SCHOLARLY PUBLICATIONS

A CURRENT AWARENESS BULLETIN
OF RESEARCH OUTPUT

@DTU

(68th Edition)

AUGUST, 2018

BY: CENTRAL LIBRARY

DELHI TECHNOLOGICAL UNIVERSITY
(FORMERLY *DELHI COLLEGE OF ENGINEERING)*
GOVT. OF N.C.T. OF DELHI
SHAHBAD DAULATPUR, MAIN BAWANA ROAD
DELHI 110042

PREFACE

This is the **Sixty Eight** Issue of Current Awareness Bulletin started by Delhi Technological University, Central Library. The aim of the bulletin is to compile, preserve and disseminate information published by the faculty, students and alumni for mutual benefits. The bulletin also aims to propagate the intellectual contribution of Delhi Technological University (DTU) as a whole to the academia.

The bulletin contains information resources available in the internet in the form of articles, reports, presentations published in international journals, websites, etc. by the faculty and students of DTU. The publications of faculty and student which are not covered in this bulletin may be because of the reason that the full text either was not accessible or could not be searched by the search engine used by the library for this purpose.

The learned faculty and students are requested to provide their uncovered publications to the library either through email or in CD, etc. to make the bulletin more comprehensive.

This issue contains the information published during **August, 2018**. The arrangement of the contents is alphabetical. The full text of the article which is either subscribed by the university or available in the web is provided in this bulletin.

Central Library

CONTENTS

1. A Generalized Method to Generate Carrier-Based 3L PWM Techniques using Two Parallel Interleaved 2L VSIs, ***7.1.Kapil Shukla*** and Ramkrishan Maheshwari, Electrical, DTU

2. A study of the sense of well-being and perceived quality of life of people in Gujarat, Rajesh Handa and ***3.Girish Chandra Maheshwari***, DSM, DTU

3. A SURVEY ON ANDROID MALWARE DETECTION TECHNIQUES, ***3.Rahul Katarya*** and ***6.Parvesh Mamgain***, IT and Computer, DTU

4. A SURVEY ON INTERNET TRAFFIC CLASSIFICATION TECHNIQUES, ***8.Sharvi Tomar***[1] and ***3.Rahul Katarya***[2], [1]Mathematics and [2]Computer science, DTU

5. Alkali-Silica Reactivity of Three River Basin (Chenab, satluj And Beas) - An Overview, ***7.1.Lalit Kumar Solanki***, S. K. Jain and B. K. Munzni, Civil, DTU

6. An aptasensor for rapid and sensitive detection of estrogen receptor alpha in human breast cancer, Rajesh Ahirwar, Anita Dalal, ***3.Jai Gopal Sharma***, Birendra Kumar Yadav, Pradip Nahar, Ashok Kumar and ***6.Saroj Kumar***, Biotechnology, DTU

7. Auto-Tuning Technique for the Cost Function Weight Factors in Model Predictive Control for Power Electronics Interfaces, Mohammad B. Shadmand, ***6.Sarthak Jain***, and Robert S, Electrical, DTU

8. BEZIER VARIENT OF THE GENERAL FAMILY OF GUPTA-SRIVASTAVA OPERATORS, ***6.RAM PRATAP*** AND ***3.NAOKANT DEO***, Mathematics, DTU

9. Blockchain and Scalability, ***3.Mrs. Anamika Chauhan***, ***8.Om Prakash Malviya***, ***6.Madhav Verma*** and ***8.1.Tejinder Singh Mor***, Information Technology, DTU

10. Community Trolling: An Active Learning Approach for Topic Based Community Detection in Big Data, Preeti Gupta · ***3.Rajni Jindal*** and Arun Sharma, CSE, DTU

11. Comparative Study on the Effect of Nitriding and Microwave Coating on Microstructure, Hardness and Wear of AISI H13 Tool Steel, Mohammad Iqbal Yunus, Kanwarjeet Singh, Gaurav Arora and ***3.Ranganath M Singari***, Mechanical, DTU

12. Design of a Cross Structure Nanoantenna, ***6.Parul Goyal***, ***6.Nishant Shankhwar*** and ***3.Yogita Kalra***, Applied Physics, DTU

13. Design, Development and Fabrication of a Go-Kart, ***3.PK Jain***, ***6.Pankaj Yadav***, ***6.Aditya Natu***, ***6.Mukesh Kumar Manda***, ***6.Parikshit Garg***, ***6.Geetanshu Ashpilya***, ***6.Ashutosh Panpalia***, ***6.Deept Madhav*** and ***6.Kunal Mathur***, Mechanical, Production and Industrial and Automobile, DTU

14. Electrochemical genosensor based on carboxylated graphene for detection of water-borne pathogen, Nandita Jaiswal, ***6.Chandra Mouli Pandey***, Amrita Soni, Ida Tiwari, Martin Rosillo-Lopez, Christoph G. Salzmann, ***3.Bansi Dhar Malhotra*** and Gajjala Sumanae, Applied Chemistry and Biotechnology, DTU

15. ELECTRON ACCELERATION BY A PLASMA WAVE IN THE PRESENCE OF A TRANSVERSELY PROPAGATED LASER WITH MAGNETIC FIELD, M. Yadav, ***3.S. C. Sharma***, ***6.M. Kaur*** and D. N. Gupta, Applied Physics, DTU

16. Electronically tunable high gain current-mode instrumentation amplifier, ***6.Sirish Oruganti***, ***3.Neeta Pandey*** and ***3.Rajeshwari Pandey***, ECE, DTU

17. Emergence of time-dependent material properties in chain extended polyureas, ***6.N. Iqbal***, ***3.D. Kumar*** and ***6.P. K. Roy***, Applied Chemistry, DTU

18. Energy storage and magnetoelectric coupling in ferroelectric–ferrite composites, ***6.S. Shankar***, Manish Kumar, Vinita Tuli1, O. P. Thakur and ***3.M. Jayasimhadri***, Applied Physics, DTU

19. Experimental Study on the Water Absorption and Surface Characteristics of Alkali Treated Pineapple Leaf Fibre and Coconut Husk Fibre, ***6.1.Mohit Mittal*** and ***3.Rajiv Chaudhary***, Mechanical, Production & Industrial, DTU

20. Exploring vitiligo susceptibility and management: a brief review, ***7.Razia Rahman*** and ***3.Yasha Hasija***, Biotechnology, DTU

21. FUZZY CONTROLLED GRAVITATIONAL SEARCH ALGORITHM FOR CLUSTERING, ***8.1.Himanshu Kaul*** and ***6.Neha Dimri***, ECE, DTU

22. Implementation of Immune Feedback Control Algorithm for Distribution Static Compensator, ***6.Manoj Badoni***, ***3.Alka Singh*** and ***6.Bhim Singh***, Electrical, DTU

23. Physical properties and electrochemical performance of Zn-substituted Na0:44Mn1□xZnxO2 nanostructures as cathode in Na-ion batteries, Mahesh Chandra, Rishabh Shukla, Rakesh Saroha, ***3.A. K. Panwar***, Amit Gupta, S. Basu and R. S. Dhaka, Applied Physics, DTU

24. Quality of Experience Framework for Cloud Computing (QoC), Asif Ali Laghari, Hui He, Asiya Khan, ***3.1.Neetesh Kumar***, and Rupak Khare, Computer Science, DTU

25. Realization of a higher fractional order element based on novel OTA based IIMC and its application in filter, ***6.Rakesh Verma***, ***3.Neeta Pandey*** and ***3.Rajeshwari Pandey***, Electronics and Communication, DTU

26. Rear contact silicon solar cells with a-SiCX:H based front surface passivation for near-ultraviolet radiation stability, Rahul Pandey and ***3.Rishu Chaujar***, Physics, DTU

27. Smaller feature subset selection for real-world datasets using a new mutual information with Gaussian gain, ***3.Seba Susan*** and Madasu Hanmandlu, IT, DTU

28. Supported matrix factorization using distributed representations for personalised recommendations on twitter, ***3.Akshi Kumar***, ***6.Himanshu Ahuja***, ***6.Nikhil Kumar Singh***, Deepak Gupta, Ashish Khanna and Joel J. P. C. Rodrigues, CSE, DTU

29. Synthesis and Electrochemical Properties of Low-Temperature Synthesized Li2MnO3/MWCNT/super P as a High Capacity Cathode Material for Lithium ion Batteries, ***6.Rakesh Saroha***, ***3.Amrish K. Panwar*** and ***6.Abhishek Bhardwaj***, Applied Physics, DTU

30. The Astropy Project: Building an Open-science Project and Status of the v2.0 Core Package, ***3.A. Kumar***, Civil, DTU

31. Thermally Grown TiO2 and Al2O3 for GaN-Based MOS-HEMTs, ***7.1.Akanksha Rawat***, Mudassar Meer, Vivek kumar Surana, Navneet Bhardwaj, Vikas Pendem, Navya Sri Garigapati, Yogendra Yadav, Swaroop Ganguly, and Dipankar Saha, Electrical, DTU

32. Thermodynamic analysis of combined cycle power plant with trans-critical cycle integrated with solar system for power generation for space heating and cooling, ***3.R.S. Mishra*** and ***7.Aakash Behl***, Mechanical & Production, DTU

33. Thermodynamic models for combined cycle power plants used in organic Rankine & Brayton Cycles, ***3.R.S. Mishra*** and ***8.Manish Kumar***, Mechanical & Production, DTU

34. Tribological behavior of thin film coating-a review, Ramesh Chandra Yadaw, Shailesh Kumar Singh, Somanth Chattopadhyaya, Sanjeev Kumar and ***3.R.C. Singh***, Mechanical, DTU

35. Uncertainty Estimation in PM10 Mass Measurements, ***6.J. Pokhariyal***, ***3.A. Mandal*** and S. G. Aggarwal, Civil, DTU

36. Video benchmarks of human action datasets: a review, ***6.Tej Singh***[1] and ***3.Dinesh Kumar Vishwakarma***[2], ECE and IT, DTU

1. *Chancellor*

2. *Pro Vice Chancellor* ***2.1.*** *Ex Pro Vice Chancellor*

3. *Faculty* ***3.1.*** *Ex Faculty*

4. *Teaching-cum-Research Fellow* ***4.1.****Asst. Librarian*

5. *Alumni*

6. *Research Scholar* ***6.1.*** *Ex Research Scholar*

7. *PG Scholar* ***7.1.*** *Ex PG Scholar*

8. *Undergraduate Student* ***8.1.*** *Ex Undergraduate Student*

This article has been accepted for publication in a future issue of this journal, but has not been fully edited. Content may change prior to final publication. Citation information: DOI 10.1109/TIE.2018.2860523, IEEE Transactions on Industrial Electronics

A Generalized Method to Generate Carrier-Based 3L PWM Techniques using Two Parallel Interleaved 2L VSIs

Kapil Shukla, and Ramkrishan Maheshwari, *Member, IEEE*

***Abstract*— Two parallel interleaved two-level (2L) three phase voltage source inverters (VSIs) can be analyzed as a single three-level (3L) VSI. A generalized carrier-based method is proposed in this paper for implementing different 3L pulse-width modulation (PWM) techniques using two parallel interleaved 2L VSIs. The proposed method modifies the given three-phase reference signals of 3L VSI for implementation of the PWM technique using two parallel interleaved 2L VSIs. The influence of non-idealities on the equivalent 3L PWM switching sequences is also discussed. To overcome the effect of non-idealities, a new modified discontinuous PWM technique (MDPWM1) is proposed. The analysis of different performance indices is carried out for different 3L PWM techniques, and the key advantages of different PWM techniques are identified. Simulation and experimental results are also presented.**

***Index Terms*— Voltage-Source inverter (VSI), Interleaving, Two-level (2L), Three-level (3L), Pulse-width Modulation (PWM).**

I. INTRODUCTION

PARALLEL interleaved voltage source inverters (VSIs) are widely used due to their distinct advantages of high power delivery, reduced current stress on switches, modularity, reduced ac side current ripple, improved thermal management, redundancy, easy maintenance, and increased efficiency [1] - [6]. In case of parallel interleaved VSIs, the dc-link is kept common, and the ac sides are connected through inductors as shown in Fig. 1. The carriers for the parallel interleaved VSIs are displaced by $2\pi/N$ for N–parallel interleaved VSIs [3] for reducing ac side current distortion.

The interleaving of carrier signals produces an instantaneous pole voltage difference between the parallel interleaved VSIs. This pole voltage difference causes circulating current. This circulating current produces additional stress on the switches, increases the losses, and could saturate the inductors connected between the VSIs [7]. Different types of inductors may be used to reduce the circulating current [4], [7] - [11]. These inductors are primarily classified as coupled inductors (CI) and common-mode (CM) inductors. The CI reduces the circulating current which is produced due to the instantaneous pole voltage difference of individual phases of a VSI [9]. While the CM inductors reduce the circulating current produced due to instantaneous CM voltage difference between the VSIs [11]. Different pulse-width modulation (PWM) techniques are also proposed in literature for reduction of circulating current [11] - [20]. In most of these techniques, the average of CM voltage difference over a switching period is kept to zero for the net change in the circulating current over a switching period to be zero. While in [20], the CM voltage is also kept to very low value for minimizing the CM current. Furthermore, these techniques consider the parallel interleaved two-level (2L) VSIs as two separate 2L VSIs.

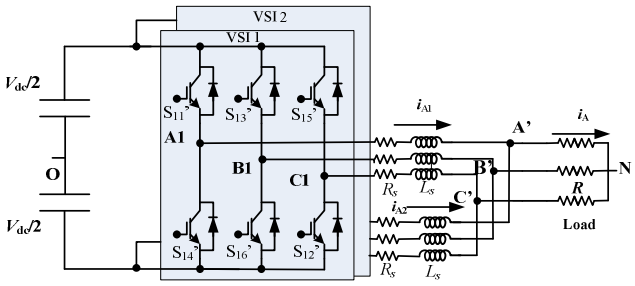


Fig. 1. Parallel interleaved VSIs connected to load fed from a common dc-link.

As the parallel interleaved 2L VSIs could also be visualized as a single three-level (3L) VSI [19] - [23], conventional 3L space-vector PWM (SVPWM) technique are used [21] – [23]. A 3L SVPWM technique is implemented in [21] and [22], using phase disposition (PD) modulation schemes. In [21], a complex state machine is used for determining the different switching states of the system. While a flux balancing technique using PD modulation scheme is proposed in [22] for implementing a 3L SVPWM technique. However, both the PD modulation schemes are limited to implementation of the conventional 3L SVPWM technique only. The conventional 3L SVPWM is also implemented for two parallel interleaved 2L VSIs in [23] using logic gates. The PWM technique proposed in [23] requires calculation of CM offset for each sub-sector within a sector. The sub-sector identification also requires many if-else loops, which increases the complexity of the code.

This paper extends the study of various 3L PWM techniques [24] - [29] for two parallel interleaved 2L VSIs by visualizing them as a single 3L VSI. A generalized carrier-based method is proposed for implementing any 3L PWM technique using two parallel interleaved 2L VSIs. For this, the

Manuscript received December 18, 2017; revised April 27, 2018 and June 23, 2018; accepted July 11, 2018.

The authors are with the department of Electrical Engineering, Indian Institute of Technology Delhi, New Delhi, India (e-mail: kapilstriker@gmail.com, rkmahesh@ee.iitd.ac.in).

0278-0046 (c) 2018 IEEE. Personal use is permitted, but republication/redistribution requires IEEE permission. See http://www.ieee.org/publications_standards/publications/rights/index.html for more information.

This article has been accepted for publication in a future issue of this journal, but has not been fully edited. Content may change prior to final publication. Citation information: DOI 10.1109/TIE.2018.2860523, IEEE Transactions on Industrial Electronics

PWM reference signals used to implement a PWM technique for a neutral-point clamped (NPC) VSI in [26] are modified. For this modification, only one if-else loop is required. As the reference signals of [26] are chosen to implement different 3L PWM techniques which requires only one CM offset addition, the method used in this paper also needs only one CM offset. Moreover, the efforts of switching sequence identification and calculation of either the CM offsets for each sub-sector or the dwell times for each voltage vector are not required in the proposed method for implementing a 3L PWM technique. The proposed method can be used to implement continuous as well as discontinuous PWM (DPWM) techniques of a 3L VSI for the two parallel interleaved 2L VSIs.

Typically, these PWM techniques cause switching state transitions, and each switching transition corresponds to turn-on or turn-off of a switch corresponding to only one phase of the 2L VSI. In this paper, it is shown that the switching state transition corresponding to 3L DPWM1 technique may result in simultaneous switching of two phases of both the VSIs. This may apply of unwanted switching state due to mismatch in device switching characteristics, dead band etc. To solve this problem, a modified DPWM technique is proposed in this paper.

Different 3L PWM techniques are compared to each other on the basis of circulating current, total ac side line current ripple, and switching loss. In summary, this paper consists of the following key features

(a) A general approach is proposed to implement any 3L NPC PWM technique while the methods of [19]-[23] are only for the conventional 3L SVPWM.
(b) Influence of non-idealities on equivalent 3L switching sequence is analyzed, and a new modified DPWM (MDPWM1) technique is proposed.
(c) Analysis of peak and root-mean square (rms) value of the circulating current for CM inductors and CI and the switching losses for different 3L PWM techniques is carried out. Based on this analysis, several recommendations are made.
(d) The average of CM voltage difference over a switching period is kept to zero.

The paper is organized as follows. Section II reviews the functioning of parallel interleaved 2L VSIs as a 3L VSI. Section III explains the proposed method. Section IV focuses on different performance indices of the two parallel interleaved 2L VSIs. Experimental results are displayed in section V. Conclusions are provided in section VI.

II. Parallel Interleaved 2L VSIs as a 3L VSI

The two parallel interleaved 2L VSIs could be analyzed as a single 3L VSI [23]. A single 3L VSI has three levels of pole voltages. These three levels could easily be obtained using thevenin's equivalent of the parallel interleaved 2L VSI system. The equivalent pole voltage of a particular phase is given by [19], [23]

$$v_{xO} = \frac{v_{x1O} + v_{x2O}}{2} \tag{1}$$

where v_{x1O} is the VSI-1 pole voltage, v_{x2O} is the VSI-2 pole voltage of phase x which is equal to {A, B, C}. Using (1), the values of equivalent pole voltages of a phase (v_{xO}) for different values of pole voltages of phase x of VSIs 1 and 2 could be generated. The different voltage levels of the equivalent pole voltage are denoted as

$$2 = +\frac{V_{dc}}{2};\quad 1 = 0\,\text{V};\quad 0 = -\frac{V_{dc}}{2} \tag{2}$$

The space-vector (SV) diagram of the equivalent pole voltages of two parallel interleaved 2L VSIs is shown in Fig. 2, which is similar to space-vector diagram of a 3L VSI [28]. The diagram is divided into 6 sectors/triangles, as displayed by bold lines. Each sector could be further divided into different sub-sectors, as displayed by dashed lines.

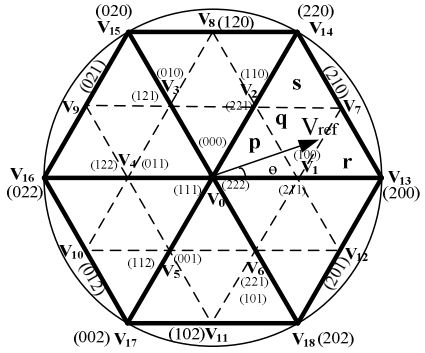


Fig. 2. Space-vector diagram of a 3L VSI.

III. Proposed Method

As discussed above, the SV diagram of two parallel interleaved 2L VSIs is same as that of a 3L VSI. Therefore, any switching sequence of a 3L VSI can be realized using two parallel interleaved 2L VSIs. To realize various 3L switching sequence using a 3L NPC VSI, various carrier based techniques are proposed [25], [26], and [29]. These techniques modify three-phase sinusoidal reference signals by adding various CM offsets to realize various switching sequences. These switching sequences lead to various PWM techniques such as space vector PWM (SVPWM) and various discontinuous PWM techniques (DPWM0, DPWM1, DPWM2, DPWM3 etc.). These PWM techniques can also be carrier-based implemented using the two parallel interleaved 2L VSIs. In this paper, a method is proposed to generate 3L PWM techniques from the two parallel interleaved 2L VSIs. The proposed method processes the three-phase reference signals used to implement a particular PWM technique of a 3L NPC VSI [26] and outputs the three-phase reference signals which can be used to carrier-based implement the same equivalent PWM technique/sequence using the two parallel interleaved 2L VSIs. Therefore, the proposed method requires less computational time to implement a 3L PWM technique as compared to the method proposed in [23]. Moreover, the proposed method is a generalized method for implementing both continuous and discontinuous 3L PWM techniques of [26] and [29] using two parallel interleaved 2L VSIs.

To understand the proposed method, it is important to review the carrier based implementation of a PWM technique

0278-0046 (c) 2018 IEEE. Personal use is permitted, but republication/redistribution requires IEEE permission. See http://www.ieee.org/publications_standards/publications/rights/index.html for more information.

This article has been accepted for publication in a future issue of this journal, but has not been fully edited. Content may change prior to final publication. Citation information: DOI 10.1109/TIE.2018.2860523, IEEE Transactions on Industrial Electronics

in a 3L NPC VSI. Typically, if the three-phase reference signals, $v_{A1,ref}$, $v_{B1,ref}$ and $v_{C1,ref}$, corresponding to the reference vector $\mathbf{V}_{ref}$ (Fig. 2) are given for the 3L NPC VSI to implement SVPWM, they can be compared with two phase disposed carrier signals to generate desired pole voltage [29], as shown in Fig. 3. The 3L switching sequences corresponding to the given three phase reference signals are marked by dashed red lines. These reference signals can be generated by methods proposed in [25], [26], or [29]. If the same reference signals are used for two parallel interleaved 2L VSIs whose carrier signals are phase shifted by 180° [3], the resultant pole voltages for individual VSIs and equivalent 3L pole voltages are shown in Fig. 4. The switching sequences generated after comparison are highlighted by dashed orange lines in Fig. 4.The highlighted switching sequences are different from the switching sequences generated in Fig. 3. However, it can be seen that the equivalent 3L pole voltage of phase B and C (Fig. 4) is same as the 3L pole voltage of phase B and C of a 3L NPC VSI (Fig. 3). While for phase A, it is not the case. That is due to mismatch in the carrier signals for positive values. As the carrier signals are not same, phase A reference signal needs to be modified. For this, the phase A reference signal is divided in two signals $v_{A1,ref1}$ and $v_{A1,ref2}$, as given by

$$v_{A1,ref1} = 0.5V_{dc} - v_{A1,ref}\ ,\ v_{A1,ref2} = 0 \qquad (3)$$

These reference signals are compared with the carrier signal as shown in Fig. 5. These two reference signals are used to generate two pulses g_{vA1O1} and g_{vA1O2}, which may have high and low levels. These pulses are passed through an EX-NOR gate to get the desired gate signal and the pole voltage signal (v_{A1O}) for phase A of VSI-1. Similarly, signal for VSI-2 (v_{A2O}) is generated. The resultant phase A equivalent pole voltage, Fig. 5, is same as the pole voltage of 3L NPC VSI, Fig. 3. Moreover, the equivalent 3L switching sequence generated using the proposed method, marked by dashed blue lines in Fig. 5, is similar to the switching sequence produced by the 3L NPC VSI with the conventional 3L SVPWM technique, marked by dashed red lines in Fig. 3. Similarly, it can be shown that the equivalent 3L switching sequences generated using the proposed method are same as the switching sequences generated by the 3L NPC VSI with different 3L PWM techniques proposed in [29]. The CM voltage difference of individual VSIs is also displayed in Fig.5, which governs the flow of circulating current as given by [7]

$$\begin{aligned} i_{cc} &= \frac{1}{2 \bullet Ls}\int (v_{cm,1} - v_{cm,2})dt \\ v_{cm,1} &= \frac{v_{A1O} + v_{B1O} + v_{C1O}}{3} \\ v_{cm,2} &= \frac{v_{A2O} + v_{B2O} + v_{C2O}}{3} \\ i_{cc} &= \frac{1}{6 \bullet Ls}\int ((v_{A1O} - v_{A2O}) + (v_{B1O} - v_{B2O}) + (v_{C1O} - v_{C2O}))dt \end{aligned} \qquad (4)$$

where $v_{cm,1}$ and $v_{cm,2}$ are the CM voltages of VSI-1 and VSI-2, respectively. Using the proposed method, the CM voltage difference averaged over a switching period (T_s) is kept to zero which makes the net change in circulating current over a switching period to zero [7] (Fig. 5). The equivalent 3L line-line output voltage (v_{AB}) waveforms corresponding to the conventional 2L SVPWM technique and 3L SVPWM technique are displayed in Figs. 6 (a) and 6(b), respectively. Here, the line-line voltage v_{AB} is given by

$$v_{AB} = v_{AO} - v_{BO} \qquad (5)$$

The voltage ripple in the resultant line-line voltage waveforms will influence the ac side line current ripple [30].

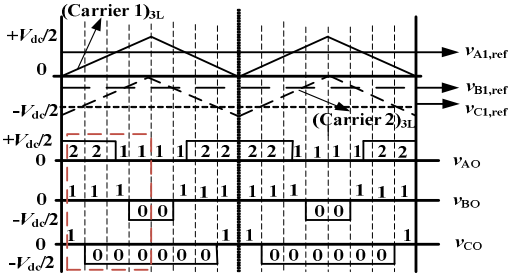


Fig. 3. Carrier Signals and pole voltages of a 3L VSI.

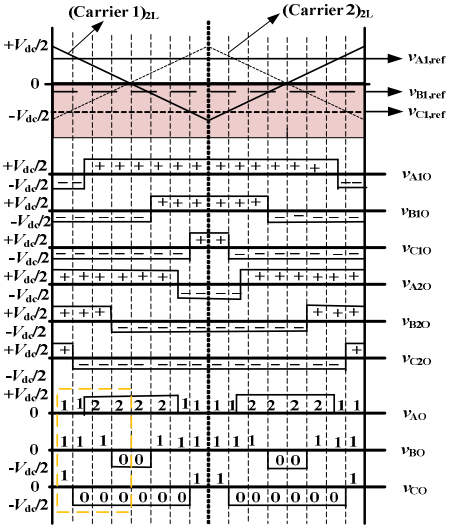


Fig. 4. Carrier signals and pole voltages of two parallel interleaved 2L VSIs when V_{ref} lies in sub-sector q.

The maximum ripple in the line-line voltages for 2L SVPWM in a switching period is $+V_{dc}$, while it is $+V_{dc}/2$ for the 3L SVPWM technique which results in less ac side line current ripple. However, this analysis is valid only for linear modulation index (m_a) range, i.e $m_a \leq 1.154$. Sometimes, the modulation index may rise above 1.154. This region of modulation index is called as over-modulation. During over-modulation, the voltage reference vector is synthesized using different methods which are already available in literature [32] - [33]. Here, the modulation index (m_a) is defined as the ratio of peak of desired fundamental ac side phase voltage and ($V_{dc}/2$).

Another approach to compare the ac side line current ripple is to check the switching sequence applied by the VSIs. Table I shows the equivalent 3L switching sequences of voltage vectors using the conventional 2L PWM techniques (column 2) and the proposed method to implement 3L PWM techniques (column 3). The 2L and 3L switching sequences corresponding to SVPWM technique are similar to the sequences shown in Figs. 4 and 5. As seen from the equivalent 3L switching sequences (Table I), the three nearest voltage vectors are always applied using the proposed method. However, in case of conventional 2L PWM techniques, the

0278-0046 (c) 2018 IEEE. Personal use is permitted, but republication/redistribution requires IEEE permission. See http://www.ieee.org/publications_standards/publications/rights/index.html for more information.

This article has been accepted for publication in a future issue of this journal, but has not been fully edited. Content may change prior to final publication. Citation information: DOI 10.1109/TIE.2018.2860523, IEEE Transactions on Industrial Electronics

equivalent sequences are not comprised of three nearest voltage vectors. As the ac side line current ripple would be minimum when the three nearest voltage vectors are applied, the proposed method cause less ac side line current ripple.

Using the six-fold symmetry of the SV diagram, a general expression of the reference signal which requires modification is given by

$$\begin{aligned} &\text{if } (v_{\text{mid}} < 0) \\ &v_{\text{max1,ref1}} = 0.5V_{\text{dc}} - v_{\text{max1,ref}},\ v_{\text{max1,ref2}} = 0 \\ &\text{else} \\ &v_{\text{min1,ref1}} = 0.5V_{\text{dc}} + v_{\text{min1,ref}},\ v_{\text{min1,ref2}} = 0 \end{aligned} \tag{6}$$

where

$$\begin{aligned} v_{\text{max1,ref}} &= \max\left(v_{\text{A1,ref}}, v_{\text{B1,ref}}, v_{\text{C1,ref}}\right) \\ v_{\text{min1,ref}} &= \min\left(v_{\text{A1,ref}}, v_{\text{B1,ref}}, v_{\text{C1,ref}}\right) \end{aligned} \tag{7}$$

The reference signals for other two phases remain unchanged. The type of gate to be used would depend on the magnitude of the middle value (v_{mid}) of the sinusoidal three phase reference voltage signals. For $v_{\text{mid}} < 0$, EX-NOR gate is used, while for the remaining conditions EX-OR gate is utilized.

TABLE I
COMPARISON OF SWITCHING SEQUENCES FOR PWM TECHNIQUES

PWM Technique	Equivalent 3L Switching Sequence using 2L PWM Technique	Equivalent 3L Switching Sequence using proposed method
SVPWM	(111), (110), (210), (200), (200), (210), (110), (111)	(211), (210), (110), (100), (100), (110), (210), (211)
DPWM1	(211), (210), (220), (220), (210), (211)	(211), (210), (110), (110), (210), (211)
DPWM3	(110), (210), (200), (200), (210), (110)	(210), (110), (100), (100), (110), (210)

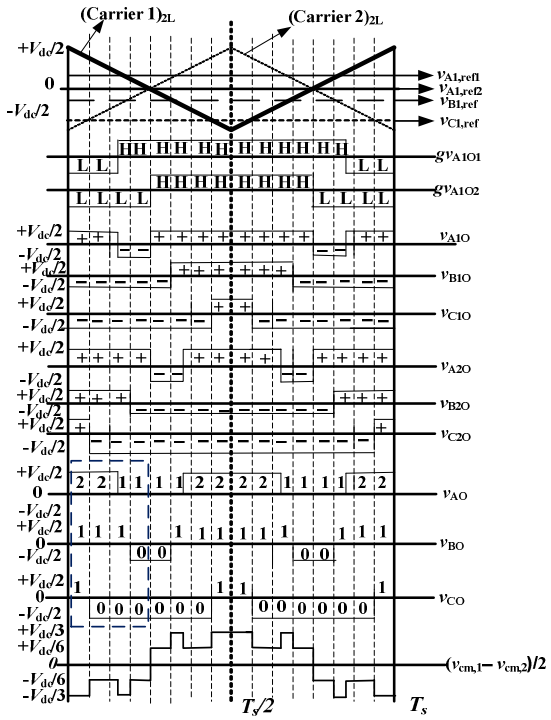


Fig. 5. Voltage waveforms for 3L SVPWM when V_{ref} lies in sub-sector q (H – High, L - Low).

A. Problem of simultaneous switching for 3L DPWM

The abovementioned proposed method of modifying the reference signal to implement a particular PWM technique can be summarized as given below:

1. Calculate the three-phase reference signals from sinusoidal reference signals using method discussed in [25], [26], or [29].
2. Modify the reference signal of phase having either the maximum or minimum value in a switching period according to (6).

The proposed method can be used to implement continuous as well as discontinuous 3L PWM techniques. The voltage waveforms corresponding to 3L DPWM3 and 3L DPWM1 technique, when the voltage reference vector ($\mathbf{V_{ref}}$) lies in sub-sector q, are displayed in Fig. 7 and Fig. 8, respectively. The switching sequence corresponding to 3L DPWM3 technique consists of three nearest voltage vectors. In addition, for implementing a 3L DPWM3 technique, there are two transitions of pole voltage signals simultaneously, as shown by green circles in Fig. 7. However, as displayed in Fig. 8, for implementing 3L DPWM1 technique, there are two instances of four transitions of pole voltage signals simultaneously. These simultaneous transitions are marked by blue circles. The two simultaneous transitions of pole voltage signals could be handled by providing a delay digitally. However, handling four simultaneous transitions of pole voltage signals is quite difficult. If these transitions do not occur at the same time, it is possible that an undesired switching state could be applied. For example, if the rising edge of v_{A1O} is delayed as shown by bold red line in Fig. 8, (010) switching state is applied instead of (110). This kind of situation may occur due to non-idealities such as delay time in switching transition, dead-band, mismatch in the switching characteristics of the devices etc.

These practical restrictions cause the shift in the transition positions of the individual pole voltage signals from the original positions. To see the effect of practical restrictions, the equivalent 3L line-line output voltage (v_{AB}) waveforms corresponding to 3L DPWM3 and 3L DPWM1 technique are displayed in Figs. 9 (a) and (b), respectively. Any shift between the transition positions of VSIs leads to an undesirable switching sequence, which is reflected in the equivalent 3L line-line output voltage (v_{AB}) waveform as shown in Fig. 9 (b). To avoid these undesirable 3L output voltage, the B phase reference signals are modified along with the phase A reference signal (Fig. 10) such that the equivalent 3L switching sequence remains undisturbed (Fig. 9 (c)). The generalized expression for the modified middle reference signal varied over a switching period is given by

$$\begin{aligned} &\text{if } (0 < t < T_s/2) \\ &v_{\text{mid1,ref}} = -0.5V_{\text{dc}},\ v_{\text{mid2,ref}} = 0.5V_{\text{dc}} \\ &\text{else} \\ &v_{\text{mid1,ref}} = 0.5V_{\text{dc}},\ v_{\text{mid2,ref}} = -0.5V_{\text{dc}} \end{aligned} \tag{8}$$

These reference signals are compared with the carrier signal as shown in Fig. 10. This new modified PWM technique is termed as 3L MDPWM1. Here, the voltage vectors applied to the individual 2L VSIs are not the nearest voltage vectors. However, the equivalent 3L switching sequences remains the same as in case of 3L DPWM1 as displayed in Fig. 8. The average of the CM voltage difference over a switching period is also kept to zero.

0278-0046 (c) 2018 IEEE. Personal use is permitted, but republication/redistribution requires IEEE permission. See http://www.ieee.org/publications_standards/publications/rights/index.html for more information.

This article has been accepted for publication in a future issue of this journal, but has not been fully edited. Content may change prior to final publication. Citation information: DOI 10.1109/TIE.2018.2860523, IEEE Transactions on Industrial Electronics

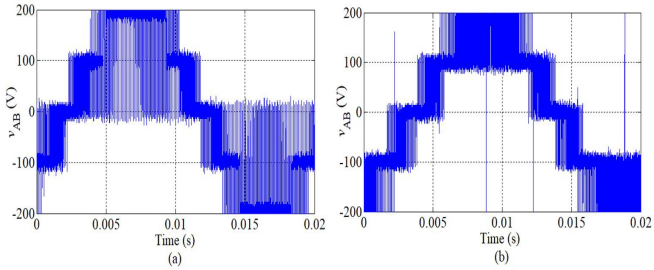


Fig. 6. Experimental results of line voltage (v_{AB}) for m_a = 1.0. (a) 2L SVPWM, (b) 3L SVPWM.

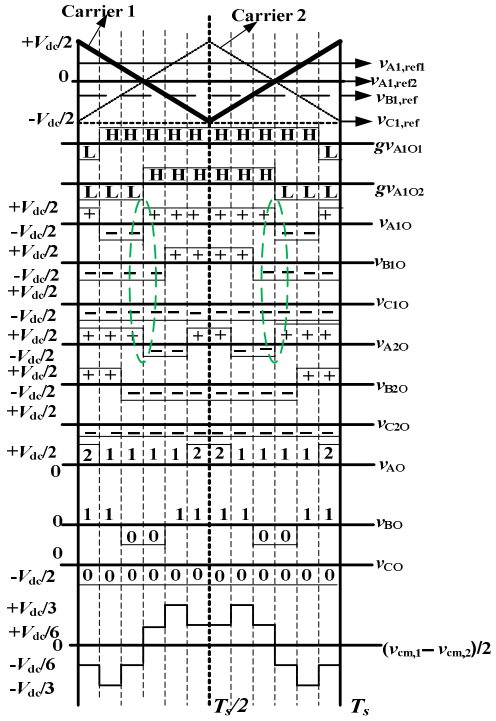


Fig. 7. Voltage waveforms for 3L DPWM3 when $\mathbf{V}_{ref}$ lies in sub-sector q (H – High, L - Low).

IV. Performance Comparison of Various PWM

The PWM techniques affect various parameters for the parallel interleaved system. The circulating current, total ac side line current ripple, and switching losses are some of the important parameters which are analyzed for various PWM techniques.

A. Circulating Current

In parallel interleaved systems, the carrier signals are interleaved to reduce the load side harmonics. However, this interleaving of carrier signals introduces a circulating current between the VSIs. The circulating current is defined by two different ways in literature. Some authors have defined circulating current as one-third of the summation of all phase currents of individual VSIs [7], [10].

$$i_{CC} = \frac{i_{A1} + i_{B1} + i_{C1}}{3} = -\frac{i_{A2} + i_{B2} + i_{C2}}{3} \tag{9}$$

Whereas some authors have defined the circulating current as half of the difference of the phase currents of individual VSIs [1], [4], [9].

$$i_{CC,x} = \frac{i_{x1} - i_{x2}}{2} \tag{10}$$

where x = {A, B, C}. The definition of the circulating current in (10) would be valid only in the case of equal current sharing. However, the circulating current defined by (9) would hold good for both equal and unequal current sharing.

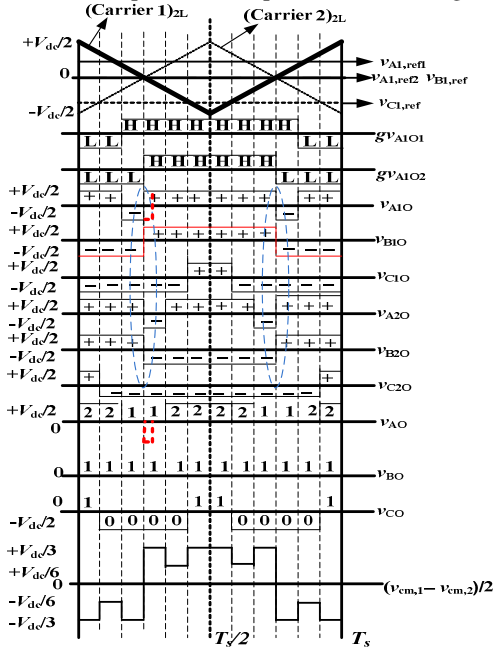


Fig. 8. Voltage waveforms for 3L DPWM1 when $\mathbf{V}_{ref}$ lies in sub-sector q (H – High, L - Low).

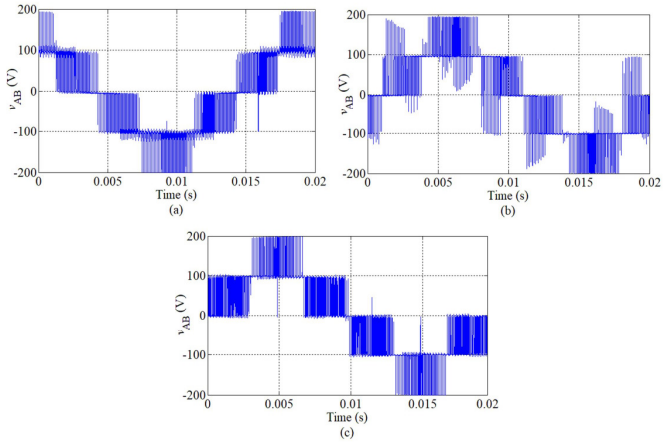


Fig. 9. Experimental results of line voltage (v_{AB}) for m_a = 0.7. (a) 3L DPWM3, (b) 3L DPWM1, (c) 3L MDPWM1.

The circulating current defined by (9) is caused by the CM voltage difference [7], and the circulating currents defined by (10) are the result of the instantaneous pole voltage difference of a particular phase [1]. The circulating current defined by (9) is limited using CM inductors. Whereas the CI are responsible for limiting the circulating currents defined by (10) [4]. Here, an analysis is carried out for normalized peak and rms values of circulating currents [7] produced due to both CM voltage difference and instantaneous pole voltage difference using different 3L PWM techniques, assuming equal power sharing among the VSIs. The analytical results for modulation index (m_a) = 1.15 are displayed in Figs. 11 and 12. The normalized

0278-0046 (c) 2018 IEEE. Personal use is permitted, but republication/redistribution requires IEEE permission. See http://www.ieee.org/publications_standards/publications/rights/index.html for more information.

This article has been accepted for publication in a future issue of this journal, but has not been fully edited. Content may change prior to final publication. Citation information: DOI 10.1109/TIE.2018.2860523, IEEE Transactions on Industrial Electronics

rms values of circulating current using (9), remains minimum for 3L DPWM3. However, the normalized peak values of circulating current using (9) turns out to be minimum for a combination of 3L DPWM3 and 3L MDPWM1 as displayed in Fig. 11 (a). Whereas, both the normalized peak and rms values of circulating current using (10) remains minimum when a combination of 3L DPWM3 and 3L DPWM1 is employed as shown in Fig. 12. Therefore, for reducing the size of CM inductors and CI, a combination of 3L DPWM3 and 3L DPWM1 could be implemented. However, this could increase the total ac side line current ripple, which is discussed in the next sub-section.

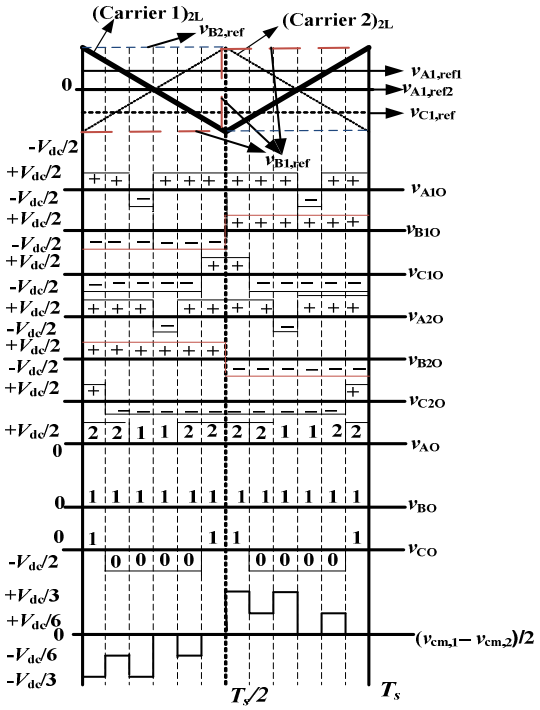


Fig. 10. Voltage waveforms for 3L MDPWM1 when V_{ref} lies in sub-sector q (H – High, L - Low).

B. Total AC Side Line Current Ripple

In parallel interleaved systems, the current flowing through the load is the sum of the individual VSIs ac side line currents and is defined as the total ac side line current. The ripple content in this total ac side line current is termed as total ac side line current ripple. The total ac side line current ripple is an important performance index which has to be looked after while selecting a PWM technique. Different PWM techniques applies different voltage vectors for different amount of time. This different application of voltage vectors produces different error voltage vectors which are responsible for producing the ac side line current ripple [30]. The ac side line current ripple will be minimum when three nearest voltage vectors are applied. Here, the two parallel interleaved 2L VSIs are analyzed as a single 3L VSI. Therefore, the ac side line current ripple would be minimum when the equivalent 3L switching sequences are composed of nearest 3L voltage vectors. The normalized rms ac side line current ripples of different 2L and 3L PWM techniques for different modulation indices (m_a) for a sector is shown in Fig. 13. Due to the application of three nearest 3L voltage vectors, the 3L PWM techniques results into low rms ac side line current ripple at all modulation indices. Moreover, the rms ac side line current ripple remains minimum for 3L SVPWM technique at all modulation indices compared to other 2L and 3L PWM techniques. The equivalent 3L voltage vectors produced by both the 3L DPWM1 and 3L MDPWM1 techniques are same. Therefore, the total ac side line current ripple of these two techniques is also same as shown in Fig. 13. The variation of normalized rms ac side line current ripple w.r.t m_a for different 2L and 3L PWM techniques is also displayed in Fig. 14.

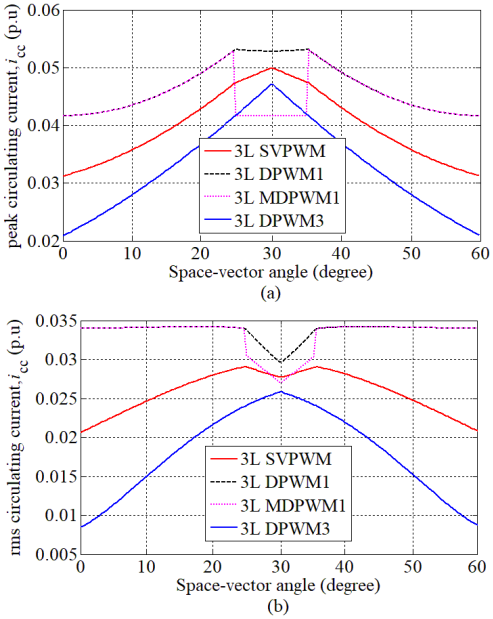


Fig. 11. Normalized circulating current (i_{CC}) defined by (9) for m_a = 1.15 (a) Peak (b) rms.

C. Switching Loss

Implementation of different 2L and 3L PWM techniques results in different amount of switching loss. It can be seen from Fig. 5 that phase A is switching four times while other two phases are switching twice in a switching period. Both the proposed 3L MDPWM1 and 3L DPWM1 techniques have same number of switching in a switching period. Therefore, the switching losses produced due to both these techniques would be same. Moreover, when the reference voltage vector $\mathbf{V}_{ref}$ lies in sub-sector r, these techniques clamp the phase having maximum value to + $V_{dc}/2$. While when $\mathbf{V}_{ref}$ lies in sub-sector s, these techniques clamp the phase having minimum value to − $V_{dc}/2$. Since in case of applications with grid-connected VSIs, unity power factor operation is desired and at unity power factor condition, the maximum and minimum values of current and voltage would appear simultaneously. Therefore, in case of 3L DPWM1 and 3L MDPWM1 techniques, there will be no switching of phase which carries maximum current. As the switching loss depends on the current flowing through the switch [31], the 3L DPWM1 and 3L MDPWM1 techniques would provide lower switching loss as compared to the 3L DPWM3 and 3L SVPWM techniques. The normalized total switching loss ($P_{SUB,TOT}$) variation over a switching period [31] for a single VSI with unity load power factor is displayed in Fig. 15.

0278-0046 (c) 2018 IEEE. Personal use is permitted, but republication/redistribution requires IEEE permission. See http://www.ieee.org/publications_standards/publications/rights/index.html for more information.

This article has been accepted for publication in a future issue of this journal, but has not been fully edited. Content may change prior to final publication. Citation information: DOI 10.1109/TIE.2018.2860523, IEEE Transactions on Industrial Electronics

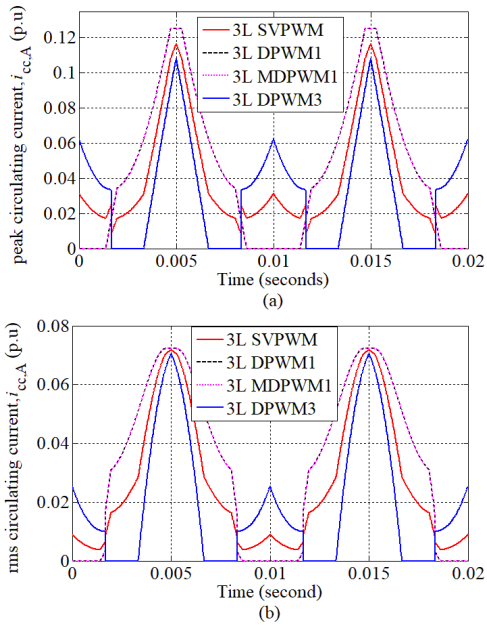


Fig. 12. Normalized circulating current ($i_{CC,A}$) defined by (10) for m_a = 1.15 (a) Peak (b) rms.

V. Experimental Results

The experimental implementation of the proposed method is done with the help of the digital signal processor (DSP) TMS320F28335 from Texas Instruments and field-programmable gate array (FPGA) MAX® 10 from Altera. The system parameters are listed in Table II. The computation time required to find the final reference signals for implementing 3L SVPWM technique are 5.2 µs and 4.1 µs using [23] and the proposed approach, respectively. Individual VSI ac side line currents (i_{A1} and i_{A2}), total ac side line current (i_A), and circulating currents (i_{CC}) corresponding to 2L SVPWM, 3L DPWM1, 3L MDPWM1, and 3L DPWM3 techniques are shown in Figs. 16 – 19. The currents i_{A1}, i_{A2}, and i_A are placed on the same axis and are zoomed to show the impact of interleaving. While implementing 3L MDPWM1, the line currents, i_{A1} and i_{A2}, shows a shift two times in a fundamental cycle, as displayed in Fig. 18. This is due to 3L MDPWM1 as the voltage vectors applied to the individual 2L VSIs are not the nearest voltage vectors, as discussed in the previous section. However, the total ac side line current (i_A) shows no deviation from its sinusoidal path. The comparison of total ac side line current ripple for different PWM techniques is tabulated in Table III.

The comparison of circulating current ($i_{CC,A}$) for different PWM techniques is also shown in Fig. 20. Among the compared PWM techniques, 3L DPWM3 results to the minimum circulating current. The comparison of circulating current (i_{CC}) for different 3L PWM techniques at different modulation indices is displayed in Table IV. The circulating current depends on the difference of the pole voltages according to (4) while the ac side line current ripple depends on the average of the pole voltages according to (1). Therefore, the modulation technique which reduces the circulating current causes high ac side line current ripple and vice versa. The harmonic analysis of total ac side line current (i_A) is also carried out and FFT plots corresponding to each PWM technique are displayed in Fig. 21. The dominant harmonics are displayed separately in the FFT plots. The switching frequency harmonic sidebands using 3L MDPWM1 reduces as compared to the 3L DPWM1 technique, which results in a lower THD.

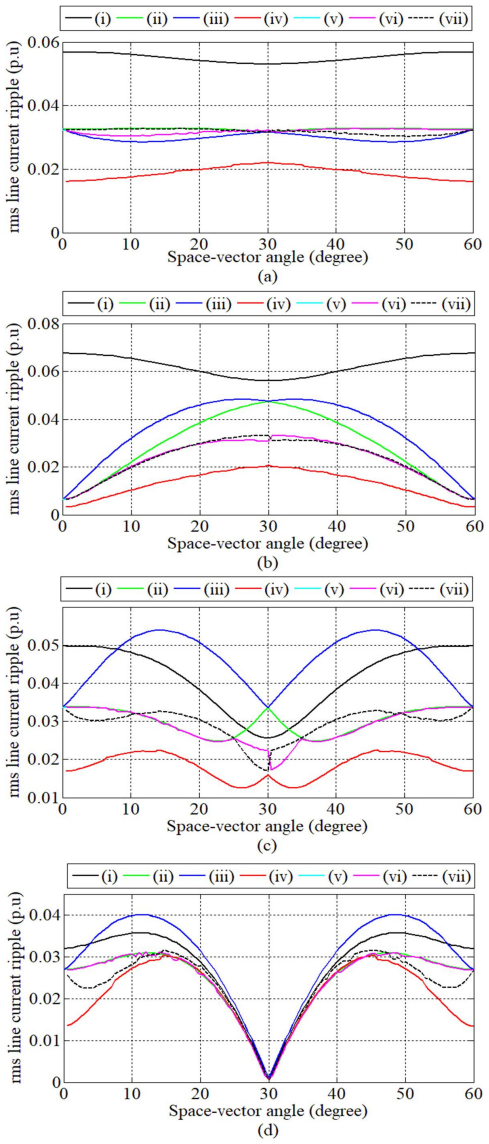


Fig. 13. Line current ripple (p.u) (a) m_a = 0.4, (b) m_a = 0.7, (c) m_a = 1.0, (d) m_a = 1.15. (i) 2L SVPWM, (ii) 2L DPWM1, (iii) 2L DPWM3, (iv) 3L SVPWM, (v) 3L DPWM1, (vi) 3L MDPWM1, (vii) 3L DPWM3.

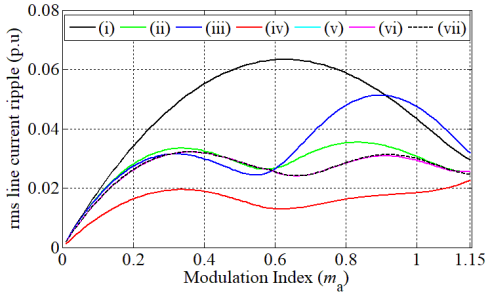


Fig. 14. Line current ripple (p.u) variation w.r.t modulation index (m_a). (i) 2L SVPWM, (ii) 2L DPWM1, (iii) 2L DPWM3, (iv) 3L SVPWM, (v) 3L DPWM1, (vi) 3L MDPWM1, (vii) 3L DPWM3.

0278-0046 (c) 2018 IEEE. Personal use is permitted, but republication/redistribution requires IEEE permission. See http://www.ieee.org/publications_standards/publications/rights/index.html for more information.

This article has been accepted for publication in a future issue of this journal, but has not been fully edited. Content may change prior to final publication. Citation information: DOI 10.1109/TIE.2018.2860523, IEEE Transactions on Industrial Electronics

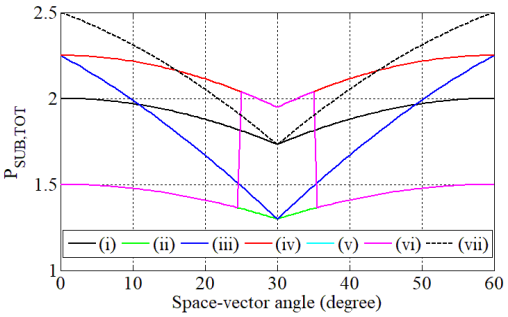


Fig. 15. Normalized total switching loss ($P_{SUB,TOT}$) variation over a sector; (i) 2L SVPWM, (ii) 2L DPWM1, (iii) 2L DPWM3, (iv) 3L SVPWM, (v) 3L DPWM1, (vi) 3L MDPWM1, (vii) 3L DPWM3.

The transient response of the proposed method is also displayed in Fig. 22. Here, both the current and frequency variations are shown for 3L DPWM1 technique. The proposed generalized method is also examined in closed loop condition. The block diagram for the closed loop control of VSI 1 is shown in Fig. 23. The load is changed from 60Ω to 40Ω keeping the current references (i_{dref1} and i_{qref1}) constant. The conventional current controllers [34] are used for generating the desired dc reference signals (v_{dref1} and v_{qref1}). These dc reference signals are then converted to three phase ac reference signals with the help of dq to ABC conversion block. The theta (Θ) required for dq to ABC conversion is generated independently, similar to the case of islanding mode operation [35]. A CM offset is added to these three phase ac reference signals to generate the required three phase reference signals (v_{A1_ref}, v_{B1_ref}, v_{C1_ref}). These reference signals are then modified as per the proposed generalized method to produce the desired 3L switching sequence. The current and voltage waveforms using 3L SVPWM technique for constant current control operation are shown in Fig. 24. The line currents (i_{A1}, i_{A2}, i_A) are maintained constant throughout. However, the load phase voltage, $v_{A'N}$, varies with respect to the load change. As load resistance is decreased from 60Ω to 40Ω, for keeping the load current constant, the voltage reference decreases and hence the load phase voltage, $v_{A'N}$, also decreases as shown in Fig. 24.

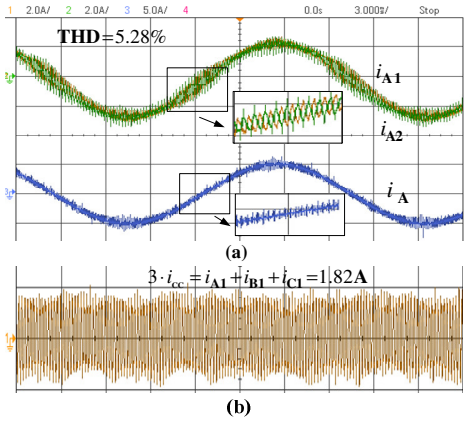


Fig. 16. Experimental results of 2L SVPWM, m_a = 1.0. (a) Line currents (2A/div, 2A/div, and 5A/div) (b) 3·Circulating current (i_{CC}), (1A/div).

TABLE II
SYSTEM PARAMETERS

Parameter	R	Rs	Ls	V_{dc}	T_s
Value	60 Ω	2.5 Ω	24 mH	600 V	200 µs

TABLE III
COMPARISON OF RIPPLE CURRENT FOR PWM TECHNIQUES

Modulation Index (m_a)	RMS Ripple current (mA)			
	3L DPWM1	3L MDPWM1	3L DPWM3	2L SVPWM
0.4	133	129	147	154
0.7	141	138	152	165
1.0	152	145	175	187

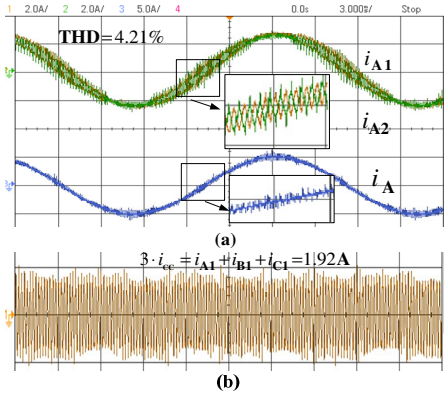


Fig. 17. Experimental results of 3L DPWM1, m_a = 1.0. (a) Line currents (2A/div, 2A/div, and 5A/div) (b) 3·Circulating current (i_{CC}), (1A/div).

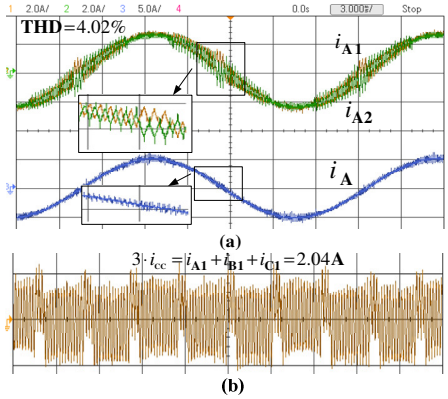


Fig. 18. Experimental results of 3L MDPWM1, m_a = 1.0. (a) Line currents (2A/div, 2A/div, and 5A/div) (b) 3·Circulating current (i_{CC}), (1A/div).

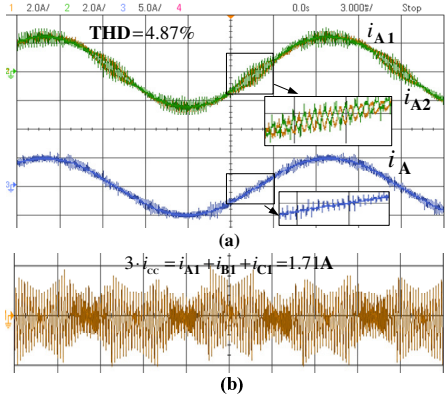


Fig. 19. Experimental results of 3L DPWM3, m_a = 1.0. (a) Line currents (2A/div, 2A/div, and 5A/div) (b) 3·Circulating current (i_{CC}), (1A/div).

0278-0046 (c) 2018 IEEE. Personal use is permitted, but republication/redistribution requires IEEE permission. See http://www.ieee.org/publications_standards/publications/rights/index.html for more information.

This article has been accepted for publication in a future issue of this journal, but has not been fully edited. Content may change prior to final publication. Citation information: DOI 10.1109/TIE.2018.2860523, IEEE Transactions on Industrial Electronics

TABLE IV
RMS & PEAK-PEAK CIRCULATING CURRENT (i_{CC})

Modualtion Index (m_a)	RMS Circulating Current (mA)				Peak-Peak Circulating Current (A)			
	3L DPWM1	3L MDPWM1	3L DPWM3	2L SVPWM	3L DPWM1	3L MDPWM1	3L DPWM3	2L SVPWM
0.4	181.13	187.23	177.13	179.8	0.87	0.94	0.84	0.89
0.7	145.45	156.3	134.3	141.2	0.77	0.82	0.74	0.75
1.0	133.42	137.8	93.8	124.5	0.64	0.68	0.57	0.61

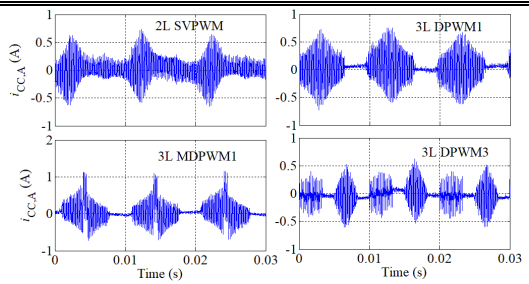


Fig. 20. Experimental results of circulating current, $i_{CC,A}$, m_a = 1.0.

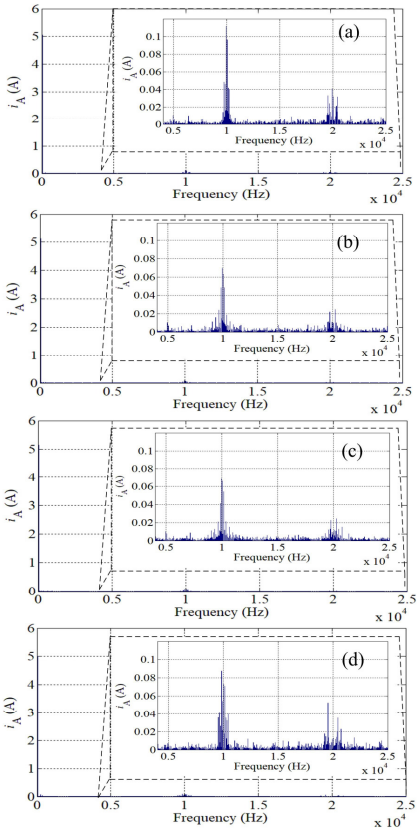


Fig. 21. FFT analysis of line current (i_A) for m_a = 1.0, (a) 2L SVPWM, (b) 3L DPWM1, (c) 3L MDPWM1, and (d) 3L DPWM3.

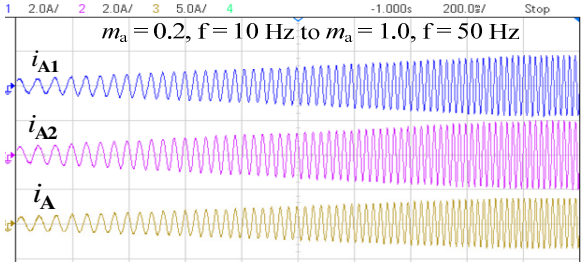


Fig. 22. Experimental results of 3L DPWM1 including current and frequency variations. Line currents (2A/div, 2A/div, and 5A/div), Time scale (200 ms/div).

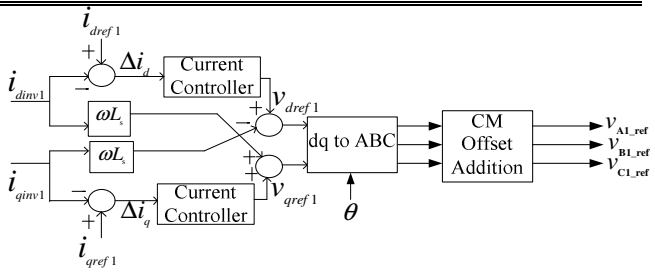


Fig. 23. Control block diagram of VSI 1.

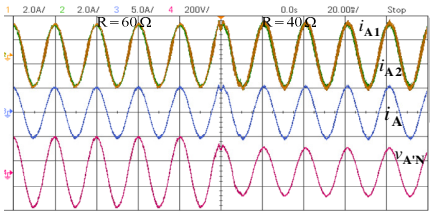


Fig. 24. Closed loop results of 3L SVPWM, Line currents (2A/div, 2A/div, and 5A/div), Load phase voltage ($v_{A'N}$), (200V/div).

The proposed generalized method is also examined experimentally under over-modulation condition. The reference signals used for over-modulation are calculated according to (12) of [33]. The final reference signals are generated by adding a CM offset corresponding to 2L SVPWM. It can be shown that the switching sequence obtained from 2L PWM technique corresponds to the switching sequence of 3L PWM technique in over-modulation. The hexagonal trajectory of Fig. 2 is traced using the modified reference signals. The average pole voltage of each phase using parallel interleaved 2L VSIs is maintained same as in the case of a 3L NPC VSI [33]. The line currents for modulation index (m_a) value of 1.21 is shown in Fig. 25.

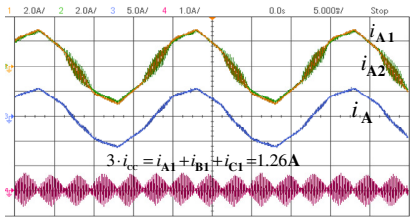


Fig. 25. Experimental results for over-modulation, m_a = 1.21, Line currents (2A/div, 2A/div, and 5A/div), 3·Circulating current (i_{CC}), (1A/div).

VI. Conclusion

A generalized method is proposed in this paper for carrier-based implementation of both continuous and discontinuous 3L PWM techniques using two parallel interleaved 2L VSIs. This paper emphasizes on the 3L PWM techniques instead of

0278-0046 (c) 2018 IEEE. Personal use is permitted, but republication/redistribution requires IEEE permission. See http://www.ieee.org/publications_standards/publications/rights/index.html for more information.

This article has been accepted for publication in a future issue of this journal, but has not been fully edited. Content may change prior to final publication. Citation information: DOI 10.1109/TIE.2018.2860523, IEEE Transactions on Industrial Electronics

2L PWM techniques for two parallel interleaved 2L VSIs. A modified PWM technique, 3L MDPWM1 is also proposed in the paper for reducing the impact of non-idealities on the equivalent 3L output voltage. Different 3L PWM techniques are compared on the basis of circulating current, total ac side current ripple, and switching losses. Inferences of the analytical comparison of different 3L PWM techniques are

(a) For minimum total ac side current ripple among 3L DPWM techniques 3L MDPWM1 should be preferred.

(b) For minimum circulating current, 3L DPWM3 should be preferred.

(c) For grid-connected VSIs with UPF with minimum switching loss, 3L DPWM1 and 3L MDPWM1 should be preferred.

REFERENCES

[1] G. Gohil, L. Bede, R. Teodorescu, T. Kerekes, and F. Blaabjerg, "Line filter design of parallel interleaved VSCs for high power wind energy conversion system," *IEEE Trans. Power Electron*., vol. 30, no. 12, pp. 6775–6790, Dec. 2015.

[2] Asiminoaei, E. Aeloiza, P. N. Enjeti, and F. Blaabjerg, "Shunt active power- filter topology based on parallel interleaved inverters," *IEEE Trans. Ind. Electron.*, vol. 55, no. 3, pp. 1175–1189, Mar. 2008.

[3] J. S. S. Prasad and G. Narayanan, "Minimization of grid current distortion in parallel-connected converters through carrier interleaving," *IEEE Trans. Ind. Electron.,* vol. 61, no. 1, pp. 76-91, Jan. 2014.

[4] G. Gohil, L. Bede, R. Teodorescu, T. Kerekes, and F. Blaabjerg, "An integrated inductor for parallel interleaved VSCs and PWM schemes for flux minimization," *IEEE Trans. Ind. Electron.*, vol. 62, no. 12, pp. 7534-7546, Dec. 2015.

[5] M. Xiaolin, A. K. Jain, and R. Ayyanar, "Hybrid interleaved space Vector PWM for ripple reduction in modular converters," *IEEE Trans. Power Electron.,* vol. 26, no. 7, pp. 1954-1967, July 2011.

[6] B.Cougo, T. Neynard, and G. Gateau, "Parallel three-phase inverters: Optimal PWM method for flux reduction in intercell transformers," *IEEE Trans. Power Electron*., vol. 26, no. 8, pp. 2184-2191, Aug. 2011.

[7] R. Maheshwari, G. Gohil, L. Bede, and S. Munk-Nielsen, "Analysis and modelling of circulating current in two parallel-connected inverters," *IET Power Electron.,* vol. 8, no. 7, pp. 1273-1283, 2015.

[8] D. Shin, J. Lee, D. Yoo, and H. Kim, "Stability improvement of interleaved voltage source inverters employing coupled inductors for grid-connected applications", *IEEE Trans. Ind. Electron*., vol. 63, no. 10, pp. 6014-6023, 2015.

[9] G. Gohil, L. Bede, R. Teodorescu, T. Kerekes, and F. Blaabjerg, "An integrated inductor for parallel interleaved three-phase voltage source-converters," *IEEE Trans. Power. Electron.*, vol. 31, no. 5, pp. 3400-3414, May. 2016.

[10] J. Ewanchuk, and J. Salmon, "Three-limb coupled inductor operation for paralleled multi-level three-phase voltage sourced inverters," *IEEE Trans. Ind. Electron.*, vol. 60, no. 5, pp. 1979–1988, Mar. 2013.

[11] D. Zhang, F. Wang, R. Burgo., and D. Boroyevich, "Common-mode circulating current control of paralleled interleaved three-phase two-level voltage-source converters with discontinuous space-vector modulation," *IEEE Trans. Power Electron.* , vol. 26, no. 12, pp. 3925-3935, Dec. 2011.

[12] M. Narimani and G. Moschopoulos, "Improved method for paralleling reduced switch VSI modules: harmonic content and circulating current," *IEEE Trans. Power Electron*., vol. 29, no. 7, pp. 3308-3317, July 2014.

[13] A. M. Hava, R. J. Kerkman, and T. A. Lipo, "Simple analytical and graphical methods for carrier-based PWM-VSI drives," *IEEE Trans. Power Electron*., vol. 14, no. 1, pp. 49-61, Jan. 1999.

[14] T. P. Chen, "Zero-sequence circulating current reduction method for parallel HEPWM inverters between AC bus and DC bus," *IEEE Trans. Ind. Electron.,* vol. 59, no. 1, pp. 290-300, Jan. 2012.

[15] C. C. Hou, C. C Shih, P. T. Cheng, and A. M. Hava, "Common-mode voltage reduction pulsewidth modulation techniques for three-phase grid-connected converters, " *IEEE Trans. Power Electron*, vol. 28, no. 4, pp. 1971-1979, April 2013.

[16] E. Ün and A. M. Hava, "A near-state PWM method with reduced switching losses and reduced common-mode voltage for three-phase voltage source inverters," *IEEE Trans. Ind. Appl*., vol. 45, no. 2, pp. 782-793, Mar./Apr. 2009.

[17] D. Zhang, F. Wang, R. Burgos and D. Boroyvich, "Total flux minimization control for integrated inter-phase inductors in paralleled, interleaved three-phase two-level voltage-source converters with discontinuous space-vector modulation,' *IEEE Trans. Power Electron*., vol. 27, no. 4, pp. 1679-1688, 2012.

[18] T. P. Chen, "Dual-modulator compensation technique for parallel inverters using space-vector modulation," *IEEE Trans. Ind. Electron*., vol. 56, no. 8, pp. 3004-3012, 2009.

[19] G. Konstantinou, J. Pou, G. J. Capella, K. Song, S. Ceballos, and V. G. Agelidis, "Interleaved operation of three-level neutral point clamped converter legs and reduction of circulating currents under SHE-PWM", *IEEE Trans. Ind. Electron*., vol. 63, no. 6, pp. 3323-3332, June 2016.

[20] Z. Quan and Y. W. Li "A three-level space vector modulation scheme for parallel converters to reduce circulating current and common-mode voltage," *IEEE Trans. Power Electron.*, vol.32, no.1, pp. 703–714, Jan. 2017.

[21] B. Cougo, G. Gateau, T. Meynard, M. Bobrowska-Rafal, and M. Cousineau, "PD Modulation Scheme for Three-Phase Parallel Multilevel Inverters," *IEEE Trans. Ind. Electron.*, vol. 59, no. 2, pp. 690-700, Feb. 2012.

[22] G. Gohil, L. Bede, R. Teodorescu, T. Kerekes, and F. Blaabjerg, "Flux-Balancing Scheme for PD-Modulated Parallel-Interleaved Inverters," *IEEE Trans. Power Electron.*, vol. 32, no. 5, pp. 3442-3457, May 2017.

[23] K. Shukla, V. Malyala, and R. Maheshwari, "A Novel Carrier-Based Hybrid PWM Technique for Minimization of Line Current Ripple in Two Parallel Interleaved Two-Level VSIs," *IEEE Trans. Ind. Electron,* vol. 65, no. 3, pp. 1908-1918, Mar. 2018.

[24] J. Rodriguez, S. Bernet, P. Steimer, and I. Lizama, "A survey on neutral-point-clamped inverters," *IEEE Trans. Ind. Electron.*, vol. 57, no. 7, pp. 2219–2230, Jul. 2010.

[25] B. P. McGrath, D. G. Holmes, and T. Meynard, "Reduced PWM harmonic distortion for multilevel inverters operating over a wide modulation range," *IEEE Trans. Power Electron*., vol. 21, no. 4, pp. 941–949, Jul. 2006.

[26] R. Maheshwari, S. B. Monge, and J. N. Apruzzese, "A Novel Approach to Generate Effective Carrier-Based Pulsewidth Modulation Strategies for Diode-Clamped Multilevel DC-AC Converters," *IEEE Trans. Ind. Electron*., vol. 63, no. 11, pp. 7243-7252, Nov. 2016.

[27] S. Das, G. Narayanan, and M. Pandey, "Space- vector-based hybrid pulsewidth modulation techniques for a three-level inverter," *IEEE Trans. Power Electron*., vol. 29, no. 9, pp. 4580-4591, Sep. 2014.

[28] S. Das and G. Narayanan, "Novel switching sequences for a space-vector- modulated three- level inverter," *IEEE Trans. Ind. Electron*., vol. 59, no. 3, pp. 1477-1487, Mar. 2012.

[29] T. Bruckner and D. G. Holmes, "Optimal pulse-width modulation for three-level inverters," *IEEE Trans. Power Electron*., vol. 20, no. 1, pp. 82–89, Jan. 2005.

[30] G. Narayanan, D. Zhao, H. K. Krishnamurthy, R. Ayyanar, and V. T. Ranganathan, "Space vector based hybrid PWM techniques for reduced current ripple," *IEEE Trans. Ind. Electron.*, vol. 55, no. 4, pp. 1614-1627, April 2008.

[31] D. Zhao, V. S. S. P. K. Hari, G. Narayanan, and R. Ayyanar, "Space-vector-based hybrid pulsewidth modulation techniques for reduced harmonic distortion and switching loss," *IEEE Trans. Power Electron*., vol. 25, no. 3, pp. 760-774, Mar. 2010.

[32] S. Busquets-Monge, R. Maheshwari and S. Munk-Nielsen, "Overmodulation of n-level three-leg DC - AC diode-clamped converters with comprehensive capacitor voltage balance," in *IEEE Trans. Ind. Electron.*, vol. 60, no. 5, pp. 1872-1883, May 2013.

[33] R. Maheshwari, S. Munk-Nielsen, and S. Busquets-Monge, "A carrier-based approach for overmodulation of three-level neutral-point-clamped inverter with zero neutral-point current," *IEEE Energy Conversion Congress and Exposition (ECCE)*, 2012, pp. 1767-1773.

[34] J. S. S. Prasad, R. Ghosh, and G. Narayanan, "Common-mode injection PWM for parallel converters," *IEEE Trans. Ind. Electron.,* vol. 62, no. 2, pp. 789-794, Feb. 2015.

[35] G. G. Talapur, H. Suryawanshi, L. Xu and A. Shitole, "A reliable micro-grid with seamless transition between grid connected and islanded mode for residential community with enhanced power quality," *IEEE Trans. Ind. Appl.,* early access.

0278-0046 (c) 2018 IEEE. Personal use is permitted, but republication/redistribution requires IEEE permission. See http://www.ieee.org/publications_standards/publications/rights/index.html for more information.

This article has been accepted for publication in a future issue of this journal, but has not been fully edited. Content may change prior to final publication. Citation information: DOI 10.1109/TIE.2018.2860523, IEEE Transactions on Industrial Electronics



Kapil Shukla was born in Dungarpur, India. He received the bachelor of technology (B.Tech.) degree in electrical engineering from the Rajasthan Technical University, Kota, India in 2010 and the master of technology (M.Tech.) degree in power systems from the Delhi Technological University (DTU), New Delhi, India in 2012. Since 2015, he has been working toward the Ph.D degree in the Department of Electrical Engineering, Indian Institute of Technology Delhi, New Delhi, India.

From 2012 to 2014, he was with the Department of Electrical and Electronics Engineering, Galgotias University, Greater Noida, U.P, India, as an Assistant Professor. He then joined the Electrical Engineering Department, Manipal University Jaipur, India as an Assistant Professor. His research interests include parallel operation of voltage source inverters and pulse-width modulation techniques.



Ramkrishan Maheshwari (S'10 – M'11) was born in Allahabad, India. He received the master of engineering (M.E.) degree in electrical engineering from the Indian Institute of Science (IISc), Bangalore, India in 2005 and the Ph.D. degree in electrical engineering from Aalborg University, Aalborg, Denmark in 2012.

From 2005 to 2008, he was with Honeywell Technology Solution Lab, Bangalore, India. From 2012 to 2014, he was with the Department of Energy Technology, Aalborg University, Denmark. He is currently working as an assistant professor with the Department of Electrical Engineering, Indian Institute of Technology, Delhi, India. His research interests include modeling and control of power converters.

0278-0046 (c) 2018 IEEE. Personal use is permitted, but republication/redistribution requires IEEE permission. See http://www.ieee.org/publications_standards/publications/rights/index.html for more information.

A study of the sense of well-being and perceived quality of life of people in Gujarat

A Thesis submitted to Gujarat Technological University

for the Award of

Doctor of Philosophy

in

MANAGEMENT

by

Rajesh Handa
[119997392025]

under supervision of

Prof. (Dr.) Girish Chandra Maheshwari



GUJARAT TECHNOLOGICAL UNIVERSITY
AHMEDABAD

[July – 2018]

A study of the sense of well-being and perceived quality of life of people in Gujarat

A Thesis submitted to Gujarat Technological University

for the Award of

Doctor of Philosophy

in

MANAGEMENT

by

Rajesh Handa
[119997392025]

under supervision of

Prof. (Dr.) Girish Chandra Maheshwari

GUJARAT TECHNOLOGICAL UNIVERSITY
AHMEDABAD

[July – 2018]

© [Rajesh Handa]

DECLARATION

I declare that the thesis entitled **"A study of the sense of well-being and perceived quality of life of people in Gujarat"** submitted by me for the degree of Doctor of Philosophy is the record of research work carried out by me during the period from September 2011 to October 2017 under the supervision of **Prof. (Dr.) Girish Chandra Maheshwari** and this has not formed the basis for the award of any degree, diploma, associateship, fellowship, titles in this or any other University or other institution of higher learning.

I further declare that the material obtained from other sources has been duly acknowledged in the thesis. I shall be solely responsible for any plagiarism or other irregularities, if noticed in the thesis.

Signature of the Research Scholar: …… Date:

Name of Research Scholar: **Rajesh Handa**

Place Mahesana

CERTIFICATE

I certify that the work incorporated in the thesis **"A study of the sense of well-being and perceived quality of life of people in Gujarat"** submitted by **Shri Rajesh Handa** was carried out by the candidate under my supervision/guidance. To the best of my knowledge: (i) the candidate has not submitted the same research work to any other institution for any degree/diploma, Associateship, Fellowship or other similar titles (ii) the thesis submitted is a record of original research work done by the Research Scholar during the period of study under my supervision, and (iii) the thesis represents independent research work on the part of the Research Scholar.

Signature of Supervisor: …… Date: ……

Name of Supervisor: **Prof. (Dr.) Girish Chandra Maheshwari**

Place: ……

Course-work Completion Certificate

This is to certify that Mr./Mrs./Ms. _____ enrolment no. _____ is a PhD scholar enrolled for PhD program in the branch _____ of Gujarat Technological University, Ahmedabad.

(Please tick the relevant option(s))

☐ He/She has been exempted from the course-work (successfully completed during M.Phil Course)

☐ He/She has been exempted from Research Methodology Course only (successfully completed during M.Phil Course)

☐ He/She has successfully completed the PhD course work for the partial requirement for the award of PhD Degree. His/ Her performance in the course work is as follows-

Grade Obtained in Research Methodology (PH001)	Grade Obtained in Self Study Course (Core Subject) (PH002)

Supervisor's Sign

Prof. (Dr.) Girish Chandra Maheshwari

Originality Report Certificate

It is certified that PhD Thesis titled **"A study of the sense of well-being and perceived quality of life of people in Gujarat"** by **Rajesh Handa** has been examined by us. We undertake the following:

a. Thesis has significant new work / knowledge as compared already published or are under consideration to be published elsewhere. No sentence, equation, diagram, table, paragraph or section has been copied verbatim from previous work unless it is placed under quotation marks and duly referenced.
b. The work presented is original and own work of the author (i.e. there is no plagiarism). No ideas, processes, results or words of others have been presented as Author own work.
c. There is no fabrication of data or results which have been compiled / analyzed.
d. There is no falsification by manipulating research materials, equipment or processes, or changing or omitting data or results such that the research is not accurately represented in the research record.
e. The thesis has been checked using < **Turnitin** > (copy of originality report attached) and found within limits as per GTU Plagiarism Policy and instructions issued from time to time (i.e. permitted similarity index <=25%).

Signature of the Research Scholar: …… Date: ……

Name of Research Scholar: **Rajesh Handa**

Place: ……

Signature of Supervisor: …… Date: ……

Name of Supervisor: **Prof. (Dr.) Girish Chandra Maheshwari**

Place: ……

Thesis: A study of the sense of well-being and perceived quality of life of people in Gujarat.

ORIGINALITY REPORT

11%	5%	11%	3%
SIMILARITY INDEX	INTERNET SOURCES	PUBLICATIONS	STUDENT PAPERS

PRIMARY SOURCES

1	Social Indicators Research Series, 2000. Publication	2%
2	"Self-Evaluation", Encyclopedia of Quality of Life and Well-Being Research, 2014. Publication	1%
3	Michalos, . "Connections, Social", Encyclopedia of Quality of Life and Well-Being Research, 2014. Publication	1%
4	Submitted to Sree Sankara University of Sanskrit, Kalady Student Paper	1%
5	www.welldev.org.uk Internet Source	1%
6	www.efdergi.hacettepe.edu.tr Internet Source	1%

PhD THESIS Non-Exclusive License to GUJARAT TECHNOLOGICAL UNIVERSITY

In consideration of being a PhD Research Scholar at GTU and in the interests of the Facilitation of research at GTU and elsewhere, I, **Rajesh Handa** having **119997392025** hereby grant a non-exclusive, royalty free and perpetual license to GTU on the following terms:

a) GTU is permitted to archive, reproduce and distribute my thesis, in whole or in part, and/or my abstract, in whole or in part (referred to collectively as the "Work") anywhere in the world, for non-commercial purposes, in all forms of media;

b) GTU is permitted to authorize, sub-lease, sub-contract or procure any of the acts mentioned in paragraph (a);

c) GTU is authorized to submit the Work at any National / International Library, under the authority of their "Thesis Non-Exclusive License";

d) The Universal Copyright Notice (©) shall appear on all copies made under the authority of this license;

e) I undertake to submit my thesis, through my University, to any Library and Archives. Any abstract submitted with the thesis will be considered to form part of the thesis.

f) I represent that my thesis is my original work, does not infringe any rights of others, including privacy rights, and that I have the right to make the grant conferred by this non-exclusive license.

g) If third party copyrighted material was included in my thesis for which, under the terms of the Copyright Act, written permission from the copyright owners is required, I have

obtained such permission from the copyright owners to do the acts mentioned in paragraph (a) above for the full term of copyright protection.

h) I retain copyright ownership and moral rights in my thesis, and may deal with the copyright in my thesis, in any way consistent with rights granted by me to my University in this non-exclusive license.

i) I further promise to inform any person to whom I may hereafter assign or license my copyright in my thesis of the rights granted by me to my University in this non-exclusive license.

j) I am aware of and agree to accept the conditions and regulations of PhD including all policy matters related to authorship and plagiarism.

Signature of the Research Scholar: _____

Name of Research Scholar: **Rajesh Handa**

Date: _____ Place: _____

Signature of Supervisor: _____

Name of Supervisor: **Prof. (Dr.) Girish Chandra Maheshwari**

Date: _____ Place: _____

Seal:

Thesis Approval Form

The viva-voce of the PhD Thesis submitted by **Shri Rajesh Handa** (**119997392025**) entitled **"A study of the sense of well-being and perceived quality of life of people in Gujarat"** was conducted on ……..…… (day and date) at Gujarat Technological University.

(Please tick any one of the following option)

☐ The performance of the candidate was satisfactory. We recommend that he/she be awarded the PhD degree.

☐ Any further modifications in research work recommended by the panel after 3 months from the date of first viva-voce upon request of the Supervisor or request of Independent Research Scholar after which viva-voce can be re-conducted by the same panel again.

(briefly specify the modifications suggested by the panel)

☐ The performance of the candidate was unsatisfactory. We recommend that he/she should not be awarded the PhD degree.

(The panel must give justifications for rejecting the research work)

---------- ----------

Name and Signature of Supervisor with Seal 1) (External Examiner 1) Name and Signature

---------- ----------

2) (External Examiner 2) Name and Signature 3) (External Examiner 3) Name and Signature

ABSTRACT

This study examined the perceived quality of life (well-being) of people in Gujarat state, with 785 respondents. It investigated the overall life satisfaction of people with the help of "satisfaction with life scale" (Dinner et al.). Semantic differential scale (Campbell et al.) has used to measure sense of well-being in terms of positive affect and negative affect. Factors were extracted by doing an exploratory factor analysis of scores of semantic differential scale. Means of factors were compared with overall life satisfaction score. Decision Tree method has used for classification of overall life satisfaction score of people with different demographic and socio-economic variables. Parametric tests used like One-sample t-test, Independent sample t-test, One Way ANOVA for Identifying the relationship between Perceived Quality of Life (PQoL) and variables (demographic, socio-economic and geographical area) like gender, age, education, marital status, income and area of residence. The study found that people of Gujarat were somewhat satisfied with their overall Quality of life; also their PQoL has varied with age, marital status and income level. Exploratory factor analysis was used to identify underlying construct (factors) of Quality of life in Gujarat, then after by applying multiple regression analysis, a model has revealed which shows the relationship between Overall Quality of life and different factors (domains of life satisfaction). Finally, Covariance Based Structural Equation Modeling (CB-SEM) has used to validate the model. Construct validity, Convergent validity and Discriminant validity has validated.

Keywords: Quality of Life, Overall Life satisfaction, Domains of Life Satisfaction, Perceived Quality of Life, Covariance Based Structural Equation Modelling (CB-SEM).

Acknowledgement

With immense pleasure, I express my hearty thanks to my Guide **Prof. (Dr.) Girish Chandra Maheshwari**, Ex-Dean, M. S. Patel Institute of Management, Faculty of Management Studies, M. S. University of Baroda, Gujarat, currently working as Professor, Delhi School of Management, Delhi Technological University, Delhi, for his guidance, motivation and constant support throughout the research. You have given your valuable time for this research, without which it was not possible for me to complete this research.

I express my sincere thanks to my DPC members **Dr. Rekha S. Savnani**, Assistant Professor, Manish Institute of Management, Sankalchand Patel University, Visnagar and **Dr. Rajesh Patel**, Principal, Nootan Science and Commerce College, Sankalchand Patel University, Visnagar, for your valuable and constant support throughout the research. You had kindly spared your valuable time for this research for which I shall always be thankful to you.

Sincere thanks expressed to **Dr. Balvinder Singh**, Associate Professor, Department of Commerce, Guru Nanak Dev University, Amritsar. I express my sincere thanks to **Prof**. (**Dr.) Vina Vani**, Professor, MICA, Ahmedabad. I have learnt many things from her and it helped build up confidence in me, which helped completion of this research work.

I wish to acknowledge my sincere gratitude to all the individuals who assisted me in this work. I express my sincere thanks to all respondents, friends, volunteers for your constant support and help during my data collection. You all had spared your valuable time behind this study, because of which such type of research work has completed.

It is my privilege to thanks the honourable Vice-chancellor, the Registrar, the Controller of Examinations and Officers of the PhD Section especially **Ms. Rajani Bhandari, Ms. Arpita** and **Ms. Radhika** of Gujarat Technological University, Ahmedabad for their guidance, timely help, prompt response, constant support and to resolving student's problems.

Rajesh Handa
PhD Scholar
Gujarat Technological University

Table of Contents

SR. NO.	CONTENT	PAGE NO.
	Title page	i
	Declaration	iii
	Certificate	iv
	Course-work completion certificate	v
	Originality report certificate	vi
	Non-exclusive license certificate	viii
	Thesis approval form	x
	Abstract	xi
	Acknowledgement	xii
	List of abbreviations	xv
	List of figures	xvi
	List of tables	xvii
	List of appendices	xx
CHAPTER 1	**INTRODUCTION**	1
1.1	Introduction	2
1.2	Research problem	3
1.3	Rational of the study	4
1.4	Objectives and research hypothesis	6
1.5	Nominal definitions	7
1.6	Conclusion	8
CHAPTER 2	**REVIEW OF LITERATURE**	**10**
2.1	Introduction	11
2.2	Brief of related studies	11
2.3	Summary of review of literature	37
2.4	Research gap	81
2.5	Conclusion	83
CHAPTER 3	**RESEARCH METHODOLOGY**	**85**
3.1	Introduction	86

3.2	Research design	86
3.3	Variables under study	86
3.4	Operation definitions	87
3.5	Conceptual framework	88
3.6	Pilot study	89
3.7	Sampling design	90
3.8	Research tools	96
3.9	Statistical design	96
3.1	Limitations of the study	97
3.11	Conclusion	98
CHAPTER 4	**RESULTS**	99
4.1	Introduction	100
4.2	Results of compare means	101
4.3	Results of tree segmentation	106
4.4	Results of hypothesis testing	110
4.5	Results of confirmatory factor analysis	135
4.6	Conclusion	143
CHAPTER 5	**DISCUSSION**	144
5.1	Introduction	145
5.2	Findings of the study	145
5.3	Conclusion of the study	148
5.4	Contribution to knowledge	150
5.5	Implications of the study	151
5.6	Scope for further research	153
5.7	Comparison of the result with earlier study	154
	BIBLIOGRAPHY	156
	LIST OF PUBLICATIONS	167
	APENDIX- A	168
	APENDIX- B	173

List of Abbreviation

CB-SEM	Covariance Based Structural Equation Modeling
CFA	Confirmatory Factor Analysis
GDP	Gross Domestic Product
GNH	Gross National Happiness
GSDP	Gross State Domestic Product
HDI	Human Development Index
HDR	Human Development Report
HRQOL	Health-Related Quality of Life
OECD	Organization for Economic Co-operation and Development
PLS-SEM	Partial Least Square. Structural Equation Modeling
PQOL	Perceived Quality of Life
QOL	Quality of Life
UNDP	United Nations Development Programes
NFI	Normed Fit Index.
TLI	Tucker–Lewis Index.
CFI	Comparative Fit Index.
AGFI	Adjusted Goodness of Fit Index.
GFI	Goodness of Fit Index.
RMSEA	Root Mean Square of Error Approximation.

List of Figures

FIG. NO.	CONTENT	PAGE NO.
3.1	Conceptual framework	89
3.2	Sampling framework	95
4.1	Tree classification	108
4.2	Means of perceived quality of life of people with different age groups	113
4.3	Means of perceived quality of life of people with different educational status	115
4.4	Means of perceived quality of life of people with different marital status	118
4.5	Means of perceived quality of life of people of Central- Gujarat, South-Gujarat, Saurashtra and North-Gujarat	120
4.6	Unstandardized coefficients of predictor's variables	131
4.7	Histogram	132
4.8	Normal p-p plot	132
4.9	Scatterplot	133
4.10	Standardized regression weights of six domains of overall life satisfaction	137
4.11	Perceived quality of life (measurement model)	138
4.12	Perceived quality of life (structural model - second order CFA)	139

List of Tables

TAB. NO.	CONTENT	PAGE NO.
2.1	Review of literature	37
3.1	Sample collection in North -Gujarat	93
3.2	Sample collection in Central –Gujarat	93
3.3	Sample collection in Saurashtra	94
3.4	Sample collection in South -Gujarat	94
4.1	Descriptive statistics of overall life satisfaction	101
4.2	Classified groups based on overall life satisfaction	101
4.3	KMO and BARTLETT'S test	102
4.4	Initial and final communalities	102
4.5	Correlation matrix of eleven variables	103
4.6	Total variance explained	103
4.7	Rotated component matrix	104
4.8	Compare means of three classified groups	105
4.9	Tree classification model summary	107
4.10	Risk estimate of Tree classification model	109
4.11	Classification, percentage correctly classified	109
4.12	One-sample t-test statistics description	110
4.13	One-sample t-test result of people’s perceived quality of life	110
4.14	Statistics description of perceived quality of life of males and females	111
4.15	Independent samples t-test result of perceived quality of life of male and females	111
4.16	Test of homogeneity of variances of perceived quality of life of people with different age groups	112
4.17	One Way Anova of perceived quality of life of people with different age groups	112
4.18	Tukey test result of perceived quality of life of people with different age groups	112

4.19	Test of homogeneity of variances of perceived quality of life of people with different educational status	114
4.20	One Way Anova of perceived quality of life of people with different educational status	114
4.21	Tukey test result of perceived quality of life of people with different educational status	114
4.22	Group statistics of perceived quality of life of people with different marital status	116
4.23	Independent sample t- test of perceived quality of life of people with different marital status	116
4.24	Test of homogeneity of variances of perceived quality of life of people with different income groups	117
4.25	One Way Anova perceived quality of life of people with different income groups	117
4.26	Tukey test result perceived quality of life of people with different income groups	117
4.27	Test of homogeneity of variances of perceived quality of life of people of Central-Gujarat, South-Gujarat, Saurastra and North-Gujarat	119
4.28	One Way Anova of perceived quality of life of people of Central-Gujarat, South-Gujarat, Saurastra and North-Gujarat	119
4.29	Tukey test result of perceived quality of life of people of Central-Gujarat, South-Gujarat, Saurastra and North-Gujarat	120
4.30	Group statistics of perceived quality of life of people of rural and urban Gujarat	121
4.31	Independent sample t- test of life of people of rural and urban Gujarat	121
4.32	KMO and BARTLETT'S Test	122
4.33	Communalities	123
4.34	Correlation Matrix of initial pool of constructs	124
4.35	Total variance explained	125
4.36	Rotated component matrix	126
4.37	Exploratory factor analysis showing factor loadings and reliability	127

4.38	Variables entered/removed	128
4.39	Regression model summary	128
4.40	One way ANOVA test result	128
4.41	Coefficients of regression model	129
4.42	Residuals statistics	132
4.43	Deleted items	135
4.44	Standardized regression weights and significance level of six domains of life satisfaction	136
4.45	CFA report for every construct in the model	140
4.46	CFA model fit summary	141
4.47	Discriminant validity index summary for the constructs	142

List of Appendices

Appendix A	Questionnaire (English)
Appendix B	Questionnaire (Gujarati)

CHAPTER 1

INTRODUCTION

1.1 INTRODUCTION

1.2 RESEARCH PROBLEM

1.3 RATIONAL OF THE STUDY

1.4 OBJECTIVES AND RESEARCH HYPOTHESIS

1.5 NOMINAL DEFINITIONS

1.6 CONCLUSION

1.1 INTRODUCTION

Human beings are in search of well-being (Happiness) since the advent of men & women on this planet always putting efforts to improve it. They find happiness through different ways: like a spiritual seeker such as Gautam Buddha, Swami Vivekananda, Rajneesh Osho, Dalai Lama, etc., and some of the human beings are relating happiness with the wealth (materialism) and start running in the race of accumulation of wealth. Not only human beings, but countries are also running in the ace of making more and more wealth as it is considered a source of happiness. The whole world focuses on the attainment of economic well-being. Economic well-being is measured in GDP (Gross Domestic Product) growth rates, the resultant majority of the countries of the world are measuring the well-being of nations in term of GDP growth rates. This has led to the classification of the world into three categories; underdeveloped nations, developing nations, and developed nations. The people of the developed nations are considered as a happy person in comparison with the rest of the two.

Somewhere in this race of wealth accumulation, the people as well as nations start ignoring their basic needs, i.e., feeling of satisfaction or happiness. In 1972, Bhutan had introduced the concept of Gross National Happiness (GNH) and started measuring well-being in terms of GNH instead of GDP. The GNH Index includes nine domains:

a) Psychological well-being;
b) Health.
c) Education.
d) Time use.
e) Cultural diversity and resilience.
f) Good governance.
g) Community Vitality.
h) Ecological diversity and resilience.
i) Living standards.

GNH attracted the attention of the whole world and put a question on the method of measuring the quality of life. In 1990, the UN launched its Human Development Report with Human Development Index (HDI). Education, Health, and Quality of Life were the three components of the Human Development Index (HDI) and accordingly assessment of

human well-being across the world was done. Objective indicators were used in measuring well-being. A few years ago, World Happiness Report (2012), introduced by United Nations Sustainable Development Solutions Network, which was a good example of measuring the quality of life through a subjective well-being approach. Now, the World has considered happiness as the proper measure of social progress and the goal of public policy. On World Happiness Day, March 20, World Happiness Report 2017 was released publicly.

Researchers like Edward F. Diener, Robert A. Cummins, Martin Seligman, Ulrich Schimmack and Bruno S. Frey has introduced the world to the concept of subjective well-being (Happiness) and its measurement. This study is also based on a subjective approach to measuring well-being or quality of life of people in Gujarat. Gujarat is considered as one of the fastest growing and prosperous states of the country. As we compared HDI ranking then it comes out that Gujarat (HDI Ranking- 11, 2015) is far behind in the state called Kerala (HDI Ranking -1, 2015). On the other hand, Gujarat has better GDP data compared to Kerala, (nominal GSDP report-2017). These facts raised the question over the quality of life in Gujarat. This study has explored the overall quality of Life of people in Gujarat and also expounded on the domains of life satisfaction, which affects the quality of life.

1.2 RESEARCH PROBLEM

The study is focused on measuring subjective well-being or perceived quality of life of people in Gujarat. By literature review, we came to know that Quality of life varies with different age groups and classes (adolescent, university students, working class, non-working class, senior citizens, etc.). This study is restricted up to examine the perceived Quality of life of people in Gujarat. The study has focused on only working persons, specifically who are doing jobs with an age group of 26 to 55 years, income level INR 1.2 lakhs to INR12 lakhs per annum, education level with minimum S.S.C. Pass, either married or unmarried and lives in urban or rural areas of Gujarat. Respondents from tribal areas of Gujarat are not included in this study. The study is based on the following key variables such as life satisfaction, subjective well-being and quality of life. The influence of demographic and socioeconomic factors (age, gender, income, education, and area of residence) on the key variables has been studied.

This study mainly finds out solutions to certain questions: 1) what is the overall life satisfaction of people in Gujarat. Thus the people of Gujarat are satisfied with their overall life satisfaction? 2) Whether overall Life-satisfaction varies with their demographic (age, gender, marital status) and socioeconomic variables (education, income, locality of residence). 3) Whether the quality of life remains the same in all four geographic zones/areas of Gujarat. 4) Whether the quality of life remains the same in urban and rural areas of Gujarat? 5) What are the factors (domains) which affect the quality of life of people in Gujarat? Also, what are the weights of these factors in terms of their impact on overall quality of life? Besides this, this study also tries to explore the sense of well-being of people in Gujarat. Thus, whether there is any difference between a sense of well-being (positive affect & negative affect) of people, which are highly satisfied compared, moderately satisfied and dissatisfied people?

This study is based on Diener's (1999) theory of subjective well-being, where three components of subjective well-being have stated; a) positive and negative affect, b) life satisfaction, and c) satisfaction with specific domains. Key outputs of the study are 1) research design framework, 2) Life-domain satisfaction scale, and 3) findings of the study, i.e. a brief but clear idea about the factors which affecting quality of life of people in Gujarat has explored.

1.3 RATIONAL OF THE STUDY

Like most of the other countries in the world, India also depends on the objective indicators to measure growth and particularly gives more weight to GDP growth rate to examine the well-being of people in India. Yes, the USA and other developed nations did the same, but their public welfare policies and budgets are made in consideration with many other parameters. At the India GDP growth rate has projected throughout the year and its impact has measured by socioeconomic surveys, resultant economic budgets and public welfare policies are a frame out. Besides India is one of the fastest growing economies and the largest democracy in the world. However, after 70 years of independence, approx. 1/3 population lives in below poverty line and the rest are also having moderate to a poor quality of life as per HDI ranking (Rank- 131, HDR-2016). India's HDI ranking is just ahead of the countries like Bhutan, Bangladesh, Pakistan,

Nepal, Myanmar and Afghanistan in SAARC countries. The country like Srilanka (Rank-73, HDR-2016) and the Maldives (Rank- 105, HDR-2016) having far better HDI ranking than India. Even in worse cases Iraq (Rank- 121, HDR-2016) and Vietnam (Rank- 115, HDR-2016) having better HDI ranking than India. Richer become rich and the poor become poorer because of weak socioeconomic policy frameworks in India. According to Global Wealth Report 2016, compiled by Credit Suisse Research Institute expounded that India is the second most unequal country in the world with the top one percent of the population owning nearly 60% of the total wealth.

The subjective approach to measuring well-being is based on people's self-report judgment/assessment of life events. On the other side, an objective approach is based on a quantitative measurement of standard of living. Hence, an objective approach is comparatively less informative. Also, people participation is comparatively very less; resultant an actual problem will never come out and a gap between economic growth and public welfare increases. The only mediator between economic growth and the well-being of people is the policy framework of the nation. In India socioeconomic surveys conducted every year, where objective indicators of quality of life played a significant role and people self-report life judgments had got less space in it. Even countries like U.A.E (Rank- 42, HDR-2016) realized the importance of focusing on policy formation by considering subjective measurements of quality of life of people. Ohood bint Khalfan Al Roumi is the Minister of State for Happiness in the new UAE Cabinet; In February 2016, she said that the new ministry aims to promote the UAE's plans, programmes, and policies to promote the happiness of the UAE society.

The subjective approach to measuring well-being is a multi-dimensional measure, where the quality of life has been assessed at 360 degrees. In India also, we have a strong need to put more focus on the subjective approach of measuring the well-being of people. This study is an attempt to demonstrate the methodology of measuring subjective quality of life/ happiness of people where people's self-report judgment about their quality of life reveals areas where the government needs to put a focus on and accordingly public welfare policies need to be crafted. Subjective approach is not only more informative, but also gives many useful solutions for various human development issues.

In India, a single standardized measurement of quality of life is used, irrespective of people belonging to the different socioeconomic class, genders, age groups, geographical areas, etc. Resultant the public welfare policies give support to only a few particular groups of people and a large number of people deprive of any kind of welfare measure. It not only creates differences in the welfare of people, but it also increases the gap among different social classes in society. In a subjective well-being approach, first categorized people into groups and accordingly factors have been decided to assess their quality of life. Subjective well-being approach will play a significant role to reduce the differences of well-being among various groups of Indian society and resultant uniform growth may take place. To make India as an ideal country, where all age group people, from children to senior citizen lives happily, all income level people lives a happy life, etc. The implementation of a subjective approach to measuring the well-being of people is much needed.

If we relate the Maslow's hierarchy of needs theory with an objective approach and subjective approach of measuring well-being, then we found that an objective approach is restricted up to assess only lower level needs like physiological needs, which is its biggest limitation. On the other side, a subjective approach can measure human needs of each level like physiological needs, safety needs, social need to higher level needs like self-esteem need and self-actualization needs. So we can conclude that the subjective approach of measuring the quality of life is a complete measure of assessing the well-being of people.

1.4 OBJECTIVES AND RESEARCH HYPOTHESIS

Objectives

The study seeks to examine the sense of well-being /happiness in the Gujarat state. Specifically, it attempts to:

I. Assess the overall life satisfaction of people.
II. Study the sense of well-being among highly satisfied people, moderately satisfied people, and poorly satisfied people.
III. Examine whether the perceived quality of life varies with demographic and socioeconomic variables like sex, age, marital status, education status, income level and residential area.

IV. Ascertain the relationship between overall life satisfaction and different domains of life satisfaction, and

V. Comparing the life satisfaction with selected people of towns and villages in the State of Gujarat.

Research Hypothesis

1. People are not neutral towards their perceived quality of life.
2. There is a significant difference in perceived quality of life of males and females.
3. There is a significant difference in perceived quality of life of people with different age groups.
4. There is a significant difference in perceived quality of life of people with different educational status.
5. There is a significant difference in perceived quality of life of people with different marital status.
6. There is a significant difference in perceived quality of life of people with different income groups.
7. There is a significant difference in perceived quality of life of people of Central-Gujarat, South-Gujarat, Saurashtra, and North-Gujarat.
8. There is a significant difference in perceived quality of life of the people of rural and urban Gujarat.
9. There is a significant relationship between overall life satisfaction and different domains of life satisfaction.

1.5 NOMINAL DEFINITIONS

People

The members of a particular nation, community, or ethnic group.

Quality of Life

World Health Organization QOL Group (1994) defined Quality of Life as an individual's perception of his/her position in life in the context of the culture and value systems in which he/she lives and in relation to his/her goals, expectations, standards and concerns. It

is a broad-ranging concept, incorporating in a complex way the person's physical health, psychological state, level of independence, social relationships, and their relationship to salient features of their environment.

Well-being

The state of being comfortable, healthy or happy.

Subjective Well-being

Schimmack et al.(2008) defined well-being as preference realization which can be measured with an affective and cognitive measure.

Life Satisfaction

Life satisfaction is an overall assessment of feelings and attitudes about one's life at a particular point in time ranging from negative to positive. It is one of three major indicators of well-being: life satisfaction, positive affect, and negative affect. Hedonic level or balance refers to the pleasantness minus unpleasantness of one's emotional life (Diener, 1984).

Overall Quality of Life

Overall quality of life is a composite assessment of the quality of the social, economic and physical environments.

1.6 CONCLUSION

This chapter introduces readers to this study by drawing a broad picture where the concern of this study has shown and describes how this study touches crucial elements of the society. Also, Researcher portrays his thinking and understanding of the societal issue and try to give it solution. Research problem identification is a major contribution of this chapter. The outlook of the research problem has picturized and then narrows it down to the specific research question. A research question on which the whole study is put focuses on. The rationale of the study has discussed in this chapter, where the need of this

study and its contribution has shown which justifies its meaningfulness to the society. As per a systematic study, Research question gets fractioned into points and accordingly to Research objectives are a frame out. Research hypothesis which are probable solutions of the research questions and which are going to be tested is get formulated in this chapter. Nominal definitions of the key terms are mentioned in this chapter. Overall, this chapter gives a preview of the research topic, its origin and its contribution to the society. A review of the literature chapter follows this chapter in the study.

CHAPTER 2

REVIEW OF LITERATURE

2.1 INTRODUCTION

2.2 BRIEF OF RELATED STUDIES

2.3 SUMMARY OF REVIEW OF LITERATURE

2.4 RESEARCH GAP

2.5 CONCLUSION

2.1 INTRODUCTION

This chapter deals with the review of the literature, which is relevant to the subject matter of the thesis. The word ‘review’ means to summarize the broad content of the research article or study and also indicates clearly any linkage with other studies in the field. The principal purpose of the literature review is to establish the academic and research area which is of relevance to the subject of the research (Oliver, 2016). It seeks to lay the foundation for the current study. It sets the thesis within a research context consisting of relevant research studies and other analyses of related ideas.

2.2 BRIEF OF RELATED STUDIES

This part of the study reviewed 101 research papers. Selection of research papers is on the basis of a) relevance to the current study and b) published in reputed International Journal/database. Research extracts, suggestions and conclusions of national and international studies have given a base for the current study. Also, it has contributed to achieving fundamental clarity about the study and helped in many ways like the selection of key variables, measurement scales (Questionnaire), statistical methods, etc.

Abdel-Khalek (2010) examined the associations between Quality of Life, Subjective Well-being and Religiosity in Arabic, Muslim. A convenience sample of 224 Kuwait University undergraduates aged between 18 to 28 years was studied. A researcher found that there was a significant and positive correlation between QoL, SWB, and religiosity. Also, religiosity was suggested to be a salient component and a contributing factor to QOL.

Alcala and Carmen (2011) examined the quality of life of 100 respondents from Purok Matahimik (Isla) in Barangay Cottat, Lucena City. Respondents were female, married, approximately 40 years old and housewife. They measured the respondent's life satisfaction in seven domains: community services, public safety & security, work life, family life and relationships, leisure, self- development and satisfaction. They found a high level of satisfaction in respondents, also respondents scored high in domains; Family life and relationships, Material possession and consumption, Public safety and security.

Ali et al. (2009) examined the Quality of Life of people in Amman, Jordan. It was found that among domains of life satisfaction, health ranked higher compared to city profile and transportation. Domain as equity and satisfaction with local government-sub-domains of community participation impacted more Quality of Life compared to sub-domain as working conditions under the domain of economy. Economy stood in rank one, while community participation ranked ninth in order of preference.

Amao (2014) studied the well-being of the poor residential neighbourhood. The researcher explored the problems that had influenced poor neighbourhoods; poverty, the growth of the informal sector and housing shortage. A researcher found that poor residential neighbourhoods had a negative impact on respondents. The study found that a majority of the respondents were poor and employed in the informal sector. The study suggested that urban renewal and slum upgrading programmes were the methods to make improvement in the socioeconomic conditions of the respondents.

Angur et al. (2015) examined the value of subjective and objective indicators of neighbourhood quality of life. Both types of indicators are found to be significantly correlated with resident evaluations of overall neighbourhood quality. Subjective indicators of neighbourhood conditions were more highly correlated to overall neighbourhood quality (also subjective), than being objective indicators of neighbourhood conditions. Researchers suggested that both types of indicators have value for decision makers.

Anzilli, Facchinetti, and Mastroleo (2013) investigated eight indicators: material Well-being (income, consumption, and assets), health, education, personal activities, work, political participation, social relations, and environment. They had introduced a macro fuzzy inference system that has "Well-being" as a final output of the aggregation of eight sub-indexes. Each sub-index was the final output of other fuzzy inference systems. They concluded that environmental and health along with the other six variables might produce the aggregated evaluation of wellbeing.

Biswas-Diener and Diener (2001) investigated the quality of life of 83 people in the slums of Calcutta (now called Kolkata), India. They had conducted in-depth interviews. The respondents belonged to three groups: those living in slum housing, sex workers (prostitutes) residing in brothels, and homeless individuals living on the streets. Their mean

score of overall quality of life was negative, but mean ratings of satisfaction with specific domains were positive. Researchers concluded that the slum dwellers of Calcutta were generally experienced a poor sense of life satisfaction, but relatively more satisfied than our estimate. It might be because of a strong association with social relationships.

Biswas-Diener and Diener (2006) examined the quality of life of 186 homeless people in Calcutta (now called Kolkata), India, California, and a tent camp in Portland (Oregon). Mean of the life satisfaction rating of both American samples was negative, but positive for the pavement dwellers in Calcutta (now Kolkata). It was found that satisfaction with self-related domains were positive otherwise material related satisfaction domains were negative. Social factors and basic material needs were identified as the most significant indicators of the overall subjective well-being of the homeless.

Biswas-Diener, Diener, and Lyubchik (2015) examined the quality of life of Bhutan. They compared 11 nations with Bhutan on 4 domains – Psychological, Social, Environmental, and Income and Material wellbeing. They found mixed results of Bhutan's wellbeing. Researchers found that Bhutan scores high on environmental wellbeing and Social Wellbeing. On the other side scores very low in terms of overall psychological well-being.

Bourke and Geldens (2007) examined the subjective wellbeing of 91 young people (aged 16-24) of rural centre in south-east Australia. They found that factors as relationships, psychological dimensions and personal issues in family and 'pressure' impacted their well-being. They found that the Deiner et al. satisfaction with life scale was an appropriate measure of young people's well-being, but for measurement of health, sociology of youth and psychological approaches to young people's wellbeing, there was a need to incorporate a variable to make the measure more holistic of subjective well-being of young people.

Brajša-Žganec, Ivanović, & Lipovčan (2011) investigated the association between personality traits, social desirability and subjective well-being. The sample size was of 392 students (195 females and 197 males), aged 19 to 26 years. They found that personality, specifically extraversion, emotional stability and conscientiousness had a high association with subjective well-being. Intellect significantly showed positive affect and agreeableness

predicted a significant indicator of the absence of negative affect. Social desirability had a significant relationship with all three subjective well-being components.

Brown, Woolf, and Smith (2008) examined the determinants of subjective well-being using data from the 2008 New Zealand General Social Survey. Indicators included: health status, particularly mental health status, unemployment, income and social relationships. Each of the indicators had a strong significant impact on life satisfaction. Mental health and physical health both show the expected relationship between increases in life satisfaction with an increase in health status, but the relationship was stronger for mental health. Unemployment and not owning one's home both had a negative coefficient, while household income had a positive coefficient. The social/community relationship and safety/security variables all had significant negative coefficients. The picture for education was mixed. Neither the school nor vocational qualification measures had a significant relationship with life satisfaction. Sex, being female, was positively correlated with life satisfaction, although the coefficient was small.

Camfield, Chaudhury, and Devine (2006) examined the wellbeing in Bangladesh; data were collected from six sites (two rural, two semi-urban and two urban sites from two different Districts) in Bangladesh. The main criteria used to select respondents for the Quality of Life study were gender, age (18-44 and 45+), religious affiliation (85 percent were Muslim and 15 percent Hindu), and socioeconomic status. Structured interviews (n = 68), the Person Generated Index (n = 22, urban sample only) and focus group discussions (n = 240) were conducted. Life domains were studied like employment, health, education. They found that besides Bangladesh considered poorly developed county in the world, but their people enjoys levels of happiness the same as was found in many developed nations.

Cantarero, Potter, and Leach (2007) examined the key indicators affecting the elderly population's perception of Quality of Life (QoL) in two rural Nebraska communities--Crete and Schuyler. The sample size was 46 respondents aged 60 years or more. Researchers examined the quality of life by evaluating the perception of current health, Access to public transportation, Housing satisfaction, neighbourhood conditions, safety, perceived support from friends, access to basic services, finances and stress. They found that a majority of the elderly were satisfied. Also, stress was found to be negatively related to Quality of life. They also used a sense of community index to measure the quality of life.

They found elders' perception of the sense of community in their town and their overall sense of satisfaction was positively correlated and elders are satisfied with the sense of community in their town.

Chan et al. (2004) investigated the quality of life of Chinese older persons in Hong Kong with a sample size of 1,616 aged 60 or above. A researcher had conducted a multi-stage study carried out between 1999 and 2001 with an objective to develop an instrument to measure the quality of life. The researcher developed the overall QoL scale had a Cronbach's alpha of 0.72 with its domains ranging from 0.65 to 0.77 which indicated a high degree of statistical reliability. The name of the scale as suggested was 'Hong Kong Quality of Life for Older Persons Scale' - abbreviated as 'HKQoLOCP'.

Chavda and Rai (2015) examined the impact of culture and gender on the well-being of adolescents. The sample consisted of 180 adolescents belonging to Vernacular and Convent schools of Ahmedabad City of Gujarat (India). Overall Well-being Scale developed by Dr. Ashok Kalia and Anita Deswal was used to investigate the physical, emotional, social and school well-being of adolescents. They found that there was a significant difference between culture and well-being in adolescents. Also, gender had a significant impact on the well-being of adolescents.

Chen and Davey (2009) examined the quality of life in Zhuhai City (South China) by conducting a survey of 449 respondents. There were four objectives: (1) to judge overall life satisfaction of residents, (2) Comparing findings with Hong Kong and Macau study, (3) to investigate the equivalence of the International well-being Index (IWI) and (4) to study the applicability of the Theory of Homeostasis Wellbeing. The study found that a moderate level of personal (PWI score = 64.4.) and national (NWI score = 57.4) wellbeing was consistent with recent findings from Hong Kong and Macau.

Cramer, Torgersen, and Kringlen (2004) studied the well-being of common people with a sample of 2066 individuals between 18 and 65 years old. They developed seven sub-indexes. Good somatic health, living in a stable relationship with a partner, preferably married, in a less densely populated area, having a good education, a good income and being a younger female was the indicators of global quality of life. However, seven sub-

indexes were related to different socio-demographic variables. Age was found to be negatively related to different sub-indexes.

Das (2008) examined the quality of life (QOL) in the city of Guwahati, Assam. The survey was conducted in the area under the jurisdiction of the Guwahati Municipal Corporation (GMC) at the household level. The researcher studied the physical, social and economic environment. It had found that both objective and subjective conditions where the important dimension of QOL. But the correlation between objective and subjective QOL was not strong enough. Further added, satisfaction of traffic conditions was the lowest among all satisfaction indicators.

Dasgupta and Majumdar (1996) studied the perceived quality of life of people of Calcutta (now called Kolkata), India, with a sample size of 400. They found that socioeconomic status was not significantly related to perceived quality of life. They found that people of 21-35 years and 56 years or older were comparatively more satisfied than the people of 36-55 years age group. The sex difference was found insignificant. They examined the association between overall life satisfaction on 13 domains of life satisfaction (i.e., health, family life, local government administration, life in India, self-development, work life, material possession, health care quality, spiritual life, social life and central government administration). Out of these 13 domains, satisfaction with self-development, family life, material possession, and local government administration was found significant.

Diener and Seligman (2002) studied 222 undergraduates. Researchers compared the upper 10% of very happy people with average and very unhappy people. They found that the very happy people were highly social and had stronger romantic and other social association than less happy people. They were more extroverted, more agreeable, and less neurotic and scored lower on several psychopathology scales of the Minnesota Multiphasic Inventory. Compared with the less happy people, the happiest people have not significantly participated in religious activities. Healthy social relations were required for happiness.

Diener and Suh (1997) re-examined the strengths and weaknesses of the various approaches of measuring the quality of life. It was concluded that social indicators and subjective well-being measures were necessary to evaluate social and economic indicators also needed which was favoured by policymakers. They opined that each approach to

measuring the quality of life was essential and contain information that was not contained by other measures.

Dobewall et al. (2012) studied the role of personality traits in happiness and life-satisfaction of self-other agreement. Self-reports on the subjective well-being (SWB) measure and the NEO Personality Inventory-3 were obtained from 1,251 Estonians aged between 18 and 86 years. Result of subjective well-being measure was showed significant to self-other agreement, $r = .55$ ($p = .000$). The study explored that when a respondent measured someone's happiness or life-satisfaction, his/her rating was influenced by the personality of that person. In addition, self-reported subjective well-being reflects, what other people think about his/her personality.

Dost (2006) examine the quality of life of 700 university students of Hacettepe University. A study demonstrated that there was no significant difference in the subjective well-being levels of male and female students. There were significant differences in the subjective well-being levels of the students according to their perceived economic level, perceived attitude of parents, satisfaction with physical appearance, religious belief, and locus of control. The results revealed that subjective well-being levels of students from middle and higher economic statuses were higher than those in the low economic status. Students with perceived democratic parental attitude reported higher levels of subjective well-being than those with overly protective and avoidant parents. Subjective well-being level of students who were satisfied with their physical appearance was higher than those who weren't satisfied with their physical appearance. In addition, subjective well-being levels of students who reported having religious beliefs higher than those who did not have any religious beliefs. Finally, compared to students with an external locus of control, those with an internal locus of control had higher levels of subjective well-being.

Dunning et al. (2006) investigated the quality of life of 2000 people of Saskatoon, Saskatchewan, Canada. The study examined as to whether the factors that explained the low quality of life does remain the same for men and women. It was found that men and women were very similar in: (1) their QoL ratings, (2) neighbourhood QoL ratings. It was found that (1) separation/widowhood was the significant predictor of poor QoL, (2) Negative perception about community security issues was associated with deterioration in perceived neighbourhood quality of life. Qualitative analysis explored that there was the

difference in perception of men and women about general areas such as safety and neighbourhood supports.

Epley and Menon (2008) developed a new methodology of measuring the quality of life at the local and state level that combined heterogeneous indicators from various fields, such as economics, social, and health, into one total measurement. This technique might be used to compare one region to another or compare one metro area with its own performance over time.

Eroglu (2012) examined the subjective well-being of university students in a comparative way. The study included 240 students (120 foreign; 120 Turkish) of Selcuk University. Decision Making Styles Questionnaire, Subjective Well-Being Questionnaire and Personal Information Form were used. A researcher found that the subjective well-being levels of university students from different cultures differentiated at significant levels.

Fleche, Smith, and Sorsa (2012) studied the wellbeing in OECD countries based on self-reported life satisfaction surveys in a pooled regression over time and countries, at the country level and the OECD average. They found that apart from income, the state of health, not being unemployed and social relationships was specifically important for wellbeing with only some differences across countries. It was found that cultural differences were not major drivers of differences in life satisfaction. Correlations between the rankings of measures of life satisfaction and other indicators of well-being such as the Human Development Index and better Life Index were also relatively high.

Fu et al. (2006) examined the quality of life of the population of aged 40-59 years-old in Taiwan and Australia (278 Australians and 398 Taiwanese men and women). The result proved that country of residence had a significant effect on quality of life with differences seen between midlife Australian and Taiwanese men and women. They found that midlife of Australian men and women had a better quality of life than midlife Taiwanese men and women. Midlife of women was enjoying a better quality of life compared to midlife of men in both Australia and Taiwan. It was found that Midlife Australian men were more dissatisfied with their sleep and rest and more dissatisfied with their sexual activities in compared to midlife Australian women.

Fuentes and Rojas (2001) examined the relationship between subjective and economic well-being in Mexico. They studied the association of demographic, social, and economic variables on subjective well-being in Mexico. It was found that there was no strong association between income and well-being. They found a positive correlation between economic well-being (socioeconomic status) and subjective well-being (happiness). However, this positive relationship was weak and a large part of human happiness remains unanswered. The relationship between income and the sense of basic need satisfaction was also examined. It was found that subjective well-being was positively correlated with the sense of basic need satisfaction but not with income.

Groenland (1990) examined the quality of life of Dutch people with a sample size of 1187. The sample included four groups: People on welfare (N- 483), Employed (N- 291), Unemployed (N- 112) and Disabled (N- 301). The researcher found that indicators of socioeconomic well-being contribute significantly to the prediction of happiness. It was concluded that socioeconomic characteristics of well-being might be highly associated with the quality of life of people on social security.

Gupta and Sharma (1998) studied how to assess the quality of life. They examined a sample of 455 Indian working women. They found that the family life was a critical indicator of one's quality of life. Further added they said the family life quality was a support for better work motivation, commitment and overall work performance.

Gutierrez (2005) examined the relationship among the Big Five personality dimensions, demographic variables (sex, age and relationship status), and subjective well-being. The survey included 236 nursing professionals. Regression analysis showed personality had a critical association with subjective well-being, especially through Extraversion and Neuroticism. There was a positive association between Openness to experience and the positive and negative components of affect. Likewise, demographic variables (sex, age and relationship status) were found to be differentially associated with the different elements of subjective well-being.

Haq (2008) examined the quality of life of Punjab in Pakistan. A researcher found that quality of life was considered poor in one area than in other areas. It was noticed that the majority of the districts and Tehsils from the north and central Punjab was better in terms

of quality of life. On the other side, regions like west and south Punjab were identified as experiencing poor quality of life.

Haq (2009) examined the objective indicators versus subjective perceived well-being of people in Pakistan. Wellbeing was studied in four domains: education, health, living conditions and economic situation. The author had given weight to the education domain in assessing the human wellbeing. It was found those objective indicators of education: literacy rate, net primary enrollment and gender equality in education were positively associated with subjective perception in education facilities. A researcher found that the economic status was the key variables of the households and communities to determine their subjective perception of well-being. The result showed that differences were found in objective wellbeing among districts of Pakistan.

Hsieh (2015) examined the quality of life of the people of America. The researcher studied 10 domain satisfaction variables; family life, health, neighbourhood, friendships, life in the United States, community, non-work (leisure/hobbies), housing, a standard of living, and savings (finances). A researcher found that the relationship between global life satisfaction and the sum of domain satisfaction scores did not remain constant across groups of different domain importance rating patterns. On an average, respondents were most satisfied with family life, while least satisfied with the financial situation.

Hudders and Pandelaere (2011) examined the subjective well-being of 584 Dutch-speaking, Belgium students. A study explored the relations between luxury consumption, materialism and cognitive and affective subjective well-being by structural modelling. A researcher found that materialistic consumers were more interested to consume luxury goods than less materialistic. Luxury consumption boosts their positive mood, lowered down negative mood and helped to increase satisfaction with life. A study found that materialistic consumers engaged more in luxury consumption than less materialistic consumers, but also got more benefit out of it.

Hussien and Heshmat (2009) investigated the factors of happiness and life satisfaction of people in Egypt. They found that old people, the unemployed and men were unhappy. There was a positive association between happiness and income level, and physical health and life satisfaction. Further added, higher education had no significant effect on the

happiness level. The study concluded with a suggestion to some policymakers that might increase people's happiness and life satisfaction.

Hutchinson et al. (2004) examined the key indicators of psychological well-being in the Caribbean country, Jamaica. The sample consisted of 2580 respondents of which 1601 were women and 979 men. Interviews were conducted on young adults aged 15–50 years as part of a sexual decision-making survey in Jamaica. The mean age was 29.7 years (standard deviation of 9.2 years). Satisfaction with life was predicted by younger age, marital status and employment. They suggested that a health variable was more important for psychological well-being while social circumstances were more significant for satisfaction with life. There were important gender differences in the mediation of psychological well-being as well as age differences in the variables associated with satisfaction with life. Women had lower levels of psychological well-being and satisfaction with life.

Inoguchi and Fujii (2009) studied the quality of life of 1003 respondents (502 males, 501 females) of 20-69 years of the age group in Japan. They grouped sixteen specific life domains into three life spheres; material, post-material, and public. It was found that Japanese people were highly satisfied with the post-material sphere of life and poorly satisfied with the public sphere of life like the condition of the environment and the welfare system. Further, added the public life domain had no significant effect on the quality of life, while friendships and spiritual life from the post-material sphere of life had a significant impact. It was found that educational attainment and household income had no significant impact on subjective well-being. Finally, being married and satisfaction with marital life was found as a most powerful and significant variable impacting the quality of life in Japan.

Jongudomkarn and Camfield (2005) examined the quality of life of the Thais. Indicators were studied like family relations, health, money, occupation, and housing. Family relationship was the most critical indicator for all groups. People were very much concerned with their health, largely due to the inconvenience and cost of illness, and aware of the psychological impact on other areas of their lives. All groups were concerned with money to experience the good life, and lack of it, was a problem for all age groups.

Everyone needed to buy their own house. People in semi-urban areas were the only one who concerned about the appearance and size of hose.

Karlsson et al. (2013) examined the quality of life of Roma people, in West Sweden. Data was collected through interviews. The data were analyzed qualitatively using a phenomenological hermeneutic approach. The respondents mainly understood the concept of Health as "being healthy" and "feeling good". Important indicators of respondent's life where health, education, social support from family and friends, freedom and security, and the extent of involvement in society. A researcher found that the Roma people perceived their health and life situation as good, despite their poor situation and discrimination.

Keng and Hooi (1995) investigated the quality of life of the people of Singapore. They studied the relationship between quality of life and demographic characteristics of respondents. They found that there were no significant relationships between life satisfaction and demographic characteristics. Singaporeans were more conscious about being healthy and live a happy family life. A study found that people of Singapore were generally very satisfied with family life and life in Singapore as a whole.

Kennedy and Kanthamani (1995) proposed a model showing a causal relationship between religious commitment and well-being. The model suggested that the religious commitment influences a person's sense of meaning in life, which, in turn, influences well-being. The model also suggested that the transcendent experiences can affect religious commitment, which then influences meaning in life and well-being.

Keyes, Shmotkin, and Ryff (2002) studied the sample of 3,032 Americans aged 25–74. Researchers found that the related-but-distinct status of subjective well-being (SWB) and psychological well-being (PWB). The probability of optimal well-being (high SWB and PWB) increased as age, education, extraversion, and conscientiousness increased and as neuroticism decreased. Compared with adults with higher SWB than PWB, adults with higher PWB than SWB were younger, had more education and showed more openness to experience.

Khan, Shirazi, and Ahmed (2011) examined the relationship between spirituality and life satisfaction between male and female among adolescent students. A sample of 80 students from Aligarh Muslim University was studied. The sample included both male and female in equal number. A researcher found that spirituality was a positive significant predictor of life satisfaction and there was a positive correlation between spirituality and life satisfaction, also there was a significant difference between male and female students in spirituality and life satisfaction.

Kusago (2008) studied the life satisfaction of people and economic growth in Japan after the World War II. They realized the differences in GDP and HDI. The study had used secondary data about people's life satisfaction collected by the government of Japan every three years from 1978 to 2002. The study found that demographic and socioeconomic characteristics like age, gender, marital status, house ownership, income level and educational attainment were impacted by people's life satisfaction levels.

Larson (1978) examined the life satisfaction of older Americans with life domains: level of education, occupational status, marital status, availability of transportation, housing, and nonamorous forms of social interaction. The research concluded that the health was strongly linked to well-being, then after socioeconomic factors and degree of social interaction. Marital status and living standard of people's was also linked to well-being. Age, sex, race, and employment were found to be insignificant. The researcher further added that negative life situation like poor health and low income were linked to poor well-being.

Leelakulthanit and Day (1992) studied the satisfaction level of people of Thailand, with 500 respondents of aged 21 years or above lives in Bangkok Metropolitan area. They investigated the overall life satisfaction and various domains of their lives. They found Thai people were somewhat happy with their overall life satisfaction and became more satisfied with personal domains of life compared to environmental domains of life. Further added, two significant factors of quality of life are economic well-being and better education. The rank orders of domains of life from most satisfied to least satisfied was spiritual life, family life, self, personal health, social life, work life, material possessions, purchase and consumption of goods and services, recreation, health care, life in Thailand, the Thai government, and Bangkok administration.

Lever (2000) developed a valid and reliable instrument to measure Quality of Life among the inhabitants of Mexico City. This study was implemented in two stages. In the first, 18 neighbourhoods in Mexico City and its surroundings were randomly selected, and the voluntary participation of 320 inhabitants of those neighbourhoods was included. The sample for the second stage was composed of 768 subjects from Mexico City, male and female, from four socioeconomic levels and two age groups i.e. 21 to 35 and 36 to 50 years of age.

Liao (2008) studied the correlation between objective indicators and subjective perception of quality life in a ranking of cities in Taiwan. The Quality of life was examined in seven domains: medical services, domestic finances, work, education, leisure, public safety, and environmental quality. He found that there was no significant correlation between objective indicators and subjective perceptions, besides Education and Environmental Quality. Environmental Quality indicators (air pollution and garbage) were positively correlated with subjective satisfaction with a residential environment. But unexpectedly, higher levels of literacy and educational attainment were negatively correlated with satisfaction with the educational system.

Liao, Fu, and Yi (2005) examined the subjective quality of life in Taiwan and Hong Kong and appeared that two Chinese societies differ on societal and individual levels. Taiwan and Hong Kong, two Chinese societies that shared their cultural heritage, but have different social and political systems. A sample size of 1222 for Taiwan and 1044 for Hong Kong was used in the study. They found that for both societies; Life-satisfaction at the societal level affects the respondents' quality of life. They concluded that the perception of socioeconomic conditions in the larger society contributed to the variation in happiness and satisfaction with personal life. A higher level of satisfaction with overall social and economic conditions enhances residents' happiness and perceived the quality of personal life. They suggested that by improvement in social, economic, and political conditions will lead to increase the quality of life at the individual level.

Liu (1974) developed a systematic methodology for assessing social, economic, political, and environmental indicators to reflect the quality of life in the U.S. Nine indicators, including Individual Status, Individual Equality, Living Conditions, Agriculture, Technology, Economic Status, Education, Health and Welfare and State and Local

Governments were compiled from more than 100 variables for 50 states and the District of Columbia. Based primarily on 1970 data, QOL indexes were generalized and the states were rated.

Lloyd and Auld (2002) examined the relative importance of selected place and person-centered leisure attributes in predicting the quality of life. The study tested a set of objective and subjective indicators that people are most concerned with their leisure lives. Overall, it was found that the person-centered leisure attribute, leisure satisfaction, was the best predictor of quality of life. Place centered attributes failed to influence the quality of life. Further analysis revealed that people who engage in social activities more frequently and who are more satisfied with the psychological benefits they derive from leisure, experience higher levels of perceived quality of life.

Loewe et al. (2013) examined the quality of life of Chilean workers. With a sample size of 530, the causal effect of seven life domain satisfaction and subjective well-being were studied. Life domains: satisfaction with health, financial situation, social relationships, one's self-worth, leisure-time, family, and work. It was found that the financial situation was the strongest predictor of overall life satisfaction of workers, with a regression weight of .36. Satisfaction with family, work, and health had regression weights of .25, .14, and .14, respectively. There were no significant effects of one's self-worth, leisure-time, and social relationships on life satisfaction.

Maditinos, Papadopoulos, and Prats (2013) examined the quality of life in Greece with a sample size of 353 respondents. They studied the relationship between the free time slot with the Perceived Quality of Life (QoL) and the Satisfaction with Life (SwL). They revealed that the paid labour was a very critical factor in explaining the perceived QoL, followed by the active leisure and to a lesser degree by the passive leisure. A researcher found that the satisfaction of life influenced more from the perceived QoL and less by time allocation and leisure.

Malik, Shukla, and Bhat (2015) examined the sensitiveness among the sample wards of Srinagar city towards their quality of life. Environmental quality was analyzed objectively based on facts and figures. A researcher found that overall environmental quality was "Fair" in the sample wards of Srinagar city. "Poor" in the wards of Mukhdoom Sahib, Bud

Dal, & Khonmoh housing facility & density of persons per room were “poor” in Mukhdoom Sahib, Bud Dal & Khonmoh while resting of the wards with "fair" to good condition. There was a variation in the perception on rating the environmental quality by the residents in the sample households eight wards depict their perception in “high” category Mukhdoom Sahib, Bud Dal, Khonmoh, Batmaloo, Maharaj Ganj, AloochiBagh, Malik Agan, Barbarshah. More than 38 % of the population was not aware whether to participate in any development programme to solve environmental problems in the city. This was mainly because people were not well aware of the quality of environment its management & conservation. These areas were either congested or poor areas of the city & at the same time govt. authorities are not up to date to provide the basic amenities.

Mastekaasa and Moum (1984) examined the perceived quality of life and its relationship with socio-demographic variables in Norway. They studied that the regional differences at the county level in Norway had an impact to the subjective well-being of individuals, even when the effects of individual-level, sociodemographic variables were removed. Contextual analyses explored that the relationship between education and QoL was positive and moderately strong in affluent counties, near zero or negative in economically poorest areas.

Michalos (2004) studied health-related quality of life of 8076 undergraduates in Korea. First, 56% of the variance was explained by health indicator in the overall happiness of respondents. Then, using the Multiple Discrepancies Theory, 51% of the variation in satisfaction with one's own health scores was explained with 76% for a sample of Finnish females and 72% for Korean males. The researcher concluded that people were satisfied with their own health, the potential predictors assembled in MDT which gave better results as compared to any other method.

Michalos and Orlando (2006) examined the Quality of life of students of the University of Northern British Columbia from 1998 to 2005 with a sample size of 3407. They studied life domain like satisfaction with family relations and university-related variables like satisfaction with UNBC instructors on some global quality-of-life variables like life satisfaction. They found that the combination of the life domain variables and the university-related variables were insignificant to judge life satisfaction of students. The

most powerful university-related variable was the students' satisfaction with their instructors.

Michalos and Zumbo (1997) investigated about the relationship between public services and quality of life of the people of Prince George, British Columbia, Canada in 1997. The researcher studied correlations among perceived satisfaction, perceived value for money, use, spending preferences and demand and by using multiple regression analysis, 66% variance explained in life satisfaction scores, 57% of the variance in satisfaction with the quality of life scores and 37% of the variance in happiness scores. The researcher concluded that a Bottom-Up model was better than the Top-Down model.

Mingtao (2010) examined the quality of life of the people of Germany with a sample size of 2870 respondents. The researcher found that Happiness varies significantly from life satisfaction by regression analysis and life satisfaction can be judged better by controllable, non-psychological variables than happiness. Household income was a significant influence on people's happiness. Unemployed people showed lower life satisfaction and there were significant interaction effects between unemployed statuses and household income suggest that unemployed people, those in actively seeking for jobs, with a certain amount of household income, reported higher life satisfaction compared to other people.

Moller (2007) used a general survey (N=26'000) to find determinants of satisfaction and dissatisfaction of South Africans in relation to their material living standards. Results suggested that the improved living standards afforded to many black South Africans under democracy were few to be associated with increases in life satisfaction. Political factors continue to play an important role in shaping subjective well-being.

Moller and Schlemmer (1983) examined the quality of life of socioeconomically and socio-politically divided society of South Africa. The researcher investigated the perceptions of well-being among white, Indian and black residents of Durban, South Africa. This study found that there were big differences in the social circumstances of the three groups, also highlighted the materially underprivileged situation of Blacks than Whites and Indians.

Mookherjee (1997) studied the General Social Survey data of the National Opinion Research Centre of 10-years (1982-1991) and examined the relationship between marital status and gender to a perception of well-being. The result found that marriage increases the perception of well-being for both men and women. Married women showed higher satisfaction than men.

Mukherjee (1981) investigated the role of value systems and life goals in quality of life in India in consideration of societal structural variations and the existing socioeconomic conditions. The researcher puts more focus on the methodology of studying the quality of life in any society instead of substantial findings.

Narayana (2009) examined the indicators and variables in the construction of education index in the Human Development Index (HDI) at the global, national and 18 sub-national human development reports in India since 1990. There was non-comparability of measurement of the education indicators and variables. The researcher concluded that that vertical and horizontal comparability of HDI may not be possible in India. Measurement of the education variables was highly diversified between global, national and sub-national HDRs, and between sub-national HDR. The diversity of measurement was highest in enrollment ratio variable.

Neuendarf (2000) examined the quality of life of 321 respondents from a metropolitan area in U.S. Researcher studied six indicators of quality of life (metro area, neighborhood, job, family, personal life, and nation). A study found that the sense of humour had a significant association with to Quality of Life perceptions of the people, while a state of depression was strongly associated with Quality of Life reports regarding family, job, and personal life. The results were reported with underlying consideration of psychological differences of an individual in assessing perceptions of quality of life.

Oluwaye (1990) examined the quality of life of rural women of eleven villages of Oyo State of Nigeria with a sample size of 308. The study focused on (a) respondent’s awareness about “quality of life", (b) indicators of good quality of rural life in Nigeria, and (c) comparison of the quality of life with the previous generation. The study found that the ability to have plenty of children, good health, wealth and good personality were the

indicators of quality of life in rural areas. Respondents perceived a sense of satisfaction with their present conditions of quality of life compared to the last generation.

Ozcan, Boke, and Kara (2008) examined Life Satisfaction of Household and Individual of Turkish. Their study was based on data of Life Satisfaction of 2006 Study; Households and Individuals were surveyed by Turkish Statistical Institute (TUIK). They studied general (over-all) happiness and happiness in different domains: health and social security, education, worklife and income, individual security and justice services, personal environment and personal support networks. They found that higher income and having a job are two crucial determinants of happiness. Male and married people were happier than singles and females. Less educated people were happier than university educated people. In addition, they noticed that there was not a big difference between developing and developed countries when it comes to determinants of happiness.

Ozmete (2011) examined the life satisfaction as a cognitive component of subjective well-being of a sample of 108 women and men with a measurement of life satisfaction. A researcher found that mean ratings of life satisfaction were generally positive. Men perceived that their life was more satisfied compared to women. Men felt better about their future; they perceived that they were more fulfilled and better satisfied with their life compared to women. Further added, men have a greater sense of well-being about the direction in which their life is headed and they felt a better sense of harmony within themselves compared to women.

Park (2009) examined the quality of life of 1,023 respondents of Korea. It was found that their lives were highly modernized and digitalized without being much globalized. Despite the modernization and digitalization of their lifestyles, ordinary people still prioritized materialistic values more than post-materialistic values, and they remain least satisfied in the material life sphere. A study explored that their positive assessments of their standard of living and marriage were the most critical indicators on the quality of life they perceived.

Plagnol and Scott (2009) studied data from the British Household Panel Survey (BHPS), an annual longitudinal study that was started in 1991 with a sample size of 40,248. They investigated whether the quality of life was stable over the life course or do they vary with

age and between genders? The study found that quality of life does not remain stable over the life course. A difference in the quality of life between men and women takes place and its changes with time. They concluded that people's perceived quality of life is linked with important life events, such as the birth of a first child and retirement. They identified that at later stages of life, both men and women mention health as being an important part of their own quality of life, however, at young ages, family and finances were priorities for both genders.

Rodgers and Converse (1975) examined the quality of life of respondents on the basis of fifteen domains of their lives. The two indexes had generated from the analysis, the Index of Well-being and the Index of Domain Satisfactions. These indices had examined relation to a variety of demographic and situational variables, including age, indicators of socioeconomic status, employment status, and size of a community. Researchers concluded that both of these indices create valid indicators of the perceived overall quality of life.

Rojas (2004) examined the quality of life of 579 people in Mexico. A study explored the relationship between Life satisfaction and the seven domains of life satisfaction. A researcher found that satisfaction in the family domain, satisfaction with spouse, children, and the rest of family, satisfaction with Economic and Personal domains were significant for life satisfaction. The economic domain included satisfaction with housing and living condition, financial solvency, and income, while the Personal domain included satisfaction to engage in personal hobbies and interests, in recreational activities and personal growth. The health and job domains were also found significant. In addition, a study found that education was a very critical variable in explaining overall life satisfaction.

Royo and Velazco (2006) examined the Quality of life of the Thais. It was found that objective indicator; food shortages, chronic ill health and wealth had a significant impact on household's happiness and domain satisfaction in Thailand. People's perception of the economic position of the household was the key indicator of overall happiness and domain satisfaction. All household head characteristics were not significant for every domain. Like, age is only positively significant for satisfaction with family’s housing and the family’s income. Gender and marital status were not significant variables for any life domain. Years of education had a positive significance for satisfaction with children’s education, family’s health care and income. Larger numbers of educated household heads

were more satisfied with their income which signals a direct and strong relationship between human capital and income.

Ruta, Camfield, and Donaldson (2006) studied the Sen's (the 1980s) capability theory of quality of life by taking a view of health care and re-defined quality of life as a gap between desired and actual capabilities. They introduced a cognitive homeostasis to justify a curvilinear relationship between resources, capabilities, and quality of life. They found that the spirituality, loss of a partner, chronic pain, etc. as indicators of quality of life.

Ryff and Keyes (1995) studied the psychological well-being that included 6 indicators of wellness; Autonomy, Environmental Mastery, Personal Growth, Positive Relations with Others, Purpose in Life and Self-Acceptance. Data gathered a sample of adults (N = 1,108), aged 25 and older, who participated in telephone interviews. Comparison of the theory-based indicators of well-being with other frequently used measures indicated moderate to strong associations between two scales (Self-Acceptance and Environmental Mastery) and single- and multi-item scales of happiness, life satisfaction, and depression. However, the remaining four dimensions of well-being (Positive Relations with Others, Purpose in Life, Personal Growth, and Autonomy) showed mixed or weak relationships with these prior indicators.

Sawatzky, Ratner, and Chiu (2005) investigated; (a) whether there was empirical support for a relationship between spirituality and quality of life, (b) about the strength of this relationship and (c) to expound critical indicators affecting this relationship. The study found that a relationship between spirituality and quality of life was of $R^2 = 0.27$.

Schimmack (2008) examined the similarities and differences between cognitive and affective measures of wellbeing. He had created a composite subjective measure of wellbeing by combining average domain satisfaction, life-satisfaction, and affect balance. The weights of cognitive indicators were assigned slightly more than the affect balance measure, but the results would be quite similar if both components were weighted equally. He found that strong predictors (e.g., unemployment) produced consistent correlations with all measures, although the effect size varied slightly. In contrast, weak predictors (e.g., gender) produced inconsistent results.

Schneider (1975) examined intercity comparisons of objective and subjective measures of well-being based on data from the U.S. Census and from other governmental agency reports. A researcher found that the level of well-being of cities, as described by objective social indicators alone, apparently tells us nothing about the 'welfare' or the 'life quality' actually experienced by individuals living in those cities. While intercity comparisons of life conditions based on objective social indicators may alert us to inequalities or injustices in the distribution of an important aspect of well-being. The researcher suggested that objective social indicators cannot be taken as direct measures of the welfare or the quality of life actually experienced by individuals.

Selim (2008) studied the quality of life in Turkey. World Values Survey (WVS) was conducted to explore the factors affecting individual happiness and life satisfaction. A researcher found that middle education had a negative impact on life satisfaction among females and the upper education level was insignificant to the life satisfaction.

Shin and Rutkowski (2003) examined the quality of life of North-Korean people. They studied the data collected by two sets of national sample surveys in 1981 and 2001. They found that North-Korean people felt highly dissatisfied than they were 20 years ago. They also felt that in last 20 years the domains of health, education, work, and the community had changed for the better, while the domains of leisure, the government, and the country had changed for the worse. North-Koreans found dissatisfied from the domains of income and housing. A study found that North-Koreans were highly dissatisfied with the elected democratic government than they did about the military regime of 20 years ago.

Shu and Zhu (2009) examined lifestyles, value priorities, satisfaction with life domains, and subjective well-being in China using a national sample of 2,000 men and women aged 20-69. They conceptualized subjective well-being as a multidimensional and multilevel phenomenon and measured it in terms of happiness, enjoyment, and accomplishment. They also hypothesized that it has to be shaped by a multitude of forces, including demographic characteristics, lifestyles, value priorities, and satisfaction with various life domains. They found that the Chinese people were having a high level of satisfaction with their interpersonal, material, and nonmaterial life domains, their positive assessments of their relative living standards, and their high rate of successful marriage was having direct positive influences on subjective well-being.

Silva, Keulenaer, and Johnstone (2012) studied the impact of contextual and individual factors on satisfaction with the environmental quality and life satisfaction. Data from OECD and non-OECD countries collected was used for the study. They concluded that actual and perceived environmental quality had a significant impact on life satisfaction.

Sing (2009) examined the quality of life of 1,000 respondents of Hong Kong. It was found that a high attraction towards materialistic attainment was negatively affecting their quality of life. Negative results found under public life sphere, which included the natural environment, the social welfare system, and the democratic system. A researcher found that access to digital communication devices helped Hong Kong people to perceive a higher quality of life.

Somarriba and Pena (2009) examined the cross-comparison among three methodologies for assessing the welfare and quality of life in the European Union (EU). This study was helpful in the view that, the European Union had immersed in a deep transformation process and with deep cultural, economic and social inequalities. Therefore, a study of the quality of life and well-being of its people could play a critical role in exploring the differences.

Somarriba, Pena, and Bernardo (2008) examined the determinants of quality of life at European level with the European Survey of Quality of Life. People of 18 year or more and resident adults in the countries were considered in a study (N=26,000). They found that demographic variables as age and sex were significant. Women and young people were comparative more satisfied. Level of labour satisfaction was found significant. Good job supports a better quality of life. Health & education variable found insignificant. They found that a correlation between satisfaction in the life is greater for the subjective variables that the objective variables. Income variable was significant.

Sores and Peto (2015) studied the factors which affected the quality of life. A sample size of 804 local respondents at tourist destinations of Hajdúszoboszlo (Hungry) was considered for the study. They found factors such as earnings, employment, health and relationships play significant roles in determining life satisfaction. The majority of respondents were dissatisfied with their lives. The highest satisfied category was the age

group 15-24 with 67%. The least satisfied category was the age group of 40-54 with 70% of those who found their present conditions far from being ideal.

Stevenson and Wolfers (2008) studied the "Easterlin paradox" which suggests that there was no link between a society's economic development and its average level of happiness. They proved that a clear association between levels of subjective well-being and GDP per capita across countries. They explored that the average relationship was found consistent across many data sets and a similar relationship between subjective well-being and income was observed within countries. Further, added that there was a relationship between changes in subjective well-being and income over time within countries, economic growth associated with rising happiness.

Tambyah et al. (2009) studied the quality of life of 1,038 respondents in Singapore. It was found that most of Singaporeans were happy and enjoyed life, although they did not perceive a high level of accomplishment. Good health, a comfortable home, a job, time with family and having enough to eat emerged as key priorities in life. It was found that the Singaporeans were highly satisfied with their marriages, family life, friendship, housing, and public safety; their perceptions of their overall quality of life were mostly influenced by their relationships with others and their satisfaction with their homes.

Tiliouine (2007) investigate the impact of physical health on the wellbeing of 2,909 people of Algeria in 2004. A researcher found significant differences between the two groups (Healthier and non-healthier) in feelings of pain, anxiety and level of normal sleep. The results explored the small difference in the Personal Wellbeing Index score was in favour of the healthier group. Moreover, the healthier group showed significantly higher satisfaction with marriage, friendship and family relationships.

Tiwari (2009) examined the Quality of Life of 102 rural households in Dhar district of Madhya Pradesh in India. Household heads from three income categories of households—those below the poverty line, marginal and ‘comfortable’; non-poor households were interviewed using semi-structured methods. It was expanded that rural respondents tend to judge their situations with better-off people within a visible local context. However, their views on what causes poverty to appear to be informed by the broader debates at the

regional and national levels. Awareness of political and national issues observed amongst the respondents.

Tsai et al. (2013) examined the applicability of the spiritual indicators in GNH, which mainly evolved in Bhutan, in Taiwan in a comparison of their religion. Although both the countries shared some commonalities in religious participation level, they proposed to consider the multi-religious behaviour in Taiwan for the applicability. The adjustment of indicators to present the influence of multi-religious impacts, avoid the bias of Buddhism as well. They suggested that the Taiwan government must adopt the impact of how religious pursuit influences wellbeing while measuring the happiness in Taiwan.

Viswanathan and Sharma (2013) examined that whether high assertive women managers have better subjective well-being (SWB) or not. Sixty women managers from the IT, ITES and manufacturing sectors were included in the study. Rathus Assertiveness Schedule (RAS) and Subjective Well-Being Inventory were (SUBI) administered. The sample was split into low and high assertiveness groups, and they were compared with each of the 11 dimensions of SWB. A researcher found the high assertiveness group scored significantly higher on the dimensions of general well-being; positive, expectation, achievement, congruence, confidence in coping, and family group support. Scores on the deficiency in social contacts and the general well-being negative were higher in the low assertiveness group.

Wahl et al. (2004) studied the quality of life of the Norwegian population by associating socio-demographic and health variables. 1893 was the sample size of aged 19-81. It was found that women were having a better quality of life than men. People with higher levels of education were found to be enjoying a better quality of life. Married and employed showed the high quality of life. People suffering from diseases had significant poor relationship indicating the importance of health on quality of life.

Wills (2007) examined the domains of subjective well-being (SWB) and a global measure of satisfaction with life as a whole (SWLS) in three major cities- Bogota (N=830) of Colombia, Belo-Horizonte (N=600) of Brazil and Toronto (N= 605) of Canada. Individuals of 18 years aged or more were included. The personal and National Well-being indexes were applied and validated in these cities. Cities were chosen have similar

democratic institutions, but different cultures and standard of living. Significant differences were found across cities in the three indexes as well as significant interaction effects with demographic variables. Researcher proposed that Individual evaluation of subjective well-being was determined by a dispositional factor, context and cultural values. Three additional domains of subjective well-being were suggested; 1) Satisfaction with spirituality and religiosity. 2) Social status and Cultural Diversity.

Wood, Rhodes, and Whelan (1989) examined the sex differences in well-being. Women were found to report greater happiness and life satisfaction than men. The sex difference was explained in terms of men's and women's social roles i.e. (The female vs. male) gender role specified greater emotional responsiveness. Furthermore, past role-related experiences provide women with appropriate skills and attitudes. Women's vs. men's greater well-being was also found to hold for married but not for unmarried. For both sexes, the married state vs. unmarried was associated with favourable well-being, but the favourable outcomes proved stronger for women than men. Given that most respondents were married, the overall sex difference in well-being can be attributed to respondents' marital status.

Yao et al. (2009) examined the quality of life of 1,006 people of Taiwan. A researcher found that people were used modern utilities and digital media. Signs of materialistic achievement had present, still, they concerned more about physical security and financial safety than personal growth. Irrespective of demographic characteristics, the people of Taiwan like other Confucian publics, was very satisfied with the interpersonal life sphere and poorly satisfied with the public life sphere. It was found that contribution of material and nonmaterial life domains was comparatively higher than interpersonal and public domains.

Zhang (2010) studied the quality of life of 1600 respondents from eight typical cities representing different developmental levels in China. It was found that most of the respondents were highly satisfied with their overall life satisfaction. People from different cities had differences in their perceptions about overall life satisfaction. But the difference was not due to changes in developmental levels. It was found that characteristics like income had a significant impact on residents' satisfaction with QoL, while gender, age, education and marriage had no significant impact. Domains like health, working status and family life were the most significant indicators of overall life satisfaction.

Zullig (2005) investigated the relationship between perceived life satisfaction and health-related quality of life (HRQOL) in South Carolina, USA. The sample size was 4914 adolescents aged 13-18 years. A study had examined perceived life satisfaction by six domains (self, family, friends, living environment, school, and overall) and HRQOL-Health-Related Quality of Life (self-rated health). The researcher concluded that there was a strong relationship between poor physical health and perceived life satisfaction.

2.3 SUMMARY OF REVIEW OF LITERATURE

In this part of a study, key elements of related studies (Literature) have shown in summary form, so it will be easy for readers as well as for researchers to make a comparison of variables and other elements of related studies. Findings and conclusions of related studies were discussed in the former part of the study under the brief of related studies, but to formulate Research Gap it was an essential and systematic way to cross-comparison of related studies. Research Gap follows this part, where the research gap will be identified after careful comparative analysis of related studies. Review of Literature table was divided into certain columns as per the requirement of research gap analysis.

Table: 2.1 Review of literature

Sr. No	Author	Year	Title of The Research	Respondents	Sample Size	Place	Variables Studied
1	Abdel-Khalek	2010	Quality of life, subjective well-being, and religiosity in Muslim college students	Kuwait University undergraduates aged between 18 to 28 years	224	Kuwait	1. General Quality of life, 2. General health, 3. Physical, Psychological, 4. Social, Environment, 5. Total Quality of life, 6. Subjective Wellbeing, 7. Physical health, 8.Mental health, 9.Happiness, Satisfaction, 10. Religiosity, 11.General religiosity, & 12.Religious

							belief.
2	Alcala and Aldovino	2011	Sense of well-being and perceived quality of life in Purok Mathimik (isla), barangay cotta, Lucena city	Female, married, Age of nearly 40 year old and housewife	100	Purok Matahimik (Isla) in Barangay Cottat, Lucena City	Domains of life satisfaction: 1.Community services, 2. Public safety and security, 3. Material possession, 4.Consumption, 5.Work life, 6.Self-development, 7. satisfaction, 8.Family life, and 9. Relationship & Leisure as an activity.
3	Ali et al.	2009	Quality of life in cities: setting up criteria for Amman-Jordan	Experts	33	Amman (Jordan)	Overall Quality of Life, Domains: 1.City profile referring to community composition, 2. Community participation, 3.Culture and recreation, economy, 4.Education, 5. Environment, 6. Health, 7. Housing, 8. Infrastructure and public services, 9. Means of transportation, and 10. Security for life and property.
4	Amao	2014	Quality of life of poor residential neighbourhoods in Oshogbo, Nigeria	Poor residential neighbourhood	500	Oshogbo (Nigeria)	1. Gender, 2.Age, 3. Marital status, 4. Income status, and 5.Quality of house.

5	Angur et al.	2015	Congruence among objective and subjective quality-of-life (QoL) indicators	Households	3000	Flint (Michigan-U.S.A.)	1. Satisfaction with neighbours, 2. Satisfaction with Home, 3. Satisfaction with Aesthetic Quality, 4. Satisfaction with Security against Crime, 5. Satisfaction with Government and Community Service, 6. Satisfaction with Racial Mix of Neighbourhood, and 7. Satisfaction with Educational System.
6	Anzilli, Facchinetti and Mastroleo	2013	"Beyond GDP": a fuzzy way to measure the country wellbeing	Fuzzy Methodology			1. Material Well-being (income, consumption, assets), 2. Health, education, 3.Personal activities and work, 4. Political participation, 5. Social relations, 6. Environment, and 7. Insecurity (economic and physical).
7	Biswas – Diener and Diener	2001	The subjective well-being of the homeless, and lessons for happiness	People lives in the slums aged age from 15 to 70 years	67	Kolkata (India)	1. Life Satisfaction, 2. Material Domains, 3. Social Domains, 4. Self-related Domains, and 5. Positive and negative affects: Affection, Joy, Anger, Sadness, Guilt, Worry and Pride.

8	Biswas-Diener and Diener	2006	Sen and the art of quality of life maintenance: towards a working definition of quality of life.	Homeless people	186	Kolkata (India)	1. Quality of Life, 2. Income, 3. Social relationship, 4. Religious and spiritual beliefs, 5. Political participation, and 6. Life events.
9	Biswas-Diener, Diener and Lyubchik	2015	Wellbeing in Bhutan	Individuals	38580 (164 Nations) Bhutan (1000)	Bhutan	1. Psychological wellbeing, 2.Social wellbeing, 3.Environmental wellbeing, and 4.Income and Material wellbeing
10	Bourke and Geldens	2007	Subjective wellbeing and its meaning for young people in a rural Australian center	young people (aged 16-24)	91	Rural center in Australia	1. Subjective wellbeing, 2. Satisfaction with life, 3. Relationships, 4. Emotional/psychological dimensions, 5. Personal dimensions, 6. Physical dimensions, and 7. Structural Issues.
11	Brajša-Žganec, Ivanović, & Lipovčan	2011	Personality traits and social desirability as predictors of subjective	Students aged 19 to 26 years	392	University of Zagreb, Croatia	1. Gender, 2.Life satisfaction, 3.Positive affect, 4.Negative affect, 5.Extraversion, 6.Agreeableness, 7.Conscientiousness,

			well-being				8.Emotional stability, 9.Intellect, and 10.Social desirability.
12	Brown, Woolf and Smith	2008	The determinants of subjective wellbeing in New Zealand: an empirical look at New Zealand's social welfare function	People aged 15 years and above	8721	New Zealand	1. Personality and genetic factors, 2. Demographic factors: gender, age, health and education, 3.economic and work factors, 4.social life and community relationships, and 5.safety and security.
13	Camfield, Chaudhury and Devine	2006	Relationships, happiness and well-being: insights from Bangladesh	People with age of 21 years or above	330	Bangladesh	1.Age, 2.Gender, 3.Occupation, 4.Socio-economic status, and 5.Overall Life Satisfation
14	Cantarero, Potter and Leach	2008	Perceptions of quality of life, Sense of community, and life satisfaction among elderly resident in Schuyler and Crete,	People aged 60 years or more	46	Rural Nebraska communities-Crete and Schuyler	1.Perception of current health, 2.Access to public transportation, 3.Housing satisfaction, 4.Perception of neighborhood conditions, 5.Perception of safety, 6.Perceived support from friends, 7.Access to basic services, 8.Finances, and 9.Stress.

			Nebraska.				
15	Chan et al.	2004	Constructing a quality of life scale for older Chinese people in Hong Kong (HKQoLOCP)	Individuals aged 60 or above	1616	China	1. Subjective well-being, 2.Health, 3.Interpersonal relations, 4.Achievement-recognition, 5.Finance, and 6.Living condition.
16	Chavda and Rai	2015	Well-being of adolescents in context of culture and gender: an empirical analysis	adolescents	180	Ahmedabad (Gujarat)	1.Culture, 2.Gender, and 3.Well-being
17	Chen and Davey	2009	Subjective quality of life in Zhuhai city, south china: a public survey using the international wellbeing index	Individuals of age group of 18 years to 70 years	449	Zhuhai City (China)	1.Gender, 2.Age, 3.Educational level, 4.Marital status, 5.Length of residency, 6.Life as a whole, 7.Standard of living, 8.Health Life, achievement, 9.Personal relationships, 10.Personal safety, 11.Community connection, 12.Future security, 13.PWI score, 14. Economic situation, 15. State of the environment, 16. Social conditions, 17.Government, 18. Business, 19. National

							security, and 20 NWI score.
18	Cramer, Torgersen and Kringlen	2004	Quality of life in a city: the effect of population density	Individuals aged 18 to 65 years	2065	Oslo	1. Age, 2.Education, 3.Income, 4.Married today, 5. Living with partner, 6.Somatic health, 7.Population density, 8.Subjective well-being, 9.Self-realisation, 10.Contact with friends, 11.Support if ill, 12.Absence of negative life events, 13.Relation to family of origin, and 14. Neighbourhood quality.
19	Das	2008	Urban quality of life: a case study of Guwahati	Households	379	Guwahati, Assam (India)	1. Satisfaction from health facility in locality, 2.Satisfaction from welfare service by local administration, 3.Satisfaction from availability of parks and green areas, 4.Satisfaction from cost of living, 5.Satisfaction from own economic condition, 6.Satisfaction from conditions of housing, 7.Satisfaction from sense of personal security, 8.Satisfaction from level of environmental pollution in city, and 9.Satisfaction

							from condition of traffic.
20	Dasgupta and Majumdar	1996	Sense of well-being and perceived quality of life in Calcutta	People with age of 21 years or above	400	Kolkata (India)	1. Overall Life satisfaction, 2.Demographic variables (Age, Gender & Income), and 3.Domain of life satisfaction: satisfaction with self-development, family life, material possession, local government administration.
21	Diener and Seligman	2002	Very happy people	College students (Undergraduates)	222	University of Illinois (Chicago-U.S.A.)	1.Satisfaction with life, 2.Global self-reported affect balance, 3.Informant affect balance, 4.Daily affect balance, 5.Memory event recall balance, 6.Trait self -description, 7.Interview suicide measure, 8.Self-rating of relationships, 9.Peer rating of target relationships, 10.Daily activities, 11.Self-report affect intensity, and 12.Big five personality type.
22	Diener and Suh	1997	Measuring quality of life: economic, social and	Meta-analysis		U.S.A., Japan & France	1. Life satisfaction, 2.Unemployment, and Health.

			subjective indicators				
23	Dobewall et al.	2012	Self-other agreement in happiness and life-satisfaction: the role of personality traits	People aged between 18 and 86 years	1251	Estonian Genome Center (University of Tartu - Estonia)	1. Subjective Wellbeing, 2.Anxiety, 3.Angry 4.Hostility, 5.Depression, 6.Self-Consciousness, 7.Impulsiveness, 8.Vulnerability, 9.Warmth, 10.Gregariousness, 11.Assertiveness, 12.Activity, 13.Excitement Seeking, 14.Positive 15.Emotions, 16.Fantasy, 17.Aesthetics, 18.Feelings, 19.Actions, 20.Ideas, 21.Values, 22.Trust, 23.Straightforwardness 24.Altruism, 25.Compliance, 26.Modesty, 27.Tender-Mindedness, 28.Competence, 29.Order, 30. Dutifulness, 31. Achievement Striving, 32. Self-Discipline, and 33.Deliberation.
24	Dost	2006	Subjective well-being among university students	university students	700	Hacettepe University	1. Gender, 2.Satisfaction with Physical Appearance, 3.Locus of Control, 4.Perceived Economic Status, 5.Perceived Parental Attitude, and

							6.Religious Belief.
25	Dunning et al.	2006	A gender analysis of quality of life in Saskatoon, Saskatchewan	Individuals.	968 & 90	Saskatoon, Saskatchewan, Canada	1. Gender, 2. Neighborhood quality of life, 3.Age, 4.Marital status, 5.Children under 18 in household, neighborhood SES, 6.Feeling a part of neighborhood, 7.Level of comfort in participating in neighborhood projects, 8.Comfortable calling on neighbours in a crisis, 9.Volunteers in organizations, 10.Community security, 11.Human services, 12.Community services, 13.Micro quality of environment, and 14. Macro quality of environment.
26	Epley and Menon	2008	A method of assembling cross-sectional indicators into a community quality of life	Census		U.S.A.	1. Crime Sector, 2.Health Sector, 3.Employment Sector, 4.Education Sector, and 5. Recreation.

27	Eroglu	2012	Examination of university students' subjective well-being: a cross-cultural comparison	Students	240	Selcuk University, Turkey	1. Nationality, 2.Gender, and 3.Subjective wellbeing.
28	Fleche, Smith and Sorsa	2012	Exploring determinants of subjective wellbeing in OECD countries: evidence from the world values survey	Adults	92338	OECD countries	1. Income, 2.Health, 3.Employment status, 4.Education, 5.Environment, 6.Personal activities, 7.Community, Governance, 8.Life satisfaction, and 9.Individual Control.
29	Fu et al.	2006	The relationship between country of residence, gender and the quality of life in Australian and Taiwanese midlife residents	Individuals aged 40-59 years	278 Australians and 398 Taiwanese	Taiwan and Australia	1.Gender, 2.Country of Residence, 3.Physical Health, 4.Psychological Health, 5.Social Health, 6.Environmental Health, 7.Social Health plus respected by others, and 8.Environmental Health plus able to get desired things to eat.

30	Fuentes and Rojas	2001	Economic theory and subjective well-being: Mexico	Individuals	339	Mexico	1. Demographic and 2.Social Variables: education, age, gender, civil status, religion and participation in church, 3.health, 4.working situation and nature of job. 5. Economic Variables: current household income, former economic level, future income expectations and perception of material needs concern for the family's economic situation, house ownership, and 6. Subjective well-being.
31	Groenland	1990	Structural elements of material well-being: an empirical test among people on social security	People on welfare, Employed, Unemployed & Disabled	1187	Dutch	1. Income, 2.Minimum Income, 3.Satisfaction, Financial evaluation, 4.Cantril indicator, 5.Affective evaluations, and 6. Future Financial.
32	Gupta and Sharma	1998	Measuring quality of family life	Working women	455	India	1. Family life and 2.Quality of Life.

33	Gutierrez	2005	Personality and subjective well-being: big five correlates and demographic variables	Nursing professionals	236	Madrid (Spain)	1. Sex, 2.Age, 3.Relationship status, 4.Neuroticism, 5.Extraversion, 6.Openness, 7.Agreeableness, 8.Conscientiousness, 9.Positive affect, 10.Negative affect, and 11. Affect balance.
34	Haq	2009	Measuring human wellbeing in Pakistan: objective versus subjective indicators	Households	73953	Punjab (Pakistan)	Domains of Life satisfaction Objective: 1.education, 2.health, living conditions and 3.economic situation. Subjective: 4.Education, 5.Health, 6.Public safety, 7.Household's economic status, and 8.Community economic status.
35	Haq	2008	Variation in quality of life within Punjab: evidence from MICS, 2007-08	Households	91280	Pakistan	Domains of Life satisfaction: 1.Health, Education, 2.Child Protection, 3.Environment, and 4.Socio-economic development.

36	Hsieh	2015	Domain importance in subjective well-being measures	Individuals of 18 years of age and older	2164	U.S.A	1.Gender, 2.Race, 3.Education, 4.Marital status, 5.Employment, 6.Resident Location, 7.Family income, 8.Age, 9.Housing, Community, 10.Finances, Leisure/hobbies , 11.Family life ,12.Friendships, 13.Health, Government,14. Job, 15.Organizations, 16.Marriage, 17.Religious faith, 18.Neighbourhood, 19. Life in US, and 20. Standard of living.
37	Hudders and Pandelaere	2011	The silver lining of materialism: the impact of luxury consumption on subjective well-being	Dutch-speaking, Belgium students	584	Flemish part of Belgium	1. Sex, 2.Age, 3.Luxury, 4.Materialism, 5.Positive affects, 6.Negative affects, and 7.Life satisfaction.

38	Hussien and Heshmat	2009	Determinants of happiness and life satisfaction in Egypt "An empirical study using the world values survey - Egypt 2008"	Individuals aged 18 or above	3050	Egypt	1.Demographic Indicators (Education level, Illiteracy, No. of children, Nationality, Gender, Marital status, Being the household head, Age), 2.Work and employment, 3.Overall Life satisfaction, 4.Social relations between individuals of the society, 5.Gender discrimination, 6.National aspects (aims of the country in the coming ten years), 7.Political and institutional indicators, 8.Environment, 9.Economic indicators, and 10.Place of residence.
39	Hutchinson et al.	2004	Social and health determinants of well-being and satisfaction in Jamaica	Young adults aged 15–50 years	2580	Jamaica	1.Age, 2.Education, 3.Union status, 4.Employment status, 5.Religiosity, 6.Church Attendance, 7.Well-being, self-esteem, 8.Satisfaction with life, and 9.Health status.

40	Inoguchi and Fujii	2009	The quality of life in japan	Individuals aged 20-69 years	1003	Japan	1. Happiness, 2.Enjoyment, 3.Achievement, 4.Overall quality of life, 5.Gender, 6.Age, 7.Marital status, 8.Education, 9.Household 10.Income, 11.Community size, 12.Life styles, 13.Value priorities, 14.Housing, 15.Standard of living, 16.Household income, 17.Education, 18.Work, 19.Health, 20.Friendships, 21.Marriage, 22.Family life, 23.Leisure, 24.Spiritual life, 25.Neighbours, 26.Public safety, 27.Condition of environment, 28.Welfare system, and 29.Democratic system.
41	Jongudomkarn and Camfield	2005	Exploring the quality of life of people in north eastern and southern Thailand	Households	1000	Thailand	1. Age, 2.Gender, 3.Religion, 4.Geographical area, 5.Locality, 6.Life Domain Satisfaction: Family relations, Health, Money, Assets, Occupation, and Accommodation.
42	Karlsson et al.	2013	The meaning of health, well-being,	Roma People aged 18–	27 Qualitative	Västra Götaland	1. Health perception, 2.Being employed 3. Having an education,

			and quality of life perceived by roma people in west Sweden	64 years	Interv iews	(Sweden)	4. Social support from family and friends, 5.freedom and security, 6. The extent of involvement in society, 7.Well-being, and 8. Quality of Life.
43	Keng and Hooi	1995	Assessing quality of life in Singapore: an exploratory study	Individua ls aged 15 to 54 years	329	Singapo re	1.Sex, 2.Age group, 3.Ethnic group, 4.Marital status, 5.Educational status, 6.Personal income, 7.Household Size, 8.Residential type, 9.Overall life satisfaction, 10.Family life, 11.Life in Singapore, 12.Personal health, 13.Living environment, 14.Material possessions, 15.Health care services, 16. Acquisition & consumption of goods, 17. Social life, 18. Self-development, 19. Working life, 20.Mass media, 21.Leisure, and 22.School life.
44	Kennedy and Kanthama ni	1995	Empirical support for a model of well-being, meaning in life, importance of	People aged 16 to 89 years	182	Prince George, British Columbi a, Canada	1. Importance of Religion to Well-Being, 2.Transcendent Experiences to Well-Being, and 3.Transcendent Experiences to Meaning in

			religion, and transcendent experiences				Life.
45	Keyes, Shmotkin and Ryff	2002	Optimizing well-being: the empirical encounter of two traditions	Individuals aged 25–74 years	3032	U.S.A.	1. Age, 2.Gender, 3.Education Status, 4.Marital Status, 5.Race, Life satisfaction, 6.Positive affect, 7. Negative affect, 8.Self-acceptance, 9.Positive relations, 10. Personal growth, 11. Purpose in life, 12.Environmental mastery, and 13. Autonomy.
46	Khan, Shirazi and Ahmed	2011	Spirituality and life satisfaction among adolescent in India	Students	80	Aligarh Muslim University, India	1. Gender, 2.Spirituality, and 3. Life satisfaction.
47	Kusago	2008	Japan's development: what economic growth, human development and subjective well-being measures tell	Individuals aged 15 or above	7519, 3437 & 4159	Japan	1. Age, 2. Gender, 3. Marital status, 4. Job status, 5. House ownership, Income, and 6. Life satisfaction.

			us about?				
48	Larson	1978	Thirty years of research on the subjective well-being of older Americans	Individuals aged 60 or older	Meta-analysis	U.S.A.	1. Health, 2.physical disability, 3.Socioeconomic variables, 4.Age, 5.Race, 6.Sex, 7.Employment, 8.Marital status, 9.Transportation, 10.Housing, 11.Social activity, and 12.Subjective Well-Being.
49	Leelakulthanit and Day	1992	Quality of life in Thailand	People with age of 21 years or above	500	Bangkok city (Thailand)	Domains of Life satisfaction: 1.Life in general, 2. Family, 3.Self, 4.Material possession, 5. Work, 6. Social life, 7.Personal health, 8.Thailand gov. Life in Thailand, 9.Healthcare, 10.Recreation, 11.Consumption, 12.Spiritual life, and 13.Bangkok Administration.
50	Lever	2000	The development of an instrument to measure quality of life in Mexico city	20 to 35 and 36 to 50 years of age for first stage, Second stage: 21	320 & 768	Mexico City (Mexico)	1.Socio-economic Level, 2.General Quality of Life, 3.Couple relationship, 4.Family relationships, 5.Work, Children, 6.Economic well-being, 7.Personal development, 8.Self-image, 9.Health and

				to 35 and 36 to 50 years of age			physical well-being, 10.Sociability, 11.Social area, 12.Recreational activities, 13.Close friends, 14.Housework, Environment, 15. Emotional losses, 16.Moral aspect, 17.Religious aspect, 18.Personal expression and creativity, and 19. Personal Knowledge.
51	Liao	2008	Parallels between objective indicators and subjective perceptions of quality of life: a study of metropolitan and county areas in Taiwan	Citizens of age 20 or older	4070	Taiwan	1. Medical Service, 2.Domestic Finances, 3.Work, Education, 4.Leisure, 5.Public safety, and 6.Environment quality.

52	Liao, Fu and Yi	2005	Perceived quality of life in Taiwan and Hong Kong: an intra-culture comparison	Person aged above 20 years	Taiwan (1222) & Hong Kong (1044)	Taiwan & Hong Kong	1. Age, 2.Gender, 3.Marital Status, 4.Educational Level, 5.Working status, 6.Personal income, 7.Health, 8.Perceived fairness, 9.Social satisfaction, 10.Overall societal satisfaction, 11.Satisfaction with economy, 12.Satisfaction with security, 13.Satisfaction with government, 14.Satisfaction with mandatory education, 15.Optimism about the society, 16.Optimism about the economy, and 17.Optimism about the politics.
53	Liu	1974	Quality of life indicators: a preliminary investigation	Secondary data		U.S.A.	1. Individual Status, 2.Individual Equality, 3.Living Conditions, 4.Agriculture Production, 5.Technological Development, 6.Economic Status, 7. Education, 8.Health and Welfare, 9.State and Local Governments, 10.Overall SEPE Index, and 11.Personal Income Per

							Capita.
54	Lloyd and Auld	2002	The role of leisure in determining quality of life: issues of content and measurement	Individuals aged 15 years or more	571	Brisbane city in Queensland, Australia	1.Gender, 2.Age, 3.Socioeconomic status, 4.Marital status, 5.Household composition, 6.Perceptions of environmental quality, 7.Satisfaction with leisure resources, 8.Satisfaction with natural resources, 9.Satisfaction with cultural resources, 10.Satisfaction with man-made resources, and 11. Quality of Life.
55	Loewe et al.	2013	Life domain satisfactions as predictors of overall life satisfaction among workers: evidence from Chile	Workers	530	Chile	1. Age, 2.Marital status, 3.Education, 4.Occupation and 5.Life Domains satisfaction: Health, Finance, Social Self, Leisure, Family, and Work.
56	Maditinos, Papadopoulos and Prats	2013	The free time allocation and its relationship with the perceived quality of life (QoL) and satisfaction	Individuals	353	Greece	1.Physical Health, 2.Mental Health ,3.Satisfaction with Life, 4.Sleep (hours / week), 5.Paid labour, 6.Unpaid household labour,7. Personal care, 8.Leisure, 9.Mass Media leisure, 10.Computer use, 11.

			with life (SWL)				Mental leisure, 12.Cultural leisure, 13.Social leisure, 14.Passive leisure, and 15.Active leisure.
57	Malik, Shukla and Bhat	2015	Spatial variation in the perception of urban residential environmental, quality of life in Srinagar city (j &k)	Households	711	Srinagar city (India)	1. Housing facility by ward, 2.Distribution of disease by ward, 3.Distribution of diseases by prevalence of certain diseases in sample areas, 4.Density of persons per room in sample households, 5.Built up of Srinagar city, 6.Perception of Residents Annoyed by Noise Pollution, 7.Perception of Residents Annoyed by Water Pollution, 8. Perception of Residents Annoyed by Crowding, 9.Perception of Residents Annoyed by Litter, 10.Perception of Residents on Total Environmental Pollution of Sample Households, 11.Resident's awareness & participation to environmental Problems, and 12. Level of Literacy.

58	Mastekaasa and Moum	1984	The perceived quality of life in Norway: regional variations and contextual effects	Individuals of 15 to 64 years of age	1005	Norway	1. Education, 2.Age, 3.Income, 4.Marital status, 5.Sex, 6.Household size, 7.Degree of Urbanization, and Overall Quality of Life.
59	Michalos	2004	Social indicators research and health-related quality of life research	Undergraduates	8076	Korea	1. Happiness on health, 2.Happiness on worries, 3.Happiness on social support, 4.Happiness on domain satisfaction, 5.Mental Health, 6.Social Functioning, 7. Social Support Index ,8.Fair Treatment Index, 9.Physical age identity, 10.Difficulties with housing costs, 11.Personal worries, 12.Living area, 13.Retail store access, 14.Ideal age preference, 15.Friendships, 16.Present age, 17.Self-esteem, 18.Accomplishing in life now, 19.Local government officials,20. Family relations, 21.Opportunities to socialize.

60	Michalos and Orlando	2006	A note on student quality of life	University students	3407	Northern British Columbia	1.Life satisfaction, 2.Happiness, 3.Satisfaction with quality of life, 4.Satisfaction with standard of living, 5.Subjective well-being, 6.Satisfaction with housing, 7. Satisfaction with family relations, 8.Satisfaction with friendships, 9.Satisfaction with recreation, 10.Satisfaction with financial security, 11.Satisfaction with self-esteem, 12.Satisfaction with instructors, 13.Satisfaction with course offerings, 14.Satisfaction with student services, 15.Satisfaction with library services, 16.Satisfaction with food services, 17.Satisfaction with fitness services, 18.Satisfaction with bookstore services, 19.University useful preferred work, 20.University useful any work, 21.Age, and 22. Academic credits earned.

61	Michalos and Zumbo	1997	Public services and the quality of life	Individual aged 18 to 88 years	715	Prince George, British Columbia, Canada	1. Happiness, 2.Satisfaction with life as a whole, satisfaction with the quality of life, 3. Satisfaction with Local Government Officials, 4.Satisfaction with Provincial Government Officials, 5.Satisfaction with Federal Government Officials, and 6.Satisfaction with All Government Officials.
62	Mingtao	2010	A microeconomic analysis of happiness and life satisfaction: a statistical study in Germany	Individuals aged over 15 years	2870	Germany	1. Age, 2.Gender, 3.Education status, 4.Marital status, 5.Subjective General health, 6.Employment status, 7. Social meet, 8.Religiosity, 9.Household income, 10.Number of rooms household have, 11.Satisfaction of Life, and12.Happiness.
63	Moller	2007	Satisfied and dissatisfied South Africans: results from the General Household Survey in international	Households	26000	South Africa	1. Race, 2.Overall Life satisfaction, 3.Domains: Housing, 4.Infrastructure, Service delivery, 5.Ownership, 6.Education, 7.Livelihoods, and 8.Poverty.

			comparison				
64	Moller and Schlemmer	1983	Quality of life in south Africa: towards an instrument for the assessment of quality of life and basic needs	People (Whites, Indian, Black)	409	South Africa	1.Overall life satisfaction, 2.Average satisfaction among all salient aspects of life as chosen by respondents (group priorities), 3.Average satisfaction with subtle issues in life not necessarily recognised as important by individual and 4.Average satisfaction with all salient aspects of major life domains and criteria : nutrition, religion, identity, social relationships, health, family, leisure and recreation, participation, self , neighbourhood issues, education, physical security, transport, housing, employment and work, financial and social security, rural ties, wages, and prices, race relations.
65	Mookherjee	1997	Marital status, gender and perception of well-being	Individuals aged 18 to 89 years.	12168	U.S.A.	1. Perception of well-being, 2.Marital status, 3.Gender, 4.Race, and 5. Financial status.

66	Mukherjee	1981	On the quality of life in India: an exploratory survey	People	143	Kolkata (India)	1.Livelihood categories, 2.Family organization, caste affiliation, 3.Education, 4.Sex, 5.Age, 6.Religion, 7.Ethnicity, 8.General Quality of Life, 9.Personal Career, 10.Life at work, 11.Family life, 12.Neighbourhood conditions,13. Network of family and neighbourhood, 14. Recreation and leisure, 15.Personal wellbeing, 16.Appreciation of a peaceful, and 17.Happy and progressive life.
67	Narayana	2009	Education, human development and quality of life: measurement issues and implications for India		HDR (UNDP)-HDI data	India	1. Education index, 2.Human Development Index (HDI), 3.Physical Quality of Life Index (PQLI), 4. Literacy rate, and 5. Gross enrolment ratio.
68	Neuendarf	2000	Perceptions of quality of life and affective characteristics: an urban examination	Adults	321	U.S.A.	1. Age, 2.Education, 3.Gender, 4.Income, 5.Marital Status, 6.Political Ideology, 7.Political Party Affiliation, 8.Race/Ethnicity, 9.Media Use, 10.New Technology

							Adoption, 11.Public Opinion, 12.Affective Filters, and 13.Quality of Life.
69	Oluwaye	1990	Determinants of quality of rural life in Nigeria: the women's view	Rural Women	308	Oyo State of Nigeria	1. Age, 2.Educational level, 3.Income per month, 4.Occupation, 5.Quality of rural life, 6. Many children, 7. Educated (good quality) children, 8.Good housing, 9.Wealth, 10.Good personality (good social relationships), and 11. Motor (vehicle) ownership, and 12. Good health.
70	Ozcan, Boke and Kara	2008	The determinants of the perception of happiness and quality of life amongst Turkish people	Households and Individuals	2140 households & 5304 individuals	Turkey	1. Sex, 2.Age, 3.Marital status, 4.Education status, 5.Employment status, 6.Environment of Life, 7.Health Status, and 8. Future outlook.
71	Ozmete	2011	Subjective well-being: a research on life satisfaction as cognitive component of	Individuals aged 18 to 54 years attending in English	108	London (Britain)	1. Gender and 2.Life - satisfaction.

			subjective well-being	Language Education Programmed in London			
72	Park	2009	The quality of life in South Korea	People aged below 14 years to 65 years and above	1023	Korea	1.Gender, 2.Age, 3.Marital status, 4.Education, Income, 5.Community, Lifestyles, 6.Needs, Happiness, 7.Enjoyment, Achievement, 8.Housing, Friendships, 9.Marriage, 10.Standard of living, 11.Household income, 12.Health, Education,13. Job, 14.Neighbours, 15.Public safety, 16.Environment, 17.Welfare system, 18.Democratic system, 19.Family life, 20.Leisure, and 21.Spiritual life.
73	Plagnol and Scott	2009	What matters for well-being: individual perceptions of quality of life before and after important life	Households	40248	England	1. Age, 2.Gender, 3.Health, 4.Family, 5.Finance, 6.Happiness, 7.Friends, 8.Leisure, 9.Home comforts and 10.Employment.

			events				
74	Rodgers and Converse	1975	Measures of the perceived overall quality of life	Household (18 years of age or older)	2164	U.S.A.	1. Friendly-lonely, 2.Enjoy-life, 3.Easy-hard, 4.Overall life satisfaction, 5.Interesting-boring, 6. Free-tied down, 7.Happiness, 8.Full-empty, 9.Hopeful-discouraging, 10.Worthwhile-useless, 11.Rewarding-disappointing, 12. Brings best-no chance, 13.Enjoyable-miserable, 14. Health, Savings, 15. Job, Education, 16.Standard of living, 17. Life in United States, 18.Marriage, 19.Community, 20. Family life, Housing, 21.Non-working time, and 22.Friendships, Neighborhood.
75	Rojas	2004	The complexity of well-being a life satisfaction conception and a domains-of-life approach	Individuals	579	Mexico	1. Life satisfaction, 2.Health, 3.Economic, 4.Job, 5.Family, 6.Friendship, 7.Personal, and 8.Community.

76	Royo and Velazco	2006	Exploring the relationship between happiness, objective and subjective well-being: evidence from rural Thailand	Households	4315	Thailand	1. Age, 2.Gender, 3.No. of family members, 4.No. of childrens, 5.Health, Education, 6.Housing, Food, 7. Relationship, 8.Wealth, and 9.Long term shocks
77	Ruta, Camfield and Donaldson	2006	Making the best of a bad situation: satisfaction in the slums of Calcutta	People age from 18 to 75 years .Living in slums	20	Kolkata (India)	1.Age, 2.Gender, 3.Income, 4.Housing, 5.Satisfaction With Life, 6.Satisfaction With Memory Balance, 7.Material Satisfaction, 8.Income Satisfaction, 9.Housing Satisfaction, 10.Food Satisfaction, 11.Social Satisfaction, 12.Family Satisfaction, 13.Romantic Satisfaction, 14.Friendship Satisfaction with Self, 15.Morality Satisfaction, 16.Intelligence Satisfaction, and 17.Satisfaction with Physical Appearance.

78	Ryff and Keyes	1995	The structure of psychological well-being revisited	People with age of 25 years or above	1108	U.S.A.	1. Age, 2.Gender, and 3.Domains of Life satisfaction: Self-Acceptance, Environmental Mastery, Positive Relations, Purpose in Life, Personal Growth and Autonomy.
79	Sawatzky, Ratner and Chiu	2005	A meta-analysis of the relationship between spirituality and quality of life				Meta-analysis
80	Schimmack	2008	Measuring wellbeing in the SOEP	Households	18196	Berlin (Germany)	1. Average domain satisfaction (DS), 2. Life satisfaction judgment (LS), 3.Affect balance (AB), 4.Subjective wellbeing measures (SWB), 5.Neuroticism, 6. Unemployment, 7.Disability, 8.Divorce, 9.Widowhood, 10.Gender, 11.Birth Year, and 12.Income.

81	Schneider	1975	The quality of life in large American cities: objective and subjective social indicators	Census		U.S.A.	1. Satisfaction with Job, 2.Satisfaction with Home, 3.Satisfaction with Money and Income, 4.Personal Efficacy, 5. Satisfaction with Level of Services, 6. Citizen Competence, 7. Government Distrust, 8. Constructed Measure of Total Life Satisfaction. 9. Income, wealth and employment, 10.Environment, 11.Health, 12.Education, 13.Participation and alienation, and 14.Social disorganization.
82	Selim	2008	Life satisfaction and happiness in turkey	Individuals aged 15 or above	6338	Turkey	1.Life satisfaction, 2.Happiness, 3.Gender, 4.Age, 5.Marital status, 6.No. of children, 7.Educational level, 8.Type of employment, 9.Importance of Religion, 10.Importance of family, 11.Importance of friend, 12.Importance of leisure time,13. Importance of politics, 14. Importance of work, 15.Political orientation, 16.Trust to the people, and 17.Proud of nationality.

83	Shin and Rutkowski	2003	Subjective quality of Korean life in 1981 and 2001	People aged 20 or older	1215	North-Korea	1. Happiness, 2.Enjoyment, 3.Satisfaction, Accomplishment, and 4.Life domain: Health, Education, Leisure, Marriage, Family, Children, Friendship, Income, Housing, Work, Government, Community, Life in Korea.
84	Shu and Zhu	2009	The quality of life in china	Individuals aged 20-69 years	2000	China	1. Gender, 2. Age, 3.Education, 4.Marital status, 5.Household income, 6.Employment, 7.Urban/rural resident, and 8.Life domain satisfaction: Personal life, Interpersonal life, Material life, Nonmaterial life, Public life, Subjective wellbeing: Happiness, Enjoyment, Accomplishment, Value priorities and Lifestyle.
85	Silva, Keulenaer and Johnstone	2012	Environmental quality and life satisfaction	People aged 15 or older	150000	OECD and non-OECD countries	1. Gender, 2.Age, Education, 3.Health status, 4.Employment status, 5.Income, and 6.Satisfaction with air quality.
86	Sing	2009	The quality of life in	Hong Kong	1000	Hong Kong	1.Gender, 2.Age, 3.Educational attainment,

			Hong Kong	residents aged 20 years to 69 years			4.Household annual income, 5.Marital status, 6.Religion, 7.Overall Quality of life, 8.Education, 9.Job, 10.Health, 11.Family life, 12.Friendship, 13.Marriage, 14.Neighbours, 15.Standard of living, 16.Household Income, 17.Housing, Leisure, 18.Spiritual life, 19.Public safety, 20.Environment, 21.Welfare system, 22.Democratic system. 23. Personal life sphere, 24.Interpersonal life sphere, 25.Material life sphere, and 26.Non-material life sphere.
87	Somarriba and Pena	2009	Synthetic indicators of quality of life in Europe	HDI Ranking		European Union (EU)	1. Satisfaction with standard of living, 2.Happiness, 3. Life satisfaction, 4.Home satisfaction, 5.Social life satisfaction, 6.Income, 7.Job satisfaction, 8.Health system satisfaction, 9. Living satisfaction area, 10.Health satisfaction, and 11.Life expectancy at birth, 12.Unsafely,

							13.Trust people, 14. Life Expectancy at the age of 65, 15.Family satisfaction, 16.School life expectancy, 17.Employment, 18.Education satisfaction, 19.Leisure time, 20. Trust in judicial system, 21.Inequality, and 22.Distance to school, stress.
88	Somarriba, Pena and Bernardo	2008	Quality of life and subjective welfare in Europe: an econometric analysis	People of 18 year or more	26000	Europe	1. Age, 2. Gender, 3.Satisfaction with the job, 4.Socio-economic status, 5.Satisfaction with the house, 6. Problems with the accommodation, shortage of space, 7.Satisfaction with one's education, 8. Age of ended education, 9.Level of education, 10.Satisfaction with the standard of living, 11.Income, 12.Difficulties in making ends meet, 13.Satisfaction with one's health, 14.Chronic illness, 15.Satisfaction with the family,16.Trust in people, 17.Satisfaction with social life, 18.Number of children,19. Marital Status, 20.Activity in a

							charitable organization, 21.Absence green and recreative zones, and 22.Air pollution.
89	Sores and Peto	2015	Measuring subjective quality of life	Adult	804	Hungry	1. Age, 2.Gender, 3.Marital Status, 4.Income level, 5.Regular exercises, 6.Personal relationships, 7. Workplace atmosphere, 8. Income, 9.Presence of thermal waters, 10.Public security, 11.Infrastructure, 12.Family, 13.Jobs and employment possibilities, 14.Comfort and physical state of homes,15. Availability of health services, 16.Political atmosphere, and 17. Traveling.
90	Stevenson and Wolfers	2008	Economic growth and subjective well-being: reassessing the Easterlin paradox	People aged 15 or older	38000	44 Countries	1. Real GDP per Capita, 2.Life satisfaction and 3.Happiness.

91	Tambyah et al.	2009	The quality of life in Singapore	Individuals aged 15 years or over	1038	Singapore	1.Gender, 2.Age, 3.Education, 4.Household income, 5.Marital status, Religion, 6.Lifestyles, 7.Digital life, 8.Global life, 9.Spirituality, 10.Value priorities, 11.Having, 12.Relating, Being, 13.Personal domains, 14.Standard of living, 15.Household income, 16.Health, Education, 17.Job, 18.Interpersonal domains, 19.Housing, 20.Friendships, , 21.Marriage, 22.Neighbours, 23.Family life, 24.Leisure, 25.Spiritual life, 26.Public domains, 27.Public safety, 28.Environment, 29.Welfare system, and 30.Democratic system.

92	Tiliouine	2007	Health and subjective wellbeing in developing countries: the case of Algeria	Healthier and non-healthier	2909	Algeria	1. Age, 2.Gender, Education, 3. Marital status, 4.Income, 5.Standard of living, 6.Health, 7.Life achievements, 8.Personal relationships, 9.Personal security, 10.Belongingness to the society, 11.Future security, 12.Neighborhood , 13.Friendship , 14.Housing ,15.Marriage, 16.Scientific culture, 17.Literature and Artistic culture, 18.Religious culture ,19.Family, relationships, 20.Use of spare time , 21.Own personality, 22.Extent of personal optimism, 23.Physical appearance, 24.Health factors, 25.Degree of daily, 26.Physical pain, 27.Degree of daily, 28.Anxiety, 29. Degree of daily, and 30. Normal sleep.

93	Tiwari	2009	Poverty and wellbeing at the 'grassroots' - how much is visible to researchers?	Rural households	102	Madhya Pradesh (India)	1. Poverty and 2.Wellbeing.
94	Tsai et al.	2013	Applicability of gross national happiness index to Taiwan	Individuals	950	Taiwan	1. Psychological Well-being, 2.Education, and 3.Culture.

95	Viswanathan and Sharma	2013	Subjective well-being in high assertive women managers	Women manager aged 23−56 years and working in the information technology (IT), information technology-enabled services (ITES), and Manufacturing sectors	60	India	1.General well-being positive, 2.Expectation-achievement congruence, 3.Confidence in coping, Transcendence, 4.Family group support, 5.Social support, 6.Primary group concern, 7.Inadequate mental mastery, 8.Perceived ill-health, 9.Deficiency in social contacts, and General well-being negative.
96	Wahl et al.	2004	Quality of life in the general Norwegian population, measured by the quality of life scale (QoL-N)	Norwegian population aged 19-81 years	1893	Norway	1. Age, 2.Gender, 3.Educational status, 4.Marital status, 5.Work, and 6.Health condition.

97	Wills	2007	Subjective well-being in cities: individual or collective? A cross cultural analysis	Individuals aged 18 years or older	2035	Brazil and Toronto of Canada.	1.Standard of living, 2.Health, 3.Achievement in Life, 4.Personal relationships, 5.Safe, 6.Feeling part of community, 7.Future security, 8.Economic situation, 9.State of Environment,10. Social conditions, 11.Government, 12.Business, and 13. Local security.
98	Wood, Rhodes and Whelan	1989	Sex differences in positive well-being: a consideration of emotional style and marital status	Marrieds	103	Texas (U.S.A.)	1. Age, 2. Marital status, 3.Happiness, 4.Life satisfaction, 5.Positive affect, and 6.General evaluation.
99	Yao et al.	2009	The quality of life in Taiwan	Individuals aged 20 to 69 years	1006	Taiwan	1.Age, 2.Gender, 3.Education, 4.Marital status, 5.Monthly household income, 6.Personal health, 7.Medical care, 8.Job, education, 9.Successful at work, 10.Being famous, 11.Winning over others, 12.Expressing personality/ talents, 13. Interpersonal: family, good with others,

							raising children; material), 14. Eat 15.Comfortable home, 16.Nice things, 17.Income, and 18.Dressing up, 19. Nonmaterial: enjoying pastimes, appreciating art/culture, being devout, and 20.public-life: living without fear of crime, contributing to community/ society, freedom, government, community, and environment.
100	Zhang	2010	Urbanites' life satisfaction research in China: a case study of quality of life in eight cities	Individuals of age group of 25 years to 55 years	1600	Cities of China	1. Gender, 2.Age, 3.Educational level, 4.Marital status, 5. Health, 6.Working status, 7.Family life, 8.Self-development, 9.Material possession and consumption, 10.Social communication, 11.Public service and policy, and 12.Leisure and entertainment.

101	Zullig	2005	Adolescent health-related quality of life and perceived satisfaction with life	adolescents aged 13-18 years	4914	South Carolina, USA	1.Race, 2.Gender, 3.Self-rated health, 4.Physical health days, 5.Mental health days, 6.Activity limitation days, 7.Satisfied with family, 8.Satisfied with friends, 9.Satisfied with school, 10.Satisfied with environment, and 11.Satisfied with overall life.

2.4 RESEARCH GAP

The funnel method (Hofstee, 2006) was implemented for writing research gap of the study. While several studies have addressed different approaches to measuring quality of life of people e.g., a) Objective approach (e.g., Narayana, 2009), b) Subjective approach e.g., Dasgupta and Majumdar, 1996), c) Mixed approach (e.g., Haq, 2009), etc., and unit of analysis studied by researchers were e.g., university students, adult with different age group, elder people (having age group 60 years or more), homeless people, households, etc. This study focuses on a subjective approach of measuring the quality of life of people of Gujarat with attention to people who are doing jobs and belongs to an age group of 25 to 55 years.

In India, subjective well-being approach of measuring the quality of life is a comparative new area of research, due to which large scope of work is present e.g., perceived quality of life can be a measure of people with different age groups, socio-economic class, states, cities, whole countries, etc. Perceived Quality of Life model where a relationship of overall quality of life with different variables is described has not established as per review of selected research papers. In practically, where developed nations are working on Happiness measurement or Subjective well-being approach, In India, even in economically sound states like Gujarat, Government of Gujarat still measuring the well-being of people by using objective indicators of Human Development Index. No concrete presence of

subjective measures of Quality of Life has found in literature as per Indian context. The study was inspired by the work of Dasgupta and Majumdar (1996) where a good attempt had made to measure subjective quality of life of people of Kolkata but the model of Quality of life was not validated in that research. This was the one of the gaps identified for the research. Therefore in this research Structural Equation Modeling technique will be used and the model of perceived quality of life will be validated to fulfil such gap.

After reviewing all selected research papers, like research by Leelakulthanit and Day (2011), Liao, Fu, and Yi (2005), Somarriba, Pena, and Bernardo (2008) and Biswas – Diener and Diener (2001), it was clearly identified that a subjective assessment of well-being of people was based on Hierarchical model of happiness given by Diener, Scollon, and Lucas (1999). Where subjective well-being has four components a) Positive affect, b) Negative affects, c) Overall all Life satisfaction and d) Domains of Life satisfaction. In the study, the same hierarchical modal of happiness was used but with changes in variables which were in the context of Gujarati culture. Diener, Diener, and Diener (1995) identified that at the cultural level there is a positive relationship between individualism and subjective well-being.

Variables of subjective well-being were studied under selected researches. A difference of variables in researches took place in developed, developing and poor nations were clearly noticed. Common variables of subjective well-being in context of developing countries and Indian cultural context were identified, which also used by other researches. These selected variables were taken for the study e.g., age, gender, marital status, education level, income level, Overall Life satisfaction, Positive and Negative affects and Domains of Life satisfaction. The Gap in a selection of variables was also realized. Certain important variables were absent in previous researches e.g., people having a residence in the urban or rural area. Therefore, such variables added in the study like Location of residence which adds value to the study by comparing the rural and urban quality of life. Geographical location of residential area was also added in the study to compare the quality of life of four regions of Gujarat state.

Diener, Lucas, Oishi, and Suh (2002) found that happy individuals were more likely to weight the worst domains in their life heavily. Thus, domains of life satisfaction can provide unique information about a person’s overall well-being. Domains of life satisfaction may important for a researcher to find out the effect of well-being in a

particular area. Researchers, who work with a particular relevant group like students, elderly people, etc., have chosen the domains accordingly. Quality of life domains as notified in previous researches were e.g., satisfaction with self-development, family life, material possession, and local government administration (Dasgupta and Majumdar,1996), satisfaction with income, social relationship, religious and spiritual beliefs, political participation, life events (Biswas-Diener and Diener,2006), general quality of life, personal career, life at work, family life, neighbourhood conditions, network of family and neighborhood, recreation and leisure, personal well-being, appreciation of a peaceful, happy and progressive life (Mukherjee, 1981), etc. There are many domains has identified which were not studied in Indian context by past researchers. Such domains identified were; satisfaction with material possession, spirituality, physical health, government, environment and work life. Therefore, the purpose of this study was to determine the effects of these domains on overall life satisfaction of people.

After reviewing selected research papers it was also found that statistical analysis did by researchers had used tests; parametric tests like t-tests, z-tests, One Way ANOVA, Multiple Regression Analysis, Logistic regression, etc. non-parametric tests like Chi-square test, etc. Multivariate tests like factor analysis, etc. But to validate the conceptual model or to evaluate the structural relationship between measured variables and latent constructs, use of validity test like Structural Equation Modelling was missing, particularly in Indian researches (e.g., Dasgupta & Majumdar, 1996). Such gaps will be removed in the study by applying appropriate statistical tests.

2.5 CONCLUSION

This chapter works as a backbone of the study. As we know a research is a systematic way of finding a solution to the problem. This chapter adds value in terms of by adding a deductive approach to smoothing the research topic, starting from a wide scope to narrow down the scope of the research. This chapter explored many dimensions, which was helpful to understand the problem in-depth. A careful study of literature helps to decide the variables of the study. Research gaps have given space to the study into the existing literature and open opportunity to contribute. Another major contribution of this chapter was it has given an idea of how to conduct research in terms of selection of research methodology in comparison with other researchers. Subjective evaluation of the quality of

life in India (Gujarat) is a challengeable task in terms of decision regarding selection of variables and research design (sampling techniques and sample size determinations) which can justify this study. More or less after this chapter, research topic becomes crystal clear and research design was visible. This chapter worked as a case study of many related research problems, due to which pathway of this study may smoothly be constructed and it provided help in the decision of selection of research tools & techniques like Questionnaire design, scales of measurements, statistical tests, etc. Last but not least, as the topic of the study associated with a new era of measuring the well-being of people and this concept is still new for the Indian society, because of this chapter it becomes familiar to a researcher. This chapter worked as a sailor who takes this study towards its goal. A research methodology chapter follows this chapter in the study.

CHAPTER 3

RESEARCH METHODOLOGY

3.1 INTRODUCTION

3.2 RESEARCH DESIGN

3.3 VARIABLES UNDERSTUDY

3.4 OPERATION DEFINITIONS

3.5 CONCEPTUAL FRAMEWORK

3.6 PILOT STUDY

3.7 SAMPLING DESIGN

3.8 RESEARCH TOOLS

3.9 STATISTICAL DESIGN

3.10 LIMITATIONS OF THE STUDY

3.11 CONCLUSION

3.1 INTRODUCTION

This chapter is a spirit of the study, in other words, it works as a roadmap where details mentioned regarding the plan or blueprint of the study. The previous chapter presented a review of the literature to highlight the gaps in research. This chapter presents the variables of the study, operational definition, conceptual framework, pilot study, sampling design, research tools and statistical design. This chapter is the most critical part of the study where a clear, complete and systematic way of conducting the research has been stated. At each stage, clear reasons and an adequate justification have been given for the way in which study was conducted; starting from the selection of variables for the study of the limitations of the study. This chapter is a mix of knowledge and art of designing a research plan. Whole framework or plan of research was discussed in a sequential order so that research may meet its objectives.

3.2 RESEARCH DESIGN

Characteristics of this study are: study having a clear research question, the research process is formal and structure, an objective of the research is testing the specific hypothesis and examine the relationship between and among selected variables, larger sample size (785 respondents), Data analysis is Quantitative in nature. Finding and results are conclusive, Finding used as input into decision making. Hence, this study has a conclusive research design, where both descriptive research and causal research design is part of it.

3.3 VARIABLES UNDERSTUDY

Variable selection for the study: Variables are derived from a literature review. It was stated in a literature gap analysis that this study having objectives to fulfil gaps present in selected research. Variables are taken from selected researches like Dasgupta and Majumdar (1996), Leelakulthanit and Day (1992), etc. Classification is done by using concepts to club together. The variables intend to test are as follows.

Demographic & Socioeconomic variables: Gender, Age**,** Educational status, Marital status, Income status, Location of residence (Urban/ Rural), Location of residence (Geographic zone).

Key Variables:

1. Overall Life satisfaction
2. Positive and Negative affect:
    a. Enjoyable - Miserable
    b. Interesting-Boring
    c. Active -Inactive
    d. Happy -Unhappy
    e. Meaningful-Meaningless
    f. Worthwhile-Useless
    g. Rewarding-Disappointing
    h. Easy -Hard
    i. Relaxed -Tightened up
    j. Full of fun -No fun at all
    k. Comfortable -Uncomfortable
3. Domains of Life-satisfaction;
    a. Government satisfaction
    b. Material possession satisfaction
    c. Environmental quality satisfaction
    d. Work life satisfaction
    e. Spirituality satisfaction
    f. Physical health satisfaction

3.4 OPERATIONAL DEFINITIONS

People: In this study 'People' refers to the persons who are doing a job, aged 26 or above, but not exceeding 55 years and residing in Gujarat State with, at least for 5 years at the same place (Village / Town / City).

Overall Life Satisfaction/ Perceived Quality of Life: In this study 'Overall life satisfaction' refers to happiness, a satisfaction of the people in their lives and their achievements in life. It is assessed by using The Life Satisfaction Scale is given by Diener, E., Emmons, R. A., Larsen, R. J., and Griffin, S. (1985).

Positive and Negative affect: Positive affect refers to the extent to which one feels active, enthusiastic, alert, etc., whereas negative affect is a dimension of distress and unpleasurable engagement (Diener, Suh, Lucas and Smith, 1999). It is assessed by Semantic Differential Scale.

Domains of Life satisfaction: Well-being relates to the life satisfaction in work, family, marriage, leisure, health, and finances (Diener, Suh, Lucas and Smith, 1999).

Lowe Income Group: Persons belong to a minimum income level of ₹ 1.2 lakhs per annum and not exceeding ₹ 2.5 lakhs per annum.

Middle Income Group: Persons belong to a minimum income level of ₹ 2.51 lakhs per annum and not exceeding ₹ 6 lakhs per annum.

Higher Income Group: Persons belong to a minimum income level of ₹ 6.01 lakh per annum and not exceeding ₹ 12 lakhs per annum.

Rural: According to Census 2011 Report, the basic units of rural areas are the revenue village.

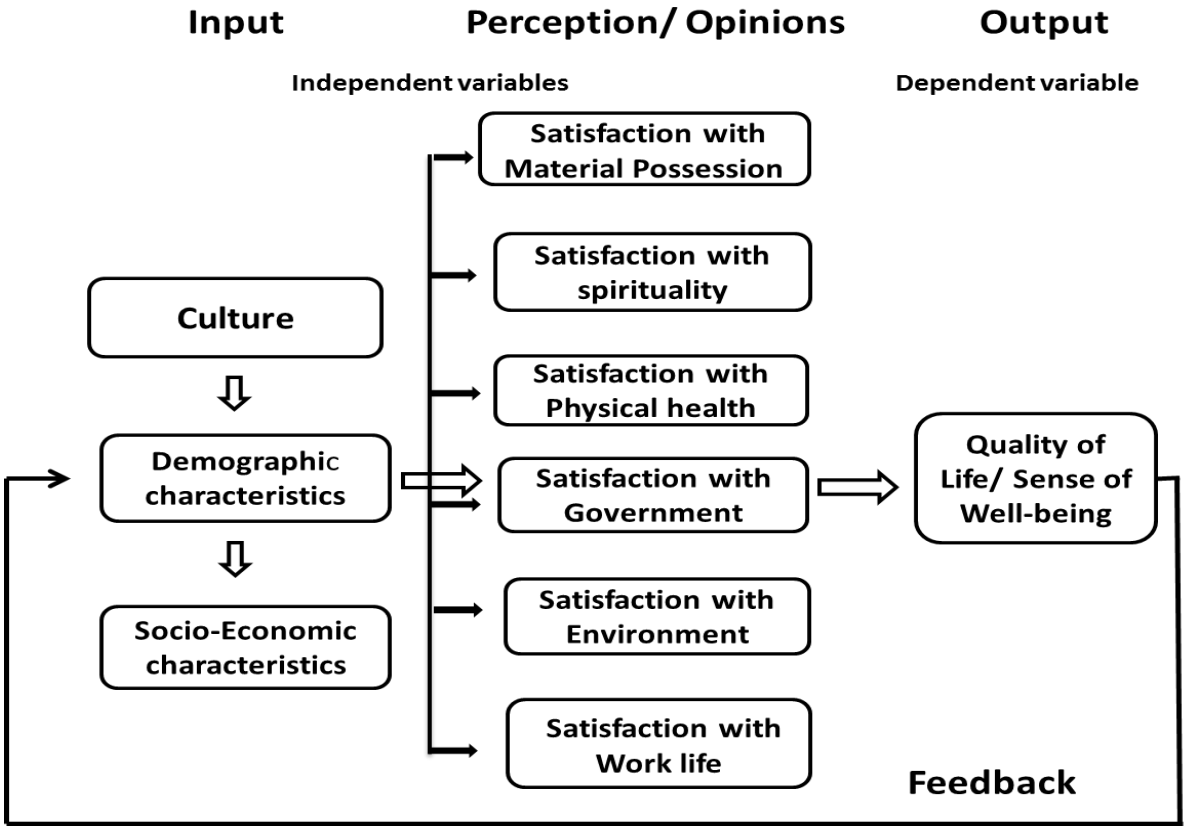
Urban: According to census 2011 report, constituents of urban areas are statutory towns, Census towns and, Out Growths.

3.5 CONCEPTUAL FRAMEWORK

The conceptual framework which is used here is inspired from a system Model of Quality of Life by The University of Oklahoma School of Social Work. Overall quality of life is a composite assessment of the quality of the social, economic and physical environments.

Nine domains have been used to assess the external and internal conditions of overall quality of life. Six of them found significant and shows strong linear association with the overall quality of life. Six Domains of Life Satisfaction are Satisfaction with Material Possession, Satisfaction with spirituality, Satisfaction with Physical Health, Satisfaction with Government, Satisfaction with Environment and Satisfaction with Work Life. The quality of life of each domain was assessed by several indicators, which were then combined to create an overall quality of life.

Fig. 3.1 Conceptual framework



3.6 PILOT STUDY

The pilot study was carried on to ascertain the variables and research design of the research. A PILOT study was conducted in Ahmedabad City in Gujarat state, with a 400 adult (aged 26-55years) sample. It investigated first the relation between variables (demographic and socioeconomic characteristics) and perceived quality of life and then the

relation between domain satisfaction and perceived quality of life. Both descriptive and causal research design has used. The survey instrument measures the residents' life satisfaction in 10 domains: satisfaction with government, Infrastructure, Work-life, Material possession, Relationships, Self-development, Physical health, Environmental quality, Children's education and Recreation activity. EFA, Multiple Regression analysis, PLS-SEM and CB-SEM techniques were used to predict perceived life-satisfaction of people in Ahmedabad city. A discussion with respondents also was conducted to give a brief about research topics to them and their suggestions were incorporated regarding the usefulness and other aspects of the study. Results and conclusions of the pilot study were used to finalize the questionnaire and research design.

3.7 SAMPLING DESIGN

Universe or Target population of the study: The universe/target population of the study includes all persons aged 26 years and above and range up to 55 years and living in the rural or urban areas of Gujarat for more than 5 years at the same place (Village / Town/ City).

Inclusion criteria:

1) The study has included only those persons who are doing a job.
2) The study has included the persons belongs to an age group of 26-55 years;
3) The study has included the persons with a minimum educational qualification of S.S.C.
4) The study has included the persons belonging to a minimum income level of ₹ 1.2 lakh per annum but, maximum income not exceeding ₹ 12 lakhs per annum.
5) The study has included those persons who are either married or unmarried.
6) The study has included both men and women.
7) The study has included respondents from both urban and rural areas.

Exclusion criteria:

1) The study has excluded the physically and mentally challenged persons.
2) The study has excluded the persons residing in tribal areas due to the inconvenience on approaching them.

Sampling frame: As per study requirement, no appropriate sampling frame was present. To prepare such type of source list/ sampling frame at a state level is also not possible under time and resource constraint.

Sampling method: Quota sampling method was used for the study, which is a non-probability sampling method. Quotas were decided in a proportion of the sample as similar to the composition of the population (Bajpai 2017).

A Census of India 2011 was taken as a base to decide the sample in the exact proportion of the distributed population. Approx. 57% percent of the population lives in rural areas and 43 % percent of the population in the urban areas of Gujarat. Approx. 60% percent of the urban population lives in the cities (Municipal Corporation's area). A total population of Gujarat was divided into four zones of Gujarat; Central Gujarat, North Gujarat, Saurashtra and South Gujarat. Their proportions in respective zones are 37% in Central Gujarat, 17% North Gujarat, 29% Saurashtra and 17% in South Gujarat.

Here, four major cities were selected (Ahmedabad, Vadodara, Rajkot and Surat), One Notified Area (Gandhinagar), 5 towns (Palanpur, Surendranagar, Gandhidham. Palitana and Nadiad) and 22 villages of Gujarat (Denap, Rajpur, Tavadia, Sojitra, Dodhiya, Beraja, Panvi, Mesvan, Rampur, Vadala, Gudel, Khada, Vansal, Nar, Nikol, Rampura, Kareli, Kavi, Karjan, Rander, Abrama, Tarsadi). Details of the sample collection, analysis as explained in figure 3.2.

Method of data collection: Survey method was used for data collection. Different modes of a survey were conducted; a) Personal Interviews, b) Office Interviews, c) Self-Administered Questionnaire and d) Mail Survey.

Sample size determination: The Cochran formula allows calculating an ideal sample size given a desired level of precision, desired confidence level, and the estimated proportion of the attribute present in the population. Cochran's formula is considered especially appropriate in situations with large populations.

$$\mathbf{N} = \frac{\boldsymbol{z^2(pq)}}{\boldsymbol{e^2}}$$

Where;

N = the sample size.

z = standard error associated with the chosen level of confidence.

p = estimated percent in the population

q = 100 - p

e = the amount of precision or allowable error in the sample estimate of the population.

Source: Bartlett, J. et al. (2001). Organizational Research: Determining Appropriate Sample Size in Survey Research.

95% level of confidence is used, so z = 1.96. Next, the p = q = 50% situation is customarily assumed as it is the worst possible case of variability. Let's take a ±3.5% sample error.

Using the sample size formula, the sample size, n, is calculated as follows.

Sample size computed with p = 50%, q = 50%, and e = 3.5%

$$\mathbf{N} = \frac{\mathbf{1.96^2(0.5*0.5)}}{\mathbf{0.035^2}}$$

$$\mathbf{N} = \frac{\mathbf{3.84(0.25)}}{\mathbf{0.001225}} = \frac{\mathbf{0.96}}{\mathbf{0.001225}} = \mathbf{784\ (rounded\ up).}$$

Source: Burns, Veeck, and Bush (2017), Marketing Research, pp.276.

- The Sample size for the study was determined by two parameters; a) supervisor as well as expert's advice and b) by considering resource and time limitation.

- Initially, a sample of 1000 responded was shortlisted but after the data cleaning process, 785 respondents constituted for this study.

Sampling framework has described by tables and charts as mentioned below.

Table 3.1 Sample collections in North-Gujarat

North- Gujarat (Ss =132)				
Urban (Town) - 57		Rural-75		
Municipal Corporation- 30	Municipality -27	District	Taluka	Village
Gandhinagar (30)	Palanpur (27)	Mahesana	Visnagar	Denap (20)
		Mahesana	Kadi	Rajpur (20)
		Patan	Sidhpur	Tavadia (20)
		Patan	Chanasma	Sojitra (15)

Table 3.2 Sample collections in Central-Gujarat

Central-Gujarat (Ss =290)				
Urban (Town) - 125		Rural-165		
Municipal Corporation- 109	Municipality -16	District	Taluka	Village
Ahmedabad (85)	Ankleshwar (16)	Anand	Khambhat	Gudel (21)
Vadodara (24)		Anand	Tarapur	Khada (21)
		Anand	Umret	Vansol (21)
		Anand	Petlad	Nar (21)
		Kheda	Kapadvanj	Nikol (20)
		Kheda	Kapadvanj	Rampura (20)
		Bharuch	Jambusar	Kareli (20)
		Bharuch	Jambusar	Kavi(21)

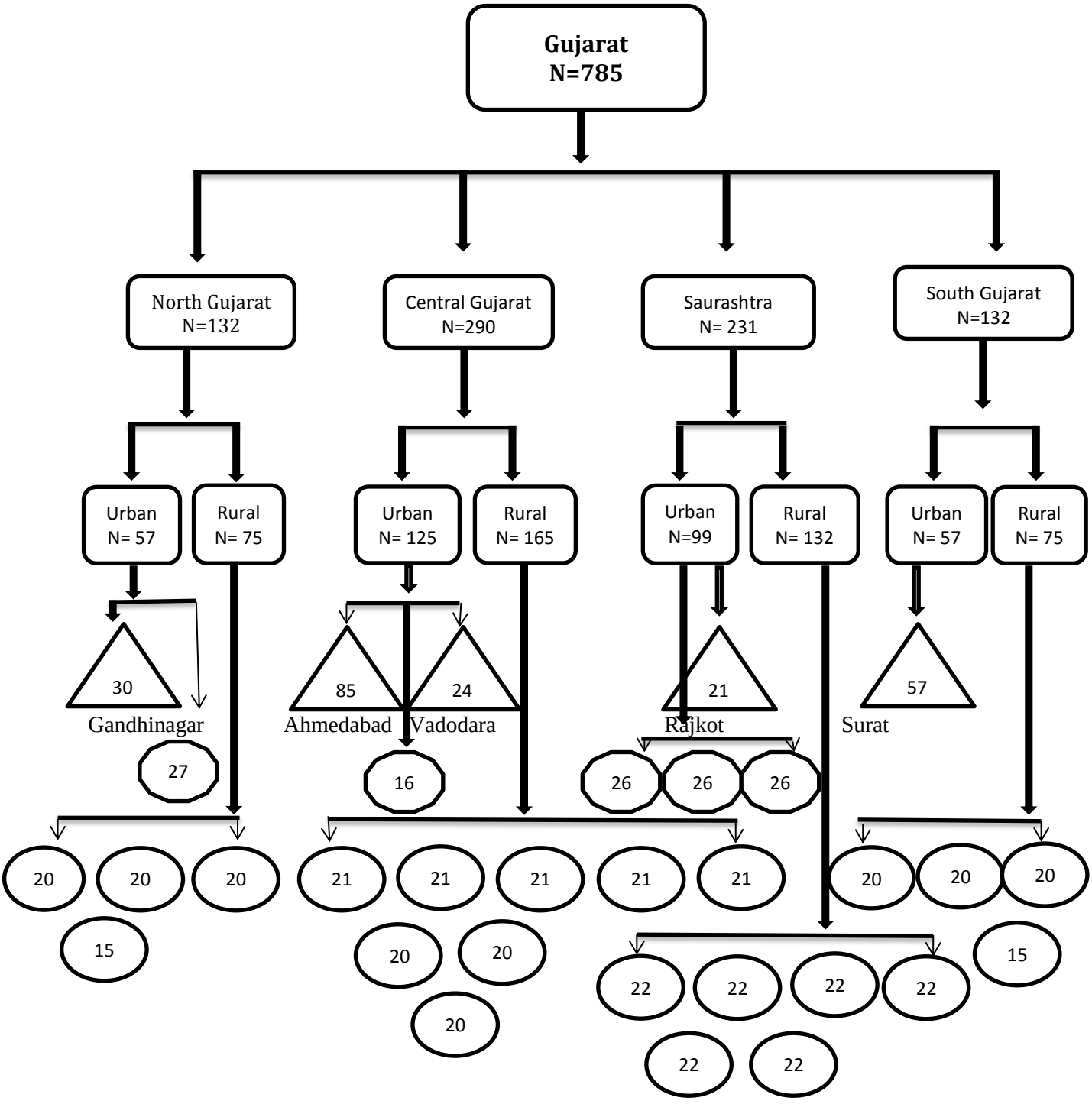
Table 3.3 Sample collection in Saurashtra

Saurastra (Ss =231)				
Urban (Town) - 99		Rural-132		
Municipal Corporation- 21	Municipality -78	District	Taluka	Village
Rajkot (21)	Surendranagar (26)	Jamnagar	Jamnagar	Dodhiya (22)
	Gandhidham (26)	Jamnagar	Jamnagar	Beraja (22)
	Palitana (26)	Junagadh	Visavadar	Panvi (22)
		Junagadh	Keshod	Mesvan (22)
		Amreli	Kunkavav Vadia	Rampur (22)
		porbandar	Porbandar	Vadala (22)

Table 3.4 Sample collection in South-Gujarat

South- Gujarat (Ss =132)				
Urban (Town) - 57		Rural-75		
Municipal Corporation- 57	Municipality -00	District	Taluka	Village
Surat (57)		Surat	Kamrej	Karjan (20)
		Surat	Olpad	Rander (20)
		Navsari	Jalalpore	Abrama(20)
		Navsari	Navsari	Tarsadi (15)

Fig. 3.2 Sampling framework



3.8 RESEARCH TOOLS

Life satisfaction scale

The Life Satisfaction Scale of Diener, E., Emmons, R. A., Larsen, R. J., and Griffin, S. (1985) has been used in the study. A 5-item scale was designed to measure global cognitive judgments of one's overall life satisfaction. Participants expressed how much they disagreed or agreed with each of the 5 items using 7-point scales that range from 1 strongly disagree to 7 strongly agree. Test-retest reliability coefficient (Cronbach's alpha value) of this scale in the present sample was found to be as high as **0.681.**

Semantic differential scale

Campbell et al. (1976) designed a scale using "Semantic Differential Technique." With the help of 17 bi-polar adjectives they solicited from people how do they feel about their present life. The current study has modified the same scale and used 11 bipolar adjectives for measuring how they feel about their present life. Test-retest reliability coefficient (Cronbach's alpha value) of this scale in the present sample was found to be as high as **0.886.**

Life-domain satisfaction scale

A sense of wellbeing was assessed by using the "life domain satisfaction scale." Initially, 38 statements (variables) were drafted, but later on, at the model validation stage, it was reduced to 20 variables which give six latent factors. A seven-point scale (from strongly disagree to strongly agree) has been used to measure satisfaction with each domain. Test-retest reliability coefficient (Cronbach's alpha value) of this scale in the present sample was found to be as high as **0.884**.

3.9 STATISTICAL DESIGN

Analysis of the collected data was subjected by statistical methods using M. S. Excel: 2010, SPSS (Statistical Package for Social Sciences): 21 and AMOS: 21 software. Tables and charts used for presentation of statistical method output are for clear understanding and to derive inferences.

I. The scores of the Semantic Differential Scale were subjected to exploratory factor analysis with varimax rotation to determine the underlying latent factors of one's Quality of Life. Ratings of satisfaction with life scale were further classified into groups. Compare means, method has been used to compare means of factors of semantic differential scale and means of classified groups.

II. Classification methods like Tree Segmentation Method have been used for data mining and better graphical segmentation of the sample of overall life satisfaction with different demographic and socioeconomic variables. The Tree Segmentation technique gives an idea to the reader that how the whole sample has segmented.

III. General characteristics of the sample in terms of age, gender, marital status, education, income, residence and other key variables were identified by calculating descriptive statistics such as mean and percent.

IV. The Likert's scale has been used for data measurement. Normality of data was assumed. Parametric tests like one sample t-test, Independent sample t-test; One Way ANOVA has been used for hypothesis testing.

V. Multiple regression analysis was used to predict the relationship between overall life satisfactions with six domains of life satisfaction.

VI. Confirmatory factor analysis was used to confirm the reliability and validity of the Perceived Quality of Life (PQoL) model.

3.10 LIMITATIONS OF THE STUDY

The present study targets persons only from two areas i.e., rural and urban areas of Gujarat, as such the findings cannot be generalized to tribal areas of Gujarat and also persons residing all over India. The study is restricted up to persons who are doing a job with a certain age group, income group, and education status. Advance aged people were excluded from the sample as they were non-earners/ unemployed.

Three scales have been used: a) Satisfaction with life scale; b) Semantic differential scale; and c) Life domain satisfaction scale. The whole study examines the Subjective Well-Being of people in Gujarat, following the theory of Diener et al. (1999).

3.11 CONCLUSION

In this chapter, the practical way in which the whole research project was organized has discussed. To conduct this research in a systematic way a proper justification and supportive arguments added in each sub-parts of the study, so that the reader, as well as examiners, may understand the spirit behind each move of the research. This chapter was divided into many subparts: research design, variables under study, operational definitions, conceptual framework, pilot study, sampling design, research tools, statistical design and limitations of the study. Here, both theoretical and practical aspects of the conduct of the research were discussed in order to achieve sense and simplicity. The discussion starts with how the epistemological stance which has been adopted provides a link between the aims and the practical methodological issue of collecting data. An epistemological approach was used which consists of the assumptions regarding the study, concerning the nature of the knowledge which is as valid in order to resolve the research question.

CHAPTER 4

RESULTS

4.1 INTRODUCTION

4.2 RESULTS OF COMPARE MEANS

4.3 RESULTS OF TREE SEGMENTATION

4.4 RESULTS OF HYPOTHESIS TESTING

4.5 RESULTS OF CONFIRMATORY FACTOR ANALYSIS

4.6 CONCLUSION

4.1 INTRODUCTION

In this chapter, different data analysis strategies and statistical tests were discussed. The data analysis is one of the important chapters of this study and one of the most critical parts where statistical tests have been used. Selection of the appropriate statistical tests was the biggest challenge of this part. Here, both logical and artistic minds were used to give proper justification to each part of the data analysis. Sequence of tests was carefully designed as per the requirement of analysis of data. The chapter has been divided into many subparts as per the results of different statistical test.

The normality of the data was verified which is the prime requirement before applying any statistical test. The normality of the data was tested through data visualization like Histogram and P-P plot test (Hair Jr., Black, Babin, and Anderson, 2015). Shapiro Wilk Test was also applied. According to Central Limit Theorem, higher sample size leads to achieve normality (Black, 2013). Mostly Parametric tests were used because 1) data were collected on an interval scale, 2) normality of data was assumed and 3) parametric tests are more powerful (Cooper et al., 2012) for qualitative analysis. Results of statistical tests were presented in sequence to meet the objectives of the study.

4.2 RESULTS OF COMPARE MEANS

Result of overall life satisfaction through life satisfaction scale is as shown in Table: 4.1.

Table 4.1 Descriptive statistics of overall life satisfaction

	N	Mean	Std. Deviation
Overall Life Satisfaction	785	5.1070	.86559
Valid N	785		

The sample data was classified into three groups on the basis of the life satisfaction scale ratings as shown in Table: 4.2.

Table 4.2 Classified groups based on overall life satisfaction

	Frequency	Percent	Cumulative Percent
Highly satisfied	161	20.5	20.5
Moderately satisfied	476	60.6	81.1
Poorly satisfied	148	18.9	100.0
Total	785	100.0	

Three groups were classified namely: a) highly satisfied group, b) moderately satisfied group, and c) poorly satisfied group. Classification was done on the basis of methodology (Dasgupta and Majumdar, 1996) mentioned as under.

On the basis of Mean and Standard Deviation of the Life satisfaction ratings (ratings given by respondents on life satisfaction scale) the total sample was classified in to three groups: a) highly satisfied (whose life satisfaction rating > Mean + Standard deviation), b) moderately satisfied (Whose life satisfaction rating > Mean - Standard deviation but less than Mean + Standard deviation), and c) poorly satisfied (Whose life satisfaction rating < Mean - Standard deviation).

Exploratory Factor Analysis: Semantic Differential Scale

The study was initiated with a view to understand as to what constitutes the quality of life. For this Semantic differential scale was subjected to Exploratory Factor Analysis with Varimax rotation to determine the underlying attributes of one's Quality of life. This was done with a view to explain the power of the attributes in helping us to rank the variables.

Table 4.3 KMO and BARTLETT'S test

Kaiser-Meyer-Olkin Measure of Sampling Adequacy.		**.889**
Bartlett's Test of Sphericity	Approx. Chi-Square	4688.152
	df	55
	Sig.	**.000**

KMO is the measure of sampling adequacy and used to examine the appropriateness of data. The KMO = **0.889** > 0.7 implies that the sample data is good for factor analysis. Significance level for Bartlett's Test of Sphericity =0.000 < 0.05 (5% level of significance) indicates that factor analysis is useful for reduction of data. The KMO as well as Bartlett's Test yielded very good results. So, Factor Analysis was considered appropriate.

The initial and final communalities were obtained as given in Table 4.4. It is desirable that extracted factors explain minimum 50% of the variance of each of the variables (Hair Jr. et. al., 2015). Here, all communalities > 0.5 means that, extracted factors explain more than

Table 4.4 Initial and final communalities

	Initial	Extraction
Enjoying	1.000	.612
Interesting	1.000	.645
Active	1.000	.659
Happy	1.000	.672
Meaningful	1.000	.665
Worthwhile	1.000	.640
Rewarding	1.000	.544
Easy	1.000	.646
Relaxed	1.000	.808
Full of Fun	1.000	.657
Comfortable	1.000	.659

Extraction Method: Principal Component Analysis.

50% of the variance for each of the variables and so extraction of factors was appropriate (Brace, Kemp, and Snelgar 2006).

Table 4.5 Correlation matrix of eleven variables

	Enjoying	Interesting	Active	Happy	Meaningful	Worthwhile	Rewarding	Easy	Relaxed	Full of fun	Comfortable
Enjoying	1.00	.663	.483	.556	.508	.574	.523	.308	.289	.494	.320
Interesting	.663	1.00	.500	.667	.606	.525	.444	.348	.273	.432	.252
Active	.483	.500	1.00	.609	.584	.516	.468	.104	.079	.285	.159
Happy	.556	.667	.609	1.00	.614	.544	.488	.323	.280	.434	.321
Meaningful	.508	.606	.584	.614	1.00	.644	.495	.284	.253	.402	.280
Worthwhile	.574	.525	.516	.544	.644	1.00	.615	.349	.267	.462	.306
Rewarding	.523	.444	.468	.488	.495	.615	1.00	.367	.384	.478	.354
Easy	.308	.348	.104	.323	.284	.349	.367	1.00	.671	.498	.475
Relaxed	.289	.273	.079	.280	.253	.267	.384	.671	1.00	.583	.647
Full of fun	.494	.432	.285	.434	.402	.462	.478	.498	.583	1.00	.586
Comfortable	.320	.252	.159	.321	.280	.306	.354	.475	.647	.586	1.00

In table 4.5, Variables had good correlation coefficients among them; this was a good indication of factorability (Brace et. al., 2006). Data were fit for factor analysis.

Table 4.6 Total variance explained

Component	Initial Eigenvalues			Extraction Sums of Squared Loadings			Rotation Sums of Squared Loadings		
	Total	% of Variance	Cumulative %	Total	% of Variance	Cumulative %	Total	% of Variance	Cumulative %
1	5.411	49.188	49.188	5.411	49.188	49.188	4.251	38.642	38.642
2	**1.795**	**16.318**	**65.507**	**1.795**	**16.318**	**65.507**	**2.955**	**26.864**	**65.507**
3	.653	5.934	71.441						
4	.587	5.341	76.781						
5	.561	5.101	81.883						
6	.449	4.084	85.967						
7	.372	3.380	89.347						
8	.349	3.173	92.520						
9	.328	2.984	95.504						
10	.254	2.312	97.816						
11	.240	2.184	100.000						

Extraction Method: Principal Component Analysis.

Initial Eigen values: Eigen value for each component in the table is a variance of the component/factor extracted (Hair Jr. et al. 2015).

Component 1 explains **49.188%** and Component 2 explains **16.318%** of the variance. The variance explained by both the factors = **65.507 %.**

In the above table, **65.507 %** of the variance is explained by two factors extracted which were quite good.

Table 4.7 Rotated component matrix

	Component	
	Exhilarating	Relaxing
Active	**.810**	
Meaningful	**.797**	
Happy	**.791**	
Interesting	**.774**	
Worthwhile	**.757**	
Enjoying	**.733**	
Rewarding	**.633**	
Relaxed		**.894**
Comfortable		**.796**
Easy		**.784**
Full of fun		**.707**

Rotation Method: Varimax with Kaiser Normalization.[a]

a. Rotation converged in 3 iterations.

A factor loading matrix for extracted factors had mentioned in Table 4.7. Factor loadings are the correlation coefficients between variables and factors. Good factor loadings were observed in Table 4.7. Approx. all factors had loading more than 0.7, which was a quiet good sign. Higher factor loading shows a strong association between variable and factor.

Labelling Factors: Factors were labelled by considering higher values of factor loadings. The combination of attributes under factor: 1 named as **"Exhilarating"** and under the factor: 2 named as **"Relaxing".** New dimensions were named as**; exhilarating** and **relaxing.**

Compare Means

Compare means statistical method was applied by comparing means of three classified groups (Refer Table: 4.2); 1) highly satisfied, 2) moderately satisfied and 3) poorly satisfied group by means of factors extracted from semantic differential scale ratings (Refer Table: 4.7). Result of compare means as shown in Table: 4.8.

Table 4.8 Compare means of three classified groups

	Perceived Quality of Life			
	Highly satisfied	Moderately satisfied	Poorly satisfied	Total
Exhilarating				
Enjoying	6.37	5.71	4.74	5.66
Interesting	6.24	5.57	4.95	5.59
Active	6.54	5.82	5.37	5.89
Happy	6.52	5.83	5.07	5.83
Meaningful	6.25	5.65	4.95	5.64
Worthwhile	6.24	5.55	4.87	5.56
Relaxing				
Rewarding	6.17	5.36	4.72	5.40
Easy	5.50	4.53	4.13	4.65
Relaxed	5.34	4.67	3.93	4.67
Full of fun	5.78	5.08	4.23	5.07
Comfortable	5.54	4.96	3.83	4.87

As shown in Table: 4.8, highly satisfied group (Overall life satisfaction) predominantly scores high on both factors 1 (Exhilarating) and 2 (Relaxing). Their orientation towards life is positive. They live life with a sense of well-being like Enjoying, Interesting, Active, Happy, Meaningful, Worthwhile, Rewarding, Easy, Relaxed, Full of Fun and Comfortable. Moderately satisfied group (Overall life satisfaction) shows the same pattern like highly satisfied one, but in comparative lessor degree. Dissatisfied group (Overall life satisfaction) also shows the same pattern like first two, but in comparative poorest degree.

4.3 RESULTS OF TREE SEGMENTATION

What factors influence overall life satisfaction?

To give an answer of this question, Tree classification method was used. The Tree segmentation method used for graphical representation of data mining (Rao, 2016). To get an idea about key variables which help in identifying segments. The iterative process works with repeated application of Chi-square test between target variable Y and each one of the different predictor variables. The Predictor variable which gives the smallest p-value provides the basis for the first partition from the root node.

Dependent variable: Sample data were classified into three groups on the basis of the life satisfaction scale ratings as shown in Table: 4.2. P.98. Three Groups were: highly satisfied group, moderately satisfied group and poorly satisfied group.

Independent variables: Individual's Gender, Age, Education, Marital status, Income, Residence (zones of Gujarat) and Residence (rural-urban).

1. Gender: Male, Female.
2. Age: 26–35 years, 36-45 years and 46 -55 years.
3. Education: Postgraduate, Graduate, Undergraduate.
4. Marital status: Unmarried, Married.
6. Annual income: ₹ 1.2- ₹ 2.5 lakhs, ₹ 2.51- ₹ 6 lakhs, ₹ 6.01- ₹ 12 lakhs.
7. Residence: Geographical zones.
8. Residence: Village, Town.

∴ **CHAID (Chi-square Automatic Interactive Detection)** algorithm was used for classification. Tree segmentation model summary as shown in Table: 4.9.

CHAID is a combination of heuristic as well as statistical methods, which examines relationships between many categorical predictor variables and categorical target variables. It applies the Chi-square test of independence, also called contingency table, between the target variable and each of the predictor independent variable using the multi-way cross tab table.

Table 4.9 Tree classification model summary

Growing Method	CHAID
Dependent Variable	swcoding
Independent Variables	Gender, Age, Education, Marital status, Income, Residence3(zones), Residence2(rural-urban)
Validation	None
Maximum Tree Depth	3
Minimum Cases in Parent Node	100
Minimum Cases in Child Node	50
Independent Variables Included	Income, Gender
Number of Nodes	5
Number of Terminal Nodes	3
Depth	2

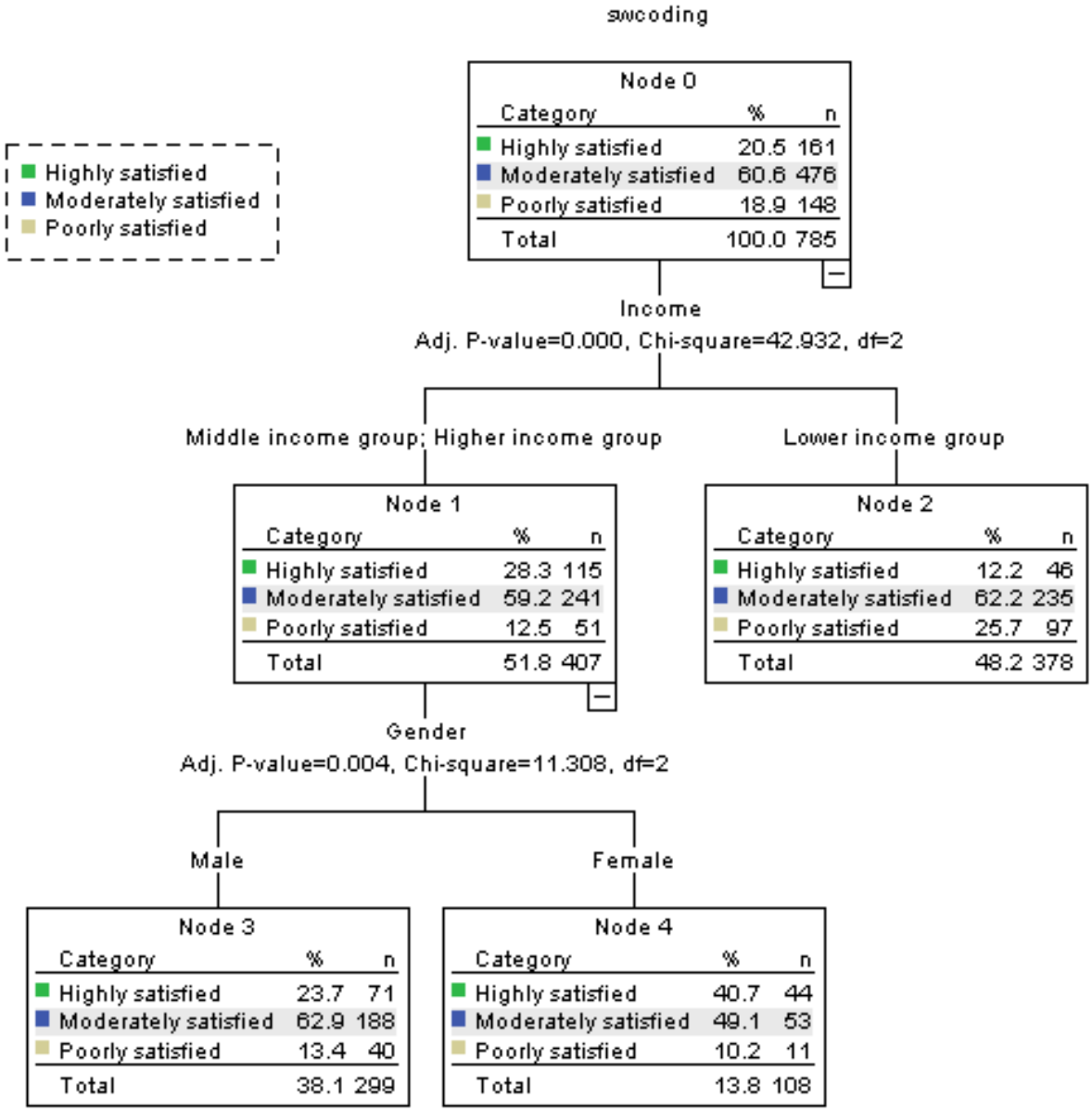
How the Algorithm works: The algorithm starts with a target variable, usually taking up values of 1 or 0. It starts with a base node called the root node (node 0) in CHAID. The root node gives the response rate as well as the total size of the sample being considered in the database (Rao, 2016).

Thereafter the Chi-square test of Independence is carried out multiple times, every time the two variables considered in the cross-tab are target variable and each of all the other variables in the database. The variable having the largest Chi-square value is selected, which is associated with the smallest level of p-value. The tree split from the root node based on the variable.

A node, which only has branches coming out, is the root node and any node which only has branches coming in is called terminal node. A node which has branches coming out and leading to other nodes is called parent node and the nodes which follow the parent node is called child node. After the tree has grown, each terminal node may be considered as a candidate to be a target market, provided the response rate (response percentage) of this terminal node is greater than the response percentage of the root node.

Tree segmentation graph as shown in Figure: 4.1

Fig. 4.1 Tree classification



Interpretation: Node 0 became the parent node to child Nodes 1 and 2. Nodes 3 and 4 became the terminal Nodes. Annual income and gender are the most significant variables in deciding factor of overall life satisfaction of individuals. Node 1: Individuals belong to middle income group and higher income group are mostly either highly satisfied or moderately satisfied with their overall life satisfaction. Further split of Node 1 into Node 3 and Node 4, based on the gender of the respondents. It reveals that females are comparatively highly satisfied in their overall life satisfaction than males. Node 2:

Individuals who belong to lower income group are mostly either moderately satisfied or dissatisfied in their overall life satisfaction.

As an indicator of model fit CHAID provides a risk estimate (Rao 2016). The risk estimate was computed as follows:

The hit ratio (p) = $\frac{number\ of\ individuals\ correctly\ classified}{total\ number\ of\ individuals\ in\ the\ sample}$

The risk estimate, q= 1- p.

Standard error of the risk = sqrt $\frac{p*(1-p)}{n}$

Table 4.10 Risk estimate of Tree classification model

Estimate	Std. Error
.394	.017

Growing Method: CHAID, Dependent Variable: swcoding

Risk estimate and its standard error: It is a measure of the tree's predictive accuracy. The risk estimate is the proportion of cases incorrectly classified after adjustment for prior probabilities and misclassification costs. Here, percentage of risk on prediction accuracy was 39.4% (Refer Table: 4.10 & Table: 4.11).

Table 4.11 Classification, percentage correctly classified

Observed	Predicted			
	Highly satisfied	Moderately satisfied	Poorly satisfied	Percent Correct
Highly satisfied	0	161	0	0.0%
Moderately satisfied	0	476	0	100.0%
Poorly satisfied	0	148	0	0.0%
Overall Percentage	**0.0%**	**100.0%**	**0.0%**	**60.6%**

Growing Method: CHAID
Dependent Variable: swcoding

4.4 RESULTS OF HYPOTHESIS TESTING

1. H_O: People are neutral towards their perceived quality of life.
   H_1: People are not neutral towards their perceived quality of life

Table 4.12 One-sample t-test statistic description of people's perceived quality of life

	N	Mean	Std. Deviation	Std. Error Mean
SW	785	**5.1070**	.86559	.03089

Table 4.13 One-sample t-test result of people's perceived quality of life

	Test Value = 4					
	t	df	Sig. (2-tailed)	Mean Difference	95% Confidence Interval of the Difference	
					Lower	Upper
SW	35.832	784	**.000**	1.10701	1.0464	1.1677

Interpretation: Here, p-value **0.000 < 0.05**. So, we reject the null hypothesis. The alternate hypothesis is accepted. People are not neutral towards their perceived quality of life.

As shown in Table: 4.12, Mean value = 5.1070 which shows people were somewhat satisfied toward their perceived quality of life.

2. H_O: There is no significant difference in perceived quality of life of males and females

   H_1: There is a significant difference in perceived quality of life of males and females

Table 4.14 Statistics description of perceived quality of life of males and females

	Gender	N	Mean	Std. Deviation	Std. Error Mean
SW	Male	579	5.0656	.83104	.03454
	Female	206	5.1699	1.02670	.07153

Table 4.15 Independent samples t-test result of perceived quality of life of male and females

		Levene's Test for Equality of Variances		t-test for Equality of Means						
		F	Sig.	t	df	Sig. (2-tailed)	Mean Difference	Std. Error Difference	95% Confidence Interval of the Difference	
									Lower	Upper
SW	Equal variances assumed	16.591	**.000***	-1.450	783	.147	-.10427	.07191	-.24544	.03690
	Equal variances not assumed			-1.313	305.818	**.190****	-.10427	.07943	-.26058	.05204

***Interpretation:** Sig. value **0.000 < 0.05,** condition of homogeneity of variances is not satisfied.

****Interpretation:** Here, p-value **0.190 > 0.05**. So, we accept the null hypothesis. There is no significant difference in perceived quality of life of males and females.

3. H_0: There is no significant difference in perceived quality of life of people with different age groups.

H_1: There is a significant difference in perceived quality of life of people with different age groups.

Table 4.16 Test of homogeneity of variances of perceived quality of life of people with different age groups

Levene Statistic	df1	df2	Sig.
.358	2	782	**.699**

Interpretation: Sig. value **0.699 > 0.05**, condition of homogeneity of variances is satisfied.

Table 4.17 One Way Anova of perceived quality of life of people with different age groups

	Sum of Squares	df	Mean Square	F	Sig.
Between Groups	8.542	2	4.271	5.769	**.003**
Within Groups	578.870	782	.740		
Total	587.411	784			

Interpretation: Here, p-value **0.003 < 0.05**. So, we reject the null hypothesis. The alternate hypothesis is accepted. There is a significant difference in perceived quality of life of people with different age groups.

Table 4.18 Tukey test result of perceived quality of life of people with a different age groups

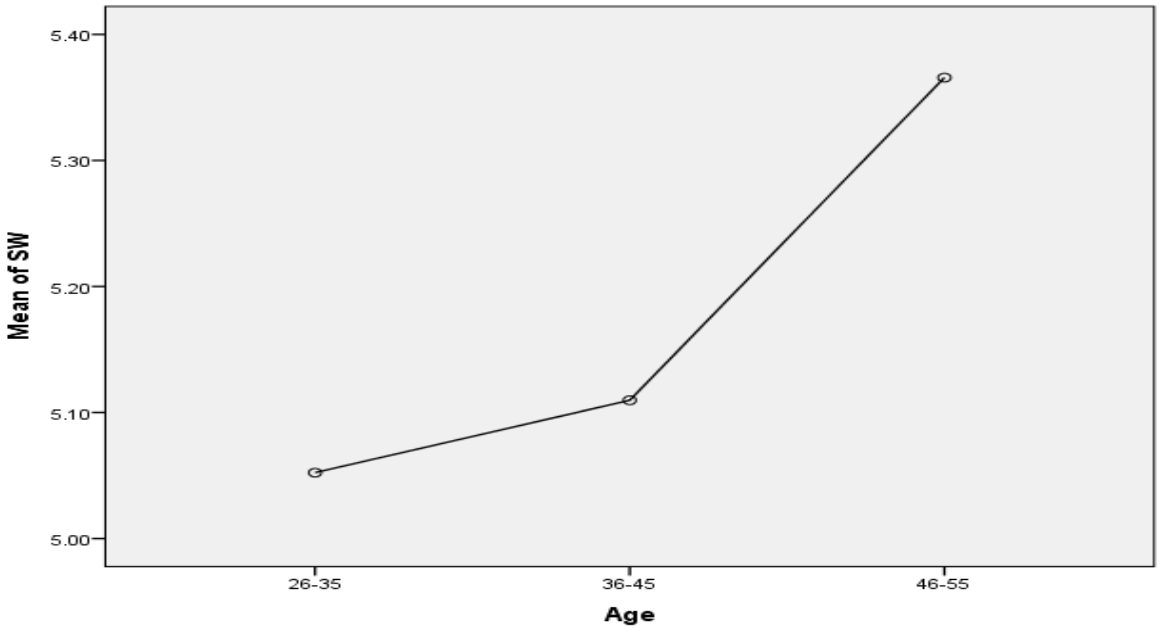
Age	N	Subset for alpha = 0.05	
		1	2
26-35	505	**5.0523**	
36-45	175	**5.1097**	
46-55	105		**5.3657**
Sig.		.807	1.000

Means for groups in homogeneous subsets are displayed.

a. Uses Harmonic Mean Sample Size = 174.233.

b. The group sizes are unequal. The harmonic mean of the group sizes is used. Type I error levels are not guaranteed.

Fig. 4.2 Means of perceived quality of life of people with different age groups



Interpretation: As per table 4.18 and fig. 4.2, Mean value of life satisfaction ratings of People in the age group 46-55 years was higher in comparison to Mean value of life satisfaction ratings of people of age group 26-35 years and 36-45 years, So it clearly shows that people of age group 46-55 years were more satisfied with their quality of life compared to people of age group 26-35 years and 36-45 years.

4. H_0: There is no significant difference in perceived quality of life of people with different educational status.

   H_1: There is a significant difference in perceived quality of life of people with different educational status.

Table 4.19 Test of homogeneity of variances of perceived quality of life of people with different educational status

Levene Statistic	df1	df2	Sig.
2.923	2	782	**.054**

Interpretation: Sig. value **0.054 > 0.05,** condition of homogeneity of variances is satisfied.

Table 4.20 One Way Anova of perceived quality of life of people with different educational status

	Sum of Squares	df	Mean Square	F	Sig.
Between Groups	3.506	2	1.753	2.348	**.096**
Within Groups	583.905	782	.747		
Total	587.411	784			

Interpretation: Here, p-value **0.096 > 0.05**. So, we accept the null hypothesis. There is no significant difference in perceived quality of life of people with different educational status.

Table 4.21 Tukey test result of perceived quality of life of people with different educational status

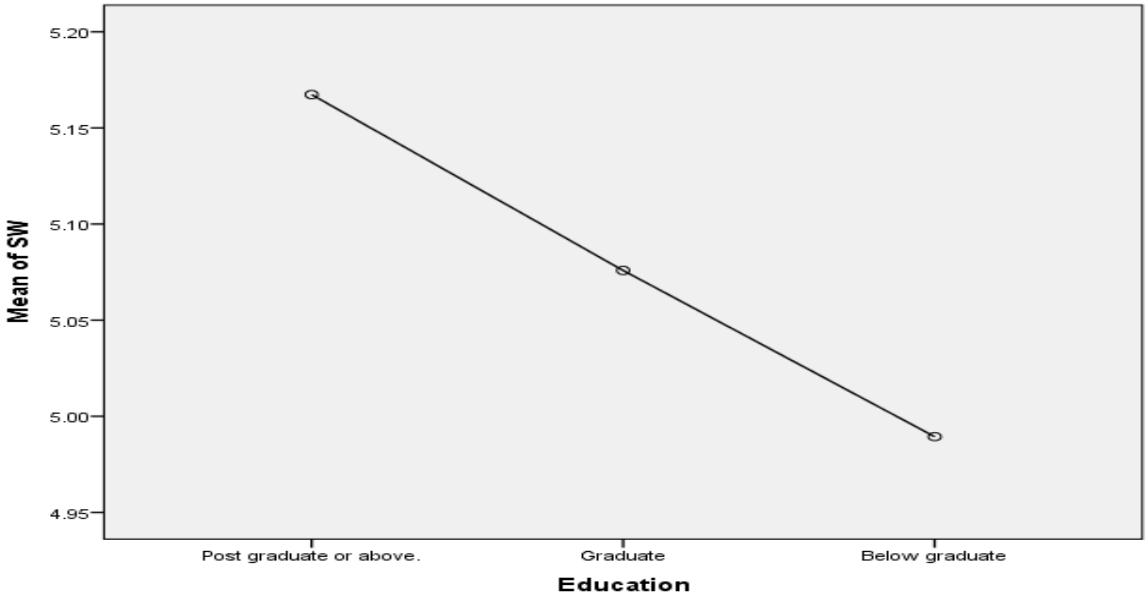
Education Status	N	Subset for alpha = 0.05
		1
Below graduate	132	**4.9894**
Graduate	261	**5.0759**
Postgraduate or above.	392	**5.1673**
Sig.		.084

Means for groups in homogeneous subsets are displayed.

a. Uses Harmonic Mean Sample Size = 214.927.

b. The group sizes are unequal. The harmonic mean of the group sizes is used. Type I error levels are not guaranteed.

Fig. 4.3 Means of perceived quality of life of people with different educational status



Interpretation: As per Table 4.21 and Fig. 4.3, Mean values of life satisfaction ratings of Individuals with different education status were comparative same. No significant difference found. There was no difference in the quality of life of people with different education status.

5. H_0: There is no significant difference in perceived quality of life of people with different marital status.

   H_1: There is a significant difference in perceived quality of life of people with different marital status.

Table 4.22 Group statistics of perceived quality of life of people with different marital status

	Marital status	N	Mean	Std. Deviation	Std. Error Mean
SW	Unmarried	211	**4.8948**	.85173	.05864
	Married	574	**5.1850**	.85825	.03582

Table 4.23 Independent sample t- test of perceived quality of life of people with different marital status

	Levene's Test for Equality of Variances		t-test for Equality of Means						
	F	Sig.	t	df	Sig. (2-tailed)	Mean Difference	Std. Error Difference	95% Confidence Interval of the Difference	
								Lower	Upper
Equal variances assumed	.409	**.523***	-4.209	783	**.000****	-.29023	.06896	-.42559	-.15487
Equal variances not assumed			-4.224	376.781	.000	-.29023	.06871	-.42534	-.15512

***Interpretation:** Sig. value **0.523 > 0.05,** condition of homogeneity of variances is satisfied.

****Interpretation:** Here, p-value **0.000 < 0.05**. So, we reject the null hypothesis. The alternate hypothesis is accepted. There is a significant difference in perceived quality of life of people with different marital status. By comparing mean scores as shown in Table: 4.22, it was found that perceived qualities of life of married are higher than unmarried.

6. H_0: There is no significant difference in perceived quality of life of people with different income groups.

H_1: There is a significant difference in perceived quality of life of people with different income groups.

Table 4.24 Test of homogeneity of variances of perceived quality of life of people with different income groups

Levene Statistic	df1	df2	Sig.
1.463	2	782	**.232**

Interpretation: Sig. value **0.232 > 0.05**, condition of homogeneity of variances is satisfied.

Table 4.25 One Way Anova perceived quality of life of people with different income groups

	Sum of Squares	df	Mean Square	F	Sig.
Between Groups	33.876	2	16.938	23.929	**.000**
Within Groups	553.535	782	.708		
Total	587.411	784			

Interpretation: Here, p-value **0.000 < 0.05**. So, we reject the null hypothesis. The alternate hypothesis is accepted. There is a significant difference in perceived quality of life of people with different income groups.

Table 4.26 Tukey test result perceived quality of life of people with different income groups

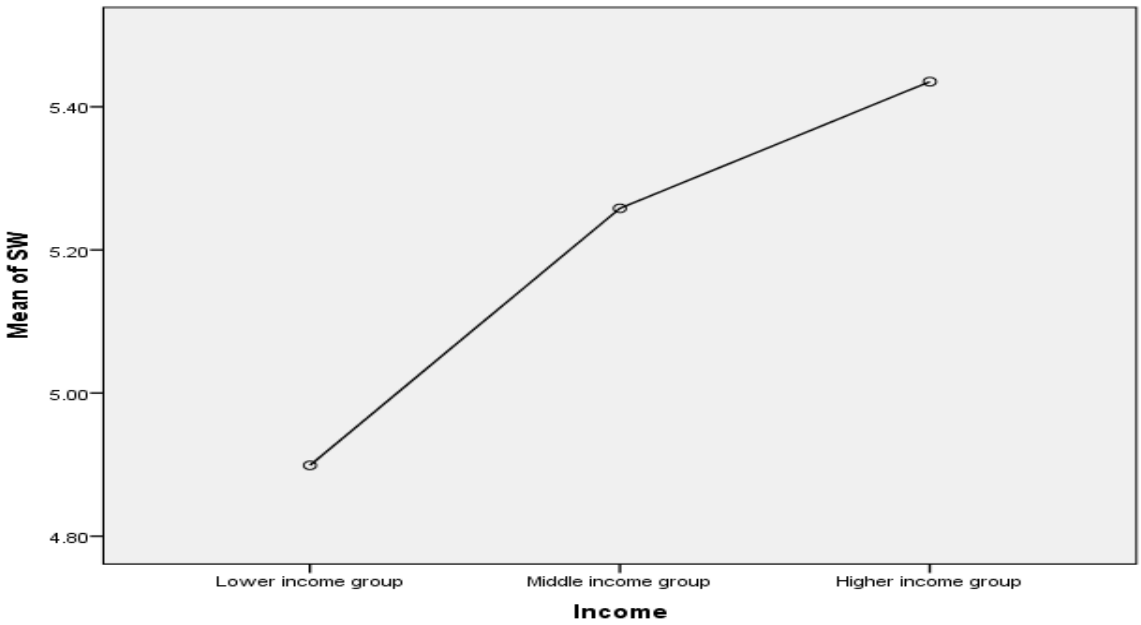
Income Group	N	Subset for alpha = 0.05	
		1	2
Lower income group	378	4.8989	
Middle income group	310		**5.2581**
Higher income group	97		**5.4351**
Sig.		1.000	.107

Means for groups in homogeneous subsets are displayed.

a. Uses Harmonic Mean Sample Size = 185.407.

b. The group sizes are unequal. The harmonic mean of the group sizes is used. Type I error levels are not guaranteed.

Fig. 4.4 Means of perceived quality of life of people with different marital status



Interpretation: As per table 4.26 and fig. 4.4, Mean values of life satisfaction ratings of people of higher and middle income groups were higher in comparison to Mean value of life satisfaction ratings of people of lower income group. So, it was clearly shown that individuals with higher and middle income groups were more satisfied with their quality of life compared to people of lower income group.

7. H_0: There is no significant difference in perceived quality of life of people of Central-Gujarat, South-Gujarat, Saurashtra and North-Gujarat.

H_1: There is a significant difference in perceived quality of life of people of Central-Gujarat, South-Gujarat, Saurashtra and North-Gujarat.

Table 4.27 Test of homogeneity of variances of perceived quality of life of people of Central-Gujarat, South-Gujarat, Saurastra and North-Gujarat

Levene Statistic	df1	df2	Sig.
3.548	3	781	**.014**

Interpretation: Sig. value **0.014 < 0.05**, condition of homogeneity of variances is **not satisfied.**

Table 4.28 One Way Anova of perceived quality of life of people of Central-Gujarat, South-Gujarat, Saurastra and North-Gujarat

	Sum of Squares	df	Mean Square	F	Sig.
Between Groups	2.082	3	.694	.926	**.428**
Within Groups	585.329	781	.749		
Total	587.411	784			

Interpretation: Here, p-value **0.428 > 0.05**. So, we accept the null hypothesis. There is no significant difference in perceived quality of life of people of Central- Gujarat, South-Gujarat, Saurastra and North-Gujarat.

∴ As the Levene test of Homogeneity of Variances is not satisfied (Refer Table: 4.27). Test result of One Way ANOVA is not reliable.

Table 4.29 Tukey test result of perceived quality of life of people of Central-Gujarat, South-Gujarat, Saurastra and North-Gujarat

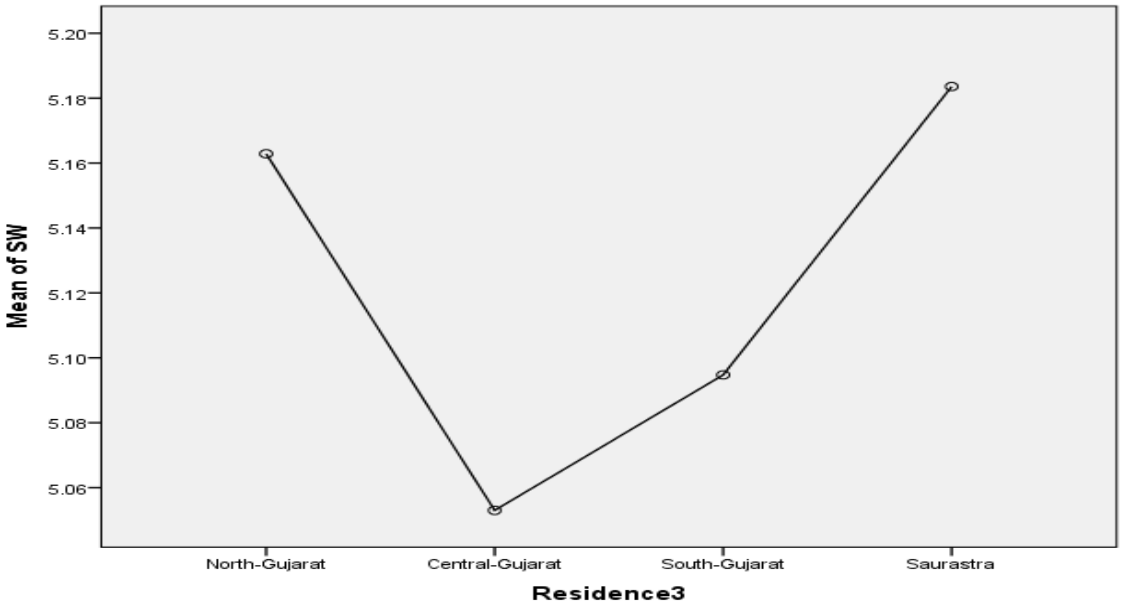
Residence	N	Subset for alpha = 0.05
		1
Central-Gujarat	283	**5.0530**
South-Gujarat	228	**5.0947**
North-Gujarat	140	**5.1629**
Saurashtra	134	**5.1836**
Sig.		.486

Means for groups in homogeneous subsets are displayed.

a. Uses Harmonic Mean Sample Size = 177.580.

b. The group sizes are unequal. The harmonic mean of the group sizes is used. Type I error levels are not guaranteed.

Fig. 4.5 Means of perceived quality of life of people of Central- Gujarat, South-Gujarat, Saurashtra and North-Gujarat



Interpretation: As per table 4.29 and fig. 4.5, Mean values of life satisfaction ratings of the people of Central-Gujarat, South-Gujarat, Saurastra and North-Gujarat were nearly same. No significant difference found. It was found that the perceived quality of life of people of Central-Gujarat, South-Gujarat, Saurashtra and North-Gujarat were same.

8. H_0: There is no significant difference in perceived quality of life of people of rural and urban Gujarat.

H_1: There is a significant difference in perceived quality of life of people of rural and urban Gujarat.

Table 4.30 Group statistics of perceived quality of life of people of rural and urban Gujarat

Residence	N	Mean	Std. Deviation	Std. Error Mean
Rural	447	**5.0881**	.89924	.04253
Urban	338	**5.1320**	.81963	.04458

Table 4.31 Independent sample t- test of life of people of rural and urban Gujarat

	Levene's Test for Equality of Variances		t-test for Equality of Means						
	F	Sig.	t	df	Sig. (2-tailed)	Mean Difference	Std. Error Difference	95% Confidence Interval of the Difference	
								Lower	Upper
Equal variances assumed	2.839	**.092***	-.702	783	**.483****	-.04381	.06241	-.16633	.07871
Equal variances not assumed			-.711	756.251	.477	-.04381	.06162	-.16477	.07715

***Interpretation:** Sig. value **0.092 > 0.05,** condition of homogeneity of variances is satisfied.

****Interpretation:** Here, p-value **0.483 > 0.05**. So, we accept the null hypothesis. There is no significant difference in perceived quality of life of the people of rural and urban Gujarat.

9. Ho: There is no significant relationship between overall life satisfaction and different domains of life satisfaction.

H_1: There is a significant relationship between overall life satisfaction and different domains of life satisfaction.

Exploratory Factor Analysis

The Life Domains Satisfaction scale was subjected to Exploratory Factor Analysis with Varimax rotation to determine the underlying attributes of Overall Life Satisfaction.

Table 4.32 KMO and Bartlett's test

Kaiser-Meyer-Olkin Measure of Sampling Adequacy.		**.838**
Bartlett's Test of Sphericity	Approx. Chi-Square	9133.654
	df	190
	Sig.	**.000**

KMO is a measure of sampling adequacy and used to examine the appropriateness of data (Brace et al. (2006). KMO = **0.838** > 0.7 implies that sample data was good for factor analysis (Brace et al. (2006). Significance level for Bartlett's Test of Sphericity = 0.000 < 0.05 (5% level of significance) indicates that factor analysis is useful for reduction of data.

The KMO as well as Bartlett’s Test yielded very good results. So, Factor Analysis was considered appropriate to apply.

The initial and final communalities were obtained as follows (Table 4.33):

Table 4.33 Communalities

	Initial	Extraction
LDS2	1.000	.582
LDS3	1.000	.686
LDS4	1.000	.763
LDS5	1.000	.572
LDS6	1.000	.811
LDS7	1.000	.920
LDS8	1.000	.829
LDS12	1.000	.724
LDS14	1.000	.682
LDS15	1.000	.763
LDS16	1.000	.792
LDS17	1.000	.833
LDS18	1.000	.870
LDS19	1.000	.765
LDS29	1.000	.548
LDS30	1.000	.666
LDS31	1.000	.757
LDS36	1.000	.730
LDS37	1.000	.873
LDS38	1.000	.825

Extraction Method: Principal Component Analysis.

It is desirable that extracted factors explain minimum 50% of the variance of each of the variables (Hair Jr. et al., 2015). Here, all communalities > 0.5 means that, extracted factors explain more than 50% of the variance for each of the variables and so extraction of factors is appropriate.

Correlation matrix as shown in Table: 4.34, Data is fit for factor analysis.

Table 4.34 Correlation matrix of initial pool of constructs

	LDS 16	LDS 17	LDS 18	LDS 19	LDS 2	LDS 3	LDS 4	LDS 5	LDS 6	LDS 7	LDS 8	LDS 36	LDS 37	LDS 38	LDS 29	LDS 30	LDS 31	LDS 14	LDS 15	LDS 12
LDS16	1.00	.759	.748	.681	.240	.182	.195	.224	.387	.421	.403	.236	.238	.211	.247	.193	.202	.308	.474	.384
LDS17	.759	1.00	.812	.692	.204	.189	.205	.175	.353	.335	.322	.222	.214	.230	.223	.152	.218	.232	.395	.276
LDS18	.748	.812	1.00	.779	.210	.158	.205	.176	.349	.408	.381	.215	.228	.219	.256	.212	.217	.232	.356	.273
LDS19	.681	.692	.779	1.00	.150	.129	.149	.158	.316	.349	.358	.175	.182	.222	.245	.218	.182	.219	.349	.312
LDS2	.240	.204	.210	.150	1.00	.510	.530	.357	.269	.220	.160	.157	.153	.183	.061	.070	.046	.180	.251	.286
LDS3	.182	.189	.158	.129	.510	1.00	.620	.447	.206	.179	.158	.191	.241	.246	.165	.102	.057	.156	.235	.276
LDS4	.195	.205	.205	.149	.530	.620	1.00	.586	.318	.284	.183	.270	.272	.284	.219	.112	.094	.197	.224	.275
LDS5	.224	.175	.176	.158	.357	.447	.586	1.00	.324	.311	.240	.221	.249	.220	.198	.197	.101	.163	.308	.393
LDS6	.387	.353	.349	.316	.269	.206	.318	.324	1.00	.821	.680	.277	.299	.238	.171	.114	.159	.225	.251	.312
LDS7	.421	.335	.408	.349	.220	.179	.284	.311	.821	1.00	.832	.315	.346	.292	.174	.127	.128	.225	.263	.309
LDS8	.403	.322	.381	.358	.160	.158	.183	.240	.680	.832	1.00	.226	.250	.210	.100	.143	.109	.188	.277	.304
LDS36	.236	.222	.215	.175	.157	.191	.270	.221	.277	.315	.226	1.000	.704	.626	.207	.108	.140	.164	.213	.190
LDS37	.238	.214	.228	.182	.153	.241	.272	.249	.299	.346	.250	.704	1.00	.816	.283	.167	.203	.234	.230	.199
LDS38	.211	.230	.219	.222	.183	.246	.284	.220	.238	.292	.210	.626	.816	1.00	.311	.144	.203	.236	.248	.203
LDS29	.247	.223	.256	.245	.061	.165	.219	.198	.171	.174	.100	.207	.283	.311	1.00	.344	.470	.247	.287	.195
LDS30	.193	.152	.212	.218	.070	.102	.112	.197	.114	.127	.143	.108	.167	.144	.344	1.00	.559	.235	.324	.216
LDS31	.202	.218	.217	.182	.046	.057	.094	.101	.159	.128	.109	.140	.203	.203	.470	.559	1.00	.233	.208	.130
LDS14	.308	.232	.232	.219	.180	.156	.197	.163	.225	.225	.188	.164	.234	.236	.247	.235	.233	1.00	.564	.496
LDS15	.474	.395	.356	.349	.251	.235	.224	.308	.251	.263	.277	.213	.230	.248	.287	.324	.208	.564	1.00	.618
LDS12	.384	.276	.273	.312	.286	.276	.275	.393	.312	.309	.304	.190	.199	.203	.195	.216	.130	.496	.618	1.00

In table 4.34, Variables having good correlation coefficients among them, this is a good indication of factorability (Brace et al., 2006). A good correlation among variable induces factors formations and also gives higher factor loadings. By above table, it clearly visualizes that the data are appropriate to proceed for further step of the factors extraction process.

Table 4.35 Total variance explained

Component	Initial Eigenvalues			Extraction Sums of Squared Loadings			Rotation Sums of Squared Loadings		
	Total	% of Variance	Cumulative %	Total	% of Variance	Cumulative %	Total	% of Variance	Cumulative %
1	6.468	32.341	32.341	6.468	32.341	32.341	3.266	16.328	16.328
2	2.239	11.194	43.535	2.239	11.194	43.535	2.626	13.130	29.458
3	1.878	9.388	52.923	1.878	9.388	52.923	2.547	12.734	42.192
4	1.771	8.854	61.777	1.771	8.854	61.777	2.471	12.353	54.545
5	1.419	7.097	68.874	1.419	7.097	68.874	2.105	10.523	65.067
6	**1.216**	**6.082**	**74.956**	**1.216**	**6.082**	**74.956**	**1.978**	**9.888**	**74.956**
7	.679	3.397	78.352						
8	.665	3.323	81.675						
9	.485	2.423	84.099						
10	.481	2.405	86.504						
11	.414	2.070	88.574						
12	.398	1.992	90.565						
13	.369	1.846	92.411						
14	.301	1.504	93.915						
15	.294	1.469	95.384						
16	.266	1.329	96.713						
17	.228	1.142	97.855						
18	.179	.894	98.749						
19	.145	.726	99.475						
20	.105	.525	100.000						

Extraction Method: Principal Component Analysis.

Initial Eigenvalues: Eigenvalues for each component in the table is a variance of the component/factor extracted.

Component 1 explains **32.341%,** Component 2 explains **11.194%,** Component 3 explains **9.388%,** Component 4 explains **8.854%,** Component 5 explains **7.097%** and Component 6 explains **6.082%** of the variance. The variance explained by all six the factors = **74.956 %.**

In the table above, **74.956 %** of the variance is explained by six factors, which is quite good and thus 6 factors were extracted.

Table 4.36 Rotated component matrix

	Component					
	Government satisfaction	Material Possession satisfaction	Environmental satisfaction	Physical Health satisfaction	Work-life satisfaction	Spirituality satisfaction
LDS18	**.892**					
LDS17	**.880**					
LDS19	**.838**					
LDS16	**.808**					
LDS4		**.841**				
LDS3		**.810**				
LDS2		**.732**				
LDS5		**.680**				
LDS7			**.900**			
LDS8			**.867**			
LDS6			**.838**			
LDS37				**.896**		
LDS38				**.871**		
LDS36				**.823**		
LDS14					**.788**	
LDS15					**.784**	
LDS12					**.771**	
LDS31						**.856**
LDS30						**.785**
LDS29						**.668**

Extraction Method: Principal Component Analysis.

Rotation Method: Varimax with Kaiser Normalization.[a]

a. Rotation converged in 6 iterations.

Labelling Factors: Factors were labelled by considering higher values of factor loadings. As shown in Table: 4.36, Factors were labelled as under: the combination of attributes under factor: 1 named as "Government satisfaction", under factor: 2 named as "Material Possession satisfaction", under factor: 3 named as "Environmental satisfaction", under factor: 4 named as "Physical health satisfaction", under factor: 5 named as "Work life satisfaction" and under factor: 6 named as "Spirituality satisfaction".

Table 4.37 Exploratory factor analysis showing factor loadings and reliability

Item No.	Questions	Factor Loading	Factor Name & Reliability
LDS18	I am satisfied with central government position on civil rights.	.892	Government satisfaction Cronbach's α= 0.919
LDS17	I am satisfied with international relation policies with neighbor countries of central government.	.880	
LDS19	I am satisfied with central government policies to solve the problems like unemployment, poverty, inflation, corruption, terrorism, etc.	.838	
LDS16	I am satisfied with internal economic policies of central government (like Interest rates, Income tax slab, etc.).	.808	
LDS4	I am satisfied with my clothing, accessories & jewelry.	.841	Material Possession satisfaction Cronbach's α= 0.800
LDS3	I am satisfied with my vehicle.	.810	
LDS2	I am satisfied with my furniture and appliances at home.	.732	
LDS5	I am satisfied with my saving & investment.	.680	
LDS7	I am satisfied with quality of air in my village/town/city.	.900	Environmental satisfaction Cronbach's α= 0.912
LDS8	I am satisfied with greenery in my village/town/city.	.867	
LDS6	I am satisfied with weather in my village/town/city.	.838	
LDS37	I feel sufficient energy/stamina to live full life.	.896	Physical Health satisfaction Cronbach's α= 0.879
LDS38	I feel sufficient body mobility/speed to live full life.	.871	
LDS36	I feel free from disease/ disorder.	.823	
LDS14	I am satisfied with working hours & timings.	.788	Work Life satisfaction Cronbach's α= 0.791
LDS15	I am satisfied with my career growth.	.784	
LDS12	I am satisfied with personal income.	.771	
LDS31	I had felt paranormal/spiritual experience.	.856	Spirituality satisfaction Cronbach's α= 0.718
LDS30	I am associated with Guru.	.785	
LDS29	I am working on self-discovery.	.668	

As shown in Table: 4.37 factors loading of each item and Internal Consistency (Reliability) of factors had shown. According to Hair Jr. et. al., (2015), factor loadings $\pm$ .50 or greater are considered practically significant and loadings exceeding 0.70 are considered indicative of well-defined structure. Here, most of all factors loading of six factors were greater to 0.7 and good internal consistency (All six's $\alpha > 0.7$).

Multiple Regression analysis

Extracted factors (table 4.37) were domains of life satisfaction. To test the hypothesis no. 9 (pp.119) Multiple regression analysis technique was applied, where Overall life satisfaction taken as dependent variable and these domains of life satisfaction work as domains of life satisfaction.

Table 4.38 Variables entered/removed

Model	Variables Entered	Variables Removed	Method
1	Spirituality satisfaction, Work-life satisfaction, Physical health satisfaction, Environmental satisfaction, Material possession satisfaction, Government satisfaction[b]	.	Enter

a. Dependent Variable: Overall Life satisfaction

b. All requested variables entered.

Table 4.39 Regression model summary

Model	R	R Square	Adjusted R Square	Std. Error of the Estimate	Durbin-Watson
1	.592[a]	.350	**.345**	.70047	**1.871**

a. Predictors: (Constant), Spirituality satisfaction, Work life satisfaction, Physical health satisfaction, Environmental satisfaction, Material possession satisfaction, Government satisfaction

Interpretation: The Adjusted R^2 value tells us that our model accounts for **34.5%** of variance explained which indicate it is a respective model as per social science research. Standard error of model is **0.70047**. This is the standard deviation of actual values of Y about the estimated Y values.

TABLE 4.40 One way ANOVA test result

Model		Sum of Squares	df	Mean Square	F	Sig.
1	Regression	205.674	6	34.279	69.862	**.000[b]**
	Residual	381.737	778	.491		
	Total	587.411	784			

a. Dependent Variable: Overall Life satisfaction

b. Predictors: (Constant), Spirituality satisfaction, Work life satisfaction, Physical health satisfaction, Environmental satisfaction, Material possession satisfaction, Government satisfaction

Interpretation: p < .05 the model is significant. So, we reject the null hypothesis. The alternate hypothesis is accepted. There is a significant relationship between overall life satisfaction and different domains of life satisfaction.

Table 4.41 Coefficients of regression model

Model	Unstandardized Coefficients		Standardized Coefficients	t	Sig.	Collinearity Statistics	
	B	Std. Error	Beta			Tolerance	VIF
(Constant)	5.107	.025		204.272	.000		
Government satisfaction	.168	.025	.194	6.721	.000*	1.000	1.000
Material possession satisfaction	**.351**	.025	.406	14.047	.000*	1.000	1.000
Environmental satisfaction	.111	.025	.129	4.448	.000*	1.000	1.000
Physical health satisfaction	**.223**	.025	.257	8.906	.000*	1.000	1.000
Work life satisfation	.133	.025	.153	5.299	.000*	1.000	1.000
Spirituality satisfaction	.176	.025	.203	7.037	.000*	1.000	1.000

Interpretation: All predictors variable's *p values are less than .05. So, all predictor variables are significant.

Regression Equation:

The Generalized equation **(**Gujarati, Porter and Guasekar, 2012, pp. 203.**)** is

$$\mathbf{Y} = \beta_0 + \beta_1 X_1 + \beta_2 X_2 + \beta_3 X_3 + \ldots\ldots + \beta_n X_n + \varepsilon$$

Where

Y= dependent variable.

X_i = independent variables (the explanatory variables or repressors).

β_0 = a constant, the value of Y when all X values are zero.

β_i = the slope of the regression surface (The β represents the partial regression coefficient associated with each X_i .

$\boldsymbol{\varepsilon}$ = an error term, normally distributed about a mean 0 (For purposes of computation, the $\boldsymbol{\varepsilon}$ is assumed to be 0 (Cooper and Schindler, 2010).

The impact of sense of well-being in term satisfaction with the different domains of life was investigated by estimating the following regression model

$$\mathbf{PQoL} = \beta_0 + \beta_1 \, DOL_1 + \beta_2 \, DOL_2 + \beta_3 \, DOL_3 + \ldots\ldots + \beta_n \, DOL_n + \varepsilon$$

Where,

PQoL = Perceived Quality of Life

DOL_i = Satisfaction with an ith Domain of Life; i= 1, 2, 3, 4, 5 & 6.

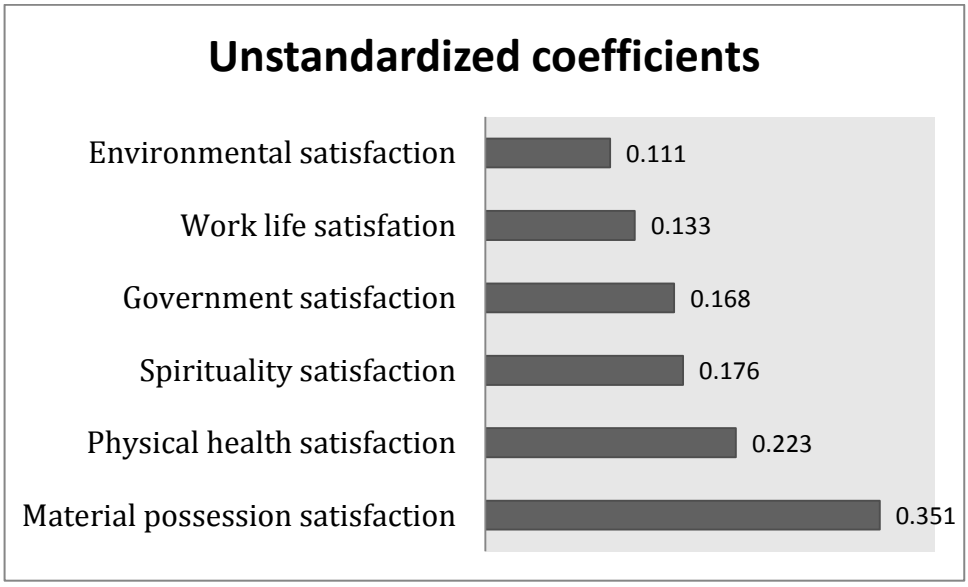
(eg. i =1 = Government satisfaction, i = 2= Material possession satisfaction, i = 3 = Environmental satisfaction, i = 4= Physical health satisfaction, i = 5 = Work life satisfaction, i = 6= Spirituality satisfaction).

The column headed "**B**" shows the unstandardized regression coefficients for the equation in Table 4.41. The Ordinary Least Square (OLS) equation may construct as

PQoL = $\mathbf{5.107} + \mathbf{0.168}$ (Government satisfaction) +
$\mathbf{0.351}$ (Material possession satisfaction) + $\mathbf{0.111}$ (Environmental satisfaction) +
$\mathbf{0.223}$ (Physical health satisfaction) + $\mathbf{0.133}$(Work life satisfation) +
$\mathbf{0.176}$ (Spirituality satisfaction).

$\therefore$ The unstandardized coefficient, for each predictor variable shows the predicted increase in the value of the criterion variable for a 1 unit increase in that predictor (while controlling for the other predictors).

Fig. 4.6 Unstandardized coefficients of predictor's variables



In Table 4.41, reveals that all six domains of life satisfactions were significant. About weightage of these domains of life satisfaction on overall life satisfaction of respondents, Material Possession Satisfaction and Physical Health Satisfaction were more influential, followed by Spirituality Satisfaction, Government Satisfaction, Work life Satisfaction and Environmental Satisfaction (Fig. 4.6).

Assumption Check of Regression Analysis

According to Gujarati et al. (2012), regression equation should satisfy following assumptions:

1. The mean of residuals is **zero**.
2. Residuals are **normally distributed.**
3. Error (Residual) variances are constant **(Homoscedascity).**
4. There is **no Multicollinearity**.
5. There is **no autocorrelation.**

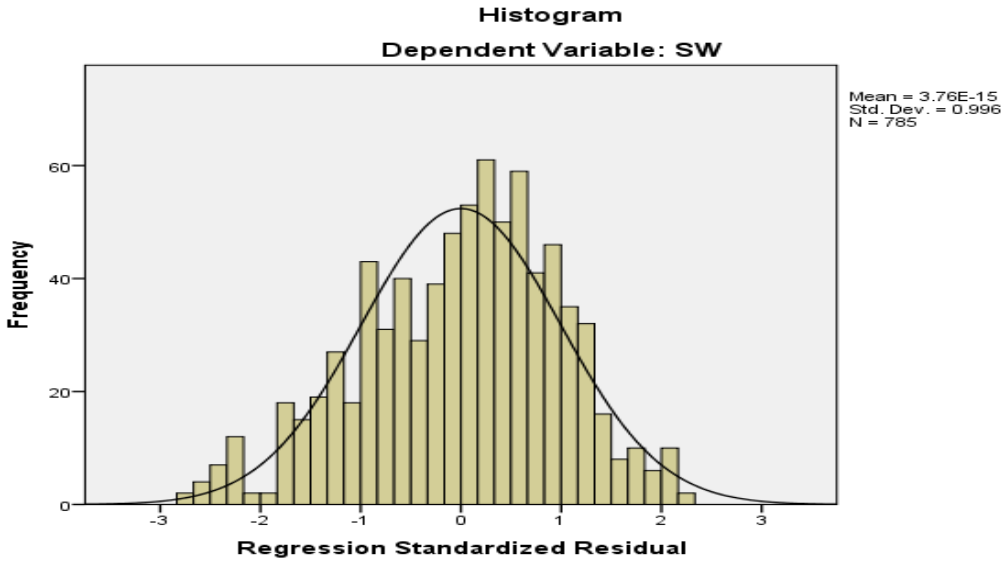
Table 4.42 Residuals statistics

	Minimum	Maximum	Mean	Std. Deviation	N
Predicted Value	3.3431	6.3083	5.1070	.51219	785
Residual	-1.89480	1.51812	.00000	.69779	785
Std. Predicted Value	-3.444	2.345	.000	1.000	785
Std. Residual	-2.705	2.167	**.000**	.996	785

a. Dependent Variable: SW

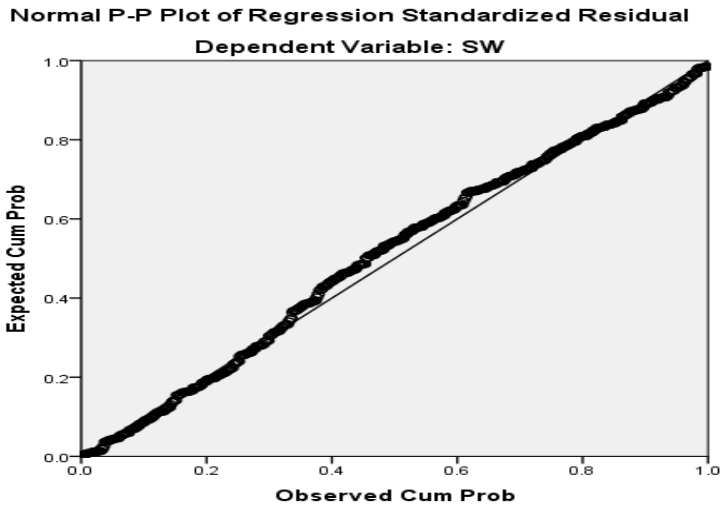
In table 4.42, Mean value of residuals is **zero.**

Fig. 4.7 Histogram



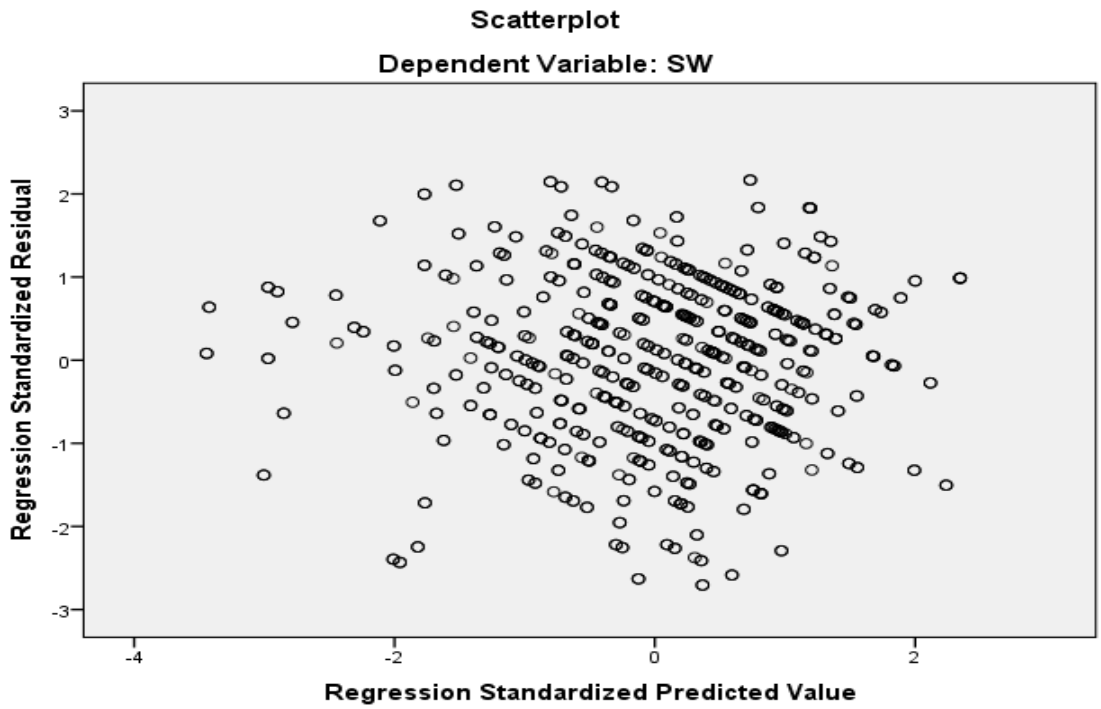
In fig. 4.7, it is found that residuals are normally distributed by constructing Bell shape.

Fig. 4.8 Normal p-p plot



In fig. 4.8, it is found that Residuals are formed straight regression line, which indicates they are normally distributed.

Fig. 4.9 Scatterplot



In fig. 4.9, No pattern was found, errors (residuals) are having constant, variance also called Homoscedascity (Field, 2006).

Multicollinearity check: All predictors variable's tolerance values greater than 0.2 and VIF values less than 5 (Field, 2006). There is no sign of multicollinearity found (Refer Table: 4.41).

Durbin Watson value is **1.871** (Ref. Table 4.39).

Durbin Watson table value: Models with an intercept (from Savin and White, 1977) at 5% significance points of dL and dU, T= 800. K=6; **DL 1.87126, DU 1.89641**

Durbin Watson value of our regression equation is under DL and DU limit of Durbin Watson table; hence null hypothesis is accepted, the residuals from an ordinary least-square regression has **no autocorrelation** at 5% significance level, T=800 and K=6 (Field 2006).

∴ K is the number of regressor excluding the intercept and T= Sample size.

Basic assumptions/conditions check in a given regression analysis:

1. Mean of residuals is **zero**: condition satisfied (Refer Table: 4.42).
2. Residuals are **normally distributed**: condition satisfied (Refer Figure: 4.7 & 4.8).
3. Error (Residual) variances are constant **(Homoscedascity):** condition satisfied (Refer Figure: 4.9).
4. There is **no Multicollinearity**: condition satisfied (Refer Table: 4.41).
5. There is **no autocorrelation** (∴Durbin Watson value **1.871** as per Table: 4.39).

All assumptions of regression line were satisfied. So, we can accept the model.

4.5 RESULTS OF CONFIRMATORY FACTOR ANALYSIS

Confirmatory factor Analysis: Validation of the Structural model (Byrne, 2001).

Unidimensionality: This requirement was achieved by item-deletion procedure of low factor loading items and cross loading items (Hair Jr. et. al., 2015), Refer Table: 4.43.

Table 4.43 Deleted items

ITEM No.	Question	Construct
LDS 1	I am satisfied with my house.	Material Possession satisfaction
LDS 13	I am satisfied from relations with coworkers.	Work life satisfaction
LDS 20	I am satisfied with my village/ town/ city growth (Expansion).	Government satisfaction
LDS 21	I am satisfied with number of bridges/ over bridges/ under bridges in my village/ town/ city.	Government satisfaction
LDS 28	I feel inner peace/harmony.	Spirituality Satisfaction
LDS 32	I feel close to God/supreme power.	Spirituality Satisfaction

Reliability: The two parameters of reliability check are:

1) The Average variance Extracted: AVE values should be greater than 0.50 (Hair Jr. et. al., 2015). For this study, it is achieved. Refer to Table 4.45.

2) Composite Reliability: CR values should be greater than 0.60 (Hair Jr. et. al., 2015). For this study, it is achieved. Refer to table: 4.45.

Validity: it is measured through four parameters:

1) Convergent validity: The Convergent validity of the measurement model has confirmed when all values of AVE is greater than 0.50. The items that are indicators of a specific construct should converge or share a high proportion of variance in common, known as convergent validity (Hair Jr. et. al., 2015). For this study, it is achieved. Refer to Table 4.45.

2) Construct Validity: The Construct validity for the measurement model has confirmed when all fitness Indexes meet the desired level of acceptance (Byrne, 2001). Construct validity is the extent to which a set of measured items actually reflects the theoretical latent construct those items are designed to measure (Hair Jr. et. al., 2015). For this study, it is achieved. Refer to Table 4.46.

3) Discriminant Validity: The Discriminant validity has confirmed when all redundant items are either deleted or constrained as a "free parameter". Discriminant validity is the extent to which a construct is truly distinct from other construct (Hair Jr. et. al., 2015). For this study, it is achieved. Refer to table: 4.47.

4) Nomological Validity and Face Validity: Construct should have Nomological validity and Face validity (Hair Jr. et. al., 2015). Nomological validity is achieved. Refer to table: 4.47. Face validity had confirmed at the time of instrument (Life Domain Satisfaction Scale) development.

CFA results of this study suggest that the measures were reliable and valid. We may conclude the model fit was good and may now look at the estimates and their level of significance.

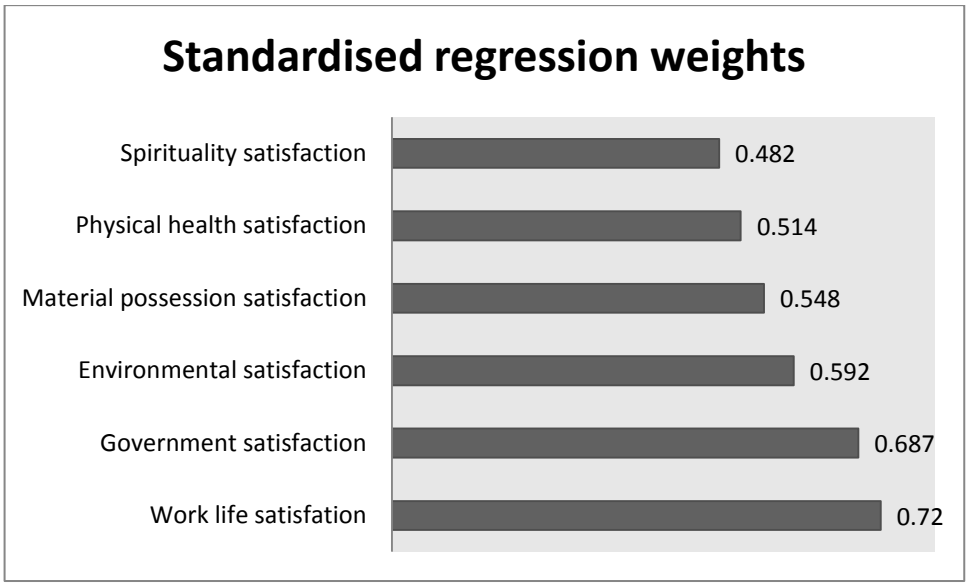
Table 4.44 Standardized regression weights and significance level of six domains of life satisfaction

	Standardized Estimate	Standard error	Critical ratio	p-value
Government Satisfation→ QOL	0.687			
Material Possession Satisfaction → QOL	0.548	0.055	10.296	***
Environmental Quality →QoL	0.592	0.087	11.769	***
Work life Satisfaction→ QoL	0.72	0.065	11.007	***
Spirituality satisfaction → QoL	0.482	0.086	8.865	***
Physical health Satisfaction→ QoL	0.514	0.061	10.422	***

P values of all six links were found significant ($p < 0.05$). The p- value for the link, individual p-value is presented as *** indicating that the link is highly significant. The result of structural equation model analysis proved that there is an association between

overall life satisfaction and different domains of life satisfaction (Ref. Table 4.44). Standardised regression weights are shown if Figure 4.10.

Fig. 4.10 Standardized regression weights of six domains of overall life satisfaction



Standardised regression weights were arranged in ascending order (Ref. Fig. 4.10).

Convergent validity check

To establish convergent validity, the specific items should share a high proportion of variance in common. As described in Table 4.45, convergent validity is indicated by:

1. All factor loadings are significant and with values greater than 0.5.
2. t- values all indicators are higher than 1.96 at 5% significance level.

3. The relatively high Average Variance Extracted (AVE) of all constructs with values greater than 0.5. Here, Government satisfaction = 71.5%, Material possession satisfaction = 53.2%, Environmental satisfaction = 79%, Work life satisfaction = 56.6%, Spirituality satisfaction = 50% and Physical health satisfaction = 72.9%.

4. Composite Reliability (CR) of all constructs is higher than 0.7 which shows measures of reliability. The correlation between the indicators is high, which is an evidence of internal consistency and the construct's Unidimensionality (Gerbing and Anderson, 1988).

Fig. 4.11 Perceived quality of life (measurement model)

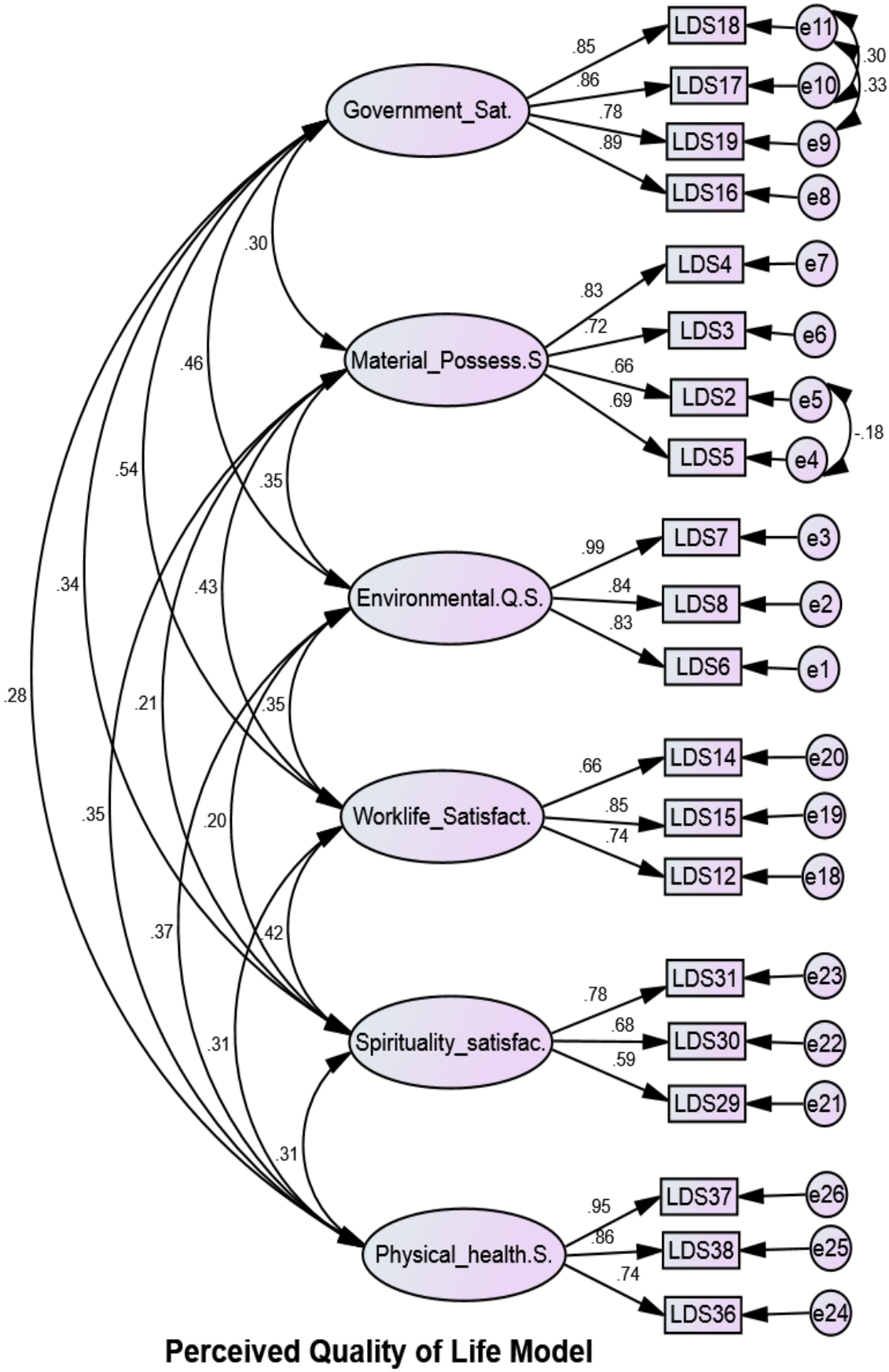


Fig. 4.12 Perceived quality of life (structural model - second order CFA)

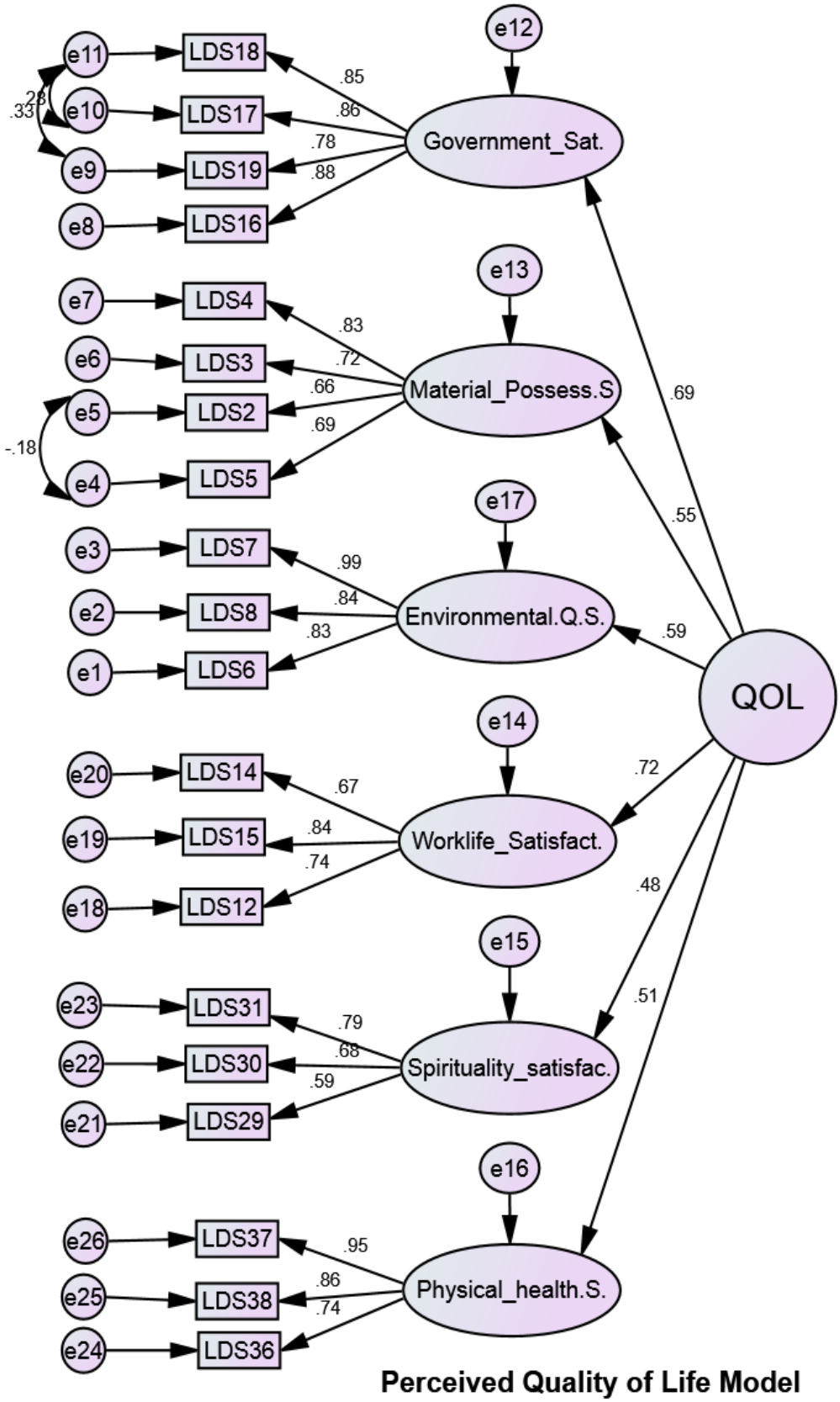


Table 4.45 CFA report for every construct in the model

The CFA Report for every construct in the model						
Construct	Item No.	Item	Factor Loading	t-value	CR (Above 0.6)	AVE (Above 0.5)
Government satisfaction	18	I am satisfied with central government position on civil rights.	0.853		0.909	0.715
	17	I am satisfied with international relation policies with neighbor countries of central government.	0.861	34.696		
	19	I am satisfied with central government policies to solve the problems like unemployment, poverty, inflation, corruption, terrorism, etc.	0.783	30.282		
	16	I am satisfied with internal economic policies of central government (like Interest rates, Income tax slab, etc.).	0.883	27.615		
Material possession satisfaction	4	I am satisfied with my clothing, accessories & jewelry.	0.834		0.818	0.532
	3	I am satisfied with my vehicle.	0.722	20.165		
	2	I am satisfied with my furniture and appliances at home.	0.66	17.4		
	5	I am satisfied with my saving & investment.	0.689	18.051		
Environmental satisfaction	7	I am satisfied with quality of air in my village/town/city.	0.989		0.918	0.790
	8	I am satisfied with greenery in my village/town/city.	0.84	36.188		
	6	I am satisfied with weather in my village/town/city.	0.829	35.105		
Work life satisfaction	14	I am satisfied with working hours & timings.	0.667		0.795	0.566
	15	I am satisfied with my career growth.	0.836	18.215		
	12	I am satisfied with personal income.	0.745	15.583		
Spirituality satisfaction	31	I had felt paranormal/spiritual experience.	0.792		0.731	0.50
	30	I am associated with Guru.	0.681	17.665		
	29	I am working on self-discovery.	0.587	14.702		
Physical health satisfaction	37	I feel sufficient energy/stamina to live full life.	0.948		0.889	0.729
	38	I feel sufficient body mobility/speed to live full life.	0.86	31.632		
	36	I feel free from disease/ disorder.	0.741	25.435		

As per Table: 4.45, all six constructs are satisfied the criteria of having Composite Reliability (CR) value greater than 0.6 and Average Variance Explained (AVE) by each construct is above 0.5. Basic conditions of reliability have satisfied (Hair Jr. et al., 2015).

Construct validity

CFA results as mention below in Table 4.46 model has satisfied all parameters of acceptance, hence we suggest that model is reliable and valid.

Table 4.45 CFA model fit summary

	Index	Level of acceptance	Observed value	Literature review	Comments
Absolute fit	Chi-square	P > 0.05	0.000**	Wheaton et. al. (1997)	**Accepted**
	RMSEA	RMSEA < 0.08	0.062	Browne and Cudeck (1993)	**Accepted**
	GFI	GFI > 0.90	0.926	Joreskog and Sorbom (1984)	**Accepted**
Incremental fit	AGFI	AGFI > 0.90	0.903	Tanaka and Huba (1985)	**Accepted**
	CFI	CFI > 0.90	0.947	Bentler (1990)	**Accepted**
	TLI	TLI > 0.90	0.937	Bentler and Bonett (1980)	**Accepted**
	NFI	NFI > 0.90	0.930	Bollen (1989)	**Accepted**
Parsimonious fit	Chisq./df	Chisq./df < 5.0	3.998	Marsh and Hocevar (1985)	**Accepted**

** Chi-square value is ignored here, because it is sensitive towards sample size. One could ignore the absolute fit index of minimum discrepancy chi-square if the sample size obtained for the study is greater than 200 (Hair et al., 1996; Joreskog and Sorbom, 1996).

Where,

RMSEA = Root Mean Square of Error Approximation.

GFI = Goodness of Fit Index.

AGFI = Adjusted Goodness of Fit Index.

CFI = Comparative Fit Index.

TLI = Tucker–Lewis Index.

NFI = Normed Fit Index.

Discriminant validity check

It is required that each construct distinct from other constructs. Discriminant validity is assessed by comparing the share variance (squared correlation) between each pair of constructs against the minimum of the AVEs for these two constructs (Fornell and Larcker, 1981), here; the discriminant validity is achieved by:

I. The absence of significant cross-loading that are not represented by the measurement model. The absence of significant cross-loading (Refer Figure. 4.11 & Figure 4.12) is also proof of a construct's Unidimensionality (Gerbing and Anderson, 1988).

II. To compare the average variance-extracted values for any two constructs with the square of the correlation estimate between these two constructs. The variance extracted estimates should be greater than the squared correlation estimate (Hair Jr. et al., 2015). The logic here is based on the idea that a latent construct should explain more of the variance in its item measures that it shares with another construct. Holmes-Smith (2001) recommended that the average AVE of the two constructs must exceed the square of their correlation to satisfy the Discriminant validity test. Referring to Table 4.47, one can conclude that the discriminant validity for all six constructs is achieved.

Table 4.46 Discriminant validity index summary for the constructs

Pair of constructs			Correlation	Square correlation	Average AVE of two constructs
Material_Possess.S	<-->	Government Sat.	0.3	0.0900	0.6235
Environmental.Q.S.	<-->	Government Sat.	0.457	0.2088	0.7528
Government_Sat.	<-->	Worklife Satisfact.	0.545	0.2970	0.6408
Government_Sat.	<-->	Spirituality_satisfac.	0.341	0.1163	0.6077
Government_Sat.	<-->	Physical_health.S.	0.285	0.0812	0.7222
Environmental.Q.S.	<-->	Material_Possess.S	0.347	0.1204	0.6610
Material_Possess.S	<-->	Worklife_Satisfact.	0.433	0.1875	0.5490
Material_Possess.S	<-->	Spirituality_satisfac.	0.208	0.0433	0.5158
Material_Possess.S	<-->	Physical_health.S.	0.351	0.1232	0.6304
Environmental.Q.S.	<-->	Worklife_Satisfact.	0.326	0.1063	0.6782
Environmental.Q.S.	<-->	Spirituality_satisfac.	0.196	0.0384	0.6451
Environmental.Q.S.	<-->	Physical_health.S.	0.366	0.1340	0.7597
Worklife_Satisfact.	<-->	Spirituality_satisfac.	0.422	0.1781	0.5331
Worklife_Satisfact.	<-->	Physical_health.S.	0.357	0.1274	0.6476
Physical_health.S.	<-->	Spirituality_satisfac.	0.312	0.0973	0.6476

Nomological validity check

The correlation among the constructs makes Nomological validity (Hair Jr. et al., 2015). In the above table 4.47, positive correlation among construct prevails the Nomological validity of the model.

4.6 CONCLUSION

This chapter played a most crucial part of the study, because a success of the study depends on the success of this chapter. In this chapter, appropriate statistical tests had applied and results were interpreted. Adequate justification and assumption's testing had done properly for all statistical tests which were used. Selections of statistical tests were determined on the basis of meeting its criteria with the characteristics of data and its capability to analyze it, so that the optimum outcome might be expected. Statistical tests had applied in a chronological sequence in aims to meet with the objectives of the study. Tables and figures were used with supportive statements with each test results, so that a summarized form of results might be presented.

CHAPTER 5

DISCUSSION

5.1 INTRODUCTION

5.2 FINDINGS OF THE STUDY

5.3 CONCLUSION OF THE STUDY

5.4 CONTRIBUTION TO KNOWLEDGE

5.5 IMPLICATIONS OF THE STUDY

5.6 SCOPE FOR FURTHER RESEARCH

5.7 COMPARISON OF THE RESULT WITH EARLIER STUDY

5.1 INTRODUCTION

In this chapter, the key points of the research are recalled and synthesized into the coherent body of understanding. In the process of summarizing, references of back sections are given so that it is easy to locate that part of the thesis at which the issues were originally discussed. Here, it was also examined that the conclusions of the study, to what extent will meet the aims or objectives of the study. A clear statement of the original contribution to knowledge made by the research has been mentioned. A practical implication had made in the thesis for various stakeholders of the society, like the Government, Welfare Organizations, People, etc. Implications were made keeping in view the thought that individual or organizations would be in the position to understand its importance and implement it. In the latter part of this chapter, possibilities for further research have been discussed.

5.2 FINDINGS OF THE STUDY

I. A sample of people of Gujarat was classified into three groups on the bases of their overall life satisfaction ratings (Refer Table 4.2): a) highly satisfied group with 20.5%, b) moderately satisfied group with 60.6%, and c) poorly satisfied group with 18.8%. It was found that highly satisfied group scored higher on all variables of a semantic differential scale. It showed that they had expressed positive orientation towards their overall life satisfaction and perceived their lives as Enjoying, Interesting, Active, Happy, Meaningful, Worthwhile, Rewarding, Easy, Relaxed, Full of fun and Comfortable. On another side, the moderately satisfied group was observed to be perceived the same as the highly satisfied group but comparative lesser degree. A poorly satisfied group having comparative lower ratings on overall life satisfaction scale and Semantic differential scale, it showed poorly satisfied group perceived same as the first two groups but the comparative lowest degree (Refer Table 4.8).

II. On the bases of the results of the Tree Segmentation method (Refer Fig. 4.1), the whole sample was classified into two groups: middle & highest income group and lower income group. It was found that the annual income of people was the most significant variable led to the classification of the whole sample into two groups. In

Node 1, Individuals belonged to middle & higher income group was found to be 28.3% highly satisfied, 59.2% moderately satisfied and only 12.5% poorly satisfied with their overall life satisfaction. On the other side, Node 2, respondents belonging to lower income group only 12.2% people were highly satisfied, 62.2% moderately satisfied and 25.7% poorly satisfied with their overall life satisfaction. Further classification of Node 1 into Node 3 and 4 took place. Gender of people was the second most significant variable found in the study under sub-group segmentation, which classified middle & higher income group income group in two categories: Node 3 of males and Node 4 of the females. It was found that in Node 3, Males were 23.7% highly satisfied, 62.9% moderately satisfied and only 13.4% poorly satisfied with their overall life satisfaction. On the other side in Node 4, Females were 40.7% highly satisfied, 49.1% moderately satisfied and only 10.2% poorly satisfied with their overall life satisfaction. It revealed that females were relatively highly satisfied in their overall life satisfaction than males.

III. On the basis of mean value **($\bar{x}$ = 5.10)** of sample data of overall life satisfaction ratings, it was found that people were somewhat satisfied in their overall life satisfaction (Refer Table 4.12).

IV. By comparing the mean values of overall life satisfaction ratings, it was found that perceived quality of life of males and females seemed to be same (Refer Table 4.15).

V. By comparing the mean values of overall life satisfaction ratings, it was found that perceived quality of life of people varied with different age groups. Perceived quality of life of people of age group 46-55 years was better than people of 26-35 years and 36-45 year age groups (Refer Table 4.17).

VI. By comparing the mean values of overall life satisfaction ratings, it is found that perceived quality of life of post-graduates, graduates and below-graduates were same (Refer Table 4.20).

VII. By comparing the mean values of overall life satisfaction ratings, it was found that perceived quality of life of people varied with their marital status. Marrieds were found to be more satisfied than unmarried (Refer Table 4.23).

VIII. By comparing the mean values of overall life satisfaction ratings, it was found that perceived quality of life of people varied with their income levels. People who belonged to the higher and middle-income group were more satisfied than lower income group in their perceived quality of life (Refer Table 4.25).

IX. By comparing mean values of overall life satisfaction ratings, it was found that perceived quality of life of people lived in different areas like Central Gujarat, South Gujarat, Saurashtra, and North Gujarat were same (Refer Table 4.28).

X. By comparing the mean values of overall life satisfaction ratings, it was found that perceived quality of life of people lived in rural and urban Gujarat was the same (Refer Table 4.31).

XI. By applying exploratory factor analysis, six latent factors were explored from 20 observed variables. Labelling of six factors had done as Government satisfaction, Material possession satisfaction, Environmental quality satisfaction, Work life satisfaction, Spirituality satisfaction and Physical health satisfaction. Going further, by applying multiple regression analysis relationships between Overall Life satisfaction and these six factors were examined. It was found that all six factors (Domains of life satisfaction) were having a significant relationship with overall life satisfaction. A regression model was found to be significant which explained 34.5% of the variance in overall life satisfaction (Refer Table 4.39). Respondents were found to be quite satisfied with Material Possession and Physical Health, while they were observed to be least satisfied with Environmental satisfaction variable among the 6 domains of life satisfaction (Refer Table 4.41).

XII. By applying confirmatory factor analysis relationship between Overall Life satisfaction and six factors (Government satisfaction, Material possession satisfaction, Environmental quality satisfaction, Work life satisfaction, Spirituality satisfaction and Physical health satisfaction) were validated. Construct validity, Convergent validity, Discriminant validity and Nomological validity were proved (Refer Table 4.45, 4.46 & 4.47).

5.3 CONCLUSION OF THE STUDY

This study had measured perceived quality of life of people in the context of Gujarat's culture. It was proved that culture, having a strong impact on the quality of life of people (Diener and Suh 2000). The culture of Gujarat had a strong influence over the quality of life of people in Gujarat. The characteristics of Gujarati culture were observed during the research were; Gujarati people are religious and spiritual in nature, most of the respondents were attached with any of the religious groups like Swaminarayan, Jainism, etc. and most of the people lived in joint families. A satisfied quality of life of people in Gujarat was one of the outcomes of a heritage culture of Gujarat.

Highly satisfied group of people were having a positive orientation towards their perceived quality of life. They sense their lives as Enjoying, Interesting, Active, Happy, Meaningful, Worthwhile, Rewarding, Easy, Relaxed, Full of Fun and Comfortable. On the other side, the moderately satisfied group was also perceived the same as a highly satisfied group but in a comparatively lesser degree. The poorly satisfied group was having poor ratings on overall life satisfaction scale and semantic differential scale, it shows dissatisfied groups perceived the same as the first two groups but in comparative lowest degree.

The annual income of people was the most significant variable which classified the whole sample into two groups; the middle & higher income group and lower income group. For further classification of sub-group segmentation, Gender of people was the second most significant variable in the study, which classified middle & higher income group in two categories, where it concluded that females were more satisfied than males.

Gujarat has a heritage culture of peace and prosperity. All over Gujarat, people were somewhat satisfied towards their overall life irrespective of different education, area, income, etc. All credit goes to a good culture of Gujarat.

In terms of gender difference, there was no gender difference in perceived quality of life of people in Gujarat. Males and females were equally satisfied in their lives. A credit goes to the culture of Gujarat and consistent efforts of the government of Gujarat in the area of women empowerment.

In terms of an age difference, perceived quality of life of people of 46-55 years age groups were significantly better than people of 26-35 years and 36-45 year age groups. Here, maybe people of 46-55 years age group perceived more stabilize in their life compared to the rest of two age groups. This is a good sign for the state.

In terms of education, perceived quality of life of post-graduates, graduates, and undergraduates were the same. This is also an impact of the good culture of Gujarat.

In terms of marital status, perceived quality of life of married was better than unmarried. This might be because of marrieds were more focused.

In terms of income status, perceived quality of life of people of a higher-income group and a middle-income group were better than a lower-income group. It is quite clearly understood that income or material possession is one of the strong influencing factors affecting the quality of life.

In terms of geographical region, perceived quality of life of the people was same in all four geographical zones of Gujarat; Central Gujarat, South Gujarat, Saurashtra, and North Gujarat. It was the biggest achievement of the Government of Gujarat to maintain uniform development all across Gujarat.

In terms of rural vs urban Gujarat, perceived quality of life of the people was same. Again, it was a very big achievement of the government of Gujarat. A balanced growth in urban and rural Gujarat has been maintained by consistent efforts of the government of Gujarat.

In terms of domains of life satisfaction, six domains of life satisfaction were identified which have an influence on the quality of life of people. These domains: Government satisfaction, Material possession satisfaction, Environmental quality satisfaction, Work life satisfaction, Spirituality satisfaction and Physical health satisfaction. Total 34.5% of the variance in overall life satisfaction of individuals had explained by these six domains of life satisfaction. Material possession satisfaction and physical health satisfaction were more influenced factors compared with rest.

5.4 CONTRIBUTION TO KNOWLEDGE

This section comprised of the original contribution of the study, which is the most important part of the research and highly recommended by the research society. Here, a list of contributions mentioned below:

1. **A Problem statement:** The problem statement of the study "To measure a perceived quality of life of people in Gujarat" is a comparative novel idea where the subjective approach of measuring the well-being of people was used.

2. **Research Methodology:** Sampling designed was one of the unique contributions of this study where an attempt was made to collect data from the whole state under a limitation of resources and time.

3. **Questionnaire Designed:** Life domain satisfaction scale was developed for the study, which was one of the most crucial contributions of the study. To measures different domains of life satisfaction for which different statements were chosen. Selection of most the appropriate statement and their sequence was the challenge. Also to maintain the length of the questionnaire was also challengeable. But in last, the questionnaire was developed through which successfully 6 factors (Domains of Life satisfaction) were extracted which accounts 34.5 % of variability defined in overall life satisfaction of people.

4. **Perceived Quality of Life Model:** The major and unique contribution given by the study is the Perceived Quality of Life (PQoL), Model. PQoL model was validated by the confirmatory factor analysis method.

5. **Implications of the study:** The implications of the study were also one of the unique contributions of the study.

5.5 IMPLICATIONS OF THE STUDY

This study having 360-degree impacts on all stakeholders of society, also its finding clarifies many misinterpretations of human psychology. Subjective well-being is a comparatively new approach to human society and having a history of approx. 50 years, but its practical implications have accepted by the world in the year 2012. World Happiness Index and ministry of Well-being in UAE are the big examples of it.

An Implication of the study to the government of Gujarat & India

The findings of the study may play a big role in policymaking. As we know, in our country a huge gap has found between the needs of society and government policies. To fulfil this gap many time feedback surveys have conducted by the government, like for Indian Railways modernization, Indian railway's continuing taking feedbacks from passengers about service quality and areas of improvements. In India, we have seen that even prestigious planning commission (now NITI Aayog) gets fail to formulate successful policies and its implementation in last 64 years. The government doesn't know about the needs of the specific sector, resultant development initiatives do not resolve problems. Budgets are prepared on the basis of socioeconomic surveys which are purely based on objective measures of households, hence very less informative. Resultants poor policies are formed and only a few people get benefits and a major portion of society which required immediate help from the government remains to deprive of any kind of action of the government.

Such studies help the government to understand the people's requirements, it may act like a voice of people and helps policymakers to make policy, its planning and implementation accordingly. Like if people are more concerned about housing issues, so the government needs to form policies which promote housing schemes in countries, If people are found dissatisfied with government economic policies, infrastructure growth, children's education, health facilities, then policies are needed to frame accordingly. Subjective well-being study is very informative, resulted in most of the developed countries; it is widely used for policy formations. In India, few NGO (Non-government Organizations) and T.V. channels conducted (public polls) people's opinion surveys during elections. That is also a subjective well-being study, which plays a significant role to determine people's

perception of their quality of life. In future, such studies will act as a performance indicator.

Other benefits of such studies are like Government policies are formed without considering the diversity among people. India is the country of diversities, here huge differences found in social, economic, demographic characteristics of people. Standardized policies will never work in India. With the help of subjective well-being studies, the government can make customized policies as per the requirement of a particular group of people.

A government may also apply the methodology of the study at sensitive areas of countries where real development is much needed and even priorities of areas of development need to know. It may very much helpful for the government to take steps for development; also it may give maximum benefit during budget preparation.

Nowadays, Happiness index is the most popular approach to measure the well-being of nations. Many countries are following it. In India, still objective approach of measuring well-being has been used and a public welfare policy has been formed accordingly. India has been used HDI Index, which is based on the few indicators of the well-being of people. In the future, India will need to adopt one holistic approach of measuring well-being like happiness Index. In future, may India apply Happiness Index to measure well-being in the country in place of Human Development Index (HDI)?

An implication of the study to the welfare organizations

Welfare organizations like NGO (Non-government Organizations), Organizations involved in CSR (Corporate social responsibility) activities, etc. are having common goals to give maximum benefits to needy people. This will only become possible when they can examine the current state of society. They require information on the quality of life of people. Such studies may provide meaningfully and customize required information to such organizations. If you can see for the last 70 years, assessing wellbeing is the biggest challenge. This study will give relief to NGOs and other welfare organizations and to policymakers.

An implication of the study of the people of Gujarat

The biggest beneficiaries of the study are people of Gujarat itself because this study had explored their quality of life and the factors which affect their overall life satisfaction. Due to such studies, people may realize the importance of their active participation in a survey of such studies. In the future by better awareness and participation of people, better results may be achieved. Due to such studies, many people start to evaluate their overall quality of life and domains of life satisfaction. It may help them to achieve happiness in life.

An implication of the study to the field of economics and public policy

Each research makes its contribution to the related field of studies. This study may also add its unique methodology of assessing well-being and its results in the field of advanced economies. The model of perceived quality of life was developed by the study is one of the major contribution to literature and helpful for upcoming researches. The study is a small example of a way of doing research, in this field. In an upcoming era, research may occur in this field because the world economics are working on this part. This research is expected to impact the following areas of public policy:

a) Economic development and well-being.
b) Cultural cohesion with diversity has overtaken on the well-being.
c) The government should certainly work on enhancing income levels for ensuring material well-being, and
d) A long-spell of "ethnic conflict free" regime has an influence on the life satisfaction. A future study must address ethnic differences.

5.6 SCOPE FOR FURTHER RESEARCH

This study has broadly focused on to examine overall life satisfaction and the factors (domains) of life satisfaction of people in Gujarat. The study has limitation like to consider a person who is doing the job with an age group of 26-55 years, an annual income of ₹ 1.20 lakhs - ₹ 12.00 lakhs and minimum education status of S.S.C. As per the time and resource constraints, 785 respondents were included in the study. The study had excluded the people of tribal areas of Gujarat.

This study may carry forward in many ways. This study has presented one research methodology for assessing the well-being of people. The same methodology may use to assess the well-being of adolescent, younger and older people. We can also measure the well-being of people in tribal areas of Gujarat. The study may also, carry forward to measure the well-being of people in slums or any other particular class or category in terms of socioeconomic categories.

Subjective assessment of the quality of life is a comparatively new concept and not much history is available. Especially countries like India this topic is new and has a very broad scope for further studies. This study was restricted up to Gujarat with a limited sample size of 785 respondents. For further studies, research may study people who are engaged in business, profession, agriculture, etc. Even measure the quality of life of the unemployed, etc. Topic has huge potential for further studies and very essential for society in numerous ways. The study may also carry forward to other states of India like North-eastern states, Jammu & Kashmir etc. also, the whole country's well-being can measure this way and Well-being Index of India will be constructed.

5.7 COMPARISON OF THE RESULT WITH EARLIER STUDY

The result of this study has been compared with the result of a study done by Dasgupta and Majumdar (1996). Finding of both studies has mentioned below:

Findings of Dasgupta and Majumdar (1996): They found that socioeconomic status was not significantly related to perceived quality of life. They found that people of 21-35 years and 56 years or older were comparatively more satisfied than the people of 36-55 years age group. The sex difference was found insignificant. They examined the association between overall life satisfactions with domains of life satisfaction. Satisfaction with self-development, Family life, Material possession, and Local government administration were found significant. Local government administration was the most influential domain.

The findings of the current study: Study found that people of Gujarat were somewhat satisfied towards their perceived quality of life. The study found that difference in people's gender, educational status, and residence area were insignificant related to perceived quality of life. The study found that people of age group 46-55 years were comparatively more satisfied with their perceived quality of life than people of age group 26-35 years and

36-45 years. The study found that married were better perceived quality of life than unmarried. The study found that individuals with higher and middle income groups were comparatively more satisfied with their perceived quality of life than people of lower income group. The study examined the association between overall life satisfactions with domains of life satisfaction. Six domains were found significant; Material Possession Satisfaction, Physical Health Satisfaction, Spirituality Satisfaction, Government Satisfaction, Work life Satisfaction and Environmental Satisfaction. Material Possession and Physical Health Satisfaction were more influential, followed by Spirituality Satisfaction, Government Satisfaction, Work life Satisfaction, and Environmental Satisfaction.

BIBLIOGRAPHY

BOOKS

1. Aczel, A. D., Sounderpandian, J., Saravanan, P., & Joshi, R. (2012). *Complete Business Statistics*. New York: Tata McGraw-Hill Companies.
2. Anderson, D. W. (2008). *Statistics for Business and Economics*. USA: Thomson Higher Education.
3. Bajpai, N. (2015). *Marketing Research: an Indian Perspective*. Delhi: Dorling Kindersley (India) Pvt. Ltd, Licensees of Pearson Education in South Asia.
4. Black, K. (2013). *Applied Business Statistics: Making Better Business Decisions*. New Delhi: Wiley India Private Limited.
5. Brace, N., Kemp, R., & Snelgar, R. (2006). *SPSS for Psychologists*. New Jercy: Lawrence Erlbaum Associates Publishers Mahwah.
6. Bruni, L., & Porta P. L. (2005). *Economics and Happiness: Framing the Analysis*. New York: Oxford University Press.
7. Burns, A.C, Veeck, A., & Bush, R.F. (2018). *Marketing Research*. India: Pearson India Education Services Pvt. Ltd.
8. Byrne B. M. (2001). *Structural Equation Modelling with AMOS Basic Concepts, Applications and Programming*. New-Jercy: Lawrence Erlbaum Associates Publishers Mahwah.
9. Chawla, D., & Sondhi, N. (2011). *Research Methodology: concepts and cases*. Noida: Vikas Publishing House Pvt. Ltd.
10. Cooper, D.R., & Schindler, P. S. (2010). *Business Research Methods*. New Delhi: Tata McGraw Hill Education Private Limited.
11. Diener, E. (2009). *Assessing Well-Being*. London: Springer Publications.
12. Diener, E., & Suh, E. M. (2000*). Culture and Subjective Well-Being*. A Bradford Book, Massachusetts: The MIT Press Cambridge.
13. Eid, M., & Larsen R. (2008*). The Science of Subjective Well-Being*. New York: The Guilford press.
14. Field, A. (2005). *Discovering Statistics Using SPSS*. New Delhi: SAGE Publications.
15. Gujarati, D. N., Porter, D. C., & Gunasekar, S. (2009). *Basic Econometrics*. New Delhi: McGraw Hill Education (India) Private Limited.

16. Hair Jr., J. F., Black, W.C., Babin, B.J., & Anderson, R. E. (2015). *Multivariate Data Analysis*. New Delhi: Dorling Kindersley (India) Pvt. Ltd, Licensees of Pearson Education in South Asia.
17. Hair, J. F., Hult, G.T.M, Ringle, C.M., & Sarstedt, M. (2014). *A Primer on Partial Least squares Structural Equation Modeling (PLS-SEM).*USA: SAGE Publications.
18. Kahneman, D., Diener, E. & Schwarz, N. (1999). *Well-being: The Foundations of Hedonic Psychology*. New York: Russell SAGE Foundation.
19. Kothari, C.R., & Garg, G. (2018). *Research Methodology Methods and Techniques*. New Delhi: New Age International (P) Limited, Publishers.
20. Kumar, R. (2005). *Research Methodology- A Step by Step Guide for Beginners*. Australia: Pearson Education.
21. Malhotra, N.K, & Dash, S. (2013). *Marketing Research an Applied Orientation*. New Delhi: Pearson.
22. Mangal, S. K., & Mangal, S. (2013). *Research Methodology in Behavioural Sciences*. Delhi: PHI learning private limited.
23. Mayers, A. (2013). *Introduction to and in psychology*. London: Pearson.
24. Nargundkar, R. (2008). *Marketing Research- Text and Cases*. New Delhi: McGraw Hill Education (India) Private Limited,
25. Oliver, P. (2016). *Writing Your Thesis*. New Delhi: Sage Publications India Pvt. Ltd.
26. Rahim, F.A. (2006). *Thesis Writing: A Manual for Researchers*. New Delhi: New Age International (P) Limited, Publishers.
27. Rao P. H (2016). *Business Analytics: An application focus*. Delhi: PHI Learning Private Limited.
28. Rapley, M. (2003). *Quality of Life Research*. New Delhi: SAGE Publications.
29. Ray, D., (1998). *Development Economics*. New Delhi: Oxford University Press.
30. Saunders, M., Lewis, P., & Thornhill, A. (2016). *Research Methods for Business Students*. UK: Pearson.
31. Sen, A., (1982). *Choice, Welfare and Measurement*. New Delhi: Oxford University Press.
32. Van, P. B., & Carbonell A. F., (2008). *Happiness Quantified-A satisfaction Calculus Approach*. New York: Oxford University Press.

JOURNALS

1. Abdel-Khalek, A.M. (2010). Quality of Life, Subjective Well-Being, and Religiosity in Muslim College Students. *Quality of Life Research*, Vol. 19, No. 8, pp. 1133-1143.
2. Alcala, V.D., & Carmen, A. A. (2011). Sense of Well Being and Perceived Quality of Life in Purok Matahimik (Isla), Barangay Cotta, Lucena City. *MSEUF Research Studies*, Vol. XIII, No 1, pp. 14-22.
3. Ali, H.H., Malkawi, F.K., & Al-Betawi, Y.N. (2009). Quality of Life in Cities: Setting up Criteria for Amman-Jordan. Social Indicators Research, Vol. 93, No. 2, pp. 407-432.
4. Amao, F.L. (2014). Quality of Life of Poor Residential Neighbourhoods in Oshogbo, Nigeria. *International Journal of Social, Behavioural, Educational, and Economic and Management Engineering*, Vol: 8, No: 4, pp. 905-908.
5. Angur, M.G., Widgery, R., &. Angur, S.G. (2015). Congruence among Objective and Subjective Quality-of-Life (QOL) Indicators. *Alliance Journal of Business Research*, 47-54.
6. Asyraf, W., & Afthanorhan, B. (2013). A Comparison of Partial Least Square Structural Equation Modeling (PLS-SEM) And Covariance Based Structural Equation Modeling (CB-SEM) For Confirmatory Factor Analysis. *International journal of engineering science and innovative technology (IJESIT)*, Vol.2, Issue 5, pp. 198-205.
7. Biswas-Diener, R., & Diener, E. (2001). Making the Best of a Bad Situation: Satisfaction in the Slums of Calcutta. *Social Indicators Research*, Vol. 55, No. 3, pp. 329-352.
8. Biswas-Diener, R., & Diener, E. (2006). The Subjective Well-Being of the Homeless and Lessons for Happiness. *Social Indicators Research-Springer*, 76, pp.185–205.
9. Biswas-Diener, R., Diener, E., & Lyubchik, N. (2015). Wellbeing in Bhutan. *International Journal of Wellbeing*, 5(2), 1-13.
10. Bourke, L., & Geldens, P.M. (2007). Subjective Wellbeing and its Meaning for Young People in a Rural Australian Center. *Social Indicators Research*, Vol. 82, No. 1, pp. 165-187.
11. Brajša-Žganec, A., Ivanović, D., & Lipovčan, L.K. (2011). Personality Traits and Social Desirability as Predictors of Subjective Well-Being. *Psihologijske teme*, 20, 2, pp. 261-276.

12. Camfield, L., Choudhury, K., & Devine, J. (2006). Relationships, Happiness and Well-Being: Insights from Bangladesh. *ESRC Research Group (WeD) on Wellbeing in Developing Countries*, WeD Working Paper 14.
13. Chan, A.C.M. et al. (2004). Constructing a Quality of Life Scale for Older Chinese People in Hong Kong (HKQOLOCP). *Social Indicators Research*, Vol. 69, No. 3, pp. 279-301.
14. Chen, Z., & Davey, G. (2009). Subjective Quality of Life in Zhuhai City, South China: A Public Survey Using the International Wellbeing Index. *Social Indicators Research*, Vol. 91, No. 2, pp. 243-258.
15. Choudhury, C.L., & Devine, J. (2006). Relationships, Happiness and Well-being: insights from Bangladesh. Wellbeing in Developing Countries. *ESRC Research Group (WeD)*. WeD Working Paper 14.
16. Cramer, V., Torgersen, S., & Kringlen, E. (2004). Quality of Life in a City: The Effect of Population Density. *Social Indicators Research*, Vol. 69, No. 1, pp. 103-116.
17. Das, D. (2008). Urban Quality of Life: A Case Study of Guwahati. *Social Indicators Research*, Vol. 88, No. 2, pp. 297-310.
18. Dasgupta, S. & Majumdar, S. (2000). Sense of well-being and perceived quality of life in Culcutta. *Advance in quality of life theory and research*, pp 65-79.
19. Diener, E., & Seligman, M.E.P. (2002). Very Happy People. *Psychological Science*, Vol 13, Issue 1, pp. 81-84.
20. Diener, E., & Suh, E. (1997). Measuring Quality of Life: Economic, Social, and Subjective Indicators. *Social Indicators Research*, Vol. 40, pp. 189–216.
21. Diener, E., Emmons, R., Larsen, R. & Griffen, S. (1985). The Satisfaction with Life. Scale. *Journal of Personality Assessment*, 49, 1.
22. Dobewall, H. et al. (2013). Self-Other Agreement in Happiness and Life-Satisfaction: The Role of Personality Traits. *Social Indicators Research*, Vol. 114, Issue 2, pp. 479–492.
23. Dost, M. T. (2006). Subjective well-being among university students. *Hacettepe University journal of education*, Vol. 31, pp. 188- 197.
24. Dunning, H., Janzen, B., Williams, A., Abonyi, S., Jeffery, B., et al. (2006). A gender analysis of quality of life in Saskatoon, Saskatchewan. *GeoJournal*, Vol. 65, No. 4, pp. 393-407.

25. Epley, D.R., & Menon, M. (2008). Method of Assembling Cross-Sectional Indicators into a Community Quality of Life. *Social Indicators Research*, Vol. 88, No. 2, pp. 281-296.
26. Eroglu, S.E. (2012). Examination of University Students' Subjective Well-Being: A Cross-cultural Comparison. *International Journal of Academic Research.* Vol. 4, No. 1, pp 168-171.
27. Fleche, S., Smith, C., & Sorsa, P. (2011). Exploring Determinants of Subjective Wellbeing in OECD Countries: Evidence from the World Values Survey. *OECD publishing*, Economics Department Working Paper No. 921.
28. Fu, S.K., Anderson. D., Courtney, M., & McAvan, B. (2006). The Relationship between Country of Residence, Gender and the Quality of Life in Australian and Taiwanese Midlife Residents. *Social Indicators Research*, Vol. 79, No. 1, pp. 25-49.
29. Fuentes, N., & Rojas, M. (2001). Economic Theory and Subjective Well-Being: Mexico. *Social Indicators Research*, Netherland: Kluwer Academic Press.
30. Groenland, E. (1990). Structural Elements of Material Well-Being: An Empirical Test among People on Social Security. *Social Indicators Research*, Vol. 22, No. 4, pp. 367-384.
31. Gupta, S., & Sharma, A. (1998). Measuring Quality of Family life. *International Journal of Sociology of the Family*, Vol. 28, No. 1, pp.115-118.
32. Gutie´rrez, J., Jime´nez, B., Herna´ndez, E., & Puente, C. (2005). Personality and subjective well-being: big five correlates and demographic variables. *Personality and Individual Differences*, Vol.38, Issue 7, pp. 1561-1569.
33. Haq, R. (2009). Measuring Human Wellbeing in Pakistan: Objective versus Subjective Indicators. *European Journal of Social Sciences*, Vol 9, No.3, pp. 516-532.
34. Haq, R., Ahmed, A., Shafique, S., & Malik, A. (2010). Variation in the Quality of Life within Punjab: Evidence from MICS, 2007-08. *The Pakistan Development Review*, Vol. 49, No. 4, pp. 863-879.
35. Hsieh, C. (2016). Domain Importance in Subjective Well-Being Measures. *Social Indicators Research*, Vol. 127, Issue 2, pp.777-792.
36. Hudders, L., & Pandelaere, M. (2012). The Silver Lining of Materialism: The Impact of Luxury Consumption on Subjective Well-Being. *Journal of Happiness Studies*, Vol.13, pp. 411–437.

37. Hutchinson, et al. (2004). Social and Health Determinants of Well Being and life Satisfaction in Jamaica. *International Journal of Social Psychiatry*, Vol. 50(1), pp. 43–53.
38. Inoguchi, T., & Fujii, S. (2009). The Quality of Life in Japan. *Social Indicators Research,* Vol. 92, No. 2, pp. 227-262.
39. Jongudomkarn, D., & Camfield, L. (2005). Exploring the Quality of Life of People in North Eastern and Southern Thailand. *ESRC Research Group (WeD) on Wellbeing in Developing Countries,* WeD Working Paper 11.
40. Kahneman, D. (2006). Developments in the Measurement of Subjective Wellbeing. *Journal of Economic Perspective,* Vol. 20, No. 1, pp. 3-24.
41. Karlsson, L. E., Crondahl, K., Sunnemark, F., & Andersson, A. (2013). The Meaning of Health, Well-Being and Quality of Life Perceived by Roma People in West Sweden. *Societies* 2013, Vol. 3, pp. 243-260.
42. Kashdan, T. (2002). The Assessment of Subjective Wellbeing (Issues Raised by the Oxford Happiness Questionnaire). *Personality and Individual Difference*, Vol.36, pp.1225-1232.
43. Keng, K. A., & Hooi, W.S., (1995). Assessing Quality of Life in Singapore: An Exploratory Study. *Social Indicators Research*, Vol. 35, No. 1, pp. 71-91.
44. Kennedy, J.E., & Kanthamani, H. (2013). Empirical Support for a Model of Well-Being, Meaning in Life, Importance of Religion, and Transcendent Experiences.
45. Keyes, C.L.M., Shmotkin, D., & Ryff, C.D. (2002). Optimizing Well-Being: The Empirical Encounter of Two Traditions. *Journal of Personality and Social Psychology,* Vol. 82, No. 6, pp. 1007–1022.
46. Khan. M., Shirazi. M., & Ahmed, M. (2011). Spirituality and Life satisfaction Among Adolescents in India. *Journal of Subcontinental Researches,* Vol.3, No.7, pp. 71-84.
47. Kusago, T. (2008). Japan's Development: What Economic Growth, Human Development and Subjective Well-Being Measures tell us about? *Thammasat Economic Journal*, Vol.26, No.2, pp. 88-116.
48. Larson, R. (1978). Thirty Years of Research on the Subjective Well-Being of Older Americans. *Journal of Gerontology*, Vol. 33, No. 1, pp.109-125.
49. Leelakulthanit, O., & Day, R. L. (1992). Quality of Life in Thailand. *Social Indicators Research,* Vol. 27, No. 1, pp. 41-57.

50. Lever, J.P. (2000). The Development of an Instrument to Measure Quality of Life in Mexico City. *Social Indicators Research*, Vol. 50, No. 2, pp. 187-208.
51. Liao, P. (2009). Parallels between Objective Indicators and Subjective Perceptions of Quality of Life: A Study of Metropolitan and County Areas in Taiwan. *Social Indicators Research*, Vol. 91, No. 1.
52. Liao, P., Fu, Y., & Yi, C. (2005). Perceived quality of life in Taiwan and Hong Kong: an intra-culture comparison. *Journal of Happiness Studies*, Vol 6, pp. 43-67.
53. Liu, B. (1974). Quality of Life Indicators: A Preliminary Investigation. *Social Indicators Research*. Vol, 1, No. 2, pp. 187-208.
54. Lloyd, K.M., & Auld, C.J. (2002). The Role of Leisure in Determining Quality of Life: Issues of Content and Measurement. *Social Indicators Research*, Vol. 57, No. 1. pp. 43-71.
55. Loewe et al., (2013). Life Domain Satisfactions as Predictors of Overall Life Satisfaction among Workers: Evidence from Chile. *Journal for Social Indicator Research*, Vol.118, pp.71–86.
56. Maditinosa, D.I., Papadopoulosb, D., & Pratsc, L. (2014). The Free Time Allocation and its Relationship with the Perceived Quality of Life (QoL) and Satisfaction with Life (SwL). *Procedia Economics and Finance*, Vol.9, pp.519 – 532.
57. Malik, T. T., Shukla, V.,& Bhat, S.A. (2015). Spatial Variation in the Perception of Urban Residential Environmental, Quality Of Life in Srinagar City (J &K). *International Journal of Social Sciences and Management*, Vol.2, Issue-3, pp. 250-262.
58. Mastekaasa, A., & Moum, T. (1984). The Perceived Quality of Life in Norway: Regional Variations and Contextual Effect. *Social Indicators Research*, Vol. 14, No. 4, pp. 385- 419.
59. Michalos, A. C., & Zumbo, B.D. (1999). Public Services and the Quality of Life, *Social Indicators Research*, Vol. 48, No. 2, pp. 125-156.
60. Michalos, A.C. (2004). Social Indicators Research and Health-Related Quality of Life Research. *Social Indicators Research*, Vol. 65, No. 1, pp. 27-72.
61. Michalos, A.C., & Orlando, J.A. (2006). A Note on Student Quality of Life. *Social Indicators Research*, Vol. 79, No. 1, pp. 51-59.
62. Moller, V. (2007). Satisfied and dissatisfied South Africans: results from the General Household Survey in international comparison. *Social Indicators Research*, Vol. 81, Issue 2, pp. 389–415.

63. Moller, V., & Schlemmer, L. (1983). Quality of Life in South Africa: Towards an Instrument for the Assessment of Quality of Life and Basic Needs. *Social Indicators Research*, Vol. 12, No. 3, pp. 225-279.
64. Mookherjee, H.N. (1997). Marital Status, Gender, and Perception of well-being. *The Journal of Social Psychology*, 137 (1), pp. 95-105.
65. Mukherjee, R. (1981), On the Quality of Life in India: An Exploratory Survey. *Social Indicators Research*, Vol. 9, No. 4, pp. 455-476.
66. Narayana, M.R. (2009). Human Development and Quality of Life: Measurement Issues and Implications for India. *Social Indicators Research,* Vol. 90, No. 2, pp. 279-293.
67. Oluwoye, O. R. (1990). Determinants of Quality of Rural Life in Nigeria: The Women's View. *Social Indicators Research*, Vol. 22, No. 3, pp. 277-286.
68. Ozcan, K.M., Böke, S.S, & Kara, M. (2008). The Determinants of the Perception of Happiness about Quality of Life amongst Turkish People. *Economic Research Forum-Working Paper Series*, Paper No. 425, pp. 1-17.
69. Ozmete, E. (2011). Subjective Well-Being: A Research on Life Satisfaction as Cognitive Component of Subjective Well-Being. *International Journal of Academic Research,* Vol. 3. No. 4. pp. 55-61.
70. Park, C. (2009). The Quality of Life in South Korea. *Social Indicators Research,* Vol. 92, No. 2, pp. 263-294.
71. Plagnol, A.C., & Scott, J. (2011). What Matters for Well-Being: Individual Perceptions of Quality Of Life Before And after Important Life Events. *Applied Research in Quality of Life*, Volume 6, Issue 2, pp 115–137.
72. Randall, J.E. et al. (2006). A Gender Analysis of Quality Of Life in Saskatoon, Saskatchewan. *GeoJournal*, Vol. 65, No. 4, pp. 393-407.
73. Rodgers, W.L., &. Converse, P.E. (1975). Measures of the Perceived Overall Quality of Life. *Social Indicators Research*, Vol. 2, No. 2, pp. 127-152.
74. Royo, M. G., & Velazco, J. (2006). Exploring the Relationship between Happiness, Objective and Subjective Well-being: Evidence from Rural Thailand. Wellbeing in Developing Countries, *ESRC Research Group (WeD).*WeD Working Paper 16.
75. Ruta, D., Camfield, L., & Donaldson, C. (2006). Sen and the Art of Quality of Life Maintenance: Towards a Working Definition of Quality of Life, *ESRC Research Group (WeD) on Wellbeing in Developing Countries,* WeD Working Paper 12.

76. Ryff, C.D., & Lee. C., &. Keyes, M. (1995). The Structure of Psychological Well-Being Revisited. *Journal of Personality and Social Psychology*, Vol. 69, No. 4, pp.719-727.
77. Sawatzky, R., Ratner, P.A., & Chiu, L. (2005). A Meta-Analysis of the Relationship between Spirituality and Quality of Life. *Social Indicators Research*, Vol. 72, No. 2, pp. 153-188.
78. Schimmack, U. (2008). Measuring Wellbeing in the SOEP. *German Socio-Economic Panel Study (SOEP),* Paper No. 145.
79. Schneider, M. (1975). The Quality of Life in Large American Cities: Objective and Subjective Social Indicators. *Social Indicators Research,* Vol. 1, No. 4, pp. 495-509.
80. Selim. S. (2008). Life Satisfaction and Happiness in Turkey. *Social Indicators Research,* Vol. 88, No. 3, pp. 531-562.
81. Shin. D. C., & Rutkowski, C.P. (2003). Subjective Quality of Korean Life in 1981 and 2001. *Social Indicators Research*, Vol. 62/63, pp. 509-534.
82. Shu, X., & Zhu, Y. (2009). The Quality of Life in China. *Social Indicators Research*, Vol. 92, No. 2, pp. 191 225.
83. Silva, J., Keulenaer, F., & Johnstone, N. (2012). Environmental Quality and Life Satisfaction: Evidence Based on Micro-Data. *OECD Environment Working Papers*, No. 44.
84. Sing, M (2009). The Quality of Life in Hong Kong. *Social Indicators Research,* Vol. 92, No. 2, pp. 295-335.
85. Smith, C. & Clay, P. M (2010). Measuring Subjective and Objective Well-being: Analysis from Five Marine Commercial Fisheries. Human Organization, Volume 69, No.2.
86. Somarriba, N., & Pena, B. (2009). Synthetic Indicators of Quality of Life in Europe. *Social Indicators Research*, Vol. 94, No. 1, pp. 115-133.
87. Somarriba, Noelia, PENA, Bernardo (2008). Quality of life and subjective welfare in Europe: an econometric analysis. *Journal of Applied Econometrics and International Development,* Vol. 8, No. 2, pp. 55-66.
88. Sores, A., & Peto, K. (2015). Measuring of Subjective Quality Of Life. *Procedia Economics and Finance,* Vol 32, pp.809 – 816.
89. Stevenson, B., & Wolfers, J. (2008). Economic Growth and Subjective Well-Being: Reassessing the Easterlin paradox. *National Bureau of Economic Research*, Working Paper No. 14282.

90. Tambyah, S.K., Tan, S.J., & Kau, A. K. (2009). The Quality of Life in Singapore. *Social Indicators Research*, Vol. 92, No. 2, pp. 337-376.
91. Tiliouine, H.(2007). Health and Subjective Wellbeing in Developing Countries: The Case of Algeria. ESRC Research Group, WeD Working Paper No.39.
92. Tiwari, M. (2009). Poverty and Wellbeing at the 'Grassroots' - How Much is Visible to Researchers? *Social Indicators Research*. 90 (1), pp. 127-140.
93. Tsai, Y.P., Lee, Y.H, & Liou, S. (2013). Applicability of Gross National Happiness Index to Taiwan - A religious perspective. *IEEE*.
94. Viswanathan, K.N., & Sharma. S. (2013). Subjective Well-being in High Assertive Women Managers. *ASCI Journal of Management*, 43 (1), pp 29–38.
95. Wahl et al. (2004). Quality of Life in the General Norwegian Population, Measured by the Quality of Life Scale (QOLS-N). *Quality of Life Research*, Vol. 13, No. 5, pp. 1001-1009.
96. Wood, W., Rhodes, R., & Whelan, M. (1989). Six Differences in Positive Well-Being: A Consideration of Emotional Style and Marital Status. *Psychological Bulletin*, Vol. 106, No. 2, pp. 249-264.
97. Yao, G., Cheng, Y., & Cheng, P. (2009). *Social Indicators Research*, Vol. 92, No. 2, pp. 377-404.
98. Zhang, L. (2010). Urbanites' Life Satisfaction Research in China: A Case Study of Quality of Life in Eight Cities. *Journal of Asian Social Science*, Vol. 6, No. 5, pp. 19-26.
99. Zullig, K.J., Valois, R.F., Huebner, E.S., & Drane, J.W. (2005). Adolescent Health-Related Quality of Life and Perceived Satisfaction with Life. *Quality of Life Research*, Vol. 14, No. 6, pp. 1573-1584.

CONFERENCE PAPERS

1. Anzilli, L., Facchinetti, G., & Mastroleo, G. (2013). *"Beyond GDP": A fuzzy way to measure the Country Wellbeing*. Paper presented at the 2013 Joint IFSA World Congress and NAFIPS Annual Meeting (IFSA/NAFIPS), Zhengzhou, Henan, China.
2. Brown, D., Wolf, J. & Smith, C. (2010). *The determinants of subjective well-being in New Zealand: an empirical look at New Zealand's social welfare function*, Paper presented at the New Zealand Association of Economists conference, New Zealand.

3. Cantarero, R., Potter, J.J., & Leach, C.K., (2007). *Perceptions of Quality of Life, Sense of Community, and Life Satisfaction Among Elderly Residents in Schuyler and Crete, Nebraska.* Paper presented at the 38th annual conference on Building Sustainable Communities, environmental design research association, University of Nebraska – Lincoln.
4. Chavda, M.D., & Rai, S.B. (2015, August). *Well-being of adolescents in context of Culture and Gender: An Empirical Analysis.* Paper presented at the Second International Conference on Advances in Economics, Social Science and Human Behaviour Study- ESSHBS 2015, Bangkok, Thailand.
5. Gough, I. (2003, November). *Human Well-being: Bridging Objective and Subjective Approaches*. Paper presented at the *ESPANET Conference*, Copenhagen.
6. Mingtao, L.U. (2010). *A microeconomic analysis of happiness and life satisfaction: a statistical study in Germany*. Paper presented at the 10th China Economics Annual Conference, Zhengzhou, Henan, China.
7. Neuendorf, K. A., Jeffres, L.W., Skalski, P., & Atkin, D. (2000, March). *Perceptions of Quality of Life and Affective Characteristics: An Urban Examination.* Paper presented at the 2nd International Conference on Quality of Life in Cities, Singapore.
8. Rojas, M. (2004, July). *The Complexity of Well-being A Life Satisfaction Conception and a Domains-of-Life Approach*. Paper presented at the International Workshop on Researching Well-being in Developing Countries. Hanse Institute for Advanced Study Delmenhorst, near Bremen, Germany.
9. Wills, E. (2007*). Subjective Well-being in Cities: Individual or Collective? A Cross Cultural Analysis.* Paper presented at the Wellbeing in International Development Conference. England.

GOVERNMENTAL BODIES' PUBLICATIONS

1. Hussien, S., & Heshmat, Y. (2009). Determinants of Happiness and Life Satisfaction in Egypt. An Empirical Study using the World Values Survey – Egypt 2008. The Egyptian Cabinet Information and Decision Support Center, Economic Issues Program.
2. Census of India 2011. (2013, May 20). Retrieved from https://www.census2011.co.in/.

LIST OF PUBLICATIONS

- Handa, R. & Maheshwari, G.C. (2016). A study of perceived quality of life of people in Gujarat, *International Journal of Science Technology and Management*, Vol. No.5, Issue No. 12, pp. 564-575. ISSN (O) 2394-1537.

- Handa, R. & Maheshwari, G.C. (2016). A study of sense of well-being and perceived quality of life of people in Central Gujarat, *International Journal of Science Technology and Management*, Vol. No.5, Issue No. 11, pp. 137-146. ISSN (O) 2394-1537.

- Handa, R. & Maheshwari, G.C. (2016). A study of sense of well-being and perceived quality of life of people in North-Gujarat & Central Gujarat, *International Journal of Advance Engineering and Research*, Vol. No.5, Issue No. 11, pp. 171-182. ISSN (O) 2319-8354.

- Handa, R. & Maheshwari, G.C. (2016). Model of quality of life in Gujarat: a subjective approach, *International Journal of Science Technology and Management*, Vol. No.5, Issue No. 12, pp. 576-583. ISSN (O) 2394-1537.

APPENDIX A- QUESTINNAIRE (IN ENGLISH)

Respected Sir/Madam,

I Rajesh Handa – working as an Assistant Professor in the Manish Institute of Management at Visnagar (Mehsana), also I am a doctoral student of Gujarat Technological University, Ahmedabad. I am doing research work on the topic "A study of the sense of well-being and perceived quality of life of people in Gujarat". I am approaching you to get your responses on the topic. You will agree that this kind of research is not possible without the support of people like you. The information provided by you will be kept confidential and used for research purpose only.

→ Place _____

→ I am staying in Gujarat from last five years at a given place. ☐ YES ☐ NO

→ Continue, if your answer is **yes.**

✓ - Please ☑ whichever box applicable in each line.

1. What is your gender? ☐ Male ☐ Female
2. What is your age? ☐ 26–35 years ☐ 36-45 years ☐ 46 -55 years
3. What is your education? _____.
4. What is your marital status? ☐ Unmarried ☐ Married
5. Your residence is located in a: ☐ Village ☐ Town (Municipality) ☐ City (Muni.Cooperation)
6. What is your Annual income? ☐ 1.20 - 2.50 lakhs ☐ 2.51- 6.00 lakhs ☐ 6.01- 12.00 lakhs

Satisfaction with Life Scale

Please ☑ whichever box applicable in each line.

		Strongly disagree	Disagree	Slightly Disagree	Neutral	Slightly Agree	Agree	Strongly agree
1	In most ways my life is close to my ideal.							
2	The conditions of my life are excellent.							
3	I am satisfied with my life.							
4	So far I have got the important things I want in life.							
5	If I could live my life over, I would change almost nothing.							

Semantic Differential Scale

Please ☑whichever box applicable in each line.

My Present Life is….

	7	6	5	4	3	2	1	
Enjoyable								Miserable
Interesting								Boring
Active								Inactive
Happy								Unhappy
Meaningful								Meaningless
Worthwhile								Useless
Rewarding								Disappointing
Easy								Hard
Relaxed								Tightened up
Full of fun								No fun at all
Comfortable								Uncomfortable

Life-domain Satisfaction Scale

Please ☑ whichever box applicable in each line.

		Strongly disagree	Disagree	Slightly Disagree	Neutral	Slightly Agree	Agree	Strongly agree
1	I am satisfied with my house.							
2	I am satisfied with my furniture and appliances at home.							
3	I am satisfied with my vehicle.							
4	I am satisfied with my clothing, accessories & jewelry.							
5	I am satisfied with my saving & investment.							
6	I am satisfied with weather in my village/town/city.							
7	I am satisfied with quality of air in my village/town/city.							
8	I am satisfied with greenery in my village/town/city.							
9	I spent joyful time with my family and friends.							
10	I give sufficient time to self for hobbies, exercise, relaxation, etc.							
11	I spent sufficient time for social gatherings, ceremonies, etc.							
12	I am satisfied with personal income.							
13	I am satisfied from relations with coworkers.							
14	I am satisfied with working hours & timings.							
15	I am satisfied with my career growth.							
16	I am satisfied with internal economic policies of central government (like Interest rates, Income							

	tax slab, etc.)							
17	I am satisfied with international relation policies with neighbor countries of central government.							
18	I am satisfied with central government position on civil rights.							
19	I am satisfied with central government policies to solve the problems like unemployment, poverty, inflation, corruption, terrorism, etc.							
20	I am satisfied with my village/ town/ city growth (Expansion).							
21	I am satisfied with number of bridges/ over bridges/ under bridges in my village/ town/ city.							
22	I am satisfied with supply of electricity in my village/ town/ city.							
23	I am satisfied with mobile network in my village/ town/ city.							
24	I am satisfied with availability of public amenities like Garden/Children's playground/ Community Centre, etc. in my village/ town/ city.							
25	I am satisfied with quality of public transportation services in my village/ town/ city.							
26	I am satisfied with quality of education institute in my village/ town/ city.							
27	I am satisfied with quality of health care services in my village/ town/ city.							
28	I feel inner peace/harmony.							
29	I am working on self-discovery.							

30	I am associated with Guru (Spiritual Guru).							
31	I had felt paranormal/spiritual experience.							
32	I feel close to God/supreme power.							
33	I am satisfied with personal safety and security in my village/ town/ city.							
34	I am satisfied with Government community services like street lights, sanitation, water supply, roads & sewerage maintenance etc. in my village/ town/ city.							
35	There is corruption free public service available in my village/ town/ city.							
36	I feel free from disease/ disorder.							
37	I feel sufficient energy/stamina to live full life.							
38	I feel sufficient body mobility/speed to live full life.							

Thanking you for your gentle support.

Any suggestion_____

APPENDIX B- QUESTINNAIRE (IN GUJARATI)

આદરણીય સાહેબશ્રી/ મેડમ

હું રાજેશ હાંડા, મનીષ ઈન્સ્ટીટ્યુટ ઓફ મેનેજમેન્ટ, વિસનગર (મહેસાણા)માં આસીસ્ટંટ પ્રોફેસર તરીકે કામ કરું છું અને હું ગુજરાત ટેકનોલોજીકલ યુનિવર્સિટી, અમદાવાદ ખાતે ડૉક્ટરલનો વિદ્યાર્થી છું. હું આ વિષય પર સંશોધન કામ કરી રહ્યો છું. ***'ગુજરાતની પ્રજાની સુખાકારી માટેની સમજ અને જીવનની ગુણવત્તા માટેના બોધનો અભ્યાસ'*** *માં આ વિષય પર તમારો પ્રતિભાવ લેવા માટે તમને અપ્રોચ કર્યા છે. આ પ્રકારના સંશોધન કાર્ય, તમારા જેવા લોકોના સહકાર વિના શક્ય નથી, એમાં તમે સહમત હશો. તમારા દ્વારા પ્રાપ્ત કરવામાં આવેલી માહિતી ગુપ્ત રાખવામાં આવશે અને તેનો માત્ર સંશોધન માટે જ ઉપયોગ કરવામાં આવશે.*

- *સ્થળ : .....*
- *હું ગુજરાતમાં છેલ્લા પાંચ વર્ષથી ઉપર દર્શાવેલા સ્થળે રહું છું.* ☐ *હા* ☐*ના*
- **ચાલુ રાખો, જો તમારો જવાબ હા હોય તો.**
- **દરેક લીટીમાં જે ખાનું યોગ્ય હોય તેમાં મહેરબાની કરીને (✓) ખરાની નિશાની કરો.**

૧. *તમારી જાતિ કઈ છે ?* ☐ *પુરુષ* ☐*સ્ત્રી*

૨. *તમારી ઉંમર કેટલી છે.* ☐*૨૬-૩૫ વષ* ☐*૩૬-૪૫ વર્ષ* ☐*૪૬-૫૫ વર્ષ*

૩. *તમારો અભ્યાસ કેટલો છે ? .....*

૪. *તમારી વૈવાવિહક સ્થિતિ શું છે ?* ☐*અપરણિત* ☐*પરણિત*

૫. *તમારું નિવાસ સ્થાન નીચેના પૈકી કયું છે ?* ☐*ગામ* ☐ *નગર* ☐*શહેર*

૬. *તમારી વાર્ષિક આવક કેટલી છે ?*

☐*૧.૨૦- ૨.૫૦ લાખ* ☐ *૨.૫૧ - ૬ .૦૦ લાખ* ☐*૬.૦૧ - ૧૨.૦૦ લાખ*

સેટીસ્ફેકશન વિથ લાઈફ સ્કેલ

→ **દરેક લીટીમાં જે ખાનું યોગ્ય હોય તેમાં મહેરબાની કરીને ✓કરો.**

		પૂર્ણ પણે અસહમત	***અસહમત***	***સહેજ અસહમત***	***તટસ્થ***	***સહેજ સહમત***	***સહમત***	***પૂર્ણપણે સહમત***
૧.	*ઘણીખરી બાબતોમાં મારું જીવન મારા આદર્શોની નજદીક છે.*							
૨.	*મારા જીવનની પરિસ્થિતિ ઘણી સારી છે.*							
૩.	*હું મારા જીવનથી સંતુષ્ટ છું.*							
૪.	*મારા જીવનમાં જોઈતી જરૂરી ચીજો લગભગ મેં મેળવી લીધી છે.*							
૫.	*જો મારું જીવન પુરુ થવાના આરે હોય, તો યે હું મારા જીવનમાં લગભગ કશું બદલવા માંગતો નથી.*							

સીમેન્ટીક ડિફન્સીયલ સ્કેલ

→ દરેક લીટીમાં જે ખાનું યોગ્ય હોય તેમાં મહેરબાની કરીને ✓કરો.

મારું હાલનું જીવન...

	૭	૬	૫	૪	૩	૨	૧	
આનંદપ્રદ								દયાપાત્ર
રસપ્રદ								કંટાળાજનક
સક્રિય								નિષ્ક્રિય
સુખી								દુખી
સાર્થક								નિરર્થક
યોગ્ય								અમસ્તુ
ઈનામી								નિરાશ
સરળ								મુશ્કેલ
આરામદાયક								ખેંચતાણવાળું
મજેદાર								મજા વગરનું
ચેનવાળું								બેચેની વાળું

લાઈફ ડોમેન સેટીસ્ફેકશન સ્કેલ

→ દરેક લીટીમાં જે ખાનું યોગ્ય હોય તેમાં મહેરબાની કરીને ✓ કરો.

		પૂર્ણ પણે અસહમત	અસહમત	સહેજ અસહમત	તટસ્થ	સહેજ સહમત	સહમત	પૂણ પણે સહમત
૧	હું મારા ઘરથી સંતુષ્ટ છું.							
૨	હું મારા ઘરના રાચરચીલું અને ઉપકરણોથી સંતુષ્ટ છું.							
૩	હું મારા વાહનોથી સંતુષ્ટ છું.							
૪	હું મારા પોશાક, ઉપસાધનો અને ઘરેણાંથી સંતુષ્ટ છું.							
૫	હું મારી બચત અને રોકાણોથી સંતુષ્ટ છે.							
૬	હું મારા ગામ / નગર / શહેરના હવામાનથી સંતુષ્ટ છું.							
૭	હું મારા ગામ / નગર / શહેરની હવાની ગુણવત્તાથી સંતુષ્ટ છે.							
૮	હું મારા ગામ / નગર / શહેરની હરિયાળીથી સંતુષ્ટ છું.							
૯	હું મારા પરિવાર અને મિત્રો સાથે આનંદીત સમય પસાર કરી શકું છું.							
૧૦	હું મારી જાતને શોખ, કસરત અને આરામ વગેરે માટે પૂરતો સમય વ્યતીત કરી શકું છું.							
૧૧	હું સામાજીક મેળા અને પ્રસંગોમાં પૂરતો સમય વ્યતીત કરી શકું છું.							
૧૨	હું પોતાની આવકથી સંતુષ્ટ છું.							
૧૩	હું સહકર્મીઓ સાથેના સંબંધોથી સંતુષ્ટ છું.							
૧૪	હું કામ કરવાના કલાક અને સમયથી સંતુષ્ટ છું.							
૧૫	હું મારી કારકિર્દીના વિકાસથી સંતુષ્ટ છું.							
૧૬	હું કેન્દ્ર સરકારની અર્થતંત્રની નીતિ સંતુષ્ટ છું. (જમે કે વ્યાજદર, આવક દર વગેરે..)							
૧૭	હું કેન્દ્ર સરકારની પાડોશી દેશો સાથેની વિદેશ નીતિ થી સંતુષ્ટ છું.							
૧૮	હું કેન્દ્ર સરકારના નાગરિક અધિકાર માટેના વલણથી સંતુષ્ટ છું.							
૧૯	કેન્દ્ર સરકારની જુદી જુદી સમસ્યાઓના જેમ કે બેરોજગારી, ગરીબી, ફુગાવો, ભ્રષ્ટાચાર,							

		પૂર્ણ પણે અસહમત	અસહમત	સહેજ અસહમત	તટસ્થ	સહેજ સહમત	સહમત	પૂણ પણે સહમત
	આંતકવાદ વગેરેના સમાધાન માટેની નીતિ સંતુષ્ટ છું.							
૨૦	હું મારા ગામ / નગર / શહેરના વિકાસ (ફેલાવો)થી સંતુષ્ટ છું.							
૨૧	હું મારા ગામ / નગર / શહેરના બ્રિજ (પુલ), ઓવરબ્રિજ અને અંડરબ્રિજની સંખ્યાથી સંતુષ્ટ છું.							
૨૨	હું મારા ગામ / નગર / શહેરના વીજપ્રવાહના પુરવઠાથી સંતુષ્ટ છું.							
૨૩	હું મારા ગામ / નગર / શહેરના મોબાઈલ નેટવર્કથી સંતુષ્ટ છું.							
૨૪	હું મારા ગામ / નગર / શહેરમાં મને મળતી સરકારી સુખસગવડો જેવી કે બગીચા / બાળકોનું રમવાનું મેદાન, કોમ્યુનીટી સેન્ટર વગેરેથી સંતુષ્ટ છું.							
૨૫	હું મારા ગામ / નગર / શહેરની પરિવહન સેવાની ગુણવત્તાથી સંતુષ્ટ છું.							
૨૬	હું મારા ગામ / નગર / શહેરની શિક્ષણ સંસ્થાની ગુણવત્તાથી સંતુષ્ટ છું.							
૨૭	હું મારા ગામ / નગર / શહેરની આરોગ્ય સંભાળની સેવાઓથી સંતુષ્ટ છું.							
૨૮	મને આંતરિક શાંતિ / સંવાદિતા લાગે છે.							
૨૯	હું પોતાની જાતની શોધ પર કામ કરી રહ્યો છું.							
૩૦	હું ગુરૂ સાથે સંકળાયેલો છું. (આધ્યાત્મિક ગુરૂ)							
૩૧	મને પેરાનોર્મલ / આધ્યાત્મિક અનુભવ થયો છે.							
૩૨	હું પોતાને ભગવાન / મહાસત્તાની નજીક અનુભવું છું.							
૩૩	હું મારા ગામ / નગર / શહેરની વ્યક્તિગત સલામતી અને સુરક્ષાથી સંતુષ્ટ છું.							
૩૪	હું મારા ગામ / નગર / શહેરની જાહેર સમાજ સેવાઓ જેવી કે							

		પૂર્ણ પણે અસહમત	અસહમત	સહેજ અસહમત	તટસ્થ	સહેજ સહમત	સહમત	પૂણ પણે સહમત
	ફળીયાની લાઈટો, સ્વચ્છતા, પાણી પુરવઠો, રોડ અને ગટરની સમારકામ વગેરેથી સંતુષ્ટ છું.							
૩૫	મારા ગામ / નગર / શહેરમાં ભ્રષ્ટાચાર રહિતની સમાજ સેવાઓ ઉપલબ્ધ છે.							
૩૬	હું મારી જાતને રોગ / બીમારીથી મુક્ત અનુભવું છું.							
૩૭	આખુ જીવન જીવવા માટે પૂરતો ઉત્સાહ અને શક્તિ મારી પાસે છે એમ લાગે છે.							
૩૮	આખું જીવન જીવવા માટે શરીરનું પૂરતું હલનચલન અને ગતિ મારી પાસે છે એમ લાગે છે.							

<u>તમારા સૌમ્ય સાથ બદલ તમારો ખૂબ આભાર.</u>

આપનું કોઈ સૂચન હોય તો .....

International Journal of Computer Engineering and Applications,
Volume XII, Special Issue, August 18, www.ijcea.com ISSN 2321-3469





A SURVEY ON ANDROID MALWARE DETECTION TECHNIQUES

Rahul Katarya
Department of Computer Science & Engineering
Delhi Technological University
New Delhi, India
rahulkatarya@dtu.ac.in

Parvesh Mamgain
Department of Information Technology
Delhi Technological University
New Delhi, India
mamgainparvesh@gmail.com

Abstract— ***Mobile Application Market has evolved and is continuously expanding with over millions of applications. Many mobile operating systems are available, most popular among them is Android. Due to its popularity and reach, malware developers are targeting android markets for distributing malware. This has led to an increase in malware growth in Android devices. Traditional detection measures are not able to cope up with the increasing growth of malware. Therefore, there is an immense need for better heuristic-based solutions that can meet the current demand of the anti-malware industry. In this paper, we have analyzed different malware detection approaches and detection vectors that may be used for effective malware detection. We have highlighted the issues and limitations of current malware detection techniques.***

Keywords—Survey, Malware Analysis, Android, Malware Detection, Analysis

I. INTRODUCTION

Android is a popular mobile platform among other platforms like iOS and windows. As of now, the majority of devices run on Android. Users mostly perform business transactions through their mobile devices. Therefore, Smartphones have become a central point for sensitive information. Due to this, malware developers are targeting Android devices by distributing malware. Malware refers to a variety of unwanted software that is used for performing malicious activities. Few commonly used malware are viruses, spyware, Trojan horses, rootkits, backdoors etc. There are various ways by which malware gets distributed to the end user like downloading and installing repacked apps, downloading the apps from the malicious website, third-party app store, play store etc. Android allows installing apps from other third-party app stores which further increase the risk of being infected by malware as most of these sources are unverified. Google Play is the official service provided by Google for downloading apps. However, it is found that it is also not secure [1]. Android has become a rich

target environment for malware because of Larger Attack Surface, Open Source and loose security in Google play store. These shortcomings have led to an increase in growth of Android malware. According to Quick heal annual report 2017, there is a 50% increase in Android samples detection count from 2016 to 2017 [2]. There is an enormous growth in malware from 2014 to 2017 (up to quarter 3) as shown in fig. 1 [3]. Reports suggest there is an increase in profit-driven malware like ransomware, adware, potentially unwanted Programs (PUP), premium SMS etc.

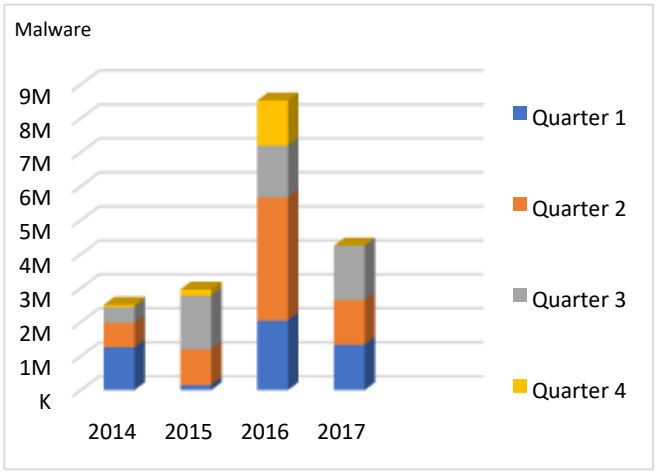


Fig. 1 Malicious Installation packages detected by Kaspersky Lab.

In this paper, we have discussed malware & its types, malware analysis techniques, and malware detection measures. The remaining part of this paper is arranged as follow. Section II begins with an overview of malware. Section III describes the Android architecture and files that are required for analysis. Section IV briefly describes General Framework for malware detection. Section V briefly describes Malware detection techniques. Section VI discusses malware analysis vectors and Lastly, Section VII presents the conclusion.

II. MALWARE

Malware is the malicious application that is used by hackers for committing unethical activities like fraud, information leak, Stealing user private data, Identity Theft etc. In 2018, A new type of malware was detected by Trend Micro which was developed using Kotlin. It can infect mobile devices with ads and secretly subscribe them to premium SMS numbers. Other features include remote code execution, SMS sending, etc. [4]. Most of the malware's are developed with some intent of profit or gain. However, Malware development may or may not be profit driven. Initially, malware was developed to showcase the proficiency of one's technical ability. However, these days trends have changed, the number of profit-driven malware has increased enormously. Various security reports from leading anti-malware products suggest the following trends and predictions - Development of more sophisticated ransomware, Machine learning based malware, the growth of potentially unwanted programs, Growth in the payment system and banking malware [5]–[8]. On the basis of the behavior of the malware, most common mobile malware types are – Expander, Worm, Trojan, and Spyware [9].

1. **Expander** - It is a type of mobile malware that targets mobile meter for additional billing by subscribing the user to premium services. Most types of malware that fall under this category targets services for profit. ANDROIDOS_BKOTKLIND.HRX is a new type of Android malware developed in Kotlin that subscribe users to premium SMS services and displays ads to them [4].

2. **Worm** - Worms are the type of malware that contains harmful instructions that do not require user interaction for executing its malicious behavior. It uses a computer network as a medium to spread itself across millions of devices. It relies on security failures of the target device to access its resources. They always cause at least some damage to the network, even if only by consuming bandwidth. SAMSAPO is an android worm that spread itself by sending an SMS message to all the contacts that are listed in the device. The message contains a malicious link to a malicious APK package. Abilities of this worm include gathering and sending information from the mobile device to a remote server, registering the phone number to a premium service etc. [10].

3. **Trojans** - Trojans are the type of mobile malware that disguises itself as a normal application, However, executes malicious behavior in the background. They are the executables that required user interaction, once activated they can cause serious damage to the victim device. They behave to be legit but performs the malicious action in the background. Trojans are usually spread through social engineering techniques. In 2017, a new mobile trojan was found by Malwarebytes called Android/Trojan.AsiaHitGroup which masquerades as multiple apps which we use in our day to day life like an alarm clock, QR scanner, compass, photo editor, Internet speed test, and file explorer. In this malware, malicious payloads are distributed over these apps [11].

4. ***Spyware*** **-** It is used for monitoring users personal and sensitive activities without user's consent. Its main objective is to gather information about a person or organization without their knowledge. GO Keyboard virtual Android application is a malware application that transmits user's personal information without user's consent. This information includes user's account details, location, network details, Android version and build, and device's model and screen size. This malware supports remote code execution attack. This app has affected millions of users worldwide. It was detected in 2017 by security researchers from AdGuard [12].

Quick Heal Report 2017 suggest that adware and premium SMS service based infections have dominated the year 2017 as shown in the fig. 2 [2]. The report indicates that the growth of Banking Trojans and ransomware have increased. The report also mentions the security vulnerability of the Android operating system like Code execution flaws, Information gain attacks etc. According to Quick heal threat report 2017 trends and predictions, android vulnerability and potentially unwanted programs are a major concern in the coming days. It also suggests that PUA's are increasing rapidly.

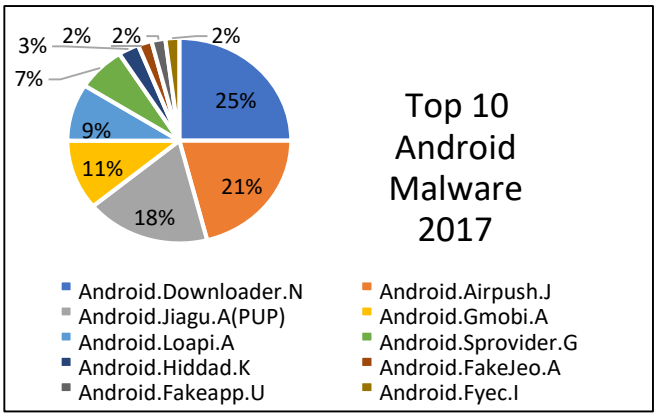


Fig. 2 Top 10 Android Malware 2017

III. ANDROID OVERVIEW

Android is a popular mobile platform. It has a large market share of 86.1% as of 2017 [13]. Android architecture can be described as a stack of components categorized into five layers as shown in the Fig. 3 [14]. The top layer consists of core applications that are included in the Android platform along with other apps. Java API framework acts as an interface between systems apps and native library & android runtime. It provides a framework for developing an android application. Native libraries consist of core features and services that are written in C and C++. Android runtime provides a runtime environment for executing dex files. HAL consist of several interfaces that are used for interacting with the corresponding hardware component. The Linux kernel forms the core of the Android platform which manages core functionalities. All applications execute separately within their own Dalvik Virtual Machine instance in ART (Android Runtime). However, After Android 5.0, this was changed to Ahead of Time compiler as opposed to dalvik just in time compiler (JIT). User-defined applications are executed on the top layer of Android architecture. They interact with each other through intents. The process is known as Interprocess communication. Intents can be implicit or explicit. They are used by various Android components for interacting with one another. Android application is packed into a special compressed file known as APK File.

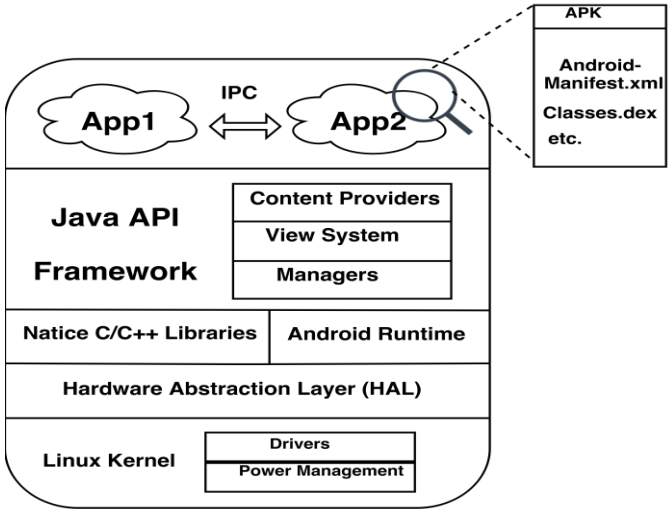


Fig. 3 Android Stack.

APK is the standard file format for the Android application. Android Package Kit (APK) is a type of archive file with a ***.apk** extension. The content of the APK file is described below.

- **META-INF** – This folder contains the metadata about the java package. It contains the manifest file, list of files along with SHA-1 digest and certificate.
- **ASSETS** – This folder contains the files or resources that can be used by the application. AssetManager class provides the access to these files or resources.
- **AndroidManifest.xml** – It is an important XML file that describes the name of the packages, permissions, version, referenced library and application components that are used in the application.

- **Classes.dex –** Android apps are written in Java which upon compilation produces bytecode which is further converted into a dalvik executable file which is interpreted by dalvik virtual machine.
- **Lib –** This directory contains processor specific compiled code.
- **Res –** It holds the raw files that are not compiled such as drawable, media etc.

Among them, Classes.dex and androidmanifest.xml is widely used for extracting malware behavior. In Android, access to a resource is granted by Android Permission System if the corresponding permission is listed in the manifest file. Android permission system acts as a primary defense against malware applications by preventing an application from gaining access to an unauthorized resource. Permissions can be further categorized into following categories based on the risk associated with them.

1. **Normal**: A low-risk permission that is automatically granted to an application on request. They provide access to features having minimal risk.
2. **Dangerous**: A high-risk permission that can grant access to user private data. It is granted by the user during installation.
3. **Signature**: This permission is only granted by the system if and only if the application that is requesting the permission is signed.
4. **Signatureorsystem**: This permission is granted by the system only to those apps that either belongs to Android system image or that are signed.

IV. GENERAL FRAMEWORK

In this section, we have discussed the general framework that is widely used by machine learning based anti-malware products. Most android analysis techniques follow this general framework with few modifications. The general framework is shown in fig. 4. In the initial phase, malware dataset and the benign dataset is created. Malware dataset can be constructed by collecting samples manually by accessing malicious sources or from online malware repositories like VirusShare [15]. The benign set can be constructed by collecting samples from play store or third-party app stores. Once samples are collected, feature extraction process is applied to the dataset which extracts the relevant features from the dataset and produces a binary representation or a graph representation of the features. Features can be extracted statically or dynamically. In static analysis, we analyze the source code of the APK while in dynamic analysis, we execute the APK and extract features by monitoring its behavior. A feature vector is generated for each application denoting the behavior of the application. Let us consider a one-dimensional feature vector $f(x)$ where x is a set of finite features such that $x = \{x_1\ x_2\ .\ .\ .\ .\ .\ .\ x_N\}$. Here a feature can be a permission, function call, system calls, hardware detail etc. They are extracted from static or dynamic analysis phase. Once features are extracted, the feature vector is constructed. We can use frequency representation and binary representation for constructing feature vector. In binary representation, 1 denotes feature is present and 0 represent feature is not present as shown in equation (1). In frequency representation, n denotes no of times that particular feature is present in the application as shown in equation (2).

$$f(x) = \begin{cases} 1 & \textit{feature present} \\ 0 & \textit{otherwise} \end{cases} \quad (1)$$

$$f(x) = n : \textit{count of feature } i \quad (2)$$

Usually, the feature set is very large which results in a large number of computations and requires a lot of resources. Therefore, feature selection techniques like Information Gain are used to minimize the dimensionality of the vector. Feature selection technique ranks the features on the basis of their contribution to malware detection. Best features are selected and rest features are removed thus reducing the size of the feature vector. Machine learning techniques are applied to the reduced feature vector to learn a model which is used for malware classification.

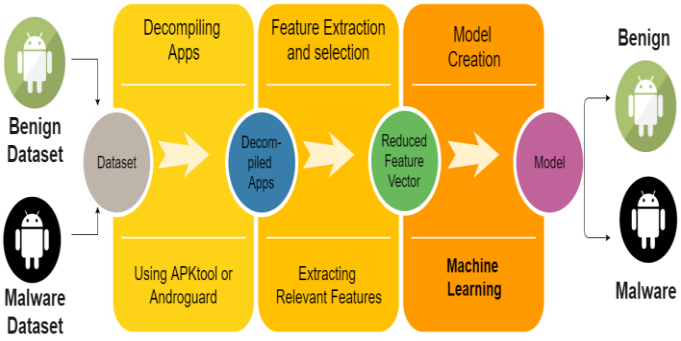


Fig 4. General Framework for malware detection

Experimental Studies shows that static analysis is widely used for detecting mobile malware as it is efficient and requires less computation [16]. However, sophisticated malware can bypass static malware detectors. On the other hand, the Dynamic analysis is computationally expensive and hence, the on-device

dynamic analysis is rarely used [17]. Combination of both techniques is preferred and yields better result [18].

V. MALWARE DETECTION TECHNIQUES

In this section, we will briefly discuss different malware detection techniques and issues associated with these techniques. Malware detection is the process of analyzing the application with the intent of determining whether the application is benign or malware. These are some issues which one should keep in mind while designing a malware detector like mobile devices have limited resources such as battery life and therefore on-device analysis is somewhat difficult. Also, Android Permission System prevents antivirus applications to introspect other application, which further limit the extent of the analysis. Therefore, most of the detection techniques are cloud-based. Considering these issues, following detection techniques are used –

1. **Signature Based Detection** - Traditional techniques for malware detection uses signatures for detecting malware applications. In this technique, A signature is computed for an application by extracting binary patterns or snippets from the code such that the signature is unique to the application. The signature is then matched with the dataset consisting of malware signatures. If a match occurs then the application is malware else benign. To further improve the detection accuracy, cloud-based detection methods were developed in which dataset is maintained at the server end and a signature is matched with the server-side dataset. The central repository is regularly updated so that accuracy of detection can be improved. This technique is highly inefficient while considering the current pace of malware development. Limitations of signature-based detection technique include Ineffective for detecting the zero-day vulnerability, Obfuscation attacks go undetected and It cannot detect encrypted malware.

2. **Static Analysis Based Detection** - In this technique, the application is examined without executing the code [16], [19], [20]. AndroidManifest.xml and Classes.dex file is widely used for feature extraction. The manifest file is decompiled and then features are extracted by developing a custom XML parser. Classes.dex is a compiled binary which needs to be decompiled before using it. Various tools are available for decompiling dex files like APK Tool [21] and Androguard [22]. Static analysis-based detection is fast and yields a better result with good accuracy. However, it has the following limitations. It is Vulnerable to obfuscation, reflection, and encryption. It cannot analyze dynamically loaded code. Some of the static analysis tools that are widely used for analyzing applications are – Smali and Baksmali [23], Androguard [22] and ApkTool.[21].

3. ***Dynamic Analysis Based Detection*** - In dynamic analysis technique, Application is examined at runtime by executing the application [17], [24]. The runtime environment can be a virtual machine, Sandbox or a real mobile device. This technique is not vulnerable to obfuscation and reflection attacks. However, malware is becoming more sophisticated and can detect an emulated environment and choose not to exhibit malicious behavior. Few limitations of this technique are - Limited coverage as the user has to interact with the application to execute different modules. However, stimulation techniques can be used to improve coverage, executing a lot of paths is a costly process, no guarantee that all execution paths are executed, Smartphones accept a wide set of touch commands which further complicates the analysis and Difficult to detect VM-Aware malware. Some of the dynamic analysis tools that are widely used for analyzing applications are – DroidBox [25] and CuckooDroid [26].

4. **Hybrid Analysis Based Detection** - Static analysis is fast but is vulnerable to obfuscation and reflection attacks. Dynamic analysis is robust to these attacks but is timeconsuming. Therefore, a combination of these two approaches is used for detecting malware [18], [27]. Hybrid analysis has the advantage of both the techniques. Combination of Virtualization technique and real devices can also be used for detecting advance sophisticated

Virtual machine aware malware. Experiments show that the combination of static and dynamic analysis yields a better result.

VI. MALWARE ANALYSIS VECTORS

This section provides a brief discussion about different vectors for malware analysis. There are different kinds of features that can be extracted from an APK file. The APK is analyzed in different areas where there is a probability of a potential leak. Many studies are carried out in different directions for malware analysis, few of them are listed below.

1. **Network Traffic** - Network access is requested by most of the applications especially by malicious

application for transferring data from victim device to a malicious destination. Taint analysis is often used to analyze the communication. Frameworks are implemented that studies network traffic for malicious behavior. Network traffic is often encrypted. However, studies show that user actions can be identified to some extent by eavesdropping network traffic [28].

2. **APIs** - Application program interface (API) is a set of methods that are used by the application for interacting with the device. Library and system API calls are monitored for malware detection [24].
3. **System Calls** - It is a method by which a user app makes a service request to the kernel of the operating system. The kernel accepts the request and perform a transition to the kernel mode and executes the service and finally, performs a transition back to user mode. A system call is hardware dependent. An app can interact with system hardware only via a system call. Malware behavior can be reconstructed by analyzing system calls [29].
4. **Dependency Graph** - It is the description of the source code of the application in which a node denotes a statement and an edge denotes the relation between the two statements. Data flow analysis is often carried out by using dependency graphs [19]. Dependency graphs can also be constructed dynamically [30].
5. **Features** - Features are extracted from the decompiled apps which consist of permissions and other relevant data from the manifest. The limitation of this analysis technique is it cannot determine the context that is when a permission request is triggered. Frameworks are developed for malware detection by analyzing features [16]. User location can also be tracked by analyzing features [31].
6. **Function Call monitoring** - Function calls such as library APIs, are monitored dynamically for reconstructing the behavior of the application. Function hooks can also be used for further analysis. Analysis framework is developed for Android malware detection [32].
7. **Taint** - In information flow analysis, transfer of information is tracked throughout the system. Detecting information flow in Android is complex. Hence, taint analysis is widely used for tracing the data flow from a tainted source to a taint sink. Taint analysis is used for identifying information leaks in an android application [17]. Implicit information flow analysis can be used for mitigating potential threats in an application.
8. **IPC** - An Android application consists of activity, services, broadcast receivers and content providers. These components interact with each other through Inter-Process Communication and Remote Procedure Calls. Data can also be leaked through IPC channels hence analyzing IPC communication is also important. Frameworks were developed that studies IPC for effective malware classification [20].
9. **Other** - Few studies are also carried out by analyzing hardware status like CPU consumption, power signature etc. [33]. Hardware features can be extracted by parsing the manifest file. Malicious behavior can also be detected by investigating energy consumption across a transmitting channel [34].

VII. CONCLUSION

In this paper, we have discussed malware, malware types and their source of distribution. We have studied different malware detection techniques and highlighted the issues and limitations of those techniques. After analyzing different trends in malware and their detection techniques we came up with the following conclusions.

- Malware is shifting towards more sophisticated obfuscation techniques which makes them harder to detect. They can easily detect emulated environments. Hence, can evade most of the current anti-malware detection techniques.
- There is a lack of a standard malware dataset for malware analysis. Most of the datasets that are available are outdated. Hence, there is an immense need for an updated diverse dataset.
- Mobile devices have limited resources especially battery life and hence on device analysis is difficult and challenging.
- Dynamic Incremental learning algorithms are required for classifying malware to deal with the new trends in malware growth.
- Hybrid techniques are required that uses mobile device and virtualization techniques for detecting sophisticated VM-Aware malware.

REFERENCES

[1] Fortune, “Google Android_ Massive Malware Infection Invades Google Play Store.” [Online]. Available: http://fortune.com/2017/09/14/google-playandroid-malware/.

[2] E. S. Solutions and Q. Heal, “Quick Heal 2017 Annual Threat Report,” 2017.

[3] Securelist, “Archive_ All - Securelist,” 2017. [Online]. Available: https://securelist.com/all/?category=919.

[4] “First Kotlin-Developed Malicious App Signs Users Up for Premium SMS Services - TrendLabs Security Intelligence Blog.” [Online]. Available: http://blog.trendmicro.com/trendlabs-

securityintelligence/first-kotlin-developed-malicious-appsigns-users-premium-sms-services/.

[5] "Malware Bytes WHite Paper.pdf," 2017.

[6] "sophoslabs-2017-malware-forecast-report.pdf."

[7] "Symantec whitepaper istr-financial-threats-review-2017-en.pdf."

[8] "F-Secure whitepaper State of Cyber Security 2017.pdf."

[9] J. Mitchell, "Mobile Malware Types," 2015. [Online]. Available: https://en.wikipedia.org/wiki/Mobile_malware. [10] "Android.Samsapo - Mobile Worm." [Online]. Available: https://www.symantec.com/security_response/writeup.jsp?docid=2014-050111-1908-99.

[11] "Android/Trojan.AsiaHitGroup - Malwarebytes Labs _ Malwarebytes Labs." [Online]. Available: https://blog.malwarebytes.com/cybercrime/2017/11/new-trojan-malware-discovered-google-play/.

[12] "Mobile Spyware- Go Keyboard app." [Online]. Available: https://www.bleepingcomputer.com/news/security/popular-android-keyboard-app-caught-collecting-userdata-running-external-code/.

[13] Statista, "Mobile OS market share 2017," *Www.Statista.Com*, 2017. [Online]. Available: https://www.statista.com/statistics/266136/global-market-share-held-by-smartphone-operating-systems/. [14] "Platform Architecture | Android Developers." 2017.

[15] "VirusShare." [Online]. Available: https://virusshare.com/.

[16] H. J. Zhu, Z. H. You, Z. X. Zhu, W. L. Shi, X. Chen, and L. Cheng, "DroidDet: Effective and robust detection of android malware using static analysis along with rotation forest model," *Neurocomputing*, 2017.

[17] W. You, B. Liang, W. Shi, P. Wang, and X. Zhang, "TaintMan: an ART-Compatible Dynamic Taint Analysis Framework on Unmodified and Non-Rooted Android Devices," *IEEE Trans. Dependable Secur. Comput.*, vol. 5971, no. c, 2017.

[18] C. Gurkok, "Securing Cloud Computing Systems," *Comput. Inf. Secur. Handb.*, pp. 897–922, 2017.

[19] A. Narayanan, S. Member, M. Chandramohan, and S. Member, "Context-Aware, Adaptive, and Scalable Android Malware Detection Through Online Learning," *Ieee Trans. Emerg. Top. Comput. Intell.*, vol. 1, no. 3, pp. 157–175, 2017.

[20] K. Xu, Y. Li, and R. H. Deng, "ICCDetector: ICC-Based Malware Detection on Android," *IEEE Trans. Inf. Forensics Secur.*, vol. 11, no. 6, pp. 1252–1264, 2016.

[21] C. Tumbleson and R. Wiśniewski, "Apktool - A tool for reverse engineering 3rd party, closed, binary Android apps." [Online]. Available: https://ibotpeaches.github.io/Apktool/.

[22] "Androguard - Reverse engineering Tool." [Online]. Available: https://github.com/androguard/androguard.

[23] "GitHub - smali_baksmali." [Online]. Available: https://github.com/JesusFreke/smali.

[24] L. Wei, W. Luo, J. Weng, Y. Zhong, X. Zhang, and Z. Yan, "Machine Learning-based Malicious Application Detection of Android," *IEEE Access*, vol. PP, no. 99, p. 1, 2017.

[25] "GitHub - pjlantz_droidbox_ Dynamic analysis of Android apps." [Online]. Available: https://github.com/pjlantz/droidbox.

[26] "GitHub - idanr1986_cuckoo-droid_ CuckooDroid - Automated Android Malware Analysis with Cuckoo Sandbox." [Online]. Available: https://github.com/idanr1986/cuckoo-droid.

[27] M. Sun, X. Li, J. C. S. Lui, R. T. B. Ma, and Z. Liang, "Monet: A User-Oriented Behavior-Based Malware Variants Detection System for Android," *IEEE Trans. Inf. Forensics Secur.*, vol. 12, no. 5, pp. 1103–1112, 2017.

[28] M. Conti, L. V. Mancini, R. Spolaor, and N. V. Verde, "Analyzing Android Encrypted Network Traffic to Identify User Actions," *IEEE Trans. Inf. Forensics Secur.*, vol. 11, no. 1, pp. 114–125, 2016.

[29] X. Xiao, Z. Wang, Q. Li, S. Xia, and Y. Jiang, "Backpropagation neural network on Markov chains from system call sequences: a new approach for detecting Android malware with system call sequences," *IET Inf. Secur.*, vol. 11, no. 1, pp. 8–15, 2017.

[30] Z. Lin, R. Wang, X. Jia, S. Zhang, and C. Wu, "Classifying android malware with dynamic behavior dependency graphs," *Proc. - 15th IEEE Int. Conf. Trust. Secur. Priv. Comput. Commun. 10th IEEE Int. Conf. Big Data Sci. Eng. 14th IEEE Int. Symp. Parallel Distrib. Proce*, pp. 378–385, 2016.

[31] S. Narain, T. D. Vo-Huu, K. Block, and G. Noubir, "The Perils of User Tracking Using Zero-Permission Mobile Apps," *IEEE Secur. Priv.*, vol. 15, no. 2, pp. 32–41, 2017.

[32] M. Fan, J. Liu, W. Wang, H. Li, Z. Tian, and T. Liu, "DAPASA: Detecting Android Piggybacked Apps Through Sensitive Subgraph Analysis," *IEEE Trans. Inf. Forensics Secur.*, vol. 12, no. 8, pp. 1772–1785, 2017.

[33] D. Arp, M. Spreitzenbarth, M. Hübner, H. Gascon, and K. Rieck, "Drebin: Effective and Explainable Detection of Android Malware in Your Pocket," *Proc. 2014 Netw. Distrib. Syst. Secur. Symp.*, 2014.

[34] L. Caviglione, M. Gaggero, J. F. Lalande, W. Mazurczyk, and M. Urbański, "Seeing the unseen: Revealing mobile malware hidden communications via energy consumption and artificial intelligence," *IEEE Trans. Inf. Forensics Secur.*, vol. 11, no. 4, pp. 799–810, 2016.

International Journal of Computer Engineering and Applications,
Volume XII, Special Issue, August 18, www.ijcea.com ISSN 2321-3469





A SURVEY ON INTERNET TRAFFIC CLASSIFICATION TECHNIQUES

Sharvi Tomar

Department of Applied Mathematics, Delhi Technological University Delhi, India
tomarsharvi24@gmail.com
Rahul Katarya
Department.of Computer Science & Engineering, Delhi Technological University Delhi, India
rahulkatarya@dtu.ac.in

ABSTRACT

To efficiently manage the resources of your network, the Internet Service Provider (ISP) needs to know the characteristics of the transported traffic flows through its infrastructure and know how to identify the application which generated the flows themselves. With this information, the ISP can establish every flow. Moreover, knowing the application that by curbing a certain flow, the quality requirements can be accurately established of the service associated with it which, if respected, determines a greater degree of user satisfaction. The analysis of Internet traffic and its identification can provide this information of strategic importance to the ISP. This paper describes the various techniques of classification used for the task and hence gives an overview of the development in this field of research

Keywords—*Internet traffic classification, feature selection, machine learning*

I. INTRODUCTION

The internet globally will continue to gain users and consume more bandwidth in the coming years. There are a number of drivers behind the growth in global IP traffic, including internet of things (IoT) growth, increased use of ultra-high-definition TVs and faster WiFi speeds to cause of internet traffic through file sharing, streaming media, video conferencing, malware etc. Knowing that internet traffic, which is the bulk load of data sent and received over the internet, grows in a manner conforming to the Moore's Law, it is expected that the volumes of traffic exchanged over the internet would be 650 Tbps in the year 2030. We thus need to push the limits of the capabilities of today's network management and solve problems which comprise of the following critical aspects of network security: (1) evaluation of vulnerabilities, (2) automatic response to infections, (3) repair of damages, (4) firewall settings and real-time scanning, and (5) manual scans.

To monitor the internet traffic for the purpose of administration in implementing security policies and/or detecting any abnormalities or threats, understanding of the internet traffic is the foremost task. Hence, we need to closely analyze the traffic over the internet network and hence internet traffic classification has become very important. Nowadays, due to the congestion of the Internet, the common strategy used by Network service providers are based on under-utilization (over provisioning) of capacity transmissive connection. Then

it is necessary, to recognize customers with needs and different

consumption for the Quality of Service (QoS) they receive which implies that all QoS systems have a certain extent of IP traffic classification implicit in their to support a network implementation based on one non-homogeneous distribution of QoS among the various users.

Among the ISPs, then, traffic classification techniques present the potential to use identifying models of network traffic and to identify, therefore, which division of applications are used by an individual subject to control, in any one moment. Then, depending on the particular identification scheme used, the information regarding the classification of network traffic can potentially be obtained without any violation of the privacy of the subject in question with the suitable Machine Learning algorithms.

II. DEFINITION

The classification of network traffic consists of distinguishing the application that generated the sequence of packets exchanged between two devices equipped with NIC (Network Interface Card), and two respective ports at the transport level. Its importance is due, essentially to two very significant areas: the quality of service of IP networks (QoS) and legal interception systems (LI).

III. CLASSIFICATION

The basis for classification of internet traffic is shown in Fig. 1.

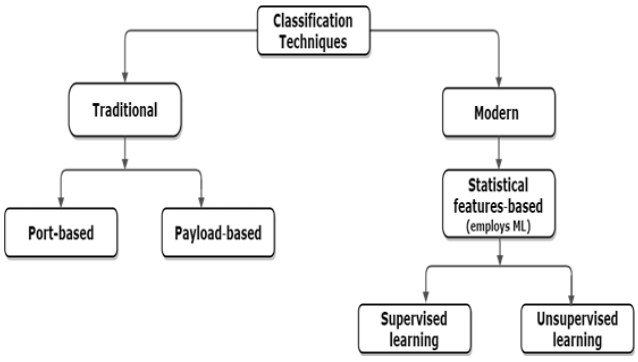


Fig. 1. Internet Traffic classification techniques

A. Classification on the basis of port number

Traditionally, the identification of the application which generates a traffic flow below the observation was performed by recognition of the doors at the transport level. The analysis of the transport ports was a simple method and effective for identifying applications by observing the belonging packages to the flow. The package reports explicitly the port number of the destination (Destination Port) in the header of TCP to identify the application which uses the data contained in the package.

Unfortunately, this method is applicable today in a small number of cases, as many applications, and precisely those that generate the most traffic, select ports dynamically and use generic ports with the aim of masquerading and to make an application indistinguishable from a normal web browsing.

B. Classification on the basis of payload

The packet inspection is another traditional method for identification. In this method, we observe the content of packages to identify protocols exchange that occurs through the flows and, therefore, identify the application.

For better understanding and validation of different applications Signature analysis is performed. Each application has different signatures related to it and correspondingly a reference database is created. These references are used by classification engines for finding the exact application, hence these references need to be updated regularly to keep latest advancements in currently deployed protocols. The methods used for Signature Analysis include:

- **Pattern analysis:** A pattern of string/characters/bytes in the payload of packets is used to classify the underlying protocol. Such pattern may not always be at a specific offset and in some cases, depending on the application, the pattern may not exist. In such cases, this method can't be deployed.
- **Numerical analysis:** This method includes the examination of numerical parameters such as the number of response packets, the size of the payload and offsets for the purpose of classification.
- **Behavioral/Heuristic analysis***:* Deep research in traffic behavior can be used for differentiating applications by providing helpful information of the applications that might be running. Similarly, by doing heuristic evaluation through decision rules or weighing methods of the packets, the protocol within them can be differentiated well

and thus, classified. Behavior and statistical analysis go side by side and many anti-viral programs follow these methods to identify the malicious software like worms and viruses.

- **Protocol/state analysis**: In some applications, there is a particular order of steps followed by the protocol. This specific series of steps followed by the protocol helps in classification of the application accordingly.

There are some problems which, in reality, make the packet inspection in general insufficient.

- In the first place, a protocol analysis must be stateful, that is, it is necessary to memorize and hold updated a

  status for each flow examined, in order to record the current status of the hypothesized protocol and, therefore, verify the goodness of the hypothesis. This produces clearly scalability problems on high links capacity and for a large number of flows.

- Furthermore, one must keep in mind that many applications encrypt the payload of the packages and, thereby making the protocol exchanges less and less observable.

- Finally, the observation of the payload of the packages yes clash with data privacy issues users' personal data in many countries.

Packet inspection can be made more scalable through a stateless approach, giving up to explicitly intercept the protocol exchanges and looking for details strings in the packet payload.

In conclusion, packet inspection is a tool effective, but whose validity is not complete above all due to the impossibility of identifying strings characteristics in the payload of an encrypted or tunneled package where all upper layer information becomes invisible and the content of the payload is not accessible.

C. Classification on the basis of statistical methods Current strategies involve classification on the basis of a statistical method which employs statistical examination of the traffic behavior such as inter-packet arrival time, session time and so on. Inter-packet arrival time has been proven to provide a relevant basis for classification of internet traffic after suitable handling [14]. These methods combine the machine learning techniques for the purpose of classification along with the statistical analysis of flow parameters and overcome the shortcomings of payload-based techniques wherein the payload content access was necessary.

Machine Learning is a science that uses an automated algorithm and gets machines to act without being explicitly programmed. Machine learning is all about ordering the findings of information collected to discern patterns and to predict new ones. Learning can be done by capturing interesting features from examples, data structures or sensors, to analyze them and evaluate the relationships between the observed variables.

The two preferred machine learning methods are supervised learning and unsupervised learning. The performance of the models employing ML-based algorithms and based on any of the learning approaches is greatly affected the technique of feature selection.

IV. FEATURE SELECTION

As for every problem that finds its solution through machine learning, feature selection is important, and internet traffic classification through machine learning is no different. Out of all the available features, all the features are not equally important and some create a negative effect on the accuracy of classification algorithms. Feature selection eliminates the redundant and uncorrelated features leaving the features that map majority of the information. The evaluation metric methods of feature selection could be divided into 3 major categories: filter methods, wrapper methods and hybrid methods [1], [2] as shown in Fig. 2.

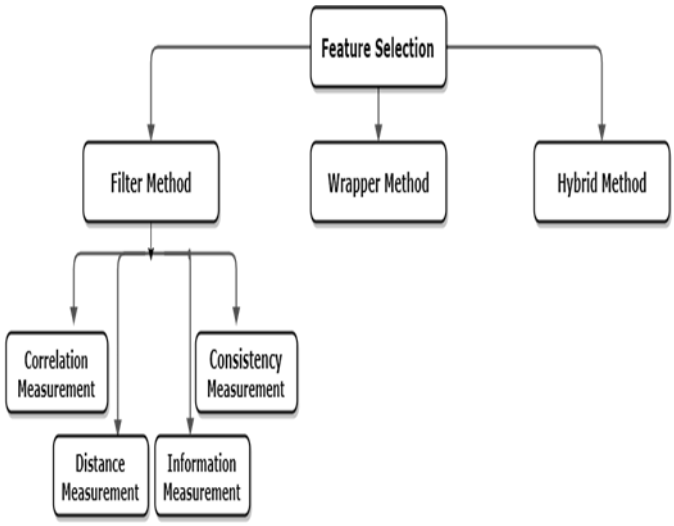


Fig. 2. Evaluation metric methods of feature selection

A. Filter Method

The filter method for evaluation of features involves ranking of features through various similarity and dissimilarity measure and creating ranked lists of the features. The features can be selected from the rank lists depending upon the quantity of information mapped by the features. Various measures of ranking in filter method are described as below
[3]:

1) **Correlation Measurement***:* With the assumption that the points lie closer to each other in feature space, features are ranked on the basis of their correlation with other features. The Pearson correlation coefficient is a commonly adopted measurement tool, as shown below:

$$R(i) = \frac{cov(X_i, Y)}{\sqrt{var(X_i) var(Y)}} \quad (1)$$

where: R(i) is the Pearson correlation coefficient and cov (X_i, Y) represents the covariance between the features X_i and Y and var(X_i) and var(Y) are the variance of the features X_i and Y respectively.

2) **Distance Measurement:** Distance measurement technique is based on the fact that the points in a class lie closer to each other than they are to the points of other class (much like unsupervised learning). Some of the popular distance measurements are Euclidean distance, Mahalanobis distance, Minkowski distance etc [3].

3) **Information Measurement***:* Measurement of the information delivered about a variable by the other variable is carried out on the basis of an information gain formula. Assuming the fact that dissimilar information carries increased or additional knowledge or insight, the information gain formulas, as described in [4], [5] are:

$$H(Y) = \sum_{i=1}^{m} P_i log(P_i) \quad (2)$$

where H(Y) is the entropy of feature Y.

After subjecting the variable X to the condition (X = X_i), the conditional entropy of Y is:

$$H(Y|X) = \sum_{i=1}^{m} * H(Y|X = X_i) \quad (3)$$

Now, the uncertainty of Y has decreased, thereby implying an increase in certainty represented as information gain and is represented as:

$$IG(Y|X) = H(Y) - H(Y|X) \quad (4)$$

where IG(Y|X) is the information gain on Y given the condition X.

4) **Consistency Measurement***:* As described in [4], the object belonging to same class should have a very similar set of features and those belonging to different class should have different. If the feature values of the objects belonging to different classes are same, the feature should not be favored.

B. Wrapper Method

Wrapper method evaluates the subsets of features based on some property to find any possible kind of relationship between them. Wrappers classify feature sets using the selected subset. For the selection of feature sets both forward and backward searches are employed, mainly based on a heuristic function. Mainly the wrapper method works on backward selection method and goes on elimination the features rather than selecting them. The two main disadvantages of this method are Over-fitting and availability of insufficient data.

C. Hybrid Method

The hybrid method combines the speed of wrapper method with the accuracy of filter method. The hybrid method works by combining the forward selection feature of filter method. It takes two steps forward for feature selection. But in the forward selection, the size of the set to be searched upon should be limited. Moreover, the filter method is also of less use in the case of less correlated features. In case of larger sets and low correlated features, the features of wrapper method i.e. the backward selection is employed.

V. SUPERVISED AND UNSUPERVISED LEARNING

A. Supervised Learning

The term supervised learning (or supervised learning) refers to the machine learning methodology in which the machine is passed an example composed of a pair of data containing the original data and the expected result. The task of the machine is to find the rule (function or model) with which to create a relationship between the two in such a way that, when a previously unknown example occurs, it can obtain the correct result.

A number of different supervised machine learning techniques have been employed for the task of traffic classification such as:

1) Using Nearest Neighbour

This classifier assigns the class to the test sample to which it belongs based on the distance of this from the objects inserted into memory. M. Roughan [20] combined the parametric approach of classification wherein we presuppose a

multi-normal analysis of the variables, such as the Discriminant Analysis (LDA and QDA) with the non-parametric approach wherein we take into account only

the distances between objects in space, regardless of their distribution, as ad example the K-Nearest Neighbor.

2) Using Bayesian *Techniques*

Bayesian methods offer an alternative to the statistical approach and employ Bayes theorem: they consider the parameter as a random variable and define the probability as a "degree of trust" (i.e. a measure of the researcher's expectation on the occurrence of the study event).Since probabilities are "subjective" (different individuals may have different expectations on the same phenomenon) there are probabilistic laws defined on the parameter of interest.

Naive Bayes with Discretisation (NBD), Naive Bayes with Kernel Density Estimation (NBK), Bayesian Network, and Naive Bayes Tree have been used for classification. The work by Williams et al. [12] provides a performance evaluation of these algorithms in terms of the speed of classification i.e. the number of classification results computed per second and the associated classification model build time. TABLE I. shows the comparison of various Bayesian techniques by Williams et al. [12] in order of decreasing classification speeds and increasing build time for the models.

TABLE I. Comparison of Bayesian Techniques

	Classification Speed	Build Time
1.	C4.5	NBK
2.	NBD	NBD
3.	Bayes Net	Bayes Net
4.	NBTree	C4.5
5.	NBK	NBTree

His work also revealed the fact that the feature reduction methodology effectively reduces the computational time for classification and the time required in building the respective model without much loss of accuracy.

3) Using C4.5 Decision Tree

A new technique was proposed which comprised of combining machine learning methods like decision tree C4.5 with Entropy-MDL (Minimum Description Length) discretization algorithm to attain remarkable performance results (97.92% accuracy) at the task of classification in significant applications [21]. This boost in accuracy can be attributed to integrating the classifier with a discretization algorithm which involves transforming a continuous environment into a discrete environment. In discretization, we group the values of a continuous data set in buckets, so as to limit the number of possible states. The buckets themselves are considered as ordered and discrete values. In mathematics, discretization consists in a process of transformation of mathematical models based on continuous equations to the ones based on discrete equations.

4) Using SVM

Support Vector Machines (SVM) constitute a class of "learning machines". SVMs originate from concepts concerning the statistical theory of learning and have theoretical generalization properties. SVM classifiers find the hyperplane that separates the two classes. The SVMs define the optimal hyperplane as the one maximizes the "margin" by a method of convex minimization which is not probabilistic but geometric.

Tristan Groleat [19] proposed the use of SVM classifier with a novel architecture for implementation at the immensely high data generation rate. The proposal of hardware accelerated solution employing FPGAs for processing traffic, which are integrated circuits suited for a wide array of applications by providing solutions to the issues arising due to the advancements brought by technology. The key benefits of FPGA are due to its ability to provide parallelism in hardware along with flexibility in design and application at a reduced cost. The SVM classifier was shown to provide better results after suitable feature selection than the C4.5 Decision trees.

But due to lack of availability of labeled training data, we resort to unsupervised learning approaches.

B. Unsupervised Learning

In this type of learning, the objective is not to estimate or predict the outcome of an event but to segment the data into similar groups so as to improve the understanding of the data through the structured presentation. The unsupervised approach, SeLeCT [22] is employed for classification and involves adaptive seeding mechanism for achieving high accuracy results in precision and recall.

The whole idea of Unsupervised Learning centers around clustering approaches. As described in [7] the clustering approaches could be subdivided into 4 major categories.

1) Flow clustering using Expectation Maximization As described by McGregor et al in [8], the expectationmaximization could be performed by them using the following properties:

• Measurement of Packet Length

- The difference in arrival time
- No. of Bytes
- Length of connection Interval
- Number of transitions between transaction mode and bulk transfer mode
- Idle time this method studies HTTP, FTP, SMTP, IMAP, NTP, and DNS properties of the network and divide the packet in a 6-hour interval into flows.

Based on the features mentioned above their EM algorithm groups the flows into initial clusters based on some property. The flows not having a significant influence on the classification are therefore removed and new cluster centers are calculated and the flows are regrouped based on the new cluster centers. This process is repeated until the desired accuracy. McGregor et al in [8] found this method to divide the network traffic according to the user interest.

2) Automated application identification using AutoClass In the work published in 2005 by Zander et al [9], there was an introduction to the usage of an unsupervised classifier which implements the Bayesian theory in its operation, called the AutoClass. The properties considered in their work were:

- Statistical Measurement of Packet Length
- Statistical Measurement of difference in arrival time
- Size of flow
- Duration of flow

The network packets in an interval of 60 sec are considered as flows. AutoClass needs a value representing the number of classes to work upon that should be either already known or should be estimated. Then a simple search is performed for the maximum likelihood and repeated until a global maxima is found and the class with maximum likelihood is chosen.

3) TCP-based application identification using Simple Kmeans

Bernaille [18] proposed the classification of TCP packets into clusters using K-Means clustering and using only the initial few packets of the network. This helped in early detection of the query since a flow was not defined as earlier but only a few initial packets were used. The features used were:

- Level of Packet
- Level of flow
- Level of connection.
- Intra-flow/Connection features
- Multi-flow features

A simple distance dissimilarity measure is used to determine the belongingness of a TCP packet cluster. In the training phase, a long chain of varied query packet collection of TCP packets is provided in offline phase considering the abovementioned features.

4) Identifying Web and P2P traffic in the network core In 2007 Erman et al used this approach, where the information about the flow was limited. The features considered are:

- Total packets.
- Mean length of a packet.
- Mean payload length (excluding headers).
- Bytes transferred
- Duration of flow.
- Mean inter-arrival time

He also used the simple K-Means Clustering approach with distance as dissimilarity measure. But unlike the previous approaches, this approach could also work in case the information about the flow of TCP, their origin and direction were limited. This is accounted for in training mode by training with the 3 different sets containing server-client, client-server direction packets and the third set containing a random mixture of both in varying proportions which is to be expected in actual data. The work helped in case only the TCP packets are available and no information about their origin is published.

VI. CONCLUSION AND FURTHER STUDY

This paper illustrates the various methodologies applied to solve the problems of network management by working in the area of identifying and classifying the traffic over the internet. The methodologies adopted in the early years emphasized on classification on the basis of transport port and field of the payload. The modern techniques managed to provide solutions to the limitations of the early adopted strategies and enhance the performance of outcomes. The application of ML-based classification algorithms has proved to be pioneering in this task. A great improvement in performance from the approaches like the supervised learning algorithms using Bayesian techniques and the Nearest Neighbour is provided by C4.5 Decision Tree and SVM employing FPGA provide good results but due to limited availability of labeled data, we resort to the use of unsupervised methods. With unsupervised methods, we do not have to attach the similarity information with the network packets. While the k-means approach seems to work well in case of unsupervised learning, the segregation into P2P and web traffic is useful when the information is limited during the transmission.

The advanced study should be encouraged to design a framework which incorporates a combination of classification models to improve results and make it more robust and applicable in diverse scenarios. Ensembling can, therefore, be a potential research breakthrough. Another branch of research could be devising approaches to tackle the grayware traffic.

REFERENCES

[1] Yogesh Dhote, Shikha Agrawal, Anjana Jayant Deen3, "A Survey on Feature Selection Techniques for Internet Traffic Classification", *International Conference on Computational Intelligence and Communication Networks, 2015.*

[2] Taoufik En-Najjary, Guillaume Urvoy-Keller, Marcin Pietrzyk, JeanLaurent Costeux "Application-based Feature Selection for Internet Traffic Classification".

[3] Bo Zhu and Alberto Mozo, "A Survey of Feature Selection in Internet Traffic Characterization*".

[4] Foithong, S., Pinngern, O., Attachoo, B., "Feature subset selection wrapper based on mutual information and rough sets", Expert Systems with Applications, vol. 39, Issue 1, pp. 574–584, 2012.

[5] Peng, H., Long, F., Ding, C., "Feature Selection Based on Mutual
Information: Criteria of Max-Dependency, Max-Relevance, and MinRedundancy", IEEE Transactions on Pattern Analysis and Machine Intelligence, vol. 27, issue 8, pp. 1226–1238, 2005.

[6] Sanmay Das, "Filters, Wrappers and a Boosting-Based Hybrid for Feature Selection".

[7] Thuy T.T. Nguyen and Grenville Armitage,"A Survey of Techniques for
Internet Traffic Classification using Machine Learning", *IEEE Communications Surveys & Tutorials, vol. 10, no. 4, Fourth Quarter 2008.*

[8] A. McGregor, M. Hall, P. Lorier, and J. Brunskill, "Flow clustering using machine learning techniques," *Proc. Passive and Active Measurement Workshop (PAM2004)*, Antibes Juan-les-Pins, France, April 2004.

[9] S. Zander, T. Nguyen, and G. Armitage, "Automated traffic classification and application identification using machine learning," in *IEEE 30th Conference on Local Computer Networks (LCN 2005)*, Sydney, Australia, November 2005.

[10] T. Nguyen and G. Armitage, "Training on multiple sub-flows to optimise the use of Machine Learning classifiers in real-world IP networks," in *Proc. IEEE 31st Conference on Local Computer Networks*, Tampa, Florida, USA, November 2006.

[11] J. Erman, A. Mahanti, M. Arlitt, and C. Williamson, "Identifying and discriminating between web and peer-to-peer traffic in the network core," in *WWW '07: Proc. 16th international conference on World Wide Web*. Banff, Alberta, Canada: ACM Press, May 2007, pp. 883–892.

[12] N. Williams, S. Zander, and G. Armitage, "A preliminary performance comparison of five machine learning algorithms for practical IP traffic flow classification," *Special Interest Group on Data Communication (SIGCOMM) Computer Communication Review*, vol. 36, no. 5, pp. 5– 16, 2006.

[13] M. Crotti, M. Dusi, F. Gringoli, and L. Salgarelli, "Traffic classification through simple statistical fingerprinting," *SIGCOMM Comput. Commun. Rev.*, vol. 37, no. 1, pp. 5–16, 2007.

[14] Mohamad Jaber, Roberto G. Cascella and Chadi Barakat, "Can we trust the inter-packet time for traffic classification?"

[15] P. Haffner, S. Sen, O. Spatscheck, and D. Wang, "ACAS: automated construction of application signatures," in *MineNet '05: Proceeding of the 2005 ACM SIGCOMM workshop on Mining network data.* Philadelphia, Pennsylvania, USA: ACM Press, August 2005, pp. 197– 202.

[16] A. Moore and D. Zuev, "Internet traffic classification using Bayesian analysis techniques," in *ACM International Conference on Measurement and Modeling of Computer Systems (SIGMETRICS) 2005*, Banff, Alberta, Canada, June 2005.

[17] Michael Finsterbusch, Chris Richter, Eduardo Rocha, Jean-Alexander Muller, and Klaus Hanssgen, "A Survey of Payload-Based Traffic Classification Approaches", *IEEE Communications Surveys & Tutorials*, volume: 16, issue: 2, Second Quarter 2014.

[18] Bernaille, L., Teixeira, R., Salamatian, K.: Early application identification. In: Proc. of ACM International Conference on Emerging Networking Experiments and Technologies (CoNEXT) 2006, Lisboa, Portugal (2006)

[19] Tristan Groléat, Matthieu Arzel, and Sandrine Vaton, "Stretching the Edges of SVM Traffic Classification With FPGA Acceleration", *IEEE Transactions on Network and Service Management* , Volume: 11, Issue: 3, Sept. 2014.

[20] M. Roughan, S. Sen, O. Spatscheck, and N. Duffield, "Class-of-service mapping for QoS: A statistical signature-based approach to IP traffic classification," in *Proc. ACM/SIGCOMM Internet Measurement Conference (IMC) 2004*, Taormina, Sicily, Italy, October 2004. [21] Da Tong, Yun Rock and Voktor K. Prasanna, "Accelerating Decision Tree Based Traffic Classification on FPGA and Multicore Platforms," *IEEE Transactions on Parallel and Distributed Systems*, Volume: 28, Issue: 11, Nov. 1 2017.

[22] Luigi Grimaudo, Marco Mellia, Elena Baralis and Ram Keralapura, "SeLeCT: Self-Learning Classifier for Internet Traffic,' *IEEE Transactions on Network and Service Management* , Volume: 11, Issue: 2, June 2014.

Alkali-Silica Reactivity Of Three River Basin (Chenab, Satluj And Beas) - An Overview

Lalit Kumar Solanki, S. K. Jain, B. K. Munzni

Abstract— **Alkali-silica reaction is one of the most recognized deleterious phenomenon in concrete that results in excessive expansion, cracks, loss in mechanical properties and serviceability problems. Aggregates constitute about three-quarter of the volume of concrete, and therefore their physical, mechanical and chemical properties need to be correctly assessed before their use in concrete. Aggregate component in concrete define its thermal, elastic properties and mineralogical composition which influences the durability of concrete. This paper presents research on the influence of strain quartz percentage in aggregates for the occurrence of potentially deleterious alkali-silica reaction in concrete. The aggregates susceptible to ASR were evaluated using petrographic analysis, aggregate mineralogy, chemical method of ASTM C 289 and the standard methods of ASTM C 1260 and ASTM C 1293. Aggregate classifications into innocuous and reactive based on the stated mineralogy tests and the potential expansion limits based on the standard test methods and their modifications were compared. The study demonstrated that none of the single method is an ideal approach to evaluate the alkali-silica reactivity of an aggregate in a better way and a suitable combination of various methods can be utilized to better predict the potential ASR of an aggregate.**

Index Terms— **Alkali-Silica Reaction, Aggregate Mineralogy, Alkalis, Moisture, Petrographic Analysis.**

I. INTRODUCTION

Alkali-aggregate reaction has two forms: alkali-silica reaction (ASR) and alkali-carbonate reaction (ACR). Alkali-silica reaction (ASR) is a reaction that takes place between the reactive silica contained in aggregates and the alkalis in the cement paste. For the reaction to take place in concrete, three conditions must exist: high pH, moisture, and reactive silica. Various types of silica present in aggregates react with the hydroxyl ions present in the pore solution in concrete. The silica, now in solution, reacts with the sodium (Na+) and potassium (K+) alkalis to form a volumetrically unstable alkali silica gel. Once formed, the gel starts imbibing water and swelling to a greater volume than that of the reacted materials. Water absorbed by the gel can be water not used in the hydration reaction of the cement, free water from rain, melted snow, tides, rivers, or water condensed from air moisture (ACI 221, 1998).

Alkali carbonate reaction (ACR) is the reaction between the cement hydroxides and certain dolomitic limestone aggregates, which can also result in deleterious expansion. This problem is relatively less prevalent in India and is not specifically addressed here.

Lalit Kumar Solanki, Scientist B CSMRS, Delhi, India,
Sanjay Kumar Jain, Scientist C, CSMRS, Delhi, India,
Bimal Kumar Munzni, Scientist D, CSMRS, Delhi, India,

In general, the reaction can be viewed as a two-step process (Farny, 1996):

Step 1:

Silica + alkali $\longrightarrow$ alkali-silica gel (sodium silicate)

$SiO_2 + 2NaOH + H_2O \longrightarrow Na_2SiO_3.2H_2O$ (2KOH can replace 2NaOH)

Step 2

Gel reaction product + water $\longrightarrow$ expansion

Since the gel is restrained by the surrounding mortar, an osmotic pressure is generated by the swelling. Once that pressure is larger than the tensile strength of the concrete, cracks occur, leading to additional water migration or absorption and additional gel swelling (ACI 221, 1998).

II. PRESENT STUDY

The overall objective of the study was to closely examine the alkali-silica reaction expansion potential in portland cement concrete containing different aggregate sources in the river basins in Himachal Pradesh, India. Fourteen aggregate sources were selected from three river basins (Chenab, Satluj and Beas) at various locations of Himachal Pradesh as shown in Fig.1. Ten coarse aggregate samples were obtained from rock quarry and the remaining four from river bed material (RBM). Both were analyzed for ASR and their reactivity was determined from different tests that were carried out on the coarse aggregate samples as per existing test methods and results were evaluated.

Petrographic analyses of all these rock types were carried out to find the strained quartz percentage, undulatory extinction angle and its mineralogical composition. Three samples for each fourteen rock type were studied and respective minimum and maximum values of their constituents are presented in Table 2



Table 1: Rock type and sources

ID	Rock Type	River Basin	Type of Source	Location
A1	Granite Biotite Schist	Chenab river basin	Rock Quarry	Himachal Pradesh
A2	Granite Biotite Gneiss	Chenab river basin	Rock Quarry	Himachal Pradesh
A3	Calcareous Quartzite	Chenab river basin	Rock Quarry	Himachal Pradesh
A4	Micaceous Quartzite	Chenab river basin	Rock Quarry	Himachal Pradesh
A5	Gneiss	Chenab river basin	Rock Quarry	Himachal Pradesh
A6	Feldspathic Schist	Chenab river basin	RBM	Himachal Pradesh
A7	Biotite Schist	Chenab river basin	RBM	Himachal Pradesh
A8	Meta Siltstone	Chenab river basin	Rock Quarry	Himachal Pradesh
A9	Quartzite	Chenab river basin	Rock Quarry	Himachal Pradesh
A10	Garnet Biotite-Schist	Beas Basin	RBM	Himachal Pradesh
A11	Dolomitic Limestone	Beas Basin	Rock	Himachal Pradesh
A12	Sandstone	Beas Basin	RBM	Himachal Pradesh
A13	Granite Gneiss	Satluj river basin	Rock	Himachal Pradesh
A14	Quartzitic Phyllite	Chenab river basin	Rock Quarry	Himachal Pradesh

Table 2: Mineralogical composition of aggregate samples

ID	Rock Type	Strain Quartz in %	UEA in degree	Quartz in %	Feldspar in %	Biotite in %	Muscovite in %	Iron Oxide in %	Dolomite in %
A1	Granite Biotite Schist	35-45	25-35	30-38	25-31	14-20	4-9	1-3	-
A2	Granite Biotite Gneiss	30-45	9-27	39-53	21-31	8-13	2-6	1-3	-
A3	Calcareous Quartzite	30-45	9-17	44-59	10-18	4-7	9-16	2-4	-
A4	Micaceous Quartzite	30-32	10-15	50-55	13-16	5-6	8-9	3-4	-
A5	Gneiss	80-86	26-35	35-40	22-30	5-18	2-13	<2	-
A6	Feldspathic Schist	80-85	23-25	44-49	33-38	6-11	2-3	-	-
A7	Biotite Schist	81-86	31-36	35-40	25-30	17-20	3-5	-	-
A8	Meta Siltstone	15-22	16-22	40-49	24-31	7-12	4-7	2-4	0
A9	Quartzite	22-26	29-33	73-78	6-9	<2	2-3	2-3	0
A10	Garnet Biotite-Schist	45-50	18-22	40-50	11-27	18-21	1-8	5-10	-
A11	Dolomitic Limestone	30-40	16-18	8-10	0	0	0	10	15-20
A12	Sandstone	45-51	19-23	70-71	8-18	5-7	1-5	1-6	-
A13	Granite Gneiss	18-22	16-21	56-64	12-20	8-12	8-12	2-4	-
A14	Quartzitic Phyllite	32-45	17-27	36-54	12-27	3-8	3-12	2-3	-

Chemical method test as per ASTM C 289 was then carried out on all these rock types for quick understanding of the reactiveness of the aggregate. Out of fourteen samples, eleven were found innocuous and three deleterious as per Figure - 2. The details are presented in the Table -3

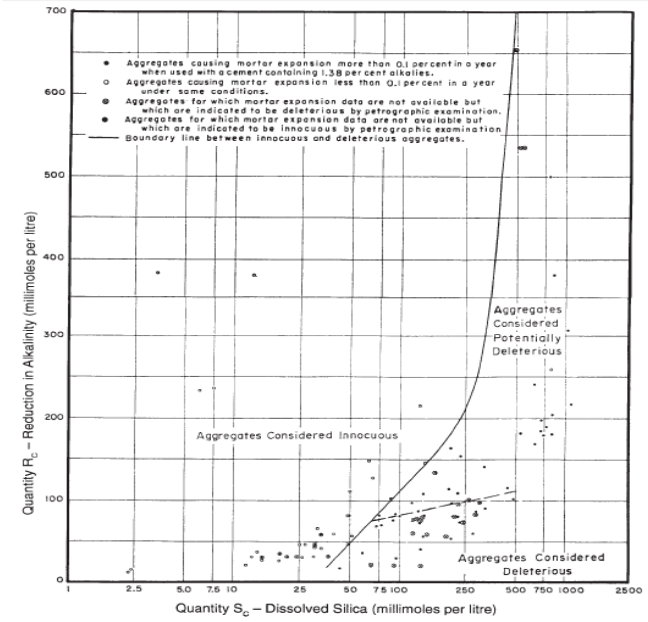


Fig. 2: Illustration of division between Innocuous and Deleterious aggregates on basis of reduction in Alkalinity test

Table 3: Silica dissolved and reduction in alkalinity of rock samples

ID	Rock Type	Silica dissolved (Sc) Milli moles/litre	Reduction in alkalinity (Rc) Milli moles/litre	Reactivity
A1	Granite Biotite Schist	4.40	95.33	Innocuous
A2	Granite Biotite Gneiss	10.60	94.67	Innocuous
A3	Calcareous Quartzite	15.00	52.50	Innocuous
A4	Micaceous Quartzite	26.45	44.66	Innocuous
A5	Gneiss	10.50	95.00	Innocuous
A6	Feldspathic Schist	10.65	198.00	Innocuous
A7	Biotite Schist	6.50	140.00	Innocuous
A8	Meta Siltstone	30.00	103.55	Innocuous
A9	Quartzite	22.10	91.50	Innocuous
A10	Garnet Biotite-Schist	80.00	35.00	Deleterious
A11	Dolomitic Limestone	140.00	37.00	Deleterious
A12	Sandstone	65.00	18.00	Deleterious
A13	Granite Gneiss	10.70	72.50	Innocuous
A14	Quartzitic Phyllite	15.80	435.33	Innocuous

After petrographic and chemical method investigation, all rock types were investigated by adopting test procedure as per ASTM C1260 because of the presence of reactive strain quartz. This method is generally prevalent and preferred by the construction industries because of its rapidity in

determining its potential to undergo alkali aggregate reaction within a months' time which is very helpful in preliminary investigation for rock selection of any project. The test results are presented in Table 4 and the same plotted in Fig 3

Table 4: Results of 16 days expansion of rock samples

ID	Rock Type	ASTM 1260 % expansion at 16 days after casting	Reactivity
A1	Granite Biotite Schist	0.023	Innocuous
A2	Granite Biotite Gneiss	0.027	Innocuous
A3	Calcareous Quartzite	0.019	Innocuous
A4	Micaceous Quartzite	0.016	Innocuous
A5	Gneiss	0.053	Innocuous
A6	Feldspathic Schist	0.118	Innocuous/Deleterious
A7	Biotite Schist	0.125	Innocuous/Deleterious
A8	Meta Siltstone	0.029	Innocuous
A9	Quartzite	0.040	Innocuous
A10	Garnet Biotite-Schist	0.204	Deleterious
A11	Dolomitic Limestone	0.130	Innocuous/Deleterious
A12	Sandstone	0.210	Deleterious
A13	Granite Gneiss	0.072	Innocuous
A14	Quartzitic Phyllite	0.039	Innocuous

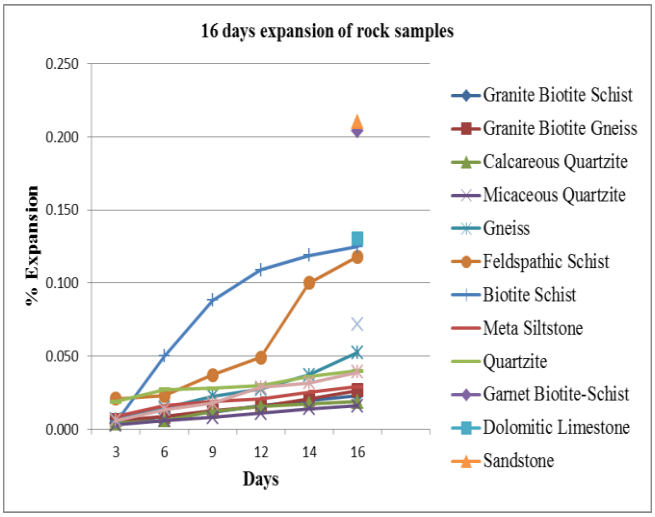


Fig. 3: 16 days expansion of rock samples

A graph is then plotted to understand the relation between % strain quartz (weighted value or by weight of highly strain quartz) and % expansion of rock type and is as presented in Fig. 4

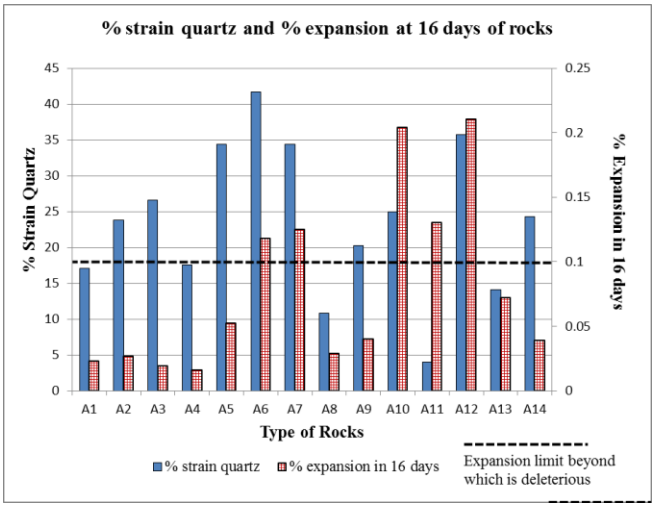


Fig. 4: % strain quartz and % expansion at 16 days of rocks

There is a clear trend from fig. 3 that with increase of % strain quartz in rock type, there is an increase of expansion. Rock type (A1, A2, A3, A4, A5, A8, A9, A13 & A14) were found to be innocuous, (A6, A7 & A11) were found to be innocuous and deleterious and (A10 & A12) were found to be potentially deleterious. Even though rock type A11 has low percentage of strain quartz yet increase of expansion is more, this could be due to dolomitic type of rock or presence of any other potentially deleterious reactive minerals other than strained quartz.

Further tests of Rock type A10 & A11 were carried out by adopting test procedure as per ASTM C1293 and the results are as presented in Table 5.

Table 5: One year expansion of rock samples

ID	Rock Type	ASTM 1293 Prism Bar test results	Reactivity
A10	Garnet Biotite-Schist	0.0508	Deleterious
A11	Dolomitic Limestone	0.0340	Innocuous

III. Conclusion

The following conclusions were generated on the use of ASTM C 1260 and ASTM C 1293 for predicting the potential reactivity of aggregates:

- ASTM C 1260 is too severe for some rock type (A11) indicating that they are reactive while the rock type passes ASTM C 1293.
- ASTM C 1260 should not be solely used to determine the potential reactivity of rock type but should be confirmed by ASTM C 1293 in case the rock type is found to be reactive.
- Since A11 rock type is of Dolomite type, so ASTM C 586 & ASTM C 1105 should be used to determine the potential reactivity.

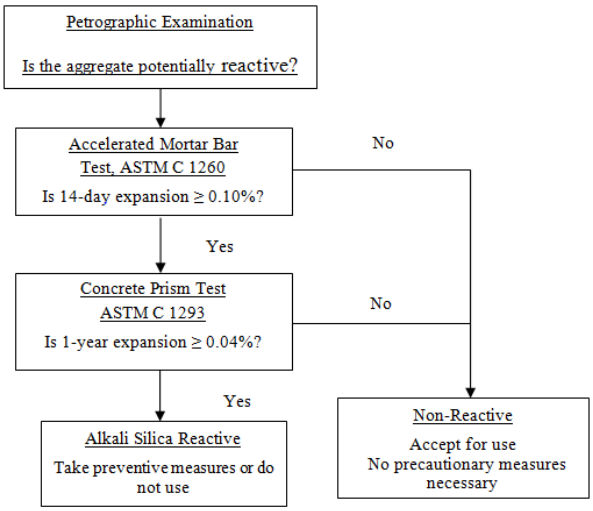


Fig. 5: Sequence of Laboratory tests for evaluating ASR

The flowchart in Fig. 5 shows the general sequence of testing and decisions that should be made when evaluating a source of aggregate for potential ASRof aggregate for potential ASR

In view of the above aggregate samples must be tested with different test procedures for arriving at conclusive judgement of the potential reactivity of the aggregate. The use of supplementary cementitious materials must always be suggested, what so ever may be the percentage of strain quartz and undulatory extinction angle. This will not only help in mitigating the ASR, but also some more advantages like less heat of hydration in case of massive structures, formation of more C-S-H gel because of pozzolanic activity, pore refinement, eco-friendly and in totality improves the durability of the concrete produced.

ACKNOWLEDGMENT

The authors sincerely thank the project staff in arranging the materials and staff of concrete group of CSMRS for facilitating different test methods in evaluation of their expansion potential under different test conditions.

REFERENCES

[1] ASTM C 227-03: Standard test method for potential Reactivity of cement-aggregate combination (Mortar-Bar Method)
[2] ASTM C 289: Test methods for potential Alkali-Silica Reactivity of aggregate (Chemical Method)
[3] ASTM C 295: Guide for petrographic Examination of aggregates for concrete
[4] ASTM C 1260 : Standard Test Method for potential Alkali Reactivity of Aggregates (Mortar-Bar Method)
[5] ASTM C 1293: Standard Test method for Determination of length change of concrete due to alkali silica reaction
[6] ASTM C 1567 Standard test method for potential alkali reactivity of aggregates (Mortar bar method)
[7] Highway Research Program, National Research Council, Washington,DC
[8] Diagnosis and control of alkali aggregate reactions in concrete, James A, Farny and Steven H. Kosmatka, Concrete Information, PCA
[9] The alkali silica reaction in concrete, R.N.Swamy
[10] ACI221.1R-98, Report on Alkali-aggregate Reactivity
[11] Alkali-aggregate reaction in concrete dams, ICOLD Bulletin 79

Lalit Kumar Solanki, B Tech and ME 'Structural' Civil Engineering from Delhi College of Engineering (Gold Medalist) and having 15 years of experience in construction industry.

Sanjay Kumar Jain, M.Sc. (Chemistry) from Jabalpur University and having 20 years of experience in physical and chemical characterization of construction materials.

Bimal Kumar Munzni, M Tech, Building Science and Construction Management from IIT Delhi, having 25 years of experience in concrete discipline.

This article has been accepted for publication in a future issue of this journal, but has not been fully edited. Content may change prior to final publication. Citation information: DOI 10.1109/JESTPE.2018.2849738, IEEE Journal of Emerging and Selected Topics in Power Electronics

Auto-Tuning Technique for the Cost Function Weight Factors in Model Predictive Control for Power Electronics Interfaces

Mohammad B. Shadmand, *Member, IEEE*, Sarthak Jain, *Student Member*, *IEEE*, and Robert S. Balog, *Senior Member*, *IEEE*

***Abstract*— This paper presents an auto-tuning technique for online selection of the cost function weight factors in model predictive control (MPC). The weight factors in the cost function with multiple control objectives directly affect the performance and robustness of the MPC. The proposed method in this paper determines the optimum weight factors of the cost function for each sampling time; the optimization of the weight factors is done based on the prediction of the absolute tracking error of the control objectives and the corresponding constraints. The proposed method eliminates the need of trial-and-error approach to determine a fix weight factor in the cost function. The application considered is a capacitor-less static synchronous compensator (STATCOM) based on MPC of a direct matrix converter (DMC). This technique compensates lagging power factor loads using inductive energy storage elements instead of electrolytic capacitors (e-caps). The result demonstrates that the proposed auto-tuning approach of cost function weights makes the control algorithm robust to parameter variation and other uncertainties in the system. The proposed capacitor-less reactive power compensator based on auto-tuned MPC cost function weight factor is verified experimentally.**

***Index Terms*—Auto-tuned weight factors, model predictive control (MPC), reactive power compensation, Capacitor-less STATCOM**

I. Introduction

The application of model predictive control (MPC) to power electronic converters dates back to the 1980's for high power applications, but with low switching frequency due to slow speed processors which limits the control loop frequency [1, 2]. Due to this limitation, wide spread adoption of MPC was not feasible and practical at that time. Past decade saw the massive improvements in high-speed microprocessors which renewed the interest in the application of MPC to power electronics requiring higher switching frequencies [3-6]. One of the main advantages of MPC over the conventional multi-loop controllers is its ability to include several control variables with different characteristics such as voltage, current, torque, and switching frequency into a single cost function or single loop which eliminates the designing and tuning of nested loops [7, 8].

Weight factors in the cost function can accommodate different units and scales as well as allow prioritization of specific control variable over others by appropriately choosing the ratio of the weight factors of the variables. However, selection of these weight factors is not straight forward [2] and requires trial and error approximation. Several empirical approaches to determine a fixed weight factor using trial-and-error have been investigated in the literature [9]. However, a fixed weight factor is not robust to parameter variation and other uncertainties of the system [10].

One of the major challenges while designing the model predictive controller in multi-objective control system is to appropriately tune the respective weight factors to achieve the control objectives within the desired performance constraint. This can be cumbersome and even lead to instability of the whole controller if the weight factors are not chosen properly. Nowadays, auto-tuning methods for MPC have been under study to decrease the burden of designing the controller and to ensure robust operation by automatically assigning weight factors. The auto-tuning of the weight factors in MPC for power electronics converters is a new topic of study, however few methods on tuning of MPC for application in other fields have been reported in literature. The authors of [11] discussed various tuning methods for MPC in chemical engineering applications. The work proposed in [12] introduced the particle swarm optimization method to tune the MPC. This can be a very computationally heavy approach and limit the high bandwidth requirement of the power electronics converters thus overshadowing one of the main advantages of MPC. The authors of [13] introduced an auto-tuning method based on the convergence of differential of the objectives and trust region algorithm to change the controller radius which is defined by the weight factors. The algorithm is not as computationally heavy but becomes very complex as the number of objectives increases and depends on solving the quadratic equations of the model.

This publication was made possible by NPRP grant # 9-204-2-103 from the Qatar National Research Fund (a member of Qatar Foundation). The statements made herein are solely the responsibility of the authors.

M. B. Shadmand is with the Department Electrical & Computer Engineering at Kansas State University, Manhattan, KS (email: mohamadshadmand@gmail.com). S. Jain and R. S. Balog are with the Department of Electrical and Computer Engineering at Texas A&M University, College Station, TX (emails: jainsarthak2091@gmail.com, robert.balog@ieee.org).

2168-6777 (c) 2018 IEEE. Translations and content mining are permitted for academic research only. Personal use is also permitted, but republication/redistribution requires IEEE permission. See http://www.ieee.org/publications_standards/publications/rights/index.html for more information.

This article has been accepted for publication in a future issue of this journal, but has not been fully edited. Content may change prior to final publication. Citation information: DOI 10.1109/JESTPE.2018.2849738, IEEE Journal of Emerging and Selected Topics in Power Electronics

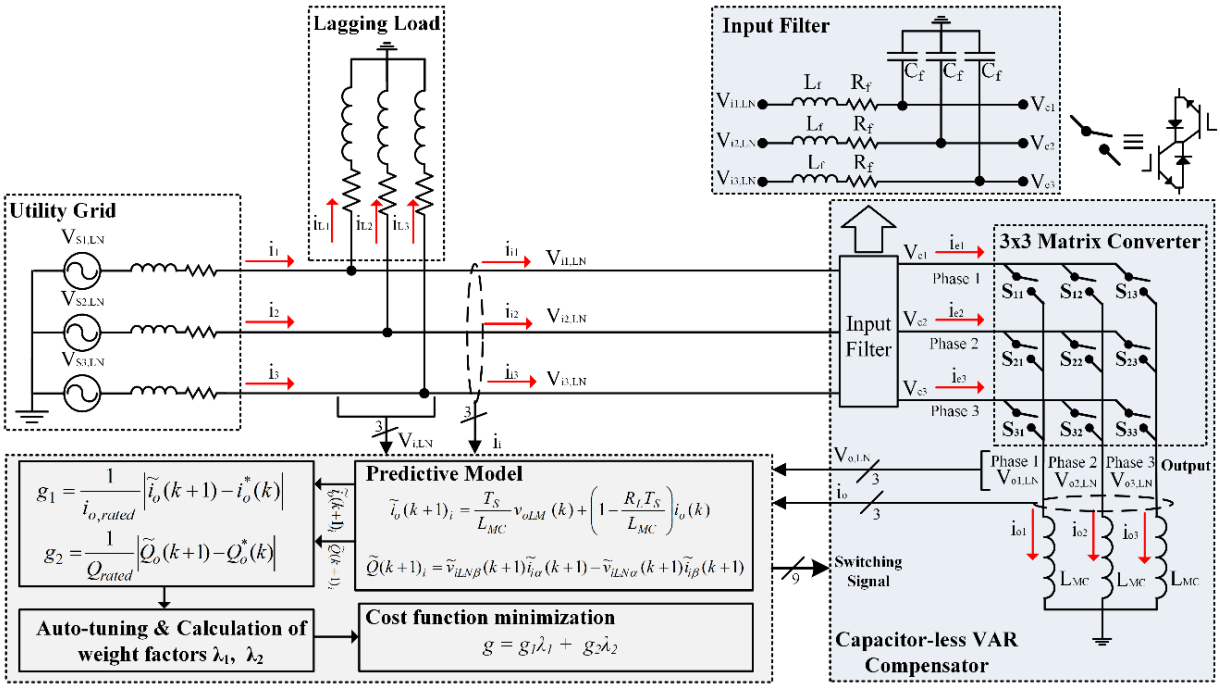


Fig. 1. Capacitor-less VAR compensator employing a matrix converter for the lagging load.

This paper presents a technique to select optimal values for the weight factors in the MPC cost function for each iteration of the MPC loop for power electronics converters. The online optimal selection of the weight factors is robust and is shown to improve the performance of the system when compared to the conventional fixed-value weight factor for MPC. The proposed approach is verified by its application to a capacitor-less static synchronous compensator (STATCOM) technique that uses only inductors combined with a model predictive controlled matrix converter (MPC-MC) [10, 14].

Reactive power compensation techniques can broadly be classified as passive and active. Passive techniques generally employ large capacitor banks which can be discretely switched individually or in group to control reactive power. This discrete variation doesn't allow precise control of reactive power control and results in over/under compensation in most cases. This can be eliminated by using active methods which employs power-electronics interfaces employing semi-conductor devices which switches capacitors at high frequency as compared to utility to precisely compensate for reactive power amongst which STATCOM has been widely studied and developed due to its flexible operation [15, 16].

Capacitors are one of the most vulnerable components to fail in power electronics systems [17] and have reliability problems due to their aging characteristics [18]. The associated failure modes including increased leakage currents and other effects from the loss of electrolyte that increases losses and hasten further degradation leading to open or short circuit failure modes [19-24] with the most frequent failure types listed in [25]. Yet due to the high energy density, low cost and suitable voltage rating of DC electrolytic capacitors, they are widely used in power electronics converters for VAR compensation even though approximately 60% of power electronic devices failures are due to the use of aluminum electrolytic capacitors [26]. The voltage-source inverter based STATCOM which uses electrolytic capacitors is vulnerable to this high-rate failure mode [10]. Thus, to ensure long service life and reliability, capacitors need to be replaced periodically and requires health monitoring equipment/techniques [26-28] which adds additional cost and complexity to the system.

The VAR compensation technique in this paper does not employ energy storage capacitors; instead the topology uses inductors to compensate VAR. Inductors are known to be robust and reliable elements with long service-life as compared to capacitors; but unlike capacitors, they consume reactive power making it impossible to use them directly as reactive power compensators. The application employed in this paper, interfaces a 3×3 Direct Matrix Converter (DMC) to the inductor bank, which is controlled by MPC with auto-tuning weight factor approach to operate it as STATCOM. The general schematic with control overview of the proposed system is illustrated in Fig. 1. DMC has a unique property of phase inversion between its input and output port which can basically reflect the inductor as a capacitor to the grid thus allowing reactive power compensation [29]. By using the property of current phase reversal of DMC, the converter provides leading currents to the AC network while the inductor absorbs lagging current at the output side of the converter. As a result, a STATCOM can be derived without using energy storage electrolytic capacitors by the matrix converter appropriately controlled by MPC. Also, the proposed solution is more reliable, robust, and provides long service life of the system. The main contributions of this paper can be summarized as follows:

2168-6777 (c) 2018 IEEE. Translations and content mining are permitted for academic research only. Personal use is also permitted, but republication/redistribution requires IEEE permission. See http://www.ieee.org/publications_standards/publications/rights/index.html for more information.

This article has been accepted for publication in a future issue of this journal, but has not been fully edited. Content may change prior to final publication. Citation information: DOI 10.1109/JESTPE.2018.2849738, IEEE Journal of Emerging and Selected Topics in Power Electronics

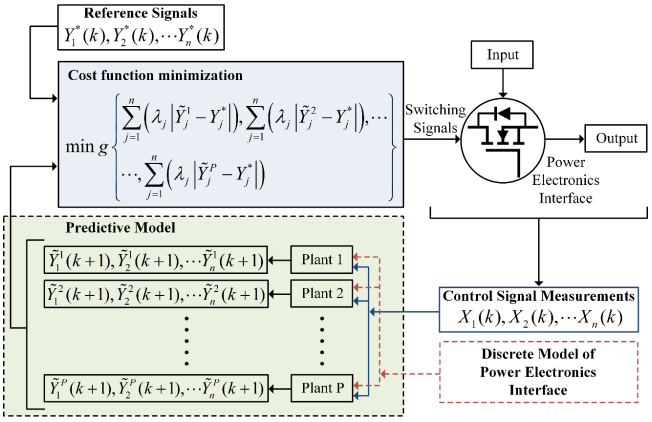


Fig. 2. MPC implementation for power electronics converters.

1) Eliminating the need of trial-and-error approach to determine a fixed weight factor in the cost function of MPC.
2) Development of a MPC approach for power electronic interfaces (PEI) robust to model parameter variation.
3) Verification of guaranteed stable operation of the proposed MPC method with auto-tuned weight factors.
4) Performance verification of a STATCOM with long service life by eliminating the need of e-caps energy devices and robust to disturbances in the system by auto-tuning the weight factors.
5) Improvement of the grid side power quality i.e. grid current compared to conventional MPC method with fix weight factor method. In particular, for the considered application, model parameter error has lower effect on the performance of the proposed MPC and meets IEEE-519 [30, 31] Total Harmonics Distortion (THD) standards with high disturbance rejection.

II. Principle of Model Predictive Control

With the rapid advancement of microprocessor technologies in last couple of decades, MPC is becoming more reliable and efficient in power electronics applications [3, 32-35]. The main characteristic of MPC is predicting the future behavior of the desired control variables [2, 3] until a specific time in horizon. The predicted control variables will be used to obtain the optimal switching state by minimizing a cost function. The discrete time model of the control variables will be used for prediction; which can be presented as state space model as follow [2]:

$$x(k+1) = Ax(k) + Bu(k) \tag{1}$$

$$y(k) = Cx(k) \tag{2}$$

Then a cost function that takes into consideration the future states, references and actuations can be defined [2], as a general cost function given by:

$$g(x(k), u(k)) = \sum_{\ell=k}^{k+N} \lambda(x(\ell), u(\ell)) \tag{3}$$

The defined cost function g is the sum of the weighed objective function over the finite horizon of N time steps. The cost function uses $x(k)$ and a sequence of manipulated variables as arguments:

$$u(k) = \left[u^T(k) \quad u^T(k+1) \quad \cdots \quad u^T(k+N) \right]^T \tag{4}$$

The future states and control objectives can be predicted for penalizing the cost function (3) by using $x(k)$, argument given in (4), and system dynamic model.

The implementation of MPC for power electronics converters is illustrated in Fig. 2. In this block diagram, measured variable $X_i(k)$, where, $i \in (1, \cdots, n)$ and $i \in \mathbb{N}$ are used along with the discrete model of the converter to estimate predictions $\tilde{Y}_i(k+1) = f(X, t)$ using measured variables for all of the P possible switching states (Plants), where $P \in \{1 \cdots P\}$. These predictions are then evaluated using a cost function which compares them to the reference values $Y_i(k)$, where, $i \in (1, \cdots, n)$ and $i \in \mathbb{N}$ by considering the design constraints. Finally, the optimal actuation S is selected and applied to the converter. The general form of the cost function

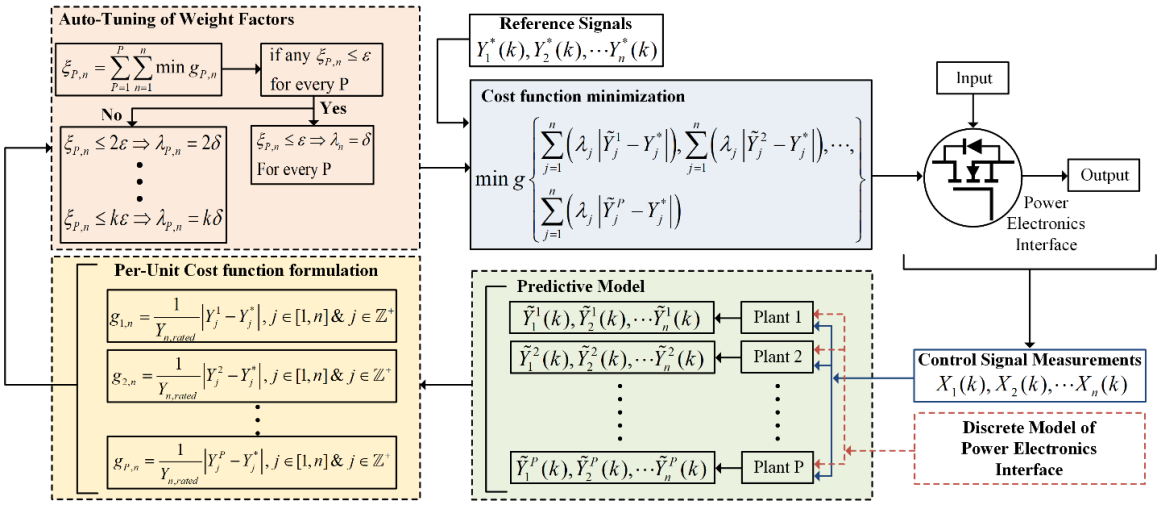


Fig. 3. Overview of the Proposed Auto-Tuned MPC for Power Electronics Converters

2168-6777 (c) 2018 IEEE. Translations and content mining are permitted for academic research only. Personal use is also permitted, but republication/redistribution requires IEEE permission. See http://www.ieee.org/publications_standards/publications/rights/index.html for more information.

This article has been accepted for publication in a future issue of this journal, but has not been fully edited. Content may change prior to final publication. Citation information: DOI 10.1109/JESTPE.2018.2849738, IEEE Journal of Emerging and Selected Topics in Power Electronics

g for reference tracking subject to minimization can be formulated as:

$$g = \sum_{j=1}^{n} \left(\lambda_j \left| \tilde{Y}_j^1(k+1) - Y_j^*(k) \right| \right)$$
$$\text{subject to } x(k+1) = Ax(k) + Bu(k) \quad (5)$$
$$y(k) = Cx(k) + Du(k)$$

The implementation of the modified MPC algorithm with *auto-tuning* of the weight factors of the cost function is illustrated in Fig. 1 and explained in Fig. 4 using flowchart. In the proposed approach, an inner loop is added before the final optimization of the cost function for the purpose of online optimal selection of the weight factors at each sampling time. The cost functions $g_1, g_2, \ldots, g_n$ corresponding to individual objectives of the controller are converted to a per-unit system. By evaluating the magnitude of these cost functions separately, their weight factors will be optimally selected to meet the predefined constraints. Finally, the general cost function (5) subject to minimization will be constructed. A more detailed explanation of the algorithm for the auto-tuning approach of the weight factors will be presented in the section IV of this paper.

The schematic of the proposed auto-tuning MPC control is comprehensive and can be applied to any power electronic interface with multiple control objectives. Fig. 3 shows the generalized control diagram of the proposed auto-tuning MPC for power electronics converter. The block diagram is shown for a power converter with 'P' plant models each having 'n' number of objectives to be met by MPC. The error tolerance ε denotes a small acceptable error in the control objectives and λ denotes the small value of weight factor which is increased in integral steps as shown in the algorithm of Fig. 4. In this paper the considered case study is a 3x3 DMC and inductive load with STATCOM functionality.

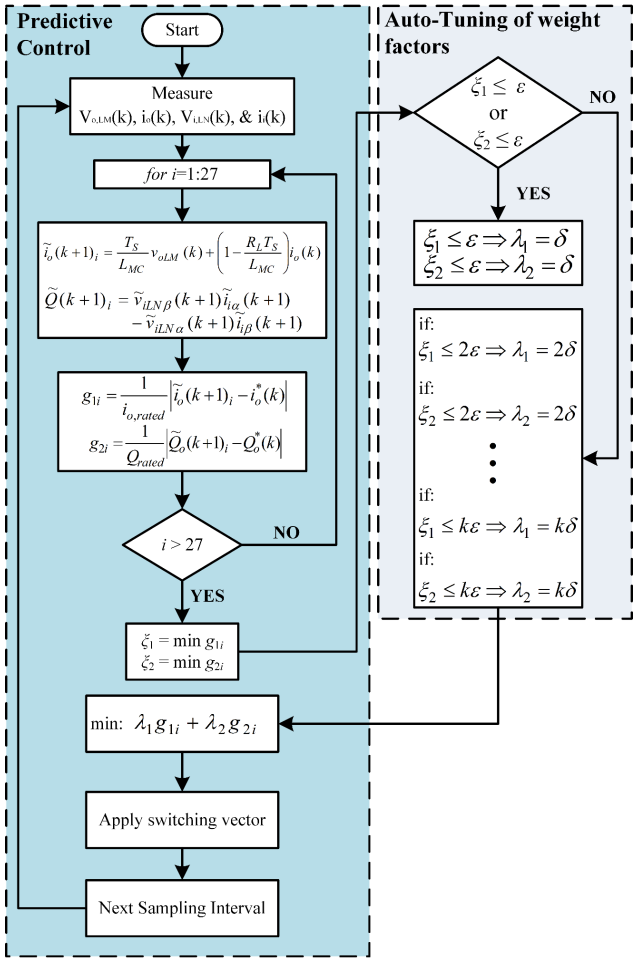


Fig. 4. Model predictive control algorithm of the matrix converter for VAR compensation with dynamic weight factor selection.

III. Ground Work: Predictive Model Formulation of the STATCOM

A. System Description

The VAR compensator system illustrated in Fig. 1 consists of three phase AC grid, an inductor bank used for compensation, a 3x3 DMC, an interface filter between utility and DMC and an inductive load as a reactive load to be compensated by DMC based STATCOM. The reactive power compensator consists of the inductors L_{MC} connected to the AC network through a 3×3 matrix converter. The line-neutral voltages at the Point of Common Coupling (PCC) of the matrix converter are denoted by $v_{i1,LN}$, $v_{i2,LN}$, and $v_{i3,LN}$, while the output voltages of the DMC are given by $v_{o1,LM}$, $v_{o2,LM}$, and $v_{o3,LM}$. The currents drawn by the lagging load are denoted by i_{L1}, i_{L2}, and i_{L3}, while currents drawn by the matrix converter including the filter from the network are i_{i1}, i_{i2}, and i_{i3}. The currents at the filter-DMC interface are i_{e1}, i_{e2}, and i_{e3}, while the currents drawn by the choke from the matrix converter are given by i_{o1}, i_{o2}, and i_{o3}.

The working principle of MC have been explained in detail in literature [36, 37] and will not be covered in this paper. Several papers in literature have investigated the model predictive control for MCs [3, 38-40]. By keeping in mind MC switching scheme restrictions, we can say that the 3×3 MC has 27 possible switching states to be considered during the prediction of variables and optimization of the cost function by MPC. In this paper all possible 27 switching states are considered for evaluating the cost function. These switching states can be classified as:

1) Space vectors with constant amplitude and variable angle at the source angular frequency: all output phases connected to different input phases.
2) Stationary space vectors with fixed direction and variable amplitude: one output phase connected to a different input phase, and the other two output phases connected to the same input phases.
3) Space vectors with zero amplitude: all output phases connected to the same input phases.

B. Current Phase Reversal Property for Matrix Converter

The 3x3 DMC topology for VAR compensator shown in Fig. 1. The detailed proof of the current phase reversal is explained in [10] and is explained here briefly. The DMC can be mathematically modeled using transfer function as:

2168-6777 (c) 2018 IEEE. Translations and content mining are permitted for academic research only. Personal use is also permitted, but republication/redistribution requires IEEE permission. See http://www.ieee.org/publications_standards/publications/rights/index.html for more information.

This article has been accepted for publication in a future issue of this journal, but has not been fully edited. Content may change prior to final publication. Citation information: DOI 10.1109/JESTPE.2018.2849738, IEEE Journal of Emerging and Selected Topics in Power Electronics

$$\begin{bmatrix} v_{o1,LM} \\ v_{o2,LM} \\ v_{o3,LM} \end{bmatrix} = \mathbf{H} \times \begin{bmatrix} v_{i1,LN} \\ v_{i2,LN} \\ v_{i3,LN} \end{bmatrix}, \quad \text{where } \mathbf{H} = \mathbf{H}^T = \begin{bmatrix} H_1 & H_2 & H_3 \\ H_2 & H_3 & H_1 \\ H_3 & H_1 & H_2 \end{bmatrix} \tag{6}$$

The **H** is known as *modulation matrix* or *instantaneous transfer matrix*. For a lossless system, the instantaneous output and input power of DMC should always be equal. Using Kirchhoff's current law, the relationship between input and output currents can be given as:

$$\begin{bmatrix} i_{i1} \\ i_{i2} \\ i_{i3} \end{bmatrix} = \mathbf{H}^T \times \begin{bmatrix} i_{o1} \\ i_{o2} \\ i_{o3} \end{bmatrix} \tag{7}$$

Taking particular modulation function **H** comprised of three single-phase functions H_1, H_2, and H_3 from [29] as:

$$\underset{k=1,2,3}{H_k} = \frac{1}{3}\left(1+2\left(\frac{V_o}{V_i}\right)\cos\left(2\omega t - \frac{2(k-1)\pi}{3}\right)\right) \tag{8}$$

The line-voltage of a three-phase utility can be represented as:

$$\underset{k=1,2,3}{v_{Sk,LN}} = v_{ik,LN} = \sqrt{2}\times V_{LN,rms}\cos\left(\omega t - 2(k-1)\pi/3\right) \tag{9}$$

Applying **H** matrix from (6) and (8) to compensator of Fig. 1, will result in three-phase MC output voltages can be given by [29]:

$$\underset{k=1,2,3}{v_{ok,LM}} = \sqrt{2}\times\frac{V_o}{V_i}\times V_{LN,rms}\cos\left(\omega t - 2(k-1)\pi/3\right) \tag{10}$$

For a balanced system, the magnitude of the current for each phase will be identical. Thus, the currents can be represented in Euler phasor form as follows:

$$i_{o1} = \mathrm{Re}\left\{\sqrt{2}\times|I_o|\times e^{j(\omega t-\pi/2)}\right\} = \mathrm{Re}\left\{\sqrt{2}\times|I_o|e^{j\omega t}\times e^{-j\pi/2}\right\} \tag{11}$$

where, $|I_o| = \left(\frac{V_o}{V_i}\right)\times\frac{V_{LN,rms}}{\omega L_{MC}}$, the phasor representation of the output current can be written as:

$$I_{o1} = |I_o|\angle -\pi/2 \tag{12}$$

Similarly, the input current i_{i1} can also be expressed as a phasor form as:

$$i_{i1} = \mathrm{Re}\left\{\sqrt{2}\times|I_i|\times e^{j(\omega t+\pi/2)}\right\} = \mathrm{Re}\left\{\sqrt{2}\times|I_i|e^{j\omega t}\times e^{j\pi/2}\right. \tag{13}$$

where, $|I_i| = \left(\frac{V_o}{V_i}\right)^2\times\frac{V_{LN,rms}}{\omega L_{MC}} = \left(\frac{V_o}{V_i}\right)\times|I_o|$, and input current phasor can be represented by:

$$I_{i1} = \left(\frac{V_o}{V_i}\right)|I_o|\angle\pi/2 \tag{14}$$

Thus, from (12) and (14) the MC input current of each phase leads the corresponding output current by $\boldsymbol{\pi}$.

C. Input filter Modeling

The conventional LC filter is used as shown in Fig. 1 with R_f as loss resistance. Input filter is required between MC and AC source to eliminate the high order harmonics [29, 36, 37]. Input filter may introduce an additional phase shift in voltage, but without loss of generality, it can be assumed that the filter resonances are well damped in properly designed filter and the phase shift will be compensated by the model predictive controller. The detailed modeling of the input filter have been adopted from the literature [10].

For the filter-grid interface, the discrete-time input current is:

$$\begin{aligned} i_i(k+1) &= A'(2,1)V_e(k) + A'(2,2)i_i(k) \\ &\quad + B'(2,1)V_{i,LN}(k) + B'(2,2)i_e(k) \end{aligned} \tag{15}$$

with coefficient matrices as:

$$A' = e^{AT_S},\ B' = \int_0^{T_S} e^{A(T_S-\tau)}Bd\tau \tag{16}$$

D. Controller Design

A load model needs to be obtained in order to predict the value of the load current at the next step sampling interval for all 27 possible switching states. The inductive load at the output side of the MC can be represented as

$$L_{MC}\frac{di_o(t)}{dt} = v_{o,LM}(t) - R_L i_o(t) \tag{17}$$

where, L_{MC} is the inductance and R_L is the inductor resistance. Using the Euler forward method, the derivative in (17) is approximated using (20) as (21).

$$\frac{di_o(t)}{dt} \approx \frac{i_o(k+1)-i_o(k)}{T_S} \tag{18}$$

$$\tilde{i}_o(k+1) = \frac{T_S}{L_{MC}+R_L T_S}\left(v_{oLM}(k) + \frac{L_{MC}}{T_S}i_o(k)\right) \tag{19}$$

where, T_s is the sampling period.

Equation (19) estimates the value of the output current of MC for the next sampling interval, $(k+1)$, and the corresponding voltage, $v_{o,LM}$, which is calculated for the 27 possible switching states of the MC. Control of reactive power and the output current are the control objectives for the MPC in this work. The reactive power can be determined by:

$$Q(t) = \mathrm{Im}\left\{v_{iLN}(t).\overline{i}_i(t)\right\} \tag{20}$$

where $\overline{i}_i(t)$ is the complex conjugate of $i_i(t)$. The current phase reversal property of the matrix converter indicates that the $i_i(t)$ and $i_o(t)$ are out of phase, thus the reactive power can be predicted by using:

$$\begin{aligned} \tilde{Q}(k+1) &= \mathrm{Im}\left\{v_{iLN}(k+1).\overline{i}_i(k+1)\right\} \\ &= v_{iLN\beta}(k+1)i_{i\alpha}(k+1) - v_{iLN\alpha}(k+1)i_{i\beta}(k+1) \end{aligned} \tag{21}$$

where α and β correspond to the real and imaginary components of the associated vector. The value of $v_{i,LN}(k+1)$ can be approximated to be $v_{i,LN}(k)$ because the line voltages are low frequency signals compared to the switching frequency. By keeping in mind the current phase reversal property of the matrix converter and (19), the $i_i(t)$ can be calculated [14]. The control objectives of the MPC cost function are the input reactive power of the matrix converter (at the point of common coupling of utility grid, load, and DMC) and the current in the

2168-6777 (c) 2018 IEEE. Translations and content mining are permitted for academic research only. Personal use is also permitted, but republication/redistribution requires IEEE permission. See http://www.ieee.org/publications_standards/publications/rights/index.html for more information.

This article has been accepted for publication in a future issue of this journal, but has not been fully edited. Content may change prior to final publication. Citation information: DOI 10.1109/JESTPE.2018.2849738, IEEE Journal of Emerging and Selected Topics in Power Electronics

inductive load of DMC. The inductive load current is controlled to minimize the THD of the grid current. From (5), (19), and (21) the cost function *g* is formulated as:

$$g = \lambda_1 \left| \tilde{i}_{o,\alpha\beta}(k+1) - i^*_{o,\alpha\beta} \right| + \lambda_2 \left| \tilde{Q}(k+1) - Q^*(k) \right| \quad (22)$$

where the asterisk indicates the reference value and the tilde indicates the predicted value to regulate input reactive power and current into the inductive load.

IV. Auto-tuning of Weight Factors & Stability Analysis

A. Auto-tuning Algorithm

This section presents an auto-tuning technique for the online selection of the cost function weight factors in model predictive control. The weight factors in the cost function with multiple control objectives directly affect the performance and robustness of the MPC. The proposed method in this section determines the optimum weight factors of the cost function for each sampling time. The optimum weight factor results in better current quality at the grid side and robustness to disturbances in the model parameters of the system. The optimization of the weight factors is done based on the prediction of the absolute tracking error of the control objectives and the corresponding constraints. Without loss of generality, this technique is applied to the application considered in this paper, a capacitor-less STATCOM technique using MPC of a DMC.

The proposed dynamic weight factor selection of MPC algorithm for the matrix converter is shown in detail in Fig. 4. After minimization of the cost function *g*, the switching that corresponds to the minimum *g* will be applied to the converter. Then the algorithm moves into auto-tuning of weight factors. The tuned weight factors will be used for the minimization of (22) at the next sampling period for sufficiently small sampling time. In practice, much of the evaluations for tuning of weight factors are based on the computations that have been already done. Thus, using the already computed cost function, we are able to split the cost function (22) into two parts where each corresponds to individual control objectives:

$$g_1 = \left| \tilde{i}_{o,\alpha\beta} - i^*_{o,\alpha\beta} \right| \le \Psi_1 \quad (23)$$

$$g_2 = \left| \tilde{Q} - Q^* \right| \le \Psi_2 \quad (24)$$

The Ψ_1 and Ψ_2 are the acceptable error of tracking commanded values. From the computed g_1 and g_2 for all 27 switching states, the minimum value of g_2 will be selected as,

$$\xi = \min g_2 \quad (25)$$

The next step is to evaluate the magnitude of minimum g_2 with a sufficiently small number ε_1 as following,

$$\xi \le \varepsilon_1 \Rightarrow \lambda = \varepsilon_2 \quad (26)$$

The statement (26) is presenting that, if g_2 is small enough (less than a defined small number ε_1), then the weight factor λ is determined to be equal to a sufficiently small number ε_2, considering the fact that g_2 is within an acceptable error range Ψ_2.

If the condition in (26) is not satisfied, a larger value for weight factor λ should be selected in order to give higher value to g_2 for minimization at the next sampling time (k+1). This evaluation of ξ when its value is more than ε_1 is as following,

$$\begin{aligned} &\xi \le 2\varepsilon_1 \Rightarrow \lambda = 2\varepsilon_2 \\ &\xi \le 3\varepsilon_1 \Rightarrow \lambda = 3\varepsilon_2 \\ &\quad \vdots \\ &\xi \le \kappa\varepsilon_1 \Rightarrow \lambda = \kappa\varepsilon_2 \\ &where: \kappa \in \{1,2,3,\ldots,N\} \end{aligned} \quad (27)$$

The statements in (27) quantized the ξ, which corresponds to the magnitude of g_2, the weight factor λ is determined based on ξ magnitude when comparing to n multiples of ε_1 till the statement in (27) is satisfied. The corresponding value of λ is multiplication of n by ε_2. This strategy for selecting the weight factor λ, based on the absolute error of g_2 is illustrated in right hand side of Fig. 4. This procedure will be repeated every sampling time, thus during every sampling period the weight factor will be tuned online and applied to the minimization procedure of the cost function (22) at next sampling time.

B. Stability Analysis of the system

The system stability is analyzed using Lyapunov stability criteria. The system is proved to be bounded and shown to asymptotically converge the error function towards zero over the time period. For the presented system, there are 27 switching states which can be applied to the DMC in order to regulate the reactive power. In finite-set MPC, the future actual voltage vector $v^{opt}_{o,LM}(k+1)$ required for perfect tracking can be represented as:

$$v^{conv}_{o,LM}(k+1) = v^{conv,opt}_{o,LM}(k+1) + \phi(k+1) \quad (28)$$

where, $v^{conv}_{o,LM}(k+1)$ shows the converter output voltage vector based on 27 switching states, $v^{conv,opt}_{o,LM}(k+1)$ is the optimum voltage vector that can make the current error in next sampling instant to zero, and $\phi(k+1)$ represents the quantization error in the voltage vectors, here, $\|\phi(k+1)\| \le l$ and $l \in \mathbb{R}^+$.

Since, $v^{conv}_{o,LM}(k+1)$ is bounded and is in finite sets, the hysteresis bounds of $\phi(k+1)$ are also bounded, thus the existence of *'l'* is guaranteed. Taking control parameters defined above, $i_{o-error}$ can be defined as:

$$i_{o-error}(k+1) = i_o(k+1) - i_{o-ref}(k+1) \quad (29)$$

From (19),

$$i_{o-error}(k+1) = \frac{T_S}{L_{MC} + R_L T_S}\left(v^{conv}_{o,LM}(k) - \frac{L_{MC}}{T_S} i_o(k) \right) - i_{o-ref}(k) \quad (30)$$

The goal of the control function is to reduce tracking error $i_{o-error}$ asymptotically to zero or a very small error tolerance value ε.

The Lyapunov function $L(k)$ is defined as:

$$L(i_{o-error}) = \frac{1}{2}\left[i_{o-error}(k) \right]^T \left[i_{o-error}(k) \right] \quad (31)$$

2168-6777 (c) 2018 IEEE. Translations and content mining are permitted for academic research only. Personal use is also permitted, but republication/redistribution requires IEEE permission. See http://www.ieee.org/publications_standards/publications/rights/index.html for more information.

This article has been accepted for publication in a future issue of this journal, but has not been fully edited. Content may change prior to final publication. Citation information: DOI 10.1109/JESTPE.2018.2849738, IEEE Journal of Emerging and Selected Topics in Power Electronics

Using (31), the rate of change of Lyapunov function can be defined as:

$$\Delta L(i_{o-error}) = L(i_{o-error}(k+1)) - L(i_{o-error}(k)) = \frac{1}{2}[x]^T[x] - \frac{1}{2}[i_{o-error}(k)]^T[i_{o-error}(k)]$$

where (32)

$$x = \frac{T_S}{L_{MC} + R_L T_S}\left(v_{o,LM}^{conv}(k) - \frac{L_{MC}}{T_S} i_o(k)\right) - i_{o-ref}(k+1)$$

According to Lyapunov theorem, for convergence of $i_{o-error}$ and for system to be stable, the rate of change of Lyapunov function $\Delta L(i_{o-error})$ should be always negative, thus, $i_{o-error} \to 0$, *iff* $\Delta L(i_{o-error}) < 0$. To check the above condition, system should follow the following criteria:

$$\begin{aligned} &L(i_{o-error}(k)) \geq C_1 |i_{o-error}(k)|^{\sigma}, \forall i_{o-error}(k) \in \Upsilon \\ &L(i_{o-error}(k)) \geq C_2 |i_{o-error}(k)|^{\sigma}, \forall i_{o-error}(k) \in \Gamma \\ &L(i_{o-error}(k+1)) - L(i_{o-error}(k)) < -C_3 |i_{o-error}(k)|^{\sigma} + C_4 \\ &C_1, C_2, C_3, C_4 \in \mathbb{R}^+, \sigma \geq 1 \\ &\Upsilon \in \mathbb{R}^+, \Gamma \subset \Upsilon \end{aligned} \quad (33)$$

From above equations,

$$\Delta L(k) = \frac{1}{2}\left(\frac{T_S}{L}\right) I^2 - \frac{1}{2}[i_{o-error}(k)]^T[i_{o-error}(k)] \quad (34)$$

Also, the current vector converges to compact set given by

$$\Omega = \left\{ \|i_{o-error}(k)\| \|i_{o-error}(k)\| \leq \frac{T_S}{L} I \right\} \quad (35)$$

Therefore, all the signals will be bounded and will satisfy the Lyapunov stability criterion.

V. Results and Discussions

The system is mathematically modeled and simulated in Simulink-MATLAB. The sampling time (T_S) of the MPC is 60μs, the reference reactive power of grid Q^* is zero VAR (unity power factor), and other system parameters are given in Table 1. A characteristic of MPC is the use of system models for selecting optimal actuations, thus evaluating the effect of model parameter mismatch on control effectiveness is of interest. The proposed dynamic weight factor selection illustrates that the effect of model parameter errors (sometimes called as model parameter uncertainties) on performance of the system is significantly reduced. In order to demonstrate this fact, the matrix converter output-side inductance (L_{MC}) model value is changed from 30mH to 15mH, while the nominal value is 30mH. The model parameter error is defined as the mismatch between the actual inductor used in the experiment versus the model inductance value in the MPC algorithm.

The simulation results illustrated in Fig. 5 demonstrate the MPC performance of reactive power compensation of matrix converter; with conventional fixed weight factor selection based on trial-and-error tuning method. The optimum weight factor based on conventional trial-and-error approach is determined as 0.008 [14] and the reference reactive power Q^* set as zero VAR (unity PF). Fig. 5(a) and (b) demonstrate the phase 1 of utility side voltage and current which are required to be in-phase, in addition to the output voltage of matrix converter. At time 60ms, the mismatch in the inductance at the output side of the matrix converter is applied and its value is dropped to 15mH from its nominal value (30mH), as it is shown in Fig. 5(a) and (b). After this parameter variation, the current became highly distorted and the STATCOM fails to operate appropriately.

Now by using the proposed auto-tuning approach of weight factor of MPC the distortion can be significantly reduced with inductance model parameter error. The simulation results in Fig. 6 demonstrate this fact. The cost function weight factor is updated instantaneously at each sampling time to achieve real time auto-tuning. Phase 1 of the utility voltage and load current are illustrated in Fig. 6 (a), and the lagging load power factor are illustrated in Fig. 6 (b). As it is shown and required for the STATCOM the grid side voltage and current are in-phase with very small distortion after time 60ms. Thus, a robust MPC with auto-tuned cost function weight factor for the objective of capacitor-less STATCOM is achieved. The current phase reversal property is illustrated in Fig.6 (c) which shows the input and output current of the matrix converter. The phase 1 of output voltage of the matrix converter is illustrated in Fig. 6 (d). These results demonstrate negligible distortion in current and voltage waveforms even with this high model error in the output inductance of the matrix converter.

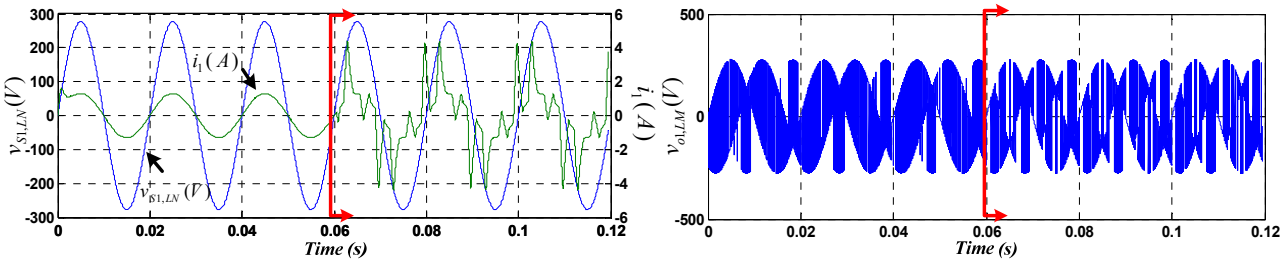
The performance of the proposed auto-tuned MPC for the considered application is verified experimentally. Fig. 7 shows the experimental setup block diagram used for the analysis of the proposed algorithm. The experimental setup includes a California Instrument MX45 programmable AC power source, dSPACE DS1006 platform to implement the controller and interface with the matrix converter hardware with 9 bidirectional switches. Fig. 8 and Fig. 9 illustrates the utility grid voltage, utility grid current, and MC output voltage with fixed cost function weight factor with and without model parameter error in the output inductance of MC. The model parameter error is triggered at instant t_1. As it is captured, the conventional MPC scheme is not robust to model parameter error, and the STATCOM failed to operate appropriately. Fig. 10 - Fig. 12 demonstrate the performance of the proposed auto-

TABLE 1: PARAMETERS FOR THE SYSTEM IN FIG. 1.

Parameter	Value
Line-to-neutral grid voltage $V_{LN,rms}$	277.13 V
Angular frequency of grid voltage ω	2π*50 rad/s
Per-phase resistance of load $R_{Load,\ per\ phase}$	10 Ω
Per-phase inductance of load $L_{Load,\ per\ phase}$	30mH
Total rated real power of load P_{Load}	2.2 kW
Power factor at the load side *p.f.*	0.9
Total maximum load reactive power requirement Q_{load}	2kVAR
MC output-side inductance L_{MC}	30mH
Per-phase filter inductance L_f	1mH
Per-phase filter capacitance C_f	20 μF
Sampling time (T_s)	60 μs
Weight factor λ of conventional approach	0.008

2168-6777 (c) 2018 IEEE. Translations and content mining are permitted for academic research only. Personal use is also permitted, but republication/redistribution requires IEEE permission. See http://www.ieee.org/publications_standards/publications/rights/index.html for more information.

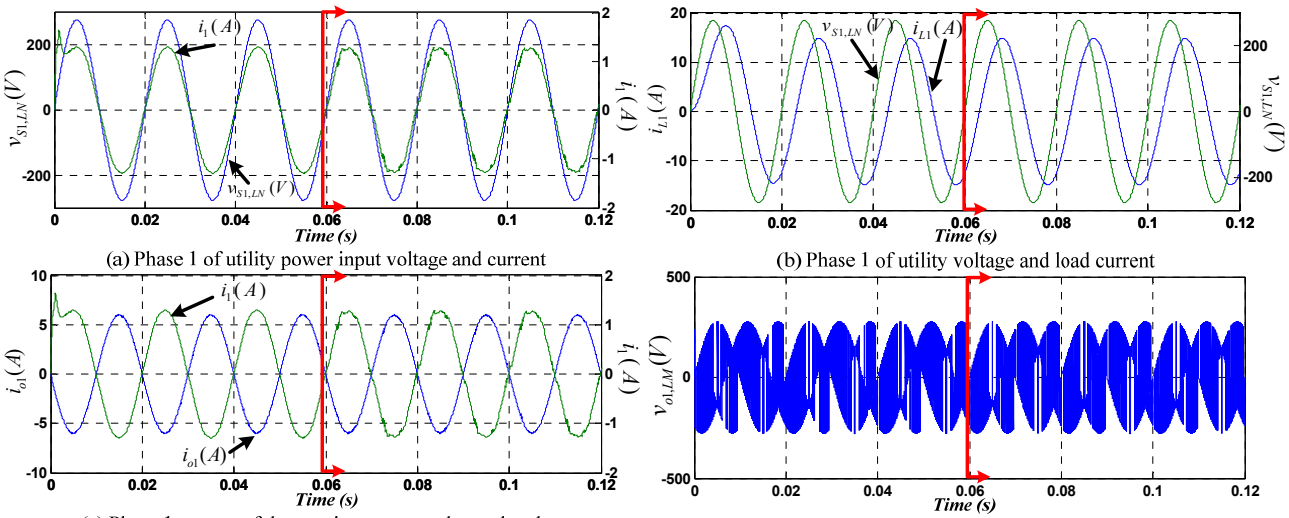
This article has been accepted for publication in a future issue of this journal, but has not been fully edited. Content may change prior to final publication. Citation information: DOI 10.1109/JESTPE.2018.2849738, IEEE Journal of Emerging and Selected Topics in Power Electronics



(a) Phase 1 of utility power input voltage and current

(b) Phase 1 of output voltage of the matrix converter

Fig. 5. Simulation results of the conventional fixed weight factor for MPC cost function for VAR compensation by matrix converter without and with error in the inductance model at time 0.06 s.



(a) Phase 1 of utility power input voltage and current

(b) Phase 1 of utility voltage and load current

(c) Phase 1 current of the matrix converter shows the phase reversal from input to output

(d) Phase 1 of output voltage of the matrix converter

Fig. 6. Simulation results of the proposed auto-tuning approach of weight factor for MPC cost function for VAR compensation by matrix converter without and with error in inductance model at time 0.06 s.

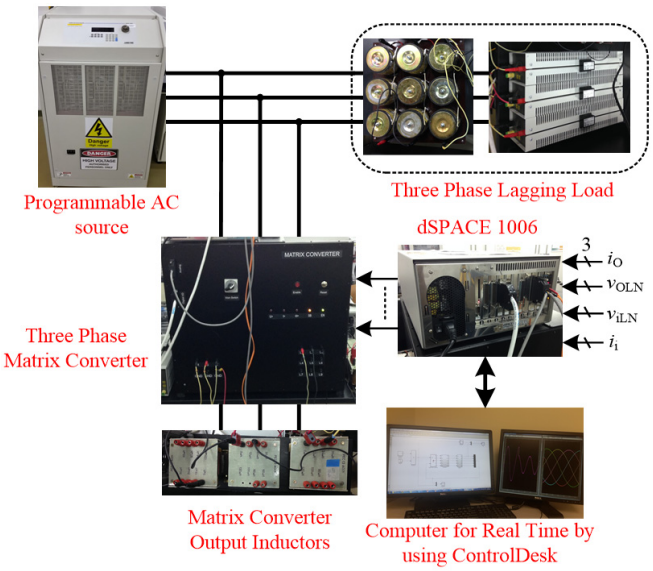


Fig. 7. Experimental setup of the proposed system.

tuning approach of MPC weight factor. Utility grid voltage, utility grid current, and the output voltage of the MC are shown in Fig. 10 and Fig. 11. The reactive power compensation performance, current phase reversal property, and lagging load current are shown by Fig. 12. As it is captured, even after instant *t1* with model parameter error, the STATCOM operates appropriately and continues to compensate the reactive power required by the utility. Thus, the proposed approach improves the robustness of the MPC scheme to model parameter errors in addition to elimination of "trial-and-error" design process of weight factor in MPC cost function.

The grid side reactive power using the proposed auto-tuned cost function weight factor and conventional fixed weight factor are shown in Fig. 13. The error to the model of the MC output-side inductance (L_{MC}) from 30mH to 15mH is applied at time 0.06 s. As it is shown, without error in the inductance model, the proposed auto-tuned method has negligible reactive power tracking error of less than 0.3%, however the reactive power tracking error of conventional fixed weight factor is 1.1%. The tracking performance improvement and robustness to system parameter error is shown after time 0.06 s, as it is shown the proposed method has tracking error of 1.04% with error in the inductance model which shows good disturbance rejection. However, the conventional fixed weight factor method failed to track the zero reactive power (unity power factor).

2168-6777 (c) 2018 IEEE. Translations and content mining are permitted for academic research only. Personal use is also permitted, but republication/redistribution requires IEEE permission. See http://www.ieee.org/publications_standards/publications/rights/index.html for more information.

This article has been accepted for publication in a future issue of this journal, but has not been fully edited. Content may change prior to final publication. Citation information: DOI 10.1109/JESTPE.2018.2849738, IEEE Journal of Emerging and Selected Topics in Power Electronics

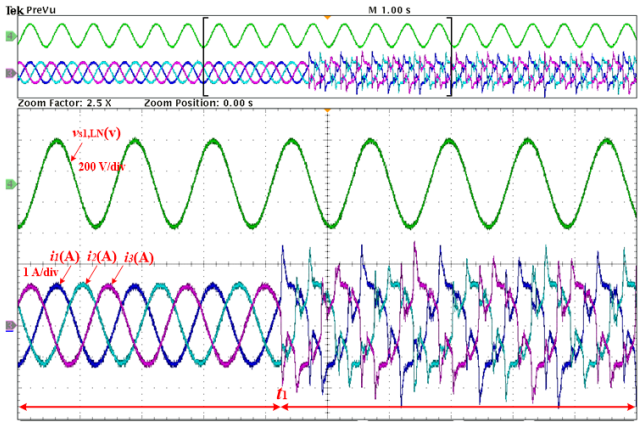


Fig. 8. Conventional MPC with fixed weight factor, model parameter error triggered at instant t_1: utility grid voltage ($v_{s1,LN}$) and current (i_1, i_2, i_3).

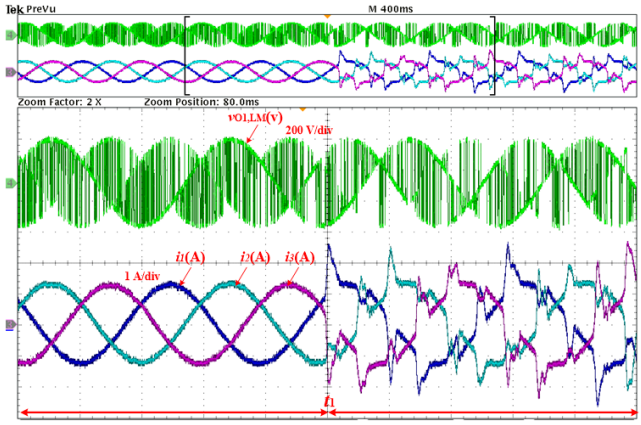


Fig. 9. Conventional MPC with fixed weight factor, model parameter error triggered at instant t_1: MC output voltage ($v_{O1,LM}$) and current (i_1, i_2, i_3).

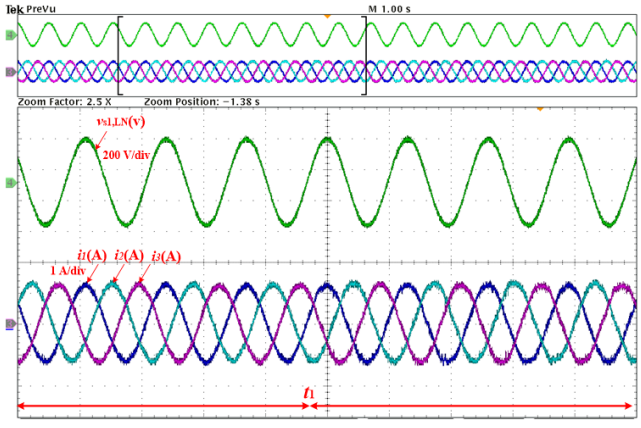


Fig. 10. Proposed MPC with auto-tuned weight factor, model parameter error triggered at instant t_1: utility grid voltage ($v_{s1,LN}$) and current (i_1, i_2, i_3).

The spectrum analysis of phase 1 of the utility side current (i_1) without error in the inductance model from 30mH to 15mH is illustrated in Fig. 14 by using conventional fixed weight factor in the cost function, as it is shown the THD is 5.52%. The spectrum analysis of phase 1 of the utility side current (i_1) without error in the inductance model by using proposed auto-tuned weight factor in the cost function is illustrated in Fig. 15, as it is depicted the THD is dropped to 1.67%. By comparing Fig. 14 and Fig. 15, even without any disturbances in the models of the system, the proposed auto-tuned weight factor method

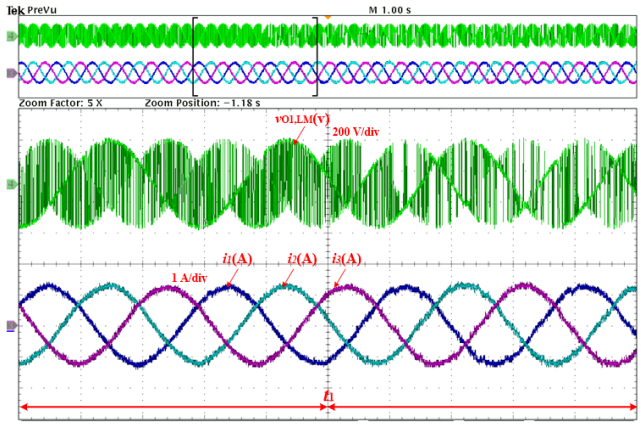


Fig. 11. Proposed MPC with auto-tuned weight factor, model parameter error triggered at instant t_1: MC output voltage ($v_{O1,LM}$) and current (i_1, i_2, i_3).

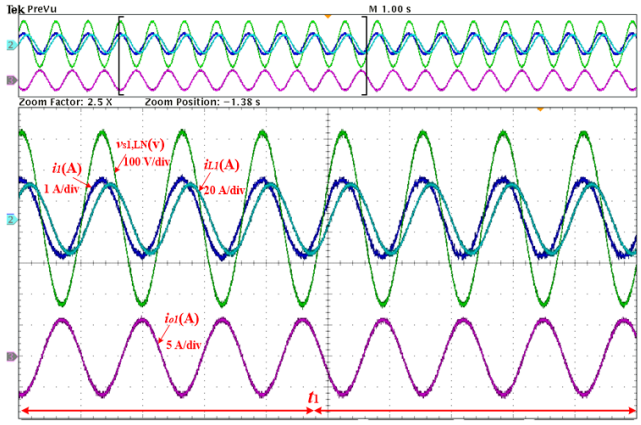
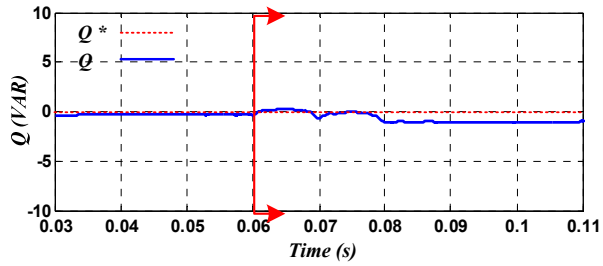
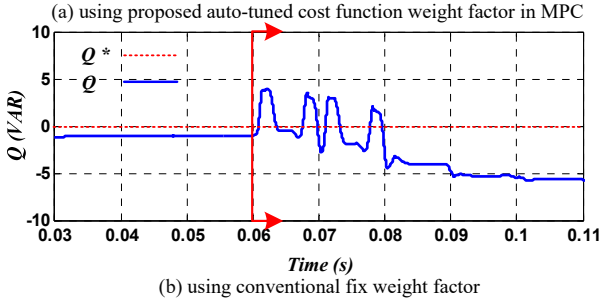


Fig. 12. Proposed MPC with auto-tuned weight factor, model parameter error triggered at instant t_1: utility grid voltage ($v_{s1,LN}$), utility grid current (i_1), MC output current (i_{o1}), and load current (i_{L1}).



(a) using proposed auto-tuned cost function weight factor in MPC



(b) using conventional fix weight factor

Fig.13. Grid side reactive power without and with error in inductance model after time 0.06 s.

significantly improves the grid side current quality. The spectrum analysis of phase 1 of the utility side current is shown in Fig. 16 after applying error to the inductance model at time 0.06ms. The THD is increased to 4.37% when using auto-tuned

2168-6777 (c) 2018 IEEE. Translations and content mining are permitted for academic research only. Personal use is also permitted, but republication/redistribution requires IEEE permission. See http://www.ieee.org/publications_standards/publications/rights/index.html for more information.

This article has been accepted for publication in a future issue of this journal, but has not been fully edited. Content may change prior to final publication. Citation information: DOI 10.1109/JESTPE.2018.2849738, IEEE Journal of Emerging and Selected Topics in Power Electronics

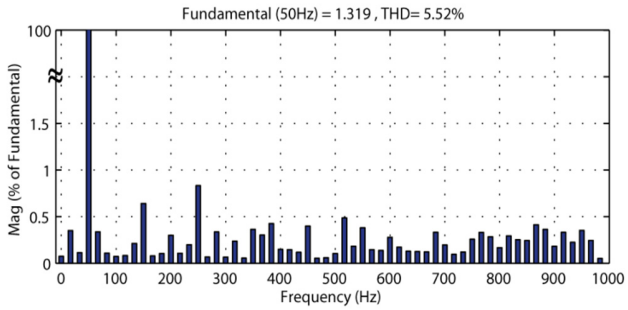


Fig. 14. Spectrum analysis of phase 1 of utility side current (i_1), without error in the inductance model at time 60ms by using conventional fix weight factor.

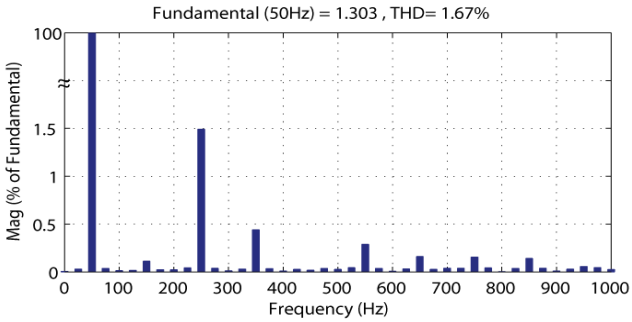


Fig. 15. Spectrum analysis of phase 1 of utility side current (i_1), without error in the inductance model at time 60ms by using proposed auto-tuned weight factor.

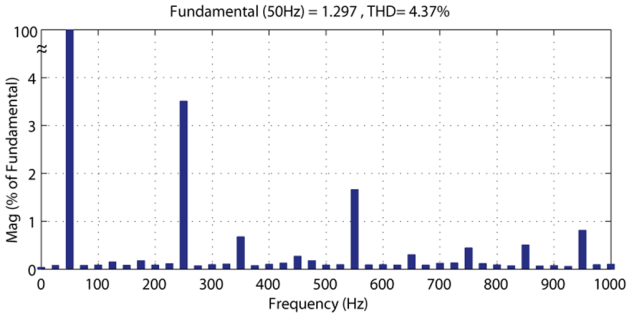
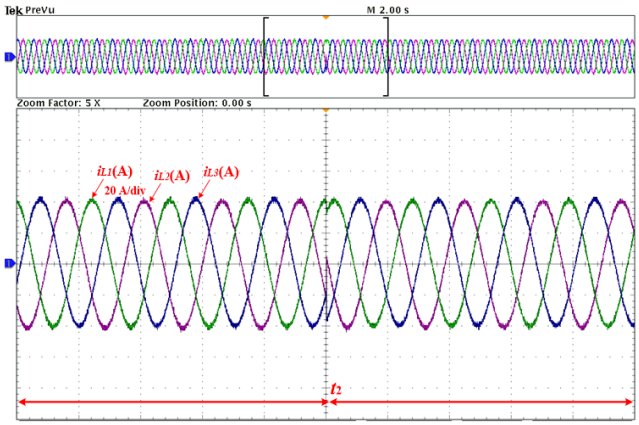


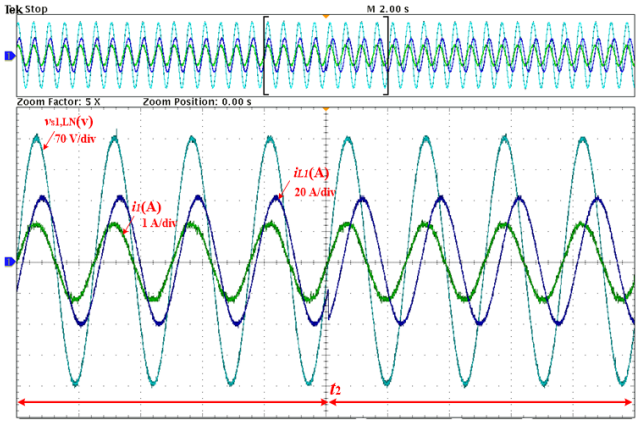
Fig.16. Spectrum analysis of phase 1 of utility side current (i_1), after applying error in the inductance model at time 60ms by using proposed auto-tuned weight factor.

weight factor method, but still it meets the IEEE-519 [30, 31] standards limits. However, if conventional fixed weight factor is used, the grid side current will be highly distorted. Thus, the proposed auto-tuning weight factor technique overcomes one of the main limitations of MPC by improving the robustness of MPC to model parameter errors.

The power factor step response on the utility side has been shown in Fig. 17. The power factor of the load has been stepped at instant t_2 from 0.9 to 0.6. Fig. 17(a) shows the 3 phase balanced load currents before and after the step change in the load power factor command at instant t_2. Fig. 17(b) shows utility current in first phase and the load phase current in first phase along with utility first phase voltage to demonstrate the controller performance. As can be observed, the utility currents are providing the real part of the currents and are in phase with the utility voltage before and after the step response in the load power factor. The extra reactive power demand is supplied by the DMC.



(a) Load current (i_{L1}, i_{L2}, i_{L3}) with step change in p.f.



(b) Utility current (i_1) and voltage ($v_{O1,LM}$), and load current (i_{L1}) before and after step change in p.f.

Fig. 17. Proposed MPC with auto-tuned weight factor, step change in load p.f. from 0.9 to 0.6 occurred at instant t_2.

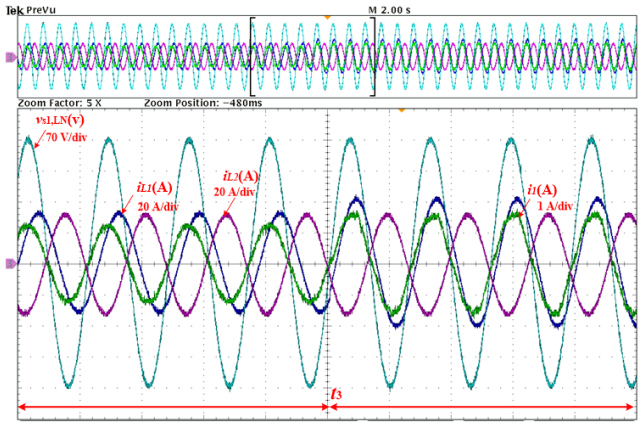
Fig. 18 shows the effect of load unbalancing on the system. The load first phase current *(i_{L1})* has been triggered at instant t_3 to create an unbalanced condition on that load. Fig. 18 (a) shows the utility voltage and currents for first phase. The utility current in first phase has been increased accordingly with respect to load unbalance to cater the extra active demand in that phase. Fig. 18 (b) shows all phases of the load current.

Finally, the voltage sag condition on the utility side has been analyzed and is shown in Fig. 19. A voltage sag at instant t_4 has been introduced on the utility side. Load being the passive type, thus the power requirement also comes down and can be observed in Fig. 19. The DMC based STATCOM is still compensating the full reactive power of the load and maintaining the unity power factor on the utility grid side.

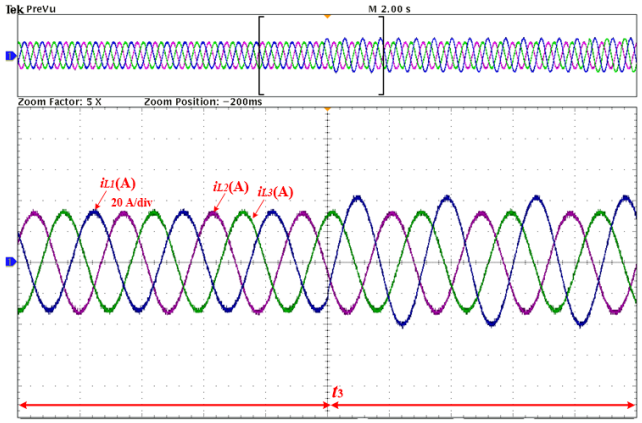
In order to evaluate the computational burden of the proposed control scheme, its execution time has been measured. The required average time to perform all calculations is roughly 50 µs. The sampling time is 60 µs, this sampling time is chosen based on the desired performance and complexity of the control scheme while considering the capability of the hardware microprocessor (dSPACE platform) we used for the system test. It turns out that the proposed control scheme uses approximately 85% of the available time. The execution time measurement shows that the implementation of the proposed

2168-6777 (c) 2018 IEEE. Translations and content mining are permitted for academic research only. Personal use is also permitted, but republication/redistribution requires IEEE permission. See http://www.ieee.org/publications_standards/publications/rights/index.html for more information.

This article has been accepted for publication in a future issue of this journal, but has not been fully edited. Content may change prior to final publication. Citation information: DOI 10.1109/JESTPE.2018.2849738, IEEE Journal of Emerging and Selected Topics in Power Electronics



(a) Utility current (i_1) and voltage ($v_{O1,LM}$), and load current (i_{L1}, i_{L2}) before and after triggering the unbalance scenario.



(b) Load current (i_{L1}, i_{L2}, i_{L3}) before and after triggering the unbalance scenario.

Fig. 18. Proposed MPC with auto-tuned weight factor, unbalance load occurred at instant t_3.

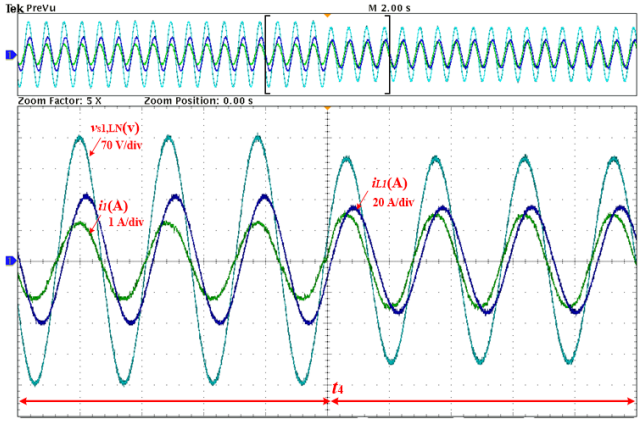


Fig.19. Proposed MPC with auto-tuned weight factor, utility voltage sag of 40 V occurred at instant t_4.

control algorithm is feasible by most of the micro-controllers. The use of an embedded system like dSPACE is intended for expedited prototyping; however, when it comes to the real application and implementation, many cheaper boards like the Altera DEO-Nano FPGA, that costs around $85 is capable of handling the proposed controller.

VI. Conclusion

The performance of MPC with multiple objectives in the cost function is directly affected by the weight factors. The proposed method in this paper determines the optimum weight factor of the cost function at each sampling time, the optimization of weight factor is done based on the prediction of objectives absolute tracking error and their corresponding constraints. This technique eliminated the conventional trial-and-error approach to design weight factor in MPC cost function. Furthermore, the proposed approach improves the robustness of the model based predictive control schemes to model parameter error.

Reactive power in the AC power system network, while fundamental to the system is detrimental to the reliability, efficiency and overall performance of the AC network. The application considered in this paper is a STATCOM by using MPC of a direct matrix converter. MPC of the matrix converter provides reactive power compensation by controlling the input reactive power and the output current into the inductive storage elements. The proposed auto-tuned technique for the MPC of the capacitor-less STATCOM by matrix converter shows: lower THD at the grid side current, robustness to the system model disturbances, and lower tracking error. Thus, the proposed control strategy and STATCOM is more reliable and robust technique for long service life of the device.

References

[1] J. Holtz and S. Stadtfeld, "A predictive controller for the stator current vector of AC machines fed from a switched voltage source," in *International Power Electronics Conference (IPEC)*, 1983, pp. 1665–1675.

[2] J. Rodriguez and P. Cortes, *Predictive control of power converters and electrical drives*. John Wiley & Sons, 2012.

[3] J. Rodriguez *et al.*, "State of the Art of Finite Control Set Model Predictive Control in Power Electronics," *IEEE Transactions on Industrial Informatics,* vol. 9, no. 2, pp. 1003-1016, 2013.

[4] L. Tarisciotti, P. Zanchetta, A. Watson, P. Wheeler, J. C. Clare, and S. Bifaretti, "Multiobjective Modulated Model Predictive Control for a Multilevel Solid-State Transformer," *IEEE Transactions on Industry Applications,* vol. 51, no. 5, pp. 4051-4060, 2015.

[5] H. Jiefeng, Z. Jianguo, and D. G. Dorrell, "Model Predictive Control of Grid-Connected Inverters for PV Systems With Flexible Power Regulation and Switching Frequency Reduction," *IEEE Transactions on Industry Applications,* vol. 51, no. 1, pp. 587-594, 2015.

[6] L. Tarisciotti, P. Zanchetta, A. Watson, J. C. Clare, M. Degano, and S. Bifaretti, "Modulated Model Predictive Control for a Three-Phase Active Rectifier," *IEEE Transactions on Industry Applications,* vol. 51, no. 2, pp. 1610-1620, 2015.

[7] A. Ayad, P. Karamanakos, and R. Kennel, "Direct Model Predictive Current Control Strategy of Quasi-Z-Source Inverters," *IEEE Trans. on Power Elect.,* vol. PP, no. 99, pp. 1-1, 2016.

[8] L. Wang *et al.*, "A finite control set model predictive control method for matrix converter with zero common-mode voltage," *IEEE Journal of Emerging and Selected Topics in Power Electronics,* 2017.

[9] P. Cortes *et al.*, "Guidelines for weighting factors design in Model Predictive Control of power converters and drives," in *IEEE International Conference on Industrial Technology (ICIT)*, 2009, pp. 1-7.

2168-6777 (c) 2018 IEEE. Translations and content mining are permitted for academic research only. Personal use is also permitted, but republication/redistribution requires IEEE permission. See http://www.ieee.org/publications_standards/publications/rights/index.html for more information.

This article has been accepted for publication in a future issue of this journal, but has not been fully edited. Content may change prior to final publication. Citation information: DOI 10.1109/JESTPE.2018.2849738, IEEE Journal of Emerging and Selected Topics in Power Electronics

[10] M. B. Shadmand, M. Mosa, R. S. Balog, and H. Abu-Rub, "Model Predictive Control of a Capacitorless Matrix Converter-Based STATCOM," *IEEE Journal of Emerging and Selected Topics in Power Electronics,* vol. 5, no. 2, pp. 796-808, 2017.

[11] J. L. Garriga and M. Soroush, "Model predictive control tuning methods: A review," *Industrial & Engineering Chemistry Research,* vol. 49, no. 8, pp. 3505-3515, 2010.

[12] R. Shridhar and D. J. Cooper, "A tuning strategy for unconstrained multivariable model predictive control," *Industrial & engineering chemistry research,* vol. 37, no. 10, pp. 4003-4016, 1998.

[13] W. Liu and G. Wang, "Auto-tuning procedure for model-based predictive controller," in *IEEE International Conference on Systems, Man, and Cybernetics*, 2000, vol. 5, pp. 3421-3426: IEEE.

[14] M. B. Shadmand, R. S. Balog, and H. Abu Rub, "Model predictive control of a capacitor-less VAR compensator based on a matrix converter," in *IEEE Annual Conference of Industrial Electronics Society (IECON)*, 2014, pp. 3311-3317.

[15] S. R. Arya and B. Singh, "Performance of DSTATCOM using leaky LMS control algorithm," *IEEE Journal of Emerging and Selected Topics in Power Electronics,* vol. 1, no. 2, pp. 104-113, 2013.

[16] Z. He *et al.*, "Reactive Power Strategy of Cascaded Delta-Connected STATCOM Under Asymmetrical Voltage Conditions," *IEEE Journal of Emerging and Selected Topics in Power Electronics,* vol. 5, no. 2, pp. 784-795, 2017.

[17] H. Wang *et al.*, "Transitioning to physics-of-failure as a reliability driver in power electronics," *IEEE Journal of Emerging and Selected Topics in Power Electronics,* vol. 2, no. 1, pp. 97-114, 2014.

[18] B. Shi, B. Zhou, Y. Zhu, X. Qin, J. Lei, and N. Han, "Open-Circuit Fault Analysis and Diagnosis for Indirect Matrix Converter," *IEEE Journal of Emerging and Selected Topics in Power Electronics,* 2017.

[19] S. Harb, Z. Haiyu, and R. S. Balog, "AC-link, single-phase, photovoltaic Module Integrated Inverter," in *IEEE Applied Power Electronics Conference and Exposition (APEC)*, 2013, pp. 177-182.

[20] A. S. Farag *et al.*, "Failure analysis of composite dielectric of power capacitors used in distribution systems," in *Electrical Insulation Conference, 1997, and Electrical Manufacturing & Coil Winding Conference. Proceedings*, 1997, pp. 557-564.

[21] W. Huai and F. Blaabjerg, "Reliability of Capacitors for DC-Link Applications in Power Electronic Converters: An Overview," *IEEE Transactions on Industry Applications,* vol. 50, no. 5, pp. 3569-3578, 2014.

[22] J. Bebic, R. Walling, K. O'Brien, and B. Kroposki, "The sun also rises," *IEEE Power and Energy Magazine,* vol. 7, no. 3, pp. 45-54, 2009.

[23] M. Makdessi, A. Sari, P. Venet, P. Bevilacqua, and C. Joubert, "Accelerated Ageing of Metallized Film Capacitors Under High Ripple Currents Combined With a DC Voltage," *IEEE Transactions on Power Electronics,* vol. 30, no. 5, pp. 2435-2444, 2015.

[24] M. Arias *et al.*, "High-Efficiency Asymmetrical Half-Bridge Converter Without Electrolytic Capacitor for Low-Output-Voltage AC-DC LED Drivers," *IEEE Transactions on Power Electronics,* vol. 28, no. 5, pp. 2539-2550, 2013.

[25] A. S. Farag *et al.*, "Failure analysis of composite dielectric of power capacitors in distribution systems," *IEEE Transactions on Dielectrics and Electrical Insulation,* vol. 5, no. 4, pp. 583-588, 1998.

[26] A. M. Imam, D. M. Divan, R. G. Harley, and T. G. Habetler, "Real-Time Condition Monitoring of the Electrolytic Capacitors for Power Electronics Applications," in *IEEE Applied Power Electronics Conference (APEC)*, 2007, pp. 1057-1061.

[27] P. Venet, H. Darnand, and G. Grellet, "Detection of faults of filter capacitors in a converter. Application to predictive maintenance," in *IEEE Telecommunications Energy Conference (INTELEC)*, 1993, vol. 2, pp. 229-234 vol.2.

[28] A. Braham, A. Lahyani, P. Venet, and N. Rejeb, "Recent Developments in Fault Detection and Power Loss Estimation of Electrolytic Capacitors," *IEEE Transactions on Power Electronics,* vol. 25, no. 1, pp. 33-43, 2010.

[29] D. Balakrishnan and R. S. Balog, "Capacitor-less VAR compensator based on matrix converter," in *IEEE North American Power Symposium (NAPS)*, 2010, pp. 1-7.

[30] C. K. Duffey and R. P. Stratford, "Update of harmonic standard IEEE-519: IEEE recommended practices and requirements for harmonic control in electric power systems," *IEEE Transactions on Industry Applications,* vol. 25, no. 6, pp. 1025-1034, 1989.

[31] I. W. Group, "IEEE recommended practices and requirements for harmonic control in electrical power systems," *IEEE STD,* pp. 519-1992, 1992.

[32] H. Abu-Rub, J. Guzinski, Z. Krzeminski, and H. A. Toliyat, "Predictive current control of voltage-source inverters," *IEEE Transactions on Industrial Electronics,* vol. 51, no. 3, pp. 585-593, 2004.

[33] B. Arif, L. Tarisciotti, P. Zanchetta, J. Clare, and M. Degano, "Grid Parameter estimation using Model Predictive Direct Power Control," *IEEE Transactions on Industry Applications,* vol. PP, no. 99, pp. 1-1, 2015.

[34] T. Geyer, "A Comparison of Control and Modulation Schemes for Medium-Voltage Drives: Emerging Predictive Control Concepts Versus PWM-Based Schemes," *IEEE Transactions on Industry Applications,* vol. 47, no. 3, pp. 1380-1389, 2011.

[35] S. Mariethoz, A. Domahidi, and M. Morari, "High-Bandwidth Explicit Model Predictive Control of Electrical Drives," *IEEE Transactions on Industry Applications,* vol. 48, no. 6, pp. 1980-1992, 2012.

[36] P. W. Wheeler, J. Rodriguez, J. C. Clare, L. Empringham, and A. Weinstein, "Matrix converters: a technology review," *IEEE Transactions on Industrial Electronics,* vol. 49, no. 2, pp. 276-288, 2002.

[37] J. Rodriguez, M. Rivera, J. W. Kolar, and P. W. Wheeler, "A Review of Control and Modulation Methods for Matrix Converters," *IEEE Transactions on Industrial Electronics,* vol. 59, no. 1, pp. 58-70, 2012.

[38] R. Vargas, J. Rodriguez, U. Ammann, and P. W. Wheeler, "Predictive Current Control of an Induction Machine Fed by a Matrix Converter With Reactive Power Control," *IEEE Transactions on Industrial Electronics,* vol. 55, no. 12, pp. 4362-4371, 2008.

[39] M. Rivera, J. Rodriguez, J. R. Espinoza, and H. Abu-Rub, "Instantaneous Reactive Power Minimization and Current Control for an Indirect Matrix Converter Under a Distorted AC Supply," *IEEE Transactions on Industrial Informatics,* vol. 8, no. 3, pp. 482-490, 2012.

[40] F. Villarroel, J. R. Espinoza, C. A. Rojas, J. Rodriguez, M. Rivera, and D. Sbarbaro, "Multiobjective Switching State Selector for Finite-States Model Predictive Control Based on Fuzzy Decision Making in a Matrix Converter," *IEEE Transactions on Industrial Electronics,* vol. 60, no. 2, pp. 589-599, 2013.

2168-6777 (c) 2018 IEEE. Translations and content mining are permitted for academic research only. Personal use is also permitted, but republication/redistribution requires IEEE permission. See http://www.ieee.org/publications_standards/publications/rights/index.html for more information.

This article has been accepted for publication in a future issue of this journal, but has not been fully edited. Content may change prior to final publication. Citation information: DOI 10.1109/JESTPE.2018.2849738, IEEE Journal of Emerging and Selected Topics in Power Electronics



Mohammad B. Shadmand (S'09, M'15) received the B.S. degree in electrical engineering from Qatar University, Doha, Qatar, in 2010. He received the M.S. and PhD degrees in electrical engineering from Texas A&M University, College Station, TX, USA in 2012 and 2015.

He was a research associate in renewable energy and advanced power electronics research laboratory, TX, USA from 2010-2015. He was a visiting researcher with Smart Grid Center, Texas A&M University at Qatar, 2014. He was an instructor in Department of Electrical and Computer Engineering, Texas A&M University, College Station, TX, USA from 2015-2016. He was a TEES research engineer in renewable energy and advanced power electronics research laboratory, TX, USA from 2016-2017. He is currently an Assistant Professor in the Department of Electrical and Computer Engineering and Director of the Renewable Energy and Power Quality Research Laboratory at Kansas State University, Manhattan, KS, USA since 2017. He has published more than 50 journal and conference papers. His current research interests include advanced model predictive control, grid-tied power electronics interfaces with advance functionalities, matrix converter, and control of smart microgrid systems.

Dr. Shadmand was awarded second place in the IEEE Industrial Application Society Graduate Thesis Contest for his M.S. thesis in 2013. He received the IEEE Standard Education award for the project "fixed-step model predictive control of grid-tied photovoltaic inverter" in 2014. He was awarded Michelle Munson_serban Simu Keystone Research Scholar, Kansas State University in 2017.



Sarthak Jain (S'13) received the B.Tech. degree in electrical engineering from GGSIPU, Delhi, India, in 2014. He is currently working towards his master's degree in electrical engineering from Texas A&M University, College Station, TX, USA.

He was research associate in Renewable Energy and Advanced Power Electronics Laboratory from 2016-2017. Before joining Texas A&M University, he was research associate at Delhi Technological University, Delhi, INDIA from 2014-2016. There, he worked on a project titled 'Reliability and Efficient System for Community Energy Solutions (RESCUES)' under Imperial College London and DST INDIA. His research interest includes power electronics circuit design, DC/AC PV grid tied inverters, DC/DC resonant converters, etc.



Robert S. Balog (S'92–M'96–SM'07) received the B.S. degree in electrical engineering from Rutgers – The State University of New Jersey, New Brunswick, NJ in 1996 and the M.S. and Ph.D. degrees in electrical engineering from the University of Illinois at Urbana-Champaign, Urbana, IL in 2003 and 2006 respectively.

He was an Engineer with Lutron Electronics, Coopersburg, PA from 1996 to 1999, a Researcher with the U.S. Army Corp of Engineers, Engineering Research and Development Center (ERDEC), Construction Engineering Research Lab (CERL), Champaign, IL from 2005-2006, a Senior Engineer at SolarBridge Technologies (now SunPower Inc.), Champaign, IL from 2006 to 2009, then joined Texas A&M University, College Station, Tx, where he is currently an Associate Professor in the Department of Electrical and Computer Engineering and Director of the Renewable Energy & Advanced Power Electronics Research Laboratory. He holds a joint faculty appointment with the Department of Electrical Engineering at Texas A&M University in Qatar.

He holds 18 issued U.S. patent with additional patents pending. His current research interests include power converters for solar energy, particularly microinverters for ac photovoltaic (ACPV) modules and highly reliable electrical power and energy systems including dc microgrids. Dr. Balog is a Registered Professional Engineer in Illinois. He received the IEEE Joseph J. Suozzi INTELEC Fellowship in Power Electronics in 2001. He is a member of Eta Kappa Nu, Sigma Xi, the National Society of Professional Engineers, the American Solar Energy Society and the Solar Electric Power Association. He is the 2011 recipient of the Rutgers School of Engineering Distinguished Engineer award.

2168-6777 (c) 2018 IEEE. Translations and content mining are permitted for academic research only. Personal use is also permitted, but republication/redistribution requires IEEE permission. See http://www.ieee.org/publications_standards/publications/rights/index.html for more information.

arXiv:1808.02520v1 [math.CA] 7 Aug 2018

BEZIER VARIENT OF THE GENERAL FAMILY OF GUPTA-SRIVASTAVA OPERATORS

RAM PRATAP AND NAOKANT DEO

Abstract. Gupta and Srivastava [6] introduced the family of sequence of linear positive operators. In the present paper, we proposed the Bezier varient of the Gupta-Srivastava operators and studied the rate of convergence for the functions of bounded variation.

1. introduction

In 2003, Srivastava and Gupta [5] introduced a sequence of linear positive operators and studied the convergence properties. After two year Ispir and Yuksel proposed the Bezier varient of Srivastava and Gupta operators and discussed the rate of convergence for the proposed operators [2].
Several Scholars have taken in to out with the modification of the Srivastava and Gupta operators (see, [1], [3], [7], [8]). One of them, Yadav [8] introduced the modification of Srivastava and Gupta operators which preserve the constant functions as well as linear functions and established the Voronvskaya type theorem and statistical convergence. It may have better approximation. In the year 2017, Neer, Ispir and Agrawal [4] proposed the Bezier varient of the operators which is introduced by Yadav [8] and discussed several convergence properties.

Recently Gupta and Srivastava [6] proposed a general family of positive linear operators, which preserve constant as well as linear functions for all $c \in \mathbb{N}\cup\{0\}\cup\{-1\}$. They have considered the general sequence of positive linear operators containing some well-known operators as special cases of Srivastav-Gupta operators [5], and for $m \in \mathbb{Z}$, and $c \in \mathbb{N} \cup \{0\} \cup \{-1\}$ operators defined as:

$$L_{n,c}\left(f\left(t\right);x\right) = \{n+(m+1)c\}\sum_{k=1}^{\infty} p_{n+mc,k}(x;c)\int_{0}^{\infty} p_{n+(m+2)c,k-1}(t;c)f(t)dt + p_{n+mc,0}(x;c)f(0), \tag{1.1}$$

where

$$p_{n,k}\left(x;c\right) = \frac{\left(-x\right)^{k}}{k!}\phi_{n,c}^{(k)}(x),$$

and

$$\phi_{n,c}^{(k)} = \begin{cases} e^{-nx}, & c=0 \\ (1-x)^{-n}, & c=-1 \\ (1+cx)^{\frac{-n}{c}}, & c=1,2,3,\ldots \end{cases}$$

Key words and phrases. Baskakov operators, Hypergeometric function,Function of Bounded variation .

From the above work, we proposed the Bezier varient of the operators (1.1) as follows:

$$F_{n,c}^{(\alpha)}\left(f\left(t\right);x\right)=\{n+(m+1)c\}\sum_{k=1}^{\infty}Q_{n+mc}^{(\alpha)}(x;c)\int_{0}^{\infty}p_{n+(m+2)c,k-1}(t;c)f(t)dt$$
$$+Q_{n+mc,0}^{(\alpha)}(x;c)f(0), \tag{1.2}$$

where $Q_{n+mc,k}^{(\alpha)}(x;c)=\left(J_{n+mc,k}(x,c)\right)^{\alpha}-\left(J_{n+mc,k+1}(x,c)\right)^{\alpha}$, $\alpha\geq 1$ with

$$J_{n+mc,k}(x,c)=\sum_{j=k}^{\infty}p_{n+mc,k}(x,c),$$

where $k<\infty$ and otherwise zero.It is obvious, $F_{n,c}^{(\alpha)}\left(.;x\right)$ is linear positive operators. For $\alpha=1$ the operators reduce to (1.1).
The special cases of operators (1.2) are as follows:

(i) For $c=0$, $\alpha=1$ and $\phi_{n,0}(x)=e^{-nx}$, we get Phillips operators

$$L_{n,0}\left(f\left(t\right);x\right)=n\sum_{k=1}^{\infty}p_{n,k}(x;0)\int_{0}^{\infty}p_{n,k-1}(t;0)f(t)dt+p_{n,0}(x;0)f(0),$$

where

$$p_{n,k}(x,0)=\frac{e^{-nx}(nx)^{k}}{k!}\ \text{ and }\ x\in[0,\infty).$$

(ii) For $c\in\mathbb{N}$, $\alpha=1$ and $\phi_{n,c}(x)=(1+cx)^{-\frac{n}{c}}$, we get genuine Baskakov-Durrmeyer type operators. These operators are similar to (1.1) except for $c=\{0,-1\}$, called summation integral type of operators. where

$$p_{n,k}(x;c)=\frac{\left(\frac{n}{c}\right)_{k}}{k!}\frac{(cx)_{k}}{(1+cx)^{\frac{n}{c}+k}}$$

and $(n)_i$ denotes the rising factorial given by

$$(n)_{i}=n(n+1)(n+2)...(n+i-1)\ \ \&\ \ (n)_{0}=1(i\in\mathbb{N}).$$

(iii) For $c=-1$, $\alpha=1$ and $\phi_{n,-1}(x)=(1-x)^{-n}$, we have sequence of Bernstein-Durrmeyer operators

$$L_{n,-1}\left(f,x\right)=(n-m-1)\sum_{k=1}^{n-m-1}p_{n-m,k}\left(x,-1\right)\int_{0}^{1}p_{n-m-2,k-1}\left(t,-1\right)f(t)dt$$
$$+p_{n-m,0}\left(x,-1\right)f(0)+p_{n-m,n-m}\left(x,-1\right), \tag{1.3}$$

where

$$p_{n,k}(x;-1)=\left(\begin{array}{c}n\\k\end{array}\right)x^{k}(1-x)^{n-k}.$$

For the proposed operators, we establish the rate of convergence for the functions of bounded variation.

2. auxilary Results

Lemma 2.1. *Let $f(t) = e_i$, $i = 0, 1, 2$ and $c \in \mathbb{N} \cup \{0\} \cup \{-1\}$, then we have*

(i) $L_{n,c}(e_0; x) = 1$;
(ii) $L_{n,c}(e_1; x) = x$;
(iii) $L_{n,c}(e_2; x) = \frac{(n+(m+1)c)}{(n+(m-1)c)}x^2 + \frac{2}{(n+(m-1)c)}x$;

All the moments of operators (1.1) can be obtained in terms of hyper geometric function of order $r \in \mathbb{N}$ for details see [6].

Remark 2.1. *The second central moment of the operators* (1.1) *is as follows:*

$$L_{n,c}\left((e_1 - x)^2; x\right) = \frac{2x(1+cx)}{(n+(m-1)c)}. \tag{2.1}$$

For sufficient large n, (2.1) *can be written as:*

$$L_{n,c}\left((e_1 - x)^2; x\right) \leq \frac{2x(1+cx)}{n}.$$

Remark 2.2. *From* (1.2)*, we have*

$$\begin{aligned} F_{n,c}^{(\alpha)}(1; x) &= \{n + (m+1)c\} \sum_{k=1}^{\infty} Q_{n+mc}^{(\alpha)}(x; c) \int_0^{\infty} p_{n+(m+2)c,k-1}(t; c)dt \\ &\quad + Q_{n+mc,0}^{(\alpha)}(x; c) \\ &= \sum_{k=0}^{\infty} Q_{n+mc}^{(\alpha)}(x; c) = \left(J_{n+mc,0}(x, c)\right)^{(\alpha)} \\ &= \left(\sum_{k=0}^{\infty} p_{n+mc,j}(x, c)\right)^{(\alpha)} = 1, \end{aligned}$$

since $\sum_{j=0}^{\infty} p_{n+mc,j}(x, c) = 1$.

Lemma 2.2. *For each $f \in C[0, \infty)$ then, we have*

$$\left|F_{n,c}^{(\alpha)}(f(t); x)\right| \leq \|f\|.$$

Proof. It is easy to prove by using Remark 2.2, so here we skip the proof. □

Lemma 2.3. *For every $f \in [0, \infty)$ then, we have*

$$\left|F_{n,c}^{(\alpha)}(f(t); x)\right| \leq \alpha L_{n,c}(\|f\|; x).$$

Proof. For $0 \leq c \leq d \leq 1$, $\alpha \geq 1$, using the inequality

$$|c^{\alpha} - d^{\alpha}| \leq \alpha |c - d|,$$

from the definition of $Q_{n+mc,k}^{(\alpha)}(x; c)$, for all $k \in \mathbb{N} \cup \{0\}$, we get

$$\begin{aligned} 0 < \left(J_{n+mc,k}(x, c)\right)^{\alpha} - \left(J_{n+mc,k+1}(x, c)\right)^{\alpha} &\\ &\leq \alpha \left(J_{n+mc,k}(x, c) - J_{n+mc,k+1}(x, c)\right) \\ &= \alpha p_{n+mc}(x, c). \end{aligned}$$

Hence, we get

$$\left|F_{n,c}^{(\alpha)}\left(f(t);x\right)\right| \leq \alpha L_{n,c}\left(\|f\|;x\right)$$

□

3. function of bounded variation

The operators (1.2) can be rewritten in the following form:

$$F_{n,c}^{(\alpha)}\left(f(t);x\right) = \int_0^\infty M_{n,m,c}^{(\alpha)}(x,t)f(t)dt, \tag{3.1}$$

where

$$M_{n,m,c}^{(\alpha)}(x,t) = \{n+(m+1)c\}\sum_{k=1}^{\infty} Q_{n+mc,k}^{(\alpha)}(x;c)p_{n+(m+2)c,k}(t,c) + Q_{n+mc,0}^{(\alpha)}(x;c)\delta(t),$$

where $\delta(t)$ is Dirac delta function.

Lemma 3.1. *For a fixed $x \in [0,\infty)$ and n is sufficient large then, we have*

(i) $\zeta_{n,c}^{(\alpha)}(x;y) = \int_0^y M_{n,m,c}^{(\alpha)}(x;t)dt \leq \frac{2\alpha x(1+cx)}{n(x-y)^2}, \;\; 0 \leq y \leq x;$

(ii) $1-\zeta_{n,c}^{(\alpha)}(x;z) = \int_0^y M_{n,m,c}^{(\alpha)}(x;t)dt \leq \frac{2\alpha x(1+cx)}{n(z-x)^2}, \;\; x \leq z \leq \infty.$

Proof. Using Remark 2.1 and 2.3 then, we have

$$\begin{aligned}
\zeta_{n,c}^{(\alpha)}(x;y) &\leq \int_0^y M_{n,m,c}^{(\alpha)}(x;t)\left(\frac{x-t}{x-y}\right)^2 dt \\
&\leq \frac{\alpha}{(x-y)^2} L_{n,c}\left((e_1-x)^2;x\right) \\
&\leq \frac{2\alpha x(1+cx)}{n(x-y)^2}.
\end{aligned}$$

We can prove the second part of the Lemma in same way. □

Theorem 3.1. *Let $f \in DBV[0,\infty)$ then for every $x \in [0,\infty)$ and sufficiently large n, we have*

$$\begin{aligned}\left|F_{n,c}^{(\alpha)}(f;x)-f(x)\right| \leq & \frac{1}{\alpha+1}\left|f'(x+)+\alpha f'(x-)\right|\sqrt{\frac{2\alpha x(1+cx)}{n}} \\ & + \frac{\alpha}{\alpha+1}\left|f'(x+)-f'(x-)\right|\sqrt{\frac{2\alpha x(1+cx)}{n}} \\ & + \frac{2\alpha(1+cx)}{n}\sum_{k=1}^{[\sqrt{n}]}\overset{x}{\underset{x-\frac{x}{k}}{V}} f'_x + \frac{x}{\sqrt{n}}\overset{x}{\underset{x-\frac{x}{\sqrt{n}}}{V}} f'_x \\ & \frac{2\alpha(1+cx)}{nx}\left|f(2x)-f(x)-xf(x+)\right| \\ & + \frac{2\alpha x(1+cx)}{n}\sum_{k=1}^{[\sqrt{n}]}\overset{x+\frac{x}{k}}{\underset{x}{V}} f'_x + \frac{x}{\sqrt{n}}\overset{x+\frac{x}{\sqrt{n}}}{\underset{x}{V}}(f'_x) \\ & + M(\gamma,r,x) + \frac{2\alpha(1+cx)}{nx}\left|f(x)\right| + \sqrt{\frac{2\alpha x(1+cx)}{n}}\left|f(x+)\right|.\end{aligned}$$

where $\overset{b}{\underset{a}{V}} f(x)$ denotes the total variation of f on $[a,b]$, f_x is an auxiliary operator given by

$$f_x(t) = \begin{cases} f(t)-f(x-), & 0 \leq t < x \\ 0, & t = x \\ f(t)-f(x+), & x < t < \infty \end{cases}. \tag{3.2}$$

Proof. From Remark 2.2, $F_{n,c}^{(\alpha)}(f(t);x) = 1$ and using the alternative form of the operators (3.1) for each $x \in [0,\infty)$ then, we have

$$\begin{aligned}F_{n,c}^{(\alpha)}(f(t);x) - f(x) &= \int_0^\infty M_{n,m,c}^{(\alpha)}(x,t)(f(t)-f(x))dt \\ &= \int_0^\infty M_{n,m,c}^{(\alpha)}(x,t)\left(\int_x^t f'(u)du\right)dt\end{aligned} \tag{3.3}$$

For each $f \in DBV[0,\infty)$ and from (3.2), we can write

$$\begin{aligned}f'(u) =& f'_x(u) + \frac{1}{\alpha+1}(f'(x+)+\alpha f'(x-)) \\ & + \frac{1}{2}(f'(x+)+\alpha f'(x-))\left(\operatorname{sgn}(u-x)+\frac{\alpha-1}{\alpha+1}\right) \\ & \times \delta_x(u)\left[f'(u)-(f'(x+)+f'(x-)\right],\end{aligned} \tag{3.4}$$

where

$$\delta_x(u) = \begin{cases} 1 & u = x \\ 0 & u \neq x. \end{cases}$$

From (3.3) and (3.4), we have

$$F_{n,c}^{(\alpha)}(f(t);x)-f(x)=\int_0^\infty M_{n,m,c}^{(\alpha)}(x,t)\int_x^t\Bigg(f_x^{'}(u)+\frac{1}{\alpha+1}(f^{'}(x+)+\alpha f^{'}(x-))+\frac{1}{2}(f^{'}(x+)+\alpha f^{'}(x-))\left(\operatorname{sgn}(u-x)+\frac{\alpha-1}{\alpha+1}\right)\times\delta_x(u)[f'(u)-\frac{1}{2}(f'(x+)+f'(x-)]\Bigg)dudt. \tag{3.5}$$

It is easy to say that

$$\int_0^\infty M_{n,m,c}^{(\alpha)}(x,t)\int_x^t[f'(u)-\frac{1}{2}(f'(x+)+f'(x-)]\delta_x(u)dudt=0. \tag{3.6}$$

Now

$$\begin{aligned}B_1&=\int_0^\infty M_{n,m,c}^{(\alpha)}(x,t)\int_x^t\frac{1}{\alpha+1}(f'(x+)+\alpha f'(x-))dudt.\\&=\frac{1}{\alpha+1}(f'(x+)+\alpha f'(x-))\int_0^\infty M_{n,m,c}^{(\alpha)}(x,t)(t-x)dt\\&=\frac{1}{\alpha+1}(f'(x+)+\alpha f'(x-))F_{n,c}^{(\alpha)}\left((t-x);x\right),\end{aligned} \tag{3.7}$$

and

$$\begin{aligned}B_2&=\int_0^\infty M_{n,m,c}^{(\alpha)}(x,t)\int_x^t\frac{1}{2}(f'(x+)+\alpha f'(x-))\left(\operatorname{sgn}(u-x)+\frac{\alpha-1}{\alpha+1}\right)dudt\\&=\frac{1}{2}(f'(x+)+\alpha f'(x-))\left(-\int_0^x M_{n,m,c}^{(\alpha)}(x,t)\int_x^t\left(\operatorname{sgn}(u-x)+\frac{\alpha-1}{\alpha+1}\right)dudt+\int_x^\infty M_{n,m,c}^{(\alpha)}(x,t)\int_x^t\left(\operatorname{sgn}(u-x)+\frac{\alpha-1}{\alpha+1}\right)\right)\\&\le\frac{\alpha}{\alpha+1}(f'(x+)+\alpha f'(x-))\int_0^\infty M_{n,m,c}^{(\alpha)}(x,t)\left|t-x\right|dt\\&\le\frac{\alpha}{\alpha+1}(f'(x+)+\alpha f'(x-))\left(F_{n,c}^{(\alpha)}\left((e_1-x)^2;x\right)\right)^{\frac{1}{2}}\end{aligned} \tag{3.8}$$

By using Remark 2.1 and Lemma 2.3, from (3.5) – (3.8) then, we have

$$\begin{aligned}F_{n,c}^{(\alpha)}(f;x)-f(x)\le&\left|A_n^{(\alpha)}(f';x)+B_n^{(\alpha)}(f';x)\right|\\&+\frac{2\alpha}{\alpha+1}\left|f'(x+)+\alpha f'(x-)\right|\frac{x(1+cx)}{n}\\&+\frac{\alpha}{\alpha+1}\left|f'(x+)-f'(x-)\right|\sqrt{\frac{2\alpha x(1+cx)}{n}}\end{aligned} \tag{3.9}$$

where

$$A_n^{(\alpha)}(f';x)=\int_0^x\left(\int_x^t f'_x(u)du\right)M_{n,m,c}^{(\alpha)}(x,t)dt,$$

and

$$B_n^{(\alpha)}(f';x)=\int_x^\infty\left(\int_x^t f'_x(u)du\right)M_{n,m,c}^{(\alpha)}(x,t)dt.$$

To estimate $A_n^{(\alpha)}(f';x)$, using integration by parts and applying Lemma 3.1 with $y=x-\frac{x}{\sqrt{n}}$, we obtain

$$\begin{aligned}
A_n^{(\alpha)}(f';x)&=\left|\int_0^x\left(\int_x^t f'_x(u)du\right)d_t\zeta_{n,c}^{(\alpha)}(x;t)\right|\\
&=\left|\int_0^x\zeta_{n,c}^{(\alpha)}(x;t)f'_x(t)dt\right|\\
&\le\int_0^y|f'_x(t)|\left|\zeta_{n,c}^{(\alpha)}(x;t)\right|dt+\int_0^y|f'_x(t)|\left|\zeta_{n,c}^{(\alpha)}(x;t)\right|dt\\
&\le\frac{2\alpha x(1+cx)}{n}\int_0^y\overset{x}{\underset{t}{V}}f'_x(x-t)^2dt+\int_y^x\overset{x}{\underset{t}{V}}f'_xdt\\
&\le\frac{2\alpha x(1+cx)}{n}\int_0^{x-\frac{x}{\sqrt{n}}}\overset{x}{\underset{t}{V}}f'_x(x-t)^2dt+\frac{x}{\sqrt{n}}\overset{x}{\underset{x-\frac{x}{\sqrt{n}}}{V}}f'_x,
\end{aligned}\tag{3.10}$$

substituting $u=\frac{x}{x-t}$, we get

$$\begin{aligned}
\frac{2\alpha x(1+cx)}{n}\int_0^{x-\frac{x}{\sqrt{n}}}\overset{x}{\underset{t}{V}}f'_x(x-t)^2dt&=\frac{2\alpha x(1+cx)}{nx}\int_1^{\sqrt{n}}\overset{x}{\underset{x-\frac{x}{u}}{V}}f'_xdu\\
&\le\frac{2\alpha(1+cx)}{n}\sum_{k=1}^{[\sqrt{n}]}\int_k^{k+1}\overset{x}{\underset{x-\frac{x}{k}}{V}}f'_xdu\\
&\le\frac{2\alpha(1+cx)}{n}\sum_{k=1}^{[\sqrt{n}]}\overset{x}{\underset{x-\frac{x}{k}}{V}}f'_x.
\end{aligned}\tag{3.11}$$

From (3.10) and (3.11), we get

$$A_n^{(\alpha)}(f';x)=\frac{2\alpha(1+cx)}{n}\sum_{k=1}^{[\sqrt{n}]}\overset{x}{\underset{x-\frac{x}{k}}{V}}f'_x+\frac{x}{\sqrt{n}}\overset{x}{\underset{x-\frac{x}{\sqrt{n}}}{V}}f'_x\tag{3.12}$$

We can write

$$B_n^{(\alpha)}(f';x) \leq \left| \int_x^{2x} \left(\int_x^t f'_x(u)du \right) d_t(1-\zeta_{n,c}^{(\alpha)}(x;t)) \right| + \left| \int_{2x}^{\infty} \left(\int_x^t f'_x(u)du \right) d_t M_{n,m,c}^{(\alpha)}(x,t) \right|.$$

From the second part of the Lemma 3.1, we get

$$M_{n,m,c}^{(\alpha)}(x,t) = d_t((1-\zeta_{n,c}^{(\alpha)}(x;t)) \quad for \;\; t > x.$$

Hence,

$$B_n^{(\alpha)}(f';x) = B_{n,1}^{(\alpha)}(f';x) + B_{n,2}^{(\alpha)}(f';x),$$

where

$$B_{n,1}^{(\alpha)}(f';x) = \left| \int_x^{2x} \left(\int_x^t f'_x(u)du \right) d_t(1-\zeta_{n,c}^{(\alpha)}(x;t)) \right|$$

and

$$B_{n,2}^{(\alpha)}(f';x) = \left| \int_{2x}^{\infty} \left(\int_x^t f'_x(u)du \right) d_t M_{n,m,c}^{(\alpha)}(x,t) \right|.$$

Using integration by parts, applying Lemma 3.1, $1-\zeta_{n,c}^{(\alpha)}(x;t) \leq 1$ and taking $t = x + \frac{x}{u}$ successively,

$$\begin{aligned}
B_{n,1}^{(\alpha)}(f';x) =& \left| \int_x^{2x} f'_x(u)du(1-\zeta_{n,c}^{(\alpha)}(x;2x)) - \int_x^{2x} f'_x(t)(1-\zeta_{n,c}^{(\alpha)}(x;t))dt \right| \\
\leq& \left| \int_x^{2x} (f'(u)-f'(x+))du \right| \left| 1-\zeta_{n,c}^{(\alpha)}(x;2x) \right| + \left| \int_x^{2x} f'_x(t)(1-\zeta_{n,c}^{(\alpha)}(x;t))dt \right| \\
\leq& \frac{2\alpha(1+cx)}{nx} |f(2x)-f(x)-xf(x+)| \\
&+ \frac{2\alpha x(1+cx)}{n} \int_{x+\frac{x}{\sqrt{n}}}^{2x} \frac{\overset{t}{\underset{x}{V}} f'_x}{(t-x)^2} dt + \int_x^{x+\frac{x}{\sqrt{n}}} \overset{t}{\underset{x}{V}} f'_x dt \\
\leq& \frac{2\alpha(1+cx)}{nx} |f(2x)-f(x)-xf(x+)| \\
&+ \frac{2\alpha x(1+cx)}{n} \sum_{k=1}^{[\sqrt{n}]} \overset{x+\frac{x}{k}}{\underset{x}{V}} f'_x + \frac{x}{\sqrt{n}} \overset{x+\frac{x}{\sqrt{n}}}{\underset{x}{V}} (f'_x). \qquad (3.13)
\end{aligned}$$

Using Remark 2.1 then, we have

$$\begin{aligned}
B_{n,2}^{(\alpha)}(f';x) =& \left| \int_{2x}^{\infty} \left(\int_{x}^{t} (f'(u) - f'(x+))du \right) M_{n,m,c}^{(\alpha)}(x,t)dt \right| \\
\leq & \int_{2x}^{\infty} |f(t) - f(x)| M_{n,m,c}^{(\alpha)}(x,t)dt + \int_{2x}^{\infty} |t-x| \, |f(x+)| \, M_{n,m,c}^{(\alpha)}(x,t)dt \\
\leq & \left| \int_{2x}^{\infty} f(t) M_{n,m,c}^{(\alpha)}(x,t)dt \right| + |f(x)| \left| \int_{2x}^{\infty} M_{n,m,c}^{(\alpha)}(x,t)dt \right| \\
& + |f(x+)| \left(\int_{2x}^{\infty} (e_1 - x)^2 M_{n,m,c}^{(\alpha)}(x,t)dt \right)^{\frac{1}{2}} \\
\leq & M \int_{2x}^{\infty} t^{\gamma} M_{n,m,c}^{(\alpha)}(x,t)dt + |f(x)| \left| \int_{2x}^{\infty} M_{n,m,c}^{(\alpha)}(x,t)dt \right| \\
& + \sqrt{\frac{2\alpha x(1+cx)}{n}} \, |f(x+)| \, . \qquad (3.14)
\end{aligned}$$

For $t \geq 2x$, we get $t \leq 2(t-x)$ and $x \leq t-x$, applying Holder's inequality, we have

$$\begin{aligned}
B_{n,2}^{(\alpha)}(f';x) \leq & M 2^{\gamma} \left(\int_{2x}^{\infty} (e_1 - x)^{2r} M_{n,m,c}^{(\alpha)}(x,t)dt \right)^{\frac{\gamma}{2r}} \\
& + \frac{2\alpha(1+cx)}{nx} \, |f(x)| + \sqrt{\frac{2\alpha x(1+cx)}{n}} \, |f(x+)| \\
= & M(\gamma, c, r, x) + \frac{2\alpha(1+cx)}{nx} \, |f(x)| + \sqrt{\frac{2\alpha x(1+cx)}{n}} \, |f(x+)| \, . \qquad (3.15)
\end{aligned}$$

From (3.13) and (3.15), we get

$$\begin{aligned}
B_{n}^{(\alpha)}(f';x) = & \frac{2\alpha(1+cx)}{nx} \, |f(2x) - f(x) - xf(x+)| \\
& + \frac{2\alpha x(1+cx)}{n} \sum_{k=1}^{\lceil \sqrt{n} \rceil} \overset{x+\frac{x}{k}}{\underset{x}{V}} f'_x + \frac{x}{\sqrt{n}} \overset{x+\frac{x}{\sqrt{n}}}{\underset{x}{V}} (f'_x) \\
& + M(\gamma, c, r, x) + \frac{2\alpha(1+cx)}{nx} \, |f(x)| + \sqrt{\frac{2\alpha x(1+cx)}{n}} \, |f(x+)| \, . \qquad (3.16)
\end{aligned}$$

From (3.9), (3.12) and (3.16), we get our desired result. □

References

[1] Deo N., *Faster rate of convergence on Srivastava-Gupta operators*, Appl. Math. Comput., **218(21)**(2012), 10486-10491.

[2] Ispir N. and Yuksel I., *On the Bezier variant of Srivastava-Gupta operators*, Appl. Math. E-Notes, **5**(2005), 129-137.

[3] Maheswari (Sharma) P., *On modified Srivastava-Gupta operators*, Filomat, **29(6)**(2015), 1173-1177.

[4] Neer T., Ispir N., and Agrawal P. N., *Bezier variant of modified Srivastava-Gupta operators*, Revista de la Unio In Matema Itica Argentina, **58(2)**(2017), 199-214.
[5] Srivastava H. M. and Gupta V., *A Certain family of summation-integral type operators*, Math. Comput. Modelling, **37**(2003), 1307-1315.
[6] Srivastava H. M. and Gupta V., *A General family of the Srivastava-Gupta operators preserving linear functions*, European J. Pure Appl. maths, **11(3)**(2018).
[7] Verma D. K. and Agrawal P. N., *Convergence in simultaneous approximation for Srivastava-Gupta operators*, Math. Sci., Springer, **6**(2012).
[8] Yadav R., *Approximation by modified Srivastava-Gupta operators*, Appl. Math. Comput., **226**(2014), 61-66.

Delhi Technological University
Formerly Delhi College of Engineering
Department of Applied Mathematics
Bawana Road, 110042 Delhi, India
E-mail address: rampratapiitr@gmail.com
E-mail address: naokantdeo@dce.ac.in

2018 IEEE International Conference on Software Quality, Reliability and Security Companion

Blockchain and Scalability

Mrs. Anamika Chauhan
Department of Information Technology
Delhi Technological University
New Delhi, India
anamika@dce.ac.in

Om Prakash Malviya
Department of Information Technology
Delhi Technological University
New Delhi, India
omprakashmlv9@gmail.com

Madhav Verma
Department of Information Technology
Delhi Technological University
New Delhi, India
madhavverma48@gmail.com

Tejinder Singh Mor
Department of Information Technology
Delhi Technological University
New Delhi, India
tejindersinghmor@gmail.com

***Abstract* — Bitcoin has shown great utility around the world with the drastic increase in its value and global consensus method of proof-of-work (POW). Over the years after the revolution in the digital transaction space, we are looking at major scalability issue with old POW consensus method and bitcoin peak limit of processing only 7 transactions per second.With more companies trying to adopt blockchain to modify their existing systems, blockchain working on old consensus methods and with scalability issues can't deliver the optimal solution. Specifically, with new trends like smart contracts and DAPPs, much better performance is needed to support any actual business applications. Such requirements are pushing the new platforms away from old methods of consensus and adoption of off-chain solutions. In this paper, we discuss various scalability issues with the Bitcoin and Ethereum blockchain and recent proposals like the lighting protocol, sharding, super quadratic sharding, DPoS to solve these issues. We also draw the comparison between these proposals on their ability to overcome scalability limits and highlighting major problems in these approaches. In the end, we propose our solution to suffice the scalability issue and conclude with the fact that with better scalability, blockchain has the potential to outrageously support varied domains of the industry.**

Keywords – Blockchain, Bitcoin, Ethereum, Lightning Protocol, Sharding, DPoS, Inspector Node.

I. Introduction

Blockchain has shown its tremendous ability in disrupting how digital transactions are carried out in a more secure and transparent manner. But the question still stands - does it have the ability to serve other real-world applications? Such confusion is because of the hindrance caused by its scalability issues.

Scalability issues arise due to limited block size and current consensus method where every node in the network sequentially validate the transaction before it being published in the blockchain. This problem intensifies with an increase in the number of transactions requiring more nodes to support the network but simultaneously increasing the number of steps for the transaction to travel and reach full consensus with every node. We can also see a proportional relationship between fall in scalability of the blockchain and increase in the network size. This flaw is the major setback that is stopping the mass adoption of blockchain for real-world applications.

II. What is Blockchain ?

The concept of blockchain recently came into limelight when the hype around Bitcoin and other cryptocurrencies gained momentum. Blockchain is the underlying principle behind cryptocurrencies. At the centre of blockchain, is a distributed ledger that records all the transactions that take place in the network. A blockchain network is usually described as decentralized because it is replicated across many network participants, each of which collaborate in its maintenance. In addition to being decentralized and collaborative, the information recorded on the blockchain is also immutable which guarantees that once a transaction has been added to the ledger it cannot be modified. This property of immutability assures the participants that their information is safe and secure.

At the very beginning of a blockchain is the 'genesis block'. Each block has certain attributes associated with it like-timestamp, nonce, version etc. The primary attribute among all of them is the 'hash' of the block which is generated by the merkle root of the current block and the hash of the previous block in the chain. It is this 'hash' which imparts two major properties to blockchain:

1. Linking of a block to its next block in the chain.
2. Any change to the data present in the block, would be immediately reflected in the hash of the block and all the blocks succeeding it.

The major advantage of a blockchain is that it doesn't depend on a central entity like some traditional banking system. Cryptocurrency investors are heavily encouraged by this property of the blockchain because instead of a central authority, it is the users and the developers joined to the network, who take important decisions.A big example of this is the inability to reach the 80% consensus on an upgrade in Bitcoin which lead to a hard fork in Bitcoin few months ago.

III. What is Bitcoin

Bitcoin is the first digital currency based on the blockchain technology. The concept of bitcoin and blockchain came into existence through a whitepaper named Bitcoin: a

978-1-5386-7839-8/18/$31.00 ©2018 IEEE
DOI 10.1109/QRS-C.2018.00034

peer to peer electronic cash system in the year 2008 and was released as an open source software in the year 2009 [1].

The main characteristic of Bitcoin is that it works in a decentralised manner. No single individual or organisation controls the Bitcoin network. The whole network is maintained by a group of dedicated computer or servers spread across the world which we call 'nodes'. It is these nodes which help in the verification and validation of all the transactions taking place in the Bitcoin network. This property of decentralization has attracted many individuals to adopt this new technology , who are not in the favour of a central authority controlling all their funds.

Another property of the bitcoin network is that each node or individual joined to it is represented by his/her public key instead of his real identity. While the senders of the traditional electronic payments are generally identified by some process of verification, the users of Bitcoin operate in an anonymous manner.

Bitcoin uses Elliptical Curve Digital Signature Algorithm to sign transactions [2]. This signing of transactions ensures that only the rightful owners have access to their assets and no one else. This signature is essential for maintaining the authenticity and integrity of the bitcoin network.

Unlike fiat currencies, Bitcoin has a limited supply that is tightly controlled by an underlying algorithm. In total there will be 21 million Bitcoins that will ever be produced. The reward for currently mining a block in the Bitcoin network is 12.5 coins. This reward is reduced in a proportional way every 4 years. This hard cap on the total supply makes Bitcoin a more tempting asset. In theory, if demand grows and the supply remains the same, the value will automatically increase.

IV. WHAT IS ETHEREUM ?

Ethereum has scored itself the second spot in the hierarchy of cryptocurrencies. The Ethereum project was proposed by Vitalik Buterin in the year 2013 and launched completely in the year 2015, after raising 19 million dollars in its presale. Ethereum is expected to surpass Bitcoin in the long run due to a major technological differences and applications that it can offer.

Ethereum is a distributed public blockchain similar to Bitcoin but the most important distinction between the two is in terms of its desire and potential [3]. Where Bitcoin offers only a single application of the blockchain technology that is peer to peer electronic cash transfer, Ethereum on the other hand opens up a new dimension of running decentralised applications on the blockchain network using certain programming code called "smart contracts".

A smart contract is a piece of code written in a certain programming language (Solidity in case of Ethereum) that can facilitate the exchange of money or anything of value. When smart contracts are deployed, they become independent entities that can execute certain commands when a series of conditions are met [4].

In the Ethereum network when a node mines a block, it is rewarded in the form of a crypto-token called Ether. Ether is the currency used to deploy smart contracts and pay the transaction fees associated with each transactions. Apart from being used as a token, Ether can also be used for trading and buying other cryptocurrencies.

The vision of Ethereum was to provide developers a platform to build decentralised applications. It has an aim to become the second Internet which runs in a decentralized manner and where the major decisions are taken by the users and developers that are joined to the network instead of a central authority.

Due to this reason, the DAO project was launched in the year 2016. The DAO (Decentralized Autonomous Organization) was the first of its kind - a fully decentralized organization with no single leader. It was made using a collection of smart contracts written on the Ethereum blockchain. It was owned by everyone who purchased tokens, but in this case tokens acted as contributors that gave the token holders voting rights on major decisions instead of giving them equity shares and ownership in the organisation.

V. SCALABILITY ISSUES ASSOCIATED WITH BITCOIN AND ETHEREUM

With the increasing popularity and adoption of cryptocurrencies like Bitcoin and Ethereum, they are compelled to think about a very basic problem in the initial design i.e. the lack of scalability. As cryptocurrencies are becoming more mainstream day by day, the number of transactions are also increasing in an exponential manner. Let's have a look at the increase in the number of transactions in Bitcoin and Ethereum in the past few years.

The below figures indicate that cryptocurrencies are being adopted at a very fast rate but as they have gotten more popular, a series of issues have come up regarding them and the major issue among it is the problem of scalability. Actually, the main problem lies in the basic principle on which the Bitcoin principle is based that is the mining nodes have to verify each and every transaction that occurs in the network [5] .

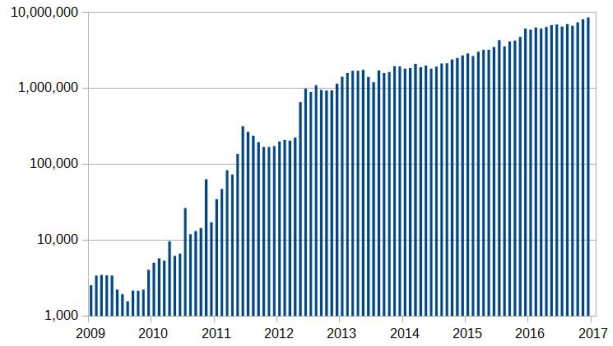


Figure 1 : A graph denoting the increase in bitcoin transactions over the last 10 years.
Source : blockgeeks.com

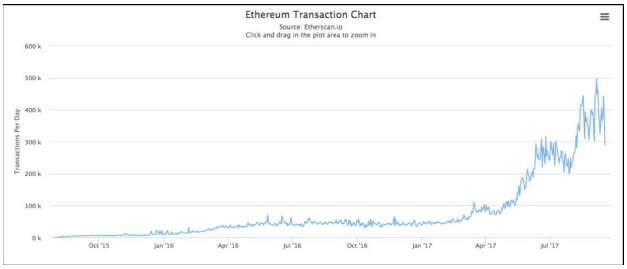


Figure 2 : A graph denoting the increase in ethereum transactions over the last 10 years.
Source : blockgeeks.com

Eventually, it is the miners who become the bottleneck in the transaction process. The process of verification was achievable when Bitcoin started in 2008 but as more and more people joined the network the number of transactions every second changed in a very drastic manner.

In the previous year itself there were at least 130,000 transactions occurring every day. Since this is a huge amount, it has become very difficult for the mining nodes to verify this lot. As a result of this, the waiting time for a transaction has increased upto 29 minutes. This means that more often than not, people would have to wait for a new block to be mined in order for their transaction to be verified.

Unfortunately, Ethereum isn't doing any better in this regard as well. Theoretically, Ethereum is expected to verify atleast 1000 transaction per second but due to the gas limit imposed on each block it is only able to process around 20. This number is very small in front of electronic payment giants like Paypal and Visa, that are able to verify around 193 and 1670 transactions per second respectively.
Supporters of cryptocurrencies have argued to switch to other Altcoins but have always feared this step due to two main reasons:

1. No coin is widely accepted and trusted as Bitcoin and Ethereum
2. If any other cryptocurrency becomes as popular as Bitcoin and Ethereum it will probably face same problem.

Due to these problems, the developers of Bitcoin are proposing a new Lightning Protocol to speed up the verification process and similarly the makers of Ethereum have proposed the method of sharding to overcome this situation.

VI. BITCOIN LIGHTNING PROTOCOL

A. Opening of Channel

Let's say there are two parties who want to create a bi-directional payment channel between them for multiple transactions during a fixed time period. The first thing they need to do is to fund the payment channel where the funding should be equal to the amount of trades they are going to do with each other. Both the parties need to send their funds for the payment channel to a specific multisignature address. Once the fund is sent, it is locked up in multisig address where signatures of both parties will be needed to unlock or spend any fund/BTC [6].

Both the parties can create transactions from their regular bitcoin address and it will need signatures from both sides to become a valid transaction. There is also a time period for each transaction which if not fulfilled, within a particular time period, both the parties will get their refund after that (eg. 30 days from when the address is created)

Now, if one party wants to back out in between the transaction, it needs to get the incomplete transaction signed by the counterparty. But the asymmetry here is that his counterparty will get the refund after 1000 blocks (a week). This prevents unnecessary cancellations and cheating.

B. Exchange

Once the funds are locked, parties can perform exchange of amount. This means that they can transact with each other, and the fresh transaction after the funding transaction, is achieved by exchange of fraud-protection proof, with signing of transaction by each party. So, if a party tries to cheat by broadcasting false transaction, counter-party can show the fraud to the miners by showing them previous transactions and it will cause the guilty party to lose all of its funds. Though, counterparty will have the time of one week to notify guilty party. Even if anybody else recognizes the fraud or the false transaction, he will get a small bounty from that money. This practice discourages cheating and fraud.

C. *Closing of Channel*

There can be two ways to close the channel. First, as discussed above, will be if any of the party chooses to opt out of the transaction, and is ready to face 1000 blocks delay for the refund. Second will be when all the transactions are done and channel reaches end of the duration.
Once the channel is closed, regardless of the number of transactions between both the parties, only two transaction will be recorded in the blockchain, opening and closing transaction.

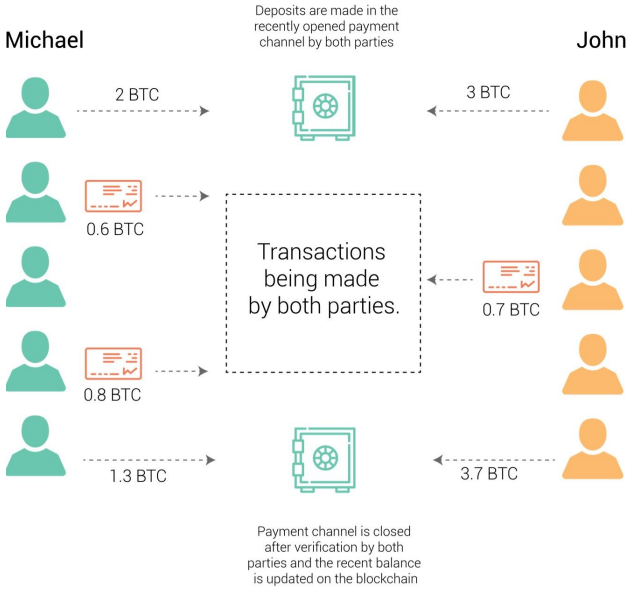


Figure 3 : A figure showing an off channel exchange between two parties.

D. *Multiple Channels Connections*

Now let's see how lightning network is going to help get the transactions done among multiple network channels. Let's say if there are 3 parties and there is already a channel established between party 1 and party 2, then there is a channel between party 2 and party 3. Now, if party 1 wants to transact with party 3 then he doesn't need to create another channel, because they can transact with each other by routing payment through already existing networks. Here, for routing payments, party 1 is given a secret key by party 3. As there is already a connection established between 2 & 3, Party 1 lets party 2 pay on its behalf to party 3 in exchange of a secret key. Now, Party 2 shows this secret key to party 1 and if both of their secret keys match, it would mean that party 2 has paid party 3 and is not lying.Such a system of multiple network channels can be extended to any number of participant channels.

VII. ETHEREUM SHARDING

Ethereum developers proposed another method to scale the blockchain by dividing them into shards where each shard has its own history of transactions and states. Certain nodes will verify only certain shards, thus the load on network will be reduced. This would allow to get transactions processed across a bunch of partitions 'Shards' rather than the mainchain handling all the transactions itself [7].

Elements of a Shard:

Collators : Nodes in a certain shard will be called Collators, which will be creating Collations. Collation is a specific structure containing important data like transaction and state history about certain shard. Each Collation will have a Collation header which will contain the following information:

1. Which shard the collation will respond to.
2. Current state of shard (before all the transactions are processed).
3. State of the shard after all the transactions are processed.
4. Digital signatures from at least ⅔'s shards confirming that the Shard is legit.

Supernodes : Supernodes will be the nodes taking all collations across all the shards and putting them in a single block which will be later added in Ethereum blockchain. This new kind of Block will be valid if :

1. All transactions are valid in all of the collations.
2. Collations have the same state as their current state before processing transactions.
3. Collations have the same state as specified in collation header, after processing transactions.
4. Collations must be digitally signed by ⅔'s of collators.

Now let's see what happens when a transaction happens across shards.

Receipts : The idea of receipts is what makes the cross shards transactions easy. Let's say there is party 1 in shard 1 and party 2 in shard 2, then to process a transaction between party 1 and party 2 (party 1 wants to pay 'x' ether to party 2) first the transaction is sent to shard 1 which reflects changes in party 1's balance, and system then generates a receipt for the transaction, which is gonna be stored in merkle root because they can be easily verified. Then a transaction is sent to shard 2 with receipt data as well which checks whether receipt has been spent or not.
It then reflects changes in party 2's balance and also marks the receipt as spent. Now, shard 2 can create new receipt for subsequent transaction.

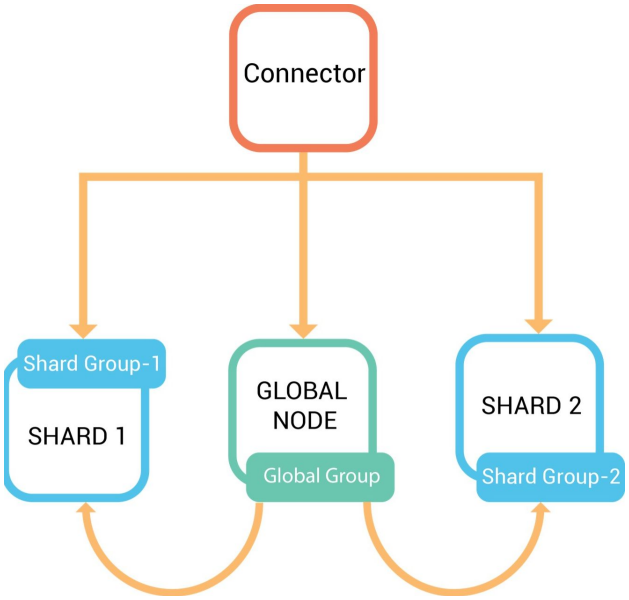


Figure 4 : Sharding Structure

Super Quadratic Sharding

In order to further scale the Ethereum network after sharding, there comes the concept of super quadratic sharding, which means dividing network into shards of shards. Such a complex system is too complex to imagine at this point of time, but if in future sharding becomes successful, then super quadratic sharding might become a useful technique to scale the network which will provide the network massive potential that can be scaled up till any level.

VIII. DPOS SOLUTION BY EOS

DPoS is a solution provided by EOS to scale blockchain for 100,000 transactions per second. Let's see how this solution is going to help the blockchain meeting the demand of ever rising crypto economy.

In DPoS systems, token holders select the block producers by continuous voting procedure. Anyone can become a block producer on the basis of the votes that he gets, and then he can produce the Block in proportion to his vote collection relative to other producers. In DPoS system, Blocks are produced in the rounds of 21. At the beginning of each round top 20 unique producers are selected automatically by total approval and the last producer is chosen on the basis of its proportional vote count relative to other producers [8].

In this system, a new block is produced exactly every 3 seconds by exactly one producer at a given time. Such a system has 100% block producer participation so transaction will be confirmed with 99.9% certainty in average 1.5 second after the time of broadcast.

Problem:

A new block in every 3 seconds is an exceptional performance measure for a blockchain which will get transaction confirmed much faster, but this system lacks something which is known as 'fraud proofs'.

Let's see how this affects the system and other problems as well:

1. DPoS removes merkle proofs that prevent regular users to audit execution of any part of the system. If regular users want to audit, they will have to run a full node which is not feasible at all.
2. Nodes producers are fired or hired on the basis of votes they collect. Voting power depends upon stake of user in EOS tokens. More tokens one holds more will be his voting power which shows a slight way towards centralization just like the concept of having more hashing power combined meaning more control over the chain.
3. In every 3 seconds, exactly one full node will produce a block which defines the way for a scalable blockchain. But, for a single full node to produce one block would mean much higher computational energy, which only large enterprises can afford. So, its scalability depends on much higher computational power like every other scalability solution.

IX. WHICH IS MOST OPTIMAL SOLUTION ?

Well, when we talk about scaling Blockchain there can be two ways to scale it:

1. Offchain scaling
2. Onchain scaling

Let's see which solution holds the basic functionalities of Blockchain.

Problems with Off chain scaling (Lightning network):

1. For a lightning network, every time a party wants to pay another, it will have to open a channel between both the parties. Where opening and closing are the transaction which will be recorded on the main chain that would mean both transactions are going to take traditional mainchain transaction time. So it won't be a real time transfer of value because of the time taken by one party to open a channel.
2. In a lightning network, duration for a channel to last is fixed so there will be a recurring problem of opening and closing transaction time period between

the two parties who want to transact even after closing their channel in future.
3. In order to open a channel on lightning network there must be sufficient funds put by both parties to transact with each other.
4. On Bitcoin network, current transaction fees is too high around 30$ per transaction. So, in such a system opening and closing transaction will cost too much if the transaction is of just 10$.
5. Fifth, and the most important, factor that worries is all of these transactions are being verified and validated off mainchain, which violates the very basic rule of blockchain where every transaction is verified by some predefined set of rules, basically where for each transaction participating full nodes compete with each other to verify and validate them.

Problems with current model of Sharding

1. The main problem that comes with sharding is 'single-shard takeover attack'. Where if an attacker takes over majority of collators in a single shard, he could manipulate them to create a malicious shard and submit malicious transaction as well.
2. Well, solution proposed for above mentioned problem is to assign each shard validator nodes or collators by random sampling. Each shard will be assigned a bunch of collators but the nodes that will be verifying transactions will be selected by random sampling from that set of collators.
3. Then there comes another problem that after each reshuffling of collators, each node will have to download and install a new shard, which is a problem that we can't' ignore because it will affect the speed of transaction as well.

X. OUR SOLUTION - INSPECTOR NODE

Well, we can't deny that lightning network is a powerful solution to scale blockchain, like a second layer of Blockchain which routes payment across various payment channel on the network. But, it doesn't carry core functionalities of Blockchain, as it is a offchain solution. So operations of a blockchain network are not applied at this layer.

Among all of other scaling solutions, Sharding seems the most effective solution. As it holds core functionalities of Blockchain with it. Each shard works like a seperate blockchain network, which operates completely as Satoshi Nakamoto visioned a blockchain to work.

Let's see how we can remove the problems that currently Sharding model is facing, and how can we make the solution more effective and secure.

Inspector Node:

We need to ensure that only a fixed no. of Collators should validate the transactions for a shard, without reshuffling or random sampling. That would mean each shard will be assigned a fixed no. of nodes for validation and verification of transactions over shard. Then there comes the problem,

If an attacker takes over majority of the shards, He can submit malicious transaction in shard, which is gonna spoil the main property of a blockchain which is 'Highly secured'.

Here we propose the concept of 'Inspector nodes', which will contribute only to investigate and eliminate malicious activity going on in a shard.

Functions of Inspector node:

1. This node will keep checking whether a majority is being developed among collators. If it sees that an attacker is trying to take over some shards (if it has already acquired a minimum percentage of hashing power from the nodes, which will be different for each shard), it will prevent the attacker from doing so and would reshuffle the nodes assigned to a shard instantly. In such a case, only when an attack is likely to happen, nodes will be reshuffled by random sampling.
2. There will be a fixed number of inspector nodes assigned to each shard, which will keep an eye on every broadcasted transaction in the network to see if there is anything suspicious about that transaction or not.
3. To prevent majority from being formed inside a network, we need to keep the competition tight among validating nodes. This is where we propose a unique incentive model for Inspector nodes.

Incentive Model for Inspector Nodes:

1. Every Inspector node, who finds the malicious activity first inside shard, will be rewarded with all the funds involved in the malicious transaction, and that fund will be cut from suspect node's account (which will be cut in a ratio if there is more than one node).
2. Apart from that, Inspector nodes will be paid inspection fees as well if there is not any malicious activity happening in the network and that inspection fees will be cut from block reward of every node in a specific ratio (How many Ethereum a node has mined, a percentage of that reward will be paid to inspector nodes) as network maintenance fee, which

will be minimal as no. of Inspector node will be much less than validating nodes.

3. If any other validating node finds malicious activity and submit it, then inspector nodes will reward that node with all the funds involved in that transaction, it will keep competition in place among nodes.
4. This incentive model will prevent the attackers from practicing malicious operations as it can cost them their funds.

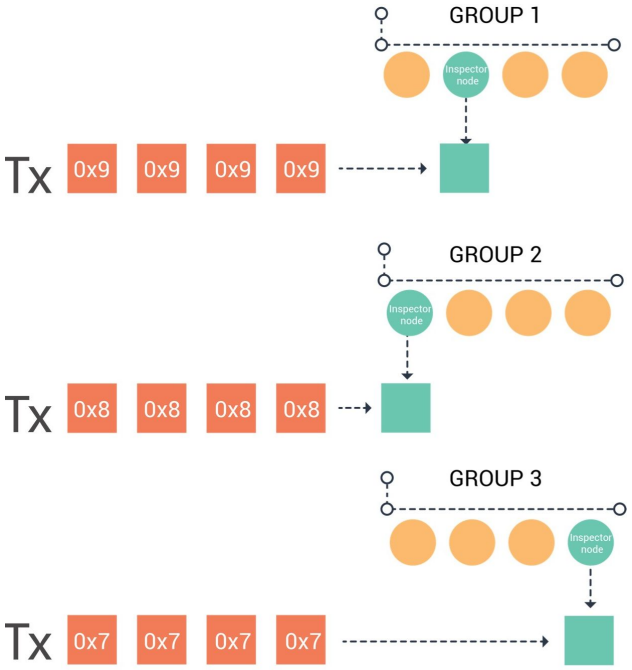


Figure 5 : Inspector nodes in action

XI. CONCLUSION

The only hurdle in Blockchain technology's way to scale upto masses is its scalability issue. There are various solutions floating in the technology space but each one comes with some problems associated with it. After analysing several possibilities of faults in all solutions, we have extracted that Sharding is the best possible method for scaling the blockchain as it includes core values and features of Blockchain. Having included our newly introduced Inspector node model in the current Sharding model, we can make this solution even better and faultless. The proposed solution contains three core functionalities of Blockchain : Decentralization, Security and Scalability. With having three main pillars of a solid and disruptive invention together, we can surely create the biggest disruption in industries, after Internet. Blockchain is still in its early stages, and we hope within next 5 years, it will transform a lot of things where transformation will be driven by scalability.

REFERENCES

[1] S. Nakamoto, "A Peer-to-Peer Electronic Cash System", (2008).
[2] "Elliptic Curve Digital Signature Algorithm," *Elliptic Curve Digital Signature Algorithm - Bitcoin Wiki*. [Online]. Available: https://en.bitcoin.it/wiki/Elliptic_Curve_Digital_Signature_Algorithm.
[3] "What is Ethereum? - CoinDesk Guides," *CoinDesk*, 31-Mar-2017. [Online] Available: https://www.coindesk.com/information/what-is-ethereum/.
[4] "What are smart contracts in Ethereum," *Smart Contracts Ethereum* [Online] Available: https://blockgeeks.com/guides/smart-contracts/.
[5] "The Raiden Network a Beginner's Guide.". [Online]. Available: https://blog.springrole.com/lightning-protocol-the-raiden-network-a-beginners-guide-c9d7bc702748
[6] "What is the bitcoin lightning protocol.". [Online]. Available: https://99bitcoins.com/what-is-the-bitcoin-lightning-network-a-beginners-explanation/
[7] "How to Scale blockchain using Ethereum Sharding.". [Online]. Available: https://medium.com/@rauljordan/how-to-scale-ethereum-sharding-explained-ba2e283b7fce
[8] "How EOS can solve the blockchain scaling problems". [Online]. Available : https://itsblockchain.com/eos-scaling/

J Grid Computing
https://doi.org/10.1007/s10723-018-9457-z

Community Trolling: An Active Learning Approach for Topic Based Community Detection in Big Data

Preeti Gupta · Rajni Jindal · Arun Sharma

Received: 25 August 2017 / Accepted: 1 August 2018
© Springer Nature B.V. 2018

Abstract Community detection plays an important role in creation and transfer of information. Active learning has been employed recently to improve the performance of community detection techniques. Active learning provides a semi-automatic approach in a selective sampling of data. Based on this, a community trolling approach for topic based community detection in big data is proposed. Community trolling selectively samples the data relevant to the current context from polluted big data using active learning. Fine-tuned data is then used to study community and its sub-communities. Community trolling as a precursor to community detection leads to a reduction of the huge unreliable dataset into a reliable dataset and results in the better prediction of community elements such as important topics and important entities. Finally, the effectiveness of approach was evaluated by implementing it on a real world Tumbler dataset. The results illustrate that community trolling provides a richer dataset resulting in more appropriate communities.

P. Gupta (✉) · A. Sharma
Department of IT, Indira Gandhi Delhi Technical University for Women (IGDTUW), Kashmere Gate, Delhi, 110006, India
e-mail: preeti.cool80@gmail.com

R. Jindal
Department of CSE, Delhi Technological University(DTU), Delhi, India

Keywords Active learning · Unlabeled big data · Community trolling · Community detection

1 Introduction

Social media provides us with a rich and easily available source of information due to which its usage is increasing day by day. It consists of entities with varied profiles which are connected to others for multiple reasons. Social network of these entities represents communities. Communities are the group of users who have similar interests and interact with the members of the community more often than members outside the community. Communities also play an important role in creation and transfer of information. Community detection is used as a tool to gather interesting links, entities and patterns from communities under study. Social media has been widely utilized to study community detection in applications such as recommendation, spam detection, terrorist tracking and fraud detection. There has been extensive research done in the field of community detection.

Social Media Proliferation is one of the major source of digital transformation which needs to be handled in scalable and distributed fashion. Big data analytics have been applied in various domains and fields to achieve scalability. Big data processing provides distributing parallel processing. The massive

Published online: 10 August 2018

amount of social media data accounts for one of the major sources of big data and community detection techniques could be easily adapted to big data context by converting these approaches or techniques into embarrassingly parallel problems [19]. However, the data should be provided in such a way that I/O and network cost is minimized. The various measures adopted by the researchers to achieve this objective are sampling, indexing, intelligent partitioning, special data structure, in-memory computation and asynchronous processing [19]. These measures reduce the number of MapReduce(MR) jobs, resulting in data shuffling reduction and better speedup [19]. Big data contains a huge amount of data from varied sources which also contain a lot of noise. The quality of big data needs to be improved for accurate and good results [26].

The focus of our current research is on the topic based communities which are based on the content of network. However, big social media data is polluted in nature consisting of a lot of noisy data. It is difficult to read through all the text documents present online for extracting relevant datasets thus necessitating the need to explore semi-automatic data filtering and data classification techniques [11]. This makes active learning an important field in the area of big data analytics.

Active learning provides selective sampling of data which leads to substantial reduction in size leading to reduce I/O and network cost. It helps us in selecting the most informative samples from the pool of unlabeled data with least cost. It also provides quality enhancement by adjusting the data to the underlying domain. This has motivated us to propose a community trolling approach using active learning for topical community detection in big data. In the proposed approach, active learning is used to select the relevant samples which are most probabilistic to be part of the current context. We have termed the active learning phase as community trolling which acts as a precursor to community detection. Community trolling would provide a broader community of interest and also leads to reduction of the huge unreliable dataset into the reliable dataset. The richer dataset provided by community trolling provides more appropriate communities and results in the better prediction of community elements such as important topics and important entities. It enables to handle the volume, velocity and veracity of big data. Community trolling is also the key difference which differentiates this work from other related work proposed. Community trolled is further explored by the topic based community to better understand the dynamics of the community.

The fundamental principle of a big data paradigm is to move computation to data rather than to bring data to computation [6]. Apache Spark [41, 44] is one of such big data computational framework which is widely adopted. It is an enhanced form of MapReduce, more suitable for iterative tasks due to its in-memory and asynchronous computation [6]. Apache Spark helps in reduction of disk I/O operations in comparison with MapReduce Framework making it better suited for tasks such as machine learning [29, 41]. Apache Spark provides immutable data structure such as a Resilient Distributed Dataset (RDD) for efficient parallel processing. It also provides special data structures such as Broadcast variables for efficient data handling over the network. Motivated by all these features, the proposed approach is implemented in Apache Spark.The main contributions of our paper are as follows:

1. To the best of our knowledge, this is the first work which has applied active learning to select rich samples in the context of topic based community detection.
2. The performance of active learning is also enhanced by incorporating domain knowledge in word2vec model which is used for pre-processing of data.
3. Most of the existing solutions are based on centralized approach; however proposed approach is implemented on distributed framework making it easily scalable in big data paradigm.
4. The proposed approach is implemented on Apache Spark Framework which is an in-memory based distributed framework thereby increasing the performance from traditional machine learning algorithms

The following is the outline of this paper. Section 2 presents the literature review of our work. Section 3 presents a detailed description of approach followed by its implementation details and analysis in Section 4. Section 5 discusses the importance of our approach. Finally, Section 6 draws out conclusions and suggests some future work.

2 Related Work

Community detection plays an important role in studying various domains such as social network analysis. There have been a number of state of the art research proposed for community detection [14, 23, 33, 42, 43] which has discussed and compared various community detection algorithms. Community detection algorithms can be classified into two main approaches namely topology based and topic based [1, 12]. Topological based approach is based on the structural property of community only and does not consider the content. Community detection just on the structural properties provides inconsistent results due to sparsity and noise present in the network and are not of current interest. Topic based community helps in capturing the context of interactions among the members generating better results.

There has been a lot of work done in the area of topic based community detection. Latent Dirichlet Allocation (LDA) [9] is the most commonly used technique for topic based community detection. LDA considers documents corpus as a representation of latent topics where each topic contains related words with different probabilities. LDA is a probabilistic unsupervised model which generates topics distribution hidden in training corpus. The model generated by LDA is then used to map the probability distribution of topics for each document. The number of topics generated by LDA corresponds to a number of topic communities which are then used to model the behavior of entities [47].

LDA variants which extend the base model by utilizing other information such as document title, links and authors have also been proposed in the literature for studying the latent distribution in topic based communities. Author-Topic(AT) model [34] uses authorship as an additional latent information to extend LDA. In AT model, each author is mapped to topics distribution and topics are mapped to words distribution providing inference over author and documents [39]. Similarly, Author-Recipient-Topic (ART) model [27, 28] is an extension of AT model which uses sender (author) and recipient as an additional latent information. The topic distribution inferred from ART models is based on interaction between entities. Community-Author-Recipient-Topic (CART) model [32] is an extension of ART model where distribution is the joint probability of community, author(sender), recipients, topics and words. In CART model, author and the sender belong to a latent community. TTR-LDA model [24] is another variant of LDA which uses tagger, tags and resource within communities such as web page as the latent information. BlockLDA [7], the another variant generates a joint model based on entity links and text/topics.

These techniques may be adapted to big data by converting them to embarrassingly parallel problems [19]. However, they all are based on unsupervised techniques which would produce messy results in the case of big data. A classification function needs labeled training data. Labeling of data can be performed in a number of ways as shown in Fig. 1.

Keeping up with the workload of labeling data is a challenge due to a large amount of data available in the big data era. This cannot be accomplished by manual analysis of few domain experts. Services such as Amazon Mechanical Trunk [10] have also been employed for manual crowdfunding and sourcing the task of annotation. However, an automated classification method in the context of big data is most suitable and desirable. Earlier approaches for selection of samples were based on keyword or rule based approach [25] which are difficult to frame in big data era. Some authors also used extra features such as smileys or emojis present in twitter data for classification [17]. Clustering or unsupervised techniques such as k-means [21] can be used for classifying where clusters correspond to classes but they result in messy output in case of a large dataset. Other techniques employed

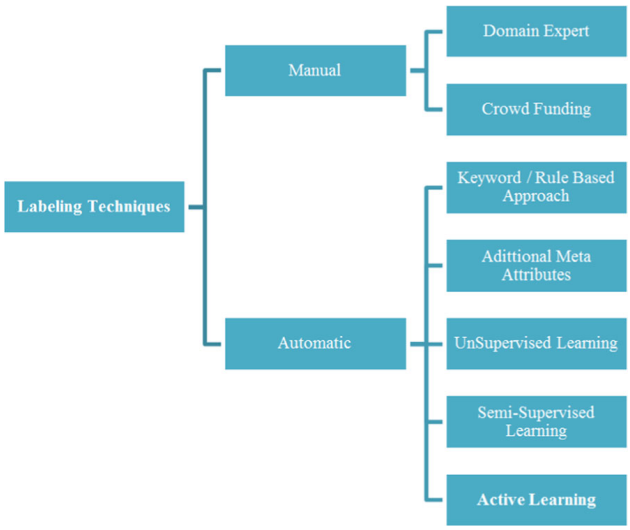


Fig. 1 Labeling Techniques

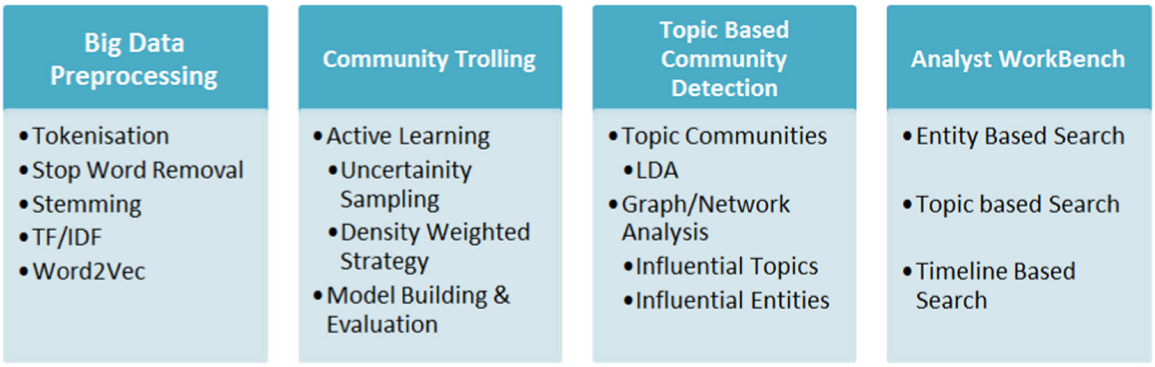


Fig. 2 Community Trolling Approach

for labeling include transfer learning [4] where knowledge from other domain is utilized. It requires labeled dataset of other domain which may also be difficult to obtain. Semi-supervised [45] and active learning [37] are the two main techniques which are used where the amount of labeled data is very less and the amount of unlabeled data is very high. Semi-supervised techniques such as co-training and self-learning make the model learn itself from the unlabeled latent variables. Active learning, on the other hand, minimizes the labeling cost by selecting only a few informative samples for labeling. It requires human annotation of few informative samples making it more apt for classification. Motivated by this, active learning for extracting relevant data out of big data was selected.

Active learning has been a widely studied area as it imposes very little labeling burden [3, 15, 36, 37]. Active learning selects the most informative samples for labeling. The informativeness of sample is directly proportional to the uncertainty of samples. High uncertainty implies its high value as the next candidate for labeling. High uncertainty also implies that the model has the least knowledge about it and adding it would increase the quality of the model.

Active learning has been adopted in the domain of community detection [16, 20, 22, 31]. Active learning in community detection helped in the selection of parameters or constraints for clustering, node selection or link selection. These techniques employ active learning for finding the most informative nodes near to the community boundaries and were applied in topological community detection.

Though active learning has also been adopted for text classification, none of the topic based community detection techniques have employed active learning. Moreover, all these techniques were not adapted to big data. This has motivated us to propose a community trolling approach using active learning for topic based community detection in big data for getting more coherent communities. The closest work to our research is of [38], which uses active learning to reduce the size of big data and minimize the classification error. In our work, we have also used the word2vec model for data preprocessing to

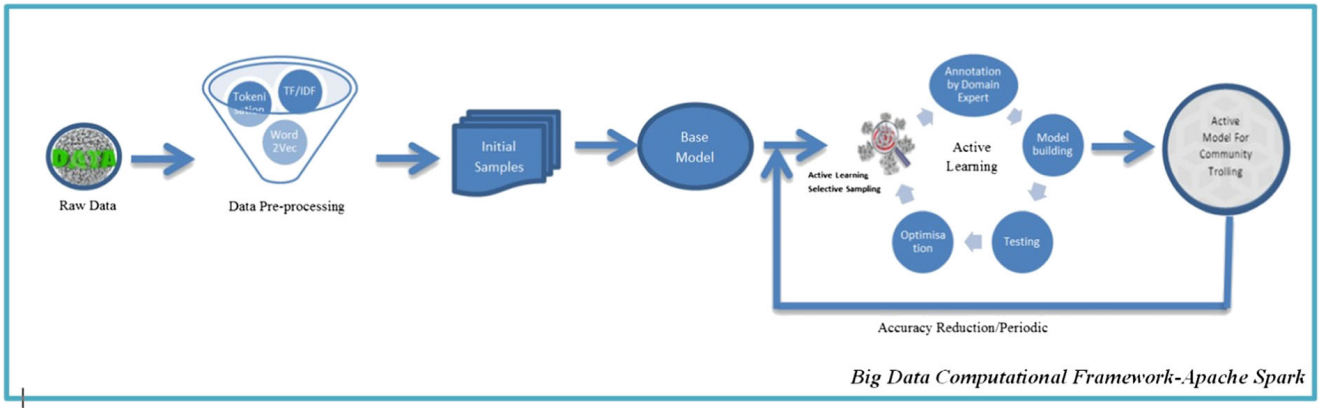


Fig. 3 Active Learning Process



Fig. 4 Data and Analysis Flow

incorporate domain knowledge which also results in better performance of active learning model.

3 Problem Statement and Design Methodology

Big data is characterized by various V's such as Velocity, Volume, Variety, Veracity, Value, Variability and Visualization [30]. However,the high volume of data is polluted in nature [41]. In order to better understand the community and its dynamics inside big data, a community trolling approach is proposed which first selects the data relevant to the current context from big data. Fine-tuned data obtained from community trolling is then used to study community and its sub-communities using topic based community detection and social network analysis. The overall design methodology of our approach is shown in Fig. 2 and is further explained below.

3.1 Big Data Pre-Processing

The pre-processing step performs the necessary cleaning and tokenization of data collected. The data considered in the current research is only textual in nature. All the links, images and videos are removed initially. The textual data is classified into distinct English Language documents or posts. Languages other than English are not considered in our approach due to lack of their understanding. The data may also contain words in which an individual character may be repeated many times such as 'loveeee' or 'warrrr'. These words are converted to their standard form i.e. 'love' or 'war'. The data is then tokenized into words followed by removal of stop words like 'and', 'the', 'or' and special characters.

After tokenization and stop word removal, the data is converted into vector format for machine learning. TF-IDF and word2vec are used for vector transformation. TF-IDF [35] is the commonly used measure and represents the importance of a term to a document in the dataset. TF-IDF is based on the frequency count of the term. Furthermore, word2vec [18] which is a distributed and deep learning representation of training corpus is also used for vectorization. Word2Vec is used to generate word vectors of fixed length from a training corpus. It provides semantically related words and is based on cosine distance rather than term frequency.

3.2 Community Trolling

Community trolling is basically a classification function which is employed for fine tuning of the data to the current context. Mathematically, this can be defined as, given a big dataset X, find Y which is a subset of X i.e $Y \square X$ such that Y contains data points relevant to the current context. This also results in data size reduction and data points related to a broader community of interest. Community trolling is thus defined as $f : X \rightarrow Y$ where f is a function which classifies the data point to be relevant for study or not. Community trolling helps in handling volume, velocity, veracity and value of big data by fine tuning polluted big data to the current context. Community trolling reduces the size of the dataset which enables in-memory processing of data more efficiently.

Big data contains the majority of unlabeled data making classification a difficult task in the big data context. Community trolling of big data is thus proposed with the help of active learning to achieve the desired classification with least labeling cost. Active learning is a machine learning task which selects most informative samples from unlabeled data [37]. The overall process is executed in Apache Spark to achieve data parallelism as shown in Fig. 3. The process starts with small number of initial samples labeled manually for building the base model.

Table 1 Accuracy and precision of base SVM

Training Sam-Ples	Accuracy	Precision
150	70.97	0.3119
1486	73.83	0.4142
2011	74.83	0.4068
2233	76.150	0.46

Active learning selects a small subset of unlabeled data. In each cycle, these selected samples are labeled manually by the domain expert and merged in the training data. The aim of selection strategy is to select and label only those samples which improve the quality of classifier accuracy. The model is rebuilt and this process is continued till a convergence criterion is achieved such as no improvement in accuracy after a point. Final model built is updated periodically or when there is a drop in accuracy below some threshold. Active learning results in the efficient utilization of available resources with least labeling cost which makes it suitable for big data analytics. Active learning can be classified into three types namely, membership query synthesis, stream based and pool based sampling [3, 37]. In the case of membership query, the annotator selects the sample or generates the new sample whereas, in the case of stream based approach, samples are queried one by one for labeling or discarding that arrive in the stream. In the case of pool based strategy which is selected in the current paper due to its wide adoptability, there exists a small set of labeled data and a large pool of unlabeled data. In every cycle, k best samples are selected by query strategy for labeling. The query strategy should select best samples from the unlabeled pool so as to maximize the classifier accuracy. There are various strategies which can be utilized for pool based sampling such as uncertainty sampling, expected error reduction, density weighted sampling, cluster based sampling, expected error reduction and query by committee [13, 15]. Uncertainty sampling is the most simple and adopted active learning query strategy. Authors [13] have compared various query strategies and found that density weighted strategy performs well in most cases. In this paper, both uncertainty sampling and density based strategy are utilized to evaluate the classifier quality. Uncertainty based strategy select the instances about which the model is least certain and including these instances in training set improves their accuracy. Density weighted strategy considers the whole input space distribution rather than individual samples [46]. The distance based similarities used for density-weighted strategy are Euclidian, Manhattan and Cosine. The base classification model employed in current approach is SVM (Support Vector Machine) due to their performance for text classification [8].

The pseudo for community trolling in big data is as shown in Algorithm 1:

Algorithm 1 PseudoCode for Community Trolling in Big Data

Input: $\langle X, C, L, U, M, \phi, \sigma, b\rangle$
$\langle BigDataSet, ClassLabels, LabeledSet, UnlabeledSet, Model, PerformanceMetric, ActiveLearningStrategy, SelectedSamples\rangle$
Output: $\langle Y = \underset{k}{\cup} X_k, M\rangle \langle SelectivelySampledBigdata, TrainedModel\rangle$
$X \leftarrow$Load dataset from bigdata storage(HDFS) and preprocess using ML pipeline
$L \leftarrow$ Choose initial b samples from X and Manually Label
Build M on L `// parallelize execution`
$PL \leftarrow U \cdot map(x \Rightarrow (x, predict(x, M)))$
`// Predicted Labels`
Compute $\phi(PL)$
while $\phi \leq threshold$ **do**
  $S = \sigma(U, M, b)$ `// parallelize selection of most uncertain b samples using active learning strategy`
  Manually Label S
  $L = L + S$
  $U = U - S$
  ReBuild M on L `// parallelize execution`
  $PL \leftarrow U \cdot map(x \Rightarrow (x, predict(x, M)))$
  `// Predicted Labels`
  Compute $\phi(PL)$
$Y \leftarrow (L.union(PL)).filter(class == k)$
return (Y, M)

3.3 Topic Based Community Detection

Community trolling in the above step classifies the documents into various categories. The documents of only relevant categories are extracted to understand the complex community dynamics using topic based community detection techniques and social network analysis. Topic based community helps in capturing the context of interactions among the members. Community profiling may thus best be performed by considering the topic of conversation first followed by network analysis.

LDA is used as a base model for topic based community detection in the current work. The topical clusters generated by LDA correspond to topic communities which are then used to model the behavior of entities. In each topic community, top words related to each topic community are determined. The documents and users are then clustered on basis of topics forming communities with users of similar interests.

A topic based star network can be constructed to determine the influence of topic. Some topics may be more popular than other. The influence of a topic is defined as the directly proportional to number of members discussing that topic. Once an influential topic is figured the network of entities involved in the conversation of that topic can be mapped. This leads to a graph with an edge between two entities representing the conversation topic. Topic based communities are by default overlapping in nature. Thus, a user may be involved in more than one topic communities.

Core or influential members are determined on the basis of centrality measures such as degree centrality, betweenness centrality, closeness centrality and Eigen vector centrality [40]. Degree centrality determines the user with a maximum number of posts and betweenness centrality determines the bridge users who control the flow between different communities. Closeness centrality determines how far entity is from other entities. Eigenvector centrality is based on the degree and is used to measure the influence of the entity.

3.4 Analyst Workbench

All the data obtained in the above step may be stored in a database preferably a columnar NoSQL database such as HBase indexed by a text search engine for visualization on the analyst dashboard. This would help in better understanding the complex process of communities and their behavior. Depending on the context, an analyst workbench may provide an entity based search, a keyword search or timeline view of entity/topic. This is of great analytical value for tasks such as finding most influential members and topics, building ontology and event detection.

4 Experiment & Results

The proposed approach was tested on publicly available and fully annotated hate data captured from Tumbler [2] on realistic settings. The experiments were performed on Databricks cloud and AWS S3. Data analysis was done on Databricks cloud which was built on Apache Spark 2.0 and Scala 2.10. Community Edition of Databricks cloud was a mini cluster with 6GB memory and 8 cores. Amazon S3 service was used for storing data. The data files were stored in Parquet format which is a binary columnar file format employed for efficient storage and processing of big data. The flow of data storage and analysis on Databricks clouds and AWS S3 is as shown in Fig. 4.

4.1 Dataset Description

Extremist communities are using the internet as their mainstream method of propaganda. The proposed approach was used to detect hate communities on the internet which is of interest to security researchers and law enforcement agencies. It was applied on Semantically Analyzed Metadata of Tumblr Posts and Bloggers available on Mendeley [2]. The dataset consists of posts from Tumbler social network which was manually classified as hate and unknown class. The total number of distinct English language posts was 2456 and the number of hate related posts was 527. The

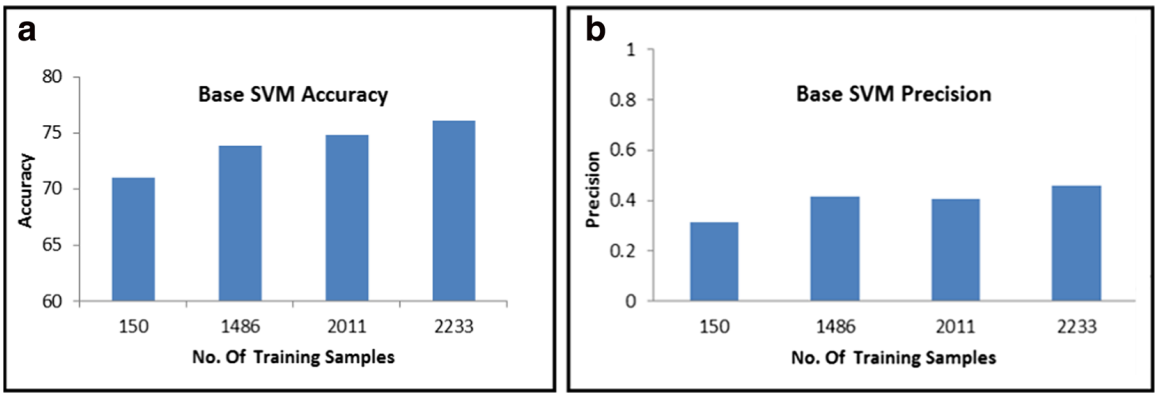


Fig. 5 **a** Base SVM Accuracy **b** Base SVM Precision

Table 2 Active learning accuracy

No. of samples	TF-IDF				Word2Vec				Word2Vec(Corpus-islamic network)			
	Uncertainty	Density-weighted			Uncertainty	Density-weighted			Uncertainty	Density-weighted		
		Euclidean	Manhattan	Cosine		Euclidean	Manhattan	Cosine		Euclidean	Manhattan	Cosine
20	73.25	74.96	74.96	74.96	73.60	73.03	73.48	73.03	73.15	73.15	73.15	73.15
40	73.36	76.93	70.81	73.23	73.63	74.67	74.75	74.67	77.94	74.83	75.08	78.52
60	75.87	76.82	70.98	74.75	46.74	74.33	74.21	74.33	77.97	78.43	78.47	78.72
80	76.88	76.63	72.53	75.67	40.30	74.37	74.24	74.37	77.28	79.17	79.13	79.09
100	77.19	76.81	72.89	76.73	37.59	74.11	74.19	74.11	77.13	79.00	79.21	79.08
120	77.76	76.62	72.62	76.79	39.19	74.23	74.19	74.23	77.93	78.60	78.77	78.77
140	78.43	77.02	73.20	76.72	49.48	74.39	74.09	74.39	78.51	78.37	78.59	78.72

dataset is fully annotated which helps in validating the results.

Another dataset, Islamic Network [5], was utilized in the absence of domain knowledge about hate communities. It consists of data from an English language forum of the dark web. The forum contains data related to Muslims, their interest and worldwide events from 2004 to 2012. It consists of 91,874 posts and 2082 members. The dataset was utilized in building word2vec model.

4.2 Results

The proposed approach is divided into four tasks which were performed on the Tumbler [2] dataset and are explained below. The dataset was converted to Parquet file format for fast processing and was stored on AWS S3.

4.2.1 Big Data Pre-Processing

In this phase, the dataset stored in S3 was loaded in the Apache Spark Dataset for pre-processing and tokenization. The text posts were pre-processed and tokenized. After tokenization, the data was vectorized using tf-idf and word2vec for comparing the results of active learning in the next step.

4.2.2 Community Trolling

In this phase, active learning for sampling the data was used to explore the community of interest. Community trolling of Tumbler text corpus was performed using active learning to detect hate promoting posts. Extensive experiments were conducted with uncertainty based sampling and density weighted sampling querying on Apache Spark. The performance was evaluated using Accuracy and Precision.

The objective of active learning is to select the least and most informative attributes which increase the performance of the underlying model. Initially, 10 samples of each class were taken for training and rest of the data was used for testing. In each step, 20 more samples were taken and added to the training set. The classification model selected was SVM. Base Line Accuracy and Precision of SVM on Tumbler text corpus is as shown in Table 1 and Fig. 5.

Also, all the experiments were performed on both term vectors and word2vec vectors. It was believed

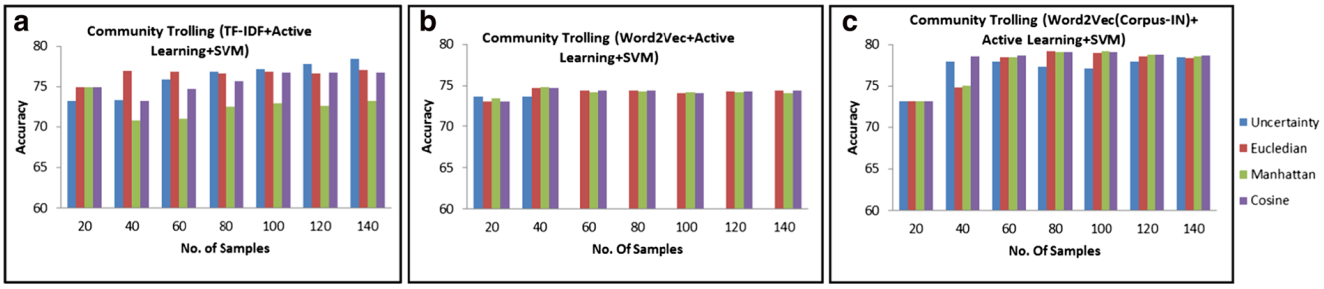


Fig. 6 **a**, **b**, **c** Active Learning Accuracy

that in the current context of hate promoting communities, it may be the case that hate terms are very less in numbers for which TF-IDF may not be relevant. Moreover, as word2vec is a deep learning module which needs a large training corpus, another dataset [5] was utilized to build the word2vec model which was then used for transformation. Table 2 and Fig. 6 represent the accuracy in each iteration for various active learning strategies. Table 3 and Fig. 7 represent the precision in each iteration for various active learning strategies.

4.2.3 Topic Based Community Detection

Community trolling using active learning provided us with the hate promoting content which was further classified into topic based communities using LDA. The standard measure used for LDA is perplexity [34]. The lower is the value of perplexity, better the model fits to dataset and is used for determining the number of topics. The result of perplexity on the hate dataset is shown in Table 4 and Fig. 8 which shows three as the optimal number of topics.

Based on the perplexity results, three topical clusters were found using LDA. For each topic, 10 related words were also found. The results of LDA before and after community trolling are shown in Tables 5 and 6.

It seems clear from above LDA output that community trolling leads to the generation of better topics. Further analysis on the resulting graph between topics and entities was also performed to figure out the strongly connected people, influential topic and influential entities shown in Fig. 9.

4.2.4 Analyst Workbench

The results of the earlier phase were stored in HBase and were also indexed by the text based search engine Solr. The results were visually represented on the dashboard for further analysis. The word cloud after selective community sampling is shown in Fig. 10. A community diagram of entities discussing topic 'muslim', 'syria' and 'racism' is also shown in Fig. 11.

4.3 Analysis

Community trolling employed active learning for selective sampling of big data. Experiments were conducted for sample selection using uncertainty based and density weighted querying strategies in Apache Spark. Besides studying the two active learning strategies, the influence of pre-processing vectorization using TF/IDF and Word2Vec was also explored. The idea was to figure out the benefits of incorporating domain knowledge in the form of word2vec corpus. The effectiveness of community trolling was computed by comparing the accuracy and precision in different scenarios.

Figure 5a shows the accuracy of SVM classification on hate dataset. It is observed from Fig. 6 that with very few samples, active learning performs better than the baseline SVM. Even with 90% of data, base SVM had an accuracy of 76.15%, which was obtained with only 40 samples in case of Euclidean based density sampling. It was found that word2vec with the text corpus of Tumbler dataset [2] has little influence on the performance. It performed the worst for both uncertainty and density based sampling. Word2Vec is a deep learning model which works well on large data. It may be the case that word2vec had the worst performance due to very less number of hate related posts in Tumbler dataset [2]. Due to lack of domain knowledge and to evaluate the effectiveness of word2vec in active learning, Islamic Network [5] text corpus was used for training of word2vec. It was observed that after training the word2vec with Islamic Network

Table 3 Active learning precision

No. Of Samples	TF-IDF				Word2Vec				Word2Vec(Corpus-Islamic Network)			
	Uncertainty	Density-Weighted			Uncertainty	Density-Weighted			Uncertainty	Density-Weighted		
		Euclidean	Manhattan	Cosine		Euclidean	Manhattan	Cosine		Euclidean	Manhattan	Cosine
20	0.1824	0.1830	0.1830	0.1830	0.3472	0.3410	0.3491	0.3437	0.3844	0.3844	0.3844	0.3844
40	0.1447	0.2105	0.3053	0.2299	0.2098	0.3408	0.3310	0.2500	0.4704	0.3982	0.3972	0.4903
60	0.1875	0.1667	0.3106	0.2573	0.1757	0.2996	0.2891	0.2524	0.4698	0.4943	0.4896	0.4932
80	0.1176	0.1975	0.3186	0.2154	0.1753	0.2809	0.2898	0.2437	0.4535	0.5540	0.5824	0.7000
100	0.1765	0.2192	0.3220	0.1974	0.1762	0.2603	0.2833	0.2389	0.4524	0.5747	0.5921	0.8750
120	0.0667	0.2029	0.3130	0.1944	0.1752	0.2593	0.2821	0.2421	0.4456	0.5345	0.5435	0.6667
140	0.0714	0.2453	0.3238	0.2381	0.1711	0.2642	0.2751	0.2449	0.4704	0.5143	0.5000	0.6667

Corpus, the accuracy of 79.21% with only 100 samples was achieved which is better than uncertainty based sampling and far better than the base SVM. The main observations are as follows:

1. Word2Vec, when trained with sufficient domain knowledge, was able to achieve better accuracy for both uncertainty and density based sampling as compared to TF-IDF based vectorization. This clearly is due to the fact that frequency of hate terms in the data may be very less and frequency of terms may not be important as compared to just their presence.
2. Word2Vec vectorization trained with sufficient domain knowledge and uncertainty based sampling was better than base SVM even with 40 samples. However, density based sampling was better than uncertainty based sampling with manhattan based sampling being the best in terms of accuracy (79.21% with just 100 samples).

As the accuracy alone is not the effective measure for evaluation, especially in the case of hate promoting communities, where a number of hate posts may be very less precision was adopted as another measure for evaluation. Figure 5b depicts the precision of true class for base SVM and Fig. 7 depicts the precision of true class in all other cases. The results were remarkably very different from accuracy results. The TF-IDF based vectorization was not able to achieve good precision in either case of uncertainty or density based sampling. Word2Vec with the text corpus of Tumbler dataset [2] was slightly better than TF-IDF based vectorization. However, its performance was still not at par with the base SVM.

Word2Vec trained with Islamic Network Corpus [5] had notable performance than base SVM in all the iterations. It was able to achieve the precision of 0.8750 with just 100 samples which is better than the precision of base SVM (0.46) with 90% of data.

It was observed that community trolling helps in extracting broader community with the help of active learning by using only a few samples. This shows the importance of active learning in big data scenario where the cost of annotation could be very high. It was further observed that adding domain knowledge in the pre-processing step helps in achieving remarkable performance.

The results contained in Tables 5 and 6 further shows the topics and their associated word extracted

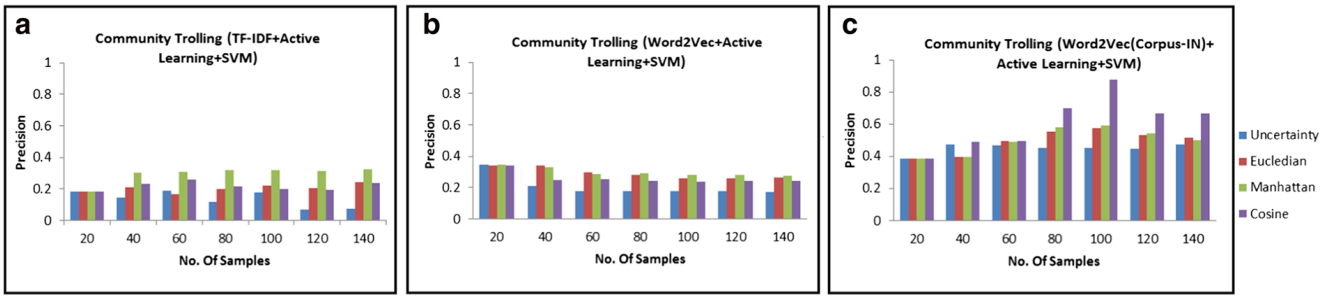


Fig. 7 **a**, **b**, **c** Active Learning Precision

by LDA before and after community trolling. Clearly, the topics represented in Table 6 are better than in Table 5. It is observed that rich data provided is a better representation of the community of interest as shown in Fig. 9. Thus, community trolling proposed helped in understanding the underlying networks more efficiently and enabled to handle polluted big data for efficient analysis.

5 Discussion

A community trolling approach for topic based community detection in big data is presented in this paper. There are various state of art community detection approaches proposed in the past [14]. These techniques could be used in big data context by converting these approaches or techniques into embarrassingly parallel problems [19]. Then, the question which hits the mind is why there is a need to apply community trolling for community detection in big data? Can big data not handle the volume of data? Big data contains a huge amount of data from varied sources which also contains a lot of noise. The quality of big data needs to be improved for accurate and good results from machine learning algorithms [26]. Community trolling using active learning provides selective sampling of data which makes the dataset richer. The advantages of using community trolling in big data are:

1. It helps in removing the unnecessary noise from big volume of data leading to better results.
2. Big data computational in-memory framework like Apache Spark will be able to handle the velocity part in a better way as substantial amount of data would be removed after community trolling.
3. The selective sampling filters the data related to current context and helps in dealing with veracity and value of big data.

Thus, community trolling would address the major V's of big data efficiently. In the growing age of big data, manual inspection of huge data is difficult thus necessitating the need to explore semi-automatic data filtering and data classification techniques [11]. Community trolling is achieved with the help of active sampling which leads to following observations:

Table 4 LDA perplexity

No. of topics	Perplexity
2	6.989
3	6.984
5	7.009
7	7.142
9	7.285
11	7.453
13	7.635
15	7.837

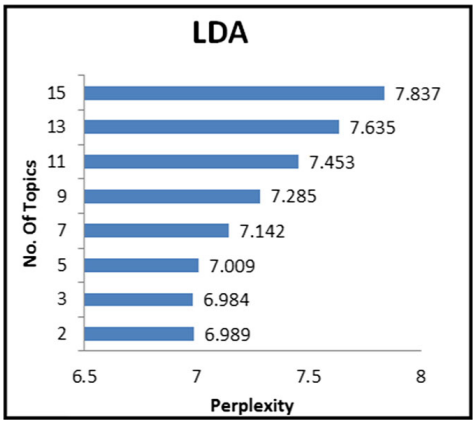


Fig. 8 LDA Perplexity

Table 5 LDA result before community trolling

Topic:0	Topic:1	Topic:2
People::0.0093529451	lesbian::0.016877250	april::0.0087173079
Time::0.0085839565	black::0.0103084298	2016::0.0067805514
Want::0.0065723844	people::0.0094526933	new::0.0054703498
Ldquo::0.0059114810	view::0.00683058250	world::0.0053557083
Love::0.0052795061	wordpress::0.0062110516	space::0.0050211470
Life::0.0049272233	allah::0.004400816	god::0.004063934
Heart::0.0049140032	h::0.004244505	seo::0.00375722179
Way::0.0047418266	racism::0.0041281097	people::0.0036645514
Things::0.0046666245	islam::0.00385448993	media::0.0034238657
Day::0.0046530694	state::0.0034686613	station::0.0032340899

Table 6 LDA result after community trolling

Topic:0 (General)	Topic:1 (Syria)	Topic:2 (Islam/Religion)
face::0.0090718435	black::0.015952630	people::0.0177366874
journey::0.0086575158	syria::0.0145795029	ldquo::0.0119855812
wearing::0.0056083113	government::0.0125380995	god::0.0083776234
day::0.0050931546	taliban::0.0121011685	muslim::0.0083033662
muslim::0.0050759366	people::0.0090375392	world::0.0081767766
thoughts::0.0043983978	united::0.0080908532	islam::0.0071513520
time::0.0040840703	nusra::0.0071883046	muslims::0.0067161187
greater::0.0039556628	islamic::0.0067959620	allah::0.0066335685
attempt::0.0039432311	support::0.0067758358	time::0.0062185089
awsat::0.0038482285	turkey::0.0067038056	love::0.006083840

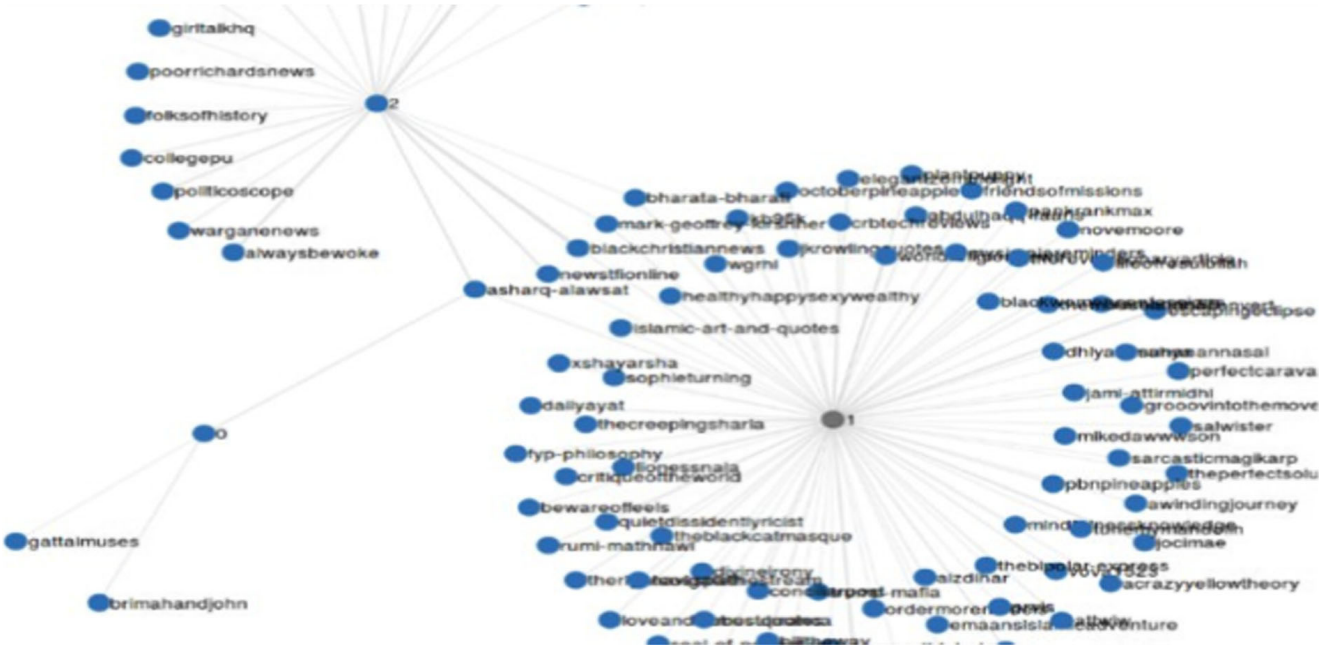


Fig. 9 Topic-Entity Communities



Fig. 10 Word cloud (Hate related posts)

1. Selection of vectorization approach such as TF/IDF or word2vec also plays an important role in results of active learning. It was observed that word2vec, when trained with sufficient domain knowledge, helps in achieving better results.
2. Density weighted sampling performs better than uncertainty based sampling in almost all the cases when word2vec trained with sufficient knowledge is used.
3. Active learning provides selective sampling of data with only a few labels reducing the annotation cost. This shows the importance of active learning in big data scenario where the cost of annotation could be very high.
4. The most expensive computation in the overall approach was iteration process of selecting the active learning samples. This is handled by the data parallelism offered by Apache Spark framework efficiently.

Community trolling extracts a broader community with the help of active learning using only a few samples. Community trolling provides a richer dataset which leads to more appropriate and qualitative information about the topics and influential members in the community. Community trolling helps in finding most appropriate and coherent communities related to current context and enables to handle polluted big data for efficient analysis. In future, the same approach may be extended to other topic based community detection.

6 Conclusion, Implication & Future Work

In this study, a community trolling approach using active learning is utilized to support topic based community detection in polluted big data. Active learning results in selective sampling of data with reduced cost and very less number of samples. The proposed approach is implemented on parallel in-memory



Fig. 11 Topical Communities

distributed Big Data Framework which makes it scalable and efficient from traditional machine learning algorithms. Community trolling enabled efficient in-memory parallel processing and provided a broader community of interest. It helps in handling noise and 4Vs (Volume, Velocity, veracity and Value) of big data. The performance of active learningis also found to be strongly related to the presence of domain knowledge which was incorporated in the word2vec model.

Online social network provides a rich source of big data and represents different communities. The experiments are conducted on a real world Tumbler dataset to evaluate the approach. It is evident from the result that Community Trolling helps in removal of noise yielding richer dataset. It was also found that featurization/vectorization also plays an important role in the overall results. It was observed that word2vec, when trained with sufficient domain knowledge, helps in achieving better performance. Results reveal that combining community trolling with community detection proved to be a useful way of finding coherent and strongly connected communities of interest.

This work Sprovides an important step towards handling noise in polluted big data which will thus enable practitioners in extracting valuable insights out of big data. The approach presented can be easily applied to various domains/areas such as image classification which present many new directions for future work. The future work which we plan to work upon include:

1. Current work focus on text based feature of the dataset, however, big social media data is heterogeneous in nature consisting of media and text. Variety aspect of big data is worth researching upon to evaluate the efficacy of proposed approach on data consisting of multi-lingual text, audio and video.
2. Temporal analysis of proposed approach may also be performed.
3. Application of community trolling on other community detection techniques.

References

1. Abdelbary, H., El-Korany, A.: Semantic topics modeling approach for community detection. Int. J. Comput. Appl. **81**(6), 50–58 (2013)
2. Agarwal, S., Sureka, A.: Semantically analyzed metadata of tumblr posts and bloggers. Accessed on February (2017)
3. Aggarwal, C.C., Kong, X., Gu, Q., Han, J., Yu, P.S.: Active learning: A survey. In: Data Classification: Algorithms and Applications, pp. 571–605. Chapman and Hall/CRC (2014)
4. Ando, R.K., Zhang, T.: A framework for learning predictive structures from multiple tasks and unlabeled data. J. Mach. Learn. Res. **6**, 1817–1853 (2005)
5. Artificial Intelligence Lab Management Information Systems Department, U.o.A.: Islamic network forum dataset. https://s3-us-west-2.amazonaws.com/azsecure-forums-darkweb/IslamicNetwork.zip (2017). (Accessed on February, 2017)
6. Bajaber, F., Elshawi, R., Batarfi, O., Altalhi, A., Barnawi, A., Sakr, S.: Big data 2.0 processing systems: Taxonomy and open challenges. J. Grid Comput. **14**(3), 379–405 (2016)
7. Balasubramanyan, R., Cohen, W.W.: Block-lda: Jointly modeling entity-annotated text and entity-entity links. In: Proceedings of the 2011 SIAM International Conference on Data Mining, pp. 450–461. SIAM (2011)
8. Basu, A., Walters, C., Shepherd, M.: Support vector machines for text categorization. In: Proceedings of the 36th Annual Hawaii International Conference on System Sciences, 2003. IEEE (2003)
9. Blei, D.M., Ng, A.Y., Jordan, M.I.: Latent dirichlet allocation. J. Mach. Learn. Res. **3**, 993–1022 (2003)
10. Buhrmester, M., Kwang, T., Gosling, S.D.: Amazon's mechanical turk a new source of inexpensive, yet high-quality, data? Perspect. Psychol. Sci. **6**(1), 3–5 (2011)
11. Cohen, K., Johansson, F., Kaati, L., Mork, J.C.: Detecting linguistic markers for radical violence in social media. Terrorism and Political Violence **26**(1), 246–256 (2014)
12. Ding, Y.: Community detection: topological vs. topical. J. Inf. **5**(4), 498–514 (2011)
13. Dos Santos, D.P., De Carvalho, A.C.: Comparison of active learning strategies and proposal of a multiclass hypothesis space search. In: International Conference on Hybrid Artificial Intelligence Systems, pp. 618–629. Springer (2014)
14. Fortunato, S.: Community detection in graphs. Phys. Rep. **486**(3), 75–174 (2010)
15. Fu, Y., Zhu, X., Li, B.: A survey on instance selection for active learning . Knowl. Inf. Syst. **35**(2), 1–35 (2013)
16. Gadde, A., Gad, E.E., Avestimehr, S., Ortega, A.: Active learning for community detection in stochastic block models. In: 2016 IEEE International Symposium on Information Theory (ISIT), pp. 1889–1893. IEEE (2016)
17. Go, A., Bhayani, R., Huang, L.: Twitter sentiment classification using distant supervision. CS224N Project Report Stanford 1(12) (2009)
18. Goldberg, Y., Levy, O.: Word2vec explained: Deriving Mikolov others's negative-sampling word-embedding method. arXiv:1402.3722 (2014)
19. Gupta, P., Sharma, A., Jindal, R.: Scalable machine-learning algorithms for big data analytics: a comprehensive review. Wiley Interdisciplinary Reviews: Data Mining and Knowledge Discovery **6**(6), 194–214 (2016)
20. Habashi, S., Ghanem, N.M., Ismail, M.A.: Enhanced community detection in social networks using active spectral clustering. In: Proceedings of the 31st Annual ACM

Symposium on Applied Computing, pp. 1178–1181. ACM (2016)
21. Kanungo, T., Mount, D.M., Netanyahu, N.S., Piatko, C.D., Silverman, R., Wu, A.Y.: An efficient k-means clustering algorithm: Analysis and implementation. IEEE Trans. Pattern Anal. Mach. Intell. **24**(7), 881–892 (2002)
22. Leng, M., Yao, Y., Cheng, J., Lv, W., Chen, X.: Active semi-supervised community detection algorithm with label propagation. In: International Conference on Database Systems for Advanced Applications, pp. 324–338. Springer (2013)
23. Leskovec, J., Lang, K.J., Mahoney, M.: Empirical comparison of algorithms for network community detection. In: Proceedings of the 19th International Conference on World Wide Web, pp. 631–640. ACM (2010)
24. Li, D., Ding, Y., Sugimoto, C., He, B., Tang, J., Yan, E., Lin, N., Qin, Z., Dong, T.: Modeling topic and community structure in social tagging: The ttr-lda-community model. J. Am. Soc. Inf. Sci. Technol. **62**(9), 1849–1866 (2011)
25. Li, X.L., Liu, B.: Rule-based classification. In: Data Classification: Algorithms and applications, pp. 121–156. CRC Press. http://www.crcnetbase.com/doi/abs/10.1201/b17320-6 (2014)
26. Liu, J., Li, J., Li, W., Wu, J.: Rethinking big data: A review on the data quality and usage issues. ISPRS J. Photogramm. Remote. Sens. **115**, 134–142 (2016)
27. McCallum, A., Corrada-Emmanuel, A., Wang, X.: Topic and role discovery in social networks. In: In Proc. of 2005 Int. Joint Conf. on Artificial Intelligence (IJCAI05), pp. 786–791 (2005)
28. McCallum, A., Wang, X., Corrada-Emmanuel, A.: Topic and role discovery in social networks with experiments on enron and academic email. J. Artif. Intell. Res. **30**, 249–272 (2007)
29. Meoni, M., Perego, R., Tonellotto, N.: Dataset popularity prediction for caching of CMS big data. J. Grid Comput. **16**(2), 1–18 (2018)
30. Mikalef, P., Pappas, I.O., Krogstie, J., Giannakos, M.: Big data analytics capabilities: a systematic literature review and research agenda. Information Systems and e-Business Management, 1–32 (2017)
31. Moore, C., Yan, X., Zhu, Y., Rouquier, J.B., Lane, T.: Active learning for node classification in assortative and disassortative networks. In: Proceedings of the 17th ACM SIGKDD International Conference on Knowledge Discovery and Data Mining, pp. 841– 849. ACM (2011)
32. Pathak, N., DeLong, C., Banerjee, A., Erickson, K.: Social topic models for community extraction. In: The 2nd SNA-KDD Workshop, vol. 8 (2008)
33. Planti'e, M., Crampes, M.: Survey on social community detection. In: Social Media Retrieval, pp. 65–85. Springer (2013)
34. Rosen-Zvi, M., Griffiths, T., Steyvers, M., Smyth, P.: The author-topic model for authors and documents. In: Proceedings of the 20th Conference on Uncertainty in Artificial Intelligence, pp. 487–494. AUAI Press (2004)
35. Salton, G., McGill, M.J.: Introduction to Modern Information Retrieval. McGraw-Hill, Inc, New York (1986)
36. Sculley, D.: Online active learning methods for fast label-efficient spam filtering. In: CEAS, vol. 7 (2007)
37. Settles, B.: Active learning. Synthesis Lectures on Artificial Intelligence and Machine Learning **6**(1), 1–114 (2012)
38. Silva, C., Antunes, M., Costa, J., Ribeiro, B.: Active manifold learning with twitter big data. Procedia Comput. Sci. **53**, 208–215 (2015)
39. Steyvers, M., Smyth, P., Rosen-Zvi, M., Griffiths, T.: Probabilistic author-topic models for information discovery. In: Proceedings of the Tenth ACM SIGKDD International Conference on Knowledge Discovery and Data Mining, pp. 306–315. ACM (2004)
40. Tang, L., Liu, H.: Community detection and mining in social media. Synthesis Lectures on Data Mining and Knowledge Discovery **2**(1), 1–137 (2010)
41. Tang, Z., Fu, Z., Gong, Z., Li, K., Li, K.: A parallel conditional random fields model based on spark computing environment. J. Grid Comput. **15**(3), 323–342 (2017)
42. Wang, M., Wang, C., Yu, J.X., Zhang, J.: Community detection in social networks: an in-depth benchmarking study with a procedure-oriented framework. Proc. VLDB Endowment **8**(10), 998–1009 (2015)
43. Xie, J., Kelley, S., Szymanski, B.K.: Overlapping community detection in networks: The state-of-the-art and comparative study. ACM Comput. Surv. (csur) **45**(4), 43 (2013)
44. Zaharia, M., Chowdhury, M., Franklin, M.J., Shenker, S., Stoica, I.: Spark: Cluster computing with working sets. HotCloud **10**(10-10), 95 (2010)
45. Zhou, X., Saha, A., Sindhwani, V.: Semi-supervised learning. In: Cost-Sensitive Machine Learning, pp. 31–59. CRC Press (2011)
46. Zhu, J., Wang, H., Tsou, B.K., Ma, M.: Active learning with sampling by uncertainty and density for data annotations. IEEE Trans. Audio Speech Lang. Process. **18**(6), 1323–1331 (2010)
47. Zou, L., Song, W.W.: Lda-tm: A two-step approach to twitter topic data clustering. In: 2016 IEEE International Conference on Cloud Computing and Big Data Analysis (ICCCBDA), pp. 342–347. IEEE (2016)

International Journal of Current Engineering and Technology
E-ISSN 2277 – 4106, P-ISSN 2347 – 5161
©2018 INPRESSCO®, All Rights Reserved
Available at http://inpressco.com/category/ijcet

Research Article

Comparative Study on the Effect of Nitriding and Microwave Coating on Microstructure, Hardness and Wear of AISI H13 Tool Steel

Mohammad Iqbal Yunus†*, Kanwarjeet Singh†, Gaurav Arora† and Ranganath M Singari†

†Department of Tool Engineering, Delhi Institute of Tool Engineering, Okhla, New Delhi, India
†Department of Mechanical Engineering, Delhi Technological University, Shahbad Daulatpur, Delhi, India

Received 25 May 2018, Accepted 28 July 2018, Available online 30 July 2018, **Vol.8, No.4 (July/Aug 2018)**

Abstract

Heat treatment and surface processing are critical aspects of design and manufacture of components in a wide range of industrial sectors. Engineering materials, such as steel, are heat treated under controlled heating and cooling to alter their chemical, physical and mechanical properties to meet desired engineering applications. Gears engaged rotating at several thousand RPM. Inner Barrels of Injection Moulding machines, which is subjected to wear when thermoplastics, glass fibres are chosen to be injection moulded, Guide pillar Guide bush which slide over each other needs to be hardened from outside to improve hardness and wear resistance, but ductile from inside to bear fluctuating load, for this types of operation Case Hardening is required, to give desired property. In this detailed and systematic investigation, we have selected AISI H13 tool steel as for our research work specimen and we have made an effort to find out the mechanical properties (EDX, Hardness HV, Pin on Disc wear test) and micro structural properties (SEM, XRD) by comparing the two process one is traditional Case hardening heat treatment process i.e. Gas Nitriding and a new process i.e. Coating of Ni-based alloy powder on H13 Tool steel by Microwave Hybrid Heating (MHH) method in household microwave oven at 900W and 2.45 GHz and further find the best process. Investigation shows that coated Sample has good Wear resistance as compared to unmodified H13 Tool Steel sample and nitrided sample, Vicker's micro-hardness of nitride sample is found to be 829.5HV, and for coated sample is 788HV, Coated sample has good Microstructure as compared to nitrided sample and is free from porous cracks.

Keywords: *H13 Tool Steel, Microwave Hybrid Heating, Case-Hardening, Gas Nitriding, Ni-based Alloy, Microwave Coating, EDX, XRD, SEM, Pin on Disc Wear Test*

1. Introduction

In the fast-growing economy, the need of people is growing day by day, that's is why growth of plastics and hybrid materials have improved, which has a good impact in the growth of tooling, extrusion and injection moulding industry. A large amount of time is being wasted in maintenance, care and sustenance, of tooling and injection moulding equipment.

Heat treatment is one of the major time consuming and tedious job to do in the industry for getting desirable property , case hardening further become more important to get desirable property Because hardened metal is normally more brittle than softer metal, through is not always a suitable choice for uses where the metal part is subject to sliding contact with hard or abrasive materials case-hardening provides a part that will not fracture (because of the soft core that can absorb stresses without cracking and hard outside which can bear sliding wear) but also satisfactorily resist wearing on the surface.

Further again if we talk about different case hardening techniques used nowadays require at least minimum of 5 hours for case hardening, further every process is not capable of performing for every metals or alloys.

Also, application of Physical vapour deposition to develop hard coatings to the substrate materials, cannot assure the optimal tribological performance without pre-treatment of the substrate materials due to plastic deformation of the substrate which results in eventual coating failure. The surface treatment provides a hardening and increases load support on substrate [Zeghni et *al*, 2005].

Many methods aim to enhance the load bearing capacity of the coated surfaces and improve the adhesion of the coatings such as deposition of an inter-layer material or compound prior to the coating or the treatment of the surface by nitriding or carburising. In terms of the cost and simplicity, surface treatment such as nitriding and carburising are better processes [Zeghni *et al*, 2005]. But at the same time the process is very tedious and time consuming.

*Corresponding author's ORCID ID: 0000-0002-1184-8133
DOI: https://doi.org/10.14741/ijcet/v.8.4.21

The innovative technique should have low cycle time, low power consumption, low cost, and be environmental friendly [Singh *et al,* 2016].

In MHH, volumetric irradiation takes place inside the material body caused volumetric heating. In volumetric irradiation, the processing time and the energy requirements gets shorten, which leads to uniform change in material properties throughout the material [Srinath *et al*, 2011]. Different range of material can be quickly and easily heated by EM energy rather than conventional types of heating because the efficiency of conversion from Electro-Magnetic radiation to heat is nearly 100%. In microwave processing, volumetric heating is done by direct transfer of energy to the bulk through interaction of EM waves with atoms and molecules of the bulk [Srinath, *et al*, 2011]. Here heat is generated internally within the material and is transferred outwards rather than origination from outside as in conventional heating . So the heating profile is inverse i.e. 'inside-out' unlike the 'outside-in' profile in conventional heating [Aravindan *et al*, 1999].

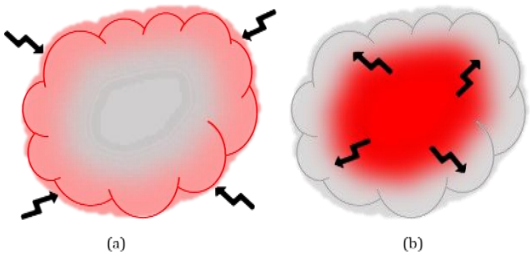


Fig.1 (a)Conventional heating versus (b)microwave heating [S. Singh *et al*, 2015]

This investigation, based on the facts stated above, intended to find out the optimum case hardening process by comparing the two processes i.e. through Gas Nitriding process and second is Coating of Ni-based Alloy Powder by Microwave Hybrid heating on substrate i.e. H13 Tool Steel and further characterization of process through Scanning Electron Microscope (SEM) to check Microstructure, X- Ray Diffraction (XRD) to check new phases developed and significance of those phases, Pin on disc wear test to check wear resistance of the specimen and microhardness to check improvement in the hardness properties after the two operation, Further develop and effective process which can be implemented in the industries and help them minimise their maintenances time.

2. Materials and Methods

The H13 tool steel substrate of 10 x10 x 5 mm3 size was prepared by different machining process for the development of Gas Nitrided and Microwave Coated surface. H13 Tool Steel is a Cr-Mo hot work steel that is widely used in hot and cold work applications. Such as hot extrusion dies [Akhtar *et al*, 2009]. The spectroscopy result of the H13 tool steel substrate was 0.401% C, 1.01% Si, 0.439% Mn, 0.004% S, <0.015% P, 5.11% Cr, 0.066% Ni, 1.31% Mo, 0.89% V.

The nominal composition of Ni-based coating powder as per EDX result was 10.65% Cr, 5.66% C, 3.66% Fe, 2.3% Si, 2.10% V, 1.98% Mn, 1.60% Mo, 1.8% B, 0.02% F, and Bal. Ni (wt.%), the particle size of Ni-based powder was 50–70 micron. Ni-based coating powders are frequently used to improve the hardness for combating wear-, corrosion-, and heat-resistant properties [Kaushal *et al*, 2015, Kaushal *et al*, 2016].

2. a Gas Nitriding

Gas Nitring samples are fine grounded with 1000 grit Silicon emery paper and further ultrasonically cleaned in acetone (C_3H_6O), before nitriding. Samples are then put in closed furnace with maintaining 520±30ºC for 72 hrs. gas mixture of NH_3 and N_2 in the ratio of 1:1 is flown in the chamber at the rate of 0.6ml/min [SH Yeh *et al*, 2011]. After 72 hrs gas supply is shut-off and continue for another 48 hrs at the same temperature, further samples are allowed to cool in an open air. The sample was heat treated at local heat treatment company i.e. M/s Coatwell India Pvt. Ltd. where proper arrangements for environmental control is accomplished by using vacuum furnace to prevent leakage of gas which causes decarburization.

2. b Microwave Coating

At room temperature, most of the metals reflect back microwaves and does not allow its penetration through the bulk due to the presence of thick electron blanket. Hence, it is difficult to coat metallic materials using microwave irradiation. But heating is due to microwave-material interaction at molecular level, if Microwave of 2.45 GHz freq. is used it means that atoms of that bulk material rubs together 2.45 billion times within a short duration of time, which causes generation of friction within the molecules and thus heating. A number of trials have been made in order to take care of these processing challenges. The following section describes the experimental procedure adopted for generation of bulk metallic clads (Fig- 2) and further different characterisation techniques employed to investigate the clad properties.

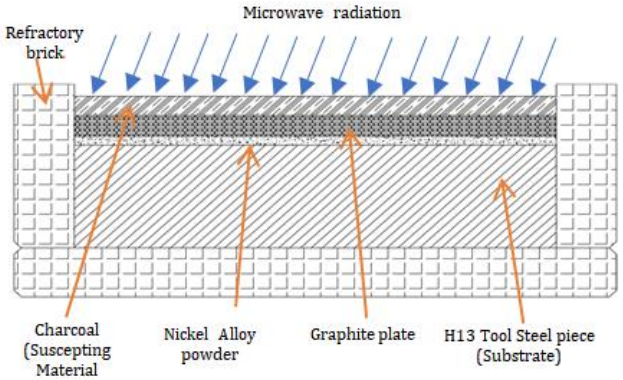


Fig 2 A Section view of the experimental setup for Microwave Cladding

In the present investigation, unmodified and modified coatings were developed at a constant power of 900 W while varying the irradiation time interval of 60 s from 330 to 810 sec for pilot experiments.

In the first step all the specimens are mechanically polished with 1000 size grit emery paper, ultrasonically cleaned in acetone (C_3H_6O), Finally dried, before Cladding (coating), Experiments were carried out in 900 W, 2.45Ghz frequency multimode microwave system of ONIDA make (Model -28CJS14). All experiments were carried out in controlled atmospheric condition.

The microwave penetration depth into the bulk material surface is much lesser than the size of bulk metallic pieces (0.12 μm) [Gupta *et al*, 2011]. This leads to throwing back of microwaves from the attacked material. In order to prevent this, use of refractory brick was used as an insulating mask. The bulk pieces were covered and sealed with refractory bricks as shown in the schematic setup in Fig 2, For initial coupling of microwaves with H13 tool steel pieces at the top of the Clad, a absorber is used which is called susceptor, charcoal powder was used in this case as it has high microwaves absorbing and high heat generating power. Carbon from charcoal does not go inside the bulk steel pieces during microwave heating as a graphite plate (1.5 mm thick) was used to separate the charcoal powder and the sandwich layer powder [Dwivedi, *et al*, 2014]. Charcoal powder enables the application of principle of microwave hybrid heating (MHH) to Clad Ni- based powder on the surface of H13 metallic pieces. The charcoal powder was placed on the top of the graphite plate. The susceptor material ingests microwave promptly at room temperature until it reaches a higher temperature, which is then transferred to the coating powder (Ni-based powder) via the conduction or radiation heat transfer until it starts absorbing microwave radiation directly at higher temperature normally between 500±100°C. As a result, the metallic materials start coupling with microwaves at higher temperature leading to further rise in temperature. The temperature rise is sufficient to cause melting and fusing of the interfaces and gives metallurgical bonding. Fig 3 gives the detailed stepwise description of microwave cladding.

Table 1 Mechanical properties of H13 tool steel

Tensile strength, U	1200-1590 N/mm^2
Tensile strength, Y	1000-1380 N/mm^2
Hardness HV	290- 370 HV
Melting Point	1427 ˚C
Density	7.8 g/cm^3

The effects of microwave heating time on cladding development used for pilot study are presented in Table 2. It was observed that cladding at 810 sec showed High standard metallurgical bonding with the substrate. Accordingly, the processing time of 810 sec for the development of all the coatings.

For microstructural investigation of samples obtained from the two process, the samples were cut transversely from the section and polished as per standards. Then etching is done on polished samples with 10% of Nital Solution (10ml HNO_3 and 90ml Ethanol C_2H_6O), and dried before SEM analysis.

Table 2 Effects of Microwave irradiation time on cladding development

Trials	Processing time, s	Observations
1	330	No melting (only powder is heated)
2	390	Charcoal and Ni-powder was red hot
3	450	Softening of powder particle was started
4	510	Presence of un melted particle
5	570	Better liquification, still presence of some un melted particle and poor bonding with bulk H13 metal Pieces
6	810	Cladding developed with good metallurgical bonding with bulk H13 metal Pieces
7	870	Overheating causes deformation in substrate

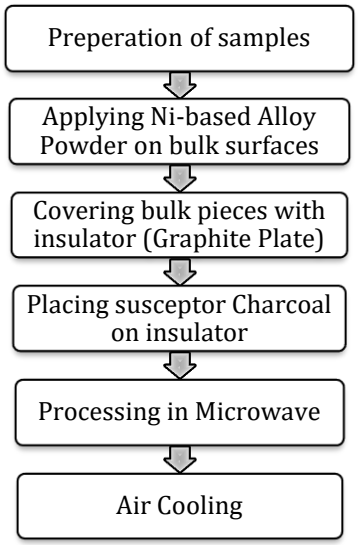


Fig 3 Typical flow chart of microwave Coating process

The wear mechanism of the worn-out surfaces of samples i.e. Unmodified, Nitrided, and Microwave coated H13 tool steel done after Pin on disc wear test, was also studied using SEM. The micro hardness of the unmodified, Nitrided, and Microwave Coated modified coatings was measured at a load of 100 g for 10sec. The average microhardness of 6 readings at one sections of the Nitriding and coating per sample was used for study. The XRD using Cu K_α radiations of unmodified, nitrided and Microwave from 10° to 100° (2θ value) at a scanning speed of 1°/min was used to identify various phases.

Abrasive Wear Study of Unmodified, Modified (Gas Nitrided), Modified (Microwave Nickle Coated) Was Performed using DUCOM (Pin on Disc) wear testing Machine, Wear Pins is of size 10x10x5 mm^3 is held against the disk having Silicon carbide abrasive paper, The track radius is fixed at 60mm, and 400 revolution per minute (rpm) of rotating disc is calculated against the the sliding speed of 150.96m/min. Abrasive wear test is divided into Three cases depending upon abrasive Paper Grit size and the specimen used, Table-2 shows the Test Structure.

Table 2 Test Structure of Pin on Disc Wear Testing

	Test Structure		
	Paper Grit Size	220	1000
1	Unmodified H13 Tool Steel of size 10x10x5mm^3 CASE A	3 nos.	3 nos.
2	Modified (Nitrided) H13 Tool Steel of Size 10x10x5mm^3 CASE B	3 nos.	3 nos.
3	Modified (Nickle Coated) H13 Tool Steel of Size 10x10x5mm^3 CASE C	3 nos.	3 nos.

The tester was allowed to run ideal for 1 min in order to obtain constant speed, and then a force of 10 N ~ 1kg was put on the H13 pins.

The samples of all coatings were cleaned with acetone and then dried. The mass loss of all the coating was calculated by weighing all samples prior to and after the wear test on an electronic weighing balance of accuracy 0.0001 g.

3. Result and Discussion

Each and every metal has got different mechanical and tribological properties. Some metals are sturdy , robust and strong, while others are much more ductile malleable and less tough. Steel are often require treatment to obtain maximum hardiness, capability and durability. We can change the mechanical properties of metals through selecting desired manufacturing process for getting desired property. One process of heat treatment is surface hardening. In this process, the metal surface is strengthened through the addition of a thin blanket of another element that increases durability and hardness of substrate. In many Industrial applications, such as guide pillar and guide bush in press tool, inner surface of injection molding, Metal gear , which requires hardness and ductility. case hardening has significant role to play

In this work, experiment has been carried out to compare the most general process of Case hardening i.e. Gas Nitriding and a new approach i.e. Microwave Coating on H13 tool steel through MHH. H13 tool steel is the very versatile grade which is used in extrusion dies and other tooling components for production of standard aluminium profiles, Injection molding nozzle and barrel, which is characterized by good resistance to wear, high toughness, uniform and high machinability, high-temperature resistance, needs to be case hardened [Akhtar, *et al*, 2009].

The particle size of Ni-based powder used in this study ranges from 50 to 70 microns, but the skin depth at 2.45 GHz of nickel powder is 0.12 microns, which is lower than the size of Ni powder to interact with microwave irradiation for the successful development of the coatings [Gupta *et al* 2011].

Thus, the coatings were developed using susceptor material i.e. charcoal powder and graphite sheet of thickness 1.5mm.

3. a Wear Test

It is clearly visible Fig- 4 that Case A Which Unmodified untampered H13 Tool Steel has got higher wear as compared with all other samples at both 220 and 1000 grit size paper, Case B which is modified Gas nitride Sample has higher rate of mass loss rather than Case C but Lower than Case A at both 220 and 1000 grit size paper, Case C Which is Microwave Coated (Nickle) H13 Tool steel has lowest mas loss as compared to all other case at both Grit size Paper test.

To analyse the abrasive wear mechanism of all the samples i.e. Case A, Case B, Case C, The SEM Images of worn-out samples of Cases A-C were taken and are shown in figure. The results of the SEM images of the unmodified, modified (nitriding), modified (Coating) shows, ploughing, cutting, and crater formation on the worn-out surfaces. The mass loss of each sample depends on the hardness and wear mechanism taking place in various cases. During ploughing, ridges were formed along the wear track and the material was displaced sideways. In the cutting mechanism, small chips are formed as wear debris, whereas in the crater the material is removed due to which small cavities are formed, the SEM images of the Samples show that the worn grooves are wider due to coarse grit size.

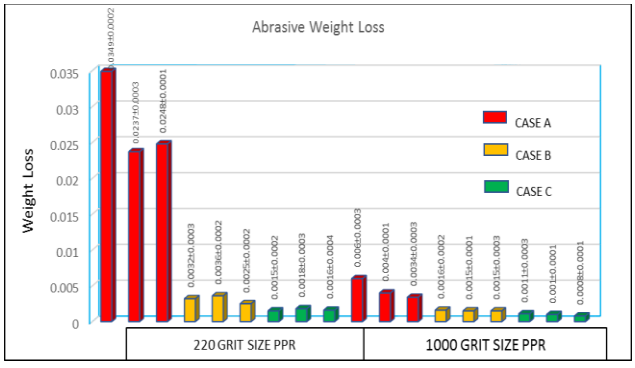


Fig 4 Abrasive Weight Loss

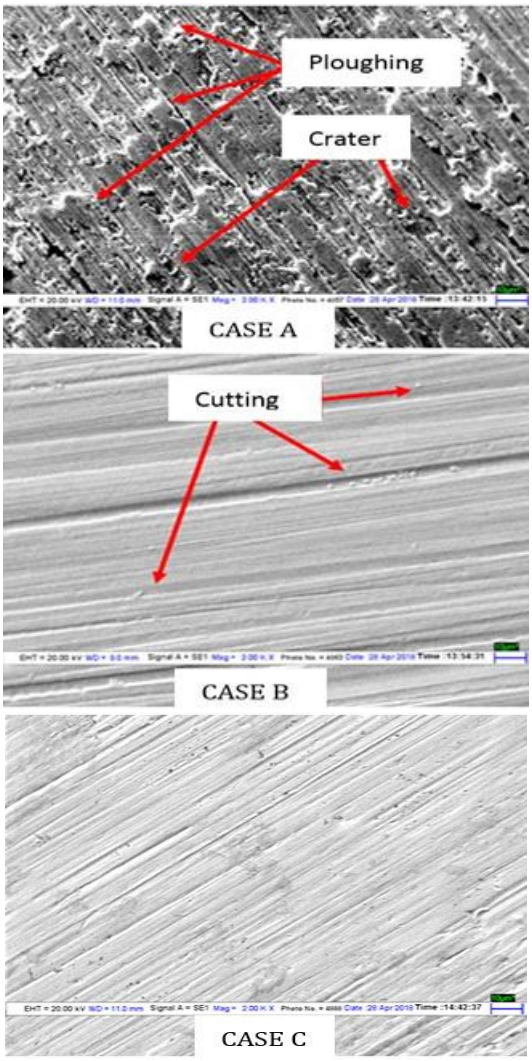
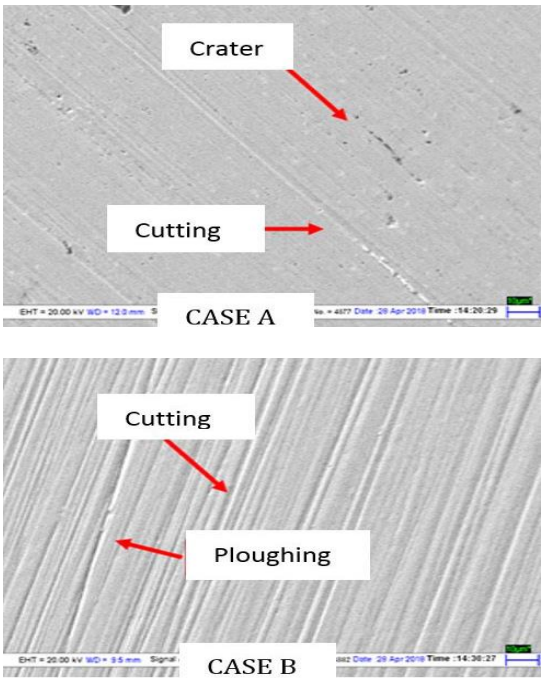


Fig 5 SEM Image to show worn out morphology of wear in the samples undergone through 220 Grit size paper Image taken at 10 µm



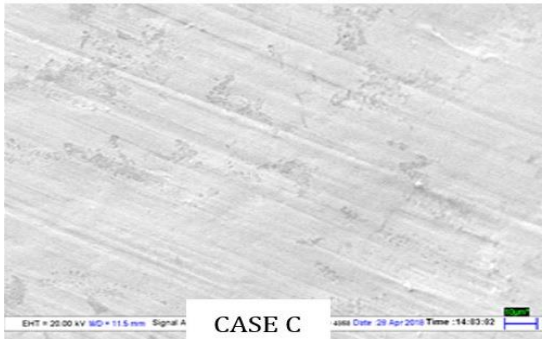


Fig 6 SEM Image to show worn out Morphology of wear in the samples undergone through 1000 Grit size paper, Image taken at 10 µm

3. b Scanning Electron Microscope (SEM)

The SEM cross-section picture of the sample (as shown in Fig- 7) reveals the presence of nitride precipitation and continuous compound layer. A White layer near the surface can be seen in SEM micrograph, which is the nitride layer. The diffusion zone exhibits a uniform distribution of nitrides depreciate slowly (somewhere abruptly) from surface to the core.

The depth of compound layer, which is considerably shallower, is an indication of controlled nitriding, as can be seen in the SEM micrograph (Figure-7). The depth of the compound layer (as seen in SEM micrograph) is of the order of 12-18.4 µm, while the nitrided layer is about 165- 180.5µm (Measured through ImageJ Software). Image is taken at magnification of 150X

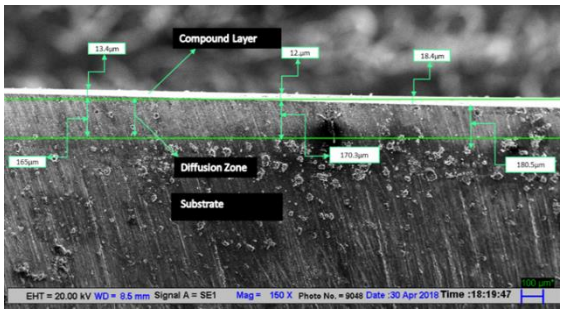


Fig 7 SEM Image of Transversely cut Nitrided Sample of H13 Tool Steel

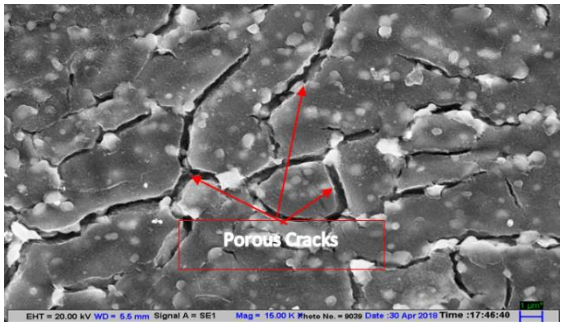


Fig 8 SEM Image of Nitrided Sample Showing its Morphology

As from SEM Image from the top surface of the nitrided Sample of H13 Tool Steel It is clearly visible that A large number of pores and cracks is seen in the compound layer while nothing is visible in Nickle coated case (Fig-8 & 9). This because the nitrogen atoms try to recombine to form N_2 as the atoms has lower energy [yang, *et al*, 2011]. SEM Image is taken at 15k X.

The SEM analysis of Nickle Alloy Powder coated on H13 tool steel through MHH is shown on Fig- 9 and that of transversely cut coated H13 tool Steel (Ni-based alloy) is shown on (BSD mode) Fig-10, the scanning electron micrograph of Nickle based powder particles used for coating H13 tool steel has been shown. The Average Particle Size of Nickle based powder is 60±10 µm which has been completely melted and formed metallurgical bond between the interfaces of Ni- clad and H13 tool steel piece, the coating is free from porosity and crack which is seen in nitrided samples so it has good mechanical property, wear strength and hardness as compared to nitrided samples, further, a dense and homogenous structure is formed, the molten powder melts interfacing surface of the substrate. The melting of the interfacing surface is limited to a thin layer only because of low skin depth of bulk material [Bansal, *et al*, 2013].

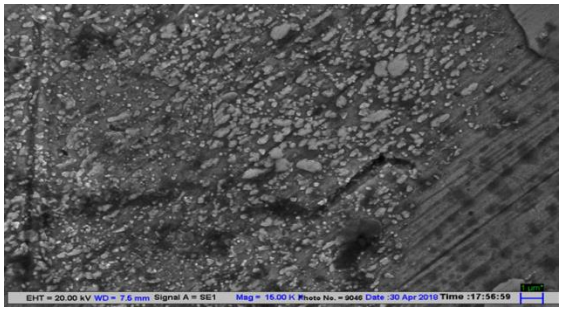


Fig 9 SEM Image of Coated (Nickle Sample) Showing its Morphology

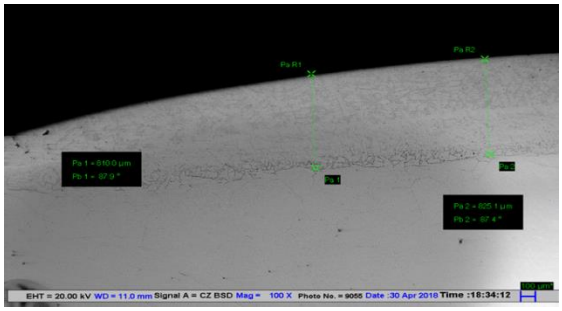


Fig 10 SEM image of transversely cut Coated (Nickle) H13 Tool Steel in BSD mode to show elements.

The average thickness of Clad is found in the range of 810-825.1µm i.e. 0.8mm approx. from SEM investigation through Back Scattered Electron Detector mode. In BSD Mode it is clearly visible the thickness of clads as it distinguishes two elements easily. The susceptor material ingest microwave promptly at the room temperature until it reaches a higher temperature which is then transferred to coating powder via the conduction/radiation mode of heat transfer until it starts absorbing microwave radiation directly at higher temperatures normally between 400ºC and 600ºC which result in development of Cladding. The microstructure of Cladding consists of eutectic, Ni Grains and dendrite form.

3. c X-Ray Diffraction (XRD)

X-Ray Diffraction is a crystallography technique which is used to find out the atomic and molecular form, shape, and composition of a crystal, when incident beam of X-rays bombards the surface of crystalline atom it diffracts into many specific direction . In this Experiment XRD Patterns are obtained through Bruker instrument AXS with Cu- K_α radiation. The Scan Rate is maintained at 1º/min and the scan range from 10º to 90º of 2θ.

The Typical XRD spectrum of H13 tool Steel used as a base metal for all comparison is shown in Fig 11 , It is seen from the XRD spectrum that that few Iron Nitride (Fe_2N) is present in the surface of H13 tool steel , which is strongest naturally magnetic material, and found in α-FeN state having BCC Structure of ferrite. The highest peak Corresponds to 2θ~44.41º shows the formation of Iron (II, III) oxide (Fe_3O_4), known as mineral magnetite. Further peaks corresponding to 2θ~ 82.16º formation of Cementite (Fe_7C), which improves the hardness of material. While other peaks have less intensity, peaks corresponding to 2θ~ 82.01º is Iron Disilicide ($FeSi_2$) and is found in β- $FeSi_2$ Phase.

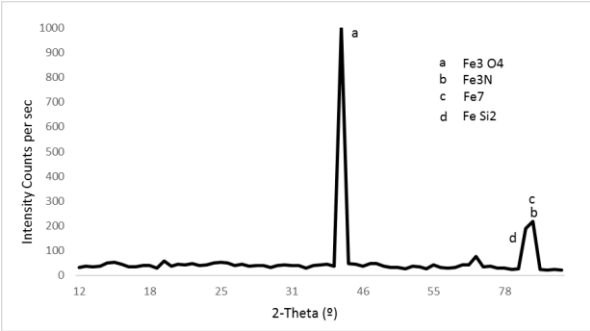


Fig 11 H13 Tool Steel XRD Spectrum

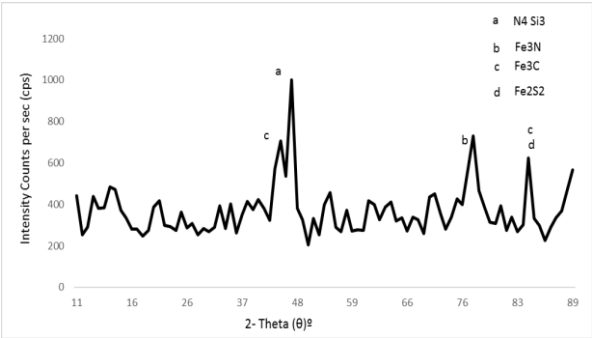


Fig 12 Nitrided H13 Tool Steel XRD Spectrum

XRD spectrum of nitrided H13 tool Steel shown in Fig-12, Gradual graph shows uniform and controlled Nitriding. It is seen from the XRD spectrum that presence of Iron Carbide in ε- Phase, with small amount of chromium vanadium oxide. Highest peak corresponds to 2θ~ 47.74º which is consists of N_4Si_3 Silicon Nitrite in α & β Phase, which provides high melting point, High hardness and Thermal inertness to the crystal, Further Peak Correspond to 2θ~76.99º Shows the formation of Fe_3N which is siderazot and is found in ε- phase. Peak corresponds to 2θ~44.58º shows α-Fe with cementite, and Chevral phase, this line also includes Iron carbide in cohenite which forms a hard, shiny, silver surface. Some traces of Fe_2S_2 Iron sulphide is also found which is an impurity.

XRD spectrum of microwave coated H13 tool Steel shown in Figure- 13, It is seen from the XRD spectrum that there is a presence of lanthanum fluoride carbonate ($FLaO_3$) and Barium carbonate ($BaCO_3$) also called Witherite, the crystals are constantly twinned together in groups of three, which features pseudo-hexagonal forms somewhat looks like bipyramidal crystals of quartz. This forms helps in hardening of steel, as it act as a flux, a matting and crystallizing agent. Highest peak corresponds to 2θ~50.96º which is consists of Bismuth Ferrite ($BiFeO_3$) and Strontium Nickle Oxide (NiO_2Sr), $BiFeO_3$ provides rhombohedral phases, another Peak Corresponds to 2θ~43.94º is Iron Nitride (Fe_3N) and also some traces of Cubic Boron Nitride (C_2BN), Fe_3N Provides HCP Structure to the crystal, which is in ε-Phase, C_2BN is the hardest material after Diamond, Provide High Hardness to the Coating.

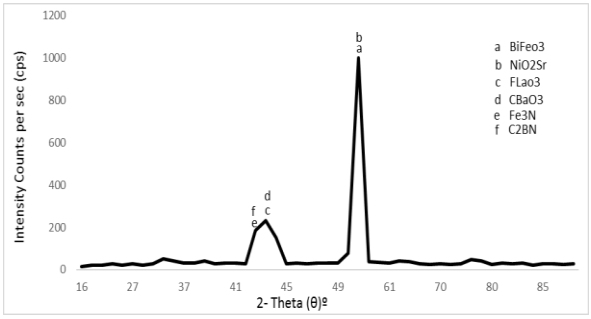


Fig 13 Coated (Nickle) H13 Tool Steel XRD Spectrum.

3. d Microvicker's Hardness (Hv)

Hardness of material has a great influence on the tribological and surface behaviour of all three specimen, for checking Hardness the Specimen is transversely cut and polished as per standard. Profile hardness on micro vicker's hardness is taken at 6 different points and average of the value is taken on HV Scale weight applied is 100g for 10sec. Mitutoyu MVK-H1 Instrument is used to measure micro vicker's hardness.

Table 3 Hardness $HV_{0.1}$

	Specimen	Hardness
1	Unmodified Untreated H13 TS	185.5
2	Unmodified and Heat treated (nitriding)	610
3	Unmodified and Heat treated (Coating)	573
4	Modified Nitrided H13 TS at Nitrided zone	829.5
5	Modified Coated Nickle H13 TS at Coating	788

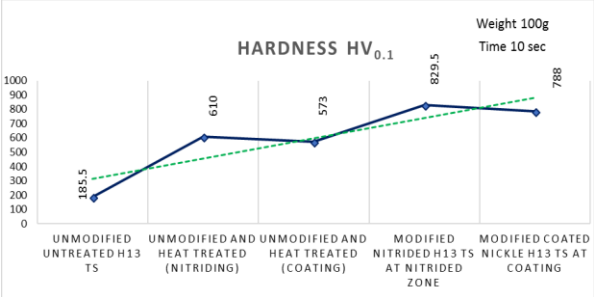


Fig 14 Hardness Profile graph ($HV_{0.1}$)

Conclusion

It is very difficult task to coat metallic material using microwave energy as metallic material does not absorb microwaves at room temperature. In this present experiment nitriding of H13 Tool Steel metallic piece through Gas nitriding and microwave coating of Nickel on H13 Tool Steel through microwave hybrid heating in a 900W microwave system of Frequency 2.45Ghz.

The Major Conclusion drawn from present Work are Discussed Below.

1) Case Hardening of H13 Tool Steel Through Gas Nitriding is Successfully done in Total 120 Hrs.
2) Case Hardening of H13 Tool Steel Through Microwave Coating Is Successfully done in 810 Sec.
3) SEM Image Of Nitrided Sample has Some pores and crack but Nickle coated H13 Tool steel doesn't show these defects.
4) Interfacing at Coating Zone shows Good Metallurgical bonding with the substrate material i.e. H13 Tool Steel.
5) The Interfacing Layer of Nickle Powder is completely melted but melting of interfacing surfaces of H13 Tool Steel is limited to only thin layer due to low depth penetration of surface by microwaves in bulk material.
6) Coating Has the Hardness of HV0.1 788 and Gas Nitriding is of HV0.1 829.5.
7) Due to excellent melting in Coating of Nickle Through MHH it has got perfect interface bonding.
8) Hardness Of gas nitrided sample is Little more than of Coating but coating has little high Wear resistance than Gas nitriding.
9) Hardness of microwave coated sample can be increased by increasing the microwave time.

Acknowledgement

The author acknowledges M/s Coatwell India Pvt. Ltd, India, to provide Gas Nitriding Facility for research work. The authors are also thankful to Mr. Kuldeep, SEM Lab, Dept of Textile Engineering Indian Institute of Technology, New Delhi for SEM, XRD and EDX studies.

References

A.E. Zeghni . and M.S.J. Hashmi (2005), The Effect of Coating and Nitriding on the Wear Behaviour of Tool Steels. *Journal of Materials Processing Technology*, 155-156, 1918-1922

K. Singh & S. Sharma (2016), Development of Ni-based and CeO2-modified coatings by microwave heating, *Materials and Manufacturing Processes,* ISSN: 1042-6914 ,1532-2475 (Online) Journal.

S. S. Akhtar & A. F. M. Arif & B. S. Yilbas (2009), Evaluation of gas nitriding process with in-process variation of nitriding potential for AISI H13 tool steel, *International Journal of Advance Manufacturing and Technology*, 47,687–698

S.H. Yeh, L.H. Chiu, H. Chang (2011), Effects of Gas Nitriding on the Mechanical and Corrosion Properties of SACM 645 Steel, *Engineering*, 3, 942-948

S. Chandrasekaran, S. Ramanathan, and T. Basak (2012), Microwave Material Processing—A Review, *Journal Review AIChE J*, 58: 330–363,

B. Yahaya, S. Izman, M. Konneh, N Redzuan (2014), Microwave Hybrid Heating of Materials Using Susceptors- A brief review, *Advanced Materials Research* Vol. 845 pp 426-430

H. Ollendorf, D. Schneider (1998), A comparative study of adhesion test methods for hard coatings, *Surface and Coatings Technology* 113 (1999) 86–102

S. S. Akhtar & A. F. M. Arif & B Sami Yilbas (2009), Evaluation of gas nitriding process with in-process variation of nitriding potential for AISI H13 tool steel, *International Journal of Advance Manufacturing and Technology*, 47,687–698

J. Yang, Y. Liu, Z. Ye, D. Yang, Shiyu He (2011), Microstructural and tribological characterization of plasma- and gas-nitrided 2Cr13 steel in vacuum, *Materials and Design*, 32 ,808–814

S. Singh, D. Gupta, V. Jain (2015), Recent applications of microwaves in surface coating and material joining; *Journal of Engineering manufacture,* Review Article, 1–15

D. Agarwal (2010), Latest global development in the field of microwave processing; *Material research innovations,* Vol 14 No 1

S. P. Kochhar A.P. Singh (2011), Developments in Microwave Processing of Materials, *Asian Journal of Chemistry*, Vol. 23, No. 8, 3307-3312

M. Yang (2012), Nitriding – fundamentals, modelling and process optimization, Worcester Polytechnic Institute.

D.U. Hong, M. A. J. Somers , J. Agren (2000), Microstructural and compositional evolution of compound layers during gaseous nitrocarburizing, *Metallurgical and Materials Transactions A*,31:195

D. Pye (2003), Practical nitriding and ferritic nitrocarburizing, *Materials Park, OH: ASM International*. ISBN: 0-87170-791-8

B. Wang (2016), An Investigation Of The Adhesion Behavior Of Aluminum On Various PVD Coatings Applied To H13 Tool Steel To Minimize Or Eliminate Lubrication During High Pressure Die Casting. *Journal of Materials Processing Technology.*

F. Czerwinski (2012), Thermochemical Treatment of Metals, *Thermochemical Treatment of Metals,* Intech

M. Avijit, U. Anish (2009), Microwave heating of pure copper powder with varying particle size and porosity, *Journal of Microwave Power Electromagnetic Energy*, ISSN: 0832-7823 (Print) (Online) Journal

M. Oghbaei, O. Mirzaee (2010), Microwave versus conventional sintering: a review of fundamentals, advantages and applications; *Journal of Alloys and Compound*, 494, 175–189

A. M. Hebbale M.S. Srinath (2016), Microstructure and Experimental Design Analysis of Nickel Based Clad Developed Through Microwave Energy, *Perspectives in Science* S2213-0209(16)30066-0;

R.B. Lohit. M. Bhovi (2017), Development of Ni-WC composite clad using microwave energy, *Materials Today: Proceedings*, 4 ,2975–2980.

J. Hardell, B. Prakash (2008), High-temperature friction and wear behaviour of different tool steels during sliding against Al–Si-coated high-strength steel, *Tribology International* 41, 663–671

M. A. Terres, L. Ammari, A. Chérif (2017), Study of the Effect of Gas Nitriding Time on Microstructure and Wear Resistance of 42CrMo4 Steel, *Materials Sciences and Applications*, 8, 493-507

A. Zhecheva, W. Sha, S. Malinov, Ad. Longa (2005), Enhancing the microstructure and properties of titanium alloys through nitriding and other surface engineering methods, *Surface & Coatings Technology*, 2192– 2207

S. Kaushal, D. Gupta, H. Bhowmick (2016), On microstructure and wear behavior of microwave processed composite clad, *Journal of Tribology.*

S. Kaushal, V. Sirohi, D. Gupta, H. Bhowmick and S. Singh (2015), Processing and characterization of composite cladding through microwave heating on martensitic steel, *Journal of Materials: Design and Application;* 0(0) 1–7

V. Sirohi (2015), Surface Modification Of Martenistic Stainless Steel Through Microwave Hybrid Heating; *Journal of Materials: Design and Applications.*

D. Agarwal (2006), Microwave sintering, brazing and melting of materials, *Advanced Processing of Metalsa and Materials, Volume 4*

A. Prasad, D. Gupta, M. Ravi Sankar, A. N. Reddy (2014), Experimental Investigations of Ni/La_2O_3 Composite Micro-Cladding on AISI 1040 Steel through Microwave Irradiation. *All India Manufacturing Technology, Design and Research Conference,* 55, 1-6

D. E. Clark, D. C. Folz, J. K. West (2000), Processing materials with microwave energy; *Materials Science and Engineering* A287, 153–158.

S. Aravindan, R. Krishnamurthy (1999), Joining of ceramic composites by microwave heating; *Materials Letters* 38, 245–249

G.S. Fox-Rabinvich, L. Shuster, G.K. Dosbaeva,(2001), Impact of ion modification of HSS surfaces on the wear resistance of cutting tools with surface engineered coatings, *Wear* 294, 1051–1058.

D. Gupta, A.K. Sharma (2011), Development and microstructural characterization of microwave cladding on austenitic stainless steel, *Surface and Coatings Technology,* 205 (21–22), 5147–5155.

SP Dwivedi, S Sharma (2014), Effect of Process Parameters on Tensile Strength of 1018 Mild Steel Joints Fabricated by Microwave Welding, *Metallogr. Microstruct. Anal,* Springer Science and ASM International, 3:58–69

M.S. Srinath, A. K. Sharma and Pradeep Kumar (2011), A new approach to joining of bulk copper using microwave energy, *Materials and Design* 32 ,2685–2694

A. Bansal, A. K. Sharma, S. Das (2013), Metallurgical and mechanical characterization of mild steel-mild steel joint formed by microwave hybrid heating process, *Indian Academy of Sciences,* pp. 679–686.

D. Gupta, A.K. Sharma (2011), Copper coating on austenitic stainless steel using microwave hybrid heating, *J. Process Mechanical Engineering,* Proc. IMechE Vol. 226 Part E

Design of a cross structure nanoantenna

Parul Goyal, Nishant Shankhwar, and Yogita Kalra

Citation: AIP Conference Proceedings **2009**, 020044 (2018); doi: 10.1063/1.5052113
View online: https://doi.org/10.1063/1.5052113
View Table of Contents: http://aip.scitation.org/toc/apc/2009/1
Published by the American Institute of Physics



Design of a Cross Structure Nanoantenna

Parul Goyal, Nishant Shankhwar, and Yogita Kalra*

TIFAC-center of Relevance and Excellence in Fiber Optics and Optical Communication, Department of Applied Physics, Delhi Technological University, Delhi-110042, India
*Email:dryogitakalra@gmail.com

Abstract. In this paper, a metallic cross nanoantenna (four fold symmetric dual dipole cross-structure) has been presented which exhibits high radiation enhancement and localization of field in the feed gap region of the cross nanoantenna at a wavelength of 500 nm. The modeling and optimization of the designed nanoantenna has been done using COMSOL Multiphysics software. Further properties have been enhanced using geometric optimization.

INTRODUCTION

Optical Nanoantenna is a device which efficiently converts free propagating optical radiation into localized energy [3]. It is analogous to the radio frequency (RF) antenna as former works at terahertz (THz) frequency range while latter at gigahertz (GHz) frequency range. The most highly claimed advantage of optical nanoantenna is their higher efficiency than their classical analogues and their tunability depending on the dimensions of the antenna [4]. A nanoantenna can work as a transmitter or a receiver. When light of certain frequency is made incident on it, an alternating current is induced on its surface that resonates at the same frequency as that of the incident light leading to electric field enhancement in the feed gap of the nanoantenna.

In this paper, a cross structure nanoantenna which is made using gold has been analyzed in ultra violet, visible and infrared region and its various characteristics like scattering cross-section, far field pattern, field enhancement, effect of antenna arm length on scattering have been studied. This nanoantenna has applications in numerous fields that make use of highly localized UV, visible and IR radiation. Techniques such as fluorescence spectroscopy and surface enhanced Raman spectroscopy (SERS) have immense scope for use of this nanoantenna as efficient emitters of localized UV, visible and IR radiation.

DESIGN

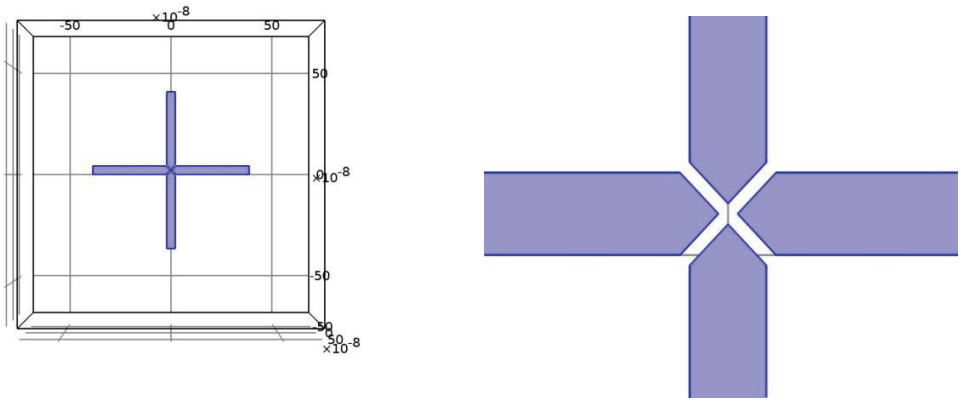
The resonant cross structure nanoantenna consists of four antenna arms of equal lengths made up of gold, two of which are placed parallel to each other and other two are perpendicular meeting at a common local spatial region, the feed gap as shown in Fig 1.

The cross resonant nanoantenna is modeled through finite element method (FEM) simulation using COMSOL Multiphysics®. The length of each of the antenna arm is taken to be 340 nm and the cross section of each arm is 40 nm x 40 nm. The central feed gap is of 10 nm length each between the two parallel arms.

RESULTS AND DISCUSSION

An input power of 1W is made incident on the antenna and light intensity is observed in the feed gap region of the nanoantenna. The field enhancement in the feed gap at resonant wavelength is observed. The various parameters of cross structure nanoantenna like scattering cross section, far field pattern, electric field enhancement, effect of antenna arm length on scattering cross section have been analyzed.

National Conference on Advanced Materials and Nanotechnology - 2018
AIP Conf. Proc. 2009, 020044-1–020044-4; https://doi.org/10.1063/1.5052113
Published by AIP Publishing. 978-0-7354-1725-0/$30.00



a) b)

FIGURE 1.Design of cross structure nanoantenna (a) complete design, (b) zoomed-in design in which centre feed gap is clearly visible.

Scattering Cross Section of Cross Structure Nanoantenna

The variation of scattering cross section of cross structure nanoantenna with respect to wavelength has been analyzed as shown in Fig 2. The maximum scattering cross section has been observed at a resonant wavelength of 500 nm.

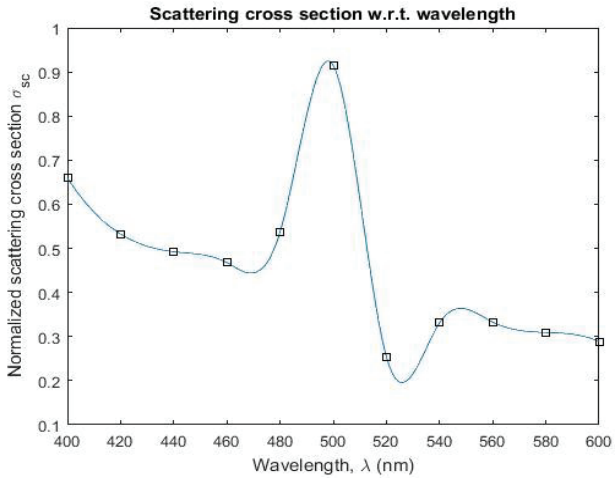


FIGURE 2. Scattering cross section with respect to Wavelength

The electric field in the cross structure nanoantenna was observed at the resonant wavelength of 500 nm and a strong field enhancement in the feed gap region was obtained as shown in Fig 3.

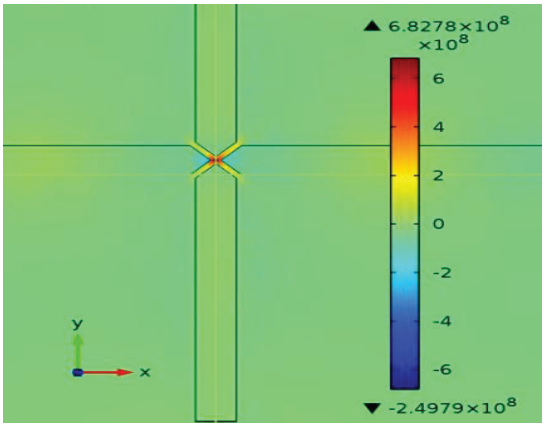


FIGURE 3. Electric field enhancement in the feed gap of the cross structure nanoantenna.

Effect of Antenna Arm Length on Scattering Cross Section

The length of the antenna arm has been varied from 250 nm to 450 nm at the step size of 10 nm at a wavelength of 500 nm. It has been observed that at the length of 340 nm, the maximum scattering has been observed as shown in the Fig 4.

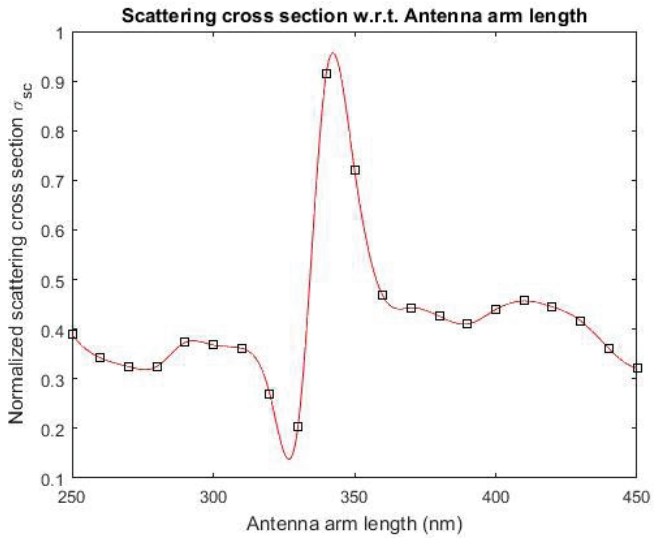
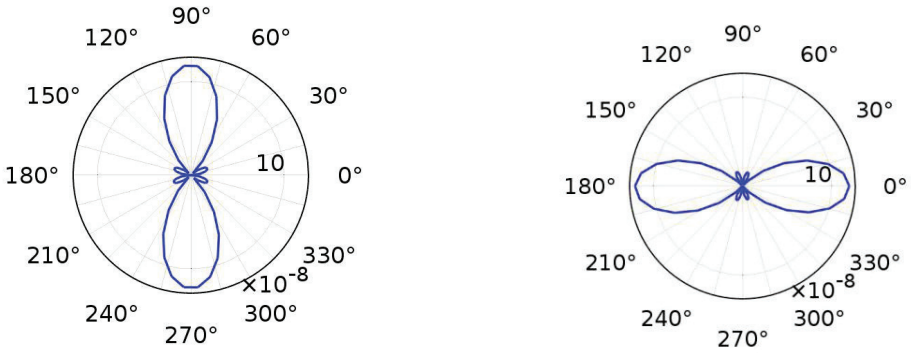


FIGURE 4. Effect of antenna arm length on scattering cross section

Far Field Pattern of Cross Structure Nanoantenna

The far field pattern of the cross structure nanoantenna for x and y polarized wave which is highly directive as observed at the resonant wavelength of 500 nm has been shown in Fig 5.



a) b)

FIGURE 5. Far field pattern of the cross structure nanoantenna (a) For x-polarized wave (b) For y-polarized wave

CONCLUSION

A cross structure nanoantenna has been successfully designed and a strong field enhancement has been observed in the feed gap region at the resonant wavelength. Effect of the variation of the antenna arm length on scattering cross section has been studied. The electric field distributions in the feed gap of the nanoantenna and far field analysis have been successfully analyzed.

ACKNOWLEDGMENT

The authors gratefully acknowledge the initiatives and support provided by the establishment of the TIFAC-Centre of Excellence in Fiber Optics and Optical Communication at Delhi Technological University (Formerly Delhi College of Engineering) Delhi, through the "Mission REACH" program of Technology Vision-2020 of the Government of India.

REFERENCES

1. P. Biagioni, J. S. Huang, L. Duò, M. Finazzi, and B. Hecht, Phys. Rev. Lett. **102**, 256801 (2009).
2. P. Mühlschlegel, H. Eisler, O. Martin, B. Hecht, and D. Pohl, Science **308**, 1607 (2005).
3. A E Krasnok, I S Maksymov, A I Denisyuk, P A Belov, A E Miroshnichenko, C R Simovski, and Yu S Kivshar, Physics-Uspekhi, **56**, 539 (2013)
4. A. Alu and N. Engheta, IEEE Transactions on Antennas and Propagation **61**, 1508 (2013).
5. A. Sundaramurthy, K. Crozier, G. Kino, D. Fromm, P. Schuck, and W. Moerner, Phys. Rev. B **72**, 165409 (2005).

Volume 6 Issue 2 (2018) 145-161 ISSN 2347 - 3258
International Journal of Advance Research and Innovation

Design, Development and Fabrication of a Go-Kart

PK Jain[1], Pankaj Yadav [1], Aditya Natu[2], Mukesh Kumar Mandal[2], Parikshit Garg[1], Geetanshu Ashpilya[1], Ashutosh Panpalia[1], Deept Madhav[3], Kunal Mathur[1]
[1]Department of Mechanical Engineering, Delhi Technological University, New Delhi-110042, India
[2] Department of Production and Industrial Engineering, Delhi Technological University, Delhi, India
3Department of Automobile Engineering, Delhi Technological University, Delhi, India

Article Info
Article history:
Received 24 January 2018
Received in revised form
10 March 2018
Accepted 20 May 2018
Available online 15 June 2018

Keywords- Go-Kart, ANSYS Workbench, Catia, Solidworks, FEA

Abstract
Go-Karts are widely used across the world for recreational or professional racing purposes. The following paper includes the whole designing methodology of the various components of a go-kart, designed and manufactured by students of Delhi Technological University. The go-kart was designed conforming with standard principles and considering all major factors and parameters for design and simulation, developing a fully failure analyzed ergonomic go-kart, powered by an internal combustion engine of capacity 125cc. Detailed calculations were done for all the components and 3-d modelling and simulation were performed on professional softwares. The go-kart was fabricated following the industrial norms

1. Introduction

The main objective behind this effort was to design and manufacture a fully functional racing Go-Kart according to industrial parameters that will perform as per expectations and the standards set by the industry, and in the process enhance our technical skills. The aspects of ergonomics, safety, ease of manufacture and reliability are taken into consideration while designing. Incorporating standard design methodology enabled us to achieve an optimum design. This project provides an opportunity to students like us having ample theoretical knowledge of engineering concepts, to get familiar with the challenges faced during the actual designing and manufacturing phases of real life products, which are very crucial for a practicing engineer.

The initial design of the chassis was made in Solidworks 2016 considering the ease of manufacturability and a proper methodology was followed for production which enabled us to manufacture the Go-Kart at a faster and efficient way. Many parameters were optimized by using higher grade material which weighed less, and ANSYS 18.1 with the feature of topology optimization also played a crucial role. The use of CATIA V5 R20 for making the chassis more ergonomic, hence improving on the driver comfort and performance, as well as the kart performance.

2.Literature Review

The research field in the domain of automobile chassis has evolved a lot with time and progress has been made according to the type of utility of a specific vehicle. Most of the research papers on chassis design focus on factors like proper handling of a variety of loads and perform crash tests for driver safety assurance [1][13] without analyzing the ergonomic aspects. [21] uses finite element techniques to perform analysis on the Go-Kart chassis for stress distribution and deflection but does not include ergonomics and driver comfort. [17] focuses on designing an optimum Ackermann steering geometry using rack and pinion by developing a new mathematical model, but it does not elaborate on design and simulation of real time mechanical components used in the steering assembly, such that the limitations of a particular geometry are highlighted. [19] uses the engine parameters to calculate sprocket dimensions, frictional torque and the factor of safety of the Go-Kart shaft designed, but does not consider the parameters like transmission efficiency that affects the performance of spur gears and chain sprocket assembly and it does not state the maximum corresponding acceleration in each gear.

While designing the Go-Kart chassis, a lot of parameters like driver safety and ergonomics, optimization in weight, rear jacking effect for shock absorption, space for engine cooling have been considered and successfully implemented. Preference of pitman arm over rack and pinion type has been illustrated as well as a comparison graph between the steering angle and the tyre angle was generated using MSCAdams. In addition to steps in [19], maximum acceleration in each gear, load shift calculations, consideration of transmission efficiency and a relation between the tractive force and the kart speed for each gear have been calculated.

***Corresponding Author,**
E-mail-address: pkjain@dce.ac.in
All rights reserved: http://www.ijari.org

3. Kart Specifications

The kart specifications have been chosen so as to achieve the required performance and maximum output, while also keeping in mind the constraints mentioned in the guidelines. Table 1 summarizes a list of the kart specifications.

Table 1 : Kart Specifications [6]

Dimensional Data	
Wheelbase	1100mm
Track Width	880mm
Ground Clearance	1.25inch
Length/Width/Height	1925.4mm/985.4mm/845.1mm
Kerb Weight	95 kg
Fuel Tank Capacity	5 litres
Performance Data	
Engine	Honda CBF Stunner
Engine Technology	PGM-Fi
Max Torque	11 Nm
Max Power	11.15 HP
Power to Weight Ratio	85.27 bhp/tonnes
Transmission Type	5 speed sequential
No. of Speed Gears	5
Ignition Type	Single Spark
Steering System	
Steering wheel diameter	304.8 mm (12 inch)
Spindle to spindle distance	700 mm
Length of steering arm	115 mm
Steering arm angle	17.65 degree
The rod length	305.41 mm
Maximum steering wheel angle	38.78 degree
Brakes System	
Brake pedal ratio	6:1
Master cylinder piston diameter	0.75 inch
Caliper piston diameter	1 inch
Brake disc diameter	170 mm

3.1. Chassis and Design

3.1.1. Definition and Purpose

The chassis is the central frame of a vehicle which has to carry all the components and support all the loads. These loads include the weight of each component and the forces which manifest during acceleration, deceleration and cornering. [13]

Chassis of a go-kart plays a significant role in the jacking of the kart while the kart is cornering. In the absence of a differential in a kart, chassis frame plays following pivotal roles in the performance [22]:

It allows, lifting of the rear inside wheel of the kart while cornering by the virtue of its flexibility and relatively low torsional stiffness. This can cause the kart to turn very smoothly even without a differential.

It acts as a shock absorber which absorbs various shocks and vibrations from the road to provide maximum comfort to the driver.

3.1.2. Design Objectives

The frame of the kart chassis was designed with following aims [5]:

- To have minimum wheelbase and track-width as permitted by rulebook and ergonomic norms to improve cornering performance
- To weigh less than 15 kg.
- To be flexible enough to allow rear 'jacking' effect and absorb road shocks.
- To protect the driver in front and side crash events.
- To provide comfortable posture to a large range of driver statures.
- To be easy to fabricate.
- To have an open airflow over the engine compartment for cooling.

Keeping the above-mentioned objectives in mind, a *tubular ladder chassis* incorporating features of *space frame chassis* was used to facilitate an open ergonomically suitable compartment. The space frame type is commonly used in race car due to its rigidity and ease of construction. [13]

3.1.3. Design Methodology

Figure 1 shows the design workflow that was adopted for this project.

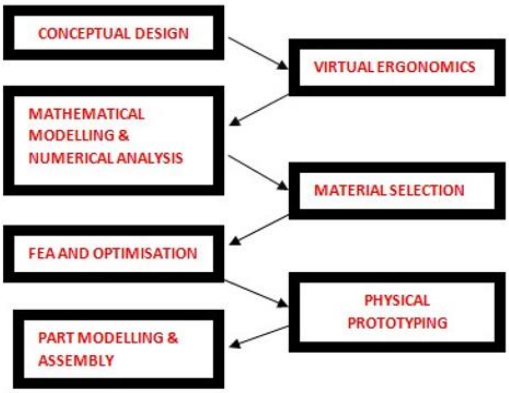


Fig. 1 : Design Methodology

Table 2 : Properties of AISI 1020 [7]

Conceptual design was initially agreed upon keeping all the initial design parameters in view. Thereafter, a virtual model of the go-kart frame was developed using SolidWorks 2016, then static and dynamic simulations were carried out using ANSYS Workbench 12.0. The stress and modal analysis techniques are significantly essential for automotive chassis structure design. It is important to study the dynamic characteristic of the chassis so that resonance and structure failure does not occur on the chassis in working condition. [14].

These softwares greatly reduce the effort and finance required for developing prototypes by providing a platform using which virtual models can be developed and tested.

The model was further analyzed in ANSYS for cornering performance and vibrational analysis etc. and ergonomic analysis was done in CATIA V5 R20. Some changes were made in the design to satisfy all conditions necessary. Multi-body modelling has been performed to accommodate all the other components on the frame.

3.1.4. Chassis Specifications

Material Selection: Various parameters were kept in mind while selecting the frame material which includes availability, cost, machinability and tensile strength. Fig. 2 shows a comparison of the deciding parameters for 3 different materials. After analyzing these 3 materials it was concluded that AISI 1020 will be the material for the chassis due to its following properties:

- Low cost
- High Machinability
- High Availability
- Moderate Strength

Table 3 : Chemical Composition of AISI 1020 [7]

Property	Value
Density	7.87 g/cc
Elastic Modulus	205 GPa
Poisson's Ratio	0.290
Yield Strength	350 MPa
Ultimate Tensile Strength	420 MPa
Thermal conductivity	51.9 W/kg
Coefficient of thermal expansion	11.7 um/m
Brinell hardness	111

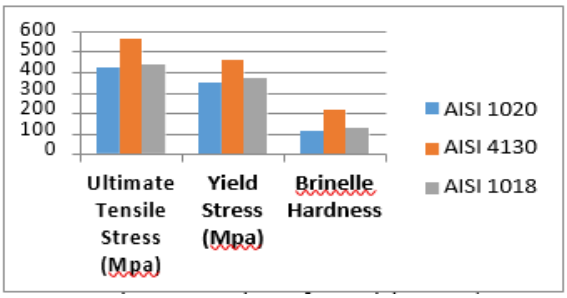


Fig. 2 : Comparison of Material Properties [7]

Table 3 : Chemical Composition of AISI 1020 [7]

Element	Content
Carbon, C	0.17-0.23%
Iron, Fe	99.08 - 99.53 %
Manganese, Mn	0.30 - 0.60 %
Phosphorous, P	≤ 0.040 %
Sulphur, S	≤ 0.050 %

According to American Iron and Steel Institute, following is depicted by 1020:

- The first digit shows that it is plain carbon steel.
- Second digit shows that there are 0 alloying elements.

The last two digits show that the steel contains approximately 0.20% carbon which depicts the best machinability

3.2Cross Section

The cross section for the members was chosen as circular tubular for its higher torsional stiffness for a given area of cross section compared to square and other sections and because of its uniform distribution of stresses resulting in low stress concentrations. The standard cross section determined after market research was 25.4mm outer diameter and 22.4mm inner diameter.

3.3 Equivalence Calculations of Cross Section of Tubes Used :

3.3.1Material AISI 1020

Modulus of Elasticity, E=205 GPa

3.3.2 Case-1

For Outer diameter = 1 inch, Thickness = 1.5 mm

Moment of Inertia, I = π (D⁴ - d⁴)/64 [9]= 8073.32 mm^4

Bending stiffness = EI [9]= 205 * 1000 * 8073.32 $N\text{-}mm^2$

= 1655030655 $N\text{-}mm^2$ = 1655.03 $N\text{-}m^2$

Polar Moment of Inertia, $I_p = \pi(D^4 - d^4)/32$ [9]= 16146.64 mm^4

Torsional Stiffness (per unit length) = GI_p [9]= 1291.73 Nm/rad

3.3.3 Case-2

For Outer diameter = 1 inch, Thickness = 1.65 mm

Moment of Inertia, I = π(D⁴ - d⁴)/64 = 8722.20 mm^4

Bending Stiffness = EI = 205 * 1000 * 8722.20 $N\text{-}mm^2$ = 1788051264 $N\text{-}mm^2$ = 1788.05 $N\text{-}m^2$

Polar Moment of Inertia, $I_p = \pi(D^4 - d^4)/32$ [9]= 17444.40 mm^4
Torsional Stiffness (per unit length) = GI_p =1395.55 Nm/rad

Table 4 : Bending Stiffness of Different Materials

Material	Bending Stiffness (Nm^2)			
	At D=1 in & t= 1.5mm	At D=1.25 in & t=1.5 mm	At D=1 in & t=1.65 mm	At D= 1.25 in & t=1.65 mm
AISI 1020	1655.03	3350.8	1788.05	3633.29
AISI 4130	1695.4	3432.52	1831.67	1831.67
AISI 1018	1655.03	3350.84	1788.07	3633.29

3.4 Final Chassis Layout

The three normal views of frame are shown in figures 3-6.

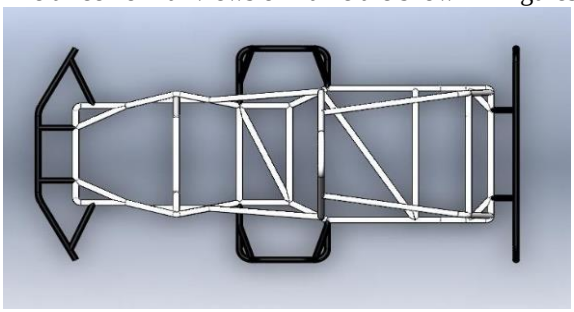


Fig. 3 : Top View of Chassis

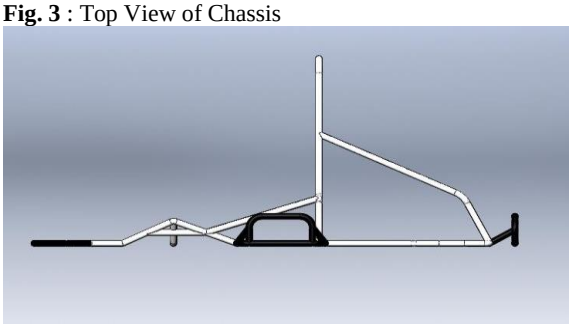


Fig. 4 : Side View of Chassis

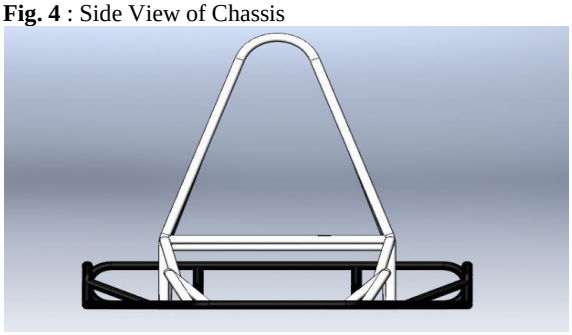


Fig. 5 : Front View of Chassis

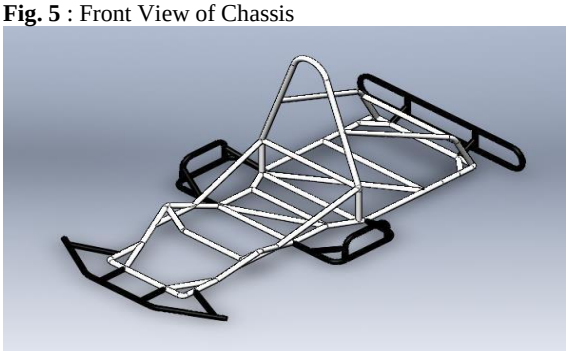


Fig. 6 : Isometric View of Chassis

3.5Final Geometrical Parameters

Major dimensions which associated with the frame have been tabulated in Table 5.

Table 5 : Frame Parameters

Parameter	Value
Wheelbase	1100 mm
Front Track	880 mm
Rear Track	880 mm
Total Length	1925.4 mm
Total Height	845.1 mm
Total Width	985.4 mm
Total Chassis Weight	12.885 kg
Cross Sectional Data	
Type	Tubular
Outer Diameter	25.4 mm
Inner Diameter of Chassis Members	22.4 mm
Inner Diameter of Bumper Members	22.1 mm

3.6. Finite Element Analysis

3.6.1FEA methodology

The finite element theory was employed for predicting the behaviour of chassis under the methods proposed in the Fig.7.

FEA is a method in which the model is divided into small elements, properties of which are then evaluated using general equations of motion and boundary conditions specified during a test. This involves solution of the equation: [2]

[Reaction]=[Stiffness]∗[Displacement]+ [Load]

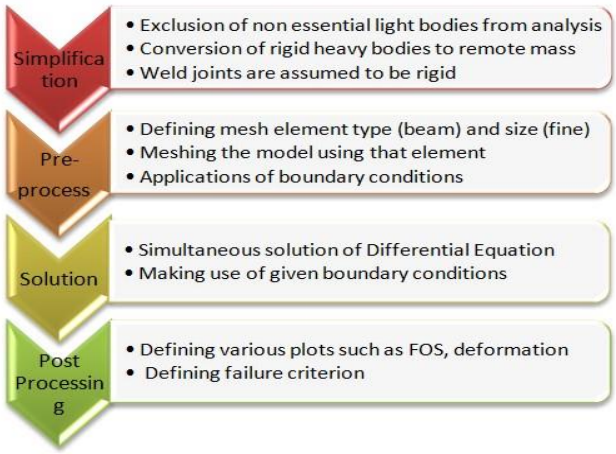


Fig. 7 : Design Methodology [4]

The non-structural elements such as driver and engine were modelled as remote mass acting on their respective mounting positions. Also, the analysis was done in ANSYS Workbench to get better validated results under same loaded conditions.

3.6.2Grid Characteristics

The frame was meshed from beam elements for analysis. In ANSYS Workbench, the model was generated automatically from beam elements with 6 degrees of freedom for every element.

The members which were predicted to be the heaviest loaded were applied 'fine' mesh control to gain better accuracy. The final mesh for ANSYS Workbench is shown in Fig. 8.

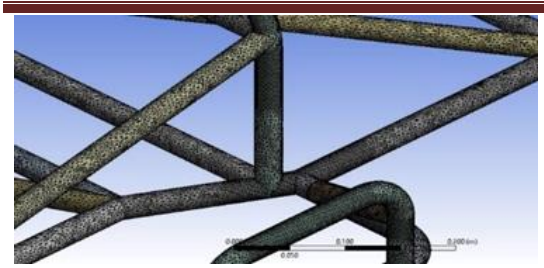


Fig. 8 (a) : Beam mesh in ANSYS Workbench



Fig. 8 (b) : Fine Mesh on the Members

Table 6 : Meshing in Ansys Workbench

Meshing Characteristics	
Physics Preference	Mechanical
Relevance	50
Relevance Center	Fine
Smoothing	Medium
Span Angle Center	Fine
Minimum Edge Length	5.7633e-004 m
Nodes	2242114
Elements	1117384

After setting the mesh, 5 static studies were performed on the model:

a) Static Bending Test
b) Torsional Stiffness Test
c) Front Impact Test
d) Side Impact Test
e) Rear Impact Test

These models have been discussed in detail in the upcoming section.

Loading Diagram Abbreviations: -

- Red Arrows- Driver Weight (600N)
- Red Arrows- Engine Weight (300N)
- Red Arrows- Impact Forces (N)
- Blue Tags- Fixed Supports
- Yellow Arrows- Gravity (m/s^2)

(a) Static Bending Test: In this test, various stresses developed in a fully loaded chassis were analysed.

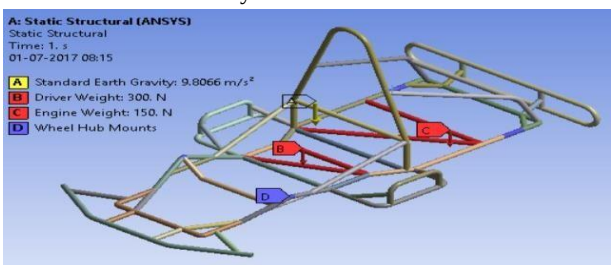


Fig.9 (a) : Loading Diagram

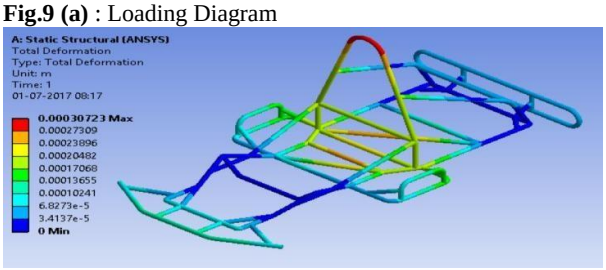


Fig.9 (b) : Total Deformation

Fig.9 (c) Equivalent Stress

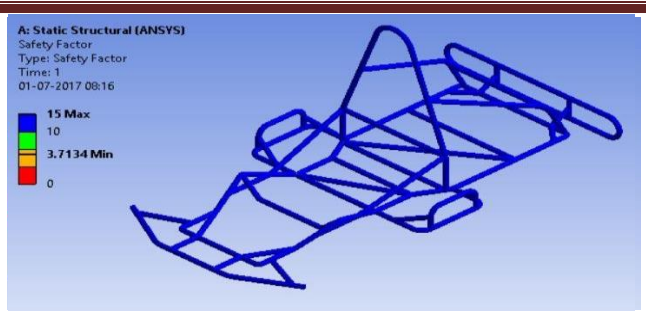


Fig.9 (d) Factor of Safety

Fig. 9 : Results of Static Bending Test

It can be seen from the chart, maximum deformation in base member is 0.27 mm at driver seat during sagging which is acceptable. The highest combined stress was encountered at the side bumpers and its value was 129.5MPa.

The yield stress of AISI 1020 is 350MPa.

$FOS = \frac{Yield\ Stress}{Max\ Combined\ Stress} = 3.71$ [9]

So, the minimum FOS evaluated is 3.71 which is safe against an industrial reference value of 1.5. So, our design is validated for static bending.

(b) Torsional Stiffness test: This test determines the resistance offered by the chassis frame against a twist which is normally developed during cornering, or when the vehicle encounters a bump in the road.

Table 7 : Boundary Conditions

Loads	Driver, Engine, and Gravity loads at mounting positions. A couple of 6035N is applied on the Rear Wheel Hub Mount positions of
Constraints	Front Wheel Hub mounting positions
Gravity	On

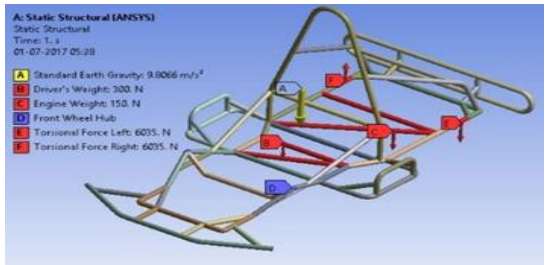


Fig.10 (a) : Loading Diagram

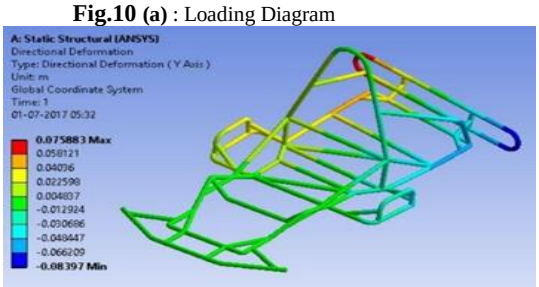


Fig.10 (b): Directional Deformation

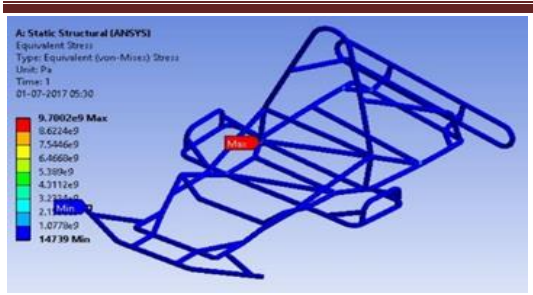


Fig.10 (c): Equivalent Stress

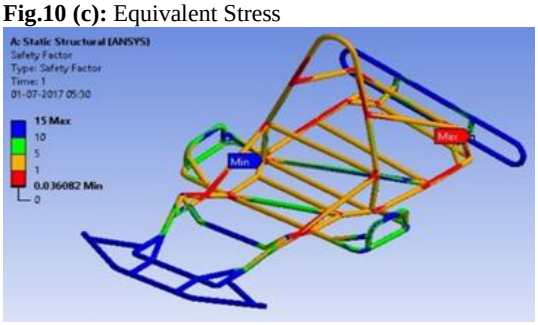


Fig.10 (d): Factor of Safety

Fig. 10 : Results of Torsional Rigidity Test

Directional Deformations at the Rear Wheel Hub Mount positions are 44 mm and 54 mm.

Twist = $\tan^{-1}\left(\frac{D_1 + D_2}{L}\right) = \tan^{-1} 0.1633 = 9.276°$

Torque = 3621 Nm

Torsional Rigidity = Torque⁄Twist

= 3621⁄9.276 = 390.36 Nm/deg

Since this value lies within the standards adopted, it is acceptable.

(c) Front Impact test: This test determines the effect of a crash on the chassis at speeds up to 70 km/h (determined to be the maximum speed when brakes are applied at least for 0.5 seconds before crash).

The collision time in a chassis without a crumple zone is statically averaged to 150ms. But the chassis of this go kart has a mild steel bumper and a thin deformable tube which can act as a crumple zone and increase the collision time to 200ms.

$F = m*(\Delta v/\Delta t)*0.5 = 150 * 70/0.2 * 5/18 *1/2$

F = 7.29 kN

In terms of G, F = 4.955G

Table 8 : Boundary Conditions

Loads	7.29kN applied on front bumper members
Constraints	Front and Rear Wheel Hub Mount Positions
Gravity	On

The FOS of the front cross members amounts to 3, which indicates that they will not fail during collision. However, the FOS in the cockpit has a minimum value of 15, which is safe enough.

Our model can be said to be validated against front impact test at a speed of up to 70 km/h against an industrial reference value of 1.5.

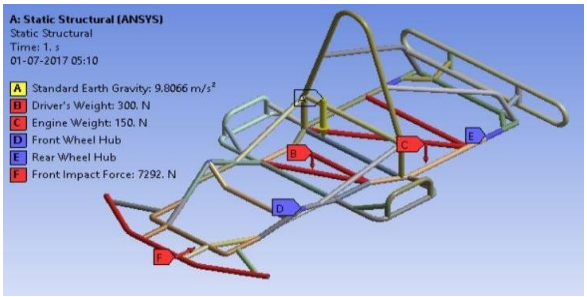
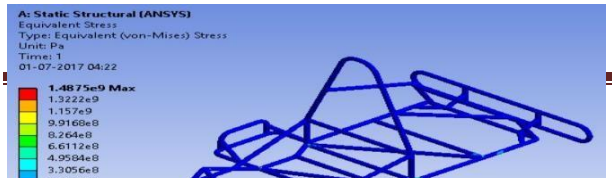


Fig.11 (a): Loading Diagram



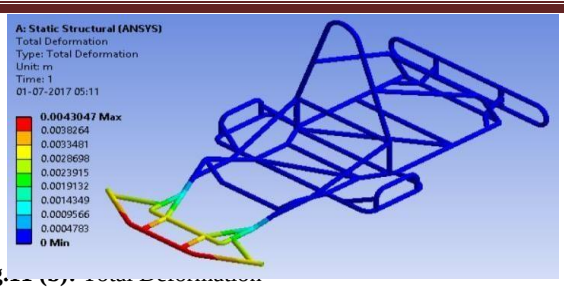


Fig.11 (b): Total Deformation

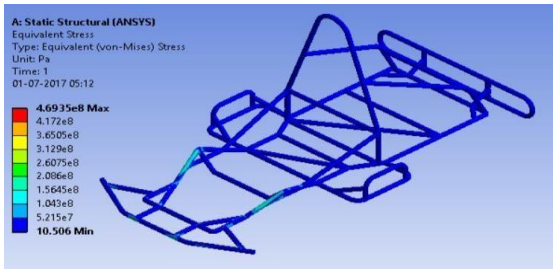


Fig.11 (c): Equivalent Stress

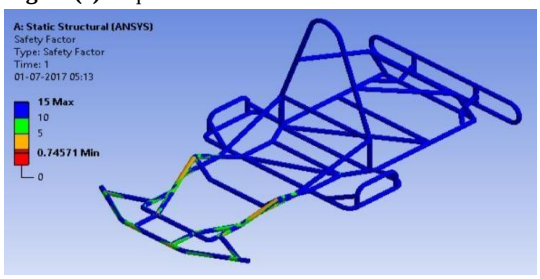


Fig.11 (d): Factor of Safety

Fig. 11: Results of Front Impact Test

(d) Side Impact test: This test determines the effect of a crash on the chassis when another kart collides with it on the side members at an angle of 90°. The maximum speed difference between the karts in such a collision is taken to be 80 km/hr.

$F = m*(\Delta v/\Delta t)*0.5 = 150*(22.22/0.2)*0.5$

F = 8.33 kN, In terms of G, F = 5.66 G

Table 9 : Boundary Conditions

Loads	8.33kN applied on side bumper members
Constraints	Front and Rear Wheel Hub Mount
Gravity	On

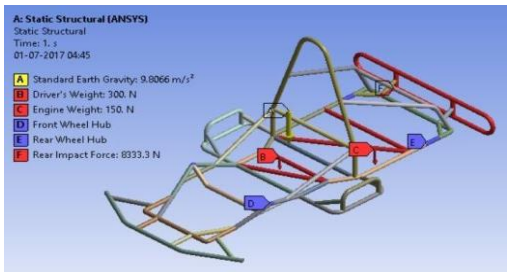


Fig.12 (a): Loading Diagram

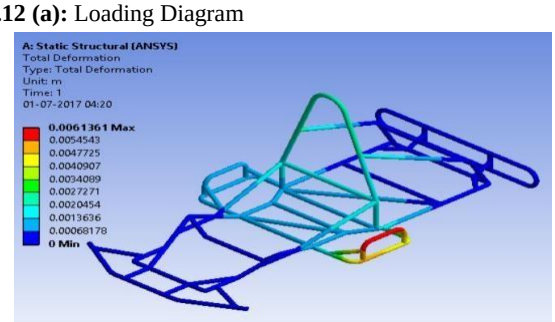


Fig.12 (b): Total Deformation

Fig.12 (c): Equivalent Stress

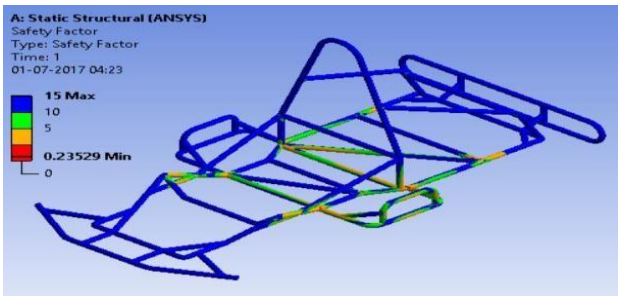


Fig.12 (d): Factor of Safety

Fig. 12 : Results of Side Impact Test

The FOS of the cockpit amounts to 5 which indicates that they will not fail during collision. Our model can be said to be validated against side impact test at a speed difference of up to 80 km/hr against an industrial reference value of 1.5.

(e) Rear Impact test: This test determines the effect of a crash on the chassis when another kart collides with it on the rear members. The maximum speed difference between the karts in such a collision is taken to be 80 km/hr.

$F = m * (\Delta v/\Delta t)*1/2 = 150 * 22.22/0.2 = 8.33$ kN

In terms of G, F= 5.66G.

Table 10 : Boundary Conditions

Loads	8.33 kN applied on side bumper members
Constraints	Front and Rear Wheel Hub Mount Positions
Gravity	On

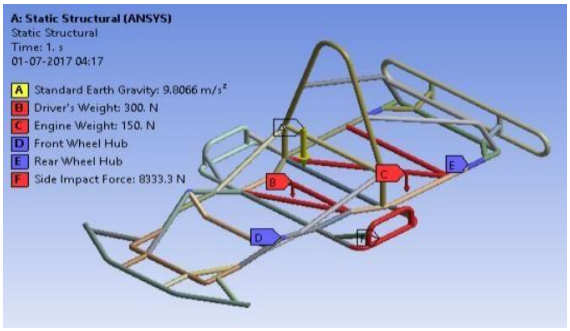


Fig.13 (a): Loading Diagram

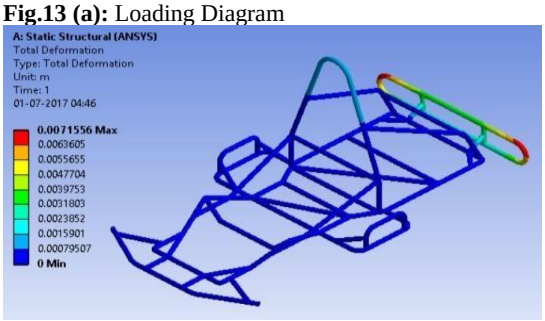


Fig.13 (b): Total Deformation

Fig.13 (c): Equivalent Stress

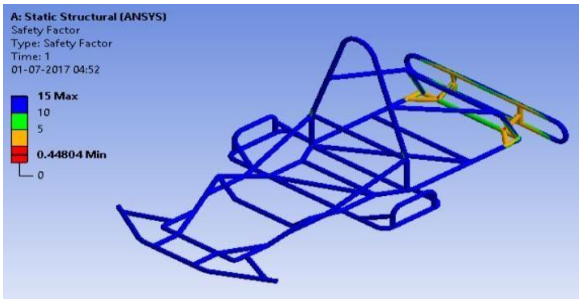


Fig.13 (d): Factor of Safety

Fig. 13 : Results of Rear Impact Test

The FOS of the cockpit amounts to 15 which indicates that they will not fail during collision. Our model can be said to be validated against side impact test at a speed difference of up to 80 km/hr against an industrial reference value of 1.5.

F. Modal Analysis

The global vibrational characteristic of a vehicle is related to both its stiffness and mass distribution. The frequencies of the global bending and torsional vibration modes are commonly used as benchmarks for vehicle structural performance. Bending and torsion stiffness influence the vibrational behavior of the structure, particularly its first natural frequency [16].

This study utilizes modal analysis to generate the natural frequencies and mode shapes of the chassis structure. If any of the excitation frequencies coincides with the natural frequencies of the chassis, then resonance phenomenon occurs. The chassis will undergo dangerously large oscillations, which may lead to excessive deflection and failure. The vibration of the chassis will also cause high stress concentrations at certain locations, fatigue of the structure, loosening of mechanical joints, creation of noise and vehicle discomfort [15]. Result from Modal Analysis is important as it can also predict the response of structural parameters under dynamic loading condition. Mode shapes simulated from Modal Analysis can provide the information of how the chassis structure will naturally displace. ANSYS Workbench Mechanical is used as pre-processor, solver and post-processor for the modal analysis [4]. The mode shapes are extracted using Block Lanczos method. Block Lanczos method has been used in studies for extracting mode shapes and natural frequencies.

Table 11 : Frequencies and Deformations at each modes

Mode	Frequency	Maximum Deformation
1	47.048	0.88484m
2	55.138	0.77644m
3	69.569	0.85726m
4	77.261	1.3113m
5	88.132	0.94202m
6	94.939	0.66217m
7	107.76	0.76488m
8	115.12	1.1874m
9	125.01	0.77368m
10	141.79	0.66935m

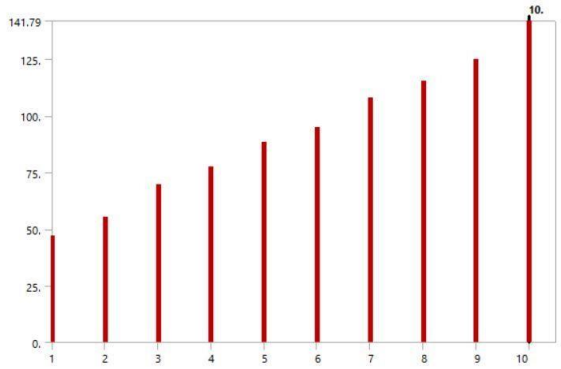


Fig. 14 : Natural Frequencies of Chassis

The analysis found that the natural frequencies extracted using Block Lanczos Method produced 10 mode shapes within 40-150 Hz frequency range. All mode shapes produced natural frequencies which is not coinciding with the primary imbalance frequency 166.66 Hzor secondary imbalance frequency 333.33Hz of engine, which is safe and comfortable. Thus, no resonance will occur, and design is hence validated.

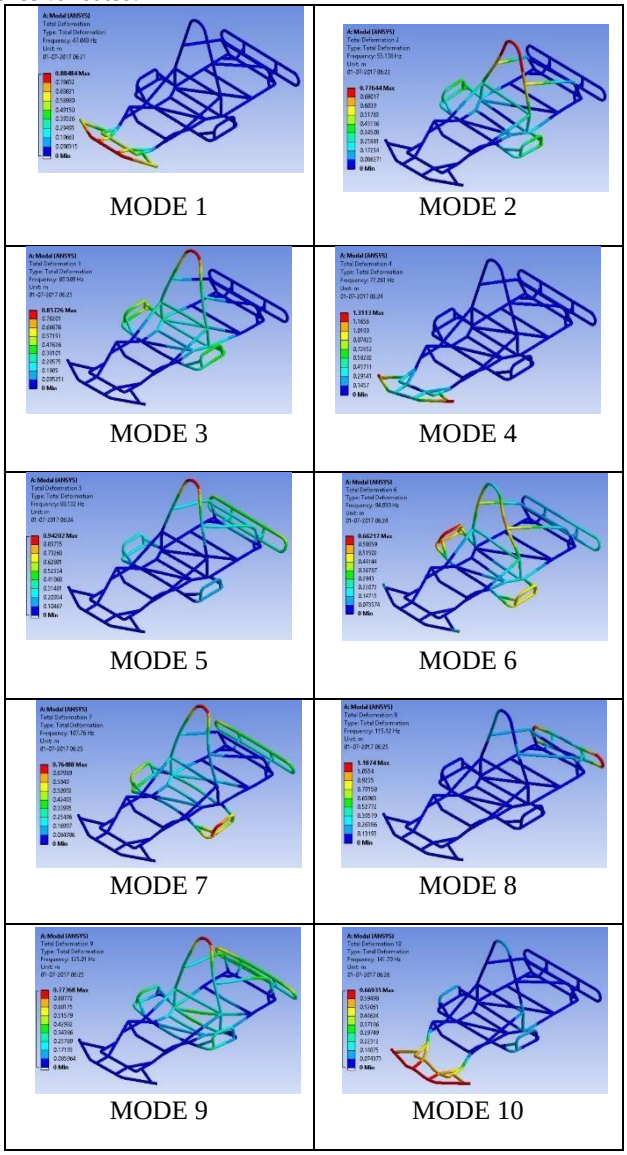


Fig. 15 : Deformation Plots at Different Frequencies

G. Ergonomics

(a) Purpose

Ergonomics is the study of designing equipment and devices that fit the human body and its cognitive abilities. In this project the design of the go kart should be such that all its controls should be comfortably in the reach of the driver's upper body [4].

Also, the vision of the driver should be unobstructed by any part of the go kart as in a dynamic event, vision plays a key role in the driver's and ultimately kart's performance.

(b) Methodology

Ergonomic analysis for the kart was performed in CATIA V5 R20 using its Human Builder and Human Activity Analysis workspaces. The test model or the manikin was first selected on the basis of the stature of the driver. Details are given in Table 12.

Table 12 : Manikin Properties

Property	Value
Population	Korean
Stature Percentile	90
Weight Percentile	6.4
Height	1780 mm
Weight	55 kg
Posture	Custom
CG Height from Ground	170 mm

The manikin was then positioned into the Kart using I-K behaviours and posture-editing.

The Fig. 16 shows the manikin model positioned in the kart, which shows that the knees should be bended outwards for maximum comfort. The red dot represents the C.G. of the driver.

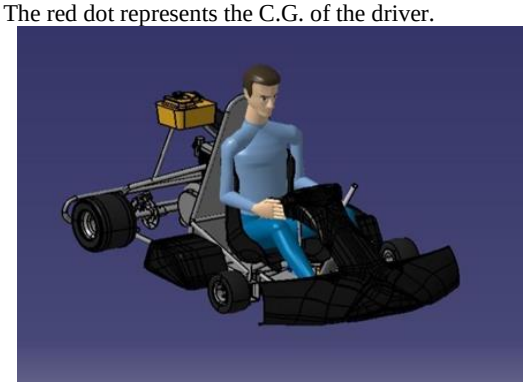


Fig. 16 : Ergonomic Model Isometric

The Fig. 17 shows the peripheral vision contours from the driver's point of view in binocular vision mode. The clear area in the middle represents good focus while the blurred region represents unfocussed vision range. The solid red contour shows the blind spots of the driver without moving.

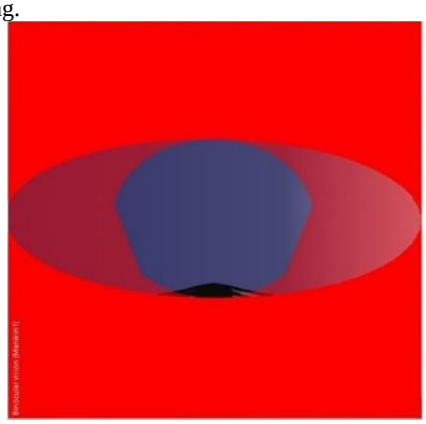


Fig. 17 : Field of Vision

Next an upper limb movement test was performed on the test model to evaluate the reaction performance of the driver in the current

posture setting. This test is known as RULA (Rapid Upper Limb Assessment).
The driver model was evaluated by RULA and an average score of 3 was given.
This score category shows that the driver does have a fine reflex action. However, this score may be attributed to correct posture application in the model.

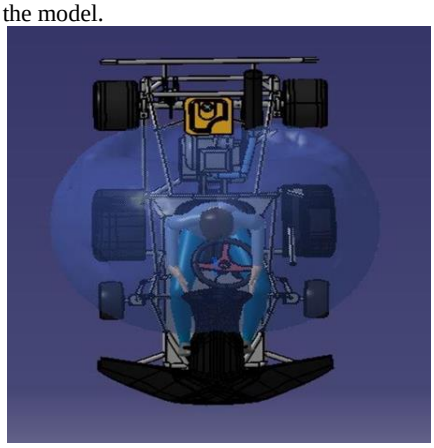


Fig. 18 : Reach Envelope

The above figure shows the reach of the hands of the driver while being properly positioned in the kart. The envelope validates that the driver can reach out for all control and emergency systems in dynamic and emergency conditions such as steering wheel, gear shifter, kill switch, fire extinguisher etc.

4. Steering

(a) Design Methodology

The methodology according to which steering system is designed is: it should have high sensitivity, directional stability, low minimum turning radius, desired steering ratios and the most important, it should follow Ackermann geometry to reduce tire wear. During turning if I-centers of all wheels meet at a point, then the vehicle will take turn about that point which results in pure rolling of the vehicle. The condition is called the Ackermann condition and this principle is known as Ackermann principle [17].
To select suitable steering system for the Go-Kart, 2 types of steering systems i.e Pitman Arm steering and Rack and Pinion arrangement have been studied. Amongst these, we chose Pitman Arm arrangement over the rack and pinion arrangement to its simplicity and low cost. Different properties of these two steering systems is shown in Table 13.

Table 13 : Pitman Steering VS Rack and Pinion Steering

Pitman Steering	Rack and Pinion
Simple 4 bar arrangement	Complex
Provides stiffness	Excessive free-play
Easy to fabricate	Difficult to fabricate/construct
Low cost of manufacturing	High cost of manufacturing
High chances of failure for long use of triangular plate	Less chances of failure for long use of rack and pinion gear

(b) Geometry Specifications

An optimum steering geometry was determined keeping in mind the desired steering ratio required for excellent vehicle control and following the Ackermann principle to the highest degree.
Factors keeping in mind for steering geometry design-

- Assumed values considering ergonomics and IKC rulebook.
- Wheel base- 1100mm
- Track width-880mm (80% of wheel base)
- Kingpin pivot to kingpin pivot point – 700mm.
- Minimizing turning radius
- Ackerman deviation for less range.

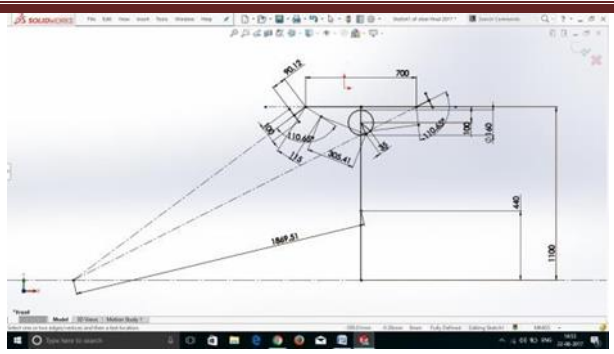


Fig. 19 (a) 2D sketch of steering linkage

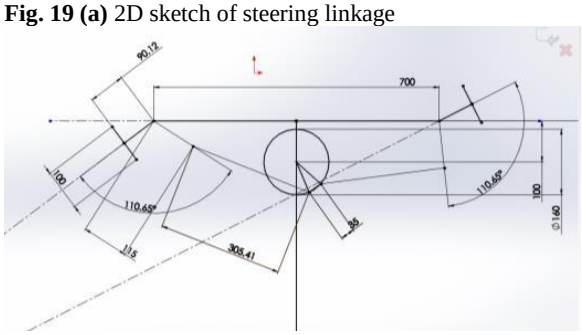


Fig. 19 (b) 2D sketch of steering linkage

Fig. 19 (a) and Fig. 19 (b) shows a 2D sketch of steering linkage which is made with the help of SolidWorks 2016. Fig. 20 shows the CAD model of steering system

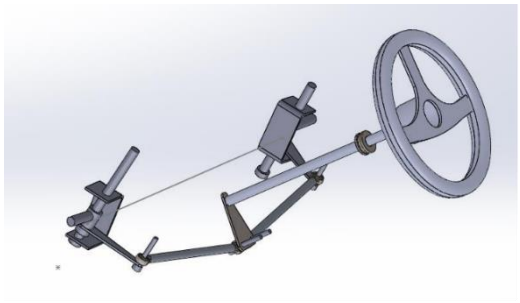


Fig. 20 : CAD model of Steering system

Table 14 : Values of Different Steering Parameters

Wheelbase	1100 mm
Track width	880 mm
Steering wheel diameter	304.8 mm (12
Spindle to spindle distance	700 mm
Length of steering arm	115 mm
Steering arm angle	17.65 deg
The rod length	305.41 mm
Maximum steering wheel angle	38.78 degree
Deviation of inner wheel at Ackermann	36.85 degree
Deviation of outer wheel at Ackermann	26.03 degree

(c) Turning Radius

The minimum turning radius of kart, as calculated came to be about 1.89m but due to deviation from Ackermann principle it will be locked at 1.79m so steering stops needed at position where turning radius is 1.89m to avoid over or under steering effect and wear and tear of tires.

(d) Steering Ratio

For providing a proper control over the kart, the steering ratio was kept nearer to 1:1 since it helps in good handling at high speeds and a better sense of control for the driver while maintaining high sensitivity for a faster response during turning.
Curve was generated with model in MSCAdams shown in figure 21.

e) Calculated Results

1. Steering Effort = 110-120 N (115.95 N at static condition)
2. Ackermann percentage = 105.3% (The values of Ackermann percentage come out to be greater than 100% which means the kart will have a tendency to oversteer).

3. Steering ratio= 1:1

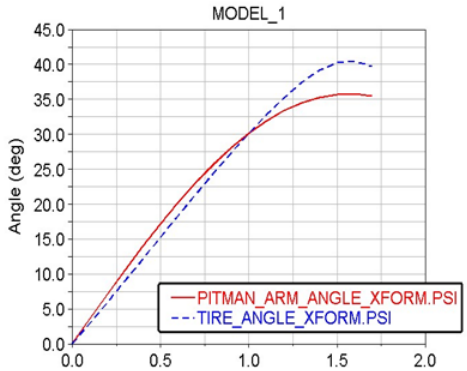


Fig. 21 : Comparison between steering angle and tyre angle

(e) Calculated Results

1. Steering Effort = 110-120 N (115.95 N at static condition)
2. Ackermann percentage = 105.3% (The values of Ackermann percentage come out to be greater than 100% which means the kart will have a tendency to oversteer).
3. Steering ratio= 1:1

(f) CAE on Steering

The following stress and strain simulations have been done using ANSYSv12. It accounts for the deformation under applied stress for the member used on the front wheels connected to chassis with fixed and knuckle and ultimately to the tires of the kart.

(i) Knuckle Mount Simulations

The following simulations were done on the ANSYS V12 which accounts for the deformation under the applied force of about 320 N approximately.

On the basis of load applied the following results have been obtained. Different iterations for different materials has been performed out of the iterations, mild steel hardened suits best.



Fig. 22 (a) : Kingpin mounting

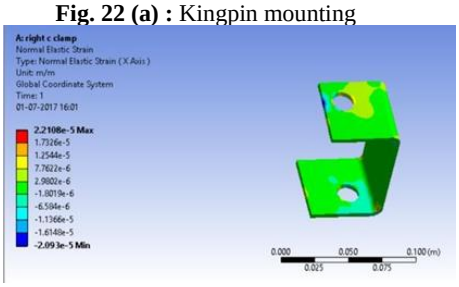


Fig. 22 (b) : Normal Elastic Strain Developed

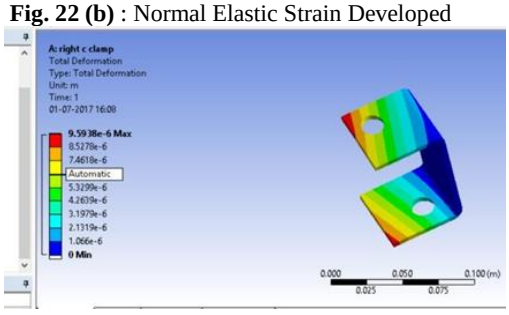


Fig. 22 (c) : Total Deformation under the Applied Stress

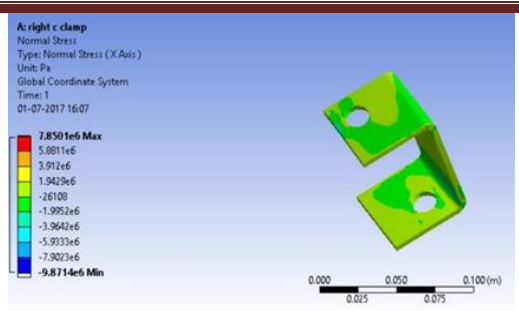


Fig. 22 (d) : Normal Stresses Developed

(ii) Knuckle Simulations

The following simulations have been done on the ANSYSv12 which accounts for the deformation under the applied force of 320 N approx. On the basis of load applied the following results have been obtained. For knuckle EN9 suits best as it has high weldability low hardness and is easily available.

Table 15 : Material Properties [7]

Materials	**EN8**	**EN9**	**EN 24**	**Plain Carbon Steel**
Density	7.8	7.8	8.17	7.8
Yield Strength(MPa)	465	480	680	220.6
Hardness (HRC)	51	48	55-65	38-40
Machinability	Very Good	Best	Worse	Good

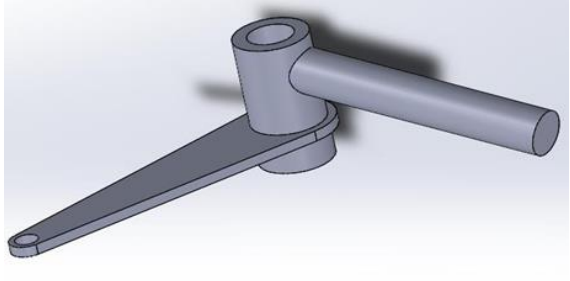


Fig. 23 (a) : CAD model of Steering Knuckle

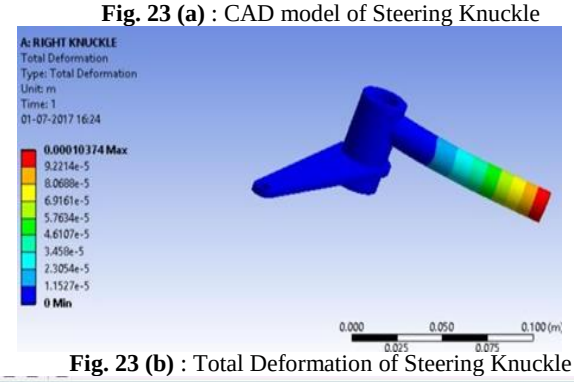


Fig. 23 (b) : Total Deformation of Steering Knuckle

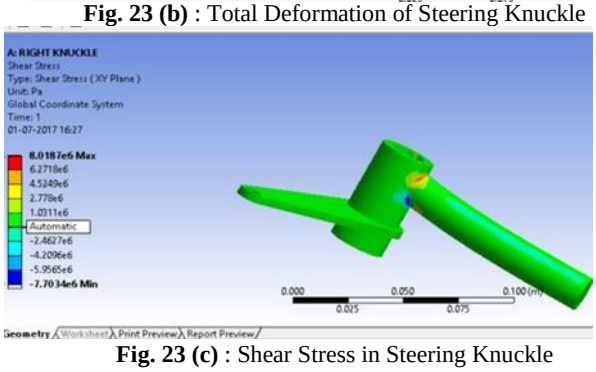


Fig. 23 (c) : Shear Stress in Steering Knuckle

Fig. 23 (a) shows the CAD model of steering knuckle.

Fig. 23 (b) shows the total deformation in the steering knuckle under the applied load or stress.

Fig. 23 (c) shows the distribution of the shear stress induced in the knuckle.

(g) Wheel Alignment Selection

Castor: We will provide positive caster angle of 10 degrees, since it will be helpful in proper weight transfer of the kart and the driver to the rear outer wheel of the kart during a turn which significantly reduces the weight on the inner rear wheel.

Camber: We provided zero camber angle because providing camber in go-kart will increase the wire wear during straight lines movement. Providing a caster angle also helps in giving a favorable automatic camber effect to the kart.

Toe: We gave toe of 3 degrees of angle for reducing turning radius and in dynamic condition tyres tend to toe out due to scrub radius so toe is compensated. It also helps in straight line stability with cornering compromised a little.

Kingpin axis inclination: We have provided 10 degrees, since it decreases scrub radius and induce jacking of rear inner tyre while turning at high speed.

5. Engine and Transmission

(a) Engine

For selecting the engine for our project, the following factors were considered in the listed order of priority:

- High Initial Torque
- High Torque at corner exits
- Cost
- Availability
- Power by weight ratio
- High power

Based on these factors, it was concluded that a manual transmission drive is essential for obtaining the desired performance characteristic curves. Further, the limitation on size of the engine confines the available choices of engines. The models of vehicle engines studied on the basis of the above mentioned criteria were: By considering factors such as maximum power, torque delivered by the engine, we have chosen the Honda Stunner engine for our go kart. The engine is heavier and more expensive than the Bajaj Discover engine, but this factor has been compromised due to the fact that Honda stunner engine is mounted vertically straight unlike the Bajaj Discover engine, which reduces our wheel base, thus making our chassis more compact.

Table 16 : Engine Specifications [8]

Displacement	124.7cc
Type of Fuel	Petrol (Spark Ignition)
Number of Strokes	4
Type of Cooling	Air cooled
Maximum Power	11.6 bhp @ 8000 rpm
Maximum Torque	11 Nm @ 6250 rpm
Air Filter	Viscous type
Bore of Engine	52.4 mm
Stroke of Engine	57.8mm
Compression Ratio	9.2:1
Clearence Volume	15.2073cc
Volumetric Efficiency	0.85
Mileage	60kmpl

(b) Engine Mounting

Engine mounting is a very crucial point that is needed to be taken care of. Proper mounting of the engine prevents the engine from possible damage as well it damps the engine vibrations.

The engine is bolted to the space frame chassis using high strength nut-bolts and washers at three points.

(c) Engine Support Base

The 28.64 Kg 124.7cc Honda CBF Stunner engine is mounted on a U-shaped member placed on a flat metal plate with 6mm. This support member is made from AISI 1020 steel and the failure while minimizing the weight. FEA simulation using Ansys of the support are carried out in order to check if the used system will perform adequately or not.

Static analysis result of the ANSYS Static Structural solver is shown. The analysis showed that the maximum stress within this member is 16.414 MP which is way beyond the yield strength of the AISI 1020 material, hence there are no chances of member failure during a race. The modal analysis results are shown in Fig. 25. As we know that the maximum speed of the engine is 10000 RPM which gives a primary imbalance frequency of 166.66 Hz and secondary imbalance of 333.33Hz. The modal analysis shows that the smallest natural frequency of the base member is 921.3Hz which is larger than the engine's frequency.

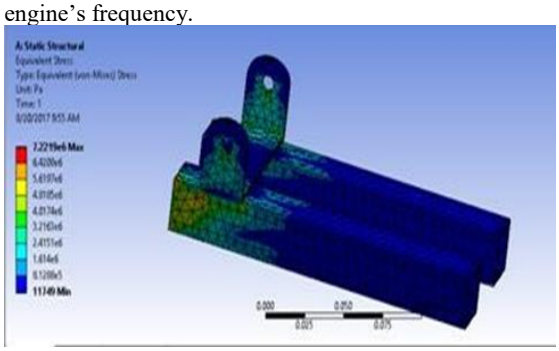
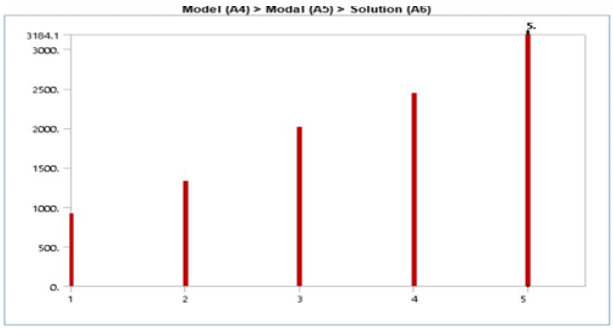


Fig. 24 : Equivalent Stress on Engine Support Base



Model (A4) > Modal (A5) > Solution (A6)

Mode	Frequency [Hz]
1.	921.83
2.	1331.5
3.	2011.6
4.	2443.4
5.	3184.1

Fig. 25 : Modal Analysis

(d) Fuel Tank

Fuel tank is mounted just above the engine slightly backwards and sufficient space is provided between engine and fuel tank. The fuel tank is bolted to the chassis, which has a capacity of 5 litres.

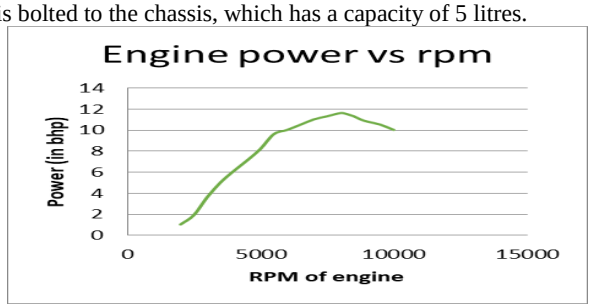


Fig. 26 (a) : Engine Power vs RPM

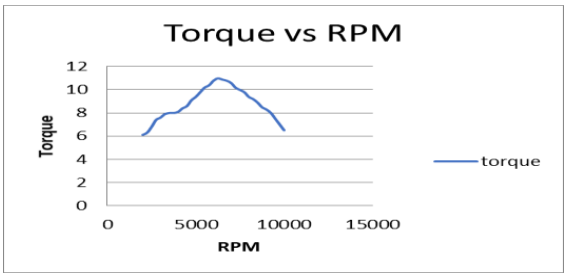


Fig. 26 (b) : Torque vs RPM
Fig. 26 : Engine Performance Curves

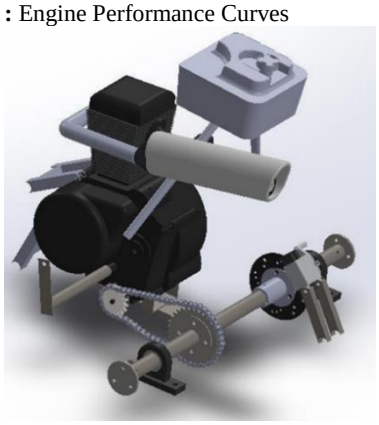


Fig. 27 : Engine CAD Model and Transmission Assembly
CAD model of the engine and transmission of the kart made using Solidworks.

(e) Transmission

A transmission is a machine that consists of a power source and a power transmission system, which provides controlled application of the power. Often the term transmission refers simply to the gearbox that uses gears and gear trains to provide speed and torque conversions from a rotating power source to another device. Often, a transmission has multiple gear ratios with the ability to switch between them as speed varies [18].

Honda CBF Stunner 125cc engine is accompanied by a five speed sequential gearbox with the following gear ratios.

Table 17 : Gear Ratios [8]

Primary Reduction Ratio	3.35
1st gear	3.076:1
2nd gear	1.944:1
3rd gear	1.473:1
4th gear	1.19:1
5th gear	1.038:1
Secondary or Final Reduction Ratio	3.071:1

For secondary reduction:
No. Of teeth on driver sprocket =14
No. Of teeth on driven sprocket =43
Calculation of maximum speed of bike:
Max Speed = r * ω
r = radius of rear tyre; ω = angular velocity of rear wheel
Aspect ratio is= 90 % and the width of tyre is 100mm.
Therefore, height of tyre= (90*100) / 100 = 90mm
Radius of Tyre (r) = (Rim Diameter * 0.5) + Tyre Height
= 309.5mm = 0.3095m. (Rim Diameter = 17 inches)
Angular velocity Maximum (ω)

$$= \frac{Max\ Engine\ RPM * 2\pi}{Primary\ Reduction * 5th\ gear\ ratio * secondary\ reduction * 60}$$

= (10000*2π) / (3.35*3.071*1.038*60)
= 98.063 rad/s.
Speed = 0.3095 * 98.063 = 30.35 m/s
= 109.26 km/hr

We made an indirect approach to calculate the appropriate size of the sprocket for limiting the maximum speed of the go-kart to 70 kmph (19.44m/s), by using the max. speed of the Honda stunner.
Max. Speed of the Honda stunner= 109.26 kmph = 30.35 m/s
∴ Max. RPM of the bike wheel (rear)= 936.41 rad/s.
∴ Max. RPM of secondary reduction driver sprocket
= Max wheel rpm * secondary reduction = 936.41 * 3.071 = 3003.1558 rad/s.
Also, RPM of the go-kart wheel at the Max Speed.

$$\frac{\max speed * 60}{2\pi * radius\ of\ wheel} = \frac{19.44 * 60}{2\pi * 0.1397} = 1328.83 \text{ rpm}$$

Required sprocket ratio (secondary reduction) * RPM of the go-kart wheel= 3003.155 rad/s. Required sprocket ratio = 3003.155/1328.83 = 2.26
No. of teeth on the required sprocket = 2.26*14 = 31.64 ≈ 32 (No. of teeth has to be a whole number).
Hence, we choose a sprocket ratio of 2.26, because it will serve both the purpose of giving high initial acceleration and limit the top speed to 70 kmph.
Coefficient of friction = 0.85 (For dry slick tyres)
Max force due to friction = Vertical force on wheels*coefficient of friction = (104*9.8)*0.85 = 866.32N
Maximum frictional torque on the rear wheels = Force on rear wheels * radius of rear wheel= 866.32*0.1397 = 121.024 Nm
866.32 N is the maximum external force available to the rear wheels for driving the kart.

Table 18 : Maximum theoretical speed for each gear at maximum RPM

Gear	Maximum Velocity
1st gear	6.28m/s = 22.60 kmph
2nd gear	9.939m/s = 35.78 kmph
3rd gear	13.11m/s = 47.196kmph
4th gear	16.23m/s = 58.42kmph
5th gear	19.44m/s = 70kmph

5.1 Sprocket Calculations in Accordance With Race Track



Fig. 28 : Mohite Racing Academy [23]

We decided to make a sprocket on the basis of a proper standard racing track by using Google maps we took out the maximum length of the track and scaled it with the scale available from the map and designed the kart's maximum velocity in accordance with it. The length came out be 160 meters.
We take the minimum turning radius to be 6 meters we found out the maximum velocity of the kart at which it could turn without skidding.
Velocity = √μ*r*g = √ .85*6*9.8 = 7.06 m/s = 25.45 kmph.
When the kart reaches the end of the other end of the longer part of the track, it needs to slow down and after calculation of the breaking force it is determined that 30 m of distance will be required to bring the kart to 25 kmph for making the other turn. Now the kart has 130 metres distance for it to reach the top speed maintain it for a certain distance and then again slow down.
Lets calculate the acceleration due to the rolling resistance.
Rolling Resistance = Fr = (0.02) * (160 kg) * (9.81 m/s^2)
= 31.392 Newtons
Kart acceleration due to rolling resistance
= - (31.392/160)= - 0.1962 m/s^2.
→Maximum acceleration in 3rd gear =

$$\frac{\text{Max. engine torque} * \text{primary red} * \text{Secondary Red} * \text{3rd gear ratio}}{\text{Wheel radius} * \text{mass of kart}}$$

$= \frac{11*3.35*2.26*1.473}{0.1397*60} = 5.3$ m/s^2.

Maximum acceleration in 3rd gear after consideration of rolling resistive force = 5.3 – 0.1962 = 5.1038 m/s^2.

Distance travelled till max speed is achieved in 3rd gear

Let us consider that it takes 1 sec for the gear shift to take place. Now during this time the force acting on the kart will be due to rolling resistance.

Hence distance travelled

= (13.11*1) – (0.5)*(0.1962)*(1^2) = 13.0119 m

Speed at the end of 1 second

= 13.11 - (0.1962*1) = 12.9138 m/s

→Maximum acceleration in 4th gear =

$$\frac{Max.engine\ torque * primary\ redn * Secondary\ redn * 4th\ gear\ ratio}{Wheel\ radius * mass\ of\ kart}$$

$= \frac{11*3.35*2.26*1.19}{0.1397*160} = 4.4$ m/s^2

Maximum acceleration in 4th gear after consideration of rolling resistive force = 4.4 – 0.1962= 4.2038 m/s^2

Distance travelled till max speed is achieved in 4th gear

$= (16.23^2 - 12.91^2) / (2*4.2038) = 11.50$ m

Let us consider that it takes 1 sec for the gear shift to take place. Now during this time the force acting on the kart will be due to rolling resistance.

Hence distance travelled = (16.23*1) – (0.5) * (0.1962) * (1^2)= 16.1319 m

Speed at the end of 1 second = 16.23 – (0.1962*1)= 16.0338 m/s

→ Maximum acceleration in 5th gear

$$= \frac{Max.\ engine\ torque * primary\ redn * secondary\ redn * 5th\ gear\ ratio}{Wheel\ ratio * mass\ of\ kart}$$

$= \frac{11*3.35*2.26*1.038}{0.1397*160} = 3.8$m/s^2

Maximum acceleration in 5th gear after consideration of rolling resistive force = 3.8 -0.1962 = 3.6038 m/s^2

Distance travelled till max speed is achieved in 5th gear

$= (19.442 - 16.03382) / (2*3.8) = 16.76$ m

Total distance required

= (11.891+13.0119+11.50+16.1319+16.76)= 69.2948 m

This distance obtained is less than the actual distance required as we have in our calculations taken into consideration peak torque available from the engine at all time which is not possible. We still have 60 m of distance available with us to reach top speed and maintain it for some period of time.

Hence limiting the top speed of kart to 70 kmph is appropriate.

5.2 Maximum Accleration At Different Gears:

The maximum acceleration in the 3rd, 4th, 5th gears have been stated earlier. The acceleration in the 1st, 2nd gears will be decided by the maximum frictional force available to the wheels as in both the gears the max force generated by engine exceeds frictional force.

Max. Force in 1st gear = (11*3.35*3.071*2.26) / 0.1397

= 1830 N, which is greater than the force available due to friction.

Max. Force in 2nd gear = (11*3.35*2.26*1.944) / (0.1397) = 1158.9 N, which is greater than the force available due to friction.

Hence, we use the max. available frictional force for the calculation of acceleration for both 1st, 2nd gear.

Max Acceleration = (866.32/160) = 5.41 m/s^2

Max Acceleration after consideration of rolling resistance = 5.41 – 0.1962 = 5.2 m/s^2

Table 19 : Maximum acceleration at different gears

Gear	Maximum Acceleration
1st gear	5.2 m/s^2
2nd gear	5.2 m/s^2
3rd gear	5.1 m/s^2
4th gear	4.2 m/s^2
5th gear	3.6 m/s^2

5.3 Tractive Force Vs Kart Speed Graph:

The graph plotted is on the basis of maximum force that the can be extracted from the engine and the kart speed. The maximum limiting frictional force is not considered.

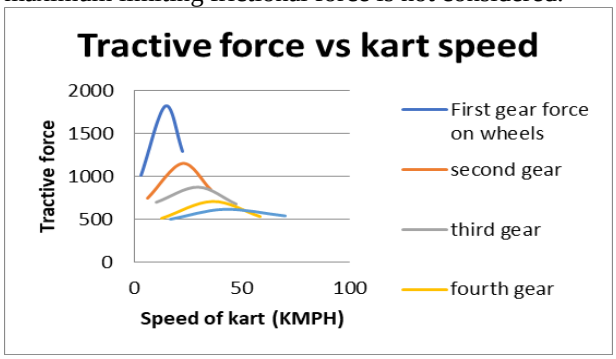


Fig. 29 : Tractive Force vs Kart Speed

5.4 Minimum Torque Required To Start The Vehicle

When we are just required to start the kart on a horizontal plane we just need to overcome the rolling resistance of the kart so we calculate the torque to overcome the rolling resistance of the kart.

Air resistance will not act as the kart is needed to just start from rest. We take rolling resistance into account for the calculation of minimum torque.

Rolling Resistance = Fr

= (0.02) * (160 kg) * (9.81 m/s^2) = 31.392 N

This is the resistance offered when the vehicle is moving. For the starting of the kart this will be more.

We multiply the force by a factor of 2.5

Therefore, total force = 2.5 * 31.392 = 78.48N

Torque = 78.48 * 1397 = 10.9636 Nm

5.5 Transmission Efficiency

At lower gear ratios and relatively lower loads the transmission efficiency is assumed to be the following:

Transmission efficiency of a spur gear transmission = 97%.

Transmission efficiency of a chain and sprocket transmission = 98%. [11]

So, there is primary reduction using spur gears.

Another spur gear contact when there is transmission from input to output shaft. Final one is the chain and sprocket reduction.

Therefore, the total efficiency = 0.97 * 0.97 * 98 = 0.922 =92.2%

5.6 Power In Each Gear At Maximum Engine Torque:

Power = 2π*N*T/60*G

Here N = Engine rpm at maximum torque,

T = torque at the axle

(Max torque * Primary reduction * gear ratio * secondary reduction)

G= total gear reduction

(Primary reduction * gear ratio * secondary reduction)

N = Engine rpm corresponding to maximum torque.

Therefore Power $= \frac{2\pi*n*\text{Max torque}*\text{primary redn}*\text{gear ratio}*\text{secondary redn}}{60*\text{primary redn}*\text{gear ratio}*\text{secondary redn}}$

$= \frac{2\pi*N*\text{Max torque}}{60} = 9.6$ hp= 9.6 * 746 = 7161W

Power at axle depends only upon the engine.

5.7 Rear Axle

We studied about various materials and then we concluded from it which material has to be chosen for the various things such as axle, hubs, and sprocket. We had analysed many materials on the basis of their properties, availability, and cost and then picked up the best one from amongst the choices available. Table 20 shows the details of the various materials that we studied.

Machinability comes out best for EN9, we are compromising the yield strength factor being maximum for EN24 for the sake of getting a lower hardness value to decrease the brittleness of the material. The hardness of EN9 is considered suitable, hence we choose EN9 as the material for our sprocket.

For hub selection, considering the above mentioned factors plus the weldability of the material, EN 9 can be welded much easily, hence we choose EN9 as the material for our hubs (Table 21).

AISI 1020 is chosen as the material for our axle as it is comparatively cheaper and readily available. It has lower yield strength as compared

to AISI 4130 and lower Machinability has been compromised with low cost of AISI 1020.

The outer diameter of the AISI 1020 is near to our requirement (35mm) comparative to other materials so that we can easily put our key into the axle. Moreover its bending stiffness is better than others and suits our requirements.

AISI 1020 is better than others due to its low cost, easy availability and high bending stiffness which is suitable for our engine mounting material.

Table 20 : Comparison of shaft materials [7]

Table 21 : Comparison of sprocket and hub materials [7]

Material	AISI - 1020	AISI - 4130	AISI - 4140	AISI - 1018
Density (g/cc)	7.87	7.85	7.85	7.87
Yield Stress (MPa)	350	460	415	370
Ultimate Stress (MPa)	420	670	655	440
Bending Stiffness (SI)	6150	3382.5	3408.4	5947.05
Outer Diameter of Axle (mm)	34.86	33.6	34.1	34.8
Thickness (mm)	3.21	2.743	2.77	3.17
Plummer Block Inner Diameter (mm)	32.1	27.486	27.7	31.64
Machinability (wrt AISI - 1212)	65 %	70 %	65 %	70 %

Materials	EN8	EN9	EN24	Plain Carbon Steel
Density	7.8	7.8	8.17	7.8
Yield Strength (MPa)	465	480	680	220.6
Hardness (HRC)	51	48	55-65	38-40
Machinability	Very Good	Best	Worse	Good

For Hubs of sprocket and wheel:

We chose Aluminium for the manufacturing of sprocket and the wheel hubs for the following properties it has:

- Light Weight (Density 2.7 g/cc)
- High Yield Strength
- Excellent Machinability
- Is easily weldable

Table 22 : Parameters used in calculation of loads

Property	Symbo	Value
Max. allowable shear stress	τ	30% of elastic limit =0.3*350=105MPa
Inner to outer diameter ratio	K	0.7
Radius of tire	R_T	0.1397 m
Distance b/w wheel & bearing	D	125 mm
Distance b/w sprocket & bearing (max.)	L_B	380 mm
Sprocket ratio	R_S	2.26
Outer Diameter of axle	D_o	-
Inner diameter of axle	D_i	-

When the kart is in motion, various bending and torsional forces act on axle, that is:

1. Bending moment due to the weight of the kart
2. Bending & twisting moment due to the engine torque
3. Twisting moment due to the Braking torque
4. Bending moment due to the braking force developed
5. Equivalent bending and twisting moment due to the combined effect of torsional and shear forces.

The maximum shear stress/normal stress theory is used to calculate the O.D. of the rear axle, which is subjected to the above described moments and torques and a combination of them.

5.8 Maximum Calculated Dynamic Weight Shift On The Rear Axle:

Weight shift due to the kart acceleration.

$W_r = W_{rs} + (W*H*a)/Lg$ [20]

Here W_{rs} = Weight on the rear wheels in the static condition.

H = Height of C.O.G from the ground (in mm)

L = Wheelbase of kart (in mm)

a = Maximum acceleration

$W_r = 104 + (160*5.2*200) / (1100*9.8) = 115.54$ kg.

Weight shift due to the gradient in the track.

$W_r = W_{rs} + (W*H*\sin\Theta)/L$ [20]

Max track gradient is assumed to be 4m rise in height for 100m run.

Therefore $\sin\theta = 4/100.7 = 0.0399$

$W_r = 104 + (160*200*0.399)/1100 = 105.16$ kg

Maximum weight on rear wheels = (104+15.4+.346) = 120.56 kg

Therefore, maximum force on rear wheels = 1037.4868 N

Common Constants Used: Calculation of the force that causes the bending in the axle:

calculate no of teeth in contact with the chain using the geometry of the sprockets. We can calculate the force shared by each teeth.

The no of teeth came out to be 21.

Now force will act tangentially on each of the sprocket teeth. We need to calculate the resultant of the forces.

The angle at which the forces act is calculated and then we add them vectorially.

Now the net resultant of these forces will cause the bending moment to take place.

Total force = (Total torque at shaft / Sprocket radius) = 255.75/.0645 = 3965.11 N

Force on each teeth acting tangentially to sprocket= (3965.11/21) = 188.80 N

Now the net resultant of these forces is calculated. Angles are calculated using Solidworks.

Therefore, the net resultant of the forces is =1783.2 N

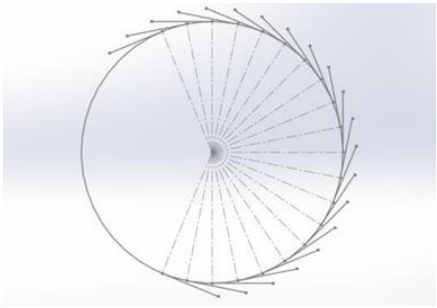


Fig. 30 : Force shared by each teeth

Table 23 : Formulae used in calculation of loads

Type of Loading (max. values)	Formula	Calculated
Bending moment due to the weight of the kart	MW = (reaction at wheels*distance between wheel and bearing)	64.75 Nm
Twisting moment due to the engine torque	TE = engine torque*final max. gear ratio	255.75 Nm
Bending moment due to the engine torque	ME = (bending force*max. dist. b/w sprocket & bearing)	677 Nm
Twisting moment due to the Braking torque (in case of hard braking)	TB = (reaction at one wheels*friction coefficient*wheel radius)	49.83 Nm
Bending moment due to the engine torque	MB= (Friction force on one wheel*distance between wheel and bearing)	44.59 Nm

5.9 Outer Diameter Calculations For Different Loading Conditions.

5.9.1 Type of Loadings

(a) Twisting of axle under the action of bending moment due to weight and engine torque and torsion caused by the engine.

$$D_o = \sqrt[3]{\frac{16\sqrt{[M_W+M_E]^2+T_E^2}}{\pi\tau(1-k^4)}} = 34.86 \text{ mm. [9]}$$

(b) Twisting of axle under the action of bending braking moment due to weight + force on wheels and torsion caused by braking torque.

$$D_o = \sqrt[3]{\frac{16\sqrt{[M_W+M_B]^2+T_B^2}}{\pi\tau(1-k^4)}} = 19.72 \text{ mm. [9]}$$

We have an axle available of material 35mm outer diameter and 25 mm inner diameter.

So we choose this one as one as the axle material.

Here are the Ansys results of the 2 cases that we calculated.

5.9.2 Type of Loadings: Twisting of axle under the action of bending moment due to weight and engine torque and torsion caused by the engine.

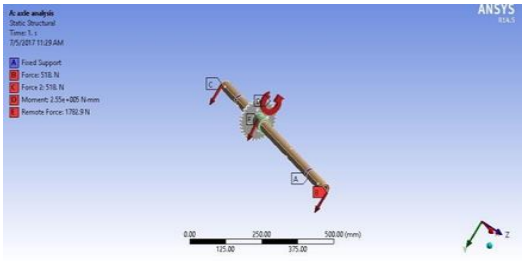


Fig. 31 (a) : Input of forces and moments

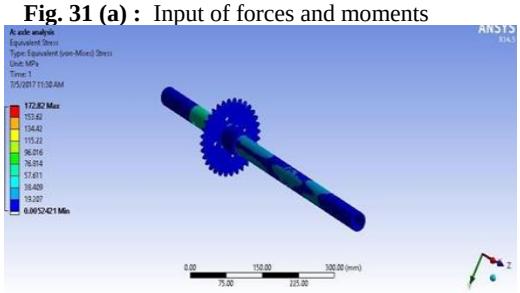


Fig. 31 (b) : Equivalent Stress

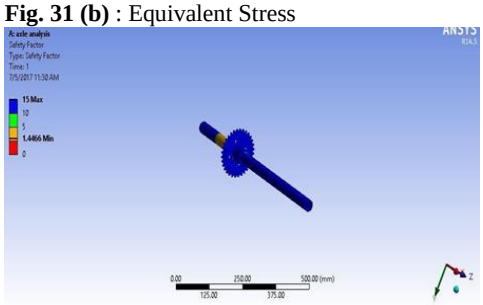


Fig 31 (c) : Factor of Safety

Fig. 31 : Type of Loadings

The equivalent stresses obtained in the axle are not exceeding the maximum value. The higher stresses that are present are induced in the key. Thus, we conclude that the axle shaft chosen is appropriate.

5.9.3 Type of Loadings: Twisting of axle under the action of bending braking moment due to weight + force on wheels & torsion caused by braking torque.

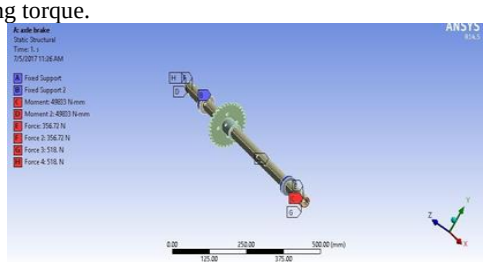


Fig. 32 (a) : Input of forces and moments

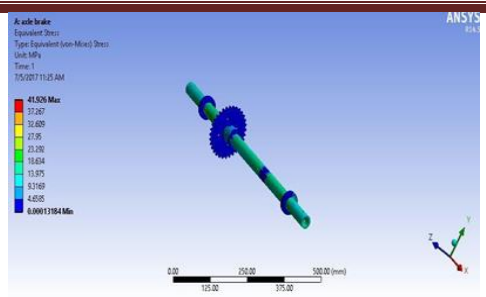


Fig. 32 (b) : Output of equivalent stresses

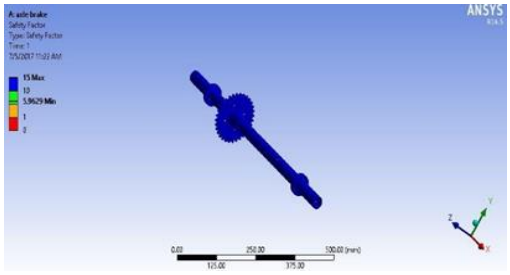


Fig. 32 (c) : Factor of safety

Fig. 32 : Type of Loadings

The stresses obtained in braking are way less than the maximum one which the axle can sustain during braking. Thus the axle will not fail.

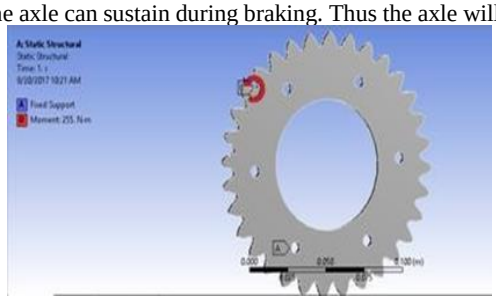


Fig. 33 (a) : Input of forces and moments

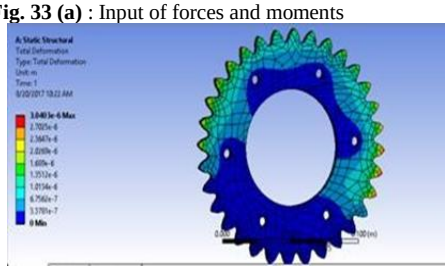


Fig. 33 (b) : Output of Equivalent Deformation

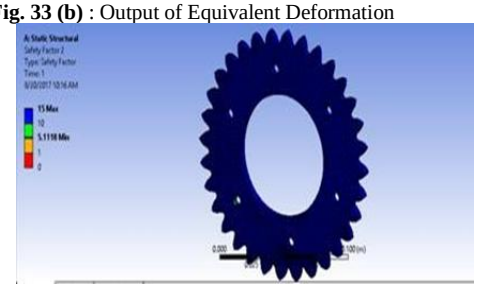


Fig. 33 (c) : Factor of safety

Fig. 33 : Analysis of Sprocket

In the case of sprocket the minimum factor of safety is 5, which is very high and hence sprocket will not fail

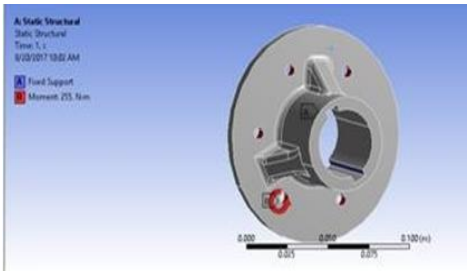


Fig. 34 (a) : Input of forces and moments

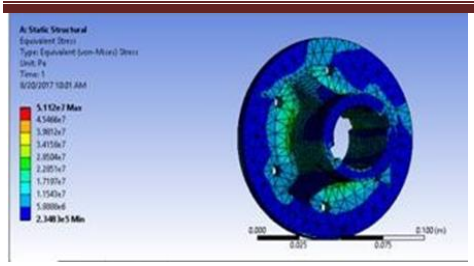


Fig. 34 (b) : Output of equivalent stresses

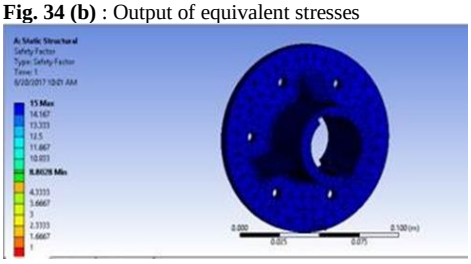


Fig. 34 (c) : Factor of safety

Fig. 34 : Analysis of Sprocket Hub

In the case of sprocket hub the max equivalent stress is just 51.253MPa, which is very low and hence sprocket hub will not fail.

6. BRAKES

6.1 Introduction

Brakes are an important mechanism on any vehicle because the safety of the driver depends on proper operation of the braking system. Brakes are an energy absorbing mechanism that convert the vehicle's kinetic energy into thermal energy, i.e. heat.

6.2 Objective

To design a braking system that can produce more than adequate braking force fulfilling IKC rules and regulations. The braking system should have following features:

1. The brakes must be strong enough to stop the vehicle within a minimum distance in an emergency.
2. The driver must have proper control over the vehicle during braking and vehicle must not skid.
3. The brakes must have well anti fade characteristics i.e. their effectiveness should not decrease with constant prolonged application.

6.3 Braking System Design

The brake system was designed according to the rules, restrictions, and requirements provided by the IKC rulebook. The Go-Kart has a hydraulic brake system which can be actuated by the brake pedal. DOT-4 has been chosen as the brake fluid. A comparison between drum brakes and disc brakes was done. Disc brakes were used in our vehicle due to these features-

1. Better stopping power.
2. Better heat dissipation due to increased effective area.
3. Drilled rotors enhance cooling whereas slotted rotors help in dirt removal.
4. Easy design, easy to inspect and completely self adjusting.

6.4 Brake Parts

The main parts used in the hydraulic braking system are –

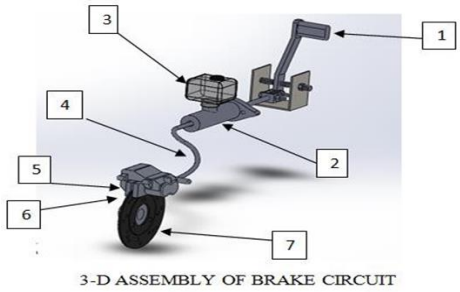
1. Brake Pedal
2. Master Cylinder
3. Reservoir
4. Brake Hose
5. Brake Caliper
6. Brake Pads
7. Rotor

A single rotor was used on the rear axle of vehicle. Calculations were carried out for the condition of braking torque being greater than the frictional torque and it was observed that a single heavy caliper would be enough to stop the kart in a reasonable distance. A single master cylinder was used. The pedal was designed, analysed and manufactured by us.

Also, the rotor was manufactured after choosing the appropriate material, i.e. gray cast iron.

-Weight of the vehicle (W) = 160 kg -Max speed of vehicle (v) = 70 kmph = 19.44 m/s

-Radius of front tire(R_{front}) = 0.122m
-Radius of rear tire (R_{rear}) = 0.1397m
- Coefficient of Friction b/w road and tyre (μ) = 0.7
-Wheelbase (L) = 1.1m
-Horizontal distance from rear axle to C.O.G (X) = 0.405 m
-Vertical height of vehicle's C.O.G (h) = 0.1504 m
-Maximum deceleration(a) = 0.7g



3-D ASSEMBLY OF BRAKE CIRCUIT

Fig. 35 : 3-D Assembly of Brake Circuit

6.5 Static Load Distribution On Axle [3]

Static load on rear axle = mg(L-X) / L = 990.7 N
Static load on front axle = mgX / L = 577.3 N
Distribution in static conditions is 63 : 37

6.5.1 Dynamic Load Transfer [3]

Dynamic load transfer of vehicle = mμgh / L = 150.07 N
Dynamic load on rear axle while braking (W_{rear}) = Static load on rear axle - Dynamic load transfer = 990.7 – 150.07 = 840.63
Dynamic load on front axle while braking (W_{front}) = Static load on front axle + Dynamic load transfer = 577.3+150.07 = 727.37 N
After braking, distribution is 53.5 : 46.5
Torque required to stop two rear wheels [3]=W_{rear} * μ * R_{rear} = 82.2 Nm
Frictional Torque at front wheels [3] = W_{front} * μ* R_{front} = 62.07 Nm

6.5.2 Braking System

Pedal effort = 200 N
Pedal Ratio = 6:1
Manual Pushrod Force (F_{mc}) = Pedal Effort * Pedal Ratio = 1200 N
Master Cylinder Bore = 19.05 mm
Area of MC Piston (A_{mc}) = 284.87 mm^2
Pressure in brake lines (P)= F_{mc} / A_{mc} = 4.212 MPa
Number of calipers = 1
Number of pistons in caliper = 2
Diameter of Caliper Piston = 25.4 mm
Area of Caliper Piston (A_{cal})= 506.45 mm^2
Force exerted by the caliper (F_{cal}) = P*A_{cal} = 4266.34 N
Coefficient of friction between pads and rotor = 0.3
Frictional force between pads and rotor (F_f)=0.3* 2 * F_{cal} = 2559.8 N
Effective rotor radius = 60mm
Braking Torque produced to stop the rotor= F_f * R_{eff} = 153.58 N
We can see that, Braking Torque > Frictional Torque
Rotor outer diameter = 170mm
Stopping Distance = $v^2 / 2a$
At v = 40kmph = 11.11 m/sec
For dry roads (μ = 0.7), stopping distance= 8.99 m
For wet roads (μ = 0.4), stopping distance= 15.74 m
Time to stop = v/a = 1.7 sec

Table 24 : Comparison of Disk Materials [7]

Grey Cast Iron (GCI)	Carbon Ceramic Composite (CCC)	Aluminum Composites (AC)
High Density Material	Moderate Density Material	Very Low Density Material
Moderate Specific Heat	High Specific Heat	High Specific Heat
Low Wear Rate	Very Low Wear Rate	Very High Wear Rate
Moderate Weight	Moderate Weight	Light Weight
Easily Available, Cheap to Manufacture	Expensive and Low Availability	Easily Available and Cheap

Preference of Materials is CCC > GCI > AC.
Although Carbon Ceramic composite had better properties, it was not chosen because of its high cost and low availability. Grey cast iron was chosen because of its easy availability, manufacturing and appropriate properties.

6.5.3 Pedal Effort Vs Deceleration

We have assumed a range of our driver's pedal effort from 100 N to 200 N. A graph between pedal force and corresponding deceleration has been plotted.
In braking conditions, force on rear wheels, = $F_f * R_{eff} / R_{rear}$
Deceleration = Force / W

Table 25 : Pedal effort vs Deceleration

Pedal Effort (N)	Deceleration(g units)
100	0.350
125	0.4375
150	0.525
175	0.6125
200	0.7

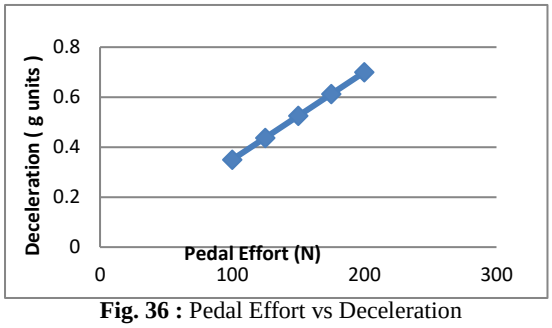


Fig. 36 : Pedal Effort vs Deceleration

6.6 Brake Fluids

A comparison of different types of fluids is given in table 26

Table 26 : Comparison of Brake Fluids [12]

DOT 3	DOT 4	DOT 5
Polyglycol Based-Glycol Ether	Polyglycol Based-Glycol Ether	Silicon Based
Amber Color	Amber Color	Purple Color
Absorbs moisture quickest	Lower absorbing power than DOT 3	Doesn't absorb moisture
Lowest boiling of °	Boiling Point- 2 °C	Highest Boiling Point
Restricted for road use only	High temperature tolerance	

DOT 4 brake fluid was used in the braking system because of the desired properties and its availability, low cost and eco friendliness.

6.7 Properties of Rotor and Pad Material

Material of Rotor - Grey Cast Iron
Material of Brake Pads - Mixture of semi-metallic and ceramic material.

Table 27 : Material properties of rotor and pad [7]

Material Properties	Pad	Disc
Thermal conductivity K (W/m-K)	56	47
Density (kg/m^3)	2400	7060
Elastic modulus (GPa)	2.76	124
Coefficient of friction	0.3	

6.7 CAE Reports of Braking System

The rotor and pedal were designed in Solidworks 2016 and their analysis was done on ANSYS for the calculated forces.

6.7.1 Rotor Analysis

Outer Diameter of Disc = 170mm Thickness = 3mm The following simulations have been done using ANSYS .

6.7.1Total Deformation : It accounts for the deformation under applied stress for the disc used on the rear axle of the kart.

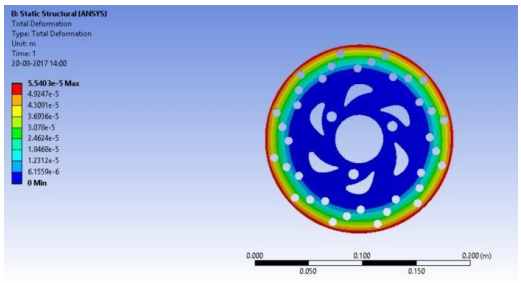


Fig. 37 (a) : Total Deformation

6.7.2 Thermal Analysis : It accounts for the distribution of temperature along rotor surface when it is stopped.

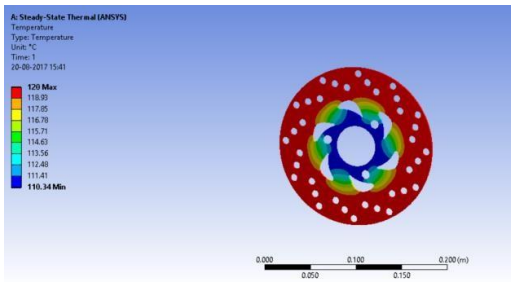


Fig. 37 (b) : Thermal Analysis
Fig. 37 : Rotor Analysis

6.7.3 Pedal Analysis

Pedal Ratio = 6:1.
The pedal effort ranges from 100N to 200 N, however, we tested our design for an application of maximum of 500N. The following simulations have been done on the pedal using ANSYS

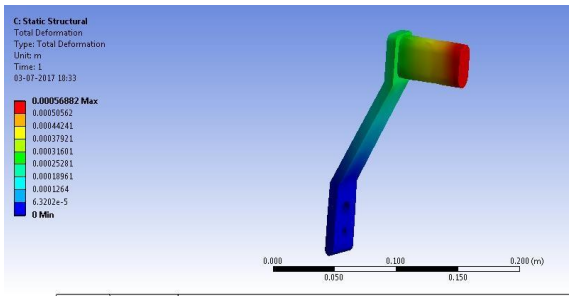


Fig. 38 (a) : Total Deformation

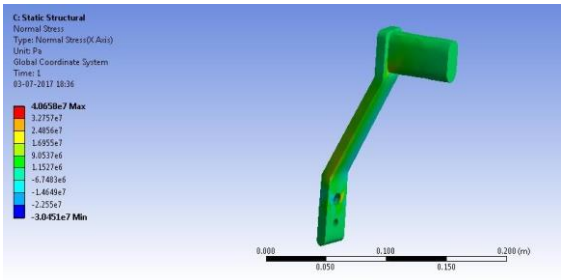


Fig. 38 (b) : Normal Stress

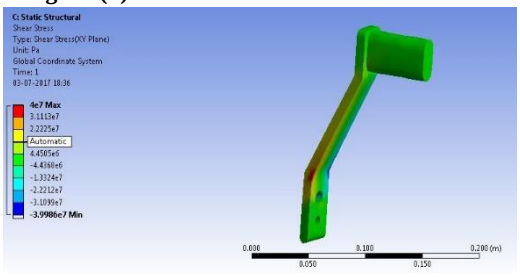


Fig. 38 (c) : Shear Stress
Fig. 38 : Pedal Analysis

Minimum factor of safety was found out to be 1.7 which approves our design.

6.8 Mounting Methods

The caliper mounting has been chosen such that bleeding point is at the top. Also, the brake rotor is attached to the axle with the help of a hub and keyway.

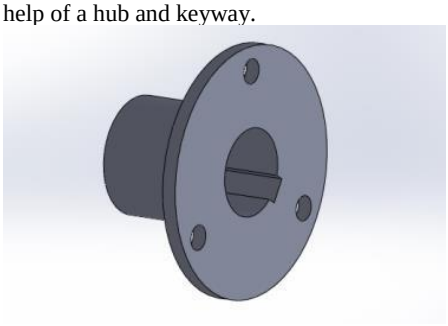


Fig. 39 : Hub and Keyway

6. Conclusions

The research paper has introduced new design concepts for the design of the Go-Kart chassis. The various in depth analysis performed on the design iterates and ensures that it meets the industrial safety standards. Focus has been laid on the new safety features that are feasible to implement and also monumental in an ever changing scientific landscape.

References

[1] K Parihar, N Negi, D Dimri, G Ramola, D Bhatt, S Gadal, N Singh, J Singh. Study and Examine the Go-kart Working Mechanism, International Journal of Scientific & Engineering Research, 8(12), 2017

[2] OC Zienkiewicz, RL Taylor. The Finite Element Method, Solid Mechanics, Fifth Edition.

[3] Limpert, Rudolf. Brake Design and Safety Society of Automotive Engineers, 1999 Second Edition.

[4] A Natu. Go-Kart Chassis Analysis: Design Methodology Integrating Revolutionary Safety Features, RAME Conference, ISBN: 987194523970-0

[5] KJ Wakeham. Introduction to Chassis Design, 1st edition, Memorial University of Newfoundland and Labrador, 2009.

[6] Indian Karting Championship (IKC) Rulebook, Season 4, 2018.

[7] www.azom.com, for material properties of all the components.

[8] https://bikeadvice.in/honda-cbf-stunner-125-review-sankesh/

[9] FP Beer, ER Johnston, JT Dewolf, DF Mazurek. Mechanics of Materials, Sixth Edition, ISBN: 978-0-07-338028-5.

[10] WF Milliken, DL Milliken. Race Car Vehicle Dynamics, ISBN: 978-1-56091-526-3.

[11] NPTEL: National Program on Technology and Enhanced Learning

[12] Ch7, Basic Hydraulic Systems- Peter Verdone Designs, 64-65, for the comparison of brake fluids.

[13] MH Mat, ARA Ghani. Design and Analysis of Eco Car Chassis, Procedia Engineering 41, 2012, 1756 – 1760.

[14] M Mahmoodi-k, I Davoodabadi, V Višnjić, A Afkar. Stress and Dynamic Analysis of Optimized Trailer Chassis, Technical Gazette 21(3), 2014, 599-608.

[15] R Rajappan, M Vivekanandhan. Static and Modal Analysis of Chassis by Using Fea, The International Journal of Engineering And Science (IJES), 2(2), 2013, 63-73.

[16] PA Renuke. Dynamic Analysis of A Car Chassis, International Journal of Engineering Research and Applications (IJERA), 2(6), 2012, 955-959

[17] D Koladia. Mathematical Model to Design Rack And Pinion Ackerman Steering Geomtery, International Journal of Scientific & Engineering Research, 5(9) 2014, 716-720.

[18] B George, A Jose, AJ George, A Augstine, AR Thomas. Innovative Design and Development of Transmission System for an Off-road Vehicle, International Journal of Scientific & Engineering Research (IJSER), 7(3), 2016.

[19] CR Prasad, MF Ahmed, MK Mohiuddin. Transmission System of Go-Kart, International Advanced Research Journal in Science, Engineering and Technology (IARJSET), 4(5), 2017 25-27.

[20] Gillespie, D Thomas. Fundamentals of Vehicle Dynamics, 1-14, ISBN: 978-1-56091-199-9, February 1992.

[21] G Mekalke. Static Analysis of a Go-Kart Chassis, International Journal of Mechanical and Industrial Technology, 3(2), 2015, 73-78

[22] A Singh, PK Jain, A Gupta. Design Analysis of the Chassis for the Go-Kart, V th International Symposium on Fusion of Science & Technology, New Delhi, India, January 18-22, 2016, ISBN: 978-93-84935-64-1

[23] Google Maps for race track satellite image.

Sensors & Actuators: B. Chemical 275 (2018) 312–321

Contents lists available at ScienceDirect

Sensors and Actuators B: Chemical

journal homepage: www.elsevier.com/locate/snb

Electrochemical genosensor based on carboxylated graphene for detection of water-borne pathogen

Nandita Jaiswal[a,1], Chandra Mouli Pandey[a,b,1], Amrita Soni[e], Ida Tiwari[a,*], Martin Rosillo-Lopez[c], Christoph G. Salzmann[c], Bansi Dhar Malhotra[d], Gajjala Sumana[e]

[a] Department of Chemistry (Centre of Advanced Study), Institute of Science, Banaras Hindu University, Varanasi, 221005, India
[b] Department of Applied Chemistry, Delhi Technological University, Delhi, 110042, India
[c] University College London, Department of Chemistry, 20 Gordon Street, WC1H 0AJ, London, UK
[d] Department of Biotechnology, Delhi Technological University, Delhi, 110042, India
[e] CSIR-National Physical Laboratory, New Delhi, 110012, India

ARTICLE INFO

Keywords:
E.coli
Graphene nanoflakes
Biosensors
Reduced graphene oxide
Electrophoretic deposition

ABSTRACT

This work reports the application of newly synthesized carboxylated graphene nanoflakes (Cx-Gnfs). The Cx-Gnfs were synthesized by wet chemical method in sulfuric acid/nitric acid mixture and was further electrophoretically deposited on indium tin oxide (ITO) coated glass substrates using Mg^{2+} ions which provides an overall charge to the materials for deposition onto the anode. The materials were characterized using SEM, TEM, contact angle, UV–vis spectroscopy, FT-IR, XRD and electrochemically characterized by cyclic voltammetry, chronocoulometry and electrochemical impedance spectroscopy. The sensitive quantitative determination of nucleic acid *Escherichia coli* O157: H7 (*E. coli*) has been achieved using Cx-Gnfs and r-GO as the sensing layer using electrochemical impedance spectroscopy. The electrochemical results reveal that the Cx-Gnfs based genosensor exhibits a linear response to complementary DNA (10^{-6} M to 10^{-17} M) with a detection limit of 1×10^{-17} M while the rGO based genosensor shows a detection limit of 1×10^{-15} M. Under optimal conditions, this Cx-Gnfs based genosensor was found to retain about 85% of its initial activity after being used for 6 times.

1. Introduction

Pathogenic bacteria are considered to be serious threat to human health mainly due to food borne and water borne illnesses [1,2]. The consumption of less processed products such as fruits, vegetables and ready to eat foods are the major sources of food borne outbreaks which has created a major concern for their immediate monitoring to ensure the safety of food products for consumption. In spite of the availability of regulations, good manufacturing practices, hazard analysis and critical control points for keeping a check on the presence of *E.coli* in food it has not been possible to achieve the desired result.

The most commonly practiced techniques in the area of food and safety for detection and enumeration of *E. coli* O157:H7 are conventional culture and molecular based methods. The culture-based method includes enumeration of bacterial colonies by growing bacteria in nutrient rich medium. While in the molecular based method enumeration are done by polymerase chain reaction (PCR) technique which is highly specific and sensitive for the detection of specific sequences of nucleic acid for the targeted bacteria using the hybridization methods. The molecular based method is known to be more rapid as compared to the conventional culture method [3–5].

The conventional methods such as culturing, PCR, flow cytometry, solid-phase cytometry and ATP bioluminescence etc. are used in the public health laboratories all over the world for the detection of *E.coli* O157:H7. Inspite of some advantages these conventional methods have drawbacks such as need of bulky instrumentations, large amount of medium which creates biological waste, time for culture and enumeration, interference by other substances of food matrices, requirement of proper training for careful handling of the instrument and a certain level of expertise for interpretation of results [6–9]. Hence, there is a need for the development of method for rapid and low cost detection of *E.coli* with improved specificity, reliability, feasibility, miniaturization, and enumeration. In this respect, biosensors are one of the most helpful and applied devices for monitoring the chemical and

* Corresponding author.
E-mail address: idatiwari@bhu.ac.in (I. Tiwari).
[1] These authors contributed equally.

https://doi.org/10.1016/j.snb.2018.07.055
Received 3 February 2018; Received in revised form 14 June 2018; Accepted 12 July 2018
0925-4005/ © 2018 Elsevier B.V. All rights reserved.

biological analytes. With the advent of nanotechnology, the construction of biosensors has become more fascinating. The use of nanoscale material helps to achieve a direct wiring of electrode with the biomolecules, providing a larger surface area for electrochemical reactions, and also creates a nano-encryption for biomaterials so that the sensitive and selective signal of biological recognition element can be amplified. The nanostructured materials such as nanoparticles, nanotubes, nanowires etc. of carbon or metal oxides are used for recognition of biological events in electrochemical biosensors due to their enhanced properties [10–13]. Recently, graphene as a true 2-dimensional material, has received much attention due to its unique physicochemical properties like high mechanical strength, excellent conductivity, high surface area, ease of functionalization and mass production [14,15]. The unique structure of graphene provides a remarkable electronic, optical, mechanical, thermal, and electrochemical properties; and makes them a potential candidate for next generation biosensing materials. In comparison to CNTs, graphene shows potential advantages of cost-effectiveness, high surface area and ease of processing [16,17]. Further, the presence of oxygen-containing groups at the edges/surface of graphene influence the electrochemical performance in terms of the heterogeneous electron transfer rate. These functional groups provide a conducive environment for controlled functionalization and immobilization of biomolecules on its surface.

Many reports for detection of *E.coli* using different nanomaterials and electrodes are available [18–45]. Biosensors based on different biological recognition entities such as antigen/antibody [18–21], single strain DNA [22–42], whole cell [43] and aptamer [44,45] have been reported for *E. coli* detection. Among these nucleic acid biosensors have been widely used for *E. coli* detection due to their enhanced sensitivity, reproducibility, and selectivity. In this context, Xu et al. fabricated a simple and sensitive electrochemical DNA biosensor based on graphene oxide/chitosan hybrid nanocomposites modified glassy carbon electrode for detection of *E.coli* O157:H7 [24]. Tiwari et al. have used graphene oxide modified iron oxide–chitosan hybrid nanocomposite film for *E. coli* O157:H7 detection and obtained a detection limit of 1×10^{-14} M [26]. Zainudin et al. have reported a label-free impedimetric *E. coli* genosensor based on graphene nanosheets displaying a wide range of linear response (1.0×10^{-10} M to 1.0×10^{-14} M) and low detection limit (0.7×10^{-15} M) [32]. Although numerous work has been done towards the detection of *E. coli* DNA using different platforms but still the sensitivity, selectivity, detection time and reusability of the sensor is a challenge which curbs its transfer to a technology. Table 1 consists of detailed discussion of non-labeled and labeled *E. coli* genosensor reports available in literature for a decade.

Here in this work, efforts have been made to fabricate a genosensor based on carboxylated graphene nanoflakes (Cx-Gnfs) for *E.coli* O157:H7 detection. A new protocol has been used for the synthesis of graphene nanoflakes in which graphene edges have been modified with carboxylate groups [46,47]. The main purpose of choosing this material as the electrode modifier is due to the presence of carboxylated groups which facilitate the targeted attachment of the nucleic acid. The results were compared with chemically reduced graphene oxide (r-GO) using electrochemical impedance spectroscopy technique. The sensor performance of the Cx-Gnfs was found to be better than r-GO and most of the reported works [Table 1].

2. Chemicals and material required

Graphite powder, multiwall carbon nanotubes (MWCNT), 1-ethyl-(dimethylaminopropyl) carbodiimide (EDC), N-hydroxysuccinimide (NHS) of analytical grade were purchased from Sigma-Aldrich. The specific sequence of *E. coli* probe (17 mer.) has been identified from the 16 s rRNA coding region of the *E. coli* genome. The complementary, non-complementary and one-base mismatch target sequences were obtained from Sigma Aldrich, Milwaukee, USA. Sequences of oligonucleotide probes are listed as below:

Probe I: probe DNA (pDNA): amine-5′-GGT CCG CTT GCT CTC GC-3′.

Probe II: complementary DNA (cDNA): 5′-GCG AGA GCA AGC GGA CC-3′.

Probe III: non-complementary DNA: 5′-CTA GTC GTA TAG TAG GC-3′.

Probe IV: one-base mismatch DNA: 5′-GCG AGA GAA AGC GGA CC-3′.

The oligonucleotide solution was prepared in Tris–EDTA buffer (1 M Tris − HCl, 0.5 M EDTA) of pH 8.0 and is stored at -20 °C prior to use.

3. Experimental section

3.1. Synthesis of Cx-Gnfs

MWCNT (1.00 g, Bayer Materials Science) were dispersed in 100 mL of a 3:1vol% mixture of H_2SO_4 (97 w/w) and HNO_3 (70 w/w) via ultrasonication for 30 min. The mixture was heated at 100 °C for 2 h, then cooled, and diluted three-times with deionized water. The resulting black dispersion was filtered (0.2 µm Whatman track-etched polycarbonate membrane) to remove any unreacted carbon material on the membrane. Finally the black filtrate was neutralized by the addition of KOH pellets under external ice bath cooling. After neutralization a large amount of white precipitates (consisting of K_2SO_4 and some KNO_3) were formed, which were separated from the black filtrate by filtration. The dispersion was re-acidified by the addition of diluted formic acid and then dialyzed against high purity *Milli-Q* deionized water using a pre-treated Spectra Por 3 regenerated cellulose dialysis membrane (MWCO 3.5 kDa, Spectrum laboratories). The dialysis procedure was considered complete when the conductivity of the water surrounding the membrane decreased below 5 $\mu S.cm^{-1}$, which was determined using a Mettler Toledo conductivity meter using a Mettler Toledo LE703 conductivity sensor. The pure brown-black dispersion underwent lyophilization to obtain 222 mg of a pure brown-black material, identified as Cx-Gnfs [46].

3.2. Synthesis of r-GO

The reduction of graphene oxide (GO) has been conducted using the two-step reduction procedure. Upon dispersion in deionized water, the pH of the solution was increased to 10.0 using 5 wt% sodium carbonate solution. Sodium borohydride (800 mg) was directly added to a 400 mL GO suspension (1 mg mL^{-1}) under magnetic stirring, and the mixture was kept at 80 °C for 1 h with constant stirring, leading to a change in the color from brown to black. The solid product was purified using water and washed with ethanol, followed by drying. Further, the obtained product was re-dispersed in H_2SO_4 at 120 °C and filtered through Millipore filter paper to yield reduced graphene oxide (r-GO) [48].

3.3. Fabrication of electrodes

For electrophoretic deposition (EPD), a very well dispersed stock solution of Cx-Gnfs (20 mg dL^{-1}) in acetonitrile was ultrasonicated (80 W, 0.25 A) for about 2 h. Then, 100 µL of this stock solution was dispersed in 10 mL of acetonitrile to make the colloidal suspension of Cx-Gnfs. The film was electrophoretically deposited using two-electrode cell by applying a DC voltage (140 V, 2 min), where platinum foil was used as the cathode and a precleaned ITO-coated glass substrate as anode. To create surface charge on the Cx-Gnfs, 10^{-5} M of Mg $(NO_3)_2.6H_2O$ was added into the suspension as electrolyte [49,50]. The deposited film (Cx-Gnfs/ITO electrode) was then removed from the suspension followed by washing with deionized water and drying. The schematic view of electrodeposition and fabrication of Cx-Gnfs/ITO electrode and pDNA/Cx-Gnfs/ITO bioelectrode has been illustrated in Fig. 1.

Table 1
Comparison of result with the previously reported work of *E.coli* genosensor.

S.No	Working electrode	Detection range	Limit of detection	Reproducibility	References
Non-labelled *E.coli* genosensor					
1.	CysFl/Au	1.0×10^{-6} M to 1.0×10^{-15} M	1.0×10^{-15} M.	6 times	[22]
2.	GO-GNP/PPY	1.0×10^{-6} M to 1.0×10^{-15} M	1.0×10^{-15} M	5–6 times	[23]
3.	GO/CS/GCE	1.0×10^{-14} to 1.0×10^{-8} M	3.58×10^{-15} M	5 times	[24]
4.	denCys/Au	1.0×10^{-14} to 1.0×10^{-8} M	1.0×10^{-14}M	4 times	[25]
5.	GIOCh/ITO	10^{-14} to 10^{-6} M	1.0×10^{-14} M	5 times	[26]
6.	GO/NiF/ch/ITO	10^{-16} to 10^{-6} M	1.0×10^{-16} M	9 times	[27]
7.	PlgNPs/ITO	1.0×10^{-13} to 1.0×10^{-6} M	8.7×10^{-14} M	9 times	[28]
8.	Gold electrode/mesoporous silica thin films	–	25×10^{-15} M	–	[29]
9.	SWCNT-modified SPE	–	0.15 mg/ml	–	[30]
10.	DNA/FNAB/ODT/Au bioelectrode	0.5×10^{-18} to 1×10^{-6} M	0.5×10^{-18} M	10 times	[31]
11.	1-pyrenebutyric acid (PyBA) functionalized graphene/GCE	1.0×10^{-10} to 1×10^{-14} M	0.7×10^{-15} M	4 times	[32]
12.	NanoZrO$_2$/ITO	1.0×10^{-6} to 1×10^{6} pM	1.0×10^{-6} pM	–	[33]
13.	Monolayer structure self assembled at nanoporous gold (NPG)/ Gold electrode	1×10^{-5} to 1×10^{-1} μM	1.0×10^{-6} μM	–	[34]
14.	Cx-Gnfs/ITO	1.0×10^{-6} M to 1.0×10^{-17} M	1.0×10^{-17} M	6 times	Present work
Labelled *E.coli* genosensor					
15.	Q-PCR amplified *E.coli* biosensor based on avidin biocomposite (Av-GEB) and magneto bead(m-GEC) modified electrode	–	4.5×10^{-15}(Av-GEC) and 0.45×10^{-15} (m-GEC)	–	[35]
16.	aMB E-sensor	1×10^{-12} to 1×10^{-9}M	–	–	[36]
17.	2-mercaptobenzoth iazole (MBT)/Au electrode	1.59×10^{-8} to 2.4×10^{-6} M	2.38×10^{-9}	–	[37]
18.	GOx–Thi–Au@SiO$_2$/GCE	0.02–50.0 nM	0.01 nM	–	[38]
19.	ST-AP/gold electrode	1 pM–10 nM	0.30 pM	5 times	[39]
20.	BdE avidin-PANI bioelectrode/Pt disk electrode	–	0.01 ng/μL	6–7 times	[40]
21.	Cadmium sulfide nanoparticles (CdSNPs)/GCE	–	1.97×10^{-14} M	–	[41]
22.	DZ5T3-hemin DNAzyme/carbon electrode	0.05–0.5 μM	144 nM	–	[42]

4. Result and discussion

4.1. Physical characterization

4.1.1. SEM studies

SEM studies were carried out to study the surface morphology of the electrophoretically deposited nanomaterial on ITO electrode. Fig. 2(A) reveals the surface of ITO after electrophoretic deposition of Cx-Gnfs nanoflakes. A uniform deposition of nanoflakes was observed on the surface of ITO electrode [*cf.* Fig. 2(A)]. The inset to Fig. 2(A) clearly reveals that the flaky structures of the Cx-Gnfs have been lost and the nanoflakes are aggregated to form cauliflower structures of uniform size. The Fig. 2(B) shows the SEM image of r-GO after electrodeposition on the ITO electrode. From the figure the uneven electrodeposition of large nanostructures on the surface of ITO can be observed. The large structure might be due to flake-like cripple glossy sheets of rGO which is further confirmed at higher magnification [*cf.* inset of the Fig. 2(B)].

4.1.2. TEM studies

The structure and crystal pattern of the nanomaterial was analysed using TEM and selected area electron diffraction (SAED). Fig. 3(A) depicts the nano-flaky structure of Cx-Gnfs having an average diameter of 50 nm [46]. The SAED pattern of Cx-Gnfs, shows the rings of the pattern possesses bright spots which is due to the polycrystalline nature of the nanomaterial [*cf.* inset Fig. 3(A)]. Crumbled and agglomerated but well exfoliated sheets of rGO can be observed in Fig. 3(B). The inset of the Fig. 3(B) illustrated a SAED pattern of r-GO having six-fold symmetric pattern owing to the crystalline nature of the nanomaterial.

4.1.3. Contact angle studies

Contact angle (CA) measurements carried out using the sessile drop method shows that after the deposition of Cx-Gnfs on ITO electrode there was a decrease in the CA from 85.4° [*cf.* Suppl. material Fig. S1 (i)] to 44.8° [Fig.S1 (ii)]. The decrease in CA is due to the introduction of Cx-Gnfs having polar groups $-COO^-$ which increases the hydrophilicity of the electrode surface. A further decrease [*cf.* Suppl. material Fig.S1 image (iii)] in CA (22.52°) after the immobilization of pDNA onto Cx-Gnfs/ITO electrode was observed. This may be due to enhancement of hydrophilicity caused by the presence of negatively charged phosphodiester backbone of DNA.

4.1.4. UV–vis studies

The UV–vis spectroscopic studies for Cx-Gnfs and r-GO were carried out in the wavelength range of 200–800 nm as indicated in Suppl. material Fig. S2, curve (a) and curve (b) respectively. There was a monotonic increase in the absorbance from 500 nm in Cx-Gnfs and from 350 nm in r-GO. This might be due to $\pi - \pi^*$ transition of C—C aromatic bonds of both the carbon nano-materials. The band gap of Cx-Gnfs was found to be 2.4 eV which is lower than that of r-GO (3.5 eV) using the Tauc equation. The difference in band gaps might be due to non-availability of functional groups on the basal plane of Cx-Gnfs as compared to the oxygen functionalities present in the r-GO [46,48].

4.1.5. FT-IR analysis

FTIR analysis of Cx-Gnfs shows an intense peak at 1722 cm^{-1} that signifies the presence of C=O group [*cf.* Suppl. material Fig. S3(A)], while the band at 3400 cm^{-1} is due to O—H stretching vibration [46]. The bands seen at 1710 and 1410 cm^{-1} are due to C=O stretching and O—H bending vibrations of the carboxyl group present in r-GO respectively. The band appearing at 1585 cm^{-1} is due to a C=C stretching mode while the band observed at 1207 cm^{-1} is due to C—OH stretching vibration. C—H stretching and bending vibrations are observed at 2950 and 866 cm^{-1}, respectively. A broad band found at 3400 cm^{-1} is due to O—H stretching vibration of the hydroxyl group present in the r-GO [*cf.* Suppl. material Fig. S3(B)].

4.1.6. XRD analysis

The XRD analysis is important in the characterization of the materials as it gives an idea about interlayer spacing and its corresponding diffraction angle. The XRD of Cx-Gnfs and r-GO is presented in Fig. 4(A)

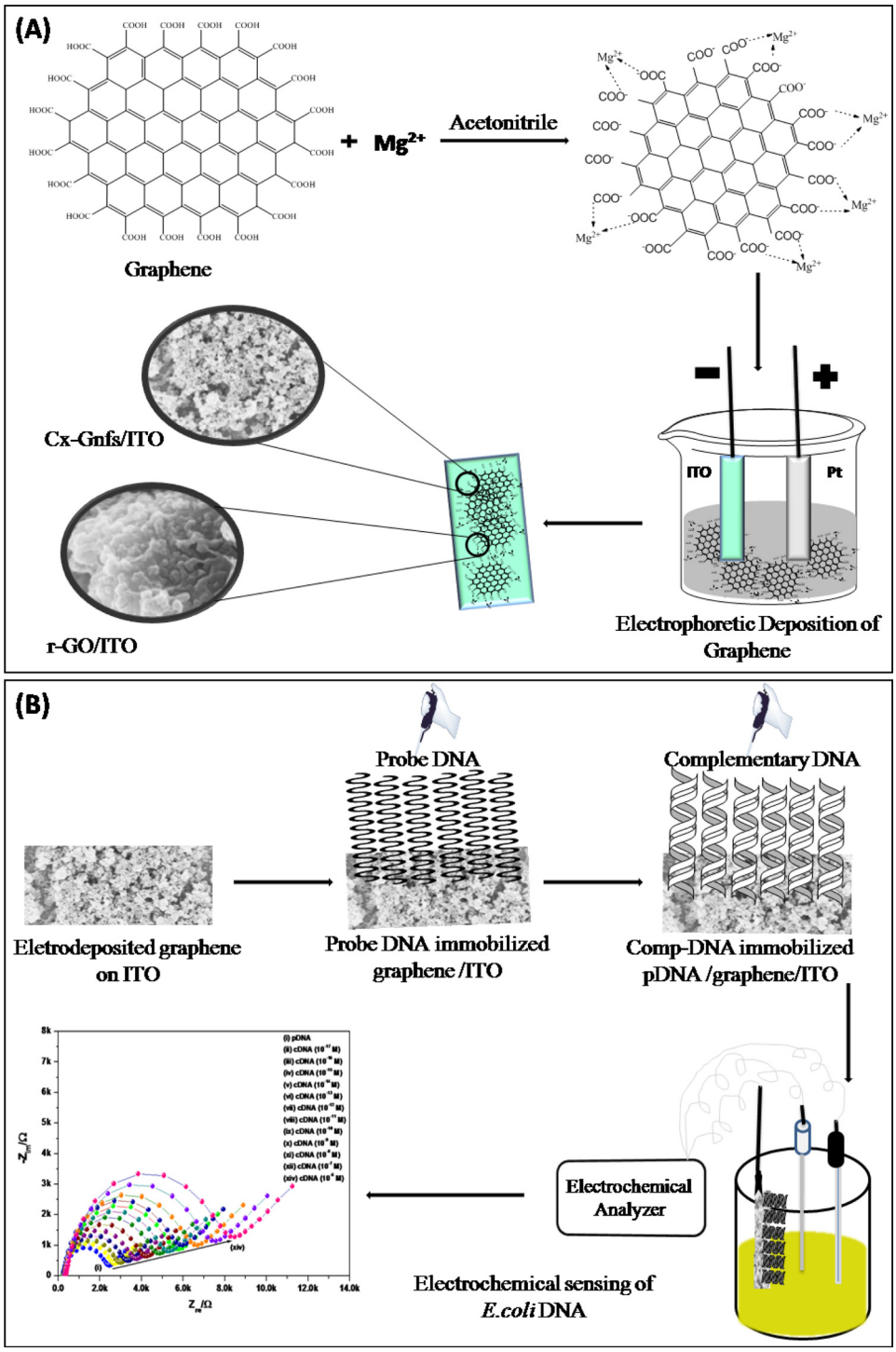


Fig. 1. Schematic representation of **(A)** fabrication of electrode based on graphene materials and **(B)** electrochemical genosensing of *E.coli* using the fabricated electrode.

and (B) respectively. The characteristic broad peaks at 22.9° and 40.4° in Cx-Gnfs can be corroborated with the data of carboxyl (COOH) functionalized MWCNTs (since MWCNTs are used as starting material in the synthesis of Cx-Gnfs) [51] and a broad reflection between 25°–30° suggests the formation of disordered graphitic structure as observed in reduced graphene. The Fig. 4(B) shows a broad reflection in the range of 21.6°–36.8° in the case of r-GO which may be due to the reduction of GO by sodium borohydride which causes a shift in diffraction angle of GO (10.2°) suggesting the poor arrangement of the layers [52].

4.2. Electrochemical characterizations

4.2.1. Cyclic voltammetry

The electrochemical behavior of the Cx-Gnfs was compared to that of the r-GO using the cyclic voltammetry (CV) technique in 5 mM $[Fe(CN)_6]^{3-/4-}$ (PBS, 100 mM, pH 7.0, 0.9% NaCl), which provides an insight in the electron transfer mechanism. The mechanism for the electron transfer by any electrode material can be best explained by the heterogeneous rate constant. This rate constant further depends upon another parameter of electron property named as the density of

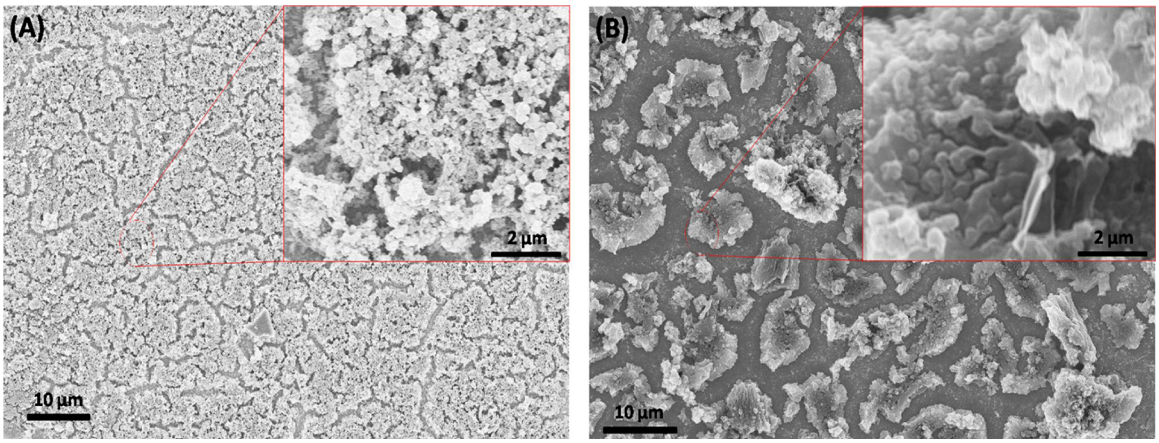


Fig. 2. SEM image showing the morphology of the surface after electrodeposition of **(A)** Cx-Gnfs and **(B)** r-GO on the ITO electrode.

electronic state, a high value of which signifies that the electron of correct energy is available for transfer from the electrode to redox species [53,54].

Various kinetic parameters were calculated using CV technique for the electrophoretically deposited Cx-Gnfs and r-GO on ITO electrode. Fig. 5(A) depicts the voltammogram of (a) bare ITO, (b) Cx-Gnfs/ITO and (c) r-GO/ITO in 5 mM $[Fe(CN)_6]^{3-/4-}$ (PBS, 100 mM, pH 7.0, 0.9% NaCl). There is an increase in the redox peak current of Cx-Gnfs/ITO and rGO/ITO as compared to that of bare ITO [*cf.* Fig. 5(A) curve (a)] which might be due to the fast electron transfer kinetics at the carbon materials modified electrodes suggesting the carbon based nanomaterial provides an electrical wiring between the electrode and the redox active species ($[Fe(CN)_6]^{3-/4-}$). The electrocatalytic performance of the Cx-Gnfs/ITO [*cf.* Fig. 5(A) curve (b)] towards the redox species is found to be low as compared to r-GO/ITO [*cf.* Fig. 5(A) curve (c)]. The plausible reason of low catalytic nature of Cx-Gnfs is the presence of negatively charged carboxylate groups on the edges of the Cx-Gnfs which might create hindrance in electron transfer between electrode and $[Fe(CN)_6]^{3-/4-}$. Besides this the peak currents [both anodic (I_{pa}) and cathodic (I_{pc})] is found to vary linearly with the square root of scan rate ($\upsilon^{1/2}$) depicting the process to be diffusion limited. The Fig. 5(B) denotes the linear variation of peak current with $\upsilon^{1/2}$ for Cx-Gnfs/ITO [plot (a)] and r-GO/ITO [plot (b)] in 5 mM $[Fe(CN)_6]^{3-/4-}$ (PBS, 100 mM, pH 7.0, 0.9% NaCl). The corresponding linear Eqs. (1) and (2) are for Cx-Gnfs/ITO and (3) and (4) are for r-GO/ITO respectively.

$$I_{pa} / A = 4.5430\ \upsilon / Vs^{-1} + 0.1651 \qquad R^2 = 0.997 \tag{1}$$

$$I_{pc}/A = -3.7210\ \upsilon/Vs^{-1} - 0.3070 \quad R^2 = 0.993 \tag{2}$$

$$I_{pa}/A = 8.200\ \upsilon/Vs^{-1} + 0.0309 \quad R^2 = 0.997 \tag{3}$$

$$I_{pc}/A = -5.3331\ \upsilon/Vs^{-1} - 0.4060 \quad R^2 = 0.991 \tag{4}$$

The Fig. 5(C) and (D) correspond to the Laviron plot (plot between peak potentials and log υ) of Cx-Gnfs/ITO and r-GO/ITO in 5 mM $[Fe(CN)_6]^{3-/4-}$ (PBS, 100 mM, pH 7.0, 0.9% NaCl) respectively. The linear equations for the linear part of Laviron plot for Cx-Gnfs/ITO are Eqs. (5) and (6) and for r-GO/ITO Eqs. (7) and (8) are depicted below:

$$E_{pa}/V = 0.4849/V + 0.2050 \log \upsilon \quad R^2 = 0.998 \tag{5}$$

$$E_{pc}/V = -0.1410/V - 0.1993 \log \upsilon \quad R^2 = 0.992 \tag{6}$$

$$E_{pa}/V = 0.4973/V + 0.2131 \log \upsilon \quad R^2 = 0.999 \tag{7}$$

$$E_{pc}/V = -0.1536/V - 0.1174 \log \upsilon \quad R^2 = 0.998 \tag{8}$$

The kinetic parameters such as α_{ec} (electron transfer co-efficient) and k_{avg} (heterogenous rate constant) were calculated using the Laviron Eqs. (9) and (10) [55,56];

$$\alpha_{ec} = S_{pa}/S_{pa} + S_{pc} \tag{9}$$

$$K_{avg} = \frac{nF\alpha_{ec}\upsilon_c}{RT} = \frac{nF(1-\alpha_{ec})\upsilon_a}{RT} \tag{10}$$

where S_{pa} and S_{pc} are the anodic and cathodic slopes of Laviron plot respectively, υ_a and υ_c are the respective scan rates. The α_{ec} and k_{avg} value for Cx-Gnfs/ITO are 0.50 and 3.89 s^{-1} while that of r-GO/ITO are 0.64 and 2.80 s^{-1} respectively in 5 mM $[Fe(CN)_6]^{3-/4-}$ (PBS, 100 mM, pH 7.0, 0.9% NaCl).

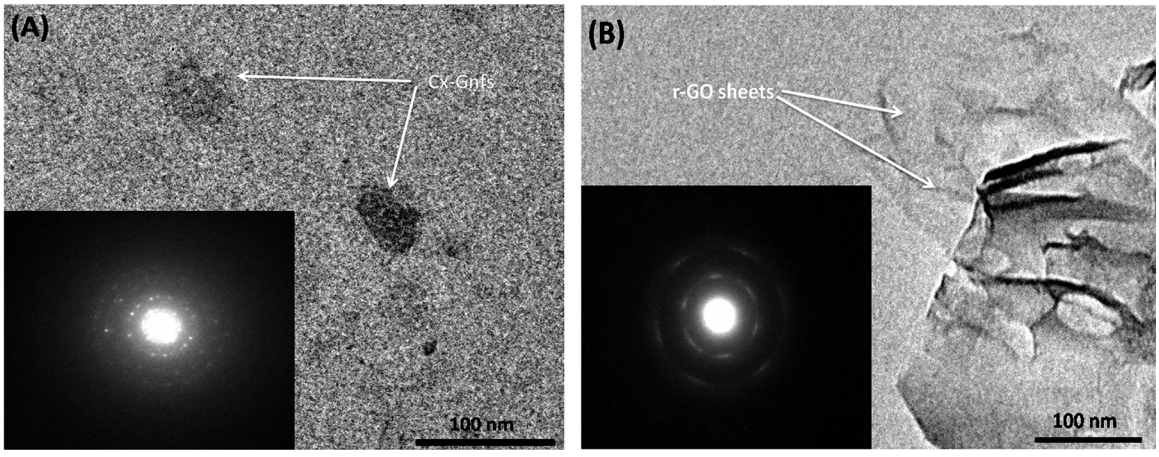


Fig. 3. TEM image showing the nanostructured **(A)** Cx-Gnfs and **(B)** r-GO with the respective inset showing the SAED pattern of the nanomaterials.

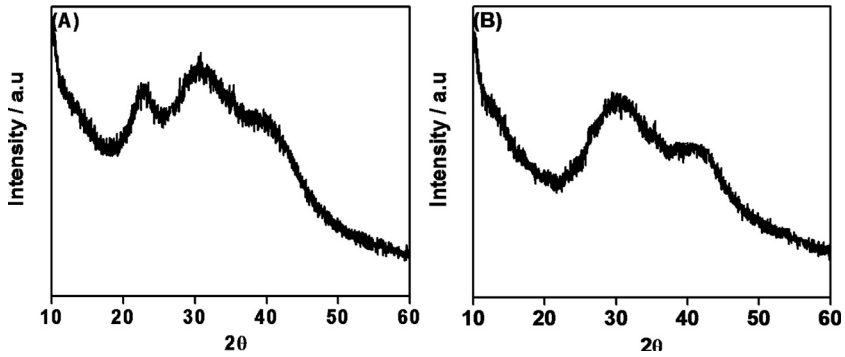


Fig. 4. XRD pattern of **(A)** Cx-Gnfs and **(B)** r-GO.

The surface coverage (Ţ) of the electrodeposited Cx-Gnfs and r-GO on ITO were also determined using Eq. (11) [57];

$$I_p = \frac{n^2F^2A\text{Ţ}\upsilon}{4RT} \tag{11}$$

The anodic and cathodic average of Ţ value for Cx-Gnfs/ITO is found to be 9.25×10^{-8} molcm^{-2} and for r-GO/ITO is 0.21×10^{-8} molcm^{-2}.

Based on the comparison of the results of both the electrode materials it can be clearly inferred that Cx-Gnfs shows a better electron tranfer kinetics. Hence, the electrodeposited Cx-Gnfs on ITO provides a larger surface area for immobilization of the probe DNA segment as compared to r-GO on ITO.

4.2.2. Chronocoulometry

The charge can be obtained by integration of current with respect to time that is the response of the chronocoulometry experiment [58]. The relation of the charge (Q) with time (t) can be given by Anson Eq. (12) obtained by integrating the Cottrell equation;

$$Q = \frac{2nFAD^{1/2}C_O t^{1/2}}{\prod^{1/2}} \tag{12}$$

Where, Q, n, A, D, C_0, and t stands for charge, number of electron transferred, area of the electrode (here 0.22 cm^2), diffusion coefficient, bulk concentration and time respectively. The Fig. 6(A) shows the forward scan of the choronocoulometric response of (a) bare ITO, (b) Cx-Gnfs/ITO, and (c) r-GO/ITO in 5 mM $[Fe(CN)_6]^{3-/4-}$ (PBS, 100 mM, pH 7.0, 0.9% NaCl). Whereas plots in Fig. 6(B) shows the linear dependence of Q on $t^{1/2}$, called as Anson plot for the (a) bare ITO, (b) Cx-Gnfs/ITO, and (c) r-GO/ITO. The slopes of the Anson plot is used for calculating the diffusion co-efficient using above Eq. (12) which will be further helpful in explaining the electron transfer kinetics of both the materials (Cx-Gnfs and r-GO). The diffusion coefficient (D) for Cx-Gnfs/ITO and r-GO/ITO were found to be 4.79×10^{-10} cm^{2}s^{-1} and 4.12×10^{-10} cm^{2}s^{-1} respectively. The higher value of D for Cx-Gnfs/ITO further corroborates the better electron transfer kinetics of the Cx-Gnfs as compared to that of r-GO.

4.2.3. Electrochemical impedance spectroscopy (EIS)

EIS is a widely used electrochemical technique, due to its fast and

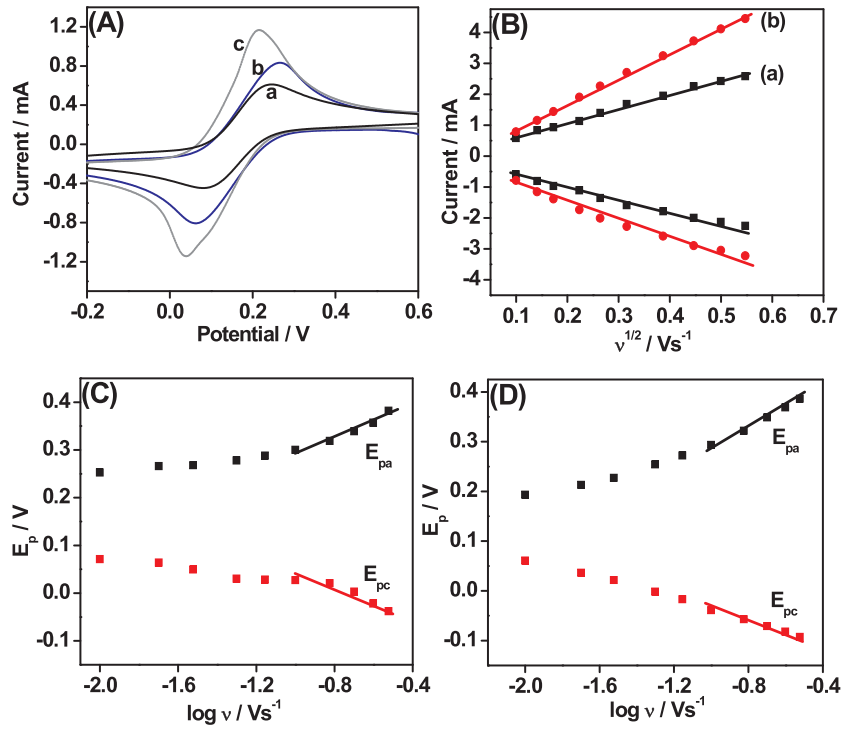


Fig. 5. (A) Cyclic voltammetry response of (a) bare ITO, (b) Cx-Gnfs/ITO and (c) r-GO/ITO in 5 mM $[Fe(CN)_6]^{3-/4-}$ (PBS, 100 mM, pH 7.0, 0.9% NaCl), **(B)** plot between current and $\upsilon^{1/2}$, **(C)** Laviron Plot for Cx-Gnfs/ITO and **(D)** Laviron plot for r-GO/ITO.

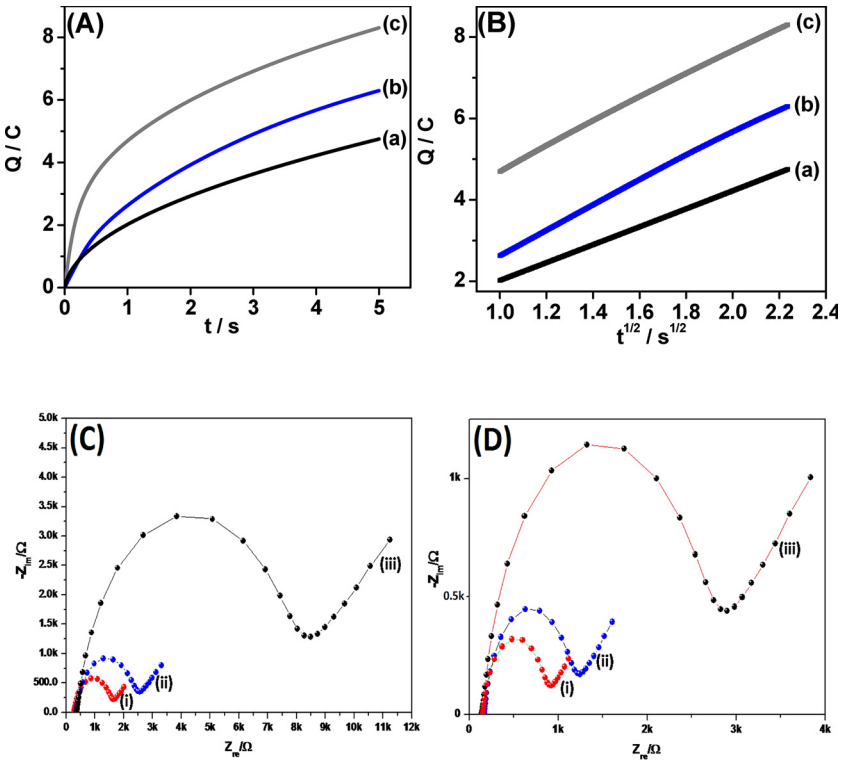


Fig. 6. (A) Chronocoulometric response of (a) bare ITO, (b) Cx-Gnfs/ITO and (c) r-GO/ITO in 5 mM $[Fe(CN)_6]^{3-/4-}$ (PBS, 100 mM, pH 7.0, 0.9% NaCl), **(B)** Anson Plot showing linear dependency of Q and $t^{1/2}$. EIS characterization of materials **(C)** (i) Cx-Gnfs/ITO, (ii) p-DNA/Cx-Gnfs/ITO and (iii) cDNA/pDNA/Cx-Gnfs/ITO and **(D)** (i) r-GO/ITO, (ii) p-DNA/r-GO/ITO and (iii) cDNA/pDNA/r-GO/ITO in 5 mM $[Fe(CN)_6]^{3-/4-}$ (PBS, 100 mM, pH 7.0, 0.9% NaCl).

sensitive response occurring at the electrode-electrolyte interface. EIS consist of a semicircle portion, observed at higher frequencies that corresponds to the electron transfer limited process, followed by a linear part at the lower frequencies attributed to a diffusion limited electron transfer process. The semicircle diameter of EIS spectra gives value of charge transfer resistance (R_{ct}) [26,59]. The increase in the diameter of the semicircle reflects increase in the R_{ct} and the numerical values of R_{ct} can be derived from experimental impedance spectra by fitting an equivalent circuit based on modified Randles and Ershler model to the data. To investigate the electrochemical response of the fabricated pDNA/Cx-Gnfs/ITO bioelectrode, EIS technique has been adopted. As the oligonucleotide chain is composed of amine-rich nucleoside residues, it is expected that the presence of free functional groups on the Cx-Gnfs/ITO surface may lead to chemisorption of the complementary targets thereby providing false positive signal. Hence, to avoid the competition of hybridization event with the non-specific adsorption of cDNA, a study for optimization of the pDNA concentration has been performed. As shown in Suppl. material Fig. S4(A), by increasing the amount of pDNA from 10^{-10} M to 10^{-4} M, the electrochemical signal is levelled off at 10^{-6} M. So, it was presumed that the maximum immobilization was achieved at this concentration (10^{-6} M).

To understand the hybridization process the analytical performance of the pDNA/Cx-Gnfs/ITO bioelectrode towards recognition of the target oligonucleotides has also been optimized. The EIS response of the pDNA/Cx-Gnfs/ITO bioelectrode in the presence of 1 μM complementary target DNA at different incubation time (5–25 min) was conducted. It was observed that the R_{ct} value increases with increase in the incubation time upto 15 min [*cf.* Suppl. material Fig. S4(B)], showing that the extent of hybridization is accomplished within this duration.

The change in R_{ct} value after each modification step was analysed using PBS containing 5 mM $[Fe(CN)_6]^{3-/4-}$ as the redox probe. Under the optimal conditions, the bare ITO electrode shows the R_{ct} value of 1.9 KΩ (curve not shown). After electrophoretic deposition of Cx-Gnfs [*cf.* Fig. 6(C); curve (i)], there was a decrease in the R_{ct} value (1.2 KΩ). This decrease in the R_{ct} value clearly indicates that there was a significant change in the reactivity after deposition of Cx-Gnfs which might be due to structural change that facilitates strong adsorption leading to faster electron transfer kinetics. Under similar conditions the R_{ct} value obtained for the rGO/ITO electrode [*cf.* Fig. 6(D); curve (i)] was found to be 0.8 KΩ, which was lower, compared to that of Cx-Gnfs/ITO electrode. This change in the R_{ct} value is due to the good conductivity of r-GO compared to Cx-Gnfs. Further, covalent binding of *E. coli* pDNA on Cx-Gnfs/ITO electrode [*cf.* Fig. 6(C); curve (ii)] and r-GO/ITO electrode [*cf.* Fig. 6(D); curve (ii)] results in enhancement of R_{ct} in each case which is due to the negatively charged phosphate backbone of pDNA exposed to the electrolyte, which in turn repels the $[Fe(CN)_6]^{-3/-4}$ ion. When the pDNA is incubated with its complementary target DNA sequence (cDNA), the hybridization reaction occurs and more negatively charged phosphate backbones are introduced. Hence, the R_{ct} value further increases due to the formation of double-stranded DNA [*cf.* Fig. 6(C) and (D); curve (iii)]. It can thus be inferred that with a change in negative charge and conformation transition, there is a change in the interfacial properties.

4.3. Electrochemical response studies

EIS was used for the quantitative determination of *E. coli*, as it provides an instant response, showing the efficiency of electron transfer between the electrode surface and the electro-active substances. The difference between the value of R_{ct} for the pDNA immobilized electrode after hybridization with cDNA ($\Delta R_{ct} = R_{ct}$ cDNA - R_{ct} pDNA) has been used as the measurement signal. The EIS response of pDNA/Cx-Gnfs/ITO bioelectrode towards the hybridization of cDNA can be seen from the Fig. 7(A). The analytical signal for pDNA/Cx-Gnfs/ITO bioelectrode (in terms of ΔR_{ct}) shows linear relationship with the logarithmic value of the complementary target DNA concentration ranging from 10^{-17} to 10^{-6} M [*cf.* Fig. 7(B)] and follows the subsequent equation:

$$\Delta R_{ct} = 7981.90 + 462.25\,[\log(\text{concentration of cDNA})] \quad R^2 = 0.995 \tag{13}$$

The detection limit is calculated to be 1×10^{-17} M using the expression 3σ/sensitivity, where σ is the standard deviation of the blank

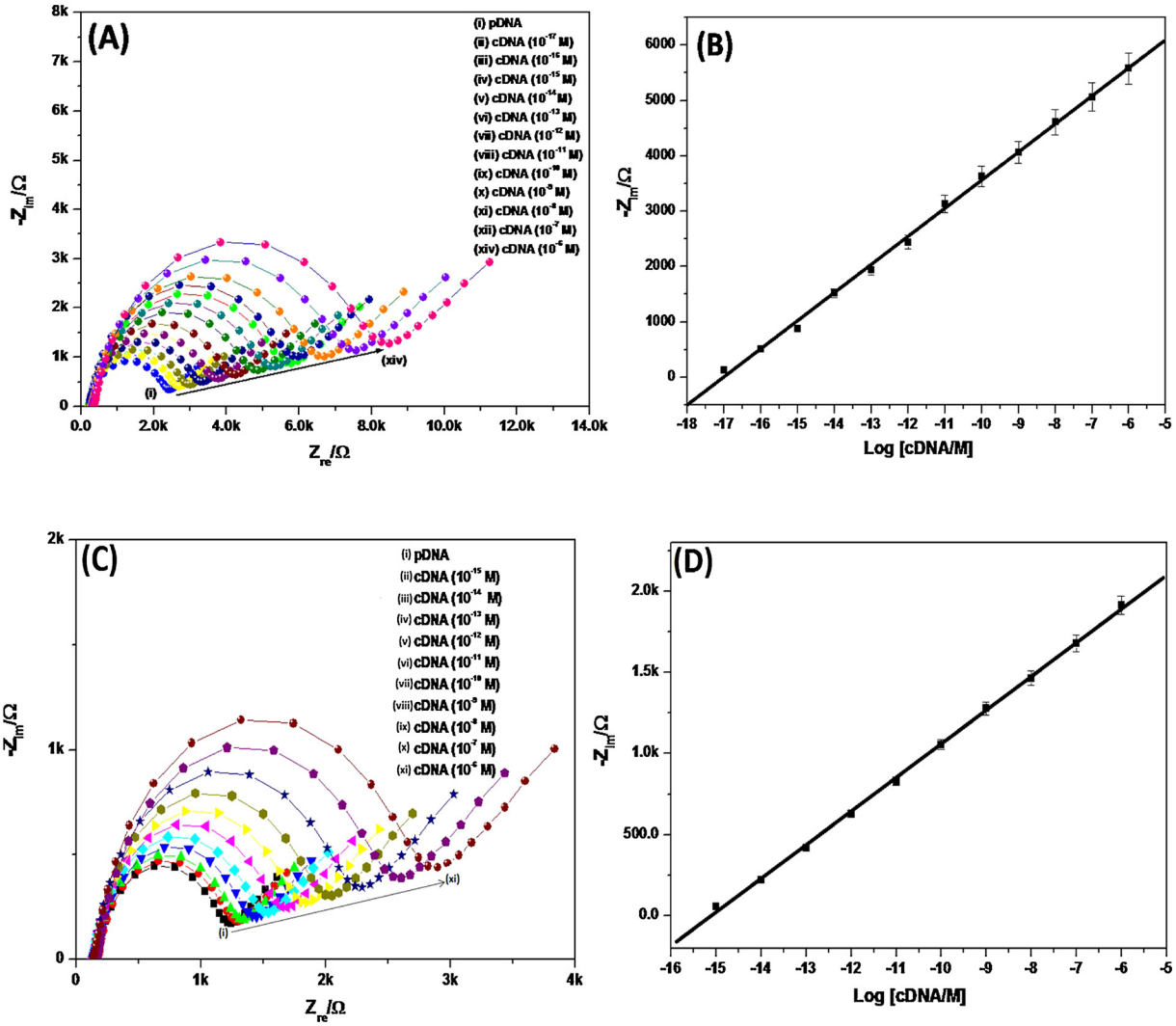


Fig. 7. (A) EIS data for detection of cDNA on pDNA immobilized on electrodeposited Cx-Gnfs/ITO electrode, **(B)** the calibration plot for detection of cDNA on pDNA/Cx-Gnfs/ITO, (**C**) detection of cDNA on pDNA immobilized on electrodeposited r-GO/ITO electrode and **(D)** the calibration plot for detection of cDNA on pDNA/r-GO/ITO in 5 mM $[Fe(CN)_6]^{3-/4-}$ (PBS, 100 mM, pH 7.0, 0.9% NaCl).

electrode. The response of pDNA/rGO/ITO bioelectrode towards hybridization with cDNA can be observed in Fig. 7(C) and similar linear relationship with the logarithmic value of the complementary target DNA concentration for pDNA/rGO/ITO bioelectrode was obtained in the range from 10^{-15} to 10^{-6} M [*cf.* Fig. 7(D)] which follows the subsequent equation:

$$\Delta R_{ct} = 2420.36 + 170.33\,[\log(\text{concentration of cDNA})] \quad R^2 = 0.995 \tag{14}$$

Whereas the detection limit for pDNA/rGO/ITO bioelectrode was calculated to be 1×10^{-15} M by using the expression 3σ/sensitivity.

The detection limit obtained for pDNA/Cx-Gnfs/ITO bioelectrode was found to be better as compared to that obtained using pDNA/rGO/ITO bioelectrode, which might be attributed to the presence of more functional groups (-COOH groups) on the edges of Cx-Gnfs compared to rGO. These functional groups provide a conducive environment for the immobilization of pDNA on Cx-Gnfs/ITO electrode.

4.4. Selectivity study

The specificity of the pDNA/Cx-Gnfs/ITO bioelectrode towards different target DNA sequences (non-complementary, one base mismatch and complementary) has been studied using EIS [Suppl. material Fig. S5]. After incubation of the bioelectrode with non-complementary DNA [*cf.* Suppl. material Fig. S5 curve (ii)], there was a slight or negligible change in the R_{ct} value with respect to the pDNA (curve i). Since, the non-complementary DNA bases do not match with the pDNA bases it is expected that there is no hybridization taking place and hence the R_{ct} should result in a semicircle diameter similar to that of pDNA/Cx-Gnfs/ITO bioelectrode. When the pDNA/Cx-Gnfs /ITO bioelectrode was immobilized with one base mis-match DNA sequence there was a slight increase in semicircle diameter in comparison to that of the pDNA/Cx-Gnfs/ITO bioelectrode (curve iii). This explains the partial hybridization of pDNA with the complementary bases of the one base mis-match DNA resulting in increased negative charge on the electrode surface which repels the marker ion. These results reveal the selectivity of the pDNA/Cx-Gnfs/ITO bioelectrode towards different target DNA sequences. The negligible change in the value of R_{ct} has been observed when pDNA/Cx-Gnfs/ITO bioelectrode was treated with non-complementary DNA and one-base mismatch, which shows that fabricated bioelectrode is highly specific for *E. coli* detection.

4.5. Reusability and stability of the bioelectrode

The fabricated sensor seems to be stable enough to allow the regeneration of pDNA/Cx-Gnfs/ITO bioelectrode after incubating with

cDNA. The removal of the cDNA is done by thermal denaturation in which the used electrodes were immersed in a mixture solution containing Tris buffer-HCl (10 mM) with pH 8.0 and 1 mM EDTA at 100 °C for 5 min, further taking it to the low temperature using an ice bath for 30 min. There was decrease in the R_{ct} value after each regeneration step and an average loss of ~15% was noted after 6th cycle of regeneration [*cf.* Suppl. material Fig. S6(A)]. The decrease in the signal might be due to the surface fouling of the bioelectrode after every regeneration process. The storage stability of fabricated bioelectrode was investigated by recording five times by measuring the signal every week over a continuum of 30 days. The fabricated bioelectrode shows a decrease in the signal response of about ~18% (stored at 4 °C) [*cf.* Suppl. material Fig. S6(B)]. The sensor performance of the Cx-Gnf/ITO electrode was found to be better than r-GO/ITO electrode and most of reported works [Table 1] indicating the suitability of prepared material for biosensing applications.

5. Conclusions

Herein we report a highly sensitive nucleic acid sensor for the determination of *E.coli* using a newly synthesized carbon material (Cx-Gnfs) [46]. The electrophoretic method for the deposition of material was used to fabricate the working electrode and further the material was characterized using physical methods such as SEM, TEM, contact angle, UV–vis spectroscopy, FT-IR, XRD and electrochemically using cyclic voltammetry, chronocoulometry and EIS. The application of the proposed electrode was carried out for the genosening of *E.coli* nucleic acid strand using EIS technique. It was observed that the deposited Cx-Gnfs based electrode shows enhanced sensitivity, selectivity, detection limit and reproducibility. The efforts are in progress for the development of technology for *E.coli* monitoring.

Acknowledgements

N. Jaiswal is thankful to UGC, India for providing fellowship and CSIR, India for awarding SRF. C.M. Pandey acknowledges the financial support received from Department of Science and Technology, India under DST-INSPIRE Faculty project (Grant No. DST/INSPIRE/04/2015/000932). A.S. is thankful to CSIR, India, for the award of SRF. The authors are sincerely thankful to Prof. O.N Srivastava (Dept. of Physics, I.Sc. B.H.U) and Prof. Rajiv Prakash (IIT B.H.U) for providing access to TEM and SEM facilities respectively.

Appendix A. Supplementary data

Supplementary material related to this article can be found, in the online version, at doi:https://doi.org/10.1016/j.snb.2018.07.055.

References

[1] E. Scallan, R.M. Hoekstra, F.J. Angulo, R.V. Tauxe, M.A. Widdowson, S.L. Roy, J.L. Jones, P.M. Griffin, Foodborne illness acquired in the United States-major pathogens, Emerg. Infect. Dis. 17 (2011) 7–15.
[2] Reports of Selected *E. coli* Outbreak Investigations, CDC (Centers for Disease Control and Prevention), 2016.
[3] G.R. Campbell, J. Prosser, A. Glover, K. Killham, Detection of *Escherichia coli* in soil and water using multiplex PCR, J. Appl. Microbiol. 91 (2001) 1004–1010.
[4] O. Lazcka, F.J.D. Campo, F.X. Munoz, Pathogen detection: a perspective of traditional methods and biosensors, Biosens. Bioelectron. 22 (2007) 1205–1217.
[5] S. Radu, G. Rusul, O.W. Ling, E. Purwati, M. Mustakim, S. Lihan, Rapid isolation and detection of *Escherichia coli* O157:H7 by use of rainbow agar O157 and PCR assay, J. Trop. Med. Public Health 31 (2000) 77–79.
[6] A.K. Deisingh, M. Thompson, Strategies for the detection of *Escherichia coli* O157:H7 in foods, J. Appl. Microbiol. 96 (2004) 419–429.
[7] C.R. Newton, A. Graham, PCR, Bios Scientific Publishers, Oxford, UK, 1997.
[8] Y. Hu, Q. Zhang, J.C. Meitzler, Rapid and sensitive detection of *Escherichia coli* O157:H7 in bovine faeces by multiplex PCR, J. Appl. Microbiol. 87 (1999) 867–876.
[9] J. Logan, K. Edwards, N. Saunders, Real-Time PCR: Current Technology and Applications, Caister Academic Press, London, UK, 2009.
[10] P.R. Solanki, A. Kaushik, V.V. Agrawal, B.D. Malhotra, Nanostructured metal oxide-based biosensors, NPG Asia Mater. 3 (2011) 17–24.
[11] C. Zhu, G. Yang, H. Li, D. Du, Y. Lin, Electrochemical sensors and biosensors based on nanomaterials and nanostructures, Anal. Chem. 87 (2015) 230–249.
[12] H. Karadeniz, A. Erdem, A. Caliskan, Electrochemical monitoring of DNA hybridization by multiwalled carbon nanotube based screen printed electrodes, Electroanalysis 20 (2008) 1932–1938.
[13] N. Jaiswal, I. Tiwari, Recent build outs in electroanalytical biosensors based on carbon-nanomaterial modified screen printed electrode platforms, Anal. Methods 9 (2017) 3895–3907.
[14] Y. Shao, J. Wang, H. Wu, J. Liu, I.A. Aksay, Y. Lin, Graphene based electrochemical sensors and biosensors: a review, Electroanalysis 22 (2010) 1027–1036.
[15] M. Pumera, Graphene-based nanomaterials and their electrochemistry, Chem. Soc. Rev. 39 (2010) 4146–4157.
[16] K. Geim, K.S. Novoselov, The rise of graphene, Nat. Mater. 6 (2007) 183–191.
[17] A. Ambrosi, C.K. Chua, A. Bonanni, M. Pumera, Electrochemistry of graphene and related materials, Chem. Rev. 114 (2014) 7150–7188.
[18] Y. Wang, J. Ping, Z. Ye, J. Wu, Y. Ying, Impedimetric immunosensor based on gold nanoparticles modified graphene paper for label-free detection of *Escherichia coli* O157:H7, Biosens. Bioelectron. 49 (2013) 492–498.
[19] C.M. Pandey, G. Sumana, K.N. Sood, B.D. Malhotra, Electrochemical studies of cystine modified self-assembled monolayer for *Escherichia coli* detection, Thin Solid Films 519 (2010) 1178–1183.
[20] C.M. Pandey, G. Sumana, I. Tiwari, Copper oxide assisted cysteine hierarchical structures for immunosensor application, Appl. Phys. Lett. 105 (2014) 1–5.
[21] C.M. Pandey, I. Tiwari, V.N. Singh, K.N. Sood, G. Sumana, B.D. Malhotra, Highly sensitive electrochemical immunosensor based on graphene-wrapped copper oxide-cysteine hierarchical structure for detection of pathogenic bacteria, Sens. Actuators B 238 (2017) 1060–1069.
[22] C.M. Pandey, I. Tiwari, G. Sumana, Hierarchical cystine flower based electrochemical genosensor for detection of *Escherichia coli* O157:H7, RSC Adv. 4 (2014) 31047–31055.
[23] I. Tiwari, M. Gupta, C.M. Pandey, V. Mishra, Gold nanoparticle decorated graphene sheet-polypyrrole based nanocomposite: its synthesis, characterization and genosensing application, Dalton Trans. 44 (2015) 15557–15566.
[24] S. Xu, Y. Zhang, K. Dong, J. Wen, C. Zheng, S. Zhao, Electrochemical DNA biosensor based on graphene oxide- chitosan hybrid nanocomposites for detection of *Escherichia coli* O157:H7, Int. J. Electrochem. Sci. 12 (2017) 3443–3458.
[25] C.M. Pandey, G. Sumana, B.D. Malhotra, Microstructured cystine dendrites-based impedimetric sensor for nucleic acid detection, Biomacromolecules 12 (2011) 2925–2932.
[26] I. Tiwari, M. Singh, C.M. Pandey, G. Sumana, Electrochemical genosensor based on graphene oxide modified iron oxide–chitosan hybrid nanocomposite for pathogen detection, Sens. Actuators B 206 (2015) 276–283.
[27] I. Tiwari, M. Singh, C.M. Pandey, G. Sumana, Electrochemical detection of a pathogenic *Escherichia coli* specific DNA sequence based on a graphene oxide–chitosan composite decorated with nickel ferrite nanoparticles, RSC Adv. 5 (2015) 67115–67124.
[28] C.M. Pandey, A. Sharma, G. Sumana, I. Tiwari, B.D. Malhotra, Cationic poly(lactic-co-glycolic acid) iron oxide microspheres for nucleic acid detection, Nanoscale 5 (2013) 3800–3807.
[29] M. Saadaoui, I. Fernández, G. Luna, P. Díez, S. Campuzano, N. Raouafi, A. Sánchez, J.M. Pingarrón, R. Villalonga, Label-free electrochemical genosensor based on mesoporous silica thin film, Anal. Bioanal. Chem. 408 (2016) 7321–7327.
[30] K. Kerman, Y. Morita, Y. Takamura, E. Tamiya, *Escherichia coli* single-strand binding protein–DNA interactions on carbon nanotube-modified electrodes from a label-free electrochemical hybridization sensor, Anal. Bioanal. Chem. 381 (2005) 1114–1121.
[31] C.M. Pandey, R. Singh, G. Sumana, M.K. Pandey, B.D. Malhotra, Electrochemical genosensor based on modified octadecanethiol self-assembled monolayer for *Escherichia coli* detection, Sens. Actuators B 151 (2011) 333–340.
[32] N. Zainudin, A.R.M. Hairul, M.M. Yusoff, L.L. Tan, K.F. Chong, Impedimetric graphene-based biosensor for the detection of *Escherichia coli* DNA, Anal. Methods 6 (2014) 7935–7941.
[33] P.R. Solanki, A. Kaushik, P.M. Chavhana, S.N. Maheshwari, B.D. Malhotra, Nanostructured zirconium oxide based genosensor for *Escherichia coli* detection, Electrochem. Comm. 11 (2009) 2272–2277.
[34] K. Li, J. Huang, G. Shi, W. Zhang, L. Jin, A sensitive nanoporous Gold-based electrochemical DNA biosensor for *Escherichia coli* detection, Anal. Lett. 44 (2011) 2559–2570.
[35] A. Lermo, E. Zacco, J. Barak, M. Delwiche, S. Campoy, J. Barbe´, S. Alegret, M.I. Pividori, Towards Q-PCR of pathogenic bacteria with improved electrochemical double-tagged genosensing detection, Biosens. Bioelectron. 23 (2008) 1805–1811.
[36] D. Jiang, F. Liu, C. Liu, L. Liu, X. Pu, An electrochemical sensor based on allosteric molecular beacons for DNA detection of *Escherichia coli.* O157:H7, Int. J. Electrochem. Sci. 8 (2013) 9390–9398.
[37] S.S. Zhang, Q.Q. Tan, X.M. Li, F. Li, Recognition and detection of ssDNA using 2-mercaptobenzothiazole self-assembled monolayer modified gold electrode, Sens. Actuators B 128 (2008) 529–535.
[38] Y. Li, J. Deng, L. Fang, K. Yu, H. Huang, L. Jiang, W. Liang, J. Zheng, A novel electrochemical DNA biosensor based on HRP-mimicking hemin/G-quadruplex wrapped GOx nanocomposites as tag for detection of *Escherichia coli* O157:H7, Biosens. Bioelectron. 63 (2015) 1–6.
[39] W. Zhang, C. Luo, L. Zhong, S. Nie, W. Cheng, D. Zhao, S. Ding, Sensitive detection of enteropathogenic *E. coli* using a bfpA gene-based electrochemical sensor, Microchim. Acta 180 (2013) 1233–1240.
[40] K. Arora, N. Prabhakar, S. Chand, B.D. Malhotra, *Escherichia coli* genosensor based

on polyaniline, Anal. Chem. 79 (2007) 6152–6158.
[41] M.H. Abdalhai, A.M. Fernandes, X. Xia, A. Musa, J. Ji, X. Sun, Electrochemical genosensor to detect pathogenic bacteria (*Escherichia coli* O157:H7) as applied in real food samples (fresh beef) to improve food safety and quality control, J. Agric. Food Chem. 63 (2015) 5017–5025.
[42] G. Longinotti, G. Ybarra, J. Montserrat, Optical and electrochemical detection of a verotoxigenic *E. coli* gene using DNAzyme-labeled stem-loops, J. Electrochem. Sci. Eng. 7 (2017) 193–200.
[43] D. Wang, J. Chen, S.R. Nugen, Electrochemical detection of Escherichia coli from aqueous samples using engineered phages, Anal. Chem. 89 (2017) 1650–1657.
[44] Y. Huang, X. Dong, Y. Liu, L.J. Li, P. Chen, Graphene-based biosensors for detection of bacteria and their metabolic activities, J. Mater. Chem. 21 (2011) 12358–12362.
[45] G. Wu, Z. Dai, X. Tang, Z. Lin, P.K. Lo, M. Meyyappan, K.W.C. Lai, Graphene Field-effect transistors for the sensitive and selective detection of Escherichia coli using pyrene-tagged DNA aptamer, Adv. Healthc. Mater. 6 (2017) 1–9.
[46] M. Rosillo-Lopez, T.J. Lee, M. Bella, M. Harta, C.G. Salzmann, Formation and chemistry of carboxylic anhydrides at the graphene edge, RSC Adv. 5 (2015) 104198–104202.
[47] C.G. Salzmann, S.A. Llewellyn, G. Tobias, M.A.H. Ward, Y. Huh, M.L.H. Green, The role of carboxylated carbonaceous fragments in the functionalization and spectroscopy of a single-walled carbon-nanotube material, Adv. Mater. 19 (2007) 883–887.
[48] S. Srivastava, V. Kumar, M.A. Ali, P.R. Solanki, A. Srivastava, G. Sumana, P.S. Saxena, A.G. Joshid, B.D. Malhotra, Electrophoretically deposited reduced graphene oxide platform for food toxin detection, Nanoscale 5 (2013) 3043–3051.
[49] A.R. Boccaccini, S. Keim, R. Ma, Y. Li, I. Zhitomirsky, Electrophoretic deposition of biomaterials, J. R. Soc. Interface 7 (2010) 581–613.
[50] M. Das, C. Dhand, G. Sumana, A.K. Srivastava, R. Nagarajan, B.D. Malhotra, Electrophoretically fabricated core-shell CNT-DNA biowires for biosensing, J. Mater. Chem. 22 (2012) 2727–2732.
[51] S.K. Mishra, S.N. Tripathi, V. Choudhary, B.D. Gupta, Surface plasmon resonance-based fiber optic methane gas sensor utilizing graphene-carbon nanotubes-poly (methyl methacrylate) hybrid nanocomposite, Plasmonics 10 (2015) 1147–1157.
[52] Q. Yang, Q. Li, Z. Yan, X. Hu, L. Kang, Z. Lei, Z.H. Liu, High performance graphene/manganese oxide hybrid electrode with flexible holey structure, Electrochim. Acta 129 (2014) 237–244.
[53] C.P. Chen, W.R. Luo, C.N. Chen, S.M. Wu, S. Hsieh, C.M. Chiang, T.Y. Dong, Redox-active π-conjugated organometallic monolayers: pronounced coulomb blockade characteristic at room temperature, Langmuir 29 (2013) 3106–3115.
[54] M. Pumera, Graphene-based nanomaterials for energy storage, Energy Environ. Sci. 4 (2011) 668–674.
[55] A.J. Bard, L.R. Faulkner, Electrochemical Methods Fundamentals and Applications, Wiley, India, 2006.
[56] E. Laviron, General expression of the linear potential sweep voltammogram in the case of diffusionless electrochemical systems, J. Electroanal. Chem 101 (1979) 19–28.
[57] H.Y. Gu, A.M. Yu, H.Y. Chen, Direct electron transfer and characterization of hemoglobin immobilized on a Au colloid–cysteamine-modified gold electrode, J. Electroanal. Chem. 516 (2001) 119–126.
[58] G. Perenlei, T.W. Tee, N.A. Yusof, G.J. Kheng, Voltammetric detection of potassium ferricyanide mediated by multi-walled carbon nanotube/titanium dioxide composite modified glassy carbon electrode, Int. J. Electrochem. Sci. 6 (2011) 520–531.
[59] E. Ivers-Tiffée, A. Weber, H. Schichlein, Electrochemical impedance spectroscopy, Handbook of Fuel Cells, John Wiley & Sons, Ltd, Chichester, 2010.

Nandita Jaiswal did her B.Sc. (Hons.) in Chemistry in 2012 from Banaras Hindu University, Varanasi, India. She received her M.Sc. in Analytical Chemistry in 2014 from Banaras Hindu University, Varanasi, India. She is currently working as senior research fellow, for her doctoral degree under guidance of Prof. Ida Tiwari in Department Of Chemistry, Institute of Science, Banaras Hindu University, Varanasi, India. Her interest of research includes electrochemical sensors and electrochemical biosensors based on composites materials.

Chandra Mouli Pandey received his PhD (Chemistry; 2015) from Banaras Hindu University, Varanasi, India, in collaboration with National Physical Laboratory, New Delhi, India. He is presently working as DST-INSPIRE Faculty in Department of Chemistry, Delhi Technological University, Delhi, on the development of microfluidics based biosensors for cancer biomarker detection. He has published more than 20 research papers in international journals and has recently authored a book entitled 'Biosensors: Fundamentals and Applications'. His main interest of research is development of biosensors for health care based on nano-materials, conducting polymers, Langmuir–Blodgett Films, self-assembled monolayers and bio-nanocomposites.

Amrita Soni has received her Master of Technology degree from Deen Bandhu Chotu Ram University of Science and Technology, Sonepat, Haryana, India. She is currently working as senior research fellow under Dr. Gajjala Sumana, Biomedical Instrumentation Section at National Physical Laboratory, New Delhi, India. Her interest of research are biosensors based on polymeric nanocomposites.

Ida Tiwari received her doctorate in 2001 in the field of electroanalytical sensors from Banaras Hindu University, Varanasi, India. There after she was awarded Research Associateship from C.S.I.R., New Delhi, India in which she worked on sensors. She joined Analytical Chemistry Division, Department of Chemistry, Faculty of Science, Banaras Hindu University, Varanasi, India as Assistant Professor in 2004 and is working as full time Professor from 2017. She has 15 years research experience in field of sensors, biosensors, composite materials, nanotechnology. She has handled projects from various funding agencies and has more than 60 publications.

Martin Rosillo-Lopez received his Ph.D degree from University College London, London, UK. He is presently working with Dr. Christoph G. Salzmann research group. His major research interest are preparation, characterisation, chemistry and application of novel carbon nanomaterials as an alternative to conventional graphene oxide.

Christoph G. Salzmann is Reader at University College London, London, UK. He is also a Royal Society University Research Fellow. He joined UCL in 2011 before working at Durham and Oxford. His research activities focus on the structural characterisation of disordered materials including disordered crystals, amorphous and nanomaterials as well as liquids.

Bansi D. Malhotra received his PhD from the University of Delhi, Delhi in 1980. He has published more than 300 papers in refereed international journals, has filed 13 patents, and has recently co-authored text books on 'Nanomaterials for Biosensors: Fundamentals and Applications' and 'Biosensors: Fundamentals and Applications'. He is a recipient of the National Research Development Corporation Award (2005) for invention on 'Blood Glucose Biochemical Analyzer' and is a Fellow of the Indian National Science Academy, the National Academy of Sciences, India and Academician of Asia Pacific Academy of Materials. His current research activities include Nanobiomaterials, Biosensors, Bio-fuel cells, Ordered Molecular Assemblies, Conducting Polymers, Langmuir-Blodgett Films, Self-assembled Mono-layers, Nano-Biotechnology, Biomedical Engineering and Biomolecular Electronics. He is currently a Professor at the Department of Biotechnology, Delhi Technological University, Delhi, India.

Gajjala Sumana received her Ph.D. (1998) from Jiwaji University in Chemistry, India. She is currently working as a principal scientist at the Biomedical Instrumentation Section, National Physical Laboratory, New Delhi, India. She has a research experience of 20 years in controlled drug delivery, liquid crystal polymers, polymer dispersed liquid crystals and biosensors. She has published more than 70 publications in the area of biomedical applications.

ISBN: 978-3-95450-184-7 doi:10.18429/JACoW-IPAC2018-THPML051

ELECTRON ACCELERATION BY A PLASMA WAVE IN THE PRESENCE OF A TRANSVERSELY PROPAGATED LASER WITH MAGNETIC FIELD

M. Yadav† and S. C. Sharma, Department of Applied Physics, Delhi Technological University, 110042, New Delhi, India
M. Kaur and D. N. Gupta, Department of Physics and Astrophysics, University of Delhi, 110007, New Delhi, India

Abstract

In this paper, we study the enhancement of electron acceleration by plasma wave in presence of a laser propagated perpendicular to the propagation of the wakefield and a static magnetic field. Electrons trapped in the plasma wave are highly accelerated by the additional field of the laser combined with the wakefield. The additional resonance provided by the laser field as well by the magnetic field contributes to the large energy gain of the electrons. The resonant enhancement of electron acceleration has been validated by single particle simulation. The dependence of energy gain on laser intensity, static magnetic field, laser spot size, initial electron energy and electron trajectories have been investigated.

INTRODUCTION

Advancement in laser technology has led to the development of very high-power and ultra-short laser pulse, based on chirped pulse amplification. Laser driven plasma wakefields have generated the great interest in last few decades owing to its ability to sustain very high accelerating gradients. It enables compact devices by producing electric fields of the order of 10-100 GeV/m. The concept of laser-driven plasma wakefield was first proposed by Tajima and Dawson [1]. Further experimental achievements led to the production of quasi-mono-energetic electron beams with energies in the range of 100 MeV to 1GeV. The plasma waves utilized for accelerating electrons to ultra-high energies can be excited using different schemes, such as laser wakefield acceleration (LWFA), plasma beat-wave acceleration (PBWA), plasma wakefield acceleration (PWFA), self-modulated wakefield acceleration (SMWFA).In LWFA, single laser pulse having pulse duration comparable to the plasma period is used to excite the plasma wave. The electrons may get trapped in the longitudinal wake of the field and accelerated to GeV energies. While in PBWA, two laser pulses with their frequency difference comparable to plasma wavelength are used to excite the plasma wakefield. Wave particle dephasing is the major limitation of these schemes. Surfatron concept [2] was also utilized, where a magnetic field is applied in the transverse direction to the plasma wave to prevent trapped electrons from outrunning the plasma wave.

* Work supported by University Grant Commission (UGC), Delhi, Govt. of India
† email address : raomonika7@gmail.com

The electron acceleration by plasma wave in plasma channel in the presence of guiding magnetic field to stabilize the electron motion and get higher accelerating gradients, was studied in Ref. [3]. In Ref. [4] the electron acceleration in plasma in the presence of static electric and magnetic fields in plasma is also discussed. Sharma and Tripathi [5] observed the electron energy gain up to 100 MeV using laser pulse in magnetized plasma. It was also observed that electron attains maximum energy near Doppler shifted cyclotron resonance.

ELECTRON DYNAMICS

In an underdense plasma, the nonlinear profile of plasma wave can be taken as:

$$\mathbf{E}_p = \hat{z}A\exp\left[\frac{-x^2}{r_p^2}\right]\cos(\eta) + \hat{x}A\left(\frac{2x}{k_p r_p^2}\right)\exp\left[\frac{-x^2}{r_p^2}\right]\sin(\eta), \quad (1)$$

where $\mathbf{E}_p = \mathbf{E}_{px}\hat{z} + \mathbf{E}_{pz}\hat{x}$, r_p is the radius of wakefield and $\eta=\omega t-kz+\delta$is the phase of the wave.The scalar potential ϕ of the wakefield can be calculated using $\mathbf{E} = -\nabla\phi$ .Let the plane polarised laser propagates through the plasma in transverse direction. The form of the laser field taken is

$$\mathbf{E}_l = \hat{z}A_0\exp\left[\frac{-r^2}{2r_0^2}\right]\exp\left[-i(\omega_0 t - k_0 x)\right] = \mathbf{E}_z\hat{z}, \quad (2)$$

where r_0 is the laser spot size. The magnetic field associated with the laser can be calculated using Maxwell equations as

$$\mathbf{B}_l = -\hat{y}\left(\frac{k_0}{\omega_0}\right)A_0\exp\left[\frac{-r^2}{2r_0^2}\right]\exp\left[-i(\omega_0 t - k_0 x)\right], \quad (3)$$

A static magnetic field B_0 is also applied in negative y-direction ($-\mathbf{B}_0\hat{y}$), which is parallel to the laser magnetic field.

In the presence of plasma wave, laser, and constant magnetic field, the relativistic equation of motion and energy gain equation can be written as

$$\frac{d\mathbf{p}}{dt} = -e(\mathbf{E}_l + \mathbf{v}\times\mathbf{B}) - e\mathbf{E}_p \quad (4)$$

$$\frac{d\gamma}{dt} = -\frac{e}{mc^2}(\mathbf{E}_l + \mathbf{E}_p).\mathbf{v} \quad (5)$$

where $\mathbf{p}$ is the electron momentum and γ is the 2-D relativistic Lorentz factor for electrons given by $\gamma^2 = 1+(p_x^2 + p_z^2)/m_0^2c^2$. Substituting the plasma wave field and laser field in Eqs. (4) and

Content from this work may be used under the terms of the CC BY 3.0 licence (© 2018). Any distribution of this work must maintain attribution to the author(s), title of the work, publisher, and DOI.

ISBN: 978-3-95450-184-7 doi:10.18429/JACoW-IPAC2018-THPML051

Content from this work may be used under the terms of the CC BY 3.0 licence (© 2018). Any distribution of this work must maintain attribution to the author(s), title of the work, publisher, and DOI.

(5) and taking components of momentum equation, the electron dynamics can be investigated.
Here we have normalized the physical quantities as $a_0 = eA_0/m_0\omega_0 c$, $a_p = eA/m\omega_p c$, $b_0 = eB_0/m\omega$, $t \to \omega t$, $r_0 = kr_0$, $r_p = kr_p$, $v_z = v_z/c$, $v_x = v_x/c$, $z \to k_0 z$, and $x \to k_0 x$,where e and m are the electron charge and rest mass, respectively. The ordinary coupled differential equations are obtained describing single electron dynamics. These equations are solved numerically using relativistic single particle code.

RESULTS AND DISCUSSION

We solved the relativistic equation of motion and energy equation numerically using fourth order Runge-Kutta method in MATLAB. The dimensionless parameters have been used during entire study. The electron dynamics has been investigated for distinct laser and plasma parameters in presence of static magnetic field $b_0 = 0.01$ (estimated using $B_0 = mc\omega/e$). These parameters are optimised to get the maximum acceleration. Here, a_0=0.25 corresponds to the laser intensity of 8.6×10^{16} W/cm^2, given laser wavelength equal to 1μm. Other laser and plasma wave parameters chosen are: laser spot size r_0=30 (corresponds to r_0~8.8μm), radius of the wakefield r_p=50 (corresponds to rp~14.7μm), initial positions x_0 and z_0 are 0.6 and 0.4 respectively, initial velocities v_{x0} and v_{z0} are 0.5 and 0.8 respectively. The ratio of plasma frequency to the laser frequency ($\omega_p/\omega = 0.5$) has been optimised to a value of 0.5.

To observe the effect of the additional laser field, we have given the estimation of electron energy with laser intensity parameter (a_0). Figure 1 represents the variation of electron energy γmc^2 with respect to normalized distance z. It is observed that the electron gains the energy during acceleration due to the additional acceleration imparted by the laser field. Next, we have kept the plasma wave amplitude constant at 0.8 to estimate the effect of only laser field.Energy gain for different valuesof a0 (a_0=0.15, a_0=0.20, a_0=0.25) has been plotted both in presence and absence of static magnetic field.It is observed that energy gain increases with a0 ranging from 0.15 to 0.25..The maximum electron energy reached is about 2 GeV. This gain is due to the combined effect of transverse electric field of laser and longitudinal electric field of plasma wave. The electrons accelerate up to GeV energy level due to the combined accelerating field in the interaction region. It can be understood from momentum and energy equations which shows that due to coupling of transverse electric field of laser E_z with plasma field, the electrons get additional momentum in the direction of propagation of the plasma wave. The electron energy obtained in presence of magnetic field is approximately twofolds the energy obtained in absence of magnetic field, as shown in Fig. 1. This is due to the fact that the electrons rotates at the cyclotron frequency (ω_c) about the lines of force in the magnetic field. Thus at $\omega = \omega_c$, cyclotron resonance occurs, and the resonant increment in electron acceleration is obtained.

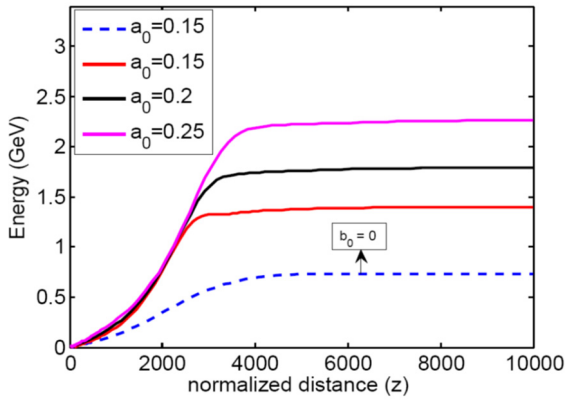


Figure 1: Variation of electron energy (γmc^2 in GeV) as a function of normalized distance z for electrons originated at x_0=0.6, and z_0=0.4 with normalized initial velocities v_{x0}=0.5,and v_{z0}=0.8.Other parameters are as ap=0.8, r_0=30 , r_p=50 , $\omega_p/\omega = 0.5$.

One of the worthmentioning observation here is that the energy gain is noted only for values of a0 less than ap(a_0<a_p). This could be due to the reason that at low laser intensity, the laser magnetic field contribution (**v**×**B**) to the elctron motion may be negligible. If we increase a_0, larger effect of laser magnetic field is experienced by the electron and it is scattered away from the propagation axis.

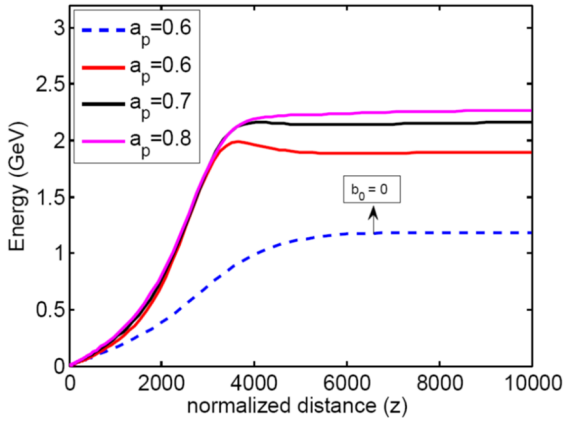


Figure 2: Variation of electron energy (γmc^2 in GeV) as a function of normalized distance z keeping a_0=0.25.

Figure 2 shows the variation of electron energy with normalized distance at a_0=0.25 for different plasma intensity parameter (a_p=0.6,0.7,0.8). Other parameters are same as used in Fig. 1. The laser field (a_0) is kept constant to observe the electron acceleration only by the plasma wave. It is observed that varying ap leads to an increase in the energy of the accelerated electrons. A higher value of a_p corresponds to larger longitudinal electric field. Hence electrons trapped in plasma wave experience a larger force in longitudinal direction and gain high energies. In the absence of external static magnetic field, the energy of electron obtained is approximately half of the energy obtained in presence of the magnetic field. This is because of the cyclotron resonance. As for $\omega > \omega_c$, resonance

ISBN: 978-3-95450-184-7 doi:10.18429/JACoW-IPAC2018-THPML051

condition is satisfied and electrons attain their maximum energy.

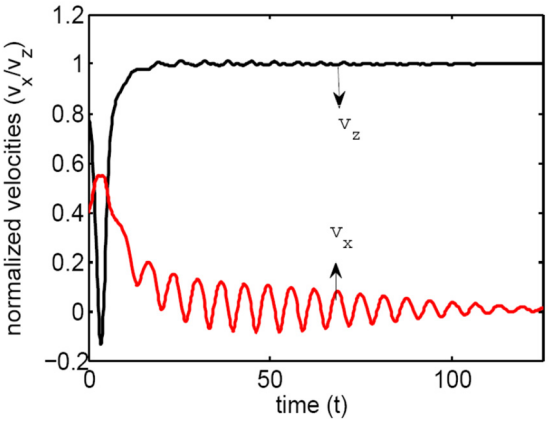


Figure 3: Plot of normalised velocities v_x and v_z with time for a_0=0.25. Other parameters are same as in Fig. 1.

Initial kinetic energy of electron is also an important factor in determinig the electron energy gain and trajectories during acceleeation. In Fig. 3, variation of normalised velocity of electron in x and z-direction with time is shown for different initial kinetic energies. Other parameters considered are same as in Fig. 1. As the electron is mainly accelerating in z-direction, the velocity of electron in that direction is expected to be increasing with time. Hence it accelerates and attains a maximum velocity approximately equal to the speed of light c.

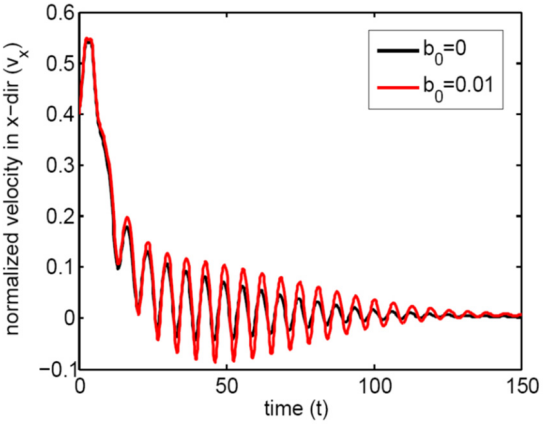


Figure 4: Plot of v_{x0} with time for b_0=0, 0.01. Other parameters are same as in Fig. 2.

The initial velocity given to electron in x-direction is 0.4c. Initially the electron velocity increases and then starts decreasing with time. And finally, almost all of the velocity is transfered in z-direction. This indicates that after a certain time the electron traverses in z-direction without much scattering in transverse direction.

In Fig. 4, electron velocity plot is shown both in the presence as well as absence of static magnetic field. Other parameters are same as in Fig. 3. In the presence of magnetic field, electron velocity oscillation amplitude is greater than in the absence of magnetic field. This is due to the additional lorentz force of external static magnetic field in x-direction.

CONCLUSION

In this study, we observed a significant increment in the electron energywhen a laser is propagated transversely to the plasma wave in the presence of a magnetic field. This electron energy gain is further enhanced in the presence of an external static magnetic field due to cyclotron resonance. We observed approximately twofold increment in the electron energy in the presence of an external constant magnetic field.It is due to an additional $\boldsymbol{v} \times \boldsymbol{B}$ term in z-direction. The role of laser intensity, plasma wave amplitude, and initial electron energies on electron energy has also been observed. Electron energy increases with the laser intensity as long as plasma wave amplitude is kept higher than laser intensity parameter. Initial energy of electrons is also a major factor in determining the electron energy and electron trajectory. It has been noticed that the electrons with higher initial kinetic energies are less scattered. This study may be useful in producing very high energy electrons, which may further be used in medicine, high energy physics, free-electron lasers and so.

REFERENCES

[1] T. Tajima and J. M. Dawson, “Laser electron accelerator”, *Phys. Rev. Lett.*, vol. 43, no. 4, p. 267, Jul. 1979, doi:10.1103/PhysRevLett.43.267.

[2] M. E. Dieckmann, P. Ljung, A. Ynnerman, K. G. McClements, “Three-dimensional visualization of electron acceleration in a magnetized plasma”, *IEEE Trans Plasma Sc.,* vol. 30, no. 1, p. 20-21, Aug. 2002, doi: 10.1109/TPS.2002.1003903.

[3] D. N. Gupta, M. Kaur, K. Gopal, and H. Suk, “Space-Charge field assisted electron acceleration by plasma wave in magnetic plasma channel”, *IEEE Trans. Plasma Sc.,* vol. 44, no.11, p. 2867-29873, Nov. 2016, doi:10.1109/TPS.2016.2615649.

[4] G. D. Tsakiris, C. Gahn, and V. K. Tripathi, “Laser induced acceleration in the presence of static electric and magnetic fields in plasma”, Phys. Plasmas, vol. 7, no. 7, p. 3017-3029, Jul. 2000, doi:10.1063/1.874154.

[5] A. Sharma and V. K. Tripathi , “Ponderomotive acceleration of electrons by a laser pulse in magnetized plasma”, *Phys. Plasmas*, vol. 16, no. 4, p. 043103, Apr. 2009, doi:10.1063/1.3098537.

Content from this work may be used under the terms of the CC BY 3.0 licence (© 2018). Any distribution of this work must maintain attribution to the author(s), title of the work, publisher, and DOI.

Int. J. Electron. Commun. (AEÜ) 95 (2018) 16–23

Contents lists available at ScienceDirect

Int. J. Electron. Commun. (AEÜ)

journal homepage: www.elsevier.com/locate/aeue

Regular paper

Electronically tunable high gain current-mode instrumentation amplifier

Sirish Oruganti, Neeta Pandey*, Rajeshwari Pandey

Dept. of Electronics & Communication Engg., Delhi Technological University, Shahbad Daulatpur, Main Bawana Road, Delhi 110042, India

ARTICLE INFO

Keywords:
CDTA
Current mode
High gain
Instrumentation amplifier

ABSTRACT

A new design for electronically tunable current mode (CM) instrumentation amplifier (IA) is presented in this paper. It employs Modified Z copy Current Differencing Transconductance Amplifier (MZC-CDTA) along with a resistor. The gain of the proposed CM IA is controlled by a single resistor and can theoretically approach infinite value. Electronic tuning feature is augmented by using a MOS based resistor. The functionality is verified through simulations on Cadence Virtuoso using TowerJazz's 180 nm Technology Node and performance against PVT variations is also examined. Feasibility of on-chip implementation is confirmed by the post-layout simulations carried out.

1. Introduction

Instrumentation Amplifiers (IA) play a major role in sensor signal acquisition and readout [1,2] which amplify differential signals to be processed further by secondary stages such as ADCs. At the same time, IAs also suppress common mode signals like offsets and noise. It is thus essential that an IA has high differential gain, and more importantly, high common mode rejection ratio (CMRR). It is also desirable if the IA is tunable, and that its gain depends on as few passive components as possible, as the gain is sensitive to component values, and any mismatch could lead to errors.

A preliminary survey on IAs reveals that a wide range of topologies are reported in literature [3–29] and references cited therein. The available IAs may be categorized in two different ways which is based either on kind of active building blocks (ABB) employed or on type of input signal processed and output signal made available/provided. As per the first scheme, if the constituent active block in IA is voltage (current) mode then corresponding topology is called voltage (current) mode IA. The second categorization is based on the type of input signal processed and output signal provided. The IAs that process signal sensed through voltage sensor are termed as Voltage-Mode (VM) or Trans-Admittance-Mode (TAM) IAs if the output signal is available in form of voltage or current respectively for further processing. The Current-Mode (CM) and Trans-Impedance-Mode (TIM) IAs on the other hand process signal available from current sensors and provide current and voltage signal at output respectively. An in-depth investigation of [3–29], and references cited therein reveals that only few IAs exist that use CM ABBs having both input and output as current [23–29]. The salient features of these topologies are as follows:

- The CM blocks Current Feedback Operational Amplifier (CFOA) [23,24], Second-Generation Current Controlled Conveyor (CCCII) [25], Operational Floating Current Conveyor (OFCC) [26], Current Operational Amplifier (COA) [27] and Current Difference Buffer Amplifier (CDBA) [28] have been used for IA designs. The MOS based IA is reported in [29]
- Single ABB is used in [23], whereas [24–28] employ two or more ABBs.
- Single resistor is employed in [25], whereas others [23,24,26,27,28] make use of two or more resistors.
- The input and output impedances are proper in all topologies except [23,24], therefore additional active block(s) may be needed in [23,24] while interfacing.
- Large resistor ratio is needed for higher gain in [23,24,25,26,27,28] while [29] requires large aspect ratio to achieve high gain.
- Component matching is essential in [23,24,26,27].

Further, it is observed that the only single ABB based CM IA available [23] provides output through a passive component, and there is requirement of an additional active block to drive the next stage/load. It may therefore be inferred that no single ABB based CM IA topology is available in open literature that uses single passive component; provides output at high impedance; and facilitates higher gain with small component spread. To fill this gap, a single ABB based CM IA that does not put any constraint on component values, is put forward in this paper.

The contents of this paper are arranged in five sections. Section 2 briefly discusses the ABB MZC-CDTA [30], and the proposed CM IA. The effect of non-idealities on performance of proposed CM IA is

* Corresponding author.
E-mail addresses: sirishoruganti@ieee.org (S. Oruganti), n66pandey@rediffmail.com (N. Pandey).

https://doi.org/10.1016/j.aeue.2018.07.035
Received 15 February 2018; Accepted 30 July 2018
1434-8411/ © 2018 Elsevier GmbH. All rights reserved.

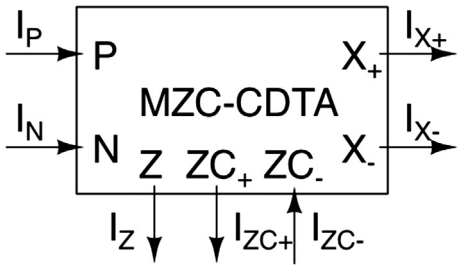


Fig. 1. MZC-CDTA circuit symbol.

addressed in Section 3, which covers the CMRR expression as well. The verification of the proposal is done through both pre and post layout simulations, and the findings are placed in Section 4. The paper is finally concluded in Section 5.

2. The MZC-CDTA and the proposed CM IA

The MZC-CDTA is based on the CDTA [31], with additional terminals provided to copy the current through Z terminal and add flexibility to the design. The circuit symbol of the MZC-CDTA is shown in Fig. 1. The terminal equations for the MZC-CDTA are as shown in (1).

$$\begin{bmatrix} V_P \\ V_N \\ I_Z \\ I_{ZC+} \\ I_{ZC-} \\ I_{X+} \\ I_{X-} \end{bmatrix} = \begin{bmatrix} 0 & 0 & 0 & 0 & 0 & 0 \\ 0 & 0 & 0 & 0 & 0 & 0 \\ 1 & -1 & 0 & 0 & 0 & 0 \\ 1 & -1 & 0 & 0 & 0 & 0 \\ -1 & 1 & 0 & 0 & 0 & 0 \\ 0 & 0 & g_m & 0 & 0 & 0 \\ 0 & 0 & -g_m & 0 & 0 & 0 \end{bmatrix} \begin{bmatrix} I_P \\ I_N \\ V_Z \\ V_{ZC+} \\ V_{ZC-} \\ V_{X+} \\ V_{X-} \end{bmatrix} \quad (1)$$

Here, g_m is the transconductance of the MZC-CDTA. The circuit diagram for the proposed MZC-CDTA based CM IA is shown in Fig. 2.

The proposed IA employs a single MZC-CDTA and a resistor and can provide both non-inverting and inverting outputs. Applying KCL at both the input nodes, we get

$$I_P = I_{IN+} + I_{X+} \quad (2)$$

and

$$I_N = I_{IN-} + I_{X-} \quad (3)$$

Thus, the expression for I_Z becomes

$$I_Z = I_{IN+} + I_{X+} - I_{IN-} - I_{X-} \quad (4)$$

where

$$I_{X+} = g_m R I_z \quad (5)$$

and

$$I_{X-} = -g_m R I_z \quad (6)$$

Substituting (5) and (6) in (4) gives

$$I_z = I_{IN+} - I_{IN-} + 2g_m R I_Z \quad (7)$$

Also,

$$I_{OUT1} = -I_{OUT2} = I_Z \quad (8)$$

Thus, the differential gain of the proposed CM IA at positive and negative output terminals is as computed in (9) and (10) respectively.

$$A_{ID1} = \frac{I_{OUT1}}{I_{IN+} - I_{IN-}} = \frac{1}{1 - 2g_m R} \quad (9)$$

$$A_{ID2} = \frac{I_{OUT2}}{I_{IN+} - I_{IN-}} = \frac{-1}{1 - 2g_m R} \quad (10)$$

It may be observed that:

- By tuning the value of $g_m R$ close to 0.5, the denominator becomes much smaller value than unity, thereby very high values of differential gain may be achieved.
- It is possible to achieve both non-inverting and inverting outputs from the proposed configuration. This provides flexibility to the designer in situations where current inversion is required for further processing.

Any common mode signal present at the input of the IA is mitigated due to differential input structure of MZC-CDTA. Therefore, if a common mode signal, whether it be in the form of a dc offset, a current bias in the previous stage, or a noise signal at the input terminals, will automatically be rejected by the proposed structure, as can be seen from (2), (3), and (4).

Considering perfect matching within the ABB, and neglecting the second-order effects, those IAs in literature which rely on component values/aspect ratios of external circuitry outside the ABB for the expression of gain are susceptible to lowering of CMRR if a mismatch occurs. Thus, in such structures, component/aspect ratio matching is essential. The proposed circuit uses single ABB, and one passive component, thus eliminating external component mismatch, and ensuring a high CMRR value. Fig. 3 shows the proposed CM IA with electronically tunable MOS resistor.

The expression for electronically tunable resistor is given by

$$R = \frac{1}{k_n (V_B - V_{Tn}) + k_p (V_B - |V_{Tp}|)} \quad (11)$$

where $k_n = \mu_n C_{OX} W/L$ and $k_p = \mu_p C_{OX} W/L$ are device transconductances of M_1 and M_2 respectively, and V_B is gate bias voltage.

Thus, the gain can be derived as a function of V_B by substituting (11) in (9) as

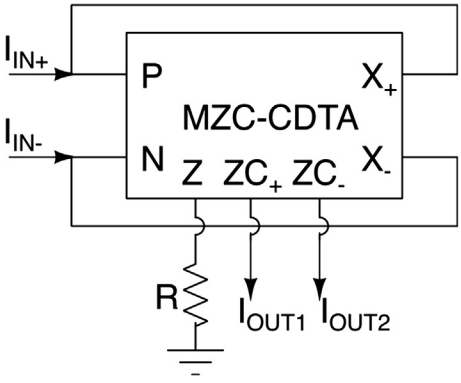


Fig. 2. Proposed CM IA.

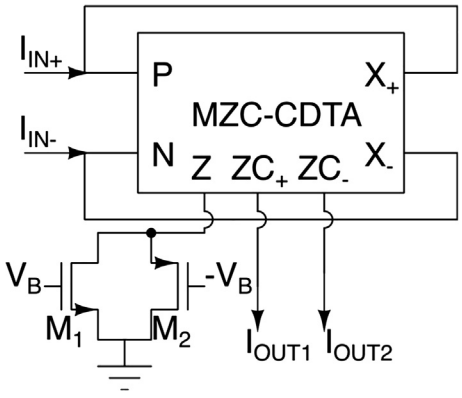


Fig. 3. Proposed electronically tunable CM IA.

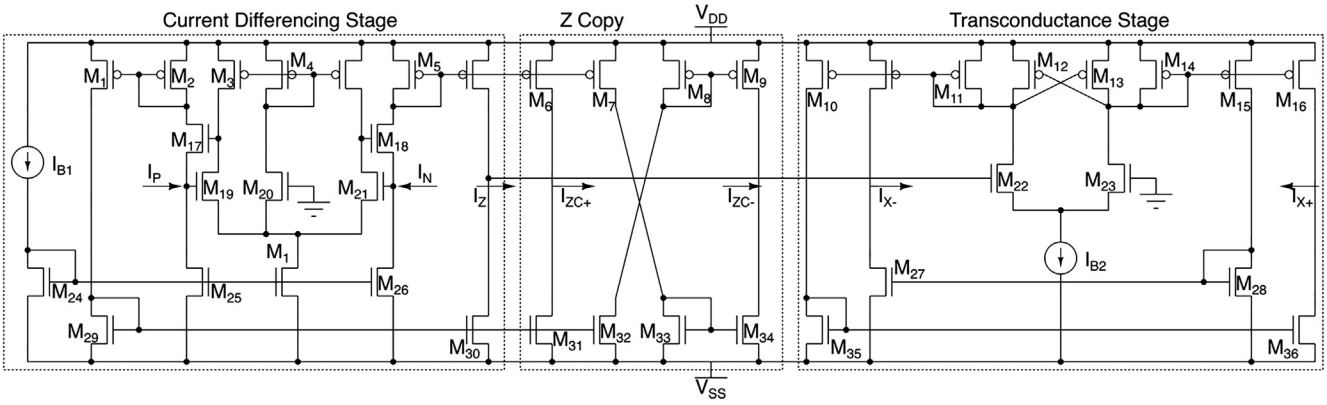


Fig. 4. CMOS implementation of MZC-CDTA.

$$A_{ID1} = \frac{1}{1-\frac{2g_m}{V_B(k_n+k_p)-(k_nV_{Tn}-k_p\,|V_{Tp}\,|)}} \tag{12}$$

Similarly, expression for A_{ID2} may be obtained by substituting (11) in (10).

3. Non-ideal analysis

Two types of non-idealities [32] arise while using the CDTA Active Block. The first is tracking error at the input terminals, represented as α_P and α_N, and the error in transconductance, represented by β. Taking these non-idealities into account, (4) and (7) respectively become

$$I_{Z_n1} = \alpha_P(I_{IN+} + I_{X+}) - \alpha_N(I_{IN-} + I_{X-}) \tag{13}$$

$$I_{Z_n1} = \alpha_P I_{IN+} - \alpha_N I_{IN-} + (\alpha_P + \alpha_N)\beta g_m R I_{Z_n1} \tag{14}$$

The differential gain A_{ID1} and A_{ID2} of (9) and (10) modify to A_{ID1_n1} and A_{ID2_n1} respectively.

The gains A_{ID1_n1} and A_{ID2_n1} are computed respectively as

$$A_{ID1_n1} = \frac{I_{OUT1_n1}}{\alpha_P I_{IN+} - \alpha_n I_{IN-}} = \frac{1}{1-(\alpha_p + \alpha_n)\beta g_m R} \tag{15}$$

$$A_{ID2_n1} = \frac{I_{OUT2_n1}}{\alpha_P I_{IN+} - \alpha_n I_{IN-}} = \frac{-1}{1-(\alpha_p + \alpha_n)\beta g_m R} \tag{16}$$

With $\alpha_P = \alpha_N = 1$ and $\beta = 1$, the gains A_{ID1_n} and A_{ID2_n} become

$$A_{ID1_n1} = -A_{ID12_n1} = \frac{1}{1-2g_m R} \tag{17}$$

Thus, the differential gain reduces to the ideal case as exhibited by (9) and (10).

For common mode, we take $I_{IN+} = I_{IN-} = I_C$. The common mode gains A_{IC1_n1} and A_{IC2_n1} at I_{OUT1} and I_{OUT2} may be computed as

$$A_{IC1_n1} = -A_{IC2_n1} = \frac{\alpha_P - \alpha_N}{1-(\alpha_P + \alpha_N)\beta g_m R} \tag{18}$$

The common mode rejection ratio can be computed as

$$\text{CMRR} = \frac{A_{ID_n1}}{A_{IC_n1}} = \frac{1-(\alpha_P + \alpha_N)\beta g_m R}{(\alpha_P - \alpha_N)(1-2\beta g_m R)} \tag{19}$$

It can be seen from (19) that the CMRR approaches infinity for $\alpha_P = \alpha_N$. Thus, it is possible to achieve very high values of CMRR.

The second type of non-ideality is parasitic impedances. The parasitics at Z, X+ and X− nodes reflect as a parallel combination of R_i and C_i (i = Z, X+, X−). Since we are connecting X+ and X− nodes to the P and N nodes, which are internally grounded, the effect of the parasitics R_{X+}, C_{X+}, R_{X-}, and R_{X-} is mitigated. The parasitics at Z terminal appear in parallel with R and modifies the differential gains of (9) and (10) respectively to

$$A_{ID1_n2} = \frac{I_{OUT1_n2}}{I_{IN+} - I_{IN-}} = \frac{1}{1-2g_m(R||R_Z||1/sC_Z)} \tag{20}$$

$$A_{ID2_n2} = \frac{I_{OUT2_n2}}{I_{IN+} - I_{IN-}} = \frac{-1}{1-2g_m(R||R_Z||1/sC_Z)} \tag{21}$$

Typically, $R_Z \gg R$, which reduces (20) and (21) to

$$A_{ID1_n2} = \frac{I_{OUT1_n2}}{I_{IN+} - I_{IN-}} = \frac{1}{1-2g_m(R||1/sC_Z)} \tag{22}$$

$$A_{ID2_n2} = \frac{I_{OUT2_n2}}{I_{IN+} - I_{IN-}} = \frac{-1}{1-2g_m(R||1/sC_Z)} \tag{23}$$

The CMRR also modifies to

$$\text{CMRR} = \frac{A_{ID_n2}}{A_{IC_n2}} = \frac{1-(\alpha_P + \alpha_N)g_m(R||1/sC_Z)}{(\alpha_P - \alpha_N)(1-2\beta g_m(R||1/sC_z))} \tag{24}$$

It may be observed from (22)–(24) that differential gain and CMRR deviate from their ideal values due to presence of parasitics, and this effect is evident in the frequency response.

4. Simulation and results

To test the efficacy of the proposed CM IA, as detailed in Section 3, Cadence Virtuoso simulations on TowerJazz's 180 nm Technology Node were performed. The CMOS implementation of the MZC-CDTA is shown as in Fig. 4. The transconductance stage proposed in [33] is appended to the current differencing stage and Z-copy modification stage as proposed in [30]. All the transistor dimensions have been kept the same as those in the works cited.

For all simulations, V_{DD} was 1.8 V and V_{SS} −1.8 V. I_{B1} for the current differencing unit was taken to be 100 μA and I_{B2} for the transconductance Unit as 500 μA. The aspect ratio of transmission gate transistors was set to 6.6 μ/180 n and bias voltage $|V_B|$ was varied for 1.8–3.3 V to ensure linear region of operation. The value of transconductance of CDTA was observed to be 7.198 mS, and this value has been used for calculations all through this work.

4.1. DC Analysis

The proposed CM IA was analysed for DC response to input current for various values of $|V_B|$. The input current was swept from −500 nA to 500 nA. The DC response plot is shown in Fig. 5. The curves show output current vs input current for various values of $|V_B|$ from 2.3 V to 3.3 V in steps of 0.25 V, which are shown in the legend of Fig. 5.

4.2. AC response

The proposed CM IA was tested for AC response and Common Mode

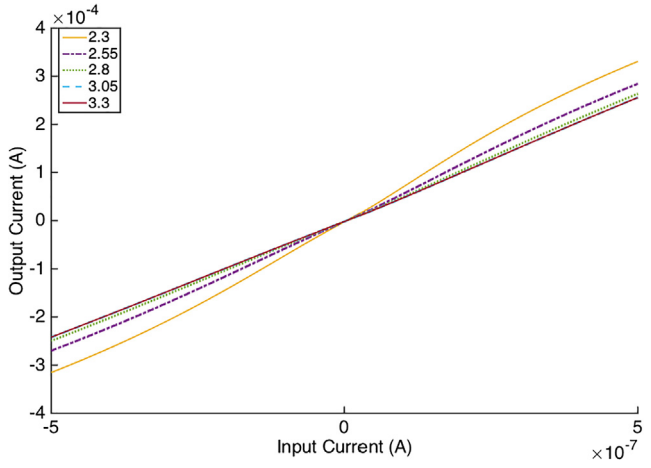


Fig. 5. DC analysis.

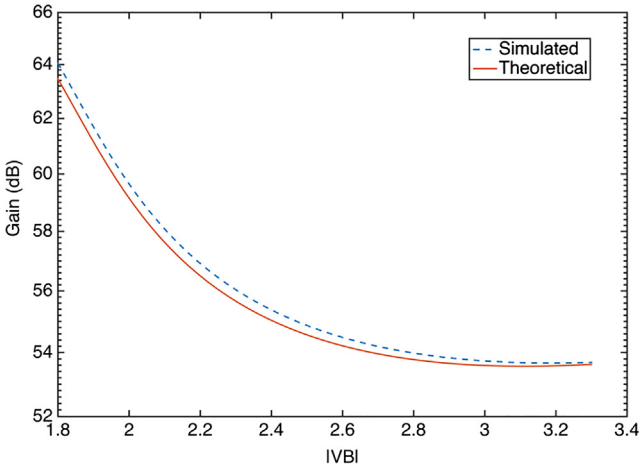


Fig. 7. Theoretical and simulated gain vs $|V_B|$.

Rejection Ratio (CMRR) for various values of $|V_B|$ from 1.8 V to 3.3 V in steps of 0.25 V, and the results are shown in Fig. 6. An AC signal of 100 nA amplitude was taken for this analysis.

The gain of the proposed CM IA, as found theoretically should reach infinity when g_mR is 0.5. The $|V_B|$ varied from 1.8 V to 3.3 V in steps of 0.25 V. The maximum gain was found as 64.055 dB with a 3 dB bandwidth of 0.9 MHz, and the minimum was 53.6903 dB with a 3 dB bandwidth of 4.8 MHz. The variation of theoretical and simulated gain against $|V_B|$ is shown in Fig. 7, which was obtained by analysing 100 points from 1.8 V to 3.3 V. It is observable that the simulated gain closely follows the theoretical gain for the entire range.

4.3. Transient analysis

Transient analysis was performed to test the proposed circuit for its output quality in the time domain. An input current of 5 kHz frequency and 100 nA amplitude was applied. $|V_B|$ was swept from 1.8 V to 3.3 V in steps of 0.25 V. The transient response is shown in the Fig. 8. The obtained waveforms are perfectly sinusoidal, and there is no distortion or offset observed.

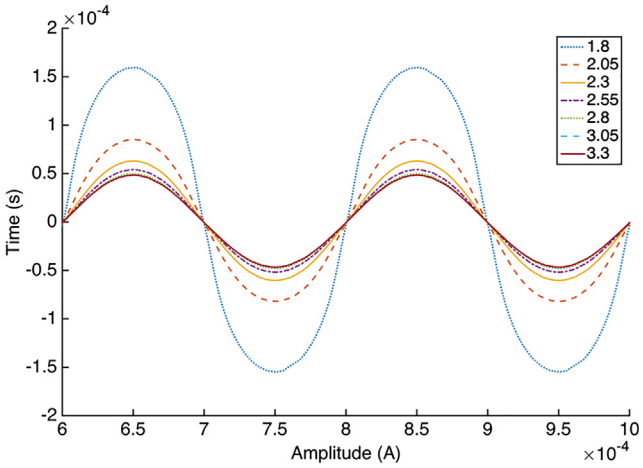


Fig. 8. Transient analysis.

4.4. Noise analysis

The figure of merit for any IA is noise immunity at the input. To test for this property on the proposed circuit, noise analysis simulation was performed. The results for input referred input/output noise in A/√Hz are shown in Fig. 9(a) and (b) respectively. The corresponding maximum values are 2.14×10^{-7} A/√Hz and 2.56×10^{-7} A/√Hz. Therefore, it may be interpreted that the proposed circuit is resilient to noise.

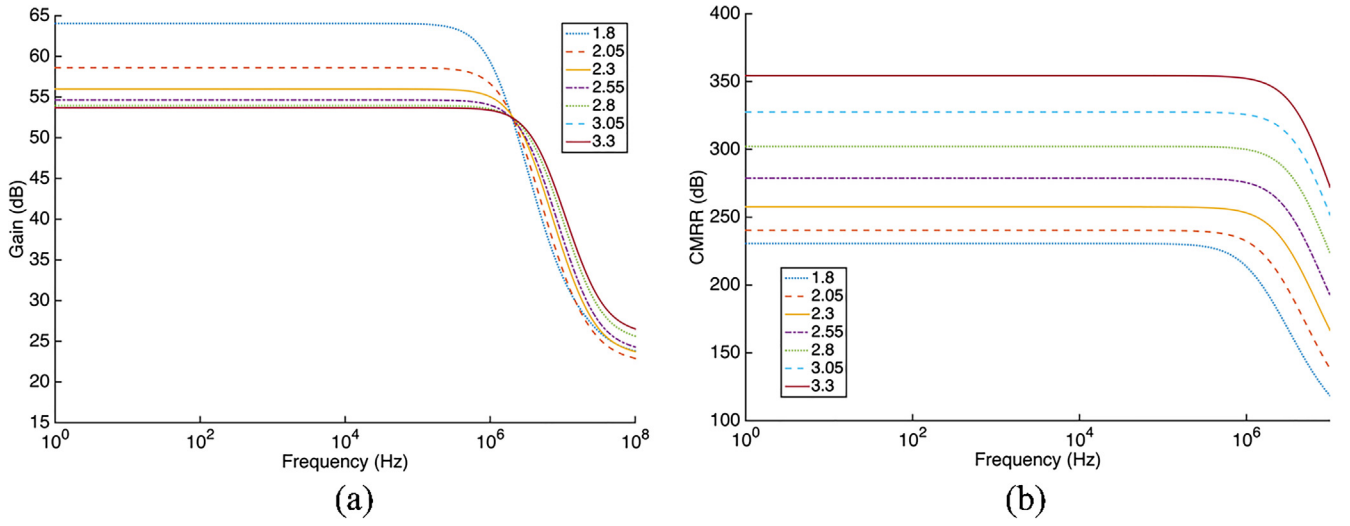


Fig. 6. AC analysis. (a) Gain and (b) CMRR.

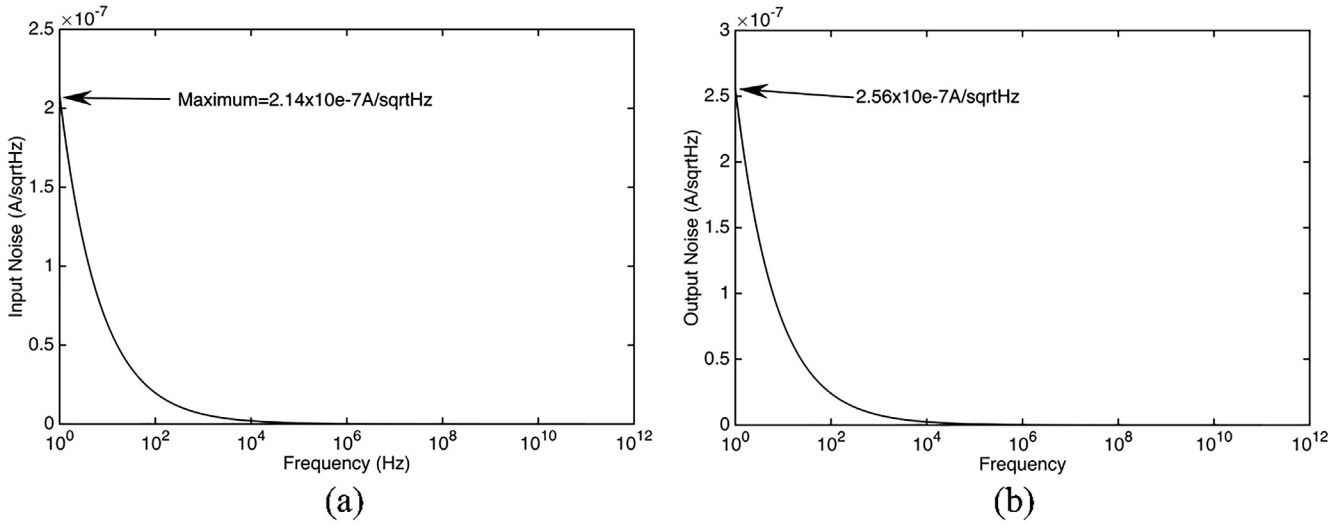


Fig. 9. Noise analysis. Input referred. (a) Input noise and (b) output noise.

4.5. Performance analysis

The transient performance of proposed CM IA is investigated under process corner, supply voltage, and temperature variations. The $|V_B|$ was set to 2.8 V. Typical Slow-Slow, Slow-Fast, Fast-Slow, and Fast-Fast Corners were analysed for process variation. The supply voltage was varied ± 5% in 5 steps. The temperature was swept from −20 °C to 70 °C in steps of 10 °C. The simulation results for process corner, supply voltage, and temperature variations are shown in Fig. 10(a), (b), and (c) respectively. A maximum deviation of 11% is observed in output amplitude against PVT variations. Thus, the circuit exhibits resilience to process, voltage, and temperature variations.

4.6. Post-layout simulation

To test the proposed circuit for performance once fabricated as an

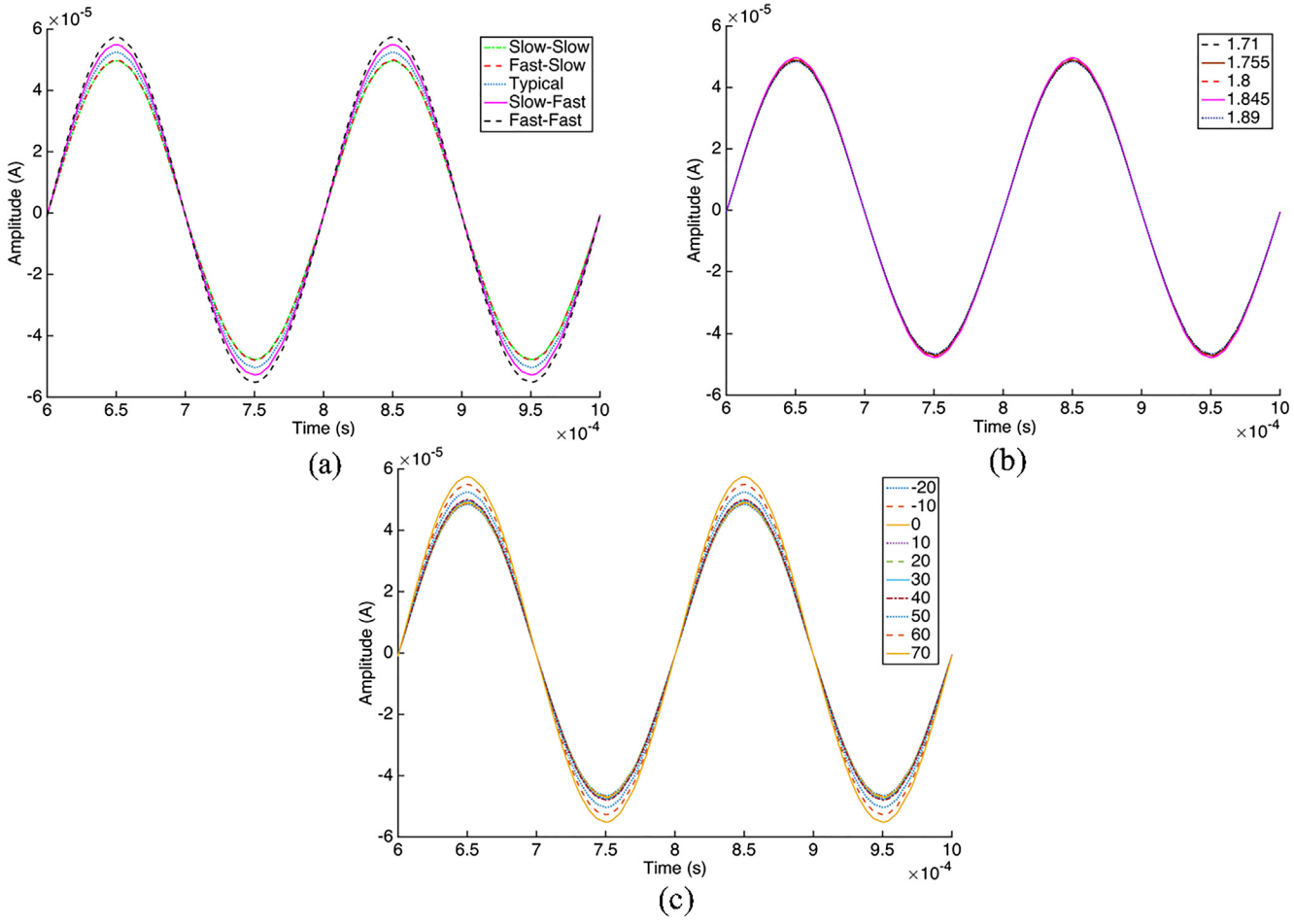


Fig. 10. Performance (PVT) analysis. (a) Process variation, (b) voltage and (c) temperature sweep.

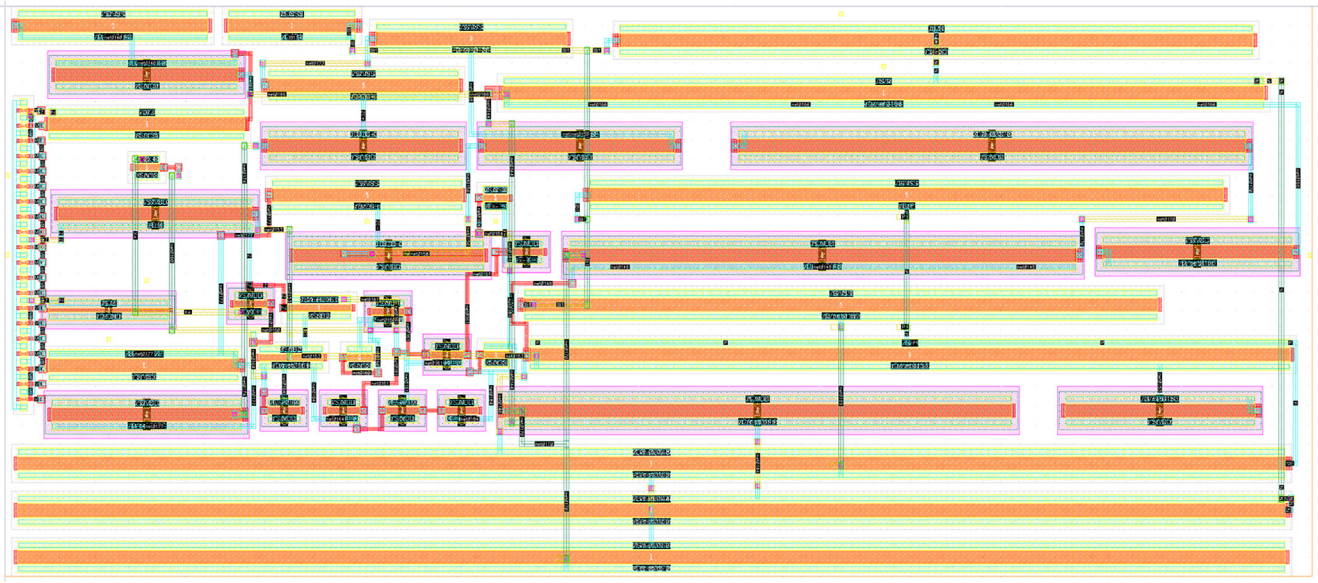


Fig. 11. Layout of proposed CM IA.

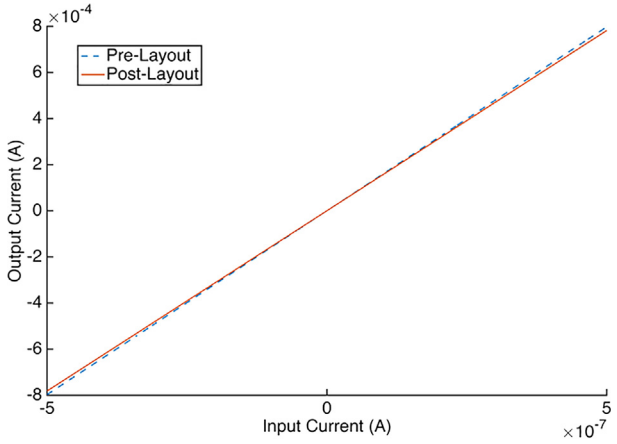


Fig. 12. Post-layout DC sweep.

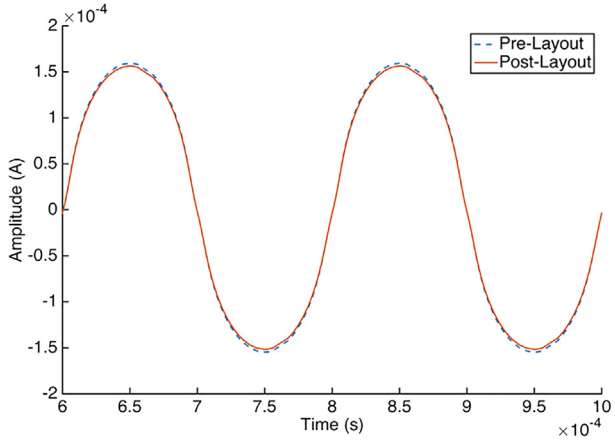


Fig. 13. Post-layout transient analysis.

IC, its layout was prepared as shown in Fig. 11, and post-layout simulations were performed. The area of the layout is 71.17 µm × 29.93 µm. Only one value of $|V_B|$ was taken to compare pre and post layout results.

The pre and post layout DC response curves for $|V_B| = 2.3$ V are shown in Fig. 12. A close matching can be observed between the pre and post layout curves, with a maximum variation of 0.15%.

Transient analysis was performed on the proposed IA for $|V_B| = 1.8$ V, by applying an input current of 100 nA, 5 kHz, and the resulting transients are shown in Fig. 13. The pre and post layout sinusoid waveforms can be seen bearing a close resemblance.

Pre and post layout frequency responses of differential gain and CMRR for $|V_B| = 1.8$ V are shown in Fig. 14(a) and (b) respectively. The effect of IA non-idealities may be observed from the curves as the gain reduces from 64.055 dB to 62.676 dB, and the CMRR from 230.7 dB to 219.4 dB.

In case of a mismatch or second-order effect such as channel length modulation within the current mirrors (M1-M2), (M4-M5), (M29-M30) (Fig. 4) in the current differencing unit, and other current mirrors, there will be input tracking errors due to the different signal paths, which may be represented by α_P and α_N. These effects indeed lower the CMRR and are detailed in Section 3. Eq. (24) captures the effect of these phenomenon in the final expression for CMRR. Monte-Carlo Analysis has been performed on the proposed CM IA. Two set of data were recorded by taking 5% mismatch in aspect ratio of (i) M29-M30 current mirror; and (ii) all current mirrors. The CMRR value reduces in both cases from 219 dB to 209 dB. Thus, it is clear that the device mismatch lower the CMRR value, however, the reduced value is also quite high.

5. Conclusion

A new single MZC-CDTA based CM IA is proposed in this work, which uses a single resistor. An electronically tunable MOS based resistor is used to obtain variable gain. The differential gain of the proposal can theoretically reach infinity by making g_mR close to 0.5. Extensive simulations are carried out to bolster the proposed concept, and post-layout simulations substantiate the feasibility of this circuit to be implemented and fabricated on chip.

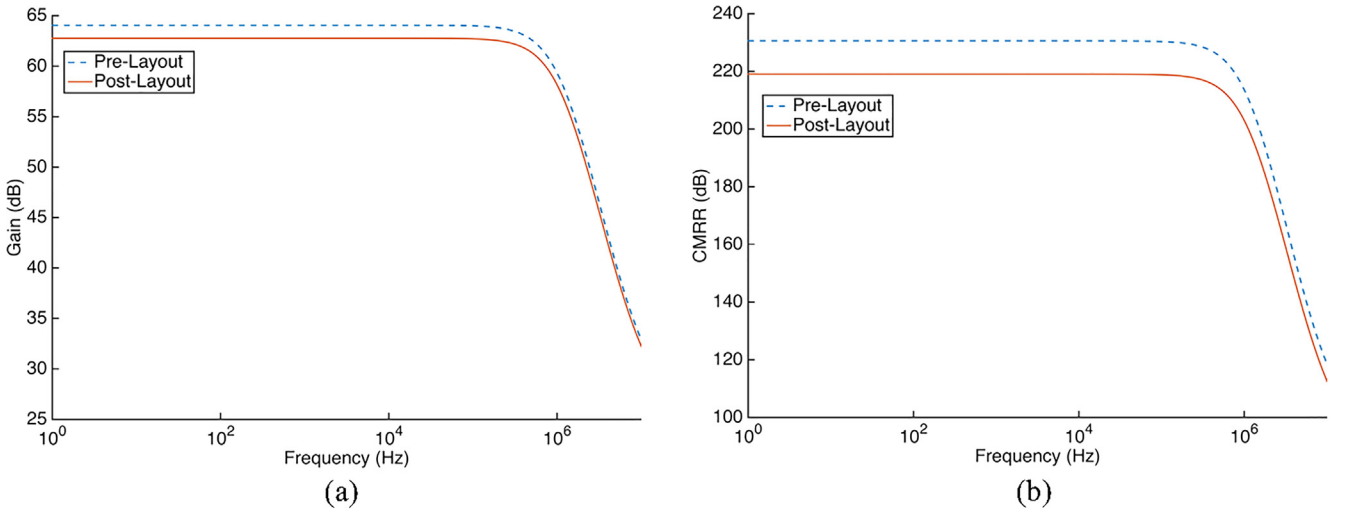


Fig. 14. Post-layout AC analysis. (a) Gain and (b) CMRR.

Acknowledgements

The authors thank Mr. Deva Nand, Assistant Professor, Department of Electronics and Communication Engineering, Delhi Technological University, for technical discussions.

Conflict of interest

The authors hereby declare that there exists no conflict of interest in this work, or in publishing this work in the AEÜ Journal of Electronics and Communication Engineering.

References

[1] Wu R, Huijsing JH, Makinwa KA. Precision instrumentation amplifiers and read-out integrated circuits. Springer; 2012.
[2] Counts L, Kitchen C. A designer's guide to instrumentation amplifiers, analog devices; 2006.
[3] Cini U, Toker A. DVCC based very low-offset current-mode instrumentation amplifier. Int J Electron 2017;104(8):1346–57. https://doi.org/10.1080/00207217.2017.1296592.
[4] Eldeeb MA, Ghallab YH, Ismail Y, El-Ghitani H. A 0.4 V miniature CMOS current mode instrumentation amplifier. IEEE transactions on circuits and systems II: Express briefs. https://doi.org/10.1109/TCSII.2017.2685589 [in press].
[5] Ercan H, Tekin SA, Alci M. Voltage and current controlled high CMRR instrumentation amplifier using CMOS current conveyors. Turk J. Electr. Eng. Comp. Sci. 2012;20:547–56.
[6] Ghallab YH, Badawy W, Kaler KVIS, Maundy BJ. A novel current mode instrumentation amplifier based on operational floating current conveyor. IEEE Trans Instrum Measur 2005;54:1941–9.
[7] Yang T, Liu K, Wang H. Novel high-CMRR DVCC-based instrumentation amplifier. In: 2nd International conference on engineering and industries (ICEI); 2011.
[8] Gupta P, Pandey N, Pandey R. High CMRR wide bandwidth instrumentation amplifier based on VDBA. Rec Adv Electr Electron Eng 2018;11(2):239–47.
[9] Maheshwari S. High CMRR wide bandwidth instrumentation amplifier using current controlled conveyors. Int J Electron 2002;89:889–96.
[10] Pandey N, Nand D, Kumar VV, Ahalawat VK, Malhotra C. Realization of OFCC based transimpedance mode instrumentation amplifier. Adv Electr Electron Eng 2016;14(2):162–7.
[11] Safari L, Minaei S, Yuce E. A new transresistance-mode instrumentation amplifier with low number of MOS transistors and electronic tuning opportunity. J Circuits Syst Comput 2016;25(4). https://doi.org/10.1142/S0218126616500225.
[12] Pandey R, Pandey N. A electronically tunable transimpedance instrumentation amplifier based on OTRA. J Eng 2013. ID 648540.
[13] Ren MY, Zhang CX, Sun DS. Design of CMOS instrumentation amplifier. Proc Eng 2012;29:4035–9.
[14] Zeinalzadeh F, Zare M. Instrumentation amplifier for the heart rate measurement with low power consumption. IOSR J Electr Electron Eng 2016;11(4–1):159–62.
[15] Zhu QS, Lidgey FJ, Su WJ. High CMRR, second generation current-mode instrumentation amplifiers. In: International symposium on circuits and systems (ISCAS 93), Chicago. p. 1326–8.
[16] Zhu QS, Lidgey FJ, Vere Hunt MA. Improved wide-band, high CMRR instrumentation amplifier. Clin Phys Physiol Measur (Sup. A) 1992;13:51–5.
[17] Hassan TM, Mahmoud SA. New CMOS DVCC realization and applications to instrumentation amplifier and active-RC filters. Int J Electron Commun (AEÜ) 2010;64:47–55.
[18] Schaffer V, Snoeij MF, Ivanov MV, Trifonov DT. A 36 V programmable instrumentation amplifier with sub-20 μV offsetand CMRR in excess of 120 dB at all gain settings. IEEE J Solid State Circuits 2009;44(7):2036–46.
[19] Bai W, Zhu Z. A 0.5-V power-efficient low-noise CMOS instrumentation amplifier for wireless biosensor. Microelectron J 2016;51:30–7.
[20] Johnston JE. A 24-bit delta–sigma ADC with an ultra-low noise chopper-stabilized programmable gain instrumentation amplifier. Comput Stand Interfaces 2001;23(2):123–8.
[21] Nizamuddin M. Design & performance analysis of instrumentation amplifier at nanoscale. Int J Adv Res Ideas Innov Technol 2017;3(1):793–8.
[22] Abidin Z, Tanno K, Mago S, Tamura H. Low common-mode gain instrumentation amplifier architecture insensitive to resistor mismatches. Int J Electr Comput Eng 2010;6(6):3247–54.
[23] Yuce E, Minaei S. New CCII-based versatile structure for realizing PID controller and instrumentation amplifier. Microelectron J 2010;41:311–6.
[24] Yuce E. Various current-mode and voltage-mode instrumentation amplifier topologies suitable for integration. J Circuits Syst Comput 2010;19(3):689–99.
[25] M'harzi Z, Alami M, Temcamani F. Low voltage, high CMRR, and wide bandwidth novel current mode current controlled instrumentation amplifier. Analog Integrated Circuit Signal Process 2017;90(1):199–205.
[26] Pandey N, Nand D, Pandey R. Generalised operational floating current conveyor based instrumentation amplifier. IET Circuits, Dev Syst 2016;10(3, 5):209–19.
[27] Safari L, Minaei S. A novel COA-based electronically adjustable current-mode instrumentation amplifier topology. Int J Electron Commun 2017;82:285–93. https://doi.org/10.1016/j.aeue.2017.08.051.
[28] Gupta K, Gupta P, Pandey N, Pandey R. CDBA-current based instrumentation amplifier. J Commun Technol Electron Comput Sci 2016;4:11–5.
[29] Safari L, Minaei S. A novel resistor-free electronically adjustable current-mode instrumentation amplifier. Circuits Syst Signal Process 2013;32(3):1025–38.
[30] Pandey N, Pandey R. Current mode full-wave rectifier based on a single MZC-CDTA. Active Passive Electron Comp 2013:967057https://doi.org/10.1155/2013/967057.
[31] Biolek D. CDTA-building block for current-mode analog signal processing. Proceedings of the ECCTD'03, Krakow, Poland. vol. 3. 2003. p. 397–400.
[32] Tangsrirat W, Tanjaroen W, Pukkalanun T. Current-mode multiphase sinusoidal oscillator using CDTA-based allpass sections. Int J Electron Commun (AEU) 2009;63(7):616–22.
[33] Rai SK, Gupta M. Current differencing transconductance amplifier (CDTA) with high transconductance and its application in filter and oscillator. Optik - Int J Light Electron Opt 2016;127(6):3388–96. https://doi.org/10.1016/j.ijleo.2015.12.112.



Sirish Oruganti was born in Visakhapatnam, Andhra Pradesh, India. He is currently an undergraduate student, pursuing his Bachelor of Technology in Electronics and Communication Engineering from Delhi Technological University. His research interests include Analog and Mixed-Signal VLSI Design and Low-Power VLSI Design.



Neeta Pandey is currently a Professor in Department of Electronics and Communication Engineering, Delhi Technological University. She did her M.E. in Microelectronics from BITS, Pilani and Ph.D. from GGS Indraprastha University Delhi. She is a Senior Member of IEEE and IEEE WIE. Her research interests are Analog and Digital VLSI Design.



Rajeshwari Pandey is currently a Professor in Dept. of Electronics and Comm. Engg., DTU. She did her M.E in Electronics and Control from BITS, Pilani, and Ph.D. from Faculty of Technology, Delhi University. She is a member of IEEE and IEEE WIE for over 12 years. Her research interests are Analog Integrated Circuits, and Microelectronics.

Journal of Applied Polymer Science

Emergence of time-dependent material properties in chain extended polyureas

N. Iqbal,[1,2] D. Kumar,[2] P. K. Roy [1]

[1]Centre for Fire, Explosive and Environment Safety, DRDO, Timarpur, Delhi 110054, India

[2]Department of Applied Chemistry and Polymer Technology, Delhi Technological University, Delhi, 110042, India

Correspondence to: P. K. Roy (E-mail: pk_roy2000@yahoo.com or pkroy@cfees.drdo.in)

ABSTRACT: In this article, we report the emergence of material properties of polyurea over a finite time frame. Due to the rapid isocyanate–amine reaction, polyurea formation occurs practically instantaneously. Despite being an "instant-curing" system, the material properties of polyurea evolve substantially with time: phenomenon, which warrants a methodical study. The curing process of polyurea formulations, containing both aliphatic and aromatic chain extender, has been studied systematically with an aim to gain insight into the time frame associated with its curing and subsequent stress relaxation. Formulations containing aromatic chain extender mandated relatively lesser time to "gel," but the complete disappearance of NCO absorbance mandated much longer periods ~7 h. Interestingly, in all the formulations, mechanical properties improved with time and reached their optimal properties over a period of 15 days. This improvement has been attributed to several processes simultaneously occurring within the matrix; the foremost being the relaxation of internal stresses which tend to buildup in the polymer during the spray coating process. In addition, significant changes occur in the internal morphology of segmented polymers, which in turn is a result of H-bond rearrangement. © 2018 Wiley Periodicals, Inc. J. Appl. Polym. Sci. **2018**, *135*, 46730.

KEYWORDS: differential scanning calorimetry; glass transition; mechanical properties; spectroscopy; structure-property relationships

Received 19 March 2018; accepted 17 May 2018

DOI: 10.1002/app.46730

INTRODUCTION

In the last two decades, elastomeric polyurea has garnered a lot of interest both from academia as well as industry, in view of its ability to exhibit a wide range of mechanical properties.[1–3] Polyurea is formed as a result of the polymerization reaction of isocyanates (—N═C═O) with amines (—NH_2).[4] The rapid kinetics associated with amine-isocyanate reaction led to processing complications, which withheld its commercialization. Subsequently, the development of improved spray equipment made it possible to overcome these technological issues, thereby rendering the process commercially realizable.[5]

This rapid curing attribute of polyurea is particularly beneficial for field applications, where an instantaneous return to service is desired. Certain products, i.e., pipes, freight wagon liners, industrial floors, need to be brought back to service as soon as possible, and in such cases, the fast curing nature of polyurea is extremely beneficial. Polyurea is also entering into areas like personnel-protective gear,[6] retrofits for unreinforced structures,[7,8] and as ballistic-penetration resistant metallic armor,[9] where rapid curing has enormous advantages.

Unfortunately, in view of the high reactivity of isocyanate and amine, polyurea coatings tend to build up huge internal stresses during the initial stages of solidification associated with the instantaneous curing process. It is to be noted that although the curing process has been studied using various analytical techniques, the time frame over which these studies have been performed is rather short.[5,10] The microstructure of polyurea comprises of two distinct domains: "hard" realms formed by hydrogen bonded polar urea linkages (—NH—CO—NH—) and "soft" domains comprising of long aliphatic polyether chains.[1,11] The phase-segregated structure of polyurea bestows extremely interesting properties to the polymer, especially enhanced modulus, high extensibility, and resiliency.[12,13] The formation of hard phase in polyurea, as studied using fluorescence and infrared spectroscopy, has been reported to reach completion within 400 min of reaction.[5] It is to be noted that although the solidification occurs in a matter of seconds, the relaxation of internal stresses mandate much longer periods. In view of the increasing application of this material in specialized fields, it is extremely

Additional Supporting Information may be found in the online version of this article.

© 2018 Wiley Periodicals, Inc.

important to be cognizant about the time frame required for polyurea to reach its optimal properties.

Further, the properties of polyurea can be tuned by choosing the raw materials judiciously, particularly isocyanates and amines.[14] However, all commercial polyurea formulations contain chain extenders, which can be either aliphatic or aromatic in nature depending upon the targeted final properties. The presence of chain extender in polyurea formulation increases the vicinity of the urea groups, which increases the probability of hydrogen bond formation,[15] without altering the total number of urea linkages in the polymer.[16] In view of the increased H-bonds, the mechanical properties of chain-extended polyurea are substantially better than their non-chain extended counterparts. In the present work, we monitor the evolution of structural and physical properties in polyurea formulations containing both aliphatic as well as aromatic chain extenders. Of particular interest is to gain insight as to how the structural changes in the polymer manifest in the form of its mechanical properties.

EXPERIMENTAL

Materials

Commercial isocyanate prepolymer, Suprasec 2054 (Huntsman, Woodland, Texas), NCO = 15.5% and propylene carbonate was used as source of isocyanate feed (Part A) without any further purification. Poly(propylene oxide) based polyether amines JEFFAMINE D-230 and JEFFAMINE D-2000 were procured from Huntsman: the designation number referring to the approximate molecular weight of each species, with D referring the functionality (D: difunctional). An aromatic chain extender, diethyltoluene diamine (DETDA 80, Lonzacure, Basel, Switzerland) was used as a source of amine feed (Part B) without any further purification. The same has been reported to be a mixture of 3,5-diethyltoluene-2,4-diamine (2,4-DETDA) (75%–81%), 3,5-diethyltoluene-2,6-diamine (2,6-DETDA) (18%–20%), and the remaining being dialkylated *m*-phenylenediamine (0.5%–3%). The structure and physical properties of all the reactants are presented in Table I.

Spraying of Polyurea

For the purpose of polyurea preparation, duly diluted Suprasec 2054 was used as the source of isocyanate (NCO),[17] and formulated mixture containing requisite amounts of D-230, D-2000 and DETDA was used as the source of amine (NH_2). The amount of the amine used for each formulation was calculated as follows

$$m_{iso} \cdot n_{eq.iso} = [m_{amine} \cdot n_{eq.amine}] i_{NCO} \quad (1)$$

Table I. Structure and Physical Properties of Reactants

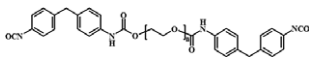
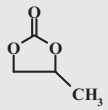
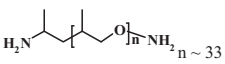
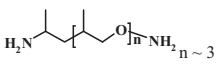
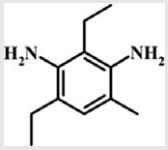
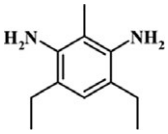
Reactant	Structure	Density (g/cm^3)	n_{eq}	Viscosity (30 °C, mPa s)
Side A				
Suprasec 2054		1.09	3.57	878.3
Propylene carbonate		1.2	—	2.2
Side B				
Long chain amine				
Jeffamine D 2000	 $n \sim 33$	0.98	1	182.9
Chain extender				
Jeffamine D 230	 $n \sim 3$	0.93	8.1–8.7	7.46
DETDA	 3,5-diethyltoluene-2,4-diamine	1.022	11.24	106.8
	 3,5-diethyltoluene-2,6-diamine			

Table II. Details of Polyurea Formulations Prepared

	Amine (part per unit volume)				
	Chain extender				
Sample designation	D 230	DETDA	D2000	Total Hard segment (%)	Contribution of aromatic chain extender (%)
PUAr-76	—	21.2	78.8	60.9	76
PUAr-63	5.5	17.5	77.0	61.7	63
PUAr-36	16.4	11.1	72.5	63.7	36
PUAr-10	27.4	2.7	69.9	64.8	10
PUAr-0	31.3	—	68.7	65.4	—

where, m_{iso} and m_{amine} refer to the mass of isocyanate and amine respectively and $n_{eq.iso}$ and $n_{eq.amine}$ refer to the equivalent number of isocyanate and amine, respectively. The isocyanate index (i_{NCO}) was maintained at a slight over-index (1.1) for all formulations to compensate for the "loss" of isocyanate-groups during storage in view of the reactivity of the isocyanate with humidity. The amount of amine (parts by volume) used for preparing different polyurea formulations are presented in Table II. For the sake of spraying, it is important to maintain a mix ratio of 1:1 for isocyanate and resin blend, which mandates dilution of the former with propylene carbonate.[17] In view of the same, the volume percent of Suprasec 2054 and propylene carbonate was maintained at 90.8 and 9.2, respectively, to attain a similar rheological profile for both side "A" and "B" during spray processing conditions (70 °C) (Supporting Information Figure S1). The hard segment (HS) content was determined as per established procedure [eq. (2)].[18]

$$HS = \frac{m_{iso} + m_{chain\,extender}}{m_{iso} + m_{chain\,extender} + m_{amine}} \quad (2)$$

t is to be noted that the m_{iso} used for the calculation of HS refers to the mass of isocyanate prepolymer which also includes the contribution of the long polyether chain. Therefore, this estimated figure of HS is much higher than the actual HS content in the polymer. For the sake of designation, the samples will be referred to as PU-Ar followed by the contribution (%) of the aromatic chain extender to the total urea content in the polymer. Detailed calculations involving the individual contributions of amines and the chain extenders to the total urea present in the sample is presented in the Supporting Information section, and have been tabulated and depicted pictorially in Supporting Information Table S1 and Figure S2, respectively.

The thickness of the polyurea films was measured using a digital micrometer (Mitutoyo make, least count 0.001 mm). Polyurea films of uniform thickness (3 ± 0.01 mm) were prepared using a spray-coating machine (Graco E 10 HP) equipped with a fusion air-purge spray gun (AW2222, Graco).

A schematic of the spray coating technique is presented in Supporting Information Scheme S1. For all runs, the block and hose heaters were maintained at a constant temperature of 70 °C and the spraying operation was performed at 2000 ± 100 psi. The mixing ratio of A and B components was 1:1 (vol/vol).

Characterization

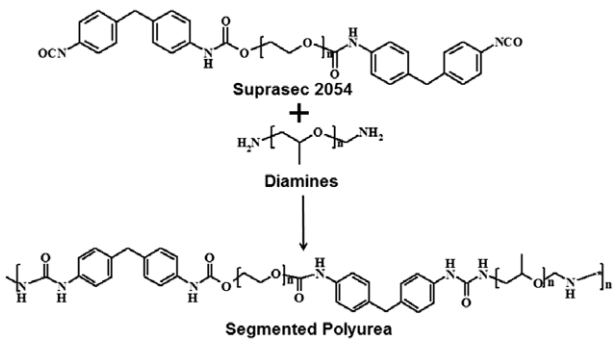
Rheological measurements were performed using Anton Paar (Graz, Austria) MCR 102 rheometer. Oscillatory shear experiments were performed using 25-mm-diameter disks, where the samples were reacted isothermally at 70 °C. The evolution of storage (G') and loss (G'') moduli at constant frequency (1 Hz) was recorded as a function of reaction time (time-sweep).

Thermal behavior of samples was investigated using differential scanning calorimetry (TA instruments, Q 20 module, Hertfordshire, UK) under nitrogen atmosphere. About 5 mg of the sample was placed in a 40 μL aluminum cap without pin and sealed with a lid. Samples were heated under a nitrogen gas flow of 50 mL min^{-1} from −80 to 150 °C at a rate of 10 °C min^{-1} to prevent oxidative degradation of the sample during analysis. The T_g was estimated from the midpoint of the glass transition phenomenon. Fourier transform infrared (FTIR) spectra of samples were recorded in the wavelength range 4000–600 cm^{-1} using FTIR spectroscopy on a Thermo Fisher FTIR (NICOLET 8700, Thermo Fisher, Waltham, Massachusetts) with an attenuated total reflectance (ATR) crystal accessory.

The mechanical properties were measured in tensile mode using Universal Testing Machine (International Equipments, Mumbai, India) as per ASTM D 412C standard. The tear strength was determined as per ASTM D 624C (Testing speed: 500 mm min^{-1}). At least five identical specimens were tested for each composition and the average results along with the standard deviation values have been reported. Dynamic mechanical analysis (DMA) (Artemis 242E, Netzsch, Bavaria, Germany) was performed on rectangular specimens (50 mm × 8 mm × 3 mm) using Dynamic mechanical analyzer (Artemis 242E, Netzsch). A dual-cantilever bending mode was used, which permitted controlled movement of the sample during testing. The nominal sample size for the DMA test is 50 mm × 8 mm × 3 mm ($l \times b \times h$). The experiments were conducted at 1 Hz, over a broad temperature range (−80 to 150 °C at 2 °C min^{-1}).

RESULTS AND DISCUSSION

The emergence of time-dependent mechanical and structural properties in various chain extended polyurea formulations has been systematically studied with an aim to understand the timeframe required for relaxation of internal stresses, thereby achieving maximal properties.



Scheme 1. Representative diisocyanate–diamine reaction leading to formation of polyurea.

Structural Evolution in Polyurea

A representative schematic depicting the formation of a representative polyurea macromolecule through the reaction of a diisocyanate with diamine is presented in Scheme 1.

Isocyanate exhibits high reactivity toward all compounds containing active hydrogen. Amongst these, the reaction rate of isocyanate with primary amine is the fastest. The relative reaction rates are presented in the Supporting Information Table S2. It is clear from the scheme that the reaction is accompanied with several structural changes, which renders this a perfect system to be followed through FTIR spectroscopy.[19–22] The FTIR spectra of all the reactants are presented in the Supporting Information Figure S3. In the spectra of the primary amines (D230 and D2000), two separate N—H stretching bands are noticeable: a broad peak due to asymmetrical stretching at ~3300–3400 cm^{-1} and the other due to symmetrical stretching at ~3330–3250 cm^{-1}. The formation of polyurea was followed by the disappearance of the absorption band at 2263 cm^{-1} ($\nu_{N=C=O}$) and the significant red shift associated with the position of the >C═O and N—H stretching bands due to inter-molecular or intra-molecular hydrogen bonding.[5,23–25] Characteristic frequencies associated with the >C═O and N—H groups are presented in the Supporting Information Table S3.

The reaction with amine and isocyanate led to similar changes in the FTIR spectra of all the formulations, and the change in the spectra of a representative formulation (PU-Ar 63) is presented in Figure 1. It can be seen that the intensity of NCO absorbance at 2263 cm^{-1} decreased exponentially within the first few minutes of the reaction, however its complete disappearance mandated ~7 h. Subsequently, the spectra remained practically unaltered even after 1 month of curing under ambient conditions. It is interesting to note that although the reaction between isocyanate and amine appears to be instantaneous, with solidification occurring in a matter of seconds, structural changes continue within the polymer over much longer periods. Further, due to the existence of polyurea in the rubbery regime at room temperatures, the possibility of polyurea chains restructuring, including H-bond rearrangement is highly probable, however it is not possible to follow these subtle changes through FTIR spectroscopy.

The FTIR spectra of the different polyurea formulations are presented in the Supporting Information Figure S4. It is interesting to note that the formulations containing aromatic chain extenders exhibited N—H band stretching at much lower frequencies, which are indicative of stronger H bonding in aromatic chain extended polyureas. The shift in the frequency associated with the free groups and the hydrogen-bonded ones present qualitative information regarding the strength of the interactions. Notably, a concomitant shift in the position of the N—H and >C═O band with increasing amount of aromatic chain extender in the formulation.

Evolution of Rheological Properties

The rheological parameters under isothermal conditions (70 °C) were monitored with an aim to gain an insight into the kinetics associated with the polymerization process. The evolution of storage (G') and loss modulus (G'') in representative formulations due to the amine–isocyanate reaction is presented in Figure 2. In the initial stages of the reaction, where the reactants are in the liquid state, the loss modulus was substantially higher than the storage modulus. As a result of the polymerization reaction, both G' and G'' increased rather rapidly, and a crossover gelation region was observed, where the storage modulus increases to the level of loss modulus.[17] This region marks a sudden transition of the viscous liquid to an elastic solid, where the amount of energy stored by the material becomes equal to the amount of energy dissipated. The time required for the same is referred to as the "gelation time" (t_{gel}). It can be seen that the "t_{gel}" of PU-Ar76 (formulation containing only DETDA) is 40 s, which increases with increasing amount of aliphatic chain extender (D 230), clearly reflecting upon its ease of processability. For formulations

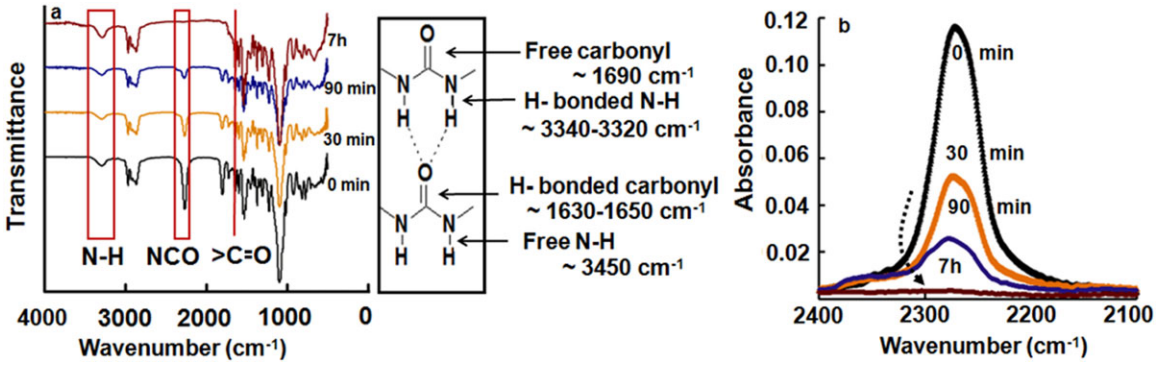


Figure 1. (a) Change in the FTIR spectra due to reaction of isocyanate with amine. (b) Decrease in isocyanate absorbance. [Color figure can be viewed at wileyonlinelibrary.com]

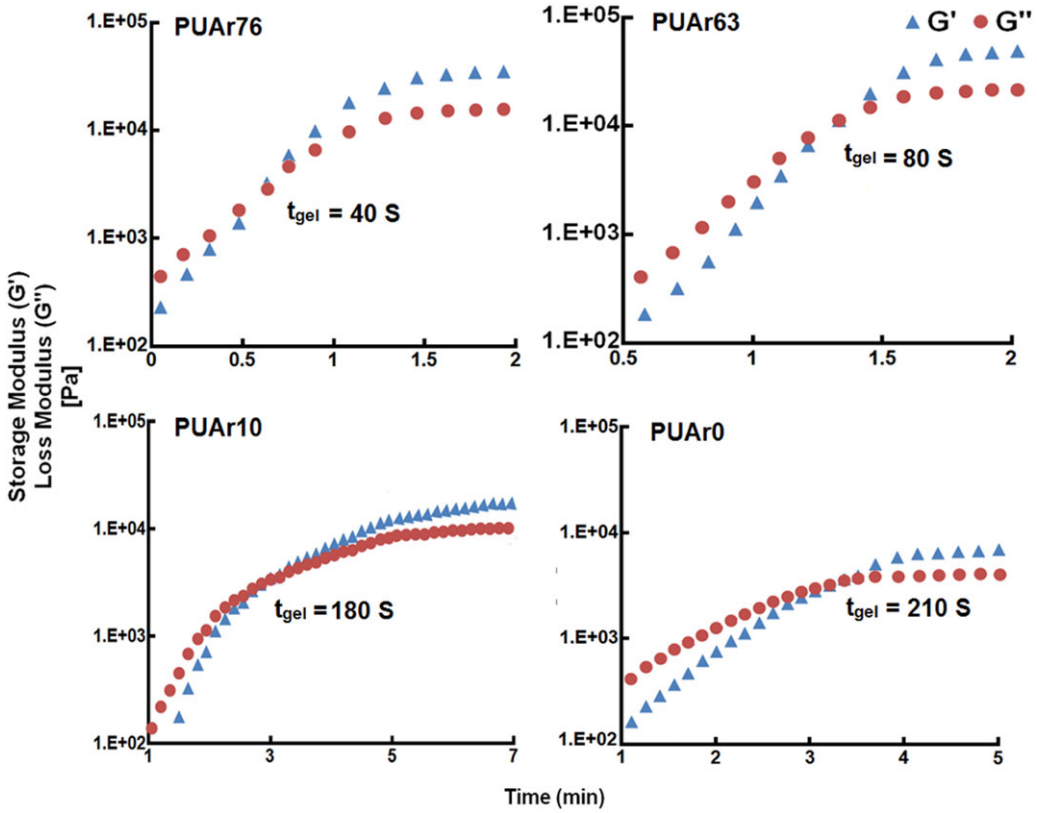


Figure 2. Evolution of storage and loss modulus in polyurea formulations (T = 70 °C). [Color figure can be viewed at wileyonlinelibrary.com]

prepared in the absence of aromatic chain extender (PU-Ar0), the gelation time is significantly higher (~3.5 min), which is undesirable, as it would lead to non-uniform coating thickness. It is interesting to note that, in none of the formulations, the storage and loss modulus level off completely in the time frame of experimentation, although the slope of the curve decreases significantly. This essentially implies that the reaction continues within the polymer, even post-solidification.

Evolution of Mechanical Properties

The mechanical properties of polyurea are strongly dependent on the nature of isocyanate, amine, and the chain extender included in the formulation. The attainment of a sufficiently robust state to resist damage by handling is a critical point during curing, commonly indicated by "tack-free" time. The tack-free time associated with the formulations is presented in Supporting Information Table S4, which reveal that this stage is achieved within 2 min of spraying.

Although, the solidification process occurs rapidly, the mechanical properties keep on evolving with time. All the formulations exhibited a similar trend of mechanical property evolution, and the development of tensile properties of a representative polyurea formulation (PU-Ar 63) is presented in Figure 3. The evolution

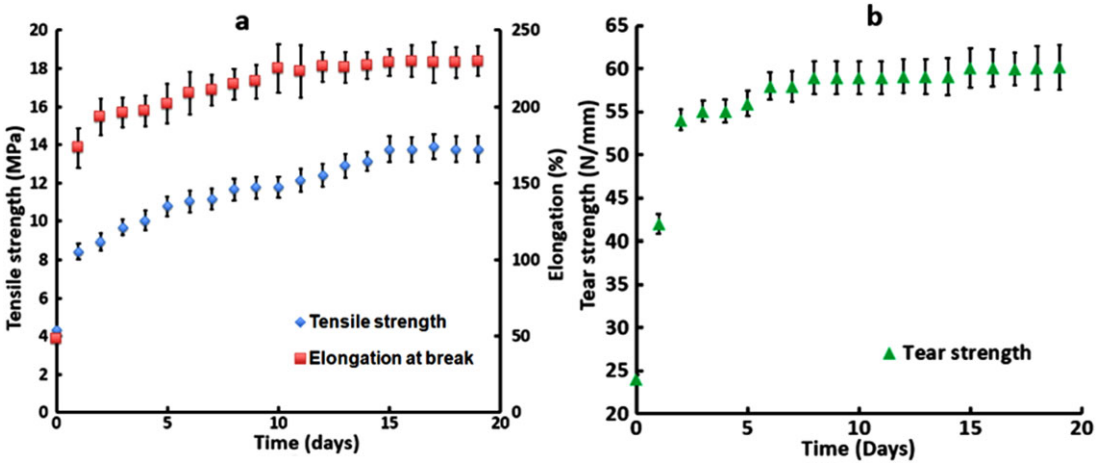


Figure 3. Variation of tensile properties and tear strength as a function of time (PU-Ar 63). [Color figure can be viewed at wileyonlinelibrary.com]

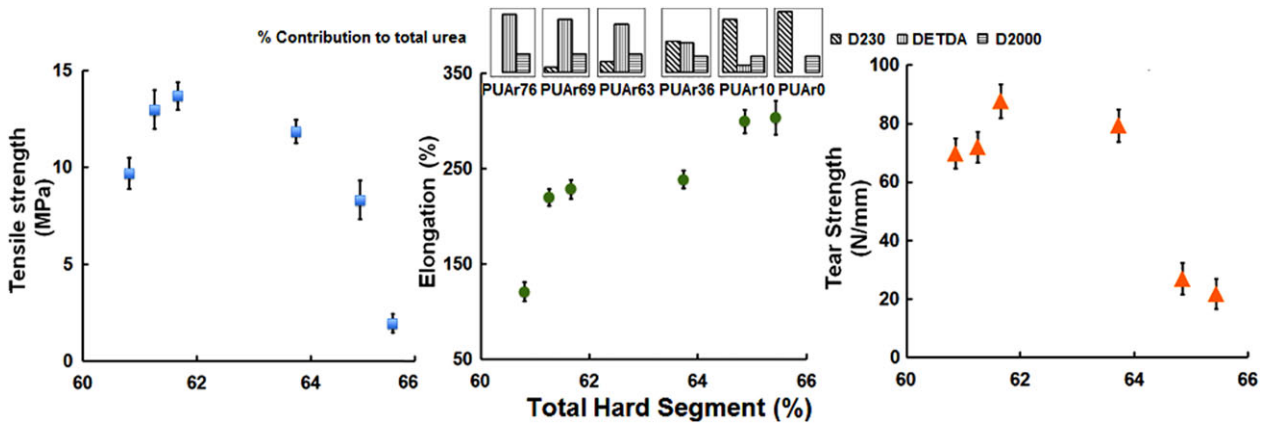


Figure 4. Variation in (a) tensile strength, (b) elongation, and (c) tear strength of polyurea formulations. The relative contribution of aromatic and aliphatic HS is also included in the figure. [Color figure can be viewed at wileyonlinelibrary.com]

of properties of all the formulations prepared is presented in the Supporting Information Figures S5 and S6). It is clear that the mechanical properties of polyurea tend to improve with time, and require ~15 days to reach a plateau.

It is to be noted that the solidification process occurs in a matter of seconds, with the urea linkages suddenly "freezing" in space, leading to a precipitous build-up of stresses. Interestingly, the stress buildup in any polymer is a result of several competing phenomena.[26] In the present case of polyurea, the most significant contribution comes from the precipitous volume contraction due to fast reactivity of the raw materials. As polyurea cools to ambient conditions, further contraction ensues due to thermal shrinkage. Notably, in comparison to the core, shrinkage in the external surface occurs more rapidly, with the contraction of the core being constrained by the external rigid surface and reduced temperature gradients. This leads to an inhomogeneous stress distribution throughout the polymer, which is tensile in the core and compressive at the surface.[27] The difference in the coefficient of thermal expansion in the reinforcement and matrix has been reported to result in significant buildup of stress in composite structures.[28] The properties of polyurea are basically a result of its interesting microstructure, which in turn comprises of urea HSs distributed throughout the polyether soft segment. Since the hard and soft domains in polyurea are expected to exhibit dissimilar thermal expansion coefficients, this is expected to contribute to the development of internal stresses in the polymer. These in-built stresses manifest themselves in the form of relatively inferior mechanical properties, which develop with time due to its eventual relaxation. In addition, significant changes have been reported to occur in the internal morphology of segmented polymers, which in turn is a result of H-bond rearrangement.[27,29–31]

However, all the polyurea formulations exhibit a sub-ambient glass transition temperature, the segmental motions in polyurea can occur freely under ambient temperatures, especially in the soft segments. These motions eventually lead to a spatial structural arrangement with lowest interatomic force on each atom: a process that continues over extended time periods. This leads to the relaxation of internal stresses, which build-up within the polymer during spray coating. It is to be noted that increasing the temperature of the sample (i.e., annealing) can accelerate this process of stress relaxation, thereby shortening the time frame required for achieving optimal properties.[5]

Characteristic mechanical properties of the fully cured polyurea formulations (post 15 days of spraying) are presented in Figure 4. Distinguishing properties viz. tensile strength, elongation, and tear strength of polyurea formulation are also tabulated in the Supporting Information Table S5. It appears that an optimal ratio of aromatic to aliphatic chain extender results in optimal H bonding between the urea linkages, which in turn leads to improved mechanical properties[32] (Supporting Information section S3 and Figures S7–S10).

Evolution of Dynamic Mechanical Properties

Dynamic mechanical studies on the various polyurea formulations were performed at different stages of curing, and the results in terms of storage and loss modulus is presented in Figure 5. Complex modulus (E^*) was obtained, which can be represented as $E' + iE''$, where E' refers to the storage modulus, representative of the material stiffness, and E'' being the loss modulus, representative of the materials ability to dissipate mechanical energy.

It is interesting to note that the storage modulus increases with time and eventually level off after ~15 days of curing. The storage and loss modulus profile characteristically reveal a single relaxation peak in the temperature region studied, which is attributed to the segmental motions linked with the soft segments in the polymer. The glass transition temperature (T_g) was established from the peak of the loss modulus profile,[33,34] which remained unaltered with time. All the polyurea formulations were found to exhibit sub-zero glass transition temperature, the T_g being dependent on the amount and type of chain extender present in the formulation (Supporting Information Figure S11). The T_g was found to systematically shift toward higher temperature as the total HS content decreased. For PU-Ar0, with a HS of 65.4, T_g was evident at −40 °C (1 Hz) which increases to −28 °C for PU Ar-76(HS = 60.8). It is particularly interesting to note the large width associated with the glass transition phenomenon ($\Delta T > 80$ °C): a property rather unique to polyurea.[35]

The T_g values obtained from differential scanning calorimetry (DSC) studies vary from the one obtained by DMA studies, both being tabulated in the Supporting Information Table S6. The difference in the T_g can be attributed to the difference in the

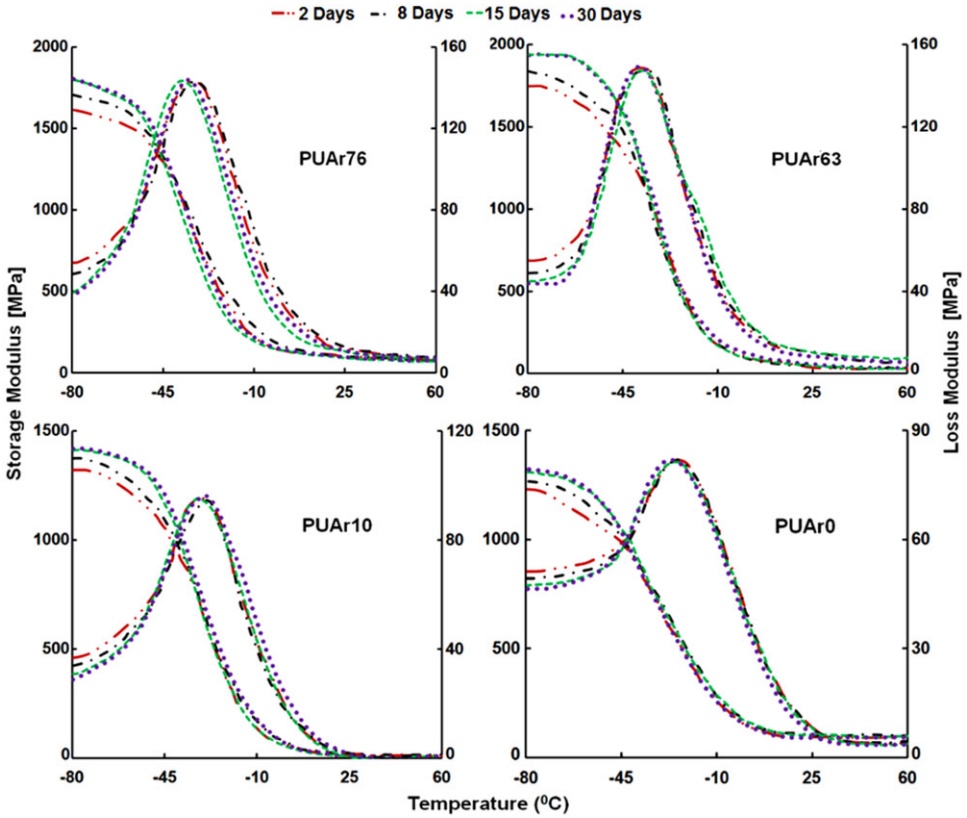


Figure 5. Variation of storage and loss modulus of polyurea formulations with temperature. [Color figure can be viewed at wileyonlinelibrary.com]

property being measured, i.e., change in specific heat capacity in DSC and that of mechanical properties in DMA. In addition, the difference in the rate of heating also leads to the observed difference in the values. DSC scans were performed at definite time periods and the traces obtained for a representative sample (PU-Ar 63) are presented in Figure 6. The shift in the baseline of the heat flow curve is indicative of the glass transition phenomenon.[36] In line with DMA results, there is not much change in the T_g values due to curing. The DSC scans of fully cured polyurea formulations are presented in the Supporting Information Figure S12. It appears that since the polymer exists much above its low temperature T_g, therefore segmental motions associated with the soft segments continue within the polymer, which lead to release of inbuilt internal stresses. In addition, there is a distinct possibility of H-bonds rearrangement, which too can lead to disbursement of internal stresses.

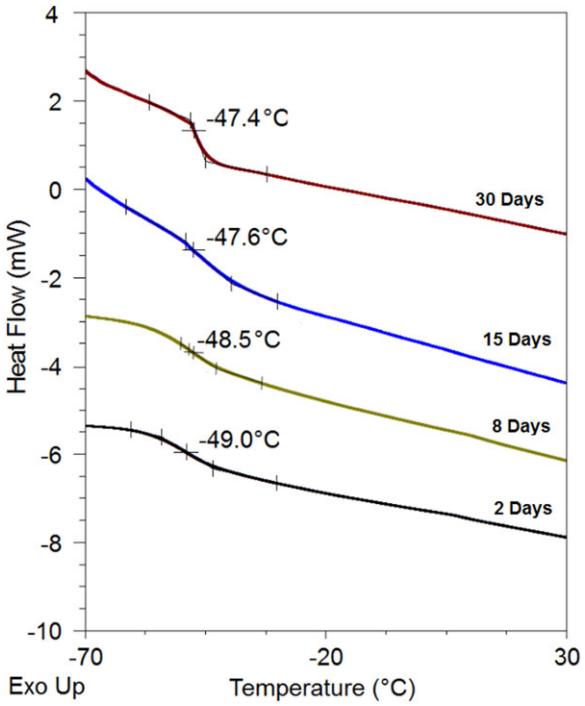


Figure 6. DSC traces of polyurea at different periods of curing. [Color figure can be viewed at wileyonlinelibrary.com]

CONCLUSIONS

The material properties of polyurea are an indirect manifestation of its nanocomposite microstructure, with the urea HSs being dispersed within a soft domain primarily comprising of polyether amines. The reaction between isocyanate and amine transpire in a matter of seconds, but the mechanical properties tend to evolve substantially over a period of time. The leveling-off of the absorbance band due to —NCO stretching mandated ~7 h, as indicated by FTIR studies. Interestingly, the mechanical properties improved significantly over a period of time and reach a plateau over ~15 days, irrespective of the type of chain extender included in the formulation. This was accompanied by a concurrent increase in the storage modulus as confirmed by DMA studies. All polyurea formulations were found to exhibit sub-zero glass

transition temperature (T_g) with the breadth of this region being exceptionally large (~80 °C), which shifted methodically toward higher temperature as the total HS content decreased. A slight increase in the T_g values was observed in all the formulations over a period of time. Under ambient conditions, all polyurea formulations exist much above its lower glass transition temperature, which permit segmental motions within the soft segments of the polymer, thereby leading to release of inbuilt internal stresses. These motions eventually lead to a spatial structural arrangement with lowest interatomic force on each atom: a process that continues over extended periods leading to optimal properties.

ACKNOWLEDGMENTS

The authors gratefully acknowledge Director, CFEES DRDO for providing logistic support to perform this work. Nahid Iqbal is pleased to acknowledge DTU for providing financial support. All the authors acknowledge DRDO for funding this research work through the grant ST/14-15/CFE-1311.

REFERENCES

1. Choi, T.; Fragiadakis, D.; Roland, C. M.; Runt, J. *Macromolecules* **2012**, *45*, 3581.
2. Fragiadakis, D.; Gamache, R.; Bogoslovov, R. B.; Roland, C. M. *Polymer* **2010**, *51*, 178.
3. Zhang, L.; Rowan, S. *J. Macromolecules* **2017**, *50*, 5051.
4. Iqbal, N.; Tripathi, M.; Parthasarathy, S.; Kumar, D.; Roy, P. K. *RSC Adv.* **2016**, *6*, 109706.
5. Zhou, Q.; Cao, L.; Li, Q.; Yao, Y.; Ouyang, Z.; Su, Z.; Chen, X. *J. Appl. Polym. Sci.* **2012**, *125*, 3695.
6. Grujicic, M.; Arakere, A.; Pandurangan, B.; Grujicic, A.; Littlestone, A. A.; Barsoum, R. S. *Multidiscipl. Model. Mater. Struct.* **2012**, *8*, 297.
7. Davidson, J.; Porter, J.; Dinan, R.; Hammons, M.; Connell, J. *J. Perform. Constr. Fac.* **2004**, *18*, 100.
8. Iqbal, N.; Sharma, P. K.; Kumar, D.; Roy, P. K. *Costr. Build. Mater.* **2018**, *175*, 682.
9. Roland, C. M.; Fragiadakis, D.; Gamache, R. M. *Compos. Struct.* **2010**, *92*, 1059.
10. Wang, S.-K.; Sung, C. S. P. *Macromolecules* **2002**, *35*, 883.
11. Grujicic, M.; Pandurangan, B.; Bell, W. C.; Cheeseman, B. A.; Yen, C. F.; Randow, C. L. *Mater. Sci. Eng. A* **2011**, *528*, 3799.
12. Chen, C.-P.; Dai, S. A.; Chang, H.-L.; Su, W.-C.; Wu, T.-M.; Jeng, R.-U. *Jong, Polymer* **2005**, *46*, 11849.
13. Mattia, J.; Painter, P. *Macromolecules* **2007**, *40*, 1546.
14. Iqbal, N.; Tripathi, M.; Parthasarathy, S.; Kumar, D.; Roy, P. *J. Appl. Polym. Sci.* **2018**, *135*, DOI: 10.1002/app.46284.
15. Negim, E. S. M.; Khatib, J. M.; Faizova, E.; Shilibekov, S.; Mussylmanbek, S. *Mid. East. J. Sci. Res.* **2013**, *16*, 890.
16. Toader, G.; Rusen, E.; Teodorescu, M.; Diacon, A.; Stanescu, P. O.; Rotariu, T.; Rotariu, A. *J. Appl. Polym. Sci.* **2016**, *133*, DOI: 10.1002/app.43967.
17. Iqbal, N.; Kumar, D.; Roy, P. K. *J. Appl. Polym. Sci.* **2018**, *135*, DOI: 10.1002/app.46284.
18. Sreenivasan, K. *Polym. J.* **1990**, *22*, 620.
19. Teo, L.-S.; Chen, C.-Y.; Kuo, J.-F. *Macromolecules* **1997**, *30*, 1793.
20. Coleman, M. M.; Skrovanek, D. J.; Hu, J.; Painter, P. C. *Macromolecules* **1988**, *21*, 59.
21. Jena, K. K.; Raju, K. S. N. *Ind. Eng. Chem. Res.* **2008**, *47*, 9214.
22. Garrett, J.; Lin, J.; Runt, J. *Macromolecules* **2002**, *35*, 161.
23. Marcos-Fernández, A.; Lozano, A. E.; González, L.; Rodríguez, A. *Macromolecules* **1997**, *30*, 3584.
24. Bergsman, D. S.; Closser, R. G.; Tassone, C. J.; Clemens, B. M.; Nordlund, D.; Bent, S. F. *Chem. Mater.* **2017**, *29*, 1192.
25. Coleman, M. M.; Sobkowiak, M.; Pehlert, G. J.; Painter, P. C.; Iqbal, T. *Macromol. Chem. Phys.* **1997**, *198*, 117.
26. White, J. R. *Polym. Test.* **1984**, *4*, 165.
27. Zoetelief, W. F.; Douven, L. F. A.; Housz, A. J. I. *Polym. Eng. Sci.* **1996**, *36*, 1886.
28. Chowdhury, N.; Wang, J.; Chiu, W. K.; Yan, W. *J. Compos.* **2016**, *2016*, 13.
29. White, J. E.; Scaia, M. D.; Snider, D. A. *Polym. Test.* **1984**, *29*, 891.
30. Yilgor, I.; Yilgor, E.; Das, S.; Wilkes, G. *J. Polym. Sci. Part B: Polym. Phys.* **2009**, *47*, 471.
31. Yilgor, I.; Yilgor, E.; Guler, I. G.; Ward, T. C.; Wilkes, G. L. *Polymer* **2006**, *47*, 4105.
32. Iqbal, N.; Tripathi, M.; Parthasarathy, S.; Kumar, D.; Roy, P. K. *Chem. Select.* **2018**, *3*, 1976.
33. Jia, Z.; Amirkhizi, A. V.; Nantasetphong, W.; Nemat-Nasser, S. *Mech. Time Depend. Mater.* **2016**, *20*, 155.
34. Huang, W.; Yang, Y.; Li, H.; Lyu, P.; Zhang, R. *DEStech. Trans. Mater. Sci. Eng.* **2017**. Available online at http://www.dpi-proceedings.com/index.php/dtmse/article/download/9926/9480.
35. Qiao, J.; Amirkhizi, A. V.; Schaaf, K.; Nemat-Nasser, S.; Wu, G. *Mech. Mater.* **2011**, *43*, 598.
36. Collins, E. A.; Bareš, J.; Billmeyer, F. W. Experiments in Polymer Science; Wiley, New York, **1973**.

Journal of Materials Science: Materials in Electronics
https://doi.org/10.1007/s10854-018-9949-4

Energy storage and magnetoelectric coupling in ferroelectric–ferrite composites

S. Shankar[1,2] · Manish Kumar[1] · Vinita Tuli[1] · O. P. Thakur[3] · M. Jayasimhadri[2]

Received: 28 April 2018 / Accepted: 27 August 2018
© Springer Science+Business Media, LLC, part of Springer Nature 2018

Abstract
Ferroelectric–ferrite composites of $BaTiO_3$–$CoFe_2O_4$ (BT–CFO) is synthesized via solid state reaction method. Powder XRD confirms the phase purity as well as composite formation with tetragonal phase of the $BaTiO_3$. The FTIR and SEM–EDS studies also confirm the formation of BT–CFO composites. The P–E loop measurement confirmed the ferroelectric nature of the sample. The maximum energy storage density and efficiency achieved for BT–5CFO (5% $CoFe_2O_4$) composite was 8.33 mJ/cm^3 and an efficiency of 59.7% respectively. The coupling between the ferroelectric and ferromagnetic phases was observed in the variation of P–E loop with magnetic field. A decrease in the maximum polarization was found with increase magnetic field. The P versus M analysis confirmed the highest magneto-electric (ME) coefficient of 13.33 mV/cm/Oe for BT–5CFO composite. These results are related to the volumetric and piezoelectric strain, suppression of ferroelectric ordering reveal the magnetoelectric nature in $BaTiO_3$–$CoFe_2O_4$ composites.

1 Introduction

An enormous effort has been focused on the study of multiferroic materials with large magnetoelectric (ME) effect in the field of physics and material science for building new types of multistate memory devices [1]. The weak coupling in single phase multiferroics owing due to atomic diffusion and undesirable chemical reactions [2] and their scarcity has motivated the research of composite materials [3]. ME composites with large magnitudes of the ME voltage coefficient have turned out to be better alternatives. These composites exploit the product property of piezomagnetic and piezoelectric phases or individual magnetostrictive and piezoelectric phases of the materials.

Usually a magnetoelectric composite consists of ferroelectric and ferromagnet for piezoelectricity and magnetostriction to exhibit multiferroism. The coupling in these magnetoelectrics arises due to the indirect mechanical strain transfer at the interface of two phases. The composites of $BaTiO_3$–$CoFe_2O_4$ has exciting magnetoelectric properties due to the contribution of their individual phases. Perovskite $BaTiO_3$ (BT) is a good functional ceramic with interesting ferroelectric and optical properties has applications as multilayer ceramic capacitors (MLCC), transducers, actuators, energy storage ferroelectric random access memories [4]. $CoFe_2O_4$ (CFO), a spinel ferrite, is well known for its remarkable electrical, optical, and magnetic properties, especially in nanometer scale [5]. The earlier work on BT–CFO composites have contributed on the magnetoelectric properties to a certain extent [6, 7]. Though the magnetoelectric coupling observed in these materials was very low due to the undesirable phases of CFO and microstructural distortion in the composites. However, the studies of addition of CFO in low concentration to BT is not completely explored to observe the origin of coupling in BT–CFO composites. The effect of smaller concentration of CFO in BT on the structural, ferroelectric P–E and magneto-electric properties has been studied both qualitatively and quantitatively.

✉ S. Shankar
sssubramaniam@arsd.du.ac.in

M. Jayasimhadri
jayaphysics@yahoo.com

[1] Experimental Research Laboratory, Department of Physics, ARSD College, University of Delhi, New Delhi 110021, India

[2] Department of Applied Physics, Delhi Technological University, New Delhi 110042, India

[3] Materials Analysis and Research Laboratory, Department of Physics, NSIT, New Delhi 110078, India

Published online: 30 August 2018

2 Experimental procedures

The solid state reaction method was employed to prepare $BaTiO_3$ and $CoFe_2O_4$ bulk ceramics by calcining them at 1000 °C and 900 °C respectively. The powders of $BaTiO_3$ (99% and 95%) of different stoichiometry were mixed with $CoFe_2O_4$ (1% and 5%) powders respectively. The samples have been named in composite as BT (pure $BaTiO_3$), BT–1CFO (1% $CoFe_2O_4$), and BT–5CFO (5% $CoFe_2O_4$). All the mixed composites were then pelletized and sintered at 750 °C for 4 h and BT was sintered at 1100 °C for 4 h. The synthesis conditions have been tabulated in Table 1. Powder X-ray diffraction (XRD) patterns were recorded using an Rikagu X-ray Diffractometer employing Cu Kα radiations. The morphological studies have been done using Scanning electron microscopy (SEM) with EDS analysis. Polarization versus electric field (PE-loop) measurements were done with the help of 'Marine India' instrument at different frequency and magnetic field upto electric field of 25 kV/cm. The FTIR studies were made using Bruker FTIR setup.

Table 1 Synthesis conditions of $BaTiO_3$, $CoFe_2O_4$ and $BaTiO_3$–$CoFe_2O_4$ composites

Composition	Calcination temperature (°C)	Duration (h)	Sintering temperature (°C)	Duration (h)
$BaTiO_3$	1000	10	1100	4
$CoFe_2O_4$	900	8	–	–
BT–1CFO	–	–	750	4
BT–5CFO	–	–	750	4

3 Result and discussion

The phase purity and content for different compositions are shown in Fig. 1. The diffraction patterns were matched and indexed JCPDS file (5-0626) with for the BT [6]. The tetragonality of BT is confirmed from the splitting of diffraction peaks at 2θ diffraction angles: 31°, 45°, 56°, 66° and 75° with miller indices (101), (002), (112), (202) and (103) for all the composites. The intensity of the BT peaks didn't decrease significantly on increasing the concentration of cobalt ferrite. However small peaks due to cubic spinel cobalt ferrite matched with JCPDS file (22-1086) are observed in BT–5CFO composite (denoted by #). This confirms the co-existence of ferroelectric and ferromagnetic phases.

The presence of CFO and formation of composite of CFO–BT has been verified by the scanning electron microscopy (SEM) and energy-dispersive X-ray spectroscopy (EDX) and have been applied on pure BT and BT–5CFO. Figure 2a show the SEM images of BT and BT–5CFO respectively. The two different colors viz. black corresponds to CFO and white corresponds to BT of SEM images confirms the presence of two different domains of BT and CFO respectively in the BT–5CFO composite. The EDX analysis confirms the presence of CFO in to BT–5CFO sample due clear percentage amount of CFO seen in Fig. 2b and the strength of the peaks enhanced after the CFO addition in to BT. High strength of the peaks of BT–5CFO comparative to pure BT is due to the magnetic nature of the CFO and also further confirms the composite formation [8–11].

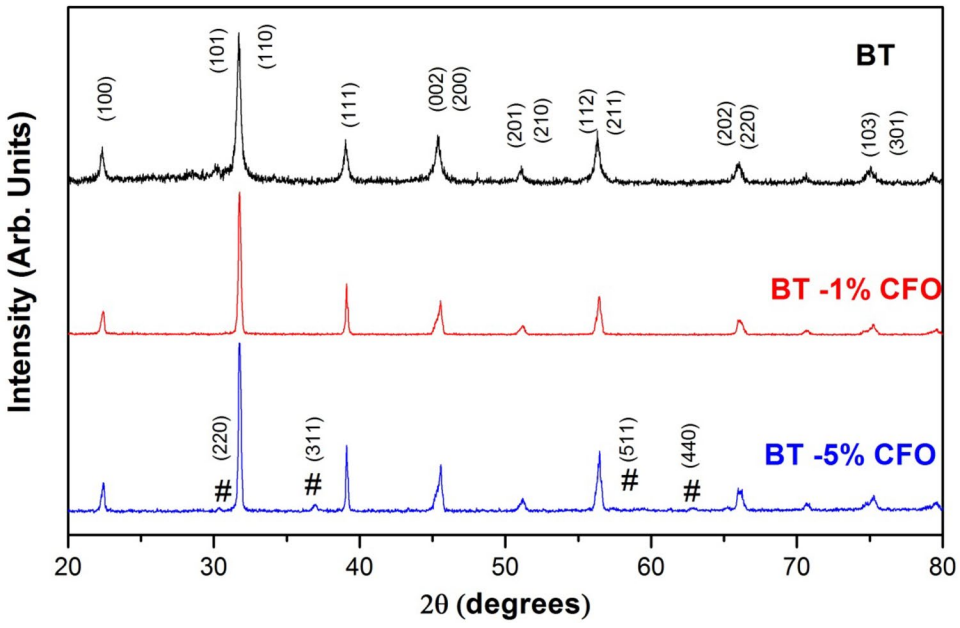
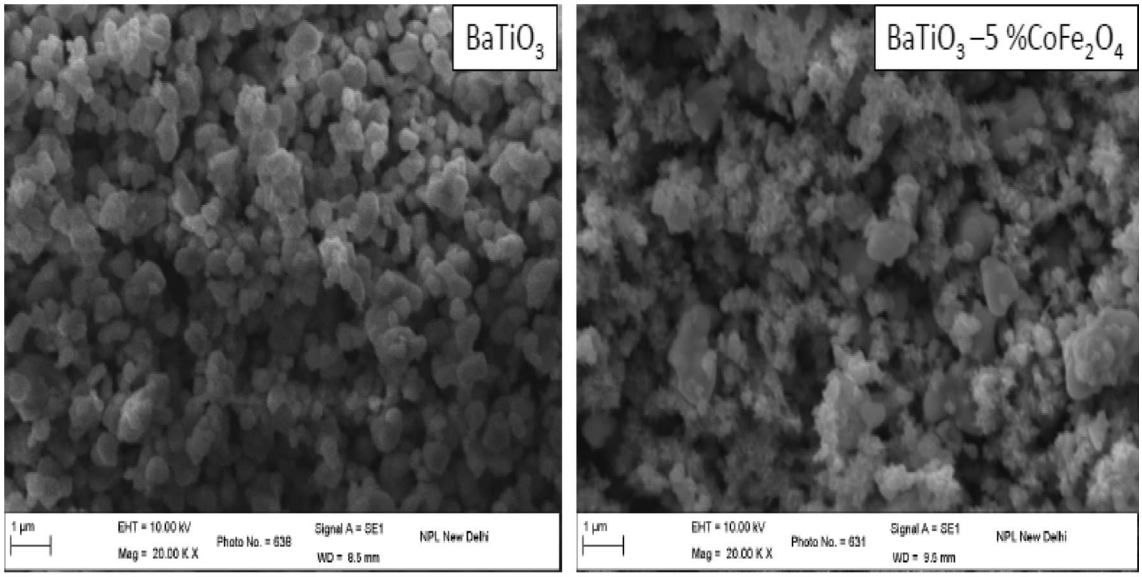
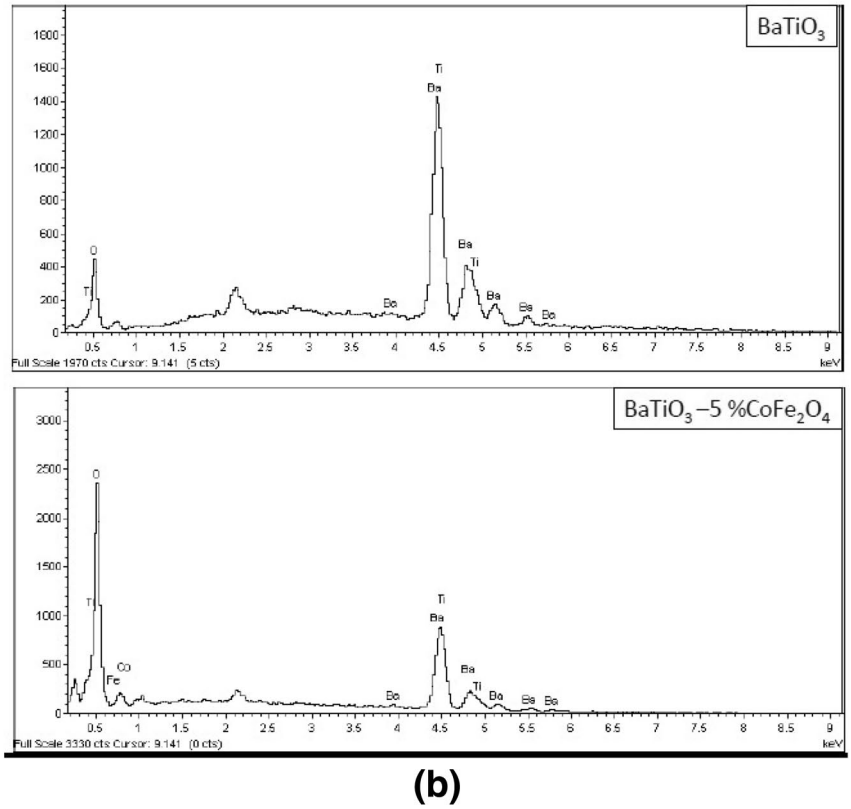


Fig. 1 XRD patterns of $BaTiO_3$ and $BaTiO_3$–$CoFe_2O_4$ composites



(a)



(b)

Fig. 2 **a** SEM micrographs of $BaTiO_3$ and $BaTiO_3$–5% $CoFe_2O_4$ composite. **b** EDS patterns of $BaTiO_3$ and $BaTiO_3$–5% $CoFe_2O_4$ composite

The FT-IR spectrum of the BT and BT–CFO composites is presented in Fig. 3. The characteristic absorption band at 3486 cm^{-1} is assigned to the O–H stretching vibration in water and confirms that the existence of the water in the BT and BT–CFO composites. The presence of the band located at 542 cm^{-1} is specific to the vibration mode of the Ti–O bond in the TiO_6 octahedra [12]. In cobalt ferrite ceramic, the FTIR spectrum has peaks near 600 and 450 cm^{-1} represent the characteristic peaks of Co_2O_3 [13]. The bands at these wavenumbers represent tetrahedral and octahedral

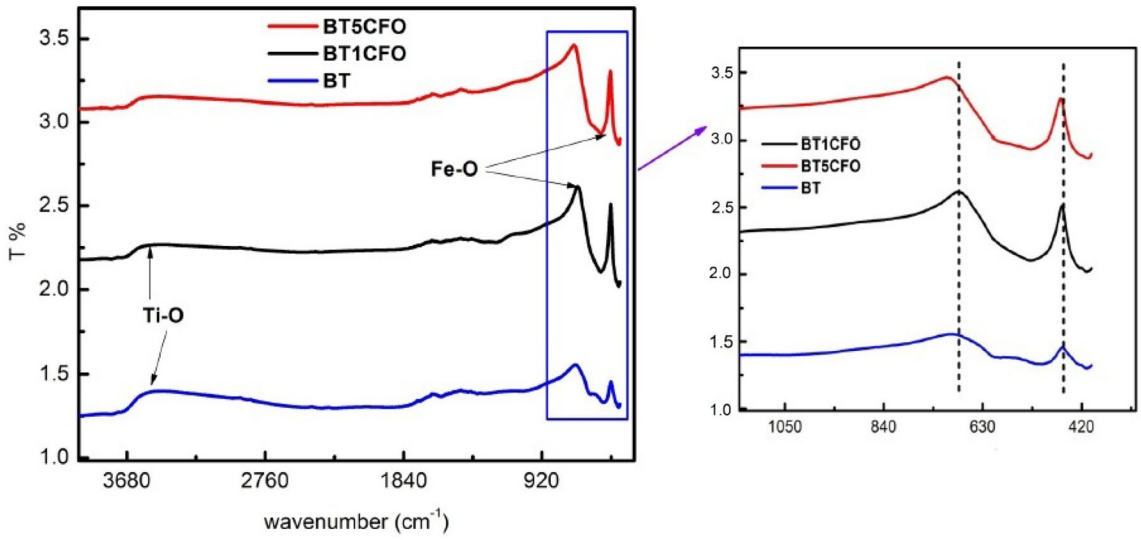


Fig. 3 FTIR spectra of $BaTiO_3$ and $BaTiO_3$–$CoFe_2O_4$ composites

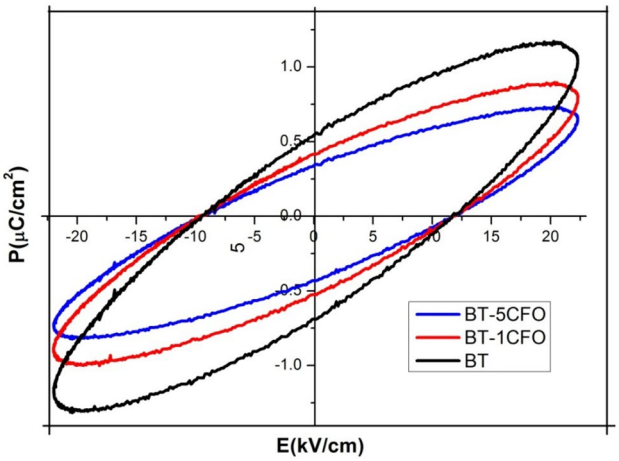


Fig. 4 P–E hysteresis loops of $BaTiO_3$ and $BaTiO_3$–$CoFe_2O_4$ composites

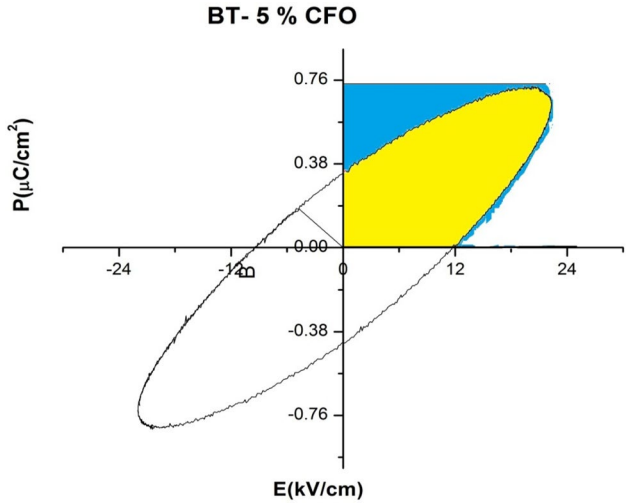


Fig. 5 P–E hysteresis loop of BT–5CFO. The blue region represents the energy loss and the yellow region represents the recoverable useful energy. (Color figure online)

clusters and also confirm the presence of Fe–O stretching vibration in cobalt ferrite. The shifting of peak at 690 cm^{-1} and sharpening of peak at 458 cm^{-1} in Fig. 3 is observed. The anomaly at bands near 600 and 400 cm^{-1} confirm the formation of BT–CFO composite.

Polarization versus electric field (P–E) hysteresis loops measured at fixed frequency of 50 Hz for BT, BT–1CFO and BT–5CFO composites are plotted in Fig. 4. These samples show extensive ferroelectric nature at an applied field of 25 kV/cm. There is an observed decrease in maximum polarization of the samples with increase in Cobalt ferrite content indicating the suppression of ferroelectric ordering [14]. The P–E loops did not display any saturation which could possibly be due to low value of electric field.

The P–E loops have been exploited for estimation of energy storage density and discharge efficiency of BT–5CFO sample (Fig. 5). The energy storage density (W_U) and efficiency (η) of a ferroelectric material are calculated as [15, 16]

$$W_U = \int_0^{Pmax} EdP$$

$$\eta = \frac{W_U}{W_L + W_U}$$

where E is applied electric field, P is polarization respectively, W_U is useful stored energy density and W_L is energy loss density. The blue region of Fig. 5 represents the loss and the yellow region represents the recoverable useful energy.

The unloaded sample of BT–5CFO displayed the energy density of 8.33 mJ/cm^3 and an efficiency of 59.7%. The efficiency can be increased by studying the sample under mechanical stress and which is currently under investigation. The variation in P–E loop due to the field-induced structural transformation is an indicative of volumetric and piezoelectric strains in the $BaTiO_3$ phase.

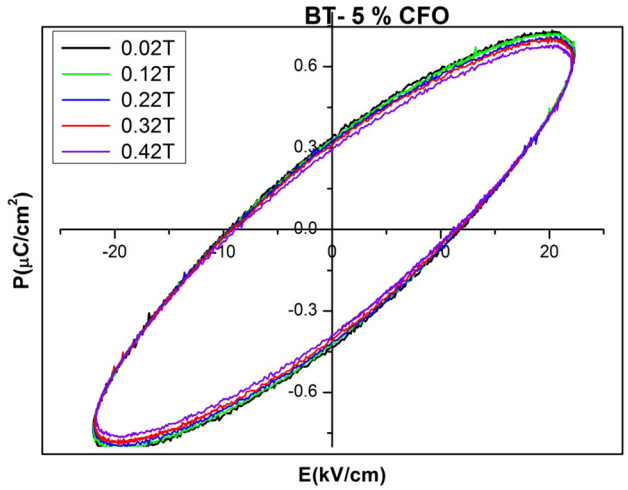


Fig. 6 Variation of P–E hysteresis loop with magnetic field (upto 0.5 T) of BT–5CFO

In order to establish the magnetoelectric effect in composites at room temperature, proving the ferroelectricity of the piezoelectric phase of barium titanate is essential. The hysteresis P–E loop of BT–5CFO composite exhibits a substantial variation with external magnetic field upto 0.4 T as shown in Fig. 6. The remnant polarization is found to decrease and the coercive field do not change with increase in magnetic field. This display the tilting of P–E loops confirming the evidence of magneto-electricity due to increase in the content of $CoFe_2O_4$ in $BaTiO_3$ [17, 18]. There was no variation in the P–E loop with magnetic field for BT–1CFO. This could be possibly due to less ferrite grains concentration in the composite which are incapable of generating magnetostriction in $BaTiO_3$.

The magneto-electric coupling quantified by ME coefficient is characterized by the appearance of an electric polarization on applying magnetic field ($\alpha = \delta E/\delta H$). Figure 7 shows the ME induced polarization as a function of the applied external magnetic field (dc). The slope of the curves is used for estimation of the direct magnetoelectric coefficient. Considering only the linear effects, the polarization can be expressed as

$$P(E, H) = P_s + (dP/dH) \times H$$

where P_s denotes the spontaneous polarization at constant field.

The values obtained from straight line fitting of P–M graph are $P_s = 0.78366$ and slope $dP/dH = -0.11801$ μC/cm^2/Oe. It can be seen that the coefficient is negative and low. This decrease in induced polarization in biphasic composites could be explained by the effect of demagnetization

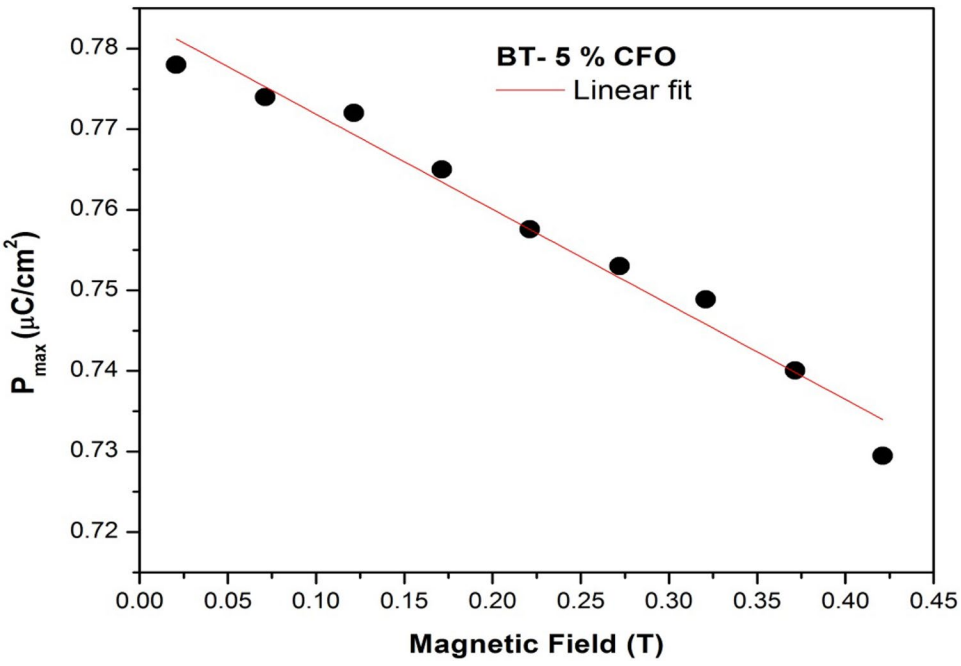


Fig. 7 Plot of maximum polarization with magnetic field and straight line fit of BT–5CFO composite

arising from local strain. As the amount of magnetic phase is increased in BT, the polar domains of BT get surrounded by the magnetic CFO phase and hinder the domain wall rotation. On the application of magnetic field, a local magnetic field is generated around the BT domains resulting in an effective strain mediated magneto-electric coupling [19]. The M–E coupling coefficient obtained for BT–5CFO composite is found to be 13.33 mV/cm/Oe which is relatively higher than reported values of 10 mV/cm/Oe and 12 mV/cm/Oe for $BaTiO_3$–20% $CoFe_2O_4$ and $BaTiO_3$–30% $CoFe_2O_4$ respectively [7].

4 Conclusion

In conclusion, we have prepared pure phase BT–CFO composites with tetragonal phase via solid state reaction route and is confirmed from XRD, SEM–EDS and FTIR studies. P versus E measurement confirmed the ferroelectric nature, high energy storage density and efficiency for BT–5CFO (5% $CoFe_2O_4$). The P versus E in the presence magnetic field and P versus M measurements confirmed the magneto-electric coupling in the composite both qualitatively and quantitatively which is related to the volumetric and piezoelectric strain, suppression of ferroelectric ordering. These features have direct influence on the application of BT–CFO composites in energy storage and multistate memory devices.

Acknowledgements Authors are thankful to University of Delhi, New Delhi for funding the Star Innovation Project (ARSD-SIP-01). The authors would like to thank Centre for Nanoscience, Jamia Millia Islamia University, New Delhi, National Physical Laboratory (NPL) New Delhi, and NSIT, New Delhi India for their characterization facilities.

References

1. X. Lu, Y. Kim, et al., Nano Lett. **11**, 3202–3206 (2011)
2. C.W. Nan, M.I. Bichurin et al., J. Appl. Phys. **103**, 031101 (2008)
3. N. Hur, S. Park et al., Nature **429**, 392–395 (2005)
4. F. Li, M. Zeng et al., J. Mater. Sci. Mater. Electron. **27**, 2836–2840 (2017)
5. S. Jabez, S. Mahalakshmi, S. Nithiyanantham, J. Mater. Sci. Mater. Electron. **28**, 5504–5511 (2017)
6. L.V. Leonel, A. Righi et al., Ceram. Int. **37**, 1259–1264 (2011)
7. C.A.F. Vaz, J. Hoffman et al., Adv. Mater. **22**, 2900–2918 (2010)
8. M. Etier, V. V. Shvartsman et al., J. Am. Ceram. Soc. **99**, 3623–3631 (2016)
9. M. Etier, C.S. Antoniak et al., Acta Mater. **90**, 1–9 (2015)
10. N. Adhlakha, K. L. Yadav, R. Singh, Smart Mater. Struct. **23**, 105024-1-16 (2014)
11. M. Naveed-Ul-Haq, V. V. Shvartsman et al., Sci. Rep. **6**, 32164-1-10 (2016)
12. D. Sun, X. Jin et al., Ferroelectrics **355**, 145–148 (2007)
13. G. Allaedini, S.M. Tasirin, P. Aminayi, Int. Nano Lett. **5**, 183–186 (2015)
14. M. Chandrasekhar, P. Kumar, Physica B **497**, 59–66 (2016)
15. M. Chandrasekhar, P. Kumar, Ceram. Int. **41**, 5574–5580 (2015)
16. V.S. Puli, D.K. Pradhan et al., J. Alloys Compd. **584**, 369–373 (2014)
17. M. Kumar, S. Shankar et al., J. Alloys Compd. **577**, 222–227 (2013)
18. M. Kumar, S. Shankar et al., J. Mater. Sci. Mater. Electron. **26**, 1427–1434 (2015)
19. D. Zhang, J. Cheng et al., J. Alloys Compd. **740**, 1067–1076 (2018)

International Journal of Applied Engineering Research ISSN 0973-4562 Volume 13, Number 15 (2018) pp. 12237-12243
© Research India Publications. http://www.ripublication.com

Experimental Study on the Water Absorption and Surface Characteristics of Alkali Treated Pineapple Leaf Fibre and Coconut Husk Fibre

Mohit Mittal [1, *], Rajiv Chaudhary [1]

[1]Department of Mechanical, Production & Industrial Engineering, Delhi Technological University, Delhi, 110042, India.

** Correspondence Author*

Abstract

Environment sustainability, depletion of raw materials, high consumption of energy during the stage of material processing, and high cost of raw & semi-finished materials are the major problems facing by industries in present days. To get rid of all these problems, scientists have focussed their attention towards the employment of agricultural residue, and plant waste fibres. The significant factor which affects the effective utilization of natural fibres in composite is interfacial adhesion between fibre and matrix polymer. Due to the presence of hydroxyl and polar groups in various constituents of cellulosic fibres, the moisture sorption is quite high which leads to dimensional instability, poor stress transfer from matrix to resin, and fibre pull out at low load conditions. Therefore, it becomes necessary to reduce hydrophilicity of natural fibres by appropriate chemical treatment which results the high strength, fracture resistant bio-composite material. In this work, experimental investigation was done to understand the water up-take behaviour of pineapple leaf fibre and coconut husk fibre. The influence of alkali treatment (NaOH) on the surface chemistry and water sorption *i.e.* swelling behaviour of natural fibres has been carried out. Surface characterization of fibres (PALF and COIR) has done by using FTIR and SEM. The results indicate that the alkali treated fibres are more roughen with regularly placed pin holes than untreated fibre due to the removal of hemicellulose, binder lignin, and waxy substances. Changes in the peaks at 1745, 1525, and 1250 cm^{-1} in FTIR spectra also confirmed the partial removal of hemicellulose and lignin. The water absorption study on alkali treated PALF and COIR shown that the alkali treated fibres absorbs more water than raw fibres. The 4% NaOH treated COIR and 8% NaOH treated PALF absorbs (5-8%) and (9-15%) more water than untreated fibres respectively.

Keywords: Pineapple leaf fibres (PALF); Coconut husk fibres (COIR); Alkali treatment; Hydrophilic nature; Water absorption; Surface morphology.

INTRODUCTION

Increasing concern about environment, depletion of petroleum reserves, high energy consumption, global warming, and high cost of raw materials etc. gives the acceleration towards lignocellulosic materials. Lignocellulosic materials include agricultural residue, grasses, wood, water plants, and plant waste fibres such as banana, sisal, jute, hemp, coir, pineapple leaf fibre, kenaf, flax etc. The current major applications of natural fibres are in automobile, packaging, building and construction, railway coach interiors, storage devices, and partition wall cabinets etc. are due to their wide varieties of advantageous properties like light weight (low density), cheaper source, good specific strength and modulus, biodegradability, high degree of flexibility, non-carcinogenic, and absence of health hazards. Moreover, the abundant and easy availability of huge and wide range of natural fibres is the main cause to select as a raw material in industries. It has been found that scientists and technologists are doing lot of efforts to utilize natural fibres in value added applications. In modern days, natural fibres and agricultural biomass are highly used as reinforcement filler in composite material. This was because of good electrical resistance, acoustic and thermal insulating properties, and high resistance to fracture.

Among all the natural fibre materials, pineapple leaf fibre (PALF) and coconut husk fibre (COIR) seems to be an outstanding material because they are abundantly available in Asia, inexpensive, and eco-friendly in nature. Pineapple leaf fibre and coconut husk fibre are waste material in agriculture sector, which has potential to replace synthetic fibres. PALF can obtain from leaves of pineapple fruit and COIR from the husk of Coconut fruit. The chemical composition of PALF and COIR is mentioned in Table 1.

Table 1. Chemical composition of pineapple leaf fiber and coir fiber [1]

Sr. No	Fiber	Cellulose (%)	Hemicellulose (%)	Lignin (%)	Pectin (%)
1	PALF	70-82	18.8	5-12.7	1.1
2	COIR	32-43	0.15-0.25	40-45	3-4

PALF is highly accepted for making of biocomposite material because of its high tensile strength and modulus, high creep resistance, good strength by weight ratio, and good flexural properties. Inspite of large profitable properties, PALF and COIR have poor resistance to moisture, low thermal stability, and poor dimensional stability. For effective utilization of these fibres in composite material, it is highly required to

reduce hydrophilicity, and increase thermal stability of natural fibres by chemical treatment. Frederick *et al.* (2004) reported that COIR fibre is more durable than other natural fibres. This was due to the presence of high lignin content in COIR fibre [2]. Lignin has the least water sorption property as compared to other natural fibre components. The hydrophilic nature of natural fibres can have undesirable effect on the effective stress transfer from matrix to the fibre (Srinivasa *et al.* 2011) [3]. Therefore, to make a high performance biocomposite material, it is necessary to modify the surface of natural fibres by chemical treatments i.e. alkali treatment, acetylation, methylation, permanganate treatment, cyanoethylation, and grafting of acrylonitrile monomer onto dewaxed PALF [4]. Among the methods, mercerization or alkaline treatment is a cost effective, mostly used surface modification technique in order to improve fibre-resin interfacial bonding [5]. Surface impurities and fibre components such as pectin, waxy substance, lignin, and hemicellulose are partially removed after alkaline treatment which results the better interfacial adhesion between fibre and resin. Currently, there is no work on the water uptake behaviour of pineapple leaf fibre and coconut husk fibre. Therefore in this study, an experimental investigation was done to understand, estimate, and compare the water absorption of untreated and alkali treated PALF and COIR. Moreover, the effect of alkali treatment on surface chemistry of PALF and COIR was studied by FTIR and SEM analysis.

MATERIALS AND METHODS

Materials

Two different types of lignocellulosic fibres were used in this study, *viz.,* coconut (*Coco- nucifera)* husk fibre (COIR), and pineapple (*Ananas comosus*) leaf fibre (PALF). Pineapple leaf fibre (PALF) and coconut husk fibre (COIR) were obtained from Go Green Products, Chennai, India. The average density of COIR and PALF was equal to 1.32 g/cm^3 and 0.98 g/cm^3 respectively. The moisture content in coir and pineapple leaf fibre ranged from 7-8% and 10-11% respectively. Sodium hydroxide (NaOH) used for alkaline treatment was of laboratory reagent (LR) grade and obtained from local supplier.

Alkali treatment of fibres

Pineapple leaf fibre and coir fibre were soaked in various concentrations (2%, 4%, 6%, 8%, and 10%) of alkaline (NaOH) solutions for 24 hrs at 25 ^{0}C, followed by washing with deionized water (until the pH was reached 7), and drying in oven at 60 ^{0}C for 24 hrs (until the constant weight was maintained). The untreated PALF and COIR fibres were also washed in deionized water and dried at 60 ^{0}C for 24 hrs.

Fourier-Transform Infrared Spectroscopy (FTIR)

Fourier-transform infrared spectroscopy, model Perkin Elmer 2000 was used to analyze the surface chemical composition of untreated and treated pineapple leaf fibre and coir fibre. FTIR spectra were analyzed with an infrared spectrophotometer in the range 4000 cm^{-1} to 400 cm^{-1}. FTIR of both untreated and alkali treated COIR and PALF had done in Analytical Instrumentation Laboratory, CSIR-CSIO Chandigarh, India.

Morphological study

Scanning electron microscopic (SEM) images of untreated and alkali treated pineapple leaf fibre and coconut husk fibre were obtained by using a scanning electron microscope (FE-SEM, Hitachi 4300) at the accelerating voltage of 10 kV in Analytical Instrumentation Laboratory, CSIR-CSIO Chandigarh, India.

Water absorption measurement

Water absorption measurement on untreated and alkali-treated PALF and COIR fibre was done in various water samples such as distilled water, river water, and hand-pump water. The pH of water samples were distilled water: 7.0, river water: 7.67, hand-pump water: 7.42. The samples were prepared from bundle of individual fibers (5g) bound together and kept inside the beaker containing various source of water at room temperature (25 ^{0}C). The weight of the fibers was measured after every 12 hrs and the moisture content was calculated by weight difference,

$$\mathbf{MC} = \frac{m_a - m_d}{m_a} \times 100$$

Where **MC** is the moisture content, m_a is the mass of the sample after exposure to moisture, and m_d is the mass of the dry sample.

RESULTS AND DISCUSSION

Fourier-Transform Infrared Spectroscopy (FTIR)

Figs. 1 and 2 shows the FTIR spectra of untreated and alkali treated coir fibers and pineapple leaf fibers respectively. It is clearly evident that surface chemistry of COIR and PALF was changed after alkaline treatment. The increase in intensity around 3300 cm^{-1} and 1000 cm^{-1} corresponds to the higher accessibility of -OH functional group after alkaline treatment. This was due to the removal of waxy and gummy substance. The increase in peak intensity at around 1600-1650 cm^{-1} and 1250 cm^{-1} after alkaline treatment also confirmed the removal of wax, adhesives, pectin, and gummy substance from the fiber surface. The absorption peak at 1745 cm^{-1} is related with

C=O stretch observed in raw fibers (PALF and COIR) but disappears after NaOH treatment. This was attributed to the removal of hemicellulose.

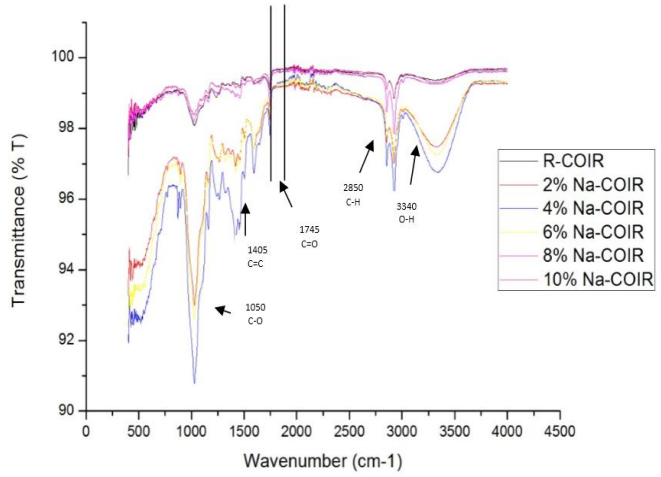


Figure 1. IR spectra of untreated and alkali treated coir fiber

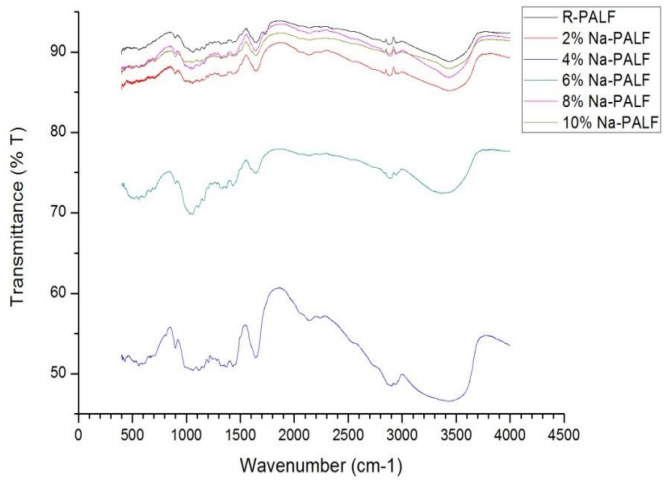


Figure 2. IR spectra of untreated and alkali treated pineapple leaf fiber

The IR spectra for raw pineapple and coconut husk fibers are shown in Fig. 3. It was observed that pineapple leaf fibers consist large amount of hydroxyl (-OH) group than COIR fibers. The broad peak in the region 3200-3500 cm^{-1} attributed to the vibration of –OH group. This O-H group provide active sites for fiber-matrix adhesion. The peak at 1244 cm^{-1} is much smaller in PALF than COIR. This peak corresponds to C=O stretch of the acetyl group of lignin.

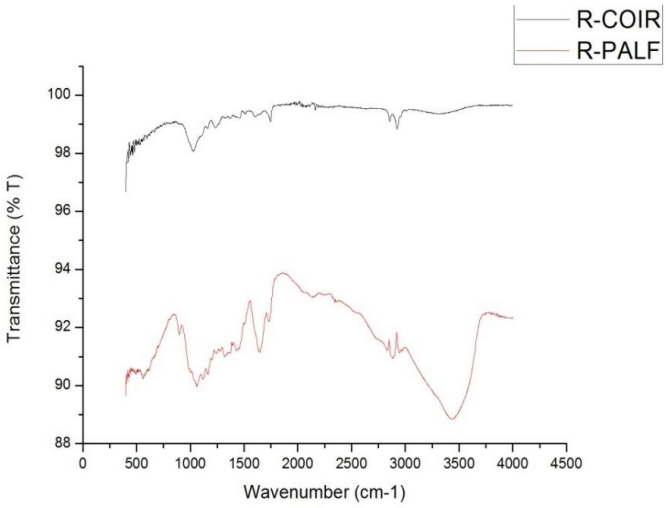
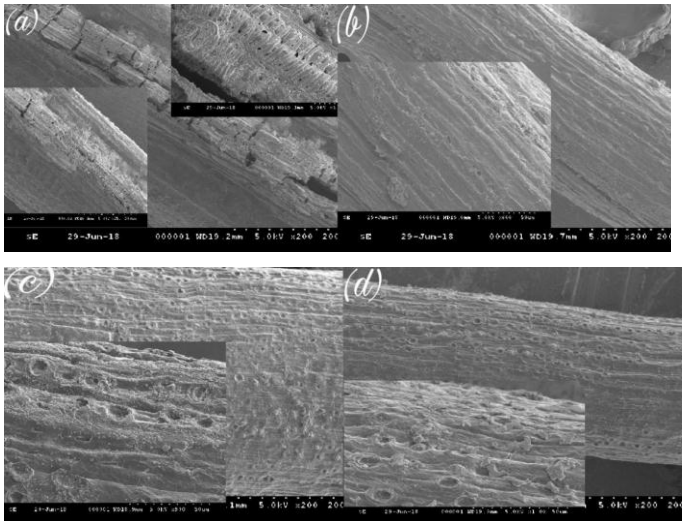


Figure 3. IR spectra of coir fiber and pineapple leaf fiber

Fibre Surface Morphology; SEM Analysis

Surface morphology of COIR fibres (untreated and alkali treated) was shown in Fig. 4 (a)-(f). The untreated COIR fibre display "rotten-wood" like apperance in which many holes, and cavities are present. The SEM micrograph shown in left bottom of Fig. 4 (a), shows network like structure that contains longituidnally oriented unit cells held together by binder lignin and fatty-waxy substances. Fig.4 (b) clearly shows that the surface topography of 2% NaOH treated COIR fibre is much smoother than untreated (raw) COIR fibre. It seems that the fibre surface being roughen again with regularly placed pin holes upon modification by high concentrated alkali solution [Fig. 4 (c)-(f)]. This might be due to the partial removal of wax, surface impurities, and fatty deposits. Similar results have also been reported by Bismarck *et al.* (2001) [6], Prasad *et al.* (1983) [7], Mwaikambo *et al.* (2002) [8].



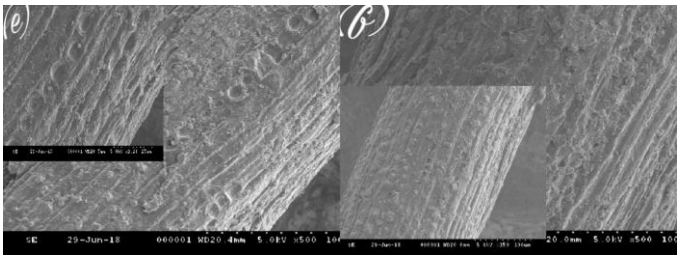


Figure 4. (a) Untreated COIR fibre, plane view (X200), and magnified plane view (X1200). (b) 2% NaOH treated COIR fibre, plane view (X200), and magnified plane view(X400). (c) 4% NaOH treated COIR fibre, plane view (X200), and magnified plane view(X900). (d) 6% NaOH treated COIR fibre, plane view (X200), and magnified plane view(X1000). (e) 8% NaOH treated COIR fibre, plane view (X500), and magnified plane view(X1200). (f) 10% NaOH treated COIR fibre, plane view (X350), and magnified plane view(X500).

Comparing the morphology of COIR fibres with PALF fibres [Fig. 5 (a)-(e)] revealed that pineapple leaf fibres are much smoother and continuous than coir fibres. As compared to COIR fibres, surface morphology of PALF shows no pin-holes. Again, we can observe from Fig. 5 that the alkali treated PALF has higher degree of roughness due to the partial removal of hemicellulose and binder lignin. Previous works [Ramadevi *et al.* (2012), Sgriccia *et al.* (2008)] have also reported the similar effect [9-10]. Fig. 5 (c)-(f) clearly shows that defibrillation increased and cracks were developed in pineapple leaf fibers after alkaline treatment. This was also because of partial removal of hemicellulose and lignin.

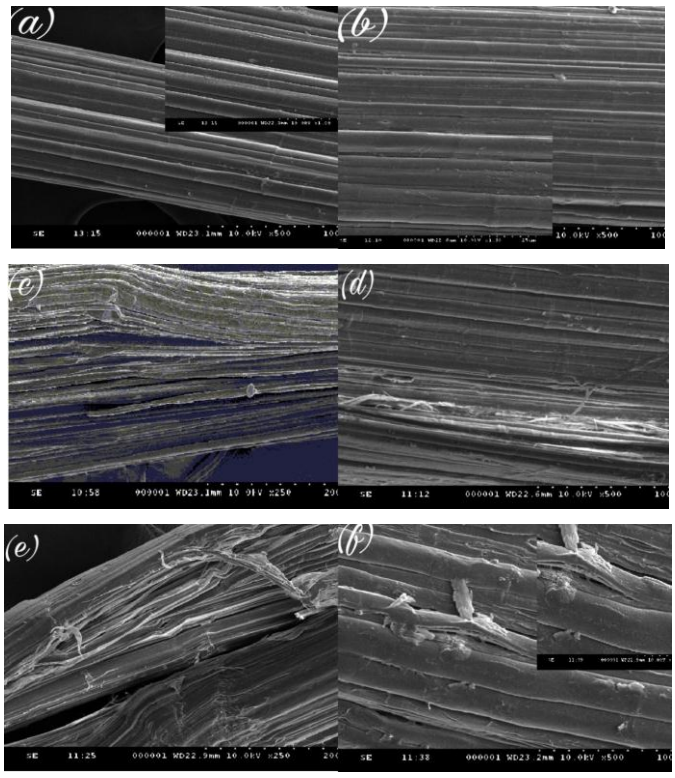


Figure 5. (a) Untreated PALF fibre, plane view (X500), and magnified view (X1000). (b) 2% NaOH treated PALF fibre, plane view (X500), and magnified plane view(X1300). (c) 4% NaOH treated PALF fibre, plane view (X250). (d) 6% NaOH treated PALF fibre, plane view (X500). (e) 8% NaOH treated PALF fibre, plane view (X250). (f) 10% NaOH treated PALF fibre, plane view (X500), and magnified plane view(X1000).

Water Absorption Measurement

The main barrier against the selection of lignocellulosic materials in engineering applications is its moisture sorption ability. The moisture absorption by cellulosic fibres leads to swelling of material, dimensional change, reduction in rigidity of cell wall, and poor strength & stiffness. In moisture sorption process; hemicellulose, non crystalline cellulose, lignin, and surface morphology of fibre plays an important role. To make first choice of lignocellulosic materials, it is greatly required to understand, estimate, and overcome the water uptake behaviour of natural fibres. To measure the water absorption of COIR and PALF fibres, the bundle of fibres were immersed in a container containing various source of water (River water, Distilled water, and Hand-Pump water). After every 12 hours, the fibres were taken out and mopped the excess water on the fibre surface before weighing. For better estimation and comparison of the water absorption of untreated and alkali treated PALF and COIR fibre, it is very important to prepare fibre bundles in the same manner. Four replicates were tested and their mean was presented as a result. The observations on the water absorption of untreated COIR and PALF fibres showed that PALF absorb more water (7.8%) than COIR fibre in distilled water (Fig. 6). It was due to the lower O/C ratio in COIR fibre than PALF fibre.

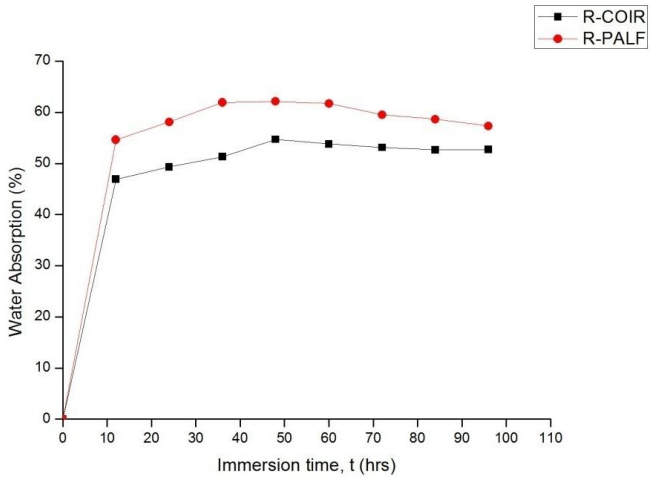


Figure 6. Comparison of water absorption by COIR and PALF fibre in distilled water.

Bessadok *et al.* (2007) reported that, when water concentration exceeds threshold limit, a significant swelling of natural fibers takes place. This was due to the linkage of water molecules to the network of polymer via hydrogen bonds [11]. The untreated COIR fibre absorbs more water in river water (60.6%) than distilled water (54.68%) and hand-pump water (52.76%). Similarly, PALF fibre absorbs more water in distilled water (62.99%) than hand-pump water

(59.6%) and river water (62%). The water absorption by fibres is attributed to the presence of free hydroxyl and polar group in amorphous and crystalline surface of fibre; presence of hollow cavity called lumen; and capillary action of micro pores, cavity, crevices, and holes in fibre surface. Figs. 7-9 clearly show the effect of immersion time (**t)** on water absorption of raw and alkali treated COIR fibre. In both cases (untreated and alkali treated fibre), the moisture sorption is a two step process. In 1st step fibre absorbs water up to saturation level due to the capillary effect and in 2nd step a decrease in the water absorption due to hydro-elastic property of fibre. We can also observe from Figs. 10-12 that capillary and water diffusion action is more pronounced in alkali treated fibres than untreated one. This was due to the fibre surface modification (changes of pore diameter and contact angle) after alkaline treatment of fibres. Alkaline treatment of fibres with various concentrations (2%, 4%, 6%, 8%, and 10%) influence capillary rise heights and capillary diffusion coefficients.

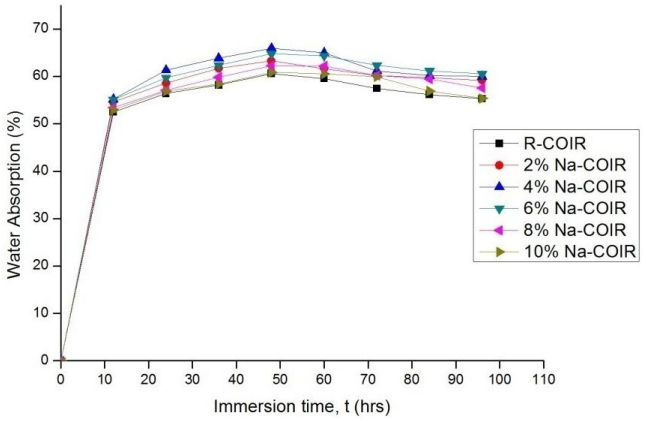


Figure 7. Effect of immersion time on water absorption of untreated and alkali treated COIR fibre in river water.

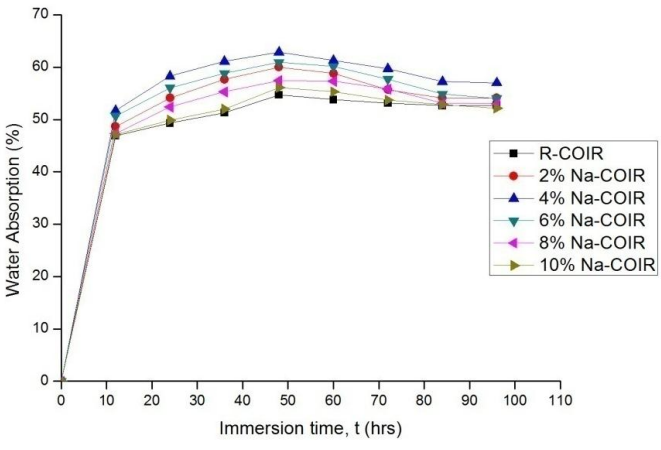


Figure 8. Effect of immersion time on water absorption of untreated and alkali treated COIR fibre in distilled water.

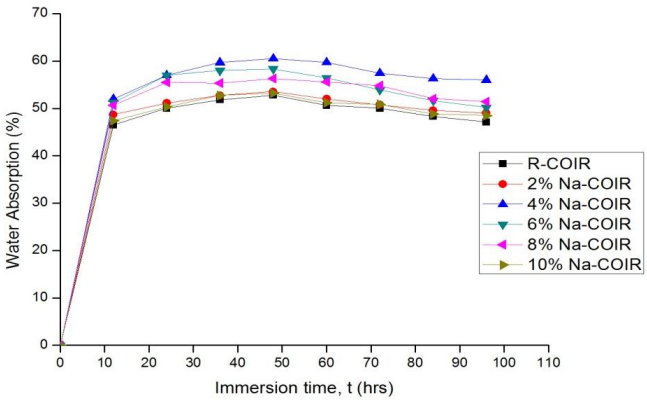


Figure 9. Effect of immersion time on water absorption of untreated and alkali treated COIR fibre in hand-pump water.

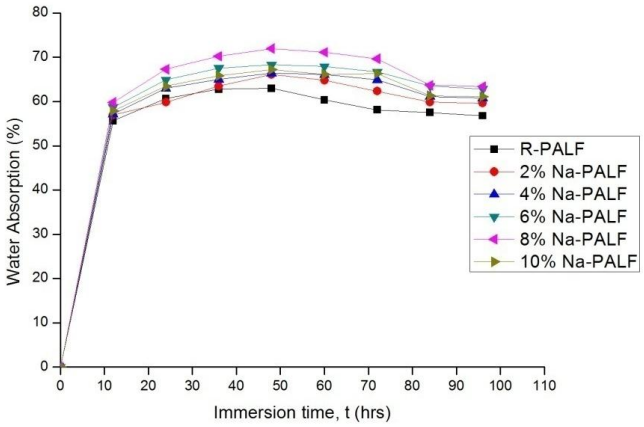


Figure 10. Effect of immersion time on water absorption of untreated and alkali treated PALF fibre in river water.

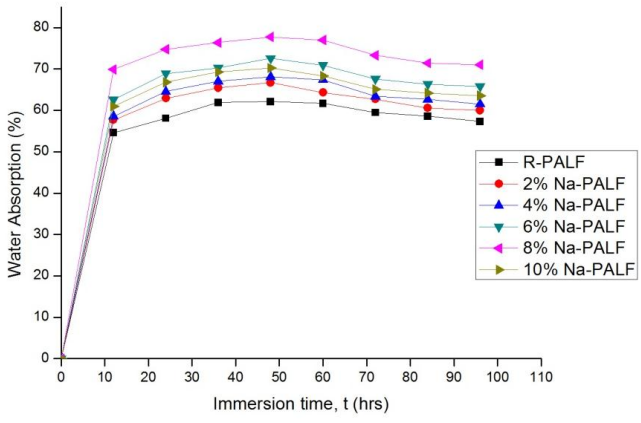


Figure 11. Effect of immersion time on water absorption of untreated and alkali treated PALF fibre in distilled water.

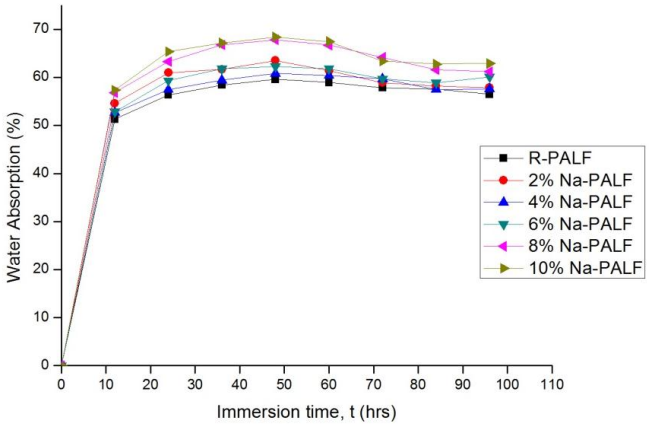


Figure 12. Effect of immersion time on water absorption of untreated and alkali treated PALF fibre in hand-pump water.

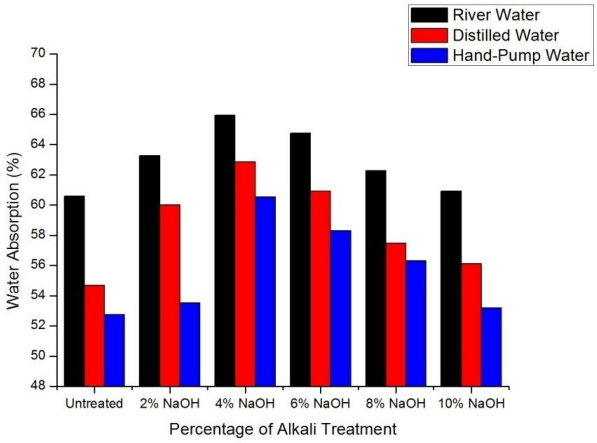


Figure 13. Effect of alkali-treatment on water absorption of COIR fibre.

Fig. 13 and 14 depicts the effect of alkali treatment on water absorption of COIR and PALF fibre respectively. It was observed that moisture sorption of fibres (PALF and COIR) were increased upon alkali treatment, which agrees with previous works (Rong *et al.* (2001), Bal *et al.* (2004), Nabi and Jog *et al.* (1999). This improvement was due to the partial removal of hemicellulose and lignin [12-14]. Bismarck *et al.* (2001) also reported the de-waxing and higher accessibility of active functional group in sisal fiber surface after alkali treatment [6]. Pejic *et al.* (2008) reported that hemicelluloses removal increases the moisture sorption and lignin removal increases the water retention ability of hemp fibre [15]. Literature studies (Buschle Diller *et al.* 1999; Wang *et al.* 2003; Kostic *et al.* 2008) concluded that non-cellulosic components (hemicellulose, lignin, pectin and waxes) negatively affect fibre processing and fibre properties (sorption property, evenness, and elasticity) [16-18]. It was observed that 4% NaOH treated COIR fibre shows maximum water uptake in all water samples [river (65.95%), distilled (62.86%), and hand-pump water (60.53%)]. The pineapple leaf fibre treated with 8% NaOH shown maximum water absorption in river (71.96%) and distilled water (77.72%); and treated with 10% NaOH shown maximum water absorption in hand-pump water (68.4%). The obtained results showed that alkaline treatment removed the pectinous gum, lignin, and hemicellulose which results faster liquid penetration in small, interconnected and uniformly distributed pores [Fig. 4 (c)-(f)]. Celino *et al.* (2014) described that heterogeneous morphologies, hydrogen bonding, and voids within the polymer are certain sites for diffusion of water [19]. The water penetration inside the fibre breaks the secondary bonds between cellulose macromolecules and formed hydrogen bonds with hydroxyl group of the polymer (cellulose) which results fibres swelling, defibrillation, close smaller pores, and reduce capillary spaces into the fibre.

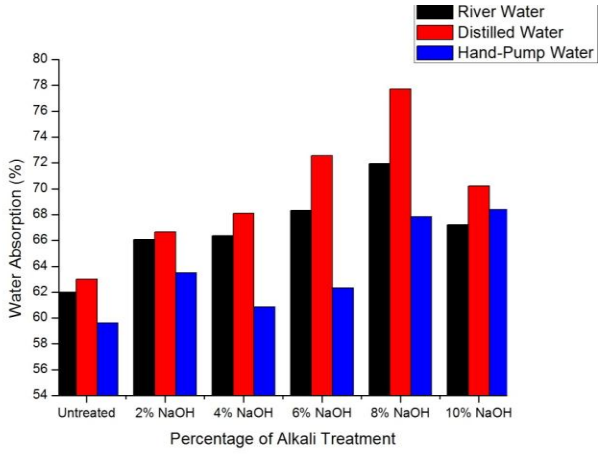


Figure 14. Effect of alkali-treatment on water absorption of PALF fibre.

CONCLUSION

We have performed the experiments to study the alkali treatment effects on surface morphology and water absorption behaviour of pineapple leaf fibre and coconut husk fibre. FTIR and SEM micrograph shows the removal of hemicellulose and binder lignin after alkali treatment. The surface of COIR fibre display many pin-holes than PALF. Defibrillation, surface cracks, porosity, and high serrated surface were produced after alkali treatment due to the partial removal of waxes and fatty substances.

PALF is more hydrophilic than COIR fibre. This was due to the presence of more holocellulose in PALF fibre. The water up-take behaviour is greatly influenced by chemical modifications. All alkali treated fibres absorb more water than untreated fibres. The 4% NaOH treated COIR and 8% NaOH treated PALF absorbs (5-8%) and (9-15%) more water than untreated fibres respectively. The capillary and water diffusion action is more pronounced in alkali treated fibres.

REFERENCES

[1] Rai, A., and Jha, C.N., Natural fibre composite and its potential as building material. BMTPC Seminar.

[2] Frederick, T.W., and Norman W., 2004, "Natural fibers plastics and composites", Kluwer Academics Publishers, New York.

[3] Srinivasa, C.V., Suresh, Y.J., and Premakumar, W.P., 2011, "Mechanical behaviour of areca fiber reinforced epoxy composites", Adv. Polym. Techno., 31(4), pp. 319-330.

[4] S. Mishra, M. Mishra, S.S. Tripathy, S.K. Nayak, and A.K. Mohanty, 2001, "Potentiality of pineapple leaf fibre as reinforcement in PALF-Polyester composite: Surface modification and mechanical performance", J. Reinf. Plas. Comp., 20(4), pp. 321-334.

[5] Ndazi Bwire S., Christian N., and Joseph T., 2007, "Chemical and thermal stability of rice husks against alkali treatment", Bioresources, 3(4), pp. 1267-1277.

[6] Bismarck, A., Mohanty, A.K., Askargorta, I.A., Czapla, S., Misra, M., Hinrichsen, G., and Springer, J., 2001, "Surface characterization of natural fibers: Surface properties and the water up-take behaviour of modified sisal and coir fibers", Gr. Chem., 3(2), pp. 100-107.

[7] Prasad, S.V., C. Pavithran, and P.K. Rohtgi, 1983, "Alkali treatment of coir fibres for coir-polyester composites", J. Mat. Sci., 18(5), pp. 1443-1454.

[8] Mwaikambo, L.Y., and Ansell, M.P., 2002, "Chemical modification of hemp, sisal, jute, and kapok fibers by alkalization", J. Appl. Polym. Sci., 84, pp. 2222-2234.

[9] Ramadevi, P., Sampathkumar, D., Srinivasa, C.V., and Bennehalli, B., 2012, "Effect of alkali treatment on water absorption of single cellulosic abaca fiber", Bioresources, 7(3), pp. 3515-3524.

[10] Sgriccia, N., Hawley, M.C., and Misra. M., 2008, "Characterization of natural fiber surfaces and natural fiber composites", Comp. Part A: Appl. Sci. Manuf., 39(6), pp. 1632-1637.

[11] Bessadok, A.S., Marias, S., Gouanve, F., Colasse, L., Zimmerlin, I., Roudesli, S., and Metyer, M., 2007, "Effect of chemical treatments of Alfa fibers on water sorption properties". Comp. Sci. Tech., 67(3), pp. 685-697.

[12] Rong, M.Z., Zhang, M.Q., Liu, Y., Yang, G.C., and Zeng, H.M., 2001, "The effect of fiber treatment on the mechanical properties of unidirectional Sisal-Epoxy composite", Comp. Sci. Tech., 61(10), pp. 1437-1447.

[13] Bal, K.E., Y. Bal, and A. Lallam, 2004, "Gross morphology and absorption capacity of cell-fibers from the fibrous vascular system of Loofah (Luffa cylindrical)", Tex. Res. J., 74(3), pp. 241-247.

[14] Nabi, D., and J.P. Jog, 1999, "Natural fiber polymer composites: A Review", Adv. Polym. Tech., 18(4), pp. 351-363.

[15] Pejic, B.M., Kostic, M.M., Skundric, P.D., and Praskalo, J.Z., 2008, "The effects of hemicelluloses and lignin removal on water uptake behaviour of hemp fibers", Bio. Tech., 99, pp. 7152-7159.

[16] Buschle Diller, G., Fanter, C., and Loth, F., 1999, "Structural changes in hemp fibers as a result of enzyme systems", Tex. Res. J., 69, pp. 244-251.

[17] Wang, H., Postle, R., Kessler, R., and Kessler, W., 2003, "Removing pectin and lignin during chemical processing of hemp for textile applications", Tex. Res. J., 73, pp. 664-669.

[18] Kostic, M., Pejic, B., and Skundric, P., 2008, "Quality of chemically modified hemp fibers", Bio. Tech., 99, pp. 94-99.

[19] Celino, A., Goncalves, O., Jacquemin, F., and Freour, S., 2014, "Qualitative and quantitative assessment of water sorption in natural fibers using ATR-FTIR spectroscopy". Carb. Polym., 101, pp. 163-170.

Rahman and Hasija *Biomedical Dermatology* (2018) 2:20
https://doi.org/10.1186/s41702-018-0030-y

Biomedical Dermatology

REVIEW Open Access

Exploring vitiligo susceptibility and management: a brief review

Razia Rahman and Yasha Hasija*

Abstract

Background: Vitiligo is a common dermatological disorder of chronic depigmentation which is phenotypically characterized by white macules on the skin caused as a result of the systematic destruction of functional melanocytes. This review provides an overview of vitiligo, its etiopathogenesis and disease management, and also discusses the scope of network-interaction studies and polypharmacological studies in understanding vitiligo disease module.

Methods: A narrative review of the relevant published literatures known to the authors that comprehensively discussed about vitiligo and its implications was conducted.

Results: Emerging evidence underlines the existing connection between deregulated miRNA function and vitiligo pathogenesis. It has also been linked with autoimmunity for the cause of melanocyte death in susceptible individuals. Alteration of genetic factors involved in immune responses and melanogenesis along with environmental factors are central to disease manifestation. Screening methods as such are not available for vitiligo, and the diagnosis is based on the assessment of the absence of melanocytes from the lesions in the affected area. With the occurrence of vitiligo at any age, most people typically develop it at a young age. Depending on the disease course and duration, clinical management primarily involves disease stabilization either by repigmentation or depigmentation of the skin.

Conclusions: Several questions remain unsolved which indeed makes vitiligo an excellent model for studying autoimmune and degenerative processes. An understanding of the underlying degenerative mechanisms and unraveling the biological mediators of melanocyte loss will open up avenues for testing novel therapeutic approaches in vitiligo management. Such studies can revolutionize our apprehension of the molecular interconnections that underpin vitiligo pathogenesis.

Keywords: Vitiligo, Autoimmunity, Genetics, Disease management

Background

Evolutionary studies indicated that skin pigmentation was the result of adaptive responses to the environment (UV radiation) after the loss of hair coat in humans. Pigmentation provides photoprotection and participates in skin barrier function and antimicrobial defenses of the skin, hence, is essential for maintaining body homeostasis (Jablonski and Chaplin 2010). Dermatological disorders have a significant psychosocial impact on the quality of patients' lives since their symptoms are visible. Although dermatological conditions are not life-threatening, it is the product of this morbidity multiplied by the high prevalence of skin disease which results in a large burden of the disease in absolute terms. Vitiligo is one such dermatological disorder that is inflicted upon almost all age groups irrespective of gender and skin type. Vitiligo is a complex acquired depigmentation disorder characterized by white non-scaly patches with distinct sharp margins distributed unilaterally in the skin. It results in the episodically selective disappearance of functional melanocytes which leads to pigment dilution in the affected areas (Le Poole et al. 1993; Ezzedine et al. 2012a, b). Vitiligo is usually asymptomatic and can appear anywhere on the skin commonly affecting the areas of the face and hands, and the genitals (Ezzedine et al. 2012a, b). It might also lead to whitening of hair although the skin and hair are affected to different degrees depending on the disease course which is unpredictable in most cases with phases of stabilized depigmentation eventually with the duration of the disease (Picardo et al. 2015).

* Correspondence: yashahasija06@gmail.com
Department of Biotechnology, Delhi Technological University, Shahbad Daulatpur, Main Bawana Road, Delhi 110042, India

© The Author(s). 2018 **Open Access** This article is distributed under the terms of the Creative Commons Attribution 4.0 International License (http://creativecommons.org/licenses/by/4.0/), which permits unrestricted use, distribution, and reproduction in any medium, provided you give appropriate credit to the original author(s) and the source, provide a link to the Creative Commons license, and indicate if changes were made. The Creative Commons Public Domain Dedication waiver (http://creativecommons.org/publicdomain/zero/1.0/) applies to the data made available in this article, unless otherwise stated.

The onset of vitiligo and its subsequent progression is thought to be impelled by several inherited genes and can develop at any age irrespective of the type of skin, gender, race, or geographical location. Additional stochastic or environmental factors are also likely to further influence the pathogenesis of vitiligo (Spritz 2013). It affects the life of patients both biologically and psychologically due to its unsightly appearance inflicting significant psychological stress and exerting a pernicious influence on the quality of life in patients concerning self-esteem and social interactions. The development of new lesions resulting in enlarged macules is classified as an active form of the disease that warrants more aggressive therapy (Taieb 2012). Friction has also been indicated to trigger vitiligo development in areas such as the neck, elbows, and ankles, a phenomenon known as the Koebner phenomenon (Gauthier et al. 2003). It has been proposed that in some vitiligo cases, Koebner phenomenon could be used to predict and analyze the clinical profile and disease course (van Geel et al. 2012). Various genetic, experimental, and clinical studies have unraveled significant pathways in vitiligo pathogenesis that have helped in identifying targets for the development of efficient treatment approaches for disease management.

Epidemiology and prevalence

Vitiligo is the most common depigmentation disorder with an overall estimated worldwide prevalence of 0.5 to 2% (Krüger and Schallreuter 2012) but a higher prevalence rate up to 8.8% has been reported in India (Sehgal and Srivastava 2007). It has also been reported to occur at an early age in the women population. The largest epidemiological study of the prevalence of vitiligo was carried out on 47,033 inhabitants on the island of Bornholm in Denmark in 1977, where vitiligo was found to affect 0.4% of the population (Howitz et al. 1977). Similar results were obtained in French West Indies, predominantly in the black population (Boisseau-Garsaud et al. 2000). Reports from China, Mexico, and Japan also indicate high incidences of vitiligo with an overall prevalence rate of 0.6% (Sehgal and Srivastava 2007; Wang et al. 2013).

The vitiligo prevalence rates of 0.06 to 2.3% in the general population and 0 to 2.2% in children have been reported in earlier studies (Nicolaidou et al. 2012). Findings also indicate an increased rate of prevalence with respect to age (Alikhan et al. 2011) (Table 1), increasing from 0.5% in children of less than 1 year of age to 1% in children of 1–5 years of age and further expanding to 2.1% in 5–12 year olds. The onset of vitiligo before the age of 12 years is reported to range from 0–2.6% (Halder 1997; Nicolaidou et al. 2012). In almost half of the patients, vitiligo develops before the age of 20 years with nearly about 70 to 80% developing it before 30 years of age. Segmental vitiligo also tends to occur at a younger age with 87% of cases reported in patients before 30 years of age and 41.3% cases before 10 years of age (Ezzedine et al. 2012a, b). Discrepancies between prevalence and incidence data leads to variability in epidemiological data which is attributable to the diverse populations and its genetics, differences in disease classification, cultural and social differences, lack of screening or diagnostic tests, social and cultural stigma attached to the disease, and inconsistent reporting by patients. Despite the same prevalence ratio of 1:1 in males and females, the ratio of treatment requests is 1:2. This signifies that females seek treatments more frequently, which apparently might be due to the ramifications of greater social burden (Alikhan et al. 2011).

Table 1 Increased prevalence rate of vitiligo with respect to age

Prevalence rates	Percentage
General population	0.06–2.3%
Children	0–2.2%
Of less than 1 year	0.5%
1–5 years of age	1%
5–12 year olds	2.1%
Before the age of 12 years	0–2.6%
Onset of disease	Percentage
Before 20 years of age	50%
Before 30 years of age	70–80%

Classification of vitiligo

Figure 1 shows the major classifications of vitiligo, namely, non-segmental or generalized vitiligo, segmental vitiligo, and mixed vitiligo according to international consensus (Ezzedine et al. 2012a, b). The onset of mixed vitiligo is the same as segmental vitiligo which eventually develops into non-segmental vitiligo, thus, the name mixed vitiligo.

In non-segmental (generalized) vitiligo, which is the most common form of vitiligo, the depigmented patches develop on both sides of the body and usually progresses slowly (Picardo et al. 2015). While in segmental vitiligo, the patches are limited to only one side of the body, particularly in the face and trunk area, and do not usually cross the midline of the body. It initially progresses rapidly which spontaneously stabilizes after a period of 6 months (Ezzedine et al. 2012a, b). In segmental vitiligo, typical distribution patterns on the face and trunk have been described, which aid in differential diagnosis (Kim et al. 2011; Geel et al. 2014). Mixed vitiligo, on the other hand, has been described as a rare combination of both segmental vitiligo and non-segmental vitiligo. The onset of mixed vitiligo is the same as segmental vitiligo which eventually develops into non-segmental vitiligo, thus the name mixed vitiligo (Ezzedine et al. 2011). The markedly different distribution patterns aid in recognition of the type of vitiligo as the evolution and the kind of treatment are different for the different subtypes of vitiligo.

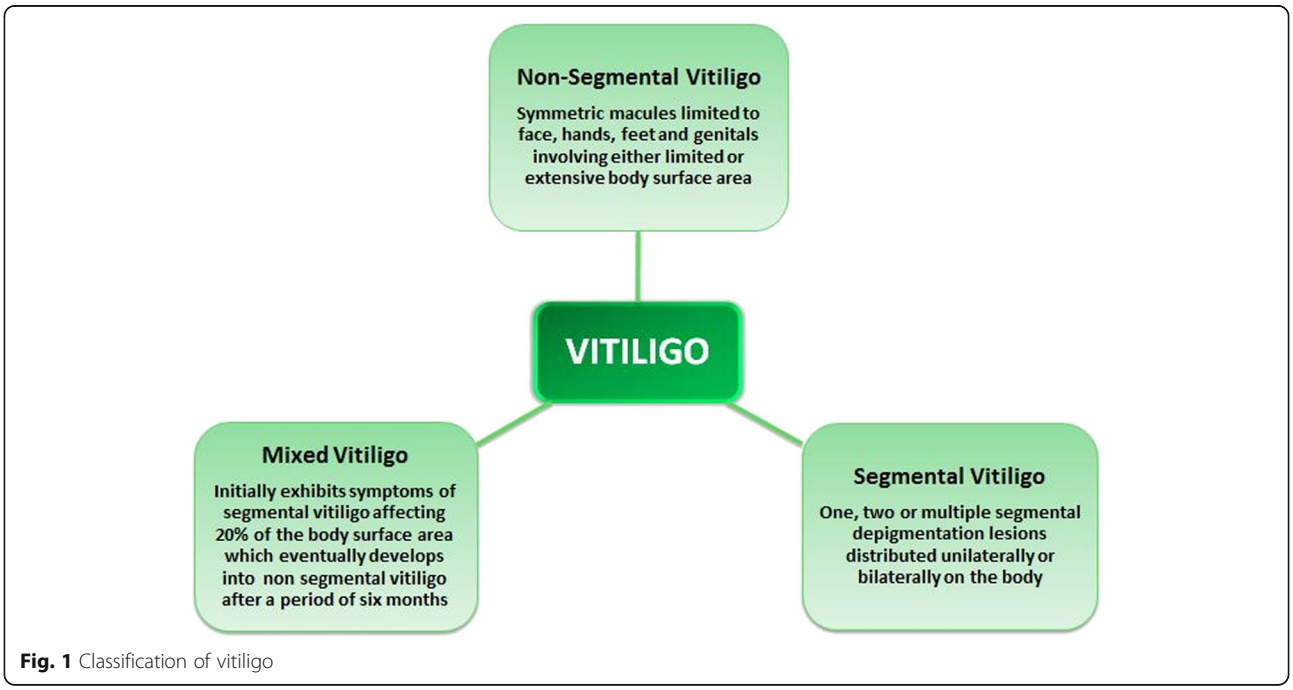


Fig. 1 Classification of vitiligo

Etiopathogenesis of vitiligo

Stress responses in the skin eliciting an autoimmune response in genetically susceptible individuals are thought to be instigated by a trigger event that eventually targets the melanocytes predisposing individuals to develop vitiligo. Though recent studies have started to reveal the etiopathogenesis of vitiligo, the mechanisms leading to vitiligo are yet a debatable topic. However, several hypotheses have been presented signifying its association with the development of vitiligo (Fig. 2). Among the different theories developed, namely, autoimmunity, oxidative stress, melanocyte growth and defective melanocyte adhesion, viral infections, and neural mechanisms, the autoimmune theory is currently considered and accepted

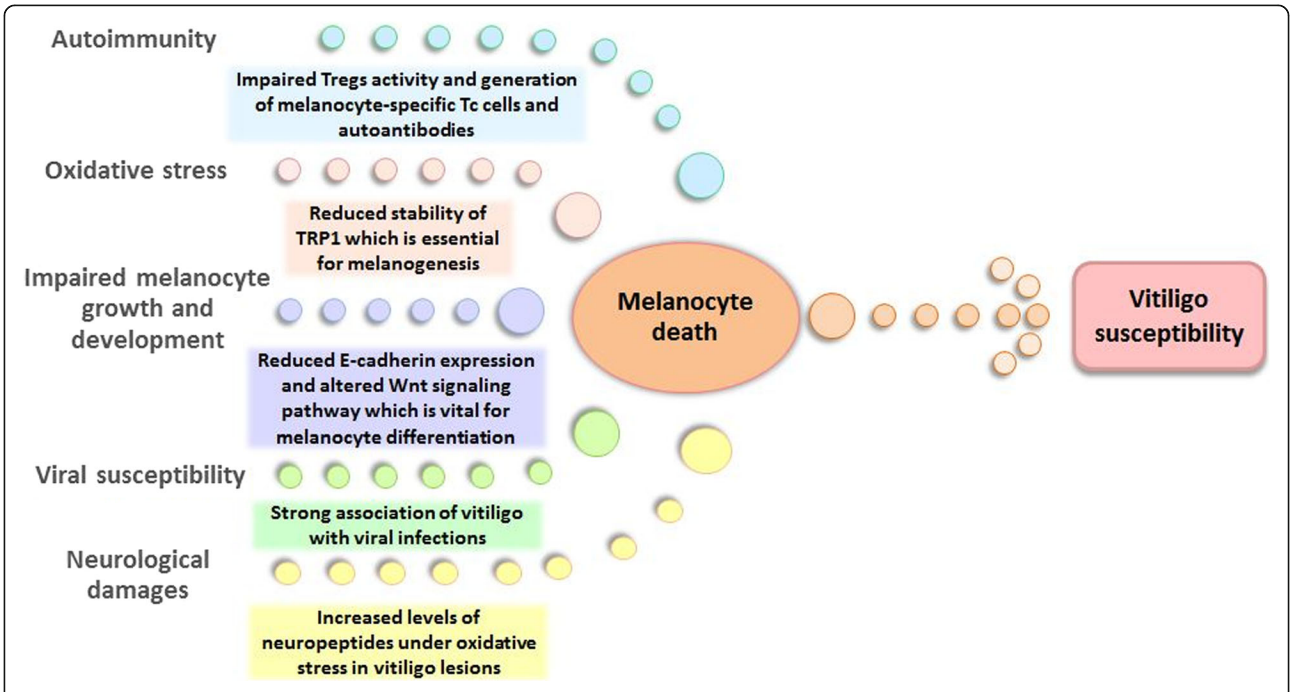


Fig. 2 Etiopathogenetic mechanisms associated with the development of vitiligo

as the leading theory globally, which has been substantiated by several reports on the frequent association of vitiligo with autoimmune diseases (Rezaei et al. 2007; Le Poole and Luiten, 2008; Kasumagic-Halilovic et al. 2013; Strassner and Harris 2016). Also, the association of vitiligo with halo naevus, which is characterized by depigmented halo-like area circumscribing a mole encompassing dense immune cell infiltrate, further supports the importance of immune mechanisms in vitiligo development (Spritz 2010).

Autoimmune theory

The loss of self-tolerance in the pathogenesis of vitiligo is unclear and not yet well understood. High levels of circulating melanocyte autoantibodies recognized by T cells specifically against tyrosinase (TRP-1 and TRP-2) have been found in many vitiligo patients with their role being linked to the destruction of keratinocytes and melanocytes (Jimbow et al. 2001; Kemp et al. 2011). Autoimmunity in vitiligo has been suggested to develop owing to the failure of inherent mechanisms which are intended to control melanocyte proliferation (Le Poole and Luiten 2008). Other antigenic proteins related to disease activity, namely, glycoprotein 100 (gp100) and melanoma antigen recognized by T cells 1 (MART-1) have also been detected in the blood and tissues of vitiligo patients (Lang et al. 2001). Several studies have shown the accumulation of T helper (TH) and T cytotoxic (TC) cells suggesting the formation of a silent micro-inflammatory process that kills melanocytes in the junction of the dermal and epidermal area of vitiligo lesion implying cell-mediated immune response activity (Oyarbide-Valencia et al. 2006). Certain major histocompatibility complex (MHC) alleles have been suggested to be associated with vitiligo as a vital link between the disease etiology and the aberrant self-antigen presentation to the T cells. Moreover, human leukocyte antigen (HLA)-A2 restricted, melanocyte-specific CD8+ T lymphocytes identified to kill melanocytes in the perilesional skin, has been detected in vitiligo patients (Van Den Boorn et al. 2009; Spritz 2010). Also, the fundamental role of regulatory T cells (Tregs) in the pathogenesis of vitiligo has been implicated in several reports with a reduction in their number in the peripheral blood of vitiligo patients along with their dysfunctional activity (Ben Ahmed et al. 2012; Lili et al. 2012). Also considered as a Th1-related disease, a significant increase in the concentration of the cytokines, namely, TNF-α, IFNG, IL-10, IL1B, and IL-17 has also been reported to be associated with the onset as well as persistence of vitiligo in patients (Taher et al. 2009; Levandowski et al. 2013). Therefore, vitiligo serves as an eminent disease model to understand the initiation and progression of organ-specific autoimmune diseases.

Oxidative stress theory

Oxidative stress, which is the result of an increase in the levels of reactive oxygen species (ROS) and subsequent reduction of antioxidant enzymes, compromises the function of cellular proteins and membrane lipids, thus impairing the activity of the antioxidant system in both lesional and non-lesional skin (Maresca et al. 1997). This imbalanced status of the antioxidant system in vitiligo has been indicated to cause increased sensitivity of melanocytes to oxidative stress leading to cellular death. Excess levels of ROS have been reported in active vitiligo skin suggesting oxidative stress as the plausible cause of vitiligo pathogenesis (Jimbow et al. 2001). Superoxide dismutase, an antioxidant enzyme, has been reported to be altered in vitiligo skin indicating that ROS generation causes an alteration in the expression of the antioxidant system affecting melanocyte function (Sravani et al. 2009). Oxidative stress-driven reduction of TRP1 expression triggers the production of intermediates of toxic melanin leading to subsequent immune-mediated melanocyte destruction (Dell'anna and Picardo 2006). Experimental data revealed a close association between oxidative stress and immune responses that promote intrinsic damage. Histological analysis shows the expression of NLR family pyrin domain containing 1 (NLRP1), IL-1, and catalase (CAT) in developing lesions (Marie et al. 2014). Several polymorphisms have been reported in the CAT gene, which impairs the enzyme function of X-box binding protein 1 (XBP1) which is primarily involved in mitigating stress-induced inflammation (Wood et al. 2008). These factors are involved in stress responses which ultimately triggers innate immune responses.

Deficient melanocyte adhesion and melanocyte growth theory

Evidence of the decreased adhesive property of melanocytes in vitiligo has been reported in earlier studies (Gauthier et al. 2003). Reduced expression levels of E-cadherin have been observed in melanocytes prior to depigmentation development in vitiligo skin. During oxidative or mechanical stress, an altered E-cadherin expression incites the loss of adhesion in epidermal melanocytes due to the increased levels of anti-adhesion molecule, tenascin (Le Poole et al. 1997; Wagner et al. 2015). Loss of melanocytes from the epidermal layer due to deficient adhesion of melanocytes could be an early phenomenon in vitiligo. Also, alteration in the factors influencing successful differentiation and proliferation of melanocytes due to oxidative stress, such as altered Wnt signaling, may also render susceptibility to vitiligo.

Viral theory

Several studies have depicted a strong association between vitiligo and hepatitis C virus (HCV) and hepatitis B virus (HBV) infections in vitiligo patients (Akbayir et al. 2004;

Akcan et al. 2006). Also, the association of cytomegalovirus (CMV) infection with vitiligo was also suggested to provoke the deterioration of skin conditions in vitiligo (Toker et al. 2007). Furthermore, the suspicious association of herpes virus and the human immunodeficiency virus (HIV) infection with vitiligo has also been reported (Niamba et al. 2007).

Neuronal mechanisms theory

Clinical observations addressing the correlation of local neurological damage to skin depigmentation (whitening) suggest that neuronal mechanisms do have a role to play in vitiligo pathogenesis. Current evidence of the detection of neuropeptides in vitiligo lesions supports the neural hypothesis which might be the effect of inflammation rather than a triggering factor. An increased level of neuropeptides such as neuropeptide Y (NPY) has been observed in the marginal areas of vitiligo lesions triggered under the conditions of oxidative stress that is thought as a reason for the induction of vitiligo (Lazarova et al. 2000).

Diagnosis and screening

The diagnosis of vitiligo does not require confirmatory laboratory tests in the majority of cases irrespective of its clinical subtype. The absence of melanocytes from lesions can be assessed by in vivo confocal microscopy (non-invasive) or a skin biopsy with the use of specific markers. There are no screening methods available for vitiligo (Ezzedine et al. 2012a, b). The clinical screening of associated disorders on the diagnosis of vitiligo is currently a debatable topic. However, female patients and those with longer disease duration and involving greater body surface area are more likely to have autoimmune thyroid disease. Therefore, proper thyroid function and the presence of anti-thyroglobulin and anti-thyroid peroxidase antibodies need to be checked regularly in vitiligo patients (Gey et al. 2013).

Therapeutic options and management of vitiligo

The management of vitiligo becomes challenging considering its complex etiopathogenesis. There is no definite cure available for vitiligo. Therefore, the current optimal management options according to the recent consensus guidelines involves a personalized approach with the therapeutic choice influenced by several factors such as disease course and its impact, skin type, age, gender, age, affected area and its extent, and social and cultural life influences (Taieb 2012). Also, general measures of avoiding factors of mechanical stress, Koebner phenomenon and UV-exposure might be helpful in limiting depigmentation conditions (van Geel et al. 2012). Figure 3 shows a flowchart depicting the clinical management of vitiligo depending on the disease course and treatment outcomes.

Topical corticosteroids, immunomodulators, and antioxidants

Topical corticosteroids being the first-line of treatment option manage disease progression by initiating anti-inflammatory responses with trivial outcomes. Although repigmentation is observed in the face and neck, the trunk area and the extremities show limited repigmentation. Oral corticosteroid involving moderate dosage of corticosteroids (mini-pulse therapy) is used to arrest disease progression in active disease conditions where the repigmentation outcomes are rare (Njoo et al. 1998). However, the associated side effects oral corticosteroids limit its long-term use.

Topical immunomodulators such as tacrolimus and pimecrolimus attenuate the production of proinflammatory cytokines by inhibiting T cell activity, thereby enhancing melanocyte migration and pigmentation in vitiligo patients (Ormerod 2005). Similar to corticosteroids, the results mostly show repigmentation in the face with moderate effects at other sites of the body.

Although, according to the current consensus guidelines, the use of topical antioxidants is not recommended, however, they are frequently prescribed in relatively limited trials (Leone and Paro 2015). The use of oral antioxidants in combination therapy is sometimes considered in patients undergoing phototherapy.

Phototherapy

Narrow-band UVB (NB-UVB) phototherapy is an effective treatment choice that has long been recognized to induce repigmentation. The majority of the patients are observed to develop the signs of repigmentation with phototherapy. Topical treatments are also advised after completed phototherapy sessions to prevent recurrence of depigmentation (Sitek et al. 2007).

Photochemotherapy is also an option, but the recurrent side effects often accompany carcinogenic risk along with limited successful outcomes which restrict its use over NB-UVB where such risks are less evident (Bhatnagar et al. 2007).

Surgery

Pigment cell transplantation techniques such as cellular and tissue graft transplantation may offer a valuable alternative treatment option. The necessity of the disease stability, which is the primary criteria linked to successful outcomes, limits this treatment option to selective patients only (van Geel et al. 2010). It is effective in both stable non-segmental and segmental vitiligo patients. Regardless of the technique used, the stability of the lesions is a major criterion related to the outcome of the procedure.

Combination therapy

The complexity of the disease makes it necessary to use a combination of different treatments to address both

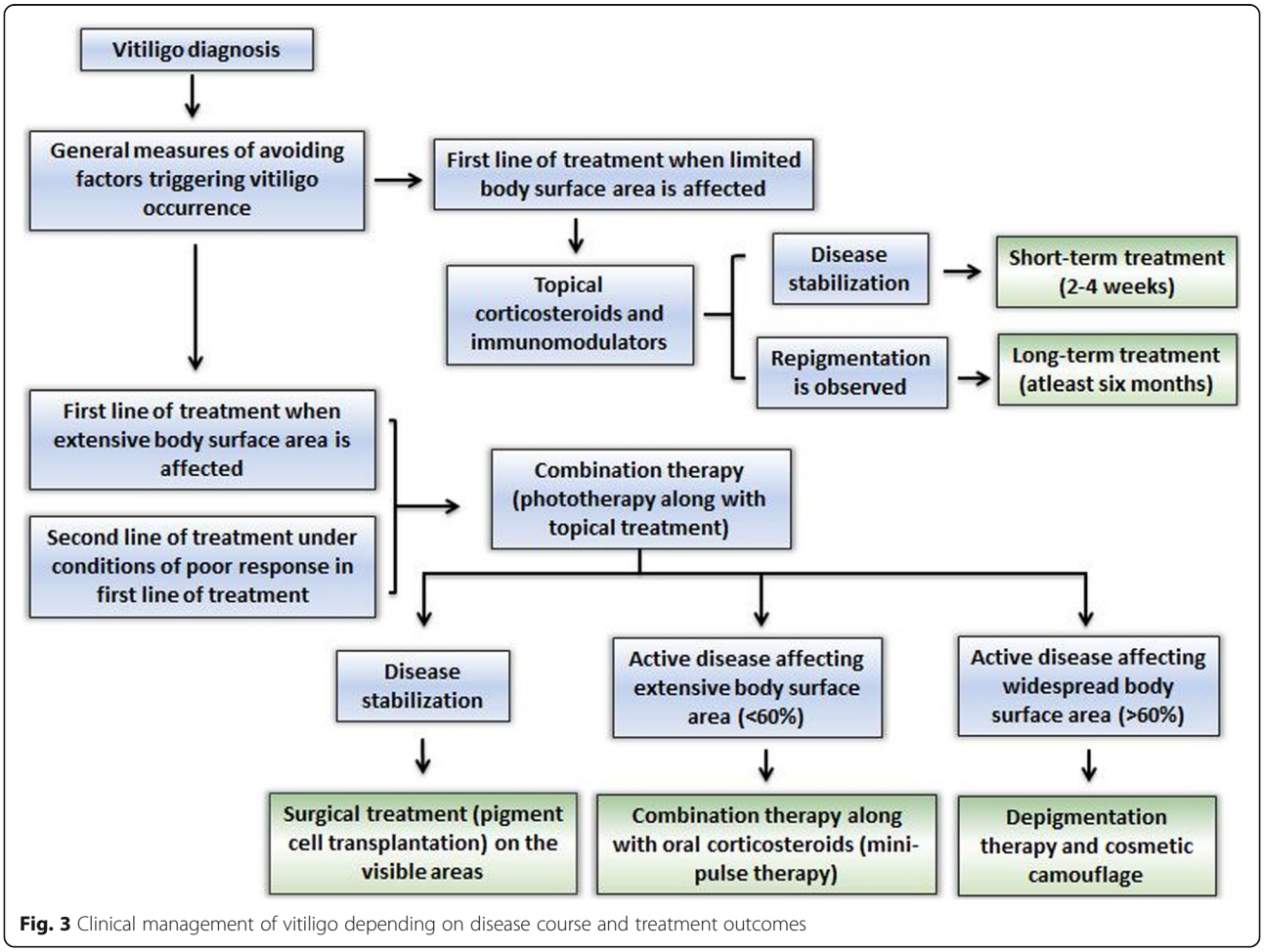


Fig. 3 Clinical management of vitiligo depending on disease course and treatment outcomes

inflammatory responses on melanocyte differentiation and proliferation. Currently, NB-UVB is prescribed along with topical corticosteroids and immunomodulators, instead of its use as a monotherapy. Such combination therapies have been shown to accelerate the repigmentation rates (Nordal et al. 2011). However, the risk of skin cancer due to the combined use of immunosuppressants is a topic of both concern and debate.

Depigmentation and cosmetic camouflage

In conditions of extensive vitiligo where most parts of the body are affected by depigmentation, depigmenting the remaining pigmented areas is considered as a better option instead of repigmentation treatments. Bleaching creams, laser therapy, and cryotherapy are some of the options for depigmentation therapy (AlGhamdi and Kumar 2011). Regardless of this treatment method, repigmentation on the treated depigmented areas might occur and as such a permanent cure cannot be assured.

Camouflaging the depigmented areas with cosmetic products could aid to reduce the daily impact of the disease on social life (Hossain et al. 2016). However, specialized advice is required to be taken before going for such alternatives of cosmetic exposure to vitiligo skin.

Association with other diseases

Due to the polygenic nature of vitiligo, it is frequently associated with several autoimmune or autoinflammatory diseases, namely, thyroid disorders (Kasumagic-Halilovic et al. 2011), psoriasis, atopic dermatitis (Ezzedine et al. 2012a, b), diabetes mellitus, pernicious anemia, and Addison's disease (Rezaei et al. 2007). Antibodies directed against melanocytes and other organ-specific tissues have been found in vitiligo patients. Recent observations strongly point to vitiligo as an autoimmune disease sharing genes with other autoimmune disorders (Zhang and Xiang 2014). Recent studies reported the expression of markers on vitiligo melanocytes that have been detected in cells from neurodegenerative diseases, such as Alzheimer's (Bellei et al. 2013). Therefore, vitiligo might represent a degenerative disease model as well. Although the definite link between vitiligo and melanoma has not been fully elucidated yet, it has been reported that they both share an inverse relationship meaning that vitiligo-affected people are relatively protected

having a much lower risk of developing melanoma' and vice-versa (Spritz 2010). Melanoma patients experiencing successful treatment responses were observed to consequently develop vitiligo. Both melanoma and vitiligo share CD8+ T cell antigens, and the allelic variants associated with vitiligo were found to confer protection from melanoma directly (Paradisi et al. 2014). This observation has contributed significantly to the development of improved therapeutic interventions to regulate melanoma in patients and depicts the similarity in the generation of immune responses and the target of similar antigens in both vitiligo and melanoma.

Impact on the quality of life

The implications of disease progression influence the potential psychiatric comorbidity associated with vitiligo. Skin integrity is considered relevant in many cultural and religious contexts, and any modification in the color or aspect of the skin influences the physical functioning and psychological state of the affected ones. Vitiligo has a major impact on the quality of patients' life relating to social and cultural stigma that eventually affects self-esteem and self-concept due to negative evaluation by others. Several factors including the patients' age at the onset of disease, the extent and distribution of the depigmented patches in the body, and stigmatization causing psychological trauma have a considerably influences the impact that vitiligo has on its patients. Furthermore, the discrepancies prevailing between the efficiency of treatment strategy, therapy response evaluation, and expectations of the patient and overall clinical management further add to the consternation of both the patients and their families (Kruger and Schallreuter 2013). Stigmatization has been shown to be the most influential factor in patient well-being and perceived quality of life, even more than disease duration and treatment inefficiency. In most cases, patients have reported discomfort owing to the uncontrolled progression of the disease rather than noting the development of new lesions in visible areas (Teovska Mitrevska et al. 2012). This suggests that the impaired quality of life is linked to the activity of the disease at a greater extent rather than to the involvement of exposed areas well indicating that the presence of visible lesions did not much affect the global pattern.

The onset of vitiligo in adolescence can have a long-lasting impact on a child's self-esteem directly affecting their psychological state causing interaction anxiousness and depression and thus pose as a risk factor for impaired quality of life in such children. Vitiligo has been found to cause more embarrassment and self-consciousness as children with vitiligo grow older with almost 95% of the teenagers within the age group of 15 to 17 years to be tribulated by their condition as compared to children (50%) of age group between 6 to 14 years (Parsad et al. 2013).

Stress and anxiety caused by vitiligo being a precipitating factor for considerable psychosocial stress can be mitigated by self-help cognitive behavioral therapy (Shah et al. 2014). Treatment according to disease severity might not alone address a patient's suffering adequately. Increased awareness of the quality of life impairments is necessary to address the physical and psychological state that encompasses several factors from the patient's perspective and will help to assure that vitiligo patients are not under-treated and under-appreciated. More than a third of vitiligo patients experience symptoms of depression without necessarily fulfilling the criteria for clinical depression (Parsad et al. 2013). New vitiligo-specific impact scales that better reflects the burden caused by vitiligo have been recently developed such as VitQoL (Lilly et al. 2013), Vitiligo Life Quality (Senol et al. 2013), and Vitiligo Impact Patient Scale (Gupta et al. 2014; Salzes et al. 2016) since the high rate of depressive symptoms signifying the psychological impact in vitiligo patients is evident.

Role of miRNAs and genetic variants on vitiligo susceptibility

Vitiligo appears to be a multifaceted disorder underlying both genetic and non-genetic factors in a complex interactive manner. A comprehensive understanding of the molecular mechanisms that determine disease susceptibility, its onset, and phenotypic expression remains a challenge since the entire spectrum of this disorder is not yet clearly understood. Recent advances in genetic studies have led to the considerable progress in defining the genetic epidemiology and pathogenesis of vitiligo, and its relationships to other autoimmune diseases offering a real insight into its biological framework (Spritz 2013). These studies have improved our knowledge on vitiligo pathogenesis and have opened up new avenues for novel targeted therapies for lack of melanocyte regeneration in vitiligo leading to effective treatment approach as well as disease prevention.

miRNA signatures

MicroRNAs are conserved, small, endogenous non-coding RNA molecules that regulate post-transcriptional gene expression and promote translational repression leading to the cleavage and degradation of mRNA. Recent studies have shown that miRNAs play prime roles in various cellular, regulatory, and signaling processes maintaining physiological homeostasis. They are also essential for cellular morphogenesis, and any disruption in its architecture leads to disease development and progression. Serum miRNA expression profiles have been observed in vitiligo patients (Shi et al. 2013). Moreover, deregulated miRNA metabolism has been reported to be indicative of inflammatory skin conditions and linked to vitiligo pathogenesis (Mansuri et al. 2016). At present, characterization of interpretative miRNA expression

and function in human melanocytes has elucidated them to be promising biomarkers for disease prognosis.

The collective role of miRNAs in oxidative stress and autoimmunity results in melanocyte destruction and leads to further progression of the disease. The expression levels of miR-1, miR-135a, and miR-9 targeting sirtuin 1 (SIRT1) which regulates stress response and inflammation have been found to increase in response to oxidative stress (Saunders et al. 2010), while heme oxygenase 1 (HO1) mRNA targeted by miR-183 is a stress-responsive antioxidant and anti-inflammatory factor (Chang et al. 2011). Increased expression of these miRNAs has been found in vitiligo patients suggesting their potential role in the destruction of melanocyte and formation of inflammatory micro-environment in the skin lesions caused as a result of oxidative stress. Increased levels of miR-133b expression have been observed in the lesional skin of vitiligo patients that suggests its role in the pathogenesis of vitiligo (Mansuri et al. 2014). let-7c targets the 3′ UTR of IL10 and regulates its expression which is a pleiotropic cytokine possessing both anti-inflammatory and immunosuppressive properties (Jiang et al. 2012). A decrease in the level of IL10 expression has been noted in skin biopsies, peripheral blood mononuclear cells, and sera obtained from vitiligo patients well indicating towards its contribution to disease development (Ratsep et al. 2008). An increased expression of miR-99b, miR-125b, miR-155, and miR-199a-3p has also been reported in vitiligo-affected skin which is related to the inhibition of expression of melanogenesis-associated genes which demonstrates that the expression of these miRNAs are dysregulated in the skin of patients with vitiligo and suggests its contribution to vitiligo pathogenesis (Sahmatova et al. 2016). Another miRNA, miR-30b targets platelet-derived growth factor receptor β (PDGFRB) mRNA and represses its ability to regulate cell proliferation in melanocytes resulting in melanocyte death in vitiligo patients (Shi et al. 2013). A significant increase in miR-183, miR-30a-3p, and miR-487a expression have also been shown in the lesional skin of vitiligo patients suggesting the importance of miR-183, miR-30a-3p, and miR-487a expression in rendering vitiligo susceptibility (Ruksha et al. 2017). Apart from the upregulated expression of miRNAs being responsible for vitiligo disease pathogenesis, individual miRNAs have been found to be significantly downregulated in the lesional skin as compared to controls. A downregulated miR-145 can restrict melanocyte proliferation and cause melanocyte death by inducing apoptosis via caspase-3 and caspase-7 activation, thereby playing a prime role in disease initiation (Sahmatova et al. 2016). The expressions of miR-211, miR-141, miR-136, miR-296, and miR-328 have been found to be specifically downregulated in vitiligo skin exhibiting their potential role in the development and progression of the disease (Mansuri et al. 2016).

Genetic susceptibility

In the recent years, several genome-wide association and linkage studies have been conducted in vitiligo which is a polygenic disorder with a complex mechanism of pathogenesis. Although multiple studies have demonstrated the genetic background of vitiligo development, however, the genetic risk is not absolute. Strong evidence for genetic factors in the pathogenesis of generalized vitiligo from various gene expression and association studies identified candidate genes. These candidate genes were found to be involved in encoding components of biological networks that primarily regulate the elements of the immune system and their targeted destruction of melanocytes mediating vitiligo susceptibility (Spritz 2012). Accordingly, several potent disease-contributing loci has been identified to be associated with vitiligo. Between 15 and 20% of patients have one or more familial first-degree relatives with vitiligo indicating the sporadic nature of occurrence of non-segmental vitiligo. Moreover, a 23% concordance of the disease has been noted in monozygotic twins (Spritz 2013). This signifies the penetrance of the genetic predisposition to vitiligo and heritability of vitiligo-associated genes (Alikhan et al. 2011). Identifying vitiligo susceptibility genes and characterizing the stress responses against trigger events that delineate autoimmune components causing disease progression would impel towards significant progress in understanding vitiligo etiology. Various studies have identified that the majority of the susceptible gene variants inculpates modulation of the immune system along with genes linked with melanocytes proliferation and migration (Zhang and Xiang 2014). It is the modulation and alteration exerted by specific genetic variations and their interactions that predispose inflammatory responses targeting melanocyte death owing to the onset of vitiligo.

Genetic studies have identified a majority of the genes that are associated with vitiligo to be a subset of immune regulatory genes concerning immuno-modulatory functions. However, a small number of genes have been identified to be linked to functions involving the regulation of melanocytes growth and proliferation, thus supporting immune regulatory mechanisms as the process that manifest vitiligo. The functional role of the many identified susceptibility loci in the pathogenesis of vitiligo is not known yet which remarkably overlaps with the genes that influence other autoimmune disorders underlining our incomplete knowledge of the disease mechanism (Shen et al. 2016). Genetic mutations that have the potential to modulate both the innate and adaptive immune responses increase the risk for vitiligo susceptibility. Table 2 lists the genetic variants that have been reported to be associated with vitiligo susceptibility. Mutations in several genes in the HLA class I and II regions encoding MHC have been discovered to be associated with vitiligo (Spritz 2012; Shen et al. 2016). MHCs are responsible for the processing and presentation

Table 2 Vitiligo susceptible genetic variants

Gene	Locus	Protein	Role
BACH2	6q15	BTB domain and CNC homolog 2	B cell regulator
BTNL2	6p21.32	Butyrophilin-like 2	T cell regulator
CASP7	10q25.3	Caspase 7	Apoptosis
CAT	11p13	Catalase	Oxidative stress regulator
CCR6	6q27	C-C motif chemokine receptor 6	B cell, T cell and dendritic cell regulator
CD44	11p13	CD44 antigen	T cell regulator
CD80	3q13.33	T-lymphocyte activation antigen CD80	T cell priming by B cells, T cells and dendritic cells
CLNK	4p16.1	Cytokine-dependent hematopoietic cell linker	Positive regulator of mast cells
C1QTNF6	22q12.3	Complement C1q tumor necrosis factor-related protein 6	Immune response-induced apoptosis
CTLA4	2q33.2	Cytotoxic T-lymphocyte protein 4	T cell inhibition
CXCR5	11q23.3	C-X-C motif chemokine receptor 5	B cell activity
FGFR1OP	6q27	Fibroblast growth factor receptor 1 oncogene partner	Cell growth and proliferation
FOXP3	Xp11.23	Forkhead box protein P1	T cell activity and development
GSTP1	11q13.2	Glutathione S-transferase Pi 1	Oxidative stress regulator
GZMB	14q12	Granzyme B	Cytotoxic T lymphocyte-mediated death
HLA-A, HLA-B and HLA-C	6p22.1	Human leukocyte antigen A, B and C	Peptide antigen presentation
HLA-DQB1 and HLA-DRB1	6p21.32	Human leukocyte antigen DQB1 and DRB1	Peptide antigen presentation
IFIH1	2q24.2	Interferon-induced helicase C domain containing protein 1	Innate immune activity
IFNAR1	21q22.11	Interferon alpha and beta receptor subunit 1	T cell signaling
IKZF4	12q13.2	Zinc finger protein Eos	T cell regulator
IL2RA	10p15.1	Interleukin-2 receptor subunit alpha	Interleukin 2-dependent T cell activation
LTA	6p21.33	Lymphotoxin alpha	Immune response-induced apoptosis
MC1R	16q24.3	Melanocortin 1 receptor	Melanogenesis regulator
MTHFR	1p36.22	Methylenetetrahydrofolate reductase	Oxidative stress regulator
NLRP1	17p13.2	NLR family pyrin domain containing 1	Innate immune Activity
OCA2	15q12-13-1	P protein	Melanosomal transporter
PMEL	12q13.2	Premelanosome protein	Melanosomes regulator
PTPN22	1p13.2	Tyrosine-protein phosphatase non-receptor type 22	T cell signaling
RERE	1p36.23	Arginine-glutamic acid dipeptide repeats protein	Lymphoid co-repressor
SH2B3	12q24.12	SH2B adaptor protein 3	T cell signaling
SLA	8q24.22	Src-like adaptor	T cell signaling
SOD2 and SOD3	6q25.3, 4p15.2	Superoxide dismutase 2 and 3	Oxidative stress regulator
TICAM1	19p13.3	Toll-like receptor adaptor molecule 1	Innate immune activity
TLR2 and TLR4	4q31.3, 9q33.1	Toll-like receptor 2 and 4	Innate immune activity
TNF	6p21.33	Tumor necrosis factor	Cell proliferation, differentiation and apoptosis
TYR	11q14.3	Tyrosinase	Melanogenesis regulator
UBASH3A	21q22.3	Ubiquitin associated and SH3 domain containing A	T cell signaling
ZMIM1	10q22.3	Zinc finger MIZ-type containing 1	Transcriptional co-activator

of antigens and are associated with autoimmune diseases in the incidence of derailed recognition of self-antigens. Failure of the immune system to recognize self-antigens leads to the development of autoreactive T cells that eventually restrict the formation of an efficient regulatory T cell (Treg) population (Simmonds and Gough 2007). Also, genetic variants of CTLA4 that are involved in T cell inhibition have been implicated to have a role in vitiligo pathogenesis (Birlea et al. 2009). Genome-wide association studies (GWAS) have found alteration in the genes that encode for factors involved in B cell regulation (BACH2), T cell development and priming (CD44, CD80), T cell receptor signaling (SLA, PTPN22, UBASH3A, CLNK, IFNAR1), and T cell activation (IKZF4, IL2RA, BTNL2, FOXP3) to be associated with vitiligo. Altered expression of the genes that regulate the innate immune response (IFIH1, NLRP1, TICAM1, TLR) and chemokine or cytokine receptors (CXCR5, CCR6, SH2B3) have also been found to be associated with vitiligo (Jin et al. 2012; Karaca et al. 2013; Shen et al. 2016).

Polymorphisms in non-immune-related genes have also been identified as risk factors. The melanocyte-specific genes (TYR, PMEL, MC1R, OCA2) encode for proteins or enzymes that participate in melanin production, and the ZMIZI gene is involved in the regulation of melanocyte development and survival (Sun et al. 2014). Genetic variants of these genes may serve as T cell antigens (autoantigens) which facilitates the initiation of an anti-melanocyte immune response contributing to cellular stress and melanocyte damage resulting in the development of vitiligo (Jin et al. 2010; Spritz 2013). Variation in the genes FGFR1OP, RERE, and CASP7 which have a central role in apoptosis along with GZMB, C1QTNF6, LTA, and TNF which are involved in immune response-induced apoptosis has also been linked with vitiligo (Lee and Bae 2015; Shen et al. 2016). Recently, an elevated plasma level of homocysteine has been described in patients with vitiligo which is associated with the polymorphic expression of MTHFR. MTHFR regulates homocysteine levels in the plasma, and an increased expression renders higher susceptibility to oxidative stress thereby contributing to the damage of melanocytes in vitiligo patients (Chen et al. 2014). Additionally, the genes GSTP1, SOD, and CAT are all broadly expressed in defense against oxidative stress wherein altered expression of these genes impairs their defense mechanisms contributing to ROS-induced melanocyte death in vitiligo patients (Wood et al. 2008; Liu et al. 2009; Laddha et al. 2013).

Scope of network-interaction studies and polypharmacological studies in understanding vitiligo disease module

Network science and analysis involve systemic cataloging of molecular interactions that offer unforeseen perspective prospects to understand and analyze the internal cellular organization and the interconnections between disease-related genes and functional proteins. Network-based studies facilitate in elucidating the extensive complex cellular networks presenting an ideal framework of their cellular organization. Protein-protein interaction networks composed of multiple nodes connected by edges accommodate better estimation of network statistics contributing to a comprehensive assistance in discerning the cellular organizing principles and molecular mechanisms that dictate the manifestation of a disease cycle (Barabasi and Oltvai 2004). This is particularly propitious when interpreting polygenic disorders having intricate patterns. Protein-protein interactions are of prime importance for various cellular and regulatory processes. Genetic variation alters or damages protein structure inciting disruption in protein-protein interactions constituting the pretext of disease development. These interaction networks usually consist of a few essential nodes (called hubs) that show maximum interaction to a large number of neighboring nodes. According to the phenomena of the centrality-lethality rule, the identification of such hub proteins and their inhibition may be lethal for the network. The magnitude of the change in structure caused by the removal of a node in a network determines the relative importance of the node in the network. Removal of such structurally critical nodes (hubs) in a network is widely believed to reflect the significance of the network architecture to better ascertain the network functionality (He and Zhang 2006). These hubs in a protein-protein interaction network may represent potential drug candidates. Since drug discovery and development is a complicated and expensive process, polypharmacology has emerged as the next paradigm of drug discovery. The transformation in the philosophy of current drug designing from one drug-one target to multiple targets of a single drug incorporates polypharmacological analysis that intends to discover the unknown targets for the existing drugs (Yildirim et al. 2007). Polypharmacology-based integrated systems biology approaches along with computational modeling, pharmacological, and clinical studies are productive for identification of novel molecular determinants essential in drug discovery and development. It also aids in unraveling the understanding of the significant impact of a new drug on complex human diseases (Rahman et al. 2018). A drug showing connections with multiple nodes (targets) in a network implies its high efficacious potential to control or inhibit the function of the particular target that is detrimental for regulatory pathways (Boran and Iyengar 2010). The identification of such hub proteins in vitiligo disease network together with polypharmacological studies will serve as an effective practical approach towards improved therapeutic interventions for better vitiligo management.

Conclusions

Cellular and molecular genetics studies have improved our knowledge on disease pathogenesis opening possibilities for new targeted therapies. An understanding of the mechanisms leading to melanocyte degeneration and autoimmunity and how melanocytes interact with their surroundings may help to unravel the rationale for the lack of melanocyte regeneration in vitiligo. Also, profiling the biological mediators of disease mechanisms might identify new therapeutic targets that may arrest disease progression and promote cell regeneration thereby stimulating repigmentation in the affected areas. Improved therapeutic and diagnostic modalities would substantially increase the compliance and satisfaction of patients. Also, the association of vitiligo with other diseases indicates that the knowledge of vitiligo pathogenesis could be of importance other than the skin as well.

Abbreviations

CMV: Cytomegalovirus; GWAS: Genome-wide association studies; HBV: Hepatitis B virus; HIV: Human immunodeficiency virus; HLA: Human leukocyte antigen; HO1: Heme oxygenase 1; MART-1: Melanoma antigen recognized by T cells 1; MHC: Major histocompatibility complex; NB-UVB: Narrow-band UVB; NLRP1: NLR family pyrin domain containing 1; NPY: Neuropeptide Y; PDGFRB: Platelet-derived growth factor receptor β; ROS: Reactive oxygen species; SIRT1: Sirtuin 1; TRP: Tyrosinase; UTR: Untranslated region; XBP1: X-box binding protein

Acknowledgements

Not applicable.

Funding

This work was supported by the Department of Biotechnology, Government of India [No.BT/PR5402/BID/7/508/2012].

Availability of data and materials

Not applicable.

Authors' contributions

YH conceived and designed the study. RR and YH prepared the manuscript. Both the authors read and approved the final manuscript.

Ethics approval and consent to participate

Not applicable.

Consent for publication

Not applicable.

Competing interests

The authors declare that they have no competing interests.

Publisher's Note

Springer Nature remains neutral with regard to jurisdictional claims in published maps and institutional affiliations.

Received: 4 January 2018 Accepted: 27 June 2018
Published online: 15 August 2018

References

Akbayir N, Gokdemir G, Mansur T, Sokmen M, Gündüz S, Alkim C, Barutcuoglu B, Erdem L. Is there any relationship between hepatitis C virus and vitiligo? J Clin Gastroenterol. 2004;38:815–7.

Akcan Y, Kavak A, Sertbas Y, Olut AI, Korkut E, Bicik Z, Kisacik B. The low seropositivity of hepatitis B virus in vitiligo patients. J Eur Acad Dermatol Venereol. 2006;20(1):110–1.

AlGhamdi KM, Kumar A. Depigmentation therapies for normal skin in vitiligo universalis. J Eur Acad Dermatol Venereol. 2011;25(7):749–57.

Alikhan A, Felsten LM, Daly M, Petronic-Rosic V. Vitiligo: a comprehensive overview Part, I Introduction, epidemiology, quality of life, diagnosis, differential diagnosis, associations, histopathology, etiology, and work-up. J Am Acad Dermatol. 2011;65:473–91.

Barabasi AL, Oltvai ZN. Network biology: understanding the cell's functional organization. Nat Rev Genet. 2004;5(2):101–13.

Bellei B, Pitisci A, Ottaviani M, Ludovici M, Cota C, Luzi F, Dell'Anna ML, Picardo M. Vitiligo: a possible model of degenerative diseases. PLoS One. 2013;8(3):e59782.

Ben Ahmed M, Zaraa I, Rekik R, Elbeldi-Ferchiou A, Kourda N, Belhadj Hmida N, Abdeladhim M, Karoui O, Ben Osman A, Mokni M, Louzir H. Functional defects of peripheral regulatory T lymphocytes in patients with progressive vitiligo. Pigment Cell Melanoma Res. 2012;25(1):99–109.

Bhatnagar A, Kanwar AJ, Parsad D, De D. Comparison of systemic PUVA and NB-UVB in the treatment of vitiligo: an open prospective study. J Eur Acad Dermatol Venereol. 2007;21(5):638–42.

Birlea SA, LaBerge GS, Procopciuc LM, Fain PR, Spritz RA. CTLA4 and generalized vitiligo: two genetic association studies and a meta-analysis of published data. Pigment Cell Melanoma Res. 2009;22(2):230–4.

Boisseau-Garsaud AM, Garsaud P, Cales-Quist D, Helenon R, Queneherve C, Claire RC. Epidemiology of vitiligo in the French West Indies (Isle of Martinique). Int J Dermatol. 2000;39(1):18–20.

Boran AD, Iyengar R. Systems approaches to polypharmacology and drug discovery. Curr Opin Drug Discov Devel. 2010;13(3):297.

Chang CL, Au LC, Huang SW, Fai Kwok C, Ho LT, Juan CC. Insulin up-regulates heme oxygenase-1 expression in 3T3-L1 adipocytes via PI3-kinase- and PKC-dependent pathways and heme oxygenase-1-associated microRNA downregulation. Endocrinology. 2011;152:384–93.

Chen JX, Shi Q, Wang XW, Guo S, Dai W, Li K, Song P, Wei C, Wang G, Li CY, Gao TW. Genetic polymorphisms in the methylenetetrahydrofolate reductase gene (MTHFR) and risk of vitiligo in Han Chinese populations: a genotype-phenotype correlation study. Br J Dermatol. 2014;170(5):1092–9.

Dell'Anna ML, Picardo M. A review and a new hypothesis for non-immunological pathogenetic mechanisms in vitiligo. Pigment Cell Melanoma Res. 2006;19(5):406–11.

Ezzedine K, Diallo A, Leaute-Labreze C, Seneschal J, Boniface K, Cario-Andre M, Prey S, Ballanger F, Boralevi F, Jouary T, Mossalayi D. Pre-vs. post-pubertal onset of vitiligo: multivariate analysis indicates atopic diathesis association in pre-pubertal onset vitiligo. Br J Dermatol. 2012a;167(3):490–5.

Ezzedine K, Gauthier Y, Leaute-Labreze C, Marquez S, Bouchtnei S, Jouary T, Taieb A. Segmental vitiligo associated with generalized vitiligo (mixed vitiligo): a retrospective case series of 19 patients. J Am Acad Dermatol. 2011;65(5):965–71.

Ezzedine K, Lim HW, Suzuki T, Katayama I, Hamzavi I, Lan CC, Goh BK, Anbar T, Silva de Castro C, Lee AY, Parsad D. Revised classification/nomenclature of vitiligo and related issues: the vitiligo global issues consensus conference. Pigment Cell Melanoma Res. 2012b;25(3)

Gauthier Y, Cario-Andre M, Lepreux S, Pain C, Taieb A. Melanocyte detachment after skin friction in non lesional skin of patients with generalized vitiligo. Br J Dermatol. 2003;148(1):95–101.

Geel N, Bosma S, Boone B, Speeckaert R. Classification of segmental vitiligo on the trunk. Br J Dermatol. 2014;170(2):322–7.

Gey A, Diallo A, Seneschal J, Leaute-Labreze C, Boralevi F, Jouary T, Taieb A, Ezzedine K. Autoimmune thyroid disease in vitiligo: multivariate analysis indicates intricate pathomechanisms. Br J Dermatol. 2013;168(4):756–61.

Gupta V, Sreenivas V, Mehta M, Khaitan BK, Ramam M. Measurement properties of the Vitiligo impact Scale-22 (VIS-22), a vitiligo-specific quality-of-life instrument. Br J Dermatol. 2014;171(5):1084–90.

Halder RM. Childhood vitiligo. Clin Dermatol. 1997;15:899–906.

He X, Zhang J. Why do hubs tend to be essential in protein networks? PLoS Genet. 2006;2(6):e88.

Hossain C, Porto DA, Hamzavi I, Lim HW. Camouflaging agents for vitiligo patients. J Drugs Dermatol. 2016;15(4):384–7.

Howitz J, Brodthagen H, Schwartz M, Thomsen K. Prevalence of vitiligo: epidemiological survey on the Isle of Bornholm, Denmark. Arch Dermatol. 1977;113(1):47–52.

Jablonski NG, Chaplin G. Human skin pigmentation as an adaptation to UV radiation. Proc Natl Acad Sci USA. 2010;107(Supplement 2):8962–8.

Jiang L, Cheng Z, Qiu S, Que Z, Bao W, Jiang C, Zou F, Liu P, Liu J. Altered let-7 expression in myasthenia gravis and let-7c mediated regulation of IL-10 by directly targeting IL-10 in Jurkat cells. Int Immunopharmacol. 2012;14:217–23.

Jimbow K, Chen H, Park JS, Thomas PD. Increased sensitivity of melanocytes to oxidative stress and abnormal expression of tyrosinase-related protein in vitiligo. Br J Dermatol. 2001;144(1):55–65.

Jin Y, Birlea SA, Fain PR, Ferrara TM, Ben S, Riccardi SL, Cole JB, Gowan K, Holland PJ, Bennett DC, Luiten RM. Genome-wide association analyses identify 13 new susceptibility loci for generalized vitiligo. Nat Genet. 2012;44(6):676.

Jin Y, Birlea SA, Fain PR, Gowan K, Riccardi SL, Holland PJ, Mailloux CM, Sufit AJ, Hutton SM, Amadi-Myers A, Bennett DC. Variant of TYR and autoimmunity susceptibility loci in generalized vitiligo. N Engl J Med. 2010;362:1686–97.

Karaca N, Ozturk G, Gerceker BT, Turkmen M, Berdeli A. TLR2 and TLR4 gene polymorphisms in Turkish vitiligo patients. J Eur Acad Dermatol Venereol. 2013;27(1):e85–90.

Kasumagic-Halilovic E, Ovcina-Kurtovic N, Jukic T, Karamehic J, Begovic B, Samardzic S. Vitiligo and autoimmunity. Med Arch. 2013;67(2):91.

Kasumagic-Halilovic E, Prohic A, Begovic B, Ovcina-Kurtovic N. Association between vitiligo and thyroid autoimmunity. J Thyroid Res. 2011;3:938257.

Kemp EH, Emhemad S, Akhtar S, Watson PF, Gawkrodger DJ, Weetman AP. Autoantibodies against tyrosine hydroxylase in patients with non-segmental (generalised) vitiligo. Exp Dermatol. 2011;20:35–40.

Kim DY, Oh SH, Hann SK. Classification of segmental vitiligo on the face: clues for prognosis. Br J Dermatol. 2011;164(5):1004–9.

Krüger C, Schallreuter KU. A review of the worldwide prevalence of vitiligo in children/adolescents and adults. Int J Dermatol. 2012;51(10):1206–12.

Kruger C, Schallreuter KU. Cumulative life course impairment in vitiligo. Curr Probl Dermatol. 2013;44:102–17.

Laddha NC, Dwivedi M, Gani AR, Shajil EM, Begum R. Involvement of superoxide dismutase isoenzymes and their genetic variants in progression of and higher susceptibility to vitiligo. Free Radic Biol Med. 2013;65:1110–25.

Lang KS, Muhm A, Moris A, Stevanovic S, Rammensee HG, Caroli CC, Wernet D, Schittek B, Knauss-Scherwitz E, Garbe C. HLA-A2 restricted, melanocyte-specific CD8+ T lymphocytes detected in vitiligo patients are related to disease activity and are predominantly directed against MelanA/MART1. J Invest Dermatol. 2001;116(6):891–7.

Lazarova R, Hristakieva E, Lazarov N, Shani J. Vitiligo-related neuropeptides in nerve fibers of the skin. Arch Physiol Biochem. 2000;108(3):262–7.

Le Poole IC, Das PK, van den Wijngaard RM, Bos JD, Westerhof W. Review of the etiopathomechanism of vitiligo: a convergence theory. Exp Dermatol. 1993;(4):145–53.

Le Poole IC, Luiten RM. Autoimmune etiology of generalized vitiligo. Curr Dir Autoimmun. 2008;10:227–43.

Le Poole IC, van den Wijngaard RM, Westerhof W, Das PK. Tenascin is overexpressed in vitiligo lesional skin and inhibits melanocyte adhesion. Br J Dermatol. 1997;137(2):171–8.

Lee YH, Bae SC. Associations between TNF-α polymorphisms and susceptibility to rheumatoid arthritis and vitiligo: a meta-analysis. Genet Mol Res. 2015;14(2):5548–9.

Leone G, Paro VA. Effect of an antioxydant cream versus placebo in patients with vitiligo in association with excimer laser: a pilot randomized, investigator-blinded, and half-side comparison trial. G Ital Dermatol Venereol. 2015;150(4):461–6.

Levandowski CB, Mailloux CM, Ferrara TM, Gowan K, Ben S, Jin Y, McFann KK, Holland PJ, Fain PR, Dinarello CA, Spritz RA. NLRP1 haplotypes associated with vitiligo and autoimmunity increase interleukin-1β processing via the NLRP1 inflammasome. Proc Natl Acad Sci U S A. 2013;110(8):2952–6.

Lili Y, Yi W, Ji Y, Yue S, Weimin S, Ming L. Global activation of CD8+ cytotoxic T lymphocytes correlates with an impairment in regulatory T cells in patients with generalized vitiligo. PLoS One. 2012;7:e37513.

Lilly E, Lu PD, Borovicka JH, Victorson D, Kwasny MJ, West DP, Kundu RV. Development and validation of a vitiligo-specific quality-of-life instrument (VitiQoL). J Am Acad Dermatol. 2013;69(1):e11–8.

Liu L, Li C, Gao J, et al. Genetic polymorphisms of glutathione S-transferase and risk of vitiligo in the Chinese population. J Invest Dermatol. 2009;129(11):2646–52.

Mansuri MS, Singh M, Begum R. miRNA signatures and transcriptional regulation of their target genes in vitiligo. J Dermatol Sci. 2016;84(1):50–8.

Mansuri MS, Singh M, Dwivedi M, Laddha NC, Marfatia YS, Begum R. MicroRNA profiling reveals differentially expressed microRNA signatures from the skin of patients with nonsegmental vitiligo. Br J Dermatol. 2014;171:1263–7.

Maresca V, Roccella M, Roccella F, Camera E, Del Porto G, Passi S, Grammatico P, Picardo M. Increased sensitivity to peroxidative agents as a possible pathogenic factor of melanocyte damage in vitiligo. J Investig Dermatol. 1997;109(3):310–3.

Marie J, Kovacs D, Pain C, Jouary T, Cota C, Vergier B, Picardo M, Taieb A, Ezzedine K, Cario-Andre M. Inflammasome activation and vitiligo/nonsegmental vitiligo progression. Br J Dermatol. 2014;170(4):816–23.

Niamba P, Traore A, Taieb A. Vitiligo in a black patient associated with HIV infection and repigmentation under antiretroviral therapy. Ann Dermatol Venereol. 2007;134:272.

Nicolaidou E, Antoniou C, Miniati A, Lagogianni E, Matekovits A, Stratigos A, Katsambas A. Childhood- and later-onset vitiligo have diverse epidemiologic and clinical characteristics. J Am Acad Dermatol. 2012;66:954–8.

Njoo MD, Spuls PI, Bos JT, Westerhof W, Bossuyt PM. Nonsurgical repigmentation therapies in vitiligo: meta-analysis of the literature. Arch Dermatol. 1998;134(12):1532–40.

Nordal EJ, Guleng GE, Rönnevig JR. Treatment of vitiligo with narrowband-UVB (TL01) combined with tacrolimus ointment (0.1%) vs. placebo ointment, a randomized right/left double-blind comparative study. J Eur Acad Dermatol Venereol. 2011;25(12):1440–3.

Ormerod AD. Topical tacrolimus and pimecrolimus and the risk of cancer: how much cause for concern? Br J Dermatol. 2005;153(4):701–5.

Oyarbide-Valencia K, van den Boorn JG, Denman CJ, Li M, Carlson JM, Hernandez C, Nishimura MI, Das PK, Luiten RM, Le Poole IC. Therapeutic implications of autoimmune vitiligo T cells. Autoimmun Rev. 2006;5(7):486–92.

Paradisi A, Tabolli S, Didona B, Sobrino L, Russo N, Abeni D. Markedly reduced incidence of melanoma and nonmelanoma skin cancer in a nonconcurrent cohort of 10,040 patients with vitiligo. J Am Acad Dermatol. 2014;71(6):1110–6.

Parsad D, Dogra S, Kanwar AJ. Quality of life in patients with vitiligo. Health Qual Life Outcomes. 2013;1:58.

Picardo M, Dell'Anna ML, Ezzedine K, Hamzavi I, Harris JE, Parsad D, Taieb A. Vitiligo. Nat Rev Dis Primers. 2015;1:15011.

Rahman R, Sharma I, Gahlot LK, Hasija Y. DermaGene and VitmiRS: a comprehensive systems analysis of genetic dermatological disorders. Biomed Dermatol. 2018;2(1):18.

Ratsep R, Kingo K, Karelson M, Reimann E, Raud K, Silm H, Vasar E, Koks S. Gene expression study of IL10 family genes in vitiligo skin biopsies, peripheral blood mononuclear cells and sera. Br J Dermatol. 2008;159:1275–81.

Rezaei N, Gavalas NG, Weetman AP, Kemp EH. Autoimmunity as an aetiological factor in vitiligo. J Eur Acad Dermatol Venereol. 2007;21(7):865–76.

Ruksha TG, Komina AV, Palkina NV. MicroRNA in skin diseases. Eur J Dermatol. 2017;27(4):343–52.

Sahmatova L, Tankov S, Prans E, Aab A, Hermann H, Reemann P, Pihlap M, Karelson M, Abram K, Kisand K, Kingo K. MicroRNA-155 is dysregulated in the skin of patients with vitiligo and inhibits melanogenesis-associated genes in melanocytes and keratinocytes. Acta Derm Venereol. 2016;96(6):742–8.

Salzes C, Abadie S, Seneschal J, Whitton M, Meurant JM, Jouary T, Ballanger F, Boralevi F, Taieb A, Taieb C, Ezzedine K. The Vitiligo Impact Patient Scale (VIPs): development and validation of a vitiligo burden assessment tool. J Investig Dermatol. 2016;136(1):52–8.

Saunders LR, Sharma AD, Tawney J, Nakagawa M, Okita K, Yamanaka S, Willenbring H, Verdin E. miRNAs regulate SIRT1 expression during mouse embryonic stem cell differentiation and in adult mouse tissues. Aging (Albany NY). 2010;2:415–31.

Sehgal VN, Srivastava G. Vitiligo: compendium of clinico-epidemiological features. Indian J Dermatol Venereol Leprol. 2007;73(3):149.

Senol A, Yucelten AD, Ay P. Development of a quality of life scale for vitiligo. Dermatology. 2013;226(2):185–90.

Shah R, Hunt J, Webb TL, Thompson AR. Starting to develop self-help for social anxiety associated with vitiligo: using clinical significance to measure the potential effectiveness of enhanced psychological self-help. Br J Derm. 2014;171:332–7.

Shen C, Gao J, Sheng Y, Dou J, Zhou F, Zheng X, Ko R, Tang X, Zhu C, Yin X, Sun L. Genetic susceptibility to vitiligo: GWAS approaches for identifying vitiligo susceptibility genes and loci. Front Genet. 2016;7:3.

Shi YL, Weiland M, Li J, Hamzavi I, Henderson M, Huggins RH, Mahmoud BH, Agbai O, Mi X, Dong Z, Lim HW. MicroRNA expression profiling identifies potential serum biomarkers for non-segmental vitiligo. Pigment Cell Melanoma Res. 2013;26(3):418–21.

Simmonds MJ, Gough SC. The HLA region and autoimmune disease: associations and mechanisms of action. Curr Genomics. 2007;8(7):453–65.

Sitek JC, Loeb M, Ronnevig JR. Narrowband UVB therapy for vitiligo: does the repigmentation last? J Eur Acad Dermatol Venereol. 2007;21(7):891–6.

Spritz RA. The genetics of generalized vitiligo: autoimmune pathways and an inverse relationship with malignant melanoma. Genom Med. 2010;2(10):78.

Spritz RA. Six decades of vitiligo genetics: genome-wide studies provide insights into autoimmune pathogenesis. J Investig Dermatol. 2012;132(2):268–73.

Spritz RA. Modern vitiligo genetics sheds new light on an ancient disease. J Dermatol. 2013;40(5):310–8.

Sravani PV, Babu NK, Gopal KV, Rao GR, Rao AR, Moorthy B, Rao TR. Determination of oxidative stress in vitiligo by measuring superoxide dismutase and catalase levels in vitiliginous and non-vitiliginous skin. Indian J Dermatol Venereol Leprol. 2009;75(3):268.
Strassner JP, Harris JE. Understanding mechanisms of autoimmunity through translational research in vitiligo. Curr Opin Immunol. 2016;43:81–8.
Sun Y, Zuo X, Zheng X, Zhou F, Liang B, Liu H, Chang R, Gao J, Sheng Y, Cui H, Wang W. A comprehensive association analysis confirms ZMIZ1 to be a susceptibility gene for vitiligo in Chinese population. J Med Genet. 2014; 51(5):345–53.
Taher ZA, Lauzon G, Maguiness S, Dytoc MT. Analysis of interleukin-10 levels in lesions of vitiligo following treatment with topical tacrolimus. Br J Dermatol. 2009;161(3):654–9.
Taieb A. Vitiligo as an inflammatory skin disorder: a therapeutic perspective. Pigment Cell Melanoma Res. 2012;25(1):9–13.
Teovska Mitrevska N, Eleftheriadou V, Guarneri F. Quality of life in vitiligo patients. Dermatol Ther. 2012;25(Suppl. 1):S28–31.
Toker SC, Sarycaoglu H, Karadogan SK, Mistik R, Baskan EB, Tunaly S. Is there any relation between vitiligo and cytomegalovirus? J Eur Acad Dermatol Venereol. 2007;21:141–2.
Van Den Boorn JG, Konijnenberg D, Dellemijn TA, Van Der Veen JW, Bos JD, Melief CJ, Vyth-Dreese FA, Luiten RM. Autoimmune destruction of skin melanocytes by perilesional T cells from vitiligo patients. J Invest Dermatol. 2009;129(9):2220–32.
van Geel N, Speeckaert R, De Wolf J, Bracke S, Chevolet I, Brochez L, Lambert J. Clinical significance of Koebner phenomenon in vitiligo. Br J Dermatol. 2012; 167(5):1017–24.
van Geel N, Wallaeys E, Goh BK, De Mil MA, Lambert J. Long-term results of noncultured epidermal cellular grafting in vitiligo, halo naevi, piebaldism and naevus depigmentosus. Br J Dermatol. 2010;163(6):1186–93.
Wagner RY, Luciani F, Cario-Andre M, Rubod A, Petit V, Benzekri L, Ezzedine K, Lepreux S, Steingrimsson E, Taieb A, Gauthier Y. Altered E-cadherin levels and distribution in melanocytes precede clinical manifestations of vitiligo. J Investig Dermatol. 2015;135(7):1810–9.
Wang X, Du J, Wang T, Zhou C, Shen Y, Ding X, Tian S, Liu Y, Peng G, Xue S, Zhou J, Wang R, Meng X, Pei G, Bai Y, Liu Q, Li H, Zhang J. Prevalence and clinical profile of vitiligo in China: a community-based study in six cities. Acta Derm Venereol. 2013;93(1):62–5.
Wood JM, Gibbons NC, Chavan B, Schallreuter KU. Computer simulation of heterogeneous single nucleotide polymorphisms in the catalase gene indicates structural changes in the enzyme active site, NADPH-binding and tetramerization domains: a genetic predisposition for an altered catalase in patients with vitiligo? Exp Dermatol. 2008;17(4):366–71.
Yildirim MA, Goh KI, Cusick ME, Barabasi AL, Vidal M. Drug-target network. Nat Biotechnol. 2007;25(10):1119–26.
Zhang Z, Xiang LF. Genetic susceptibility to vitiligo: recent progress from genome-wide association studies. Dermatol Sin. 2014;32(4):225–32.

Ready to submit your research? Choose BMC and benefit from:

- fast, convenient online submission
- thorough peer review by experienced researchers in your field
- rapid publication on acceptance
- support for research data, including large and complex data types
- gold Open Access which fosters wider collaboration and increased citations
- maximum visibility for your research: over 100M website views per year

At BMC, research is always in progress.

Learn more biomedcentral.com/submissions



International Journal of Engineering Applied Sciences and Technology, 2018
Vol. 3, Issue 2, ISSN No. 2455-2143, Pages 7-15
Published Online June 2018 in IJEAST (http://www.ijeast.com)



FUZZY CONTROLLED GRAVITATIONAL SEARCH ALGORITHM FOR CLUSTERING

Himanshu Kaul
Delhi Technological University
Shahbad Daulatpur, New Delhi 110042, India

Neha Dimri
Indian Institute of Technology
Hauz Khas, New Delhi 110016, India

Abstract— **Clustering is a key activity in numerous data mining applications such as information retrieval, text mining, image segmentation, etc. In this paper, a clustering approach, Fuzzy-GSA, based on gravitational search algorithm (GSA) has been proposed. The proposed Fuzzy-GSA algorithm utilizes a fuzzy inference system to effectively control the parameters of gravitational search algorithm. The performance of Fuzzy-GSA algorithm has been evaluated against four benchmark datasets from the UC Irvine repository. The results illustrate that the Fuzzy-GSA algorithm attains the highest quality clustering over the selected datasets when compared with several other clustering algorithms namely, k-means, particle swarm optimization (PSO), gravitational search algorithm (GSA) and, combined gravitational search algorithm and k-means approach (GSA-KM).**

Keywords— **Clustering, Fuzzy-GSA, Gravitational Search Algorithm, Fuzzy Inference System**

I. INTRODUCTION

Clustering or cluster analysis refers to the process of grouping a set of data objects such that objects belonging to the same group are similar, whereas those belonging to different groups are distinct. The final groups are called clusters or classes. It is a major data mining task and is used as a common technique for analysis of statistical data in many fields such as pattern recognition, machine learning, information retrieval etc. In the process of clustering, it is important to define an appropriate similarity or dissimilarity measure over which the data objects are to be clustered. The same set of objects may be partitioned into different groups depending on the choice of similarity or dissimilarity measure. The number of clusters in the final partition may be pre-assigned or may be considered as an internal parameter of the clustering algorithm to be deduced based on the input data.

Clustering is an unsupervised learning task since it groups data objects into clusters without any prior information such as class labels. The clustering techniques, thus, should be able to deduce the structure embedded in data without any extra information. Clustering algorithms have been successfully applied in several fields such as information retrieval (Jardine and Rijsbergen 1971; Tombros et al. 2002), medicine (Liao et al. 2008), biology (Kerr et al. 2008), customer analysis (Saglam et al. 2006), image segmentation (Xia et al. 2007) and many others. Clustering has been an area of active research and many clustering algorithms have been proposed in the literature. The most widely used and the most popular algorithm for clustering is the k-means algorithm, proposed by J. MacQueen in 1967 (MacQueen 1967). K-means algorithm is fairly straightforward, simple to implement and has been employed by several researchers (Jain 2010; Forgy 1965; Kaufman and Rousseeuw 1990). However, it may be easily trapped in a local optimum and fail to achieve a global optimum in several cases since the algorithm's performance is highly dependent on the initial centroids chosen.

To overcome this problem, several heuristic based approaches have been proposed for clustering. Selim and Alsultan (1991) provided a simulated annealing (SA) algorithm for clustering. They have demonstrated that the simulated annealing algorithm converges to a global optimum for the clustering problem. Maulik and Bandyopadhyay (2000) presented a clustering technique based on genetic algorithm, known as GA-clustering. The centers of a pre-defined number of clusters were encoded using chromosomes and the improved performance of GA-clustering over k-means algorithm was demonstrated with the help of three real datasets. A tabu search based method was presented for solving the clustering problem in (Al-Sultan 1995; Sung and Jin 2000).

Shelokar et al. (2004) presented an Ant Colony Optimization (ACO) based technique for optimally assigning objects to a pre-defined number of clusters. The ACO based technique provided very promising results when compared with other heuristic methods such as genetic algorithm, simulated annealing and tabu search. Fathian et al. (2007) proposed an algorithm for clustering based on honeybee mating optimization (HBMO). The performance of HBMO based approach was better compared to SA, GA, tabu search and ACO when evaluated over several well-known datasets. Ching-Yi and Fun (2004) provided a Particle Swarm Optimization (PSO) based approach for clustering. They compared the performance of PSO-based approach with

International Journal of Engineering Applied Sciences and Technology, 2018
Vol. 3, Issue 2, ISSN No. 2455-2143, Pages 7-15
Published Online June 2018 in IJEAST (http://www.ijeast.com)

traditional clustering algorithms and demonstrated that the PSO-based approach performed better using four artificial datasets.

Hatamlou et al. (2011) applied the Gravitational Search Algorithm (GSA) to data clustering. The results over four well-known datasets depicted that GSA based approach performed better than several other clustering algorithms namely PSO, HBMO, ACO, GA, SA and k-means. Hatamlou et al. (2012) presented a technique combining the benefits of k-means algorithm with GSA, called GSA-KM, in clustering. In GSA-KM approach, the initial population for GSA was generated with the help of k-means algorithm, which allowed GSA to converge faster. When compared with other well known algorithms, such as k-means, GA, SA, ACO, HBMO, PSO and the conventional GSA approach, GSA-KM approach provided better results over several real datasets.

Gravitational Search Algorithm (GSA) uses a constant value of parameter α for the calculation of gravitational constant. In the beginning, smaller value of α allows for a greater exploration of the search space. Furthermore, higher value of α during the last few iterations enhances the search space exploitation. Therefore, the approach based on GSA can be improved by adapting and controlling the value of parameter α, as the algorithm proceeds.

This paper proposes an algorithm for clustering, called Fuzzy-GSA, based on Gravitational Search Algorithm (GSA). The proposed algorithm uses fuzzy rules for controlling the parameter α in GSA algorithm as the search progresses. In Section II, an overview of the Gravitational Search Algorithm (GSA) proposed by Rashedi et al. (2009) has been presented. Section III describes the proposed clustering algorithm, Fuzzy-GSA, where Section III–A describes the developed fuzzy inference system and Section III–B presents the proposed algorithm for clustering. Section IV discusses the experimental results and comparison with other clustering algorithms. Section V lists the conclusions of the present study.

II. Gravitational Search Algorithm

Gravitational Search Algorithm (GSA) is an optimization algorithm proposed by Rashedi et al. (2009). It is based on the Newton's laws of gravity and motion. The law of gravity states that "Every particle in the universe attracts every other particle with a force that is directly proportional to the product of the masses of the particles and inversely proportional to the square of the distance between them". By this definition, the gravitational force is determined using the following equation (Rashedi et al. 2009):

$$F = G\,\frac{M_1 M_2}{R^2} \tag{1}$$

where, F is the gravitational force acting between two masses $M_1$and M_2, G is the gravitational constant with a value of 6.67259×10^{-11} N m^2/kg^2, and R is the distance between the two masses.

Newton's second law of motion states that when a force acts on a mass, acceleration is produced. The magnitude of acceleration produced is obtained using the equation below (Rashedi et al. 2009):

$$a = \frac{F}{M} \tag{2}$$

where, F and M denote the net force acting on a given particle and its mass, respectively.

The Gravitational Search Algorithm (GSA) employs this physical phenomenon for solving optimization problems. Consider a system with N masses or agents. The position of i^{th} mass is defined as:

$$X_i = (\, x_i^1, \ldots, x_i^d, \ldots, x_i^n) \text{ , for } i = 1,2, \ldots, \text{N} \tag{3}$$

where, x_i^d is the position of i^{th} agent in d^{th} dimension and n is the total number of dimensions in the search space. The positions of agents correspond to the solutions of the problem. The mass of each agent is computed, after evaluating the present population's fitness, using the following equations:

$$m_i(t) = \frac{fit_i(t) - worst(t)}{best(t) - worst\,(t)} \tag{4}$$

$$M_i(t) = \frac{m_i(t)}{\sum_{j=1}^{N} m_j(t)} \tag{5}$$

where, $fit_i(t)$, denotes the fitness value of i^{th} agent at time t, and *best(t)* and *worst(t)* are computed as follows (for minimization problems):

$$best(t) = \min\, fit_j(t)\,,\ j = 1, 2, \ldots, N \tag{6}$$

$$worst(t) = \max\, fit_j(t)\,,\ j = 1, 2, \ldots, N \tag{7}$$

Similarly, for maximization problems *best(t)* and *worst(t)* are computed by taking the maximum and minimum fitness values respectively.

International Journal of Engineering Applied Sciences and Technology, 2018
Vol. 3, Issue 2, ISSN No. 2455-2143, Pages 7-15
Published Online June 2018 in IJEAST (http://www.ijeast.com)

The acceleration of an agent is computed next, by considering the total forces from a set of heavier masses using the laws of gravity and motion using Eqs. (8) and (9). The new velocity of an agent is computed next by adding a fraction of its current velocity to its acceleration (Eq. (10)), followed by the calculation of its new position (Eq. (11)).

$$F_i^d(t) = \sum_{j \in kbest, j \neq i} rand_j \, G(t) \frac{M_j(t) M_i(t)}{R_{ij}(t) + \varepsilon} \left(x_j^d(t) - x_i^d(t) \right) \quad (8)$$

$$a_i^d(t) = \frac{F_i^d(t)}{M_i(t)} = \sum_{j \in kbest, j \neq i} rand_j \, G(t) \frac{M_j(t)}{R_{ij}(t) + \varepsilon} \left(x_j^d(t) - x_i^d(t) \right) \quad (9)$$

$$v_i^d(t+1) = rand_i \times v_i^d(t) + a_i^d(t) \quad (10)$$

$$x_i^d(t+1) = x_i^d(t) + v_i^d(t+1) \quad (11)$$

where, $rand_i$ and $rand_j$ are two random numbers uniformly distributed in the range of [0, 1], ε is a small value to prevent division by zero, $R_{ij}(t)$ is the Euclidean distance between agent *i* and agent *j*. *Kbest* is the set of first *K* agents with best fitness values and thus, largest mass. *Kbest* is dependent on time, initialized to K_o at the start and decreases as time progresses. The gravitational constant, $G(t)$, decreases with time to control the search accuracy. The value of $G(t)$ is calculated using the following equation:

$$G(t) = G_o e^{\frac{-\alpha t}{T}} \quad (12)$$

where, G_o is the initial value of gravitational constant, α is a parameter which governs the degree of exploration versus exploitation of the search and *T* is the maximum number of iterations.

III. Fuzzy-GSA Clustering Algorithm

In this section, the proposed algorithm, called Fuzzy-GSA, has been described for data clustering. The proposed approach is based on Gravitational Search Algorithm (GSA), described in section II, and uses fuzzy inference rules for controlling the parameter α as search progresses. This section is divided into two subsections. Section III–A describes the Fuzzy Inference System (FIS) developed, and the section III–B presents the proposed Fuzzy-GSA algorithm for clustering.

A. The Developed Fuzzy Inference System –

The FIS is developed with two input variables and one output variable. The input variables are as follows:

- *IT*: The current iteration number.
- *Fbest*: The best value of fitness achieved till the current iteration.

IT enables us to consider how far we have reached in the search process. During the initial iterations, i.e. when *IT* is low, a lower value of α is desired since lower the value of α, higher the value of gravitational constant, *G(t)*, will be (Eq. (12)) and thus, higher the force, *F*, (Eq. (8)) resulting in a higher acceleration, *a*, (Eq. (9)) and velocity, *v(t)* (Eq. (10)). This allows for higher exploration at the beginning of search. Similarly, towards the final few iterations, i.e. when *IT* is high, a higher value of α is desired to promote higher exploitation. Fig. 1 depicts the membership function for *IT*. The iterations are represented as a fraction of the maximum number of iterations allowed, such that 0.5 means half of the total iterations and 1 represents the maximum iterations.

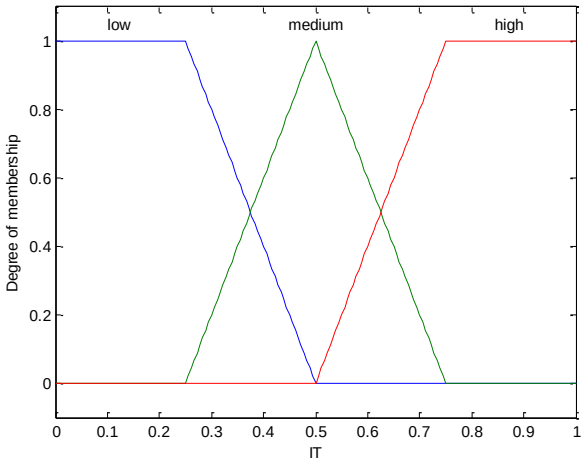


Fig. 1. Membership function for *IT*

Fbest represents the lowest value of fitness, since clustering is a minimization problem with the fitness function as mean square error, achieved till the current iteration. If the value of *Fbest* is high, then we need to reduce α to promote a greater exploration, since higher values for *Fbest* mean we are still far from the solution. However, if *Fbest* is low, we should increase α to allow for a higher exploitation as we are near the

International Journal of Engineering Applied Sciences and Technology, 2018
Vol. 3, Issue 2, ISSN No. 2455-2143, Pages 7-15
Published Online June 2018 in IJEAST (http://www.ijeast.com)

solution. Fig. 2 shows the membership function for *Fbest*. Note that the membership function for *Fbest* needs to be tuned as per the input dataset being considered, since the acceptable values of fitness function will vary for different datasets.

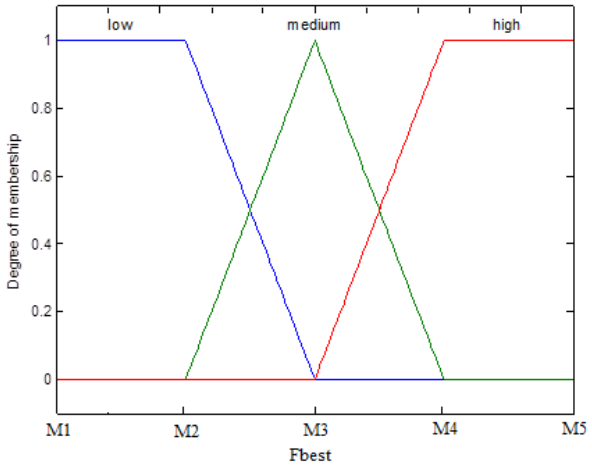


Fig. 2. Membership function for *Fbest*

To obtain the marked value M5 in Fig. 2, we executed five independent runs of GSA for a single iteration and equated M5 to the maximum value of *Fbest* obtained, after adding hundred and then rounding it off to the nearest hundred. For the value of M3, we considered the integer part of the best fitness value obtained using GSA (Hatamlou et al. 2011), for that dataset. M4 was computed by adding one to the value of M3, and M2 was calculated by rounding off M3 to the nearest ten smaller than M3. Finally, M1 was obtained by subtracting ten from M2.

It should be noted that the fitness function, representing the total mean square error or the sum of intra-cluster distances, is computed using the following equation (Yang et al. 2010):

$$f(O,C) = \sum_{l=1}^{k} \sum_{O_i \in C_l} d(O_i, CC_l)^2 \tag{13}$$

where, CC_l represents the centroids of the cluster C_l, $d(O_i, CC_l)$ denotes the distance or dissimilarity between object O_i and cluster centroid CC_l. The most popular and widely used distance metric is the Euclidean distance, which we have used in this work. Euclidean distance between two objects X_i and X_j with d dimensions is calculated as:

$$d(X_i, X_j) = \sqrt{\sum_{p=1}^{d} (x_i^p - x_j^p)^2} \tag{14}$$

where, x_i^p denotes the value of p^{th} dimension for the object X_i and x_j^p denotes the value of pth dimension for the object X_j.

The developed FIS consists of one output variable, i.e. *alpha(t)*, which denotes the value of parameter α in Eq. (12). Fig. 3 shows the membership function for *alpha(t)*. The range of parameter α is taken as [0, 50] to provide a wide range of search on the value of *alpha(t)*.

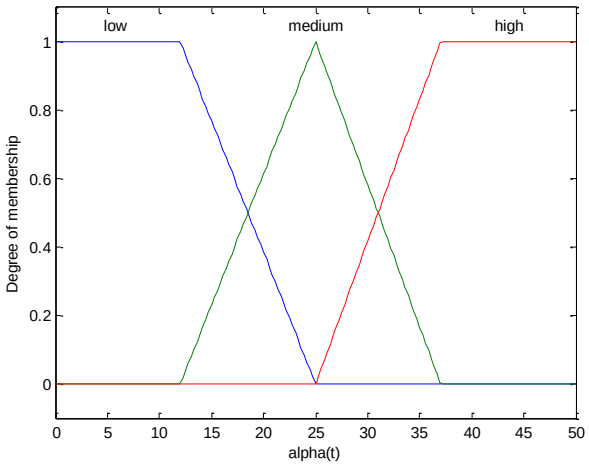


Fig. 3. Membership function for *alpha(t)*

The following eight fuzzy rules were formulated to control the parameter α in the calculation of the gravitational constant (Eq. (12)):

i. If (*IT* is low) and (*Fbest* is low) then (*alpha(t)* is high)
ii. If (*IT* is low) and (*Fbest* is medium) then (*alpha(t)* is medium)
iii. If (*IT* is low) and (*Fbest* is high) then (*alpha(t)* is low)
iv. If (*IT* is medium) and (*Fbest* is high) then (*alpha(t)* is low)
v. If (*IT* is medium) and (*Fbest* is medium) then (*alpha(t)* is medium)
vi. If (*IT* is high) and (*Fbest* is high) then (*alpha(t)* is medium)
vii. If (*IT* is high) and (*Fbest* is medium) then (*alpha(t)* is medium)
viii. If (*IT* is high) and (*Fbest* is low) then (*alpha(t)* is high)

The discussed fuzzy inference system is developed using Mamdani's method, in which the operator for "And" is min and "Or" is max. The implication method is min, aggregation method is max and defuzzification method is centroid.

International Journal of Engineering Applied Sciences and Technology, 2018
Vol. 3, Issue 2, ISSN No. 2455-2143, Pages 7-15
Published Online June 2018 in IJEAST (http://www.ijeast.com)

B. Proposed algorithm –

The proposed algorithm, Fuzzy-GSA, comprises of two steps. The first step is to generate an initial population for GSA. We have generated the initial population by considering three agents (or candidate solutions) corresponding to the maximum, minimum and median values for all features in a given dataset, respectively. This provides a better initial population, which would allow for a higher exploration since a wide range of values, including maximum, minimum and median, are present while searching the solution space. The rest of the agents are generated randomly by considering the range of features in the given dataset.

The second step involves application of GSA, described in Section II, to the given dataset and using the fuzzy inference system developed to control the parameter α while searching for the solution. The flow diagram for the proposed Fuzzy-GSA algorithm is depicted by Fig. 4.

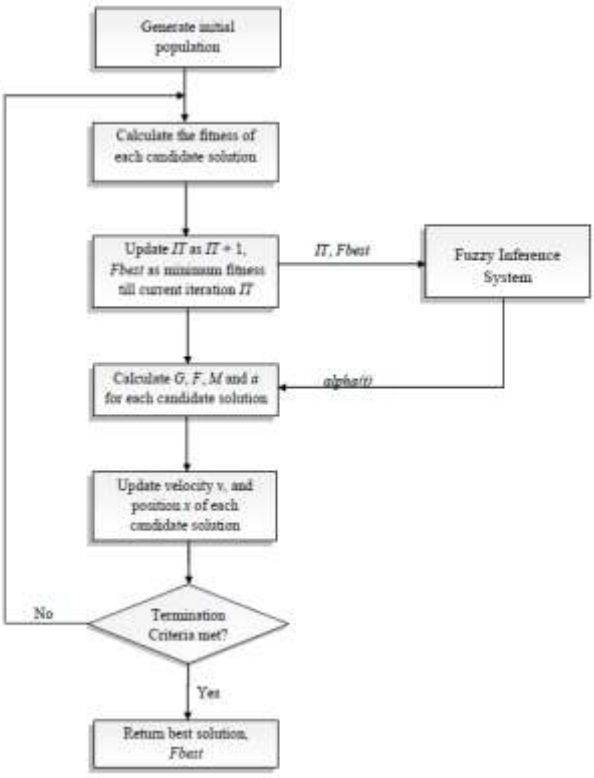


Fig. 4. Flow diagram for the proposed Fuzzy-GSA clustering algorithm

The step-by-step algorithm for the proposed Fuzzy-GSA clustering is stated next. Let N denote the population size, C_i be the i^{th} candidate solution or agent, k be the number of clusters, d be the number of features in a given dataset.

Step 1: Generate initial population, $P = \{C_1, C_2, \ldots, C_N\}$.

- Generate C_1 consisting of maximum values of all the features.
- Generate C_2 consisting of minimum values of all the features.
- Generate C_3 consisting of median values of all the features.
- Generate the remaining N-3 candidates randomly within the range of minimum to maximum values for all features.

Step 2: Apply GSA and use the developed FIS, described in Section III–A, for parameter adaptation.

- Calculate the fitness function, as per Eq. (13), for all the candidate solutions.
- Feed the values of *IT*, current iteration number, and *Fbest*, best fitness achieved, as inputs to the developed FIS, and obtain the value of parameter α.
- Calculate G, F, M and a for all the candidate solutions using Eqs. (5), (8), (9) and (12), respectively.
- Update the velocity and position of each candidate solution as per Eq. (10) and (11) respectively.
- Check if termination criteria, i.e. maximum number of iterations allowed is reached or fitness function is not exhibiting a minimum improvement, are met. If yes, then return the best value of fitness function achieved as the final solution, else reiterate through step 2.

The final solution consists of the best value of fitness function, i.e. the minimum mean square error, achieved by running the proposed Fuzzy-GSA algorithm.

IV. Results and Discussion

The proposed Fuzzy-GSA algorithm for clustering is implemented in MATLAB R2014b. Each candidate solution, in the population, consists of cluster centers for each of the k clusters, and each cluster center comprises of values for each feature in a dataset. Fig. 5 illustrates the representation of the i^{th} candidate solution C_i. CC_{ij} denotes the j^{th} cluster center of the i^{th} candidate solution and F_{ij} represents the value of j^{th} feature for i^{th} cluster center. Therefore, each candidate solution consists of $(d \times k)$ values. The design parameters used in numerical computations have been defined in Table 1.

The performance of the proposed approach, Fuzzy-GSA, has been measured by calculating the sum of intra-cluster distances as defined by Eq. (13) by considering four benchmark datasets namely, Iris, Wine, Breast Cancer Wisconsin and Contraceptive Method Choice (CMC) for

International Journal of Engineering Applied Sciences and Technology, 2018
Vol. 3, Issue 2, ISSN No. 2455-2143, Pages 7-15
Published Online June 2018 in IJEAST (http://www.ijeast.com)



evaluation. The selected datasets for evaluation have been obtained from UC Irvine repository of machine learning databases (Blake and Merz 2016), and are the benchmark datasets used by many researchers to validate the performance of clustering algorithms.

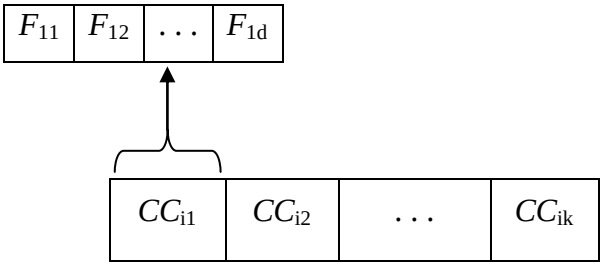


Fig. 5. Representation of i^{th} Candidate Solution, C_i

Table -1 Design parameters used in the proposed Fuzzy-GSA clustering algorithm

Parameters	**Value**
N (population size)	50
maximum number of iterations	300
G_o	100
minimum acceptable improvement	1×10^{-6}

A description of each benchmark dataset is provided below:

- *Iris Dataset*: It consists of three classes with 50 instances each, where each class refers to a species of iris flower. There are four features in the dataset namely, petal length, petal width, sepal length and sepal width which report certain characteristics of iris flower. The dataset comprises of a total of 150 instances. There no missing feature values in this dataset.

- *Wine Dataset*: It consists of three classes representing different types of wine. The data is a result of a chemical analysis of wines grown in the same region in Italy but derived from three different cultivators. There are 13 features which represent quantities of different constituents found in each of the three types of wines. The dataset consists of 178 instances with no missing values.

- *Breast Cancer Wisconsin Dataset*: This dataset comprises of two classes namely, malignant and benign representing the severity of cancer. There are a total of 683 instances, without missing values. It has 9 attributes or features namely, clump thickness, uniformity of cell size, uniformity of cell shape, marginal adhesion, single epithelial cell size, bare nuclei, bland chromatin, normal nucleoli and mitoses.

- *Contraceptive Method Choice (CMC) Dataset*: It consists of three classes namely, no-use, long-term and short-term. There are 1473 instances in this dataset, without any missing values. It contains 9 features or attributes namely, wife's age, wife's education, husband's education, number of children ever born, wife's religion, whether wife's working, husband's occupation, standard of living and media exposure.

Sum of intra-cluster distances has been calculated over each of the four benchmark datasets considered, using Eq. (13). Further, the performance of the proposed Fuzzy-GSA algorithm has been compared with existing clustering algorithms such as conventional GSA (Hatamlou et al. 2011), combined k-means and GSA (Hatamlou et al. 2012), PSO (Ching-Yi and Fun 2004) and k-means (MacQueen 1967) algorithms on selected datasets. Due to the stochastic nature of these algorithms, 20 independent runs for each algorithm over each dataset have been considered. The results are then compared in terms of best, average and worst solutions over 20 independent simulations. Moreover, the standard deviation of the achieved solutions through each clustering algorithm is calculated. It should be noted that, a lower value of the sum of intra-cluster distances denotes a higher quality clustering.

Fig. 6 illustrates the three clusters assigned by the proposed Fuzzy-GSA algorithm over the Iris dataset. It shows a 3-D plot considering the three dimensions namely, petal length, sepal width and sepal length of the Iris dataset. The remaining dimension, petal width, is highly correlated with the dimension, petal length, and thus, can be ignored without losing the quality of cluster representation. The three clusters, corresponding to the three types of iris flower, are depicted by three different colour coded symbols namely, blue squares, green circles and red triangles. The X-axis represents the dimension sepal length, the Y-axis represents the dimension sepal width and the Z-axis represents the dimension petal length. The respective cluster centers are represented by black coloured circles.

The best, average, worst and standard deviation of the obtained solutions over 20 independent simulations by different clustering algorithms on the selected datasets are shown in Table 2.

International Journal of Engineering Applied Sciences and Technology, 2018
Vol. 3, Issue 2, ISSN No. 2455-2143, Pages 7-15
Published Online June 2018 in IJEAST (http://www.ijeast.com)

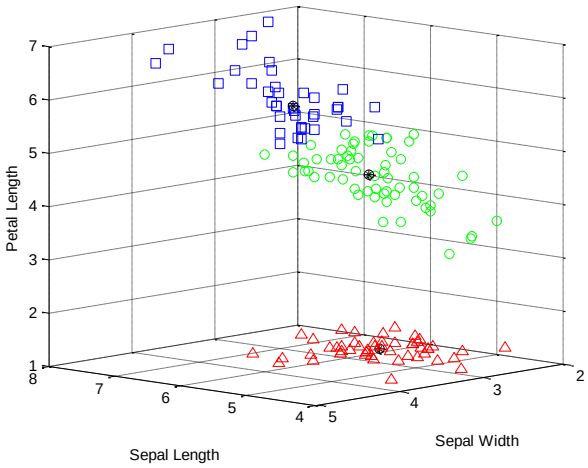


Fig. 6. Cluster plot by Fuzzy-GSA algorithm over Iris Dataset

As can be seen from Table 2, the proposed algorithm, Fuzzy-GSA, demonstrates the highest quality solutions in terms of best, average and worst intra-cluster distances over all the four benchmark datasets. Furthermore, the standard deviation of Fuzzy-GSA is lower, which indicates that it can locate a near-optimal solution in most of the cases when compared with other clustering algorithms.

For Iris dataset, the best, average and worst solutions by the proposed Fuzzy-GSA algorithm are 96.5403, 96.5425 and 96.5581, respectively with a standard deviation of 0.0054. For Wine dataset, the best, average and worst solutions achieved by the Fuzzy-GSA algorithm are 16292.23, 16293.369 and 16294.35 respectively, with a standard deviation of 0.82. For Breast Cancer Wisconsin dataset, the achieved best, average and worst solutions are 2964.38, 2964.38 and 2964.39, respectively with a standard deviation of 0.003. Lastly, for CMC dataset, the best, average and worst solutions obtained by Fuzzy-GSA algorithm are 5532.2, 5532.6 and 5533.7, respectively with a standard deviation of 0.5831.

To summarize, the proposed Fuzzy-GSA algorithm achieves the best quality clustering when compared with several popular clustering algorithms, depicted in Table 2, over four benchmark datasets considering 20 independent runs.

Table -2 Simulation Results for different clustering algorithms over 20 independent simulations

Dataset	Criteria	K-means	PSO	GSA	GSA-KM	Fuzzy-GSA
Iris	Best	97.2046	96.7170	96.6700	96.6173	96.5403
	Avg	101.2562	97.8962	96.6952	96.6687	96.5425
	Worst	124.2155	99.7773	96.8961	96.6989	96.5581
	Std	9.8954	0.9306	0.0485	0.0227	0.0054
Wine	Best	16555.6794	16340.1288	16319.0752	16300.0862	16292.23
	Avg	16990.4711	16378.4879	16351.3308	16301.6686	16293.369
	Worst	18294.8465	16505.4147	16481.6366	16302.5723	16294.35
	Std	772.6452	44.7783	34.3939	0.6280	0.8200
Cancer	Best	2988.4278	2974.6453	2965.1822	2965.0778	2964.38
	Avg	2988.4278	3078.4729	2975.0247	2965.6777	2964.38
	Worst	2988.4278	3336.6453	2997.7815	2966.7573	2964.39
	Std	0	113.8010	8.8999	0.4191	0.003
CMC	Best	5543.5119	5710.8682	5544.6439	5543.5119	5532.2
	Avg	5543.7652	5840.8038	5627.3252	5544.5250	5532.6
	Worst	5545.2005	5987.0105	5697.1460	5545.2005	5533.7
	Std	0.6186	82.3954	48.8495	0.8487	0.5831



V. CONCLUSIONS

This paper proposes an algorithm, *Fuzzy-GSA*, for clustering. *Fuzzy-GSA* algorithm is based on the conventional Gravitational Search Algorithm (GSA) with a provision for adapting the value of parameter α used in the calculation of the gravitational constant. In the beginning, a smaller value of α is desired to achieve a higher exploration, whereas towards the end of search, a relatively higher value of α helps in achieving a higher exploitation. *Fuzzy-GSA* algorithm incorporates Fuzzy Inference System (FIS) into the conventional GSA to allow for parameter adaptation. The parameter α is controlled by using eight formulated fuzzy inference rules, in *Fuzzy-GSA*. Also, *Fuzzy-GSA* algorithm generates a better quality initial population for GSA by considering the nature of dataset being considered. It generates three candidate solutions consisting of maximum, minimum and median values, respectively in a dataset thereby building an initial population, which covers a wider range. This helps in achieving a higher exploration. The performance of *Fuzzy-GSA* is evaluated by comparing its best, average and worst solutions with several other clustering algorithms over four selected benchmark datasets namely, Iris, Wine, Breast Cancer Wisconsin and CMC, considering 20 independent runs. The results show that *Fuzzy-GSA* achieves the highest quality clustering with very small standard deviation, when compared with several other clustering algorithms.

VI. REFERENCES

Al-Sultan K.S. (1995) A tabu search approach to the clustering problem, Pattern Recognition, vol. 28, issue 9, pp. 1443–1451.

Blake C.L., Merz C.J. (2016) UCI repository of machine learning databases. Available from: http://www.ics.uci.edu/-mlearn/MLRepository.html. Accessed 20 June 2016.

Ching-Yi C., Fun Y. (2004) Particle swarm optimization algorithm and its application to clustering analysis, in IEEE International Conference on Networking, Sensing and Control.

Fathian M., Amiri B., Maroosi A. (2007) Application of honey-bee mating optimization algorithm on clustering, Applied Mathematics and Computation, vol. 190, issue 2, pp. 1502–1513.

Forgy E.W. (1965) Cluster analysis of multivariate data: efficiency versus interpret- ability of classifications, Biometrics, vol. 21, issue 2.

Hatamlou A., Abdullah S., Nezamabadi-pour H. (2011) Application of gravitational search algorithm on data clustering, Rough Sets and Knowledge Technology, Springer, pp. 337–346.

Hatamlou A., Abdullah S., Nezamabadi-pour H. (2012) A combined approach for clustering based on K-means and gravitational search algorithms, Swarm and Evolutionary Computation, vol. 6, pp. 47–52.

Jain A.K. (2010) Data clustering: 50 years beyond K-means, Pattern Recognition Letters, vol. 31, issue 8, pp. 651–666.

Jardine N., Rijsbergen C.J. van (1971) The use of hierarchic clustering in information retrieval, Information Storage and Retrieval, vol. 7, issue 5, pp. 217–240.

Kaufman L., Rousseeuw P.J. (1990) Finding Groups in Data: An Introduction to Cluster Analysis, John Wiley & Sons, New York.

Kerr G., Ruskin H.J., Crane M., Doolan P. (2008) Techniques for clustering gene expression data, Computers in Biology and Medicine, vol. 38, issue 3, pp. 283–293.

Liao L., Lin T., Li B., (2008) MRI brain image segmentation and bias field correction based on fast spatially constrained kernel clustering approach, Pattern Recognition Letters, vol. 29, issue 10, pp. 1580–1588.

MacQueen J. (1967) Some methods for classification and analysis of multivariate observations, In Proceedings of the Fifth Berkeley Symposium on Mathematical Statistics and Probability, vol. 1, pp. 281-297.

Maulik U., Bandyopadhyay S. (2000) Genetic algorithm-based clustering technique, Pattern Recognition, vol. 33, issue 9, pp. 1455–1465.

Rashedi E., Nezamabadi-pour H., Saryazdi S. (2009) GSA: a gravitational search algorithm, Information Sciences, vol. 179, issue 13, pp. 2232–2248.

Saglam B., Türkay M., Salman F.S., Sayın S., Karaesmen F., Örmeci E.L. (2006) A mixed-integer programming approach to the clustering problem with an application in customer segmentation, European Journal of Operational Research, vol. 173, issue 3, pp. 866–879.

Selim S.Z., Alsultan K. (1991) A simulated annealing algorithm for the clustering problem, Pattern Recognition, vol. 24, issue 10, pp. 1003–1008.

Shelokar P.S., Jayaraman V.K., Kulkarni B.D. (2004) An ant colony approach for clustering, Analytica Chimica Acta, vol. 509, issue 2, pp. 187–195.

Sung C.S., Jin H.W. (2000) A tabu-search-based heuristic for clustering, Pattern Recognition, vol. 33, issue 5, pp. 849–858.

Tombros A., Villa R., Rijsbergen C.J. van (2002) The effectiveness of query-specific hierarchic clustering in



information retrieval, Information Processing & Management, vol. 38, issue 4, pp. 559–582.

Xia Y., Fenga D., Wangd T., Zhaob R., Zhangb Y. (2007) Image segmentation by clustering of spatial patterns, Pattern Recognition Letters, vol. 28, issue 12, pp. 1548–1555.

Yang S., Wu R., Wang M., Jiao L. (2010) Evolutionary clustering based vector quantization and SPIHT coding for image compression, Pattern Recognition Letters, vol. 31, issue 13, pp. 1773–1780.

This article has been accepted for publication in a future issue of this journal, but has not been fully edited. Content may change prior to final publication. Citation information: DOI 10.1109/TIA.2018.2867328, IEEE Transactions on Industry Applications

Implementation of Immune Feedback Control Algorithm for Distribution Static Compensator

Manoj Badoni, Alka Singh, *Senior Member*, *IEEE* and Bhim Singh, *Fellow*, *IEEE*

***Abstract*—This paper presents an immune feedback control algorithm for a three phase Distribution Static Compensator (DSTATCOM) to mitigate several power quality problems such as harmonics, reactive power and load unbalancing at distribution level. A configuration chosen for DSTATCOM is based on a three-phase voltage source converter (VSC), which is suitably controlled as a shunt compensator for performing these functions. The underlying principle of an immune feedback is based on adaptive control and the designed control estimates fundamental reference grid currents from nonlinear load currents. This control algorithm proposed for DSTATCOM, is validated for maintaining power factor to unity, load balancing and harmonics reduction of supply currents. An improved performance of immune feedback control is presented along with its comparison with conventional control algorithms such as d-q frame, normalized least mean square (NLMS) and other recently developed control algorithms such as leaky LMS, LLMF and synchronous extraction. Experimental results are obtained with the proposed control, which is tested on a prototype developed in the laboratory using a VSC. It is observed from simulation and experimental results that the proposed control algorithm of DSTATCOM is able to achieve mitigation of most of the power quality problems at the distribution level.**

Keywords—Power quality; power factor correction; PI controller; immune feedback principle, DSTATCOM

I. INTRODUCTION

Power engineers are concerned about the rapid increase in power quality (PQ) problems and solutions in the distribution level. Consumers even in developing nations are realizing the importance of good PQ and willing to spend extra cost. Several reasons account for PQ problems in distribution systems viz. an unprecedented increase in power electronics loads, which include converters, switch mode power supplies (SMPS), variable frequency drives, electric arc furnaces, computers etc. Common power quality problems include load unbalancing, voltage regulation, harmonics injection into the grid supply and poor power factor [1]. Guidelines for limiting harmonics and other power quality related problems are specified in IEEE-519 standard [2]. An improvement in quality of power is achieved using different custom power devices and one such recent shunt compensating device is a DSTATCOM (Distribution Static Compensator) [3]. It is used for mitigating power quality problems related to currents, such as reduction of harmonics in grid currents, reactive power compensation, balancing of unbalanced load at distribution level and it can be controlled in different operating modes.

An exhaustive literature review has shown a number of control techniques for the control of shunt compensator [4-19], which are used to estimate the fundamental component of grid reference currents and switching pulses for DSTATCOM. In past few decades, various conventional time domain control methods have been reported for example instantaneous reactive power theory (IRPT) [4], dq frame theory [5], symmetrical components-based modified technique [6], vector resonant controller [7], one-cycle control for three phase shunt compensator with unbalance source and load [8], model predictive control [9]. Several new and promising techniques are also popular viz. unified adaptive linear neuron based control [10], adaptive synchronous extraction [11], normalized least mean square (NLMS) [12-14], recursive least square [15], dual-tree complex wavelet transform [16], predictive current control [17], neural network control [18], and adaptive neuro-fuzzy inference based control [19]. These techniques differ on the basis of complexity, tracking performance, stability and ease of implementation.

Kawafuku et. al. [20] have reported a control algorithm based on biological immune system. The structure of immune feedback system consists of various cells and these have to function in a manner that neutralizes the attack of antigens or foreign invaders. The immune system is a highly evolved system just as the brain. Although neural networks based on working of brain are relatively common. The full potential of biological immune systems is not realized. Its working is based on activities of B-cell, helper and suppressor T-cells and how they work rapidly to respond to foreign particles while quickly stabilizing itself. Its properties of fast control, stabilization, learning and elimination, make it an ideal technique for adaptive control system. These features are helpful in optimization problems, abnormality detection and pattern recognition. However, due to complexity of immune system, such controls have received less attention. Still, some of these controls are successfully used in varied engineering applications [21]. Some of recent applications of immune feedback algorithm include the control of a single phase inverter [22] and a three phase inverter [23], where dead time elimination and space vector PWM control have been used. Simulation studies are reported on the application of immune based feedback principle for a single STATCOM for voltage control [24] as well as multiple STATCOM [25]. However, design, application and experimental implementation of an immune control for solving power quality problems are not reported in the literature.

An immune feedback based control, devised on the working of biological immune system of the human body resembles and works as an adaptive and self-corrective system [26]. In this work, the basic immune technique is utilized for designing a control to mitigate power quality problems. The attack of antigens can be viewed as analogous to the variations in the operating conditions in the system. The control

0093-9994 (c) 2018 IEEE. Personal use is permitted, but republication/redistribution requires IEEE permission. See http://www.ieee.org/publications_standards/publications/rights/index.html for more information.

This article has been accepted for publication in a future issue of this journal, but has not been fully edited. Content may change prior to final publication. Citation information: DOI 10.1109/TIA.2018.2867328, IEEE Transactions on Industry Applications

algorithm is designed to work in two different modes i.e. improvement of power factor for grid currents to unity and regulating AC terminal voltage and to provide load compensation, appropriately. Simulation and test results with the proposed algorithm, demonstrate the unique features of learning, memory and anomaly recognition associated with this algorithm. Performance of proposed control is compared with already reported control algorithms for DSTATCOM such as normalized least mean square (NLMS), dq frame, leaky LMS [27], leaky least mean fourth (LLMF) [28], and adaptive synchronous extraction. The application of this algorithm for shunt compensation is innovative and has not been reported in the literature till date. This also opens a new opportunity to use biologically inspired algorithms on real systems.

II. System Configuration

A block diagram of a three phase DSTATCOM is shown in Fig. 1. A three-phase AC mains with grid impedance, shown using series R_s-L_s branch, feeds a three phase load. The DSTATCOM is designed using a three-phase VSC with a DC bus capacitor at DC side. Passive filters comprising series connected capacitive (C_f) and resistive (R_f) elements at the PCC, are used to suppress switching noise produced by IGBTs (Insulated Gate Bipolar Transistors). This noise contains high frequency components. A nonlinear load is represented in form of a three-phase diode bridge rectifier. A scaled down prototype is implemented in the laboratory and the immune feedback based control is verified under a variety of load changes. Design specifications for simulation and hardware implementation are given in Appendix-A and B.

III. Mathematical Formulation of Control Algorithm

Fig. 2 shows a block diagram of the immune feedback based control algorithm, which is based on the functions of biological immune system of human body and works as an adaptive and self-corrective system. The mathematical expressions related to the immune feedback based control algorithm are given in this section and categorized further in into three sub-sections. The purpose of using the immune feedback principle is to extract the weighted values of the load currents, which correspond to fundamental positive sequence value. The estimation of reference currents is discussed next section followed by the use of PWM (Pulse Width Modulation) current controller for generation of gating pulses.

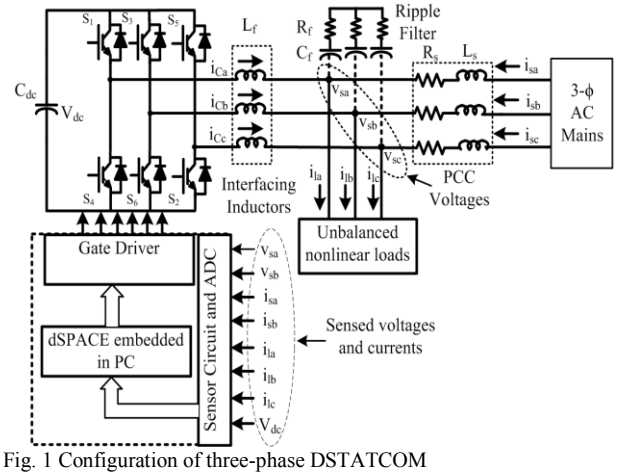


Fig. 1 Configuration of three-phase DSTATCOM

A. Mathematical Approach for Estimation of Weighted Values Using Immune Feedback Algorithm

The peak of PCC (Point of Common Coupling) voltages, is calculated by using 3-phase voltages (v_{sa}, v_{sb}, v_{sc}) as,

$$V_t = \sqrt{2(v_{sa}^2 + v_{sb}^2 + v_{sc}^2)/3} \quad (1)$$

This magnitude (V_t) is used to compute unit inphase and quadrature vectors, which are used to estimate active and reactive components of reference supply currents. In-phase unit vectors of PCC voltages, u_{pa}, u_{pb} and u_{pc} are calculated as follows,

$$u_{pa} = v_{sa}/V_t;\ u_{pb} = v_{sb}/V_t \text{ and } u_{pc} = v_{sc}/V_t \quad (2)$$

These unit inphase vectors are also utilized in the computation of updated active weighted value of reference currents.

The incremental weight based on immune feedback principle at $(n+1)^{th}$ sampling moment is expressed as,

$$\Delta w(n+1) = \eta[1 - \gamma\{\Delta w(n) - \Delta w(n-1)\}^2]\frac{\delta J(n)}{\delta w(n)} + \alpha\Delta w(n) \quad (3)$$

where α is multiplication factor of the foreign materials, parameter η (learning rate) controls the response speed, parameter γ (stabilization factor) controls the stabilization effect and $J(n)$ is the cost function to be minimized and expressed as,

$$J(n) = \frac{1}{2}e(n)^2 \quad (4)$$

Here in (4), $e(n)$ is the error between the sensed value of load current (i_l) and estimated value of current (i_e), is given as,

$$e(n) = i_l - i_e \quad (5)$$

The estimated current is computed using weight vector w^T=[w_p, w_q…] and input vector $x(n)$=[u_p, u_q…], where weight w_p corresponds to the fundamental active component and w_q, is the fundamental reactive weight value extracted from the load current. The parameter u_p, is unit in-phase template and u_q is unit quadrature template of PCC voltages. The estimated load current is product of weight vector (w) and input vector ($x(n)$) given as,

$$i_e = wx^T(n) \quad (6)$$

This weight update rule for immune feedback at $(n+1)^{th}$ sampling moment is stated as,

$$w(n+1) = w(n) + \Delta w(n+1) \quad (7)$$

Rewriting (7) by replacing value of $\Delta w(n+1)$ from (3) and stated at $(n+1)^{th}$ sampling moment as [20],

$$w(n+1) = w(n) + \eta[1 - \gamma\{\Delta w(n) - \Delta w(n-1)\}^2]\frac{\delta J(n)}{\delta w(n)} + \alpha\Delta w(n) \quad (8)$$

The partial differentiation $\frac{\delta J(n)}{\delta w(n)}$ is simplified by the differentiation using chain rule. According to this partial differentiation can be written as, $\frac{\delta J(n)}{\delta w(n)} = \frac{\delta J(n)}{\delta e(n)} \times \frac{\delta e(n)}{\delta w(n)}$.

0093-9994 (c) 2018 IEEE. Personal use is permitted, but republication/redistribution requires IEEE permission. See http://www.ieee.org/publications_standards/publications/rights/index.html for more information.

This article has been accepted for publication in a future issue of this journal, but has not been fully edited. Content may change prior to final publication. Citation information: DOI 10.1109/TIA.2018.2867328, IEEE Transactions on Industry Applications

Differentiation of $\frac{\delta J(n)}{\delta e(n)}$ and $\frac{\delta e(n)}{\delta w(n)}$ give estimated error (*e(n)*) and input vector (*x(n)*) respectively. Therefore, partial differentiation $\frac{\delta J(n)}{\delta w(n)}$ is written in terms of product of estimated error (*e(n)*) and input vector (*x(n)*). Apart from it, weight update equation shows negative learning action if $1>\gamma\{\Delta w(n)-\Delta w(n-1)\}^2>0$ and positive learning action if $1<\gamma\{\Delta w(n)-\Delta w(n-1)\}^2$ and the system is kept stable by choosing appropriate value of learning rate.

The weight updation given in (8), is modified for weighted values corresponding to active power components (w_{lpa}, w_{lpb} and w_{lpc}) of load currents and are given as follows,

$$w_{lpa} = w_{pa} + \eta\left[1-\gamma\{\Delta w_{pa}-\Delta w_{pa}'\}^2\right]e_a u_{pa} + \alpha\Delta w_{pa} \quad (9)$$

$$w_{lpb} = w_{pb} + \eta\left[1-\gamma\{\Delta w_{pb}-\Delta w_{pb}'\}^2\right]e_b u_{pb} + \alpha\Delta w_{pb} \quad (10)$$

$$w_{lpc} = w_{pc} + \eta\left[1-\gamma\{\Delta w_{pc}-\Delta w_{pc}'\}^2\right]e_c u_{pc} + \alpha\Delta w_{pc} \quad (11)$$

The unit quadrature vectors u_{qa}, u_{qb} and u_{qc} are computed from in-phase templates as follows [1],

$$u_{qa} = -u_{pb}/\sqrt{3} + u_{pc}/\sqrt{3} \quad (12)$$

$$u_{qb} = \sqrt{3}\,u_{pa}/2 + (u_{pb}-u_{pc})/2\sqrt{3} \quad (13)$$

$$u_{qc} = -\sqrt{3}\,u_{pa}/2 + (u_{pb}-u_{pc})/2\sqrt{3} \quad (14)$$

These unit quadrature vectors are utilized in computations of reactive weighted values of load currents. The weight update given in (8), is modified for weighted values corresponding to reactive power components (w_{lqa}, w_{lqb} and w_{lqc}) of load currents and are given as,

$$w_{lqa} = w_{qa} + \eta\left[1-\gamma\{\Delta w_{qa}-\Delta w_{qa}'\}^2\right]e_a u_{qa} + \alpha\Delta w_{qa} \quad (15)$$

$$w_{lqb} = w_{qb} + \eta\left[1-\gamma\{\Delta w_{qb}-\Delta w_{qb}'\}^2\right]e_b u_{qb} + \alpha\Delta w_{qb} \quad (16)$$

$$w_{lqc} = w_{qc} + \eta\left[1-\gamma\{\Delta w_{qc}-\Delta w_{qc}'\}^2\right]e_c u_{qc} + \alpha\Delta w_{qc} \quad (17)$$

The average active (w_{lp}) and reactive (w_{lq}) weights are as,

$$w_{lp} = \frac{w_{lpa}+w_{lpb}+w_{lpc}}{3} \quad (18)$$

$$w_{lq} = \frac{w_{lqa}+w_{lqb}+w_{lqc}}{3} \quad (19)$$

The average weight values are used to estimate reference active and reactive weighted values, which is discussed in the next sub section.

B. Estimation of Reference Grid Currents

The DC voltage error (v_{de}) is generated by comparing the sensed voltage at DC bus (V_{dc}) with the reference value (V_{dc}^*). The voltage at DC bus (V_{dc}) is regulated to its reference magnitude by passing error value (v_{de}) to the proportional integral (PI) controller. This control provides an output value which is estimated to be component, w_{pdc}. This component is given at n^{th} sampling instant as,

$$w_{pdc}(n) = w_{pdc}(n-1) + k_{pd}\big(v_{de}(n)-v_{de}(n-1)\big) + k_{id}\big(v_{de}(n)\big) \quad (20)$$

This equation is an expression of PI controller, which is used to regulate voltage at DC bus. Here in (20), parameter w_{pdc} denotes the output of PI controller, k_{pd} is proportional and k_{id} is integral gains. The reference active power weight is calculated by adding w_{lp} and w_{pdc} and is given as,

$$w_p = w_{lp} + w_{pdc} \quad (21)$$

Reference active grid currents (i_{pa}^*, i_{pb}^* and i_{pc}^*) representing three phase components are calculated using inphase unit templates (u_{pa}, u_{pb} and u_{pc}) and reference weight (w_p) as,

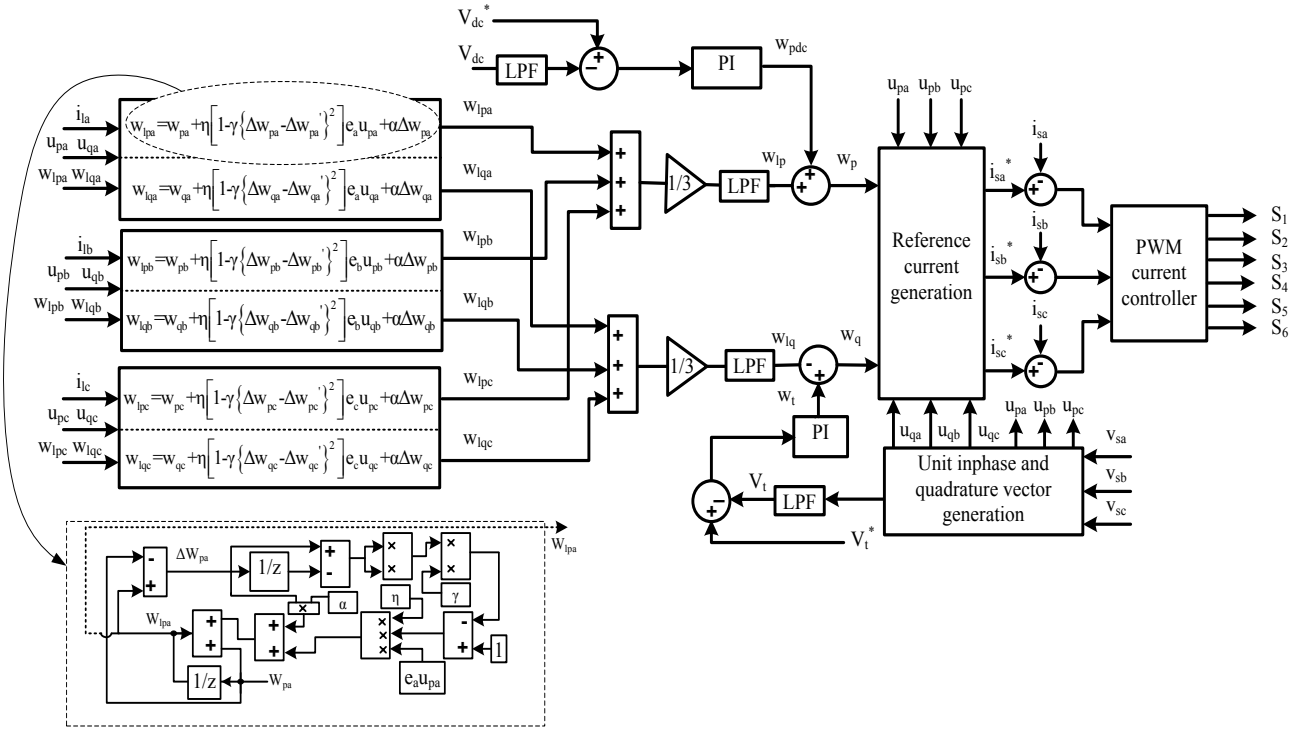


Fig. 2 Block diagram of immune feedback based control algorithm for shunt compensator

0093-9994 (c) 2018 IEEE. Personal use is permitted, but republication/redistribution requires IEEE permission. See http://www.ieee.org/publications_standards/publications/rights/index.html for more information.

This article has been accepted for publication in a future issue of this journal, but has not been fully edited. Content may change prior to final publication. Citation information: DOI 10.1109/TIA.2018.2867328, IEEE Transactions on Industry Applications

$$i_{pa}^{*} = w_p u_{pa}, i_{pb}^{*} = w_p u_{pb} \text{ and } i_{pc}^{*} = w_p u_{pc} \quad (22)$$

These reference active grid currents given in (22) are used to estimate total grid currents.

The PCC voltage magnitude (V_t) is calculated by using (1) and compared with reference PCC voltage (V_t^*), thus the error generated (V_{te}) is passed through a second PI controller to set PCC voltage magnitude at reference value. The output of PCC voltage at n^{th} sampling instant is given as,

$$w_t(n) = w_t(n-1) + k_{pq}\big(V_{te}(n) - V_{te}(n-1)\big) + k_{iq}\big(V_{te}(n)\big) \quad (23)$$

This equation is an expression for a second PI controller used in control algorithm, which is used to regulate voltage at PCC. Here in (23), parameters w_t, k_{pq} and k_{iq} denote PI controller output, its proportional gain and integral gain.

The reference reactive weight (w_q) corresponding to load current, is computed using the average reactive weight (w_{lq}) and the output of second PI controller on AC bus, which gives an estimated output (w_t). This weight w_q, is calculated as follows,

$$w_q = w_t - w_{lq} \quad (24)$$

The reactive reference currents (i_{qa}^*, i_{qb}^* and i_{qc}^*) are computed from the unit quadrature templates (u_{qa}, u_{qb} and u_{qc}), given in (12), (13) and (14), and reference reactive power weight (w_q) as,

$$i_{qa}^{*} = w_q u_{qa}, i_{qb}^{*} = w_q u_{qb} \text{ and } i_{qc}^{*} = w_q u_{qc} \quad (25)$$

Currents computed using (22) and (25) are used to estimate total reference grid currents, which is explained in the next sub section.

C. *Generation of Switching Pulses*

The estimated reference active and reference reactive components of currents given in (22) and (25) are added to estimate reference grid currents. The addition of these current components is given as,

$$i_{sa}^{*} = i_{pa}^{*} + i_{qa}^{*} \quad (26)$$

$$i_{sb}^{*} = i_{pb}^{*} + i_{qb}^{*} \quad (27)$$

$$i_{sc}^{*} = i_{pc}^{*} + i_{qc}^{*} \quad (28)$$

The sensed grid currents (i_{sa}, i_{sb} and i_{sc}) are sensed by the currents sensors and compared with estimated reference currents (i_{sa}^*, i_{sb}^* and i_{sc}^*).Thus, the current errors (i_{sae}, i_{sbe} and i_{sce}) are generated. After the generation of these error signals; these are processed through PWM current controller to produce six switching pulses for six IGBTs switches of VSC.

IV. Simulation Results

The simulation model of the proposed system is developed in MATLAB using the Simulink and Sim Power System (SPS) tool boxes. The behavior of DSTATCOM with the immune feedback principle based control method is verified for power factor correction (PFC) and voltage regulation modes under dynamic load conditions.

A. *Steady State and Dynamic Behavior of DSTATCOM in PFC Mode*

The behavior of a shunt compensator in PFC mode is presented in Figs. 3(a) and (b). These results depict waveforms of PCC voltages (v_s), grid currents (i_s), load currents (i_l), DSTATCOM currents (i_C) and DC bus voltage (V_{dc}). It is noticed from Figs. 3(a) and (b) that the system operates in steady state (before t=0.3s) and the value at DC bus voltage is maintained at reference voltage of 700V by the PI controller.

One phase (phase '*c*') of the load is now turned off (t=0.3s to t=0.4s) and it is noticed that the load currents become unequal and unbalanced. However, the grid currents still remain balanced due to the DSTATCOM action. It is observed from simulated results that under unbalanced load condition, the maximum overshoot, which occurs in DC bus voltage is around 25V. However, it is controlled to 700V (reference value) with a PI controller action within a couple of cycles. The in-phase relationship between the voltages at PCC and the corresponding grid currents is observed and thus power factor correction capability of DSTATCOM is achieved.

The harmonic spectra of grid current (i_{sa}) after compensation and load current (i_{la}) in PFC mode are depicted in Fig. 4. The values of THDs of grid current and load current are observed 2.15%, and 27.10%, respectively. It may be

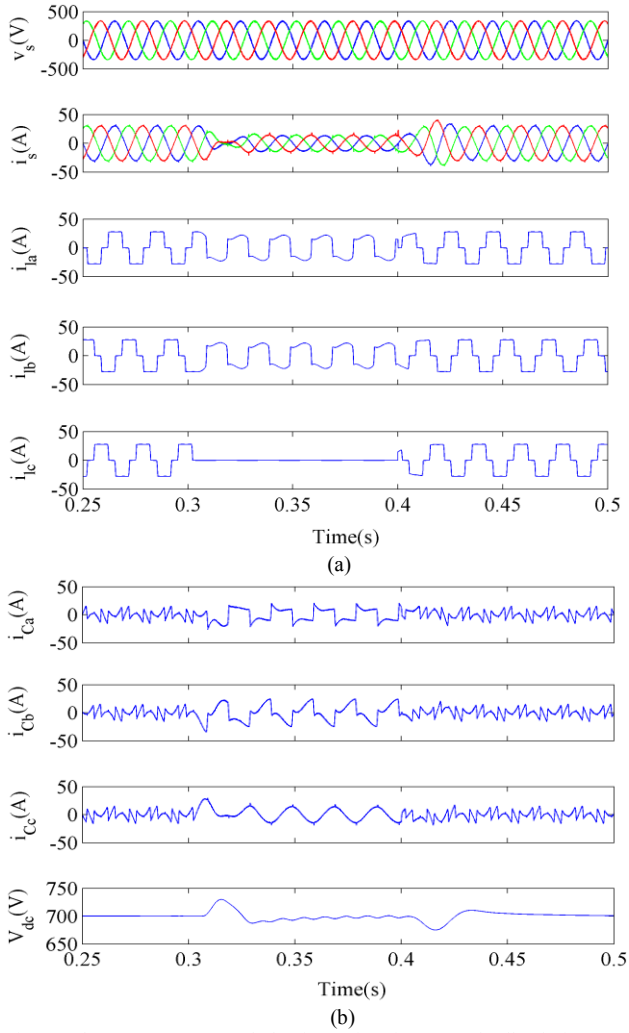
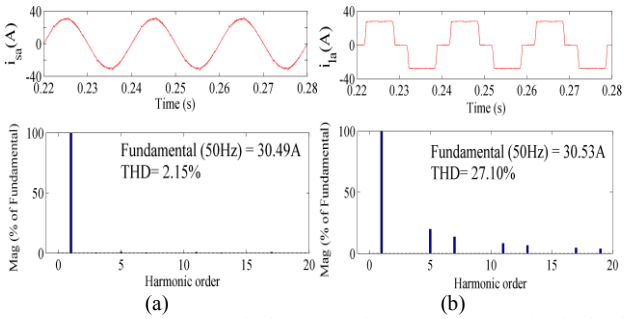


Fig. 3 Shunt compensator behavior using immune feedback in PFC mode

0093-9994 (c) 2018 IEEE. Personal use is permitted, but republication/redistribution requires IEEE permission. See http://www.ieee.org/publications_standards/publications/rights/index.html for more information.

This article has been accepted for publication in a future issue of this journal, but has not been fully edited. Content may change prior to final publication. Citation information: DOI 10.1109/TIA.2018.2867328, IEEE Transactions on Industry Applications



(a) (b)

Fig. 4 Harmonic spectra of phase 'a' of (a) grid current, i_{sa} (b) load current, i_{la} in PFC mode

inferred from these results that the harmonic distortion of i_{sa}, is less than a limit (<5%) imposed by international standard such as IEEE-519.

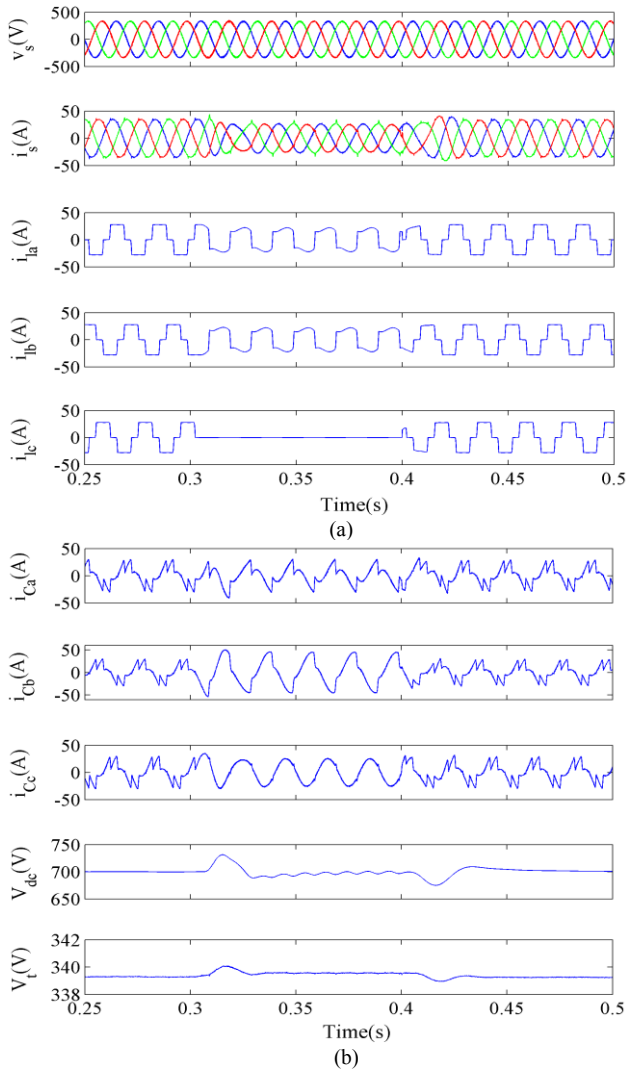
B. *DSTATCOM Performance in Voltage Regulation Mode Under Varying Loads*

The behavior of DSTATCOM is tested at nonlinear load to observe if the voltage is regulated at PCC using proposed control algorithm. The waveforms shown in Figs. 5(a) and (b) represent three-phase voltages at PCC (v_s), 3-phase grid currents (i_s), three-phase load currents (i_l), compensator currents (i_C), self-sustained DC bus voltage (V_{dc}) voltage at the VSC and PCC voltage magnitude (V_t). The system reaches the steady state condition and the voltage at DC bus, V_{dc} of the VSC and PCC voltage magnitude, V_t are regulated at 700V and 338.89 V, which is desired from the control algorithm. The load is changed at t=0.3s, when unbalancing is created in the load and phase 'c' of load is instantly thrown off from the system from t=0.3s till t=0.4s; thereby creating a dynamic load change in the system. However, the grid currents are still observed to be perfectly sinusoidal, having the same peak magnitude and 120° phase displaced from each other due to DSTATCOM operation. The action of the two PI controllers at the PCC voltage and DC bus voltage, regulates both of these voltages to 338.89V and 700V, respectively. Thus, the control algorithm based on an immune feedback adaptively extracts weights under different loading conditions including unbalanced load condition. The voltage regulation is achieved by the action of PI controller within a couple of cycles.

Fig. 6 shows the harmonic spectra of grid current (i_{sa}) after compensation and load current (i_{la}) in voltage regulation mode. Harmonic distortion in phase 'a' of grid current is observed to be 2.97% when the distortion in load current is 27.18%. Fig. 6 clearly highlights that phase 'a' of the grid current, after compensation is maintained sinusoidal and the distortion limits of i_{sa} from harmonics point of view, follow a limit of less than 5% specified by an IEEE-519 standard [2].

C. *Comparative Performance of Immune Feedback Control with NLMS and SRF Control Algorithms*

The critical evaluation of a developed immune feedback control algorithm is made and its performance is compared with NLMS and dq frame control algorithms. The basic mathematical weight update equation for the NLMS control is shown in Appendix-C. Fig. 7 shows a comparative performance of immune feedback and NLMS based control [12-14] developed for control of DSTATCOM.

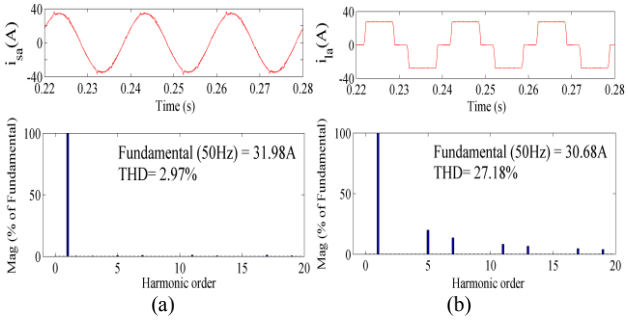


(a)

(b)

Fig. 5 Shunt compensator behavior with immune feedback based control algorithm in voltage regulation mode

A comparison is also presented in terms of speed of weight convergence, error between sensed and estimated load current, harmonics compensation in grid currents and computational time required for processing both the algorithms. Fig. 7(a) shows convergence of weight corresponding to phase 'a' of load current with immune feedback and NLMS control algorithms. These results present fast weight convergence with immune feedback control algorithm (steady state is obtained at



(a) (b)

Fig. 6 Harmonic spectra of Phase 'a' of (a) grid current, i_{sa} (b) load current, i_{la} in voltage regulation mode

0093-9994 (c) 2018 IEEE. Personal use is permitted, but republication/redistribution requires IEEE permission. See http://www.ieee.org/publications_standards/publications/rights/index.html for more information.

This article has been accepted for publication in a future issue of this journal, but has not been fully edited. Content may change prior to final publication. Citation information: DOI 10.1109/TIA.2018.2867328, IEEE Transactions on Industry Applications

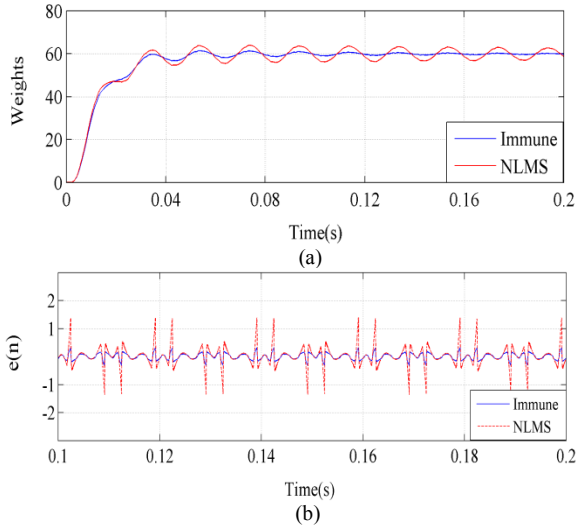


Fig. 7 Comparative performance of immune and NLMS controls in terms of (a) weight convergence (b) error signal

t=0.10s), whereas large sustained oscillations about the average value of weight, are observed with NLMS based control algorithm. Fig. 7(b) shows the error *e(n)* in estimation obtained with both the control algorithms. These results show low error, good tracking speed and fast response with the developed control. Figs. 8(a) and (b) present the harmonic spectrum of grid current (i_{sa}), obtained with NLMS and dq frame control algorithms. These control algorithms are able to achieve 3.33% and 2.75% THDs in grid current, whereas 2.15% THD is achieved with immune feedback based control algorithm (shown in Fig. 4). The control algorithm developed based on immune feedback technique, achieves improved harmonics compensation, fast weight convergence, offers reduced complexity and improved performance in terms of low error and small sampling time required for execution. Another advantage is that this algorithm is PLL-less as compared to dq frame control. The comparative performances of these three control algorithms are summarized in Table-I, which definitely indicates a superiority of proposed control.

D. Comparative Performance of Immune Feedback Control with Leaky LMS, LLMF and SRF Control Algorithms

Performance of immune feedback control is also compared with other adaptive techniques recently proposed in the literature [12-14]. These include leaky LMS, LLMF and synchronous extraction control algorithms. These algorithms viz. leaky LMS and LLMF contain leaky factor and cubic error signal in the weight updation equation, which increases the complexity. A proper selection of leaky factor is a major issue in leaky LMS and LLMF control, because higher value of this factor affects the biased problem and lower value increases Eigen spread [27]. Hence, their complexity is higher due to an immune feedback based control possess less as compared with leaky LMS and leaky LMF (LLMF). Moreover, these results show that the THDs of supply current obtained with leaky LMS and LLMF controls are obtained to be 3.6% and 2.5%, whereas a lower THD value of 2.3% is obtained with an immune feedback control. Another control algorithm reported is based on adaptive theory such as synchronous-extraction based control [11]. This algorithm possesses advantages similar to an immune feedback control. However, THD of supply current obtained with synchronous-extraction based control is 4.4%, which is higher than a THD of supply current obtained (2.3%) with proposed control algorithm. Table-II presents a comparative performance of above control algorithms for DSTATCOM.

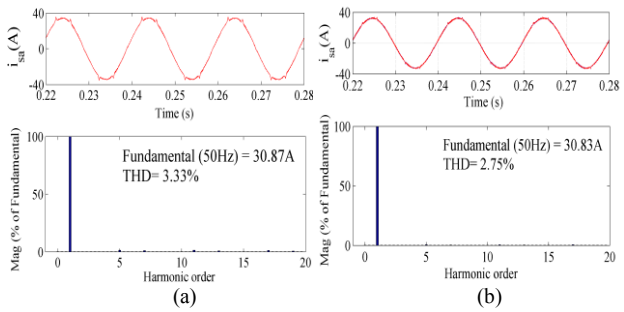


Fig. 8 Harmonic spectra of phase 'a' of grid current, i_{sa} (a) with NLMS and (b) with dq frame controllers in PFC mode

V. Experimental Results

A prototype of the DSTATCOM has been developed in the laboratory for testing the control algorithm. It consists of a three-phase VSC, interfacing inductors, three-phase bridge diode rectifier based three-phase nonlinear load. The control algorithm implementation is performed using DSP (Digital Signal Processor-dSPACE1104) where eight ADC channels are used. The experimental prototype uses Hall Effect voltage (LEM LV-25) and current sensors (LEM LA-25). Test results

TABLE I
COMPARATIVE PERFORMANCE OF IMMUNE FEEDBACK WITH NLMS AND DQ FRAME BASED CONTROL

Features		Immune Feedback	NLMS	dq frame
Modeling		Few mathematical operations are required	Complex require more mathematical operations	Complex-Required Phase lock loop (PLL)
Weight convergence		Fast (steady state at t=0.1s)	Sustained oscillations	NA
Error, *e(n)*		Small	Large	NA
Harmonic compensation	Grid current THD, i_{sa}	30.49A, 2.15%	30.87A, 3.33%	30.83A, 2.75%
	Load current THD, i_{la}	30.53A, 27.10%	30.53A, 27.10%	30.63A, 27.17%
Sampling Time (T_s)		60µs	75µs	60 µs

TABLE II
COMPARATIVE PERFORMANCE OF IMMUNE FEEDBACK WITH LEAKY LMS, LLMF AND SYNCHRONOUS EXTRACTION

Features	Immune Feedback	Leaky LMS	LLMF	Synchronous extraction
Type of Control	Adaptive	Adaptive	Adaptive	Adaptive
Weight convergence	Fast	Slow	Fast	Fast
Static Error	Less	More	Less	Less
Computation	Less	More	More	More
%Harmonics in grid current, i_{sa}	2.3%	3.6%	2.5%	4.4%

0093-9994 (c) 2018 IEEE. Personal use is permitted, but republication/redistribution requires IEEE permission. See http://www.ieee.org/publications_standards/publications/rights/index.html for more information.

This article has been accepted for publication in a future issue of this journal, but has not been fully edited. Content may change prior to final publication. Citation information: DOI 10.1109/TIA.2018.2867328, IEEE Transactions on Industry Applications

have been obtained under a variety of loading conditions and are recorded using standard meters available in the laboratory.

A. Behavior of Immune Feedback Controller for Shunt Compensator

Fig. 9 shows performance of proposed control algorithm in PFC mode at nonlinear load. Fig. 9(a) shows waveforms of phase 'a' of PCC voltage (v_{sa}), its filtered value (v_{saf}), in-phase unit template (u_{pa}) and load current (i_{la}). Fig. 9(b) shows waveforms of sensed DC bus voltage (V_{dc}), filtered DC bus voltage (V_{dcf}), error signal (V_{de}) between reference DC bus and sensed DC bus voltage and output of DC bus PI controller (w_{pdc}). Fig. 9(c) shows waveforms of error signal (e_a), incremental weighted value (Δw_{pa}), delayed weighted value (w_{pa}) and weighted value corresponding to active power component of phase 'a' of load current. Fig. 9(d) shows the average weighted value (w_{lp}) corresponding to active power component of load, output of DC bus PI controller (w_{pdc}) and reference active power weight (w_p) along with w_{lpa}. Fig. 9(e) shows reference supply currents (i_{sa}^*, i_{sb}^* and i_{sc}^*) along with phase 'a' of sensed supply current (i_{sa}). It is observed from these results that the shunt compensator performs satisfactory in steady state and unbalanced load condition using immune feedback control.

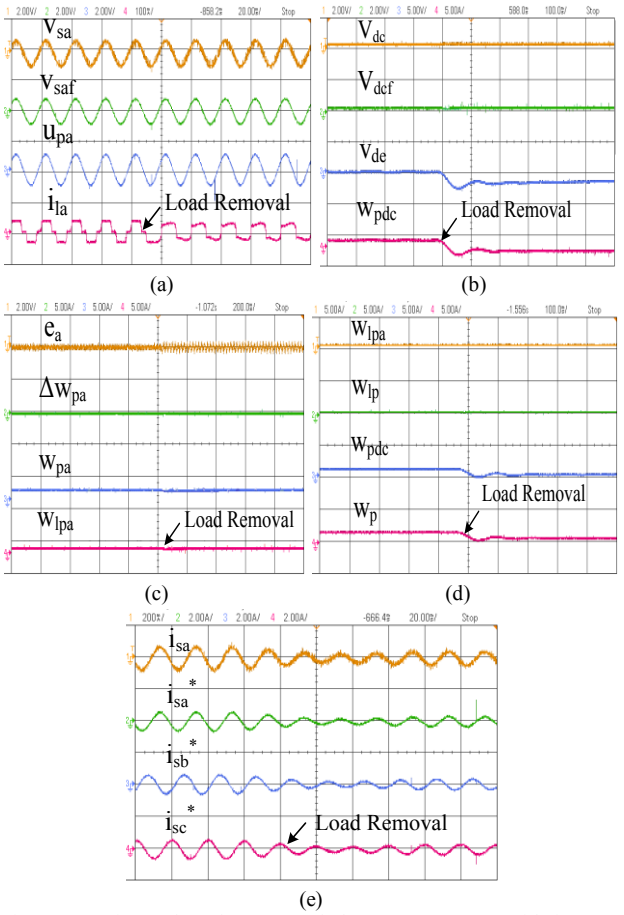


Fig. 9 Experimental performance of shunt compensator with immune feedback based control algorithm (a) v_{sa}, v_{saf}, u_{pa}, i_{la} (b) V_{dc}, V_{dcf}, v_{de}, w_{pdc} (c) e_a, Δw_{pa}, w_{pa}, w_{lpa} (d) w_{lpa}, w_{lp}, w_{pdc}, w_p (e) i_{sa}, i_{sa}^*, i_{sb}^*, i_{sc}^*

B. DSTATCOM Behavior Under Nonlinear Load

Test results are presented in Fig. 10, which show the system behavior when steady state condition has been achieved. Waveforms of PCC voltage and grid current (v_{sa} and i_{sa}), PCC voltage and load current (v_{sa} and i_{la}) and PCC voltage and compensator current (v_{sa} and i_{Ca}) are shown in Figs. 10(a)-(c). Harmonic spectra corresponding to phase '*a*' of grid current (i_{sa}), load current (i_{la}) and PCC voltage are shown in Figs. 10(d)-(f). The observed percentage of THDs in grid current, load current and PCC voltage are 2.3%, 22.9% and 3.2% respectively. It can be observed from the system responses that the DSTATCOM performs the function of correcting the power factor of grid current when nonlinear load is connected. The THD results show a reduction from 22.9% to 2.3% achieving harmonics reduction to a very large extent.

C. Dynamic Behavior Under Varying Nonlinear Load

Figs. 11(a)-(d) show the test results obtained with the shunt compensator when a nonlinear load is also varying. Fig. 11(a) shows the PCC voltage (v_{sa}) and the three phase grid currents (i_{sa}, i_{sb} and i_{sc}) when unbalanced condition is introduced suddenly. These results point out that the grid currents have decreased in magnitude, however, are sinusoidal and balanced. Fig. 11(b) shows the PCC voltage (v_{sa}) of phase 'a', and phase 'a', 'b' and 'c' currents drawn by the load (i_{la}, i_{lb} and i_{lc}) when the load in phase 'c' is suddenly disconnected. Fig. 11(c) shows the PCC voltage (v_{sa}) and the three phase compensator currents (i_{Ca}, i_{Cb} and i_{Cc}) under the same load dynamics. Moreover, it is simultaneously seen from these

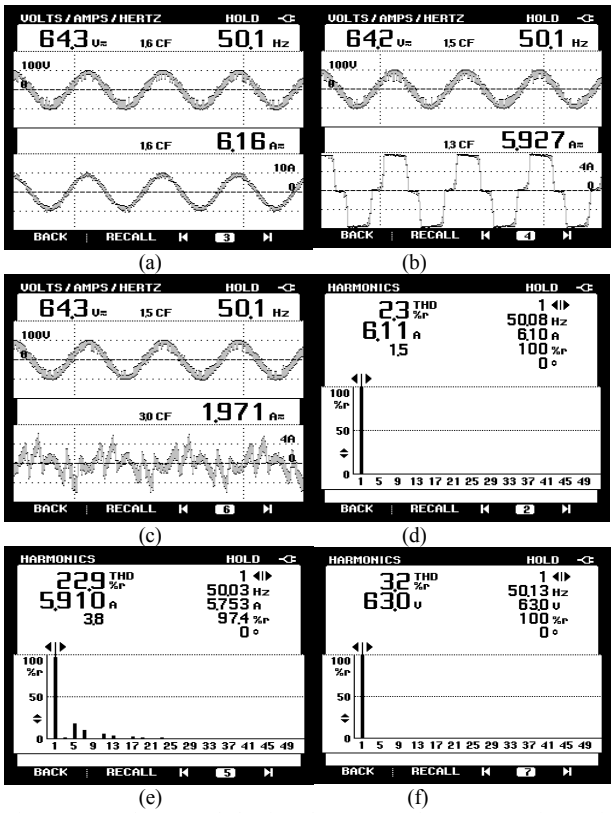


Fig. 10 Steady state behavior for power factor correction using DSTATCOM with nonlinear load (a)-(c) waveforms of grid current, i_{sa} load current, i_{la} and compensator current, i_{Ca} along with v_{sa} (d)-(f) harmonic spectra of i_{sa}, i_{la} and v_{sa}

0093-9994 (c) 2018 IEEE. Personal use is permitted, but republication/redistribution requires IEEE permission. See http://www.ieee.org/publications_standards/publications/rights/index.html for more information.

This article has been accepted for publication in a future issue of this journal, but has not been fully edited. Content may change prior to final publication. Citation information: DOI 10.1109/TIA.2018.2867328, IEEE Transactions on Industry Applications

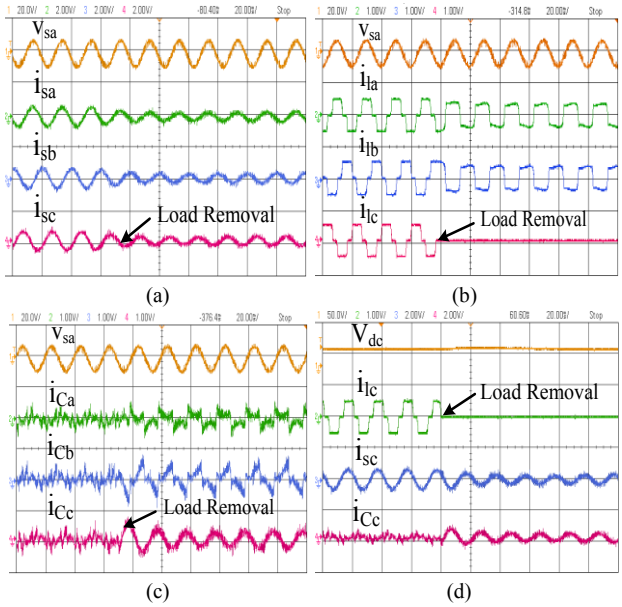


Fig. 11 Experimental results of the system under dynamic load conditions (a) v_{sa}, and grid currents (i_{sa}, i_{sb}, i_{sc}) (b) v_{sa}, and load currents (i_{la}, i_{lb}, i_{lc}) (c) v_{sa}, and compensator currents (i_{Ca}, i_{Cb}, i_{Cc}) (d) V_{dc}, i_{lc}, i_{sc}, i_{Cc}

results that the compensator now injects higher currents. Fig. 11(d) shows the waveforms of DC bus voltage (V_{dc}), load current (i_{lc}) grid current (i_{sc}) and compensator current (i_{Cc}) of phase 'c'. These results confirm that closed loop immune feedback control algorithm is stable and regulates the DC bus voltage at its 200V (set value) within couple of cycles during unbalanced load currents.

VI. Conclusions

A control algorithm based on immune feedback principle has been developed for the control of DSTATCOM. It has been designed and implemented for improving several power quality problems at distribution level. Extensive test results backed with simulation results have been presented for proposed control algorithm. The control algorithm has been developed and implemented for generating switching pulses for VSC. Superior performance of an immune feedback control algorithm has been observed in terms of convergence speed, harmonics compensation, error minimization and computational complexity then it has been compared with NLMS and dq frame based control algorithms for DSTATCOM. Further comparisons with other adaptive controls viz. leaky LMS, LLMF and synchronous extraction are tabulated in Table -II. These results show that the proposed immune control algorithm works well at closed loop conditions and also responds well under extreme load variations. Test results validating the simulation results have recorded 2.3% THD in the grid current obtained after compensation, thereby meeting the standard IEEE-519 limits for harmonics. The obtained value of THD of supply currents is among the lowest of all the considered algorithms. This work highlights the following outcomes.

- Biological immune feedback control algorithm has suitably been designed and implemented to improve power quality problems.
- The immune control algorithm has been found to have an inherent capability to adapt, recognize patterns, identify, self organize and learn. The proposed control algorithm mimics this behavior quite well.
- Experimental results highlight the feasibility of depicting a complex biological phenomenon in a simplified manner.
- A good match between experimental results and simulated results points to feasibility of such control algorithm.
- The performance of developed control has been compared to a number of conventional as well as recently proposed control algorithms and it gives improved performance. Although all the control algorithms have been successful in reducing harmonics substantially (<5%) in the supply current, however, the best performance has been achieved with the proposed control algorithms under similar test conditions.
- The concept and working of biological algorithms can be used a tool to design controllers for real time systems.

This work highlights in detail the design, working and application of the proposed control algorithm in solving power quality problems and used for load compensation.

Appendix-A

AC Supply: 415V, 3-ph and 50Hz; grid impedance: R_s=0.01Ω, L_s=1mH; reference DC bus voltage V_{dc}=700V; DC bus capacitor C_{dc}=1640μF; interfacing inductor L_f=3mH; ripple Filter R_f=5Ω, C_f=5μF, DC bus PI proportional and integral gains: k_{pd}=0.5, k_{id}=0.02; learning rate factor (η)=0.045, stabilization factor (γ)=0.32, load: diode rectifier with R=15Ω, L=100mH.

Appendix-B

AC Supply: 110V, 3-ph and 50Hz; grid impedance: R_s=0.3Ω, L_s=1mH; reference DC bus voltage V_{dc}=200V; DC bus capacitor C_{dc}=1640μF; interfacing inductor L_f=3mH; DC bus PI proportional and integral gains: k_{pd}=0.3, k_{id}=0.05; load: diode rectifier with R=15Ω, L=100mH.

Appendix-C

Mathematical formulation for NLMS controller as [12-14],

A *posteriori* estimation error at the n^{th} instant is given as,

$$\acute{\varepsilon}(n) = \varepsilon(n)\left[1 - \mu(n)x^T(n)x(n)\right] \quad (29)$$

If step size $\mu(n) = \frac{1}{x^T(n)x(n)}$, then $\acute{\varepsilon}(n)$ becomes zero. Under this condition, the recursive weight equation is formulated as,

$$w(n+1) = w(n) + \frac{e(n)x(n)}{x^T(n)x(n)} \quad (30)$$

Another variation of this NLMS algorithm is shown in (31) where α' is the new normalized adaptation constant and λ is a small positive number.

$$w(n+1) = w(n) + \frac{\alpha' e(n)x(n)}{\lambda + x^T(n)x(n)} \quad (31)$$

The need of λ arises to ensure the weight updation does not become excessively large even if $x^T(n)x(n)$ becomes small temporarily.

Acknowledgement

The authors would like to thank Department of Science and Technology, Government of India, for the sponsored project (grant EMR/2016/001874).

0093-9994 (c) 2018 IEEE. Personal use is permitted, but republication/redistribution requires IEEE permission. See http://www.ieee.org/publications_standards/publications/rights/index.html for more information.

This article has been accepted for publication in a future issue of this journal, but has not been fully edited. Content may change prior to final publication. Citation information: DOI 10.1109/TIA.2018.2867328, IEEE Transactions on Industry Applications

AUTHOR INFORMATION

Manoj Badoni (manojbadoni23@gmail.com) is with the Department of Electrical and Instrumentation Engineering Thapar University, Patiala, India. **Alka Singh** is with the Department of Electrical Engineering, Delhi Technological University, Delhi, India. **Bhim Singh** is with the Department of Electrical Engineering, Indian Institute of Technology, Delhi, India. **Alka Singh** is Senior Member of the IEEE and **Bhim Singh** is Fellow of the IEEE. This article first appeared as "DSP based implementation of an immune feedback algorithm for control of shunt compensator" at the 2016 IEEE 6th International Conference on Power Systems (ICPS). This article was reviewed by the IEEE-IAS Industrial Automation and Control Committee.

REFERENCES

[1] B. Singh, A. Chandra, K. Al-Haddad, *Power Quality: Problems and Mitigation Techniques*, John Wiley and Sons, U.K., 2015.

[2] *IEEE Recommended Practices and Requirement for Harmonic Control on Electric Power System*, IEEE Std.519, 1992.

[3] S. R. Arya, B. Singh, R. Niwas, A. Chandra and K. Al-Haddad, "Power quality enhancement using DSTATCOM in distributed power generation system," *IEEE Trans. Indu. Applications*, vol. 52, no. 6, pp. 5203-5212, Nov.-Dec. 2016.

[4] H. Akagi, Y. Kanazawa and A. Nabae, "Generalized theory of the instantaneous reactive power in three-phase circuits," in *Proc. IEEE and JIEE IPEC*, pp. 821–827, 1983.

[5] M. B. Latran, A. Teke and Y. Yoldaş, "Mitigation of power quality problems using distribution static synchronous compensator: a comprehensive review," *IET Power Electronics*, vol. 8, no. 7, pp. 1312-1328, 2015.

[6] R. Kumar, B. Singh and D. T. Shahani, "Symmetrical components-based modified technique for power-quality disturbances detection and classification," *IEEE Trans. Ind. Applications*, vol. 52, no. 4, pp. 3443-3450, July-Aug. 2016.

[7] H. Yi, F. Zhuo,Y. Zhang, Y. Li, W. Zhan, W. Chen and J. Liu, "A source-current-detected shunt active power filter control scheme based on vector resonant controller," *IEEE Trans. Indu. Applications*, vol. 50, no. 3, pp. 1953-1965, May-June 2014.

[8] J. Taotao and K. M. Smedley, "Operation of one-cycle controlled three phase active power filter with unbalanced source and load," *IEEE Trans. Power Electron.*, vol. 21, pp. 1403-1412, 2006.

[9] L. Tarisciotti, A. Formentini, A. Gaeta, M. Degano, P. Zanchetta, R. Rabbeni and M. Pucci, "Model predictive control for shunt active filters with fixed switching frequency," *IEEE Trans. Indu. Applications*, vol. 53, no. 1, pp. 296-304, Jan.-Feb. 2017.

[10] M. Qasim, P. Kanjiya and V. Khadkikar, "Optimal current harmonic extractor based on unified ADALINEs for shunt active power filters," *IEEE Trans. Power Electron.*, vol. 29, pp. 6383–6393, 2014.

[11] B. Singh, S. R. Arya, A. Chandra and K. Al-Haddad, "Implementation of adaptive filter in distribution static compensator," *IEEE Trans. Indu. Applications*, vol. 50, no. 5, pp. 3026-3036, Sept.-Oct. 2014.

[12] A. Singh, M. Badoni and B. Singh, "Application of least means square algorithm to shunt compensator: An experimental investigation," in *Proc. IEEE Inter. Conf. on Power Electronics, Drives and Energy Systems (PEDES)*, Mumbai, pp. 1-6, 2014.

[13] S. Haykin, *Adaptive Filter Theory*, Pearson Publications, 2002.

[14] R. K. Agarwal, I. Hussain and B. Singh, "Grid integration of single stage SPV system using NLMS filtering control technique," in *Proc. IEEE 6th International Conf. on Power Systems (ICPS)*, New Delhi, pp. 1-6, 2016.

[15] M. Badoni, A. Singh and B. Singh, "Variable forgetting factor recursive least square control algorithm for DSTATCOM," *IEEE Trans. Power Del.*, vol. 30, no. 5, pp. 2353-2361, 2015.

[16] R. Kumar, B. Singh, D. T. Shahani and C. Jain, "Dual-tree complex wavelet transform-based control algorithm for power quality improvement in a distribution system," *IEEE Trans. Ind. Electron.*, vol. 64, no. 1, pp. 764-772, Jan. 2017.

[17] K. Venkatraman, M. P. Selvan and S. Moorthi, "Predictive current control of distribution static compensator for load compensation in distribution system," *IET Gen., Trans. & Distri.*, vol. 10, no. 10, pp. 2410-2423, 2016.

[18] B. Singh, P. Jayaprakash, S. Kumar and D. P. Kothari, "Implementation of neural-network-controlled three-leg VSC and a transformer as three-phase four-wire DSTATCOM," *IEEE Trans. Indu. Applications*, vol. 47, no. 4, pp. 1892-1901, July-Aug. 2011.

[19] M. Badoni, A. Singh and B. Singh, "Design and Implementation of ANFIS Based Control Algorithm for DSTATCOM," *Electric Power Components & Systems*, vol. 43, no. 15, pp. 1741-1751, 2015.

[20] M. Kawafuku, M. Sasaki and K. Takahashi, "Adaptive learning method of neural network controller using an immune feedback law," in *Proc. IEEE/ASME Inter.Conf. on Advanced Int. Mech.*, pp. 641 – 646, 1999.

[21] Dipankar Dasgupta, "Advances in artificial immune systems," *IEEE Com. Intelligence Magazine*, vol. 1, iss. 4, pp. 40-49, Nov. 2006.

[22] J. Yuan, Z. Zhao, Cong Li, Jin Wang and C. Tian, "An immune algorithm based dead time elimination PWM control strategy in a single phase inverter," in *Proc. IEEE APEC*, pp. 757-764, 2013.

[23] J. Yuan, J. Pan, W. Fei, C. Cai and B. Chen, "An immune algorithm based space vector PWM control Strategy in a three phase inverter," *IEEE Trans. Ind. Electron.*, vol. 60, no. 5, pp. 2083-2094, May 2013.

[24] H. F. Wang, H. Li and H. Chen, "Application of cell immune response modeling to power system voltage control by STATCOM," *IEE Proc.-Generation, Trans. and Dist.*, vol. 149, pp. 102-107, May 2002.

[25] H. F. Wang, H. Li and H. Chen, "Power system voltage control by multiple STATCOMs based on learning humoral immune response," *IEE Proc.- Gen., Trans. & Dist.*, vol. 149, no. 4, pp. 416-426, July 2002.

[26] M. Badoni, A. Singh and B. Singh, "DSP based implementation of an immune feedback algorithm for control of shunt compensator," in *Proc. IEEE 6th Inter.Conf. on Power Systems (ICPS)*, New Delhi, pp. 1-6, 2016.

[27] S. R. Arya and B. Singh, "Performance of DSTATCOM using leaky LMS control algorithm," *IEEE Journal of Emerging and Selected Topics in Power Electronics*, vol. 1, no. 2, pp. 104-113, June 2013.

[28] R. K. Agarwal; I. Hussain; B. Singh, "Implementation of LLMF control algorithm for three-phase grid tied SPV-DSTATCOM system," *IEEE Transactions in Early Access*.

0093-9994 (c) 2018 IEEE. Personal use is permitted, but republication/redistribution requires IEEE permission. See http://www.ieee.org/publications_standards/publications/rights/index.html for more information.

arXiv:1808.04267v1 [cond-mat.mtrl-sci] 13 Aug 2018

Physical properties and electrochemical performance of Zn-substituted $Na_{0.44}Mn_{1-x}Zn_xO_2$ nanostructures as cathode in Na-ion batteries

Mahesh Chandra,[1] Rishabh Shukla,[1] Rakesh Saroha,[1] A. K. Panwar,[2] Amit Gupta,[3] S. Basu,[4] and R. S. Dhaka[1,*]

[1]*Department of Physics, Indian Institute of Technology Delhi, Hauz Khas, New Delhi-110016, India*
[2]*Department of Applied Physics, Delhi Technological University, Delhi-110042, India*
[3]*Department of Mechanical Engineering, Indian Institute of Technology Delhi, Hauz Khas, New Delhi-110016, India*
[4]*Department of Chemical Engineering, Indian Institute of Technology Delhi, Hauz Khas, New Delhi-110016, India*

(Dated: August 14, 2018)

We report the synthesis, physical properties and electrochemical performance of Zn substituted $Na_{0.44}Mn_{1-x}Zn_xO_2$ ($x = 0 - 0.02$) nanostructures as cathode in Na-ion batteries for energy storage applications. These samples stabilize in the orthorhombic structure and the morphology is found to be slab like with 100 – 200 nm width and few micrometer of length. The resistivity measurements show highly insulating nature for all the samples, where the activation energy decreases with increasing Zn concentration indicating more defect levels in the band gap. The cyclic voltammogram (CV) shows reversible oxidation and reduction peaks, which clearly shift towards higher/lower potentials with increasing Zn concentration up to 2%. We observed the specific capacity of about 100 mAh/g at current density of 4 mA/g and improved cycle life for Zn substituted $x = 0.005$ sample. However, with further increasing the Zn concentration ($x = 0.02$), the specific capacity decreases, which can be a manifestation of the decreased number of reduction peaks in the CV data.

INTRODUCTION

All electrochemical intercalation based batteries require not only ample lattice space and robust structure of an electrode, but also a multiple valance ion to maintain charge neutrality [1]. In this regard transition metal based oxides are widely studied as cathode as well as anode in Li/Na/K ion batteries [1–5]. Among transition metal oxides, $Na_{0.44}MnO_2$ with tunnel type structure and multivalent Mn ion have been studied as cathode material (in pristine form) [6, 7] as well as anode material (when doped with other appropriate transition metal ion) in a Na-ion battery [8]. The 3D lattice structure of $Na_{0.44}MnO_2$ comprise of MnO_6 octahedra and MnO_5 square based pyramids with 0.44 Mn in 3+ valence state and 0.56 Mn in 4+ valence state. Among these, all the Mn^{4+} and 50% Mn^{3+} occupy the octahedral position whereas rest of the 50% of Mn^{3+} occupy pyramidal position resulting into three different sites for Na ions in two different tunnels, one large S-shaped and other smaller one [9]. These tunnels in $Na_{0.44}MnO_2$ allow an easy insertion and reinsertion of the Na–ions during the oxidation and reduction of the cathode material.

The electrochemical properties and particularly the cycling capacity of $Na_{0.44}MnO_2$ critically depend on the synthesis method [9–11], sintering temperature [6, 9] and morphology [12–14] of the samples. Despite of the potential, two major challenges need to be overcome while using these materials as cathode in Na-ion batteries. First is the poor retention of capacity upon cycling and low capacity at higher current rates. The poor cyclic capacity is owing to the structural instability upon insertion/extraction of the Na–ions [6, 9]. Such deficiency can be resolved by altering the morphology (surface to volume ratio) by optimizing the growth technique. There have been various modified techniques employed for the synthesis of $Na_{0.44}MnO_2$ [15–18], such as reverse microemulsion method [6, 19], polymer-pyrolysis method [11], modified pechini method [14, 20] and optimized solid state reaction method [13]. Apart from the synthesis, introduction of some disorder in the electrode material, especially in the form of doping, has been found to be increasing the capacity and performance of the electrode material [1, 4, 8, 21].

Another major issue with Mn based transition metal oxides is the presence of the strong Jahn-Teller (JT) active Mn^{3+} ion. The JT distortion makes the compound vulnerable to the structural changes during the Na insertion/extraction resulting into the reduction of capacity after cycling. One approach to overcome this limitation is to substitute the transition metal site with a diavalent ion [22, 23], which eventually converts some of the Mn^{3+} to Mn^{4+}, therefore reducing the number of JT ions. One such example is substitution of Ni at Mn site where the most stable state of Ni (which is Ni^{2+}) is utilized [23]. Similarly, the most stable state of Zn is 2+ and therefore, can be a potential candidate for the replacement of Mn. Moreover, the ionic size of Zn is larger than that of Mn, so one can expect an increase in the unit cell volume with Zn substitution and hence easy insertion/reinsertion of Na ions upon charging/discharging. The larger ion in the lattice or larger unit cell volume upon substitution has been found to improve electrochemical properties in some oxides [24, 25].

Therefore, we report the synthesis of Zn-substituted tunnel type $Na_{0.44}MnO_2$ by sol-gel technique and investigation of their structural, morphological, transport and electrochemical properties. These samples stabilize in the orthorhombic structure and the activation energy decreases with increasing Zn concentration. We observed

the specific capacity of about 100 mAh/g at current density of 4 mA/g. The capacity does not increase with Zn substitution, but we observed significant improvement in the cycling life of a Na-ion battery.

EXPERIMENTAL

We have synthesized $Na_{0.44}Mn_{1-x}Zn_xO_2$ (x = 0, 0.005, 0.02) using sol gel method. The sodium nitrate (Merck, 99%), manganese nitrate (Merck, 99%), and zinc nitrate (Merck, 99.9%) were added in a stoichiometric ratio in deionized water followed by homogeneouse mixing via stirring for 2 hrs. Then, citric acid (Sigma, 99.9%) in molar ratio of 3:1 was added to the mixture as a complexing agent followed by overnight stirring at 90^{o}C, which results in the formation of the gel. The formed gel was dried at 120^{o}C for 24 hrs. The obtained powder then ground to get fine particles. The powder was first heated to 450^{o}C for 12 hrs to remove organic components before final sintering at 900^{o}C for 15 hrs.

The room temperature powder x-ray diffraction data were recorded with CuKα radiation (1.5406 Å) from Panalytical x-ray diffractometer in the 2θ range of 10 – 60^o. The surface morphology of the prepared materials has been investigated using a scanning electron microscope (SEM) at 20 keV electron energy. Raman spectra of the prepared pellets were recorded with Renishaw inVia confocal Raman microscope at wavelength of 785 nm and grating of 1200 lines/mm with 1 mW laser power. Temperature dependent resistivity measurements were done using physical property measurement system (PPMS) from Quantum Design, USA.

For the electrochemical measurements, first the slurry for cathodes were prepared by mixing $Na_{0.44}Mn_{1-x}Zn_xO_2$ (x = 0 – 0.02) active material, PVDF (Polyvinylidene difluoride) as binder and carbon black as conductive additive in a weight ratio of 80:10:10 in NMP (N-methyl-2-pyrrolidinone) solvent followed by overnight stirring. The obtained slurry was coated on a current collector (Al foil in present case). In order to evaporate the solvent, the coated material was dried in vacuum oven at 135^{o}C for 10 hrs. After that, the circular disks of 12 mm diameter were prepared. The CR2016 coin half-cells were assembled in an nitrogen-filled glove box (Jacomex, $\leq$0.5 ppm of O_2 and H_2O level). The sodium disks prepared from sodium cubes (Sigma Aldrich, 99.9%) with 16 mm diameter were used as counter as well as reference electrode. The glass fiber filter (Advantec, GB-100R) was used as separator and in house prepared $NaClO_4$ dissolved in ethylene carbonate (EC)/dimethyl carbonate (DMC) in a volume ratio of 1:1 was used as an electrolyte [26]. All the electrochemical characterizations were performed using VMP3 (Biologic) instrument and BTS-400 (Neware) at room temperature. The cyclic voltmmetry (CV) measurements were performed in the potential window of 1.8 – 4.0 V vs. Na/Na^+ at a scan rate of 0.1/0.05 mVs^{-1}. The charging/discharging of the coin cell were performed in galvanostatic mode at different current densities.

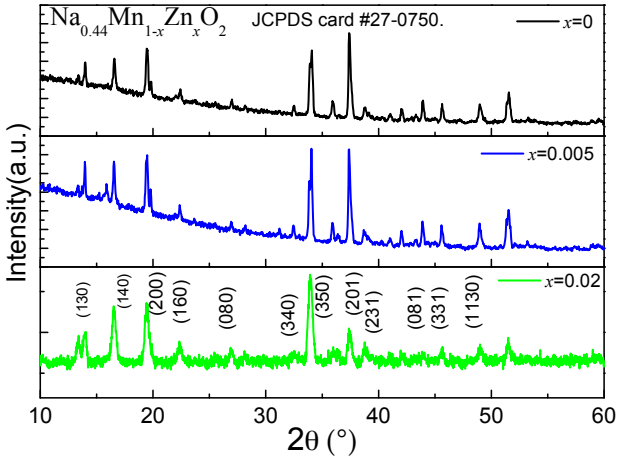


FIG. 1. The XRD patterns for the $Na_{0.44}Mn_{1-x}Zn_xO_2$ (x = 0 – 0.02) samples with peak indexing using JCPDS# 27-0750.

RESULTS AND DISCUSSION

The x-ray diffraction (XRD) patterns for the as synthesized $Na_{0.44}Mn_{1-x}Zn_xO_2$ (x = 0 – 0.02) are shown in Fig. 1. The structure for x = 0 sample is orthorhombic with Pbam space group (JCPDS No: 27-0750), which is in agreement with earlier reports [6, 9, 12]. The Zn substitution does not affect the structure and it remain orthorhombic for all the samples. The compositions of all the samples have been confirmed by energy dispersive x-ray spectroscopy (not shown). We have estimated the strain and crystallite size using Williamson Hall plots [27] from the XRD data. We found that with increasing Zn concentration, the strain increases from $(2.13\pm0.5)\times10^{-3}$ for x=0 to $(2.6\pm0.2)\times10^{-3}$ for x=0.005 and $(3.2\pm0.3)\times10^{-3}$ for x=0.02 smaples. This observation indicates that the substitution of Mn with the larger ion Zn might be causing this increase in internal strain. However, the crystallite size decreases from 100 nm to 50 nm with increasing Zn concentration.

Fig. 2 shows the surface morphology of $Na_{0.44}Mn_{1-x}Zn_xO_2$ (x = 0 – 0.02) samples, investigated using SEM technique. In the SEM images [see Figs. 2(a-c)], we observed slabs of a few nm width and μm length for $Na_{0.44}MnO_2$ sample. With Zn substitution, the morphology does not change much and slab structure prevails for x = 0.005 and 0.02 samples. However, for x = 0.02 sample there are some random shape particles also observed along with the slabs [Fig. 2(c)]. In Fig. 3, we have shown the Raman

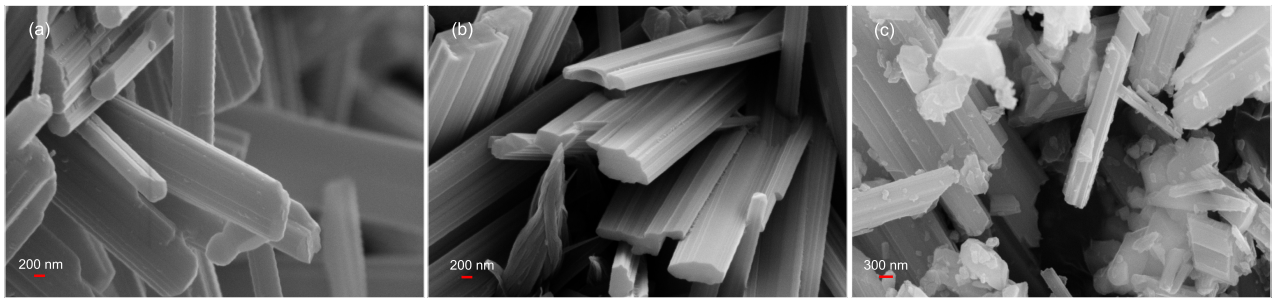


FIG. 2. The SEM images for $Na_{0.44}Mn_{1-x}Zn_xO_2$: (a) $x = 0$, (b) $x = 0.005$, and (c) $x = 0.02$ samples.

spectroscopy measurements for $x = 0$ and 0.02 samples using a 785 nm wavelength laser. There are two major peaks observed in the Raman spectra for $x = 0$ sample , i.e. at 654 and 369 cm^{-1}. These two peaks correspond to the stretching vibrations of Mn-O bonds and bending vibrations of Mn-O-Mn bonds, respectively. These peaks are slightly shifted and lower in intensity as observed at 649 and 364 cm^{-1} for $x = 0.2$ sample. Considering the diatomic approximation which assumes each metal oxygen bond as a separate and non-interacting oscillator and which has been used to explain the relation between Raman shift and bond length in many transition metal oxides [28, 29], the shift in the Raman peaks towards lower wave number with increasing Zn concentration indicates a decrease in the force constant and thus increase in the metal oxygen bond length. Apart from these major peaks there are few minor peaks observed in both the samples. These results are consistent with earlier reports [14, 30].

Now let us discuss the electronic properties which also play an important role in the electrochemical properties. The electronic band structure of 3d transition metal oxides is mainly governed by the overlapping and interaction between 3d orbitals of the neighboring transition metal ions. The substitution of the foreign ion alters the overall metal-metal distance, which manifest itself into the modification in the band structure. The intercalation of Na into the cathode material is correlated to the density of states near the Fermi level [31–34]. The high density of states (i.e. higher conductivity) results in to high rate capability, whereas the lower density of states (lower conductivity) in the cathode material leads to poor cycle life as described in the ref. [33]. In a way, lattice constant, electronic properties and electrochemical properties are correlated. Therefore, in order to get an idea about how Zn substitution affects the electronic properties, we have performed the temperature dependent resistivity measurements on the three samples by four probe method. All the samples show highly insulating nature due to which we could not measure the resistivity below 280 K, as it increases beyond the measurement limit of

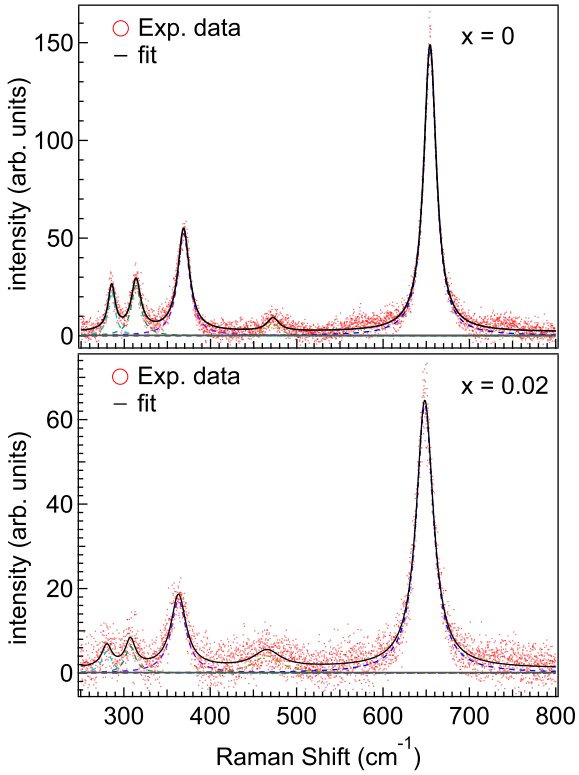


FIG. 3. Raman spectra of $Na_{0.44}Mn_{1-x}ZnO_2$ ($x = 0$ and 0.02) samples, measured at room temperature using 785 nm laser. The dashed lines are fitted with Lorentzian line shape.

the instrument. When compared with $x = 0$ sample, the resistivity first decreases for $x = 0.005$ sample and then increases for $x = 0.2$ (Fig. 4). However, the fitting of the temperature dependent resistivity data using Arrhenius equation: $\rho = \rho_0 e^{E_a/k_B T}$, where, E_a is the activation energy, shows that the activation energy systematically decreases with increasing Zn substitution. For example, the activation energy is 420 meV, 360 meV and 330 meV for $x = 0$, 0.005 and 0.2 samples, respectively. These values of the activation energies are well in agreement with

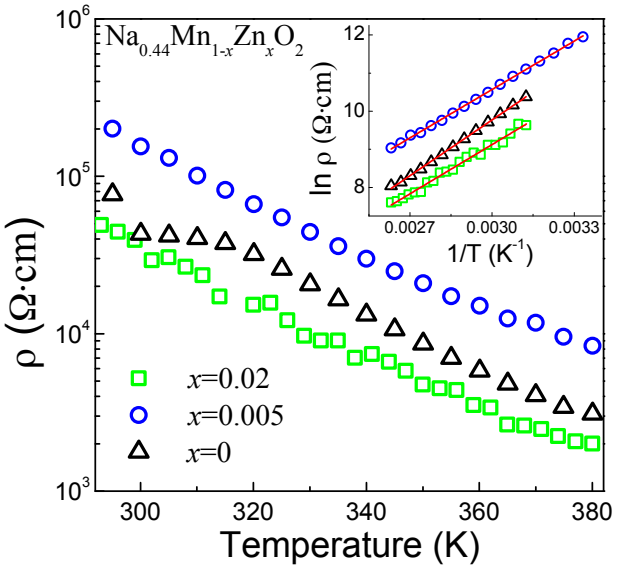


FIG. 4. The temperature dependent resistivity data of $Na_{0.44}Mn_{1-x}ZnO_2$ (x = 0 – 0.02). The inset shows a plot between ln ρ and 1/T with fitting by the Arrhenius equation.

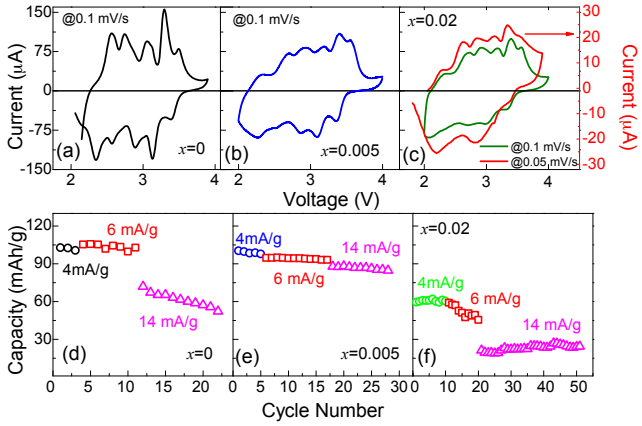


FIG. 5. (a–c) The cycling voltammogram and, (d–f) the capacity degradation upon cycling for $Na_{0.44}Mn_{1-x}Zn_xO_2$ with x = 0, 0.005, 0.02, measured at different current densities.

the previous reports on Mn based transition metal oxides [26, 35]. The plausible explanation for reduction in the activation energy can be the defect levels in the band gap due to the Zn substitution. The systematic decrease in the activation energy with Zn substitution indicates narrowing the band gap and increase in density of states with doping. As mentioned above, this increase in the density of states near Fermi level in x = 0.2 sample can be one of possible reason for better rate capability despite of lower specific capacity which is described in the following section.

The electrochemical behavior of $Na_{0.44}Mn_{1-x}ZnO_2$ (x = 0 – 0.02) as the electrode materials in Na-ion batteries has been investigated by cyclic voltametry (CV) and charging discharging measurements at different current densities on the prepared coin cells. The CV data gives information about the potentials at which the oxidation/reduction takes place, as shown in Figs. 5(a–c), the scan rate is kept as 0.1 or 0.05 mV/sec for all the CV scans. For x = 0 sample, there are six distinct peaks in the oxidation, which repeats in the reduction as well as upon cycling indicating reversibility of Na ion in extraction/insertion. The multi peaks in the CV indicate a complex phase evolution where each peak corresponds to the extraction of Na from different crystallographic sites in the structure [13]. The difference between oxidation and reduction peak values is a measure of the number of free electrons (or Na-ion) involved in the charging/discharging and is given by ΔE=59/n meV (at room temperature) [36], where, ΔE is the difference between the oxidation and corresponding reduction peaks and n is the number of electrons involved. For n=0.44 (to extract all the Na-ion), the peak separation should be 0.13 mV. For our sample the peak separation is 0.11, 0.17, 0.17, 0.18, 0.21 mV for peaks from higher voltage to lower voltage side, which correspond to n=0.53, 0.34, 0.34, 0.32, 0.28. These values are close to the expected n = 0.44 in ideal case. The CV data for all three samples (x = 0, 0.005, 0.02) are shown in Figs. 5(a–c). Now, if we look at the CV for x = 0.005 and 0.02 samples, it is clear that x = 0.005 sample contains all the oxidation and reduction peaks similar to that in x = 0 sample with a small shift in the peak position. Moreover, the similar oxidation peaks have been observed for x = 0.02 sample, but there are fewer reduction peaks when compared with the x = 0 sample. In order to resolve the redox peaks for x=0.02 cathode we performed the CV at slower scan rate of 0.05 mV/s [Fig. 5(c)], but no significance change has been observed. The separation between the oxidation and reduction peaks has also increased indicating decrease in the number of available free electrons and irreversibility of Na ion for some sites, which affect the discharge capacity with higher Zn concentration at the Mn site.

The galvanostatic charging-discharging curves at different current densities for $Na_{0.44}Mn_{1-x}Zn_xO_2$ (x = 0, 0.005, 0.02) are shown in the Fig. 6 and the capacity fading with cycling is summarized in Figs. 5(d–f). For x = 0 sample, the capacity is nearly 100 mAh/g (which is close to the theoretical capacity 121 mAh/g [37]) for slow charging rates that is with current densities 4 mA/g and 6 mA/g. It can be seen that the capacity is almost constant after 10 cycles. However, for higher current density (14 mA/g) the capacity is low and degrade rapidly with cycling (nearly 25% degradation after 10 cycles), see Fig. 5(d). The possible reason for such behavior lie in the layered structure and presence of Jahn-Teller Mn^{3+} ions in these samples. Similar capacity fading is also observed

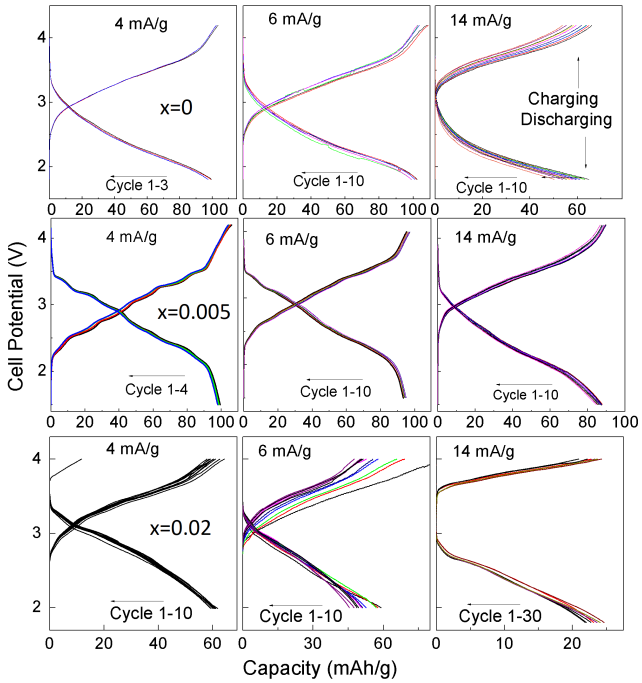


FIG. 6. The charging discharging cycles measured at different current densities for $x = 0$ sample (upper panel), 0.5% (middle panel) and 2% Zn substitutions (lower panel).

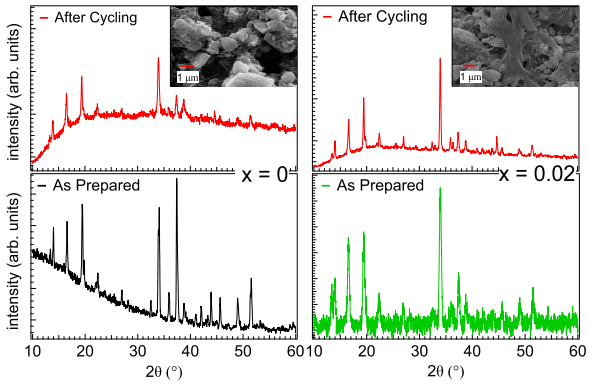


FIG. 7. The comparison of XRD patterns for the as prepared sample and cycled electrode of $x = 0$ and $x = 0.02$ samples. The insets show SEM images of the cycled electrodes.

in other Mn based oxides where Mn has 3+ oxidation sate [26, 38]. As mentioned earlier the Zn substitution would decrease the concentration of Jahn-teller active Mn^{3+} ions and one can expect improvement in the capacity degradation upon cycling. When comparing the capacity of $x = 0$ and 0.005 samples after 10 cycles at 6 mA/g current density, we find that the capacity loss is nearly 4 % for the $x = 0$ sample, whereas it is only about 1% for $x = 0.005$ sample. In addition, the capacity is higher with improved cycling capacity at 14 mA/g current density. This clearly indicate the improvement in the cycle life with small Zn concentration (0.5%). With further increasing Zn concentration (2%), the overall capacity has decreases to about 60 mAh/g at slower current density of 4 mA/g. This decrease in the capacity is a manifestation of the absence of reduction peaks in the CV for 2% substituted sample, as discussed earlier. Despite of the low capacity, the durability is improved and the capacity remain unchanged after 10 cycles at 4 mA/g current density. Upon increasing the charging/discharging current density to 14 mA/g, the capacity decreases to nearly 25 mAh/g and remains constant for more than 30 measured cycles. In this way, we reveal that Zn substitution increases the cycle life possibly due to the reduction in Jahn-Teller Mn^{3+} ions. Now, we discuss the possible explanation of the lower capacity in galvanostatic charging discharging for $x = 0.02$ sample in the view of the CV measurements. The substitution of Zn^{2+} can have the following effects in the parent sample: (1) it replaces the Mn^{3+} (not Mn^{4+}, due to larger difference in ionic radii and charge) and simultaneously converts another Mn^{3+} to Mn^{4+} in order to maintain the charge neutrality, (2) Zn^{2+} is reluctant in changing its valance state from 2+ and Mn^{4+}/Mn^{5+} redox couple is rare and not accessible at ordinary potentials. Therefore, the presence of Zn^{2+} hinders the extraction of Na from the cathode in these two ways. This hindrance clearly reflect in the CV of $x = 0.02$ sample in terms of smaller anodic/cathodic peak current as well as less number of redox peaks, which may manifest in the low specific capacity.

In order to understand how the cycling affect the structure and morphology, we recorded the XRD patterns and SEM images of the cycled electrodes. We compare the XRD data in Fig. 7 and SEM images in the insets. It is evident from the comparison of XRD data that there are no new peaks observed after cycling and the peaks in the as prepared materials matches with those in the the cycled electrode. This shows that there is no structural or phase change taking place during/after cycling process. However, in the case of $x = 0$ sample, the peak broadening and intensity of peaks found to different indicating a change in particle size and morphology. The SEM images of $x = 0$ and $x = 0.02$ electrodes show that the electrode surface for $x = 0$ is porous with large voids as compared to that for $x = 0.02$ electrode, which might be responsible for rapid capacity degradation upon cycling.

CONCLUSIONS

In conclusion, we have synthesized nano-size rod shaped $Na_{0.44}Mn_{1-x}Zn_xO_2$ ($x = 0 - 0.02$) via sol gel method and studied the physical properties and electrochemical performance for Na-ion batteries. The structure is orthorhombic (Pbam space group) and it does

not change with Zn substitution. All the samples are highly insulating and the activation energy, deduced from Arrhenius fitting, decreases with higher Zn concentration. The specific capacity for $Na_{0.44}MnO_2$ is nearly 100 mAh/g, which is close to the theoretically predicted value. The capacity does not increase with Zn substitution, but we observed significant improvement in cycling life. The capacity reduction is only 1% for the 0.5% Zn sample after 10 cycles as compared to the 4% of $x = 0$ sample, measured at 6 mA/g current density. Our study reveal that Zn substitution changes Mn ion from 3+ to 4+ valence state and improve the battery life. We observed changes in the morphology of electrodes after cycling.

ACKNOWLEDGMENTS

RSD acknowledges the financial support from SERB-DST [Early Career Research (ECR) Award, project reference no. ECR/2015/000159], BRNS (DAE Young Scientist Research Award, project sanction no. 34/20/12/2015/BRNS), and IIT Delhi (FIRP project no. MI01418). Mahesh and Rishabh thank SERB-DST (NPDF, no PDF/2016/003565), and DST-inspire, respectively, for the fellowship. Rakesh thanks IIT Delhi for postdoctoral fellowship through FIRP project. The authors acknowledge central research facility (CRF) and the physics department of IIT Delhi for providing research facilities: XRD, SEM, Raman, and PPMS EVERCOOL–II.

* rsdhaka@physics.iitd.ac.in

[1] C. Liu, Z. G. Neale, G. Cao, Understanding electrochemical potentials of cathode materials in rechargeable batteries, Materials Today, 19 (2016) 109 – 123.

[2] M. I. Jamesh, A. S. Prakash, Advancement of technology towards developing Na-ion batteries, J. Power Sources 378 (2018) 268 – 300.

[3] N. Ortiz-Vitoriano, N. E. Drewett, E. Gonzaloa, T. Rojo, High performance manganese-based layered oxide cathodes: overcoming the challenges of sodium ion batteries, Energy Environ. Sci. 10 (2017) 1051 – 1074.

[4] H. Su, S. Jaffer, H. Yu, Transition metal oxides for sodium-ion batteries, Energy Storage Materials 5 (2016) 116 –131.

[5] Y. Xiao, P.-F. Wang, Y.-X. Yin, Y.-F. Zhu, X. Yang, X.-D. Zhang, Y. Wang, X.-D. Guo, B.-H. Zhong, Y.-G. Guo, A layered tunnel inter growth structure for high-performance sodium-ion oxide cathode, Adv. Energy Mater. 8 (2018) 1800492 (1 – 7).

[6] Q. Liu, Z. Hu, M. Chen, Q. Gu, Y. Dou, Z. Sun, S. Chou, S. X. Dou, Multiangular rod-shaped $Na_{0.44}MnO_2$ as cathode materials with high rate and long life for sodium-ion batteries, ACS Appl. Mater. Interfaces 9 (2017) 3644 – 3652.

[7] Z. Chen, T. Yuan, X. Pu, H. Yang, X. Ai, Y. Xia, Y. Cao, Symmetric sodium-ion capacitor based on $Na_{0.44}MnO_2$ nanorods for low-cost and high-performance energy storage, ACS Appl. Mater. Interfaces 10 (2018) 11689 – 11698.

[8] Y. Wang, J. Liu, B. Lee, R. Qiao, Z. Yang, S. Xu, X. Yu, L. Gu, Y.-S. Hu, W. Yang, K. Kang, H. Li, X.-Q. Yang, L. Chen, X. Huang, Ti-substituted tunnel-type $Na_{0.44}MnO_2$ oxide as a negative electrode for aqueous sodium-ion batteries, Nat. Commun. 6 (2015) 6401 (1 – 10).

[9] F. Sauvage, L. Laffont, J.-M. Tarascon, E. Baudrin, Study of the insertion/deinsertion mechanism of sodium into $Na_{0.44}MnO_2$, Inorganic Chemistry, 46 (2007) 3289 – 3294.

[10] X. He , J. Wang , B. Qiu, E. Paillard, C. Mad, X. Cao, H. Liu, M. C. Stan, H. Liu, T. Gallash, Y. S. Meng, J. Li, Durable high-rate capability $Na_{0.44}MnO_2$ cathode material for sodium-ion batteries, Nano Energy, 27 (2016) 602 – 610.

[11] Y. Cao, L. Xiao, W. Wang, D. Choi, Z. Nie, J. Yu, L. V. Saraf, Z. Yang, J. Liu, Reversible sodium ion insertion in single crystalline manganese oxide nanowires with long cycle life, Adv. Mater. 23 (2011) 3155 – 3160.

[12] R. Ma, H. Jiao, H. Zhu, S. JiaoInt. Ultra-long nanorods of single-crystalline $Na_{0.44}MnO_2$ as cathode materials for sodium-ion batteries, Int. J. Electrochem. Sci. 11 (2016) 7242 – 7253.

[13] S. Demirel, E. Oz, E. Altin, S. Altin , A. Bayri, P. Kaya, S. Turan, S. Avci, Growth mechanism and magnetic and electrochemical properties of $Na_{0.44}MnO_2$ nanorods as cathode material for Na-ion batteries, Mat. Charact. 105 (2015) 104 – 112.

[14] L. Zhao, J. Ni, H. Wang, L. Gao, $Na_{0.44}MnO_2$–CNT electrodes for non-aqueous sodium batteries, RSC Advances 3 (2013) 6650 – 6655.

[15] D. Zhang, W.-j. Shi, Y.-wang Yan, S.-dong Xu, L. Chen, X.-min Wang, S.-bin Liu, Fast and scalable synthesis of durable $Na_{0.44}MnO_2$ cathode material via an oxalate precursor method for Na-ion batteries, Electrochimica Acta, 258 (2017) 1035 – 1043.

[16] G. Ma, Y. Zhao, K. Huang, Z. Ju, C. Liu, Y. Hou, Z. Xing, Effects of the starting materials of $Na_{0.44}MnO_2$ cathode materials on their electrochemical properties for Na-ion batteries, Electrochimica Acta, 222 (2016) 36 – 43.

[17] V. Dall Asta, D. Buchholz, L. G. Chagas, X. Dou, C. Ferrara, E. Quartarone, C. Tealdi, and S. Passerini, Aqueous processing of $Na_{0.44}MnO_2$ cathode material for the development of greener Na-ion batteries, ACS Appl. Mater. Interfaces 9 (2017) 34891 – 34899.

[18] X. Ju, H. Huang, H. Zheng, P. Deng, S. Li, B. Qu, T. Wang, A facile method to hunt for durable high-rate capability $Na_{0.44}MnO_2$, J. of Power Sources 395 (2018) 395 – 402.

[19] P. Zhan, S. Wang, Y. Yuan, K. Jiao, S. Jiao, Facile synthesis of nanorod-like single crystalline $Na_{0.44}MnO_2$ for high performance sodium-ion batteries, J. Electrochem. Soc. 162 (2015) A1028 – A1032.

[20] D. J. Kim, R. Ponraj, A. G. Kannan, H.-W. Lee, R. Fathi, R. Ruffo, C. M. Mari, D. K. Kim, Diffusion behavior of sodium ions in $Na^{0.44}MnO_2$ in aqueous and non-aqueous electrolytes, J. Power Sources 244 (2013) 758 – 763.

[21] Y. Wang, R. Xiao, Y.-S. Hu, M. Avdeev, L. Chen, P2-$Na_{0.6}[Cr_{0.6}Ti_{0.4}]O_2$ cation-disordered electrode for high-rate symmetric rechargeable sodium-ion batteries, Nat. Commun. 6 (2015) 6954 (1 – 9).

[22] H. Liu, Y. Wang, L. Li, K. Wang, E.Hosono, H. Zhou, Facile synthesis of NaV_6O_{15} nanorods and its electrochemical behavior as cathode material in rechargeable lithium batteries, J. Mater. Chem. 19 (2009) 7885 – 7891.

[23] Y. Li, X. Feng, S. Cui, Q. Shi, L. Mi, W. Chen, From α-$NaMnO_2$ to crystal water containing Na-birnessite: enhanced cycling stability for sodium-ion batteries, CrystEngComm 18 (2016) 3136 – 3141.

[24] R. Saroha, A. K. Panwar, Y. Sharma, P. K. Tyagi, S. Ghosh, Development of surface functionalized ZnO-doped $LiFePO_4$/C composites as alternative cathode material for lithium ion batteries, Appl. Surf. Sci. 394 (2017) 25 – 36.

[25] Y. -S. Lee, K. -S. Ryu, Study of the lithium diffusion properties and high rate performance of $TiNb_6O_{17}$ as an anode in lithium secondary battery, Scientific Reports, 7 (2017) 16617 (1 – 13).

[26] M. Chandra, R. Shukla, M. Rashid, A. Gupta, S. Basu, R. S. Dhaka, Synthesis and physical properties of Na_xTO_2 (T = Mn, Co) nanostructures for cathode materials in Na-ion batteries, Mater. Res. Bull. 105 (2018) 178 – 183.

[27] G. K. Williamson, W. H. Hall, X-Ray Line broadening from field aluminum and wolfram, Acta Metallurgica 1 (1953), 22 – 31.

[28] F. D. Hardcastle, I. E. Wachs, Determination of niobium-oxygen bond distance and bond order by Raman spectroscopy, Solid State Ionics 45 (1991) 201 – 213.

[29] F. D. Hardcastle, I.E. Wachs, Raman Spectroscopy of supported chromium oxides catalysts, J. Chem. Soc., Faraday Trans., 92 (1996) 1969–1973.

[30] N. Karikalan, C. Karuppiah, S. Chen, M. Velmurugan, P. Gnanaprakasam, Three-dimensional fibrous network of $Na_{0.21}MnO_2$ for aqueous sodium-ion hybrid supercapacitors, Chem. Eur. J. 23 (2017) 2379 – 2386.

[31] J. Xia, H. Zhao, W. K. Pang, Z. Yin, B. Zhou, G. He, Z. Guo, Y. Du, Lanthanide doping induced electrochemical enhancement of $Na_2Ti_3O_7$ anodes for sodium-ion batteries, Chem. Sci., 9 (2018), 3421 – 3425.

[32] M. Kunduraci, J. F. Al-Sharab, G. G. Amatucci, High-Power Nanostructured $LiMn_{2-x}Ni_xO_4$, High-Voltage Lithium-Ion battery electrode materials: electrochemical impact of electronic conductivity and morphology, Chem. Mater. 18 (2006), 3585 – 3592.

[33] J. Molenda, Correlation between electronic and electrochemical properties of A_xMO_2-type electrode materials. Electronic Criterion, Solid State Ionics, 21 (1986) 263 – 272.

[34] J. Molenda, A. Milewska, W. Zaja, M. Rybskib and J. Tobola, Correlation between electronic structure, transport and electrochemical properties of a $LiNi_{1-y-z}Co_yMn_zO_2$, cathode material, Phys. Chem. Chem. Phys. 19 (2017) 25697 – 25706.

[35] A. Mendiboure, C. Delmas, P. Hagenmuller, Electrochemical intercalation and deintercalation of Na_xMnO_2 bronzes, J. solid state chem. 57 (1985) 323 – 331.

[36] J.-M. Savéant, N. J. Hoboken, Elements of Molecular and Biomolecular Electrochemistry, John Wiley & Sons (2006).

[37] M. Xu, Y. Niu, C. Chen, J. Song, S. Bao, C. M. Li, Synthesis and application of ultra-long $Na_{0.44}MnO_2$ submicron slabs as a cathode material for Na-ion batteries, RSC Adv. 4 (2014) 38140 – 38143.

[38] A. Caballero, L. Hernan, J. Morales, L. Sanchez, J. S. Pena, M. A. G. Aranda, Synthesis and characterization of high-temperature hexagonal P2-$Na_{0.6}MnO_2$ and its electrochemical behaviour as cathode in sodium cells, J. Mater. Chem. 12 (2002) 1142 – 1147.

University of Plymouth

PEARL **https://pearl.plymouth.ac.uk**

Faculty of Science and Engineering School of Engineering

Quality of Experience Framework for Cloud Computing (QoC)

Laghari, A

http://hdl.handle.net/10026.1/12154

IEEE Access
Institute of Electrical and Electronics Engineers (IEEE)

All content in PEARL is protected by copyright law. Author manuscripts are made available in accordance with publisher policies. Please cite only the published version using the details provided on the item record or document. In the absence of an open licence (e.g. Creative Commons), permissions for further reuse of content should be sought from the publisher or author.

IEEE Access
Multidisciplinary | Rapid Review | Open Access Journal

Date of publication xxxx 00, 0000, date of current version xxxx 00, 0000.

Digital Object Identifier 10.1109/ACCESS.2017.Doi Number

Quality of Experience Framework for Cloud Computing (QoC)

Asif Ali Laghari[1], Hui He[1], Asiya Khan[2], Neetesh Kumar[3], and Rupak Kharel[4], Member, IEEE

[1]School of Computer Science & Technology, Harbin Institute of Technology, Harbin, China
[2]School of Marine Engineering, University of Plymouth, Plymouth, UK
[3]Indian Institute of Information Technology & Management, Gwalior, India
[4]School of Engineering, Manchester Metropolitan University, Manchester, UK

Corresponding authors: Asif Ali Laghari, Hui He (e-mail: asiflaghari@hit.edu.cn, hehui@hit.edu.cn).

ABSTRACT Cloud computing provides platform for pay per use services such as software, hardware and platforms. Previous cloud frameworks use fix policies that do not have the functionality to upgrade services on demand when the user do not receive services according to Service Level Agreement (SLA). Also, there was a lack of functionality to monitor external network and client device resources. This paper presents Quality of experience framework for Cloud computing (QoC) for monitoring the Quality of Experience (QoE) of the end user using video streaming services in the cloud computing environment. The management platform is used for administration purpose in QoC framework that provides facility to easily manage the cloud environment and provide services according to SLA via runtime policy change. The objective QoE/QoS section will automatically monitor the Quality of Service (QoS) data. It will also compare and analyze the subjective QoE submitted by the users and objective QoS data collected by agent based framework for accurate QoE prediction and proper management. The proposed QoC framework has new features of real time network monitoring, client device monitoring and allows changing policy in runtime environment which to our knowledge is currently not provided by existing frameworks.

INDEX TERMS Cloud computing, Service level agreement (SLA), Quality of Experience (QoE), Quality of Service (QoS), QoC.

I. INTRODUCTION

Multimedia usage on the Internet has increased dramatically over the last few years to access resources such as video tutorials, video-on-demand (VOD), video conferences, audio/video streaming, etc. Users can access free video services such as IPTV, online videos, video conferences etc. from the cloud servers including commercial services on a pay per use basis. In a client server architecture, the users can access these videos from video servers that have options of streaming with multiple bit rates e.g. YouTube. The user will simply make the selection or the service provider automatically defaults to a particular bit rate according to the network bandwidth and device compatibility [1, 2]. These are free of cost services, no service level agreement (SLA) between user and service provider exists for Quality of Service (QoS) provision and thus compensation on low services is irrelevant. Hence, less storage is normally provided to users for uploading their personal contents. Free service providers such as Facebook has its own settings for videos and thus when users upload video, it is automatically converted to service provider's predefined format, normally with reduced quality [3]. The free cloud service providers do not provide the QoS for video streaming but user can freely access their multimedia contents and also share publicly. Commercial cloud service provider allows video storage space on pay per use basis with better QoS for video streaming. The user can access video services (for stream, download and upload) using variety of user interfaces including mobile apps [4, 5]. Earning more revenues from the market is basic competition between the cloud service providers, so all providers try to offer better QoS to their customers to deliver better user satisfaction thus retaining the customer.

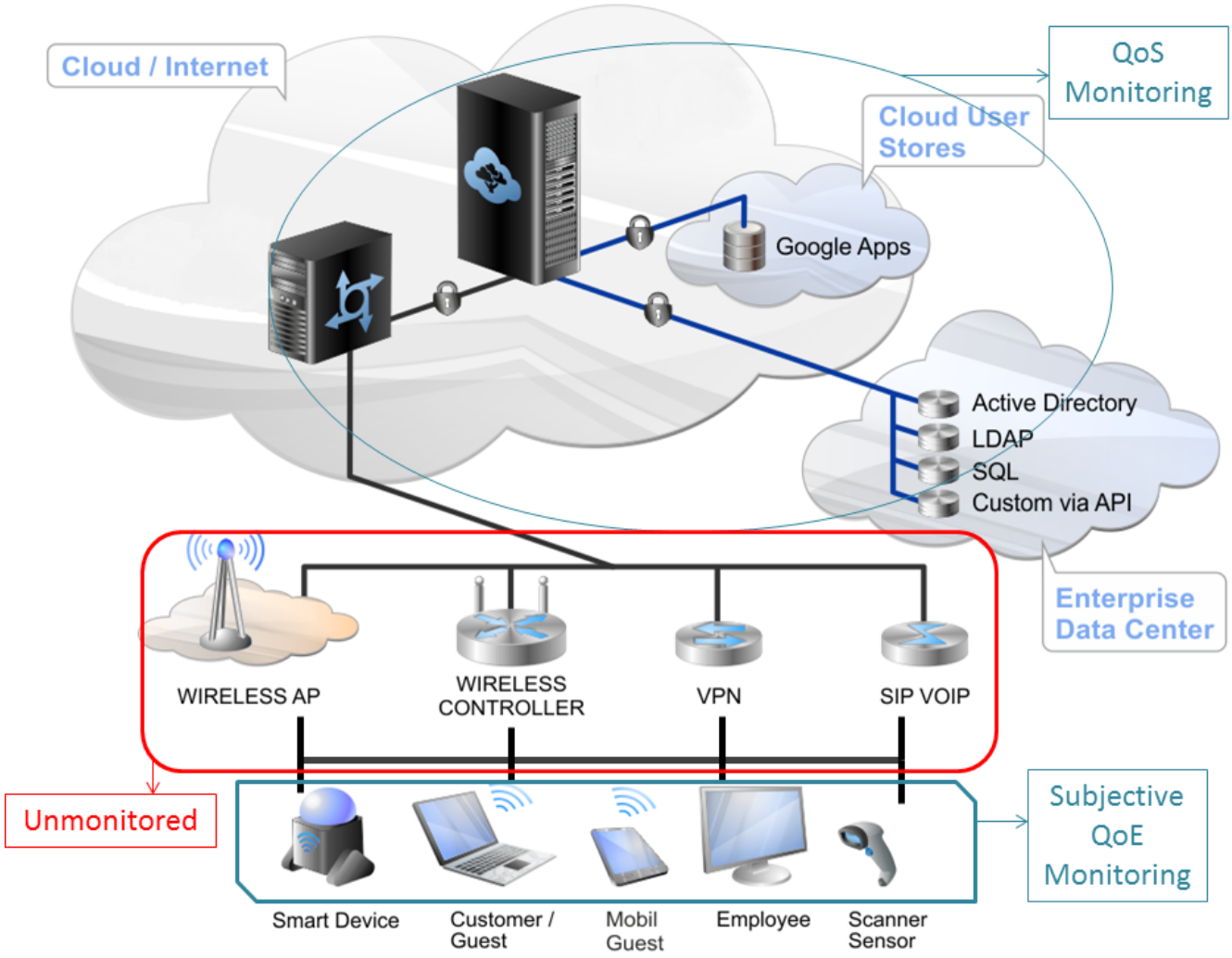


FIGURE 1. **Cloud QoE/QoS Monitoring Scenario [11].**

Poor QoS of video streaming and violation of SLA in commercial cloud infrastructure force users to move to other service provider that guarantee better QoS. However, migration of user from one provider to another is a loss of economy for the business as well as annoyance for user who have to move all the stored data from the previous cloud to a new cloud [6]. To avoid user migration problems, cloud organizations provide user feedback or user support page on their website to receive data about the user experience regarding their services or complaints about monitoring QoS and avoid violation of SLA. But organizations struggle to capture positive user experience for management of cloud services [7]. To capture positive and accurate QoE is cumbersome for cloud organizations because of the greedy behavior of the user and less knowledge of user's QoE is a problem for cloud management [8]. There are so many autonomous tools developed by cloud organizations for QoS data monitoring in cloud environment limited to their firewall and are given in Fig. 1 [9, 10, 11]. A few cloud service providers also add subjective Quality of Experience (QoE)/customer feedback/complaint pages on their websites and apps for customer feedback to improve the overall QoS and increase user experience level. Therefore, middleware network and QoS monitoring at user side are still not included in monitoring frameworks for cloud management.

QoC framework provides the solution of the above discussed problems. The proposed QoC framework based on the agent technology, automatically collects objective QoE/QoS from cloud to client device and user also have an option to subjective QoE to cloud management. The QoE data submitted by end users and objective QoE/QoS data collected by the system will be analyzed for service delivery according to SLA. The main contribution of this paper is to propose a QoE framework for Cloud computing (QoC) that is able to:

- Collect data (status) of the internal cloud environment, client's device and middle network environment from cloud to end user's device automatically.

- Submit complains and feedback about services and mobile app to access cloud services from remote locations.
- Upgrade policy for the time being if the user does not get QoS according to SLA and extend package limitation for users to complete current task.
- Distinguish the negative and positive QoE by comparison of current service delivery parameters when the user submits feedback which to our knowledge is currently not provided by existing cloud QoE frameworks.

The paper is organized as follows. In Section II, we provide related work based on the overview of the cloud infrastructure and existing QoE based frameworks. Section III depicts the architecture of the proposed framework, which contains QoE model of QOC framework and functionality. Section IV presents sequence diagram of the QoC framework and Section V provides details of the web and mobile app of QoC framework. Section VI illustrates results and discussions. Finally, in Section VII, we conclude the work and provide future research directions.

II. RELATED WORKS

This section presents the related work and is further divided into two parts. It provides an over-view of the cloud infrastructure and summarizes the existing QoE-based cloud frameworks.

A. OVERVIEW OF THE CLOUD INFRASTRUCTURE

Cloud computing is an evolution of grid computing [12]. Grid computing is a collection of shared hardware resources such as computers, network routers managed via software from multiple locations for one common goal [13]. In grid computing, all resources are used for one specific large task or workloads like weather forecast and earth simulation for earthquake alerts. Whereas, cloud computing provides high computational power with more features such as permanent storage and hardware resources or infrastructure as a service (IaaS), application software as a service (SaaS) and platforms or operating systems for application development as a service (PaaS) [14, 15]. According to the NIST Cloud Computing Definition, "Cloud computing is a model for enabling convenient, on-demand network access to a shared pool of configurable computing resources (such as, networks, servers, storage, applications, and services) that can be rapidly provisioned and released with minimal management effort or service provider interaction" [16, 17]. Cloud computing is based on the three service models - SaaS, PaaS and IaaS. SaaS is a business and consumer type of service, which is used by end users e.g. for email, the application software of database and accounting but users do not necessarily need the technical information to manage the cloud [18, 19]. PaaS provides development tools for developers, which are technically managed and configured by the end user developers according to their requirement. IaaS is fully dependent on access to cloud infrastructure and devices like servers, network and storage devices so in IaaS developer has full access to manage and change cloud infrastructure [20].

Cloud management monitor technical parameters to provide QoS to the user but customer satisfaction and accurate QoE still remains a big issue for cloud management. It is hard to capture user needs and manage the services according to their needs. There is no framework provided by industry or academia for cloud management, which provides complete solution to capture and distinguish between positive and negative QoE.

B. EXISTING QoE BASED FRAMEWORKS

QoE/QoS frameworks are designed and developed for cloud computing to analyze the user needs and their satisfaction level about cloud services. One such framework is proposed in [21], where the framework is based on the agent technology. The proposed framework works on two conditions, cloud-assisted adaptive video streaming and social-aware video prefetching. A private agent constructed in cloud center for each mobile user will analyze the network traffic and on the basis of network capacity, will adjust video quality (bitrate) by the scalable video coding technique.

CLAMS (Cross-Layer Multi-Cloud Application Monitoring as a Service Framework) is QoS monitoring based on the agent technology, which monitors applications and big data analytics in multi cloud environment and addresses the issue of cross layer monitoring of applications [22]. Follow Me Cloud: FMC Interworking Federated Clouds and Distributed Mobile Networks cloud framework presented by Tarik [23], this framework is based on the subjective evaluation of user for network delay when their services are migrated from one cloud data center to another. The idea of this framework is that services migrate to near location datacenter will enhance the QoE of the user and this will generate a high cost for cloud service providers.

Another QoE framework Cloud2Bubble is proposed by Costa, et. al [24]. This framework monitors the environment based on the user profile, addresses disconnect and service delivery status enabling the delivery of personalized services for users based on their preferences and needs. This framework proposed to provide QoS for every single user profile according to needs when multiple users use same devices in different times. QoE test is not conducted to validate the proposed framework.

Mobile Cloud Gaming (CMG) framework was proposed for multi user gaming environment for the mobile user via cloud server instead of client server architecture [25]. The purpose of the framework is providing an idea to shift mobile user load to cloud server due to the inherent hardware constraint of mobile devices (memory and graphics processing). The framework is based on the objective and subjective QoE measures. The objective factors analyzed which influence on QoE measure are four factors: cloud

server, source video, wireless network and client. The author set network based model for subjective QoE validation of framework and also propose Game Mean Opinion Score (GMOS) for measurement of end user's QoE.

The proposed QoC framework is based on agent technology, the agent monitors environment from cloud to end users and technical data for performance analysis. Previous QoE based cloud framework has limited scope of monitoring and analysis at cloud side but QoC framework monitor cloud as well as network environment and client side. No existing framework upgrades the policy in the runtime environment to provide QoS according to the SLA and is unable to differentiate between the positive and negative QoE of end users. Comparison of previous QoE frameworks with QoC framework is given in Table 1.

TABLE I
COMPARISON OF QOE FRAMEWORK OF CLOUD COMPUTING

QoE/QoE Cloud Frameworks	Wang [21]	CLAMS [22]	FMC [23]	Cloud2Bubble [24]	CMG [25]	QoC
Parameters	NQoS	AQoS	NQoS	NQoS & AQoS	NQoS & PSNR/ VQ	NQoS & AQoS
Monitoring Support	Yes	Yes	Yes	Yes	Yes	Yes
Analysis Support	Quantitative	Quantitative	Quantitative	Quantitative	Quantitative	Quantitative & Qualitative
Reporting	No	No	No	Yes	No	Yes
Policy Change	No	No	No	No	No	Yes
Client Monitoring	No	No	No	No	No	Yes
Remarks	Objective (QoS) Evaluation	Objective QoS Evaluation	Subjective Evaluation	Subjective Evaluation	Objective & Subjective Evaluation	Objective QoE/QoS & Subjective Evaluation

III. ARCHITECTURE OF THE PROPOSED QOC FRAMEWORK

This section presents the architecture of the proposed QoC framework and is further divided into two parts to describe the QoE model used in the QoC framework and the proposed QoC framework.

A. QUALITY OF EXPERIENCE (QoE)

Nowadays QoE is a major notion for organizations for developing products and providing services to end users. The QoE is a measurement of user factors like feelings enjoyment, perception, satisfaction and cognition for given service or product [26]. QoS was used in past for improvement in services and technical parameters were changed by vendors, but SLA violation and user satisfaction remains big problem [27]. SLA is a document which is signed by the user and vendor for QoS, but user needs evolve by time and vendor has fix policies for long period, so this is the main reason for merging QoE for service delivery and product development [28]. Using QoE notion vendor/service providers capture information of user needs in a timely manner for their performance of services and avoiding violation of SLA. There are two types of QoE, (i) subjective and (ii) Objective. Subjective QoE can be captured by using interviews, questionnaire, scales and web-based surveys [28]. Objective QoE is further divided into two parts, one is human physiological data which can be captured by MRI and EEG tests and other is technical parameter QoS data [29, 30]. Subjective QoE is costly and it is very difficult to distinguish positive and negative feedback of users, but objective QoE provides almost accurate results without negative feedback. Vendors mostly use subjective QoE for services or products because it is easy to capture as compared to objective QoE, but few vendors also use objective QoE for more accurate data [31, 32]. The QoE model contains components associated with management and users. Generally, management side has the database, which contains information of user and SLA. When the user starts using services, they have an option to submit experience or complains via web page commonly given from all service providers. The user experience is based on the user's level of satisfaction, learning ability, enjoyment and engagement [33-35], this feedback given for the service quality which end user received at the destination. When users submit the feedback, it is directly stored in the database and management analyze the feedback/complains. If any changes is required at their side, they manage within the limitation of SLA [28]. QoE model with detailed components are given in Fig. 2.

In Fig. 2, QoE model is based on the management side, client side and the network are in the middle of service delivery from cloud to client. Management section is based on the QoE database (DB). DB is further subdivided into user profile information, QoE data, SLA for particular user, record of evaluation and changes (log reports) and analysis section of subjective and objective QoE/QoS. User side components are QoE/complaint which is based on the user's level of satisfaction, enjoyment, learning and engagement.

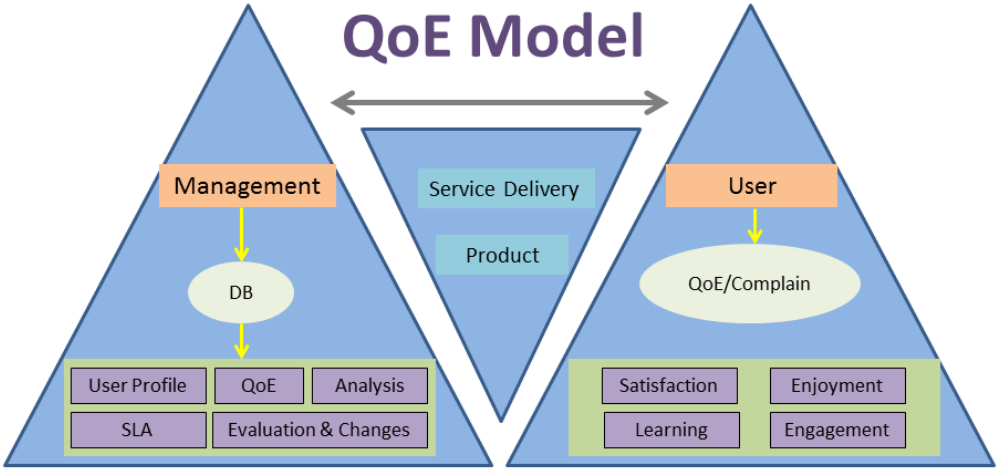


FIGURE 2. Proposed QoE Model.

Previously QoE has been used for network management in client server architectures to provide QoS to end users according to their needs [32], now academia and industry merge QoE features in cloud environment for better management and provide QoS to end users according to their needs. The proposed QoC framework automatically captures objective QoE in runtime environment from cloud management to end user and also provides a facility for the user to submit subjective QoE/complaints feedback via a web form. Objective QoE monitoring tool based on the agent technology which collects QoS data from cloud environment to destination user and finds problems.

B. THE PROPOSED QoC FRAMEWORK

The proposed QoC framework is a semi-automatic management based on agent technology. In QoC framework, cloud side components are cloud manager, QoE manager, user profile & SLA, user storage, agent framework for monitoring objective, QoE/QoS and MySQL database for storing the subjective and objective QoE of end user shown in Fig. 3. Further, the QoC framework architecture contains cloud web interface and mobile app for user to access cloud features. We develop web-based tool "QoE test cloud" for testing subjective QoE validation of QoC framework for multimedia services. QoE test cloud web-based tool provides the facility of storage video on the cloud, share and download features to users. The QoE test cloud is based on different sections, every section facilitates users to manage their videos on the cloud. This tool provides facility to user to create an account for storage and makes his profile for QoE submission in the context of complaints, needs and decline of services (QoS) mentioned in signed SLA. If a user enters negative feedback or wrong information to get more QoS mentioned in SLA from the cloud, submitted subjective QoE of the user will be analyzed and compared with monitored objective QoE/QoS then QoC framework will not take any action on user's feedback. QoC framework compares both subjective and objective QoE for accurate analysis that QoS is provided according to SLA or not. If QoS is not according to SLA then alert to user about the problem at user side is sent, if problem is on the cloud side, i.e. network speed, network error, traffic burden on cloud internal network, or storage problem, VM migration issue then it will be solved and provide QoS according to SLA.

If the user did not get QoS according to SLA and the subjective QoE is positive then the objective system will search for the problem. If the problem is found within cloud environment then it sends alert to cloud administrator, but if problem is found outside from the cloud environment then QoC framework will search exact issue for the disturbance in providing QoS to end user. For example, QoC framework found a problem at user's device and user facing the problem getting QoS because of low hardware configuration of the device or due to peak network traffic then QoC framework will send alert to the user about the problem. Sometimes end user will not get QoS from service providers due to the lack of free computational resources in their own devices. In this situation, QoC framework will send alert to the user to make their device free for use of cloud services. This is a major issue for cloud administration because nontechnical users are not always aware of resources on their side and may not understand the reason of QoS degradation and may claim for SLA violation to cloud management. The purpose of merging both subjective and objective QoE/QoS in QoC framework is that if a nontechnical user will not know about the submission of complaint using feedback form then objective QoE/QoS monitoring tool will automatically detect the services and compare to the signed SLA. If the user had not receive services according to SLA, the system will diagnose the problem and react on it. User perception could not give a precise evaluation of the problem and unable to detect accurate problem and level of performance. Users also provide negative feedback for getting more QoS because of greed, so objective QoE/QoS technical data will

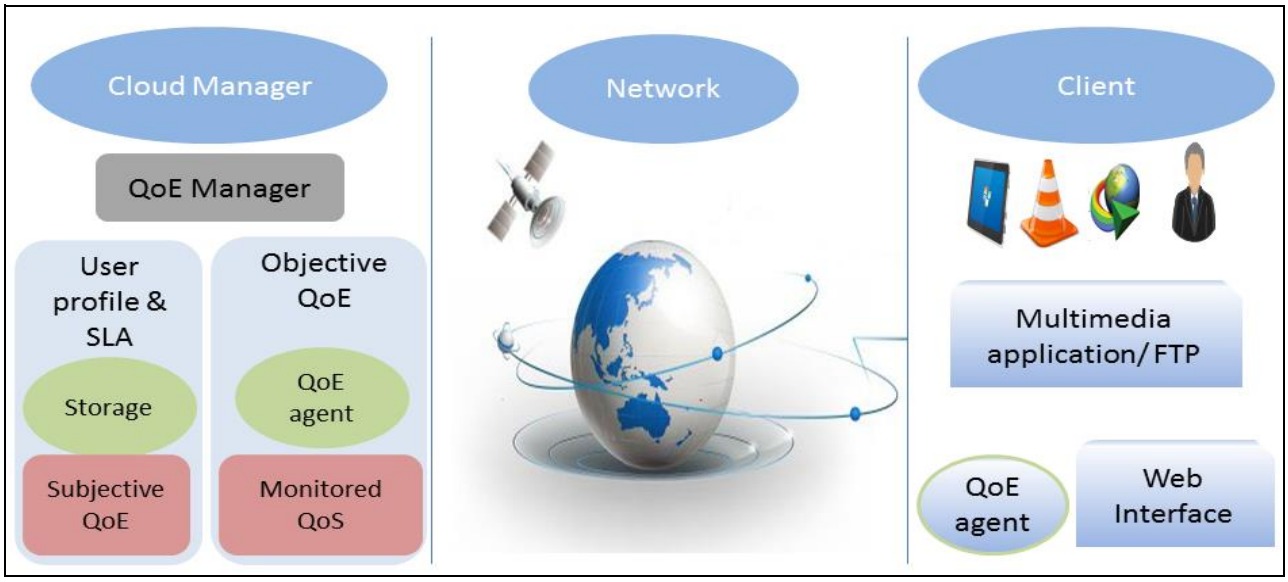


FIGURE 3. **Architecture of the proposed QoC framework.**

provide accurate information about the performance. Subjective feedback helps administrator to understand user's perception, complaints, future needs and objective QoE/QoS data will help to get final accurate user feedback for decision.

IV. SEQUENCE DIAGRAM OF PROPOSED QOC FRAMEWORK

The sequence diagram in Fig. 4 explains how our proposed QoC framework operates, how agent code collects data at the end user's device and internal cloud and the evaluation of subjective and objective QoE/QoS. The sequence diagram is based on the client and admin section. Admin section is further subdivided in 4 parts which contains QoE manager, user videos, management platform and QoE database. The operations of sequence diagram are presented in two actions.

- The user invokes services to access the cloud, the request goes to QoE manager for account verification and policy activation and the user starts video streaming from his account. Cloud transfers video streaming data to end users and after perception user will submit QoE, which will be stored in QoE database (DB). QoE manager will automatically collect objective QoS data from cloud to end user's device, which contains network information (e.g. delay, packet loss, reordering and number of routers between cloud and user), user device information (e.g., buffer information, device hardware information, battery status information and location) which is shown as 6 activity in diagram. This information will be compared by management platform with subjective QoE submitted by the user for analysis of services according to SLA and stored in QoE DB for future use. Objective QoE again is collected by agents and resent to management section for analysis, if services are low from the mentioned value in SLA then management platform updates policy and the user will receive services with the upgraded policy.
- Cloud admin will send request to QoE manager to check user reports and profile and QoE manager will forward the request to management platform to generate a report from QoE DB. Admin can select a particular user from management section and view the report. The problem report will also be forwarded to the end user for the device performance degradation for receiving services according to SLA.

V. MOBILE USER QOE MEASUREMENTS BASED ON QoC

A. CLOUD VIDEO SERVICE WEBSITE

Client side contains web interface for registration, for example a user Mike registers himself on the cloud using the web interface registration module. He must select a package for P1, or P2 etc., which contains storage data limit of 1GB and 2GB respectively on pay per use basis. Details of user like email, name and phone number will be stored in cloud database with his package. The user will log in using his ID and upload videos on the cloud storage using standard web interface.

The QoC framework supports all type of videos that contains different formats and codecs with high data volume. Other clouds support only few popular video codecs and during the upload file is compressed, decreasing the quality of the video from original quality [36]. After uploading videos on the cloud, the user has option to select a particular video to edit information, delete, move to other folder and share publicly on a different social media networks like Facebook, Twitter or Baidu. This QoC framework also provides facility for users to play online video. The user can manage and perform an operation on their uploaded videos.

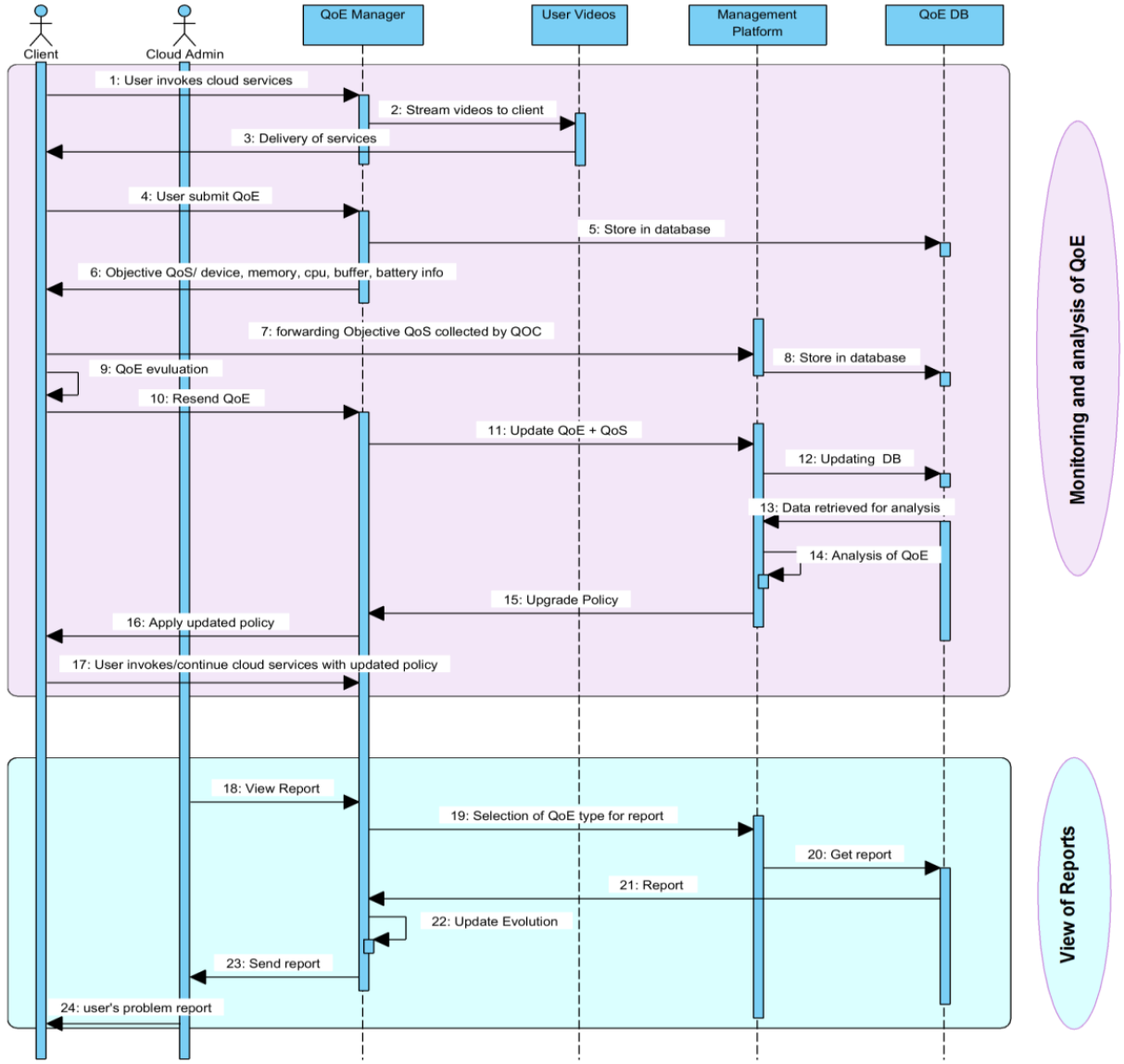


FIGURE 4. Sequence diagram of Proposed QoC framework.

The mobile app is also developed for users because most users want access to videos via mobile phones during their travel. The mobile app contains all user based functionalities for accessing, upload and download of videos. QoC framework cloud based mobile app has all the same functions which are available for the desktop system so the user can access same features via desktop or mobile phones.

VI. RESULTS AND DISCUSSIONS

A. SUBJECTIVE EXPERIMENTS

During the online playing of videos, the user feels the quality of the video is low from original or is facing delay/buffering issues then s/he can submit complaint/experience to cloud management by using the feedback form, which is also given in the QoC framework. The user will enter information about the problem currently being faced and also priority of problem that they have, either major issue to solve on the emergency basis or low level issue solved on the normal routine of management. Other information includes QoS of network, user's network connection speed, video quality information like facing buffering, low quality video and rank the quality of the video. User complaints will be submitted to the database with their profile for processing to provide QoS according to SLA. QoC framework feedback form is used to collect subjective QoE from user to analyze his problem; service delivered to user comparison with SLA and needs. Subjective QoE form of QoC framework is designed using standard web interface asshown in Fig 5.

Management Platform is another part of QoC framework, which is used for cloud administration to manage user's accounts, set SLAs, and solve problems. Management platform depends on three parts: feedback, QoE data and Objective QoE/QoS data. Feedback list provides details of user submitted complaints from the start of using services to

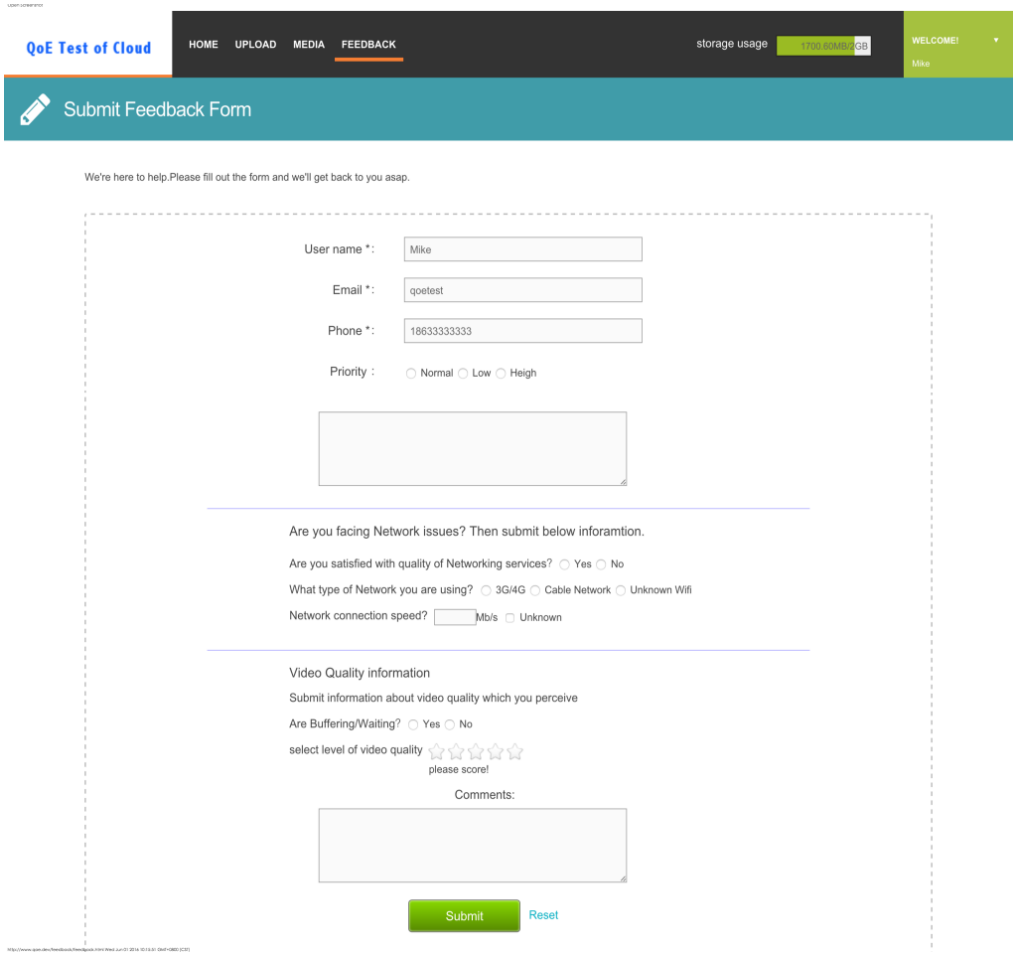


FIGURE 5. **Feedback form.**

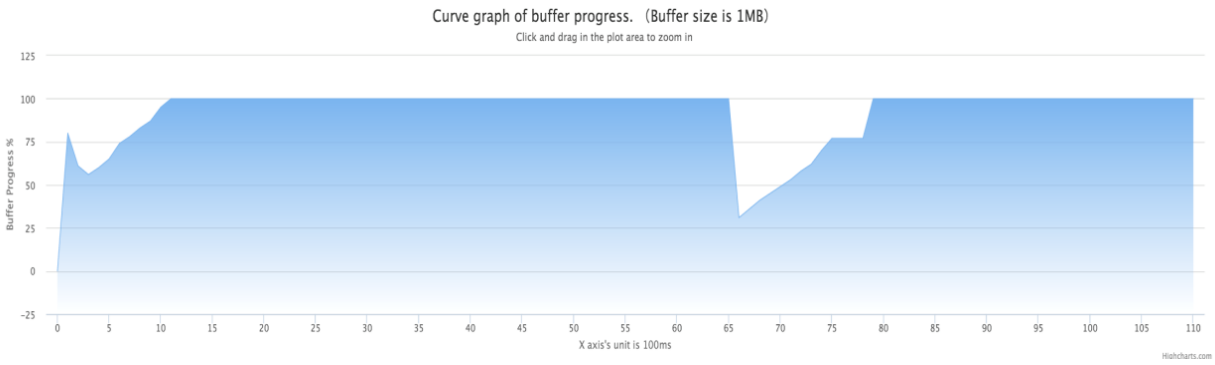


FIGURE 6. Buffer reading result via Wi-Fi network.

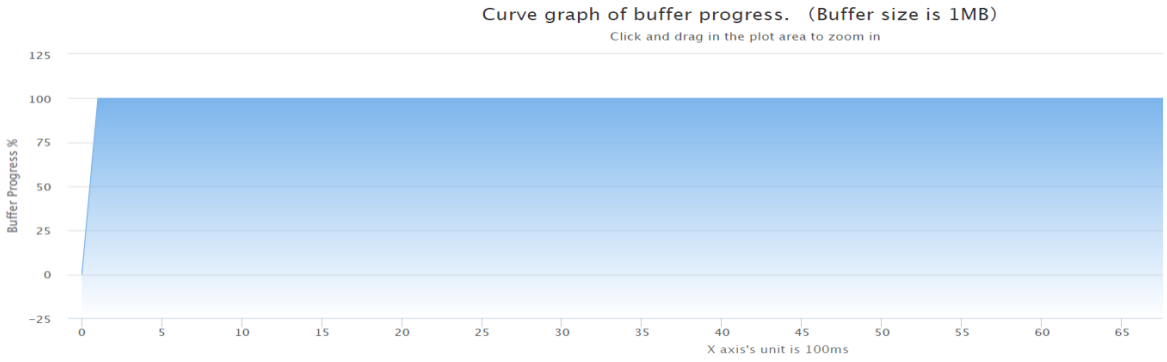


FIGURE 7. 100% buffer filled (local system).

till date. The list will provide information including user ID, name, phone, email date, reply, status and option for view details of buffer and network information using standard web interface. These are the details of components which user can input during submission of QoE.

Subjective QoE section of QoC framework also has a functionality to read user buffer status and information of video, total playing, current and roaming time with data size of the video, when user submits complaint/subjective QoE. The buffer checking agent runs across the firewall of a user device in the same way as agent work in Globus toolkit of grid computing for resource discovery [37]. Fig. 6 shows that 1Mb buffer is not filled due to network delay when video content is playing and buffer code is tested by using Wi-Fi network. But test of buffer code on the local system in android virtual environment provides results that buffer is filled every millisecond while playing the video, see Fig. 7. The agent base code is also used to extract user's device information and its power status and battery life and shown in the web interface alongside the buffer information.

B. OBJECTIVE MEASUREMENT

Objective QoE/QoS is a part of management platform of QoC framework administration side. Objective QoE monitoring is based on the agent technology and QoS data can be retrieved by applied functionalities, which are provided by simple network management protocol (SNMP) [16]. SNMP uses agents to retrieve QoS data of network such as route information from cloud to end user, number of packets in and out number of network interfaces. SIGAR (https://support.hyperic.com/display/SIGAR/Home) is used for low level system information such as total memory, used memory, actual free memory, CPU utilization and specific information e.g memory and CPU consumed by a process [38]. In QoC framework, system management software will monitor cloud environment for free resources like computation, storage and load on the internal cloud network. Monitoring of QoS data from cloud to user contains distance from cloud to user, number of routers between them, specific delay on network traffic passing from router, network bandwidth, type of network, user device capability, OS, browser, CPU usage, memory usage, route queue delay, etc. CPU and memory usage have huge impact on the performance of accessing cloud while router queue delay is important information for administration to understand the deficiencies in QoS according to SLA.

Objective QoE/QoS part is based on monitoring function, which is subdivided into three parts such as monitoring of local cloud environment, network environment, user device and usage information. Other components of objective QoE/QoS contain task section, which provides information about the task (current task, start time, estimated time of completion and remaining time). User section provides details of the list of registered users and particular information of users like email, phone and registration date etc. SLA section contains signed SLA between user and services provider and status of SLA with policy change or previous policy for providing QoS. Objective

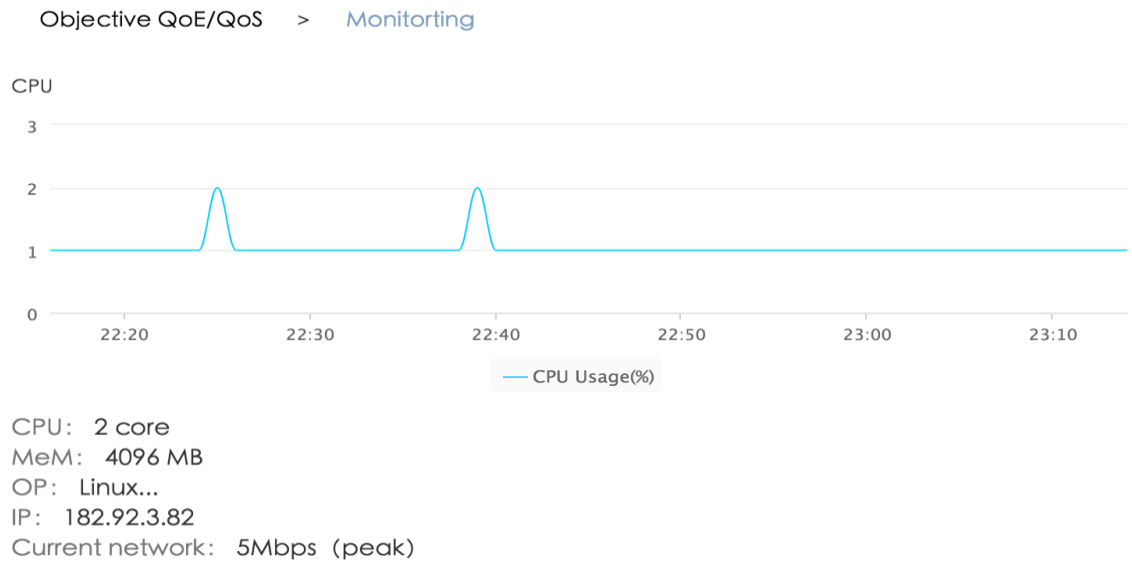


FIGURE 8. Monitoring local cloud environment.

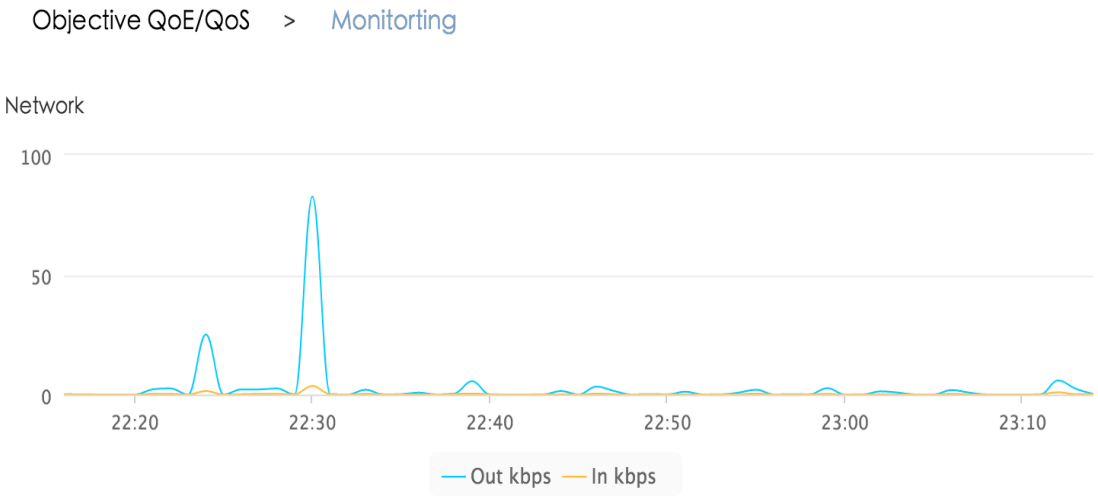


FIGURE 9. **Monitoring network environment.**

QoE/QoS also have a manual/automatic control system, in manual function administrator of cloud service provider will manage the operations for cloud management and in automatic cloud management software self-manage all operation of management like user complaint and reaction on the submitted complaints. Results of some objective QoE/QoS functions are given in Fig. 8 and Fig. 9.

The allocation of resources is provided to the user on the basis of task and previous usage pattern. For example, a user Alice always uses high computational power to process simulations for short time, so the system will manage to provide resources in the free rack where the load is minimum and the rack's internal network traffic is low for high volume data upload, which will be used in the completion of this current task. User Bob always requires low computational resources for a long time to complete his task, therefore system management will shift his resources from those racks which have less computational resources available for sharing. This approach in internal cloud management will provide better overall service to the end users. For example, if user starts the task of scientific simulation on the cloud and one hour estimated time for task completion is displayed to the user. After 50 minutes, 87% of the task is completed, but suddenly remaining time of the task is increased due to the increased traffic load on the network. The task of the user is still running on the cloud and the prepaid resources will finish after 5 minutes. The estimated time for task completion is still 40 minutes with 100% utilization of computation resources from cloud side. In this situation, cloud will provide additional time automatically for the task and it will be finished with flexible SLA. In this example, if strict SLA were to be applied, it will cause loss of 87% completed task together with uploaded data and these types of strict policies will force the user to migrate from the current provider.

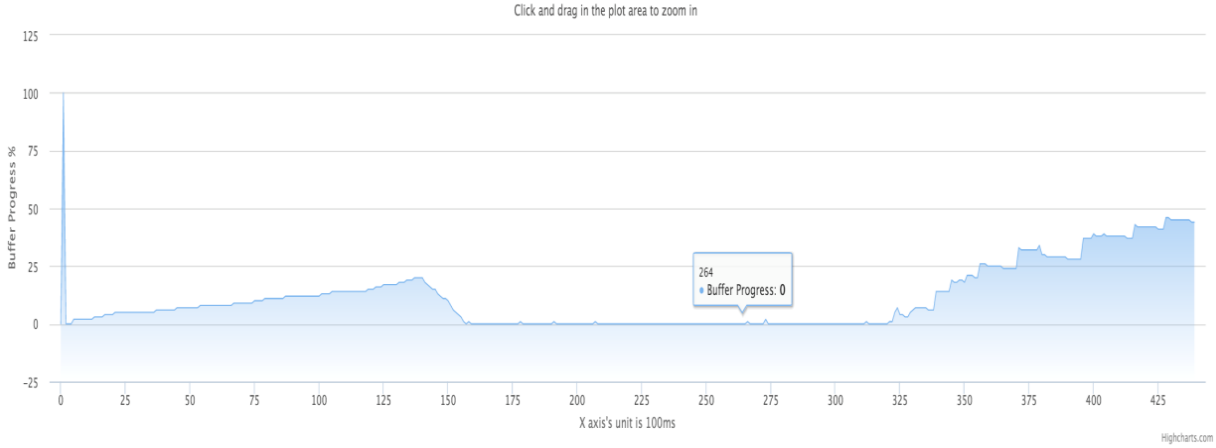


FIGURE 10. **Test sample 1.**

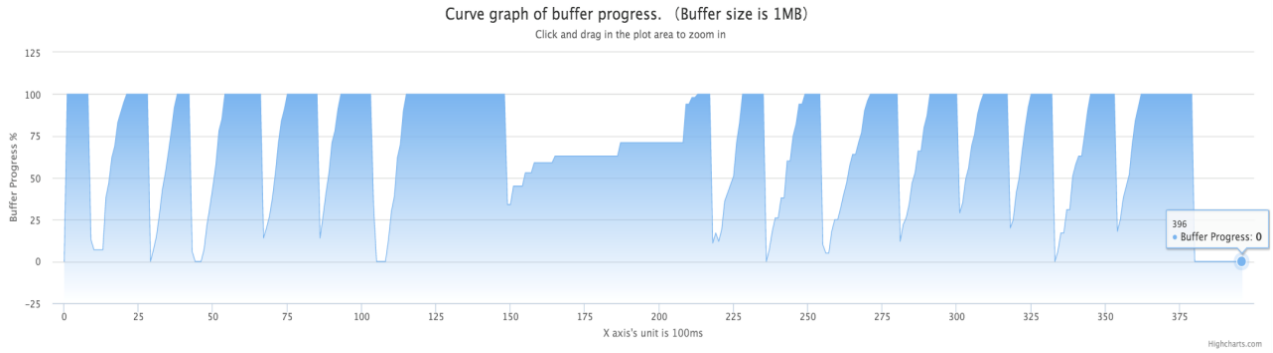


FIGURE 11. Test sample 2.

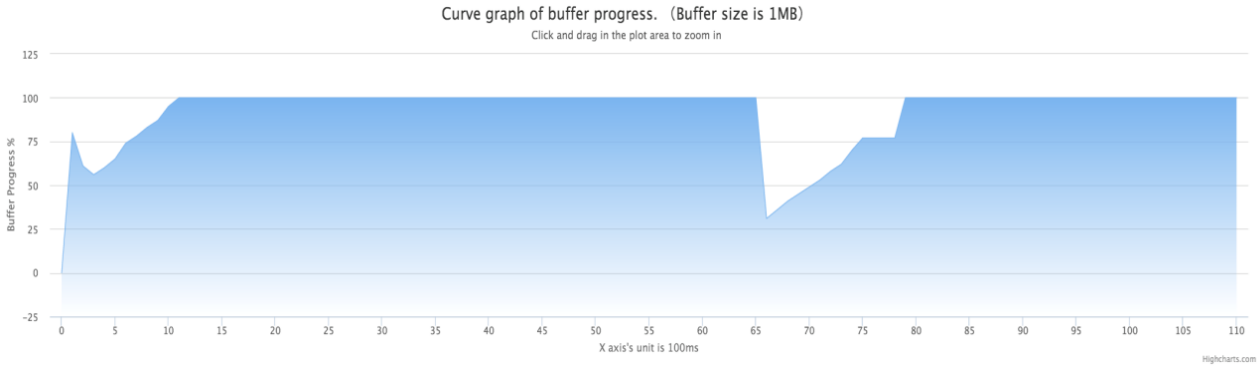


FIGURE 12. Test sample 3.

C. MOBILE USER PERFORMANCE EXPERIMENTS

Mobile user performance was measured on different network conditions where speed limits are applied and here are the three test samples (1, 2, 3) are given in Figs. 10, 11 and 12.

The first test sample is in the limit speed under the condition of the test curve and buffer is full of proportion to 0%, plays with severe video Caton. The second test sample is in normal condition under the network environment but the user frequently switches playing time point of the curve test, switch to a play between the need of re-buffer, the buffer is full of 43%, video playback is not smooth. The third test sample is normally played test results and buffer is full of proportion was 78%, smooth video playback. So through the analysis of the buffer curves can be a certain degree of response to user's playback quality of experience, and the buffer is full of proportion can direct response the user's Caton.

VII. CONCLUSION AND FUTURE WORK

We have designed and developed a QoC framework for cloud services based on the agent technology for measuring user QoE and found the QoS according to SLA, thus, avoiding violation of SLA. The QoC framework provides web interface facility for the user to manage their information, upload and share videos with HD quality among their friends via QoC cloud and social media. The QoC framework provides feedback form for submission of user complaint and their experience when using services. Subjective QoE part will also extract the device information of user and battery status if using cloud services via mobile phone or laptop. The framework also reads the buffer information of user device and measure the network speed and type of the network. The management platform is administrative part of QoC framework, which provides user interface facility to the administrator for management of cloud. The feedback, QoS data and reports of subjective QoE are submitted by the end user. The objective QoE/QoS part forms the management platform, which is only visible for the administrator of the cloud, collects QoS data such as monitoring the internal environment for computational and network resources. The QoC framework captures both subjective and objective QoE in runtime environment, analyze the captured QoE and change policy, if service degradation problem in internal cloud environment is found. In comparison with existing cloud frameworks, the proposed QoC framework provides functionality to monitor entire environment from cloud to end user's device, collect QoS data using agents and store in database for analysis of service according to SLA. The QoC automatically upgrades the policy of user in runtime and extend package limitation for task completion avoiding negative experience with users thus preventing migration to different platform of competitors.

In the future, we will design and develop image and file hosting facility in QoC framework and test the user experience for quality and size of images. The database file hosting and SaaS applications will also be embedded for online database operations. This is ongoing research work with academia and industry and the results of performance of

objective metrics, such as video quality metric (VQM) and peak signal to noise ratio (PSNR), in assessing the provided video quality will be presented in the future.

Acknowledgment: The work is supported by the National Key R&D Program of China under grant No. 2017YB0801801, the National Science Foundation of China (NSFC) under grant No. 61472108.

REFERENCES

[1] D. Culibrk, M. Mirkovic, P. Lugonja and V. Crnojevic, "Mining web videos for video quality assessment," Soft Computing and Pattern Recognition (SoCPaR), 2010 International Conference of, Paris, 2010, pp. 75-80.
[2] D. Jain, S. Agrawal, S. Sengupta, P. De, B. Mitra and S. Chakraborty, "Prediction of quality degradation for mobile video streaming apps: A case study using YouTube," 2016 8th International Conference on Communication Systems and Net-works (COMSNETS), Bangalore, 2016, pp. 1-2.
[3] S. Schmiedeke, P. Kelm and T. Sikora, "DCT-based features for categorisation of social media in compressed domain," Multimedia Signal Processing (MMSP), 2013 IEEE 15th International Workshop on, Pula, 2013, pp. 295-300.
[4] J. He, D. Wu, Y. Zeng, X. Hei and Y. Wen, "Toward Optimal Deployment of Cloud-Assisted Video Distribution Services," in IEEE Transactions on Circuits and Systems for Video Technology, vol. 23, no. 10, pp. 1717-1728, Oct. 2013.
[5] A. Ahmed, A. H. Abdullah, O. Kaiwartya, Y. Cao, M. J. Usman, S. Kumar, D. K. Lobiyal, and R. S. Raw. "Cloud Computing in VANETs: Architecture, Taxonomy, and Challenges." IETE Technical Review (2017): 1-25.
[6] V. C. Emeakaroha, T. C. Ferreto, M. A. S. Netto, I. Brandic and C. A. F. De Rose, "CASViD: Application Level Monitoring for SLA Violation Detection in Clouds," IEEE 36th Annual Computer Software and Applications Conference, Izmir, 2012, pp. 499-508.
[7] N. Samet, A. Ben Letaïfa, M. Hamdi and S. Tabbane, "Toward Quality of Experi-ence models of cloud-based mobile services," 2015 International Wireless Commu-nications and Mobile Computing Conference (IWCMC), Dubrovnik, 2015, pp. 1510-1514.
[8] A. A. Laghari, H. Hui, M. Shafiq, A. Khan, "Assessment of quality of experience (QoE) of image compression in social cloud computing‖", International Journal of Multiagent and Grid Systems, vol. 14, no. 2, 2018, DOI 10.3233/MGS-180284.
[9] A. Ahmed, A., A. H, Abdul, O Kaiwartya. M. J. Usman, and S. O. A. Rehman "Mobile Cloud Computing Energy-aware Task Offloading (MCC: ETO)." In Proceedings of the Communication and Computing Systems: Proceedings of the International Conference on Communication and Computing Systems (ICCCS 2016), p. 359. 2017.
[10] K. Alhamazani; R. Ranjan; P. P. Jayaraman; K. Mitra; F. Rabhi; D. Georgakopou-los; L. Wang, "Cross-Layer Multi-Cloud Real-Time Application QoS Monitoring and Benchmarking As-a-Service Framework," in IEEE Transactions on Cloud Computing , vol.PP, no.99, pp.1-1
[11] http://cloudessa.com/products/cloudessa-radius-service/
[12] S. M. Abdulhamid,, M. S. A. Latiff, and M. B. Bashir. "On-demand grid provi-sioning using cloud infrastructures and related virtualization tools: a survey and taxonomy." arXiv preprint arXiv: 1402.0696 (2014).
[13] S. M. Abdulhamid,, M. S. A. Latiff, and M. B. Bashir. "Scheduling techniques in on-demand grid as a service cloud: a review." Journal of Theoretical & Applied Information Technology 63, no. 1 (2014).
[14] J. K. Verma, S. Kumar, O. Kaiwartya, Y. Cao, J. Lloret, C. P. Katti, and R. Kharel. "Enabling green computing in cloud environments: Network virtualization approach toward 5G support." Transactions on Emerging Telecommunications Technologies (2018): e3434.
[15] M. Abdullahi,, and M. A. Ngadi. "Symbiotic Organism Search optimization based task scheduling in cloud computing environment." Future Generation Computer Systems 56 (2016): 640-650.
[16] M. A. Hadi, "Overview of Cloud Computing Towards to Future Net-works."International Journal of Computer Science and Innovation 2015, no. 2 (2015).
[17] A. A. Laghari, H. He, M. Shafiq, and A. Khan. "Impact of storage of mobile on quality of experience (QoE) at user level accessing cloud." In Communication Software and Networks (ICCSN), 2017 IEEE 9th International Conference on, pp. 1402-1409. IEEE, 2017.
[18] S. M. Abdulhamid,, M. S. A. Latiff, and M. B. Bashir and I. Idris. "Tasks schedul-ing technique using league championship algorithm for makespan minimiza-tion in IAAS cloud." arXiv preprint arXiv:1510.03173(2015).
[19] https://aws.amazon.com/what-is-cloud-computing/
[20] S. H. H. Madni, M. S. A. Latiff, and Y. Coulibaly. "Recent advancements in re-source allocation techniques for cloud computing environment: a systematic review." Cluster Computing (2016): 1-45.
[21] X. Wang, T. Kwon, Y. Choi, H. Wang and J. Liu, "Cloud-assisted adaptive video streaming and social-aware video prefetching for mobile users," in IEEE Wireless Communications, vol. 20, no. 3, pp. 72-79, June 2013.
[22] K. Alhamazani,, R. Ranjan, P. P. Jayaraman, K. Mitra, M. Wang, Z. G. Huang, L. Wang, and F. Rabhi. "Real-Time QoS Monitoring for Cloud-Based Big Data Analytics Applications in Mobile Environments," IEEE 15th International Confer-ence on Mobile Data Management, Brisbane, QLD, 2014, pp. 337-340.
[23] T. Taleb and A. Ksentini, "Follow me cloud: interworking federated clouds and distributed mobile networks," in IEEE Network, vol. 27, no. 5, pp. 12-19, Septem-ber-October 2013.
[24] P. M. Costa, J. Pitt, J. Falcão e Cunha, and T. Galvão, "Cloud2Bubble: Enhancing Quality of Experience in Mobile Cloud Computing Settings", Proceedings of the Third ACM Workshop on Mobile Cloud Computing and Services, New York, NY, USA, 2012, pp. 45–52.
[25] S. Wang and S. Dey. "Cloud mobile gaming: modeling and measuring user experience in mobile wireless networks." ACM SIGMOBILE Mobile Computing and Communications Review 16, no. 1 (2012): 10-21.
[26] A. A. Laghari, I. H. Sadhayo, and M. I. Channa. "Enhanced autonomic network-ing management architecture (enama)." engineering, science & technology: volume 14, no. 1, Jan – June 2015. pp. 9.
[27] A. Laghari, H. He, M. Ibrahim, and S. Shaikh. "Automatic Network Policy Change on the Basis of Quality of Experience (QoE)." Procedia Computer Sci-ence 107 (2017): 657-659.
[28] A.A Laghari, K. R. Laghari, M. I. Channa, and T. H. Falk. "QON: Quality of expe-rience (QoE) framework for network services." International Conference on Software Technology and Engineering (ICSTE 2012). ASME Press, 2012.
[29] A. A. Laghari,, H. He, S. Karim, H. A. Shah, and N. K. Karn. "Quality of Experi-ence Assessment of Video Quality in Social Clouds." Wireless Communications and Mobile Computing (2017).
[30] A. Laghari,, H. He, S. Zardari, and M. Shafiq. "Systematic Analysis of Quality of Experience (QoE) Frameworks for Multimedia Services." IJCSNS 17, no. 5 (2017): 121.
[31] www.witbe.net
[32] www.qoesystems.com
[33] A. A, Laghari,, H. He, M. Shafiq, and A. Khan. "Assessing effect of Cloud dis-tance on end user's Quality of Experience (QoE)." In Computer and Communica-tions (ICCC), 2nd IEEE International Conference on, pp. 500-505. IEEE, 2016.
[34] L. Farhan, R. Kharel, O. Kaiwartya, M. Hammoudeh, and B. Adebisi, "Towards green computing for Internet of things: Energy oriented path and message scheduling approach," Sustainable Cities and Society, vol. 38, pp. 195-204, 2018.
[35] K. Adhikari, S. Tatinati, W. T. Ang, K. C. Veluvolu, and K. Nazarpour, "A quaternion weighted Fourier linear combiner for modeling physiological tremor," *IEEE Transactions on Biomedical Engineering*, vol. 63, no. 11, pp. 2336-2346, 2016.

[36] Mascolo. "The Power of Mobile Computing in a Social Era," in Internet Compu-ting, IEEE , vol.14, no.6, pp.76-79, Nov.-Dec. 2010.
[37] M. J. Schop, P. Laura, M. Neill, K. Carl, I. Foster, M. D'Arcy, and A. Chervenak. "Monitoring the grid with the Globus Toolkit MDS4." In Journal of Physics: Confer-ence Series, vol. 46, no. 1, p. 521. IOP Publishing, 2006.
[38] https://support.hyperic.com/display/SIGAR/Home.

Biographies of Authors.



Asif Ali Laghari received the B.S. degree in Information Technology from the Quaid-e-Awam University of Engineering Science and Technology Nawabshah, Pakistan, in 2007 and Master degree in Information Technology from the QUEST Nawabshah Pakistan in 2014. From 2007 to 2008, he was a Lecturer in the Computer and Information Science Department, Digital Institute of Information Technology, Pakistan. In 2015, he joined the school of the Computer Science & Technology, Harbin Institute of Technology, where he is now a PhD student. He has published more than 10 technical articles in scientific journals and conference proceedings. His current research interests include Computer networks, cloud computing, and multimedia QoE management.



He Hui is born in 1974. Dr., associate professor, doctoral tutor. IEEE & IEEE Computer Member, China Computer Society, ACM Association. Harbin Institute of Technology School of computer science and technology. Mainly engaged in computer network, network measurement and simulation, network active defense technology, mobile network security, cloud computing, migration learning and so on. Presided over or participated in the national network information security project key projects,

Asiya Khan received the B.Eng. degree (Hons) in electrical and electronic engineering from the University of Glasgow, Glasgow, U.K., in 1992, the M.Sc. degree in communication, control, and digital signal processing from Strathclyde University, Glasgow, in 1993, and the Ph.D. degree in multimedia communication from the University of Plymouth, Plymouth, U.K. currently Dr. Asiya Khan is a lecturer in Control Systems Engineering, School of Engineering, University of Plymouth, Plymouth United Kingdom.
She worked with British Telecommunication Plc from 1993 to 2002 in a management capacity developing various



products and seeing them from inception through to launch. She has been Research Assistant in Perceived QoS Control for New and Emerging Multimedia Services (VoIP and IPTV)–FP7 ADAMANTIUM project at the University of Plymouth. She has published several papers in international journals and conferences. Her research interests include video quality of service over wireless networks, adaptation, perceptual modeling, and content-based analysis.



Dr. N. Kumar received his M.Tech in Computer Science and Technology from School of Computer and System Sciences of Jawaharlal Nehru University (JNU), New Delhi, India in 2012. He has also received his PhD from JNU in 2015. Formerly, he has worked as an assistant professor at Shri Mata Vaishno Devi University (SMVDU), Jammu & Kashmir, India. Later, he has been appointed as an assistant professor at the department of Computer Engineering, Delhi Technological University (Formerly known as Delhi College of Engineering), Delhi, India. Currently, He is working as an assistant professor in Indian Institute of Information Technology and Management (IIITM) Gwalior, India. His research interest includes HPC (Parallel & Distributed Computing, Grid Computing, Green Computing, GPU), Evolutionary Computation, Cloud Computing, Parallel Algorithms.



Dr Rupak Kharel is currently working as a Senior Lecturer in School of Engineering. He joined the school in July 2011. He has over 10 years of experience in the field of academics, R&D and software design. He received his PhD in Secure Communication Systems and MSc in Optoelectronic and Communication systems from North Umbria University, UK in 2011 and 2007 respectively. He obtained his B.Eng degree in Computer Engineering from Institute of Engineering, Pulchowk Campus, Tribhuvan University, Nepal in 2004.
He has worked on several commercial projects and have provided consultancy in software design and architecture.
His research interests are in the field of cyber security challenges especially in IoT and smart cities, smart m-health applications using biosensors, Energy efficient IoT networks, wireless sensor networks, satellite networks.

Analog Integrated Circuits and Signal Processing
https://doi.org/10.1007/s10470-018-1315-1

MIXED SIGNAL LETTER

Realization of a higher fractional order element based on novel OTA based IIMC and its application in filter

Rakesh Verma[1] · Neeta Pandey[1] · Rajeshwari Pandey[1]

Received: 5 August 2017 / Revised: 15 April 2018 / Accepted: 20 August 2018
© Springer Science+Business Media, LLC, part of Springer Nature 2018

Abstract
This paper presents higher order fractional element using the concept of impedance inverter circuit based on operational transcoductance amplifier (OTA). Firstly the concept of OTA impedance inverter is generalized in fractional domain which is followed by presentation of novel OTA based inverted impedance multiplier circuit (IIMC) and its generalization. Effect of OTA parasites on performance of proposed IIMC is also presented. The usefulness of the proposal is illustrated through implementation of fractional order filter of higher order using IIMC. The functional verification of all proposed circuits is done through SPICE simulations using 0.18 μm TSMC CMOS technology parameter. The fractional capacitors of orders 0.2 and 0.5 are realized using truncated infinite order domino RC ladder network and are considered for all simulations in this work. The proposed IIMC is experimentally verified through hardware prototyping using LM 13600N dual OTAs IC. The simulation and experimental results corroborate with theoretical prepositions.

Keywords OTA · Impedance multiplier · Fractional order · Filter

1 Introduction

The inherent capability of fractional order system (FOS) in modeling physical phenomenon more accurately has attracted researchers' interest in developing variety of applications pertaining to biomedical instrumentation [1, 2], control systems [3–6], signal processing and generation [7–9]. These applications use fractional order elements (FOE) whose impedance is $Z(s) = as^{\alpha}$ [10] (α-fractional order of FOE). The FOE with positive fraction represents fractional inductor (FI) while those with negative fraction correspond to FC. Research on hardware realization of FOE [11–16] is still in nascent stage and variety of approximations such as Oustaloup Recursive approximation [17], Carlson approximation [17], Matsuda approximation [17], Chareff approximation [17], Continued Fraction Expansion (CFE) [17], Modified Oustaloup [18] and El-Khazali reduced order approximations [19] are available in literature to emulate the behavior of FOE specially FC with $\alpha < 1$ through a semi-infinite RC tree in [10] or by other combinations of RC ladder networks [5] such as cross RC ladder network, domino ladder etc.

The FOE with non-integer fractional value > 1 (order alteration) is useful element in designing of higher order FOS. A detailed comparison of active/passive FOFs [11, 15, 20–37] which use reconfigured fractional order (FO) impedance emulator/on chip fabricated FOE/order adjustment by electronic tuning/and/or are experimentally verified is placed in Table 1. The literature survey shows that two techniques—generalized impedance converter (GIC) [11, 15, 20–26] and fractional stepping [27–34] are available for order alteration. The former approach is detailed in [24] in general form where the type/order of FOE is varied by selecting appropriate passive component used therein and it can provide FO variation in range $0 < \alpha \leq 2$ where α represents fractional order. The structures reported in [11, 15, 20–23, 25, 26] may be viewed as specific cases discussed in [24]. The later approach is based

✉ Neeta Pandey
n66pandey@rediffmail.com

Rakesh Verma
dce.rkverma@gmail.com

Rajeshwari Pandey
rajeshwaripandey@gmail.com

[1] Department of Electronics and Communication Engineering, Delhi Technological University, Bawana Road, Delhi 110042, India

Published online: 27 August 2018

Table 1 Detailed comparison of active/passive FOFs

Ref. no.	Active/passive elements	Realized filter	Hardware implementation	Reconfigurable FO impedance emulator		Silicon fabricated packaged FOE	Electronic tuning of FOE/FOF
				Used Structure	Reconfigured order		
[11]	Passive	FO parallel $RL_{1+\beta}C_{\alpha}$ resonator and filter	Y	GIC	FI order $1 < 1 + \beta < 2$	PMMA* coated FC	NA
[12]	Op-amp	FO Tow–Thomas biquad	Y	NA		Y	NA
[14]	Op-amp	FO KHN filter	Y	NA		PMMA* coated FC	NA
[15]	OTA	NA	Y	Series and parallel CPE emulator	Mixed order FO impedance using CPE emulator of order $0 < \alpha < 1$	Fabricated CPE emulator chip	Y
[16]	OTA	Low pass filter (LPF) having fractional order step	Y	NA		NA	NA
[20]	Passive	Series $RL_{\alpha}C_{\beta}$	Y	GIC	FI order $0 < \alpha < 2$	NA	NA
[21]	Op-amp	KHN and Sallen–Key	Y	GIC	FI order $0 < \alpha < 2$	NA	NA
[22]	Op-amp	Sallen–Key	Y	GIC	FC order $0 < \alpha < 2$	NA	NA
[23]	Second generation current conveyor (CCII)	Fractional order LPF (FLPF)	Y	GIC	FC order $0 < \alpha < 2$	NA	NA
[24]	Op-amp	NA	Y	GIC	Four quadrant CPE (Fractor) having order $-2 < \alpha < 2$	NA	NA
[25]	Passive	Series $RL_{1+\beta}C_{\alpha}$	Y	GIC	FI order $1 < 1 + \beta < 2$	NA	NA
[26]	Passive	FO Series $RL_{\beta}C_{\alpha}$ resonator and filter	NA	GIC	FI order $0 < \beta < 2$	NA	NA
[27]	OTA	Fractional step filter using FLF topology	NA	FLF	FOE order $0 < \alpha < 1$	NA	Y
[28]	OTA	Fractional step filter using IFLF topology	NA	IFLF	FOE order $0 < \alpha < 1$	NA	Y
[29]	Differential difference current conveyor (DDCC)	Fractional step filter using IFLF topology	NA	IFLF	FOE order $0 < \alpha < 1$	NA	NA
[30]	OTA	IFLF filter based on voltage excited CPE	NA	IFLF	FOE order $0 < \alpha < 1$	NA	Y
[31]	OTA	IFLF filter based on current excited CPE emulator	NA	IFLF	FOE order $0 < \alpha < 1$	NA	Y
[32]	Op-amp	Higher order filters with fractional stepping	Y	FLF	FOE order $0 < \alpha < 1$	NA	NA
[33]	Current feedback operational amplifier (CFOA)	LPF having fractional order step	Y	FLF	FOE order $0 < \alpha < 1$	NA	NA

Table 1 continued

Ref. no.	Active/passive elements	Realized filter	Hardware implementation	Reconfigurable FO impedance emulator		Silicon fabricated packaged FOE	Electronic tuning of FOE/FOF
				Used Structure	Reconfigured order		
[34]	Nonlinear tranconductance cell	FO-companding Filter	NA	FLF	FOE order $0 < \alpha < 1$	NA	Y
[35]	Op-Amp	FO-inverse Chebyshev LP filter on multiple input biquad	Y	NA		NA	NA
[36]	Op-Amp	High Q and asymmetric—FO band pass filter (FBPF)	Y	NA		NA	NA
[37]	CCII OTA	FLPF and FBPF	NA	NA		NA	NA
Proposed	OTA	FO parallel $RL_{n+\alpha}$ $C_{n+\alpha}$ filter	Y	IIMC	Order $n + \alpha > 1$	NA	NA

*Poly-methyl-methacrylate

on developing functional block diagram (FBD) of FOE's transfer function for given fractional order using follow the ladder feedback (FLF)/inverse follow the ladder feedback (IFLF) topology. This method is used for realizing tunable order FOE ($\alpha < 1$) and is used in various circuits such as differentiator [16, 30, 31], integrator [15, 16, 31], FC [30, 31], FI [31] for characterization of constant phase emulator (CPE) and develops α order low-pass (LP) [16, 30], $(1 + \alpha)$ order LP [32, 34], high-pass (HP) [27] and higher order fractional step filters [32, 34]. To the best of authors' knowledge, no fundamental element increasing into higher order for designing higher order FO circuits is available in open literature. Therefore, this paper puts forward an approach for order alteration $(n + \alpha)$ of FOE using FC of a specific order (α).

The proposed approach of order alteration is based on IIMC designed around OTA [38]. It adds electronic tunability to the magnitude of FOE thereby making it an attractive choice for higher order FOS realization. The remaining paper is arranged as follows: Sect. 2 entails generalization of OTA based impedance inverter in fractional domain. An OTA based IIMC and its generalization in fractional domain is proposed for approximating higher order FOE. SPICE simulations and experimental results for performance evaluation are also included in this section. Higher order FOF based on parallel resonator is presented in Sect. 3 wherein proposed fractional order IIMC (FO-IIMC) is used for emulating higher order FOE. The functional verification of the higher order FOF is put forward in Sect. 4. Conclusions are drawn in Sect. 5. The paper also includes Appendix 1 for examination of effect of OTA parasites on proposed IIMC performance.

2 Proposed OTA based IIMC

In this work a novel approach for order alteration is put forward. Operational transconductance amplifier (OTA) is used to illustrate the proposal due to its distinctive feature of providing electronic tunability to the application developed around it [39–42]. An OTA based impedance inverter is generalized in fractional domain first which is followed by proposed OTA based IIMC and its generalization in fractional domain.

2.1 Generalization of OTA based impedance inverter

The schematic of OTA based impedance inverter [38] is shown in Fig. 1(a). The input impedance of the circuit is given as

$$Z_{in} = \frac{1}{g_{m1}g_{m2}Z_1} \tag{1}$$

where g_{m1} and g_{m2} correspond to transconductances of OTA1 and OTA2 respectively.

The circuit of Fig. 1(a) can be generalized to fractional domain by replacing Z_1 by $Z_{1\alpha} = 1/s^{\alpha}C_{\alpha}$ where $Z_{1\alpha}$

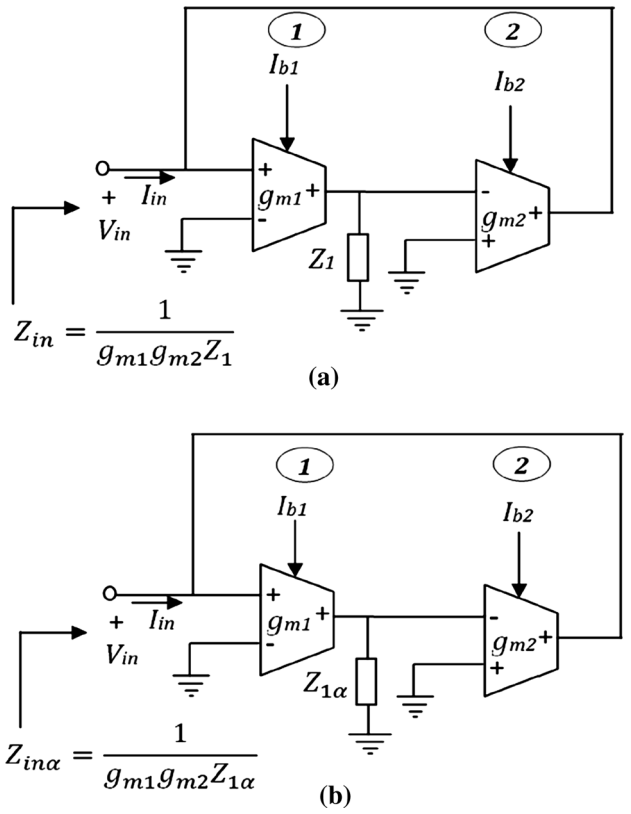


Fig. 1 OTA based **a** impedance inverter circuit [24] and **b** generalization in fractional domain

represents FO impedance of order α. Figure 1(b) shows the resulting circuit and its input impedance is expressed as

$$Z_{in\alpha} = \frac{1}{g_{m1}g_{m2}Z_{1\alpha}} \tag{2}$$

For FC as $Z_{1\alpha}$, the input impedance is expressed as

$$Z_{in\alpha} = \frac{s^{\alpha}C_{\alpha}}{g_{m1}g_{m2}} \tag{3}$$

which corresponds to FI of order α.

2.2 Proposed impedance inverter multiplier

The OTA based IIMC is shown in Fig. 2. It uses (n + 1) OTAs and n impedances. The input impedance of IIMC is given by

$$Z_{in-IIMC} = \frac{1}{g_{m0}(g_{m1}g_{m2}\ldots g_{mn})(Z_1Z_1\ldots Z_n)} \tag{4}$$

For $Z_i = 1/sC_i$ (i = 1, 2, …,n), the input impedance of (4) becomes

$$Z_{in-IIMC} = \frac{s^nC_1C_2\ldots C_n}{g_{m0}(g_{m1}g_{m2}\ldots g_{mn})} \tag{5}$$

Generalizing the IIMC in fractional domain by replacing Z_1 by FC of order α and keeping other capacitances as integer order (normal) modifies (5) to

$$Z_{in-IIMC(n-1+\alpha)} = \frac{s^{n-1+\alpha}C_{1\alpha}C_2\ldots C_n}{g_{m0}(g_{m1}g_{m2}\ldots g_{mn})} \tag{6}$$

Equation (6) presents input impedance of FI of order (n-1 + α) and its pictorial representation is given in Fig. 3. To realize fractional capacitor of same order the circuit of Fig. 1(b) is used.

Comparison of the presented scheme with the available ones yields in the following points:

- The FOE reported in [24] uses GIC structure and realizes fractors of order less than 2 only. Thus this method gives limited order alteration in higher domain.
- Higher order fractional step filters are realized by emulation of any FOE of order α ($0 < \alpha < 1$) using FLF/IFLF topology. Again order alteration of FOE is not there for FO $\alpha > 1$.
- the presented scheme realizes 1 + α order FOE. Any further integer increment may be obtained by placing OTA and integer order capacitor in the loop thus leading to a modular structure.

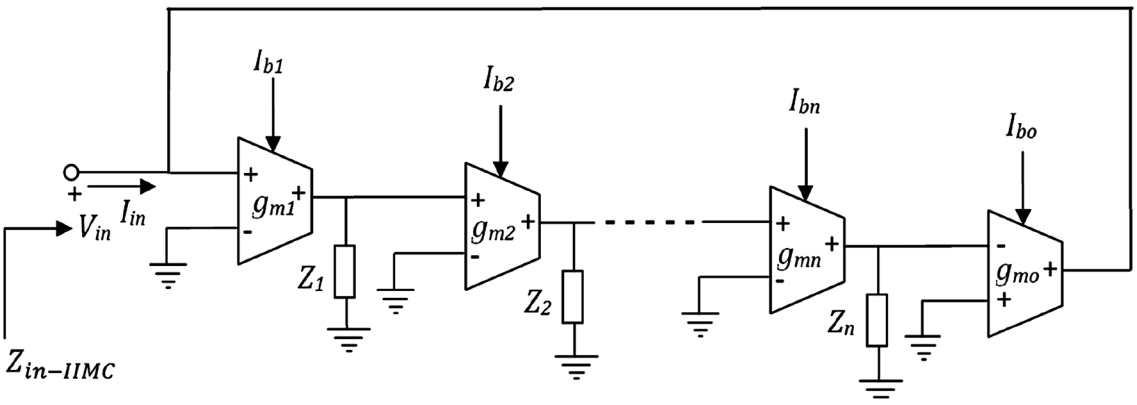


Fig. 2 OTA based IIMC

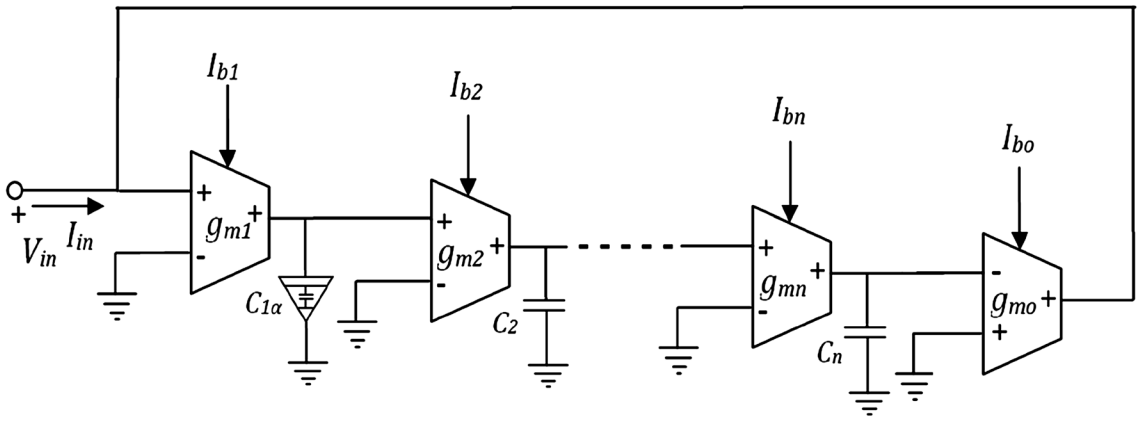


Fig. 3 Generalization of IIMC in fractional domain

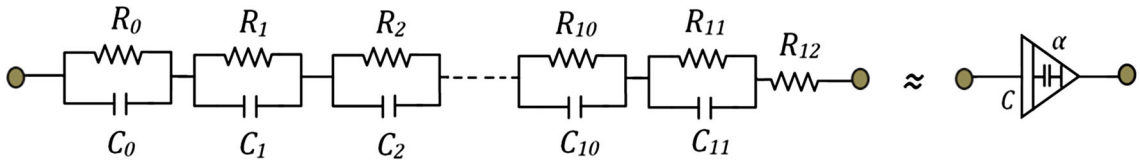


Fig. 4 Truncated RC domino ladder network realizing FC [24]

- In [24], the magnitude of FOE is varied by changing the value of one of the resistances employed in GIC. Therefore, electronic tuning of FOE's magnitude can be accomplished by electronic implementation of that resistance. In the proposed structure, magnitude variation is attained through bias current variation.

2.3 Performance evaluation

2.3.1 Evaluation through simulations

The performance of the proposal is illustrated through simulations of proposed IIMC based FI and FC wherein FC of order 0.2 and 0.5 is employed. Due to unavailability of SPICE model of FC, infinite order domino RC ladder network truncated to 12–13 numbers of blocks [24] of Fig. 4 is used to emulate the behavior of FC.

The values for Fig. 4 FC having (1) $\alpha = 0.2$ and $C_{\alpha} = 25$ µF are $R_0 = 16$ kΩ, $R_1 = 9.1$ kΩ, $R_2 = 6.6$ kΩ, $R_3 = 4.7$ kΩ, $R_4 = 3.3$ kΩ, $R_5 = 2.4$ kΩ, $R_6 = 1.8$ Ω, $R_7 = 1.5$ Ω, $R_8 = 1$ kΩ, $R_9 = 680$ Ω, $R_{10} = 470$ Ω, $R_{11} = 180$ Ω, $R_{12} = 1.1$ kΩ, $C_0 = 51.7$ µF, $C_1 = 20$ µF, $C_2 = 4.7$ µF, $C_3 = 1.33$ µF, $C_4 = 330$ nF, $C_5 = 100$ nF, $C_6 = 27$ nF, $C_7 = 8.2$ nF, $C_8 = 2.2$ nF, $C_9 = 560$ pF, $C_{10} = 150$ pF, $C_{11} = 82$ pF (2) $\alpha = 0.5$ and $C_{\alpha} = 3.75$ µF are $R_0 = 330$ kΩ, $R_1 = 82$ kΩ, $R_2 = 33$ kΩ, $R_3 = 12$ kΩ, $R_4 = 4.7$ kΩ, $R_5 = 2$ kΩ, $R_6 = 736$ Ω, $R_7 = 270$ Ω, $R_8 = 120$ Ω, $R_9 = 47$ Ω, $R_{10} = 8.2$ Ω, $R_{11} = 18.2$ Ω, $C_0 = 4.7$ µF, $C_1 = 3.1$ µF, $C_2 = 1$ µF, $C_3 = 470$ nF, $C_4 = 168$ nF, $C_5 = 68$ nF, $C_6 = 27$ nF, $C_7 = 10$ nF, $C_8 = 4.7$ nF, $C_9 = 1$ nF, $C_{10} = 2.2$ nF (R_{12} and C_{11} are not in use).

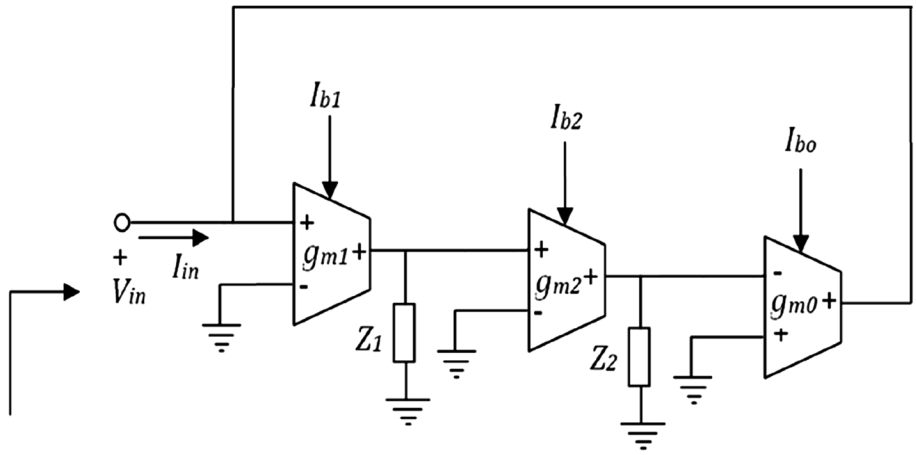
The FI and FC of order $(1 + \alpha)$ are shown in Fig. 5(a) and (b) respectively. The corresponding equivalent values of FI and FC are given as

$$L_{1+\alpha} = \frac{C_{1\alpha}C_2}{g_{m0}g_{m1}g_{m2}} \tag{7}$$

$$C_{1+\alpha} = \frac{g_{m3}g_{m4}C_{1\alpha}C_2}{g_{m0}g_{m1}g_{m2}} \tag{8}$$

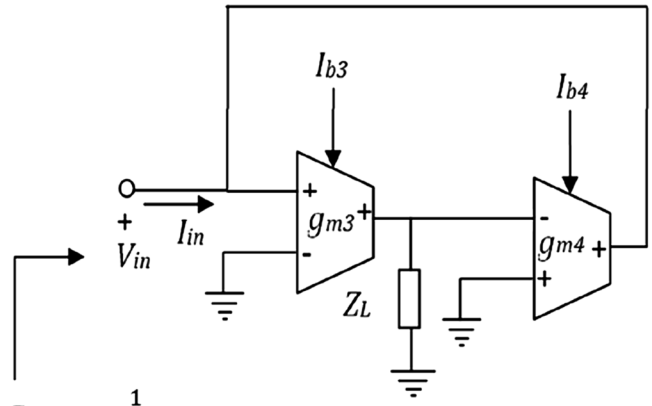
To examine the operation of proposed FI and FC (Fig. 5) of order $(1 + \alpha) = 1.2$ and 1.5, SPICE simulations are carried out by taking CMOS based schematic of OTA [42] (reproduced as Fig. 6) and TSMC process technology parameters of node 0.18 µm. The supply voltages are taken as ± 1.8 V. The aspect ratios of the transistors are

Fig. 5 Proposed IIMC based **a** FI and **b** FC of order $(1 + \alpha)$



$$\frac{s^{1+\alpha}(C_{1\alpha}C_2)}{g_{mo}(g_{m1}g_{m2})}; For\ Z_1 = 1/s^{\alpha}C_{1\alpha}\ and\ Z_2 = 1/sC_2$$

(a)



$$Z_{in} = \frac{1}{g_{m3}g_{m4}Z_L}$$

(b)

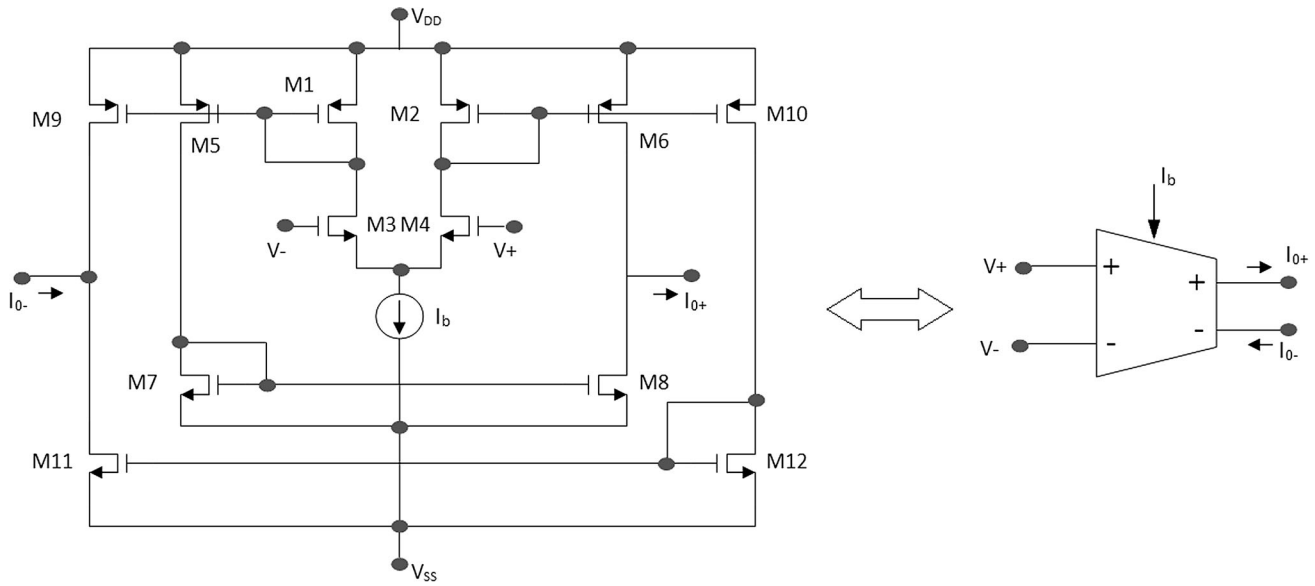


Fig. 6 CMOS realization of dual current output OTA [42]

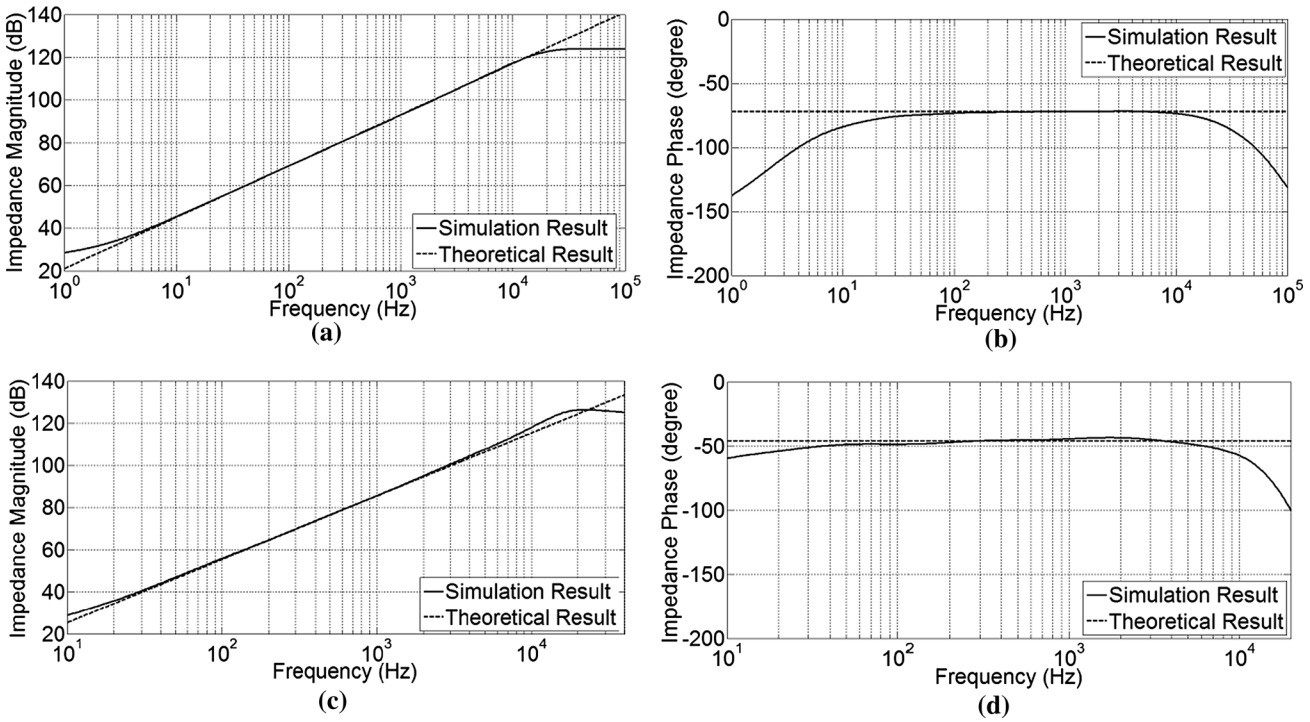


Fig. 7 Impedance responses **a**, **b** 1.2 order; and **c**, **d** 1.5 order FIs having $L_{1+\alpha} = 1.25\ \Omega/s^{1.2}$ and 37.5 $m\Omega/s^{1.5}$ respectively; **a**, **c** impedance magnitude response; **b**, **d** impedance phase response

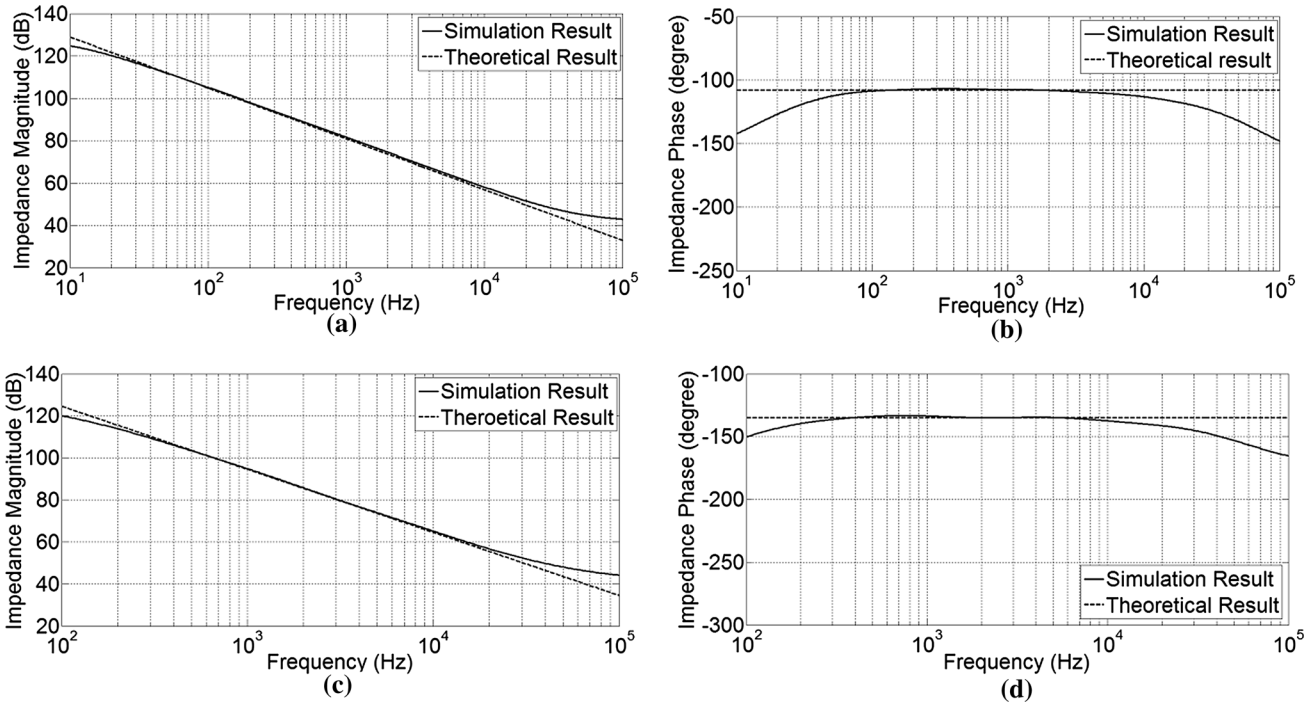


Fig. 8 Impedance responses **a**, **b** 1.2 order; and **c**, **d** 1.5 order FCs having $C_{1+\alpha} = 2.5\ n℧/s^{1.2}$ and 0.0375 $n℧/s^{1.5}$

(5.76 μm/0.72 μm), (2.16 μm/0.72 μm) and (1.44 μm/0.72 μm) for M_{3-4}, $M_{1-2,\ 5-6,\ 9-10}$ and $M_{7-8,\ 11-12}$ respectively.

The components values of circuits given in Fig. 5(a) and (b) are set such as equal transconductance gain (g_m)- = 100 μA/V, $C_{1\alpha\ (\alpha = 0.2,\ 0.5)} = 25\ \mu℧/s^{0.2}$, 3.75 $\mu℧/s^{0.5}$

Table 2 Frequency range for different FIs and FCs

Impedance response	Frequency range of operation			
	Order of FI		Order of FC	
	1.2	1.5	1.2	1.5
Magnitude	1.48 Hz–30.5 kHz	7.4 Hz–32.3 kHz	8.7 Hz–47.9 kHz	92 Hz–53.7 kHz
Phase	33.8 Hz–14.2 kHz	51.2 Hz–5.4 kHz	48.9 Hz–9.77 kHz	194 Hz–16 kHz

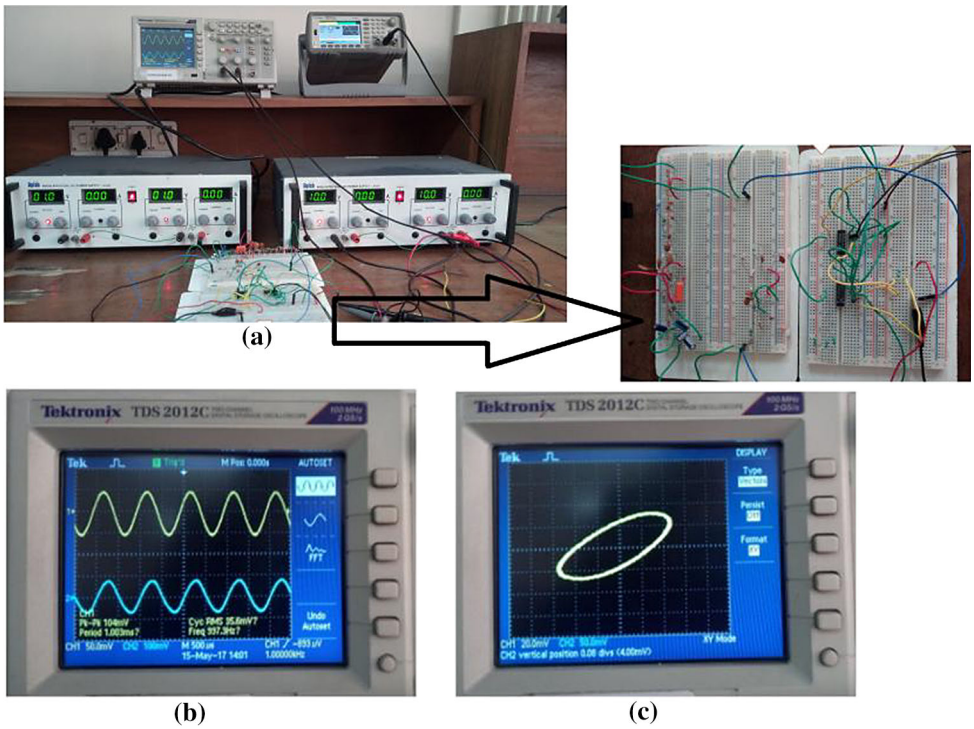


Fig. 9 **a** Hardware setup, **b** experimental results and **c** Lissajous pattern of OTA based α order FI

and the normal capacitor values C_2 of FI (FC) are 50 nF, 10 nF (10 nF, 1 nF) for $\alpha = 0.2, 0.5$ respectively.

Figures 7 and 8 show theoretical and simulated frequency responses of FI and FC of order $(1 + \alpha)$. The frequency range of operation for different FIs and FCs are summarized in Table 2 with ± 5 dB and ± 5° maximum possible deviation for impedance magnitude and phase responses respectively.

2.3.2 Evaluation through experimentation

The experimental verification of α order and $1 + \alpha$ order ($\alpha = 0.5$) FI circuits shown in Fig. 1(b) and Fig. 5(a) respectively is performed with ICs LM 13600 N (dual OTAs) using the setups depicted in Figs. 9(a) and 10(a) respectively. Here the FC of Fig. 4 is used and component values specified in Sect. 2.3 are taken.

The measurements are taken at supply voltage of ± 10 V. The transconductance gains of OTAs for FIs' order α and $(1 + \alpha)$ are set at $g_{m1} = g_{m2} = 0.393$ mA/V; and $g_{m1} = g_{m2} = 0.393$ mA/V, $g_{m3} = 0.732$ mA/V respectively. In the designing of α and $(1 + \alpha)$ order FIs, the normal capacitor of 0.47 μF is used. The responses obtained across the output capacitor of impedance inverter circuit (IIC) (Fig. 1(b)) and proposed IIMC configuration realizing FI of $(1 + \alpha)$ order (Fig. 5(a)) for sinusoidal input signal (100 mV_{pp}) are shown in Figs. 9 and 10 respectively. The Lissajous patterns also verify that FI having $1 + \alpha$ order is 90° in advance than α order. Experimental impedance phase responses of FI having $1 + \alpha$ ($\alpha = 0.5$) order is shown in Fig. 11 along with theoretical result. It may be noted that experimental impedance response of proposed FI of order 1.5 follows theoretical curve in frequency range of 50 Hz–4 kHz within ± 5° phase error band. The deviation may be attributed to the non-ideal performance of OTA as detailed in "Appendix 1".

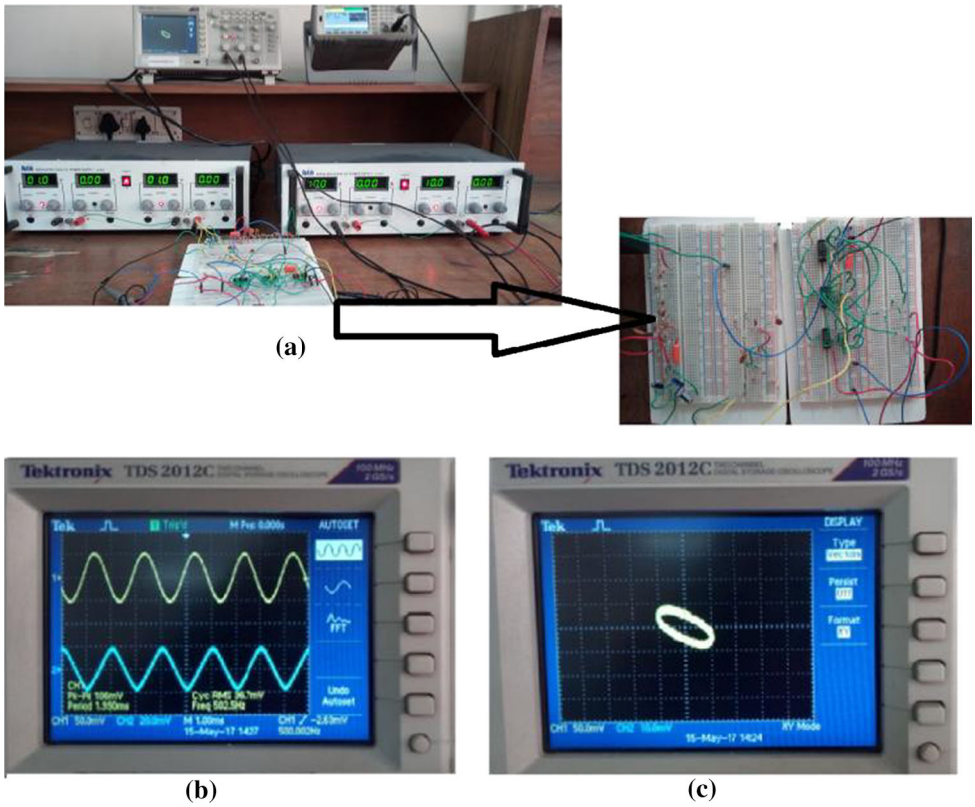


Fig. 10 **a** Hardware setup, **b** experimental results and **c** Lissajous pattern of OTA based FI having $1 + \alpha$ order

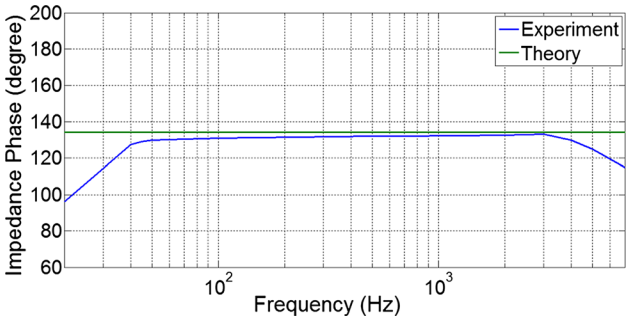


Fig. 11 Impedance phase response of FI of $1 + \alpha$ ($\alpha = 0.5$) order

2.4 Proposed higher order FOF

The proposed higher order FOF (Fig. 12) is based on parallel resonator block (PRB) wherein the inductor and capacitor of conventional PRB are replaced by FI and FC of order $(n + \alpha)$ respectively. Figure 12(b) shows OTA based realization of Fig. 12(a).

The generalized $(n + \alpha)$ order FC circuit (in Sect. 2.3) is used in designing of OTA based higher order FOF. The structure of fractional order filter (FOF) circuit (in Fig. 12 (b)) is based on the model of parallel FO $RL_{(n+\alpha)}C_{(n+\alpha)}$ circuit (in Fig. 12(a)) having current mode (CM) configuration.

The circuit analysis of Fig. 12(a) yields following filter responses:

1. Transfer function (TF) of FLPF

$$T(s)_{FLPF}^{2(n+\alpha)} = \frac{I_{FI}(s)}{I_{in}(s)} = \frac{\frac{1}{L_{n+\alpha}C_{n+\alpha}}}{s^{2(n+\alpha)} + \frac{s^{(n+\alpha)}}{RC_{n+\alpha}} + \frac{1}{L_{n+\alpha}C_{n+\alpha}}} \tag{9}$$

2. TF of FBPF

$$T(s)_{FBPF}^{2(n+\alpha)} = \frac{I_R(s)}{I_{in}(s)} = \frac{\frac{s^{(n+\alpha)}}{RC_{n+\alpha}}}{s^{2(n+\alpha)} + \frac{s^{(n+\alpha)}}{RC_{n+\alpha}} + \frac{1}{L_{n+\alpha}C_{n+\alpha}}} \tag{10}$$

3. TF of FO high pass filter (FHPF)

$$T(s)_{FHPF}^{2(n+\alpha)} = \frac{I_{FC}(s)}{I_{in}(s)} = \frac{s^{2(n+\alpha)}}{s^{2(n+\alpha)} + \frac{s^{(n+\alpha)}}{RC_{n+\alpha}} + \frac{1}{L_{n+\alpha}C_{n+\alpha}}} \tag{11}$$

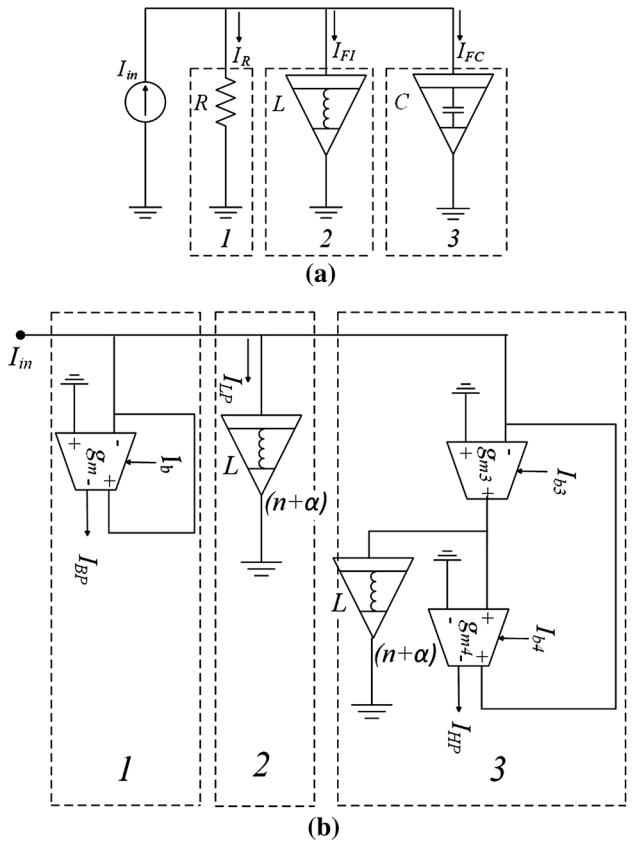


Fig. 12 **a** Higher order fractional parallel $RL_{(n+\alpha)}C_{(n+\alpha)}$ circuit and **b** its realization using OTA

2. TF of FBPF

$$T(s)_{FBPF}^{2(n+\alpha)} = \frac{I_{BP}(s)}{I_{in}(s)} = \frac{s^{(n+\alpha)}\frac{g_m}{C_{n+\alpha}}}{s^{2(n+\alpha)} + s^{(n+\alpha)}\frac{g_m}{C_{n+\alpha}} + \frac{1}{L_{n+\alpha}C_{n+\alpha}}} \tag{13}$$

3. TF of FHPF

$$T(s)_{FHPF}^{2(n+\alpha)} = \frac{I_{HP}(s)}{I_{in}(s)} = \frac{s^{2(n+\alpha)}}{s^{2(n+\alpha)} + s^{(n+\alpha)}\frac{g_m}{C_{n+\alpha}} + \frac{1}{L_{n+\alpha}C_{n+\alpha}}} \tag{14}$$

There magnitude and phase responses for proposed higher order FOF are computed as:

$$|T(j\omega)|_{FLPF} = \frac{\frac{1}{L_{n+\alpha}C_{n+\alpha}}}{|D(j\omega)|} \text{ and } \angle T(j\omega)_{FLPF} = -\tan^{-1}\theta \tag{15}$$

$$|T(j\omega)|_{FBPF} = \frac{\frac{g_m}{C_{n+\alpha}}\omega^{(n+\alpha)}}{|D(j\omega)|} \text{ and } \angle T(j\omega)_{FBPF} = \tan^{-1}((n+\alpha)\pi/2) - \tan^{-1}\theta \tag{16}$$

$$|T(j\omega)|_{FHPF} = \frac{\omega^{2(n+\alpha)}}{|D(j\omega)|} \text{ and } \angle T(j\omega)_{FHPF} = \tan^{-1}((n+\alpha)\pi) - \tan^{-1}\theta \tag{17}$$

where

$$|D(j\omega)| = \left[\begin{array}{c} \omega^{4(n+\alpha)} + 2\frac{g_m}{C_{n+\alpha}}\omega^{3(n+\alpha)}\cos\frac{(n+\alpha)\pi}{2} + \left\{\frac{g_m^2}{C_{n+\alpha}^2} + \frac{2}{L_{n+\alpha}C_{n+\alpha}}\cos(n+\alpha)\pi\right\}\omega^{2(n+\alpha)} \\ + \frac{2}{L_{n+\alpha}C_{n+\alpha}}\frac{g_m}{C_{n+\alpha}}\omega^{(n+\alpha)}\cos\alpha\pi/2 + \left(\frac{1}{L_{n+\alpha}C_{n+\alpha}}\right)^2 \end{array}\right]^{1/2} \tag{18}$$

$$\text{and } \theta = \tan^{-1}\left[\frac{\omega^{2(n+\alpha)}\sin(n+\alpha)\pi + \frac{g_m}{C_{n+\alpha}}\omega^{(n+\alpha)}\sin(n+\alpha)\pi/2}{\omega^{2(n+\alpha)}\cos(n+\alpha)\pi + \frac{g_m}{C_{n+\alpha}}\omega^{(n+\alpha)}\cos(n+\alpha)\pi/2 + \frac{1}{L_{n+\alpha}C_{n+\alpha}}}\right]$$

It may be observed from (9) to (11) that a 2(n + α) order FOF is obtained by using (n + α) order FC and FI in PRB. The corresponding responses for proposed OTA based higher order FOF are computed as:

1. TF of FLPF

$$T(s)_{FLPF}^{2(n+\alpha)} = \frac{I_{LP}(s)}{I_{in}(s)} = \frac{\frac{1}{L_{n+\alpha}C_{n+\alpha}}}{s^{2(n+\alpha)} + s^{(n+\alpha)}\frac{g_m}{C_{n+\alpha}} + \frac{1}{L_{n+\alpha}C_{n+\alpha}}} \tag{12}$$

The maximum/minimum frequency point 'ω_m' (at which gain is maximum/minimum), half power–frequency point 'ω_c' (at which power is half of pass band power) and right phase frequency 'ω_{rp}' (at which $T(j\omega)$ is pure imaginary) can be obtained by solving the equation $(d/d\omega)|T(j\omega)|_{\omega=\omega m} = 0$, $|T(j\omega_{3dB})| = (1/\sqrt{2})|T(j\omega_{passband})|$ and $\angle T(j\omega_{rp}) = \pm\pi/2$ respectively.

Table 3 Stability constraints for proposed higher order FOF

$k = \frac{4C_{n+\alpha}}{L_{n+\alpha}g_m^2}$	Stability condition	Root location in F-domain complex plane	ω_0	Q
$k \leq 1$	$(n+\alpha) < 2$	$r_{1,2} = \frac{-g_m/C_{n+\alpha} \pm \sqrt{(g_m/C_{n+\alpha})^2 - 4\left(\frac{1}{L_{n+\alpha}C_{n+\alpha}}\right)}}{2} = g_{1,2}e^{j\pi}$	$g_{1,2}^{1/(n+\alpha)}$	$\frac{-1}{2\cos\pi/(n+\alpha)}$
$k > 1$	$(n+\alpha) < 2\delta/\pi$, $\delta = \cos^{-1} -(1/\sqrt{k}) > (n+\alpha)\pi/2$	$r_{1,2} = \sqrt{\frac{1}{L_{n+\alpha}C_{n+\alpha}}}e^{\pm j\delta}$	$\left(\frac{1}{L_{n+\alpha}C_{n+\alpha}}\right)^{1/2(n+\alpha)}$	$\frac{-1}{2\cos\delta/(n+\alpha)}$

2.5 Stability analysis

The stability analysis of proposed higher order FOF is also carried out using method outlined in [43]. The stability condition, root location in F-domain (transformation of s-domain into fractional domain i.e. $s^{n+\alpha}$) complex plane, pole frequency ω_0 and quality factor Q are given in Table 3. In this work, all denominator coefficients (12), (13) and (14) are positive.

To elaborate little further, let us express the general transfer function of higher order FOF as

$$T(s) = \frac{N(s)}{s^{2(n+\alpha)} + 2as^{(n+\alpha)} + b} \tag{19}$$

where numerator N(s) will take different values according to the function type. The characteristic equation of (19) gives the pole locations at $\left\{-a \pm j\sqrt{b-a^2}\right\} = \sqrt{b}e^{\pm j\delta}$ in F-domain complex plane where $\delta = \cos^{-1}\left(-a/\sqrt{b}\right)$ (assuming all coefficients are positive and $b > a^2$ or $k = b/a^2 > 1$). The stability analysis of proposed higher order FOF is carried out by using transformation of F-plane into s-plane and comparing with a classical second order system whose poles are located at $\left\{-\omega_0/2Q \pm j\omega_0\sqrt{1-(1/4Q^2)}\right\} = \omega_0 e^{\pm j\theta}$ where $\theta = \cos^{-1}(-1/2Q)$. This comparison results in $\omega_0 = b^{1/2(n+\alpha)}$, $Q = -\frac{1}{2\cos\{\delta/(n+\alpha)\}}$ (both must be positive) and stability condition as $(n+\alpha) < 2\delta/\pi$ for higher order FOF.

3 Simulation results

The operation of proposed higher order FOF using FI and FC of order $(1+\alpha) = 1.2$ and 1.5 is examined through SPICE simulation. The CMOS based schematic of OTA [42] (Fig. 6) is used for simulations and TSMC process

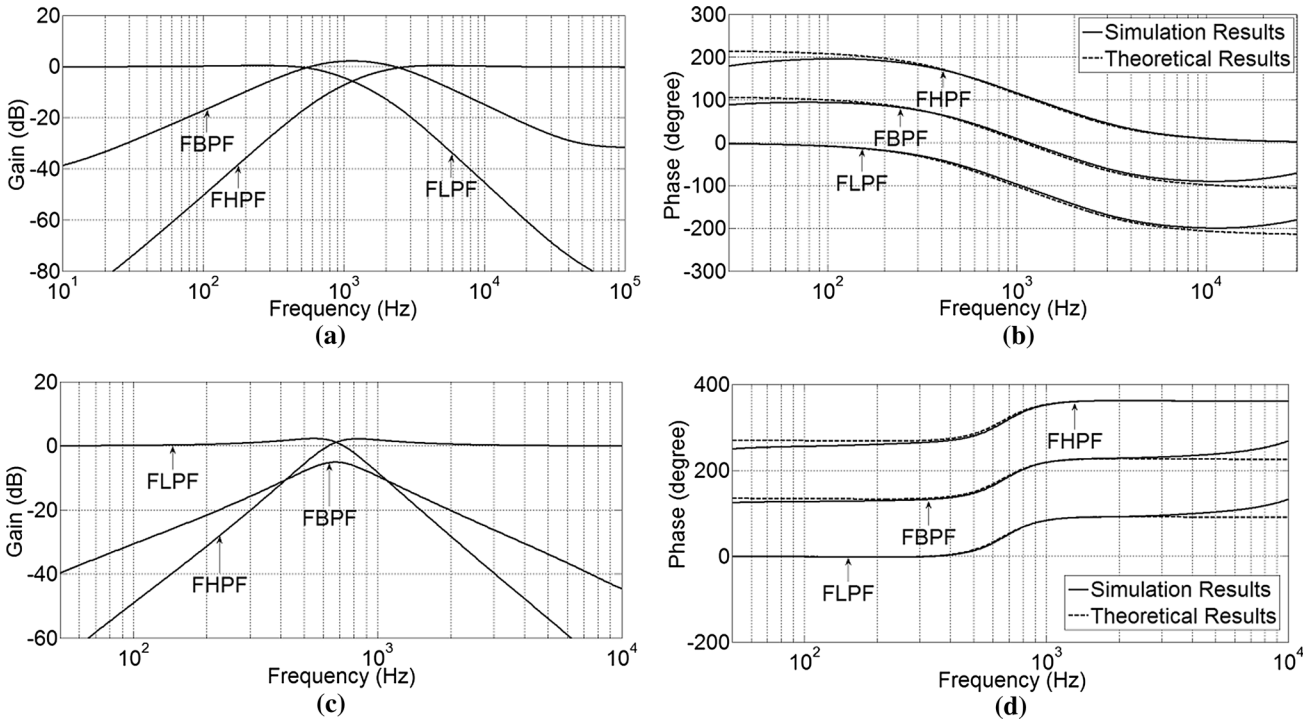


Fig. 13 Simulation frequency response of proposed FOF employing FOE of **a**, **b** 1.2 order and **c**, **d** 1.5 order

Table 4 Performance parameters for FLPF, FHPF and FBPF for order of 2(n + α)

Filter	Parameters measured	2(n + α) = 2(1.2)		2(n + α) = 2(1.5)	
		Simulation results	Theoretical results	Simulation results	Theoretical results
FLPF	Gain in pass-band frequency	0.992	1	0.998	1
	Half power frequency(Hz)	812.775	832.7	828	800
	Max/min frequency (Hz)	254	261.72	550.28	523.3
	Right phase frequency (Hz)	900	840	1.35 k	1.32 k
	Gain at max/min frequency	1.05	1.07	1.3	1.27
FHPF	Gain in pass-band frequency	0.98	1	0.994	1
	Half power frequency(Hz)	1.65 k	1.423 k	549	543.47
	Max/min frequency (Hz)	4.7 k	4.28 k	831	831.764
	Right phase frequency (Hz)	1.4 k	1.411 k	331	329.62
	Gain at max/min frequency	1.05	1.07	1.28	1.27
FBPF	Lower cut-off frequency (Hz)	519	484.72	494.735	478.14
	Higher cut-off frequency (Hz)	2.597 k	2.445 k	917.438	909.5
	Centre frequency (Hz)	1.14 k	1.09 k	676	659.37
	Right phase frequency (Hz)	192.75, 6.166 k	192.959, 6.136 k	None	None
	Gain at center frequency	1.29	1.32	0.557	0.55

technology parameters of node 0.18 μm are used. The supply voltages are taken as ± 1.8 V. In order to verify the theoretical proposition, following parameters are chosen: $g_m = 1/R = 50\mu A/V$, $L_{1+\alpha=1.2,1.5} = 0.25\ \Omega/s^{1.2}$, $37.5\ m\Omega/s^{1.5}$ and $C_{1+\alpha=1.2,1.5} = 2.5\ \mho/s^{1.2}$, $3.75\ n\mho/s^{1.5}$. The simulated and theoretical responses of proposed FOF are shown in Fig. 13 and various performances are summarized in Table 4 for FLPF, FHPF and FBPF. The simulation results for FLPF, FHPF and FBPF are found to be in close agreement with theoretical results.

Simulations are also performed to examine the stability of proposed FOF. The root-location in F-domain complex plane, pole frequency and quality factor of proposed higher order FOF are enlisted in Table 5.

The root locus technique provides stability analysis of fractional order system [44] and its graphical representation can be illustrated through W-plane transformation. The root locus of realized FLPF and FBPF having order $2(1+\alpha) = 2(1.2)$ and $2(1.5)$ respectively are plotted in Fig. 14 using forlocus function in MATLAB program. The plot of the Riemann surface has 5 and 2 Riemann sheets for order $2(1+\alpha) = 2(1.2)$ and $2(1.5)$ respectively. The boundaries of unstable region (shown by dashed dotted lines in Fig. 14) $\left\{-\pi/10 \le \arg(w)_{(1+\alpha)=1.2} \le \pi/10\right\}$ and $\left\{-\frac{\pi}{4} \le \arg(w)_{(1+\alpha)=1.5} \le \frac{\pi}{4}\right\}$ for FOFs of order 2(1.2) and

Table 5 Stability analysis

Order (n + α)	F-domain complex plane	Root location $r_{1,2}$	Pole frequency $f_{01,02}$ (Hz)	Stability condition			Quality factor Q
				(i) $\delta = \cos^{-1}\left(-\frac{1}{\sqrt{k}}\right) > (n+\alpha)\times 90^\circ$ *if* $k > 1$ (ii) $\delta = 180^\circ > (n+\alpha)\times 90^\circ$ *if* $k < 1$	$(n+\alpha) < 2\delta/\pi$	Performance	
1.2	$F = s^{1.2}$	$-2\times10^4, -8\times10^4$	610.96, 1.94 k	180° > 108°	1.2 < 2	Stable	0.577
1.5	$F = s^{1.5}$	$-6.67\times10^4 \pm j25.82\times10^4$	659.375	255.52° > 135°	1.5 < 2.839	Stable	0.507

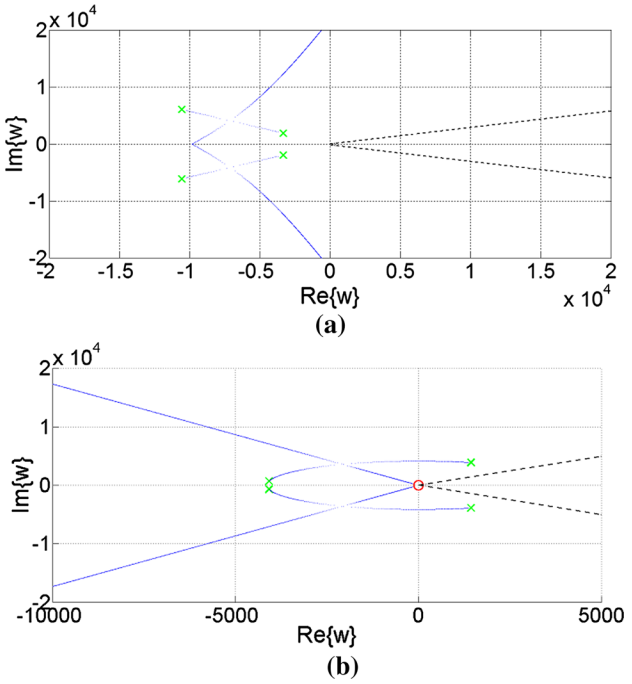


Fig. 14 Root-locus plot of **a** FLPF and **b** FBPF having order 2 (1 + α) = 2(1.2) and 2(1.5) respectively with dashed line is the unstable region

2(1.5) respectively thus confirming the stability of the said FOFs.

4 Conclusions

In this paper an approach for designing higher order fractional element has been presented. This approach is based on the concept of impedance inverter designed using OTA. In the flow of paper the concept of OTA impedance inverter of integer domain is first generalized in fractional domain by replacing the integer order capacitor by α order FC. The resulting fractional order impedance inverter is further used to propose fractional order IIMC of order (n + α). A higher order FOF is then developed as an application of the proposed IIMC. All proposed circuits are functionally verified through SPICE simulations using 0.18 μm TSMC CMOS technology parameter. The fractional capacitors (FCs) (with α = 0.2 and 0.5), are realized using truncated infinite order domino RC ladder network and are considered for all simulations in this work. The proposed IIMC is experimentally verified through hardware prototyping using LM 13600N dual OTAs IC. The simulation and experimental results are observed to be in close resemblance with theoretical prepositions.

Appendix 1

Non-ideal analysis

The OTAs have been assumed to be ideal for the development of transconductance (g_m) based higher order immitance. However the practical OTA exhibits finite output resistance ($1/g_0$) and capacitance (C_p) to ground and provides frequency dependent transconductance gain. The transconductance gain of practical OTA can be expressed by single pole model as

$$g_m = \frac{g_m}{sC_p + g_0} \tag{20}$$

Considering (20), the impedance Z_L and Z_c of Fig. 5(a) and (b) respectively become

$$Z_L = \left[g_{01} + sC_{p1} + \frac{g_{m0}g_{m1}g_{m2}}{D(s)} \right]^{-1} \tag{21}$$

$$Z_C = \left[g_{04} + sC_{p4} + \frac{g_{m4}g_{m4}}{(g_{01}+g_{04}) + s(C_{p1}+C_{p4}) + \frac{g_{m0}g_{m1}g_{m2}}{D(s)}} \right]^{-1} \tag{22}$$

where $D(s) = g_{02}g_{00} + s^{\alpha}C_{1\alpha}g_{00} + s\{g_{00}C_{p2} + g_{02}(C_{p0}+C_2)\} + s^{1+\alpha}\{C_{1\alpha}(C_{p0}+C_2)\} + s^2C_{p2}(C_{p0}+C_2)$(A4)and g_{0i} and C_{pi} $(0 \le i \le 4)$ are parasites of practical OTAs.

Thus it is clear in the non-ideal analysis of Z_L and Z_c, there is a 2nd order term $s^2C_{p2}(C_{p0}+C_2)$ added with $s^{1+\alpha}\{C_{1\alpha}(C_{p0}+C_2)\}$ (choosing high value of C_2 or $C_{1\alpha}$ or both will reduce the parasitic effect). The second order equation is independent on the value of $C_{1\alpha}$. But the least value of C_2 will reduce the non-ideal performance in the high frequency region, however it introduces non-ideal performance in the low frequency region (because of an additional term of $s^{\alpha}C_{1\alpha}g_{00}$) and this term is dependent on the α order FC, therefore in the low frequency region, the higher order $C_{1\alpha}$ approximation model may provide much better performance.

References

1. Geddes, L. A., & Baker, L. E. (1989). *Principles of applied biomedical instrumentation* (3rd ed.). Chichester: Weily.
2. Faria, A. C., Veiga, J., Lopes, A. J., & Melo, P. L. (2016). Forced oscillation, integer and fractional-order modeling in asthma. *Computer Methods Programs in Biomedicine, 128,* 12–26.
3. Chen, Y. Q., Petras, I., & Xue, D. (2009). Fractional order control: A tutorial. In *Proceeding American control conference (ACC)* (pp. 1397–1411).
4. Dorcak, L., Valsa, J., Gonzalez, E., Terpak, J., Petras, I., & Pivka, L. (2013). Analogue realization of fractional-order dynamical systems. *Entropy, 15*(10), 4199–4214.

5. Podlubny, I., Petras, I., Vinagre, B. M., Leary, P. O., & Dorcak, L. (2012). Analogue realizations of fractional-order controllers. *Nonlinear Dynamics, 29*(4), 281–296.
6. Suksang, T., Loedhammacakra, W., & Pirajnanchai, V. (2012). Implement the fractional-order, half integrator and differentiator on the OTA based $PI^{\lambda}D^{\mu}$ controller circuit. In *IEEE conference on ECTICON*. https://doi.org/10.1109/ecticon.2012.6254136.
7. Das, S., & Pan, I. (2012). *Fractional order signal processing-introductory concepts and applications*. Berlin: Springer.
8. Sheng, H., Chen, Y. Q., & Qiu, T. S. (2011). *Fractional processes and fractional-order signal processing: Techniques and applications*. Berlin: Springer.
9. Said, L. A., Radwan, A. G., Madian, A. H., & Soliman, A. M. (2015). Fractional order oscillators based on operational transresistance amplifiers. *International Journal of Electronics and Communications (AEU), 69*(7), 988–1003.
10. Nakagava, M., & Sorimachi, K. (1992). Basic characteristics of a fractance device. *IEICE Transactions on Fundamentals, E75-A* (12), 1814–1818.
11. Adhikary, A., Sen, S., & Biswas, K. (2016). Practical realization of tunable fractional order parallel resonator and fractional order filters. *IEEE Transactions on Circuits and Systems I, 63*(8), 1142–1151.
12. Freeborn, T. J., Maundy, B., & Elwakil, A. S. (2012). Fractional-step tow-thomas biquad filters. *Nonlinear Theory and Its Applications IEICE (NOLTA), 3*(3), 357–374.
13. Biswas, K., Sen, S., & Dutta, P. K. (2006). Realization of a constant phase element and its performance study in a differentiator circuit. *IEEE Transactions on Circuits and Systems, 53*(9), 802–806.
14. Tripathy, M. C., Biswas, K., & Sen, S. (2013). A design example of a fractional-order Kerwin–Huelsman–Newcomb biquad filter with two fractional capacitors of different order. *Circuits, Systems, and Signal Processing, 32,* 1523–1536.
15. Tsirimokou, G., Psychalinos, C., Elwakil, A. S., & Salama, K. N. (2017). Experimental behavior evaluation of series and parallel connected constant phase elements. *AEU-International Journal of Electronics and Communications, 14,* 5–12.
16. Suksang, T., Pirajnanchai, V., Suppitaksakul, C., & Loedhammacakra, W. (2012). Design and improve the performance of OTA low pass filter with fractional-order step. In *IEEE conference on electron devices and solid state circuit (EDSSC)*.
17. Vinagre, B. M., Podlubny, I., Hernandez, A., & Feliu, V. (2000). Some approximations of fractional order operators used in control theory and applications. *Fractional Calculus & Applied Analysis, 3*(3), 945–950.
18. Xue, D. Y., Zhao, C., & Chen, Y. Q. (2006). A modified approximation method of fractional order system. In *IEEE conference on mechatronics and automation* (pp. 1043–1048).
19. El-Khazali, R. (2015). On the biquadratic approximation of fractional order Laplacian operators. *Analog Integrated Circuits and Signal Processing, 82*(3), 503–517.
20. Tripathy, M. C., Mondal, D., Biswas, K., & Sen, S. (2015). Experimental studies on realization of fractional inductors and fractional-order bandpass filters. *International Journal of Circuit Theory and Applications, 43*(9), 1183–1196.
21. Ali, A. S., Radwan, A. G., & Soliman, A. M. (2013). Fractional order butterworth filter: Active and passive realizations. *IEEE Journal on Emerging and Selected Topics in Circuits and Systems, 3*(3), 346–354.
22. Soltan, A., Radwan, A. G., & Soliman, A. M. (2015). Fractional order Sallen–Key and KHN filters: Stability and poles allocation. *Circuits, Systems, and Signal Processing, 34*(5), 1461–1480.
23. Said, L. A., Ismail, S. M., Radwan, A. G., Median, A. H., El Yazeed, M. F. A., & Soliman, A. M. (2016). On the optimization of fractional order low pass filter. *Circuits Systems and Signal Processing, 35*(6), 2017–2039.
24. Adhikary, A., Sen, P., Sen, S., & Biswas, K. (2016). Design and performance study of dynamic fractors in any of the four quadrants. *Circuits, Systems, and Signal Processing, 35*(6), 1909–1932.
25. Adhikary, A., Sen, S., & Biswas, K. (2017). Design and hardware realization of a tunable fractional-order series resonator with high quality factor. *Circuits, Systems, and Signal Processing*, *36*(9), 3457–3476.
26. Freebom, T. J., Maundy, B., & Elwakil, A. (2013). Fractional resonance-based $RL_{\alpha}C_{\beta}$ filters. *Mathematical Problems in Engineering*. https://doi.org/10.1155/2013/726721.
27. Jerabek, J., Sotnar, R., Dvorak, J., Langhammer, L., & Kotton, J. (2016). Fractional-order high pass filter with electronically adjustable parameters. In *International conference on applied electronics*.
28. Tsirimokou, G., Psychalinos, C., & Elwakil, A. S. (2017). Fractional-order electronically controlled generalized filters. *International Journal of Circuit Theory and Applications, 45*(5), 595–612.
29. Khateb, F., Kubanek, D., Tsirimokou, G., & Psychalinos, C. (2016). Fractional-order filter based on low-voltage DDCCs. *Microelectronics Journal, 50,* 50–59.
30. Tsirimokou, G., Psychalinos, C., & Elwakil, A. S. (2015). Emulation of a constant phase element using operational transconductance amplifiers. *Analog Integrated Circuits and Signal Processing*, *85*(3), 413–423.
31. Tsirimokou, G., Psychalinos, C., Freeborn, T. J., & Elwakil, A. S. (2016). Emulation of current excited fractional-order capacitors and inductors using OTA topologies. *Microelectronics Journal, 55,* 70–81.
32. Maundy, B., Elwakil, A. S., & Freeborn, T. J. (2011). On the practical realization of higher order filters with fractional stepping. *Signal Processing, 91*(3), 484–491.
33. Tsirimokou, G., Koumousi, S., & Psychalinos, C. (2016). Design of fractional-order filters using current feedback operational amplifiers. *Journal of Engineering Science and Technology, Review, 9*(4), 77–81.
34. Tsirimokou, G., Laoudias, C., & Psychalinos, C. (2014). 0.5-V fractional-order companding filters. *International Journal of Circuit Theory and Applications, 43,* 1105–1126.
35. Geiger, R. L., & Sanchez-Sinencio, E. (1985). Active filter design using operational transconductance amplifiers: A tutorial. *IEEE Circuits and Devices Magazine, 1*(2), 20–32.
36. Ahmadi, P., Maundy, B., Elwakil, A. S., & Belostotski, L. (2012). High-quality factor asymmetric-slope band pass filters: A fractional-order capacitor approach. *IET Circuits, Devices and Systems, 6*(3), 187–197.
37. Verma, R., Pandey, N., & Pandey, R. (2017). Electronically tunable fractional order filter. *Arabian Journal for Science and Engineering, 42,* 3409–3422.
38. Geiger, R. L., & Sanchez-Sinecio, E. (1985). Active filter design using operational transconductance amplifiers: A tutorial. *IEEE Circuits and Devices Magazine, 1,* 30–31.
39. Li, Y. N. (2013). On the systematic synthesis of OTA-based Wien oscillators. *AEU-International Journal of Electronics and Communications, 67*(9), 754–760.
40. Sotner, R., Jerabek, J., Herencsar, N., Vrba, K., & Dostal, T. (2015). Features of multi-loop structures with OTAs and adjustable current amplifier for second-order multiphase/quadrature oscillators. *AEU-International Journal of Electronics and Communications., 69*(5), 814–822.
41. Senani, R., Gupta, M., Bhaskar, D. R., & Singh, A. K. (2014). Generation of equivalent forms of operational transconductance amplifier-RC sinusoidal oscillators: The Nullor approach. *IET-*

The Journal of Engineering. https://doi.org/10.1049/joe.2013.0200.
42. Senani, R., Bhaskar, D. R., Gupta, M., & Singh, A. K. (2015). Canonic OTA-C sinusoidal oscillators: Generation of new grounded-capacitor versions. *American Journal of Electrical and Electronic Engineering, 3*(6), 137–146.
43. Radwan, A. G., Elwakil, A. S., & Soliman, A. M. (2009). On the generalization of second-order filters to the fractional-order domain. *Journal of Circuits, Systems, and Computers, 18*(02), 361–386.
44. Patil, M. D., Vyawahare, V. A., & Bhole, M. K. (2014). A new and simple method to construct root locus of general fractional-order systems. *ISA Transaction, 53*(2), 380–390.



Rakesh Verma received B.Tech. degree in Electronics and Communication Engineering (ECE) from Birla Institute of Applied Sciences, Bhimtal and M.Tech. degree in Control and Instrumentation Engineering from Delhi Technological University, Delhi. He has served as Assistant Professor in ECE department, National Institute of Technology, Delhi. At present, he is a Ph.D. research scholar in ECE department, Delhi Technological University, Delhi. His research interest is focused on fractional order current mode circuits.



Neeta Pandey is Professor in ECE department, Delhi Technological University. She received her M.E. in Microelectronics from BITS Pilani and Ph.D. from Guru Gobind Singh Indraprastha University, Delhi. She has served in Central Electronics Engineering Research Institute, Pilani, Indian Institute of Technology, Delhi, Priyadarshini College of Computer Science, Noida and Bharati Vidyapeeth's College of Engineering, Delhi in various capacities. She is having approximately 27 years of teaching and research experience in Electronics and Communication Engineering. She has published papers in international, national journals of repute and conferences. Her research interests are in analog and digital VLSI design. She is life member of ISTE and senior member of IEEE, IEEE WIE for 13 years.



Rajeshwari Pandey received her B.Tech. (Electronics and Telecommunication) from J. K. Institute of Applied Physics, University of Allahabad and her M.E. (Electronics and Control) from BITS, Pilani, Rajasthan, India and Ph.D. from Faculty of Technology, Delhi University, India. She has served BITS Pilani, AERF, Noida and Priyadarshini College of Computer Science, Noida in various capacities. Currently, she is Professor in Department of Electronics and Communication Engineering, Delhi Technological University, Delhi. Her research interests include analog integrated circuits and microelectronics. She is life member of ISTE, IETE and IEEE and IEEE WIE.

Superlattices and Microstructures xxx (xxxx) xxx–xxx

Contents lists available at ScienceDirect

Superlattices and Microstructures

journal homepage: www.elsevier.com/locate/superlattices

Rear contact silicon solar cells with a-SiC$_X$:H based front surface passivation for near-ultraviolet radiation stability

Rahul Pandey[a], Rishu Chaujar[b,*]

[a] Chitkara University Institute of Engineering and Technology, Chitkara University, Jansla, Rajpura, Punjab, 140401, India
[b] Microelectronics Research Lab, Department of Applied Physics, Delhi Technological University, Bawana Road, Delhi, 110042, India

ARTICLE INFO

Keywords:
Absorption
Interface
Efficiency
Recombination
Surface passivation
Solar cell

ABSTRACT

Surface recombination (due to dangling bonds) and lower absorption (due to the low absorption coefficient of silicon (Si)) are the major hindrances in silicon-based photovoltaic (PV) devices. To overcome this, numerous complex texturing schemes are projected to enhance the light trapping. However nanostructured cells are not efficient due to the large surface to volume ratio which enhances surface recombination. Thus, the nanostructured cells require additional passivation scheme to mitigate the recombination losses. Here, we have designed a nontextured, 15% efficient, amorphous silicon carbide hydrogenated (a-SiC$_X$:H) passivated, 10-μm thick rear contact Si solar cell device. Considerable reduction in photo reflectance is obtained in the near ultraviolet (UV)/visible spectral region together with near UV stability at higher surface recombination velocity (SRV). External quantum efficiency (EQE) > 90% is achieved by the a-SiC$_X$:H based device (within the wavelength spectrum of 480–620 nm). Improvement in spectrum response give rise to 28.1 mA cm^{-2} short circuit current density (J_{SC}). Further, the performance of a-SiC$_X$:H passivated device is compared with a conventional dielectric anti-reflective coating (ARC) and high-low junction-based surface passivation techniques. Results indicate that the presence of a-SiC$_X$:H reduces the hole concentration near the front surface which eventually decreases the surface recombination. Highly efficient and reliable solar cells can be achieved by the design schemes reported in this paper, which balance both the photonic and electronic effects together.

1. Introduction

Photovoltaic (PV) market is dominated by silicon (Si) wafer technology [1], which is a reliable material present in abundance. It is employed as PV material due to its established fabrication process. However, Si-based PV devices face absorption related issues due to the low absorption coefficient of Si and hence requires thick (> 100 μm) Si wafer, in order to utilize the spectrum efficiently [2]. Therefore, the necessity of thick wafers and high-quality Si considerably raises the cost of the module, whereas cost-effective modules are required to make PV system feasible at a commercial level, with module price to be < $0.5/watt [3]. Cheaper and energy efficient solar cells with high efficiency can be realized by a reduction in the thickness of the active layer [4,5]. Nevertheless, electrical characteristics should be optimized along with optical absorption of these thin devices to enhance the performance of solar cell [6,7]. In previous years, significant effort has been made to increase the light absorption by nanoscale light trapping using nanocones [8,9], nanowires [10,11], nanodomes [12] and nanoholes [13]. Despite the success in light trapping the power conversion efficiencies (PCEs) of the thin devices remains below 11%, excluding 15.7% and 13.7% as reported by Branham et al. [14] and Jeong et al. [3]

* Corresponding author.
E-mail addresses: rahul.pandey@chitkara.edu.in (R. Pandey), chaujar.rishu@dtu.ac.in (R. Chaujar).

https://doi.org/10.1016/j.spmi.2018.08.016
Received 18 May 2018; Received in revised form 7 August 2018; Accepted 17 August 2018
0749-6036/ © 2018 Elsevier Ltd. All rights reserved.

respectively (the aforesaid research works used complex texturing schemes). Large surface to volume ratio enhances surface recombination which eventually decreases the overall performance of these devices [3]. In the 1980s the advancement in the passivation of both surfaces leads to the PCEs above 20%. Today's trend is to minimize the thickness of active materials keeping the efficiencies high. Thus, passivation of both front and back surfaces is essential for Si solar cells. This is due to higher surface to volume ratio of thin devices compared to thick devices. In crystalline Si, recombination losses occur mainly through defect states due to indirect band gap [15]. These defects are situated within the volume and the surface. They are further divided into two categories: extrinsic (process related) and intrinsic (material related and unavoidable). High-quality silicon is free from inherent defects, and external defects can be minimized to a low level using suitable growth techniques like float-zone (FZ) [16]. However, the situation becomes more complicated at the interface, due to the non-saturated dangling bond. These defect levels promote the surface recombination losses, and they must be electronically passivated, and the passivation techniques must be stable against near UV radiation. Further, most of the lower wavelength photons are absorbed near the illuminated surface, and hence, the non-metalized front surface needs to be well passivated to increase the lower wavelength response. Moreover, heavy doping near the front surface also needs to be avoided otherwise formation of dead layer occur which eventually degrades lower wavelength response. There are two fundamental approaches to minimize the surface recombination's: (1) reduction of the density of surface states, and (2) reduction of surface concentrations of electrons or holes [17]. Deposition of dielectric films (Al_2O_3, SiO_2, SiN_x) is a standard method to minimize the surface states. However, high-quality surface passivation cannot be maintained when exposed to near UV radiation. Thus, to improve the near UV stability of dielectric passivated devices, the formation of high-low junctions, i.e., p^+p and n^+n is required to reduce the concentration of charge carriers (electrons or holes) by creating a front surface field (FSF) or back surface field (BSF) [17].

In this work, simulation analysis has been done for a-SiC_X:H passivated rear contact Si solar cell, and the performance is compared with conventional dielectric passivation and high-low junction-based passivation techniques. Further, an optimized 250 μm thick 22% efficient IBC silicon have also been designed with a-SiC_X:H passivated the front surface. SiC material is an ideal choice for advanced devices due to the large indirect band (E_g = 2.2 eV) with high thermal conductivity, breakdown field and saturation velocity [18]. Deposition of silicon carbide onto silicon wafers creates interface states at SiC/Si interface, which could result in significant carrier recombination. Therefore, hydrogenated amorphous silicon carbide can be used to reduce the interface states, which will eventually prevent carrier recombination. In previous research work, plasma enhanced chemical vapour deposition of a-SiC_X:H layer led to less than 20 cm s^{-1} surface recombination velocity for n-type silicon wafer which indicates very good surface passivation induced by the a-SiC_X:H layer [19]. SiC on Si < 100 > has also been deposited by Chassagne et al. using atmospheric-pressure vapour phase epitaxy at 1350 °C [20]. Moreover, previous work shows the formation of SiC film for Si solar cell passivation by RF magnetron co-sputtering system, and the film was deposited on silicon < 100 > and glass substrates [21]. Furthermore, sub 10 μm thick SiC passivated Si, and silicon germanium (SiGe) PV devices are reported through device simulation for ultra-high efficiency; improvement in optical coupling and reduction in surface recombination is observed without employing complex texturing and passivation schemes [22,23]. Rear contact architecture Si-solar cell has been used in the present study, so as to acquire the liberty of designing its front surface for optimum electrical and optical performance [24].

2. Device architecture and model description

Device structure used in the simulation is identical to the calibrated device structure reported in our previous work [25] and is also illustrated in Fig. 1. The dimensions of the simulated device are (46 μm-wide $p+$, 50-μm-wide pitch, and 30-μm-wide $n+$). The

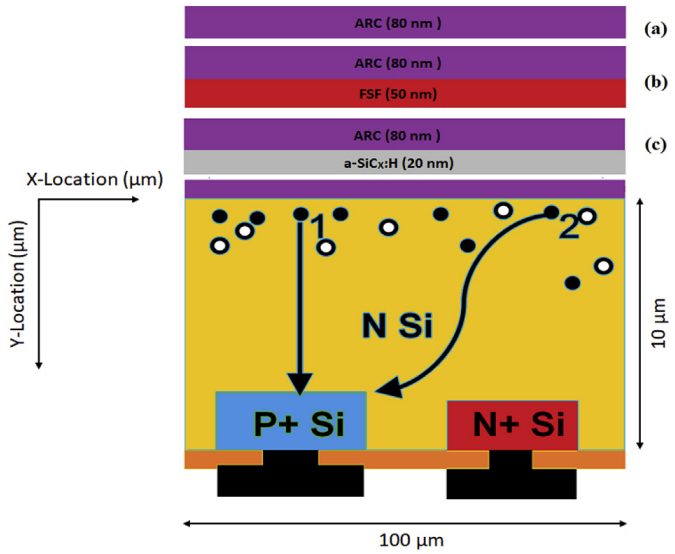


Fig. 1. Simulated device structure with different passivation scheme (a) represents ARC, (b) represents ARC with FSF, a layer of the n + region is used to create FSF, and (c) represents a-SiC_X:H with ARC.

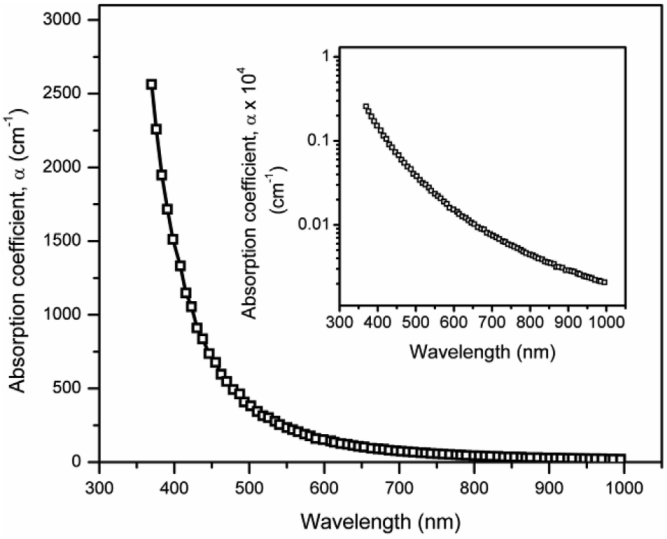


Fig. 2. Absorption coefficient of a-SiC_X:H film used in the simulation. ***INSET*** absorption in log scale.

substrate is *n-type* doped with density $3 \times 10^{15}\,cm^{-3}$. Boron with doping density ($4 \times 10^{20}\,cm^{-3}$) is used to create a $p+$ region with a diffusion depth of 300 nm, whereas $n+$ region with a diffusion depth of 100 nm is obtained by doping with phosphorous of density ($1 \times 10^{20}\,cm^{-3}$). Further, a detailed description of the models and assumptions used in simulations are shown in Table A.1 of the Appendix. The illuminated current density (J)- voltage (V) curve of the devices are obtained under standard AM1.5 solar spectrum. Optical properties for silicon and ARC are identical to as reported by Pandey et al. [25], however absorption coefficient for a-SiC_X:H has been obtained from Ref. [26] and reported in Fig. 2.

3. Results and discussions

3.1. UV reliability analysis along with the electro-optical performance of the devices

In this subsection, initial analysis has been carried out at the interface; to understand and compare the different passivation techniques. A small region at the surface is exaggerated, and photogeneration rate contour has been obtained as reported in Fig. 3(a–c). Results indicate that the presence of a-SiC_X:H increases the optical coupling and hence shows higher photon absorption rate compared to other passivation techniques as shown in Fig. 3(a–c). The performance of a PV device is related to the amount of light getting absorbed inside the active layer, and hence transparent ARC layer is required to increase the coupling of photons. Absorption coefficient as reported in Fig. 2 shows a low absorption coefficient of a-SiC_X:H at higher wavelengths, and hence the presence of a-SiC_X:H increases the optical coupling inside the silicon. Moreover, photon absorption rate in FSF/ARC based device is slightly lower compared to ARC based device, due to the heavily doped front surface as depicted in Fig. 3(a–c).

Besides, to understand the carrier dynamics and surface passivation quality, hole quasi-Fermi (HQF) energy, hole concentration and recombination rate has been obtained near the interface for all the devices and are depicted in Fig. 4 and Fig. 5(a–d) respectively. Fig. 4 shows the HQF energy for all the devices, whereas Fig. 5(a–b) shows the hole concentration along with recombination rate near the front surface (y = 0.01 μm). Fig. 4 displays increasing the doping of the FSF layer increases the barrier for minority carriers (hole) and thereby prevents the motion of holes toward the FSF/ARC interface. This results in a reduction of hole concentration as depicted in Fig. 5(a), and thereby improves the surface passivation quality as evidently represented in Fig. 5(b). Again, reconsidering the results reported in Fig. 4, the presence of a-SiC_X:H significantly increase the barrier to ~1.52eV, (0.8eV higher than the barrier achieved with FSF doping of $1 \times 10^{20}\,cm^{-3}$). The HQF data illustrates, a-SiC_X:H based device outperform in preventing the hole movements towards the interface and hence a drastic reduction in hole concentration near the interface (Fig. 5(a)) is obtained compared to other passivation schemes reported in this manuscript. The fundamental approach to minimize the recombination is reduction of minority carrier concentrations at the surface [17], and the same is proficiently achieved without the need of heavily doped front surface. Added recombination data (in linear and log scale, Fig. 5(a–b)) near the interface shows surface recombination is significantly suppressed in the case of a-SiC_X:H passivated device.

Likewise, hole concentration and recombination rate away from the interface is also analyzed and is depicted in Fig. 5(c–d). It is observed in Fig. 5(c) that the light generated hole concentration is slightly higher in a-SiC_X:H based device compared to other devices, due to higher photon absorption (as discussed earlier). And most of the generated carrier will be collected, and the rest will be balanced by the recombination process. Thereby, the enhanced hole concentration in the region away from the interface consequently results in slightly higher recombination rate for a-SiC_X:H based device compared to other devices as revealed in Fig. 5(d). Additionally, the result also supports that presence of a-SiC_X:H minimizes the hole concentration near the interface only (which is required).

In addition, a contour plot of recombination rate near the front surface is also reported in Fig. 6(a–c). Results indicated in

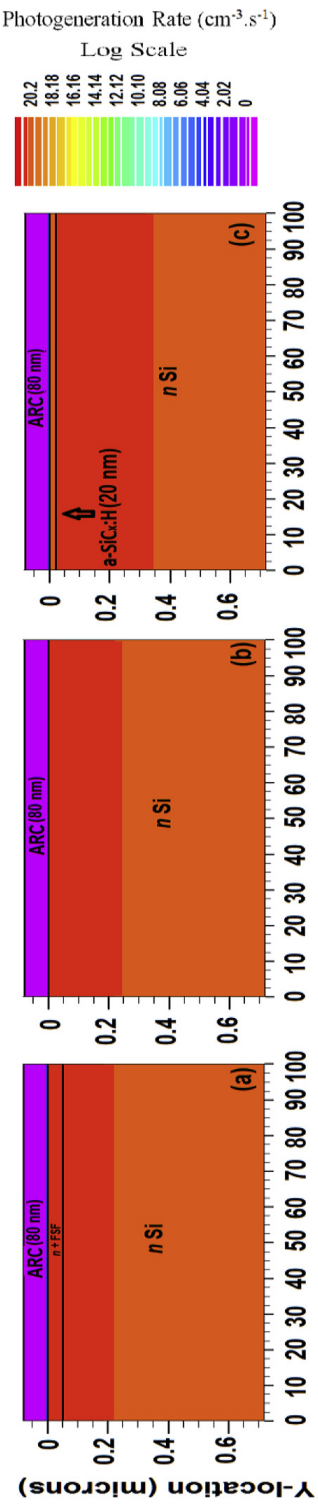


Fig. 3. Contour plot of photogeneration rate near the interface (a) FSF/ARC based device, (b) ARC based device, and (C) a-SiC_x:H/ARC based device. Results are obtained under illumination on and zero applied voltage.

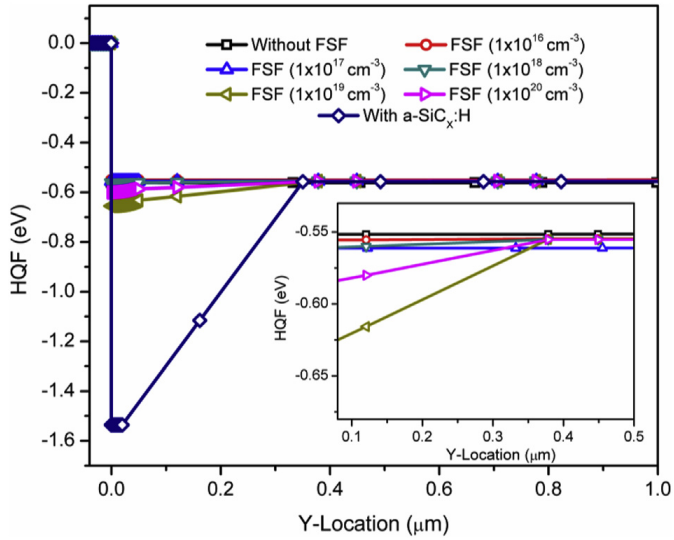


Fig. 4. HQF energy near the interface of all the simulated devices, i.e., ARC based, ARC + FSF based (with different FSF doping) and a-SiC_X:H based devices. ***INSET*** magnified view of ARC and ARC + FSF based devices. Data is obtained with zero bias with illumination ON.

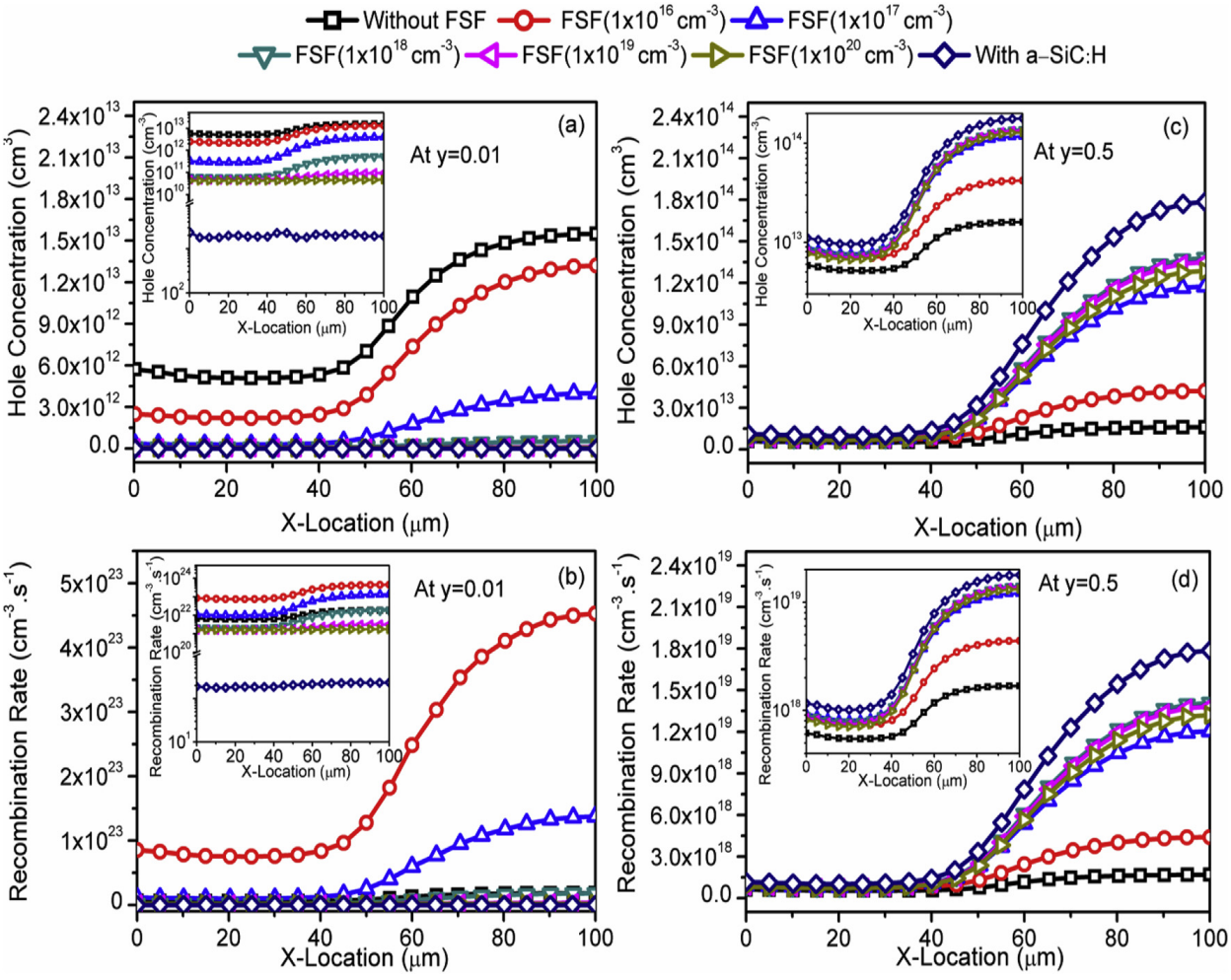


Fig. 5. Hole concentration and recombination rate of all the simulated devices, i.e., ARC based, ARC + FSF based (with different FSF doping) and a-SiC_X:H based devices. (a) and (c) hole concentration at y = 0.01 and y = 0.5, respectively. (b) and (d) recombination rate at y = 0.01 and y = 0.5, respectively. ***INSET*** of all the figure shows the data in log scale. Data is obtained with zero bias with illumination ON.

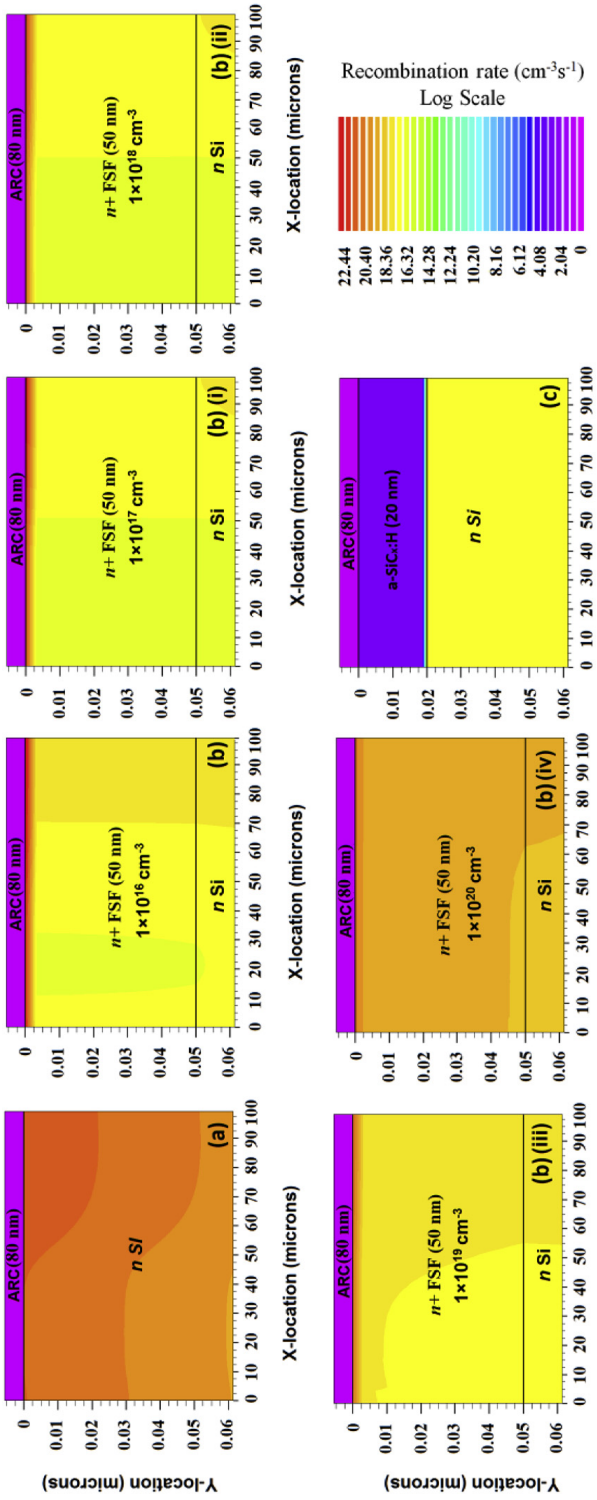


Fig. 6. Contour plot of recombination rate near the interface (a) ARC based device, (b) FSF/ARC based device. Different concentration of the n + region, i.e. FSF region is further represented in b (i-iv), and (c) a-SiC_X:H/ARC based device. Results are obtained under illumination and zero applied voltage.

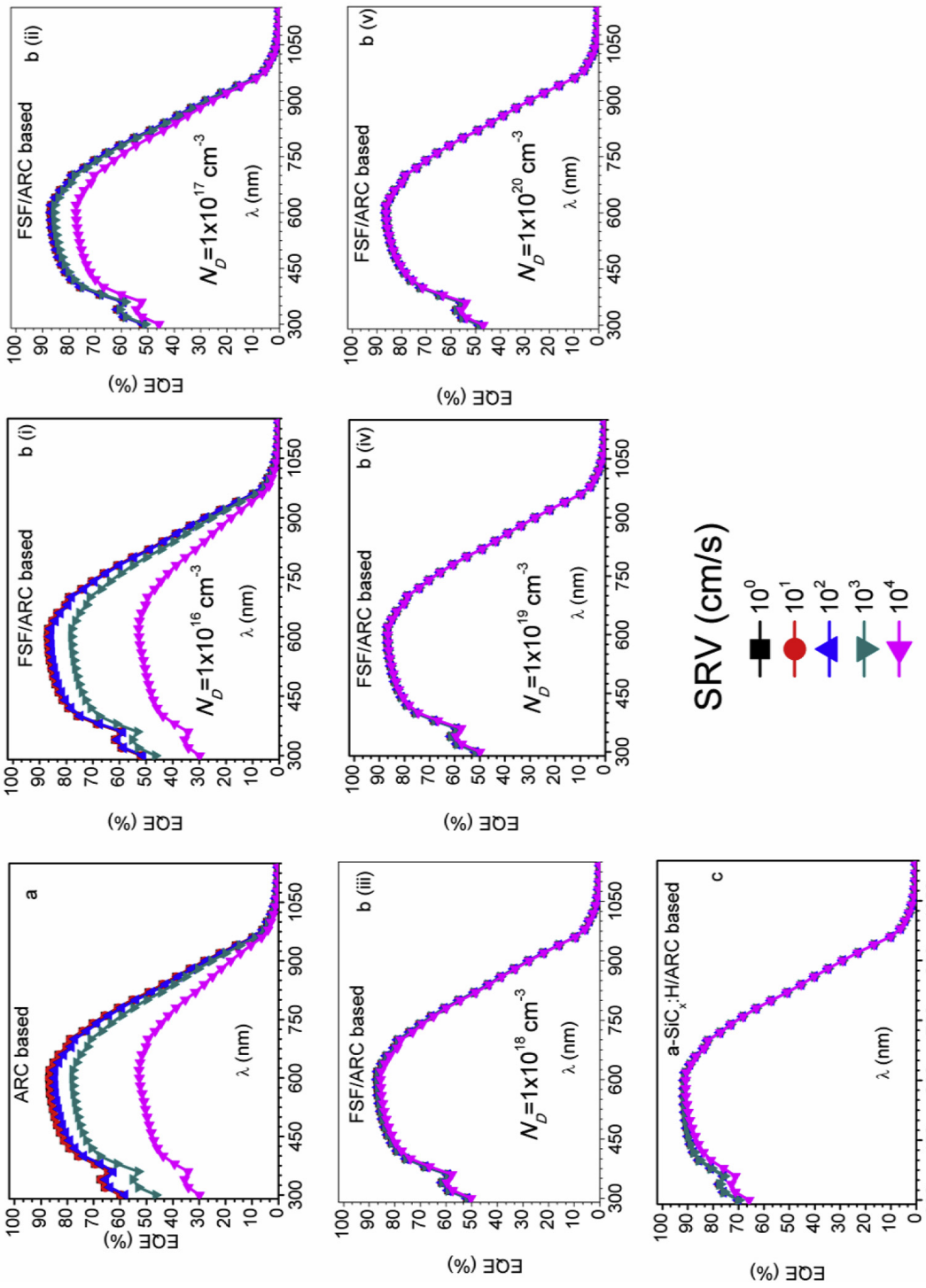


Fig. 7. Impact of SRV on the optical performance, i.e., EQE of (a) ARC based device, (b) FSF/ARC based device, different concentration of n + region, i.e., FSF region is further represented in b (i-iv), and (c) a-SiC$_x$:H/ARC based device.

Fig. 5(a–d) and Fig. 6(a–c) show hole concentration and recombination rate are low near region 1 (marked in Fig. 1) and gradually increases from region 1 to region 2 (marked in Fig. 1) and become maximum in region 2. Reported results are obtained under zero biasing condition with illumination ON, and with this condition associated electric field of $p + - n$ junction will collect and separate generated electron-hole (e-h) pairs. The collection near the $p + -n$ junction is completed, and for the region away from the $p + -n$ junction, the collection is by a diffusion process. Therefore, area away from the collecting terminal shows higher hole concentration and higher recombination rate.

Further, spectrum response, i.e., EQE of the devices at different SRV has been obtained and are reported in Fig. 7(a–c). The number of surface states is incorporated in the simulations with the help of SRV parameters in the interface statement of ATLAS device simulator. EQE of ARC, FSF/ARC, and a-SiC_X:H/ARC based devices are indicated in Fig. 7(a), (b), and Fig. 7(c), respectively. Spectrum response of the FSF/ARC based device is obtained for different donor concentration ($1 \times 10^{16}\,cm^{-3}$ to $1 \times 10^{20}\,cm^{-3}$) of the front surface and are reported in Fig. 7(b(i-v)). As discussed earlier (shown in Fig. 5(a–d) and Fig. 6), ARC coated device is more vulnerable to surface states, and the same has been supported by spectrum response also as observed in Fig. 7(a). Fig. 7(a) shows increasing the surface states in terms of SRV results in significant degradation in ARC based device. At a wavelength equivalent to 300 nm, the EQE of ARC-based device went to 30% from 60% as SRV changes from 1 cm/s to 10^4 cm/s. Generally, front surface recombination reduces the lower wavelength response of the solar cell, whereas lower diffusion length and transmitted photons translate to a reduction in midway and higher wavelength response, respectively. Nevertheless, back surface recombination also degrades higher wavelength response. Result shows, ARC coated device is unable to withstand under near UV radiation and higher surface states condition. On the other hand, EQEs of FSF/ARC and a-SiC_X:H/ARC based devices shows fewer degradations. However, selecting the appropriate doping concentration is an important parameter for FSF/ARC based device. Results show FSF doping concentration of $1 \times 10^{16}\,cm^{-3}$ will not provide any spectral improvement as shown in Fig. 7(b (i)). This implies FSF is not capable of reducing the minority carrier (holes) concentration at the interface (as already shown in Fig. 5(a)). Increasing the concentration will result in improvements in both lower as well as midway spectrum responses as shown in Fig. 7(b) (ii-v) and the improvement is attributed to the higher surface field. The increased surface field efficiently prevents the holes at the interface, and thus reduces the concentration and surface recombination. Eventually, giving rise to a stable spectrum response. FSF/ARC based device with appropriate doping provides near UV stability as shown in Fig. 7(b) (i-v), however, the performance in terms of the EQE at the lower wavelength degrades as shown in Fig. 7(b (i-v)). The formation of the dead layer at the front surface reduces the EQE since most of the high-energy photons are absorbed near the front surface, and they get recombine. Moreover, another passivation scheme, i.e., using a-SiC_X:H along with ARC coating is a possible solution to prevent the formation of the dead layer along with near UV stability. Fig. 7(c) shows the presence of a-SiC_X:H at the front surface provides significant near UV stability without degrading the lower wavelength response, due to lower surface recombination as already discussed in Figs. 5(b), and Fig. 6(c).

Further, a-SiC_X:H -based device shows EQEs > 90% in the wavelength range of 480–620 nm in addition to near UV stability under high SRV condition. The remarkable improvements are attributed to the presence of a-SiC_X:H which prevents the movement of holes toward the interface. However, the thickness of a-SiC_X:H is a critical parameter. Increasing the thickness more than 20 nm results in undesired absorption in a-SiC_X:H and reduces photon coupling in underlying Si [22]. Concluding the results obtained at the interface and spectrum response supports that presence of a-SiC_X:H provides good surface passivation quality.

Furthermore, the illuminated J-V curve along with PV parameters of the devices are also examined and reported in Fig. 8 a-SiC_X:H/ARC based device outperforms other devices due to improved optical absorption and superior surface passivation quality as discussed earlier. The short circuit current density (J_{SC}) in a-SiC_X:H/ARC based device is 26% and 8% higher compared to ARC and FSF/ARC based devices respectively. Whereas the open circuit voltage (V_{OC}) is 7% and 1% higher compared to respective devices.

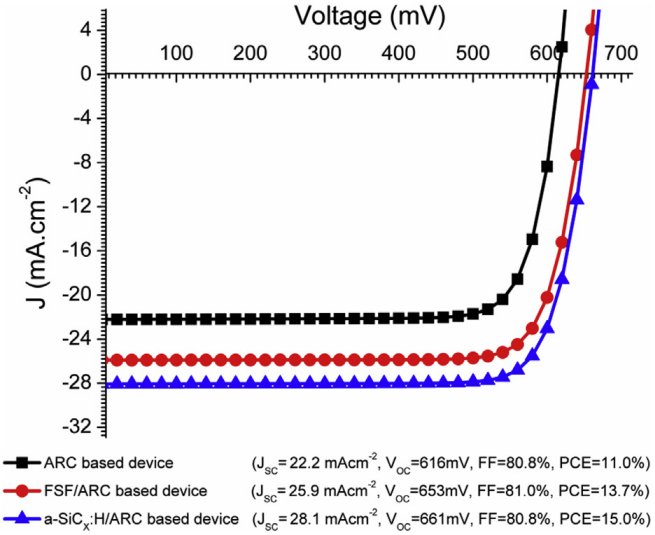


Fig. 8. Illuminated J-V curve along with photovoltaic parameters of ARC, FSF/ARC, and a-SiC_X:H/ARC based devices, respectively. The doping concentration of $1 \times 10^{19}\,cm^{-3}$ has been used for the FSF.

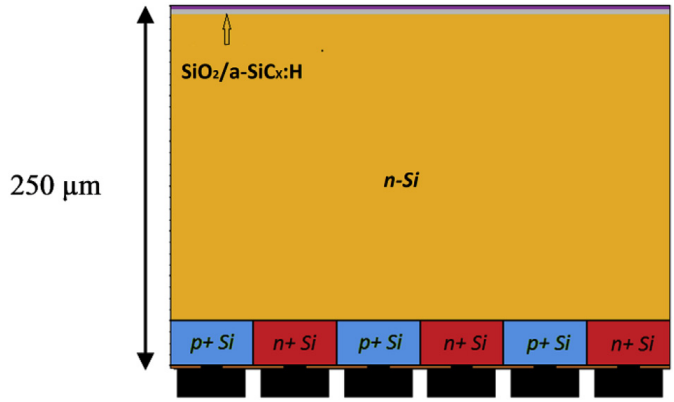


Fig. 9. a-SiC_X:H passivated 250 µm thick IBC silicon solar cell used in the simulation. Contacts are represented by black regions.

However, the improvement in fill-factor (FF) is not significant. The improved optical and electrical performance resulted in 15% efficient silicon solar cell in 10-µm thick regime.

3.2. Design and optimization of a-SiC_X:H passivated 250 µm thick IBC silicon solar cell

In this subsection, a 250 µm thick a-SiC_X:H passivated IBC solar cell, shown in Fig. 9, has been designed and optimized to obtained higher conversion efficiencies. The architecture of the device is inspired by the device reported by SunPower Corporation [27]. The width 20 µm has been used for both $n+/p+$ regions. 80 nm thick SiO_2 has been used for back surface passivation along with 5 µm contact width. The length of the contact is 700 nm. 3×10^{15} cm^{-3} doping concentration has been used for *n*-type region and doping/diffusion depth for n+/p + region is optimized to 4×10^{18} cm^{-3}/3 µm.

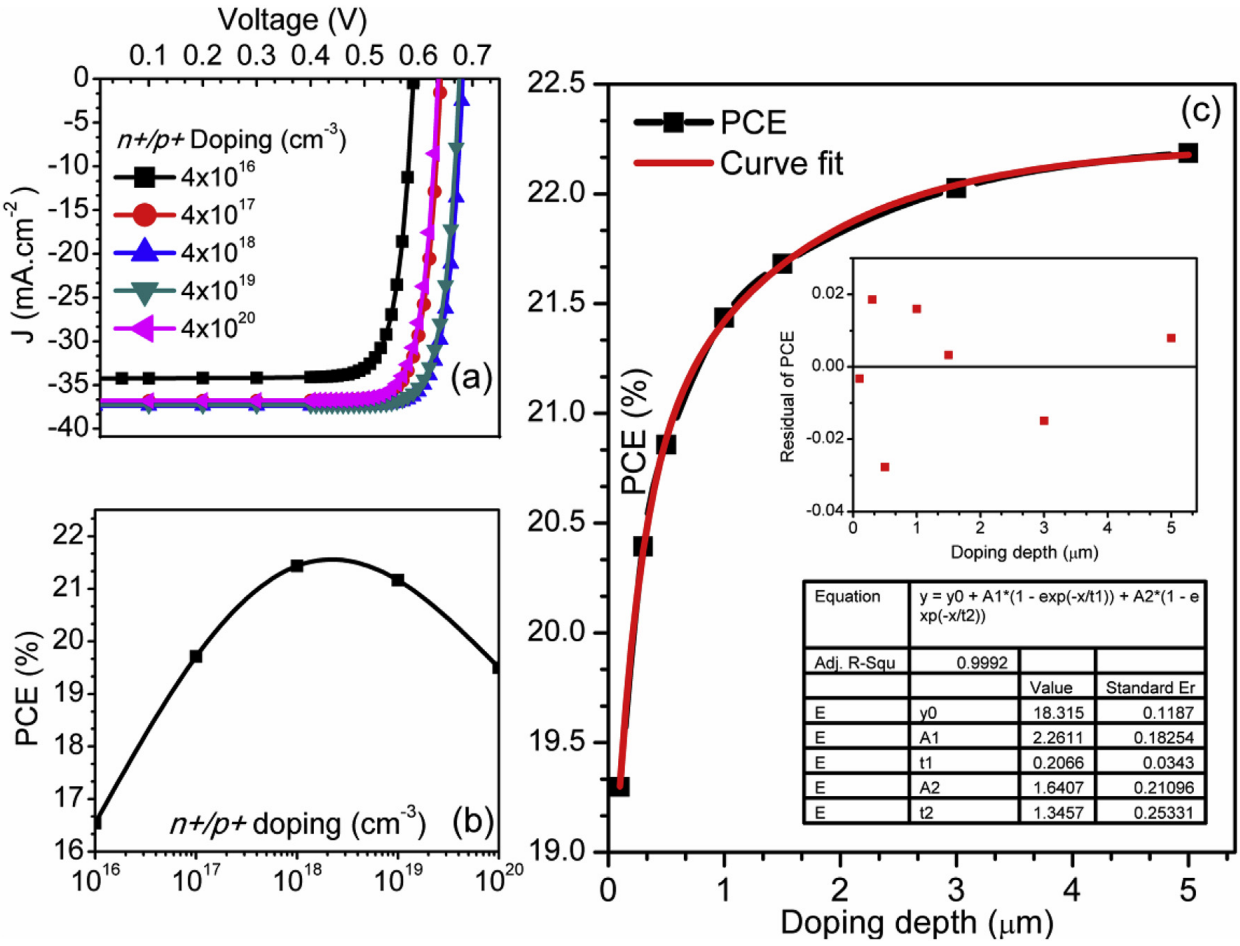


Fig. 10. (a–b) J-V and PCE curve of a-SiC_X:H passivated 250 µm thick IBC– silicon solar cell with a different doping concentration of n +/p + regions and (c) PCE curve with different diffusion depth. ***INSET*** the residual of PCE and curve fitting parameters.

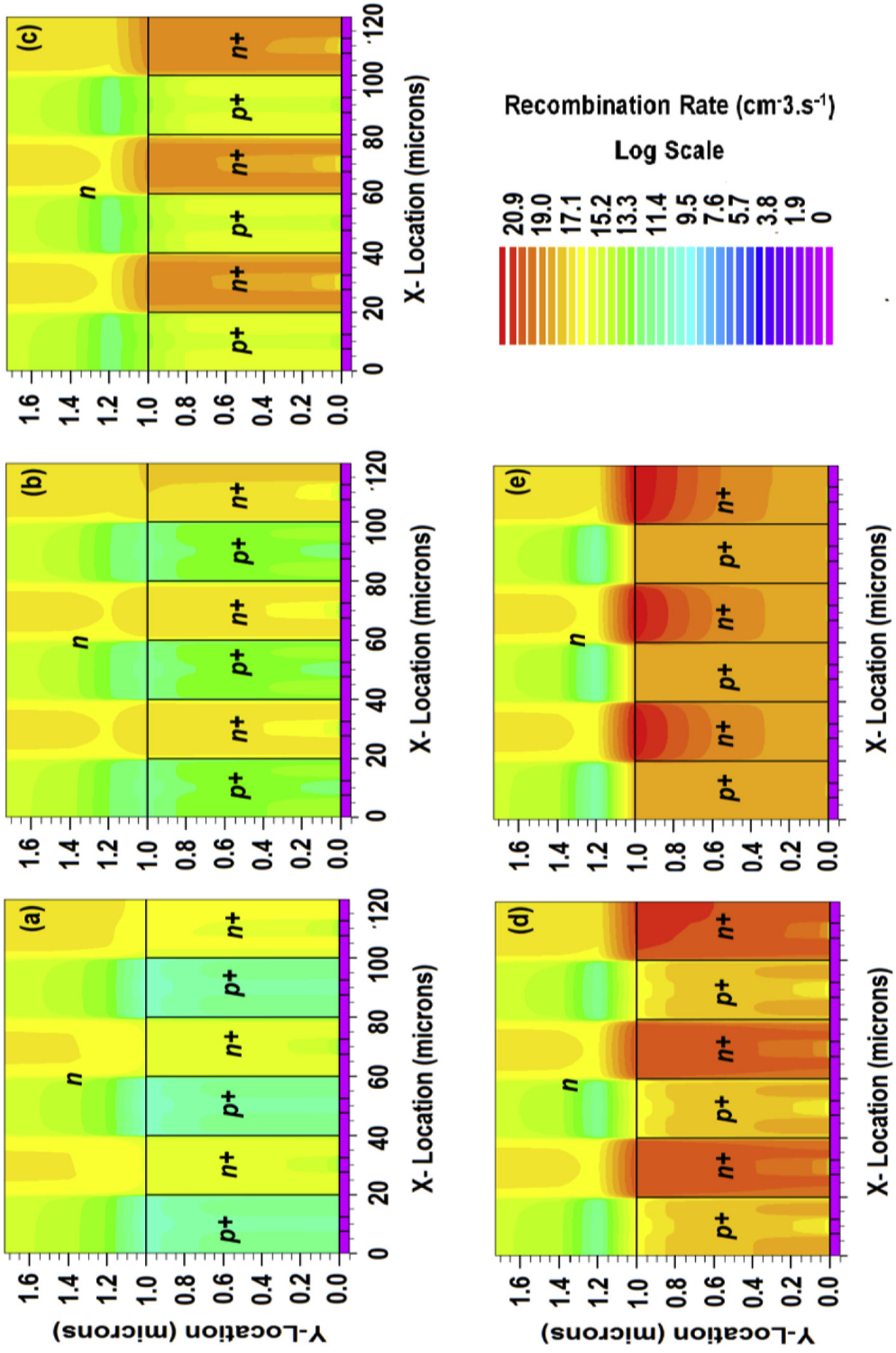


Fig. 11. Contour representation of recombination rate near n + /p + regions with different doping concentration of n + /p + : (a) 4×10^{16} cm^{-3}, (b) 4×10^{17} cm^{-3} (c) 4×10^{18} cm^{-3}, (d) 4×10^{19} cm^{-3}, and (e) 4×10^{20} cm^{-3}.

Table 1
Photovoltaic parameters of a-SiC_X:H passivated ibc silicon solar cell with different doping depth of $p+/n$ + regions.

Doping depth (μm)	J_{SC} (mA.cm^{-2})	V_{OC} (mV)	FF (%)	PCE (%)
0.1	36.6138	632.43	83.3882	19.3091
0.3	37.1274	655.30	83.8739	20.4061
0.5	37.2622	665.82	84.1183	20.8698
1.0	37.3706	681.27	84.2450	21.4482
1.5	37.4078	687.40	84.3857	21.6990
3.0	37.4453	698.73	84.2351	22.0393
5.0	37.4615	702.19	84.3904	22.1989

Fig. 10(a–c) shows the optimization of the device. Initially, the impact of the doping concentration of $n+/p$ + region has been obtained, and results are reported in Fig. 10(a). Increasing the doping concentration increases V_{OC} of the device, due to enhanced diffusion potential and low series resistance. Optimum PCE has been achieved with a doping level of 4×10^{18} cm^{-3} as shown in Fig. 10(b). However, increasing the doping further beyond 4×10^{19} cm^{-3}, the J-V curve shows significant degradation in device performance. Therefore, to understand the trend, a small region at the rear side is exaggerated, and the contour plot of the recombination rate is obtained and reported in Fig. 11(a–e). In the case of 4×10^{20} cm^{-3} $n+/p$ + doping based device, too high recombination rate is observed at and near the $n+/n$ interface, as shown in Fig. 11(e). This could be attributed to heavily doped regions. Therefore, due to the increased recombination rate of minority carrier, a significant reduction in V_{OC} and PCE has been observed at the concentration of 4×10^{20} cm^{-3}, as shown in Fig. 10(a–b). Thus, further analysis has been done with the $n+/p$ + doping concentration of 4×10^{18} cm^{-3}. Moreover, the impact of the $p+/n$ + diffusion depth has also been obtained and reported in Fig. 10(c). Increasing the diffusion depth at lower values improves the PCE, due to an increase in carrier collection probability since minority carrier generated in the *n*-type region requires to travel less distance to arrive at the collecting junction. However, increasing depth beyond 3 μm does not show significant improvement as exposed in Fig. 10(c). Furthermore, the relation between diffusion depth and PCE has also been obtained with the help of curve fitting, and equation along with fitting parameters are reported in the inset plot of Fig. 10(c). X and Y axes values represent the diffusion depth and PCE respectively. In addition, photovoltaic parameters of the devices with different doping depth are summarized in Table 1.

Further, the EQE and J-V curve of the optimized 250 μm thick device is reported in Fig. 12(a–b) along with EQE and J-V curves of 10 μm thick device, previously designed in this manuscript. The optical absorption of the 10 μm thick device is very low at higher wavelength > 800 nm, due to the lower absorption coefficient of silicon. Whereas, device structure discussed in ongoing subsection show superior optical absorption and higher EQE at longer wavelengths as shown in Fig. 12(a). The improvement is attributed to increased wafer thickness. Enhancement in spectrum response resulted in 33% higher J_{SC} for thick device. Moreover, more than 76% EQE has been obtained at lower wavelengths, without the need of the complex texturing schemes. This shows the decent optical performance of the device and suppressed surface recombination. This section concludes 22% efficient IBC silicon solar cell with a-SiC_X:H passivated front surface.

4. Conclusion

This work presents design and simulations of a-SiC_X:H passivated rear-contact solar cells. Near UV stability analysis has been done for a-SiC_X:H passivated device, and the performance is compared with conventional ARC and FSF/ARC based devices. Hole concentration along with surface recombination rate is obtained at the interface and away from the interface to understand the carrier

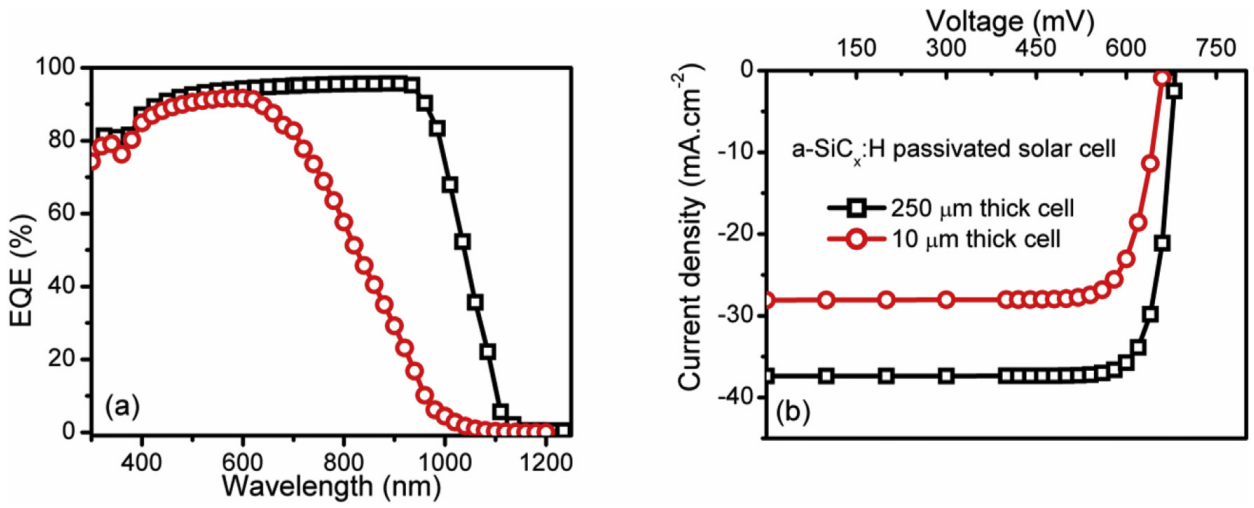


Fig. 12. (a) EQE and (b) J-V curve of a-SiC_X:H passivated 250 μm thick IBC and 10 μm thick silicon solar cell.

dynamics. Results show a significant reduction in minority carrier (hole) concentration and recombination near the front surface for a-SiC_X:H passivated device. Photon absorption rate shows higher photon coupling in the underlying silicon substrate. In the wavelength spectrum range of 480–620 nm, the device reflects EQEs > 90% together with excellent near UV stability under high SRV condition. 15% PCE is achieved, without the need of complex texturing, in 10 μm thick rear-contact solar cell. Additionally, a 250 μm thick IBC silicon solar cell with a conversion efficiency of 22.2% has also been realized and optimized. Highly efficient and cost-effective solar cells can be fabricated using the design schemes reported, which balances the photonic and electronic effects together and contributes towards energy efficient applications.

Acknowledgment

Authors would like to thank Microelectronics Research Lab, Department of Engineering Physics Delhi Technological University to carry out this work.

Appendix A. Supplementary data

Supplementary data related to this article can be found at https://doi.org/10.1016/j.spmi.2018.08.016.

Appendix

Table A.1
Semiconductor equations and models used during simulations

The Poisson equation, electron and hole continuity equation.	$\frac{d}{dx}\left(-\varepsilon(x)\frac{d\psi}{dx}\right) = -q\left[\begin{matrix} n(x) - p(x) + N_a^-(x) - N_d^+(x) + \\ n_t(x) - p_t(x) \end{matrix}\right]$ $\frac{dn_p}{dt} = D_n\frac{d^2n_p}{dx^2} + n_p\mu_n\frac{d\xi}{dx} + \mu_n\xi\frac{dn_p}{dx} + G_n - \frac{n_p - n_{p0}}{\tau_n}$ $\frac{dp_n}{dt} = D_p\frac{d^2p_n}{dx^2} - p_n\mu_p\frac{d\xi}{dx} - \mu_p\xi\frac{dp_n}{dx} + G_p - \frac{p_n - p_{n0}}{\tau_p}$	Where q the electron charge, D the diffusion coefficient, ε is the permittivity and G the generation rate. The n_s, n_t, p_s and p_t are the free electron, trapped electron, free hole, and trapped hole, respectively. ψ is the electrostatic potential. $N_a{}^-$ the ionized acceptor-like doping concentration and $N_d{}^+$ are the ionized donor-like doping concentration. ξ is the electric field and τ_n, τ_p are the carrier lifetimes.
Auger recombination	$R_{AUGER} = C_n(pn^2 - n_0n_{ie}^2) + C_p(np^2 - p_0n_{ie}^2)$	The auger coefficients, $C_p = 9.9 \times 10^{-32}\,\mathrm{cm^6\,s^{-1}}$ and $C_n = 2.8 \times 10^{-31}\,\mathrm{cm^6\,s^{-1}}$ have been used for p-type and n-type Si, respectively, at 300 K temperature. n_o, p_o are the concentration of electron and holes at equilibrium.
Shockley-Read-Hall (SRH) recombination.	$R_{SRH} = \frac{pn - n_{ie}^2}{\tau_{n0}\left[p + n_{ie}\exp\left(\frac{E_i - E_t}{k_bT}\right)\right] + \tau_{p0}\left[n + n_{ie}\exp\left(\frac{E_t - E_i}{k_bT}\right)\right]}$	The n_{ie} is the effective intrinsic carrier concentration and its value for silicon is $4.28 \times 10^9 cm^{-3}$. K_b is Boltzmann's constant and E_i and E_t are the intrinsic Fermi level and trap energy level, respectively. T is the lattice temperature in degree Kelvin. n and p are the electron and hole concentrations. Basic for the SRH model are the assumptions of one trap level in the forbidden band i.e. $E_t = E_i$ and corresponds to the most efficient recombination center. τ_{n0} and τ_{p0} are the electron and hole bulk lifetimes, 10^{-5}s has been used for 10 μm thick device and 10^{-3}s for 250 μm thick device. N is the doping concentration of Si
Surface recombination	$R_{surface} = \frac{pn - n_{ie}^2}{\tau_n^{eff}\left[p + n_{ie}\exp\left(\frac{E_i - E_t}{k_bT}\right)\right] + \tau_p^{eff}\left[n + n_{ie}\exp\left(\frac{E_t - E_i}{k_bT}\right)\right]}$ $\frac{1}{\tau_n^{eff}} = \frac{1}{\tau_n^i} + \frac{d_i}{A_i}S_{n0}$ and $\frac{1}{\tau_p^{eff}} = \frac{1}{\tau_p^i} + \frac{d_i}{A_i}S_{p0}$ With $S_{p0} = \sigma_p\nu_{th}N_{st}$ and $S_{n0} = \sigma_n\nu_{th}N_{st}$	Where, A_i and d_i are the area and the length of the interface node i and τ_n^i is the bulk lifetime calculated at a node i along the interface. $S_{p0}S_{n0}$, σ_p and σ_n are the surface recombination velocities (SRVs) parameters and capture cross section for holes and electrons respectively. N_{st} is the surface states per unit area and ν_{th} is the thermal velocity of the charge carrier ($\sim 10^7\,\mathrm{cm\,s^{-1}}$).

References

[1] I.E.E. ITRPV, 2017, ITRPV, (2017).
[2] A. Deinega, S. Eyderman, S. John, Coupled optical and electrical modeling of solar cell based on conical pore silicon photonic crystals, J. Appl. Phys. 113 (2013) 224501-224501.
[3] S. Jeong, M.D. McGehee, Y. Cui, All-back-contact ultra-thin silicon nanocone solar cells with 13.7% power conversion efficiency, Nat. Commun. 4 (2013) 2950-2950.
[4] R. Pandey, R. Chaujar, Numerical simulations of novel SiGe-based IBC-HJ solar cell for standalone and mechanically stacked tandem applications, Mater. Res. Bull. 93 (2017) 282–289.
[5] C. van Lare, F. Lenzmann, M.A. Verschuuren, A. Polman, Dielectric scattering patterns for efficient light trapping in thin-film solar cells, Nano Lett. 15 (2015) 4846–4852.
[6] N. Dwivedi, S. Kumar, A. Bisht, K. Patel, S. Sudhakar, Simulation approach for optimization of device structure and thickness of HIT solar cells to achieve ~27% efficiency, Sol. Energy 88 (2013) 31–41.
[7] E. Garnett, P. Yang, Light trapping in silicon nanowire solar cells, Nano Lett. 10 (2010) 1082–1087.
[8] K.X. Wang, Z. Yu, V. Liu, Y. Cui, S. Fan, Absorption enhancement in ultrathin crystalline silicon solar cells with antireflection and light-trapping nanocone gratings, Nano Lett. 12 (2012) 1616–1619.
[9] S. Jeong, E.C. Garnett, S. Wang, Z. Yu, S. Fan, M.L. Brongersma, M.D. McGehee, Y. Cui, Hybrid silicon nanocone–polymer solar cells, Nano Lett. 12 (2012) 2971–2976.
[10] D.R. Kim, C.H. Lee, P.M. Rao, I.S. Cho, X. Zheng, Hybrid Si microwire and planar solar cells: passivation and characterization, Nano Lett. 11 (2011) 2704–2708.
[11] T.J. Kempa, J.F. Cahoon, S.-K. Kim, R.W. Day, D.C. Bell, H.-G. Park, C.M. Lieber, Coaxial multishell nanowires with high-quality electronic interfaces and tunable optical cavities for ultrathin photovoltaics, Proc. Natl. Acad. Sci. Unit. States Am. 109 (2012) 1407–1412.
[12] J. Zhu, C.-M. Hsu, Z. Yu, S. Fan, Y. Cui, Nanodome solar cells with efficient light management and self-cleaning, Nano Lett. 10 (2010) 1979–1984.
[13] S.-F. Leung, M. Yu, Q. Lin, K. Kwon, K.-L. Ching, L. Gu, K. Yu, Z. Fan, Efficient photon capturing with ordered three-dimensional nanowell arrays, Nano Lett. 12 (2012) 3682–3689.
[14] M.S. Branham, W.-C. Hsu, S. Yerci, J. Loomis, S.V. Boriskina, B.R. Hoard, S.E. Han, G. Chen, 15.7% Efficient 10-μm-thick Crystalline Silicon Solar Cells Using Periodic Nanostructures, Advanced Materials, Deerfield Beach, Fla., 2015, pp. 2182–2188.
[15] W. Chen, V. Depauw, F. Haddad, J.-L. Maurice, P. Roca i Cabarrocas, Influence of anodic bonding on the surface passivation quality of crystalline silicon, Sol. Energy Mater. Sol. Cell. 157 (2016) 154–160.
[16] T. Niewelt, M. Selinger, N.E. Grant, W. Kwapil, J.D. Murphy, M. Schubert, Light-induced activation and deactivation of bulk defects in boron-doped float-zone silicon, J. Appl. Phys. 121 (2017) 185702.
[17] A.G. Aberle, Surface passivation of crystalline silicon solar cells: a review, Prog. Photovoltaics Res. Appl. 8 (2000) 473–487.
[18] G.S. Chung, K.S. Kim, F. Yakuphanoglu, Electrical characterization of Au/3C-SiC/n-Si/Al Schottky junction, J. Alloy. Comp. 507 (2010) 508–512.
[19] D. Klein, M. Kunst, Study of surface passivation of crystalline silicon with amorphous silicon carbide deposited by plasma enhanced chemical vapor deposition, Appl. Phys. Lett. 99 (2011) 232106.
[20] T. Chassagne, G. Ferro, D. Chaussende, F. Cauwet, Y. Monteil, J. Bouix, A comprehensive study of SiC growth processes in a VPE reactor, Thin Solid Films 402 (2002) 83–89.
[21] Y.-H. Joung, H. Kang, J. Kim, H.-S. Lee, J. Lee, W. Choi, SiC formation for a solar cell passivation layer using an RF magnetron co-sputtering system, Nanoscale Research Letters 7 (2012) 22-22.
[22] R. Pandey, R. Chaujar, Rear contact SiGe solar cell with SiC passivated front surface for > 90-percent external quantum efficiency and improved power conversion efficiency, Sol. Energy 135 (2016) 242–252.
[23] R. Pandey, R. Chaujar, Novel back-contact back-junction SiGe (BC-BJ SiGe) solar cell for improved power conversion efficiency, Microsyst. Technol. 22 (2016) 2673–2680.
[24] E.V. Kerschaver, G. Beaucarne, Back-contact solar cells: a review, Prog. Photovoltaics Res. Appl. 14 (2006) 107–123.
[25] R. Pandey, R. Chaujar, Numerical simulation of rear contact silicon solar cell with a novel front surface design for the suppression of interface recombination and improved absorption, Curr. Appl. Phys. 16 (2016) 1581–1587.
[26] S. Allen, Y. Awad, Silicon Carbide-based Antireflective Coating, US Patent App. 12/994,973, (2009).
[27] https://us.sunpower.com/company/history/, https://us.sunpower.com/company/history/.

Multidimensional Systems and Signal Processing
https://doi.org/10.1007/s11045-018-0612-2

Smaller feature subset selection for real-world datasets using a new mutual information with Gaussian gain

Seba Susan[1] · **Madasu Hanmandlu**[2]

Received: 1 April 2018 / Revised: 11 August 2018 / Accepted: 13 August 2018
© Springer Science+Business Media, LLC, part of Springer Nature 2018

Abstract
A new filter method is proposed for feature selection and ranking that incorporates a novel mutual information with Gaussian gain for evaluating the relationships between features and the class, and in-between features. The new mutual information is derived as per the axioms of classical information theory from the recently introduced non-extensive entropy with Gaussian gain. The characteristic of this entropy is its non-linearity when representing correlated information in natural texture images represented by sparse probability distributions. In this work, we trace this property in our new mutual information in the context of correlated random variables associated with real-world datasets. The non-linearity of the Gaussian function embedded in the mutual information formula is utilized for identifying the most important features in the correct order of rank, right at the outset of the incremental feature selection algorithm. This leads to formation of smaller groups of ranked feature subsets that give the highest classification accuracies. Extensive experimentation on twenty benchmark datasets from the UCI repository along with comparison to the state-of-the-art confirms the efficacy of our approach. An automated optimum feature subset selection is also proposed based on a simple statistical test on the new measure.

Keywords Feature selection · Feature ranking · Information theoretic measures · Mutual information · Non-extensive entropy with Gaussian gain

1 Introduction

Feature Selection (FS) of datasets applied for machine learning has now become a mandatory procedure to eliminate redundant features and achieve high accuracies (Liu and Lei 2005). Identifying the most relevant features that help in predicting the class label is the aim of every feature selection algorithm. Information-theoretic measures such as mutual information (MI) (Battiti 1994), entropy (Jurado et al. 2015), Kullback–Leibler (KL) divergence (Zhang et al. 2013) and correlation (Akande et al. 2015) have been in use since long for studying

✉ Seba Susan
seba_406@yahoo.in

1 Delhi Technological University, New Delhi 110042, India

2 Department of Electrical Engineering, IIT Delhi, New Delhi 110016, India

Published online: 20 August 2018

the relationship between the features and the class label. Of all these measures, mutual information emerges as the most popular choice due to its ability to represent the non-linear relationships between random variables (Yang and Ong 2012). Though the recent innovations in this area include unsupervised techniques such as clustering with mutual information-based distances (Vinh and Bailey 2013), the conventional method of supervised Mutual Information based Feature Selection (MIFS) (Battiti 1994) consistently reports high classification accuracies in literature, and so it forms the focus of interest in our paper. Partial or skewed attention to specific features for enhancing the overall performance can be observed in the works of Tang et al. (2016) that finds class-specific features for Bayesian classification, in Yang et al. (2015) that emphasizes on the features linked with the minority class, and in Song et al. (2013) that forms a set of the most representative features from each cluster. To find the smallest subset of relevant and unique features is a challenge for the real-world datasets in today's context, as observed in experiments with social media data that is inherently inter-linked (Tang and Liu 2014) and speaker verification from cepstral coefficients derived from the speech signal (Eriksson et al. 2005). Different solutions to the FS problem do exist other than these conventional techniques and some of them are listed below. Researchers occasionally have come up with varied solutions to address the optimality of the feature subsets. The problem of feature selection specifically for imbalanced datasets is tackled in Khoshgoftaar et al. (2014) by an iterative sampling process followed by aggregation of the ranked features resulting from all iterations. Modern applications of FS such as medical diagnosis has been particularly investigated in Zhou et al. (2017) wherein an iterative random forest method is used for identifying useful biomarkers from urinary micro-array data for diagnosing chronic kidney disease. The application of deep learning to the FS problem is yet another unconventional but promising direction of research and the method described in Zou et al. (2015) identifies the reconstruction errors associated with deep belief networks as the criterion for ranking features.

In this paper, we define a new mutual information measure based on the Gaussian information gain, particularly for MIFS, that gives a more compact subset of ranked feature list due to the non-linearity of the Gaussian function embedded in it. The purpose of our algorithm is more authentic feature ranking through the non-extensive mutual information that we introduce through this paper. As a result, we get higher accuracies for the smallest subset of ranked features since our ranking scheme is more accurate as compared to other methods, as we prove through extensive experimentation.

The organization of the paper is as follows. A review of related work in literature including the definition of mutual information and its application to feature selection is reviewed in Sect. 2. The new mutual information with Gaussian gain is defined in Sect. 3, and its usefulness in the iterative MI based feature selection algorithm along with the feasibility of automation of the whole process is also explored in the same section. The experimentation and the results are analyzed in Sect. 4 and the overall conclusions are drawn in Sect. 5.

2 Related work in literature

In this section, we review the Mutual Information (MI) based Feature Selection (FS) and related methods that have been prevalent since long and have a direct bearing on our approach. We also discuss some recent advents in the FS field that are quick and fast approaches and popular among researchers who desire a fast solution to the FS problem. The trade-off between accuracy of FS and the speed factor is a major research problem and one that must be negotiated by researchers prior to choosing their FS algorithms.

2.1 Feature selection techniques

Feature ranking and selection has been of great interest to the research community due to its advantages of dimensionality reduction and formation of compact feature subsets (Bolón-Canedo et al. 2017). HSIC-Lasso (Yamada et al. 2014), Fisher Score (Duda et al. 2001) based on ranking by Fisher criterion, and Relief (Kira and Rendell 1992) that is based on instance learning, are quite unlike the conventional information-theoretic FS algorithms though popular due to their quick and fast execution. The Least absolute shrinkage and selection operator (Lasso) selects non-redundant features using kernel-based independence measures (Yamada et al. 2014). A different line of research is the exploration of evolutionary and swarm-based algorithms for learning the ranks of features through classification accuracies. Differential Evolution-based Feature Selection (DEFS) (Khushaba et al. 2011) based on a real-value optimizer is an example of a wrapper method that depends on classification accuracies for ranking the features. Gravitational search algorithm has been used for feature selection recently in Bostani and Sheikhan (2017) to filter out the noisy, redundant features. Recent innovations in swarming algorithms that have been applied as a search strategy for optimal feature subset selection include the Grasshopper Optimization Algorithm (GOA) that was coupled with Evolutionary Population Dynamics in Mafarja et al. (2018) for implementing a wrapper-based FS.

It has been several decades since the term mutual information was coined by none other than Claude Shannon in his classic paper (Shannon 1948). It refers to the dependence between two random variables measured through logarithmic gain function. Researchers were quick to apply this information-theoretic measure for correlating the feature variable of a dataset with the class variable to measure the amount of inter-dependence between the two (Lisker 1957; Chow and Liu 1968). That lead to the introduction of iterative mutual information based schemes (Quinlan 1986; Ben-Bassat 1982) that selects and ranks candidate features by measuring the mutual information with respect to the class variable. Quinlan in 1986 used Mutual Information to measure the merit of an attribute as he laid the foundations of decision trees (Quinlan 1986). Battiti (1994) suggested an iterative algorithm that is now termed Mutual Information based Feature Selection (MIFS), that evaluates not only the mutual information with respect to the class variable but also the mutual information with respect to the already selected feature variables that should be at a bare minimum. The different mutual information-based feature selection schemes that evolved from MIFS are discussed in detail in Sect. 2.3. The time-complexity of all MIFS algorithms are similar since they are based on the same iterative process of selecting a candidate feature in an incremental fashion. MIFS-ND introduced recently in Hoque et al. (2014), utilizes a greedy search algorithm for ranking features based on their relevance to the class variable and in-between features. A recent survey on mutual information based feature selection methods establishes the current significance of this conventional information-theoretic measure in grading and ranking features (Pascoal et al. 2017).

2.2 Definition of mutual information

Mutual information is a popular information measure used to rank and evaluate the features or attributes of datasets with respect to their relevance to the class variable. The mutual information (Shannon 1948; Cover and Thomas 1991) (MI) between two random variables $X = \{x_i\}$ and $Y = \{y_j\}$ is defined as the reduction in the uncertainty of X if Y is known i.e.

$$I(X|Y) = H(X) - H(X|Y) \tag{1}$$

The uncertainty of the random variable X is measured by its entropy $H(X)$. The conditional entropy of X given Y is denoted by $H(X|Y)$. The mutual information in (1) is thus termed the conditional mutual information of X given Y. On similar lines, the conditional mutual information of Y given X is given by

$$I(Y|X) = H(Y) - H(Y|X) \tag{2}$$

An obvious and conventional choice of the entropy formula in (1) and (2) is Shannon entropy (Shannon 1948) with the logarithmic information gain, which when substituted in (1) yields

$$I(X|Y) = \sum_i \sum_j p(x_i, y_j)(\ln p(x_i|y_j) - \ln p(x_i)) \tag{3}$$

We next review one of the most popular feature selection algorithms incorporating mutual information called the Mutual Information based Feature Selection (MIFS).

2.3 Mutual information based feature selection (MIFS)

Mutual Information based Feature Selection (MIFS) proposed by Battiti (1994) selects features one by one in an incremental manner, with the criteria of selection being the maximization of the mutual information with respect to the class variable and the minimization of the mutual information with respect to the already selected features. Let C be the output class and F and S be the initial and the final set of features selected, respectively. Initially S is empty and F contains the entire set of features. Iteratively, we consider the candidacy of each feature in F for its inclusion in S. Let the feature f_i belong to F and the feature f_s belong to S.

MIFS requires that the feature f_i that is transferred from F to S is the one that maximizes the expression

$$I(C; f_i) - \beta \sum_{f_s \in S} I(f_s; f_i) \tag{4}$$

where $I(C; f_i)$ is the mutual information between the output C and feature f_i, and $I(f_s; f_i)$ is the Mutual Information between each selected feature f_s in S and the candidate feature f_i. The parameter β is user defined.

As a substitute to the user defined parameter β, the Maximum Relevance Minimum Redundancy (mRMR) method in Peng et al. (2005) uses the cardinality of the set S, so that the expression to be maximized in (4) now reduces to

$$I(C; f_i) - \frac{1}{|S|} \sum_{f_s \in S} I(f_s; f_i) \tag{5}$$

In the Normalized Mutual Information based Feature Selection (NMIFS) (Estevez et al. 2009), which is an improvement over mRMR, the mutual information in the second term in (5) is normalized by the minimum entropy of the features f_i and f_s as shown below.

$$I(C; f_i) - \frac{1}{|S|} \sum_{f_s \in S} \frac{I(f_s; f_i)}{\min(H(f_s), H(f_i))} \tag{6}$$

The second term of (6) is an adaptive redundancy penalization term that requires no user-defined parameters. For high dimensional data, the computational complexity increases due to the second term since the mutual information between every pair of $(\{f_s\}, f_i)$ needs to be calculated.

Table 1 Sample probabilities and their difference of logarithms

$p(x_i \mid y_j)$	$p(x_i)$	$\ln p(x_i \mid y_j) - \ln p(x_i)$
0.9	0.3	1.0986
0.6	0.5	0.182
0.05	0.02	0.9162
0.1	0.099	0.0100

3 A new non-extensive mutual information for smaller feature subset selection-motivation, definition, application and methodology

3.1 Requirement of a new mutual information for representing the sparse probabilities in real-world datasets

The mutual information measure defined by Shannon in Shannon (1948) is essentially a difference of logarithms as observed from (3). This leads to a dynamic range compression, which is correct in essentials presuming the large differences expected between the conditional probability $p(x_i \mid y_j)$ and the individual probability $p(x_i)$ for correlated random variables X and Y. However, for real-world datasets containing thousands of samples and/or hundreds of attributes, discretization of the real-valued attribute variables leads to a sparse probability representation. Scanning for correlated information amongst these sparse probabilities requires a new mutual information definition adapted to this low range of probabilities encountered in the real-world datasets. Computation of the mutual information in (3) based on these sparse probabilities could be misleading, since the logarithm function becomes unstable for very small numbers close to zero. We demonstrate this through an example in Table 1 where some sample values of $p(x_i \mid y_j)$ and $p(x_i)$, and the difference of their logarithms are shown. For the low probability values of (0.05, 0.02), the difference of logarithms gives a very high unlikely value of 0.9162.

To undo the dynamic compression that the logarithm induces, its inverse function or exponential could be substituted for a better representation of the probabilities in low ranges. We propose that the difference of logarithms in (3) be replaced by a difference of exponentials, more specifically by a difference of Gaussians, so that the low and sparse probabilities found in real-world datasets fall within the bell of the Gaussian curve and are duly highlighted. In particular, we draw inspiration from our previous work on the identification of regular textures from real world images (Susan and Hanmandlu 2013a), in which we introduced the non-extensive entropy with Gaussian gain for a better representation of the sparse probabilities that ensue from texture images when intensities were discretized into bins and compiled into a histogram. We next derive the new mutual information incorporating the difference of Gaussians from the previously defined non-extensive entropy with Gaussian gain as per the axioms of classical probability theory.

3.2 Definition of the new mutual information with Gaussian gain

The non-extensive entropy with Gaussian gain was introduced by the authors in Susan and Hanmandlu (2013a), and is defined as

$$H(P) = \sum_i p_i e^{-p_i^2} \tag{7}$$

Its name is derived from the Gaussian information gain function $e^{-p_i^2}$ embedded in the formula. The probability distribution $P = \{p_i\}$ in (7) is a complete one, i.e. $\sum_i p_i = 1$ and $0 \leq p_i \leq 1$. The entropy in (7) is non-extensive since it exhibits non-additive behavior when the entropies from the component sub-systems are summed up together, as observed for the crowd motion anomaly detection experiments in Susan and Hanmandlu (2015) and dynamically growing neural networks in Susan and Dwivedi (2014) in which only significant deviations in the sum of component entropies is recorded as a spike. This property of the non-extensive entropy has been applied successfully for automatic texture defect detection in a recent work (Susan and Sharma 2017), where the defect versus non-defect regions are distinguished by fitting a two-mode Gaussian mixture model on the non-extensive entropy values computed from different texture patches. Another application is image clustering based on the mean-shift mode distributions that assume a maximum entropy at the point of optimal clustering (Susan and Kumar 2016). It is to be noted that the probabilistic non-extensive entropy in (7) was extended for defining the non-extensive fuzzy entropy in Susan and Hanmandlu (2013b), which was then used as a simple fuzzy criterion for feature selection and ranking.

In this paper, we first propose to extend the probabilistic non-extensive entropy with Gaussian gain to define the mutual information between two correlated random variables. This measure would then serve our purpose to measure the correlation between the class variable and the feature variables, and also in-between the feature variables to check for redundancy.

The non-extensive entropy in (7) when substituted in (1) yields the new mutual information with Gaussian gain defined as

$$\begin{aligned} I(X|Y) &= \sum_i \sum_j p(x_i, y_j) e^{-p^2(x_i)} - \sum_i \sum_j p(x_i, y_j) e^{-p^2(x_i|y_j)} \\ &= \sum_i \sum_j p(x_i, y_j) [e^{-p^2(x_i)} - e^{-p^2(x_i|y_j)}] \end{aligned} \tag{8}$$

The expression in (8) can also be written as

$$I(X|Y) = \sum_i \sum_j p(x_i, y_j) e^{-p^2(x_i)} [1 - e^{-\frac{(p^2(x_i, y_j) - p^2(x_i) p^2(y_j))}{p^2(y_j)}}] \tag{9}$$

The above result is obtained by substituting, $p^2(x_i|y_j) = \frac{p^2(x_i, y_j)}{p^2(y_j)}$ in (8). The presence of exponentials in the summation in (8) implies that the new measure is non-additive since exponentials do not add up unlike logarithms (Susan and Hanmandlu 2013a). Similarly, mutual information from multiple component sub-systems do not add up due to the exponentials that constitute the formula. It is the non-extensive behavior of the exponential based information measures that is demonstrated here.

Theorem 1 *The new Mutual Information is a non-negative quantity.*

Table 2 Sample probabilities and their difference of Gaussians

$p(x_i \mid y_j)$	$p(x_i)$	$e^{-p^2(x_i)} - e^{-p^2(x_i \mid y_j)}$
0.9	0.3	0.469
0.6	0.5	0.081
0.05	0.02	2.096×10^{-3}
0.1	0.099	1.97×10^{-4}

Proof The new Mutual Information is a non-negative quantity implies

$$I(X|Y) \geq 0 \tag{10}$$

This can be explained from the fact that in (8), a reduction in uncertainty of X always occurs (or sometimes may not occur for uncorrelated variables) if Y is known, i.e.

$$p(x_i) \leq p(x_i|y_j) \tag{11}$$

Hence $I(X|Y)$ in (8) is non-negative.

In the context of the feature selection procedure described in Sect. 2, $I(C|f_i)$, $I(f_s|f_i) \geq 0$ in Eq. (6). □

Theorem 2 *The new Mutual Information is not necessarily symmetric*

Proof The new Mutual information measure is not necessarily symmetric

$$I(X|Y) \neq I(Y|X) \tag{12}$$

□

Proof This follows from the fact that the sum of the exponential terms $\left\{ e^{-p^2(x_i)}[1 - e^{-\frac{(p^2(x_i,y_j) - p^2(x_i)p^2(y_j))}{p^2(y_j)}}] \right\}$ in $I(X|Y)$ is not necessarily equal to the sum of exponential terms $\left\{ e^{-p^2(y_j)}[1 - e^{-\frac{(p^2(x_i,y_j) - p^2(x_i)p^2(y_j))}{p^2(x_i)}}] \right\}$ in $I(Y|X)$ for unequal distributions X and Y. □

To prove the effectiveness of the new measure in representing correlated information within sparse probabilities associated with real-world datasets, we redo the experiment in Table 1 and compute the difference of Gaussians instead of the difference of logarithms. The results are shown in Table 2 and indicate a low and feasible value for (0.05, 0.02) that is in order with the other values.

3.3 Application of the newly defined non-extensive mutual information for feature selection by MIFS

Maximizing the objective function in (6) means to maximize the first term (relevance) and minimize the second term (redundancy). Since the method described in Sect. 2 is incremental in nature, we would wish that the most relevant and compact feature subset be identified right at the outset. The first term $I(C; f_i)$ indicates the information obtained about

the class variable C given the candidate feature f_i and so it can be denoted as $I(C|f_i)$. On similar lines, $I(f_s; f_i)$ in the second term, which is the information obtained about the already selected feature f_s given the candidate feature f_i, can be denoted by $I(f_s|f_i)$. Taking into consideration the asymmetry of the new mutual information, we substitute our observations into the MIFS objective function to be maximized in (6), which we now rewrite as

$$I(C|f_i) - \frac{1}{|S|} \sum_{f_s \in S} \frac{I(f_s|f_i)}{\min(H(f_s), H(f_i))} \tag{13}$$

The formulae for mutual information ($I(C|f_i)$, $I(f_i|f_s)$) in (13) are substituted from (8) and those for the entropy ($H(f_i)$, $H(f_s)$) from (7).

Maximizing the first term in (13) i.e. $I(C|f_i)$, means to identify recurring patterns of the class label and feature values, a characteristic of the non-extensive entropy with Gaussian gain on which the new mutual information in (7) is based. A high co-occurrence of the feature value with a class label is translated to a higher probability of co-occurrence $p(x_i|y_j)$ that pushes $e^{-p^2(x_i|y_j)}$ further down the non-linear Gaussian curve in the second term in the MI expression in (8), yielding an overall higher mutual information $I(C|f_i)$. The second term in (13) is a summation of mutual information from multiple sources. Since the Gaussian function embedded in the MI formula is non-additive by nature, only consistently low values of $\underset{s}{\forall}\{I(f_s|f_i)\}$ will induce a negative spike in the summation in the second term thus maximizing the overall objective function in (13). For redundant features, the second term yields a high value leading to their non-selection. Thus the use of the new non-extensive mutual information for MIFS ensures that the most relevant and non-redundant features are identified right at the onset. However, the feature rankings amongst the redundant and non-relevant features at the bottom of the list could be faulty, due to the non-additive summation in the second term. Since only the most relevant and non-connected features are of interest to us and fast and quick identification is required, we assert our method to be of paramount importance in this regard. It is confirmed that in the absence of redundancy and in case all features are unique and non-connected, the first term in (13) overrides the second term, and the features are then simply ranked according to their correlation with the class label. The pseudo-code for our incremental FS algorithm is given below.

Let a selected and ranked feature at any point in the algorithm be denoted as f_s

Let the set of selected features be $S=\{f_s\}$

Initialize $S=\{\}$

Given the class column vector C for all the instances in the dataset

Initialize the feature rank $j=1$

REPEAT

For each Candidate feature f_i in the set of non-selected features

Find MutualInformation(C/f_i)

Temp=0;

For each selected feature f_s

MinEntropy=min(Entropy(f_s), Entropy(f_i));

Temp=Temp+(MutualInformation(f_s/f_i))/MinEntropy;

End

Measure(f_i)=MutualInformation(C/f_i)-Temp/size(S);

// For the very first iteration: Measure(f_i)=MutualInformation(C/f_i); //

End

Sort Measure(f_i) for all i in descending order

Include f_i at the top of sorted list in the selected feature list S with Rank j

Increment Rank $j=j+1$

UNTIL j=number of Features in original dataset

// Include the last remaining feature in S at the last rank position//

We also propose an automatic feature subset selection by plotting the (negated) second or redundancy term for the ranked feature list and locating the first positive peak in the cumulative mean of the graph to mark the closing boundary of the top ranked feature subset. The first positive peak is found in an automated manner by checking, starting from the origin, if the value of the graph at the next point along the x-axis, falls below the value at the current point on the x-axis. The x-axis here, refers to the ranked feature list returned by the proposed FS method. Positive peaks in the (negated) redundancy graph indicate non-redundant behavior that helps in maximizing the objective function in (13), and so is a desirable quality.

The overall methodology followed for implementing the proposed feature selection scheme for experimentation on real-world datasets is described next.

3.4 Overall methodology for the incremental feature selection process incorporating the new measure

Prior to the feature selection step, some pre-processing of the datasets is essential that involves normalization of the values in each feature column, in the range of 0 to 1. This is followed by discretization of the values to form the probability histograms. 100 bins with Gaussian kernel size of 0.05 are used to discretize the normalized values and derive the probability statistics.

The incremental feature selection algorithm on the lines of the existing work described in Sect. 2 and incorporating our new measure as described in the previous sub-section, we define as *Non-Extensive Normalized Mutual Information based Feature Selection (Next-NMIFS)* which is summarized below.

1. Starting from an empty set S consider each candidate feature from the feature set F that is not included in S and compute the objective function in (13).
2. Select the candidate feature that maximizes the objective function in (13) and include it in S assigning it a rank on the order of its inclusion in S.
3. Repeat the procedure in steps 1 and 2 till all the features in F have been ranked and included in S.
4. Use classification experiments exhaustively for all possible top-ranked feature subsets, and mark the accuracies.
5. Alternatively, for automatically determining the most compact and relevant feature subset with minimum redundancy, plot the negative of the second term in (13) i.e. $\left\{-\frac{1}{|S|}\sum_{f_s\in S}\frac{I(f_i|f_s)}{\min(H(f_i),H(f_s))}\right\}$ for all the features in the order of the rank. Find the cumulative mean at each point on the graph and plot it. Find the first peak in the cumulative mean graph, which is the point where the mean redundancy since the start of process reaches a low point. All the top-ranked features until this point constitute our proposed automatic compact feature subset for the particular dataset. The accuracies of this compact feature subset are tested and compared against our results of exhaustive search in step 4 to check if the automation is a feasible alternative to the conventional exhaustive search for the best feature subsets.

4 Experimental results and discussions

4.1 Experimental setup

The real-world datasets used for our experimentation comprise of twenty datasets from the UCI Repository (Frank and Asuncion 2010) whose details of (*Samples, Outputs, Features*) are given in the first column of Table 3. The software implementation is done in MATLAB 7.10 on a Pentium 2.6 GHz processor with 1 GB RAM. Each dataset is segregated in the following manner: 50% training, 50% testing with cross-validation of the training and testing inputs. The Support Vector Machine (SVM) classifier with the Gaussian radial basis function as the kernel, is used for the classification by considering various feature subsets in the rank order. The parameters C and *epsilon* of SVM are determined while training by the Pattern Search method (Momma and Bennett 2002) with intervals of 10 and tolerance of 10^{-8}. The mutual information-based feature selection methods require data discretization to construct the probability histograms. First of all, each feature column is normalized between 0 to 1 as shown below.

Table 3 Results of feature selection using the SVM classifier on 20 datasets from the UCI repository (with the method proposed in this paper shown highlighted by gray)

S. no.	*Datasets* (*Samples, Outputs, Features*)	mRMR		NMIFS		Next-NMIFS (PROPOSED)		HSIC-Lasso		Fisher Score		RELIEF		DEFS		Upper-bound normalized MIFS	
		V	CV	V	CV	V	CV	V	CV	V	CV	V	CV	V	CV	V	CV
Amongst all methods																	
1	*Glass* (214, 6, 9)	90.34 (6)	90.5 (6)	91.12 (5)	**91.28 (5)**	**91.43 (4)**	**91.28 (5)**	91.28 (7)	**91.28 (5)**	90.97 (2)	90.97 (6)	90.19 (7)	90.19 (9)	90.34 (5)	90.81 (5)	91.12 (5)	**91.28 (5)**
2	*Ionosphere* (351, 2, 34)	**94.89 (2)**	90.86 (12)	**94.89 (2)**	90.86 (12)	**94.89 (2)**	**91.43 (13)**	90.34 (6)	90.86 (9)	89.20 (3)	90.86 (12)	84.09 (4)	86.29 (8)	92.61 (5)	90.86 (9)	**94.89 (2)**	90.86 (12)
3	*SPECT-Heart* (267, 2, 22)	84.21 (9)	85.82 (14)	84.21 (9)	85.82 (14)	**85.71 (9)**	**85.82 (9)**	84.96 (6)	85.07 (11)	85.71 (11)	85.82 (13)	84.21 (21)	85.07 (11)	82.70 (20)	85.07 (20)	84.21 (9)	85.82 (14)
4	*Lung Cancer* (32, 3, 56)	79.17 (18)	85.41 (16)	79.17 (18)	85.41 (16)	**79.17 (12)**	**87.50 (12)**	75 (2)	83.33 (31)	77.08 (6)	85.41 (20)	68.75 (46)	77.08 (2)	75 (15)	75 (13)	77.08 (4)	83.33 (11)
5	*Abalone* (4177, 29, 8)	96.54 (1)	96.28 (1)	96.54 (1)	96.28 (1)	**96.55 (1)**	**96.30 (1)**	96.55 (2)	96.29 (1)	**96.55 (1)**	**96.30 (1)**	**96.55 (1)**	96.29 (1)	**96.55 (1)**	96.29 (1)	96.54 (1)	96.28 (1)
6	*Sonar* (208, 2, 60)	81.73 (10)	81.73 (8)	**84.62 (10)**	83.65 (10)	**84.62 (10)**	**83.65 (9)**	84.62 (12)	82.69 (10)	80.77 (6)	81.73 (3)	84.62 (31)	80.77 (7)	80.77 (7)	78.85 (5)	77.88 (10)	76.92 (10)
7	*Wine* (178, 3, 13)	97.38 (6)	98.13 (7)	97.38 (6)	98.13 (7)	**98.13 (5)**	**98.50 (5)**	97.00 (4)	98.50 (6)	**98.13 (5)**	**98.50 (5)**	94.76 (5)	96.25 (6)	97.75 (6)	98.13 (6)	97.38 (6)	98.13 (7)
8	*Breast Cancer Wisconsin* (699, 2, 9)	**97.13 (8)**	96.57 (7)	**97.13 (8)**	96.57 (5)	**97.13 (8)**	**97.14 (5)**	**97.13 (8)**	96.57 (6)	96.84 (9)	96.57 (8)	96.84 (9)	97.14 (7)	96.84 (9)	96.86 (5)	**97.13 (8)**	96.86 (5)
9	*Semeion* (1593, 2, 265)	98.36 (86)	98.12 (172)	98.36 (86)	98.12 (172)	98.49 (114)	**98.12 (159)**	98.11 (265)	97.87 (201)	**98.49 (113)**	**98.12 (159)**	98.11 (218)	97.62 (124)	98.36 (118)	97.49 (166)	98.36 (86)	98.19 (172)
10	*Hepatitis* (155, 2, 19)	**71.43 (5)**	**76.92 (6)**	**71.43 (5)**	**76.92 (6)**	**71.43 (5)**	**76.92 (6)**	70.13 (2)	74.36 (2)	67.53 (6)	75.64 (4)	63.64 (9)	69.23 (1)	68.83 (6)	75.64 (3)	**71.43 (5)**	**76.92 (6)**
11	*Echocardiogram* (132, 2, 12)	93.94 (10)	87.88 (12)	93.94 (10)	87.88 (12)	**93.94 (1)**	**92.42 (4)**	**93.94 (1)**	87.88 (6)	93.94 (6)	87.88 (8)	93.94 (8)	87.88 (11)	93.94 (10)	87.88 (10)	**93.94 (1)**	90.91 (7)

Table 3 continued

S. no.	*Datasets* (*Samples, Outputs, Features*)	mRMR		NMIFS		Next-NMIFS (PROPOSED)		HSIC-Lasso		Fisher Score		RELIEF		DEFS		Upper-bound normalized MIFS	
		V	CV	V	CV	V	CV	V	CV	V	CV	V	CV	V	CV	V	CV
12	*Arrhythmia* (452, 16, 279)	95.74 (4)	95.74 (4)	95.63 (2)	95.63 (2)	**95.99 (6)**	**95.99 (6)**	95.24 (8)	95.24 (8)	94.93 (5)	94.93 (5)	95.88 (74)	95.88 (74)	95.22 (8)	95.22 (8)	95.05 (28)	95.05 (28)
13	*CNAE 9* (1080, 9, 856)	95.16 (29)	94.65 (50)	95.23 (28)	94.73 (28)	**95.86 (39)**	**95.35 (41)**	92.86 (272)	92.76 (272)	95.72 (46)	95.12 (46)	93.19 (726)	93.13 (730)	92.37 (409)	92.55 (350)	93.19 (72)	93.15 (71)
14	*Internet* (3279, 2, 1558)	95.79 (135)	95.79 (135)	95.79 (135)	95.79 (135)	**96.03 (134)**	**96.03 (134)**	94.87 (2)	94.87 (2)	94.02 (163)	93.10 (163)	92.80 (310)	92.80 (310)	93.28 (57)	93.28 (57)	95.05 (17)	95.05 (17)
15	*Breast Tissue* (106, 6, 9)	**87.42 (3)**	87.74 (9)	**87.42 (3)**	87.74 (9)	**87.42 (3)**	**87.74 (4)**	86.48 (1)	87.74 (9)	86.48 (5)	87.74 (8)	87.42 (7)	87.74 (9)	86.48 (8)	87.74 (9)	**87.42 (3)**	87.74 (9)
16	*Horse Colic* (300, 2, 27)	73.56 (4)	78.89 (5)	73.56 (4)	78.89 (5)	**75.56 (5)**	**80.0 (6)**	71.78 (6)	78.22 (8)	**75.56 (5)**	78.44 (5)	75.33 (2)	78.89 (7)	72.89 (2)	78.22 (7)	73.56 (4)	78.89 (5)
17	*Dermatology* (366, 6, 34)	**91.99 (33)**	**91.62 (32)**	**91.99 (33)**	91.53 (18)	**91.99 (33)**	**91.62 (32)**	91.80 (14)	91.43 (25)	91.80 (19)	91.35 (21)	91.80 (26)	91.07 (32)	91.80 (27)	91.35 (27)	**91.99 (33)**	91.53 (18)
18	*Libra Movement* (360, 15, 90)	94.44 (7)	94.44 (7)	94.44 (7)	94.44 (7)	**94.44 (3)**	**94.44 (2)**	**94.44 (3)**	94.44 (3)	94.44 (9)	94.44 (9)	94.44 (7)	94.44 (7)	**94.44 (3)**	94.44 (3)	94.44 (7)	94.44 (7)
19	*Soybean Large* (307, 19, 35)	98.52 (23)	98.60 (23)	98.52 (23)	98.60 (23)	**98.93 (17)**	**99.15 (16)**	98.86 (17)	98.87 (15)	98.90 (23)	98.84 (25)	98.04 (15)	98.56 (18)	97.73 (18)	97.88 (16)	98.52 (23)	98.60 (23)
20	*Parkinson* (195, 2, 22)	**96.91 (7)**	95.92 (9)	95.88 (13)	93.88 (13)	**96.91 (7)**	**95.92 (8)**	91.75 (20)	92.86 (21)	89.69 (3)	93.88 (9)	94.85 (9)	93.88 (8)	94.85 (7)	92.86 (21)	95.88 (14)	93.88 (14)
Run-time (in secs) *On a per feature basis as in* (Peng et al. 2005) *and averaged across all datasets*		0.945 s		1.242 s		1.3 s		0.02 s		0.007 s		0.08 s		0.16 s		1.95 s	

The values in bold for every dataset indicate the highest classification accuracy (in %)

For each feature column f_i^{old} of the dataset, i = 1, 2,…, K, if $\max(f_i^{old}) - \min(f_i^{old}) > 0$, we have

$$f_i^{new} = \frac{f_i^{old} - \min(f_i^{old})}{\max(f_i^{old}) - \min(f_i^{old})} \tag{14}$$

If $\max(f_i^{old}) - \min(f_i^{old}) = 0$ then $f_i^{new} = f_i^{old}$.

After normalization, 100 bins with Gaussian kernel size of 0.05 are used to discretize f_i^{new} and derive the probability statistics required for the feature selection algorithm described in Sect. 3.

4.2 Discussion on feature selection results

The results of the exhaustive search for the top-ranked feature subset that gives the highest accuracies are summarized in Table 3 for the proposed method (Next-NMIFS) for both Validation (V) and Cross-Validation (CV). Our results are compared with several state-of-the-art methods of feature selection and ranking namely NMIFS (Peng et al. 2005), mRMR (Estevez et al. 2009), HSIC-Lasso (Yamada et al. 2014), Fisher Score (Duda et al. 2001), Relief (Kira and Rendell 1992), Differential evolution based feature selection (DEFS) (Khushaba et al. 2011) and upper-bound normalized MIFS (Lee et al. 2012). The best classification accuracy for minimum number of features is considered as most desirable (highlighted in bold in Table 3). The results for all possible feature subsets are plotted in the form of graphs in Fig. 1 for both Validation and Cross-Validation, for a few datasets. As seen from Table 3 and the feature graphs in Fig. 1, the proposed method Next-NMIFS performs consistently best with quick convergence at the highest accuracy (overall its graph peaks above all other graphs and is more skewed to the left than the others), followed by HSIC-Lasso, DEFS and Fisher Score. The runtime of Next-NMIFS is comparable to that of NMIFS and mRMR, for instance for the 60 feature *Sonar* dataset the runtime is 1.95 s, 1.3 s, 1.242 s, 0.945 s respectively for Upper-bound normalized MIFS, the proposed method Next-NMIFS, NMIFS and mRMR. The runtime of fisher score, RELIEF and HSIC-Lasso is significantly lesser than the mutual information methods and just takes a fraction of seconds to execute. The DEFS which is a wrapper method depends on the time taken by 100 generations of the genetic algorithm with an initial population of 50 to execute. The advantage of Next-NMIFS over NMIFS is considerable while mRMR is only marginally inferior to NMIFS. Table 4 analyzes the Wilcoxon statistic test for the classification results in Table 3, as per the guidelines in Demšar (2006) and Wilcoxon (1945). The statistic $z < -1.96$ (Demšar 2006) for all cases, implying the rejection of the null hypothesis that the two-classifier performances being compared are the same with the same ranking. The 'two classifiers' referred here represents the proposed method Next-NMIFS and each of the other methods shown in the columns of Table 4 considered one by one.

4.3 Automation results

The automated feature subset selection as per the procedure outlined in Sect. 3, is illustrated for the *Wine* dataset in Fig. 2, and the automation results for all 20 datasets are summarized in Table 5. The computed optimum feature sizes are same as that of the exhaustive search results for the best feature subset, in case of the small datasets such as *Glass* and *Wine*. For larger datasets like *Internet*, the results are comparable and the computed feature subset

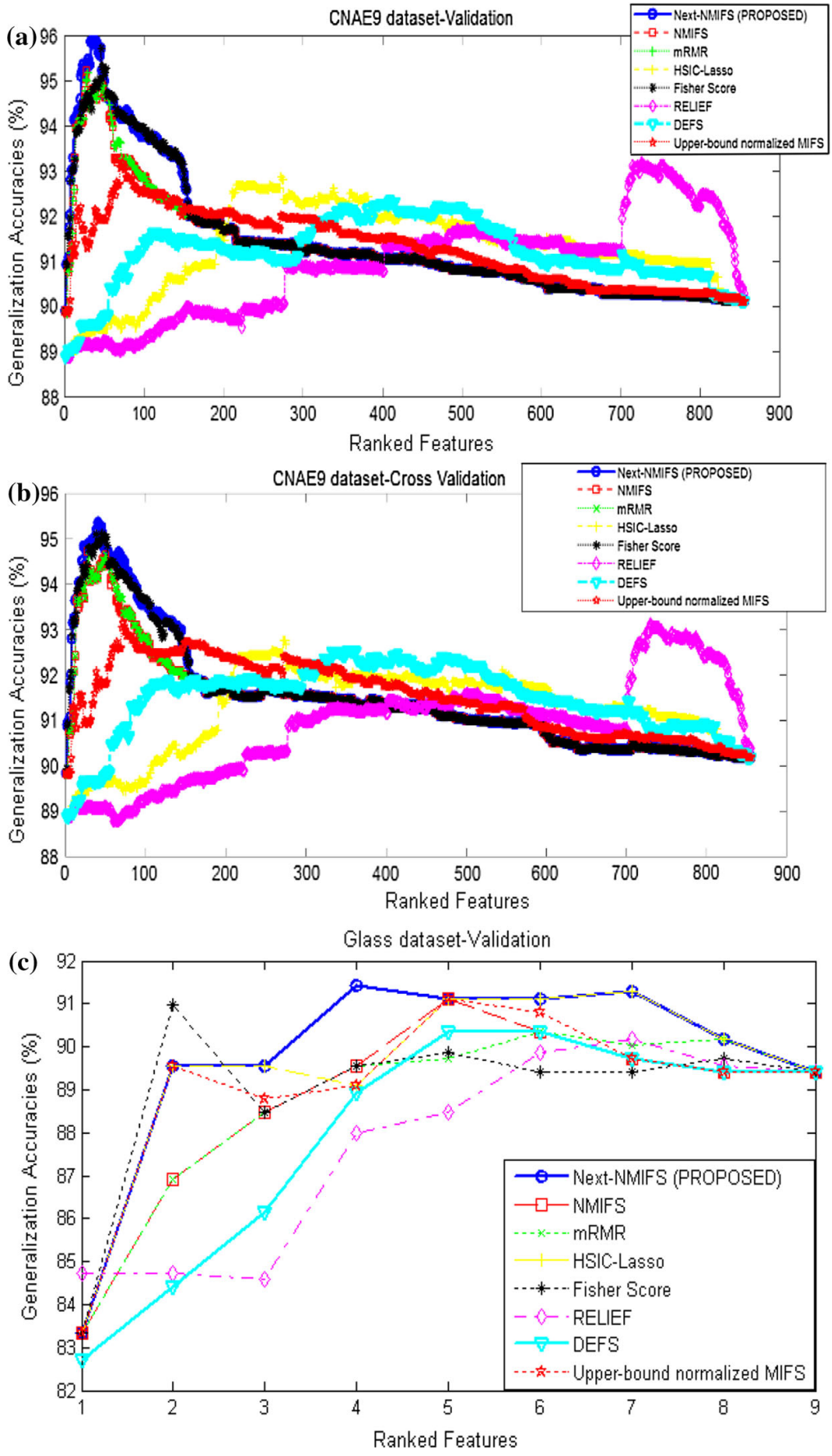


Fig. 1 Generalization classification accuracy (in %) versus number of selected features (pair-wise validation and cross-validation graphs shown) for the **a**, **b** *CNEA9* **c**, **d** *Glass* and **e**, **f** *Parkinson* datasets of the UCI repository shown for different feature selection methods, including the proposed Next-NMIFS

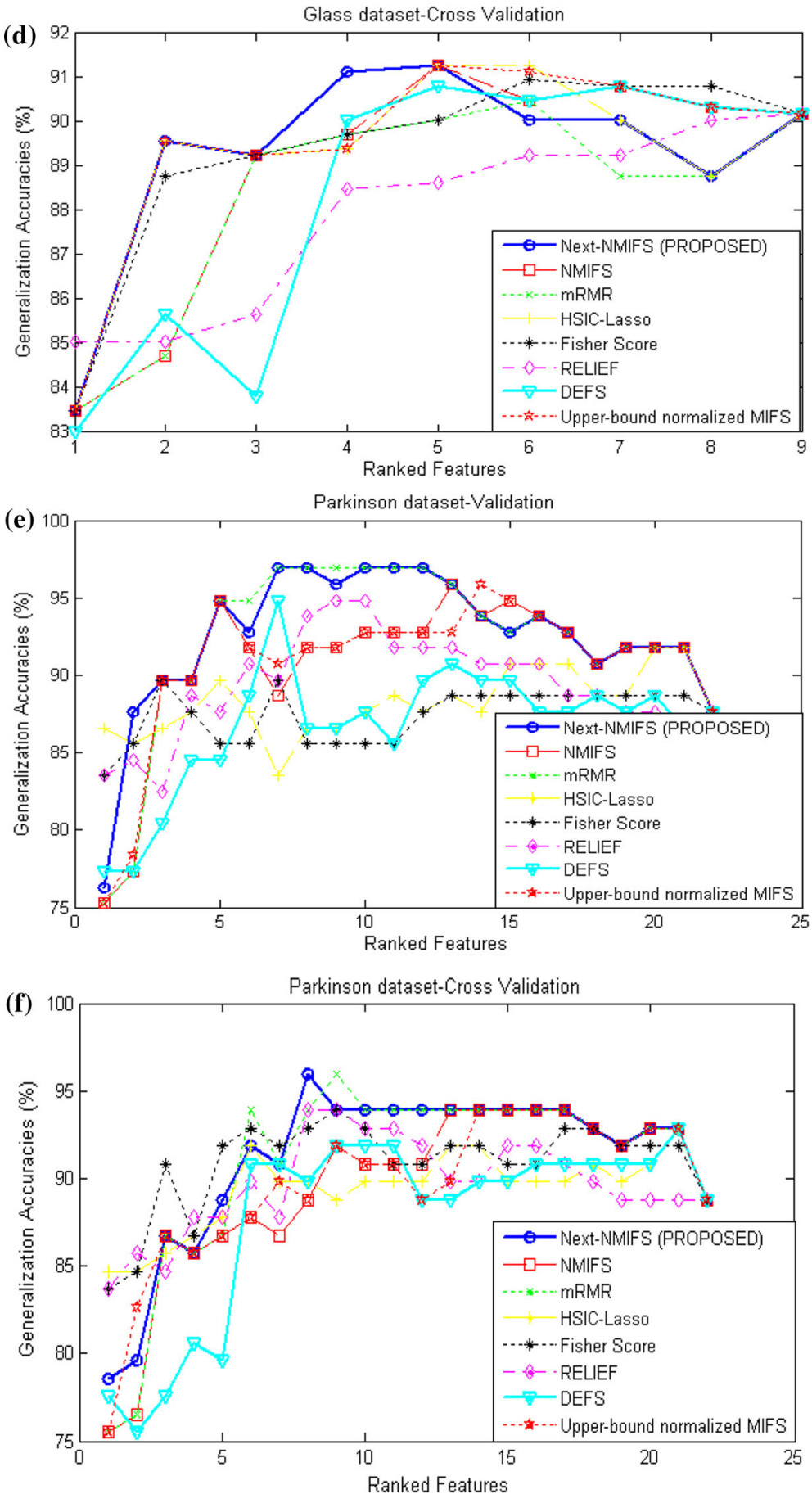


Fig. 1 continued

Table 4 Wilcoxon test statistic for the validation results in Table 3 computed over all datasets for the pairwise combination of proposed method versus all methods considered one by one

Other methods	mRMR	NMIFS	HSIC-Lasso	Fisher Score	RELIEF	DEFS	Upper-bound normalized MIFS
Wilcoxon test statistic z (Wilcoxon 1945) ($z < -1.96$ for Hypothesis rejection)	−3.77	−3.77	−4.17	−3.99	−4.17	−4.29	−3.87

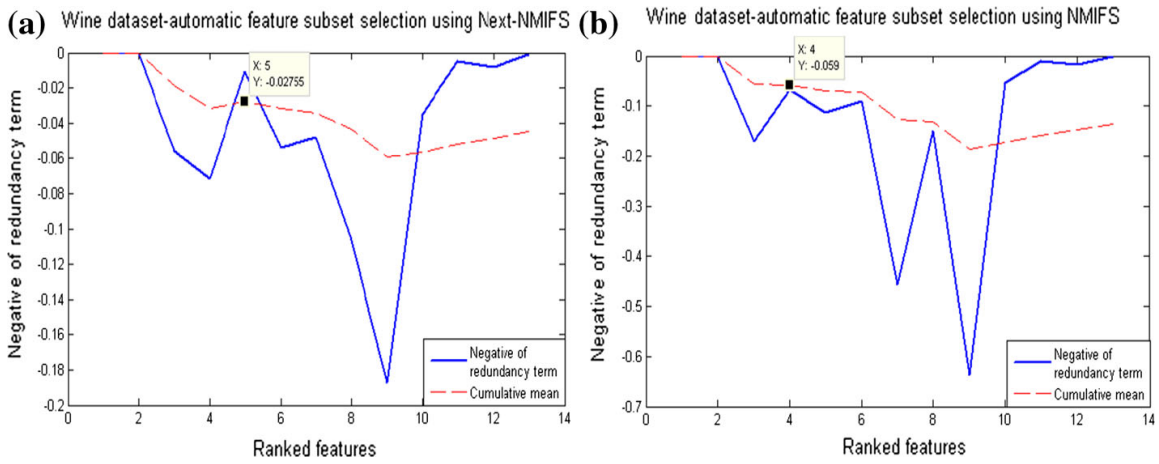


Fig. 2 Proposed automatic feature subset selection from the graph of the negative of the redundancy (second) term **a** for the *Wine* dataset using Next-NMIFS **b** for the *Wine* dataset using NMIFS

size corresponds to local maxima in the accuracy graphs in Fig. 1. This makes the proposed automation a feasible solution for determining automatically the optimum feature subset containing the top ranked features.

Comparatively, the NMIFS (Peng et al. 2005) that is based on Shannon entropy is more sensitive and leads to a more uniform response to all features making the choice of a distinct feature subset difficult. For instance, for the *Wine* dataset, in Fig. 2b NMIFS gives a less accurate answer (feature subset size = 4) as compared to Next-NMFS in Fig. 2a (feature subset size = 5). As observed from Table 3, for the *Wine* dataset, feature size = 5 does give best results with Next-NMIFS while feature size = 6 or 7 gives best results with NMIFS and not feature size = 4. So the proposed automation does not hold for MIFS based on extensive measures like Shannon entropy (e.g. NMIFS, mRMR).

5 Conclusion

A new non-additive mutual information based on the non-extensive entropy with Gaussian gain is proposed for highly efficient feature selection using the maximum-relevance minimum-redundancy approach, for the sparse probabilities derived from real-world datasets. The new mutual information formula incorporating a difference of Gaussians is highly efficient in representing the high correlations between the attributes and the class-labels, and in identifying and discarding redundant attributes. Its efficiency is proved by extensive experimentation on benchmark real-world datasets, and comparison with the state-of-the-art. The

Table 5 Proposed automatic feature subset selection for 20 datasets of UCI repository using Next-NMIFS: Feature subset size, Accuracy obtained, maximum accuracy with feature subset size from the exhaustive search in Table 1

Dataset serial no. (Table 1)	1	2	3	4	5	6	7	8	9	10	11	12	13	14	15	16	17	18	19	20
Feat. size	4	3	9	7	1	4	5	4	7	6	6	6	41	11	3	6	17	19	3	3
Accuracy	91.4	89.2	85.8	77.5	96.5	75	98.5	96.3	90.1	76.9	92.9	95.9	95.3	95.5	87.4	80	91.8	94.4	96.1	89.7
Maximum accuracy	91.4 (4)	94.8 (2)	85.8 (9)	87.5 (12)	96.5 (1)	84.6 (10)	98.5 (5)	96.8 (5)	98.4 (114)	76.9 (6)	93.9 (1)	95.9 (6)	95.3 (41)	96.0 (134)	87.4 (3)	80 (6)	91.9 (33)	94.4 (2)	99.1 (16)	96.9 (7)

selected feature subsets of top-ranked features are skewed to the left indicating a quicker convergence of the incremental feature selection process due to the more accurate ranking assigned by the new measure for highly correlated random variables. Higher accuracies for a smaller set of top-ranked features is the result of our investigation. An automation of the whole procedure is also implemented successfully as an alternative to the conventional exhaustive search for the optimal feature subset as is wont in feature selection experiments.

References

Akande, K. O., Owolabi, T. O., & Olatunji, S. O. (2015). Investigating the effect of correlation-based feature selection on the performance of support vector machines in reservoir characterization. *Journal of Natural Gas Science and Engineering, 22,* 515–522.

Battiti, R. (1994). Using mutual information for selecting features in supervised neural net learning. *IEEE Transactions on Neural Network, 5*(4), 537–550.

Ben-Bassat, M. (1982). 35 Use of distance measures, information measures and error bounds in feature evaluation. *Handbook of Statistics, 2,* 773–791.

Bolón-Canedo, V., Alonso-Betanzos, A., & Sánchez-Maroño, N. (2017). *Artificial intelligence: Foundations, theory, and algorithms feature selection for high-dimensional data*. New ork: Springer.

Bostani, H., & Sheikhan, M. (2017). Hybrid of binary gravitational search algorithm and mutual information for feature selection in intrusion detection systems. *Soft Computing, 21*(9), 2307–2324.

Chow, C., & Liu, C. (1968). Approximating discrete probability distributions with dependence trees. *IEEE Transactions on Information Theory, 14*(3), 462–467.

Cover, T. M., & Thomas, J. A. (1991). *Elements of information theory*. New York: Wiley.

Demšar, J. (2006). Statistical comparisons of classifiers over multiple data sets. *Journal of Machine Learning Research, 7,* 1–30.

Duda, R. O., Hart, P. E., & Stork, D. G. (2001). *Pattern classification* (2nd ed.). New York: Wiley.

Eriksson, T., Kim, S., Kang, H.-G., & Lee, C. (2005). An information-theoretic perspective on feature selection in speaker recognition. *IEEE Signal Processing Letters, 12*(7), 500–503.

Estevez, P. A., Tesmer, M., Perez, C. A., & Zurada, J. M. (2009). Normalized mutual information feature selection. *IEEE Transactions on Neural Networks, 20*(2), 189–201.

Frank, A., & Asuncion, A. (2010). *UCI machine learning repository* http://archive.ics.uci.edu/ml. Irvine, CA: University of California, School of Information and Computer Science.

Hoque, N., Bhattacharyya, D. K., & Kalita, J. K. (2014). MIFS-ND: A mutual information-based feature selection method. *Expert Systems with Applications, 41*(14), 6371–6385.

Jurado, S., Nebot, À., Mugica, F., & Avellana, N. (2015). Hybrid methodologies for electricity load forecasting: Entropy-based feature selection with machine learning and soft computing techniques. *Energy, 86,* 276–291.

Khoshgoftaar, T. M., Gao, K., Napolitano, A., & Wald, R. (2014). A comparative study of iterative and non-iterative feature selection techniques for software defect prediction. *Information Systems Frontiers, 16*(5), 801–822.

Khushaba, R. N., Al-Ani, A., & Al-Jumaily, A. (2011). Feature subset selection using differential evolution and a statistical repair mechanism. *Expert Systems with Applications, 38*(9), 11515–11526.

Kira, K., & Rendell, L. A. (1992). The feature selection problem: Traditional methods and a new algorithm. In *AAAI* (Vol. 2, pp. 129–134).

Lee, S., Park, Y.-T., & d'Auriol, B. J. (2012). A novel feature selection method based on normalized mutual information. *Applied Intelligence, 37*(1), 100–120.

Lisker, L. (1957). Minimal cues for separating/w, r, l, y/in intervocalic position. *Word, 13*(2), 256–267.

Liu, H., & Lei, Yu. (2005). Toward integrating feature selection algorithms for classification and clustering. *IEEE Transactions on Knowledge and Data Engineering, 17*(4), 491–502.

Mafarja, M., Aljarah, I., Heidari, A. A., Hammouri, A. I., Faris, H., Ala'M, A. Z., et al. (2018). Evolutionary population dynamics and grasshopper optimization approaches for feature selection problems. *Knowledge-Based Systems, 145,* 25–45.

Momma, M., & Bennett, K. P. (2002). A pattern search method for model selection of support vector regression. In *SDM* (Vol. 132, pp. 261–274).

Pascoal, C., Oliveira, M. R., Pacheco, A., & Valadas, R. (2017). Theoretical evaluation of feature selection methods based on mutual information. *Neurocomputing, 226,* 168–181.

Peng, H., Long, F., & Ding, C. (2005). Feature selection based on mutual Information: Criteria of max-dependency, max-relevance and min redundancy. *IEEE Transactions on Pattern Analysis and Machine Intelligence, 27*(8), 1226–1238.

Quinlan, J. R. (1986). Induction of decision trees. *Machine Learning, 1*(1), 81–106.

Shannon, C. E. (1948). A mathematical theory of communication. *The Bell System Technical Journal, 27,* 379–423.

Song, Q., Ni, J., & Wang, G. (2013). A fast clustering-based feature subset selection algorithm for high-dimensional data. *IEEE Transactions on Knowledge and Data Engineering, 25*(1), 1–14.

Susan, S., & Dwivedi, M. (2014). Dynamic growth of hidden-layer neurons using the non-extensive entropy. In *2014 Fourth international conference on communication systems and network technologies (CSNT)* (pp. 491–495). IEEE, 2014.

Susan, S., & Hanmandlu, M. (2013a). A non-extensive entropy feature and its application to texture classification. *Neurocomputing, 120,* 214–225.

Susan, S., & Hanmandlu, M. (2013b). A novel fuzzy entropy based on the non-extensive entropy and its application for feature selection. In *2013 IEEE international conference on fuzzy systems (FUZZ)* (pp. 1–8). IEEE.

Susan, S., & Hanmandlu, M. (2015). Unsupervised detection of nonlinearity in motion using weighted average of non-extensive entropies. *Signal, Image and Video Processing, 9*(3), 511–525.

Susan, S., & Kumar, A. (2016). Auto-segmentation using mean-shift and entropy analysis. In *2016 3rd international conference on computing for sustainable global development (INDIACom)* (pp. 292–296). IEEE, 2016.

Susan, S., & Sharma, M. (2017). Automatic texture defect detection using Gaussian mixture entropy modeling. *Neurocomputing, 239,* 232–237.

Tang, B., He, H., Baggenstoss, P. M., & Kay, S. (2016). A Bayesian classification approach using class-specific features for text categorization. *IEEE Transactions on Knowledge and Data Engineering, 28*(6), 1602–1606.

Tang, J., & Liu, H. (2014). An unsupervised feature selection framework for social media data. *IEEE Transactions on Knowledge and Data Engineering, 26*(12), 2914–2927.

Vinh, N. X., & Bailey, J. (2013). Comments on supervised feature selection by clustering using conditional mutual information-based distances. *Pattern Recognition, 46*(4), 1220–1225.

Wilcoxon, F. (1945). Individual comparisons by ranking methods. *Biometrics Bulletin, 1*(6), 80–83.

Yamada, M., Jitkrittum, W., Sigal, L., Xing, E. P., & Sugiyama, M. (2014). High-dimensional feature selection by feature-wise kernelized lasso. *Neural Computation, 26*(1), 185–207.

Yang, F., Mao, K. Z., Lee, G. K. K., & Tang, W. (2015). Emphasizing minority class in LDA for feature subset selection on high-dimensional small-sized problems. *IEEE Transactions on Knowledge and Data Engineering, 27*(1), 88–101.

Yang, J.-B., & Ong, C.-J. (2012). An effective feature selection method via mutual information estimation. *IEEE Transactions on Systems, Man, and Cybernetics, Part B: Cybernetics, 42*(6), 1550–1559.

Zhang, Y., Li, S., Wang, T., & Zhang, Z. (2013). Divergence-based feature selection for separate classes. *Neurocomputing, 101,* 32–42.

Zhou, L.-T., Cao, Y.-H., Lv, L.-L., Ma, K.-L., Chen, P.-S., Ni, H.-F., et al. (2017). Feature selection and classification of urinary mRNA microarray data by iterative random forest to diagnose renal fibrosis: A two-stage study. *Scientific Reports, 7,* 39832.

Zou, Q., Ni, L., Zhang, T., & Wang, Q. (2015). Deep learning based feature selection for remote sensing scene classification. *IEEE Geoscience and Remote Sensing Letters, 12*(11), 2321–2325.

Publisher's Note Springer Nature remains neutral with regard to jurisdictional claims in published maps and institutional affiliations.



Dr. Seba Susan is an Associate Professor in the Department of Information Technology at Delhi Technological University (DTU). She completed her Bachelors in Technology (B.Tech.) in Electronics Engineering from Cochin University of Science & Technology (2002), Masters in Engineering (M.E.) in Electronics & Communication (2008) from the erstwhile Delhi College of Engineering now Delhi Technological University, and Ph.D. from the Electrical Engineering Department of IIT Delhi (2014). Her research areas are Computer Vision, Data Mining, Speech and Natural Language Processing, Pattern Recognition, Image Processing & Soft Computing with the area of specialization being the use of statistical and soft computing tools for Machine Learning and Pattern Recognition. She has published 40 papers in National and International Journals and Conferences. She has a total teaching experience of 15 years and has been associated with the Department of Information Technology (IT), DTU since July 2010. She is a member of the IEEE Computational Intelligence Society, Signal Processing Society and the Computer Society and also a life member of the Computer Society of India (CSI). She is also a reviewer of IEEE Transactions on System, Man, Cybernetics, IEEE Transactions on Multimedia, Computers & Electrical Engineering (Elsevier), IET Image Processing, IET Computer Vision and IET Biometrics. She was awarded the Elsevier Outstanding Reviewer of the year award for 2015, and her biography is listed in the 2016 Marquis Whos Who of the World (33rd ed.). She is also a recipient of the DTU Research Excellence Award for 2017.



Madasu Hanmandlu (SM'06) received his B.E. degree in electrical engineering from Osmania University, Hyderabad, India, in 1973; M.Tech. degree in Power systems from Jawaharlal Nehru Technological University, Hyderabad, India, in 1976; and Ph.D. degree in control systems from the Indian Institute of Technology (IIT) Delhi, India. In 1982, he joined the Department of Electrical Engineering, IIT Delhi, as a Lecturer and became an Assistant Professor in 1990, an Associate Professor in 1995 and Professor in 1997. He has been an Emeritus Professor with the Department of Electrical Engineering, IIT Delhi since August 2014. Presently he is a Professor in CSE Department, MVSR Engineering College, Hyderabad. His current research interests include fuzzy modeling for dynamic systems and applications of fuzzy logic to image processing, medical imaging, multimodal biometrics and surveillance. He has authored a book on Computer Graphics in 2005 under PBP Publications and also has well over 325 publications in both conferences and journals to his credit. He has guided 32 Ph.Ds and 160 M.Tech. students. He has handled several sponsored projects. He was an Associate Editor of both Pattern Recognition Journal (January 2005–March 2011) and of IEEE Transactions on Fuzzy Systems and a viewer to other journals such as Pattern Recognition Letters, IEEE Transactions on Image Processing and Systems, Man and Cybernetics (January 2007–2010). He is a Senior member of IEEE and is listed in Reference Asia; Asia's who's who of Men and Women of achievement; 5000 Personalities of the World (1998), American Biographical Institute.

Computers and Electrical Engineering 71 (2018) 569–577

Contents lists available at ScienceDirect

Computers and Electrical Engineering

journal homepage: www.elsevier.com/locate/compeleceng

Supported matrix factorization using distributed representations for personalised recommendations on twitter☆

Akshi Kumar[a], Himanshu Ahuja[a], Nikhil Kumar Singh[a], Deepak Gupta[b], Ashish Khanna[b], Joel J. P. C. Rodrigues*[,c,d,e,f]

[a] Department of Computer Science, Delhi Technological University, India
[b] Maharaja Agrasen Institute of Technology, Delhi, India
[c] National Institute of Telecommunications (Inatel), Santa Rita do Sapucaí-MG, Brazil
[d] Instituto de Telecomunicações, Portugal
[e] ITMO University, St. Petersburg, Russia
[f] University of Fortaleza (UNIFOR), Brazil

ARTICLE INFO

Keywords:
Probabilistic Matrix Factorization
Twitter User Recommendation
Distributed Representations
Recurrent Neural Networks

ABSTRACT

Microblogging is one of the most prevalent media for sharing news on the Internet. Microblogging platforms, such as Twitter have proven to be of great success in targeted marketing, alerting about natural disasters and promoting government policies among others; But most of this relevant information in microblogs is side-lined, owing to information overload, rendering any practical utility of the platform as ineffective. Hence, it is crucial to filter data and recommend only relevant information to the users. Interestingly, to pertain and appeal to a certain community, users make the use of *hashtags* (#), which in turn, helps in the efficient categorization and summarization of microblogs. In this paper, we exploit this advantage through a novel framework for a recommendation system, Distributed Representation based Supported Matrix Factorization (DRSMF) build on top of Probabilistic Matrix Factorization (PMF) and Recurrent Neural Networks (RNNs). The RNNs generate character-level distributed representations for each tweet to overcome the solecistic use of sentence structure in microblogs. The framework further performs a multi-modal analysis on the microblog posts to recommend similar users and *hashtags*, which assists in countering information-overload. Our framework outperforms standard PMF techniques by the use of constrained regularisation on latent factor representations.

1. Introduction

Twitter users post more than 500 million tweets every day making Twitter one of the most popular social web service and microblogging platform. The microblog posts have been used for sentiment analysis, identifying natural disasters, event detection and numerous other applications. Microblogging platforms, such as Twitter are known to have a noisy environment [1], lacking any strict syntax. While the posts are pragmatically applicable, they are often morphologically improper making traditional Natural Language Processing (NLP) techniques to fail. Nevertheless, considering the increasing popularity and vast abundance of data, it is of utmost

☆ Reviews processed and recommended for publication to the Editor-in-Chief by Guest Editor Dr. G. R. Gonzalez.

* Corresponding author.
E-mail addresses: akshikumar@dce.ac.in (A. Kumar), himanshuahujadtu@gmail.com (H. Ahuja), nikhilksingh97@gmail.com (N.K. Singh), deepakgupta@mait.ac.in (D. Gupta), ashishkhanna@mait.ac.in (A. Khanna), joeljr@ieee.org (J. J. P. C. Rodrigues).

https://doi.org/10.1016/j.compeleceng.2018.08.007
Received 19 May 2018; Received in revised form 14 August 2018; Accepted 14 August 2018
0045-7906/ © 2018 Elsevier Ltd. All rights reserved.

importance to recommend the microblog posts (referred to as *tweets*) concisely in accordance with their relevance to the user. There is a wide variety of topics and ideas discussed on these microblogging platforms, hence recommender systems, such as ours, aims to provide the users with relevant and novel information that is coherent to their user profile.

In many social platforms, like Twitter, users utilize *hashtags* which are characteristic to the *tweet* they are contained in. An average of 14.6% tweets use *hashtags* in the text [2]. Many related research works have also stressed the role of *hashtags* as distinctive and valuable labels for the Twitter posts they are associated with [3,4]. Unlike traditional NLP methods which would assume equal importance for each word in a Twitter post, our proposed system leverages *hashtags* as nominal representatives of the content of the tweet and also the users that have utilized it. Furthermore, Twitter also contains some special explicit features, associated with each user and tweet, which are also exploited by DRSMF. To summarize, the major contributions of this work are as follows:

1. We propose a novel recommendation system which uses constrained regularization on implicit *hashtag* embeddings, for the *user-hashtag* adjacency matrix. Further, the adjacency matrix uses explicit features to quantify each *user-hashtag* entry. This constrained regularization on implicit features and explicit quantification helps in modeling user behavior using a Supported Matrix Factorization framework and overcoming data sparsity and cold-start.
2. We propose a robust recurrent neural network (RNN) based character-level embedding encoder architecture on the microblogs, which maps each tweet to a *hashtag*. The use of a character model gives DRSMF resistance against the use of improper syntax and character limit restriction prevalent in microblogs.
3. We propose an extensive qualitative and quantitative analysis of the proposed framework. We show that, using Supported Matrix Factorization and constrained regularization on implicit *hashtag* latent vectors generated via the recurrent neural network, DRSMF achieves better results than other similar architectures.

Using the explicit features and implicit semantic analysis of microblog posts, the proposed framework achieves the following tasks:

1. Given a user profile, extract similar user profiles utilizing past twitter activity behavior.
2. Predicting the *hashtags*, a user is most likely to use in a new tweet based on their past *hashtag* usage and previous interests.

The rest of the paper is organized as follows: In Section 2, we review the related literature to discuss the shortcomings and advantages of previously proposed methods. In Section 3, we present the architecture of the proposed DRSMF framework. In Section 4, we discuss the properties of data utilized for experimentation of the proposed work. In Section 5, we perform an extensive qualitative and quantitative analysis of DRSMF against other baseline recommendation systems. Finally, in Section 6, we present the concluding remarks and future direction for DRSMF.

2. Related work

User interest modeling and recommendation systems is a thoroughly investigated and reviewed research area. Many recommendation frameworks have been developed for news articles, movies, and e-commerce products, amongst others. Recommendations on microblog posts pose two major challenges that contrasts them against traditional recommender systems:

1. The length of microblog posts is small, making it difficult to extract semantic information.
2. Lack of any syntactical sentence structure, and use of erroneous spelling and grammar.

In the following paragraphs, we discuss the studies that have been conducted so far on recommendations for microblog posts.

In [5–8], knowledge-based methods for personalized recommendation on Twitter are utilized. Abel et al. [5] uses related news articles to identify the semantic meaning of individual *tweets* to model user behavior. Once relevant news articles are identified, they are analyzed for discovering entities which aid in the topical evaluation of individual *tweets*. Piao and Breslin [6] studies the synergetic effect of time-based, content-based and interest based representations. These studies fail to counter the syntactically noised environment of microblogging platforms limiting their domain of functionality.

The authors in [8], address the issue of the *Topic Model* which is based on the assumption that every record contains rich information which is not the case in user-based microblogging platforms like Twitter. This hampers the overall quality of recommendations [9–11]. Further, Kwak et al. [12] conducted a study which revealed that user-annotated *hashtags* are good identifiers of prevalent events and happenings. Numerous studies have been conducted for Hashtag Recommendation for Tweets [13–15]. Li et al. [16] uses LDA for recommending hashtags for newly created tweets, [13] exploits content similarity between tweets whereas [15] based their recommendation framework on hyper-linked tweets, leveraging content on web pages for a more affluent analysis.

Abel et al. [17] use multi-view embeddings for Twitter users which represents each user as a high dimensional vector containing information about the *tweets* posted by the user, the neighborhood of its friends and followers and the people the user *mentioned*. These high dimensional vector representations were then used for General Canonical Correlation Analysis [18] to find the similarity among users. Variations in word embedding models have been investigated in previous studies [19–22]. In [19], word embeddings were generated on the basis of syntactical analysis of words in documents.

Embedding models have been previously implemented on Twitter for various tasks [16,23]. Dhingra et al. [23] evaluates character embeddings with Bi-directional Gated Recurrent Units for prediction of *hashtags* on newly created tweets which has higher

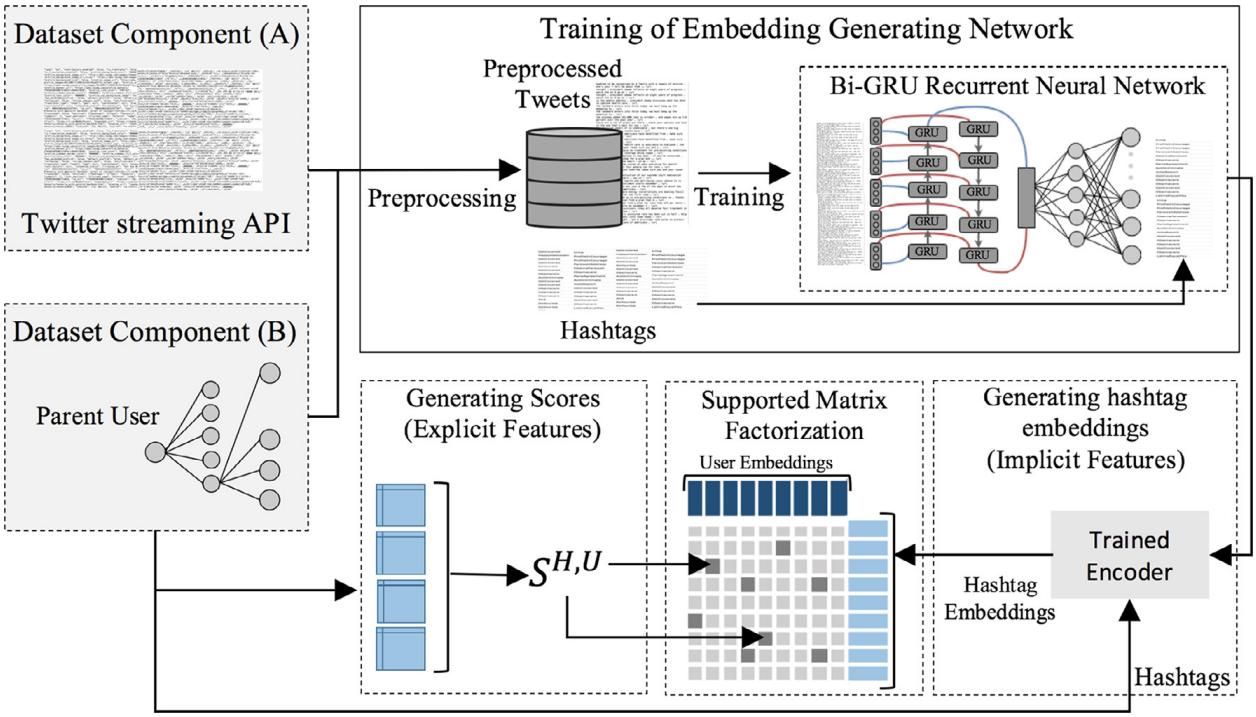


Fig. 1. Architecture of the proposed DRSMF framework.

performance than word baseline model. In [24], authors use an LSTM-RNN to generate word embeddings for *hashtag* recommendation. Whereas, in [25], authors use a feed-forward network to train on distributed representations. The results from the above *hashtag* recommendation frameworks suggest that text embeddings based models perform with better accuracy than traditional NLP models.

3. Proposed approach

The Twitter platform provides various important information about its users and *tweets*. For example, the number of times a tweet has been shared (*retweeted*), the number of times a *tweet* is *favourited* by another user, the *tweet* history of a Twitter user, and social relations amongst various users. Fig. 1 illustrates the proposed Distributed Representation based Supported Matrix Factorization framework which completely exploits this explicit information. Our framework also leverages on *hashtags* which act as topical and nominal representatives of the tweets they are contained in. These *hashtags* store the implicit characteristics of each *tweet* as a function of character level embeddings. The framework infers a latent factor representation for each user, which is based on the correlation between a *user* - *hashtag* pair. Our model is able to overcome the sparse environment of the Twitter platform through constrained regularisation on the *hashtag* embedding vector which drives the formation of the latent factors for the users. This model acts as a specialized recommendation system for microblogging platforms for a personalized user and *hashtag* recommendation (Fig. 2).

3.1. *Generation of implicit features: Hashtag embedding vectors*

The projection of a sparse hot-encoded vector representation onto a dense vector embedding representation using sequential

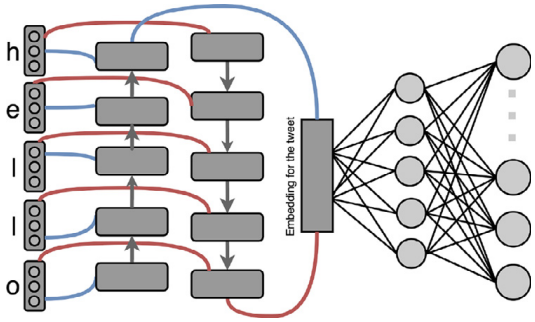


Fig. 2. Recurrent Neural Network Architecture for generating Distributed Representations of Hashtags.

modeling has been widely used in various fields of Natural Language Processing [26–28] such as sentiment classification, text summarization, and language translation. We use a Recurrent Neural Network (RNN) in DRSMF as they can process sequential data of the *tweets* of any length and generate a correlation between the items of the vocabulary. Microblogging websites like Twitter lack any strict syntax and proper vocabulary leading to a large word vocabulary for processing. Another peculiar characteristic feature of Twitter is the restriction on the number of characters in a *tweet*. Due to this restriction, the final hidden state of the encoder RNN is able to capture the essence of the *tweet* into an embedding. The noisy environment of the Twitter platform and the imposition word limit on the size of the *tweet* both favor the use of character-level embedding vectors.

The text and corresponding *hashtags* of each *tweet* are extracted from the Twitter dataset. We adopted our encoding mechanism from [23,27] where a two-pass encoder with Recurrent Units was utilized. A character set M from the text is generated, where each character $m_i \in M$ is a one-hot encoding vector of length $|M|$. This sparse representation of character set is projected onto a dense embedding space of size d_m in $\mathbb{R}^{|P|\times d_m}$. Considering a *tweet* of length k, we generate a sequence embedding vectors $x_1, x_2, x_3, \ldots, x_k$ and feed it into our sequential encoding architecture wherein at each time step t in the sequence, the hidden state h_t is generated via the following formulations.

$$r_t = \sigma(W_r x_t + U_r h_{t-1} + b_r) \tag{1}$$

$$z_t = \sigma(W_z x_t + U_z h_{t-1} + b_z) \tag{2}$$

$$\widetilde{h_t} = \tanh(W_h x_t + U_h(r_t \odot h_{t-1}) + b_h) \tag{3}$$

$$h_t = (1 - z_t) \odot h_{t-1} + z_t \odot \widetilde{h_t} \tag{4}$$

Here, $x_t \in \mathbb{R}^{d_k\times 1}$, W_r, W_z, $W_h \in \mathbb{R}^{d_h\times d_c}$ and U_r, U_z, $U_h \in \mathbb{R}^{d_h\times d_h}$ where d_h is the hidden state dimension. The processing is done in both forward and reverse order and the final hidden states for both the forward pass (h_k^f) and backward pass (h_0^b) are combined to give the final *tweet* embedding as follows:

$$e = W^f h_k^f + W^b h_0^b + b. \tag{5}$$

where W^f, $W^b \in \mathbb{R}^{d_t\times d_h}$ and $b \in \mathbb{R}^{d_t\times 1}$. The tweet embedding is then trained to classify on the hashtag it was associated with using a feed-forward neural network using a softmax output layer (Eq. (6)). Here, *hashtags* provide an added advantage of making supervised learning possible as they are user annotated representatives of the content of the microblog post. An unsupervised learning approach could have also been implemented which attempts to rebuild the original text from the hidden states [20,29].

$$P(y = j|e) = \frac{exp(w_j^T e + b_j)}{\sum_{i=1}^{L} exp(w_i^T e + b_i)} \tag{6}$$

where w_i is a vector representing the weights of the ith hashtag and $b \in \mathbb{R}^{L\times 1}$ is the vector representing the bias w.r.t each of the L hashtags. The objective function is defined as categorical cross entropy loss between the predicted and true hashtags:

$$J = \frac{1}{B}\sum_{i=1}^{B}\sum_{j=1}^{L} - t_{i,j}\log(p(i,j)) + \lambda \|\Theta\|^2 \tag{7}$$

Here, B is the batch size of the *tweet* embeddings, $p(i, j)$ is the probability calculated by the softmax for the ith *tweet* in the batch and jth *hashtag* class. The $L - 2$ rgularisation, weighted by λ is applied over the parameters of the linear layer. Once the model is trained, it is used to generate embeddings for newly created tweets. These embeddings act as nominal representatives of the *hashtags*.

3.2. Explicit features

Each *tweet* consists of various explicit features that can be used to represent its importance. Our model considers the following features to calculate the score for each *user-hashtag* pair in the Score Matrix (S):

1. **Followee Count of a User (fo_i^U):** The number of users that follow the feed of the ith user.
2. **Favourite Count of a User (fa_i^U):** The number of tweets the ith user has marked as a favourite.
3. **Friend Count of a User (fr_i^U):** The number of users' feed that is followed by the ith user.
4. **Favourite Count of a Hashtag (fa_j^H):** The number of users that have favorited the Tweet associated with the jth *hashtag*.
5. **Retweet Count of a Hashtag (rt_j^H):** The number of users that have re-tweeted the Tweet associated with the jth *hashtag*.

The weighted sum of the normalised logarithm of these factors (Eq. (9)) is taken as entry to the Score matrix (S). For ith user and jth *hashtag*:

$$\widetilde{fo_i^U} = \left\lfloor \log\left(a + \frac{fo_i^U - fo_{min}^U}{fo_{max}^U - fo_{min}^U}(b - a)\right)\right\rfloor \tag{8}$$

$$S_{ij}^{H,U} = \widetilde{fo_i^U} + \widetilde{fr_i^U} + \widetilde{fa_i^U} + \widetilde{fa_j^H} + \widetilde{rt_j^H} \tag{9}$$

3.3. Supported matrix factorization

Probabilistic Matrix Factorization is susceptible to cold-start and high data sparsity prevalent in micro-blogging platforms. To overcome these, DRSMF performs Supported Matrix Factorization. After finding a corresponding embedding for each *hashtag* and calculating the values of entries to the Collaborative Filtering Matrix [30], we construct a score matrix $S \in \mathbb{Z}^{+^{U\times H}}$ where each entry is an integer value from 1 to $S_{\max}$. We denote S_{ij} as the score of the ith user for the jth *hashtag*. The column vectors, U_i in $U \in \mathbb{R}^{D\times N}$ and H_j in $H \in \mathbb{R}^{D\times M}$ represent user and *hashtag* latent vectors respectively. The conditional distribution over the observed scores is represented as Gaussian observation noise.

$$p(S|U, H, \sigma^2) = \prod_{i=1}^{N}\prod_{j=1}^{M}[\mathcal{N}(S_{ij}|U_i^T H_j, \sigma^2)]^{I_{ij}} \tag{10}$$

Here, the Indicator function I_{ij} represents whether the ith user has used the jth *hashtag* and σ^2 is the variance of the data. $H \in D \times M$ is initialized with the *hashtag* embeddings (Section 3.1). The U matrix is initialized with random Gaussian prior. The predicted score of the ith user with the jth *hashtag* is the dot product of the ith column U i.e. U_i and jth column of H i.e. H_j.

$$\widehat{S_{ij}} = U_i^T H_j \tag{11}$$

The model minimises the square of differences error between the scores in S and the predicted scores $\widehat{S}$ with $L-2$ regularisation.

$$L = \sum_{S_{i,j}\in S}(S_{ij} - U_i^T H_j)^2 + \lambda_U \sum_i ||U_i||^2 + \lambda_H \sum_j ||H_j||^2 \tag{12}$$

The loss is minimised using Alternating Least Squares (ALS) [31] wherein one set of latent feature representation is held constant (H_j) and the other is minimised (U_i). Once, the latent factor representation is minimised, it is held constant and we take the derivative of the loss function with respect to the previously constant vectors (H_j). This alternate stepping procedure is carried on till convergence.

$$\frac{\partial L}{\partial U_i} = 0, \quad U_i^T = S_i H (H^T H + \lambda_U I)^{-1} \tag{13}$$

$$\frac{\partial L}{\partial H_j} = 0, \quad H_j^T = S_j U (U^T U + \lambda_H I)^{-1} \tag{14}$$

In the above equations (Eqs. (12)–(14)), λ_H is subjugated to heavy regularisation ($\lambda_H > > \lambda_U$). This predicted score matrix is used for determining the similarity amongst users and the *hashtags* a user is most likely to use based on previous activity behavior.

4. Dataset description

To train our model, we used tweets parsed during *September 2017* using the Twitter API. The model for generating *hashtag* embeddings (Section 3.1) was trained with a dataset composed with the union of,

- Dataset component (A): one million English tweets extracted from Twitter Streaming API, randomly. The purpose of this dataset is to train the Bi-GRU RNN encoder on a generic environment and prevent it to overfit to any class of users.
- Dataset component (B): Constructed by selecting a particular Twitter user as the parent user, fetch its *tweets* and branch to the *friends* of the parent user. Repeating this step for each friend of the parent, we collect tweets in a Breadth-First fashion with the parent user at the centre of the web. This procedure is repeated until we reach a fixed tweet limit. This graph of users is used to test DRSMF on a class of users. This dataset component is utilized in both, the training of the Bi-GRU RNN encoder along with Dataset Component (A) and in constructing user profiles in the form of distributed representation during Supported Matrix Factorization.

For each tweet, we save its *id, screen name*, text, timestamp, *retweet* count and *favourite* count. For each user, we save the *id, screen name, favourites* count, *followers* count, *statuses* count and *friends* count. These features of each tweet and user aid in the construction of entries to the Score matrix (S) (Section 3.2). Probabilistic Matrix Factorization (Section 3.3) is performed on the *hashtag* − *user* pairs found in dataset (B).

5. Results

In Section 4, we discussed how we extracted and processed data to train our model. Furthermore, we evaluated our framework on two datasets. The first experimental dataset is *unconstrained*, including all the users and *hashtags* of the Dataset Component (B). The second experimental dataset is *constrained* wherein we applied a lower limit allowance on the occurrence of a *hashtag*. Table 1 mentions the features of these datasets. We present both the qualitative and quantitative analysis of the DRSMF framework.

For quantitative evaluation of the model we calculate the precision score, on cosine distance threshold. For the kth user in the dataset, we get the top n user latent embeddings. For each of these n top users, the top h *hashtags* are then derived using the *hashtag* latent embeddings. We calculate the cosine distance of the *hashtags* such obtained with the top h *hashtags* of the kth user. A threshold

Table 1
Dataset statistics.

Dataset component (B)	#Hashtags	#Users	Sparsity
Unconstrained	12,354	340	0.37%
Constrained (*#Hashtags* > =2)	2065	283	0.84%

is then applied to this cosine distance to get the sum precision score.

Fig. 3 illustrates the precision score of the baseline Probabilistic Matrix Factorization (PMF) with embedding size 50 and 200, Tweet2Vec model by Dhingra et al. with embedding size 200 and DRSMF with embedding size (D) 50 and 200 and regularization (λ_H) 0.5 and 5.0 at various threshold levels. Further, Table 2 describes the precision score of the baseline PMF, Tweet2vec [23] and DRSMF at 0.3 threshold. On the constrained dataset, all three models PMF, Tweet2vec and DRSMF show lower precision scores compared to the unconstrained dataset. This owes to the overfitting of user profiles during matrix factorization. Even then, constrained regularization on the *hashtag* embeddings prevent the proposed framework from overfitting on the data when compared to Tweet2Vec and PMF.

A 2-D representation of the relevance between the *hashtags* is shown in Fig. 4. The hashtag embeddings are obtained through probabilistic matrix Factorization of the *tweets* subjected to heavy regularisation. It can be observed that each cluster in the relevance plot describes a collection of hashtags linked to a similar topic. The hashtag embeddings take in consideration both the explicit features and implicit features of the tweets they were contained in.

We also evaluate our model based on the *hashtags* predicted for a particular user. Given a user, their *top-n* predicted *hashtags* for a tweet are retrieved based on the trained *Score Matrix* (S). The predicted *hashtags* are compared with the actual hashtags that were used by the user in the tweet (Table 3). In case of *Topical Trends* (eg. *#MarchForScience*), the use of explicit features proved to be beneficial in recommending more apt and relevant *hashtags* but the explicit features boasted the importance of irrelevant *hashtags* in case of *General Trends* (e.g. *#Irma*). As an implication, we can overlay the discussed framework with Topical Models, to decrease the predictions that are general, yet irrelevant to the *tweet*. Our framework can be utilized for directional recommendation of users, i.e. if A is *recommended* to B, does not necessarily imply that B will be *recommended* to A. This directionality arises from leveraging explicit features of each user. In Table 4, we discuss different users, the top user they were recommended and their *hashtag-profiles*.

6. Conclusion

We presented a novel user and *hashtag* recommendation framework, DRSMF based on constrained regularization of *hashtag* embeddings. The experimental results showed that DRSMF outperforms the baseline probabilistic matrix factorization framework. The above results also show the robustness of our framework against the semantically noisy environment of microblogging platforms. Our framework is able to capture the relevance of users and *hashtags* through explicit and implicit features of the *tweets* and recommend similar users and *hashtags* for newly created microblogs. In future, we aim to extend the proposed framework to handle image and hyperlink data. Furthermore, the proposed framework can be adapted with a time series evaluation architecture for fake news detection and disaster localization.

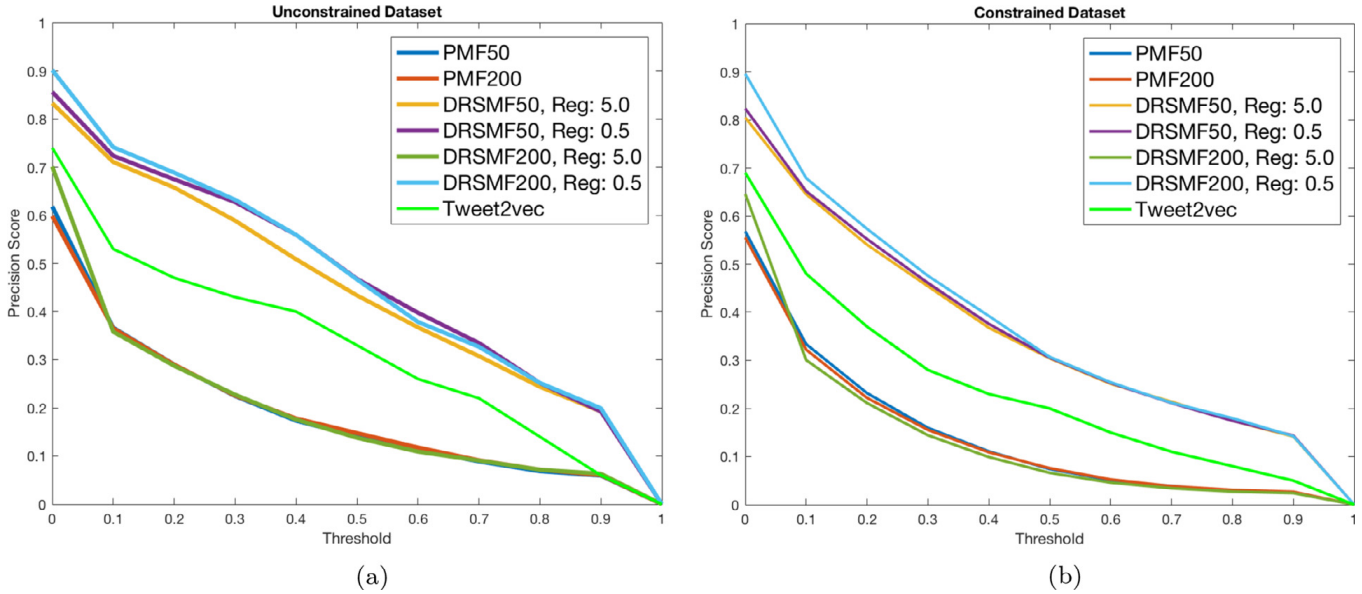


Fig. 3. The threshold *vs.* precision scores of DRSMF, Tweet2vec [23] and PMF baseline on (a) *unconstrained* and (b) *constrained* dataset.

Table 2
Precision score at Threshold = 0.3.

Dataset	PMF		Tweet2Vec [23]	DRSMF			
	D:50	D:200	D:200	D:50,λ_H:0.5	D:200,λ_H:0.5	D:50,λ_H:5.0	D:200,λ_H:5.0
Unconstrained	0.2246	0.2255	0.4306	0.5887	0.2274	0.6272	0.6321
Constrained	0.1596	0.1554	0.2814	0.4540	0.1443	0.4609	0.4757

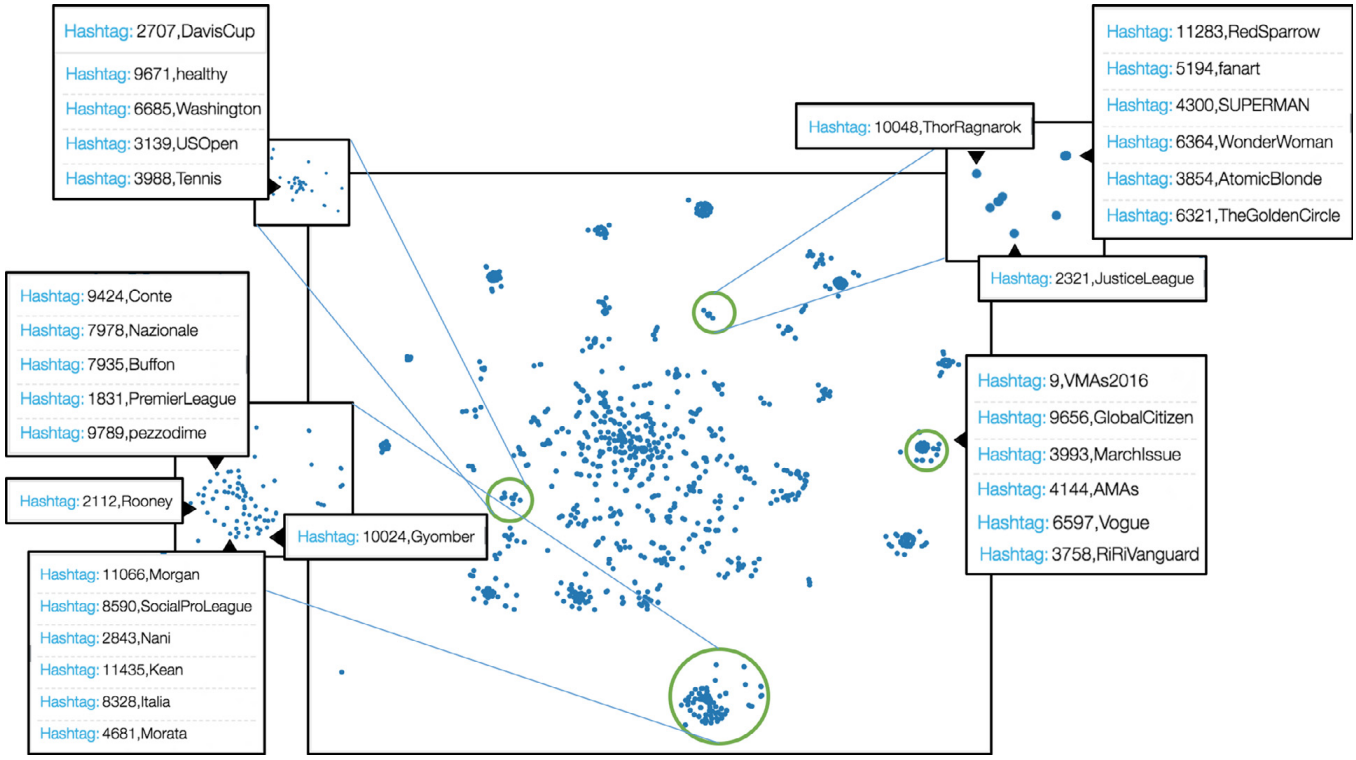


Fig. 4. The relevance between hashtag embeddings formed after supported probabilistic representation of the tweets. (on *unconstrained* dataset).

Table 3
Prediction of Hashtags for Individual Users (on *constrained* dataset).

User screen name	Actual hashtag used	Predicted hashtags
@BarackObama	**#ACA**	**#AHCA**, #USVI, **#medicaid**
	#StopTheDebtTrap	#technology, **#MadeInAmerica**, #Obama
@UNFP	**#OuraganIrma**	**#IrmaHurricane2017, #HarveyHurricaneIrma**, #Katia
@AlvaroKohn	**#MarchForScience**	**#Resilience2017**, #biosphere, **#Sustainability**, #climate #Irma
@TwitterSports	**#CFL**	**#NFL**, #eSports, #TwitterLove, **#ArgorFootball**
	#mayweather	**#MayWeathervMcGregor, #MMAHour**, #Vegas

Table 4
Predicting similar users based on *Hashtag Profiles* (on *constrained* dataset).

User	Predicted user
@FC_Basel_en	**@ChampionsLeague**
#MUFC,	#UCL,
#EuropaChallenge, #TheUEFAawards, #Eridivisie,	#ExpeditionEuropa, #ComeOnCity, #UCLFantasy,
#worldcupqualifiers	#Feyenoord
@StottPeter	**@ArcticInstitute**
#Arctic, #ActOnClimate, #StateOfClimate, #AGU16, #seaice	#SaveTheArctic, #climatechange, #AGU, #polar, #sustainability
@pitrodriguez	**@TwitterSports**
#NFL_Brasil, #NBADraft, #LoveTwitter, #UFC214noCombate	#MayweatherMcGregor, #CFL, #NBACereals, #UFC14

Acknowledgements

This work was supported by the National Funding from the FCT - Fundação para a Ciência e a Tecnologia through the UID/EEA/50008/2013 Project; by the Government of the Russian Federation, Grant 08-08; by Finep, with resources from Funttel, Grant No. 01.14.0231.00, under the Centro de Referência em Radiocomunicações - CRR project of the Instituto Nacional de Telecomunicações (Inatel), Brazil; by National Funding from the Brazilian National Council for Research and Development (CNPq) through the Grant No. 309335/2017-5.

References

[1] Honey C, Herring SC. Beyond microblogging: conversation and collaboration via twitter. System sciences, 2009. HICSS'09. 42nd Hawaii international conference on. Ieee; 2009. p. 1–10.
[2] Wang X, Wei F, Liu X, Zhou M, Zhang M. Topic sentiment analysis in twitter: a graph-based hashtag sentiment classification approach. Proceedings of the 20th ACM international conference on information and knowledge management. ACM; 2011. p. 1031–40.
[3] Efron M. Hashtag retrieval in a microblogging environment. Proceedings of the 33rd international ACM SIGIR conference on Research and development in information retrieval. ACM; 2010. p. 787–8.
[4] Huang J, Thornton KM, Efthimiadis EN. Conversational tagging in twitter. Proceedings of the 21st ACM conference on Hypertext and hypermedia. ACM; 2010. p. 173–8.
[5] Abel F, Gao Q, Houben G-J, Tao K. Semantic enrichment of twitter posts for user profile construction on the social web. Extended semantic web conference. Springer; 2011. p. 375–89.
[6] Piao G, Breslin JG. Interest representation, enrichment, dynamics, and propagation: a study of the synergetic effect of different user modeling dimensions for personalized recommendations on twitter. European knowledge acquisition workshop. Springer; 2016. p. 496–510.
[7] Kinsella S, Wang M, Breslin JG, Hayes C. Improving categorisation in social media using hyperlinks to structured data sources. Extended semantic web conference. Springer; 2011. p. 390–404.
[8] Piao G, Breslin JG. Exploring dynamics and semantics of user interests for user modeling on twitter for link recommendations. Proceedings of the 12th international conference on semantic systems. ACM; 2016. p. 81–8.
[9] Kapanipathi P, Jain P, Venkataramani C, Sheth A. User interests identification on twitter using a hierarchical knowledge base. European semantic web conference. Springer; 2014. p. 99–113.
[10] Michelson M, Macskassy SA. Discovering users' topics of interest on twitter: a first look. Proceedings of the fourth workshop on Analytics for noisy unstructured text data. ACM; 2010. p. 73–80.
[11] Sriram B, Fuhry D, Demir E, Ferhatosmanoglu H, Demirbas M. Short text classification in twitter to improve information filtering. Proceedings of the 33rd international ACM SIGIR conference on Research and development in information retrieval. ACM; 2010. p. 841–2.
[12] Kwak H, Lee C, Park H, Moon S. What is twitter, a social network or a news media? Proceedings of the 19th international conference on World wide web. ACM; 2010. p. 591–600.
[13] Ding Z, Qiu X, Zhang Q, Huang X. Learning topical translation model for microblog hashtag suggestion. IJCAI. 2013. p. 2078–84.
[14] She J, Chen L. Tomoha: Topic model-based hashtag recommendation on twitter. Proceedings of the 23rd international conference on World Wide Web. ACM; 2014. p. 371–2.
[15] Sedhai S, Sun A. Hashtag recommendation for hyperlinked tweets. Proceedings of the 37th international ACM SIGIR conference on research & development in information retrieval. ACM; 2014. p. 831–4.
[16] Li Q, Shah S, Nourbakhsh A, Liu X, Fang R. Hashtag recommendation based on topic enhanced embedding, tweet entity data and learning to rank. Proceedings of the 25th ACM international on conference on information and knowledge management. ACM; 2016. p. 2085–8.
[17] Abel F, Gao Q, Houben G-J, Tao K. Analyzing user modeling on twitter for personalized news recommendations. International conference on user modeling, adaptation, and personalization. Springer; 2011. p. 1–12.
[18] Carroll JB. Development of native language skills beyond the early years. ETS Res. Rep. Ser. 1968;1968(1).
[19] Collobert R, Weston J, Bottou L, Karlen M, Kavukcuoglu K, Kuksa P. Natural language processing (almost) from scratch. J. Mach. Learn. Res. 2011;12(Aug):2493–537.
[20] Mikolov T, Chen K, Corrado G, Dean J. Efficient estimation of word representations in vector space. arXiv:130137812013.
[21] Mikolov T, Sutskever I, Chen K, Corrado GS, Dean J. Distributed representations of words and phrases and their compositionality. Advances in neural information processing systems. 2013. p. 3111–9.
[22] Liu Y, Liu Z, Chua T-S, Sun M. Topical word embeddings. AAAI. 2015. p. 2418–24.
[23] Dhingra B, Zhou Z, Fitzpatrick D, Muehl M, Cohen WW. Tweet2vec: Character-based distributed representations for social media. arXiv:160503481 2016.
[24] Li J, Xu H, He X, Deng J, Sun X. Tweet modeling with lstm recurrent neural networks for hashtag recommendation. Neural networks (IJCNN), 2016 international joint conference on. IEEE; 2016. p. 1570–7.
[25] Tomar A, Godin F, Vandersmissen B, De Neve W, Van de Walle R. Towards twitter hashtag recommendation using distributed word representations and a deep feed forward neural network. Advances in computing, communications and informatics (ICACCI, 2014 international conference on. IEEE; 2014. p. 362–8.
[26] Santos CD, Zadrozny B. Learning character-level representations for part-of-speech tagging. Proceedings of the 31st international conference on machine learning (ICML-14). 2014. p. 1818–26.
[27] Ling W, Luís T, Marujo L, Astudillo RF, Amir S, Dyer C, et al. Finding function in form: Compositional character models for open vocabulary word representation. arXiv:150802096 2015;.
[28] Socher R, Manning CD, Ng AY. Learning continuous phrase representations and syntactic parsing with recursive neural networks. Proceedings of the NIPS-2010 deep learning and unsupervised feature learning workshop. vol. 2010. 2010. p. 1–9.
[29] Bengio Y, Ducharme R, Vincent P, Jauvin C. A neural probabilistic language model. Journal of machine learning research 2003;3(Feb):1137–55.
[30] Mnih A, Salakhutdinov RR. Probabilistic matrix factorization. Advances in neural information processing systems. 2008. p. 1257–64.
[31] Takane Y, Young FW, De Leeuw J. Nonmetric individual differences multidimensional scaling: an alternating least squares method with optimal scaling features. Psychometrika 1977;42(1):7–67.

Akshi Kumar is an Assistant Professor in the Department of Computer Science & Engineering at Delhi Technological University. She has received her doctorate degree in Computer Engineering from the University of Delhi, India. She has many publications to her credit in various International Journals with high impact factor and International Conferences with best paper awards. Her research interests include Intelligent Systems, Text Mining, Sentiment Analysis, Recommender Systems, Social & Semantic Web, User-generated Big-data.

Himanshu Ahuja is currently pursuing the B. Tech degree with the Computer Science and Engineering Department at Delhi Technological University, New Delhi, India. His current research interests encompass Computer Vision, object detection, Deep Learning, Graph representation and Sequential Data Modelling.

Nikhil Kumar Singh is currently pursuing the B. Tech degree with the Computer Science and Engineering Department at Delhi Technological University, New Delhi, India. He has an avid interest for data gathering, analysis and visualization . His current research interests encompass NLP, social networks and recommendation systems.

Deepak Gupta has completed B.Tech. from Guru Gobind Singh Indraprastha University, M.E. from Delhi College of Engineering and Ph.D. from Dr. APJ Abdul Kalam Technical University, Lucknow, UP. He has published 31 text/edited books on various topics of computer science & engineering with International Publishers, has edited two book published by Elsevier and 35 research papers in various International Journals of repute.

Ashish Khanna is a highly qualified individual with 15 years of expertise in Teaching, Entrepreneurship, and Research & Development with specialization in Computer Science Engineering Subjects. He received his Ph.D. degree from NIT, Kurukshetra. He has completed his M. Tech. and B. Tech. from GGSIPU. He has published many research papers in reputed journals. He also has papers in SCI indexed and Springer journals.

Joel J.P.C. Rodrigues is a professor and senior researcher at the National Institute of Telecommunications (Inatel), Brazil. He is the leader of the Internet of Things Research Group (CNPq), the President of the scientific council at ParkUrbis, Covilh Science & Technology Park. He has authored or coauthored over 650 papers in refereed international journals and conferences, 3 books, and 2 patents.

Synthesis and electrochemical properties of low-temperature synthesized Li_2MnO_3/MWCNT/super P as a high capacity cathode material for lithium ion batteries

Rakesh Saroha, Amrish K. Panwar, and Abhishek Bhardwaj

Citation: AIP Conference Proceedings **2009**, 020038 (2018); doi: 10.1063/1.5052107
View online: https://doi.org/10.1063/1.5052107
View Table of Contents: http://aip.scitation.org/toc/apc/2009/1
Published by the American Institute of Physics



Synthesis and Electrochemical Properties of Low-Temperature Synthesized Li_2MnO_3/MWCNT/super P as a High Capacity Cathode Material for Lithium ion Batteries

Rakesh Saroha, Amrish K. Panwar,[a)] and Abhishek Bhardwaj

Department of Applied Physics, Delhi Technological University, Delhi-110042, India.
[a)]Corresponding Author: panwaramar@gmail.com

Abstract: The present work describes the synthesis and electrochemical properties of layered-Li_2MnO_3 with different carbon additives usingball millingroute. X-ray diffraction (XRD) pattern reveals that all the prepared samplesbelong to*m*-Li_2MnO_3 phasehaving*C2/*m space group. LMOA (Li_2MnO_3sample with MWCNT's)providesmaximum discharge capacity among all the prepared samples. The LMOAcathodeoffers acapacity of 121±5 $mAhg^{-1}$ at a current density of 10 mA/g for the initial cycle in the voltage windowof 2.0-4.8 V.

Introduction

Cathode materials with formula $Li[Li_xMn_yM_z]O_2$[M represents transition metal] become apopularchoice in the recent time because of their higher experimental specific discharge capacity(>200 mAh/g) as compared to the commercially available $LiCoO_2$[1, 2].$Li[Li_{1/3}Mn_{2/3}]O_2$cathode material generally inscribed as Li_2MnO_3, possesses much higher theoretical specific discharge capacity (458 mAh/g) as compared to $Li[Li_xMn_yM_z]O_2$[1, 3-6]. Despite of high theoretical discharge capacity, its commercialization is still unfeasible because of electrochemical inactiveness in the 2.2-4.4 V (*vs.* Li^+/Li) voltage range[7-10].Several efforts have been made worldwide by research fraternity to overshadow this shortcomingusingextraction of lithium and oxygen simultaneously in the form of Li_2O to activate Li_2MnO_3[11, 12], substitutionat Li/Mnsite partially with another metal ion[4, 7, 13-15], co-doping [16-18],surface modification [19-21], synthesizing oxygen deficient phase [22]and even with different morphologies [6, 23].There have been various reports on the low-temperature synthesis of Li_2MnO_3particles,but thecombined effect of different carbon additives and low-temperature synthesis has not been reported so far for Li_2MnO_3[6, 21, 24]. The criteria of low-temperature synthesis have been adopted in the present work following the low-temperature annealing, which minimizes the loss of lithium as compared to higher annealing temperature with prolonged heating[24].The objective of the present study is to reveal the effects of different carbon additives on the electrochemical performances of the low-temperature synthesizedlayered-Li_2MnO_3. All the samples in the presentstudy have been synthesizedbywet milling method and were examined for phase analysis and microstructural investigation using scanning electron microscopy (SEM) and X-ray diffraction (XRD), respectively.Electrochemical analysis of the synthesized samples wasalso performed to analyze the electrochemical performance.

Experimental

Pristine Li_2MnO_3 and MWCNT/Super P added Li_2MnO_3samples were prepared using wet milling route. Stoichiometric amounts of lithium hydroxide monohydrate ($LiOH.H_2O$, Sigma-Aldrich grade, ≥ 99%) and Manganous(II) acetate tetrahydrate($(CH_3COO)_2$ $Mn.4H_2O$, Sigma-Aldrich grade, ≥ 99%) were used as precursors.All the precursors were ball millin a planetary ball mill of capacity 50 ml (0.693 kg). Precursors were ball milled at 400 rpm for 5 h in toluene media. The powder to ballweight ratio was kept at 10:1. The resulting solid precursor was then dry, crushed using pestle mortar and then decomposedin the airat 500ºC for 30 h in a muffle furnace.The powders thus obtained were mixed with super P (5wt. % of the remaining sample after heating)and MWCNT's (1wt. %)separately and again ball mill for 2 h. No further annealing was done for the obtained samples. The pristine and modified sample withMWCNT's and super Pwere abbreviated as LMO, LMOA and LMOB, respectively.

Phase composition and quantitative analysis of the crystal structurefor synthesized powderswas conducted using RIGAKU make X-ray diffractometerattached with $CuK_{\alpha 1}$ radiation (λ=1.540 Å). The 2θ range for XRD data collection was kept at 10º-70º with a step size of 0.02º. The morphologicalproperties of the preparedsamples wereanalyzed using HITACHI make S-3700N scanning electron microscope.

National Conference on Advanced Materials and Nanotechnology - 2018
AIP Conf. Proc. 2009, 020038-1–020038-5; https://doi.org/10.1063/1.5052107
Published by AIP Publishing. 978-0-7354-1725-0/$30.00

Electrochemical tests were performed using CR2032 coin-type halfcells. The positive working electrode was made bydispersing active material, super P (conductive carbon) and polyvinylidenedifluoride (PVDF, binder) in N-methyl-2-pyrrolidinone (NM2P, solvent) in a wt.% ratio of 70:15:15, respectively. The precise description of electrode preparation method has been described elsewhere[3].Electrochemical behavior was investigated by cyclic voltammetry (CV) testsin the potential window of 2.0-4.8 V (*vs.* Li/Li^+ metal). The cells were charged and discharged galvanostaticallyat different current density rates.

Results and discussion

Fig. 1. shows the obtained XRD patterns of the prepared samplesof LMO, LMOA and LMOB. All the prepared samplesshow diffraction peaks which correspond to the *m*-Li_2MnO_3phasehaving *C2/*m space group.The wellintense peaks indicate the crystalline nature of prepared samples.XRD graph also shows the presence of few low intense peaks around 20-30° leading to the Mn-ion ordering into Li-Mn layers giving rise to superlattice structure. The double peak around 65° can also be assigned to the layered Li_2MnO_3 structure with different cation distribution in transition metal layers in the form of Mn_2Li.No additional peak related to MWCNT/Super P was observed. It shows that the carbon present in the samples is amorphous in nature or the amount is too small to be detected.The unit cell parameters obtained for bare LMO were found to be: a = 4.931 Å, b = 8.528 Å and c = 5.019 Å. Scherrer's formula (d= kλ/β cos θ; d is the average crystallite size, k is the shape factor (0.94), λ is the wavelength of X-ray (0.154 nm), β is the FWHM and θ is the Bragg's diffraction angle) was used to calculate the mean crystallite size for pristine LMO and was found to be 62 nm.

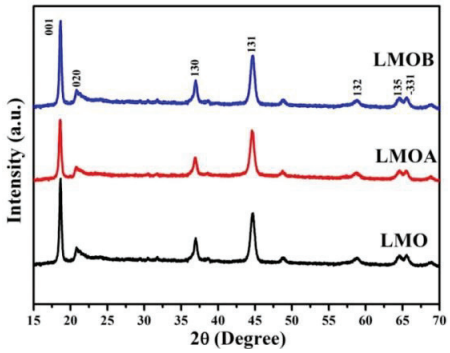


FIGURE 1. XRD patterns of synthesized samples of LMO,LMOA and LMOB.

Fig. 2(A)-(C) shows the SEM micrographs of the synthesized samples LMO, LMOA and LMOB. All prepared samples showmore or less same morphologicalfeatures with acombination of small as well as bigger sized grains. The mean grain size of LMO, LMOA and LMOBsampleswere obtainedby "imageJ" software and lie in the range of 200-300 nm.

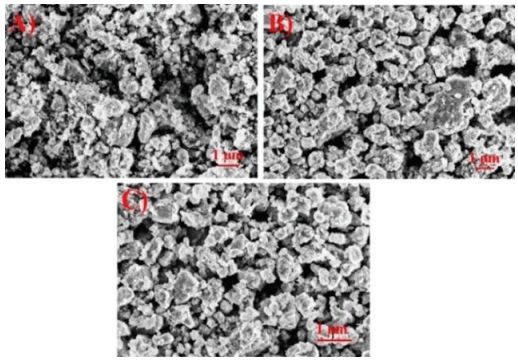


FIGURE 2. SEM micrographs of powder samples: (A) LMO; (B) LMOA; (C) LMOB.

Fig. 3 displays the CV curves of the prepared cathodes in the voltage range of 2.0-4.8 V for all samples. The CV data measurement was performed at a low scan rate of $0.05mVs^{-1}$. It can be noticed from Fig. 3that MWCNT/Super P modified Li_2MnO_3 (LMOA) shows a more intense anodic peak around 4.7 V as compared to pristine LMO.The anodic peak at 4.7 V specifies the removal of lattice oxygen alongside with lithium extraction

from the monoclinic structure which seems to be much easier in MWCNT/Super P modified Li_2MnO_3 samples[3]. However, no symmetrically situated cathodic peak around 4.7 V was observed for all the synthesized samples.Therefore, CV result suggests that the Li_2MnO_3 (LMO) activation will take place around4.7 V.Apart from anodic peak at 4.7 V, the CV profile also indicates the appearance of redox peaks at 3.0/2.8 V which may be assigned to Li-ion intercalation in the spinel structure at *16c* octahedral sites [3].Fig. 4displays the first charge/discharge profiles of LMO, LMOA and LMOB samples at 10 mA/g current density. The discharge capacities for samples LMO, LMOAand LMOB were estimated to be 52±5, 94±5 and 121±5 $mAhg^{-1}$, respectively. The charge/discharge profiles of LMO, LMOA and LMOB samples shows plateau about 2.87 V,itmay be due to the variation in the oxidation state of Mn ion during redox reactions. Among all the samples, the MWCNT modified Li_2MnO_3 i.e. LMOA display the best charge/discharge profile with highest discharge capacity value. These results are in consistent with the CV results and show excellent kinetics inside the cathode and superior reactivity for LMOA sample.Fig. 5(A)-(C) displays the GCD profiles of pristine LMO,for the 10^{th}

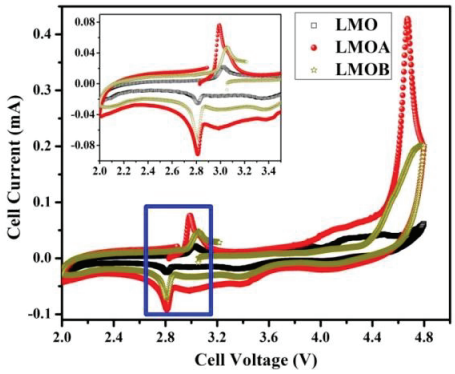


FIGURE 3. Cyclic Voltammograms of the LMO, LMOA an LMOB samples at a scan rate of 0.05 mVs^{-1}.

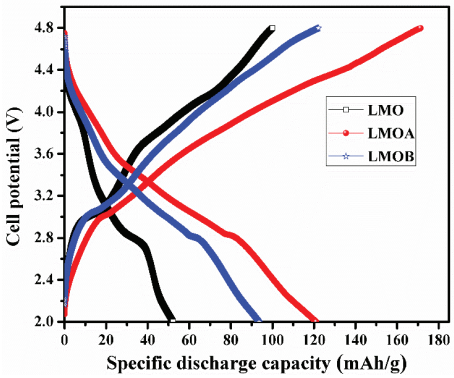


FIGURE 4.1st charge/discharge profile of prepared samples at a 10 mA/g.

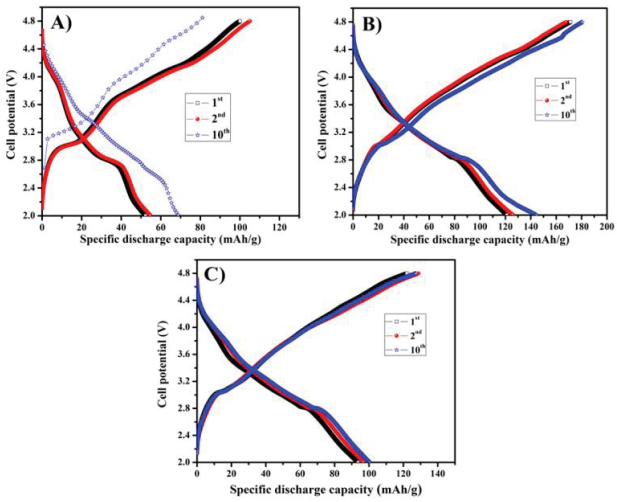


FIGURE 5. GCD curves of the samples for 1st, 2nd and 10th cycle at 10 mA/g: (A) LMO; (B) LMOA; (C) LMOB.

cycle is higher than 1stcycle which is due to exclusion of lattice oxygen alongside with lithium extraction leads to activation of LMO. LMOA and LMOB samples, respectively for 1st, 2nd and 10th cycle at a current density of 10 mA/g. From Fig. 5(A), it can be noted that capacity value of LMO samplefor the 10th cycle is higher than 1stcycle which is due to exclusion of lattice oxygen alongside with lithium extraction leads to activation of LMO.

Similar results were obtained for LMOA (Fig. 5(B)) sample for which discharge capacity value of 10th cycle was found to be higher than to 1stcycle. However, for LMOB (Fig. 5(C))sample the GCD profiles for 1st, 2nd and 10th cycle remains almost similar. Therefore, addition of MWCNT and super P not only enhances the discharge capacity but also strengthen the integrity of the synthesized samples.

Conclusions

In the present work,synthesis and electrochemical properties of layered-Li_2MnO_3 with different carbon additives have been carried outusing ball milling route. X-ray diffraction (XRD) pattern reveals that all the prepared samplesbelong to*m*-Li_2MnO_3 phasehaving *C2/*m space group and are well crystalline as indicated by sharp and intense peaks. Cyclic voltammetry curves reveal the presence of an intense anodic peak at 4.7 V for MWCNT added Li_2MnO_3 (LMOA) in the 2.0-4.8 V voltage range. Among all the synthesized samples, LMOA exhibit maximum discharge capacity, best rate performances, and cyclabilityover all range of current densities. The LMOAsampleprovides a discharge capacity of 121±5 $mAhg^{-1}$ at 10 mA/g.

References

1. Y. W. Denis, K. Yanagida, Y. Kato and H. Nakamura, J. Electrochem. Soc. **156** (6), A417-A424 (2009).
2. J. Lin, D. Mu, Y. Jin, B. Wu, Y. Ma and F. Wu, J. Power Sources **230**, 76-80 (2013).
3. R. Saroha, A. Gupta and A. K. Panwar, J. Alloys Compd. **696**, 580-589 (2017).
4. X. Dong, Y. Xu, L. Xiong, X. Sun and Z. Zhang, J. Power Sources **243**, 78-87 (2013).
5. Q. Zhang, X. Hu, D. Zhan and T. Peng, Electrochim. Acta **113**, 424-432 (2013).
6. G. Yang, L. Wang, J. Wang and W. Yan, Ceram. Int. **43** (1), 71-76 (2017).
7. L. Torres-Castro, J. Shojan, C. M. Julien, A. Huq, C. Dhital, M. P. Paranthaman, R. S. Katiyar and A. Manivannan, Mater. Sci. Eng. B **201**, 13-22 (2015).
8. D. Kim, J. Gim, J. Lim, S. Park and J. Kim, Mater. Res. Bull. **45** (3), 252-255 (2010).
9. C. Park, S. Kim, I. R. Mangani, J. Lee, S. Boo and J. Kim, Mater. Res. Bull. **42** (7), 1374-1383 (2007).
10. S. Kim, C. Kim, J.-K. Noh, S. Yu, S.-J. Kim, W. Chang, W. C. Choi, K. Y. Chung and B.-W. Cho, J. Power Sources **220**, 422-429 (2012).
11. Y. Sun, Y. Shiosaki, Y. Xia and H. Noguchi, J. Power Sources **159** (2), 1353-1359 (2006).
12. M. H. Rossouw and M. M. Thackeray, Mater. Res. Bull. **26** (6), 463-473 (1991).
13. W. Zhao, L. Xiong, Y. Xu, X. Xiao, J. Wang and Z. Ren, J. Power Sources **330**, 37-44 (2016).
14. M. Tabuchi, Y. Nabeshima, T. Takeuchi, K. Tatsumi, J. Imaizumi and Y. Nitta, J. Power Sources **195** (3), 834-844 (2010).

15. G.Singh, A. Sil, S. Ghosh and A. Panwar, Ceramic International**36,** 1831-1836(2010).
16. M. Tabuchi, H. Kageyama, K. Takamori, Y. Imanari and K. Nakane, Electrochim. Acta **210**, 105-110 (2016).
17. M. Tabuchi, M. Kitta, H. Kageyama, H. Shibuya and J. Imaizumi, J. Power Sources **279**, 510-516 (2015).
18. M. Tabuchi, Y. Nabeshima, T. Takeuchi, H. Kageyama, J. Imaizumi, H. Shibuya and J. Akimoto, J. Power Sources **221**, 427-434 (2013).
19. A. Klein, P. Axmann, C. Yada and M. Wohlfahrt-Mehrens, J. Power Sources **288**, 302-307 (2015).
20. S.-J. Kim, M.-C. Kim, D.-H. Kwak, D.-M. Kim, G.-H. Lee, H.-S. Choe and K.-W. Park, J. Power Sources **304**, 119-127 (2016).
21. F. Wang, S. Xiao, M. Li, X. Wang, Y. Zhu, Y. Wu, A. Shirakawa and J. Peng, J. Power Sources **287**, 416-421 (2015).
22. K. Kubota, T. Kaneko, M. Hirayama, M. Yonemura, Y. Imanari, K. Nakane and R. Kanno, J. Power Sources **216**, 249-255 (2012).
23. M. Cheng, K. Zhu, L. Yang, L. Zhu, Y. Li and W. Tang, J. Alloys Compd. (2016).
24. S. F. Amalraj, D. Sharon, M. Talianker, C. M. Julien, L. Burlaka, R. Lavi, E. Zhecheva, B. Markovsky, E. Zinigrad and D. Kovacheva, Electrochim. Acta **97**, 259-270 (2013).

The Astronomical Journal, 156:123 (19pp), 2018 September https://doi.org/10.3847/1538-3881/aabc4f
© 2018. The American Astronomical Society.
OPEN ACCESS

The Astropy Project: Building an Open-science Project and Status of the v2.0 Core Package*

The Astropy Collaboration, A. M. Price-Whelan[1], B. M. Sipőcz[44], H. M. Günther[2], P. L. Lim[3], S. M. Crawford[4], S. Conseil[5], D. L. Shupe[6], M. W. Craig[7], N. Dencheva[3], A. Ginsburg[8], J. T. VanderPlas[9], L. D. Bradley[3], D. Pérez-Suárez[10], M. de Val-Borro[11]
(Primary Paper Contributors),
T. L. Aldcroft[12], K. L. Cruz[13,14,15,16], T. P. Robitaille[17], E. J. Tollerud[3]
(Astropy Coordination Committee),
and
C. Ardelean[18], T. Babej[19], Y. P. Bach[20], M. Bachetti[21], A. V. Bakanov[98], S. P. Bamford[22], G. Barentsen[23], P. Barmby[18], A. Baumbach[24], K. L. Berry[98], F. Biscani[25], M. Boquien[26], K. A. Bostroem[27], L. G. Bouma[1], G. B. Brammer[3], E. M. Bray[98], H. Breytenbach[4,28], H. Buddelmeijer[29], D. J. Burke[12], G. Calderone[30], J. L. Cano Rodríguez[98], M. Cara[3], J. V. M. Cardoso[23,31,32], S. Cheedella[33], Y. Copin[34,35], L. Corrales[36,99], D. Crichton[37], D. D'Avella[3], C. Deil[38], É. Depagne[4], J. P. Dietrich[39,40], A. Donath[38], M. Droettboom[3], N. Earl[3], T. Erben[41], S. Fabbro[42], L. A. Ferreira[43], T. Finethy[98], R. T. Fox[98], L. H. Garrison[12], S. L. J. Gibbons[44], D. A. Goldstein[45,46], R. Gommers[47], J. P. Greco[1], P. Greenfield[3], A. M. Groener[48], F. Grollier[98], A. Hagen[49,50], P. Hirst[51], D. Homeier[52], A. J. Horton[53], G. Hosseinzadeh[54,55], L. Hu[56], J. S. Hunkeler[3], Ž. Ivezić[57], A. Jain[58], T. Jenness[59], G. Kanarek[3], S. Kendrew[60], N. S. Kern[45], W. E. Kerzendorf[61], A. Khvalko[98], J. King[38], D. Kirkby[62], A. M. Kulkarni[63], A. Kumar[64], A. Lee[65], D. Lenz[66], S. P. Littlefair[67], Z. Ma[68], D. M. Macleod[69], M. Mastropietro[70], C. McCully[54,55], S. Montagnac[71], B. M. Morris[57], M. Mueller[72], S. J. Mumford[73], D. Muna[74], N. A. Murphy[12], S. Nelson[7], G. H. Nguyen[75], J. P. Ninan[50], M. Nöthe[76], S. Ogaz[3], S. Oh[1], J. K. Parejko[57], N. Parley[77], S. Pascual[78], R. Patil[98], A. A. Patil[79], A. L. Plunkett[80], J. X. Prochaska[81], T. Rastogi[98], V. Reddy Janga[82], J. Sabater[83], P. Sakurikar[84], M. Seifert[98], L. E. Sherbert[3], H. Sherwood-Taylor[98], A. Y. Shih[85], J. Sick[86], M. T. Silbiger[98], S. Singanamalla[87], L. P. Singer[88,89], P. H. Sladen[90], K. A. Sooley[98], S. Sornarajah[98], O. Streicher[91], P. Teuben[92], S. W. Thomas[44], G. R. Tremblay[12], J. E. H. Turner[93], V. Terrón[94], M. H. van Kerkwijk[95], A. de la Vega[37], L. L. Watkins[3], B. A. Weaver[96], J. B. Whitmore[97], J. Woillez[61], and V. Zabalza[98]
(Astropy Contributors)

[1] Department of Astrophysical Sciences, Princeton University, Princeton, NJ 08544, USA; coordinators@astropy.org
[2] Kavli Institute for Astrophysics and Space Research, Massachusetts Institute of Technology, 70 Vassar St., Cambridge, MA 02139, USA
[3] Space Telescope Science Institute, 3700 San Martin Dr., Baltimore, MD 21218, USA
[4] South African Astronomical Observatory, P.O. Box 9, Observatory 7935, Cape Town, South Africa
[5] Univ Lyon, Univ Lyon1, Ens de Lyon, CNRS, Centre de Recherche Astrophysique de Lyon UMR5574, F-69230, Saint-Genis-Laval, France
[6] Caltech/IPAC, 1200 E. California Blvd, Pasadena, CA 91125, USA
[7] Department of Physics and Astronomy, Minnesota State University Moorhead, 1104 7th Ave S, Moorhead, MN 56563, USA
[8] National Radio Astronomy Observatory, 1003 Lopezville Rd, Socorro, NM 87801, USA
[9] eScience Institute, University of Washington, 3910 15th Ave NE, Seattle, WA 98195, USA
[10] University College London/Research IT Services, Gower St, Bloomsbury, London WC1E 6BT, UK
[11] Astrochemistry Laboratory, NASA Goddard Space Flight Center, 8800 Greenbelt Road, Greenbelt, MD 20771, USA
[12] Harvard-Smithsonian Center for Astrophysics, 60 Garden St., Cambridge, MA, 02138, USA
[13] Department of Physics and Astronomy, Hunter College, City University of New York, 695 Park Avenue, New York, NY 10065, USA
[14] Physics, Graduate Center of the City University of New York, New York, NY, USA
[15] Department of Astrophysics, American Museum of Natural History, New York, NY, USA
[16] Center for Computational Astropyhsics, Flatiron Institute, 162 Fifth Avenue, New York, NY 10010, USA
[17] Aperio Software Ltd., Headingley Enterprise and Arts Centre, Bennett Road, Leeds, LS6 3HN, UK
[18] Department of Physics & Astronomy, University of Western Ontario, 1151 Richmond St, London ON N5X4H1 Canada
[19] Department of Theoretical Physics & Astrophysics, Masaryk University, Kotlarska 2, 61137 Brno, Czech Republic
[20] Department of Physics and Astronomy, Seoul National University, Gwanak-gu, Seoul 08826, Republic of Korea
[21] INAF-Osservatorio Astronomico di Cagliari, via della Scienza 5, I-09047, Selargius, Italy
[22] School of Physics & Astronomy, University of Nottingham, University Park, Nottingham NG7 2RD, UK
[23] NASA Ames Research Center, Moffett Field, CA 94043, USA
[24] Heidelberg University, Kirchhoff Institut for Physics, Im Neuenheimer Feld 227, D-69116 Heidelberg, Germany
[25] Max-Planck-Institut für Astronomie, Königstuhl 17, D-69117 Heidelberg, Germany
[26] Unidad de Astronomía Fac. Cs. Básicas, Universidad de Antofagasta, Avda.U. de Antofagasta 02800, Antofagasta, Chile
[27] Department of Physics, UC Davis, 1 Shields Ave, Davis, CA, 95616, USA
[28] Department of Astronomy, University of Cape Town, Private Bag X3, Rondebosch 7701, South Africa
[29] Leiden Observatory, Leiden University, P.O. Box 9513, 2300 RA, Leiden, The Netherlands
[30] Istituto Nazionale di Astrofisica, via Tiepolo 11 Trieste, Italy
[31] Universidade Federal de Campina Grande, Campina Grande, PB 58429-900, Brazil
[32] Bay Area Environmental Research Institute, Petaluma, CA 94952, USA
[33] Department of Physics, Virginia Tech, Blacksburg, VA 24061, USA
[34] Université de Lyon, F-69622, Lyon, France

* The author list has three parts: the authors that made significant contributions to the writing of the paper in order of contribution, the four members of the Astropy Project coordination committee, and contributors to the Astropy Project in alphabetical order. Their position in the author list does not correspond to contributions to the Astropy Project as a whole. A more complete list of contributors to the core package can be found in the package repository and at the Astropy team webpage.

[35] Université de Lyon 1, Villeurbanne; CNRS/IN2P3, Institut de Physique Nucléaire de Lyon, France
[36] University of Wisconsin—Madison, 475 North Charter Street, Madison, WI 53706, USA
[37] Department of Physics and Astronomy, Johns Hopkins University, Baltimore, MD 21218, USA
[38] Max-Planck-Institut für Kernphysik, P.O. Box 103980, D-69029 Heidelberg, Germany
[39] Faculty of Physics, Ludwig-Maximilians-Universität, Scheinerstr. 1, D-81679 Munich, Germany
[40] Excellence Cluster Universe, Boltzmannstr. 2, D-85748 Garching b. München, Germany
[41] Argelander-Institut für Astronomie, Auf dem Hügel 71, D-53121 Bonn, Germany
[42] National Research Council Herzberg Astronomy & Astrophysics, 4071 West Saanich Road, Victoria, BC, Canada
[43] Instituto de Matemática Estatística e Física—IMEF, Universidade Federal do Rio Grande—FURG, Rio Grande, RS 96203-900, Brazil
[44] Institute of Astronomy, University of Cambridge, Madingley Road, Cambridge, CB3 0HA, UK
[45] Department of Astronomy, UC Berkeley, 501 Campbell Hall #3411, Berkeley, CA 94720, USA
[46] Lawrence Berkeley National Laboratory, 1 Cyclotron Road, Berkeley, CA 94720, USA
[47] Scion, Private Bag 3020, Rotorua, New Zealand
[48] Drexel University, Physics Department, Philadelphia, PA 19104, USA
[49] Vizual.ai, 3600 O'Donnell St, Suite 250, Baltimore, MD 21224, USA
[50] Dept of Astronomy and Astrophysics, Pennsylvania State University, University Park, PA 16802, USA
[51] Gemini Observatory, 670 N. Aohoku Pl, Hilo, HI 96720, USA
[52] Zentrum für Astronomie der Universität Heidelberg, Landessternwarte, Königstuhl 12, D-69117 Heidelberg, Germany
[53] Australian Astronomical Observatory, 105 Delhi Road, North Ryde NSW 2113, Australia
[54] Las Cumbres Observatory, 6740 Cortona Drive, Suite 102, Goleta, CA 93117-5575, USA
[55] Department of Physics, University of California, Santa Barbara, CA 93106-9530, USA
[56] Imperial College London, Kensington, London SW7 2AZ, UK
[57] Department of Astronomy, University of Washington, Seattle, WA 98155, USA
[58] BITS PILANI/Computer Science, Pilani Campus, Rajasthan, India
[59] Large Synoptic Survey Telescope, 950 N. Cherry Ave., Tucson, AZ, 85719, USA
[60] European Space Agency, Space Telescope Science Institute, 3700 San Martin Dr., Baltimore, MD 21218, USA
[61] European Southern Observatory, Karl-Schwarzschild-Straße 2, D-85748 Garching bei München, Germany
[62] Department of Physics and Astronomy, University of California, Irvine, CA 92697, USA
[63] College of Engineering Pune/Department of Computer Engineering and IT, Shivajinagar, Pune 411005, India
[64] Delhi Technological University, India
[65] Department of Physics, University of Berkeley, California, CA94709, USA
[66] Jet Propulsion Laboratory, California Institute of Technology, 4800 Oak Grove Drive, Pasadena, CA 91109, USA
[67] Department of Physics & Astronomy, University of Sheffield, Sheffield, S3 7RH, UK
[68] Department of Physics and Astronomy, University of Missouri, Columbia, Missouri, 65211, USA
[69] Cardiff University, Cardiff CF24 3AA, UK
[70] Department of Physics and Astronomy, Ghent University, Krijgslaan 281, S9, B-9000 Gent, Belgium
[71] Puy-Sainte-Réparade Observatory, France
[72] Department of Mathematics, Brown University, 151 Thayer Street, Providence, RI 02912, USA
[73] SP^{2}RC, School of Mathematics and Statistics, The University of Sheffield, UK
[74] Center for Cosmology and Astroparticle Physics, The Ohio State University, 191 West Woodruff Avenue, Columbus, OH 43210, USA
[75] VNU-HCMC, University of Natural Sciences/Faculty of IT, 227 Nguyen Van Cu St., Ward 4, District 5, Ho Chi Minh City, Vietnam
[76] Experimental Physics 5, TU Dortmund, Otto-Hahn-Str. 4, D-44227 Dortmund, Germany
[77] University of Reading, Whiteknights Campus, Reading RG6 6BX, UK
[78] Departamento de Astrofisica, Universidad Complutense de Madrid, Madrid, Spain
[79] Pune Institute of Computer Technology, Pune 411043, India
[80] European Southern Observatory, Av. Alonso de Córdova 3107, Vitacura, Santiago, Chile
[81] Astronomy & Astrophysics, UC Santa Cruz, 1156 High St., Santa Cruz, CA 95064 USA
[82] Indian Institute of Technology, Mechanical Engineering, Kharagpur, India
[83] Institute for Astronomy (IfA), University of Edinburgh, Royal Observatory, Blackford Hill, EH9 3HJ Edinburgh, UK
[84] IIIT-Hyderabad, India
[85] NASA Goddard Space Flight Center, 8800 Greenbelt Road, Greenbelt, MD 20771, USA
[86] AURA/LSST, 950 N Cherry Ave, Tucson, 85719, USA
[87] Microsoft Research, Redmond, WA 98053, USA
[88] Astroparticle Physics Laboratory, NASA Goddard Space Flight Center, 8800 Greenbelt Road, Greenbelt, MD 20771, USA
[89] Joint Space-Science Institute, University of Maryland, College Park, MD 20742, USA
[90] Zentrum für Astronomie der Universität Heidelberg, Astronomisches Rechen-Institut, Mönchhofstraße 12-14, D-69120 Heidelberg, Germany
[91] Leibniz Institute for Astrophysics Potsdam (AIP), An der Sternwarte 16, D-14482 Potsdam, Germany
[92] Astronomy Department, University of Maryland, College Park, MD 20742, USA
[93] Gemini Observatory, Casilla 603, La Serena, Chile
[94] Institute of Astrophysics of Andalusia (IAA-CSIC), Granada, Spain
[95] Department of Astronomy & Astrophysics, University of Toronto, 50 Saint George Street, Toronto, ON M5S 3H4, Canada
[96] National Optical Astronomy Observatory, 950 N. Cherry Ave., Tucson, AZ 85719, USA
[97] Centre for Astrophysics and Supercomputing, Swinburne University of Technology, Hawthorn, VIC 3122, Australia
Received 2018 January 8; revised 2018 March 27; accepted 2018 March 29; published 2018 August 24

[98] The Astropy Project.
[99] Einstein Fellow.


Original content from this work may be used under the terms of the Creative Commons Attribution 3.0 licence. Any further distribution of this work must maintain attribution to the author(s) and the title of the work, journal citation and DOI.

Abstract

The Astropy Project supports and fosters the development of open-source and openly developed `Python` packages that provide commonly needed functionality to the astronomical community. A key element of the Astropy Project is the core package `astropy`, which serves as the foundation for more specialized projects and packages. In this article, we provide an overview of the organization of the Astropy project and summarize key features in the core package, as of the recent major release, version 2.0. We then describe the project infrastructure designed to facilitate and support development for a broader ecosystem of interoperable packages. We conclude with a future outlook of planned new features and directions for the broader Astropy Project.

Key words: methods: data analysis – methods: miscellaneous – methods: statistical – reference systems

1. Introduction

All modern astronomical research makes use of software in some way. Astronomy, as a field, has thus long supported the development of software tools for astronomical tasks, such as scripts that enable individual scientific research, software packages for small collaborations, and data reduction pipelines for survey operations. Some software packages are, or were, supported by large institutions and intended for a wide range of users. These packages therefore typically provide some level of documentation and user support or training. Other packages are developed by individual researchers or research groups, are then typically used by smaller groups for more domain-specific purposes, and may have less extensive user support. For both packages meant for wider distribution and for scripts specific to particular research projects, a library that addresses common astronomical tasks simplifies the software development process by encouraging the reuse of common functions. The users of such a library then also benefit from a community and ecosystem built around a shared foundation. The Astropy project has grown to become such a community for `Python` astronomy software, and the `astropy` core package has become this shared foundation.

The development of the `astropy` core package began as a largely community-driven effort to standardize core functionality for astronomical software in `Python`. In this way, its genesis differs from, but builds upon, many substantial and former astronomical software development efforts that were commissioned or initiated through large institutional support, such as IRAF (developed at NOAO; Tody 1993), MIDAS (developed at ESO; Banse et al. 1988), or Starlink (originally developed by a consortium of UK institutions and now maintained by the East Asian Observatory; Disney & Wallace 1982; Currie et al. 2014). More recently, community-driven efforts have seen significant success in the astronomical sciences (e.g., Turk et al. 2011).

`Python`[100] is an increasingly popular, general-purpose programming language that is available under a permissive open-source software license and is free of charge for all major operating systems. This programming language has become especially popular in the quantitative sciences, where researchers must simultaneously conduct research, perform data analysis, and develop software. A large part of this success owes itself to the vibrant community of developers and a continuously growing ecosystem of tools, web services, and stable, well-developed packages that enable easier collaboration on software development, easier writing and sharing of software documentation, and continuous testing and validation of software. While dedicated libraries provide support for array representation and arithmetic (`numpy`; Van der Walt et al. 2011), a wide variety of functions for scientific computing (`scipy`; Jones et al. 2001), and publication-quality plotting (`matplotlib`; Hunter 2007), tens of thousands of other high-quality and easy-to-use packages are available to help with tasks that are not specific to astronomy but might be performed in the course of astronomical research, e.g., interfacing with databases, or statistical inferences. More recently, the development and mainstream adoption of package managers such as Anaconda[101] has significantly streamlined the installation process for many libraries, lowering the barriers to entry for new users.

The Astropy Project aims to provide an open-source and open-development core package (`astropy`) and an ecosystem of *affiliated packages* that support astronomical functionality in the `Python` programming language. "Open development" describes a process where anybody with an internet connection can suggest changes to the source code and contribute their opinion when new features, bug fixes or other code changes, governance, or any other aspect of the development process is discussed (see Sections 2.2 and 2.3 of how this is organized in practice). The `astropy` core package is now a feature-rich library of sufficiently general tools and classes that supports the development of more specialized code. An example of such functionality is reading and writing FITS files: it would be time-consuming and impractical for multiple groups to implement the FITS standard (Pence et al. 2010) and maintain software for such a general-purpose need. Another example of such a common task is in dealing with representations of and transformations between astronomical coordinate systems.

The Astropy Project aims to develop and provide high-quality code and documentation according to the best practices in software development. The project makes use of different tools and web services to reach those goals without central institutional oversight. The first public release of the `astropy` package is described in Astropy Collaboration et al. (2013). Since then, the `astropy` package has been used in hundreds of projects and the scope of the package has grown considerably. At the same time, the scientific community contributing to the project has grown tremendously and an ecosystem of packages supporting or affiliated with the `astropy` core has developed. In this paper, we describe the current status of the Astropy community and the `astropy` core package and discuss goals for future development.

We start by describing the way the Astropy Project functions and is organized in Section 2. We then describe the main software efforts developed by the Astropy Project itself: a core package called `astropy` (Section 3) and several separate packages that help maintain the infrastructure for testing and documentation (Section 4). We end with a short vision for the

[100] https://www.python.org/

[101] https://anaconda.org/

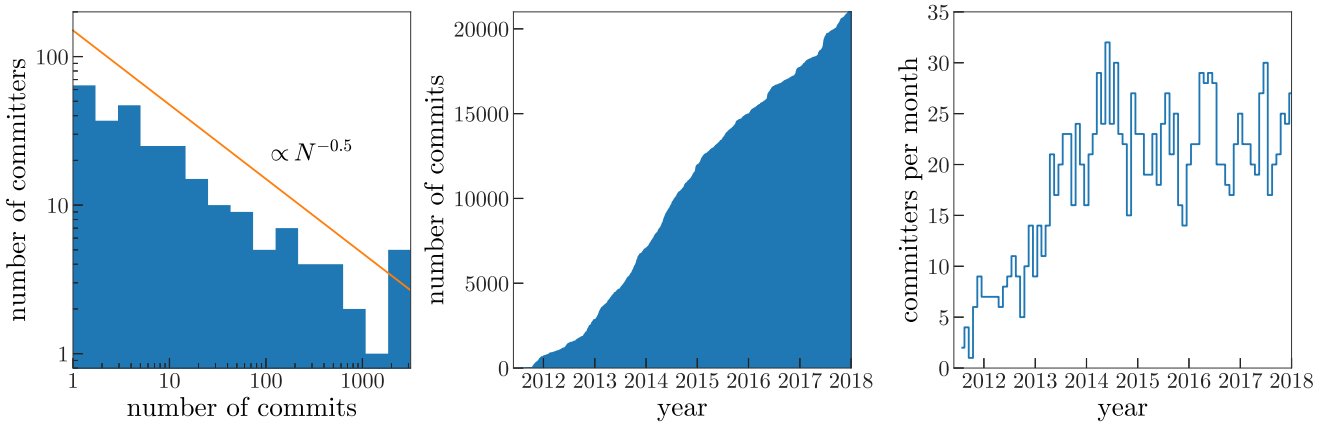


Figure 1. Left panel: distribution of number of commits per committer. Middle panel: cumulative number of commits to the `astropy` core package over time. Right panel: number of unique committers per month to the `astropy` core package.

future of Astropy and astronomical software in general in Section 5. The full paper, including the code to produce the figures, is available in a `GitHub` repository (Price-Whelan et al. 2018).[102]

This article is not intended as an introduction to `astropy`, nor does it replace the `astropy` documentation. Instead, it describes the way the Astropy community is organized and the current state of the `astropy` package.

2. Organization and Infrastructure

2.1. Coordination of Astropy

From its inception, Astropy has required coordination to ensure the project as a whole and its coding efforts are consistent and reasonably efficient. While many `Python` projects adopt a "Benevolent Dictator For Life" (BDFL) model, Astropy has instead opted for a *coordination committee*. This is partly due to the nature of the project as a large-scale collaboration between many contributors with many interests, and partly due to the sheer amount of work that needs to get done. For the latter reason, the project has expanded the committee from three to four members starting in 2016.

For resolving disagreements about the `astropy` core package or other Astropy-managed code, the coordination committee primarily acts to work toward consensus, or when consensus is difficult to achieve, generally acts as a "tie-breaker." The committee also oversees affiliated package applications to ensure that they are in keeping with Astropy's vision and philosophy,[103] as well as the associated procedures. Additionally, the committee oversees the assignment of roles (primarily driven by already-existing contributions), and increasingly has acted as the "face" of the Project, providing contact with organizations like NumFOCUS (the body that holds any potential funding in trust for Astropy) and the American Astronomical Society (AAS).

2.2. Astropy Development Model

Code is contributed to the `astropy` core package or modified through "pull requests" (via `GitHub`[104]) that often contain several `git` commits. Pull requests may fix bugs, implement new features, or improve or modify the infrastructure that supports the development and maintenance of the package. Individual pull requests are generally limited to a single conceptual addition or modification, to make code review tractable. Pull requests that modify or add code to a specific subpackage must be reviewed and approved by one of the subpackage maintainers before they are merged into the core codebase. Bugs and feature requests are reported via the `GitHub` issue tracker and labeled with a set of possible labels that help classify and organize the issues. The development workflow is detailed in the `astropy` documentation.[105]

As of version 2.0, `astropy` contains 212,244 lines of code[106] contributed by 232 unique contributors over 19,270 `git` commits. Figure 1, left, shows the distribution of total number of commits per contributor as of early 2018. The relative flatness of this distribution (as demonstrated by its log-log slope of -0.5) shows that the `astropy` core package has been developed by a broad contributor base. A leading group of six developers have each added over 1000 commits to the repository, and ∼20 more core contributors have contributed at least 100 commits. However, the distribution of contribution level (number of commits) continues from 100 down to a single commit. In this sense, the development of the core package has been a true community effort and is not dominated by a single individual. It is also important to note that the number of commits is only a rough metric of contribution, as any single commit could be a critical fix in the package or merely a fix for a typographical error. Figure 1, middle, shows the number of commits as a function of time since the genesis of the `astropy` core package. The package is still healthy: new commits are and have been contributed at a steady rate throughout its existence. Figure 1, right, shows that, ≈20–25 people contribute to the core package each month. While we would like for this number to grow, this demonstrates that the core package is still being developed and maintained by a substantial group of contributors.

2.3. APEs—Astropy Proposals for Enhancement

The Astropy project has a formal mechanism to propose significant changes to the core package (e.g., re-writing the

[102] Codebase: https://github.com/astropy/astropy-v2.0-paper.
[103] http://docs.astropy.org/en/stable/development/vision.html
[104] https://github.com/astropy/astropy/
[105] *How to make a code contribution*, http://docs.astropy.org/en/latest/development/workflow/development_workflow.html.
[106] This line count includes comments, as these are often as important for maintainability as the code itself. Without comments there are 142,197 lines of code.

coordinates subpackage; Tollerud et al. 2014), to plan out major new features (e.g., a new file format; Aldcroft 2015), or to institute new organization-wide policies (e.g., adopting a code of conduct; Cruz et al. 2015). This mechanism is called "Astropy Proposal for Enhancement" (APE) and is modeled after the "Python Enhancement Proposals" (PEP) that guide the development of the `Python` programming language. In an APE, one or more authors describe in detail the proposed changes or additions, including a rationale for the changes, how these changes will be implemented, and in the case of code, what the interface will be (Greenfield 2013). The APEs are discussed and refined by the community before much work is invested into a detailed implementation; anyone is welcome to contribute to these discussions during the open consideration period. APEs are proposed via pull requests on a dedicated GitHub repository[107]; therefore, anyone can read the proposed APEs and leave in-line comments. When a community consensus emerges, the APEs are accepted and become the basis for future work. In cases where consensus cannot be reached, the Astropy coordination committee may decide to close the discussion and make an executive decision based on the community input on the APE in question.

2.4. Concept of Affiliated Packages

A major part of the Astropy Project is the concept of "Affiliated Packages." An affiliated package is an astronomy-related `Python` package that is not part of the `astropy` core package, but has requested to be included as part of the Astropy Project's community. These packages support the goals and vision of Astropy of improving code re-use, interoperability, and embracing good coding practices such as testing and thorough documentation.

Affiliated packages contain functionality that is more specialized, have license incompatibilities, or have external dependencies (e.g., GUI libraries) that make these packages more suitable to be separate from the `astropy` core package. Affiliated packages may also be used to develop substantial new functionality that will eventually be incorporated into the `astropy` core package (e.g., astropy.visualization.wcsaxes). New functionality benefits from having a rapid development and release cycle that is not tied to that of the `astropy` core (Section 2.5). These projects may also have less stringent requirements for style, testing, or development as compared to the core package.

Affiliated packages are listed on the main Astropy website and advertised to the community through Astropy mailing lists; a list of current affiliated packages is included in Table 1. Becoming an affiliated package is a good way for new and existing packages to gain exposure while promoting Astropy's high standard for code and documentation quality. This process of listing and promoting affiliated packages is one way in which the Astropy Project tries to increase code re-use in the astronomical community.

Packages can become affiliated with Astropy by applying for this status on a public mailing list. The coordination committee (Section 2.1) reviews such requests and issues recommendations for the improvement of a package, where applicable.

[107] https://github.com/astropy/astropy-APEs

2.5. Release Cycle and Long-term Support

The `astropy` package has a regular release schedule consisting of new significant releases every six months, with bugfix releases as needed (Tollerud 2013). The major releases contain new features or any significant changes, whereas the bugfix releases only contain fixes to code or documentation but no new features. Some versions are additionally designated as "Long-term support" (LTS) releases, which continue to receive bug fixes for two years following the release with no changes to the API. The LTS versions are ideal for pipelines and other applications in which API stability is essential. The latest LTS release (version 2.0) is also the last one that supports `Python` 2; it will receive bug fixes until the end of 2019 (Robitaille 2017).

The version numbering of the `astropy` core package reflects this release scheme: the core package version number uses the form `x.y.z`, where "x" is advanced for LTS releases, "y" for non-LTS feature releases, and "z" for bugfix releases. This is similar to Semantic Versioning.[108]

The released versions of the `astropy` core package are available from several of the `Python` distributions for scientific computing (e.g., Anaconda) and from the `Python` Package Index (PyPI).[109] Effort has been made to make `astropy` available and easily installable across all platforms; the package is constantly tested on different platforms as part of a suite of continuous integration tests.

2.6. Support of Astropy

The Astropy Project, as of the version 2.0 release, does not receive any direct financial support for the development of `astropy`. Development of the software, all supporting materials, and community support are provided by individuals who work on the Astropy Project in their own personal time, by individuals or groups contributing to Astropy as part of a research project, or contributions from institutions that allocate people to work on Astropy. A list of organizations that have contributed to Astropy in this manner can be found in the Acknowledgments.

Different funding models have been proposed for support of Astropy (e.g., Muna et al. 2016), but a long-term plan for sustainability has not yet been established. The Astropy Project has the ability to accept financial contributions from institutions or individuals through the NumFOCUS[110] organization. NumFOCUS has, to date, covered the direct costs incurred by the Astropy Project.

2.7. Reuse of the Scientific Python Ecosystem

The Astropy Project is built on a philosophy of building from the existing Python scientific ecosystem wherever possible. Many of the enabling technologies like `numpy`, `scipy`, `matplotlib`, or `cython`, are necessary as the core underpinnings of Astropy packages. Often, this means using these packages as "building blocks" (e.g., the ubiquitous use of `numpy` arrays throughout `astropy`). In other cases, this means wrappers around more general algorithms that make them more convenient for astronomy use cases (e.g., the model-fitting in the `astropy.modeling` subpackage

[108] https://semver.org

[109] See the installation documentation for more information: http://docs.astropy.org/en/stable/install.html.

[110] NumFOCUS is a 501(c)(3) nonprofit that supports and promotes world-class, innovative, open-source scientific computing.

discussed in Section 3.7). Sometimes these simple wrappers evolve into more complex implementations that address astronomically relevant use cases the general tool does not support (e.g., `astropy.convolution`, see Section 3.8). As a broad rule, the Project explicitly encourages re-use of code where possible.

However, the boundaries of when this re-use is called for is often ambiguous. Some of the examples above only evolved after significant debate in the community over whether these algorithms were sufficient. Other times, even apparently general functionality did not exist in the wider ecosystem that met the Astropy community's needs, and hence the functionality had to be developed wholly from the developer resources available in the community (e.g., `astropy.units`, or `astropy.table` when it began). At the same time, however, the Astropy Project has provided the wider community with myriad bug fixes to the enabling technologies listed above, as well as the testing and documentation architecture. Functionality is only "extracted" from Astropy to other packages after careful consideration that includes considering the impact on the maintenance and support of Astropy.

3. Astropy Core Package Version 2.0

The Astropy Project aims to provide `Python`-based packages for all tasks that are commonly needed in a large subset of the astronomical community. At the foundation is the `astropy` core package, which provides general functionality (e.g., coordinate transformations, reading and writing astronomical files, and units) or base classes for other packages to utilize for a common interface (e.g., NDData). In this section, we highlight new features introduced or substantially improved since version 0.2 (previously described in Astropy Collaboration et al. 2013). The `astropy` package provides a full log of changes[111] over the course of the entire project and more details about individual subpackages are available in the documentation.[112] Beyond what is mentioned below, most subpackages have seen improved performance since the release of the version 0.2 package.

3.1. Units

The astropy.units subpackage adds support for representing units and numbers with associated units—"quantities"—in code. Historically, quantities in code have often been represented simply as numbers, with units implied or noted via comments in the code because of considerations about speed: having units associated with numbers inherently adds overhead to numerical operations. In astropy.units, Quantity objects extend `numpy` array objects and have been designed with speed in mind.

As of `astropy` version 2.0, units and quantities, prevalent in most of its subpackages, have become a key concept for using the package as a whole. Units are intimately entwined in the definition of astronomical coordinates; thus, nearly all functionality in the astropy.coordinates subpackage (see Section 3.3) depends on them. Most `astropy` subpackages have been made compatible with `Quantity` objects, although they are not always required.

[111] https://github.com/astropy/astropy/blob/stable/CHANGES.rst
[112] http://docs.astropy.org/en/stable/

The motivation and key concepts behind this subpackage were described in detail in the previous paper (Astropy Collaboration et al. 2013). Therefore, we primarily highlight new features and improvements here.

3.1.1. Interaction with `numpy` Arrays

Quantity objects extend `numpy.ndarray` objects and therefore work well with many of the functions in `numpy` that support array operations. For example, Quantity objects with angular units can be directly passed in to the trigonometric functions implemented in `numpy`. The units are internally converted to radians, which is what the `numpy` trigonometric functions expect, before being passed to `numpy`.

3.1.2. Logarithmic Units and Magnitudes

By default, taking the logarithm of a Quantity object with non-dimensionless units intentionally fails. However, some well-known units are actually logarithmic quantities, where the logarithm of the value is taken with respect to some reference value. Examples include astronomical magnitudes, which are logarithmic fluxes, and decibels, which are more generic logarithmic ratios of quantities. Logarithmic, relative units are now supported in astropy.units.

3.1.3. Defining Functions that Require Quantities

When writing code or functions that expect Quantity objects, we often want to enforce that the input units have the correct physical type. For example, we may want to require only length-type Quantity objects. astropy.units provides a tool called quantity_input() that can perform this verification automatically to avoid repetitive code.

3.2. Constants

The astropy.constants subpackage provides a selection of physical and astronomical constants as Quantity objects (see Section 3.1). A brief description of this package was given in Astropy Collaboration et al. (2013). In version 2.0, the built-in constants have been organized into modules for specific versions of the constant values. For example, physical constants have `codata2014` (Mohr et al. 2016) and `codata2010` versions. Astronomical constants are organized into `iau2015` and `iau2012` modules to indicate their sources (resolutions from the International Astronomical Union, IAU). The `codata2014` and `iau2015` versions are combined into the default constant value version: `astropyconst20`. For compatibility with `astropy` version 1.3, `astropyconst13` is available and provides access to the adopted versions of the constants from earlier versions of `astropy`. To use previous versions of the constants as *units* (e.g., solar masses), the values have to be imported directly; with version 2.0, astropy.units uses the `astropyconst20` versions.

Astronomers using astropy.constants should take particular note of the constants provided for Earth, Jupiter, and the Sun. Following IAU 2015 Resolution B3 (Mamajek et al. 2015), nominal values are now given for mass parameters and radii. The nominal values will not change even as "current best estimates" are updated.

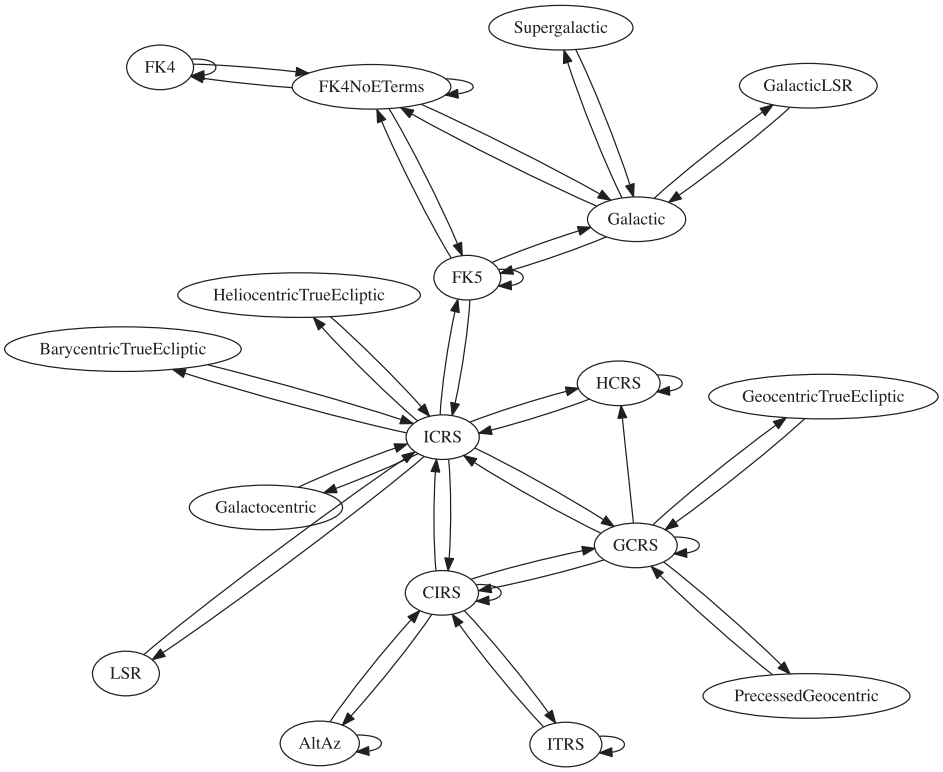


Figure 2. The full graph of possible reference frame transformations implemented in astropy.coordinates. Arrows indicate transformations from one frame to another. Arrows that point back to the same frame indicate self-transformations that involve a change of reference frame parameters (e.g., equinox).

3.3. Coordinates

The astropy.coordinates subpackage is designed to support representing and transforming celestial coordinates and—new in version 2.0—velocities. The framework heavily relies on the astropy.units subpackage, and most inputs to objects in this subpackage are expected to be Quantity objects. Some of the machinery also relies on the Essential Routines of Fundamental Astronomy (ERFA) `C` library for some of the critical underlying transformation machinery (Tollerud et al. 2017), which is based on the Standards Of Fundamental Astronomy (SOFA) effort (Hohenkerk 2011).

A key concept behind the design of this subpackage is that coordinate *representations* and *reference systems/frames* are independent of one another. For example, a set of coordinates in the International Celestial Reference System (ICRS) reference frame could be represented as spherical (right ascension, declination, and distance from solar system barycenter) or Cartesian coordinates (x, y, z with the origin at barycenter). They can therefore change representations independent of being transformed to other reference frames (e.g., the Galactic coordinate frame).

The classes that handle coordinate representations (the `Representation` classes) act like three-dimensional vectors and thus support vector arithmetic. The classes that represent reference systems and frames (the `Frame` classes) internally use `Representation` objects to store the coordinate data—that is, the `Frame` classes accept coordinate data, either as a specified `Representation` object, or using short-hand keyword arguments to specify the components of the coordinates. These preferred representation and short-hand component names differ between various astronomical reference systems. For example, in the ICRS frame, the spherical angles are right ascension (`ra`) and declination (`dec`), whereas in the Galactic frame, the spherical angles are Galactic longitude (`l`) and latitude (`b`). Each `Frame` class defines its own component names and preferred `Representation` class. The frame-specific component names map to corresponding components on the underlying `Representation` object that internally stores the coordinate data. For most frames, the preferred representation is spherical, although this is determined primarily by their common use in the astronomical community.

Many of the `Frame` classes also have attributes specific to the corresponding reference system that allow the user to specify the frame. For example, the Fifth Fundamental Catalogue (FK5) reference system requires specifying an equinox to determine the reference frame. If required, these additional frame attributes must be specified, along with the coordinate data, when a `Frame` object is created. Figure 2 shows the network of possible reference frame transformations as currently implemented in astropy.coordinates. Custom user-implemented `Frame` classes that define transformations to any reference frame in this graph can then be transformed to any of the other connected frames.

The typical user does not usually have to interact directly with the `Frame` or `Representation` classes. Instead, astropy.coordinates provides a high-level interface to representing astronomical coordinates through the SkyCoord class, which was designed to provide a single class that accepts a wide range of possible inputs. It supports coordinate data in any coordinate frame in any representation by internally using the `Frame` and `Representation` classes.

In what follows, we briefly highlight key new features in astropy.coordinates.

3.3.1. Local Earth Coordinate Frames

In addition to representing celestial coordinates, `astropy` now supports specifying positions on the Earth in a number of different geocentric systems with the `EarthLocation` class. With this, `astropy` now supports Earth-location-specific coordinate systems such as the altitude-azimuth (`AltAz`) or horizontal system. Transformations between `AltAz` and any Barycentric coordinate frame also requires specifying a time using the Time class from `astropy.time`. With this new functionality, many of the common tasks associated with observation planning can now be completed with `astropy` or the Astropy-affiliated package `astroplan` (Morris et al. 2018).

3.3.2. Proper Motion and Velocity Transformations

In addition to positional coordinate data, the `Frame` classes now also support velocity data. As the default representation for most frames is spherical, most of the `Frame` classes expect proper motion and radial velocity components to specify the velocity information. The names of the proper motion components all start with `pm` and adopt the same longitude and latitude names as the positional components. Transforming coordinates with velocity data is also supported, but in some cases the transformed velocity components have limited accuracy because the transformations are done numerically instead of analytically. The low-level interface for specifying and transforming velocity data is currently experimental. As such, in version 2.0, only the `Frame` classes (and not the SkyCoord class) support handling velocities.

3.3.3. Solar System Ephemerides

Also new is support for computing ephemerides of major solar system bodies and outputting the resulting positions as coordinate objects. These ephemerides can be computed either using analytic approximations from ERFA or from downloaded JPL ephemerides (the latter requires the `jplephem`[113] optional dependency and an internet connection).

3.3.4. Accuracy of Coordinate Transformations

In order to check the accuracy of the coordinate transformations in astropy.coordinates, we have created a set of benchmarks that we use to compare transformations between a set of coordinate frames for a number of packages.[114] Because no package can be guaranteed to implement all transformations to arbitrary precision and some transformations are sometimes subject to interpretation of standards (particularly in the case of Galactic coordinates), we do not designate any of the existing packages as the "ground truth" but instead compare each tool to all other tools. The benchmarks are thus useful beyond the Astropy Project because they allow all of the tools to be compared to all other tools. The tools included in the benchmark at the moment include the `astropy` core package, Kapteyn (Terlouw & Vogelaar 2015), NOVAS (Barron et al. 2011), PALpy (Jenness & Berry 2013), PyAST (a wrapper for AST, described in Berry et al. 2016), PyTPM,[115] PyEphem (Rhodes 2011), and pySLALIB (a Python wrapper for SLALIB, described in Wallace 1994).

[113] https://github.com/brandon-rhodes/python-jplephem
[114] http://www.astropy.org/coordinates-benchmark/summary.html
[115] https://github.com/phn/pytpm

The benchmarks are meant to evolve over time and include an increasing variety of cases. At the moment, the benchmarks are set up as follows—we have generated a standard set of 1000 pairs of random longitudes/latitudes that we use in all benchmarks. Each benchmark is then defined using an input and output coordinate frame, using all combinations of FK4, FK5, Galactic, ICRS, and Ecliptic frames. For now, we set the epoch of observation to J2000. We also set the frame to J2000 (for FK5 and Ecliptic) and B1950 (for FK4). In the future, we plan to include a larger variety of epochs and equinoxes, as well as tests of conversion to/from Altitude/Azimuth. For each benchmark, we convert the 1000 longitudes/latitudes from the input/output frame with all tools and quantify the comparison by looking at the median, mean, maximum, and standard deviation of the absolute separation of the output coordinates from each pair of tools.

Figure 3 visualizes the relative accuracy of the conversion from FK4 to Galactic coordinates for all pairs of tools that implement this transformation. In this figure, the color of the cell indicates the maximum difference (in arcseconds) between the two tools over the 1000 longitude-latitude pairs tested. This figure shows, for example, that `astropy`, Kapteyn, and PyTPM agree with sub-milliarcsecond differences (light colors, small differences), while PALpy, pySLALIB, and PyAST also agree among themselves. However, there is an offset of around $0\farcs2$ between the two groups. Finally, PyEphem disagrees with all other packages by $0\farcs4$–$0\farcs8$ (darker colors, large differences). These values are only meant to be illustrative and will change over time as the benchmarks are refined and the packages updated.

3.4. Time

The astropy.time subpackage focuses on supporting timescales (e.g., UTC, TAI, UT1) and time formats (e.g., Julian date, modified Julian date) that are commonly used in astronomy. This functionality is needed, for example, to calculate barycentric corrections or sidereal times. astropy.time is currently built on the ERFA (Tollerud et al. 2017) C library, which replicates the Standards of Fundamental Astronomy (SOFA; Hohenkerk 2011) but is licensed under a three-clause BSD license. The package was described in detail in Astropy Collaboration et al. (2013) and has remained stable for the last several versions of `astropy`. Thus, in what follows, we only highlight significant changes or new features since the previous Astropy paper.

3.4.1. Barycentric and Heliocentric Corrections

Detailed eclipse or transit timing requires accounting for light traveltime differences from the source to the observatory because of the Earth's motion. It is therefore common to instead convert times to the solar system barycenter or heliocenter where the relative timing of photons is standardized. With the location of a source on the sky (i.e., a SkyCoord object), the location of an observatory on Earth (i.e., an EarthLocation object), and time values as Time objects, the time corrections to shift to the solar system barycenter or heliocenter can now be computed with astropy.time using the `light_travel_time` method of a Time object.

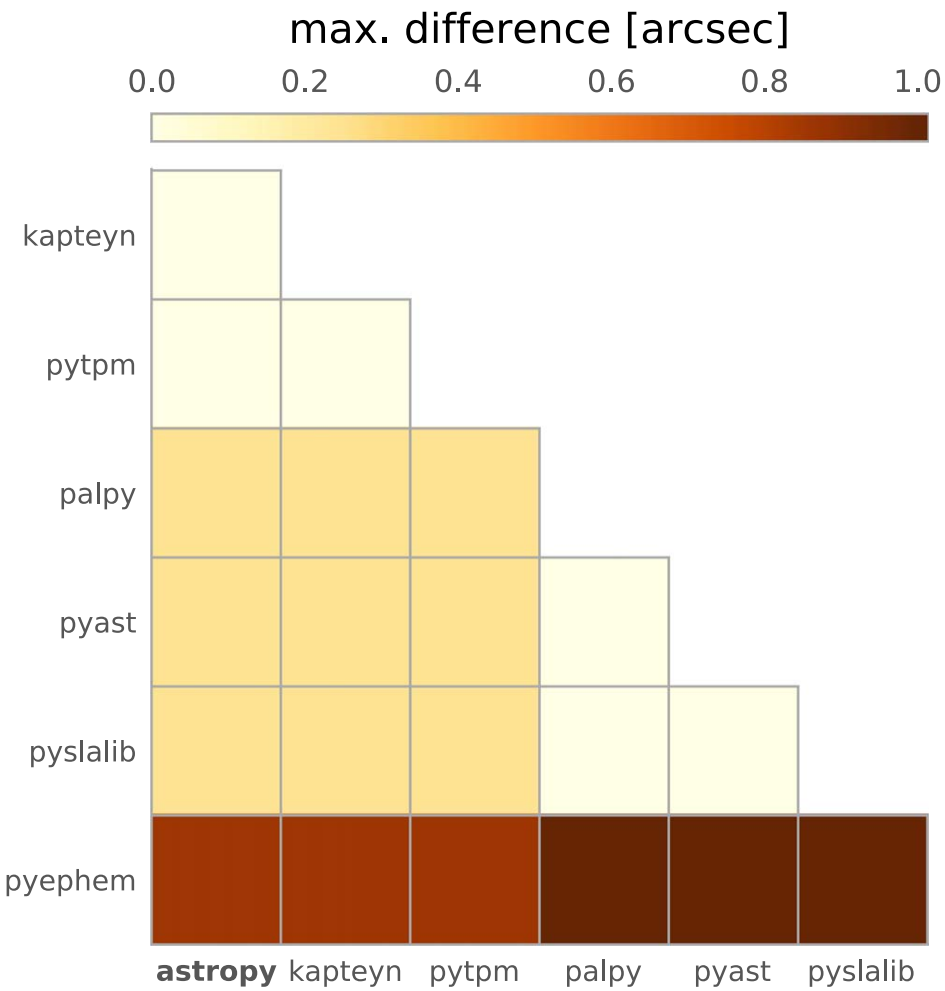


Figure 3. Comparison matrix of the maximum difference between longitude-latitude values in a set of 1000 random points transformed from FK4 to Galactic with the different packages. Darker colors (larger differences) are more significant disagreements.

3.5. Data Containers

3.5.1. `nddata`

The astropy.nddata subpackage provides three types of functionality: an abstract interface for representing generic arbitrary-dimensional data sets intended primarily for subclassing by developers of other packages, concrete classes building on this interface, and utilities for manipulating these kind of data sets.

The `NDDataBase` class provides the abstract interface for gridded data with attributes for accessing metadata, the world coordinate system (WCS), uncertainty arrays matched to the shape of the data, and other traits. Building on this interface, the `NDData` class provides a minimal working implementation for storing `numpy` arrays. These classes serve as useful base classes for package authors wishing to develop their own classes for specific use cases and as containers for exchanging gridded data.

The classes `NDDataRef`, `NDDataArray`, and `CCDData` extend the base storage functionality with options to do basic arithmetic (addition, subtraction, multiplication, and division), including error propagation in limited cases, and slicing of the data set based on grid coordinates that appropriately handles masking, errors, and units (if present). Additionally, the `CCDData` class also provides reading and writing from and to FITS files, and uses data structures from `astropy`, like `WCS`, to represent the file contents abstractly.

The http://docs.astropy.org/en/stable/nddata/utils.html `astropy.nddata.utils` module provides utilities that can operate on either plain `numpy` arrays or any of the classes in the astropy.nddata subpackage. It features a class for representing two-dimensional image cutouts, allowing one to easily link pixels in the cutout to those in the original image or vice versa, to convert between world and pixel coordinates in the cutout, and to overlay the cutout on images. Functions to enlarge or reduce an image by doing block replication or reduction are also provided.

3.5.2. Tables

The astropy.table subpackage provides functionality for representing and manipulating heterogeneous data. In some respects, this is similar to `numpy` record arrays (Van der Walt et al. 2011) or `pandas` `DataFrame` objects (McKinney 2010), but with modifications for astronomical data. Most notably, tables from astropy.table allow for table or column metadata and can handle vectors/arrays or arbitrary objects (with suitable column-like characteristics) as table entries. The subpackage was described in detail in Astropy Collaboration et al. (2013). Thus, in what follows, we only summarize key new features or updates to astropy.table since the previous Astropy paper. These are

support for grouped table operations, table concatenation, and using array-valued astropy objects as table columns.

A table can contain data that naturally form groups; for example, it may contain multiple observations of a few sources at different points in time and in different bands. We may want to split the table into groups based on the combination of source observed and the band, after which we combine the results for each combination of source and band in some way (e.g., finding the mean or standard deviation of the fluxes or magnitudes over time) or filter the groups based on user-defined criteria. These kinds of grouping and aggregation operations are now fully supported by Table objects.

Table objects can now be combined in several different ways. If two tables have the same columns, we may want to stack them "vertically" to create a new table with the same columns but all rows. If two tables are row-matched but have distinct columns, we may want to stack them "horizontally" to create a new table with the same rows but all columns. For other situations, more generic table concatenation or joining are also possible when two tables share some columns.

The Table object now allows array-valued Quantity, celestial coordinate (SkyCoord), and date/time (Time) objects to be used as columns. It also provides a general way for other user-defined array-like objects to be used as columns. This makes it possible, for instance, to easily represent catalogs of sources or time series in Astropy, while having both the benefits of the Table object (e.g., accessing specific rows/columns or groups of them and combining tables) as well as, for example, the SkyCoord or the Time classes (e.g., converting the coordinates to a different frame or accessing the date/time in the desired timescale).

Additionally, there is now interoperability between Table and pandas DataFrame objects using the Table.to_pandas() and Table.from_pandas() methods. Table.to_pandas() is, however, limited to a subset of possible Table objects, because several of the features outlined above cannot be represented as pandas data frames. While these features might be contributed to or combined with pandas at a later date, the architectural differences that enable these areas are significant, so this would be a major undertaking that would require substantial investment from the core maintainers and communities of both packages.

3.6. io

The astropy.io subpackages provide support for reading and writing data to a variety of ASCII and binary file formats, such as a wide range of ASCII data table formats, FITS, HDF5, and VOTable. It also provides a unified interface for reading and writing data with these different formats using the astropy.table subpackage. For many common cases, this simplifies the process of file input and output (I/O) and reduces the need to master the separate details of all the I/O packages within astropy. The file interface allows transparent compression of the gzip, bzip2, and lzma (.xz) formats; the latter two require the Python installation to have been compiled with support the respective libraries.

3.6.1. ASCII

One of the problems when storing a table in an ASCII format is preserving table metadata such as comments, keywords and column data types, units, and descriptions. The newly defined *Enhanced Character Separated Values* (ECSV, Aldcroft 2015) format makes it possible to write a table to an ASCII-format file and read it back with no loss of information. The ECSV format has been designed to be both human-readable and compatible with most simple CSV readers.

The astropy.io.ascii subpackage now includes a significantly faster Cython/C engine for reading and writing ASCII files. This is available for most of the common formats. It also offers some additional features like parsing of different exponential notation styles, such as commonly produced by Fortran programs. On average, the new engine is about four to five times faster than the corresponding pure-Python implementation and is often comparable to the speed of the pandas (McKinney 2010) ASCII file interface. The fast reader has a parallel processing option that allows harnessing multiple cores for input parsing to achieve even greater speed gains. By default, read() and write() will attempt to use the fast Cython/C engine when dealing with compatible formats. Certain features of the full read / write interface are unavailable in the fast version, in which case the reader will by default fall back automatically to the pure-Python version.

The astropy.io.ascii subpackage now provides the capability to read a table within an HTML file or web URL into an astropy Table object. A Table object can now also be written out as an HTML table.

3.6.2. FITS

The astropy.io.fits subpackage started as a direct port of the PyFITS project (Barrett & Bridgman 1999). Therefore, it is pretty stable, with mostly bug fixes but also a few new features and performance improvements. The API remains mostly compatible with PyFITS, which is now deprecated in favor of astropy.

Command-line scripts are now available for printing a summary of the HDUs in FITS file(s) (fitsinfo) and for printing the header information to the screen in a human-readable format (fitsheader).

FITS files are now loaded *lazily* by default, i.e., an object representing the list of HDUs is created but the data are not loaded into memory until requested. This approach should provide substantial speed-ups when using the convenience functions (e.g., getheader() or getdata()) to get an HDU that is near the beginning in a file with many HDUs.

3.6.3. HDF5

The astropy.io.misc.hdf5 subpackage provides support for binary read and write access to files in the *Hierarchical Data Format* (HDF5), if the h5py package is installed. Astropy table I/O is offered transparently through Table.read() and Table.write(), analogously to the other auto-detected formats. The keyword path='group/subgroup/data set' specifies the path to the data inside the file's hierarchical structure.

3.7. Modeling

The astropy.modeling subpackage provides a framework for representing analytical models and performing model evaluation and parameter fitting. The main motivation for this functionality was to create a framework that allows arbitrary combination of models to support the Generalized World Coordinate System (GWCS) package.[116] The current FITS

[116] https://github.com/spacetelescope/gwcs

WCS specification lacks the flexibility to represent arbitrary distortions and does not meet the needs of many types of current instrumentation. The fact that the `astropy` modeling framework now supports propagating units also makes it a useful tool for representing and fitting astrophysical models within data analysis tools.

Models and fitters are independent of each other: a model can be fit with different fitters and new fitters can be added without changing existing models. The framework is designed to be flexible and easily extensible. The goal is to have a rich set of models, but also facilitate creating new ones, if necessary.

3.7.1. Single Model Definition and Evaluation

Models are defined by their parameters and initialized by providing values for them. The names of the parameters are stored in a list, `Model.param_names`. Parameters are complex objects. They store additional information—default value, default unit, and parameter constraints. Parameter values and constraints can be updated by assignment. Supported constraints include `fixed` and `tied` parameters, as well as `bounds` on parameter values. The framework also supports models for which the number of parameters and their names are defined by another argument. A typical example is a polynomial model defined by its degree. A model is evaluated by calling it as a function.

If an analytical inverse of a model exists, it can be accessed by calling `Model.inverse`. In addition, `Model.inverse` can be assigned another model that represents a computed inverse.

Another useful settable property of models is `Model.bounding_box`. This attribute sets the domain over which the model is defined. This greatly improves the efficiency of evaluation when the input range is much larger than the characteristic width of the model itself.

3.7.2. Model Sets

Using astropy.modeling provides an efficient way to set up the same type of model with many different sets of parameter values. This creates a model set that can be efficiently evaluated. For example, in PSF (point-spread function) photometry, all objects in an image will have a PSF of the same functional form, but with different positions and amplitudes.

3.7.3. Compound Models

Models can be combined using arithmetic expressions. The result is also a model, which can further be combined with other models. Modeling supports arithmetic (+, −, *, /, and **), join (&), and composition (|) operators. The rules for combining models involve matching their inputs and outputs. For example, the composition operator, |, requires the number of outputs of the left model to be equal to the number of inputs of the right one. For the join operator, the total number of inputs must equal the sum of number of inputs of both the left and the right models. For all arithmetic operators, the left and the right models must have the same number of inputs and outputs. An example of a compound model could be a spectrum with interstellar absorption. The stellar spectrum and the interstellar extinction are represented by separate models, but the observed spectrum is fitted with a compound model that combines both.

3.7.4. Fitting Models to Data

The astropy.modeling subpackage also provides several fitters that are wrappers around some of the `numpy` and `scipy.optimize` functions and provide support for specifying parameter constraints. The fitters take a model and data as input and return a copy of the model with the optimized parameter values set. The goal is to make it easy to extend the fitting framework to create new fitters. The optimizers available in `astropy` version 2.0 are Levenberg–Marquardt (`scipy.optimize.leastsq`), Simplex (`scipy.optimize.fmin`), SLSQP (`scipy.optimize.slsqp`), and LinearLSQFitter (`numpy.linalg.lstsq` which provides exact solutions for linear models).

Modeling also supports a plugin system for fitters, which allows using the `astropy` models with external fitters. An example of this is `SABA`,[117] which is a bridge between Sherpa (Doe et al. 2007), and astropy.modeling, to bring the Sherpa fitters into `astropy`.

3.7.5. Creating New Models

If arithmetic combinations of existing models are not sufficient, new model classes can be defined in different ways. The astropy.modeling package provides tools to turn a simple function into a full-featured model, but it also allows extending the built-in model class with arbitrary code.

3.7.6. Unit Support

The astropy.modeling subpackage now supports the representation, evaluation, and fitting of models using Quantity objects, which attach units to scalar values or arrays of values. In practice, this means that one can, for example, fit a model to data with units and get parameters that also have units out, or initialize a model with parameters with units and evaluate it using input values with different but equivalent units. For example, the blackbody model (BlackBody1D) can be used to fit observed flux densities in a variety of units and as a function of different units of spectral coordinates (e.g., wavelength or frequency).

3.8. Convolution

The astropy.convolution subpackage implements *normalized convolution* (e.g., Knutsson & Westin 1993), an image reconstruction technique in which missing data are ignored during the convolution and replaced with values interpolated using the kernel. An example is given in Figure 4. In `astropy` versions $\leqslant$1.3, the direct convolution and Fast Fourier Transform (FFT) convolution approaches were inconsistent, with only the latter implementing normalized convolution. As of version 2.0, the two methods now agree and include a suite of consistency checks.

3.9. Visualization

The astropy.visualization subpackage provides functionality that can be helpful when visualizing data. This includes a framework (previously the standalone astropy.visualization.wcsaxes package) for plotting astronomical images with coordinates via `matplotlib`, functionality related to image normalization (including both scaling and stretching), smart

[117] https://github.com/astropy/saba

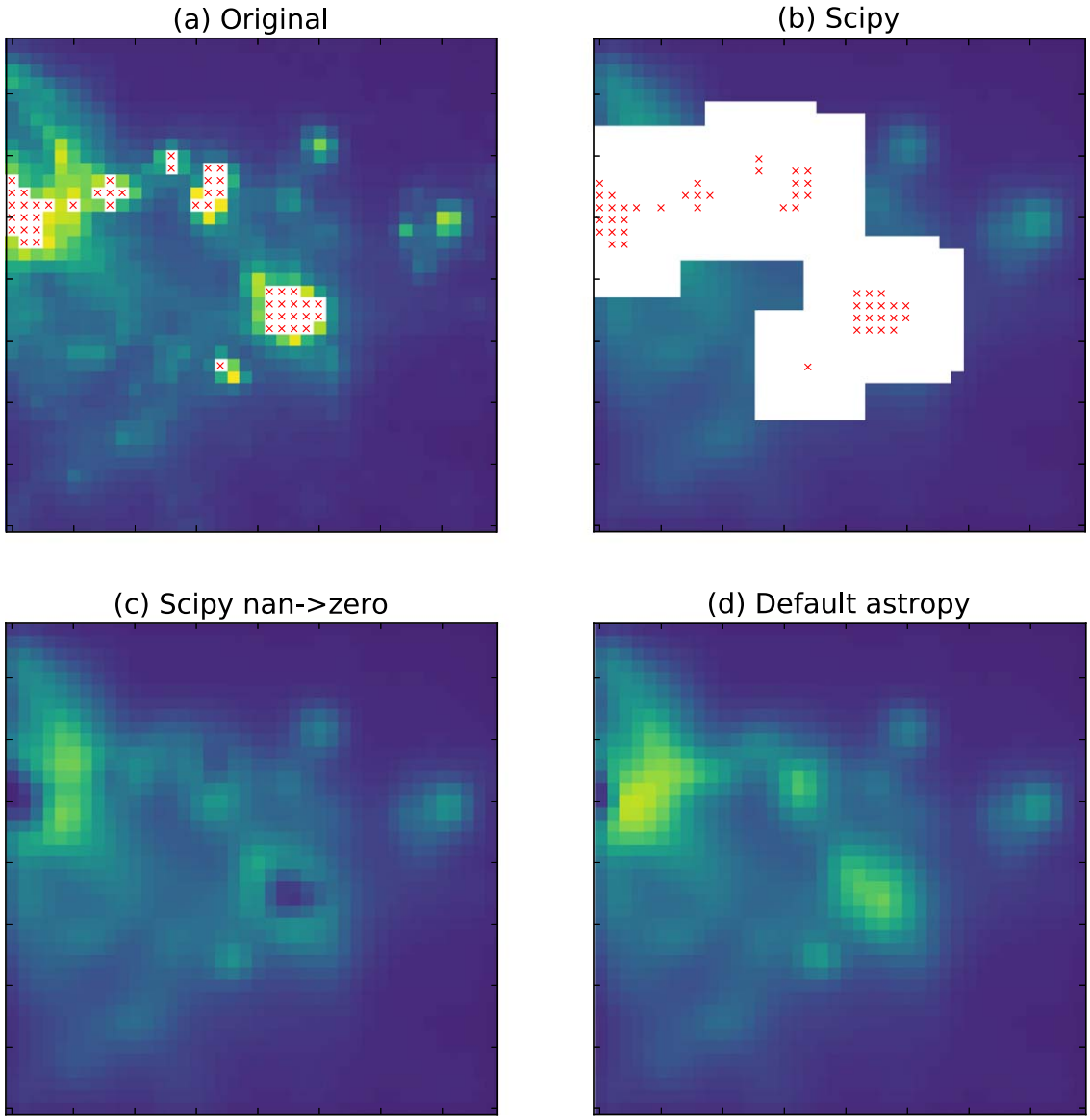


Figure 4. An example showing different modes of convolution available in the `Python` ecosystem. Each red x signifies a pixel that is set to `NaN` in the original data (top left). If the data are convolved with a Gaussian kernel on a 9×9 grid using `scipy`'s direct convolution (top right), any pixel within range of the original `NaN` pixels is also set to `NaN`. The bottom left panel shows what happens if the `NaN`s are set to zero first: the original `NaN` regions are depressed relative to their surroundings. Finally, the bottom right panel shows `astropy`'s convolution behavior, where the missing pixels are replaced with values interpolated from their surroundings using the convolution kernel.

histogram plotting, red-green-blue (RGB) color image creation from separate images, and custom plotting styles for `matplotlib`.

3.9.1. Image Stretching and Normalization

Using astropy.visualization provides a framework for transforming values in images (and more generally, any arrays), typically for the purpose of visualization. The two main types of transformations are normalization and stretching of image values.

Normalization transforms the image values to the range [0, 1] using lower and upper limits ($v_{\rm min}$, $v_{\rm max}$),

$$y = \frac{x - v_{\rm min}}{v_{\rm max} - v_{\rm min}}, \quad (1)$$

where x represents the values in the original image.

Stretching transforms the image values in the range [0, 1] again to the range [0, 1], using a linear or nonlinear function:

$$z = f(y). \quad (2)$$

Several classes are provided for automatically determining intervals (e.g., using image percentiles) and for normalizing values in this interval to the [0, 1] range.

`Using matplotlib` allows a custom normalization and stretch to be used when displaying data by passing in a normalization object. The astropy.visualization package also provides a normalization class that wraps the interval and stretches objects into a normalization object that `matplotlib` understands.

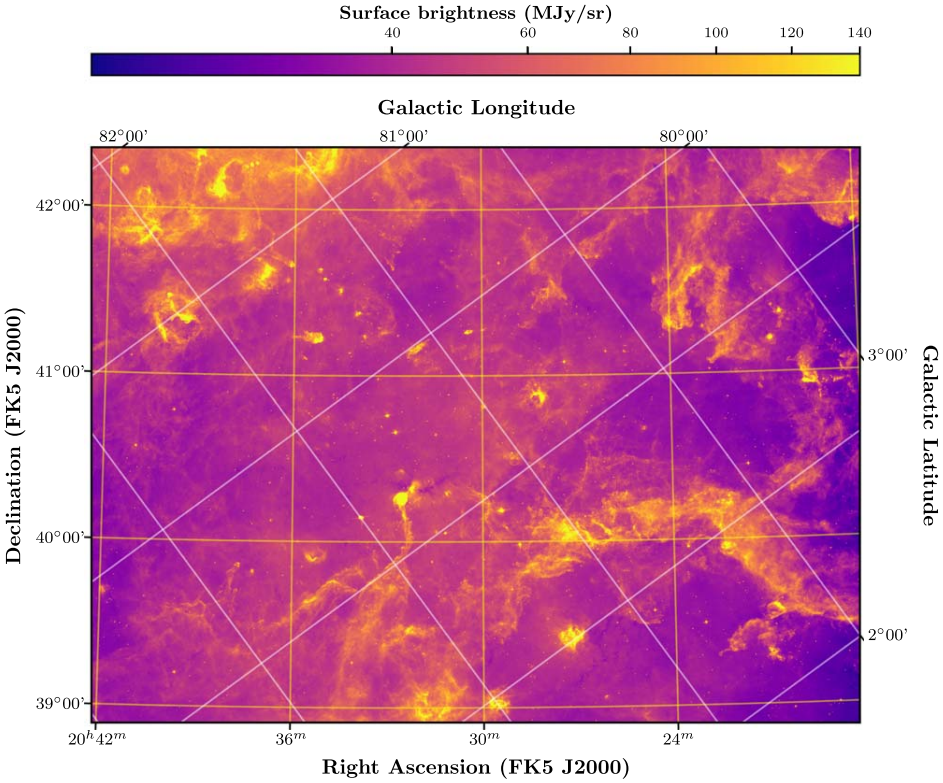


Figure 5. An example of a figure made using the astropy.visualization.wcsaxes subpackage, using *Spitzer*/IRAC 8.0 μm data from the Cygnus-X *Spitzer* Legacy survey (Beerer et al. 2010).

3.9.2. Plotting Image Data with World Coordinates

Astronomers dealing with observational imaging commonly need to make figures with images that include the correct coordinates and optionally display a coordinate grid. The challenge, however, is that the conceptual coordinate axes (such as longitude/latitude) need not be lined up with the pixel axes of the image. The astropy.visualization.wcsaxes subpackage implements a generalized way of making figures from an image array and a WCS object that provides the transformation between pixel and world coordinates.

World coordinates can be, for example, right ascension and declination, but can also include, for example, velocity, wavelength, frequency, or time. The main features from this subpackage include the ability to control which axes to show which coordinate on (e.g., showing longitude ticks on the top and bottom axes and latitude on the left and right axes), controlling the spacing of the ticks either by specifying the positions to use or providing a tick spacing or an average number of ticks that should be present on each axis, setting the format for the tick labels to ones commonly used by astronomers, controlling the visibility of the grid/graticule, and overlaying ticks, labels, and/or grid lines from different coordinate systems. In addition, it is possible to pass data with more than two dimensions and slice on-the-fly. Last but not least, it is also able to define non-rectangular frames such as, for example, Aitoff projections.

This subpackage differs from `APLpy` (Robitaille & Bressert 2012), in that the latter focuses on providing a very high-level interface to plotting that requires very few lines of code to get a good result, whereas astropy.visualization.wcsaxes defines an interface that is much closer to that of `matplotlib` (Hunter 2007). This enables significantly more advanced visualizations.

An example of a visualization made with astropy.visualization.wcsaxes is shown in Figure 5. This example illustrates the ability to overlay multiple coordinate systems and customize which ticks/labels are shown on which axes around the image. This also uses the image stretching functionality from Section 3.9.1 to show the image in a square-root stretch (automatically updating the tick positions in the colorbar).

3.9.3. Choosing Histogram Bins

The astropy.visualization subpackage also provides a histogram function, which is a generalization of `matplotlib`'s histogram function, to allow for a more flexible specification of histogram bins. The function provides several methods of automatically tuning the histogram bin size. It has a syntax identical to `matplotlib`'s histogram function, with the exception of the `bins` parameter, which allows specification of one of four different methods for automatic bin selection: "blocks," "knuth," "scott," or "freedman."

3.9.4. Creating Color RGB Images

Lupton et al. (2004) describe an "optimal" algorithm for producing RGB composite images from three separate high-dynamic range arrays. The astropy.visualization subpackage provides a convenience function to create such a color image. It also includes an associated set of classes to provide alternate scalings. This functionality was contributed by developers from the Large Synoptic Survey Telescope (LSST) and serves as an

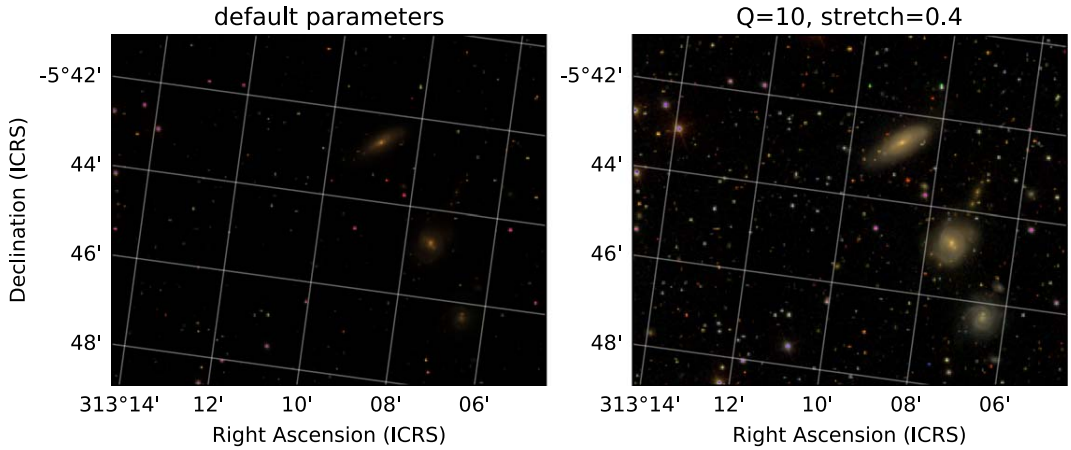


Figure 6. An RGB color image of the region near the Hickson 88 group constructed from SDSS images and the astropy.visualization tools. This example uses astropy.visualization.wcsaxes to display the sky coordinate grid, and the http://docs.astropy.org/en/stable/api/astropy.visualization.make_lupton_rgb.html `make_lupton_rgb()` function to produce the RGB image from three SDSS filter images (*g*, *r*, *i*). The image on the left shows the image with the default parameters, whereas the image on the right has parameters set to show a greater dynamical range.

example of a contribution to Astropy from a more traditional engineering organization (Jenness et al. 2016).

The Sloan Digital Sky Survey (SDSS) SkyServer color images were made using a variation on this technique. As an example, in Figure 6, we show an RGB color image of the Hickson 88 group, centered near NGC 6977.[118] This image was generated from SDSS images using the astropy.visualization tools.

3.10. Cosmology

The astropy.cosmology subpackage contains classes for representing different cosmologies and functions for calculating commonly used quantities such as look-back time and distance. The subpackage was described in detail in Astropy Collaboration et al. (2013). The default cosmology in `astropy` version 2.0 is given by the values in Planck Collaboration et al. (2016).

3.11. Statistics

The astropy.stats package provides statistical tools that are useful for astronomy and are either not found in or extend the available functionality of other `Python` statistics packages, such as `scipy` (Jones et al. 2001) or `statsmodels` (Seabold & Perktold 2010). The astropy.stats package also contains a range of functionality used by many different disciplines in astronomy. It is not a complete set of statistical tools, but rather a still growing collection of useful features.

3.11.1. Robust Statistical Estimators

Robust statistics provide reliable estimates of basic statistics for complex distributions that largely mitigate the effects of outliers. The astropy.stats package includes several robust statistical functions that are commonly used in astronomy, such as sigma clipping methods for rejecting outliers, median absolute deviation functions, and biweight estimators, which have been used to calculate the velocity dispersion of galaxy clusters (Beers et al. 1990).

[118] http://skyserver.sdss.org/dr13/en/tools/chart/navi.aspx?ra=313.12381&dec=-5.74611

3.11.2. Circular Statistics

Astronomers often need to compute statistics of quantities evaluated on a circle, such as sky direction or polarization angle. A set of circular statistical estimators based on Jammalamadaka & Sengupta (2001) are implemented in astropy.stats. These functions provide measurements of the circular mean, variance, and moment. All of these functions work with both `numpy.ndarrays` (assumed to be in radians) and Quantity objects. In addition, the subpackage includes tests for Rayleigh Test, `vtest`, and a function to compute the maximum likelihood estimator for the parameters of the von Mises distribution.

3.11.3. Lomb–Scargle Periodograms

Periodic analysis of unevenly spaced time series is common across many subfields of astronomy. The astropy.stats package now includes several efficient implementations of the Lomb–Scargle periodogram (Lomb 1976; Scargle 1982) and several generalizations, including floating mean models (Zechmeister & Kürster 2009), truncated Fourier models (Bretthorst 2003), and appropriate handling of heteroscedastic uncertainties. Importantly, the implementations make use of several fast and scalable computational approaches (e.g., Press & Rybicki 1989; Palmer 2009), and thus can be applied to much larger data sets than Lomb–Scargle algorithms available in, e.g., `scipy.stats` (Jones et al. 2001). Much of the Lomb–Scargle code in `astropy` has been adapted from previously published open-source code (VanderPlas et al. 2012; VanderPlas & Ivezic 2015). Users should be aware that correct interpretation of periodogram results involves some subtleties; for a thorough discussion of this issue, see (VanderPlas 2018, in press).

3.11.4. Bayesian Blocks and Histogram Binning

The astropy.stats package also includes an implementation of *Bayesian Blocks* (Scargle et al. 2013), an algorithm for analysis of breakpoints in nonperiodic astronomical time-series. One interesting application of Bayesian Blocks is its use in determining optimal histogram binnings, particularly binnings with unequal bin sizes. This code was adapted, with several improvements, from the `astroML` package (VanderPlas et al. 2012). An

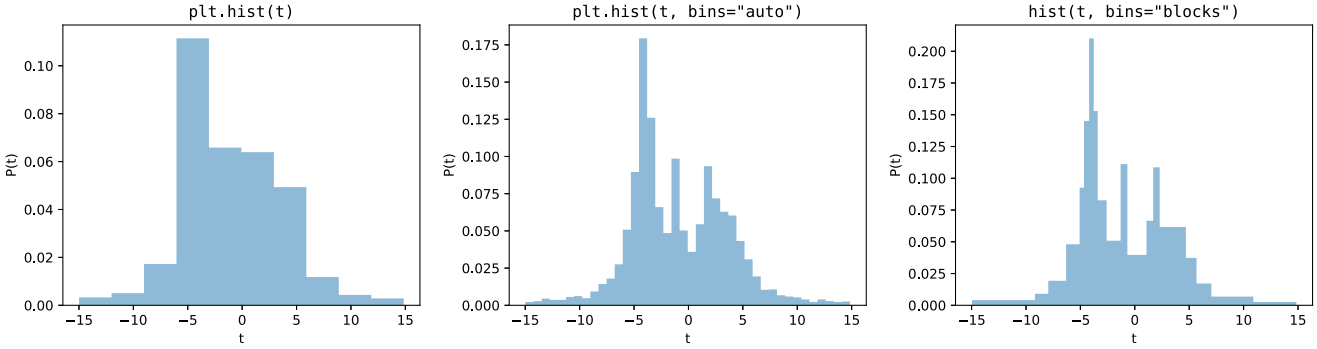


Figure 7. Three approaches to a 1D histogram. Left: a standard histogram using `matplotlib`'s default of 10 bins. Center: a histogram with the number of equal-width bins determined automatically using `numpy`'s `bins = 'auto'`. Right: a histogram created by `astropy`, with irregularly spaced bins computed via the Bayesian Blocks algorithm. Compared to regularly spaced bins, the irregular bin widths give a more accurate visual representation of features in the data set at various scales.

example of a histogram fit using the Bayesian Blocks algorithm is shown in the right panel of Figure 7.

4. Infrastructure for Astropy Affiliated Packages

In addition to astronomy-specific packages and libraries, the Astropy Project also maintains and distributes several general-purpose infrastructure packages that assist with the maintenance and upkeep of the `astropy` core package and other affiliated packages. The following sections describe the most widely used infrastructure packages developed by the Astropy Project.

4.1. Package Template

Astropy provides a package template—as a separate `GitHub` repository, `astropy/package-template`[119]—that aims to simplify setting up packaging, testing, and documentation builds for developers of affiliated packages or `astropy`-dependent packages. Any `Python` package can make use of this ready-to-go package layout, setup, installation, and `Sphinx` documentation build infrastructure that was originally developed for the `astropy` core package and affiliated packages maintained by the Astropy Project. The package template also provides a testing framework, template configurations for continuous integration services, and `Cython` build support.

4.2. Continuous Integration Helpers

Astropy also provides a set of scripts for setting up and configuring continuous integration (CI) services as a `GitHub` repository, `astropy/ci-helpers`.[120] These tools aim to enable package maintainers to control their testing setup and installation process for various CI services through a set of environment variables. While the current development is mostly driven by the needs of the Astropy ecosystem, the actual usage of this package is extremely widespread.[121] The current tools support configuration for Travis CI[122] and Appveyor CI.[123]

[119] https://github.com/astropy/package-template/
[120] https://github.com/astropy/ci-helpers
[121] Approximately 30% of the ci-helpers contributors come from outside the astropy community, and there are currently 292 repositories on github that have ci-helpers in their travis configuration file.
[122] https://travis-ci.org/
[123] https://www.appveyor.com/

4.3. Sphinx Extensions

The documentation for many `Python` packages, including all the packages in the Astropy ecosystem, is written using the `Sphinx` documentation build system. `Sphinx` supports writing documentation using plain text files that follow a markup language called `reStructuredText` (RST). These files are then transformed into HTML, PDF, or LATEX documents during the documentation build process. For the Astropy Project, we have developed several `Sphinx` extensions that facilitate automatically generating API documentation for large projects, like the `astropy` core package. The main extension we have developed is `sphinx-automodapi`,[124] which provides a convenient single RST command to generate a set of documentation pages, listing all of the available classes, functions, and attributes in a given `Python` module.

5. The Future of the Astropy Project

Following the release of version 2.0, development on the next major version of the `astropy` core package (version 3.0) began. On top of planned changes and additions to the core package, we also plan to overhaul the Astropy educational/learning materials and further generalize the infrastructure utilities originally developed for the core package for the benefit of the community.

5.1. Future Versions of the Astropy Core and Affiliated Packages

One of the most significant changes coming in this next major release will be removing the support for `Python` 2 (Robitaille 2017): future versions of `astropy` will only support `Python` 3.5 or higher. Removing `Python` 2 support will allow the use of new features exclusive to `Python` 3, simplify the code base, and reduce the testing overhead for the package. Version 3.0 was released in February 2018.

In the next major release after version 3.0, scheduled for mid-2018, the focus will be on algorithm optimization and documentation improvement. To prepare for this release, we are subjecting the core package to testing, evaluation, and performance monitoring. As a result, less new functionality may be introduced, as a trade-off for better performance.

Beyond the core code, the Astropy Project is also further developing the Astropy-managed affiliated packages. While these may not be integrated into the `astropy` core package,

[124] http://sphinx-automodapi.readthedocs.io

these projects provide code that is useful to the astronomical community and meet the testing and documentation standards of Astropy. Some of these new efforts include an initiative to develop tools for spectroscopy (Crawford et al. 2017, `specutils`, `specreduc`, `specviz`), integration of LSST software, and support for HEALPIX projection.

5.2. Learn Astropy

The documentation of the `astropy` core package contains narrative descriptions of the package's functionality, along with detailed usage notes for functions, classes, and modules. While useful as a reference for more experienced `Python` users, it is not the proper point of entry for other users or learning environments. In the near future, we will launch a new resource for learning to use both the `astropy` core package and the many packages in the broader Astropy ecosystem, under the name *Learn Astropy*.

The new *Learn Astropy* site will present several different ways to engage with the Astropy ecosystem:

Documentation: The `astropy` and affiliated package documentation contains the complete description of a package with all requisite details, including usage, dependencies, and examples. The pages will largely remain as-is, but will be focused toward more intermediate users and as a reference resource.

Examples: These are stand-alone code snippets that live in the `astropy` documentation that demonstrate a specific functionality within a subpackage. The `astropy` core package documentation will then gain a new "index of examples" that links to all of the code or demonstrative examples within any documentation page.

Tutorials: The Astropy tutorials are step-by-step demonstrations of common tasks that incorporate several packages or subpackages. Tutorials are more extended and comprehensive than examples, may contain exercises for the users, and are generally geared towards workshops or teaching. Several tutorials already exist[125] and are being actively expanded.

Guides: These are long-form narrative, comprehensive, and conceptually focused documents (roughly one book chapter in length), providing stand-alone introductions to core packages in addition to the underlying astronomical concepts. These are less specific and more conceptual than tutorials: for example, "using `astropy` and `ccdproc` to reduce imaging data."

We encourage any users who wish to see specific material to either contribute or comment on these efforts via the Astropy mailing list or `astropy/astropy-tutorials` GitHub repository.[126]

6. Conclusion

The `astropy` package is improving in stability, breadth, and reliability while the the Astropy project is still significantly growing. As the `astropy` core package becomes more mature, several subpackages have reached stability with a rich set of features that help astronomers worldwide to perform many daily tasks, such as planning observations, analyzing data or simulation results, and writing publications. The strong emphasis that the Astropy Project puts on reliability and high coding standards helps users to trust the calculations performed with `astropy` and to publish reproducible results. At the same time, the Astropy ecosystem and core package are both growing: new functionality is still being contributed and new affiliated packages are being developed to support more specialized needs.

The Astropy Project is also spreading awareness of best practices in community-driven software development. This is important because most practicing astronomers were not explicitly taught computer science and software development, despite the fact that a substantial fraction of many astronomers' workload today is related to software use and development. The `astropy` package leads by example, showing all interested astronomers how modern tools like `git` version control or CI testing can increase the quality, accessibility, and discoverability of astronomical software without overly complicating the development cycle. Within Astropy, all submitted code is reviewed by at least one (but typically more than one) member of the Astropy community. Reviewers provide feedback to contributors, which helps to improve contributors' software development skills. As a community, Astropy follows an explicit code of conduct (Cruz et al. 2015) and treats all contributors and users with respect, provides a harassment-free environment, and encourages and welcomes new contributions from all. Thus, while the Astropy Project provides and develops software and tools essential to modern astronomical research, it also helps to prepare the current and next generation of researchers with the knowledge to adequately use, develop, and contribute to those tools within a conscientious and welcoming community.

We thank the referee for an insightful report that improved the paper. We would like to thank the members of the community who have contributed to Astropy, who have opened issues and provided feedback, and who have supported the project in a number of different ways. We would like to acknowledge Alex Conley and Neil Crighton for maintaining the astropy.cosmology subpackage.

The Astropy community is supported by and makes use of a number of organizations and services outside the traditional academic community. We thank Google for financing and organizing the Google Summer of Code (GSoC) program, that has funded several students per year to work on Astropy related projects over the summer. These students often turn into long-term contributors. We also thank NumFOCUS and the Python Software Foundation for financial support. Within the academic community, we thank institutions that make it possible for astronomers and other developers on their staff to contribute their time to the development of Astropy projects. We acknowledge the support of the Space Telescope Science Institute, Harvard–Smithsonian Center for Astrophysics, and the South African Astronomical Observatory.

The following individuals would like to recognize support for their personal contributions. H.M.G. was supported by the National Aeronautics and Space Administration through the Smithsonian Astrophysical Observatory contract SV3-73016 to MIT for Support of the *Chandra* X-Ray Center, which is operated by the Smithsonian Astrophysical Observatory for and on behalf of the National Aeronautics Space Administration under contract NAS8-03060. J.T.V. was supported by the UW eScience Institute via grants from the Moore Foundation, the Sloan Foundation, and the Washington Research Foundation. S.M.C. acknowledges the National Research Foundation of South Africa. M.V.B. was supported by NASA's Planetary

[125] http://tutorials.astropy.org/

[126] https://github.com/astropy/astropy-tutorials

Astronomy Program. T.L.A. was supported by NASA contract NAS8-03060. Support for E.J.T. was provided by NASA through Hubble Fellowship grant No. 51316.01 awarded by the Space Telescope Science Institute, which is operated by the Association of Universities for Research in Astronomy, Inc., for NASA, under contract NAS 5-26555, as well as a Giacconi Fellowship. M.B. was supported by the FONDECYT regular project 1170618 and the MINEDUC-UA projects codes ANT 1655 and ANT 1656. D.H. was supported through the SFB 881 "The Milky Way System" by the German Research Foundation (DFG). W.E.K was supported by an ESO Fellowship. C.M. is supported by NSF grant AST-1313484. S.P. was supported by grant AYA2016-75808-R (FEDER) issued by the Spanish government. J.E.H.T. was supported by the Gemini Observatory, which is operated by the Association of Universities for Research in Astronomy, Inc., on behalf of the international Gemini partnership of Argentina, Brazil, Canada, Chile, and the United States of America. Y.P.B was supported by the Korea Astronomy and Space Science Institute, under the R&D program supervised by the Ministry of Science, ICT, and Future Planning.

Furthermore, the astropy packages would not exist in their current form without a number of web services for code hosting, continuous integration, and documentation; in particular, astropy heavily relies on GitHub, Travis CI, Appveyor, CircleCI, and Read the Docs.

`Astropy` interfaces with the SIMBAD database, operated at CDS, Strasbourg, France. It also makes use of the ERFA library (Tollerud et al. 2017), which in turn derives from the IAU SOFA Collection[127] developed by the International Astronomical Union Standards of Fundamental Astronomy (Hohenkerk 2011).

Software: `astropy` (Astropy Collaboration et al. 2013), `numpy` (Van der Walt et al. 2011), `scipy` (Jones et al. 2001), `matplotlib` (Hunter 2007), `Cython` (Behnel et al. 2011), `SOFA` (Hohenkerk 2011), `ERFA` (Tollerud et al. 2017).

Appendix
List of Affiliated Packages

The Appendix comprises Table 1.

Table 1
Registry of Affiliated Packages

Package Name	Stable	PyPI Name	Maintainer	Citation
APLpy	Yes	APLpy	Thomas Robitaille and Eli Bressert	Robitaille & Bressert (2012)
Astro-SCRAPPY	Yes	astroscrappy	Curtis McCully	van Dokkum (2001)
astroML	Yes	astroML	Jake Vanderplas	Vanderplas et al. (2012), Ivezić et al. (2014)
astroplan	No	astroplan	Brett Morris	Morris et al. (2018)
astroquery	Yes	astroquery	Adam Ginsburg and Brigitta Sipocz	Ginsburg et al. (2017b)
ccdproc	Yes	ccdproc	Steven Crawford, Matt Craig, and Michael Seifert	Craig et al. (2015)
cluster-lensing	No	cluster-lensing	Jes Ford	Ford (2016)
gala	Yes	astro-gala	Adrian Price-Whelan	Price-Whelan (2017)
galpy	Yes	galpy	Jo Bovy	Bovy (2015)
gammapy	No	gammapy	Christoph Deil	Deil et al. (2017)
ginga	Yes	ginga	Eric Jeschke and Pey-Lian Lim	ejeschke et al. (2017)
Glue	Yes	glueviz	Chris Beaumont and Thomas Robitaille	Beaumont et al. (2014)
gwcs	No	gwcs	Nadia Dencheva	Dencheva et al. (2017)
Halotools	Yes	halotools	Andrew Hearin	Hearin et al. (2017)
HENDRICS	Yes	hendrics	Matteo Bachetti	Bachetti (2015)
hips	No	hips	Christoph Deil and Thomas Boch	hips developers (2018)
imexam	No	imexam	Megan Sosey	Sosey (2017)
linetools	Yes	linetools	J. Xavier Prochaska, Nicolas Tejos, and Neil Crighton	Prochaska et al. (2017)
marxs	Yes	marxs	Hans Moritz Günther	Günther et al. (2017)
naima	Yes	naima	Victor Zabalza	Zabalza (2015)
omnifit	Yes	omnifit	Aleksi Suutarinen	Suutarinen (2015)
photutils	No	photutils	Larry Bradley and Brigitta Sipocz	Bradley et al. (2017)
poliastro	No	poliastro	Juan Luis Cano Rodríguez	Rodríguez et al. (2017)
PyDL	No	pydl	Benjamin Alan Weaver	Weaver et al. (2017)
pyregion	Yes	pyregion	Jae-Joon Lee and Christoph Deil	pyregions developers (2018)
pyspeckit	Yes	pyspeckit	Adam Ginsburg	Ginsburg & Mirocha (2011)
python-cpl	No	python-cpl	Ole Streicher	Streicher & Weilbacher (2012)
PyVO	No	pyvo	Stefan Becker	Graham et al. (2014)
regions	No	regions	Christoph Deil and Johannes King	pyregions developers (2018)
reproject	Yes	reproject	Thomas Robitaille	Robitaille (2018)
sncosmo	Yes	sncosmo	Kyle Barbary	Barbary (2014)
spectral-cube	Yes	spectral-cube	Adam Ginsburg	Ginsburg et al. (2017a)
specutils	No	specutils	Nicholas Earl, Adam Ginsburg, Steve Crawford, and Erik Tollerud	specutils developers (2018)
spherical_geometry	No	spherical-geometry	Bernie Simon	
stingray	No	stingray	Daniela Huppenkothen, Matteo Bachetti, Abigail Stevens, Simone Migliari, and Paul Balm	Huppenkothen et al. (2016)
synphot	Yes	synphot	Pey Lian Lim	Lim (2016)

[127] http://www.iausofa.org

ORCID iDs

A. M. Price-Whelan https://orcid.org/0000-0003-0872-7098
S. M. Crawford https://orcid.org/0000-0002-8969-5229
A. Ginsburg https://orcid.org/0000-0001-6431-9633
J. T. VanderPlas https://orcid.org/0000-0002-9623-3401
L. D. Bradley https://orcid.org/0000-0002-7908-9284
M. de Val-Borro https://orcid.org/0000-0002-0455-9384
K. L. Cruz https://orcid.org/0000-0002-1821-0650
T. P. Robitaille https://orcid.org/0000-0002-8642-1329
E. J. Tollerud https://orcid.org/0000-0002-9599-310X
M. Bachetti https://orcid.org/0000-0002-4576-9337
P. Barmby https://orcid.org/0000-0003-2767-0090
G. B. Brammer https://orcid.org/0000-0003-2680-005X
L. H. Garrison https://orcid.org/0000-0002-9853-5673
D. Homeier https://orcid.org/0000-0002-8546-9128
G. Hosseinzadeh https://orcid.org/0000-0002-0832-2974
T. Jenness https://orcid.org/0000-0001-5982-167X
S. Kendrew https://orcid.org/0000-0002-7612-0469
N. S. Kern https://orcid.org/0000-0002-8211-1892
C. McCully https://orcid.org/0000-0001-5807-7893
B. M. Morris https://orcid.org/0000-0003-2528-3409
S. Pascual https://orcid.org/0000-0002-9351-6051
A. L. Plunkett https://orcid.org/0000-0002-9912-5705
J. X. Prochaska https://orcid.org/0000-0002-7738-6875
L. P. Singer https://orcid.org/0000-0001-9898-5597
P. Teuben https://orcid.org/0000-0003-1774-3436
G. R. Tremblay https://orcid.org/0000-0002-5445-5401
A. de la Vega https://orcid.org/0000-0002-6219-5558
L. L. Watkins https://orcid.org/0000-0002-1343-134X
J. Woillez https://orcid.org/0000-0002-2958-4738

References

Aldcroft, T. 2015, Astropy Proposal for Enhancement 6: Enhanced Character Separated Values table format (APE 6), Zenodo, doi:10.5281/zenodo.1043901
Astropy Collaboration, Robitaille, T. P., Tollerud, E. J., et al. 2013, A&A, 558, A33
Bachetti, M. 2015, MaLTPyNT: Quick look timing analysis for NuSTAR data, Astrophysics Source Code Library, ascl:1502.021
Banse, K., Ponz, D., Ounnas, C., Grosbol, P., & Warmels, R. 1988, in Instrumentation for Ground-Based Optical Astronomy, ed. L. B. Robinson (New York: Springer-Verlag), 431
Barbary, K. 2014, sncosmo v0.4.2, Zenodo, doi:10.5281/zenodo.11938
Barrett, P. E., & Bridgman, W. T. 1999, in ASP Conf. Ser. 172, Astronomical Data Analysis Software and Systems VIII, ed. D. M. Mehringer, R. L. Plante, & D. A. Roberts (San Francisco, CA: ASP), 483
Barron, E. G., Kaplan, G. H., Bangert, J., et al. 2011, BAAS, 43, 344.14
Beaumont, C., Robitaille, T., Borkin, M., & Goodman, A. 2014, glueviz v0.4: multidimensional data exploration, Zenodo, doi:10.5281/zenodo.13866
Beerer, I. M., Koenig, X. P., Hora, J. L., et al. 2010, ApJ, 720, 679
Beers, T. C., Flynn, K., & Gebhardt, K. 1990, AJ, 100, 32
Behnel, S., Bradshaw, R., Citro, C., et al. 2011, CSE, 13, 31
Berry, D. S., Warren-Smith, R. F., & Jenness, T. 2016, A&C, 15, 33
Bovy, J. 2015, ApJS, 216, 29
Bradley, L., Sipocz, B., Robitaille, T., et al. 2017, astropy/photutils: v0.4, Zenodo, doi:10.5281/zenodo.1039309
Bretthorst, G. L. 2003, in Statistical Challenges in Astronomy. Third Statistical Challenges in Modern Astronomy (SCMA III) Conf., ed. E. D. Feigelson & G. J. Babu (New York: Springer), 309
Craig, M. W., Crawford, S. M., Deil, C., et al. 2015, ccdproc: CCD data reduction software, Astrophysics Source Code Library, ascl:1510.007
Crawford, S., Earl, N., Ginsburg, A., & Tollerud, E. 2017, Vision for Astropy Spectroscopic Tools (APE 13), Zenodo, doi:10.5281/zenodo.1117943
Cruz, K., Hagen, A., Robitaille, T., Tollerud, E., & Villaume, A. 2015, Astropy Proposal for Enhancement 8: Astropy Community Code of Conduct (APE 8), Zenodo, doi:10.5281/zenodo.1043913
Currie, M. J., Berry, D. S., Jenness, T., et al. 2014, in ASP Conf. Ser. 485, Astronomical Data Analysis Software and Systems XXIII, ed. N. Manset & P. Forshay (San Francisco, CA: ASP), 391
Deil, C., Zanin, R., Lefaucheur, J., et al. 2017, arXiv:1709.01751
Dencheva, N., Sipocz, B., Jones, C., et al. 2017, spacetelescope/gwcs: GWCS v0.8.0, Zenodo, doi:10.5281/zenodo.1041790
Disney, M. J., & Wallace, P. T. 1982, QJRAS, 23, 485
Doe, S., Nguyen, D., Stawarz, C., et al. 2007, in ASP Conf. Ser. 376, Astronomical Data Analysis Software and Systems XVI, ed. R. A. Shaw, F. Hill, & D. J. Bell (San Francisco, CA: ASP), 543
ejeschke, Lim, P. L., Rajul, et al. 2017, ejeschke/ginga: Ginga v2.6.6, Zenodo, doi:10.5281/zenodo.1040969
Ford, J. 2016, cluster-lensing: v0.1.2, Zenodo, doi:10.5281/zenodo.51370
Ginsburg, A., & Mirocha, J. 2011, PySpecKit: Python Spectroscopic Toolkit, Astrophysics Source Code Library, ascl:1109.001
Ginsburg, A., Robitaille, T., Koch, E., et al. 2017a, radio-astro-tools/spectral-cube: Version 0.4.1 release, Zenodo, doi:10.5281/zenodo.1013994
Ginsburg, A., Sipocz, B., Parikh, M., et al. 2017b, astropy/astroquery: v0.3.6 with fixed license, Zenodo, doi:10.5281/zenodo.826911
Graham, M., Plante, R., Tody, D., & Fitzpatrick, M. 2014, PyVO: Python access to the Virtual Observatory, Astrophysics Source Code Library, ascl:1402.004
Greenfield, P. 2013, Astropy Proposal for Enhancement 1: APE Purpose and Process (APE 1), Zenodo, doi:10.5281/zenodo.1043886
Günther, H. M., Frost, J., & Theriault-Shay, A. 2017, AJ, 154, 243
Hearin, A. P., Campbell, D., Tollerud, E., et al. 2017, AJ, 154, 190
hips developers 2018, hips—Python library to handle HiPS data, https://github.com/hipspy/hips
Hohenkerk, C. 2011, SchpJ, 6, 11404
Hunter, J. D. 2007, CS&E, 9, 90
Huppenkothen, D., Bachetti, M., Stevens, A. L., Migliari, S., & Balm, P. 2016, Stingray: Spectral-timing software, Astrophysics Source Code Library, ascl:1608.001
Ivezić, Ž., Connolly, A., Vanderplas, J., & Gray, A. 2014, Statistics, Data Mining and Machine Learning in Astronomy (Princeton, NJ: Princeton Univ. Press)
Jammalamadaka, S. R., & Sengupta, A. 2001, Topics in Circular Statistics (Singapore: World Scientific)
Jenness, T., & Berry, D. S. 2013, in ASP Conf. Ser. 475, Astronomical Data Analysis Software and Systems XXII, ed. D. N. Friedel (San Francisco, CA: ASP), 307
Jenness, T., Bosch, J., Owen, R., et al. 2016, Proc. SPIE, 9913, 99130G
Jones, E., Oliphant, T., Peterson, P., et al. 2001, SciPy: Open source scientific tools for Python, http://www.scipy.org/
Knutsson, H., & Westin, C. F. 1993, in Proc. IEEE Conf. on Computer Visionand Pattern Recognition (New York: IEEE), 515
Lim, P. L., et al. 2016, synphot User's Guide (Baltimore, MD: STScI), https://synphot.readthedocs.io/en/latest/
Lomb, N. R. 1976, Ap&SS, 39, 447
Lupton, R., Blanton, M. R., Fekete, G., et al. 2004, PASP, 116, 133
Mamajek, E. E., Prsa, A., Torres, G., et al. 2015, arXiv:1510.07674
McKinney, W. 2010, in Proc. 9th Python in Science Conf., ed. S. van der Walt & J. Millman, 51
Mohr, P. J., Newell, D. B., & Taylor, B. N. 2016, RvMP, 88, 035009
Morris, B. M., Tollerud, E., Sipőcz, B., et al. 2018, AJ, 155, 128
Muna, D., Alexander, M., Allen, A., et al. 2016, arXiv:1610.03159
Palmer, D. M. 2009, ApJ, 695, 496
Pence, W. D., Chiappetti, L., Page, C. G., Shaw, R. A., & Stobie, E. 2010, A&A, 524, A42
Planck Collaboration, Ade, P. A. R., Aghanim, N., et al. 2016, A&A, 594, A13
Press, W. H., & Rybicki, G. B. 1989, ApJ, 338, 277
Price-Whelan, A., Crawford, S., Sipocz, B., et al. 2018, astropy/astropy-v2.0-paper: final draft, Zenodo, doi:10.5281/zenodo.1211397
Price-Whelan, A. M. 2017, JOSS, 2, doi:10.21105/joss.00388
Prochaska, J. X., Tejos, N., Crighton, N., et al. 2017, linetools/linetools: Third Minor Release, Zenodo, doi:10.5281/zenodo.1036773
pyregions developers 2018, regions—ds9 region parser for python, https://github.com/astropy/pyregion
Rhodes, B. C. 2011, PyEphem: Astronomical Ephemeris for Python, Astrophysics Source Code Library, ascl:1112.014
Robitaille, T. 2017, Astropy Proposal for Enhancement: Roadmap for Python 3-only support (APE 10), Zenodo, doi:10.5281/zenodo.1038587

Robitaille, T. 2018, reproject: astronomical image reprojection in Python, Zenodo, doi:10.5281/zenodo.1162674
Robitaille, T., & Bressert, E. 2012, APLpy: Astronomical Plotting Library in Python, Astrophysics Source Code Library, ascl:1208.017
Rodríguez, J. L. C., Hidalgo, A., Márquez, A. L., et al. 2017, poliastro/poliastro: poliastro 0.8.0 (OSCW edition), Zenodo, doi:10.5281/zenodo.1058988
Scargle, J. D. 1982, ApJ, 263, 835
Scargle, J. D., Norris, J. P., Jackson, B., & Chiang, J. 2013, ApJ, 764, 167
Seabold, S., & Perktold, J. 2010, in 9th Python in Science Conf., ed. S. van der Walt & J. Millman
Sosey, M. 2017, imexam version 0.8.0 release, Zenodo, doi:10.5281/zenodo.1042809
specutils developers 2018, specutils—Affiliated package for 1D spectral operations, https://github.com/astropy/specutils
Streicher, O., & Weilbacher, P. M. 2012, in ASP Conf. Ser. 461, Astronomical Data Analysis Software and Systems XXI, ed. P. Ballester, D. Egret, & N. P. F. Lorente (San Francisco, CA: ASP), 853
Suutarinen, A. 2015, omnifit: v0.2.1, Zenodo, doi:10.5281/zenodo.35536
Terlouw, J. P., & Vogelaar, M. G. R. 2015, Kapteyn Package, version 2.3 (Groningen: Kapteyn Astronomical Institute)
Tody, D. 1993, in ASP Conf. Ser. 52, Astronomical Data Analysis Software and Systems II, ed. R. J. Hanisch, R. J. V. Brissenden, & J. Barnes (San Francisco, CA: ASP), 173
Tollerud, E. 2013, Astropy Proposal for Enhancement 2: Astropy Release Cycle and Version Numbering (APE 2), Zenodo, doi:10.5281/zenodo.1043888
Tollerud, E., Pascual, S., Nair, P., et al. 2017, liberfa/erfa: v1.4.0, Zenodo, doi:10.5281/zenodo.1021149
Tollerud, E., Price-Whelan, A., Aldcroft, T., & Robitaille, T. 2014, Astropy Proposal for Enhancement 5: Coordinates Subpackage Plan (APE 5), Zenodo, doi:10.5281/zenodo.1043897
Turk, M. J., Smith, B. D., Oishi, J. S., et al. 2011, ApJS, 192, 9
Van der Walt, S., Colbert, S. C., & Varoquaux, G. 2011, CSE, 13, 22
van Dokkum, P. G. 2001, PASP, 113, 1420
VanderPlas, J. 2018, ApJS, arXiv:1703.09824
VanderPlas, J., Connolly, A., Ivezić, Ž., & Gray, A. 2012, in Conf. on Intelligent Data Understanding (CIDU), ed. K. Das et al. (New York: IEEE), 47
VanderPlas, J. T., & Ivezic, Z. 2015, arXiv:1502.01344
Wallace, P. T. 1994, in ASP Conf. Ser. 61, Astronomical Data Analysis Software and Systems III, ed. D. R. Crabtree, R. J. Hanisch, & J. Barnes (San Francisco, CA: ASP), 481
Weaver, B. A., Barbary, K., Bradley, K., et al. 2017, weaverba137/pydl: PyDL v0.6.0, Zenodo, doi:10.5281/zenodo.1095151
Zabalza, V. 2015, Proc. ICRC, 922
Zechmeister, M., & Kürster, M. 2009, A&A, 496, 577

This article has been accepted for inclusion in a future issue of this journal. Content is final as presented, with the exception of pagination.

Thermally Grown TiO_2 and Al_2O_3 for GaN-Based MOS-HEMTs

Akanksha Rawat, Mudassar Meer, Vivek kumar Surana, Navneet Bhardwaj, Vikas Pendem, Navya Sri Garigapati, Yogendra Yadav, Swaroop Ganguly, and Dipankar Saha

***Abstract*— We have demonstrated the potential use of thermally grown TiO_2 and Al_2O_3 oxides as gate dielectrics for GaN-based high-electron-mobility-transistors. TiO_2 and Al_2O_3 are found to provide negative and positive band offsets with AlGaN, respectively. A significant performance improvement on various device characteristics provides evidence for its potential use. The oxides are formed by a combination of predeposition of a thin film and followed by oxidation in pure O_2 environment. The formation and thickness of the oxides are confirmed through the X-ray photoelectron spectroscopy and the transmission electron microscopy. The performance improvement for TiO_2- and Al_2O_3-based oxide gates have been identified in terms of a ideality factor and a reduction in the gate leakage current in comparison with that of control devices. This is further augmented by an increase in the $n_s \times \mu$ product. The ON/OFF current ratio and turn-ON voltage increase by 2–3 orders of magnitude and 0.3–0.6, respectively, for the Schottky diodes. The negative shift on the capacitance–voltage characteristics is also found to be minimal, indicating higher gate coupling with thermally grown oxides.**

***Index Terms*— GaN, gate dielectric, interface, metal–oxide–semiconductor (MOS)-high-electron-mobility transistor (HEMT).**

I. Introduction

DUE to the distinctive properties of achieving high breakdown voltage, current density, mobility, and 2-D electron gas density (2-DEG), the AlGaN/GaN high-electron-mobility transistors (HEMTs) have become a prominent candidate for radio frequency (RF) applications, high power, and high-temperature electronics [1]–[6]. For further improvements, major research is being carried out on the metal–oxide–semiconductor (MOS) gates and studying the nature of the surface states at the oxide/AlGaN interface that affect many device characteristics, such as gate leakage current, power dissipation, mobility, drain current, and saturation velocity [7], [8]. To improve these characteristics without sacrificing the 2-DEG carrier concentration and mobility,

Manuscript received January 6, 2018; revised April 21, 2018 and June 18, 2018; accepted July 13, 2018. This work was supported in part by Indian Space Research Organization, in part by Department of Science and Technology, and in part by Impacting Research Innovation and Technology. The review of this paper was arranged by Editor S. Rajan. *(Corresponding author: Dipankar Saha.)*

The authors are with the Department of Electrical Engineering, IIT Bombay, Mumbai 400076, India (e-mail: dipankarsaha@iitb.ac.in).

Color versions of one or more of the figures in this paper are available online at http://ieeexplore.ieee.org.

Digital Object Identifier 10.1109/TED.2018.2857468

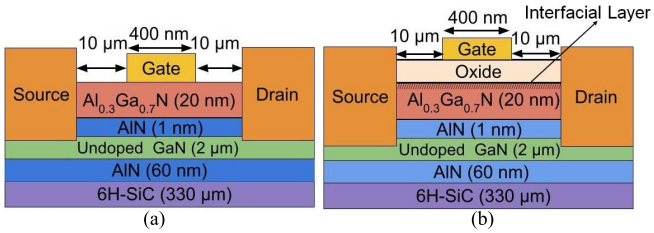


Fig. 1. Cross-sectional schematic of (a) conventional and (b) oxide HEMTs on AlGaN/GaN heterostructure.

MOS-HEMT technology is very pertinent. A desired gate oxide should have a wide energy band gap and high dielectric constant. Various high K dielectrics, such as SiO_2 [2], [9], Al_2O_3 [4], [5], [10], HfO_2 [11]–[13], ZrO_2 [14], Ta_2O_5 [15], TiO_2 [16]–[19], Ga_2O_3 [20], and Sc_2O_3 [21], have been explored to various degrees of success. We have explored the potential use of thermally grown Al_2O_3 and TiO_2 as gate dielectrics for MOS HEMTs. The choice of Al_2O_3 is based on the fact that it has a large band gap (~6.5 eV) [22] with significant conduction band offset. In addition, a good interface with AlGaN has been confirmed with atomic layer deposited Al_2O_3 [10]. TiO_2 on the other hand, however, has a very high dielectric constant with negative conduction band offset with AlGaN. Based on the different phases of TiO_2 (amorphous, anatase, and rutile), dielectric constants ranging from 20 to 100 have been reported [18], [23], [24]. Here, we have studied fundamental properties of thermally grown TiO_2 and Al_2O_3 on AlGaN by the X-ray photoelectron spectroscopy (XPS) and the transmission electron microscopy (TEM). The effectiveness of the oxide is confirmed from the gate contact characteristics. The interfacial properties are extracted from I–V and C–V characteristics.

II. Heterostructure and Device Fabrication

A schematic of the AlGaN/GaN heterostructure used in this paper is shown in Fig. 1. Large area capacitors are fabricated on this sample. The heterostructure is grown by metal–organic chemical vapor deposition technique on a 6H-SiC substrate. The fabrication of the Schottky diodes involves the formation of annular ohmic regions by depositing Ti/Al/Ni/Au (30/100/30/100 nm) in electron-beam evaporator under high vacuum and rapid thermal annealing (RTA) at 850 °C for 30 s in N_2 environment. The center region of 100-μm diameter is then selectively exposed using lithography, and the thin films of Ti (2 nm) and Al (2 nm) are deposited on two

0018-9383 © 2018 IEEE. Personal use is permitted, but republication/redistribution requires IEEE permission.
See http://www.ieee.org/publications_standards/publications/rights/index.html for more information.

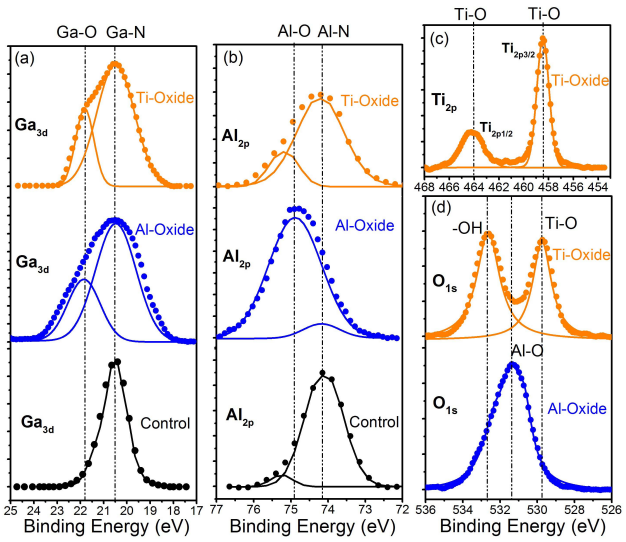


Fig. 2. XPS data of (a) Ga_{3d} and (b) Al_{2p} peaks for various samples, (c) Ti_{2p} peak for Ti-oxide sample, and (d) O_{1s} peak for the oxide samples.

TABLE I
ELEMENTAL ATOMIC PERCENTAGES IN TiO_x AND AlO_x

Element	Atomic%	Element	Atomic%
Ti_{2p}	26.9	Al_{2p}	30.5
O_{1s}	73.0	O_{1s}	69.4

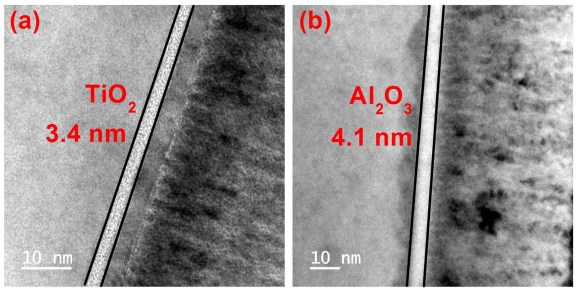


Fig. 3. TEM images of thermally grown (a) TiO_2 and (b) Al_2O_3.

different samples. The samples are then annealed by RTA in O_2 environment at 700 °C and 500 °C, respectively, for thermal oxidation. Finally, Ni/Au (30/100 nm) is deposited by an e-beam evaporation for the Schottky contacts. The Schottky-to-ohmic contact distance is maintained at 30 μm. The electrical characterizations are done in a cascade probe station using Agilent B1500A semiconductor device parameter analyzer.

III. Experimental Results and Discussion

A. Oxide Physical Characteristics

The complete formation of the oxides without any residual metal is confirmed through XPS. It may be noted that C-1's peak at 284.8 eV has been chosen as a reference for all the XPS data [see Fig. 2(a)–(d)] presented here. Fig. 2(a) shows Ga_{3d} for all the samples. It may be noted that Ga–O bond formation is also observed along with Ga–N bonds indicating part of the underlying AlGaN layer is also getting oxidized in the process. Fig. 2(b) shows the XPS spectra for the Al_{2p} core levels indicating the formation of the AlO_x. Fig. 2(c) shows the XPS spectra of Ti_{2p} core levels confirming the presence of Ti–O bonds. The corresponding O_{1s} peaks for both TiO_x and AlO_x bonds are shown in Fig. 2(d). It may be noted that a sample with TiO_x also shows some formation of hydroxides.

The stoichiometry for the oxides is calculated by integrating the corresponding peaks after normalizing by the atomic sensitivity factors. Table I shows the atomic percentages for the various species in the oxides. The Ti : O and Al : O ratios are found to be 1 : 2.7 and 1 : 2.3, respectively. The O_2 content is found to be higher for both the cases than that required for the ideal stoichiometry. This further confirms the oxidation of the part of the underlying AlGaN layer. It may be noted that the peaks for Al–Al (72.9 eV) and Ti–Ti (454.1 eV) are absent, indicating that Al and Ti are fully oxidized to Al_2O_3 and TiO_2, respectively. The physical thicknesses of the thermal oxides are determined by TEM on control samples prepared under identical conditions. Fig. 3(a) and (b) shows the TEM images for the TiO_2 and Al_2O_3 samples, respectively, indicating respective thicknesses of 3.4 and 4.1 nm.

B. Oxide/AlGaN Band Alignment

We have determined the band alignments with respect to the top AlGaN layer of the heterostructure. This is particularly interesting for TiO_2 with a band gap of 3.2 eV, which is smaller than that of AlGaN (4.1 eV). The band alignment at the Al_2O_3/AlGaN interface has been widely studied [25]–[27]. The conduction and valence band offsets have been reported to be 1.47 and 1.00 eV, respectively. We, therefore, have focused at the TiO_2/AlGaN interface here. The XPS data for both the core- and valence-level spectra from the bulk reference compounds and heterostructures are used to determine the valence band offsets [28]–[31].

The valence band offset ΔE_{VBO} at the TiO_2/AlGaN interface is determined from

$$\Delta E_{\mathrm{VBO}} = \left(E^{\mathrm{Control}}_{\mathrm{Ga}_{3d}} - E^{\mathrm{TiO_2(3.4\,nm)}}_{\mathrm{Ga}_{3d}}\right) - \left[\left(E^{\mathrm{Control}}_{V} - E^{\mathrm{TiO_2(Bulk)}}_{V}\right) - \left(E^{\mathrm{TiO_2(Bulk)}}_{\mathrm{Ti}_{2p}} - E^{\mathrm{TiO_2(3.4\,nm)}}_{\mathrm{Ti}_{2p}}\right)\right] \quad (1)$$

where E represents the energy, superscript represents the sample, and subscript represents the corresponding orbitals. The valence band maxima $E_V^{\mathrm{TiO_2(Bulk)}}$ and E_V^{Control} are obtained from the linear fitting of the leading edge of the valence band spectra, as shown in Fig. 4(a) and (b), respectively. The Ti_{2p} and Ga_{3d} binding energies for bulk and thin-film oxides are shown in Fig. 4(c)–(f), respectively. The ΔE_{VBO} for the TiO_2/AlGaN interface is found to be −0.560 eV. Fig. 5 shows the band alignment for both the TiO_2/AlGaN and Al_2O_3/AlGaN interfaces for completeness. It may be noted that TiO_2 also gives type-I band alignment with negative offsets for both conduction and valence bands.

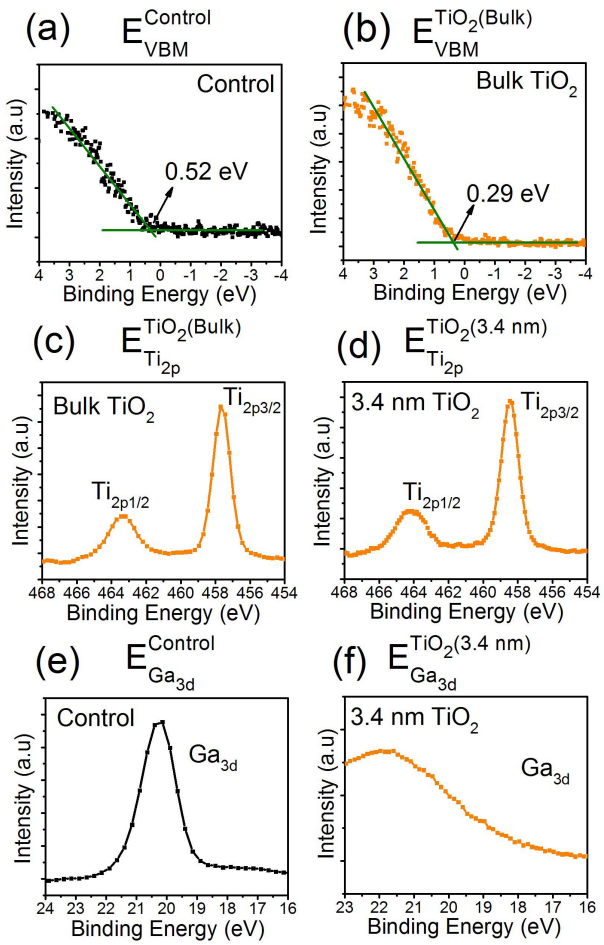


Fig. 4. Linear fitting of the valence band spectra in (a) control and (b) TiO_2 bulk sample. Ti_{2p} energy-level spectra for (c) TiO_2 bulk and (d) 3.4-nm TiO_2/AlGaN sample. Ga_{3d} energy-level spectra for (e) control and (f) 3.4-nm TiO_2/AlGaN sample.

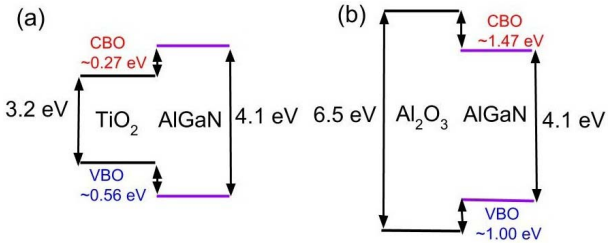


Fig. 5. Conduction band and valence band offsets in energy band diagrams for (a) TiO_2/AlGaN (b) Al_2O_3/AlGaN interfaces.

C. Hall Measurements: 2-DEG Density and Mobility

The 2-DEG and mobility are determined by Hall measurements in Van der Pauw geometry. The distance between the ohmic pads is kept 10 times the size of the pads. Table II shows the 2-DEG density (n_s) and mobility (μ) for all the samples. The 2-DEG density is found to be maximum (1.3×10^{13} cm^{-2}) for the TiO_2 sample, while the mobility is found to be maximum (1540 cm^2/V.s) for the Al_2O_3 sample. Since the product $n_s \times \mu$ determines most of the dc and RF characteristics for transistors, it is also shown in Table II. The change in

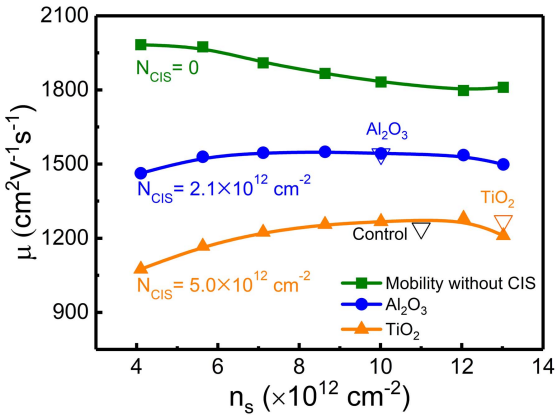


Fig. 6. Estimated μ versus n_S. The effect of N_{CIS} is found to dominate for TiO_2 and control samples.

TABLE II
MOBILITY AND 2-DEG DENSITY FOR VARIOUS SAMPLES

Parameters	Control	TiO_2	Al_2O_3
n_s (cm^{-2})	1.1×10^{13}	1.3×10^{13}	1.0×10^{13}
μ (cm^{2}V^{-1}s^{-1})	1240	1270	1540
$n_s \times \mu$ (V^{-1}s^{-1})	1.34×10^{16}	1.72×10^{16}	1.54×10^{16}

electron density for TiO_2 and Al_2O_3 samples can be explained from the negative and positive band offsets with AlGaN. They try to pull down and pull up the conduction band edge, respectively. Consequently, the difference between the Fermi level (E_F) and the first bound state (E_1) increases (pull-down case) and decreases (pull-up case), which are reflected on n_s. The fixed charges present at the interface can further modify ($E_F - E_1$).

The 2-DEG mobility dependence has been studied earlier [32]–[35]. The change in mobility, in our case, can be understood from the dependence of μ on n_s shown in Fig. 6, considering the effect of acoustic phonon and charged interface states (CISs) [36]. The effect of surface state dipole is neglected, as the impact is found to be negligible. It may be noted that μ decreases for increasing n_s in the absence of CIS. However, in the presence of CIS, there exists a critical density that is required to screen the detrimental effects; μ follows conventional trend for density larger than the critical density. A larger value of N_{CIS} moves the required critical density to a larger value. The increased mobility for the Al_2O_3 sample is probably due to a decrease in n_s and lower CIS. This indicates Al_2O_3 can effectively passify the interface states. TiO_2 sample, having higher interface traps (shown later), suffers from mobility degradation due to an increased value for N_{CIS}. The almost unchanged μ for TiO_2 in comparison with that of the control sample is probably due to similar CIS for both the cases. While we have done Hall measurements in a conventional geometry (without a gate metal), the change in mobility due to N_{CIS} is likely to be small with gate metal on top of the channel. The effect of N_{CIS} will be suppressed due to screening by the gate metal. Also, remote coulomb scattering is going to be limited by the AlGaN barrier.

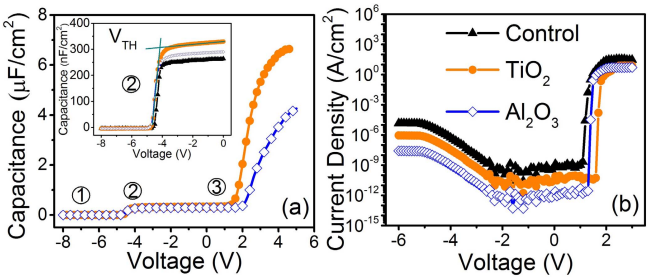


Fig. 7. (a) C–V characteristics at 1-MHz frequency and (b) I–V characteristics for control, TiO_2 and Al_2O_3-based MOS Schottky diodes.

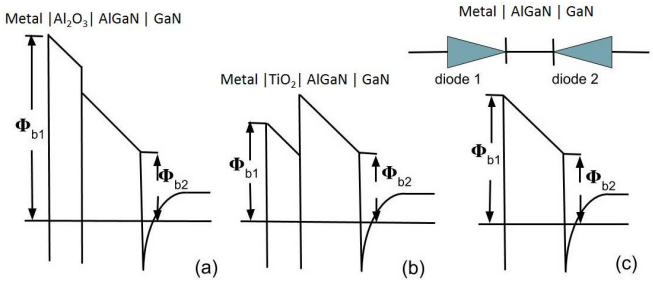


Fig. 8. Schematic conduction band diagrams for (a) Al_2O_3, (b) TiO_2, and (c) control samples along with two-diode equivalent model.

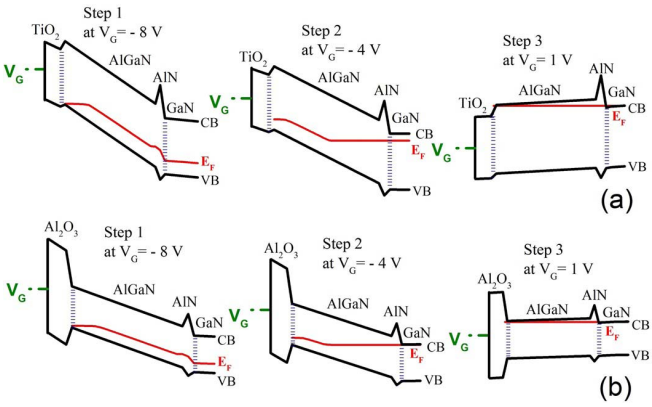


Fig. 9. Simulated energy -band diagrams for (a) TiO_2 and (b) Al_2O_3-based MOS gates at regions 1–3 marked on the C–V curve of Fig. 6(a).

D. Oxide/AlGaN Schottky Gate Characteristics

The capacitance–voltage (C–V) and current–voltage (I–V) measurements were carried out on the large area Schottky diodes to understand the gate characteristics of the MOS-HEMTs. Fig. 7(a) shows the C–V characteristics for the control and oxide samples. The oxide samples show two distinct steps in C–V indicating the presence of the oxides. It is interesting to note that the capacitance increases in spite of the additional thermal oxides [shown in the inset of Fig. 7(a)]. This further confirms that part of the AlGaN is converted to the oxide during oxidation step. The extracted threshold voltage is shown in Table III. Threshold voltage shifts slightly toward the negative direction for the oxide samples.

Fig. 7(b) shows the I–V characteristics of the control sample and oxide gates. As intuitively expected, the ON/OFF current ratio and turn-ON voltage are found to increase by 2–3 orders of magnitude and 0.3–0.6 due to the oxides, respectively. To determine the effectiveness of the oxides in the common framework of the conventional HEMTs [37], we have considered a two-diode model for the gate, where the oxide-AlGaN combination is considered as an *equivalent* single barrier with a modified effective barrier height and ideality factor. It may be noted that effective barrier height helps to understand the effectiveness of the dielectric to reduce leakage current. The Al_2O_3 sample shows the minimum reverse leakage current that is in-line with the positive band offset and higher effective barrier height. Hence, Al_2O_3 sample is likely to give higher breakdown voltage. The effect of the thin AlN barrier is implicitly considered in the barrier height and ideality factor and, therefore, not explicitly shown here. A schematic of the two-diode model is shown in Fig. 8. The extracted parameters for the control and oxide samples are shown in Table III. We have also determined energy band-diagrams (shown in Fig. 9) for positions 1-subthreshold, 2-threshold, and 3-below cutin of the C–V curve shown in Fig. 7(a). It may be noted that both Al_2O_3 and TiO_2 show fundamentally similar nature in spite of the negative band offset for the TiO_2 sample.

E. Oxide/AlGaN Interface Characteristics

The interface-state density (D_{it}) and trap time constant (τ_{it}) at the oxide–AlGaN interface are determined from frequency-dependent conductance measurements. The frequency is varied from 10 kHz to 5 MHz for various bias voltages. The equivalent circuit for the oxide/AlGaN interface considered here is shown in the inset of Fig. 10(b). We have selectively

TABLE III
COMPARISON OF DIODE PARAMETERS

Parameters	Control	TiO_2	Al_2O_3
I_{ON}/I_{OFF} (± 4 V)	5.4×10^7	2.3×10^8	5.1×10^9
η_1	1.7	1.2	1.0
η_2	29.8	31.2	31.7
$\Phi_{b1,eff}$ (eV)	1.2	2.1	2.2
V_{TH} (V)	-4.1	-4.2	-4.3

considered bias condition, where the trapping/detrapping at the AlGaN/GaN interface is inhibited. The D_{it} and τ_{it} are obtained from [38]

$$\frac{G_p}{\omega} = \frac{\omega C_0^2 G_m}{\omega^2(C_m - C_0)^2 + G_m^2} = \frac{q D_{it}\omega\tau_{it}}{1 + (\omega\tau_{it})^2} \quad (2)$$

where C_0 is the oxide capacitance and C_m and G_m are the measured capacitance and conductance at frequency ω, respectively. The relative dielectric constant for Al_2O_3 and TiO_2 is estimated to be 8.8 and 25, respectively. The trap energy level E_T with respect to the conduction band E_C [39] is then estimated from

$$\tau_{it} = \frac{1}{\sigma_{it} v_t N_C} \exp\left(\frac{E_C - E_T}{kT}\right) \quad (3)$$

where T (= 300 K) is the temperature, σ_{it} (=4×10^{-13} and 1×10^{-16} cm^{-2}) is the capture cross section, v_t (=2.60×10^7 and 2.68×10^7 cm/s) is the thermal velocity [40] and [41], and N_C (=2.20×10^{18} and 2.07×10^{18} cm^{-3}) is the effective density of states for oxide samples (Al_2O_3 and TiO_2).

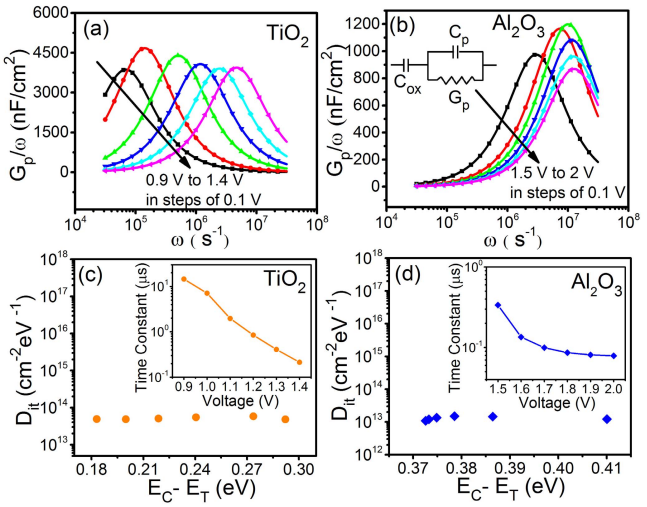


Fig. 10. Fitting of the trap conductance as a function of frequency at different voltages for (a) TiO_2 and (b) Al_2O_3 samples (inset shows the equivalent circuit at the oxide/AlGaN interface). D_{it} as a function of relative position of trap energy level with respect to the conduction band edge and inset shows the time constant as a function of voltage for (c) TiO_2 and (d) Al_2O_3 samples.

Fig. 10(a) and (b) shows the plot for $G_{p/\omega}$ versus ω for both the oxides along with analytical curve fitting using (2). The estimated values for D_{it} are found to be 4.8×10^{13} to 5.8×10^{13} $cm^{-2}\cdot eV^{-1}$ and 1.0×10^{13} to 1.5×10^{13} $cm^{-2}\cdot eV^{-1}$ for TiO_2 and Al_2O_3 samples, respectively [see Fig. 10(c)–(d)]. The corresponding time constants are found to be in the range 0.18–0.41 eV for both the oxides. Inset of Fig. 10(c) and (d) show the time constant variation with voltage for both the oxides. It may be noted that both TiO_2 and Al_2O_3 show reasonable D_{it} to be used in depletion-mode HEMTs for the benefit of decreasing leakage current and increasing $n_s \times \mu$ albeit TiO_2 shows slightly higher D_{it}. However, an enhancement mode HEMT with a thinner AlGaN will bring the dielectric/AlGaN interface closer to the 2-DEG. This may require further optimization to reduce the deteriorating effects of D_{it}.

IV. Conclusion

We have demonstrated the thermally grown TiO_2 and Al_2O_3 as potential dielectrics for GaN-based MOS-HEMTs. The physical properties of both the oxides have been investigated by XPS and TEM. The band alignments with respect to AlGaN have been experimentally determined. The Schottky characteristics show lower leakage current and larger ON/OFF ratio for both the oxides.

Acknowledgment

The authors would like to thank the Sophisticated Analytical Instrument Facility, IIT Bombay, for transmission electron microscopy.

References

[1] U. K. Mishra, P. Parikh, and Y.-F. Wu, "AlGaN/GaN HEMTs-an overview of device operation and applications," *Proc. IEEE*, vol. 90, no. 6, pp. 1022–1031, Jun. 2002, doi: 10.1109/JPROC.2002.1021567.

[2] P. Kordoš, G. Heidelberger, J. Bernát, A. Fox, M. Marso, and H. Lüth, "High-power SiO_2/AlGaN/GaN metal-oxide-semiconductor heterostructure field-effect transistors," *Appl. Phys. Lett.*, vol. 87, no. 14, p. 143501, 2005, doi: 10.1063/1.2058206.

[3] H. Kambayashi *et al.*, "Over 100 A operation normally-off AlGaN/GaN hybrid MOS-HFET on Si substrate with high-breakdown voltage," *Solid-State Electron.*, vol. 54, no. 6, pp. 660–664, 2010, doi: 10.1016/j.sse.2010.01.001.

[4] P. D. Ye *et al.*, "GaN metal-oxide-semiconductor high-electron-mobility-transistor with atomic layer deposited Al_2O_3 as gate dielectric," *Appl. Phys. Lett.*, vol. 86, no. 6, p. 063501, Jan. 2005, doi: 10.1063/1.1861122.

[5] T. Hashizume *et al.*, "Al_2O_3 insulated-gate structure for AlGaN/GaN heterostructure field effect transistors having thin algan barrier layers," *Jpn. J. Appl. Phys.*, vol. 43, no. 6B, p. L777, 2004, doi: 10.1143/JJAP.43.L777.

[6] K. Takhar, M. Meer, B. B. Upadhyay, S. Ganguly, and D. Saha, "Performance improvement and better scalability of wet-recessed and wet-oxidized AlGaN/GaN high electron mobility transistors," *Solid-State Electron.*, vol. 131, pp. 39–44, May 2017, doi: 10.1016/j.sse.2017.02.002.

[7] E. Kohn, I. Daumiller, P. Schmid, N. X. Nguyen, and C. N. Nguyen, "Large signal frequency dispersion of AlGaN/GaN heterostructure field effect transistors," *Electron. Lett.*, vol. 35, no. 12, pp. 1022–1024, Jun. 1999, doi: 10.1049/el:19990697.

[8] S. Mizuno, Y. Ohno, S. Kishimoto, K. Maezawa, and T. Mizutani, "Large gate leakage current in AlGaN/GaN high electron mobility transistors," *Jpn. J. Appl. Phys.*, vol. 41, no. 8, p. 5125, 2002, doi: 10.1143/JJAP.41.5125.

[9] S. Arulkumaran, T. Egawa, H. Ishikawa, T. Jimbo, and Y. Sano, "Surface passivation effects on AlGaN/GaN high-electron-mobility transistors with SiO_2, Si_3N_4, and silicon oxynitride," *Appl. Phys. Lett.*, vol. 84, no. 4, pp. 613–615, Jan. 2004, doi: 10.1063/1.1642276.

[10] T. Hashizume, S. Ootomo, and H. Hasegawa, "Suppression of current collapse in insulated gate AlGaN/GaN heterostructure field-effect transistors using ultrathin Al_2O_3 dielectric," *Appl. Phys. Lett.*, vol. 83, no. 14, pp. 2952–2954, Oct. 2003, doi: 10.1063/1.1616648.

[11] C. Liu, E. F. Chor, and L. S. Tan, "Investigations of HfO_2/AlGaN/GaN metal-oxide-semiconductor high electron mobility transistors," *Appl. Phys. Lett.*, vol. 88, no. 17, p. 173504, Apr. 2006, doi: 10.1063/1.2198507.

[12] F. Tian and E. F. Chor, "Improved electrical performance and thermal stability of HfO_2/Al_2O_3 bilayer over HfO_2 gate dielectric AlGaN/GaN MIS–HFETs," *J. Electrochem. Soc.*, vol. 157, no. 5, pp. 557–561, 2010, doi: 10.1149/1.3353799.

[13] S. Abermann *et al.*, "MOCVD of HfO_2 and ZrO_2 high-k gate dielectrics for InAlN/AlN/GaN MOS-HEMTs," *Semicond. Sci. Technol.*, vol. 22, no. 12, p. 1272, 2007, doi: 10.1088/0268-1242/22/12/005.

[14] Y. Dora *et al.*, "ZrO_2 gate dielectrics produced by ultraviolet ozone oxidation for GaN and AlGaN/GaN transistors," *J. Vac. Sci. Technol. B, Microelectron. Process. Phenom.*, vol. 24, no. 2, pp. 575–581, Mar. 2006, doi: 10.1116/1.2167991.

[15] D. A. Deen *et al.*, "Atomic layer deposited Ta_2O_5 gate insulation for enhancing breakdown voltage of AlN/GaN high electron mobility transistors," *Appl. Phys. Lett.*, vol. 98, p. 023506, 2011, doi: 10.1063/1.3531551.

[16] S. Yagi *et al.*, "High breakdown voltage AlGaN/GaN MIS-HEMT with SiN and TiO_2 gate insulator," *Solid-State Electron.*, vol. 50, no. 6, pp. 1057–1061, 2006, doi: 10.1016/j.sse.2006.04.041.

[17] K.-T. Lee, C.-F. Huang, J. Gong, and C.-T. Lee, "High-performance 1-μm GaN n-MOSFET with MgO/MgO-TiO_2 stacked gate dielectrics," *IEEE Electron Device Lett.*, vol. 32, no. 3, pp. 306–308, Mar. 2011, doi: 10.1109/LED.2010.2096196.

[18] S. A. Campbell *et al.*, "MOSFET transistors fabricated with high permitivity TiO_2 dielectrics," *IEEE Trans. Electron Devices*, vol. 44, no. 1, pp. 104–109, Jan. 1997, doi: 10.1109/16.554800.

[19] D. Meng *et al.*, "Low leakage current and high-cutoff frequency AlGaN/GaN MOSHEMT using submicrometer-footprint thermal oxidized TiO_2/NiO as gate dielectric," *IEEE Electron Device Lett.*, vol. 34, no. 6, pp. 738–740, Jun. 2013, doic: 10.1109/LED.2013.2256102.

[20] Y. Nakano, T. Kachi, and T. Jimbo, "Characteristics of SiO_2/n-GaN interfaces with β-Ga_2O_3 interlayers," *Appl. Phys. Lett.*, vol. 83, no. 21, pp. 4336–4338, 2003, doi: 10.1063/1.1629371.

[21] R. Mehandru *et al.*, "AlGaN/GaN metalâŁ"oxideâŁ"semiconductor high electron mobility transistors using Sc_2O_3 as the gate oxide and surface passivation," *Appl. Phys. Lett.*, vol. 82, no. 15, pp. 2530–2532, 2003, doi: 10.1063/1.1567051.

[22] N. V. Nguyen *et al.*, "Band offsets of atomic-layer-deposited Al_2O_3 on GaAs and the effects of surface treatment," *Appl. Phys. Lett.*, vol. 93, no. 8, pp. 082105-1–082105-3, Aug. 2008, doi: 10.1063/1.2976676.

[23] H. S. Kim, D. C. Gilmer, S. A. Campbell, and D. L. Polla, "Leakage current and electrical breakdown in metal-organic chemical vapor deposited TiO_2 dielectrics on silicon substrates," *Appl. Phys. Lett.*, vol. 69, no. 25, pp. 3860–3862, 1996, doi: 10.1063/1.117129.

[24] H. Fukuda, S. Namioka, M. Miura, Y. Ishikawa, M. Yoshino, and S. Nomura, "Structural and electrical properties of crystalline TiO_2 thin films formed by metalorganic decomposition," *Jpn. J. Appl. Phys.*, vol. 38, no. 10R, p. 6034, 1999, doi: 10.1143/JJAP.38.6034.

[25] T. Hashizume, S. Ootomo, and H. Hasegawa, "Al_2O_3-based surface passivation and insulated gate structure for AlGaN/GaN HFETs," *Phys. Status Solidi C*, no. 7, pp. 2380–2384, 2003, doi: 10.1002/pssc.200303446.

[26] T. Hashizume, S. Ootomo, T. Inagaki, and H. Hasegawa, "Surface passivation of GaN and GaN/AlGaN heterostructures by dielectric films and its application to insulated-gate heterostructure transistors," *J. Vac. Sci. Technol. B, Microelectron. Process. Phenom.*, vol. 21, no. 4, pp. 1828–1838, Jul. 2003, doi: 10.1116/1.1585077.

[27] X. Qin *et al.*, "A comparative study of atomic layer deposition of Al_2O_3 and HfO_2 on AlGaN/GaN," *J. Mater. Sci., Mater. Electron.*, vol. 26, no. 7, pp. 4638–4643, 2015, doi: 10.1007/s10854-015-2926-2.

[28] E. A. Kraut, R. W. Grant, J. R. Waldrop, and S. P. Kowalczyk, "Semiconductor core-level to valence-band maximum binding-energy differences: Precise determination by X-ray photoelectron spectroscopy," *Phys. Rev. B, Condens. Matter*, vol. 28, no. 4, p. 1965, 1983, doi: 10.1103/PhysRevB.28.1965.

[29] E. T. Yu, D. H. Chow, and T. C. McGill, "Commutativity of the GaAs/AlAs (100) band offset," *Phys. Rev. B, Condens. Matter*, vol. 38, no. 17, p. 12764(R), 1988, doi: 10.1116/1.584758.

[30] S. A. Chambers, Y. Liang, Z. Yu, R. Droopad, J. Ramdani, and K. Eisenbeiser, "Band discontinuities at epitaxial $SrTiO_3$/Si (001) heterojunctions," *Appl. Phys. Lett.*, vol. 77, no. 11, pp. 1662–1664, 2000, doi: 10.1063/1.1310209.

[31] S. A. Chambers, T. Droubay, T. C. Kaspar, and M. Gutowski, "Experimental determination of valence band maxima for $SrTiO_3$, TiO_2, and SrO and the associated valence band offsets with Si(001)," *J. Vac. Sci. Technol. B, Microelectron. Process. Phenom.*, vol. 22, no. 4, pp. 2205–2215, 2004, doi: 10.1116/1.1768525.

[32] M. N. Gurusinghe, S. K. Davidsson, and T. G. Andersson, "Two-dimensional electron mobility limitation mechanisms in $Al_xGa_{1-x}N$/GaN heterostructures," *Phys. Rev. B, Condens. Matter*, vol. 72, no. 4, p. 045316, Jul. 2005, doi: 10.1103/PhysRevB.72.045316.

[33] D. Jena, I. Smorchkova, A. C. Gossard, and U. K. Mishra, "Electron transport in III–V nitride two-dimensional electron gases," *Phys. Status Solidi B*, vol. 228, no. 2, pp. 617–619, 2001, doi: 10.1002/1521-3951.

[34] D. Jena, A. C. Gossard, and U. K. Mishra, "Dislocation scattering in a two-dimensional electron gas," *Appl. Phys. Lett.*, vol. 76, no. 13, pp. 1707–1709, 2000, doi: 10.1063/1.126143.

[35] D. Zanato, S. Gokden, N. Balkan, B. Ridley, and W. Schaff, "The effect of interface-roughness and dislocation scattering on low temperature mobility of 2d electron gas in GaN/AlGaN," *Semicond. Sci. Technol.*, vol. 19, no. 3, p. 427, 2004, doi: 10.1088/0268-1242.

[36] E. Ahmadi, S. Keller, and U. K. Mishra, "Model to explain the behavior of 2DEG mobility with respect to charge density in N-polar and Ga-polar AlGaN-GaN heterostructures," *J. Appl. Phys.*, vol. 120, no. 11, p. 115302, 2016, doi: 10.1063/1.4962321.

[37] C.-H. Chen, S. M. Baier, D. K. Arch, and M. S. Shur, "A new and simple model for GaAs heterojunction FET gate characteristics," *IEEE Trans. Electron Devices*, vol. 35, no. 5, pp. 570–577, May 1988, doi: 10.1109/16.2499.

[38] E. H. Nicollian *et al.*, *MOS (Metal Oxide Semiconductor) Physics and Technology*. New York, NY, USA: Wiley, 1982.

[39] D. K. Schroder, *Semiconductor Material and Device Characterization*. Hoboken, NJ, USA: Wiley, 2006.

[40] M. Silvestri, M. J. Uren, and M. Kuball, "Iron-induced deep-level acceptor center in GaN/AlGaN high electron mobility transistors: Energy level and cross section," *Appl. Phys. Lett.*, vol. 102, no. 7, pp. 073501-1–073501-4, Feb. 2013, doi: 10.1063/1.4793196.

[41] S. M. Sze and K. K. Ng, *Physics of Semiconductor Devices*. Hoboken, NJ, USA: Wiley, 2006.



Akanksha Rawat received the B.E. degree from the Shri Vaishnav Institute of Technology and Science, Indore, India, in 2010, and the M.Tech. degree from the Delhi Technological University, Delhi, India, in 2013. She is currently pursuing the Ph.D. degree with the Department of Electrical Engineering, IIT Bombay, Mumbai, India.

Her current research interests include device design, fabrication, and electrical characterization of III–V semiconductor-based electronic devices.



Mudassar Meer received the B.E. degree from North Maharashtra University, Jalgaon, India, in 2005, and the M.Tech. degree from IIT Guwahati, Guwahati, India, in 2009. He is currently pursuing the Ph.D. degree with the Department of Electrical Engineering, IIT Bombay, Mumbai, India.

His current research interests include the fabrication and electrical characterization of III–V semiconductor-based electronic devices.



Vivek Kumar Surana received the M.Tech. degree in solid-state electronic materials from IIT Roorkee, Roorkee, India, in 2013. He is currently pursuing the Ph.D. degree in electrical engineering with IIT Bombay, Mumbai, India.

His current research interests include device design, fabrication, and characterization of GaN-based power transistor.



Navneet Bhardwaj received the M.Tech. degree in nanoscience and technology from Kurukshetra University, Kurukshetra, India, in 2014. He is currently pursuing the Ph.D. degree with the Department of Electrical Engineering, IIT Bombay, Mumbai, India.

His current research interests include the fabrication and simulation of passive components in radio frequency integrated circuits and monolithic microwave integrated circuits.



Vikas Pendem received the B.Tech. degree from Jawaharlal Nehru Technological University, Hyderabad, India, in 2013, and the M.Tech. degree from the Council of Scientific and Industrial Research-Central Electronics Engineering Research Institute, Pilani, India, in 2015. He is currently pursuing the Ph.D. degree with the Department of Electrical Engineering, IIT Bombay, Mumbai, India.

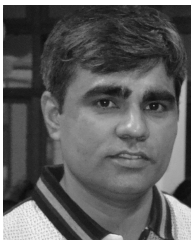
His current research interests include III-Nitride-based electronic and optoelectronic devices.

This article has been accepted for inclusion in a future issue of this journal. Content is final as presented, with the exception of pagination.



Navya Sri Garigapati received the B.Tech. degree from the Rajiv Gandhi University of Knowledge Technologies, IIT Nuzividu, Nuzvid, India, in 2014. She is currently pursuing the M.Tech. degree with the Department of Electrical Engineering, IIT Bombay, Mumbai, India.

Her current research interests include III-Nitride-based electronic and optoelectronic devices.



Yogendra Yadav received the M.Sc. degree in physics from Chaudhary Charan Singh University, Meerut, India, in 2004, and the M.Tech. degree in solid-state technology from IIT Kharagpur, Kharagpur, India, in 2009. He is currently pursuing the Ph.D. degree with the Department of Electrical Engineering, IIIT Bombay, Mumbai, India.

His current research interests include the simulation, fabrication, modeling, and electrical characterization of III-Nitride-based electronic devices.



Swaroop Ganguly received the B.Tech. degree from IIT Kharagpur, Kharagpur, India, in 1999, and the M.S.E. and Ph.D. degrees from the University of Texas at Austin, Austin, TX, USA, in 2001 and 2005, respectively.

He is currently an Associate Professor with the Department of Electrical Engineering, IIT Bombay, Mumbai, India.



Dipankar Saha received the B.E. degree from Jadavpur University, Kolkata, India, in 2001, the M.Tech. degree from IIT Bombay, Mumbai, India, in 2005, and the Ph.D. degree from the University of Michigan, Ann Arbor, MI, USA, in 2009.

He is currently an Associate Professor with the Department of Electrical Engineering, IIT Bombay. His current research interests include GaN-based electronic and optoelectronic devices.

International Journal of Research in Engineering and Innovation (IJREI)
journal home page: http://www.ijrei.com
ISSN (Online): 2456-6934

Thermodynamic analysis of combined cycle power plant with trans-critical cycle integrated with solar system for power generation for space heating and cooling

R.S. Mishra, Aakash Behl

Department of Mechanical & Production Engineering, Delhi Technological University, Delhi India

Abstract

To build up a programming code and solving it on computational numerical technique by developing energy balance equation for combine cycle power plant integrated with Trans-critical cycle. A computer programming code has been used to simulate a performance under various different conditions under different temperature and pressure circumstances and thermal performance on different cases of Brayton cycle have been analyzed using standard fluids. In this paper Brayton cycle, Rankine cycle and trans-critical cycle are combined which makes it tri-generate cycle and variations of temperature and pressure with thermal performance parameters such as thermal efficiency, exergy destructions in the various components using trans-critical cycle have been analyzed. It is observed that by increasing condenser temperature of Rankine cycle, the combined cycle efficiency , net-work are increasing and by increasing the mass flow rate of Brayton cycle, combined cycle efficiency is decreasing while combined net-work is increasing. Similarly by increasing the exit pressure of pump in the trans-critical cycle, both the combined cycle efficiency & combined net work are decreasing also is decreasing and also by increasing the inlet temperature of turbine of trans-critical cycle, the combined cycle efficiency and combined net-work is increasing. By increasing the inlet pressure of pump of trans-critical cycle, combined cycle efficiency and combined net work (i.e. both) are increasing. . © 2018 ijrei.com. All rights reserved

Keywords: Thermodynamics, Combined cycle power plant, integrated solar system

1. Introduction

The Combined cycle power plants also calls as CCPT are the combination of a gas turbine or Brayton cycle with Rankine cycle. They are designate by the high efficiency in the technology of production of electricity from fossil fuels. Simultaneously, these units are in between to the fast developing currently achieving efficiencies around 60%. Combined cycle power plants defines a number of benefits, listed as speedy construction time, mild investment costs, highly reliable and flexible. The CO_2 emission at the efficiency 0.60 is equal 330 kg--CO_2/MWh, i.e. 2 times lower than the emission from modern coal power plants (800 kgCO_2/MWh). Presently, this technology is not famous because of the high price of gas. The electric efficiency of the Brayton cycle mainly relies on the pressure ratio in the air compressor and the highest temperature in the circuit that is a Combustor Outlet Temperature (COT) of the flue gases from the combustion chamber. However, often because the most vital temperature within the rotary turbine shall be thought of the common exhaust gas temperature at the recess to the turbine, Turbine Recess Temperature (TRT).

Combined cycle power plant with the trans-critical cycle is explained here. With its combination with CO_2 trans-critical cycle it's become tri generative cycle. It has been applied in refrigeration (commercial) and heat pump water heating systems. Its cycle COP (coefficient of performance) mainly depends on high pressure optimization and control. Theoretically, the optimal high pressure increases with the increasing gas cooler outlet temp or ambient temperature. However, due to reliability and cost concerns, there is an upper limit of the high pressure in compressor design and system operation. In this work, i proposed a constrained optimization method for getting constrained optimal high pressure equation of CO_2 trans-critical cycle.

Corresponding author: R. S. Mishra
Email Id: hod.mechanical.rsm@dtu.ac.in

1.1 Combined cycle power plant

Combined cycle power plant works on two heat engines that is Brayton cycle and Rankine cycle. In order to explain the complete combine cycle power plant one need to explain the Rankine cycle and Brayton cycle separately and trans-critical cycle is also added.

1.2 The Rankine cycle

The Rankine cycle thoroughly describes the way through which team-operated heat engines largely found in thermal power generation plants for generating power. The sources used in these power plants are sometimes fission or the combustion of the fuels accessible. The power of the Rankine cycle is prohibited by the high heat of vaporization of the operating fluid. Also, unless the pressure and temperature reach to their super critical levels within the vessel, the temperature vary the cycle will operate over is sort of small: turbine entry temperatures air usually around 565°C and steam condenser temperatures air around 30°C. This low rotary turbine entry temperature (compared to a rotary turbine) is why the Rankine (steam) cycle is usually used as a bottoming cycle to recover otherwise rejected heat in combined-cycle gas turbine power plant as additionally called gas turbine power stations.

In Rankine cycle working fluid usually circulated in a close loop and keeps recycled at every initial stage. The condensed droplets of water vapour coming out form the Rankine cycle power station through the cooling tower system not actually forms closed loop. In further step addition of steam at high temperature is required for which departure of waste product form the cycle is necessary and all this happens in a closed cycle. Generally, Q_{out} is used to represent the heat coming from the exit point, it is also called as exhaust heat .Latent heat of vaporization of the working fluid is being absorbed by the cooling towers which works as a heat exchangers and simultaneously evaporating cooling water to the atmosphere. There are many substances present which can be used as working fluid but mainly water is considered as a working fluid as it is nontoxic, easily available.

Basically there are totally four process in the working of Rankine cycle which shown below in the T-s diagram of the Rankine cycle in the below parts shown in fig.2.

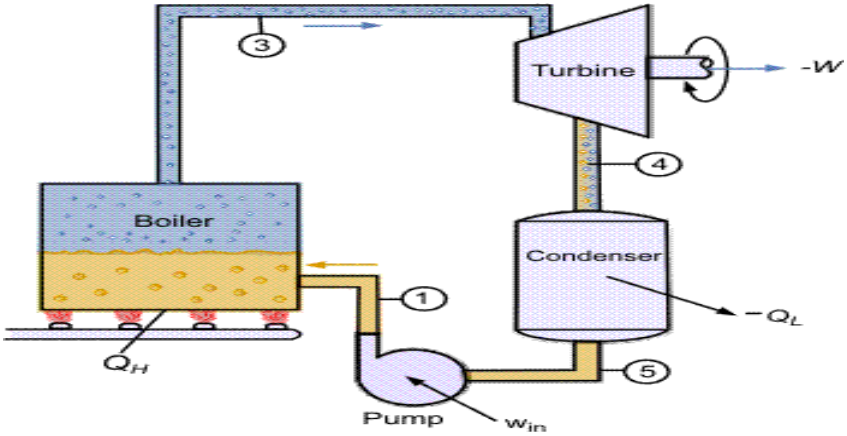


Figure 1: Basic design of Rankine cycle [1].

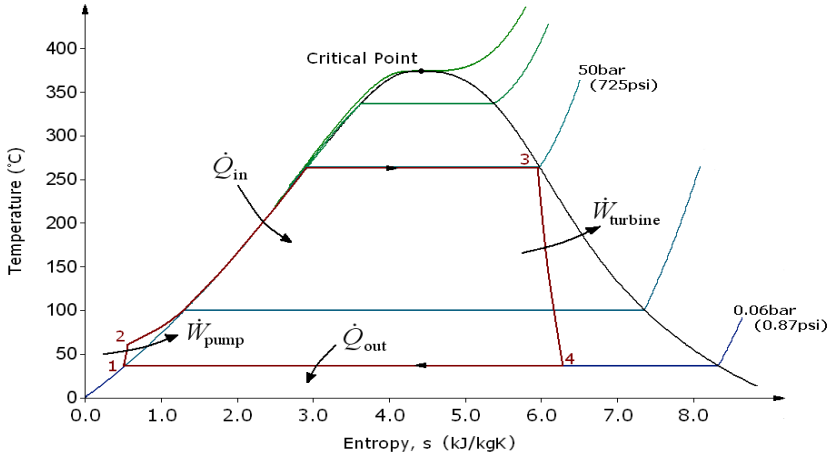


Figure 2: T-s diagram for Rankine cycle.

Process 1-2

In this process a pump is used which is shown in the Fig.2. Here pump is used to produce high pressure to the working fluid so that it can reach up to the boilers.

Process 2-3

As the working fluid reached boiler through pump, it starts getting heated through some external source so as to make working fluid as a dry saturated vapour for calculating required input energy.

Process 3-4

In this process turbine is used where expansion of dry saturated vapour takes place for the generation of power. Occurrence of condensation along with depletion of temperature and pressure is seen. Numerically using the steam tables one can calculate the outputs.

Process 4-1

Here on this process condenser is used where saturated liquid enters the condenser to condense at constant pressure.
In a perfect temperature cycle, the pump and rotary engine will be like physical property, that is no entropy will be generated by either pump or rotary engine and thus maximize output work. On T-s diagram (Fig.2), the vertical lines are used to define the process 1-2 as well as process 3-4 and additionally closely match that of the Carnot cycle. In Fig.2, it is shown that prevention of vapour ending with in the superheat region in temp unit cycle.

1.3 Brayton Cycle

The Brayton cycle is the ideal cycle for gas-turbine engines. It is used for gas turbines in which both the compression and expansion processes are implemented. There are two different types of the Brayton cycle; the open gas turbine cycles and the closed gas turbine cycle respectively. The difference between these two cycles is that during the open gas turbine cycle, a combustion process takes place, and exhaust gases are thrown out, in other words the exhaust gases cannot be recirculates, while in the other cycle (the closed gas turbine cycle), the combustion process is replaced by a heat-addition process, the exhaust gases are also utilized so as to increase the temperature of the air which enters the compressor. In Fig.3, we can see an open gas turbine. Initially, at ambient condition fresh air is taken up by the compressor, and here as a result of compressions the temperature and pressure is increased.. Here, the combustion process occurs at constant temperature. In the third process the high temperature gas enters in to turbine as you can see in Fig.3. In this operation, at atmospheric pressure gases (hot) will expand in the turbine so that power generation can take place. At last exhaust gases coming out from the turbine will move back to the heat exchanger to atmosphere.

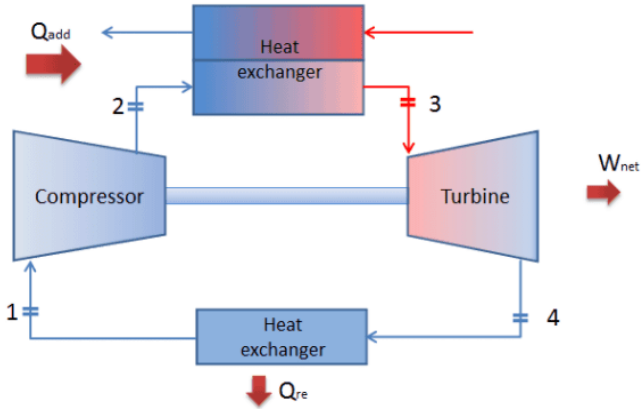


Figure 3: The Brayton cycle [3]

In the shut gas turbine cycle, in spite of the fact that the pressure and development process have in like manner, burning chamber is supplanted by a warmth exchanger in which builds the compacted air temperature. As given in Fig.3, perfect Brayton cycle is really a shut gas turbine cycle, and the means of the Brayton cycle resemble following processes.

Process 1–2

It is an isentropic compression in the compressor, in this process a pump is used which is shown in the Fig.3. Here pump is used to produce high pressure to the working fluid so that it can reach up to the boilers.

Process 2–3

It is known as constant pressure heat addition. As the working fluid reached boiler through pump, it starts getting heated through some external source so as to make working fluid as a dry saturated vapour. Graphically and numerically we can calculate the required input energy.

Process 3–4

It is an isentropic expansion in the turbine. In this process, the turbine is used where expansion of dry saturated vapour takes place for the generation of power and occurrence of condensation along with depletion of temperature and pressure is observed. Numerically using the steam tables one can calculate the outputs.

Process 4–1

It is constant pressure heat rejection, here on this process condenser is used where saturated liquid enters the condenser to condense at constant pressure.

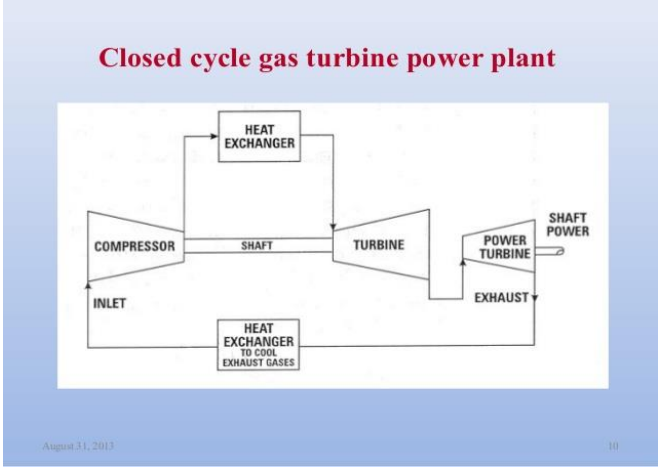


Figure 4: A closed-cycle gas turbine engine [4]

Gaseous petrol as fuel is utilized to run an open Brayton cycle, flammable gas is copied with compacted air to deliver high weight hot vent gases having temperature over 1000ºC. These gases extends in the turbine driving the generator and the fumes gases are utilized as a fuel in squander warm recuperation kettle or warmth recuperation steam generator. The superheated steam at that point drives the turbine therefore creating extra power alongside the power delivered from Brayton cycle. Once in a while the turbine from both the cycles is in single shaft and they together drive the generator to deliver power, for the most part the two turbines have their own particular generator. The gas turbine is a standout amongst the most productive one for the change of gas powers to mechanical power or power. The utilization of distillate fluid powers, generally diesel, is likewise normal as exchange energizes. All the more as of late, as straightforward cycle efficiencies have enhanced and as petroleum gas costs have fallen, gas turbines have been all the more generally embraced for base load control age, particularly in consolidated cycle mode, where squander warm is recouped in squander warm boilers, and the steam used to deliver extra power. They are installed around the world. Consolidated cycle control plant as in name recommends, it joins existing gas and steam innovations into one unit, yielding noteworthy changes in warm proficiency over traditional steam plant. Anyway the warmth recouped in this procedure is adequate to drive a steam turbine with an electrical yield of roughly 50 for every penny of the gas turbine generator. The gas turbine and steam turbine are coupled to a solitary generator. For start-up, or 'open cycle' task of the gas turbine alone, the steam turbine can be detached utilizing a pressure driven grasp. As far as general speculation a solitary shaft framework is regularly around 5 for every penny bring down in cost, with its working straightforwardness ordinarily prompting higher unwavering.

1.4 Carbon dioxide Trans-critical Power Cycle

The current study conjointly focuses on the trans-critical cycle due to its high potential usage within the trade and thanks to the restricted studies found within the literature. The trans-critical cycle, whose heat rejection takes place at a subcritical pressure, should not be confused with the entirely critical cycle.

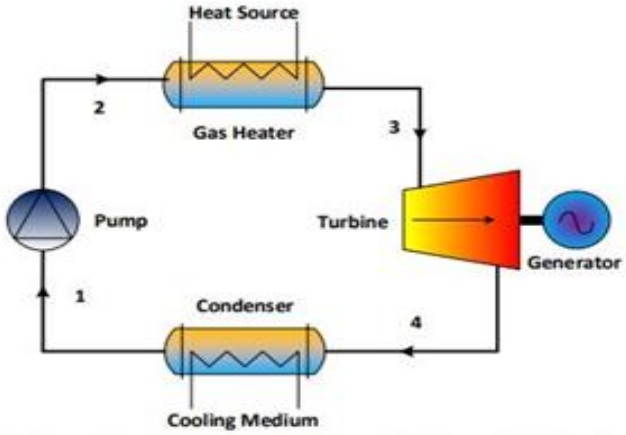


Figure 5: The trans-critical cycle [5]

Actually, coal pink-slipped trans-critical power plants at high temperatures (above five hundred °C) represent a mature technology and among the most effective playing heat engines with a thermal potency as high as forty ninth .As way because it is understood the dioxide are going to be thought-about as trans-critical cycle wherever the temperature is on top of vital temperature i.e., 31 °C. For trans-critical carbon dioxide because it is portrayed in Fig.6 and therefore the T-S diagram in Fig.6 same as Brayton cycle the trans-critical dioxide cycle can expertise processes: compression (1-2), isobaric heat provide (2-3), growth (3-4), and isobaric heat rejection (4-5). The sole distinction between these 2 cycles is whether or not a part of the cycle is found within the subcritical region or not. Therefore, each cycle' generally associated with critical cycles within the literature.

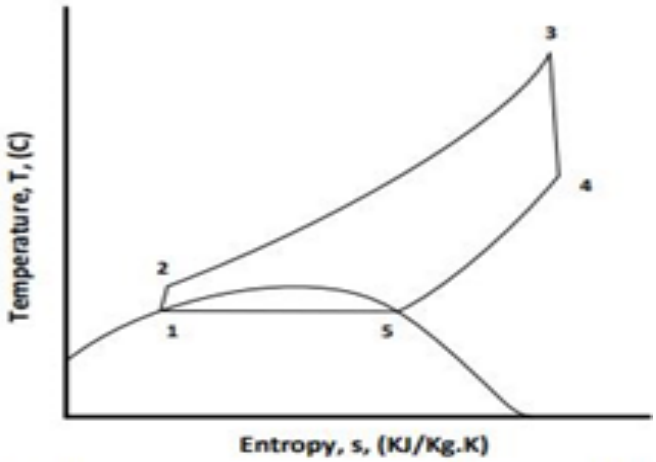


Figure 6: T-S Diagram of Trans-critical Cycle

The energy analysis relies on the primary law of physics. The thermal potency and therefore the specific internet output ar its results. With the assumptions antecedent explicit, their values rely solely on one freelance parameter: the air mass, that ar P2=P3. Above all, these results don't depend upon the operating fluid mass rate. The equations for the various parts. For the pump: $\eta_p = (h_2,s-h_1)/ (h_2-h_1)$ wherever the η_p is that the potency of the pump, h_1 is that the specific physical property of the pump recess fluid, h_2 is that the physical property of pump outlet fluid and $h_{2,s}$ is that the physical property physical property of outlet fluid. $w_p = h_2 - h_1$ wherever the w_p is that the work of the pump, $h_1$is the particular physical property of the recess fluid and h2 is that the physical property of outlet fluid. For the turbine: $\eta_t = (h_3-h_4)/ (h_3-h_{4,s})$ wherever the η_t is that the potency of the rotary engine, h3is the particular physical property of carbon dioxide at the rotary engine recess, h_4 is that the physical property of outlet fluid and h4,is is that the physical property physical property of outlet fluid. $w_t = h_3 - h_4$ wherever the w_t is that the work of the pump, $h_3$is the particular physical property of the rotary engine recess fluid and h_4 is that the specific physical property of outlet fluid. For the vapor generator: $q_{in} = h_3 - h_2$ wherever the q_{in} is that the heat transferred to the fluid in vapor generator, h_2 is that the specific physical property of the warmer recess fluid and h_3 is that the physical property of outlet fluid. For the condenser: $q_{out} = h_4 - h_1$ wherever the $q_{_out}$ is that the heat rejected from the operating fluid in condenser, h4is the physical property of the fluid coming into the condenser and h1 is that the physical property exiting of fluid deed the condenser. The thermal potency of the cycle:

$$\eta_{th} = [(W_t-W_p)/ q_{_in}] = [(h_3-h_4)-(h_2-h_1)/ (h_3-h_2)]$$

wherever the $\boldsymbol{\eta_{th}}$ is that the thermal potency of the cycle, w_t is that the rotary engine work, W_p is that the pump work and q_{in} is heat transferred to the operating fluid in warmer. In compare with associate degree organic Jeannette Rankin cycle (ORC), the carbon dioxide trans-critical power cycle encompasses a higher capability in taking blessings of the energy during an inferior waste heat with gradient temperature, like exhaust gases. The temperature glide (Temperature modification throughout take-up of warmth energy) for carbon dioxide on top of the crisis permits for an improved.

1.5 Turbine Cycle

An ignited mixture of a natural gas and air which is purified and a later on compressed makes it to expand. Spinning of a turbine blades took place due to a pressure created form expansion process, for creating electricity ay are attached with a generator as well as shaft. In further second step a generation of steam is done by utilizing a heat of gas turbine from exhaust and make it to through a heat recovery steam generator (HRSG).

1.6 Heat Recovery Steam Generator

In HRSG that stands for Heat Recovery Steam Generator is known for water flow in a tube and a flow is extremely purified and around am passing of a hot gases occurs and therefore ay produce steam .In a steam turbine rotation of steam occurs and concatenate with a generator for a production of Electricity.A steam condensing and water system is a same as in a steam power plant.

1.7 Typical Size and Configuration of CCGT Plants

Rankine and Brayton cycle combines to form a combined-cycle. It includes different configuration for shafts such as multi shaft configuration and single shaft configuration. Single-shaft systems constitute of one - one unit of each gas turbine, steam turbine, generator and Heat Recovery Steam Generator (HRSG), with a gas turbine and steam turbine concatenate to a single shaft of a single generator. Areare one or more generator in multi turbines and HRSGs to a separate single steam turbine-generator steam is supplied through it.
A chief demerit of multiple stage combined cycle power plant is that a number of steam turbines, condensers and condensate systems-and perhaps a cooling towers and circulating water systems increases to equalise a quantity of gas turbines.

1.8 Efficiency of CCGT Plant

It is essential to use a parts of a exhaust energy through gas to gas healer after a combination of Rankine cycle and a bray ton cycle, achievement of low temperature at output and high temperature at a input can be done. A efficiency of a cycles will sum up with it, as same fuel source powered am. A power of CCPT is filled by Supplementary Firing and Blade Cooling. At HRSG supplementary firing was organised and a flow of compressed gas flow is being carried out in a turbine area of a rotary engine and it was mainly opted for a cooling down of a turbine blades.

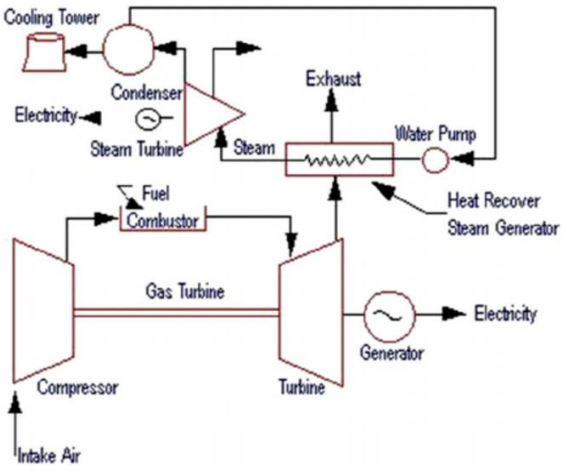


Figure 7: Combined Cycle Gas Turbine Plant HRSG [6]

1.9 Combined cycle integrated with solar system

PTS called as a parabolic trough solar energy plant. Ay are a most vital establishment of a CSP that is concentrating solar energy technique. SEGS that is PT star electricity producing technique system shows that a tendency of this present technique found to be more trust worthy as well as renewable resource. This method usually adopted on a commercial scale on large scale with some around output of 345MW. For satisfying a increasing demand for a energy resource, CSP are found to be a most promising technology. It has been seen that only CSP can fulfil a demand of energy for developing countries. Electricity produce by a CSP with in a MENA (Mediterranean & geographical region) wants to improvise a native energy production system. Trans Mediterranean renewable energy cooperation introduced a energy cooperation. ISCC is one of a most important system. It stands for integrated solar combine cycle; PTT that is parabolic trough technology is said to be coupled whenever it is supported by a star field. Are is no need to install a storage source for a backup of fuel for boilers because of a flexibility in operation and reduction in value of a system. Here a mathematical codes are built for a integrated solar combine cycle that is ISCC powerhouse operational below weaar conditions. Habib (1994)[1] presented an analysis of a cogeneration system, which quantified the irreversibility of the different components of each plant. In addition to that, the influence of the heat-to-power ratio and the process pressure on the thermal efficiency and utilization factor is presented. His results show that the total irreversibility of the cogeneration plant is 38 percent lower compared to the conventional plant. This reduction in the irreversibility is accompanied by an increase in the thermal efficiency and utilization factor by 25 and 24 percent, respectively. The results show that the exergy destruction in the boiler is the highest. Bejan, et al (1996)[2] actually provided a comprehensive and rigorous introduction to thermal system design and optimization from a contemporary perspective. The book includes current developments in engineering thermodynamics, heat transfer, and engineering economics relevant to design. The use of exergy analysis and entropy generation minimization is featured. A detailed description of engineering economics and thermo economics are also presented. Moreover, a case study is considered throughout the book for continuity of the presentation. The case study involves the design of a gas turbine cogeneration system. Rolf Kehlhofer (1997) [3] provided the study of thermodynamic principles of combined cycle power plants and co-generation system. His work includes the different layout system of combined cycle power plants. It describes the effect of operating variables and part load behavior of combined cycle power plants. Karthikeyan et al (1998) [4] derived energy balances for a one pressure level heat recovery steam generator. Effects of pinch and approach points on steam generation and also on temperature profiles across heat recovery steam generator was investigated. The effects of operating conditions on steam production and also on exit gas temperature from the heat recovery steam generator are discussed. It is concluded that low pinch point results in improved heat recovery steam generator performance due to reduced irreversibility's. Additionally, the supplementary firing enhances the steam production. Tawney, et al. (2000)[5] focused on several ranges of process steam flows and conditions in order to provide a basis for comparison of the most common cycle configurations in combined cycle applications. Plant design, cycle performance, and economics of each configuration are evaluated based on requirements of flexibility and process steam flows. Rather than self-establishing the energy balances, Gate Cycle TM Heat Balance software developed by GE Enter Software, Inc. is used to build thermal models. Additionally, a financial software tool developed within Bechtel is used to construct an economic model for each cycle configuration. It is concluded that, the selection of a cogeneration facility type and the economic parameters are very much site specific and are based on numerous variables such as site ambient conditions, the level of desired power output and steam demand, capacity factor, flexibility, power purchase agreement and steam purchase agreement requirements, and owner's economic parameters for return on equity. Boyce (2002) [6] covered all major aspects of power plant design, operation, and maintenance. It covers cycle optimization and reliability, technical details on sizing, plant layout, fuel selection, types of drives, and performance characteristics of all major components in a cogeneration or combined cycle power plant. Comparison of various energy systems, latest cycles and power augmentation techniques, reviews and benefits of latest codes, detailed analysis of available equipment, techniques for improving plant reliability and maintainability, testing and plant evaluation techniques, and advantages and disadvantages of fuels. ET. Bonataki and K.C. Gianna Koglou (2002) [7], gave a modern optimization methods based on evolutionary algorithms and game theory. They will be supported by computational methods for their thermal analysis and simple model for computing there capital cost. In this paper a detailed thermal model and a quite simple economic model will be incorporated in an evolutionary search algorithm and an automated tool combine the design of new cycle gas turbine power plant will be demonstrated. The search algorithm is used a Genetic Algorithm (GA) for single and multi-objective optimization problems. The latter is handled through game theory inspired enhancement to the G.A. based search yielding the so called optimal Pareto front, with two objectives (via electrical efficiency and investment cost), the Pareto front members can be envisaged as compromise between high cost/high efficiency and low cost/low efficiency design. Neil Petchers (2003) [8] provided a comprehensive details of thermal system design from a contemporary perspective. First part of the book provide a theoretical basis for understanding the inter relation of heat and power resources. It 18 provides and introduction to basic heat and power thermodynamic and includes sections on heat and power generation technologies and equipment. Part seconds describe the infrastructure in which the theory and technologies describe in part first must be applied. Having learned on the

theory and available technology, application cannot be effective device, analysis' for cost effectiveness and implemented without knowledge of environmental factors and utility rate structures. Yongjun Zhao, et al (2003) [9], investigated the design and cost of HRSG system and to demonstrate impact on the overall cost of electricity (COE) of a combined cycle power plant. There are numerous design parameter that can affect the size and complexity of the HRSG, and it is the plan for the project to identity all the important parameter and to evaluate each the exhaust gas pressure drop across the HRSG is chosen for evaluation. This parameter affects the performance of both the gas turbine and steam turbine and size of HRSG. Single pressure, two pressure, and there pressure HRSG are investigation with the trade-offs between design point size, performance and cost evaluated for each system. A genetic algorithm is used in the design optimization process to minimize the investment cost of the HRSG second system level metrics' are employed to evaluate a design. They are gas turbine net power, steam turbine net power, fuel consumption of the power plant, net cycle efficiency of the power plant, HRSG investment cost, total investment cost of the power plant and the operating cost measured by the cost of electricity (COE), The impacts of HRSG exhaust gas pressure drop and system complexity on these system level metrics are investigated. Zaleta-Aguilar Alejandro (2003)[10],represented the proposed exergo-economic fuel-impact models for steam turbines in power plants. They are applied to calculate the impact on the steam cycle when malfunctions are occurring during the operation of steam turbine sections. Concepts such as the exergetic consumption and the dissipation temperature are used to understand the proposed fuel-impact analysis. In order to validate these fuel-impact methods, well-known procedures, to simulate on and off-design conditions of a steam power cycle are used as references. Chih Wu, (2004) [11] provided an intelligence computer software called "cycle pad". It is powerful, mature, user friendly package developed to simulate thermodynamic devices and cycles. It makes feasible for engineers to run meaningful sensitivity analysis to consider combinations of design modifications to make engineering cost benefit analysis and to include refinements such as accounting for pressure changes and heat transfers occurring between major cycles components. Yadav, et al (2004)[12] mainly focused on to development of gas turbine related power plants such as combined 20 Mitre, et al (2005), In his paper, author evaluates the effect of operational conditions on pollutants (co, co2, so2, No) emissions levels, waste heat and waste water of a combined cycle natural gas and steam power plants. The HYSYS process simulation was used for modeling and simulation. This study clearly shown that the absolute quantity of pollutants emitted is high. Also it was possible to verify that the unit operation in the condition of minimal emissions regarding the maximum possible, and thus a reduction or elimination of such pollutants is not possible. It can be observed from this study that the ideal condition for exergy productivity is to operate with a fuel air ratio as the stoichiometric one. The first constraints to this ideal is the mechanical conditions of the turbine, which can be operate at the corresponding combustion gas exit temperature so a stoichiometric ratio in the range of (2.7-2.9) is used, and these conditions make the process viable (turbine viability) and minimize pollutants production (CO and NOx). These operational conditions are the optimal considering environmental concerns. The CO2 being a product, is maximized in the process, so there is no need to search for methodologies to minimize their production, but there is for technologies for their capture and uses parallel to the process. Xiaojun Shi and DefuChe (2007)[13]proposed an improved Liquefied Natural Gas (LNG), fuelled combined cycle power plant with a waste heat recovery and utilization system. The proposed combined cycle, which provide power output and thermal energy, consist of gas/steam combined cycle, the subsystem utilization the latent heat of spent steam from the steam turbine to vaporize LNG, the sub system that recovers both the sensible heat and latent heat of water vapour in the exhaust gas from heat recovery steam generator (HRSG), by installing a condensing heat exchanger, and the HRSG waste heat utilization sub system. The conventional combined cycle and proposed combined cycle are modeled, considering mass, energy and exergy balances for every component and both energy and exergy analysis are conducted. Parametric analysis are performed for the proposed combined cycle to evaluate the effect of several factors, such as the gas turbine temperature (TIT), the condenser pressure, the pinch point temperature different of the condensing heat exchanger and fuel gas heating temperature on the performance of the proposed combined cycle through simulation calculation. The results show that the net electrical efficiency and the exergy efficiency of proposed combined cycle can be increased by 1.6% and 2.84% than those of the conventional combined cycle 21 respectively. The heat recovery per kg of flue gas is equal to 86.27 kJ/sec. one MW of electric power for operating sea water pumps can be saved. The net electric efficiency and heat recovery ratio increase as the condenser pressure decreases. The higher heat recovery from HRSG exit flue gas is achieve at higher gas TIT and at lower pinch point temperature of condensing heat exchanger. Srinivas, et al (2008) [14].studied the optimum configuration for single pressure (SP), dual pressure (DP) and triple pressure (TP) heat steam generator (HRSG) to improve heat recovery and exergy efficiency of combined cycle. Deaerator was added to enhance efficiency and remove dissolve gases in feed water. A new method was introduced to evaluate low pressure (LP) and intermediate pressure (IP) in HRSG from local flue gas temperature to get minimum possible temperature difference in heaters instead of a usual fixation of pressures. Optimum location for deaeraor was found at 1, 3, and 5 bar respectively for SP, DP and TP in heat recovery at a high pressure (HP) of 200 bar. It is concluded that optimum pressure ratio for compressor with SP, DP and TP effects in heat recovery are 8, 10 and 12 respectively at 12000 C of gas turbine inlet temperature optimum deaerator pressure is obtained at 1.3, and 5 bar for SP, DP and TP levels respectively at steam turbine inlet pressure of 200 bar. Similarly at 200 bar of HP pressure for DP and TP, steam

reheated demands 100 bar to maximize exergy efficiency for combustion chamber. Parametric analysis exhibits that gain in efficiency from single pressure heat recovery to DP and TP recovery increasing with diminishing rate. J.Li, G.Pei, Y.Z.Li, J.Ji[15] find out that with the reducing of the Organic Rankine Cycle (ORC), the engine shaft power isn't solely determined by the enthalpy drop by the expansion method however additionally the external heat loss from the expander. Theoretical and experimental support in evaluating tiny scale expander heat loss is rare. This paper presents a quantitative study on the convection, radiation and conductivity heat transfer from a kW-scale expander. A mathematical model is constructed and valid. The results show that the external radiative or convective heat loss constant was regarding 3.2 or 7.0 W/m2K once the ORC operated around 100ºC. Radiative and convective heat loss coefficients enhanced because the expander operation temperature enhanced. Conductive heat loss because of the affiliation between the expander and also the support accounted for an oversized proportion of the warmth loss. The fitting relationships between heat loss and mean temperature distinction were established. It's recommended that low conduction material be embodied within the support of expander. Mattress insulation for compact expander may be eliminated once the operation temperature is around 100ºC. V. Lemort et al. [16] had presented the results of an experimental study administered on a model of an open-drive oil-free scroll expander integrated into an ORC operating with refrigerant HCFC-123. By exploiting the expander performance measurements, the eight parameters of a scroll expander semi-empirical model are then known. The model is ready to calculate variables of 1st importance like the mass rate, the delivered shaft power and also the discharge temperature, and secondary variables like the availability heating-up, the exhaust cooling-down, the close losses, the interior escape and also the mechanical losses. The utmost deviation between the predictions by the model and also the measurements is two hundredth for the mass rate, 5-hitter for the shaft power and 3K for the discharge temperature. The valid model of the expander is finally wont to quantify the various losses and to point how the planning of the expander can be altered to realize higher performances. Kosmadakis et al. [17] suggested the constant theoretical study of a 2 stage solar Rankine cycle for Ro distillation. The current work issues the constant study of an autonomous 2 stage solar ORC for Ro desalinization. The most aim is to estimate the efficiency similarly on calculate annual energy out there for desalinization. Aleksandra & Borsukiewicz[18]suggested pumping within Rankine cycle and created calculation based mostly result for the pumping work on ORC. Analysis has been administrated for eighteen completely different organic fluids that may be used an operating fluids within the subcritical ORC system. A trial was created to search out correlations between numerous thermo-physical properties of operating fluids, specific work and power of cycle. Kim, Y.M., C.G. Kim, and D. Favrat[19]Every year, the sun irradiates the landmasses on earth with the equivalent of 19,000 billion tons of oil equivalent (toe). Only a fraction (9 billion toe) would satisfy the world's current energy requirements. Put differently, in 20 minutes, the amount of solar energy falling on the earth could power the planet for one year. Chen, H., [20] Solar ponds are large-scale solar thermal energy collectors, which are pools filled with saltwater with a density gradient from the bottom to the top. A solar pond combines heat collection and storage. With a 20°C ambient temperature, the thermal energy obtained from the solar ponds is in the form of low-grade heat at 70 to 80°C. There are low-, medium- and high- temperature solar thermal collectors, depending on their collecting temperature.

2. System Description

2.1 Solar thermal power plants

A sun unendingly provides a vast quantity of energy. As a result of a character of this energy, which is opened up, it has to be collected and targeted to be useable. Are square measure several applications and techniques wherever solar power is utilized. In star thermal power plants, solar power is absorbed as heat that is a re-modelled into electricity. Re-modelling thermal solar power to electricity may be conducted by completely different approaches. A foremost common techniques square measure concentrating alternative energy (CSP) plants and also a star chimney. CSP techniques are: star tower, parabolic dish and parabolic trough. With a star chimney, a radiation is born-again to mechanical energy by heating a air in an air solar dish (greenhouse). A heated air is allowed to flow through a chimney settled at a center of a solar dish. A buoyancy force of a air causes flow through a chimney. A flowing air drives a rotary engine that is fastened at a doorway of a chimney to come up with electricity. A star chimney consists of a solar dish or greenhouse, high created chimney and rotary engine. A storage system will be used mistreatment this method to stay a plant engaging at night-time. A straightforward idea of its storage system is to fabricate water storage to a lower place a absorbent material plate of a star collectors. This technology blessings are; it makes use of beam and diffuse radiation therefore it's able to work throughout cloudy periods, it will work twenty four hours if a storage system is utilized, a desired materials to construct it straightforward and offered in most regions of a globe, and Are’s no want for cooling water systems, therefore it's appropriate for arid locations.

.

2.2 Concentrating Solar Power (CSP) plants

CSP plants provide high temperature energy that’s employed to work standard potency cycles like a Stirling engine. Though solar power concentrated plant square measure utilized largely for production of electricity, ay could be employed in several industrial exercise. Fig.8 depicts various practice for CSP systems. One in every foremost necessary conditions for selecting a foremost appropriate method for planned exercise is that an operative temperature.



Figure 8: CSP applications India [9]

2.3 Solar Tower

This method gives a boosted magnitude relation of radiation concentration that permits star towers to realize that for heating of an air high temp is required. Depicted in a Fig. 9. The system of tower consisting a reflectors of heliostat settled in spherical array round a star adopter. Position of a sun being tracked by a reflector to make sure leading a daylight to a adopter. Medium of transfer of heat is employed within aadopter for soak up a focused alternative energy. Rejected heat is provided to work up aarmal power station. Warmth fluid transfer within a central adopter may be air &wateer, melted salt or oils. Analysis releases this method may b accustomed workup of turbine wherever air is pressurized initial so het up within a receiver to a thousand. star tower among a evidenced CSP technologies within a field.. Air capability is ten MWe every

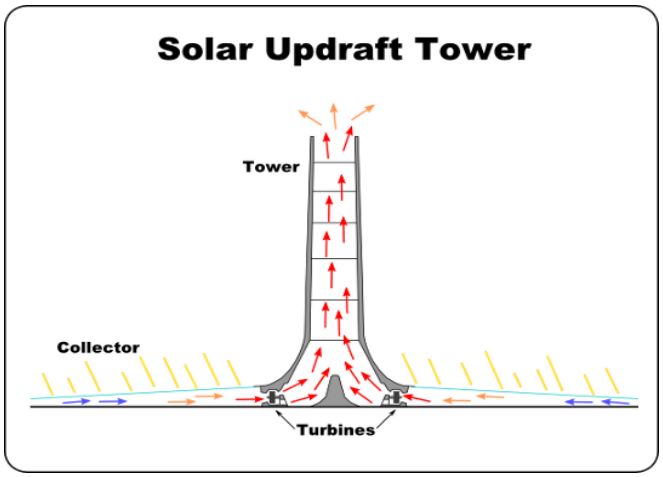


Figure 9: Solar draft (solar tower)[24]

2.4 Parabolic dish-engine

Ground level construction such method is about usage of dish having parabolic shape to focus radiations on a generator of engine within center of attention of a reflector. Under consideration of potency, umbrella dish is that a best technology among star techniques, its highest potency may be a maximum amount of twenty ninth. As you can see in fig.10. A standard umbrella dish having radius variation from five to fifteen m with five to twenty five powers. It is appropriate for redistributed potency provide and unpopulated area by taking this technique.

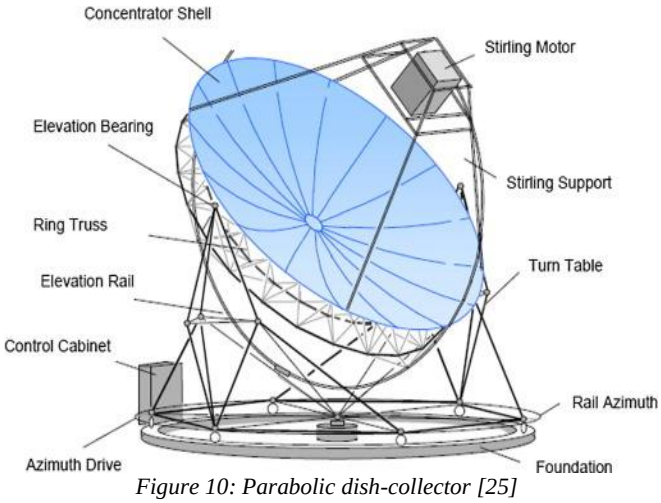


Figure 10: Parabolic dish-collector [25]

2.5 Liner Fresnel system

Setup actually have associate array of liner reflectors. A absorbent tube that is homeward on a focused radiation being

received by the focal line of the reflector and converts a sun potency to heat. Fig.11 depicts Augustin Jean Fresnel system parts. H T fluid is employed to soak up this energy to be employed in a planned application. This sort of collector offers sensible prospects for solar power use and it's appropriate for small- and large-scale applications. Some prototypes are tested. Its operation temperature was two hundred °C, its dimensions were sixteen m long × four m high and it consisted of eleven primary reflectors.

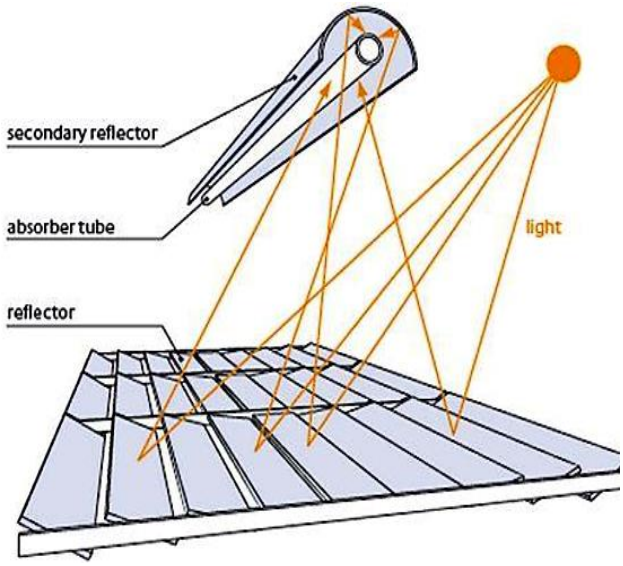


Figure 11: Linear Fresnel system [26]

2.6 Parabolic trough system

A distinction among this technique and hence a Liner Augustine Jean Fresnel system is parabolic trough system utilizes umbrella shaped formed reflectors. A concentration ratio will around eighty or additional .In absorber tube collected energy oh HT fluid will run. Parabolic trough technique provides energy at a temperature of up to 400°C. This energy is provided to run either a straightforward Jeannette Rankin cycle or hybrid system. A warmth transfer fluid that is employed to soak up warmth will be either water or artificial oils. Fig.12 depicts parabolic trough system components.

2.7 Parabolic trough solar power plants

Under this topic an operation eventualities &hence a totally different installation configuration for parabolic trough systems square measure described. Additionally, as this technique utilizes a sun following system, a used following system is in brief mentioned.

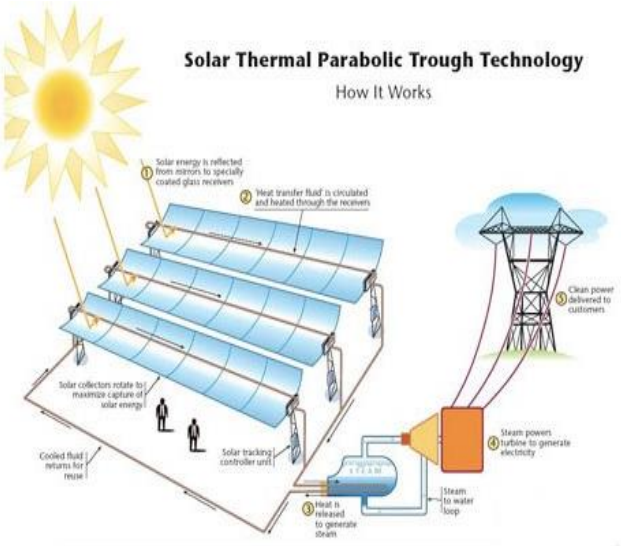


Figure 12: Parabolic trough system [27]

2.8 The sun chase system

Homeward-bound rotational axis, wherever collectors area unit. A system unceasingly drives collectors from east at sunrise to west at sunset. Little motors area unit accustomed drive this chase system. Fig.13 depicts solar furnace system concept. Since solely direct radiation is focused PTS utilizes a sun chase system for confirm most potency of a concentrating method

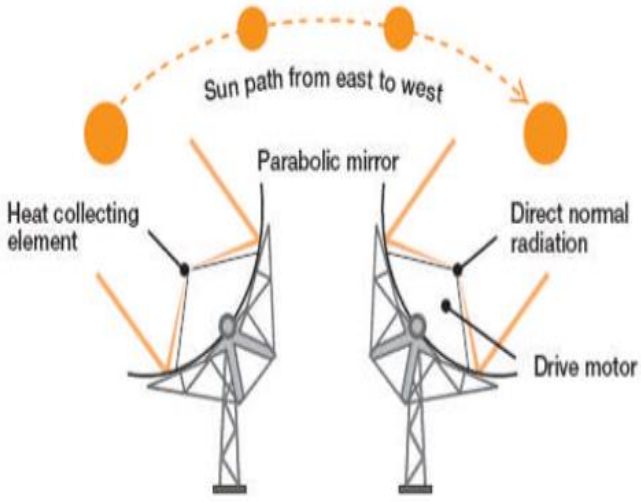


Figure 13: The sun chase system [28]

2.9 Solar desalinization

A potential of victimization star PTS in H_2O desalinization, wherever a star field is attached to water desalinization like multi-stage flash distillation (MSF) or multi impact

distillation. Below Fig. 14 depicts solar desalinization.

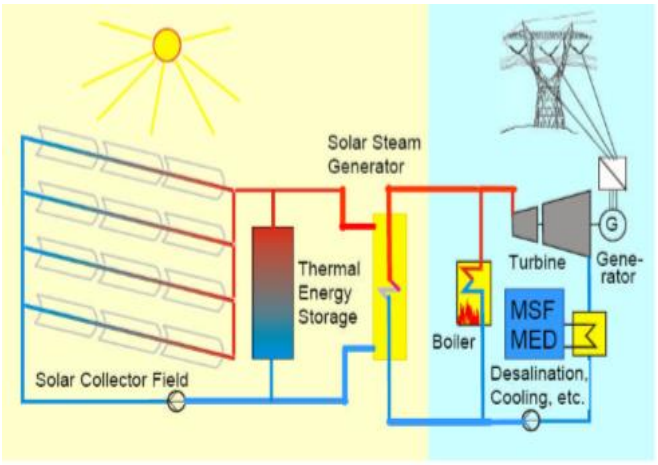


Figure 14: Solar desalinization [29]

2.10 Integrated solar combined cycle

An ISCC system may be a combination of a star field and gas turbine-combined cycle. A waste heat from a turbine is employed to come up with some steam to be distended during a turbine. Additionally, a star field provides further heat to a thermal cycle. An extra heat from a star field ends up in electricity generation increase throughout daylight time. This mixture ends up in up a thermal potency. A advantages of using this technology are to beat some issues associated with start-up and close up in alternative energy plants, scale back a cost of capital and improve a solar-to-electricity potency. Below Fig. 15 shows ISCC.

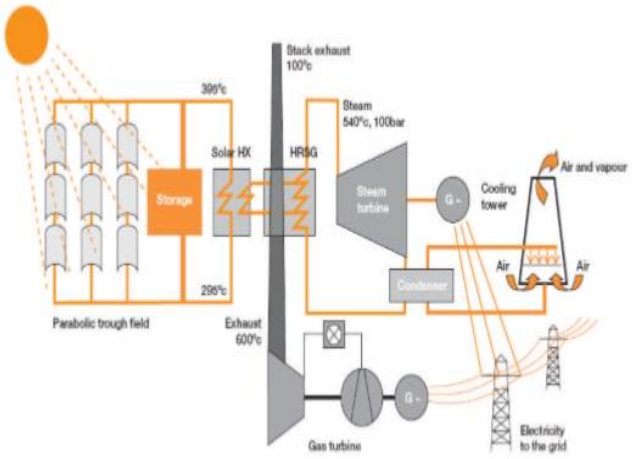


Figure 15: Integrated solar combined cycle [30]

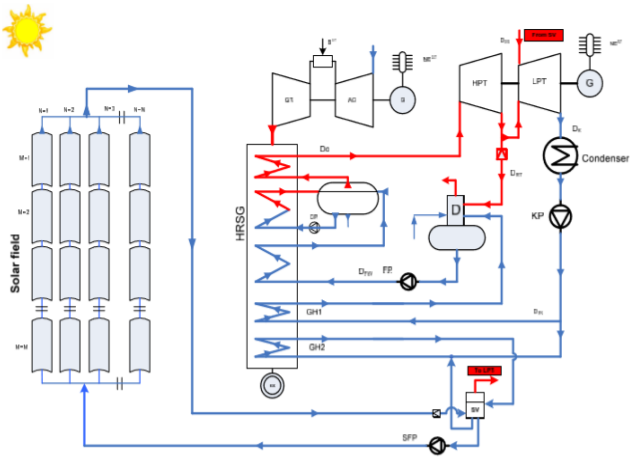


Figure 16: The proposed design for ISCC [31]

2.11 The proposed design

A planned style of a ISCC is shown in Fig.16. Its associate integration between a traditional combined cycle station (gas & steam turbine) and star field, supported a parabolic trough solar furnace. HRSG is one in every of a CC parts. It's wont to recover a warmth loss from a turbine exhaust gases. Most advanced electricity generation gas turbines area unit capable of being connected to heat recovery units. A most parts of a planned ISCC are: turbine unit, HRSG, turbine unit, and star field supported parabolic trough technology.

A turbine unit is that a major energy resource for a political leader cycle. HRSG that could be a device won't to recover heats from high temp. Gases streams (used with gas turbines). The HRSG consists 3 main sections, i.e. superheating section, evaporator & saver. The saver will pump up the feed water temp. To the saturation temperature to recover the max amount heat as potential from the gases stream. Then the steam generator (evaporator) converts the feed water to saturated steam at the HRSG drum's pressure. The superheating section will increase the steam temperature to the required temperature (HRSG, 2007). The projected style includes victimization 2 gas heaters. The primary warmer GH1 preheats water within the HRSG. Additionally an evaporator is employed within the HRSG to come up with some steam to produce some energy

3. Mathematical analysis of the integrated solar combined cycle

An approach wont to investigate various parts of a ISCC powerhouse is described. It includes a physics analysis of main objectives.

3.1 Combined cycle thermodynamics analysis

In an ISCC cycle a sole objective of analyzing a gas turbine unit. It is about to enumerate the energy's wastage in terms of gases at the exit. Under this section we will try to examine the performances of the cc that is combustion chamber,

performance of turbine, and last, compressor.
The equation for heater/heat exchanger of Brayton and Rankine cycle:

$Q_{hex} = \dot{m}_b(h_{4,b} - h_{1,b}) = \dot{m}_r(h_{1,r} - h_{4,r})$ (1)
The equation of the expander of Brayton cycle:
$n_{T,s} = h_2 - h_1 / h_3 - h_1$ (2)
$W_T = \eta_T*(h_1 - h_2)$ (3)
Where $\eta_T$is the mechanical efficiency of expander.
The equation of condenser of trans-critical cycle:
$Q_{cond} = \dot{m}(h_4 - h_1)$ (4)
The equation of fluid pump of Rankine cycle:
$W_{pump} = h_4 - h_3$ (5)
The work of turbine of trans-critical cycle.
$W_T = h_3 - h_4$ (6)
The work of turbine of Rankine cycle
$W_T = h_{1,r} - h_{2,r}$ (7)
The work of pump of trans-critical cycle.
$W_C = h_2 - h_1$ (8)
The work of pump of Rankine cycle
$W_P = h_{4,r} - h_{3,r}$ (9)
Equation for the net system output:
$W_{sys} = W_{NET,Rankine} + W_{NET,Brayton} + W_{NET,transcritical}$ (10)
Equation for finding the cycle thermal efficiency:
$\eta_{th} = W_{sys}/Q_{hex}$ (11)

3.2 Exergy Analysis

Economizer

$E_{rev,EC,b}=m_{,dot,b}*((h_{bv}-h_{5,b})-T_{amb}*(s_{bv}-s_{5,b}))$
$E_{rev,EC,r}=m_{dot,r}*((h_{4,r}-h_{rv})-T_{amb}*(s_{4r}-s_{rv}))$
$E_{rev,EC,total}=E_{rev,EC,b}+E_{rev,EC,r}$
(Total exergy in Economizer)

Heater

$E_{rev,HE,b}=m_{_dot_b}*((h_{bs}-h_{bv})-T_{amb}*(s_{bs}-s_{bv}))$
$E_{rev,HE,r}=m_{dot,r}*((h_{rv}-h_{rs})-T_{amb}*(s_{rv}-s_{rs}))$
$E_{rev,HE,total}=E_{rev,HE,b}+E_{rev,HE,r}$
(Total exergy in Heater)

Super heater

$E_{rev,SH,b}=m_{_dot,b}*((h_{4,b}-h_{bs})-T_{amb}*(s_{4,b}-s_{bs}))$
$E_{rev,SH,r}=m_{dot,r}*((h_{rs}-h_{1,r})-T_{amb}*(s_{rs}-s_{1,r}))$
$E_{rev,SH,total}=E_{rev,SH,b}+E_{rev,SH,r}$
(Total exergy in Super Heater)

Overall hex

$E_{rev,HEX,b}=m_{_dot,b}*((h_{4,b}-h_{5,b})-T_{amb}*(s_{4,b}-s_{5,b}))$
$E_{rev,HEX,r}=m_{dot,r}*((h_{4,r}-h_{1,r})-T_{amb}*(s_{4,r}-s_{1,r}))$

The exergy in Overall Heat Exchanger is given by following expression
$E_{rev,HEX},total=E_{rev,HEX,b}+E_{rev,HEX}$

4. Result and Discussion

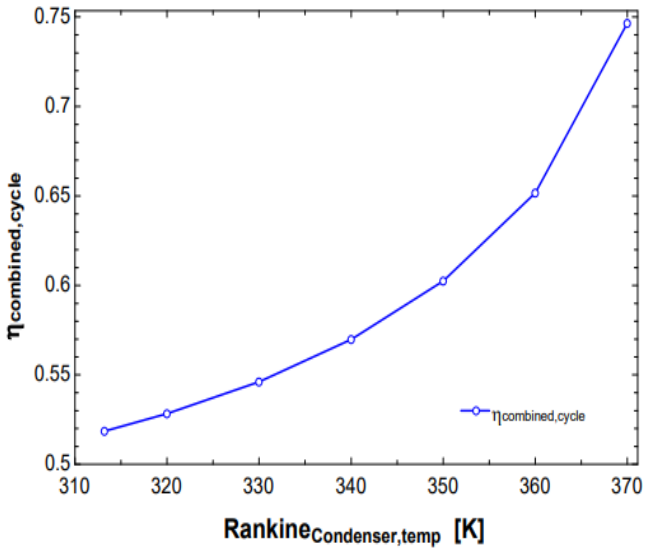


Figure 17: Variation between combined cycle efficiency and condenser temperature of Rankine Cycle

Fig. 17 shows the variation between combined cycle efficiency and condenser temperature of Rankine Cycle. It can be seen that on increasing the condenser temperature, efficiency is also increasing. The combined cycle efficiency is 56.98% at condenser temperature 340K.

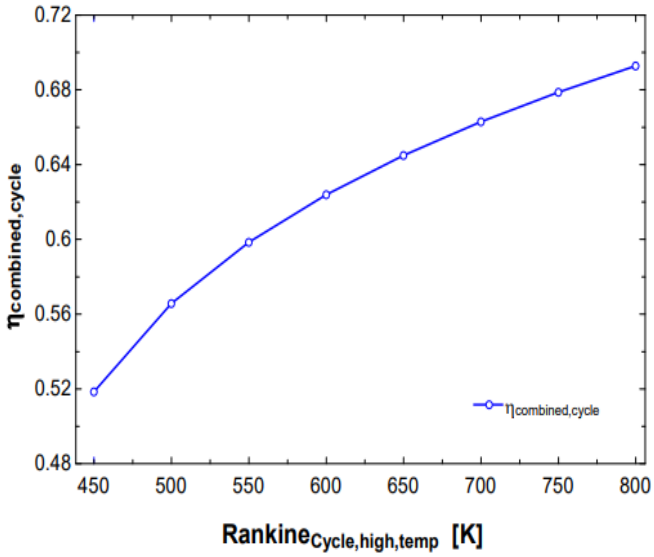


Figure 18: Variation between combined cycle efficiency and cycle high temperature of Rankine Cycle

Fig.18 shows the variation between combined cycle efficiency and cycle high temperature of Rankine Cycle. It can be seen that on increasing the cycle high temperature, efficiency is also increasing. The combined cycle efficiency is 51.85% at temperature 450K.

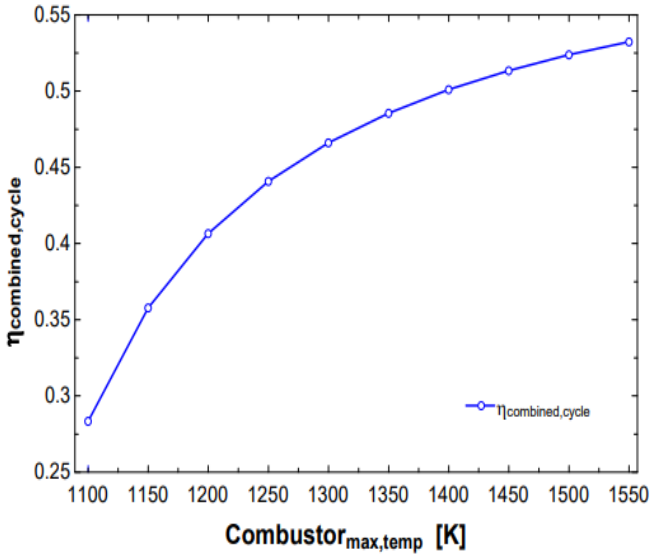


Figure 19: Variation between combined cycle efficiency and combustor maximum temperature of Brayton Cycle

Fig.19 shows the variation between combined cycle efficiency and combustor maximum temperature of Brayton Cycle. It can be seen that on increasing the combustor temperature, efficiency is also increasing. The combined cycle efficiency is 44.08% at combustor temperature 1250K

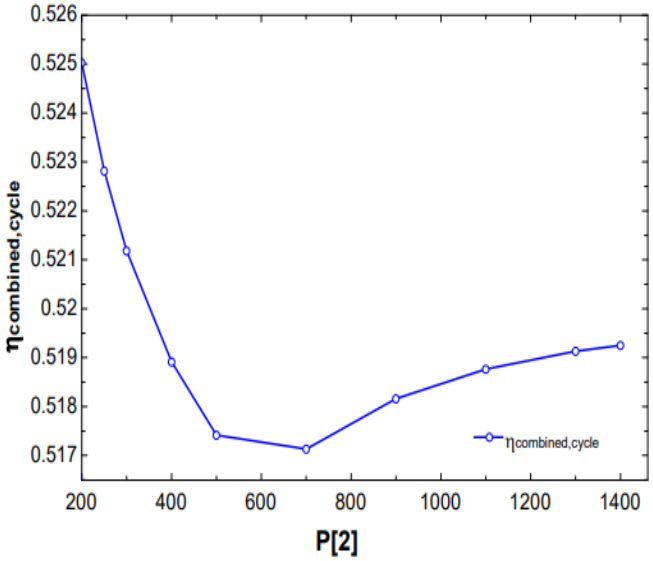


Figure 20: Variation between combined cycle efficiency and exit pressure of pump of trans-critical cycle.

Fig. 20 shows the variation between combined cycle efficiency and exit pressure of pump of trans-critical cycle. It can be seen that on increasing the pressure, efficiency is decreasing and after 700 kPa efficiency is slightly increasing. The combined cycle efficiency is 51.89% at pressure 400 kPa

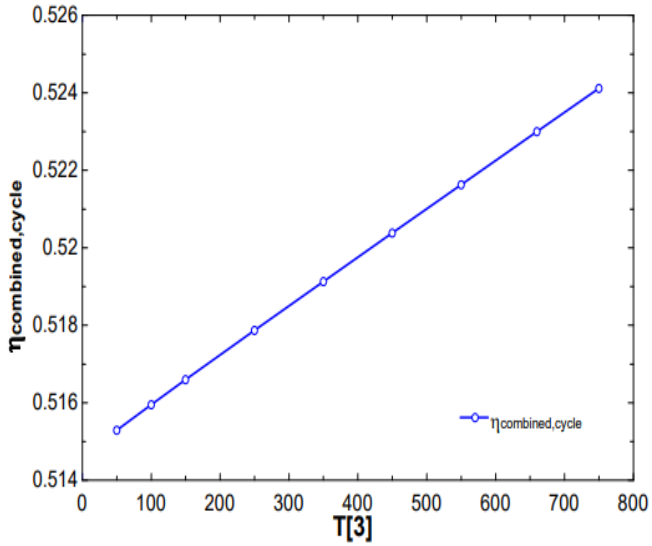


Figure 21: Variation between combined cycle efficiency and turbine inlet temperature of trans-critical Cycle.

Fig. 21 shows the variation between combined cycle efficiency and turbine inlet temperature of trans-critical Cycle. The can be seen that on increasing the temperature, efficiency is also increasing. The combined cycle efficiency is 51.79% at temperature 250ºC.

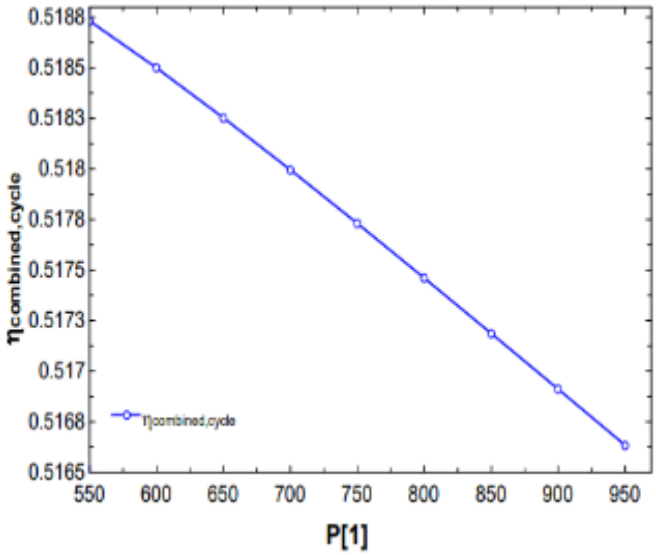


Figure 22: Variation between combined cycle efficiency and inlet pump pressure of trans-critical Cycle

Fig.22 shows the variation between combined cycle efficiency and inlet pump pressure of trans-critical Cycle. It can be seen that on increasing the pressure, efficiency is decreasing. The combined cycle efficiency is 51.8% at pressure 700 kPa.

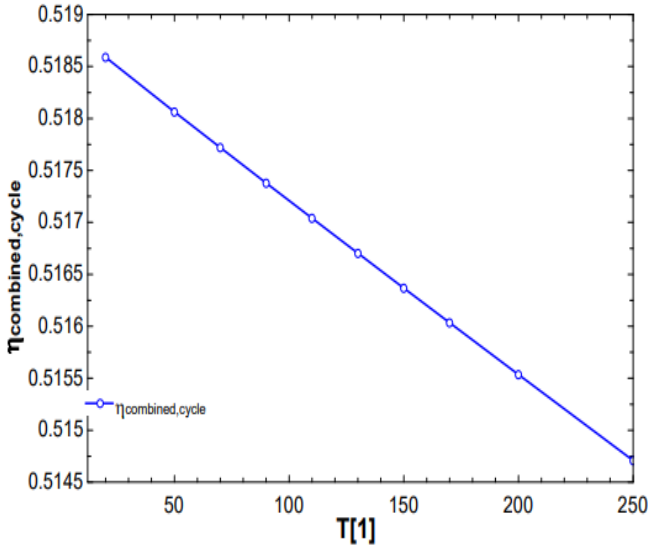


Figure 23: Variation between combined cycle efficiency and turbine inlet temperature of trans-critical Cycle

Fig.23 shows the variation between combined cycle efficiency and turbine inlet temperature of trans-critical Cycle. It can be seen that on increasing the temperature, efficiency is decreasing. The combined cycle efficiency is 51.7% at temperature 110ºC.

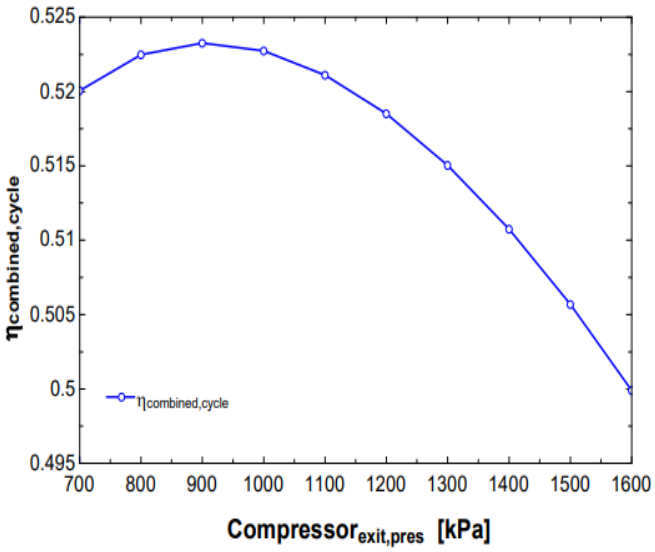


Figure 24: Variation between combined cycle efficiency and compressor exit pressure of Rankine Cycle

Fig. 24 shows the variation between combined cycle efficiency and compressor exit pressure of Rankine Cycle.

It can be seen that on increasing the pressure, efficiency is increasing up to 900 kPa and after that it keeps on decreasing. The combined cycle efficiency is 52.11% at compressor exit pressure 1100 kPa.

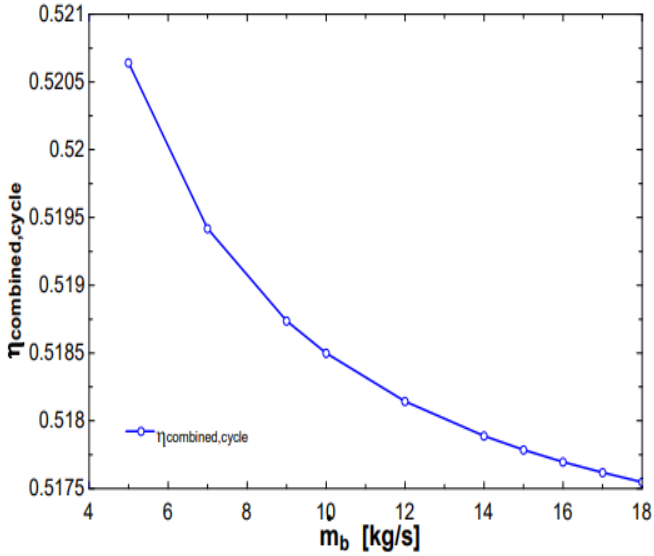


Figure 25: variation between combined cycle efficiency and mass flow rate of Brayton Cycle

Fig. 25 shows the variation between combined cycle efficiency and mass flow rate of Brayton Cycle. It can be seen that on increasing the mass flow rate, efficiency is decreasing. The combined cycle efficiency is 51.81% at mass flow rate 12 kg/sec.

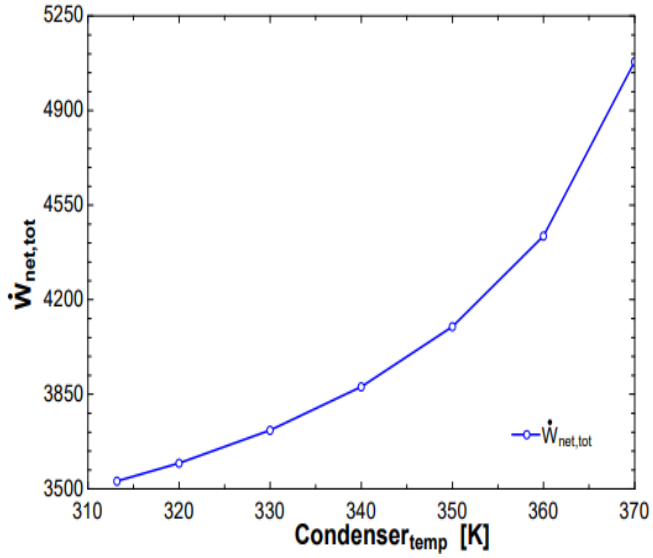


Figure 26: Variation between combined cycle net-work and condenser temperature of Rankine Cycle

Fig.26 shows the variation between combined cycle net-work and condenser temperature of Rankine Cycle. It can be seen that on increasing the condenser temperature, combined net-work is also increasing. The combined cycle net-work is 3878 kW at condenser temperature 340K.

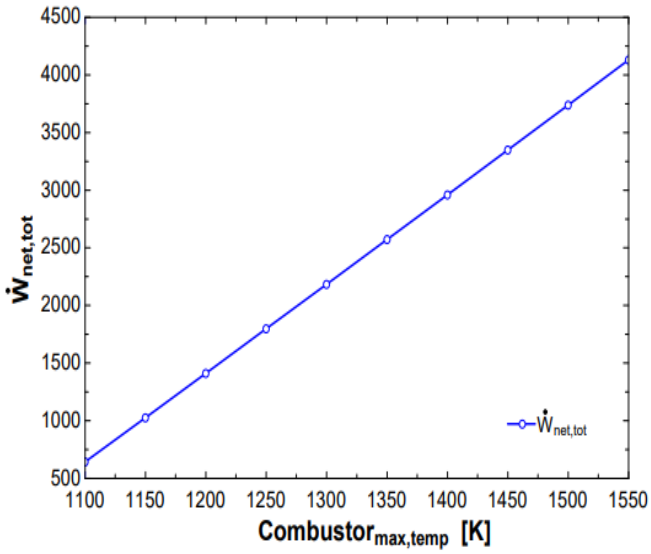


Figure 27: Variation between combined cycle net-work and cycle high temperature of Rankine Cycle

Fig.27 shows the variation between combined cycle net-work and cycle high temperature of Rankine Cycle. It can be seen that on increasing the cycle high temperature, net-work is also increasing. The combined cycle net-work is 3529 kW at temperature 450K.

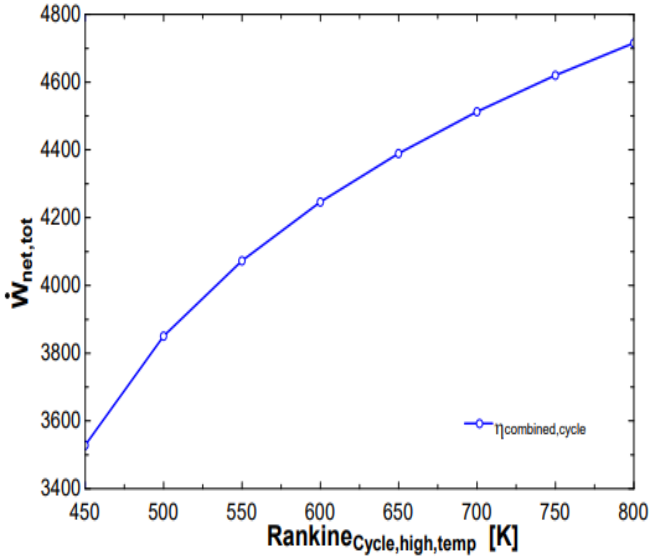


Figure 28: Variation between combined cycle net-work and combustor maximum temperature of Brayton Cycle

Fig. 28 shows the variation between combined cycle net-work and combustor maximum temperature of Brayton Cycle. It can be seen that on increasing the combustor temperature, net-work is also increasing. The combined cycle net-work is 1798 kW at combustor temperature 1250K.

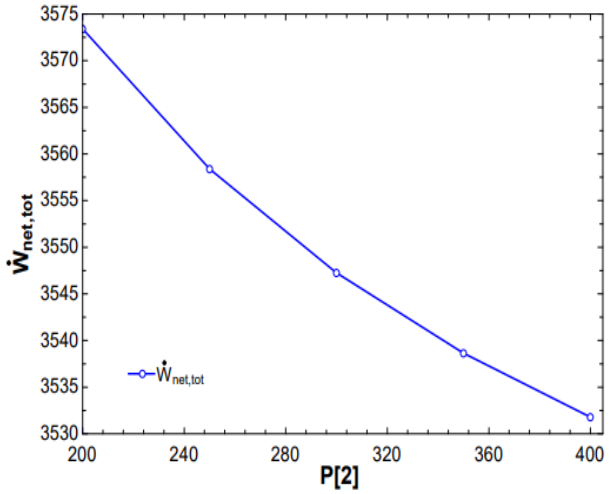


Figure 29: Variation between combined cycle net-work and exit pressure of pump of trans-critical cycle

Fig. 29 shows the variation between combined cycle net-work and exit pressure of pump of trans-critical cycle. It can be seen that on increasing the pressure, net-work is decreasing. The combined cycle net-work is 3532 kW at pressure 400 kPa.

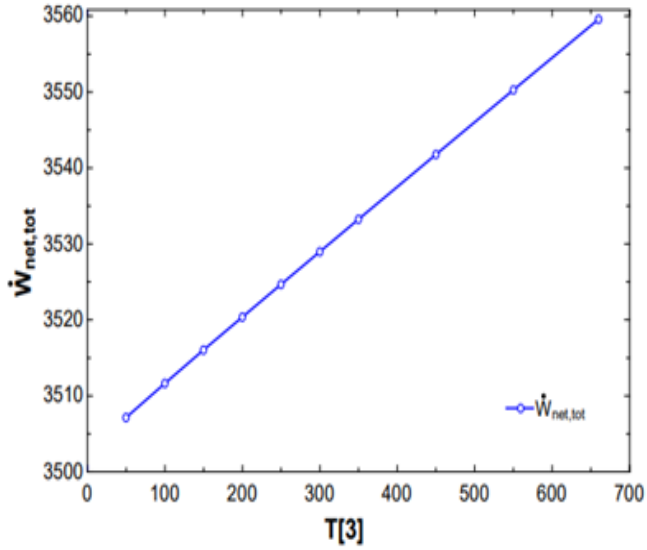


Figure 30: Variation between combined cycle net-work and turbine inlet temperature of trans-critical Cycle

Fig. 30 shows the variation between combined cycle net-work and turbine inlet temperature of trans-critical Cycle. It can be seen that on increasing the temperature, net-work is also increasing. The combined cycle net-work is 3525 kW at temperature 250ºC.

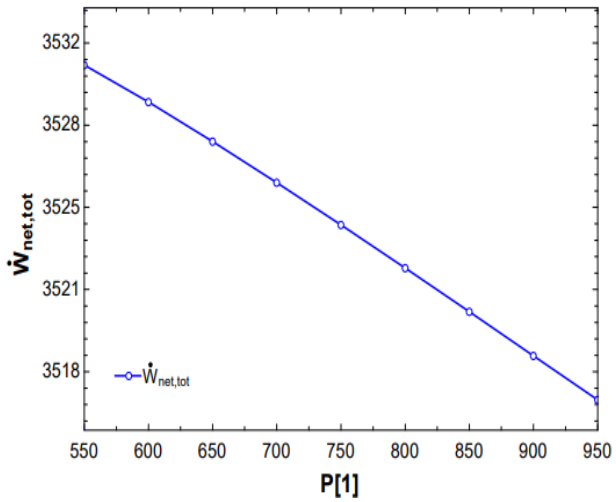


Figure 31: Variation between combined cycle net-work and inlet pump pressure of trans-critical Cycle

Fig.31 shows the variation between combined cycle net-work and inlet pump pressure of trans-critical Cycle. It can be seen that on increasing the pressure, net-work is decreasing. The combined cycle net-work is 3526 kW at pressure 700 kPa

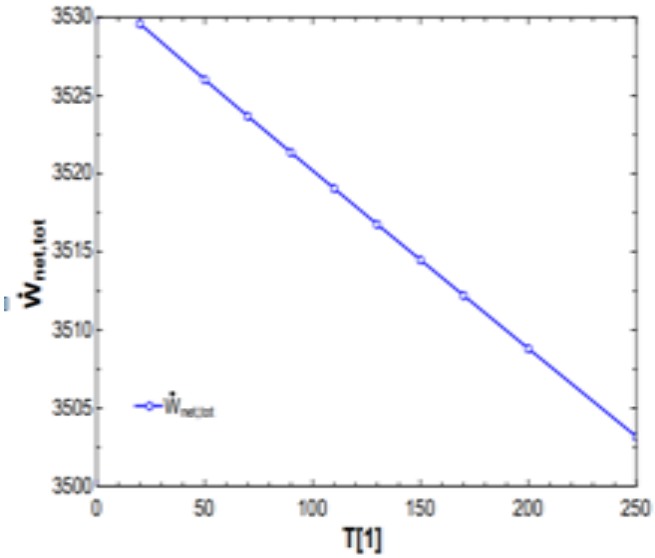


Figure 32: Variation between combined cycle net-work and turbine inlet temperature of trans-critical Cycle

Fig. 32 shows the variation between combined cycle net-work and turbine inlet temperature of trans-critical Cycle. It can be seen that on increasing the temperature, net-work is decreasing. The combined cycle net-work is 3519 kW at temperature 110ºC.

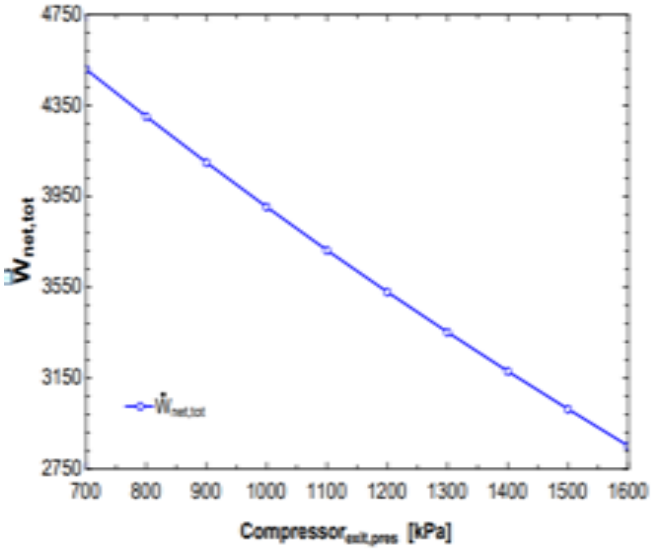


Figure 33: variation between combined cycle net-work and compressor exit pressure of Rankine Cycle

Fig.33 shows the variation between combined cycle net-work and compressor exit pressure of Rankine Cycle. It can be seen that on increasing the pressure, net-work is decreasing. The combined cycle net-work is 3713 kW at compressor exit pressure 1100 kPa.

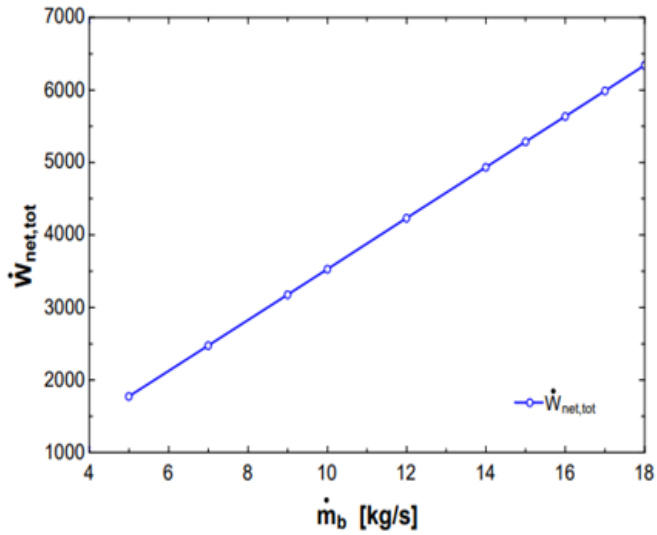


Figure 34: Variation between combined cycle net-work and mass flow rate of Brayton Cycle

Fig. 34 shows the variation between combined cycle net-work and mass flow rate of Brayton Cycle. It can be seen that on increasing the mass flow rate, efficiency is increasing. The combined cycle net-work is 4232 kW at mass flow rate 12 kg/sec

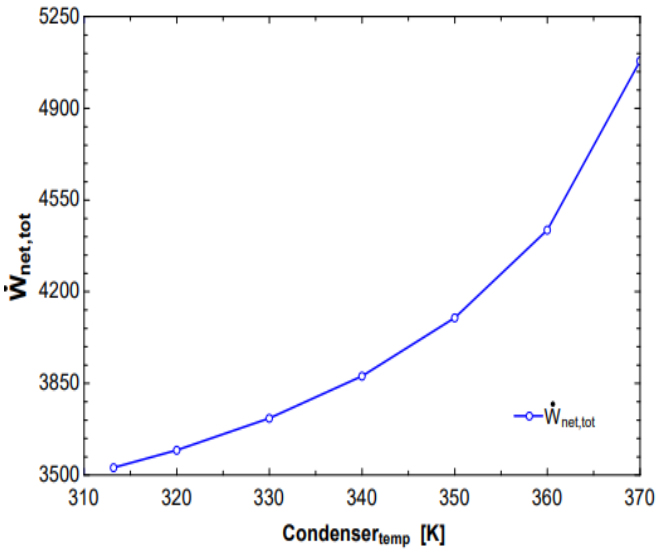


Figure 35: Variation between combined cycle net-work and condenser temperature of Rankine Cycle

Fig.35 shows the variation between combined cycle net-work and condenser temperature of Rankine Cycle. It can be seen that on increasing the condenser temperature, combined net-work is also increasing. From Table 19 combined cycle net-work is 3878 kW at condenser temperature 340K.

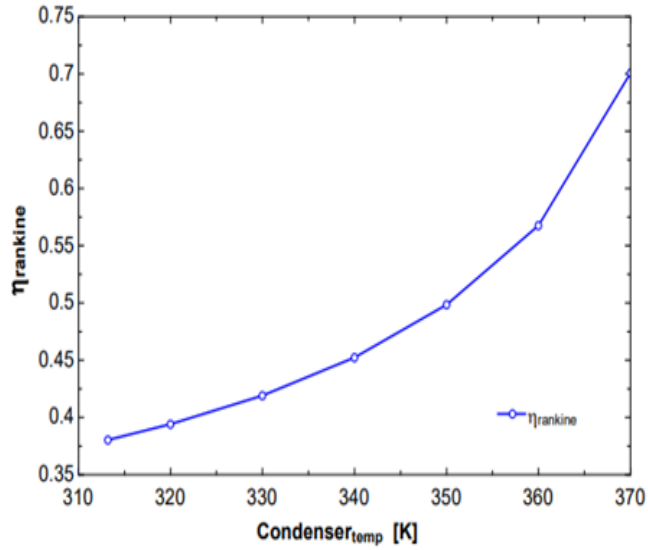
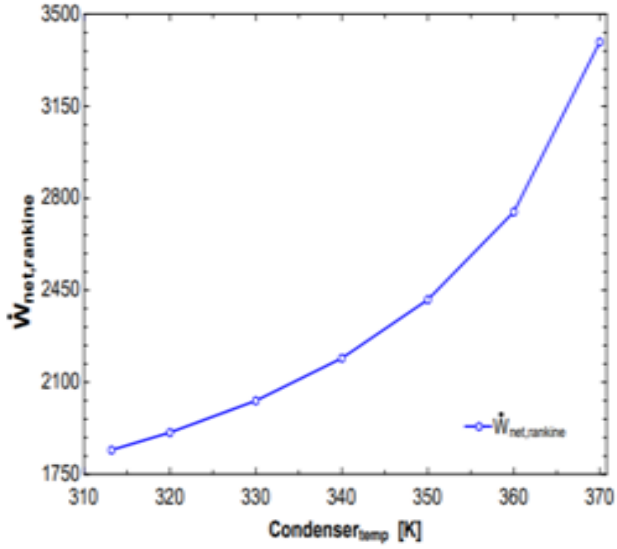


Figure 36: Variation between Rankine cycle efficiency and condenser temperature

Fig.36 shows the variation between Rankine cycle efficiency and condenser temperature. It can be seen that on increasing the condenser temperature, efficiency is also increasing. The Rankine cycle efficiency is 45.25% at condenser temperature 340K



Fig*ure 37: Variation between Rankine cycle net-work and condenser temperature.*

Fig. 37 shows the variation between Rankine cycle net-work and condenser temperature. It can be seen that on increasing the condenser temperature, Rankine net-work is also increasing. The combined cycle net-work is computed as 2191 kW at condenser temperature 340K.

5. Conclusion

In this study, carbon dioxide cycles is also investigated for recovering the low grade heat. In this thesis, three cycle are combined i.e. Brayton, Rankine and Trans critical cycle in which fluid taken are Ideal gas (air), Steam and Carbon dioxide respectively. The mass flow rate of Brayton cycle is 10 kg/sec and atmospheric temperature is 25ºC.
The following conclusions were drawn from thermodynamic analysis of above mentioned cycles have been shown below.

- On increasing condenser temperature of Rankine cycle, combined efficiency of cycle and combined net-work both are increasing.
- On increasing the mass flow rate of Brayton cycle, combined efficiency of cycle is decreasing and combined net-work is increasing.
- On increasing the exit pressure of pump in trans-critical cycle, combined net work is decreasing also combined cycle efficiency is decreasing.
- On increasing the inlet temperature of turbine of trans-critical cycle, combined cycle efficiency and combined net-work is increasing.
- On increasing the inlet pressure of pump of trans-critical cycle, combined cycle efficiency and combined net work both are increasing.

References

[1] Al-Hamdan, Q. and Ebaid, M. (2006), "Modeling and Simulation of a Gas Turbine Engine for Power Generation", vol. 128, no. 2, p. 311.

[2] Alrobaei, H. (2006a), Integrated Gas Turbine - Solar Power Plant, available at: http://www.energycentral.com/centers/knowledge/whitepapers/report.cfm?rid=102295 (accessed 20/11/2006)

[3] Alrobaei, H. (2006b), Hybrid Solar/Fossil Fuel Cogeneration Power Plant, available at: http://www.energycentral.com/centers/knowledge/Hybrid Solar/Fossil Fuel Cogeneration Power Plant/ (accessed 22/07/2007).

[4] Alrobaei, H. (2004), Effectiveness of Semi-Combined Solar Power Plant, available at: http://www.softinway.com/science/articles (Accessed 23/07/2007).

[5] Alrobaei, H. (1998), "Thermodynamic Parametric Study for Combined Cogeneration Power Plants", Journal of Engineering, vol. 38, pp. 8091.

[6] ALSTOM (2007), Product Brochure GT12E2 & GT8C2, available at: http://www.power.alstom.com/home/elib/ (accessed 30/07/2007).

[7] ANU (2007), (The Australian National University), available at: http://solar.anu.edu.au (accessed 11/05/2007).

[8] ASHRAE (2003), Applications Handbook (SI), ASHRAE, Atlanta, GA, USA.

[9] Badran, O. and Eck, M. (2006), "The application of parabolic trough technology under Jordanian climate", Renewable Energy, vol. 31, no. 6, pp. 791-802.

[10] Beasley, O. (1994), "Induced Draft Fan Innovation for Heat Recovery Steam Generators", Journal of Engineering for Gas Turbines and Power, vol. 116, pp. 402-405.

[11] Becker, M. and Trieb, F. (2000), Solar Thermal Power Plants, available at: http://www.solarpaces.org/Library/library.htm

[12] Bernardes, D. and Weinrebe, A. (2003/12), "Thermal and technical analyses of solar chimneys", Solar Energy, vol. 75, no. 6, pp. 511-524.

[13] CSES, (2007), Monthly Daily Meteorological Data, Center for Solar Energy Studies – Libya, Tripoli.

[14] Nakata, T., Hasegawa, T., Ninomiya, T. and Sato, M. (1997), Development of a 1,500°C-Class Gas Turbine Combustor for IGCC, Central Research Institute of Electric Power Industry.

[15] DLR, Institute of Technical Thermodynamics and Section Systems Analysis and Technology Assessment (2006a), Trans-Mediterranean Interconnection for Concentrating Solar Power, , Federal Ministry for the Environment; Nature Conservation and Nuclear Safety Germany, Stuttgart, Germany.

[16] DLR (2006b), Concentrating Solar Power for the Mediterranean Region, available at: http://www.dlr.de/tt/med-csp (accessed 11/11).

[17] DLR (2002), Concentrating Solar Power Now, D-11055, The Federal Ministry for the Environment, Nature Conservation and Nuclear Safety (BMU), Berlin, Germany.

[18] Duffie, J. (1991), Solar Engineering of Thermal Processes, 2nd Ed, Wiley, New York.

[19] Eastop, T. and McConkey, A. (1993), Applied thermodynamics for engineering technologists, 5th ed, Longman, London.

[20] Eck, M. and Hirsch, T. (2007/2), "Dynamics and control of parabolic trough collector loops with direct steam generation", Solar Energy, vol. 81, no. 2, pp. 268-279.

[21] Elgady, A. (2007), Data about the Libyan power sector, GECOL (the General Electricity Company Of Libya), Zawia, Libya.

[22] El-Osta, W. (2003), "Prospects of wind power plants in Libya: a case study", Renewable Energy, vol. 28, no. 3, pp. 363-371.

[23] ETB (2007), Gases and Densities, Engineering Tool Book ,available at: http://www.engineeringtoolbox.com (accessed 17/08/2007.

[24] European Commission (2004), European Research on Concentrated Solar Thermal Energy, Brussels.

[25] Flagso GmbH (2007), Brief Technical Description of the SKAL-ET Collector, available at: http://www.flagsol.com (accessed 11/08/2006).

[26] Flynn, D. (2003), Thermal power plant simulation and control, 1s Ed, Institution of Electrical Engineers, London, UK.

[27] GECOL (2006), GECOL Annual Report 2006, , General Electricity Company of Libya, Tripoli, Libya.

[28] GECOL (2005), GECOL Annual Report 2005, General Electricity Company of Libya, Tripoli, Libya.

[29] Gill, A. (1984), Power Plant Performance, 1st Ed, Butterworths, London.

[30] Greenpeace International (2003), Solar Thermal Power 2020 Exploiting the Heat from the Sun to Combat Climate Change, ISBN:9073361-82-6, Greenpeace and the European Solar Thermal Industry Association (2003).

[31] Herrmann, U., Kelly, B. and Price, H. (2004/0), "Two-tank molten salt storage for parabolic trough solar power plants", Energy, vol. 29, no. 56, pp. 883-893.

[32] Hosseini, R., Soltani, M. and Valizadeh, G. (2005/8), "Technical and economic assessment of the integrated solar combined cycle power plants in Iran", Renewable Energy, vol. 30, no. 10, pp. 1541-1555.

[33] Hottel, H. C. (1976), "A simple model for estimating the transmittance of direct solar radiation through clear atmospheres", Solar Energy, vol. 18, no. 2, pp. 129-134.

[34] HRSG User's group (2007), HRSG User's Handbook, available at: http://www.hrsgusers.org/practices.php (accessed 01/08/2007).

[35] Huang, M. and Gramoll, K. (2007), Actual Gas-turbine Cycle, available at: https://ecourses.ou.edu/home.htm (accessed 25/07/2007).

[36] Incropera, F. (2002), Fundamentals of Heat and Mass Transfer, 5th ed, John Wiley & Sons, New York.

[37] IWAI, M. (2003), "Thermodynamic Table for Performance Calculations in Gas Turbine Engine", Proceedings of the International Gas Turbine Congress, 2-7 November 2003, Tokyo.

[38] Jacobson, E., Ketjoy, N., Nathakaranakule, S. and Rakwichian, W. (2006), "Solar parabolic trough simulation and application for a hybrid power plant in Thailand", vol. 32, no. 2, pp. 187-199.

[39] Jones, J. (2007a), "CSP lifts off. Nevada Solar One comes to life ", Renewable Energy World, vol. 10, no. 3, pp. 36-42.

[40] Jones, J. (2007b), "Solar Movement", Renewable Energy World, vol. 10, no. 4, pp. 168-172.

[41] Lane, D. (2007), Brayton Cycle: The Ideal Cycle for Gas-Turbine Engines In Relation to Power Plants, available at: http://coeweb.engr.unr.edu/me/ (accessed 22/07/2007).

[42] Mills, D. (2004), "Advances in solar thermal electricity technology", Solar Energy, vol. 76, no. 1-3, pp. 19-31.

[43] Mustafa, E. (2007), Monthly Daily Meteorological Data, LREC Libyan Renewable Energy Centre.

[44] Najjar, Y. (1996/2), "Enhancement of performance of gas turbine engines by inlet air cooling and cogeneration system", Applied Thermal Engineering, vol. 16, no. 2, pp. 163-173.

[45] Natan, S., Barnea, D. and Taitel, Y. (2003/11), "Direct steam generation in parallel pipes", International Journal of Multiphase Flow, vol. 29, no. 11, pp. 1669-1683.

[46] NREL, (2007), U.S. Parabolic Trough Power Plant Data, available at: http://www.nrel.gov/csp/troughnet/power_plant_data.html

Nomenclature

A	Altitude [m]
Ap	Total outer area of the receiver tube [m^2]
ASF	Total solar field aperture area
[m^2]	The specific fuel consumption of the gas turbine unit [tonne/MWh]
BGT	Gas turbine fuel consumption [tonne/h]
C	Solar collector concentration ratio [-]
Cp	Specific heat [kJ/kg.K]
DB	Fuel saving [tonne/h]
Dci	Cover inner diameter [m]
Dco	Cover outer diameter [m]
Devap	Steam mass loss from the deaerator [kg/s]
DFW	Mass flow of feed water [kg/s]
DK	Water mass flow in plant condenser [kg/s]
DLoss	Steam loss [kg/s]
Do	Steam mass flow at the turbine inlet (reference point) [kg/s]
DRK	Water mass flow in GH1 [kg/s]

DRK2	Water mass flow in GH2 [kg/s]
DRT	The extracted steam to operate the plant deaerator [kg/s]
DSS	The generated stem due to solar field Contribution [kg/s]
Dti	Receiver inner diameter [m]
Dto	Receiver outer diameter [m]
h'	Saturated water specific enthalpy [kJ/kg]
h"	Saturated steam specific enthalpy [kJ/kg]
Ib	Beam solar radiation [W/m^2]
Id	Diffuse solar radiation [W/m^2]
Isc	Solar constant [W/m^2]
Iso	Extra-terrestrial solar radiation [W/m^2]
K	Receiver thermal conductivity [W/m. °K]
kc	Cover thermal conductivity [W/m. °K]
Ke	Cover extinction coefficient [m-1]
l	Collector length [m]
N	Number of collectors in each row [-].
M field [kg/s] m.	Water mass flow for each row in the ^{solar}
SF [kg/s]	Water mass flow for whole solar field
mC gas turbine unit	Relative air mass flow for blades cooling in
mf unit [kg fuel/kg air]	The relative fuel mass flow for gas turbine
mgas [kg/s] mK	Gases mass exhaust from gas turbine unit
N	Number of rows of solar field [-]
n2	Cover refractive index [-]
NEGT	Gas turbine output [MW]
NEST	Steam turbine output [MW]
NFP [MW]	Energy consumption by water feed pump
P	Pressure [bar]
PD	Deaerator pressure [bar]
PDE	Deaerator's evaporator pressure [bar]
Pk	Condenser pressure [bar]
PLPT	Pressure at LPT inlet [bar]
PLPTO	Pressure at LPT inlet for combined cycle operation [bar]
PSOSF	Design outlet pressure for solar field [bar]
Qc.v	Fuel calorific value [kJ/kg]
QL	Heat loss from solar collector [kW]
QSC	Useful heat from solar field [kW]
QSF	Nominal solar field output [kW]
Qu row) [kW]	Useful heat gain in solar field (for each
R	Gas constant [kJ/kg.°K]
S	Specific entropy [kJ/kg.°K]
Sb [W/m^2.°K]	Absorbed solar energy by receiver tube
T	Temperature [°C]
Ta	Ambient temperature [°C]
Tbw blades [°C]	The average temperature of gas turbine
Tex	Exhaust Gases temperature after HRSG °C]
Tfi	Water temperature at solar field inlet [°C]
Tfo	Water temperature at solar field outlet [°C]
TL	Disposed water temperature [°C]
TRFW1	Re-feed water temperature [°C]
TS [°C]	Temperature for ideal process (isentropic)
Ua	Wind Velocity [m/s]
UL	Solar collector loss coefficient [W/m^2.°K]
W	Collector aperture width [m]
Wa [kJ/kg]	Specific work done by gases in the GT
Wco GT [kJ/kg]	Specific work done by cooling air in the
We	Specific work for gas turbine unit [kJ/kg]
WK	Compressor specific work [kJ/kg]
WT	Total specific work of GT (gases + air) [kJ/kg]
XK	Steam/water dryness factor [%]

Abbreviations

AC	Air compressor
ANU	The Australian National University
CC	Combined cycle
CHP	Combined Heat and Power
CSES	Centre for Solar Energy Studies – Libya
CSP	Concentrating Solar Power
DE	The evaporator of the desecrator
DISS	Direct solar steam European project
DLR	German Aerospace Centre
DSG	Direct steam Generation
EC	European commission
ECC	Equivalent combined cycle
ETB	Engineering tool Book
EU-MENA	Europe, Mediterranean North African region
FP	Feed water pump
FV	Flash vessel
G	Electricity generator
GCC	Gas Turbine Combustion chamber
GECOL	General Electricity Company of Libya
GH	Gas heater
GT	Gas turbine
GTU	Gas turbine unit
HPT	High pressure turbine
HRSG	Heat Recovery Steam Generation
HTF	Heat Transfer Fluid
HVDC	High Voltage Direct Current
ISCC	Integrated Solar Combined Cycle Power Plant
LPT	Low pressure turbine
LREC	Libyan Renewable Energy Centre
MED	Multi Effect Desalination Unit
MSF	Multi Stage Flash Desalination Unit
NREL	National Renewable Energy Laboratory
RFWH	Re-feed water heater
SEEN	The Sustainable Energy and Economy Network
SEGS	Solar Electricity Generating Station
STU	Steam turbine unit
SV	Separator vessel
TRANS-CSP	Trans-Mediterranean Interconnection for Concentrating Solar Power
TREC	Trans-Mediterranean Renewable Energy Cooperation

International Journal of Research in Engineering and Innovation (IJREI)
journal home page: http://www.ijrei.com
ISSN (Online): 2456-6934

Thermodynamic models for combined cycle power plants used in organic Rankine & Brayton Cycles

R.S. Mishra, Manish Kumar

Department of Mechanical & Production Engineering, Delhi Technological University, Delhi India

Abstract

As global energy demand continues to grow, combined cycle power plants are becoming more relevant**.** In combined cycles**,** the power output loss in gas turbines for ambient air temperatures over the standard 15˚C**,** the gas turbine power output is increased up to 30% and also the exhaust flow is increased. However, the exhaust temperature will be reduced due to the cooling. The reduction on the gas temperature partially compensates the increase in the exhaust flow and the final effect is an increase in the steam turbine power output of 2 – 5 %. Therefore in a combined cycle , the gas turbine power increased from 20 – 30% and steam turbine power increased to 2 – 5 % In this paper thermal models were developed for Rankine cycle using organic fluids, Brayton gas turbine cycle and its performance improvements using different methods using organic fluids and combined cycle and performance were carried out and it was found that the cycle efficiency is increasing on increasing of heater pressure for both R123 and R245fa and efficiency is coming more for R123 as compared to R245fa while the net-work is also increasing on increasing of pressure ratio but more network increases in R245fa as compared to R123..
© 2018 ijrei.com. All rights reserved
Keywords: Thermodynamic Modelling, Subcritical ORC, combined cycle power plants, Organic Rankine & Brayton Cycles

1. Introduction

A combined-cycle power plant uses both a gas and a steam turbine together to produce up to 50 percent more electricity from the same fuel than a traditional simple-cycle plant. The waste heat from the gas turbine is routed to the nearby steam turbine, which generates extra power. In the combined cycle gas turbine (CCGT) plant, a gas turbine generates electricity and the waste heat is used to make steam to generate additional electricity via a steam turbine; this last step enhances the efficiency of electricity generation. Normally in the combined cycle power plants (CCPPs) a gas turbine generator generates electricity while the waste heat from the gas turbine is used to make steam to generate additional electricity via a steam turbine. The output heat of the gas turbine flue gas is utilized to generate steam by passing it through a heat recovery steam generator (HRSG), so it can be used as input heat to the steam turbine power plant. This combination of two power generation cycles enhances the efficiency of the plant. While the electrical efficiency of a simple cycle plant power plant without waste heat utilization typically ranges between 25% and 40%, a CCPP can achieve electrical efficiencies of 60% and more. Supplementary firing further enhances the overall efficiency. The high fuel utilization factor of the plant contributes to low lifecycle costs. The lot of work on thermodynamic analysis were carried out on the combined power plants using organic fluids as explained by various investigators including Sanjay Vijayaraghavan & Goswami et.al [1] developed new thermodynamic cycle for the simultaneous production of power and cooling from low temperature heat sources. The proposed cycle combines the Rankine and absorption refrigeration cycles, providing power and cooling as useful outputs. Initial studies were performed with an ammonia-water mixture as the working fluid in the cycle. This work extends the application of the cycle to working fluids consisting of organic fluid mixtures. Organic working fluids have been used successfully in geothermal power plants, as working fluids in Rankine cycles. An advantage of using organic working fluids is that the industry has experience with building turbines for these fluids. A

Corresponding author: R. S. Mishra
Email Id: hod.mechanical.rsm@dtu.ac.in

commercially available optimization program has been used to maximize the thermodynamic performance of the cycle. And also discussed the advantages and disadvantages of using organic fluid mixtures as opposed to an ammonia-water mixture and also found that the thermodynamic efficiencies achievable with organic fluid mixtures, under optimum conditions, are lower than those obtained with ammonia-water mixtures, and the refrigeration temperatures achievable using organic fluid mixtures are higher than those using ammonia-water mixtures. Mishra R.S. and Dharminder Sahu [2] carried out energy and exergy analysis of Gas turbine-Organic Rankine combined cycle with solar reheating of organic fluid is done and results are compared with simple combined cycle, combined cycle with regeneration, combined cycle with solar reheating of organic fluid. The performance of the system is compared using different organic fluids (i.e. R134a, R245fa, Acetone, and R1234yf) at different organic Rankine cycle and it is found that the maximum pressure and maximum temperature , the R1234yf shows maximum increase in efficiency by regeneration about 70%. Acetone shows maximum organic Rankine cycle efficiency of 25.96%. Exergetic efficiency of combined cycle with regeneration and reheating 64%, 72%, 64%and 82% for R134a, R245fa, R1234yf and Acetone respectively. Acetone is recommended for practical applications due to its highest energy and exergetic efficiency among all selected organic fluids but some important problem related to flammability and explosion risk have to be considered while managing it. After Acetone, R245fa can be considered as better option in solar reheated combined cycle plant with regeneration. Al-Sulaiman Fahad A, Hamdullahpur Feridun, Dincer Ibrahim"[3] carried out detailed exergy analysis of selected thermal power systems driven by parabolic trough solar collectors (PTSCs) is presented. The power is produced using either a steam Rankine cycle (SRC) or a combined cycle, in which the SRC is the topping cycle and an organic Rankine cycle (ORC) is the bottoming cycle and examined using seven organic fluids (i.e. R134a, R152a, R290, R407c, R600, R600a, and ammonia) . and found that the R134a combined cycle demonstrates the best exergetic performance with a maximum exergetic efficiency of 26% followed by the R152a combined cycle with an exergetic efficiency of 25%. Alternatively, the R600a combined cycle has the lowest exergetic efficiency, 20–21%. In this paper thermal models were developed for Rankine cycle using organic fluids, Brayton gas turbine cycle and its performance improvements using different methods using organic fluids and combined cycle and performance were carried out.

2. Thermodynamic Modelling

This chapter deals with the set of equations that are used for the different steps of analysis to be performed. They are presented in order of the showed system performance.

2.1 Energy Analysis

The Ist law of thermodynamics is the basis for the energy analysis. The final results includes the net output and the thermal efficiency. As already mentioned in the assumptions, their value is dependent only on evaporation pressure i.e. Pevap = P1 = P8. Following are the set of equations for different components.

2.1.1 Subcritical ORC

The equation for heater/heat exchanger:

$$Qhex= \dot{m}hf\ (h_{11} - h_{14}) = \dot{m}cf(h_1 - h_8) \quad (1)$$

The equation of the expander

$$\eta_{T,i} = (h_2 - h_1) / (h_3 - h_1) \quad (2)$$
$$W_T = \eta T,m^*(h_1 - h_2) \quad (3)$$

Where ηT,mis the mechanical efficiency of expander.
The equation of condenser:

$$Q_{cond} = \dot{m}cf\ (h_{18} - h_{15}) = \dot{m}r(h_2 - h_6) \quad (4)$$

The equation of fluid pump:

$$W_{pump} = (h_8 - h_6) \quad (5)$$

Equation for the net system output:

$$W_{sys} = \dot{m}hf(h_1 - h_2) - \dot{m}cf(h_8 - h_6) \quad (6)$$

Equation for finding the cycle thermal efficiency:

$$\eta_{th} = W_{sys}/Q_{hex} \quad (7)$$

Taking into account the effect of IHE, the equation (1) and (4) are changed to

$$Q_{hex} = \dot{m}_{hf*}(h_{11} - h_{21}) = \dot{m}r^*(h_1 - h_{19}) \quad (8)$$
$$Q_{cond} = \dot{m}_{cf*}(h_{22} - h_{15}) = \dot{m}r^*(h_{20} - h_6) \quad (9)$$

For the Internal Heat Exchanger:

$$(h_{20} - h_2) = (h_8 - h_{19}) \quad (10)$$

2.1.2 Subcritical ORC Using R245fa

The equation for heater/heat exchanger:

$$Q_{hex} = \dot{m}_{hf}(h_{11} - h_{14}) = \dot{m}cf(h_1 - h_8) \quad (11)$$

The equation of the expander

$$\eta_{T,i} = (h_2 - h_1) / (h_3 - h_1) \quad (12)$$

$$W_T = \eta_{T,m*}(h_1 - h_2) \quad (13)$$

Where ηT,mis the mechanical efficiency of expander.
The equation of condenser:

$$Q_{cond} = \dot{m}_{cf}(h_{18} - h_{15}) = \dot{m}_r(h_2 - h_6) \quad (14)$$

The equation of fluid pump:

$$W_{pump} = (h_8 - h_6) \quad (15)$$

Equation for the net system output:

$$W_{sys} = \dot{m}_{hf}(h_1 - h_2) - \dot{m}_{cf}(h_8 - h_6) \quad (16)$$

Equation for finding the cycle thermal efficiency:

$$\eta_{th} = (W_{sys}/Q_{hex}) \quad (17)$$

Taking into account the effect of IHE, the equation (11) and (14) are changed to

$$Q_{hex} = \dot{m}_{hf*}(h_{11} - h_{21}) = \dot{m}r*(h_1 - h_{19}) \quad (18)$$
$$Q_{cond} = \dot{m}_{cf*}(h_{22} - h_{15}) = \dot{m}_{r*}(h_{20} - h_6) \quad (19)$$

For the Internal Heat Exchanger:

$$(h_{20} - h_2) = (h_8 - h_{19}) \quad (20)$$

2.1.3 Simple Brayton Cycle

The energy equation of simple Brayton cycle are as follows:
For the compressor:

$$W_C = (h_2 - h_1) \quad (21)$$

Where WC is the work of compressor.

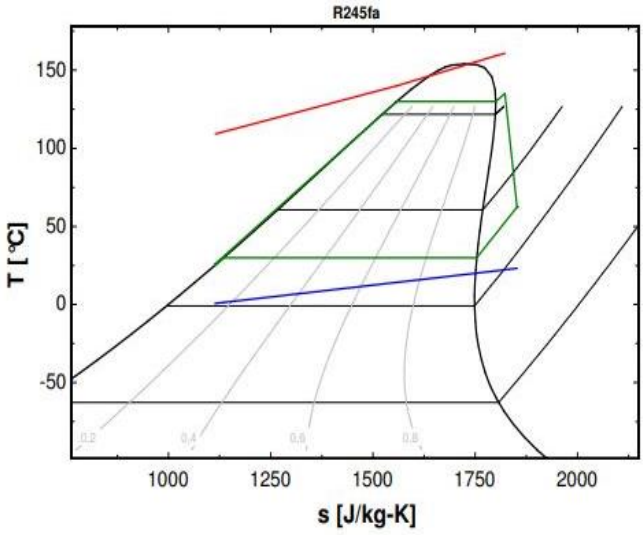


Figure 1: T-S diag. of Subcritical ORC system using R245fa

h_2 and h_1 is the enthalpy at the exit and inlet of the compressor respectively.
For the Combustion Chamber:

$$Q_{in} = (h_3 - h_2) \quad (22)$$

Where Qin is the heat input in the combustion chamber.
And h_3 and h_2 is the enthalpy at the exit and inlet of the combustion chamber respectively.
For the Turbine:

$$W_T = (h_3 - h_4) \quad (23)$$

Where WT is the work of the turbine.
And h3 and h4 is the enthalpy at the inlet and the exit of the turbine respectively.
For the cooler/ heat exchanger:

$$Q_{out} = (h_4 - h_1) \quad (26)$$

Where Q_{out} is the heat output in the cooler or heat exchanger.
And h_4 and h_1 is the enthalpy at the inlet and exit of the cooler respectively.
Net-work of the Brayton cycle:

$$W_{NET} = (W_T - W_C) \quad (27)$$

Isentropic Efficiency of the compressor:

$$\eta_C = (h_{2,s} - h_1)/(h_2 - h_1) \quad (28)$$

Where $h_{2,s}$ is the isentropic enthalpy of the compressor.
Isentropic Efficiency of the turbine:

$$\eta_T = (h_3 - h_4)/(h_3 - h_{4,s}) \quad (29)$$

Where h4,s is isentropic enthalpy of the turbine.
Cycle Efficiency of the Brayton cycle:

$$\eta_{cycle} = (W_{NET}/Q_{in}) \quad (30)$$

2.1.4 Combined Cycle

$$W_{net,combined} = W_{net,Brayton} + W_{net,Rankine} \quad (31)$$
$$E_{tacombined} = W_{net,combined} / (Q_{in,hex,Rankine} + Q_{in,combustor}) \quad (32)$$

2.2 Exergy Analysis

The drawback of energy analysis is that the conversion of energy of evaporator and condenser could not be done. Exergy analysis is an energy conversion coefficient that focuses on quantity as well as quality of energy, and this parameter more profoundly tells the essence of losses and energy conversion as compared to energy analysis. The exergy destruction in each component can also be calculated by this analysis.
The exergy analysis can be done by calculating the specific

flow exergy at exit and entry of sources and also at each state point in cycle. The following expression gives the quantity:

$$e = h - h_0 + T_0(s_0 - s) \quad (33)$$

Where the subscript 0 represents the environmental conditions which are considered to be 15ºC and atmospheric pressure. Following are the equations for different components:
Equation for Evaporator:

$$E_{d,evap} = \dot{m}_{hf*}(e_{11} - e_{14}) + \dot{m}_{r*}(e_8 - e_1) \quad (34)$$

Equation for expander:

$$E_{d,T} = \dot{m}_{r*}(e_1 - e_2) - W_T \quad (35)$$

Equation for condenser:

$$E_{d,cond} = \dot{m}_{r*}(e_2 - e_6) + \dot{m}_{cf}*(e_{15} - e_{18}) \quad (36)$$

Equation for working pump:

$$E_{d,P} = W_P + \dot{m}_{r*}(e_6 - e_8) \quad (37)$$

Expression for system total exergy destruction rate:

$$E_{d,Tot} = E_{d,evap} + E_{d,P} + E_{d,cond} + E_{d,T} \quad (38)$$

The overall exergy efficiency is calculated as:

$$\eta_{ex} = 1 - \{E_d,T_{ot} / \dot{m}_{hf} *(e_{11} - e_{14})\} \quad (39)$$

If internal heat exchanger is considered, then Eqn. 34 and 36 is changed to

$$E_{d,evap} = \dot{m}_{r*}(e_{19} - e_1) - \dot{m}_{hf*}(e_{21} - e_{11}) \quad (40)$$
$$E_{d,cond} = \dot{m}_{r*}(e_{20} - e_6) - \dot{m}_{cf*}(e_{22} - e_{15}) \quad (41)$$

Expression for internal heat exchanger:

$$E_{d,IHE} = \dot{m}_{r*}(e_8 - e_{19}) - \dot{m}_{r*}(e_{20} - e_2) \quad (42)$$

The equations 25 and 26 are modified as:

$$E_{d,Tot} = (E_{d,evap}+E_{d,P}+E_{d,cond}+E_{d,IHE} + E_{d,T} \quad (43)$$
$$\eta_{ex} = 1 - \{E_{d,Tot} / \dot{m}_{hf*}(e_{11} - e_{21})\} \quad (44)$$

3. Result and Discussion

3.1 Subcritical ORC

3.1.1 Effect of cycle efficiency

Fig.2 shows the effect of cycle efficiency by varying the heater pressure. It can be seen from the figure that by increasing the heater pressure the cycle efficiency is also increasing but there is a limit on increasing of heater pressure i.e. critical pressure of the fluid. In this study analysis is done on two fluids R123 and R245fa for subcritical case respectively. It can be seen from the fig. 2 that R123 is having more efficiency than R245fa at a same particular heater pressure. It can be seen from the fig. 2 the efficiency of the Rankine cycle at heater pressure 1326 kPa is 12.04% for fluid R123 and efficiency of Rankine cycle at heater pressure 1326 kPa is 9.08% for fluid R245fa.
So, from the results it can be seen R123 is having more efficiency than R245fa but the amount of chlorine content in R123 makes it unusable as it depletes the ozone layer and is not an ecofriendly fluid.

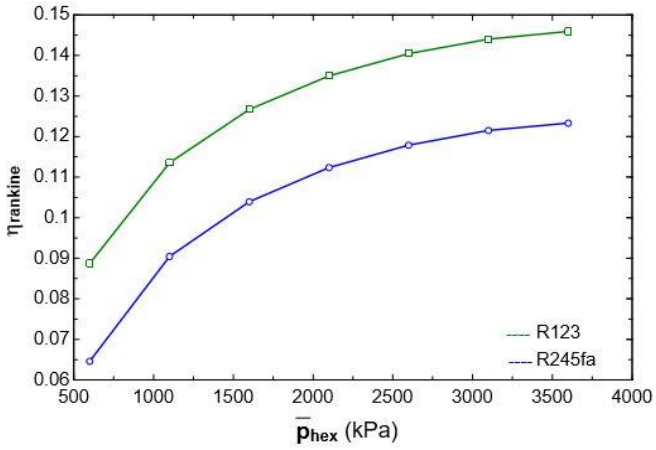


Figure 2: Variation of cycle efficiency with variation of heater pressure (kPa)

3.1.2 Effect on exergy flow rate

Fig. 3 shows the change of exergy flow rate of hot fluid by varying the heat pressure. The exergy flow rate of hot fluid is 67.75 kW at heater pressure of 1326 kPa for the fluid R123 and for fluid R245fa the exergy flow rate is 73.39 kW at heater pressure of 2127 kPa.

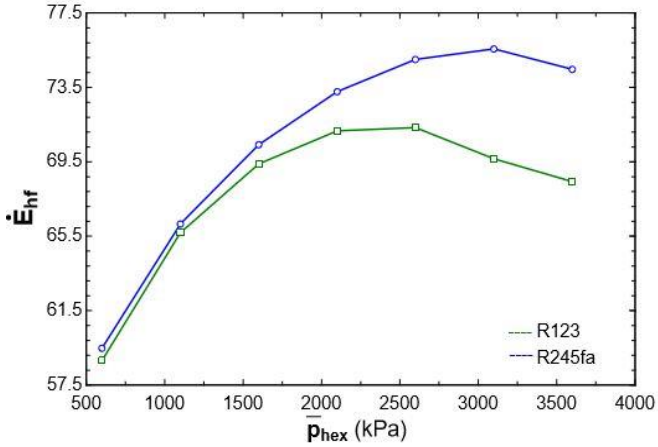


Figure 3: Variation of Exergy flow rate of hot fluid with variation of heater pressure

3.1.3 Effect on heater temperature

Fig.4 shows the change in heater temperature by varying the heater pressure. It can be seen from the Fig. 4 the heater temperature is 125 ºC at heater pressure 1326 kPa for fluid R123 and for fluid R245fa the heater temperature is 95 ºC at heater pressure 1326 kPa.

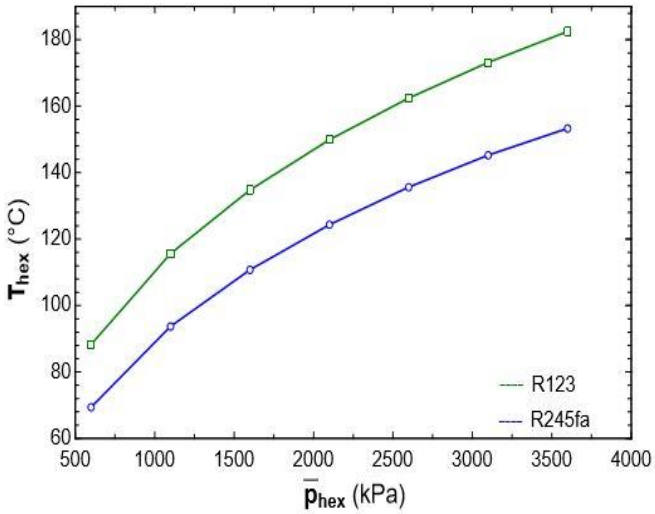


Figure 4: Variation of heater temperature with Variation of heater pressure

3.1.4 Effect of net-work

Fig.5 shows the graph between heater pressure and net-work output. It can be seen from the Fig.5 that the net-work output is 27.33 kW at heater pressure 1326 kPa for fluid R123 and 28.38 kW at heater pressure 2126 kPa for fluid R245fa. From the figure it can be seen that Net-work output is coming more for R123 than R245fa.

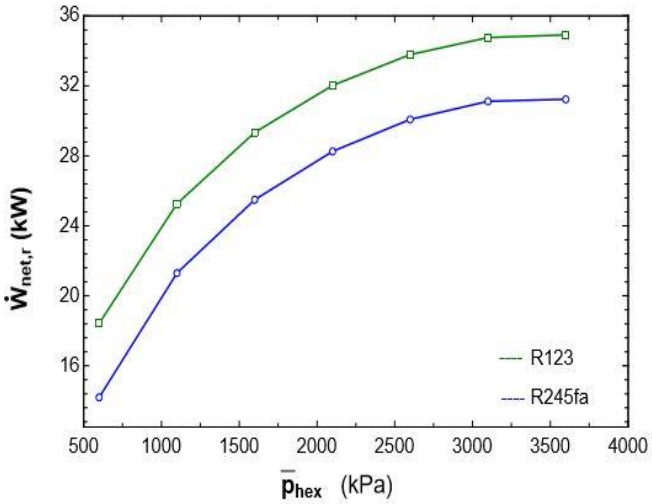


Figure 5: heater pressure Vs Net-work output

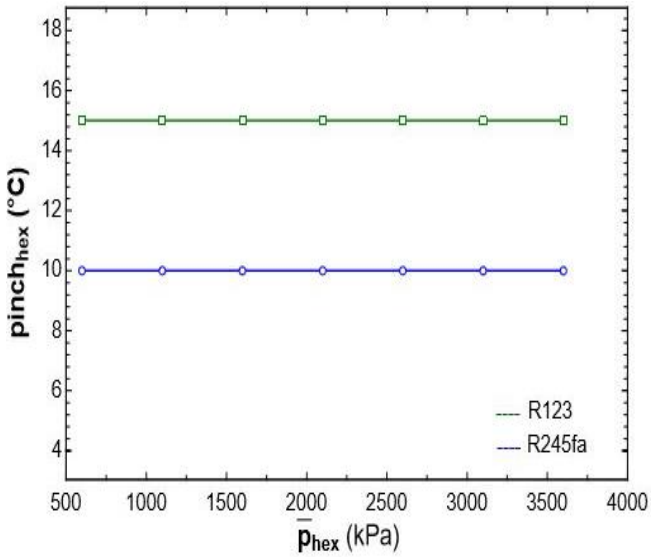


Figure 6: heater pressure Vs pinch point

3.1.5 Effect of pump work

Fig.7 shows the change in pump work by varying the heater pressure. It can be seen from the Fig. 7 that R123 fluid is taking less work to run a pump while R245fa fluid is taking more work to run a pump. The pump work is 1.047 kW at heater pressure 1326 kPa for R123 fluid and 1.832 kW for fluid R245fa at heater pressure 2127 kPa.

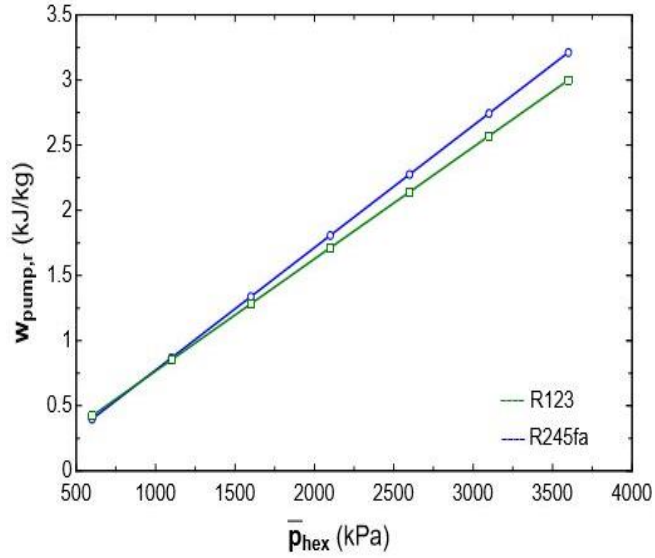


Figure 7: Variation of pump work with Variation of heater pressure

3.1.6 Effect of turbine work

Fig.8 shows the variation between heater pressure and turbine work. It can be seen from the Fig. 8 that fluid R123 is having more turbine work than fluid R245fa at same pressure. For

fluid R123 the turbine work is 28.38 kW at heater pressure 1326 kPa. For fluid R245fa the turbine work is 24.56 kW at heater pressure 1326 kPa.

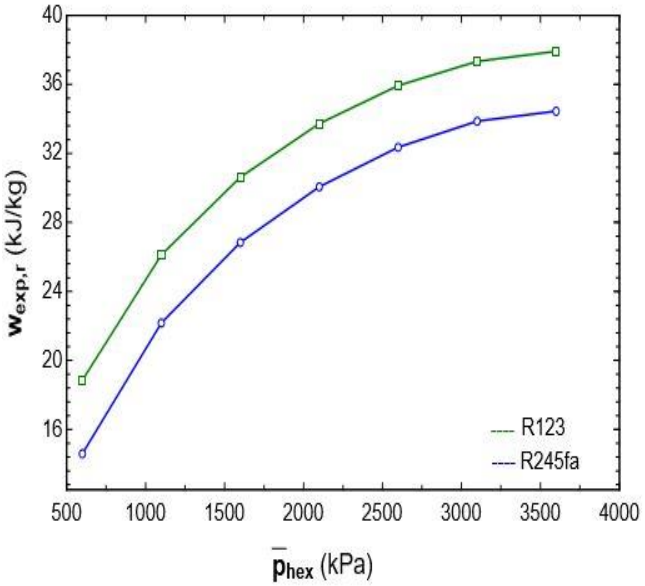


Figure 8: Variation of turbine work with Variation of heater pressure

3.1.7 Effect of second law efficiency

Fig.9 shows the graph between second law efficiency and heater pressure. It can be seen from the Fig. 9 that the second law efficiency is 40.41% at heater pressure 1326 kPa for fluid R123 and 38.67% at heater pressure 2127 kPa for fluid R245fa

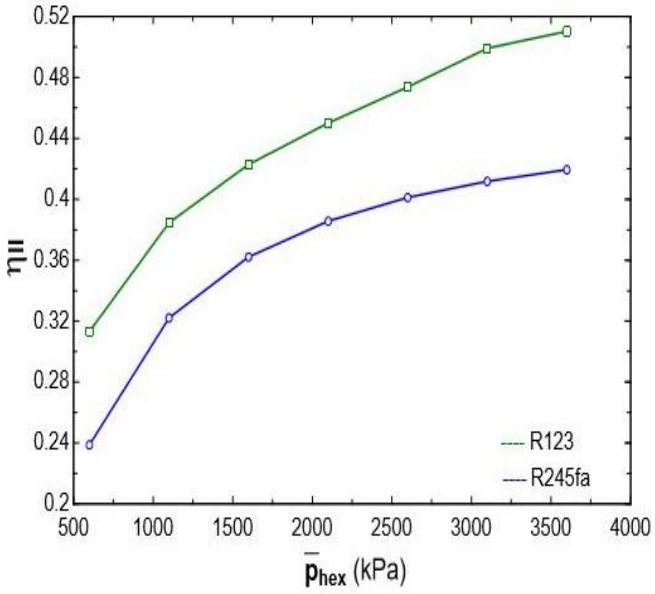


Figure 9: Variation of second law efficiency Variation of heater pressure

3.2 Simple Brayton Cycle

3.2.1 Effect of compressor inlet pressure

Fig.10 shows the effect of pressure at compressor inlet on the efficiency of Brayton cycle. The analysis is done on two fluid i.e. R123 and R245fa. It can be seen from the Fig.10 that for a given value of P1, increasing the turbine inlet temperature (T3) results in increase in efficiency of cycle. This is because ($\eta th = 1 - T4/T3$) as the T3 increases, the denominator increases and the fraction decreases which will result in increasing the efficiency. It can be seen from the Fig. 10 the cycle efficiency is 3.601 % at 94 kPa compressor inlet pressure for fluid R123 and 11.41% at 95 kPa compressor inlet pressure for fluid R245fa.

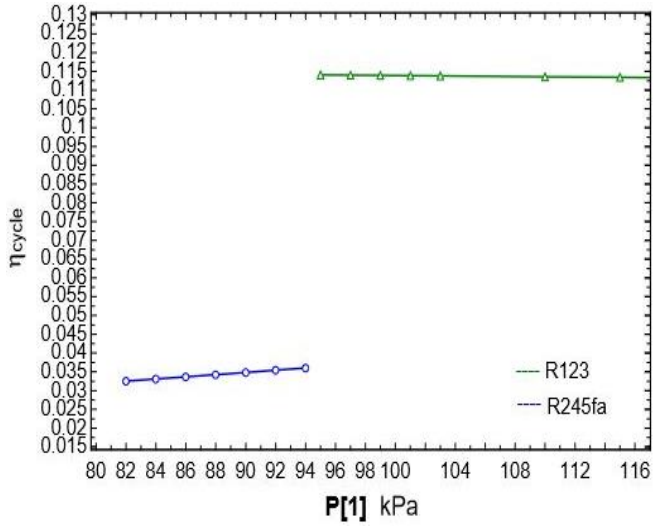


Figure 10: Variation of cycle efficiency with variation of compressor inlet pressure

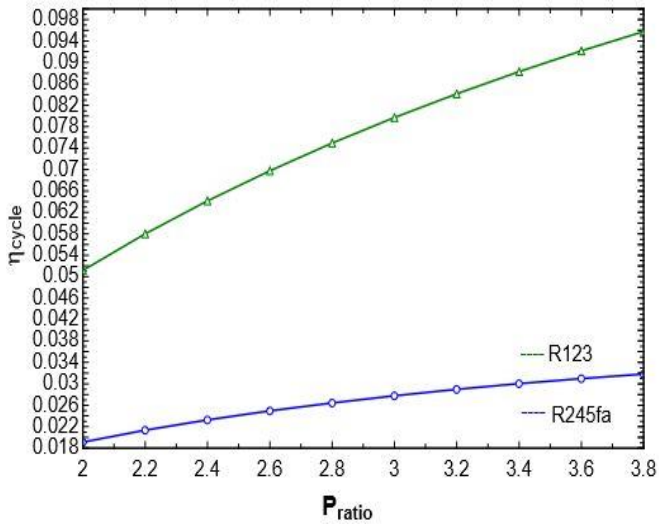


Figure 11: Variation of cycle efficiency with variation of Pressure ratio

3.2.2 Effect of pressure ratio

Fig.11 shows the variation between pressure ratio and cycle efficiency. It can be seen from the Fig.11 that the cycle efficiency is 2.896 % at pressure ratio 3.2 for fluid R245fa and 8.4 % for fluid R123 at 3.2 pressure ratio.

3.2.3 Effect of minimum operation Temperature

Fig.12 shows the graph between minimum operation temperature and cycle efficiency is 3.548 % at T1 = 25 ºC for fluid 245fa and 11.39 % for fluid R123.

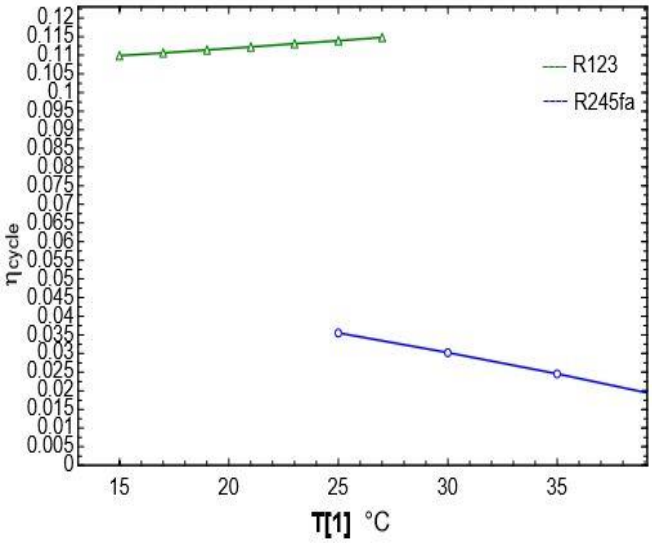


Figure 12: Variation of cycle efficiency with Variation of Minimum Operation temperature

.

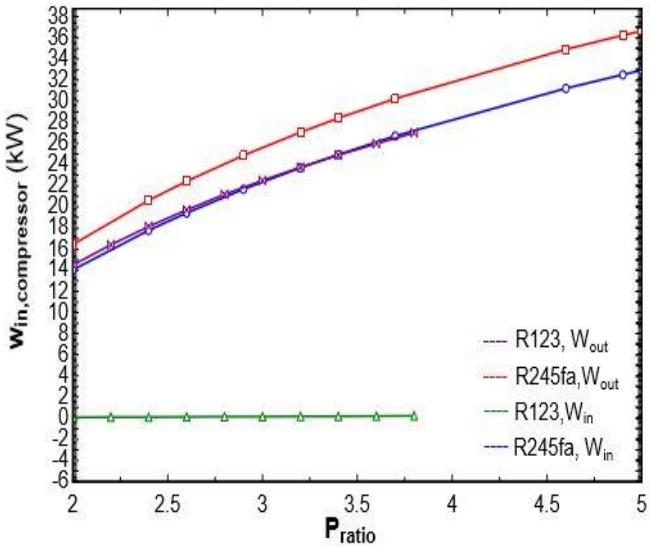


Figure 13: Variation of compressor and turbine works with Variation of Pressure ratio

3.2.4 Effect of pressure ratio on the compressor and turbine work

Fig.13 shows the variation between pressure ratio and compressor & turbine work. It can be seen from the Fig.13 that for fluid R123 the work input and work output is 0.1691 kW and 23.67 kW respectively at pressure ratio 3.2 and for fluid R245fa the work input and work output is 23.71 kW and 27.01 kW respectively at pressure ratio 3.2

3.3 Brayton cycle with Intercooling

The performance evaluation of Brayton Cycle with Intercooling is given below.

3.3.1 Effect of cooler pressure

Fig.14 show the variation of cooler pressure and cycle efficiency. It can be seen from the Fig. 14 the cycle efficiency is 11.39 % at 114 kPa cooler pressure for fluid R123 and 3.812 % at 114 kPa cooler pressure for fluid R245fa.

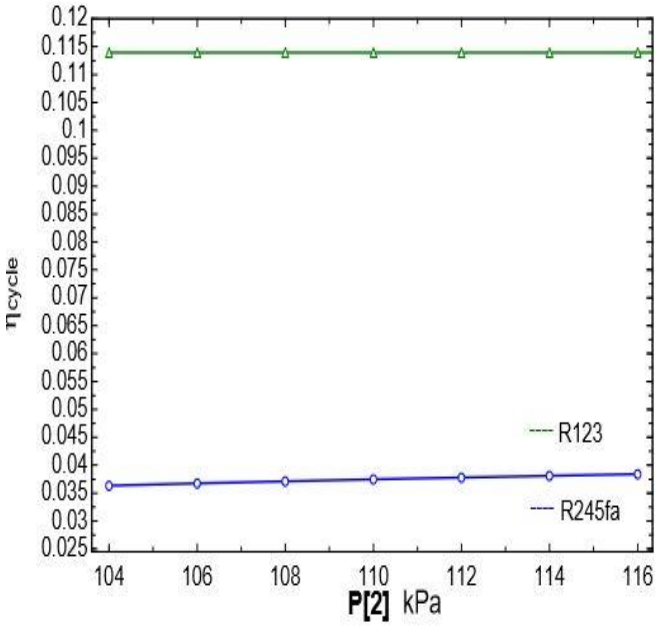


Figure 14: Variation of cycle efficiency with Variation of Cooler pressure

3.3.2 Effect of High pressure Inlet turbine temperature

Fig.15 shows the variation between turbine inlet temperature and efficiency of cycle. It can be seen from the Fig. 15 that the cycle efficiency is 11.47 % at 150 ºC for fluid R123 and 2.892 % at 150 ºC for fluid R245fa.

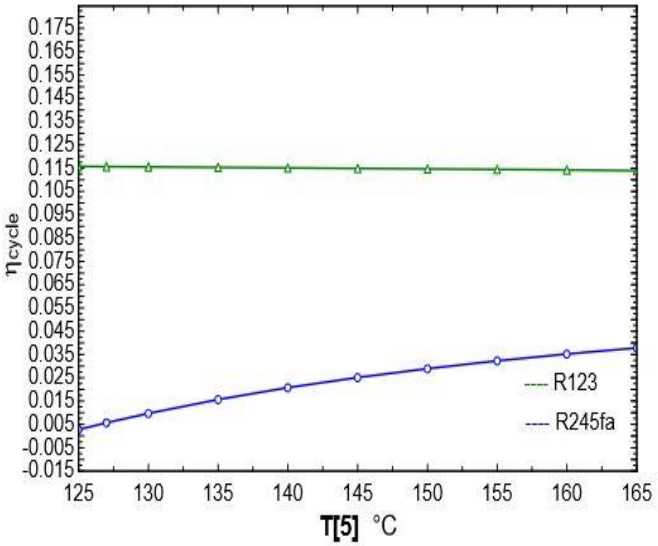


Figure 15: Variation of cycle efficiency with High pressure inlet turbine temperature

3.3.3 *Effect of cooler pressure on cycle work*

Fig.16 show the variation of cooler pressure and net-work. It can be seen from the Fig. 3.15 the net-work is 11.37 kW at 114 kPa cooler pressure for fluid R123 and 4.136 kW at 114 kPa cooler pressure for fluid R245fa.

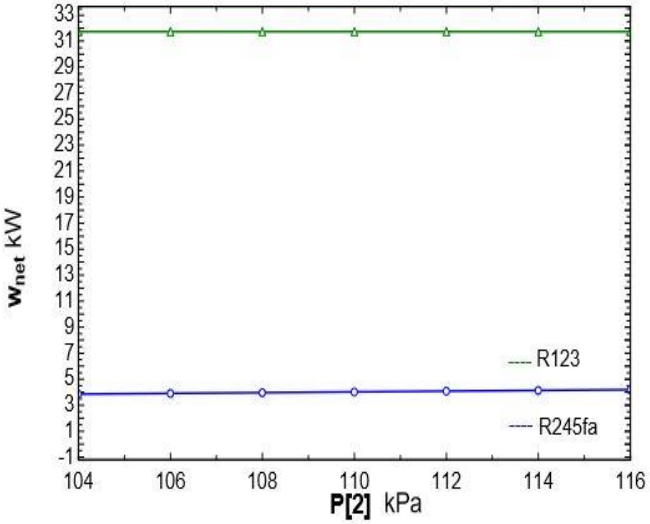


Figure 16: Variation of Cooler pressure Vs Variation of Net-work

3.3.4 *The effect of pressure ratio*

Fig 3.16 show the variation of pressure ratio and cycle efficiency. It can be seen from the Fig. 17 that the cycle efficiency is 8.412 % at pressure ratio 3.2 for fluid R123 and 3.054 % at pressure ratio 3.2 for fluid R245fa.

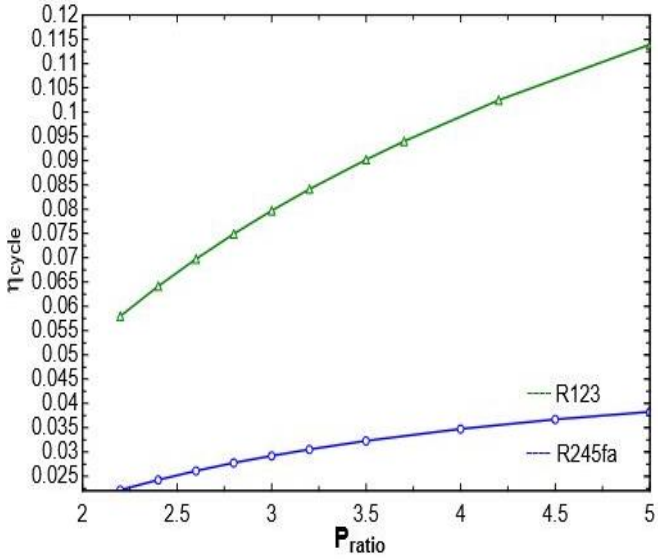


Figure 17: Pressure ratio Vs cycle efficiency

3.3.5 *Effect of pressure ratio on compressor and turbine work*

Fig.18 shows the variation between pressure ratio and compressor & turbine work. It can be seen from the Fig.18 that for fluid R123 the work input and work output is 0.1691 kW and 23.67 kW respectively at pressure ratio 3.2 and for fluid R245fa the work input and work output is 23.42 kW and 27.07 kW respectively at pressure ratio 3.2.

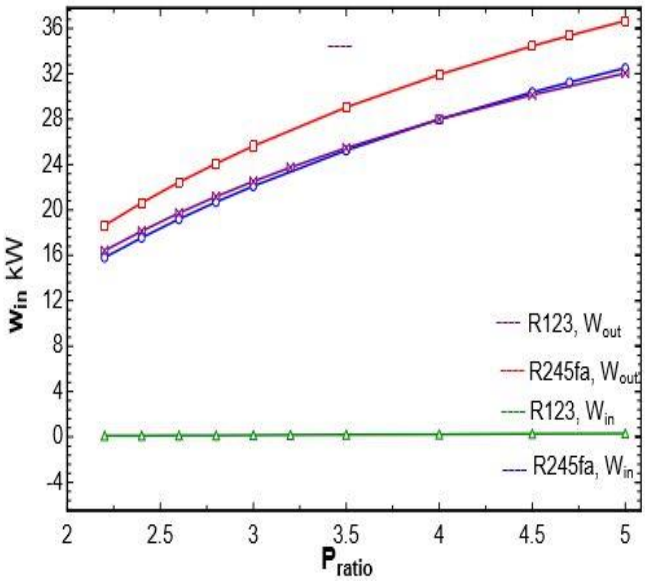


Figure 18: Variation of Pressure ratio Vs Variation of compressor and turbine work

3.3.6 The effect of Minimum cycle temperature

Fig.19 shows the graph between minimum operation temperature and cycle efficiency is 3.827 % at T1 = 25 ºC for fluid 245fa and 11.39 % for fluid R123.

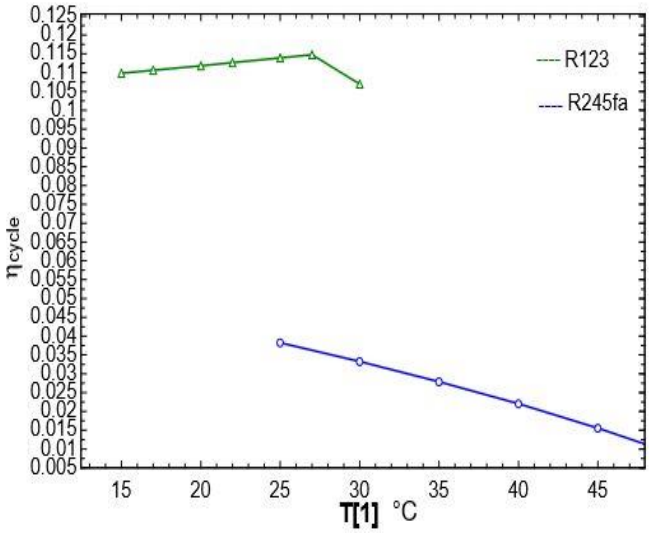


Figure 19: Variation of Minimum cycle temperature Vs Variation of cycle efficiency

3.4 Brayton with Reheating

3.4.1 The effect of Re-heater pressure

Fig. 20 show the variation of re-heater pressure and cycle efficiency. It can be seen from the Fig. 20 that the cycle efficiency is 10.69 % at 160 kPa re-heater pressure for fluid R123 and 3.372 % at 160 kPa re-heater pressure for fluid R245fa.

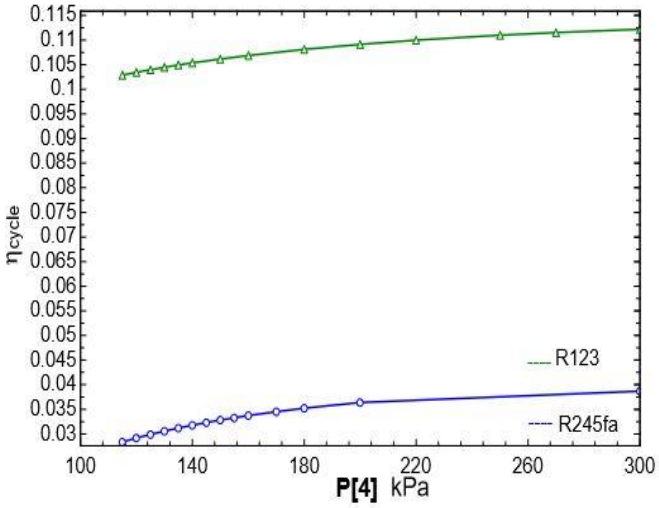


Figure 20: Variation of Re-heater pressure Vs Variation of cycle efficiency

3.4.2 The effect of high pressure turbine inlet temperature

Fig.21 show the variation of turbine inlet pressure and cycle efficiency. It can be seen from the Fig. 3.20 that the cycle efficiency is 10.31 % at 160 kPa turbine inlet pressure for fluid R123 and 2.562 % at 160 kPa turbine inlet pressure for fluid R245fa.

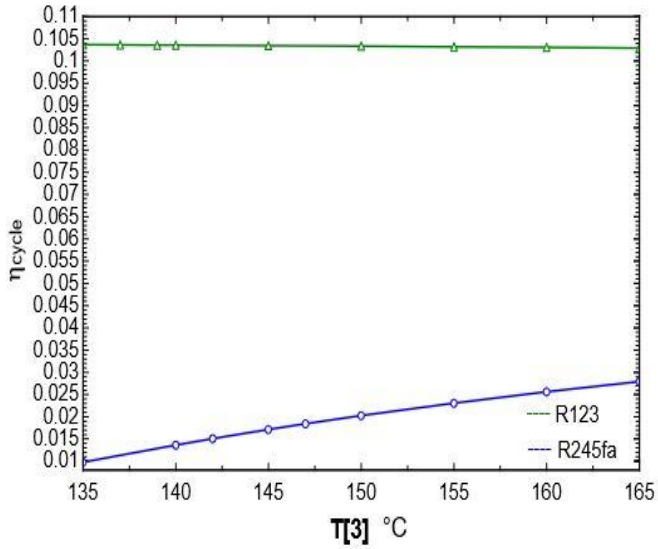


Figure 21: Variation of High pressure inlet turbine temperature Vs Variation of cycle efficiency

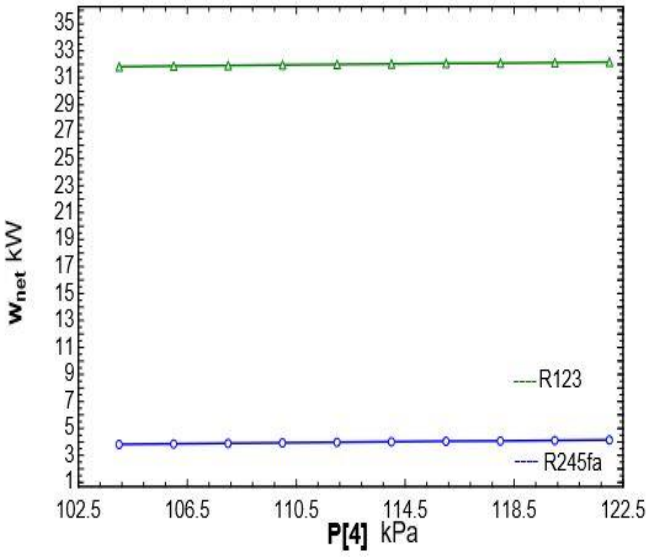


Figure 22: Variation of Re-heater pressure Vs Variation of Net-work

3.4.3 The effect of Re-heater pressure

Fig.22 show the variation of re-heater pressure and net-work. It can be seen from the Fig. 22 that the net-work is 32.13 kW at 120 kPa re-heater pressure for fluid R123 and 2.915 kW at 120 kPa re-heater pressure for fluid R245fa.

3.4.4 The effect of pressure ratio on cycle efficiency

Fig.23 show the variation of pressure ratio and cycle efficiency. It can be seen from the Fig. 23 the cycle efficiency is 7.4 % at pressure ratio 3 for fluid R123 and 2.4 % at pressure ratio 3 for fluid R245fa.

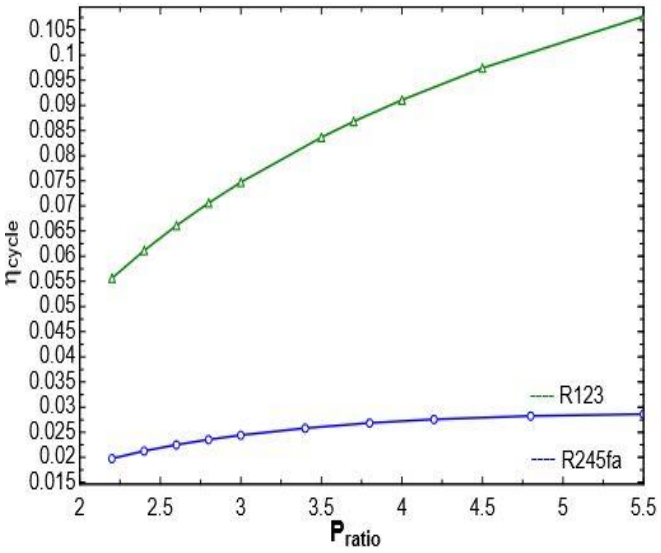


Figure 23: Variation of Pressure ratio Vs Variation of cycle efficiency

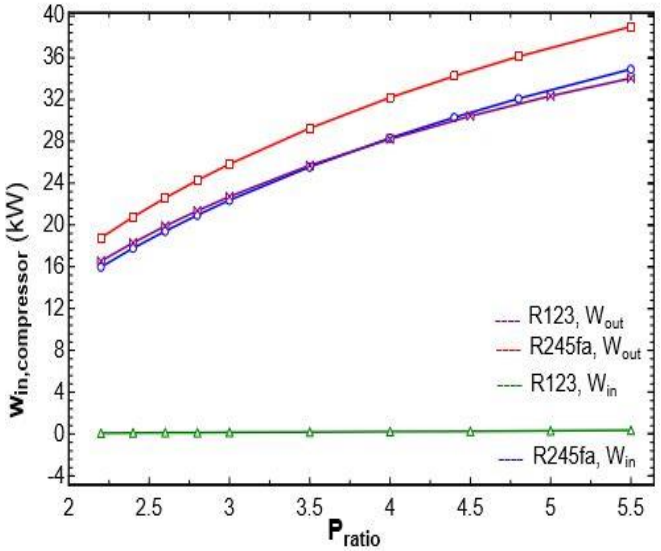


Figure 24: Variation of Pressure ratio Vs Variation of compressor and turbine works

3.4.5 The effect of pressure ratio on compressor and turbine work

Fig.24 shows the variation between pressure ratio and compressor & turbine work. It can be seen from the Fig. 24 that for fluid R123 the work input and work output is 15.38 kW and 22.72 kW respectively at pressure ratio 3.2 and for fluid R245fa the work input and work output is 22.38 kW and 25.83 kW respectively at pressure ratio 3.2.

3.4.6 The effect of minimum cycle temperature

Fig.25 shows the graph between minimum operation temperature and cycle efficiency is 2.837 % at T1 = 25 ºC for fluid 245fa and 10.29 % for fluid R123.

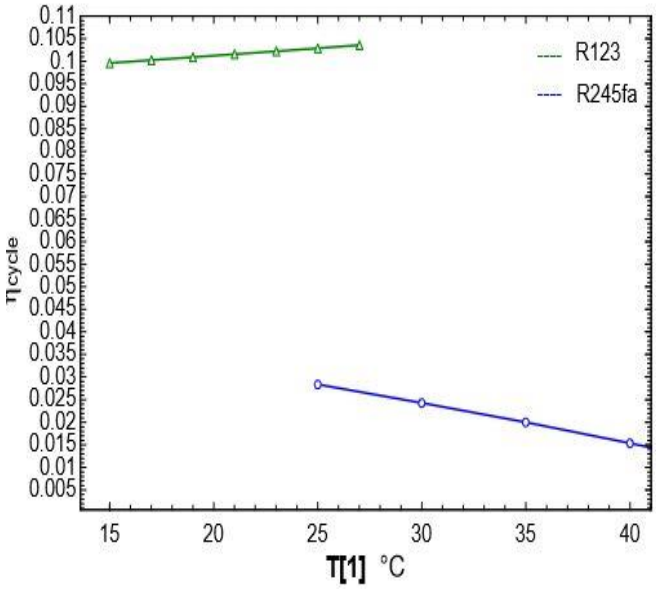


Figure 25: Variation of Minimum cycle temperature Vs Variation of cycle efficiency

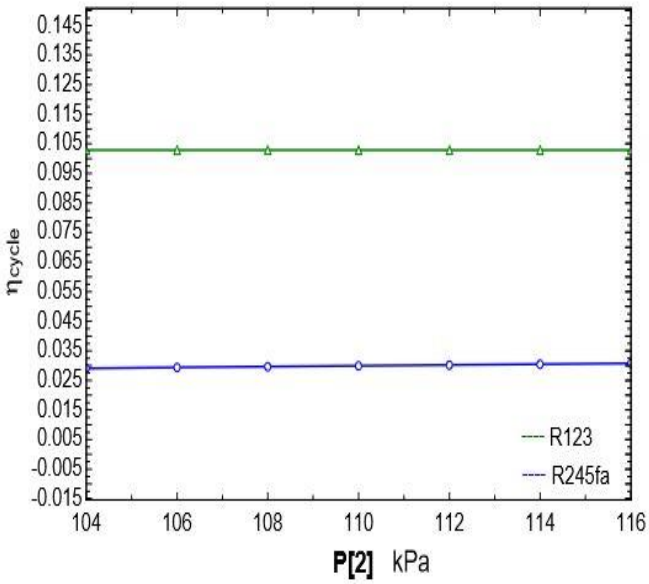


Figure 26: Variation of Cooler pressure Vs Variation of cycle efficiency

3.5 Brayton cycle with Intercooling and Reheating

3.5.1 The effect of cooler pressure

Fig.26 show the variation of cooler pressure and cycle efficiency. It can be seen from the Fig.26 that the cycle efficiency is 10.29 % at 114 kPa cooler pressure for fluid R123 and 3.051 % at 114 kPa cooler pressure for fluid R245fa.

3.5.2 The effect of high pressure Inlet turbine temperature

Fig.27 shows the graph between HP inlet turbine temperature and cycle efficiency is 2.31 % at T5 = 150 ºC for fluid 245fa and 10.33 % for fluid R123.

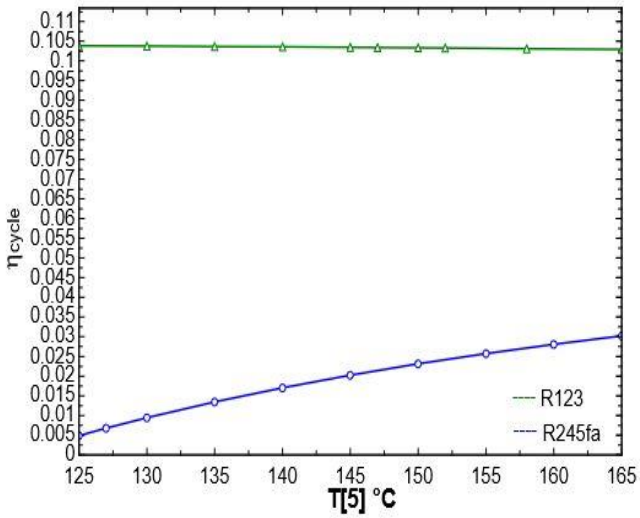


Figure 27: Variation of High pressure Inlet turbine temperature Vs cycle efficiency

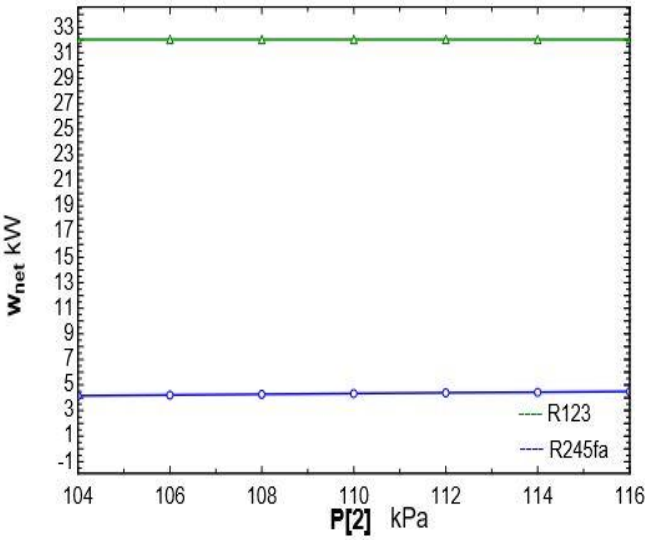


Figure 28: Variation of Heater pressure Vs Variation of Net-work

3.5.3 The effect of heater pressure on total cycle work

Fig.28 show the variation of heater pressure and Net-work. It can be seen from the Fig. 28 that the Net-work is 32.04 kW at 114 kPa heater pressure for fluid R123 and 4.439 kW at 114 kPa heater pressure for fluid R245fa.

3.5.4 Effect of pressure ratio on cycle efficiency

Fig.29 show the variation of pressure ratio and cycle efficiency. It can be seen from the Fig. 29 the cycle efficiency is 7.472 % at 3 pressure ratio for fluid R123 and 2.61 % at 3 pressure ratio for fluid R245fa.

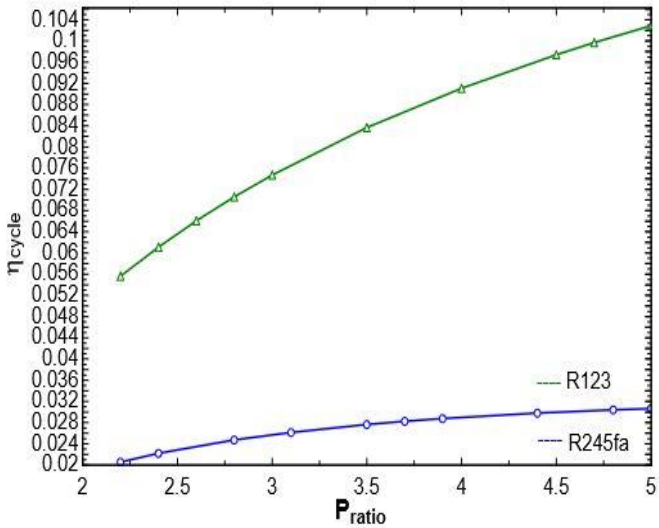


Figure 29: Variation of Pressure ratio Vs Variation of cycle efficiency

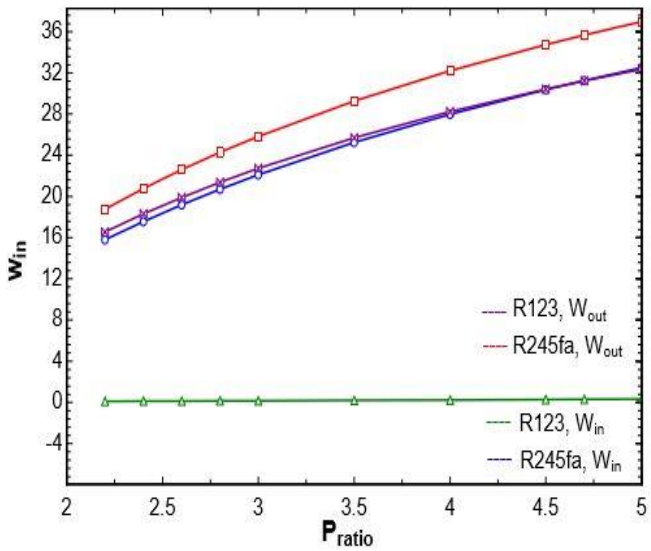


Figure 30: Variation of compressor and turbine work with variation of Pressure ratio

3.5.5 *The effect of pressure ratio on compressor and turbine work*

Fig.30 shows the variation between pressure ratio and compressor & turbine work. It can be seen from the Fig. 30 that for fluid R123 the work input and work output is 15.38 kW and 22.72 kW respectively at pressure ratio 3 and for fluid R245fa the work input and work output is 22.1 kW and 25.83 kW respectively at pressure ratio 3.

3.5.6 *The effect of Minimum cycle temperature*

Fig.31 shows the graph between minimum operation temperature and cycle efficiency is 3.064 % at T1 = 25 ºC for fluid 245fa and 10.29 % for fluid R123.

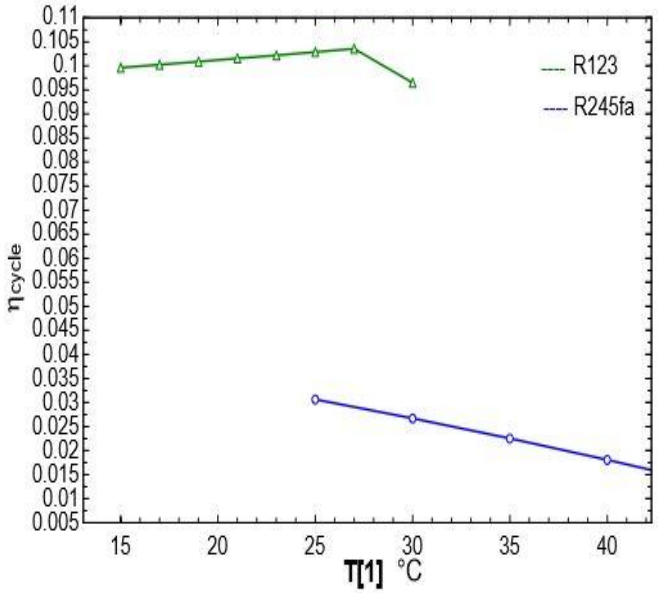


Figure 31: Variation of Minimum cycle temperature Vs Variation of cycle efficiency

3.6 *Combined cycle*

The performance evaluation of combined cycle is given below

3.6.1 *The effect of heater pressure on combined cycle efficiency*

Fig.32 shows the variation between heater pressure and combined cycle efficiency. It can be seen from the Fig. 32 that the combined efficiency, Rankine efficiency, Brayton efficiency is 12.43 %, 11.79 %, 10.72 % respectively at heater pressure 2600 kPa for fluid R245fa and 12.43 %, 14.04 %, 10.99 % respectively for fluid R123.

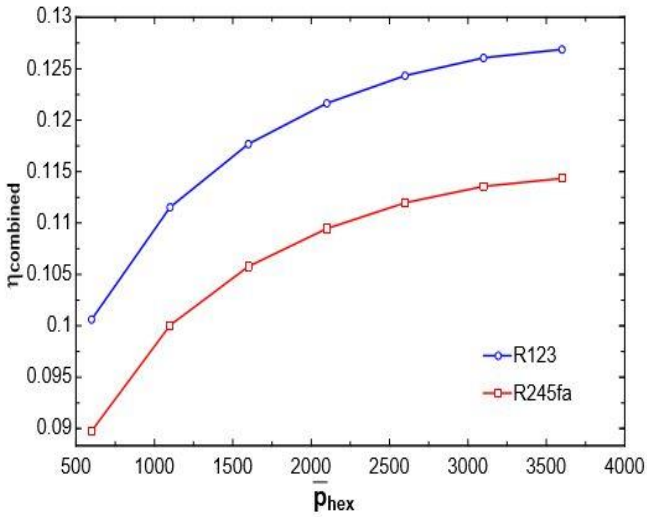


Figure 32: Variation of combined cycle efficiency with variation of heater pressure

3.6.2 *The effect of heater pressure on combined net-work*

Fig.33 shows the change in combined cycle net-work output by varying the heater pressure. It can be seen from the Fig. 33 that the combined cycle work is 63.21 kW at heater pressure 2600 kPa for fluid R123 and for fluid R245fa the combined cycle work is 64.16 kW at heater pressure 2600 kPa.

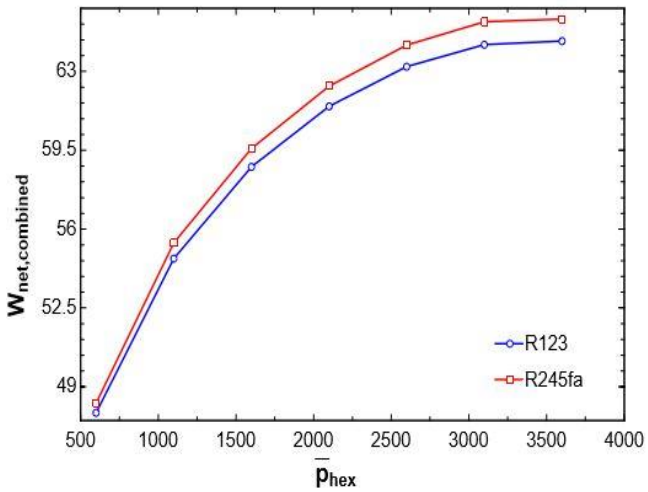


Figure 33: Variation of combined net-work with variation of Heater pressure

3.6.3 *Effect of heater pressure on Turbine work of both Brayton and Rankine*

Fig.34 shows the change in turbine work of Brayton and Rankine cycle by varying the heater pressure. It can be seen from the Fig. 34 that the turbine work for Brayton cycle is 35.93 kW and 30.08 kW for Rankine cycle at heater pressure

2600 kPa for fluid R123 and for fluid R245fa the turbine work for Brayton is 34.8 kW and for Rankine is 32.36 kW at heater pressure 2600 kPa.

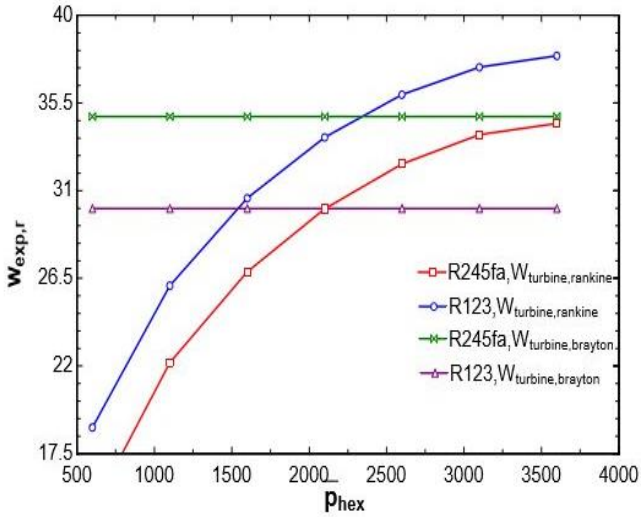


Figure 34: Variation of Turbine work with variation of heater pressure

3.6.4 *Effect of heater pressure on pump and compressor work*

Fig.35 shows the change in pump and compressor work of Brayton and Rankine cycle by varying the heater pressure. It can be seen from the Fig. 35 that the pump and compressor work for Brayton cycle is 2.142 kW & 0.6571 kW at heater pressure 2600 kPa for fluid R123 and for fluid R245fa the pump and compressor work for Rankine cycle is 2.276 kW & 0.7183 at heater pressure 2600 kPa.

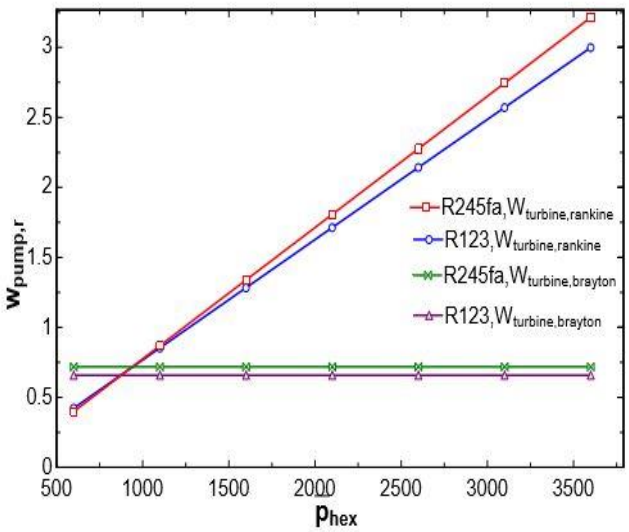


Figure 35: Variation of pump and compressor works with Variation of Heater pressure

3.6.5 *The effect on heater temperature on combined efficiency*

Fig.36 shows the change in combined cycle net efficiency by varying the heater temperature. It can be seen from the Fig. 36 that the combined cycle efficiency is 11.91 % at heater temperature 140 ºC for fluid R123 and for fluid R245fa the combined cycle efficiency is 11.27% at heater temperature 140 ºC.

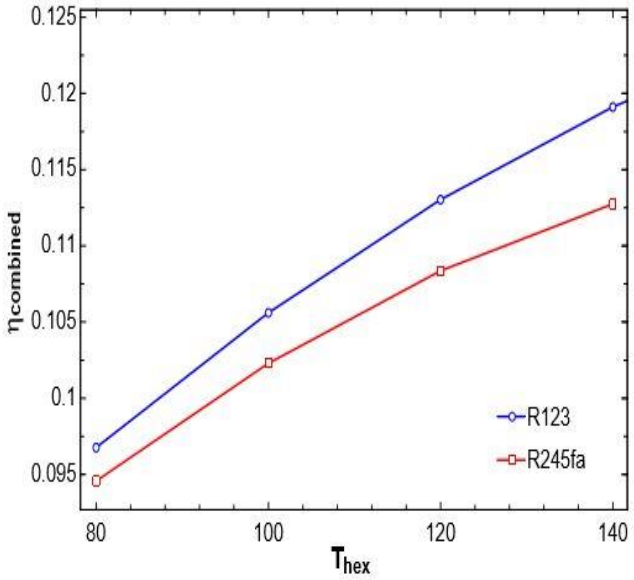


Figure 36: Variation of combined cycle efficiency with variation of Heater temperature

3.6.6 *Effect of heater pressure on combined net-work*

Fig.37 shows the change in combined cycle net-work by varying the heater temperature. It can be seen from the Fig. 37 that the combined cycle net-work is 59.74 kW at heater temperature 140 ºC for fluid R123 and for fluid R245fa the combined cycle net-work is 64.71 kW at heater temperature 140 ºC.

3.6.7 *Effect of pressure ratio on combined cycle efficiency*

Fig.38 shows the change in combined cycle net efficiency by varying the pressure ratio. It can be seen from the Fig.38 that the combined cycle efficiency is 13.43 % at pressure ratio 10 for fluid R123 and for fluid R245fa the combined cycle efficiency is 13.08 % at pressure ratio 10.

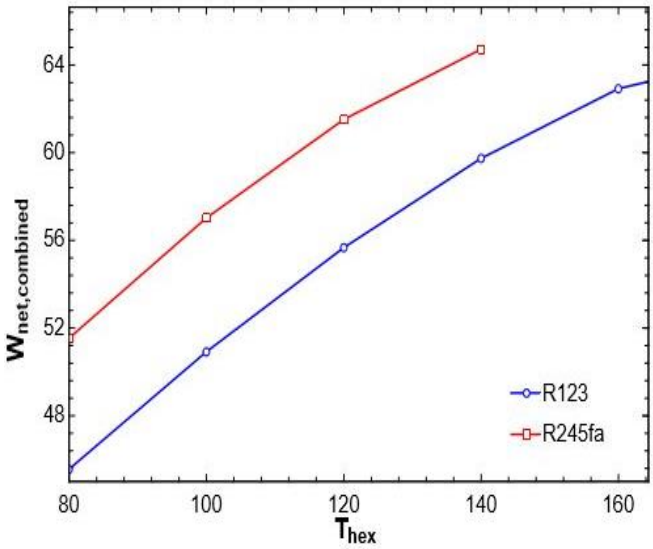


Figure 37: Variation of combined net-work with variation of Heater temperature

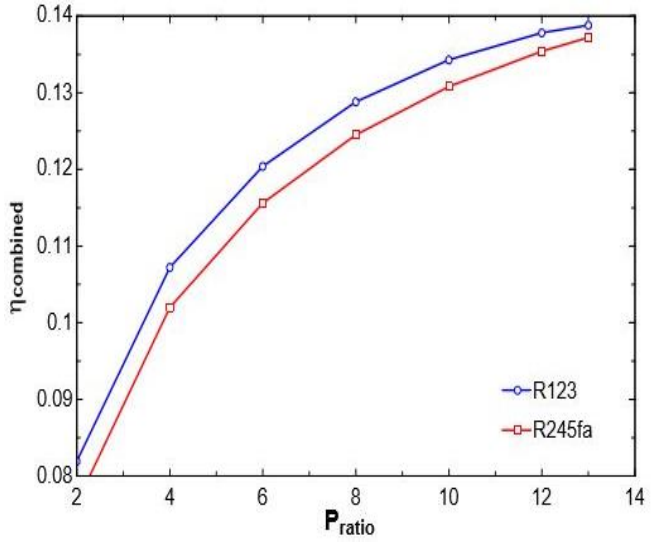


Figure 38: Variation of combined cycle efficiency with Variation of Pressure ratio

3.6.8 *Effect of pressure ratio on combined net-work*

Fig39 shows the change in combined cycle net-work by varying the pressure ratio. It can be seen from the Fig. 39 that the combined cycle net-work is 64.58 kW at pressure ratio 10 for fluid R123 and for fluid R245fa the combined cycle net-work is 72.96 kW at pressure ratio 10.

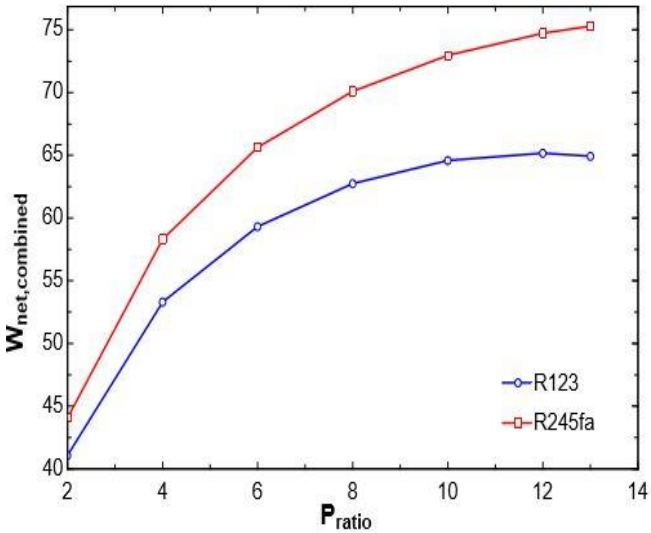


Figure 39: Variation of combined net-work with variation of Pressure ratio

3.6.9 *Effect of compressor inlet pressure on combined efficiency*

Fig.40 shows the change in combined cycle net efficiency by varying the compressor inlet pressure. It can be seen from the Fig. 40 that the combined cycle efficiency is 11.26 % at compressor inlet pressure 300 kPa for fluid R123 and for fluid R245fa the combined cycle efficiency is 10.8 % at compressor inlet pressure 300 kPa.

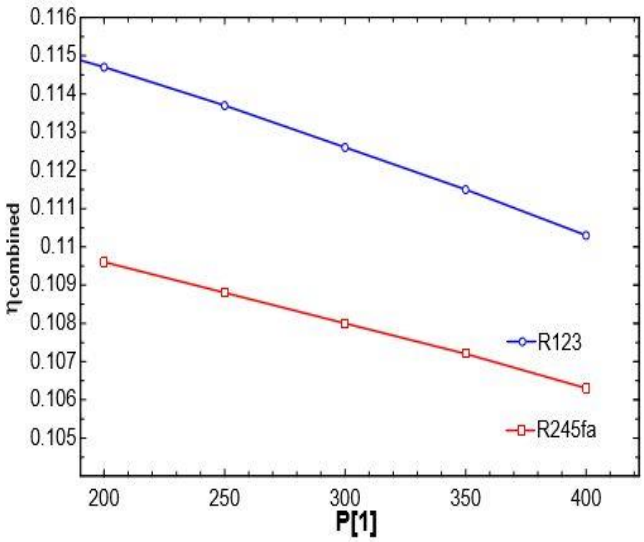


Figure 40: Variation of combined cycle efficiency with variation of Compressor inlet pressure

3.6.10 Effect of compressor inlet pressure on combined net-work

Fig.41 shows the change in combined cycle net-work by varying the compressor inlet pressure. It can be seen from the Fig. 41 that the combined cycle net-work is 55.03 kW at compressor inlet pressure 300 kPa for fluid R123 and for fluid R245fa the combined cycle net-work is 60.95 kW at compressor inlet pressure 300 kPa.

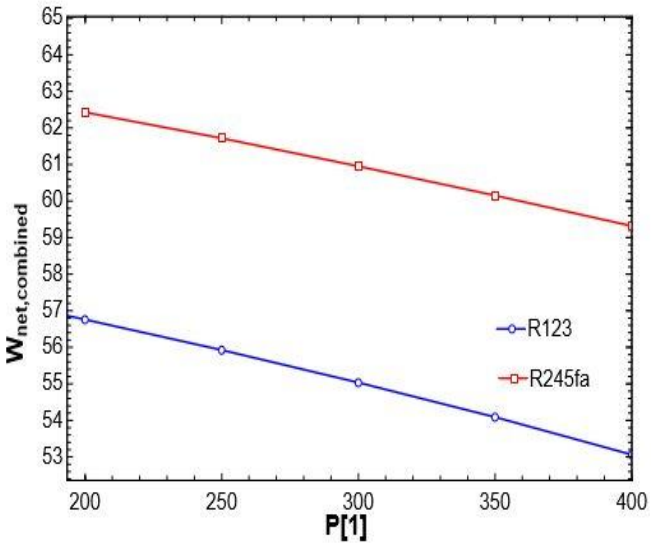


Figure 41: Variation of combined net-work with variation of Compressor inlet pressure

4. Conclusion

In this study, the simulation of subcritical organic Rankine cycle system with internal heat exchanger using R123 and R245fa is done which illustrates the impacts of IHE on ORC systems. Also, simulation is done on Brayton cycle and combined cycle. In combined cycle simulation is done using R123 and R245fa. The mass flow rate taken into account for analysis is 1 kg/s and the warmth source temperature is taken as 200ºC. The temperature difference of 10ºC is set as the minimum heat transfer temperature difference of heat exchanger. The simulation results show that there will be an optimum gas heater pressure for power cycles at certain cycle working conditions. The heater pressure will increase with increasing heat source temperature. The efficiency of the expansion machine will have more crucial influence on the cycle thermal efficiency than the pump efficiency does.

For combined cycle, the cycle efficiency is increasing on increasing of heater pressure for both R123 and R245fa. But efficiency is coming more for R123 as compared to R245fa at particular heater pressure.For combined cycle, the combined net-work of cycle is increasing on increasing of heater pressure for both R123 and R245fa but work output is more for R245fa. In combined cycle, cycle efficiency is increasing on increasing of pressure ratio but there is more increase seen in R123. Also, net-work is also increasing on increasing of pressure ratio but here more increase is seen in R245fa.In combined cycle, on increasing compressor inlet pressure the cycle efficiency and the net-work both are decreasing for R123 and R245fa.

References

[1] Sanjay Vijayaraghavan & D Yogi Goswami [2005] Organic Working Fluids for a Combined Power and Cooling Cycle in Journal of Energy Resources Technology, Vol-127, No-2 · 2005, DOI: 10.1115/1.188503.

[2] R.S. Mishra & Dharmendra Sahu [2016]Thermodynamic analysis and comparison of various organic fluids for ORC in Gas turbine-Organic Rankine combined cycle plant with solar reheating and regeneration of ORC fluids, International Research Journal of Engineering and Technology (IRJET) e-ISSN: 2395 -0056 , Vol: 03, Issue: 08 ,2016 www.irjet.net p-ISSN: 2395-0072.

[3] Al-Sulaiman Fahad A, Hamdullahpur Feridun, Dincer Ibrahim"[2012] Performance assessment of a novel system using parabolic trough solar collectors for combined cooling, heating, and power production" Renew Energy 2012;48:161–72.

Nomenclature

dP_{cf}	Total resistance at condenser cooling water side, kP_a
ε	Heat exchanger effectiveness
Q_{net}	Net heat transfer rate, W
dP_{hf}	Flow resistance in the working fluid circulation loop, kP_a
e	specific flow energy, kJ/kg
E_d	energy destruction rate, K_w
h	specific enthalpy, kJ/kg
m	mass flow rate, kg/s
P	pressure, KP_a
s	specific entropy, kJ/(kg K)
T	Temperature,
v	specific volume, m^3/kg
W	power output, kJ/s
w	specific power, kJ/kg
η_{ex}	energy efficiency
η_P	overall efficiency of the working fluid pump
$\eta_{P,i}$	isentropic compression efficiency of the working fluid pump
$\eta_{P,m}$	mechanical efficiency of the working fluid pump
η_{th}	thermal efficiency
$\eta_{T,i}$	internal efficiency of the expander
$\eta_{T,m}$	mechanical efficiency of the expander

ResearchGate

See discussions, stats, and author profiles for this publication at: https://www.researchgate.net/publication/326835903

Tribological behavior of thin film coating-a review

Article · January 2018
DOI: 10.14419/ijet.v7i3.11788

CITATIONS
0

READS
52

5 authors, including:


Ramesh Yadaw
Northern India Textile Research Association
8 PUBLICATIONS **7** CITATIONS
SEE PROFILE


Somnath Chattopadhyaya
Indian School of Mines University
115 PUBLICATIONS **360** CITATIONS
SEE PROFILE


Sanjeev Kumar
SRM University
35 PUBLICATIONS **124** CITATIONS
SEE PROFILE


R. C. Singh
Delhi Technological University
42 PUBLICATIONS **54** CITATIONS
SEE PROFILE

Some of the authors of this publication are also working on these related projects:

Physical Vapour Deposition View project

equipment failure analysis View project

All content following this page was uploaded by Ramesh Yadaw on 06 August 2018.

The user has requested enhancement of the downloaded file.

International Journal of Engineering & Technology, 7 (3) (2018) 1656-1663

International Journal of Engineering & Technology

Website: www.sciencepubco.com/index.php/IJET
doi: 10.14419/ijet.v7i3.11788
Research paper

Tribological behavior of thin film coating-a review

Ramesh Chandra Yadaw [1], Shailesh Kumar Singh *[1], Somanth Chattopadhyaya [1], Sanjeev Kumar [2], R.C. Singh [3]

[1] Department of Mechanical Engineering, Indian Institute of Technology (IIT-ISM) Dhanbad, India
[2] Department of Mechanical Engineering, Krishna Engineering College, Ghaziabad, India
[3] Department of Mechanical Engineering, Delhi Technological University, Delhi, India
**Corresponding author E-mail: shaileshsonu10@gmail.com*

Abstract

An automotive industry sectors are facing major challenges to produce materials of high hardness, low wear rate and corrosive resistant due to international intrinsic norms. Scientist and researchers are developing new materials with different surface properties to come over the international intrinsic norms and hence, they are trying to enhance tribological behavior and increase the life of automotive parts, make the parts corrosive resistant. Therefore, it has become essential to explore the new combinations of coating materials. A tribome-chanical effect of hard metal (WC-12 % Co and Cr3C2-25 % NiCr) coating on the cast iron and steel substrate were compared. Micro hardness, porosity, microstructure, corrosion and economical factor were compared and concluded that the hardness of WC-12%Co & Cr3C2-25NiCr coated on mild steel substrate were comparatively superior but the Cr3C2-NiCr coated cast iron substrate was better over WC-12%Co because it was more economical and corrosive resistant and competitive wear characteristics and as the temperature and load are increased, the Cr3C2-NiCr shows excellent wear resistances.

Keywords: *Hard Metals; Micro Hardness; Porosity; SEM; Microstructure; Environment.*

1. Introduction

An automotive industry sector is possibly among the most technologically demanding of all industry segments. In order to face the challenges & meet market competitions, Scientist and researchers are constantly exploring new technologies and materials to enhance tribological behavior, life of the automotive parts, surface morphology, fuel efficiency, reduce weight, lower emissions, corrosive resistant and in the end best economy.

Thin film metal coatings are being used for tribological applications [1-3]. In modern industrial system the major challenges are to produce materials having high hardness, low wear rate and corrosive resistant and surface engineering is a rapid growing area of research because of the high industrial demands for corrosion control and wear resistance, coupled with enabling technology that produces new kind of coatings with desirable tribological performance as well as mechanical properties.Hardmetal coatings have shown improvements in recent successful tests [4].These coatings have many tribological applications such as automotive parts, diesel engine piston rings [5-6] aerospace components, etc .The elevated friction and wears generated causes material losses and decreases efficiency of mechanical parts. In this context, there are quite a number of processes to apply coatings, as well as a nearly unlimited number of coating materials. Some processes are not suitable for certain coating materials; also, the necessary coating thicknesses are not attainable with all methods. Beyond that, the equipment necessary for some processes can be quite complex and, therefore, costly. The use of cost analysis can determine whether a coating is a practical solution. Today's regulations require that ecological criteria of the respective coating processes must also be examined, as not all methods are environmentally equal for example the hard chrome plating technology is not favorable for health and environment[7-10].Various researchers have made successful attempt on comparison of tribo-mechanical properties of thermally sprayed and hard chrome plating. some principal coating technologies, such as thermal spray (wire arc, plasma, high velocity oxy-fuel, detonation spray), laser deposition, electrolytic methods (electro deposition, electro less deposition, pulsed electro deposition, micro arc oxidation/plasma electrolytic oxidation), and vapor based techniques (physical and chemical vapor deposition, gas & plasma nitriding, nitro carburizing etc), are being introduced to fulfill specific technical needs of different automotive applications [11-16].

Each coating technique differs in many respects such as form of feed stock materials (powders, wire, rod), coating thickness, substrate temperature, component geometry and/or size constraint etc [17]. The selection of materials for wear resistant applications is influenced by the way wear takes place such as sliding, abrasive and erosive wear [18-23].The prediction of wear resistance under a given wear situation is influenced by the contact conditions, variables affecting the wear, There are many factors that influence the coating characteristics such as effect of heat treatments, compositions, binders, types of spraying method, temperatures, size of feedstock powder, types of hard metals etc.HVOF sprayed WC-12Co and75 Cr_3C_2-25NiCr coatings are used at high temperature, wear and corrosion. WC-12Co and 75Cr_3C_2- 25NiCr coatings are used under different wear conditions such as sliding wear (e.g. piston rings brake rotors and cylinder liners), abrasive wear (e.g.Aeroplane landing gear,), and erosive wear (Aircraft blades and its propellers, [24-32].WC-based metals are widely used in practice mainly for high hardness and toughness[33],[34-36]. Cr_3C_2–25 wt. %NiCr coatings are frequently used to guard against wear at increasing temperatures. [37–39].

Researchers are trying to expand the range of applications of thermal spraying and developing new types of hard metal powders and mixtures.[40-42].The process of deposition with compound or mechanical mixtures are differs in various aspects such as particle size and forms etc.[43-46]

Copyright © 2018 Ramesh ChandraYadaw et al. This is an open access article distributed under the Creative Commons Attribution License, which permits unrestricted use, distribution, and reproduction in any medium, provided the original work is properly cited.

In the current study, we have compared different coating materials with different substrates (Cast Iron, Mild steel) and their tribomechanical properties (wear, microstructure, hardness and porosity etc.).

2. Materials & methods

2.1. Types of deposition techniques

Steel and cast iron are widely used metals in construction, mechanical, tooling, aircraft and chemical industries [47 -49], as they have good mechanical properties and relatively cheaper. But its hardness, corrosion resistance and wear restrict their uses in demanding conditions and environments. Deposition techniques are very practical and effective for the improvement of hardness, corrosion resistance and wear properties of these materials [50-51].The various deposition techniques are being used for surface coating purpose, some typical techniques are as follows.

1) Thermal spraying technique
2) Physical vapor Technique
3) Chemical vapor technique
4) Galvanize
5) Baked Polymers

Thermally sprayed hard metal coatings have a typical coating thickness within the range 100–500 μm [5]. Thus, thermal spray enables the functionality of hard metals to be realized on the surface of large parts, which cannot be obtained by powder metallurgy for economical and technical reasons.

Thermal spray technology has several different deposition processes that all use heat sources to liquefy the coating materials and to project the liquefied particles on to the surface to be coated. Thermal spray processes can be based on thermal energies obtained from combustion of gases, such as hydrocarbons or hydrogen, or liquid fuels or can be obtained from electric discharges. Besides actual thermal spray processes, such as flame spray with powder or wire material, electric arc spraying, plasma arc spraying, and HVOF spraying, processes entirely based on deposition by kinetic energies are also classified under the simple term thermal spray processes. Some thermal spraying processes are as following.

2.1.1. High velocity oxy fuel (HVOF)

Fig.1 depicts the general block diagram of high velocity oxy-fuel coating, In this method, the fuel generally propylene, propane, or hydrogen, is mixed with oxygen and burned in a chamber and the products of the combustion are allowed to expand with the help of nozzle where the gas velocities may become supersonic. Powder is introduced along the axis, in the nozzle and is heated and accelerated. The powder is usually fully or partially melted and achieves velocities of near about 540 m/s. Since the powder is exposed to the products of combustion, they may be melted in either a reducing or an oxidizing medium, and oxidation of metallic and carbide is possible.HVOF processes can produce coatings of any metallic or cermets materials [52].

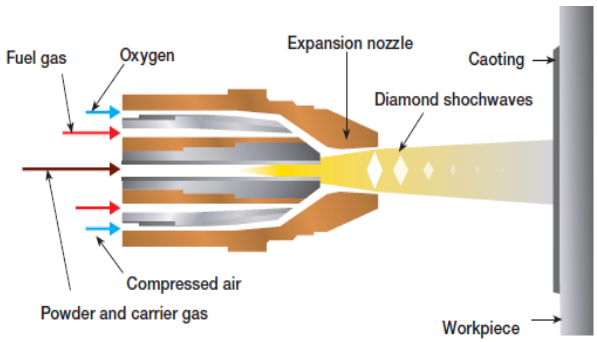


Fig. 1: Schematic of HVOF [52].

2.1.2. Detonation gun

In the detonation gun process, a mixture of oxygen and acetylene, along with a pulse of powder, is introduced into a barrel and detonated by creating spark. Virtually all metallic, ceramic, and cermets materials can be deposited using detonation gun deposition. Detonation gun coatings are used widely for wear and corrosion resistance as well as for many other types of applications [52].

2.1.3. Plasma spray technique

A plasma spray consist of a gas, usually argon, but sometimes including nitrogen, hydrogen, or helium, is allowed to flow between a tungsten cathode and a water-cooled copper anode. An electric arc is created between the two electrodes using a high frequency discharge and then sustained using do power. The arc ionizes the gas, creating high-pressure gas plasma. Powder is generally introduced into the gas stream either just outside the torch or in the diverging exit region of the nozzle (anode). It is heated and accelerated by the high-temperature, high-velocity plasma gas stream. Plasma spray may be used to produce coatings of virtually any metallic, cermets, or ceramic material [52].

A major advantage of the thermal spray processes is the extremely wide variety of materials that can be used to make a coating. Virtually any material that melts without decomposing can be used. A second major advantage is the ability of most of the thermal spray processes to apply a coating to a substrate without significantly heating it.

In Physical Vapor Deposition (PVD) and Chemical Vapor Deposition (CVD) process, the coating material is deposited onto the substrate in the form of ions. Only thin coatings ((μm range) can be deposited using these processes. This is the main limitation of CVD and PVD compared to thermal spray processes. However metals, alloys as well as refractory compounds can be deposited using CVD and PVD processes.[52-53] Baked polymer is used for corrosion resistance and aesthetics. The coating thickness varies from 1-10 μm.The galvanize method has coating thickness 1-5 μm and used for corrosion resistance purpose.

2.2 Comparison of some important thermal spraying process

There were different types of thermal spraying methods that are commercially available but some important methods are listed in the table. Also different coating materials corresponding to the different types of thermal spaying methods were compared. The coatings material may be used in a different form, some important form of the materials have been compared. Various methods of surface preparation, particle velocity and substrate temperatures are also tabulated in the table. The particle velocities have the range from 100-1000 m/s and the temperature of the substrate are varied from 95-150 ^{0}C.Mostly the coating materials are used in powder form.

Table 1: Comparison of Some Important Thermal Spraying Process [54]

S. N	Thermal spraying methods	Coating materials	Form of coating material	Method of surface preparation	Particle Velocity (m/s)	Substrate Temp. (0^0C)
1	HVOF	Cemet,Metallic,and some ceramics	Powder	Grit blasting	100-550	95-150
2	Super D Gun	Cemet,Metallic, and ceramic	Powder	Grit blasting or as-machined	850-1000	95-150
3	Detonation Gun	Cemet,Metallic, and ceramic	Powder	Grit blasting or as-machined	730-790	95-150
4	Ceramic rod spray	Ceramic and cermets coatings	rod	Grit blasting	260-360	95-135

The coating materials WC-Co and Cr_3C_2-NiCr are considered here. Tungsten carbide and chromium carbide-based coatings are often used in various industrial fields such as the steel industry and aerospace industry for improving the resistance to wear and corrosion. The Cobalt and nickel are used as binder metals. The compositions of coating materials are 75wt%Cr_3C_2-25%NiCr, WC-12%Co.

Substrates selected for the application of the coatings were cast iron and mild steel. [55]The surface was ultrasonic cleaned with acetone and then sand blasted with SiC particles under gas pressure of 4.5 bar in case of cast iron specifically for Cr_3C_2-NiCr, [56]for WC–12%Co powders with a particle size of 15–45 µm is used as the coating material. The powders were composed of 12.09 wt. % cobalt, 0.37 wt. % iron, and 5.18 wt. % carbon and balance tungsten carbide. For preparing the powders–paste mixtures, cellulose acetate and sodium carboxyl methyl cellulose were soluble in acetone firstly. Then the WC–12%Co powders were mechanically mixed, dissolved in acetone and sprayed on the substrate to form a pre layer with the thickness of 0.3 mm by means of an air spray gun.

For mild steel, Roughness of substrates prior to deposition is required, as a means of improving the mechanical bonding of the coating the substrate material was cleaned with isopropyl alcohol followed by grit blasting with coarse Al_2O_3-24mesh. [57-58]

The mild steel substrate was coated by HVOF spraying with this high flow speed of the particles to be deposited and Plasma spraying and electric contact strengthening method was used for cast iron substrate.

2.3. Wear test methods

An apparatus for wear testing is termed as wear tester, tribotester or tribometer. From a surface engineering point of view, wear test is carried out to evaluate the potential of using a certain surface engineering technology to reduce wear for a specific application, and to investigate the effect of treatment conditions (processing parameters) on the wear performance, so that optimized surface treatment conditions can be realized.

There are some important types of wear tester, discussed briefly as following.

2.3.1. Pin-on-disc wear tester

In a pin-on-disc wear tester, a pin is loaded against a flat rotating disc specimen such that a circular wear path is described by the machine. The machine can be used to evaluate wear and friction properties of materials under pure sliding conditions. Either disc or pin can serve as specimen, while the other as counterface. Pin with various geometry can be used. A convenient way is to use ball of commercially available materials such as bearing steel, tungsten carbide or alumina (Al_2O_3) as counterface, so that the name of ball-on-disc is used.

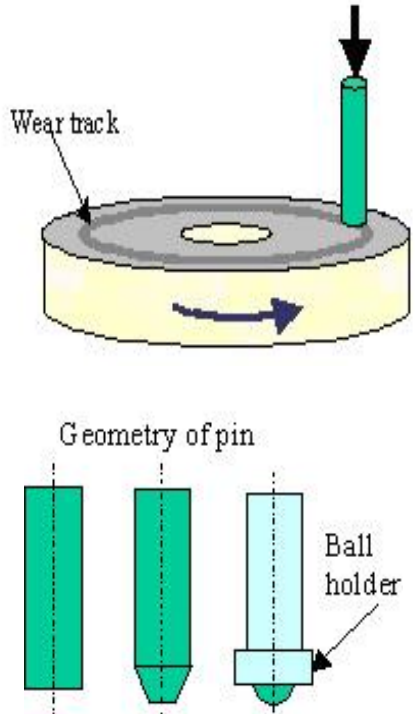


Fig. 2: Pin on Disc Wear Test [59].

2.3.2. Abrasive wear tester

The abrasive wear tester is used for abrasive wear testing of materials in reciprocating sliding. This machine has several advantages such as high reproducibility, short test time, simple flat test geometry, easy evaluation, simple operation. This machine has some disadvantages. The friction cannot be measured by this machine, some parameters such as humidity and temperature can not be controlled.

2.3.3. High temperature tribometer

The High Temperature Tribometer is made to analyze tribological behavior at elevated thermal conditions. This instrument can accurately simulate in-service conditions at high temperature and features a unique dual heating setup which makes the instrument highly reliable and stable up to 1000°C.

2.3.4. Reciprocating

The linearly reciprocating tribometer is utilized to perform wear tests of two friction pairs under relatively oscillating movement. This is performed by means of moving the upper friction partner via linear drive in a cyclical translatory motion, while the counter body is pressed under the defined normal force. An essential future of this tribometer is the big variance of applicable sample pairs and probe geometries. In addition to standard geometries (pin-disk; ball-disk) by means of using specific sample holders, the tribological performance of real geometries can be tested with or without lubricants.

The sliding wear test was performed using a standard LRT (SRVs tester). It was operated at room temperature. The frequency and the strokes were 50Hz and 2mm respectively. The coating sample surface was polished to a finish of Ra0.5µm before performing the

wearing test so that the samples remain cleaned. The cross-section of the coating as well as the wear scar was observed by SEM analysis. The porosity of the coating was measured by the image analysis using commercial software. At least 10 images from different zones were taken for the measurement. The micro hardness of the coating was tested using a FM-700 Vickers micro hardness tester with 200gf load.WC-12%Co were tested as per [56].
In case of mild steel substrate, [58]The tribological tests concerned with the sliding wear behavior of the coated samples were performed using Pin on Disk apparatus and were analyzed by Response Surface Methodology (RSM). The wear resistance of these coatings at room temperature and at 350^0C was compared. Deposition morphology and microstructure of coatings were studied using optical and electron microscopy. These measured mechanical properties were discussed with the microstructures of the coatings using electron microscopy, EDAX and X-ray diffraction. The details of these thermally sprayed powders are as presented in table 1. The calibrated Vickers micro indentation hardness indentor was used to obtain micro hardness of the coated samples. The coating characterization included optical microscopy of metallographic ally prepared cross-sections where the porosity was measured and the insight of the coating into the substrate was observed to be very secure. The wear test on the coated pins as samples was performed using the Pin-on-Disc apparatus (Ducom Tribometer) as per the ASTM G99 standard. [60].

2.4. Types of wear

Wear Undesirable removal of material from operating solid surface is known as wear. Wear may be classified as:

2.4.1. Abrasive wear

Abrasive wear, sometimes called cutting wear, occurs when hard particles slide and roll under pressure, across the tooth surface. Abrasive wear is caused by the passage of relatively hard particles/asperities over a surface. Hard particle sources are: dirt in the housing, sand or scale from castings, metal wear particles, and particles introduced into housing when filling with lube oil.

2.4.2. Adhesive wear

Adhesive wear is very common in metals. It is dependent on the mutual affinity between the materials. When brass pin under load pushed in indium block, and subsequently retracted, some particles of indium transferred on brass pin and loss of indium takes place. This loss occurs due to adhesive force between brass and indium [61].

2.4.3. Corrosive wear

The fundamental cause of corrosive wear is a chemical reaction between the material and a corroding medium which can be a chemical reagent, reactive lubricant or even air. When sliding surfaces interact with the environment, reaction takes place and form reaction product like oxide, chloride etc that causes wear [61].

2.4.4. Erosive wear

Erosive wear caused by the impact of particles (solid/liquid) against a solid surface. For example dust particles impacting on gas turbine blades and slurry impacting on pump impeller. [61].

2.4.5. Fretting wear

It refers to small amplitude (1 to 310 μm), with high frequency oscillatory movement mainly originated by vibration. This generally occurs in mechanical assemblies (press fit parts, rivet / bolt joints, strands of wire ropes, rolling element bearings), in which relative sliding on micron level is allowed. It is very difficult to eliminate such movements and the result is fretting. Fretting wear and fretting fatigue are present in almost all machinery and are the cause of total failure of some otherwise robust components. [61].

3. Result and discussion:

The various parameters were collected and compared in the following table 2.Different types of powder, their size; types of substrate materials, coating methods, coating thickness, hardness and porosity were summarized. Researchers have used powder particle size 10-50μm.The substrate materials are steels and cast iron. In most of the cases, steels were used as substrates but the focus on the cast iron was very limited. As on date, majority of the studies were based on WC-Co, WC-Ni or WC-Co-Cr or Cr_3C_2-NiCr but there was no or very rare study found with WC-NiCr or Cr_3C_2-C_O combinations. Mostly the coating methods HVOF or plasma spraying were used for tribo mechanical studies. The HVOF method was comparatively the most effective coating method.
Table.2 (ref.page no.6) Comparison of hardness, porosity and sliding wear performances

3.1.1. Effect of type of substrate and heat treatment in mass loss

There is no effect of substrate type and preheating in mass loss. The heat treatment of coating influenced significantly the mass loss. The heat treated coating had approximately 3 times lower mass loss than as sprayed coating. [14-16].

3.1.2. Effect of heat treatment on friction and abrasive wear behavior

Temperature ranges played very significant role .Its effect on friction and wear resistance were remarkable. The high temperature heat treatment of coatings was detrimental to friction and abrasive wear resistance. The low temperature heat treatment increased wear resistance of WC-12Co and Cr3C2–25NiCr coatings under benign abrasive wear conditions [78-81].

3.2. Micro hardness & porosity measurements

The hard powders having different compositions were studied and their mechanical properties mainly micro hardness and porosity were compared. The coating methods and substrate types also presented in the table 3
Micro hardness and porosity of different coating materials were studied and compared. The materials coated with mild steel substrate posses high hardness as compared to the cast iron substrate.WC-12%Co coated cast iron and mild steel substrate have high hardness than Cr_3C_2-25%NiCr coated cast iron and mild steel substrate.

Table 3: Porosity and Micro Hardness of WC-12 % Co & Cr_3C_2-25 % Nicr Coating

Composition	Micro hardness	Porosity	Coating method	Substrate Types
(WC-12%Co)DI	1073 HV	---	Electric contact strengthening	Ductile Iron(DI)
(Cr_3C_2-25%NiCr)CI	937HV	<3	Plasma sprayed	Cast Iron(CI)
(WC-12%Co)MS	1293HV	0.855	HVOF spraying	Mild Steel(MS)
(Cr_3C_2-25%NiCr)MS	1081HV	1.4946	HVOF spraying	Mild Steel(MS)

The mild steel substrates coated by WC-12%Co, Cr_3C_2-25%NiCr have lower porosity than cast iron substrate i.e. coating applied on mild steel substrate has higher density than the cast iron. From the table.2, it is very clear that Cr_3C_2-25 % NiCr coatings have more porosity than WC-12%Co and hence WC-12%Co coating has higher density than Cr_3C_2-25%NiCr.

3.3. Micro structural analysis of the coatings

The WC–12%Co coatings deposited on ductile iron using the optimum parameters were obtained, and then the microstructure from the coatings to the substrate were discussed. The cross sectional microstructures of WC–12%Co composite coatings on ductile iron by electric contact strengthening are shown. After electric contact surface deposition, a white bright layer on ductile iron substrate was formed. As shown in Fig. 3a, SEM photograph of WC–12%Co coatings revealed dark and bright regions. The typical bright WC particle microstructure can be identified clearly and the distribution was uniform and fine resulting good wear resistant property. [56].

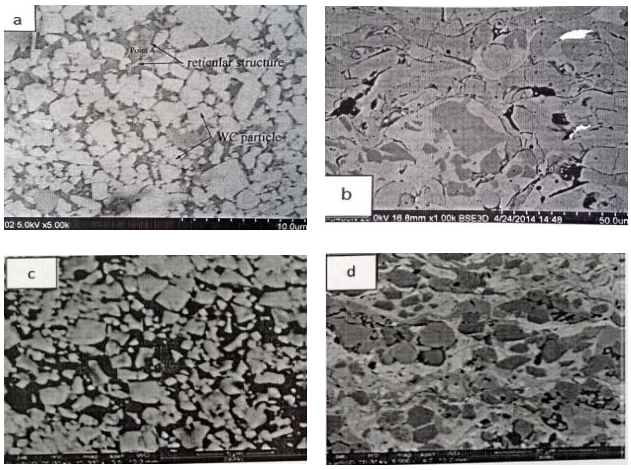


Fig. 3: SEM (A) Micro-Structure of WC-Co [56] (B) Micro- Struc Ture of Cr_3C_2-Nicr on Cast Iron Substrate [66] (C) Micro-Structure of WC-Co [60] (D) Micro-Structure of Cr_3C_2-Nicr on Mild Steel Substrate [60].

The microstructure of the plasma sprayed cermets coating is shown in Fig. 3b. The Cr_3C_2–NiCr coating presented a typical layered and dense structure, implying that the binder metal was melted and fully deformed. [66]

In case of coating applied on mild steel substrate, Cross sectional images of SEM represent that the coatings are compact, uniform and were free from defects, cracks. In fig.3c tungsten flakes appeared as white flakes and the shapes of these flakes were like hexagonal and these hexagonal shapes helps to improve hardness. In fig.3d, the flakes (Cr_3C_2-NiCr) were slightly larger in size and darker and the flakes were distributed properly. [60].

4. Conclusions

1) In the present study, the hard metal coatings WC-12Co and Cr_3C_2-25NiCr have been compared for the micro hardness, porosity and microstructure, corrosion properties. The micro structural examination and tribo mechanical properties shows that the hard metal coatings are dense, packed in and without defects and fractures.
2) In case of mild steel substrate, micro hardness, porosity of the coating was better than the cast iron substrate and the microstructure was denser than cast iron but in terms of economy and corrosion, Cr_3C_2-NiCr coated cast iron has better response. So, Cr_3C_2-NiCr coated cast iron substrate is better over WC-12%Co because of having more economical and corrosive resistant as well as competitive wear characteristics and as the temperature and load are increased, Cr_3C_2-NiCr shows excellent wear resistances.
3) Nano size powders coating shows better micro hardness than micro size powder particles.
4) HVOF method is more effective method than plasma spray.
5) The heat treated coating had approximately 3 times lower mass loss than as sprayed coating.

5. Future scope

In the present study hard metal coatings WC-12Co and Cr_3C_2-25NiCr have been compared for the micro hardness, porosity and microstructure, corrosion properties and to date, majority of the research in the field of thermal spraying has been focused on carbon steel substrate and not on cast iron substrate. To the best of authors' knowledge, only a few literatures is available in which cast iron substrates were studied by the researchers. So, this gap should be fulfilled.

There may be some more alternative compositions, e.g. such as nano materials doping can be used with Cr and also based on TiC or use of iron-based or iron-containing binders may be of importance.

As on date, majority of the studies were based on WC-Co, WC-Ni or WC-Co-Cr or Cr_3C_2-NiCr but there was no or very rare study found with WC-NiCr or Cr_3C_2-C_O combinations There may the scope to work with these combinations.

Table 2

Powders	Size (μm)	Substrate	Coating method	Coating thickness	Hardness	Porosity (%)	Wear loss&Wear Rate	Corrosion Property	Wear Test Method	references
WC-12%Co	10–45	Mild steel	HVOF	----	963.8	Dense	----	-----	---	[62]
WC-12%Co	-38/10	Mild steel	HVOF	150 to 170μm	1293	0.85	----	Inferior corrosive resistance property than NiCrBSi and Cr_3C_2-NiCr	Pin-on-Disc apparatus (DucomTribometer) ASTM G99	[60]
Cr_3C_2-25%NiCr	-45/10	Mild steel	HVOF	150 to 170 μm	1081	1.5	----	Less corrosive resistance than NiCrBSi	Pin-on-Disc apparatus (DucomTribometer) ASTM G99	[60]
NiCrBSi	-53/15	Mild steel	HVOF	150 to 170 μm	997	0.922	----	More corrosive resistance than Cr_3C_2-NiCr	Pin-on-Disc apparatus (DucomTribometer) ASTM G99	[60]
WC-12%Co	10–45	Carbon Steel	HVOF	100–500 μm	1376	----	----	----	----	[63],[64], [65]

WC-17%Co	10–45	Carbon Steel	HVOF	100–500 µm	1358	----	----	----	----	[63],[64]
Cr_3C_2-25%NiCr	10–45	Carbon Steel	HVOF	100–500 µm	1080	----	----	----	----	[63]
WC-12%Co	15–45	Ductile Iron	Electric contact surface strength-ening	100-125 µm	1073	----	----	----	----	[56],[57]
75% wt Cr_3C_2-25%wt NiCr	15–45	Cast Iron	Plasma spraying	----	937±105	<3	(0.054±0.007) mm3 at 60 N (0.079±0.006) at 100 N			[66]
60% wt TiB2–40%wt NiCr	15–45	Cast Iron	Plasma spraying	----	1128±89	<3	(0.046±0.009)mm3 at 60N (0.077±0.010)mm3 at 100 N	---	---	[66],[67]
WC–10Co–4Cr wt%	−15/+45	AISI 304 stain-less steel	HVOF	200–300 µm	1297±45	0.75 ±0.2	---	---	---	[68]
Mo	10–50	Cast iron	atmos-pheric plasma-spray	100–300 µm	500	---	0.09 at 89 N	---	pin-on-plate type apparatus for applied loads of 49, 89 and 129 N under dry and sliding speed of 1 Hz	[69]
WC-12%Co	(WC 12%Co) micro size	Carbon steel	Plasma and HVOF equip-ment	160 µm	1066 for HVOF,826 for plasma system	1.3 for HVOF and 6.6 for Plasma	---	---	---	[70]
WC-12%Co	(WC–12%Co) nano size	Carbon steel	Plasma and HVOF equip-ment	160 µm	1367 for HVOF,837 for plasma system	1.2 for HVOF and 6.4 for Plasma	---	---	---	[70]
Hardened Steel	---	Mild steel	HVOF		700±89				ASTMG-99	[71]
Hard Chrome	---	Mild steel	HVOF	290±31 µm	884±97				ASTMG-99	[71]
WC-12%Ni	---		HVOF		843 ± 123	1.9–2.8				[72]
Cr3C2-37WC-18NiCoCr	-45+15	Carbon Steel	HVOF	------	934 (±195)	0.5 (±0.2)	0.63 (±0.04)*10^{-6} mm^3/Nm	---	---	[73]
Cr3C2-50NiCr-MoNb	-45+15	Carbon Steel	HVOF	------	806 (±117)	0.8 (±0.3)	2.18*10^{-6} mm^3/Nm	---	---	[73]
Cr3C2-25NiCr	-38+10	Carbon Steel	HVOF	-----	938 (±79)	1.7 (±1.0)	1.58 (±0.75)*10^{-6} mm^3/Nm	Better ox-idation re-sistance property at higher tempera-ture	---	[73]
WC-17%NiCr	35 with devia-tion 7	ACI CD4MCu cast du-plex stainless steel	HVOF (Robot Con-trolled Spray)	250 µm	756±108	0.69 ± 0.18	0.68 ± 0.06* 10^{-5} mm3/Nm at 40 kN	---	ASTM G133-05 Standard	[74]
WC-17%NiCr	35 with devia-tion 7	ACI CD4MCu cast du-plex stainless steel	HVOF (Manual Spray)	250 µm	704±67	0.91 ± 0.31	1.28 ± 0.03* 10^{-5} mm3/Nm at 40 kN	---	ASTM G133-05 Standard	[74]

References

[1] Kamlesh V. Chauhana*, Sushant K. Rawala 'A review paper on tribological and mechanical properties of ternary nitride based coatings'Procedia Technology 14 (2014) 430 – 437.

[2] Singh, Shailesh Kumar, et al. "Wear behavior of chromium nitride coating in dry condition at lower sliding velocity and load." The International Journal of Advanced Manufacturing Technology (2017): 1-11.

[3] Lorenzo-Martin C, Ajayi O, Erdemir A, Fenske G.R, Wei R. Effect of microstructure and thickness on the friction and wear behaviour of CrN coatings. Wear; 2013. p. 963-971. https://doi.org/10.1016/j.wear.2013.02.005.

[4] L.-M. Berger, Hard but slippery-titaniumhardmetal coatings have industrial potential, met. Powder Rep. 60 (5) (2005) 28 (29, 31).

[5] L.-M. Berger, Application of hardmetals as thermal spray coatings, Int J RefractMet HardMater (2014.

[6] Barbezat Gérard Application of thermal spraying in the automobile industry Surface & Coatings Technology 201 (2006) 2028–2031 https://doi.org/10.1016/j.surfcoat.2006.04.050.

[7] Dayan, A.D., Paine, A. J.: Mechanisms of chromium toxicity, carcinogenicity and allergenicity: review of the literature from 1985 to 2000. Hum. Exp. Toxicol. 20, 439–451 (2001). https://doi.org/10.1191/096032701682693062.

[8] Von Burg, R., Liu, D.: Chromium and hexavalent chromium. J Appl. Toxicol. 13, 225–230 (1993). https://doi.org/10.1002/jat.2550130315.

[9] Costa, M.: Toxicity and carcinogenicity of Cr (VI) in animal models and humans. Crit. Rev. Toxicol. 27, 431–442 (1997). https://doi.org/10.3109/10408449709078442.

[10] Directive 2002/95/EC of the European Parliament and of the Council on the restriction of the use of certain hazardous substances in electrical and electronic equipment. Off. J. Eur. Union1, 27, pp. 19–37 (2003).

[11] Bolelli, G., Cannillo, V., Lusvarghi, L., Manfredini, T.: Wearbehavior of thermally sprayed ceramic oxide coatings. Wear 261, 1298–1315 (2006). https://doi.org/10.1016/j.wear.2006.03.023.

[12] Picas, J.A., Forn, A., Mattha¨us, G.: HVOF coatings as an alternative to hard chrome for pistons and valves. Wear 261, 477–484 (2006). https://doi.org/10.1016/j.wear.2005.12.005.

[13] Kirsten, A., Oechsle, M., Moll, R. F.: Carbide containing materials for hard chromium replacement by HVOF-spraying. In: Proceeding of the International Thermal Spray Conference ITSC 2005, Basel, 2–4 May 2005, and pp. 957–962. DVS-Verlag, Basel, Switzerland, Du¨sseldorf, (2005). CD (ISBN 3-87155-793-5).

[14] Bolelli, G., Cannillo, V., Lusvarghi, L., Soragni, E., Loreto, A., Valente, T.: A comprehensive characterization of industrially manufactured hard chrome platings and of thermally sprayed alternatives. In: Proceeding of the International Thermal Spray Conference ITSC 2005, Basel, 2–4 May 2005, and pp. 1456–1461. DVS-Verlag, Basel, Switzerland, Du¨sseldorf (2005). CD (ISBN 3- 87155-793-5).

[15] Guilemany, J.M., Espallargas, N., Suegama, P.H., Benedetti, A.V., Fernandez, J.: High-velocity oxyfuel Cr3C2–NiCr replacing hard chromium coatings. J. Therm. Spray Technol. 14, 335–341 (2005). https://doi.org/10.1361/105996305X59350.

[16] Wank, A., Schwenk, A., Wielage, B., Grund, T., Friesen, E., Pokhmurska, H.: Behavior of thermally sprayed wear protective coatings exposed to different abrasive wear conditions in comparison to hard chromium platings. In: Conf. Proc. Int. Thermal Spray Conference & Exhibition ITSC 2007, 14–16 May 2007, Beijing, China, pp. 1011–1016. ASM International, Materials Park, Ohio, USA (2007).

[17] P. Vuoristo, Thermal spray coating processes, in: D. Cameron (Ed.), Comprehensive Materials Processing, vol. 4, Elsevier, 2014, pp. 229–276. https://doi.org/10.1016/B978-0-08-096532-1.00407-6.

[18] Nitesh Vashishtha, S.G. Sapate, Abrasive wear maps for High Velocity Oxy Fuel (HVOF) sprayed WC-12Co and Cr3C2−25NiCr coatings, Tribology International 114 (2017) 290–305. https://doi.org/10.1016/j.triboint.2017.04.037.

[19] Friction, lubrication, and wear technology. Materials Park, OH: ASM International, Handbook Committee; 1992.

[20] Rasool G, Stack MM. Wear maps for TiC composite based coatings deposited on 303 Stainless steel. Tribol Int 2014; 74:93–102. https://doi.org/10.1016/j.triboint.2014.02.002.

[21] Hsu SM, Shen MC. Ceramic wear maps. Wear 1996; 200:154–7. https://doi.org/10.1016/S0043-1648(96)07326-7.

[22] Rasool G, Stack MM. Mapping wear mechanisms of TiC/Ti composite coating. Tribol Int 2015; 328–329:498– 508. https://doi.org/10.1016/j.wear.2015.03.022.

[23] M. Oechsle, Carbide containing spray powders and HVOF-coatings, Conf Proc 7.HVOF-Kolloquium 2006, 9–10 November 2006, Erding, Germany, Gemeinschaft Thermisches Spritzen EV, Unterschleißheim, 2006, pp. 57–62.

[24] Stanford MK, Jain VK. Friction and wear characteristics of hard coatings. Wear 2001; 251:990-6. https://doi.org/10.1016/S0043-1648(01)00719-0.

[25] Sahraoui T, Fenineche NE, Montavon G, Coddet C. Structure and wear behaviour of HVOF sprayed Cr3C2 –NiCr and WC–Co coatings. Mater Design 2003; 24:309-13. https://doi.org/10.1016/S0261-3069(03)00059-1.

[26] Shabanaa*,M.M.M. Sarcar b, K.N.S.Sumanc,S Kamaluddind Tribological and Corrosion behavior of HVOF Sprayed WC-Co,NiCrBSi and Cr3C2-NiCr Coatings and analysis using Design ofExperiments, Materials Today: Proceedings 2 (2015) 2654 – 2665. https://doi.org/10.1016/j.matpr.2015.07.227.

[27] Sharma S. Parametric study of abrasive wear of Co–CrC based flame sprayed coatings by response surface methodology. Tribol Int 2014; 75:39–50. https://doi.org/10.1016/j.triboint.2014.03.004.

[28] Roy M, Rao CVS, Rao DS, Sundararajan G. Abrasive wear behavior of detonation sprayed WC-Co coatings on mild steel. Surf Eng 1999; 15(2):129-36. https://doi.org/10.1179/026708499101516470.

[29] Sapate SG, Roy M. Solid particle erosion of thermal sprayed coatings. In: Thermal sprayed coatings and their tribological performances. IGI Global Publications 2015; 193- 226. https://doi.org/10.4018/978-1-4666-7489-9.ch007.

[30] Mateen A, Saha GC, Khan TI, Khalid FA. Tribological behavior of HVOF sprayed near-nanostructured and microstructured WC- 17wt.% Co coatings. Surf Coat Technol2011; 206:1077-84. https://doi.org/10.1016/j.surfcoat.2011.07.075.

[31] T. Gong, P. Yao, X. Zuo, Z. Zhang, Y. Xiao, L. Zhao, et al., Influence of WC carbide particle size on the microstructure and abrasive wear behavior of WC–10Co–4Cr coatings for aircraft landing gear, Wear 2016;362–363:135–45. https://doi.org/10.1016/j.wear.2016.05.022.

[32] Matthews S, James B, Hyland M. High temperature erosion–oxidation of Cr3C2–NiCr thermal spray coatings under simulated turbine conditions. Corros Sci 2013; 70:203-11. https://doi.org/10.1016/j.corsci.2013.01.030.

[33] C.N. Machioa,, G. Akdogana, M.J. Witcombb, S. Luyckxa, Performance of WC–VC–Co thermal spray coatings in abrasion and slurry erosion tests, Wear 258 (2005) 434–442 https://doi.org/10.1016/j.wear.2004.09.033.

[34] D.K. Shetty, I.G. Wright, J.T. Stropki, Slurry erosion of WC–Co cermets and ceramics, Trans. ASLE 28 (1) (1984) 123–133. https://doi.org/10.1080/05698198508981604.

[35] J. Zinyana, S. Broccardo, S. Hamar-Thibault, L.A. Cornish, M.J. Witcomb, C.H. Allibert, S. Luyckx, Effect of composition on the (V, W)C constitution in V-W-C-Co alloys, in: Plansee Proceedings, Austria, 2001, pp. 291–29.

[36] S. Broccardo, An investigation into the corrosion resistance of WC–VC–Co hard metals, M.Sc. Dissertation, University of the Witwatersrand, 2003.

[37] B. Lotfi a, P.H. Shipway a,, D.G. McCartney a, H. Edris b, Abrasive wear behaviour of Ni(Cr)–TiB2 coatings deposited by HVOF spraying of SHS-derived cermets powders, Wear 254 (2003) 340–349 https://doi.org/10.1016/S0043-1648(03)00014-0.

[38] J. He, M. Ice, E.J. Lavernia, Synthesis of nanostructured Cr3C2–25(Ni20Cr) coatings, Metall. Mater. Trans. A 31 (2000) 555–564. https://doi.org/10.1007/s11661-000-0290-0.

[39] B. Champange, S. Dallaire, Wear resistance of TiB2–Fe cermets, in: Proceedings of the International Conference.

[40] B. Normand, V. Fervel, C. Coddet, V. Nikitine, Surf. Coat. Technol. 123 (2000) 278. https://doi.org/10.1016/S0257-8972(99)00532-0.

[41] O.P. Solonenko, M.F. Zhukov, Thermal Plasma and New Materials Technology, Cambridge Interscience Publishing, Cambridge, UK, 1994, pp. 509 – 513

[42] Shan-Ping Lu, Oh-Yang Kwon, Surf. Coat. Technol. 153 (2002) 40 https://doi.org/10.1016/S0257-8972(01)01555-9.

[43] B. Mitin, Poroshkovaia Metalurgia I Napilenia Pokritia, Metalurgia, Moscow, 1987 (in Russian).

[44] A. Conde, F. Zibiri, J. Damborenea, Mater. Sci. Eng., A 334 (2002) 233. https://doi.org/10.1016/S0921-5093(01)01808-1.

[45] Y.S. Borisov, A.L. Borisova, Plazmennye Poroshkovye Pokritiia, Tehnika, Moscow, 1986 (in Russian).

Copyright © 2018 Ramesh ChandraYadaw et al. This is an open access article distributed under the Creative Commons Attribution License, which permits unrestricted use, distribution, and reproduction in any medium, provided the original work is properly cited.

[46] Y.S. Borisov, Gazotermicheskie Pokritia iz Poroshkovyh Materialov, Naukova Dumka, Kiev, 1987 (in Russian).

[47] M.F. Ashby, D.R.H. Jones, Engineering Materials: 2. an Introduction to Microstructures, Processing and Design, Pergamon Press, Oxford, 1986, p. 4.

[48] H. Skuleva, S. Malinovb, W. Shac,T, P.A.M. Basheer 'Microstructural and mechanical properties of nickel- base plasma sprayed coatings on steel and cast iron substrates'Surface & Coatings Technology 197 (2005) 177– 184

[49] H. Skulev, S. Malinov, P.A.M. Basheer, W. Sha, Surf. Coat. Technol. 185 (2004) 18. https://doi.org/10.1016/j.surfcoat.2003.12.012.

[50] H. Skulev, S. Malinov, P.A.M. Basheer, W. Sha, Surf. Coat. Technol. 185 (2004) 18. https://doi.org/10.1016/j.surfcoat.2003.12.012.

[51] J.R. Davis (Ed.), Surface Hardening of Steels: Understanding the Basics, ASM International, Materials Park, OH, 2002.

[52] Sulzer Metco, an Introduction to Thermal Spray, Issue 4 • c 2013 Sulzer Metco.

[53] H.M. Ortner, P. Ettmayer, H. Kolaska, The history of the technological progress of hardmetals, Int. J. Refract. Met. Hard Mater.44 (2014) 148–159. https://doi.org/10.1016/j.ijrmhm.2013.07.014.

[54] Robert C. Tucker, Jr., Praxair Surface Technologies, Inc. Thermal Spray Coatings, ASM Handbook, Volume 5: Surface Engineering C.M. Cotell, J.A. Sprague, and F.A. Smidt, Jr., editors, p 497-509

[55] Haibo Wang a,c, HuiLi b, HongbinZhu b, FangjieCheng a,n, DongpoWang,Zhuoxin'AcomparativestudyofplasmasprayedTiB2–NiCr andCr3C2–NiCr compositecoatings, Materials Letters153(2015)110–113.

[56] Xiaoben Qi, Shigen Zhu, Hao Ding, Zhengkun Zhu, Zhibing Han, Microstructure and wear behaviors of WC–12%Co coating on ductile iron by electric contact surface strengthening, Applied Surface Science 282 (2013) 672– 679. https://doi.org/10.1016/j.apsusc.2013.06.032.

[57] Friction, lubrication, and wear technology. Materials Park, OH: ASM International, Handbook Committee; 1992.

[58] Picas JA, Forn A, Mattaus G. HVOF coatings as an alternative to hard chrome for pistons and valves. Wear 2006; 261:477-84. https://doi.org/10.1016/j.wear.2005.12.005.

[59] C. X. Li, the University of Birmingham, UK, Wear Testing and Wear Measurement, Surface Engineering.

[60] Shabanaa*, M.M.M. Sarcar b, K.N.S.Sumanc, S Kamaluddind. 'Tribological and Corrosion behavior of HVOF Sprayed WC-Co,NiCrBSi and Cr3C2-NiCr Coatings and analysis using Design of Experiments' Materials Today: Proceedings 2 (2015) 2654 – 2665. https://doi.org/10.1016/j.matpr.2015.07.227 ...

[61] Singh, Shailesh Kumar, et al. "Influence of Nano-particle on the Wear behaviour of Thin Film Coatings a Review." International Journal of Applied Engineering Research 13.6 (2018): 4053-4058.

[62] DING Zhang-xiong1, CHEN Wei1, and WANG Qun2 'Resistance of cavitations erosion of multimodal WC-12Co coatings sprayed by HVOF'Received 8 December 2010; accepted 1 August 2011.

[63] F. Rastegar *, D.E. Richardson 'Alternative to chrome HVOF cermets coatings for high horse power diesel engines1'Surface and CoatingTse chnolog9y 0(1997) 1 56-163.

[64] L.-M. Berger, Hardmetals as thermal spray coatings, Powder Metall. 50 (3) (2007) 205–214. https://doi.org/10.1179/174329007X246078.

[65] L. Pawlowski, the Science and Engineering of Thermal Spray Coatings, 2nd ed. John Wiley & Sons, Chichester, 2008.

[66] Hsu SM, Shen MC. Ceramic wear maps. Wear 1996; 200:154–7. https://doi.org/10.1016/S0043-1648(96)07326-7.

[67] M. Jones, A.J. Horlock, P.H. Shipway∗, D.G. McCartney, J.V. WoodA comparison of the abrasive wear behaviour of HVOF sprayed titanium carbide- and titanium boride-based cermet coatings ,Wear 251 (2001) 1009–1016. https://doi.org/10.1016/S0043-1648(01)00702-5.

[68] Lalit Thakura, N. Aroraa,, R. Jayaganthanb, R. Soodc An investigation on erosion behavior of HVOF sprayed WC–CoCr coatings Applied Surface Science 258 (2011) 1225– 1234. https://doi.org/10.1016/j.apsusc.2011.09.079.

[69] B. Uyulgana,*, H. Cetinela, I. Ozdemira, C. Tekmena, S.C. Okumusb, E. Celika Friction and wear properties of Mo coatings on cast-iron substrates Surface and Coatings Technology 174 –175 (2003) 1082–1088.

[70] Sultan Al-Mutairi a, M.S.J. Hashmi a, B.S. Yilbas b, J. Stokes a Microstructural characterization of HVOF/plasma thermal spray of micro/nanoWC–12%Co powders Surface & Coatings Technology 264 (2015) 175–186. https://doi.org/10.1016/j.surfcoat.2014.12.050.

[71] S ˇ.Houdkova´ • F. Zaha´lka • M. Kasˇparova´ • L. -M. BergerComparative Study of Thermally Sprayed Coatings under Different Types of Wear Conditions for Hard Chromium Replacement.

[72] L.-M. Berger a,S. Saaro a , T. Naumann a , M. Wiener a , V. Weihnacht a , S. Thiele b , J. Suchánek Microstructure and properties of HVOF-sprayed chromium alloyed WC–Co and WC–Ni coatings Surface & Coatings Technology 202 (2008) 4417–4421. https://doi.org/10.1016/j.surfcoat.2008.04.019.

[73] V. Matikainen1*, G. Bolelli2, H. Koivuluoto1, P. Sassatelli2, L. Lusvarghi2, P. Vuoristo1 Sliding wear behaviour of HVOF and HVOF sprayed Cr3C2-based coatings S0043-1648(17)30566-5.

[74] Hamed Asgari, Gobinda Saha , Mohsen Mohammadi, Tribological behavior of nanostructured high velocity oxy-fuel (HVOF) thermal sprayed WC-17NiCr coatings, Ceramics International xx (xxxx) xxxx–xxxx.

[75] O. Maranhoa, D. Rodriguesb, M. Boccalini Jr. b, A. Sinatorac Mass loss and wear mechanisms of HVOF-sprayed multi-component white cast iron coatings Wear 274– 275 (2012) 162– 167.

[76] L. Pawlowski, in: The Science and Engineering of Thermal Spray Coatings, John Wiley and Sons, 1995, p. 211.

[77] L. Pawlowski, in: The Science and Engineering of Thermal Spray Coatings, John Wiley and Sons, 1995, p. 182.

[78] Nitesh Vashishtha, S.G. Sapate, Pranay Bagde, A.B. Rathod,Effect of heat treatment on friction and abrasive wear behavior of WC-12Co and Cr3C2-25NiCr coatings, S0301-679X(17)30477-2.

[79] Thiele S, Sempf k, Roessler KJ, Berger LM, Spatzier J, Thermophysical and microstructural studies on thermally sprayed tungsten carbide-cobalt coatings. J Therm Spray Technol 2011; 20:358-65. https://doi.org/10.1007/s11666-010-9558-0.

[80] Roy M, Pauschitz A, Polak R, Franek F. Comparative evaluation of ambient temperature friction behaviour of thermal sprayed Cr3C2-25(Ni20Cr) coatings with conventional and non-crystalline grains. Tribol Int 2006; 39:29-38. https://doi.org/10.1016/j.triboint.2004.11.009.

[81] Kumar, Dalip, Qasim Murtaza, and R. C. Singh. "Sliding wear behavior of aluminum alloy coating prepared by two-wire electric arc spray process." The International Journal of Advanced Manufacturing Technology 85.1-4 (2016): 237-252.

View publication stats

MĀPAN-Journal of Metrology Society of India
https://doi.org/10.1007/s12647-018-0285-1

SHORT COMMUNICATION

Uncertainty Estimation in PM_{10} Mass Measurements

J. Pokhariyal[1,2], A. Mandal[2]* and S. G. Aggarwal[1]

[1]CSIR-National Physical Laboratory, New Delhi 110012, India

[2]Delhi Technological University, Shahbad Daulatpur, Main Bawana Road, Delhi 110042, India

Received: 13 March 2018 / Accepted: 09 August 2018

© Metrology Society of India 2018

Abstract: Mass measurements of particles in the atmosphere are important for regulatory and scientific purposes. In nearly all of the countries, particulates $\leq$ 10 µm in aerodynamic size (PM_{10}) are one of the most significant parameters of National Ambient Air Quality Standards (NAAQS). In India, as given in NAAQS, the PM_{10} regulatory limit is 60 µg m^{-3} which is based on the annual mean weight of samples (minimum 104) annually at a specific site taken for two/three days in a week for 24 h. In this paper, the components of uncertainty involved in the filter-based sampling of PM_{10} along with the gravimetric determination of mass have been calculated. As per the EPA guidelines, PM_{10} mass was monitored for a year at NPL (National Physical Laboratory), New Delhi from January 2014 to January 2015. The 24-h time-weighted mean mass concentration (n = 104) for one-year measurement varied from 32.5 to 480.2 µg m^{-3}.During the study, high mass loading was observed in the month of December to February. In general, the flow rate of the sampling has been reported to be major uncertainty component in size-segregated PM sampling. In this work, the flow rate of the sampling (90.4%) and charge effect of the filter (6.7%) had the major contribution in the total uncertainty budget of PM_{10} mass measurement. Rest of the uncertainty components, e.g., balances (0.39%) and conditioning of filter (2.39%), had the least contribution.

Keywords: PM_{10}; NAAQS; Measurement uncertainty; PM

1. Introduction

The aerosol study is an important part of atmospheric chemistry and physics; hence, it has an impact on regional as well as global climate. They also affect human health adversely and therefore are major parameters of National Ambient Air Quality Standards (NAAQS). In nearly all of the countries, PM or particulate matter having size dimensions as $\leq$ 2.5 µm ($PM_{2.5}$) and $\leq$ 10 µm (PM_{10}) has been included in NAAQS as regulatory parameters on account of their measurement techniques, i.e., equivariance or reference procedures [1, 2]. For accurate and precise data of NAAQS, it is essential that the instruments used in the measurement laboratory and measurement should be in accordance with the NAAQS and ISO standard. For such measurements, instruments should be calibrated with the standards with traceability and should be as per the recommendation of NAAQS.

The international system of units (SI) measurement traceability deals with the linking of the results of measurement with the reference value, i.e., linkage of the results of measurement (results obtained by instrumental analysis, which is calibrated with the standard) with the SI. The calibration that is traceable is not so straightforward in aerosol measurements as it involves different parameters, e.g., time, size, flow, mass, and if the equipment working is dependent upon various parameters related to frequency, optical, temperature, wavelength, absorbance, pressure, then all these parameters require traceable standards [2]. Thus, SI is defined as a system of seven base units, viz. measurement of length (meter), mass (kilogram), time (second), temperature (Kelvin), electrical current (Ampere), luminous intensity (Candela) and amount of substance (mole). For traceability to SI units, it is significant that the standards used must have a calibration hierarchy of its set measured values to SI units [3]. Further, measurement results should involve uncertainty. The measurement uncertainty is defined as the dispersion of the measurement results that is reasonably attributed to the measurand value.

In summary, to produce a traceable result from a measurement exercise, as a first step, it is important to use

*Corresponding author, E-mail: anubha_mandal10@yahoo.co.in

Published online: 27 August 2018

calibrated (SI traceable) instruments, use certified reference material and also use the standard/reference method of the measurements. Secondly, measurement results should be given with the uncertainty considering all the factors (sources) from where the uncertainty can arise in the result [4].

Most of the NAAQS for PM (particulate matter) is based on the mass concentrations for particulates < 10 μm in aerodynamic diameter (PM_{10}) [5]. In 1997, Environment Protection Agency (EPA) United States introduced standards for particles < 2.5 μm in aerodynamic diameter. Therefore, mass measurements of atmospheric particles are consistently measured in monitoring stations in various regions around the world. The most commonly used technique for measuring the mass concentrations of particulate involves gravimetric filter-based method [6, 7]. An accurately controlled environment, with clean air and a stable humidity and temperature is required for processing and weighing of filter that is equilibrated at these conditions. Balances with sensitivities of ≤ 1 μg is calibrated with traceable standards and be regularly serviced [8]. In this study, we have identified and also calculated the uncertainty components associated with the filter-based sampling of PM_{10} and its gravimetric estimation of mass in New Delhi. Air pollution in Delhi is caused by various factors—meteorological conditions, sources of pollution and geographical location of Delhi. PM_{10} concentrations largely vary and are reported to have violated standards at most places in Delhi. Various uncertainty components like conditioning of filters, weighing of filters, the flow rate of low-volume sampler have been taken into account.

2. Materials and Methods

A year-round sampling of PM_{10} was done throughout the year using a low-volume (16.7 lpm) particulate sampler (Envirotech APM 550) as per the guidelines given in NAAQS. The monitoring and measurement were performed in National Physical Laboratory (NPL) CSIR, New Delhi, from January 2014 to January 2015. Year-round sampling is divided into four seasons. The monsoon season includes the days in the months from June to September. The second season is the post-monsoon which consists of days in October and November. The third season is winter, and it includes days in the months of December, January, and February. The fourth season is the summer which includes the months of March–May [9].

The PM_{10} particles were collected on prebaked, conditioned and weighed quartz filters (47 mm diameter). After sampling, filter was conditioned in a similar manner and weighed for particulate mass determination. Sampling flow rate was tested every month once before and after sampling to see the flow variation (one of the important uncertainty components). Other factors, such as humidity, temperature, evaporation loss, were also studied for the influence on the particulate collection and weighing uncertainty [2]. Meteorological data were also recorded for the year-round period of sampling. Collection of PM_{10} samples was done at the laboratory rooftop at $\sim$ 15 m above the ground. This measurement site is a good representation of urban aerosols of New Delhi with the mixed effect of vehicular, residential, industrial and agricultural emissions [10].

The air of measured volume is passed through a filter for a set period of time (24 h). The PM_{10} mass measurement was calculated by dividing the mass of PM_{10} on the filter by the air volume and is expressed in mass per unit volume [8].

$$\mathrm{PM}_{10}\ (\mu\mathrm{g/m}^3) = \frac{m_2 - m_1}{V} \tag{1}$$

where PM_{10} = mass concentration of particulate matter ≤ 10, in μg m^{-3}; m_1 = initial mass of filter, in μg; m_2 = final mass of filter, in μg; V = volume of air sampled, in m^3.

Data of hourly meteorological parameters like relative humidity, temperature, wind velocity and direction for the measurement period were obtained from the weather station of NPL, New Delhi [11].

3. Results and Discussion

Uncertainty estimation was also done for this study. Measurement of uncertainty in the mass concentration of PM_{10} is dependent on two factors: (1) the volume of the air sucked by the sampler and (2) particle mass measurement. Figure 1 shows the uncertainty components involved in these measurements in the form of cause effective diagram.

The uncertainty in the measurement of various components that belong to the mass of particle and volume measurement by means of the low-volume sampler is considered in the measurement of the mass of PM_{10}. The combined standard uncertainty (u_c) is defined as:

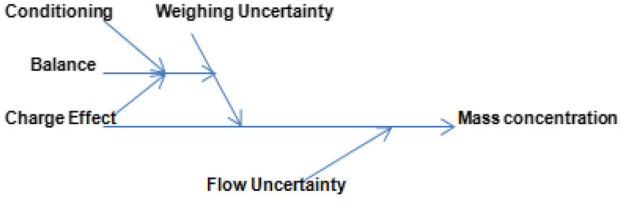


Fig. 1 Cause–effect diagram showing uncertainty components

$$u_c = \sqrt{\sum_i (u_i)^2} \quad (2)$$

$$U_e = k \times u_c \quad (3)$$

where u_i is the standard uncertainty of i and U_e is the combine expanded uncertainty at k (coverage factor). In this work, $k = 2$ at 95% confidence level.

The uncertainty involved in the measurement of the mass of the particle has a significant contribution of these parameters which are given as follows:

3.1. Uncertainty in Conditioning

While doing the conditioning of filters, there may be two possibilities:

(a) Aerosol water content/moisture may add up to the mass (positive effect).
(b) There may be some losses in particulate mass due to evaporation of volatile material from the surface of particles (negative effect).

To study their common effect and estimate the uncertainty due to these two factors, measurement of mass has to be considered.

Therefore, five PM_{10} filters were prebaked and conditioned before sampling. Uncertainty was calculated for the difference in mass of the same filter at different conditioning times, i.e., 12, 24, 36 and 72 h after sampling. The standard uncertainty is calculated by the equation given below:

$$u_1(m) = \frac{\sqrt{\frac{\sum_{i=1}^{n}(m_i - \bar{m})^2}{n-1}}}{\sqrt{n}} \quad (4)$$

where m_i is the mass of particles before conditioning, $\bar{m}$ is the average mass above m_i, and n is the number of samples. Uncertainty was calculated for different hours of conditioning for five different filters of $PM_{10,}$ and then, the average of the mass was taken. The combined standard uncertainty was calculated as 36.7139 g. The relative standard uncertainty was calculated as 0.005.

3.2. Uncertainty Due to Balance Used for Weighing of Filters

The entire filter weighing was done on Mettler Toledo AX105 balance with a maximum capacity of 100 mg. The uncertainty of the balance is estimated using the above Eq. (4). Type A uncertainty is determined as the standard deviations of repeated measurement results having a normal distribution. Type B uncertainty is based on values given in the calibration certificate of the balance with rectangular distribution. Combining both type A and type B, we get standard uncertainty as 3.7593 g. Relative standard uncertainty is calculated as 0.031.

3.3. Uncertainty Due to the Charge Effect

Aerosol mass drop from the filter, contaminations, electrostatic charging of filters and variations in relative humidity may result in the deviations from the actual mass value [12]. An electrostatic charge eliminator (Haug Mettler Toledo) was used to remove the static charge collected on the filters before each weighing. The PM_{10} filter masses were determined by taking the weight of the filters with and without using the electrostatic charge eliminator as given in Eq. (4). The standard uncertainty calculated for the difference in mass before and after the use of a static charge eliminator was found to be as 1.2041 g.

3.4. Uncertainty Due to PM_{10} Sampler Inlet Flow Rate

Rotameters are the most widely used as flow meter to determine flow rate in PM_{10} samplers. It consists of a rotating float in a tapered tube that keeps falling and rising and thus measures the flow rate. They are gravity-type flow meters because they are based on the resistance between the downward force of gravity and the upward force of the incoming air. The flow rate is indicated on a graduated scale.

Air is drawn by means of a blower into the sampler through a quartz filter, so that particulate matter collects on the surface of the filter. Due to the size-select-type inlet, particles $\leq$ 10 μm diameter are collected on the quartz filter paper. A flow-rate indicator records the volume of air sampled. A reference orifice meter is used to calibrate the flow-rate indicator [13].

PM_{10} low-volume sampler flow rate (16.7 lpm) is measured by rotameter. This rotameter is calibrated with the reference flow meter in NPL traceable to the SI unit. The flow rate was measured at the start of sampling and then at the end of the sampling. The mass of filter on loading in a sampler and removing from the sampler (after sampling) was also recorded. The sampling was performed for 24, 48, 96 and 120 h to observe any change in the flow rate of sampling (if any). The relative uncertainty in flow measurement is calculated as given in Eq. (5). The uncertainty in flow rate was calculated using the mass, volume with the corresponding sampling time. The type A uncertainty is calculated by five repeatable measurements, and the normal distribution is calculated as 0.03 lpm. Type B uncertainty as given in the calibration certificate of reference flow meter is 0.54 lpm. Standard uncertainty of flow rate $u(q_2)$ at the low-volume sampler inlet for the entire

duration of sampling is estimated using Eq. (6) as given below:

$$q_1 = \frac{u(q)}{\bar{q}}\% \tag{5}$$

$$u(q_2) = \frac{\sqrt{\sum_{i=1}^{n}\left(\frac{\Delta m}{\Delta V}xq_1\% - \frac{\Delta \bar{m}}{\Delta V}xq_1\%\right)^2}}{\sqrt{n}} \tag{6}$$

where Δm is the difference in mass of filters, ΔV is the difference in volume of the air sucked during the start and end of sampling, q_1 is the % flow rate during sampling and q_2 is the average flow rate calculated throughout the entire sampling period (for n number of samples). The total standard uncertainty (types A and B) was calculated as 0.318 μg m^{-3}.

The uncertainty parameters involved in the measurement of mass concentration are calculated for PM_{10} samples. The combined standard uncertainty for the measurement of mass concentration $u(x)$ can be calculated as:

$$u(x) = \sqrt{(u(m))^2 + (u(v))^2} \tag{7}$$

Mass concentration is calculated from measured mass and volume using Eq. (1). Figure 2 shows the mass concentration (μg m^{-3}) versus number of sampling days.

The 24-h time-weighted average of mass concentration for a year-round measurement of PM_{10} samples (n = 104) varied from 32.5 to 480.2 μg m^{-3}. High mass loading was observed during the measurement period of December–February months.

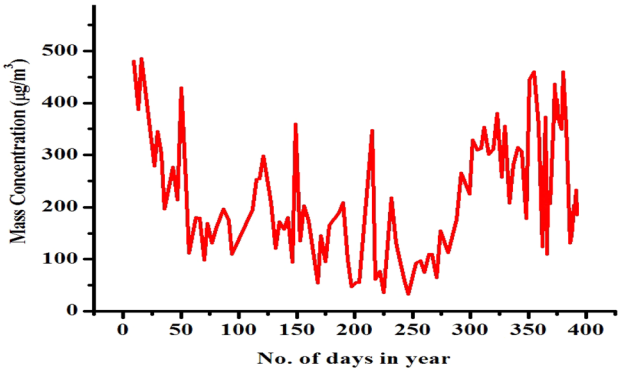


Fig. 2 Mass concentration of PM_{10} samples for the year 2014–2015

The uncertainty budget for the PM_{10} mass measurements in all the four uncertainty components is listed in Table 1. Only two uncertainty parameters had a major contribution: uncertainty in flow rate and uncertainty in charge effect. Of these, the uncertainty in flow rate had the greatest impact. The combined uncertainty for mass measurement of PM $_{10}$ samples was calculated as 1.40 μgm^{-3}.

Relative humidity effects the mass concentration of PM samples. In the atmosphere, the particle can retain water if relative humidity (RH) is around 80% or more. However, below 80% RH though particle retains water, it is not so significant. Therefore, in high RH conditions, this aerosol water content may have a major contribution toward PM_{10} mass concentration. In winter, especially on foggy days, nighttime RH is recorded to be more than 90% which influences the mass concentration. It is to be noted that we have determined particle mass after conditioning of filters [14]. Relative humidity (RH) as shown in Fig. 3 shows high values in the month of December, January and February.

The mass concentration also depends on the temperature. In Fig. 4, the mean temperature was found to be high in the month of May and June, and subsequently, the mass concentration was low in these months. When the mean temperature was low in the months of November, December, January and February, mass loading was more. In winters, there are many sources which affect the aerosol mass loading. One of the major sources is secondary aerosol formation, i.e., the uptake of gases into aerosols [15]. The reason behind heavy mass loading in winters is as follows: OC, EC, WSOC and total inorganic ion concentrations were approximately 3–4 times higher in winter as compared to summer. This is probably due to (1) increased anthropogenic activities in the winter season and (2) prominent oxidative exhaustion of particles, and because of the high humidity and temperature in the tropics, there is wet removal of particulates in summer season [16].

Table 1 Uncertainty budget for PM_{10} mass measurements

Uncertainty components	Uncertainty type	Standard uncertainty	Distribution	Relative standard uncertainty	Relative contribution to standard uncertainty (%)
Conditioning	Type A	36.7139	Normal	0.005	0.4
Balance	Type A	3.7593	Normal	0.031	2.4
	Type B		Rectangular		
Charge effect	Type A	1.2042	Normal	0.089	6.8
Flow uncertainty	Type A	0.3182	Normal	1.180	90.4
	Type B		Rectangular		

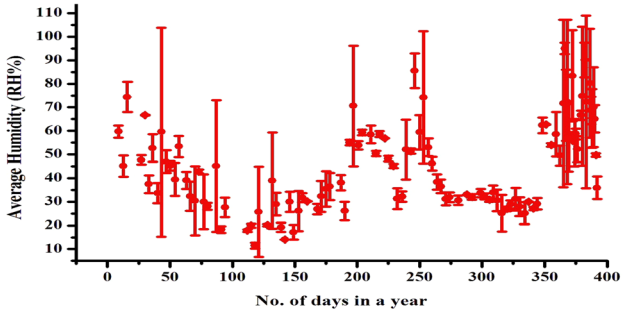


Fig. 3 Mean relative humidity (RH) during the sampling of PM_{10} samples

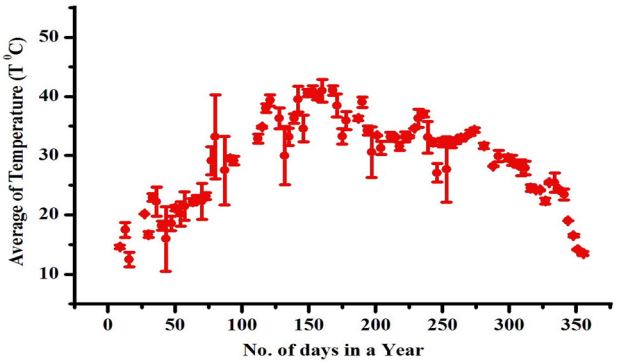


Fig. 4 Mean temperature (T °C) during the sampling of PM_{10} samples

4. Conclusion

We have measured PM_{10} mass concentration in New Delhi as per NAAQS guidelines for the year-round period from January 2014 to January 2015. It is observed that PM_{10} mass loading peaked in winters (January 396 ± 89 μg m^{-3}) and minimized in the summer (June 88 ± 27 μg m^{-3}). The increased concentration of mass can be due to the low planetary boundary layer and increased biomass burning in the winter season. Year-round average mass concentration was calculated (88 ± 27–396 ± 89 μg m^{-3}). In addition to this mass measurement, we have also estimated the measurement uncertainty. We found that the uncertainty contribution due to flow measurement in PM_{10} mass measurement could be up to 90.4%, followed by charge effect 6.8%, conditioning 2.4%, and microbalance also as 0.39%. Combined uncertainty is also calculated to increase the level of confidence in the measurement. Each primary measurement has its own contribution to the total calculated uncertainty as given in Eq. (5) [17].

Acknowledgements Authors are thankful to the Director, National Physical Laboratory, for providing experimental facilities. Dr. S. K. Mishra is acknowledged for providing PM_{10} sampler. One of the authors, Jyoti Pokhariyal, is thankful to Prof. S. K. Singh, Head, Environmental Engineering Department, Delhi Technological University, for providing the research opportunity.

References

[1] H. Hauck, A. Berner, B. Gomiscek, S. Stopper, H. Puxbaum, M. Kundi and O. Preining, On the equivalence of gravimetric PM data with TEOM and beta-attenuation measurements, J. Aerosol Sci., **35** (2004) 1135–1149.

[2] S. G. Aggarwal, S. Kumar, P. Mandal, B. Sarangil, K. Singh, J. Pokhariyal, S. K. Mishra, S. Agarwal, D. Sinha, S. Singh, C. Sharma and P. K. Gupta, Traceability issue in $PM_{2.5}$ and PM_{10} Measurements. MAPAN-J. Metrol. Soc India, **28**(3) (2013) 153–166.

[3] VIM (international vocabulary of metrology—basic and general concepts and associated terms (http://www.bipm.org/en/publications/guides/vim.html), JCGM., **200**(3) (2012) 29–30.

[4] ISO/IEC Guide: Uncertainty of measurement—Part 3: Guide to the expression of uncertainty in measurement. **98**(3) (2008).

[5] National Ambient Air Quality Standards for Particulate Matter; EPA, Federal Register., **62**(138) (1997).

[6] P.H. McMurry, A review of atmospheric aerosol measurements, Atmos. Environ., **34** (2000) 1959–1999.

[7] J. C. Chow, Measurement methods to determine compliance with ambient air quality standards for suspended particles. J. Air Waste Manage. Assoc., **45** (1995) 320–382.

[8] J. G. Watson, R. J. Tropp, S. D. Kohl, X. Wang, J. C. Chow, Filter processing and gravimetric analysis for suspended particulate matter samples, Aerosol Sci. Eng., **1** (2017) 93–105.

[9] K. Singh, S. Tiwari, A. K. Jha, S. G. Aggarwal, D. S. Bisht, B. P. Murty, Z. H. Khan and P. K. Gupta, Mass-size distribution of PM_{10} and its characterization of ionic species in fine (PM2.5) and coarse (PM10–2.5) mode, New Delhi, India. Nat. Hazards., **68** (2013) 775–789.

[10] B. Sarangi, S. G. Aggarwal and P. K. Gupta, A simplified approach to calculate particle growth rate due to self-coagulation, scavenging and condensation using SMPS measurements during a particle growth event in New Delhi, Aerosol Air Qual. Res., **15** (2015) 166–179.

[11] B. Sarangi, S. G. Aggarwal, D. Sinha and P. K. Gupta, Aerosol effective density measurement using scanning mobility particle sizer and quartz crystal microbalance with the estimation of involved uncertainty, Atmospheric Meas. Tech., **9** (2016) 859–875.

[12] S. M. Almeida, M. A. Reis, M. C. Freitas and C. A. Pio, Quality assurance in elemental analysis of airborne particles, Nucl. Instrum. Methods., **207** (2003) 434–446.

[13] L. Melymuk, P. Bohlin-Nizzetto, R. Prokeš, P.Kukučka and J. Klánová, Current challenges in air sampling of semivolatile organic contaminants: sampling artifacts and their influence on data comparability, Environ. Sci. Technol., **48**(24) (2014) 14077–14091.

[14] S. G. Aggarwal, M. Mochida, Y. Kitamori and K. Kawamura, Chemical closure study on hygroscopic properties of urban aerosol particles in Sapporo, Japan, Environ. Sci. Technol., **41** (2007) 6920–6925.

[15] C. A. Varotsos and R. Zellner, A new modeling tool for the diffusion of gases in ice or amorphous binary mixture in the polar stratosphere and the upper troposphere, Atmos. Chem. Phys., **10** (2010) 3099–3105.

[16] S. G. Aggarwal, K. Kawamura, G. S. Umarji, E. Tachibana, R. S. Patil and P. K. Gupta, Organic and inorganic markers and stable C-, N-isotopic compositions of tropical coastal aerosols from megacity Mumbai: sources of organic aerosols and atmospheric processing, Atmos. Chem. Phys., **13** (2013) 4667–4680.

[17] R. E. Lacey and W. B. Faulkner, Uncertainty associated with the gravimetric measurement of particulate matter concentration in ambient air, J. Air Waste Manage. Assoc., **65** (2015) 887–894.

Artificial Intelligence Review
https://doi.org/10.1007/s10462-018-9651-1

Video benchmarks of human action datasets: a review

Tej Singh[1] · **Dinesh Kumar Vishwakarma**[2]

© Springer Nature B.V. 2018

Abstract
Vision-based Human activity recognition is becoming a trendy area of research due to its wide application such as security and surveillance, human–computer interactions, patients monitoring system, and robotics. In the past two decades, there are several publically available human action, and activity datasets are reported based on modalities, view, actors, actions, and applications. The objective of this survey paper is to outline the different types of video datasets and highlights their merits and demerits under practical considerations. Based on the available information inside the dataset we can categorise these datasets into RGB (Red, Green, and Blue) and RGB-D(depth). The most prominent challenges involved in these datasets are occlusions, illumination variation, view variation, annotation, and fusion of modalities. The key specification of these datasets is discussed such as resolutions, frame rate, actions/actors, background, and application domain. We have also presented the state-of-the-art algorithms in a tabular form that give the best performance on such datasets. In comparison with earlier surveys, our works give a better presentation of datasets on the well-organised comparison, challenges, and latest evaluation technique on existing datasets.

Keywords Human action and activity recognition · Survey · RGB dataset · RGB-depth (RGB-D) dataset

1 Introduction

In the present era, human activity recognition (Aggarwal and Ryoo 2011; Vishwakarma and Agrawal 2013; Edwards et al. 2016; Das Dawn and Shaikh 2016; Bux et al. 2016) in videos has become a prominent area of research in the field of computer vision. It has many daily living applications such as patient monitoring, object tracking, threat detec-

✉ Dinesh Kumar Vishwakarma
dvishwakarma@gmail.com

Tej Singh
ttomar07@gmail.com

[1] Department of Electronics and Communication Engineering, Delhi Technological University, New Delhi, India

[2] Department of Information Technology, Delhi Technological University, New Delhi, India

Published online: 17 August 2018

tion, and security and surveillance. The key motivation to work in this field is to recognise human gestures, actions, and interactions in videos and utilised it into practical scenarios. The recognition of human activities in video involves various steps such as preprocessing, segmentation, feature extraction, dimension reduction, and classification. These human activity datasets divided into two categories based on the modalities in which they are recorded such as RGB and RGB-D. Before 2010, a large number of RGB video dataset was available (Chaquet et al. 2013). After the advancement of low-cost depth sensor, e.g. Microsoft Kinect, there has been a drastic increase in the 3D dataset, and multi-modal videos dataset (Li et al. 2010; Aggarwal and Xia 2013; Lun and Zhao 2015; Zhang et al. 2016). Due to low cost and lightweight sensors datasets are recorded with multiple modalities such as depth frames, accelerometer, IR sensors frames, acoustical data, and skeleton data information. The RGB-D datasets having multiple modalities which reduces the loss of information in 3D videos as compared to traditional RGB datasets at the cost of increased complexities.

These HAR datasets provide an open challenge to the researcher to measure their accuracy and compare the state-of-the-approaches with each other work. It is a difficult task to collect videos and maintained a standard format for the new dataset, so it is important to know exact knowledge of these benchmarks in the relevant area of applications which leads to the advanced research in the community and saves precious time. With the advancement of labelling algorithms, it becomes an opportunity to label the dense dataset videos for activity recognition, object tracking, and scene reconstruction. This work covers gesture, action/interaction, daily living activity, shopping, fine-grained activity, sports actions, and human–object interaction datasets and focused on datasets specifications such as year of publication, frame rates, spatial resolution, the total number of action and number of actors (subjects) performing in videos and state-of-the-art solutions on existing benchmarks.

Chaquet et al. (2013), focused on twenty-eight publically available RGB datasets of human action and activity. The dataset characteristics are discussed such as ground truth, numbers of action/actors, views and area of applications. Their work does not cover the RGB depth dataset available at that time. Edwards et al. (2016), proposed a good survey on RGB and RGB-D dataset. However, they are missing the essential datasets. Also, they are not discussed various challenges present in the video, state-of-the-art results, and future recommendation for HAR dataset. Our survey paper including all of such issues on latest as well as famous HAR dataset. Wang et al. (2017), discussed specific novel techniques on RGB-D-based motion recognition. Hassner (2013), focused on action recognition and accuracy of most of the RGB datasets. The very limitation of this work is the action in depth datasets and area of applications. Firman (2016), analysed the depth dataset such as semantics, identification, face/pose recognition and object tracking. Borges et al. (2013), discussed the advantages and shortcomings of various methods for human action understanding. Zhang et al. (2016), present an excellent survey on RGB-D video dataset with state-of-the-art results. However, they do not cover the RGB dataset in their work as well as missing larger depth dataset NTU RGB+D, PKU-MMD which is most suitable for Deep Learning Architecture. It is a fact that latest RGB dataset is more realistic and appropriate to address the real problem of the world as compared to RGB-D that are recorded in indoor environments and face the limitations of sensors as Mocap, or Kinect. Therefore, there is a need for such a review paper to the community that covered both types of dataset across all application domains. Zhua et al. (2016), discussed the comprehensive analysis of both handcrafted and learning-based actions representations on RGB and RGB-D datasets and the advantages and limitations of existing techniques. Han et al. (2017), discussed an overview of the existing space–time representation of people on

RGB-D datasets with modalities, representation encoding, and feature engineering. Herath et al. (2017) provided a comprehensive review on human activity solutions in videos from handcrafted to deep recognition. Compared with the existing surveys, our objective of this review work to discussed the characteristics and various challenges present in the famous HAR datasets and highlighted the higher state-of-the-art accuracy on both RGB and RGB-D benchmarks and the key contribution of our work is as follows:

- A unified literature review on RGB and RGB-D human action datasets are presented.
- The key challenges involved and practical consideration of these datasets are identified and presented in tabular form.
- The details of the technical specifications such as resolution, frame rate, the number of actions, background, etc. are outlined in tabular form.
- The highest classification accuracies achieved on these datasets using existing state-of-the-art algorithms are compared.
- The popular architecture of deep learning and handcrafted feature-based models for human action recognition datasets are highlighted.

The rest of the paper is arranged as follows: Sect. 2, explain the basic terminology used throughout the survey work. Section 3 describes the different kind of RGB and RGB-D human action datasets in details. Section 4 includes various challenges present in the datasets. Section 5, gives the comparison of RGB and RGB-D datasets regarding merits, demerits and applications, advantages, disadvantages, and future recommendations for datasets are discussed. Finally, in Sect. 6, work has been concluded.

2 Basic definitions

Gestures It is defined (Aggarwal and Ryoo 2011) as basic or atomic movements of body parts, for example, hand waving, moving the head up and down, etc.

Actions It is defined (Aggarwal and Ryoo 2011) as a body activity of one person or actors such as running, walking, and jogging, etc. Actions can consider as combinations of atomic gestures.

Interactions It is defined (Aggarwal and Ryoo 2011) as two or more peoples/objects involved in one to one communications. Interactions may be with two type human–human interactions and human objects interactions. Examples of human–human interactions are high-five, fighting with each other, etc. Human objects interactions may see as the person making tea, answering the phone calls, and the crowd.

Group Activity It is defined (Aggarwal and Ryoo 2011) as multiple persons or groups involved in common objectives such as a group meeting, two groups fighting each other, etc. The word RGB dataset and 2D dataset have the same meaning. Similarly, RGB-D dataset and 3D dataset have a similar sense.

Modality It is defined as methods to record and collect data in a particular dataset. A multi-modal dataset has more than two sensors, devices to record a dataset but increases the complexity. Examples of modalities are a video camera, depth map camera (Kinect), Motion Capture (MoCap) marker tracking, accelerometer, audio devices, Bluetooth devices, and skeletal tracking.

View It is defined as the way of looking or observing something by a recording apparatus. It can be divided into two types of single view and multi-view. In a single view, only one recording device is used while multi-view is having more than one.

RGB (Colour) It is available in various resolutions and formats. The format determines the type of colour image data whether it is encoded as RGB or Grey. High-resolution images have high data per frames as compared to low-resolution images.

Depth data It is a measure of distance, in millimetre, to the nearest object at that particular spatial coordinates in the depth sensor's (Kinect) field of view. The depth images can be captured in three different spatial resolutions: 640×480, 320×240, and 80×60 according to specified image format. This data can be used in to track a person's motion and background segmentation.

Skeleton data It consists of the 3D position of data for human skeletons which are visible in the depth sensors. In tracking mode, the position of a skeleton and each of the skeleton joints are stored in three-dimensional coordinates in meters.

Infrared stream This invisible infrared light (IR) stream is generated by a depth sensor to determine an object's depth distance from the sensor. The main aims for this IR stream are to enhance external camera calibration using a test pattern observed from both the RGB and IR camera. It is also used to measure accurate coordinates from one camera space to other and also capture IR image in darkness.

Table 1 summarises and covered most famous video RGB(2D) datasets related to simple human action/interaction, human-object, sports, ADLs, cooking, shopping and smart home activities applications during last two decades. These datasets are arranged according to the chronological order of year in which they were published, modalities, and application domains for which they were recorded.

Similarly, Table 2 contains RGB-D (3D) datasets in the same fashion as the previous table. The RGB-D datasets are recorded with more than one modalities such as RGB, depth frames, skeleton data, acoustical data, and IR sensors for better presentation of actions. It can be observed that there have been a significant increase in the RGB-D (3D) datasets after the development of Microsoft Kinect Sensors in the last decades. The majorities of 3D dataset were recorded in indoor environments due to limitations of sensors.

Table 3 given the comparison between related video dataset surveys. Our review work to discussed the characteristics and various challenges present in the famous 48 human activity datasets and highlighted the higher state-of-the-art accuracy on both RGB and RGB-D benchmarks.

3 Detail descriptions of RGB and RGB-D datasets

In this section, the most familiar RGB and RGB-D datasets related to the various area of applications are discussed in detail.

3.1 RGB (2D) datasets

In this section, RGB colour datasets from the various applications are discussed in chronological order with details such as published year, institute, authors, the total number of actions, actors, the motive of creation, and application of proposed dataset in different approaches. The datasets belonging to normal human actions/activities, movies, surveillance, sports actions, human–human interaction and human-objects interaction are discussed in the subsequent section. Table 4 summarises, the technical specifications of RGB datasets such as spatial resolutions, frames per second, number of actions/actors, and videos samples.

Table 1 RGB (2D) human action dataset

Dataset	Year	Modality	Application domain
KTH (Laptev and Lindeberg 2004)	2004	Grey	Human action recognition in real outdoor conditions
Weizmann (Gorelick et al. 2005)	2005	RGB	Human action recognition
IXMAS (Weinland et al. 2007)	2006	RGB	Multi-view-invariant action recognitions
CASIA Action (Wang et al. 2007)	2007	RGB	Human behaviour and human–human interaction
UIUC Sport (Tran and Sorokin 2008)	2008	RGB	Sports actions recognition
UCF Sports (Lan et al. 2011)	2008	RGB	Sports actions recognition
Olympic Games (Niebles et al. 2010)	2008	RGB	Sports actions recognition
Hollywood (Laptev et al. 2008)	2008	RGB	Realistic actions recognition from movies
Hollywood2 (Marszaek et al. 2009)	2009	RGB	Realistic actions recognition from movies
UT-Interaction (Ryoo and Aggarwal 2009)	2009	RGB	Human–Human interaction activity recognition
BEHAVE (Blunsden and Fisher 2009)	2009	RGB	Human Group behaviour activity analysis
HMDB51 (Kuehne et al. 2011)	2011	RGB	Human activity recognition, human–human interaction, human – object interaction
UCF50 (Reddy and Shah 2012)	2011	RGB	Human Sports activity recognition
BIT-Interaction (Kong et al. 2014)	2012	RGB	Human–human interaction in realistic scenarios
MPII Cooking (Rohrbach et al. 2012)	2012	RGB	Daily cooking activity
UCF101 (Soomro et al. 2012)	2013	RGB	Human Sports activity recognition
YouTube Sports 1M (Karpathy et al. 2014)	2013	RGB	Human Sports activity recognition
ActivityNet (Heilbron et al. 2015)	2015	RGB	Human activity understanding
THUMOS'15 (Gorban et al. 2015)	2015	RGB	Action recognition in wild video
ChaLearn: Action/Interaction (Baró et al. 2015)	2015	RGB	Automatic learning of human action and interactions
FCVID (Jiang et al. 2017)	2015	RGB	Human activity understanding
MOBISERV-AIIA (Iosifidis et al. 2015)	2015	RGB	Assistant daily living (ADLs) activity recognition
MERL Shopping Dataset	2016	RGB	Human object interaction, shopping activities
YouTube 8M (Haija et al. 2016)	2016	RGB	Human activity recognition, human interaction
Okutama Action (Barekatain M 2017)	2017	RGB	Concurrent human action recognition form aerial view
Something–Something (Goyal et al. 2018)	2018	RGB	Human–object interaction

Table 2 RGB-D (3D) human action datasets

Dataset	Year	Modality	Applications domain
i3DPost Multi-View (Gkalelis et al. 2009)	2009	RBG, Depth	Human action/interaction and behaviour
MSR Action 3D (Li et al. 2010)	2010	Depth + skeleton	Sports Gesture recognition
CAD-60 (Sung et al. 2012)	2011	RGB, Depth, skeleton	Daily activity recognition
RGB-D HuDaAct	2011	RGB, Depth	Daily activity recognition
50- Salads (Stein and McKenna 2013)	2013	RGB, Depth	Complex gestures Recognition
Berkeley MHAD (Ofli et al. 2013)	2013	RGB, Depth, skeleton	Human behaviour Recognition
CAD-120 (Sung et al. 2012)	2013	Depth, skeleton	Action labelling, human and object tracking
Hollywood 3D	2013	RGB, Depth	Natural action recognition in movies
MSR Action Pairs (Oreifej and Liu 2013)	2013	Depth	Action pairs recognitions
UWA3D Multi-View (Rahmani et al. 2014)	2014	RGB, Depth, skeleton	Similar and cross view action recognition
Northwestern UCLA (Wang et al. 2014)	2014	RGB, Depth, skeleton	Cross- view action recognition
LIRIS (Wolf et al. 2014)	2014	RGB, Depth, grey	Human activity recognition
IM-Daily Depth (Jalal et al. 2014)	2014	RGB, Depth, skeleton	Daily human activity in real scenarios
Human Manipulation Actions (Pieropan et al. 2014)	2014	RGB, Depth, audio	Fusion of multiple information for activity recognition
UTD-MHAD (Chen et al. 2015)	2015	RGB, Depth, skeleton	View- invariant human action recognition
M^2I (Xu et al. 2015)	2015	RGB, Depth, skeleton	Human–human, human–object interaction
SYSU-3D HOI (Hu et al. 2015)	2015	RGB, Depth, skeleton	Human–object interaction
G3Di	2015	RGB, Depth, skeleton	Gaming interaction activity
NTU RGB+D (Shahroudy et al. 2016)	2016	RGB, Depth, skeleton, IR sequences	Human Action Recognition
DAHLIA (Vaquette et al. 2017)	2017	RGB, Depth, skeleton	Smart home daily life activities
PRAXIS GESTURE (Negin et al. 2018)	2018	RGB, Depth	Elderly care assistive activities
PKU-MMD (Liu et al. 2017)	2017	RGB(image and video), Depth, skeleton, IR sequences	Multi-modal action recognition

3.1.1 Weizmann action

Gorelick et al. (2005) introduced this dataset (http://www.wisdom.weizmann.ac.il/~vision/SpaceTimeActions.html). It is the most common and straightforward benchmark for human actions recognition in video format with a static background, fixed camera, and even illumination environment conditions. The objective of creations in this dataset was to recognise simple human actions in videos. It consists of 9 actors each performing 10 activities such as walking, running, jumping, galloping sideways, bending, one hand waving, two-hand waving, jumping in place, jumping jack, and skipping. The application of proposed dataset

Table 3 A brief comparison of related datasets surveys

Reference work	Datasets	Number of datasets	Key ingredient
Chaquet et al. (2013)	RGB	28	RGB action, human interaction, surveillance dataset
Edwards et al. (2016)	RGB, RGB-D	51	Containing pose, action/activity datasets Introduced new dataset: Converse
Hassner (2013)	RGB	18	Most of RGB web/online based datasets
Zhang et al. (2016)	RGB-D	44	RGB-D action dataset only
Wang et al. (2017)	RGB-D	13	RGB-D based actions benchmarks, deep driving methods
Ours	RGB, RGB-D	48	RGB and RGB-D human action/activity recognitions datasets, challenges in datasets, state-of-art-results

found in Yadav et al. (2016), Vishwakarma and Singh (2017), Vishwakarma et al. (2016a, b), Vishwakarma and Kapoor (2015) and Junejo et al. (2014) (Fig. 1).

3.1.2 KTH action

The KTH Actions dataset introduced (http://www.nada.kth.se/cvap/actions) by Schuldt et al. (2004) and Laptev and Lindeberg (2004). It is a more difficult action video dataset than the Weizmann dataset. It consists of 25 actors each performing 6 activities such as walking, jogging, running, boxing, hand waving, and hand clapping. All the activities performed both indoor as well as an outdoor environment with changing illumination condition several times in four different scenarios. The application of proposed dataset is found in Vishwakarma and Singh (2017), Vishwakarma et al. (2016a, b), Vishwakarma and Kapoor (2015), Pei et al. (2016), Schuldt et al. (2004), Liu et al. (2013) and Li et al. (2015).

3.1.3 IXMAS: INRIA Xmas motion acquisitions sequence

This multi-view dataset (http://4drepository.inrialpes.fr/public/viewgroup/6) (Weinland et al. 2007) is introduced by INRIA, France in 2006. The objective of this dataset was to recognise view-invariant human action from the multi-view camera platform. This dataset consists of 11 actors performing 13 daily living activities such as nothing, checking watch, crossing arms, scratching head, sitting down, getting up, turning around, walking, waving, punching, kicking, pointing, picking up, throwing overhead, and throwing from bottom up. Each activity performed three times by individual actors in an uncontrolled manner. The application of proposed dataset is found in Vishwakarma et al. (2016a), Junejo et al. (2014) and Liu et al. (2013) (Fig. 2).

Table 4 Technical specification RGB dataset

Dataset	Resolution	FPS	Actions	Actors	Videos
KTH	160 × 120	25	6	25	600
Weizmann	180 × 144	50	10	9	90
IXMAS	390 × 291	23	13	11	1650
CASIA Action	320 × 240	25	8	24	1446
UIUC Sport	1024 × 768	15	14	8	532
UCF Sports	720 × 480	10	10	–	150
Olympic Games	–	–	16	–	783
Hollywood	400 × 300, 300 × 200	24	8	–	233
Hollywood2	400 × 300, 300 × 200	24	1	–	3669
UT-Interaction	720 × 480	30	6	–	160
BEHAVE	640 × 480	25	6	5	163
HMDB51	320 × 240	30	51/–	–	6766
UCF50	320 × 240	25	50	–	6681
BIT-Interaction	320 × 240	30	8	–	400
MPII Cooking	1664 × 1224	29.4	65	12	44
UCF101	320 × 240	25	101	–	13,320
YouTube Sports 1 M	–	–	487	–	1,133,158
ActivityNet	1280 × 720	30	203	–	27,801
THUMOS'15	–	–	101	–	5600
ChaLearn: Action/Interaction	480 × 360	15	235	14	235
FCVID	–	–	239	–	91,223
MOBISERV-AIIA	640 × 480	15	2	12	384
MERL Shopping	1980 × 1080	15	5	32	96
YouTube 8 M	–	–	4716	–	~800, 000
Okutama Action	3840 × 2160	30	12	9	44
Something–Something	100 × (~)	12	174	1133	108,499



Fig. 1 Example video frames from Weizmann Action Dataset (Gorelick et al. 2005)



Fig. 2 Example video frames from IXMAS Dataset (Weinland et al. 2007)



Fig. 3 Example video frames from Hollywood Dataset (Laptev et al. 2008)

3.1.4 CASIA action

This dataset (http://www.cbsr.ia.ac.cn/english/Action%20Databases%20EN.asp) is (Wang et al. 2007) introduced by the Institute of Automation, Chinese Academy of Sciences (CASIA). These videos are recorded with multiple cameras in an outdoor environment. This dataset consists of total 1446 video sequences. There are total twenty-four subjects and two subjects performing seven human interactions activities such as fight, rob, following and gathering, meeting and part, overtake, follow, and meet and gather. In this dataset, a single person is performing 8 actions such as jump, bend, walk, punching a car, wander, run, crouch, and faint. The application of proposed dataset is found in Zhang et al. (2007, 2008), Xu et al. (2017), Du et al. (2016) and Aggarwal and Vishwakarma (2016).

3.1.5 UIUC sports action

This dataset (http://vision.cs.uiuc.edu/projects/activity) is introduced by Tran et al. (2008). It was created for two primary objectives to recognised abnormal activities and training with fewer data samples. This dataset divided into two sub-datasets. The first dataset consists of 8 actors performing 14 sports activities such as walking, running, jumping, waving, jumping jacks, clapping, jumping from a sit-up, raise one hand, stretching out, turning, sitting to standing, crawling, pushing up and standing to sit. The applications of proposed dataset is found in Shan et al. (2015).

3.1.6 Hollywood

It is introduced (https://www.di.ens.fr/~laptev/download.html) by Laptev et al. (2008) at the IRISA Institute in France, in 2008. This dataset was created to recognised human activities in real and variant conditions. These dataset videos were collected from 32 Hollywood movies. There are total eight labelled actions classes such as Handshake, Hug Person, Kiss, Sit-down, Sit-up, Stand-up Answerphone, and Get out from the car. The test set contains 211 samples with manually verified labels. The application of proposed dataset is found in Abbasnejad et al. (2016) (Fig. 3).

3.1.7 Hollywood 2

This dataset (https://www.di.ens.fr/~laptev/download.html) was introduced by Laptev et al. (2009). It consists of twelve actions such as get out the car, handshake, hug person, kiss, run, sit-down, driving a car, eat, fight, sit up, stand up, and answer phone. There are total 3669 videos collected from 69 Hollywood movies and approximately 20 h in length. The dataset overcomes the constrained that were caused by the physical properties of scenes, high correlation with particular scene classes. The application of proposed dataset is found in Marszaek et al. (2009), Pei et al. (2016), Liu et al. (2017) and Yu et al. (2017).

3.1.8 UT-interaction

It was created (http://cvrc.ece.utexas.edu/SDHA2010/Human_Interaction.html) by Ryoo et al. (2009). This dataset provides challenges such as aerial view and a wider area of activity videos. It focused on high-level activity such as human–human interaction. This dataset consists of 6 actions such as hugging, kicking, handshaking, pushing, punching, and pointing. The videos are recorded in the natural environment. The dataset divided into two sub-datasets. The first subset contains ten videos captured with minor zoom rate on a parking lot scenario. The backgrounds in the first video dataset are static with little camera jitter. The second subset has the dynamic background and more camera jitters than the first subset. The application of proposed dataset is found in Ryoo et al. (2010) and Kong et al. (2012).

3.1.9 Behave

This dataset was introduced by Blunsden et al. (2009) (http://groups.inf.ed.ac.uk/vision/BEHAVEDATA/INTERACTIONS/index.html) at the University of Edinburgh. The objective of this dataset is to recognized multi-person behavioural interactions on ground truth. This dataset contains around 90,000 frames of humans, annotated by bounding boxes and interacting groups classified into one of six different behaviours classes. The dataset consists of two views of the different environment and people performing interactions activities. It consists of 10 interactions activities following, meet, split, ignore, chase, fights, running together, approach, and the group. The application of proposed dataset is found in Lopez et al. (2016) and Kim et al. (2014).

3.1.10 Olympic sports

This dataset (http://vision.stanford.edu/Datasets/OlympicSports) was introduced by Niebles et al. (2010). It consists videos of different athletes is practising different sports activities. This dataset is useful for modelling motion by exploiting the temporal structure of the human activities. The sources of the video sequences were taken from YouTube. It contains 50 videos from 16 different sports events viz. high jump, long jump, triple jump, pole vault, basketball lay-up, bowling, tennis-serve, platform, discus, hammer, javelin, shot put, springboard, snatch, clean jerk, and vault. The application of proposed dataset is found in Ni et al. (2015).

3.1.11 UCF sports action

Lan et al. (2011) introduced this dataset (http://crcv.ucf.edu/data/UCF_Sports_Action.php) in CVPR Conference, Barcelona. It contains different actions classes collected from sports

activities channel BBC and ESPN. This dataset consists of 10 action classes such as skate-boarding, swing-bench, swing side, walking, diving, golf swing, kicking, lifting, riding a horse, and running. The applications of proposed dataset is found in Pei et al. (2016), Li et al. (2015), Rodriguez et al. (2008) and Soomro and Zamir (2014).

3.1.12 Hmdb51

The HMDB51 dataset (http://serre-lab.clps.brown.edu/resource/hmdb-a-large-human-motion-database) was introduced by Kuehne et al. (2011). This dataset collected from various source such movie, public databases Prelinger Archive, YouTube and Google videos. There were total 6849 videos in this dataset, and they are further divided into 51 actions classes. Each action class has more than a hundred clips. All activity classes split into 5 groups such as general body movements, public facial actions, body movements for human interactions, facial actions with objects manipulations and body movements with objects interactions. The videos in the dataset have been annotated with an action label and meta-label details. The application of proposed dataset is found in Liu et al. (2013), Li et al. (2015), Sadanand and Corso (2012), Gross et al. (2012), Jiang et al. (2012), Wang et al. (2013), Jain et al. (2013), Guo et al. (2017) and Fu et al. (2017).

3.1.13 Ucf 50

This dataset (http://crcv.ucf.edu/data/UCF50.php) introduced by Reddy et al. (2012). It is video clips collected from an online source such as YouTube. All action video has the realistic environment. It was an updated version of the UCF11 dataset. This dataset contains 50 actions classes such as Breaststroke, Clean and Jerk, Diving, Drumming, Baseball Pitch, Basketball Shooting, Bench Press, Biking, Biking, etc. The application of proposed dataset is found in Gopalan (2013) and Hao et al. (2017).

3.1.14 BIT interaction

Kong et al. (2014) introduced this dataset at (https://sites.google.com/site/alexkongy/software) Beijing Laboratory, China in 2012. The videos of the dataset provide a challenge to a researcher with varying conditions in subject appearance, scale, illumination condition, and viewpoint. The video sequences recorded in realistic scenarios with a cluttered background. The people involved in interactive activity annotated with bounding boxes and behave entirely different with diverse motion attributes. It contains 8 action class of human interaction such as a bow, boxing, handshake, high-five, hug, kicks, Pat, and push. Each interaction class consists of 50 videos. The application of proposed dataset is found in Kong et al. (2012), (2014) and Xu et al. (2017).

3.1.15 MPII cooking

This dataset was introduced by Rohrbach et al. (2012) (https://www.mpi-inf.mpg.de) at the Max Planck Institute for Informatics, Germany in 2012. This dataset contains cooking activities recorded in a realistic kitchen environment. All the events categorised into two parts fine-grained body movements that have low inter-class variability and diverse subjects high intra-class variability. This dataset consists of 12 actors performing 65 different cooking activities such as pour, cut slice, or spice etc. There are total 44 videos with a length of more



Fig. 4 Examples video sequence from ActivityNet dataset (Heilbron et al. 2015)

than 8 h and 881,755 frames. The application of proposed dataset is found in Amin et al. (2013) and Cippitelli et al. (2016).

3.1.16 UCF 101

It is introduced by Soomro et al. (2012). This dataset (http://crcv.ucf.edu/data/UCF101.php) is useful for action recognition of realistic environment videos. All videos of this dataset collected from YouTube. It is an advanced version of UCF 50 dataset. It contains 101 action classes such as Boxing Speed Bag, Breaststroke, Brushing Teeth and so on. There is total more than 13 thousand videos, which are further divided into 25 groups. Each group contains 4–7 action clips and has a similar type of characteristics such as viewpoint and background. The videos in the dataset provide challenge due to various background conditions, camera motion, lighting conditions, and different objects appearance. The application of proposed dataset is found in work Abbasnejad et al. (2016), Xu et al. (2016), Yu and Yuan (2015) and Hu et al. (2016).

3.1.17 YouTube Sports 1M

It is introduced by Karpathy et al. (2014) (https://github.com/gtoderici/sports-1m-dataset/blob/wiki/ProjectHome.md) at Google Research at Computer Science Department, Stanford University in 2013. It is a sports activity dataset collected from one million YouTube videos. There are 487 annotated action classes. These sports classes are divided into categories such as team sports, aquatic sports, winter sports, ball sports, combat sports, and sports with animals. This dataset includes six bowling, seven American football, and 23 billiards action styles. The application of the proposed dataset is found in Karpathy et al. (2014).

3.1.18 ActivityNet

It is introduced by Heilbron et al. (2015) (http://activity-net.org/) at University of Del Norte, Colombia. The objective of this large-scale dataset is to provide a semantic taxonomy of videos showing human activities and to cover a rich area of interest for each activity. All the videos of this dataset were downloaded from social videos sharing sites such as YouTube. The ActivityNet dataset divided into three subgroups by application domain such as untrimmed videos classification, trimmed videos classification, and Activity detection on all the untrimmed videos. The untrimmed video dataset consists of 27801labelled videos having 203 activity classes. The trimmed activity dataset consists of 203 activity classes with average 193 samples for each category and objective to predict the label of single activity videos clips. The application of proposed dataset is found in Ma et al. (2016), Yeung et al. (2016), Wu et al. (2016) and Fu et al. (2017) (Fig. 4).

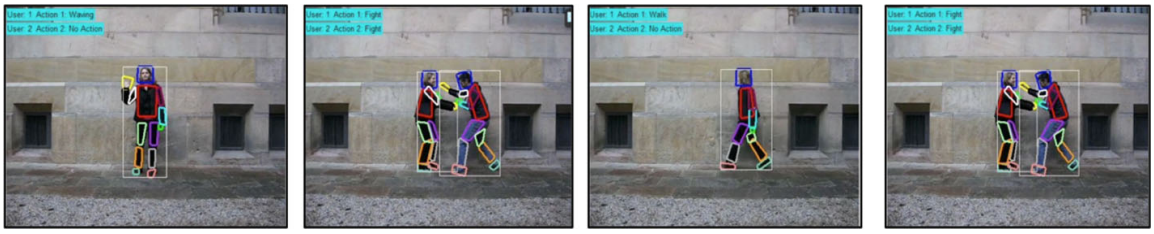


Fig. 5 Example videos sequences from ChaLearn Dataset (Baró et al. 2015)

3.1.19 THUMOS'15 challenge

It was introduced by Gorban et al. (2015) http://www.thumos.info/download.html). The THUMOS challenge has two main objectives, classification of action in a particular video and temporal action detection in each video. THUMOS'15 provides new challenges and approaches for large-scale action and classes from temporally untrimmed videos in realistic scenarios. The videos in this dataset was collected from YouTube and consists of 101 action classes. THUMOS'15 focused on two main tasks (a) action classification for 101 action classes and (b) temporal action localisation on a subset of 20 action classes. This dataset also has 3000 background set videos. The application of the proposed dataset is found in Idrees et al. (2017).

3.1.20 ChaLearn: action/interaction

This dataset is introduced for the ChaLearn LAP 2015 challenge by Baro et al. (2015) (http://chalearnlap.cvc.uab.es/dataset/15/description/) at the University Oberta de Catalunya, Barcelona, Spain. It focused on the automatic learning of a different set of actions performed by individual actors and spotting of independent continuous gestures. It contains 14 different actors performing 235 action/interaction labelled sequences. There are 11 actions categories (7 actions and four interactions) such as Wave, Point, Clap, Crouch, Jump, Walk, Run, Shake Hands, Hug, Kiss, and Fight. This dataset provides challenge due to the high intra-class variability of actions, self-occlusions, clothing, poses and skin colour (Wang et al. 2015) (Fig. 5).

3.1.21 FCVID

It was introduced by Jiang et al. (2017) (http://bigvid.fudan.edu.cn/FCVID). This dataset was composed of web internet videos for deep learning features. It contains 91,223 internet videos with manually annotated in 239 different categories of real-life scenarios. This dataset is equally divided into training and test samples videos.

3.1.22 MOBISERV-AIIA database

This dataset was introduced by Iosifidis et al. (2015) (http://www.aiia.csd.auth.gr/MOBISERV-AIIA/index.html). This novel multi-view dataset was created to assists daily living (ADLs) activities of individuals with the objective to solve and manage dementia in elderly people, and malnutrition problems. It contains 12 performers of different height, age, sex, and colour performing 3 actions: eating, drinking, and apraxia which consists of 13 sub actions of meals activities four times in a day. Two light sources of 800 W each and daylight lamps were



Fig. 6 Examples video sequence from MOBISERV-AIIA Database (Iosifidis et al. 2015)



Fig. 7 Examples frames from MERL Shopping Dataset (Singh et al. 2016)

used to improve the recorded illuminations environment. All videos were compressed using Lagarith compression technique to reduce the storage spaces. The application of proposed dataset is found in Yan (2016), Iosifidis et al. (2013) and Iosifidis and Tefas (2013) (Fig. 6).

3.1.23 MERL shopping dataset

Singh et al. (2016) introduced this shopping activity dataset (http://www.merl.com/demos/merl-shopping-dataset). This dataset is used for fine-grained action detection and localising the action in a long video frame. It consists of 96 videos each having 2 min long and 32 actors were performing 5 different action class: "Inspect Shelf", "Inspect Product", "Retract from Shelf ", "Reach to Shelf", "Hand in Shelf", and "Inspect Product". The dataset recorded with fixed position mounted on the head of the actors. All videos are having spatial resolution 1980×1080 with frame rate 15fps. The application of proposed dataset is found in Lea et al. (2017) (Fig. 7).

3.1.24 YouTube 8M

It is introduced by Haija et al. (2016) (https://research.google.com/youtube8m/) at Google Research laboratory, US. It is the largest multi-label video classification dataset consist of eight million videos with annotated 4800 visual entities. Its primary objective is to identify the contemporary theme of a video and adaptation of various learning approaches on large-scale videos. All videos annotated similarly like You-Tube annotation system and excellent representation for content-based methods. This dataset provides 7 million video URL, 450,000 h of videos, 3.2 billion/audio/visual feature, 4716 classes, and 3.4 average labels per videos. Each video sequences are having 120–500 s in length and more than one thousand views.

3.1.25 Okutama action

It is introduced by Barekatain (2017) (http://okutama-action.org/) at Technical University of Munich, Munich. Its main aim to recognise concurrent human action from aerial view platform. This dataset contains 9 actors performing 12 low and high-level activities such as running, sitting, walking, lying, standing, reading, drinking, pushing/pulling, carrying,

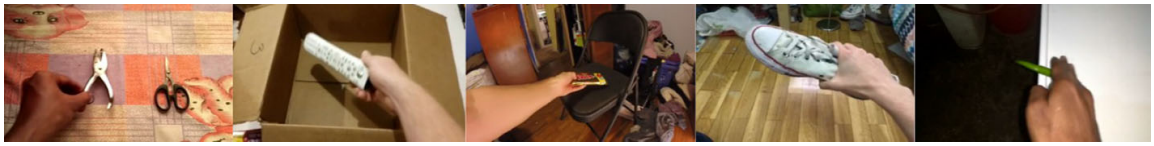


Fig. 8 Examples frames from Something–Something dataset (Goyal et al. 2018)

calling, handshaking, hugging. It consists of 43 min fully annotated videos sequences and were recorded using 2 UAV flying at the height of 10–45 m at an angle of 45° or 90°.

3.1.26 The 20 BN something–something dataset

Goyal et al. (2018) introduced this dataset (https://20bn.com/datasets/something-something). This publically available dataset is an extensive collection of human object interaction of densely labelled 174 videos sequences. It consists of 1133 workers performing pre-trained daily human–object interaction physical activities. Total 108,499 videos and jpg images are having variable spatial resolutions and lengths (Fig. 8).

3.2 RGB-D (3D) datasets

This section summarises the most important RGB-D datasets from various applications such as human activity recognition, daily activities, complex gestures, human behaviour, object tracking, realistic action recognition from movies, and cross-view actions recognitions. It can be noticed that a number of actions in 3D datasets are less as compared to the 2D datasets. We noticed that the NTU RGB+D dataset has a number of actions and actors than any other depth datasets. Most of the RGB-D dataset is recorded in control, static background conditions. Some datasets as Berkeley MHAD, Hollywood 3D, and Northwestern-UCLA is more challenging due to dynamic background conditions. At present, the most of the depth dataset recorded with multiple sensors system. The different dataset is discussed in the following section according to chronological order with details such as published year, Institute, authors, the total number of actions, actors, objectives, and challenges in the dataset. Table 5 summarises the technical specifications of RGB-D datasets such as spatial resolutions, frames per second, number of actions/actors, and videos samples.

3.2.1 I3DPost multi-view human action dataset

This multi-view and 3D human action/interaction dataset are introduced by Gkalelis et al. (2009) (http://kahlan.eps.surrey.ac.uk/i3dpost_action/) with the collaboration project i3DPost of University of Surrey and CERTH-ITI in 2009. It consists of 8 actors (6 male, 2 female) performing 12 different motion action classes such as: Running, Walking, Bending, Jump-in-place, Sit-Stand Up, Jumping, Pull, Handshake, Walk-sit, Run-fall, Run-jump-walk, and Hand waving and basic Facial-expressions sequences for each person. There are total 104 multi-view high definition (HD) videos, recorded with 8 different angle viper cameras positioning above 2 m height and 8 m diameter in a circle. All camera videos were synchronised and save on hard disk in an uncompressed format. These multi-view videos are further processed to create a 3D human model for each action frames. The applications of proposed dataset is found in Vishwakarma et al. (2016a), Iosifidis et al. (2014), Mademlis et al. (2018) and Mygdalis et al. (2016) (Fig. 9).

Table 5 Technical specification RGB-D dataset

Dataset	Resolutions	Fps	Actions	Actors	videos
i3DPost Multi-view	1920 × 1080	25	12	8	104/832
MSR Action 3D	640 × 480	15	20	7	567
RGB-D HuDaAct	640 × 480	30	12	30	1189
CAD-60	640 × 480	25	12	4	60
50-Salads	640 × 480	30	2	25	966
Berkeley MHAD	640 × 480	30	11	12	
CAD-120	640 × 480	25	10	4	120
Hollywood 3D	1920 × 1080	24	14	–	650
MSR Action Pairs	320 × 240	30	10	6	180
UWA3D Multi-view	640 × 480	30	30	10	900
Northwestern-UCLA	640 × 480	30	10	10	1475
LIRIS	640 × 480, 720 × 576	25	828	21	–
IM-Daily Depth	640 × 480	30	15	15	45
Human Manipulation Actions	640 × 480	30	6	8	140
UTD-MHAD	512 × 424	30	27	8	861
M^2I	320 × 240	30	22	22	1784
SYSU-3D HOI	640 × 480	30	40	12	~480
G3Di	640 × 480	30	12	15	574
NTU RGB+D	512 × 424, 1920 × 1080	30	60	40	56,880
DAHLIA	1920 × 1080, 640 × 480	15	7	44	51
PRAXIS	960 × 540, 512 × 424	–	29	60	–
PKU-MMD	512 × 424, 1920 × 1080	30	66/60	51/40	1076

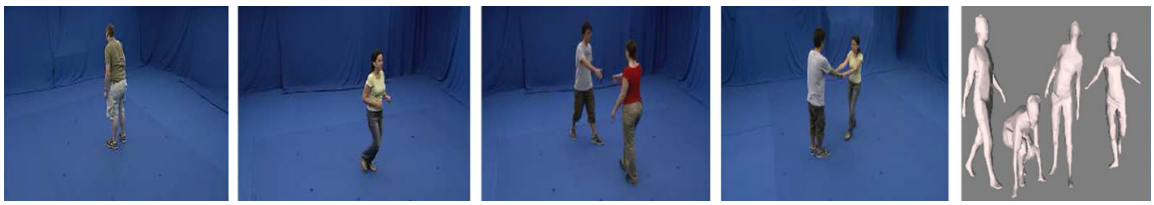


Fig. 9 Examples video sequence from i3DPost Multi-view Human Action Datasets (Gkalelis et al. 2009)

3.2.2 MSR action 3D

This dataset (http://research.microsoft.com/en-us/um/people/zliu/ActionRecoRsrc) is introduced by Li et al. (2010) in Microsoft Research laboratory at Redmond, the US. The dataset videos were captured using depth sensors and consists of seven actors performing 20 action classes such as draw circle, hand clap, two hand wave, side-boxing, bend, high arm wave, horizontal arm wave, hammer, hand catch, forward kick, throw, pickup, punch, high throw, draw x, draw tick, sidekick, jogging, tennis swing, tennis serve, and golf swing. All twenty actions are divided into three sub-groups, each having 8 actions because this makes it handle a large amount of computation of different clustering techniques training samples into salient postures. Both subset 1 and subset 2 were grouped for similar actions movements.

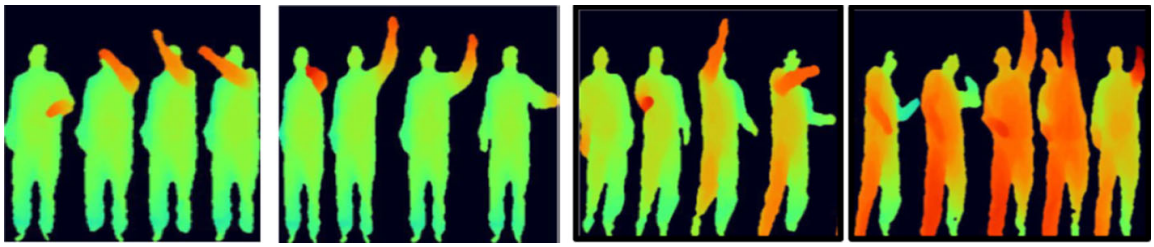


Fig. 10 Examples video sequence from MSR Action3D Dataset (Li et al. 2010)



Fig. 11 Examples video sequence from CAD-60 Dataset (Sung et al. 2012)

The subset 3 consists of high-level actions activities and these actions are categorised as about interactions with game consoles and different movement of arms, legs, torso and their combinations. The application of proposed dataset is found in Li et al. (2010), Wang et al. (2012) and Zhou t al. (2015) (Fig. 10).

3.2.3 RGB-D HuDaAct

It is introduced by Ni et al. (2011) (http://filezilla-project.org/download.php) at the Advanced Digital Sciences Centre, Singapore. Its main aim of monitoring daily human activities by using multimodal data sensors such as RGB colour, and depth frame images. This dataset provides synchronised colour and depth videos with the help of Kinect sensors in a lab environment. It contains 12 students performing 12 different class activities such as making a call, sit down, stand up, take off the jacket, put on the jacket, exit the room, etc. and also includes random types of background activities. Each student performed each activity two to four times. There are 1189 labelled videos and each having length 30–150 s long.

3.2.4 Cad-60

This dataset was introduced by Sung et al. (2012) (http://pr.cs.cornell.edu/humanactivities/data.php). These dataset videos were recorded in five different scenarios such as a living room, office, kitchen, bedroom, and bathroom. It consists of 4 actors performing 12 activities such as brushing teeth, wearing contact lens, talking on the phone, rinsing mouth, opening pill container, chopping, stirring, talking on the couch, working on the computer, writing on a whiteboard, and relaxing on the couch. The application of proposed dataset is found in Mo et al. (2016), Gaglio et al. (2015) and Zhu et al. (2015) (Fig. 11).

3.2.5 Cad-120

This dataset was introduced by Sung et al. (2012) (http://pr.cs.cornell.edu/web3/CAD-120). It contains 4 subjects performing 10 high-level activities such as having a meal, microwaving food, picking objects, cleaning objects, making cereal, taking medicine, stacking objects,

unstacking objects, taking food, arranging objects, and taking medicine. The dataset videos also have 12 affordance labels: placeable, closable, scrubbable, reachable, movable, stationary, pourable, pourto, scrubber, openable, containable, and drinkable. The application of proposed dataset is found in Hu et al. (2016) and Liu et al. (2016).

3.2.6 50 Salads

This dataset (http://cvip.computing.dundee.ac.uk/datasets/foodpreparation/50salads) is introduced by Stein and McKenna (2013). The RCUK Digital Economy Research Hub and SIDE jointly funded this research. The primary objective of this dataset was to recognised complex manipulative gestures. The manipulative gestures defined as the interaction between hands, tool, etc. and while objects like cooking food, industrial work and assembly assignment, etc. some applications containing situational support, automated supervision, and skill development. It consists of 25 people each preparing two mixed salads. There are three-axis Activity WAX3 wireless accelerometers. These sensors were mounted on the knife, spoon, peeler, glass, oil bottle, and pepper dispenser. This dataset can be utilised in many research areas such as activity recognition, spotting, video analysis, tracking, sensor fusion, transfer learning, and user adoption. The application of proposed dataset is found in Lea et al. (2017) and Awwad and Piccardi (2016).

3.2.7 Berkeley MHAD

It is created by Ofli et al. (2013). This dataset (http://tele-immersion.citris-uc.org/berkeley_mhad) was a part of the NSF-funded project: A Bio-Inspired Approach to Recognition of Human Movements and Movement Styles. It was collaborative research between the UC at Berkeley and Johns Hopkins University. This dataset consists of 12 actors performing 11 actions such as sit down, stand up, jumping, jumping jacks, bending, punching, waving two hands, waving one hand, clapping, throwing and sit down/stand up. Each actor repeats each action by five times. Five different systems instantly recorded each action, which was optical motion capture, four multi-view stereo vision camera arrays, two Kinect devices, six wireless accelerometers and four microphones. The Bluetooth protocol used to send the data to a computer with a time stamp. The application of proposed dataset is found in Chaudhry et al. (2013).

3.2.8 UWA3D activity

It is introduced by Rahmani et al. (2014) at the University of Western Australia, Crawley. This dataset (http://staffhome.ecm.uwa.edu.au/~00053650/databases.html) was collected using Kinect camera device with a focus on three aspects scale variations among subjects, viewpoint variation, and continuity of actions while performing the activity. It consists of 10 subjects performing 30 activities viz phone answering, jumping jack, one hand waving, one hand Punching, sitting down, standing up, holding chest, holding head, picking up, putting down, dancing, coughing, holding back, walking, turning around, drinking, bending, vibrating, falling, irregular walking, lying down, running, kicking, jumping, moping floor, sneezing, sitting down on chair, squatting, two hands waving, and two hand punching. There are 5 subjects, performing 15 activities to captured cross-view action activities. This dataset provides challenge due to self-occlusions and high similarity in actions. The application of proposed dataset is found in Rahmani et al. (2014) and Chen et al. (2015).



Fig. 12 Examples video sequence from LIRIS Dataset (Wolf et al. 2014)

3.2.9 Northwestern-UCLA Action3D

Wang et al. (2014) introduced this dataset (http://users.eecs.northwestern.edu/~jwa368/my_data.html) at UC, Los Angeles. It is a Multi-view 3D event based dataset. It consists of RGB, depth image and skeleton data captured with Kinect cameras. This dataset contains 10 actors each performing 10 action classes stand up, pick up with one hand, pick up with two hands, drop trash, walk around, carry, donning, doffing, throw, and sit down. The application of proposed dataset is found in Wang et al. (2014).

3.2.10 LIRIS

This dataset (http://liris.cnrs.fr/voir/activities-dataset) is introduced by Wolf et al. (2014) at LIRIS Laboratory, CNRS, France. It was primarily recorded for the ICPR-HARL 2012 competition. These dataset videos have various activities taken from daily life. It consists of three type fully annotated video sub-dataset grey, RGB, and depth. The annotation contains information on the action class as well as its spatial and temporal positions in the video. There are different activities such as discussion between two or more people, giving an object to another person, put/take an object into/from a box/desk, enter/leave a room (pass through a door) without unlocking, try to get into a room (unsuccessfully), unlock and enter (or leave) a room, leave baggage unattended, handshaking, typing on a keyboard, and telephone conversation. The Kinect device mounted on a remotely controlled Wany Robotics Pekee II mobile robot that is part of the LIRIS-VOIR platform. Both sub-dataset are partially independent because the second dataset captured from the similar scenes captured in the first dataset which taken from a different viewpoint. The application of proposed dataset is found in Wolf et al. (2014) (Fig. 12).

3.2.11 Hollywood 3D

Hadfield et al. (2017) introduced this dataset (http://cvssp.org/Hollywood3D) at the University of Surrey, Guildford, UK, in the year 2013. EPSRC funded this project. This 3D dataset used for action recognition in natural scenarios and collected from various Hollywood films. It consists of 14 activities classes such as no actions, runs, punches, kicks, shoots, eat, drive, uses phone, kiss, hug, stands up, sits down, swims, and dance. There are 650 manually labelled videos in the dataset approximately. This dataset provides both RGB video and depth sequences which are useful for baseline recognition using both depth and appearance. The application of the proposed dataset is found in Hadfield et al. (2017), Iosifidis et al. 2014 and Hadfield and Bowden (2013).

3.2.12 MSR action pairs (3D action pairs)

Oreifej and Liu (2013) introduce this dataset (http://www.cs.ucf.edu/~oreifej/HON4D.html#) at the University of Central Florida, Orlando. This dataset focused on two most important aspects, skeleton trajectories for similar actions and correlation of actions pairs. In this dataset, pairs of activities are selected to believe that shape cues may be similar, but their correlations vary such as Pick up and Put down activities. It contains 10 actors performing 6 pairs of actions Pick up a box/Put down a box, Lift a box/Place a box, Push a chair/Pull a chair, Wear a hat/Take off a hat, Put on a backpack/Take off a backpack, and Stick a poster/Remove a poster. The actors perform each action three times and five actors used for testing and rest for training. The application of proposed dataset is found in Ofli et al. (2013) and Althloothi et al. (2014).

3.2.13 IM-daily activity

Jalal et al. (2014) introduced this dataset (http://imlab.postech.ac.kr/databases.htm). It can use for continuous online human activity recognition. This dataset contains daily routine activities recorded in real scenarios like labs, classroom and halls. It consists of 15 different peoples are performing 15 various activities such as both hands waving, bending, boxing, clapping, cleaning, eating, exercise, kicking, phone conversation, reading an article, right hand waving, sit down, stand up, throwing and take an object. The video files are available in (.bin files,.txt files,.jpeg) formats. The dataset consists of RGB as well as depth images with human silhouettes. This dataset is challenging due to a similar type of activity present in the videos. The application of proposed dataset is found in Jalal and Kim (2014).

3.2.14 Human manipulation

It is introduced by Pieropan et al. (2014) . This dataset (https://imatge.upc.edu/web/resources/human-manipulation-dataset) was a collaborative project of TOMSY and the Swedish Research Council. Its primary objectives of creation were that robots need to merge information from multiple modalities and autonomously in an unstructured environment. It consists of 8 actors are performing 6 actions classes pour milk, close milk box, open milk box, open cereal box, close cereal box, and pour cereals. Each action performed by the actors in an uncontrolled manner. The application of proposed dataset is found in Lin et al. (2016).

3.2.15 UTD-MHAD

Chen et al. (2015) introduced this dataset (http://www.utdallas.edu/~cxc123730/UTD-MHAD.html). The dataset was created to recognized view-invariance human activities. It consists of 8 subjects performing 27 action classes viz cross arms in the chest, basketball shoot, right-hand draw x, right-hand draw circle clockwise, jogging in place, walking in place, sit to stand, stand to sit, forward lunge (left foot forward), squat two arms stretch out, right arm swipe to the left, right arm swipe to the right, right-hand wave, two hand front clap, right arm throw, right-hand draw circle (counter-clockwise), draw triangle, arm curl (two arms), tennis serve, two hand push, right-hand knock on door, bowling (right hand), Front boxing, baseball swing from right, tennis right-hand forehand swing, right hand catch an object, right hand pick up and throw. It was recorded with multiple sensors such as Kinect camera, depth sensors and inertial sensors simultaneously. The application of proposed dataset is found in Mahjoub and Atri (2016), Elmadany et al. (2016), Imran and Kumar (2016) (Fig. 13).

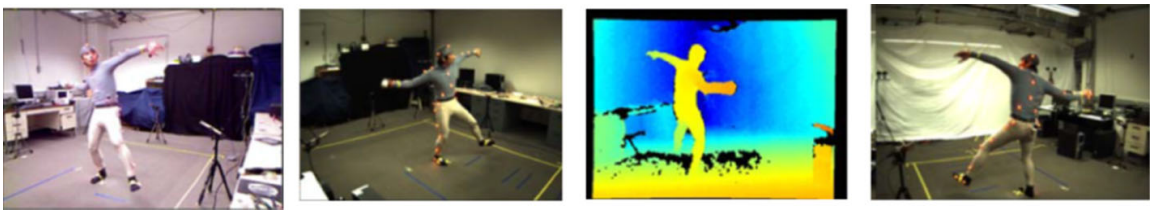


Fig. 13 Examples video sequence from MHAD Dataset (Ofli et al. 2013)

3.2.16 M^{2}I dataset

It is introduced by Xu et al. (2015) (http://media.tju.edu.cn/m2i.html), at Multimedia Institute of Tianjin University, CHINA. It is a multi-view and multimodal interactive action dataset. This dataset provides challenge due to clutter background, illumination variation, and intra-class similarities actions. It focused on human–human, and human–object interaction and actions were recorded with two static Kinect cameras simultaneously. It contains 22 actors are performing 22 actions categorised into three main classes: (A) Multi-person interactive actions: Walk Together, Cross, Wait, Chat, Hug, Handshake, High Five, Bow, and Box. (B) Multi-person with object interactive actions: play football, pass the basketball, and carry box. C) Person-object interactive actions: Throw Basketball, Bounce Basketball, Hula Hoop, Tennis Swing, Call Cell phone, Drink Take Photo, Sweep Floor, Clean Desk, and Play the Guitar. There are twenty groups each containing two actors and each action performed twice the time. This dataset consists of total 1760 samples of RGB, depth, and skeleton data. The application of proposed dataset is found in Gao et al. (2017), Hao et al. (2017).

3.2.17 Sysu-3d hoi

It is introduced by Hu et al. (2015) (http://isee.sysu.edu.cn/resource) at School of Mathematics and Computational Science, Sun Yat-sen University, China . This dataset provides a challenge due to manipulated similar object activities and more number of actors. This dataset was captured with Kinect sensors with three modalities such as RGB frames, depth sequences, and skeleton data. It focuses on human–object interactions activities. It consists of 40 actors performing 12 different object interactive activities such as phone, chair, bag, wallet, mop, and besom, and so on. There are total 480 videos clips in the dataset. The application of proposed dataset is found in (Hu et al. 2016).

3.2.18 G3Di

It was introduced by Bloom et al. (2016) (http://dipersec.king.ac.uk/G3D/G3Di.html). It is a realistic, complex human activity dataset used for multiplayer gaming showcase. It is a multi-modal dataset having RGB, depth, and skeleton data. All the activities performed by the 12 people into six different pairs. Each pair is performing a competitive or collaborative sports activity such as boxing, volleyball, football, table tennis, sprint, and hurdles depending on gaming mode. The application of proposed dataset is found in Bobick and Davis (2001).

3.2.19 Ntu rgb-d

This dataset (https://github.com/shahroudy/NTURGB-D) is introduced by Shahroudy et al. (2016) at Nanyang Technological University, Singapore. It was captured using Microsoft



Fig. 14 Examples video sequence from NTU RGB-D Dataset (Shahroudy 2016)



Fig. 15 Examples video sequence from DAHLIA dataset (Vaquette et al. 2017)

Kinect v2 sensors. It is a multi-modal dataset with made viz depth maps, 3D joint Information, RGB frames, and IR sequences. It consisted of 60 actions classes and divided into three groups: 40 daily activities, nine health-related actions and 11 mutual actions. It consists of 40 subjects of different age, height, and gender. Each subject is having a unique identification number while performing activities in the videos. The actors perform each action twice before left and right camera. There are three cameras installed at an equal height to capture different view angle videos. Each camera has a unique number and fixed angle position. The first camera captured 45° views while second and third captured front and side view respectively. The application of proposed dataset is found in Cippitelli et al. (2016) (Fig. 14).

3.2.20 DAHLIA (daily human life activity)

Vaquette et al. (2017) introduced this dataset (http://www-mobilemii.cea.fr/?page_id=20). These dataset videos focused on monitoring the elderly people activities context to smart home. It contains 51 long daily activities untrimmed videos captured in a kitchen environment. There are total 44 subjects of different age, sex, and height performing 7 high semantic level activities such as house working, washing dishes, clearing table, cooking, having lunch, laying the table, and working. All the videos are recorded with 3 Kinect V2 cameras with RGB, Depth, and skeleton modalities. The RGB and depth frames are having spatial resolution 1920×1080 and 512×424, respectively (Fig. 15).

3.2.21 PRAXIS gesture

PRAXIS gesture dataset introduced by Negin et al. (2018) (https://team.inria.fr/stars/praxis-dataset/). Kinect v2 sensors record this RGB-D dataset in office environment. The camera position is fixed and only upper body of subject is to appear for camera view. There are total 64 subject (60 patients and 4 clinicians) performing continuously each gesture 2–3 times in the videos. It consist of total 29 annotated gesture (14 dynamic and 15 static gestures), which are divided into Abstract, Symbolic, and Pantomimes for Praxis test. All the gesture are captured in sequence in natural way without time limitations. The RGB and depth frames having spatial resolution 960×540 and 512×424, respectively (Fig. 16).

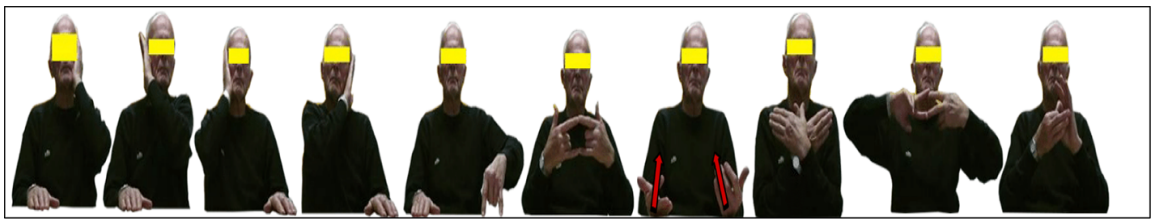


Fig. 16 Examples video sequence from PRAXIS Gesture Dataset (Negin et al. 2018)

3.2.22 PKU-MMD

Liu et al. (2017) introduced this large-scale dataset (http://www.icst.pku.edu.cn/struct/Projects/PKUMMD.html) at Institute of Computer Science and Technology, Peking University, and funded by Microsoft Research Asia. It focused on long continuous sequences action detection and multi-modal action analysis. Kinect version 2.0 sensor captured this dataset. This dataset divided into two phases of long and short sequences videos respectively. Phase 1 consist of total 1076 long videos sequences of 3–4 min in length recorded at 30 fps. Phase 1 contains 66 actors performing 51 action classes that are divided into two parts 41 daily actions and ten human interaction actions. Phase 2 consists of 2000 short videos sequence of 1–2 min recording at 30 fps. Phase 2 contains 60 actors performing 49 actions classes. This dataset recorded with five modalities RGB image, depth maps, skeleton joints, infrared sequences, and RGB videos.

4 Challenges in HAR dataset

In this section, we discuss different existing challenges in RGB and RGB-D dataset. The recorded videos are facing limitations in at least one of aspects such as similarity of actions, cluttered background, viewpoints variations, illuminations variations, and occlusions. Initial human action recognition datasets are less challenging as compared to current dataset due to less number of action classes, subjects, and reasonably recorded in controlled environmental conditions. The performance measure of algorithm depends on depends on these crucial factors present in the datasets. The RGB dataset is facing more challenges like view changes, intra-class variations, cluttered background, partial occlusions, and camera movements than RGB-D datasets.

4.1 Background and environment conditions

The background information is useful for a broad area of applications e.g. tracking, action/gestures recognition, surveillance, and video retrieval. The natural environment contains various objects such as trees, waves, rain, and water and these factors effects the recognition activity in videos. The characteristics of good feature descriptors directly influence by background subtraction techniques or foreground detection. The KTH Action dataset is more challenging due to changing background as compared to Weizmann dataset. To recognized human activity in videos is a crucial task when the presence of moving object or background. The background in videos may be different types such as slow/high dynamic, static, occluded, airy, rainy, and dense populated. The datasets recorded in indoor or controlled manner are IXMAS, MOBISERV-AIIA, PRAXIS Gesture, i3DPost, DAHLIA, MSR

Action 3D, CAD-60, CAD-120, 50 Salads, multimodal human action, UWA3D, LIRIS, 3D Online Action, IM-Daily Activity, human manipulation, UTD-MHAD, NTU RGB+D, and PKU-MMD. The foreground subtraction in i3DPost multi-view dataset become so easy due to blue screen backdrop background. The UT-Interaction, BEHAVE, BIT Interactions datasets having more complexities because of the larger outdoor area and changing background conditions. The various datasets such as UCF sports activity, UIUC Sports, Olympic sports, Hollywood1, Hoolywood2, HMDB51, THUMOS'15, ActivityNet, and YouTube 8 M recorded from online sources YouTube, and various movies, are challenging due to having both dynamic objects and backgrounds conditions.

4.2 Applications domain

To identify the interesting activity, we have to specify the area of the application domain. In our survey work, we attempt to cover datasets from wide application domains such as human activity recognition, object detection, surveillance system, patients monitoring, ambient assisted living, Human–Human interaction, and sports activities. To address the daily life problems, there is need to expand dataset to realistic applications. The datasets discussed here for simple human action/activities are KTH, Weizmann, IXMAS, MSR Action 3D, i3DPost multi-view. Human–Human interaction and Human–Object Interaction dataset are BIT Interactions Breakfast action, UT-Interaction, NTU RGB-D, PKU-MMD, and SYSU-3D HOI, MERL Shopping, 20BN Something–Something. The MOBISERVE-AIIA, PRAXIS Gesture, and DAHLIA dataset are targetting the daily living activities problem to assists elderly people for smart home environment. The Hollywood, Hollywood 2, HMDB51, and Hollywood 3D dataset recorded from movies and used for actions or interactions are, The dataset taken from YouTube or movies to recognized sports activities are UCF 50, UCF101, UIUC Sports, Olympic Sport, THUMOS, FCVID, ChaLeran, and YouTube Sports 8M.

4.3 Similarity and dissimilarity of actions

The similarity between the actions classes in the datasets provides a fundamental challenge to the researcher. Many actions seem to be similar in videos such as jogging, running, walking, etc. The same type of actions affects the accuracy of classification. The same actions performed by different actors increase the complexity in the dataset such as YouTube Sports 1 M, or 8 M dataset having thousands of videos of same action class. The scale variations among subjects, the action classes, and continuity of actions while performing activity provides a challenge to classification such as UWA3D Activity, M^2I datasets etc.

4.4 Occlusion

Occlusion is a thing where another object hides the object of interest. For the human action and activity recognition, occlusion can categorized as self-occlusion and occlusion of another object/partial occlusion. It is a challenging task to recognize human action/interaction activities from occluded videos. The occlusion is a bigger challenge in the field of computer vision applications such as human pose/action estimation, object tracking, video surveillance, 3D foreground reconstruction, and traffic monitoring applications. It occurs due to the relative motion of static and dynamic occluding objects. Occlusion is two types in human pose estimation self-occlusion and occlusion by another object. Self–occlusion is occurring

when body parts occlude each other due to different viewpoints while other occlusions occur when an object obstructs the view. Self-occlusion will not be considered as a disturbance as that in inter-person occlusion (Fu et al. 2017). Self-occlusion frequently took place in various human action datasets viz. sports action datasets such as UCF 50, UCF101, MOBISERV–AIIA, MERL Shopping, and 20BN Something–Something, YouTube 1 M, and UIUC action. The online, downloaded videos datasets are Hollywood, HMDB51, THUMOS'15, and ActivityNet. In 3D datasets occlusion is still a problem since current depth sensors provides 2.5D estimation of the scene. Most of the RGB-D dataset ignored the occlusions case. The depth sensor is severely affected by internal noise data and self- occlusion by performing users (Liu et al. 2016) such as in CAD-60, 50 salad, Berkeley MHAD, i3dPost Multi-view, PRAXIS Gesture, UWA3D activity, LIRIS, MSR Action pair, UTD-MHAD, M2I, SYSU-3D HOI, NTU RGB+D, and PKU-MMD datasets.

4.5 View-variations

The viewpoint of any activity recorded inside the video dataset is a key attribute in the human activity recognition system. The multiple views have more robust information than single view and independent of captured view angle inside the dataset. However, multiple views increase the complexity such as more training as well as test data is required for classification analysis. Here, KTH, Weizmann, PRAXIS Gesture, MERL Shopping, 20BN something–something UIUC Sport, Hollywood, Hollywood2, UCF Sports, MSR Action 3D, and Hollywood 3D are single view datasets. The multi-view datasets are CAD-60, CAD-120, UWA3D, MOBISERVE-AIIA, DAHLIA Northwestern-UCLA, LIRIS, UTD- MHAD, NTU RGB-D, IXMAS, CASIA Action, UT-Interaction, BEHAVE, and BIT-Interaction. Some of the outdoor/indoor datasets recorded for view-invariant human activity recognition with the help of multiple cameras and more than one modalities are IXMAS, UT-Interaction, BEHAVE, and CAD-60.

Tables 6 and 7 contains different challenges existing in both types of the datasets such as occlusions, varying illumination, view variant, and labelling of videos. The RGB-D dataset have advantages over normal colour frames such as view, illuminations, and object detections in scenes but fewer occlusions in videos make this type of dataset unrealistic for robust algorithms. It can be observed that most of the RGB-D dataset having a fixed camera position and orientation while capturing the videos.

Table 8 consists of comparisons of RGB and RGB-D datasets by single activity, multiple activities, group activity, human–human interaction, human–object interaction, sports activity, and surveillance activity. Earliest benchmarks datasets are having single actor and single activity such as KTH, Weizmann, and IXMAS dataset. Such datasets, which are downloaded from the internet or recorded from various movies, are having all types of major activities in trimmed videos clips such as Hollywood datasets. There is a massive increase in RGB dataset in aspects of a number of action samples, actors, videos lengths, multi-modal and multi-view datasets such as ActivityNet, THUMOS'15 challenge, and ChaLearn challenges datasets.

5 Analysis and discussion on RGB and RGB-D datasets

In this section, the analysis of various types of activities, and the highest accuracies achieved on the available dataset and their advantages and disadvantages are discussed in details.

Table 6 Challenge comparison of RGB datasets

Dataset	Illumination variations	View variant	Labelling/annotation	Background				View	
				Static	Dynamic	Indoor	Outdoor	Single	Multi
KTH	√	√		√			√	√	
Weizmann	√			√			√	√	
IXMAS	√	√		√		√			√
CASIA Action	√	√			√	√	√		√
UIUC Sport	√				√	√	√	√	
UCF Sports	√	√	√		√	√	√	√	
Olympic Games	√	√			√	√	√	√	
Hollywood		√			√	√	√	√	
Hollywood2	√	√	√		√	√	√	√	
UT- Interaction	√	√			√		√		√
BEHAVE	√		√		√		√		√
HMDB51	√	√			√	√	√	√	
UCF50	√	√			√	√	√	√	
BIT-Interaction	√	√	√		√		√		√
MPII Cooking	√			√		√			√
UCF101	√	√			√	√	√	√	
YouTube Sports 1 M	√	√	√		√	√	√	√	
ActivityNet	√	√	√		√	√	√		√
THUMOS'15	√	√	√		√	√	√		√
ChaLearn: Action/Interaction	√	√	√		√		√	√	
FCVID	√	√	√		√	√		√	
MOBISERV-AIIA		√	√	√		√		√	√
MERL Shopping				√		√		√	
YouTube 8 M	√	√	√		√	√	√	√	
Okutama Action	√	√	√		√	√			√
Something–Something		√	√		√	√		√	

Table 7 Challenge comparison of RGB-D datasets

Dataset	Illumination variations	View variant	Labelling annotation	Background				View	
				Static	Dynamic	Indoor	Outdoor	Single	Multi
i3DPost Multi-view		√		√		√		√	√
MSR Action 3D		√		√		√		√	
RGB-D HuDaAct				√		√			√
CAD-60	√	√		√				√	
50- Salads		√	√	√					√
Berkeley MHAD					√				√
CAD-120	√	√	√	√					√
Hollywood 3d	√	√	√		√				√
MSR Action Pairs				√		√		√	
UWA3D Multi-view				√					√
Northwestern –UCLA				√	√				√
LIRIS	√	√	√	√		√			√
IM-Daily Depth		√		√		√		√	
Human Manipulation Actions	√		√	√					√
UTD-MHAD				√					√
M^2I	√	√		√					√
SYSU-3D HOI				√					√
G3Di				√		√			
NTU RGB+D		√		√					√
DAHLIA		√	√	√		√			√
PRAXIS Gesture			√	√		√		√	
PKU-MMD		√	√	√					√

Table 8 Classification of 2D and 3D datasets based on activity-wise

Dataset	Single person activity	Multiple person activity	Group activity	Human–human interaction	Human–object interaction	Sports activity
KTH	√					
Weizmann	√					
IXMAS	√					
CASIA Action	√			√		
UIUC Sport	√				√	√
UCF Sports Action	√				√	√
Olympic Games	√				√	√
Hollywood1	√	√	√	√	√	
Hollywood2	√	√	√	√	√	
UT- Interaction		√	√	√		
BEHAVE		√	√	√		
TV human interactions		√	√	√		
HMDB51	√	√	√	√	√	
UCF50	√				√	√
BIT-Interaction		√	√	√		
MPII Cooking	√				√	
UCF101	√	√	√	√	√	
YouTube Sports 1 M	√	√	√	√	√	√
Breakfast actions	√				√	
ActivityNet	√	√	√	√	√	
THUMOS'15	√	√	√	√	√	√
ChaLearn: Action/Interaction	√	√		√		
FCVID	√	√	√	√	√	
MOBISERV-AIIA	√					
MERL Shopping	√				√	

Table 8 continued

Dataset	Single person activity	Multiple person activity	Group activity	Human–human interaction	Human–object interaction	Sports activity
YouTube 8 M	√	√	√	√	√	
Okutama Action	√	√		√		
Something–Something	√				√	
i3DPost Multi-view	√					
MSR Action 3D	√					√
RGB-D HuDaAct	√				√	
CAD-60	√				√	
50- Salads	√				√	
Berkeley MHAD	√					
CAD-120	√				√	
Hollywood 3D	√	√	√	√	√	
MSR Action Pairs	√				√	
3D Online RGB-D	√				√	
UWA3D Multi-View	√					
Northwestern –UCLA	√					
LIRIS		√	√	√		
IM-Daily Depth	√					
Human Manipulation Actions	√				√	
UTD-MHAD	√					
M^2I	√	√		√	√	
G3Di	√			√		√
SYSU-3D HOI	√				√	
NTU RGB+D	√	√		√		
DAHLIA	√				√	
PRAXIS Gesture	√					
PKU-MMD	√	√		√		

Tables 9 and 10 consists of the highest recognition accuracies on RGB and RGB-D datasets through various state-of-the-art techniques. The different feature extractors and classification techniques are developed in the past two decades on these datasets. It can observe that no unique solution that can apply to both categories of RGB and RGB-D datasets. Earlier HAR datasets were small and recorded in a controlled manner with few numbers of action classes. That is why they are suitable for handcrafted features solutions such as in KTH, Weizmann, IXMAS, MSR Action 3D, CAD-60, Berkeley MHAD, and 50 salad datasets. Latest benchmarks recorded in an uncontrolled manner with multiple modalities in real scenarios or downloaded from web or movies such as UCF101, HMDB51, Hollywood, or YouTube 1 M or 8 M datasets. It is challenging an algorithm to fit everywhere for distinct actions datasets. With the advancement of artificial intelligence, deep learning based methods become popular. Deep knowledge-based solutions require a considerable amount of time to recognised human activity recognition in videos as compared to still images. That is why handcrafted action representation is still used for activity recognition in videos. However, these representations are over-fitted to a specific application, so they are not well suited for generalised realistic scenarios. On the other hand, deeply learned feature approaches is a natural choice for human action recognition.

5.1 Discussion on existing solutions for video benchmarks

Human activity recognition in video is far completeted as compared to static images due to temporal cues in videos. The developed solutions should overcome the challenges present in videos dataset due to the cluttered background, view-variation, occlusion, intra-class similarity and application scenarios. Based on the existing solution present for activity recognition we can broadly categorise this solution in two parts: Handcrafted solutions and Learned feature representation and the details classification taxonomy can be seen from Fig. 17. The handcrafted feature based on spatiotemporal volume dominated the research from 2001 to 2012. The main disadvantages of handcrafted feature-based space–time solution are an average performance for the complex dataset and generalisation of the algorithm to realistic scenarios. Later on, deep learning based solutions outperform handcrafted solutions due to robust feature extraction and classification in videos. With the advancement of high computational power and increasing size of the video dataset, deep learning based solution is beneficial for real-life applications.

5.1.1 Handcrafted feature representation

The handcrafted feature solutions are classified into two parts based on the extraction of a feature from the body such as edge, shape, and motions. Further, this representation can be categorised into various solutions depending on feature extraction from the input video.

Global representation In this feature extraction techniques, human activity recognition based on body shape and motion of action. In this context, Bobick and Davis (2001) presented the Motion History Images (MHI) and Motion Energy Images (MEI) to recognised human simple human action and extracted the global motion feature from videos sequences in static background conditions. Shechtman and Irani (2005) proposed a 3D space–time volume video template to measure the similarity between the recognised actions. Rodriguez et al. (2008) introduced a maximum average correlation height (MACH) filter based approach 3D XYT volume for action recognition. Tian et al. (2012) improvised activity recognition using the

Table 9 2D Dataset with state-of-the-art accuracy and techniques

Dataset	Classification technique	Max Avg. accuracy (%)	Evaluation protocol	Reference year
Weizmann	Hybrid (SDGs + AESIs)	100 (Vishwakarma and Singh 2017)	LOOCV	2016
KTH	Interest points (IP) with differential motion information	98.20 (Yadav et al. 2016)	3-fold cross-validation	2016
IXMAS	HC-MTL + L/S Reg	94.7 (Liu et al. 2017)	Cross-view	2017
CASIA Action	Hierarchical Spatio-Temporal model (HSTM)	95.24 (Xu et al. 2017)	–	2017
UIUC Sport	Adaptive Slicing feature, MFCC, SVM	98.9 (Shan et al. 2015)	LOSO	2015
Olympic Games	Motion Part Regularisation	92.3 (Ni et al. 2015)	LOOCV	2015
Hollywood	Joint max margin semantic features, DCNN, SVM	48.58 (Abbasnejad et al. 2016)	–	2016
Hollywood2	(GEAN), RGP	92.40 (Yu et al. 2017)	–	2017
UT-interaction	Hierarchical Spatio-Temporal Model	94.17 (Xu et al. 2017)	LOOCV	2017
UCF-YouTube	Interest points (IP) with differential motion information	91.30 (Yadav et al. 2016)	3-fold cross-validation	2016
BEHAVE	Group interaction zone(GIZ), (ARF + GCT + AF)	93.74 (Kim et al. 2014)	3-folds-cross-validation	2014
HMDB51	Spatiotemporal Multiplier Networks	72.20 (Feichtenhofer et al. 2017)	–	2017
UCF50	ST-VLMPF(DF)	95.10 (Duta et al. 2017)	LOGO (Cross-View)	2017
BIT-Interaction	4-level, Pachinko Allocation Model	93 (The et al. 2016)	10-fold cross-validation	2016
MPII Cooking	GRP + IDT-FV	75.5 (Cherian et al. 2017)	–	2017
UCF101	Spatiotemporal Multiplier Networks	94.9 (Feichtenhofer et al. 2017)	–	2017
YouTube Sports 1 M	HC-MTL + L/S Reg	89.7 (Liu et al. 2017)	LOGO (Cross-View	2017
ActivityNet	UntrimmedNet (hard)	91.3 (Wang et al. 2017)	–	2017
THUMOS'15	Pyramid of Score Distribution Feature (PSDF)	40.9(0.1) (Yuan et al. 2016)	–	2016
ChaLearn: Action/Interaction	Fisher vector + Idt features	53.85 (Wang et al. 2015)	LOOCV	2015
FCVID	Rdnn	76.0 (Jiang et al. 2017)	–	2017
MOBISERV-AIIA	DSP + OEML	68.0 (Yan 2016)	–	2016
MERL Shopping	MSB-RNN	80.31 (Singh et al. 2016)	–	2016
YouTube 8 M	NetVLAD + CG after pooling and MoE	83.0 (Miech et al. 2017)	–	2017
Okutama Action	SSD(RGB)	18.80 (Barekatain M 2017)	Cross validation	2017
Something–Something	2D + 3D-CNN (top-1)	63.80 (Goyal et al. 2018)	–	2018

Table 10 3D dataset with state-of-the-art accuracy and techniques

Dataset	Classification technique	Max Avg. accuracy (%)	Evolution protocol	Reference year
i3DPost Multi-view	SDEG, +R transform	92.92 (Vishwakarma et al. 2016a)	LOOCV	2016
MSR Action 3D	ConvNets	100 (Wang et al. 2015, 2016)	Cross-subject	2015
RGB-D HuDaAct	BoW with χ^2 kernel SVM	82.9 (Chen et al. 2014)	Cross subject validation	2014
CAD-60	Bag-of-Poses, ELM	99.0 (Agahian et al. 2018)	LOSO-CV	2018
50-Salads	ED-TCN	73.40 (Lea et al. 2017)	–	2017
Berkeley MHAD	Hierarchy of LDSs, HBRNN-L	100 (Chaudhry et al. 2013)	–	2013
CAD-120	QQSTR with feature selection	95.2 (Tayyub et al. 2015)	4-fold cross validation	2015
Hollywood 3D	Bag of features (BoF) with Disparity Pyramids	36.09 (Iosifidis et al. 2014)	Cross-validation	2014
MSR Action Pairs	Skeleton embedded features + depth maps	97.70 (Ji et al. 2018)	Cross validation	2018
UWA3D Multi-view	MSO-SVM	91.79 (0°) (Chen et al. 2015)	Cross-view	2015
Northwestern–UCLA	CNN + Synthesized + Pre-trained	92.3 (Liu et al. 2017)	Cross-view	2017
LIRIS	Pose + Appearance + context	74 (recall) (Wolf et al. 2014)	–	2014
IM-Daily Depth	Muti-fused features, ICP + KNN	81.17(body parts) (Jalal and Kim 2014)	Cross-subject	2014
Human Manipulation Actions	HMM + Euler angle distance	73 (Pieropan et al. 2014)	Cross-validation	2014
UTD-MHAD	Bag-of-Poses, ELM	95.0 (Agahian et al. 2018)	LOSO-CV	2018
M^2I	FV/BoVW	92.33 (Hao et al. 2017) (v1 + v2)	Cross-view	2017
SYSU-3D HOI	Joint heterogeneous features learning (JOULE)model	84.89 ± 2.29 (S2) (Hu et al. 2016)	Cross subject	2016
G3Di	Hierarchical Transfer Segments (HiTS)	Average latency time 2 frames (66 ms) (Bloom et al. 2016)	Cross –subject	2016
NTU RGB+D	CNN + Synthesized + Pre-trained	87.21 (Liu et al. 2017)	Cross-view	2017
DAHLIA	Multi cam HOG	82.14 (Vaquette et al. 2017)	Cross-subject	2017
PRAXIS Gesture	CNN + LSTM	84.74 (Negin et al. 2018)	–	2018
PKU-MMD	Joint classification regression RNN	64.20 (Liu et al. 2017)	Cross-view	2017

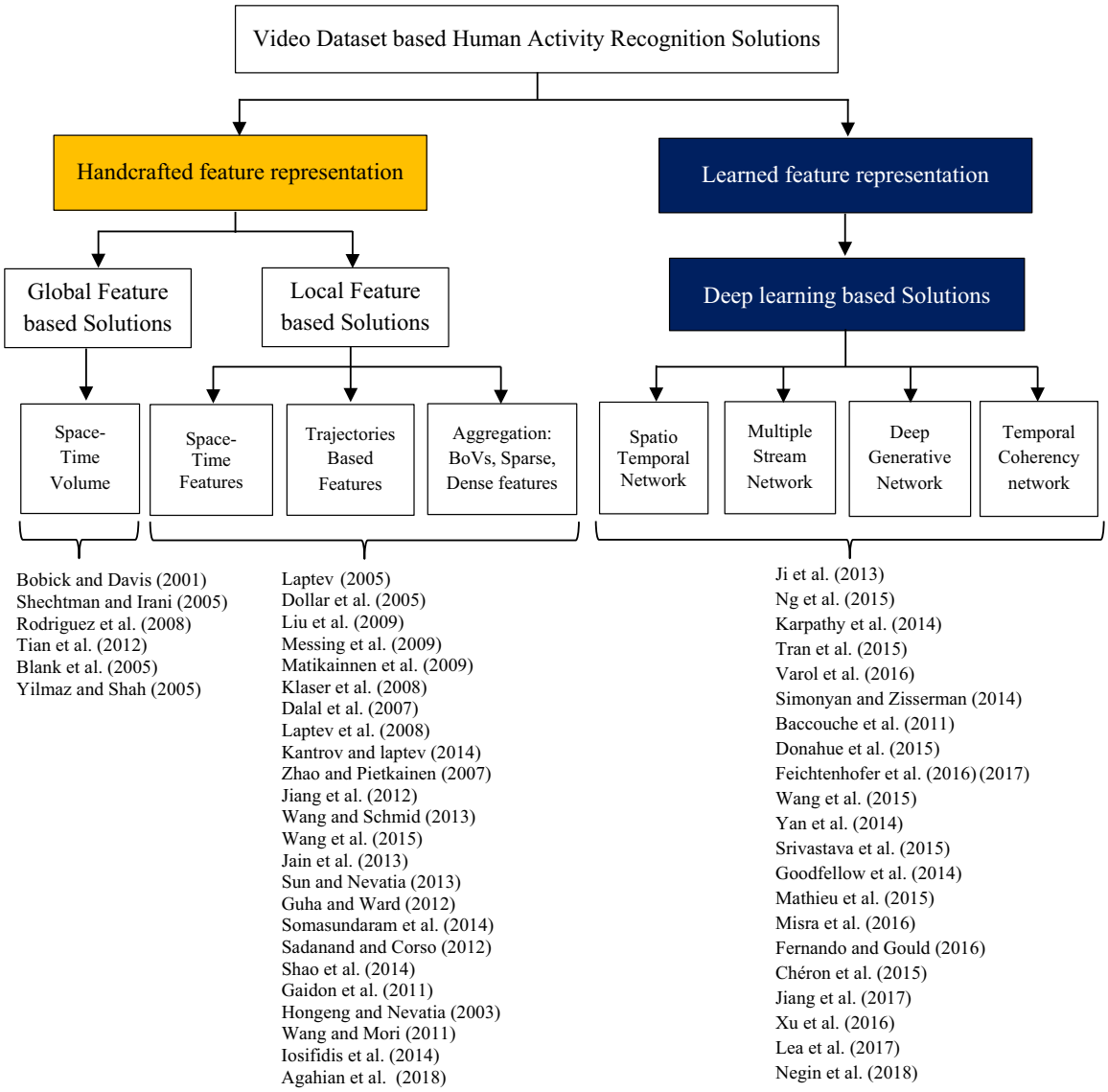


Fig. 17 A taxonomy of Video Dataset based Human Activity Recognition Solutions

gradient of MHI template. Blank et al. (2005) proposed the Space–Time 3D shape model of MEI template using binary silhouettes which outperform over previous approaches of human action recognition. A similar approach is adopted by Weinland et al. (2006) using spatiotemporal volumes to recognised view-invariant activities. Yilmaz and Shah (2005) introduced the Space–Time Volume to identified action sketch. The main disadvantages of global feature-based space–time solution are the poor performance for the complex dataset, i.e. having more number of actors present in video frames and action cannot segment spatially properly.

Local feature representation These techniques are based on to extract the local feature from the body shape. These techniques outperform over global feature-based techniques due to robust feature extraction. These feature descriptors used both cuboids as well as trajectories for action recognition. In trajectories based approaches a human motion is represented as 3D XYT or 4D XYZT points with respect to their joints positions and analysed the view-invariant activity.

Towards the first step of local representation, Laptev (2005) introduced the Space—Time Interest Points (STIPs) based on an extension of 2D Harris Detector to 3D (Harris and Stephens 1988). Similarly, Willems et al. (2008) proposed a Hessian Detector based approached to localised action using second derivatives of the corner detector. Dollar et al. (2005) introduced the spatial filtering approaches to recognised complex motion in action video. To addressed the problem of cluttered background Liu et al. (2009) proposed a statistical background invariant approach to detect interest points. In Kläser et al. (2008) proposed the histogram of the gradient (HOG) based motion descriptor HoG3D descriptor. In Laptev et al. (2008) introduced the Histogram of Optical flow (HOF) spatiotemporal descriptor that gave a robust feature to localised the action motion. In Kantorov and Laptev (2014) proposed the reduced the video size through MPEG compression and tried to compensate for the complexities of HoFs. Zhao and Pietikainen (2007) introduced 2D LBP (Local Binary Pattern) descriptors in spatiotemporal feature extraction. In Kellokumpu et al. (2008), Norouznezhad et al. (2012) a variant of LBP introduced to overcome the problem of three orthogonal planes. The spatiotemporal interest point extracted from cuboids not so efficient as compared to trajectories of local features (Matikainen et al. 2009; Messing et al. 2009). In Jiang et al. (2012), Wang and Schmid (2013) human actions and interaction recognised using trajectories features. However, these features are not so robust when camera motion and occlusions are present in videos, so sparse feature extraction is introduced for action detection (Wang et al. 2009). The earlier sparse coding technique was useful for face recognition, image restoration, and sub-space clustering. Zhu et al. (2011) introduced a learned dictionary based on max-pooling sparse coding using spatiotemporal cuboids from unannotated videos. In Guha and Ward (2012) suggested a common dictionary approach to recognised action classes. Somasundaram et al. (2014) presented saliency feature of spatiotemporal for dictionary learning. Sadanand and Corso (2012) introduced a high-level dictionary based on 'action bank' features for activity recognition. In Shao et al. (2014) a pyramid structure based on Laplacian and 3D Gaussian filter is used as an action bank. Gaidon et al. (2011) introduced atomic actions with the extension of temporal structure in Bag of Words (BoVs) to recognised variable length action videos. The initial success of Hidden Markov Models (HMMs) (Rabiner 1989) in speech processing motivates the researcher for action recognition in videos because videos can be considered as a sequence of transition frames like state transition in HMMs. Hongeng and Nevatia (2003) proposed a model using HMMs for event detection in videos. The inconsistency occurs due to first order state transition improvised in the work of Tang et al. (2012) using the max-margin variable HMM model. Sun and Nevatia (2013) introduced a HMMs model using short video clips to recognised complex activities. In Wang and Mori (2011) a max-margin approached is used for modelling action classes.

Vishwakarma and Singh (2017) proposed a unified model based on Average energy silhouettes (AESIs) which is a projection of 3D pose into a 2D pose of human activity. They computed spatial edge histogram (SDG) to recognised action in KTH, Weizmann action dataset. In Yadav et al. (2016) dense information based spatiotemporal local feature descriptor is introduced which outperform over existing state-of-the-art methods on UCF YouTube and KTH datasets. In Liu et al. (2017) proposed a multi-task learning based method using hierarchical clustering for recognition of high-level activities present in multi-view datasets such as IXMAS and realistic datasets as Hollywood 2, YouTube 1M, UCF101 and HMDB51. Xu et al. (2017) proposed a two-layer hierarchical spatiotemporal model for recognition task in interaction datasets as BIT Interaction, CASIA, and UT interactions. These model utilised a high-level feature for temporal information present in video sequences. Shan et al. (2015) used a different slicing spatiotemporal to model action sequences rather than XY plane, e.g. XT slicing. They projected 3D spatiotemporal feature to 1D using maximum entropy princi-

ple. They showed higher accuracy on the UIUC Sports dataset and MSR Action 3D datasets. In Yu et al. (2017) they addressed the problem of event detection using max-margin semantic features classifier with IDT. They tested their approach on Hollywood, UCF101, and MPII Cooking Activities dataset that gives out good performances compare with existing methods. In The et al. (2016) proposed to recognised human interaction activities using human pose joints coordinates' estimation. They were able to discriminate complex activities utilising the correlation between generated body features and codebooks and validated the results on BIT interaction and UT Interaction dataset. In Yan (2016) addressed an approach using discriminative sparse projections (DSPs) to recognise person based daily activity dataset MOBISERVE AIIA and CASIA B. Yuan et al. (2016) focused on action classification and annotations using temporal action localisation in untrimmed videos. They introduced the Pyramid distribution feature (PDF) to model motion cues in videos at multiple resolutions. Their approach outperforms existing methods on THUMOS'15 challenges and MPII Cooking datasets. Wang et al. (2015) introduced a deep network, which utilised the Fisher vector, and IDT features for action localisation and classification. Their model outperforms in ChaLearn (LAP) challenge 2015. Vishwakarma et al. (2016a) proposed a unified framework for based on spatial distribution of edges gradient (SDEG) and R- transform to recognised human activity. The hybrid model showed robust performance on IXMAS, KTH, Weizmann, and i3DPost Multi-view datasets. Agahian et al. (2018) proposed 3D skeleton joints based bag-of-poses a spatiotemporal model for action recognition. The K-means algorithm is used to train the pose descriptor and SVM to classify action pose. The proposed approach gives a robust performance on CAD-60, UTD MHAD, UT Kinect, MSR Action 3D and MSRC-12 datasets.

Over the year several handcrafted approaches introduced for action representation such as MEI, MHI, optical flow, MBH, HOG, HOF, Sparse representation, and dense trajectories. The most effective existing work for action recognised given by Wang and Schmid (2013), Peng et al. (2014) IDT with fisher vectors (FV). However high computations complexity of IDT methods limits its implementation for real-time applications.

5.1.2 Learned feature representations

The heart of the deep architecture is 3D Convolutional Neural Network (CNN) due to its power of robust low to high features extraction from raw input data signal. A CNN model uses the nonlinear activation function based on stochastic gradient descent and effectively sharing the weighs between the hidden layer and max-pooling layers filter architectures. After the successful implementation of CNN in image processing, various approaches for action recognition in videos were adopted during the last 6 years.

The first step toward deep architecture for video analysis introduced by Ji et al. (2013) a spatiotemporal based 3D convolutional network, which outperforms over the 2D convolutional network but accepts a fixed number of frames from input data. The different videos have a different time span, hence, to overcome this difficulty, Ng et al. (2015) proposed temporal pooling deep structure for video analysis. Karpathy et al. (2014) introduced the concept of slow fusion in convolutional network layers with consecutive parts of input videos. They showed that multi-resolution network improved the accuracy with the help of parameter sharing among layers. Tran et al. (2015) introduced a constant filter depth based deep convolutional network, C3D descriptor for video analysis. Later on, Long Short-Term Memory (LSTM), which is a combination of parallel recurrent neural network (RNN) structure introduced and good efficient model for video analysis. The main drawback of RNN is training

the network due to vanishing gradient. To overcome the difficulty of exploding gradient Baccouche et al. (2011) proposed a model in which two architecture 3D ConvNet and the LSTM are trained separately. Donahue et al. (2015) the main drawback of 3D ConvNet structure larger parameters and training time. Simoyan and Zisserman (2014) introduced two streams (spatial and temporal) network parallelly for action recognition. The spatial network receives raw input video frames while temporal network accepts optical flow motion as input data. The spatial stream network fine-tuned to pre-trained network Imagenet while temporal stream trained using early fusion in the network on input optical flow fields. The temporal stream has multiple classification layers due to the limitation of medium dataset UCF 101 and HMDB 51 and each layer is trained separately, which leads to multiple task learning. Feichtenhofer et al. (2016) proposed a multiple stream network with intermediate fusion with improved accuracy and reduced parameters as compared to the original network. Deep learning generative model trains the temporal data in an unsupervised manner. It is a good option for video analysis because labelling the data is a difficult task and time-consuming. A deep generative model predicts the future sequences accurately for motion dynamics. Yan et al. (2014) proposed a deep autoencoders model called Dynecoder, which contains three hidden layers to estimate the next input sequences. Later on, Srivastava et al. (2015) introduced the LSTM based auto encoders model to predicts the future of sequences. Goodfellow et al. (2014) presented a discriminative adversarial network to overcome the difficulties present in the deep generative network. During training, this model learns with judgement whether the given input sequence is authenticated or not. Mathieu et al. (2015) proposed a multi-scale adversarial network for activity recognition. Mishra et al. (2016) introduced the deep feature model based on temporal coherency to recognised action and posed. However, the temporal coherency based model is not a perfect choice for dynamic background videos such as on YouTube 1 M dataset. To overcome abrupt scene change difficulty in Fernando et al. (2015) rank-pooling solutions is introduced. Fernando and Gould (2016) proposed end-to-end learning with backpropagation and pooling mechanism. The majority of deep learning architectures are based on CNN, and it only differs on how the input is applied. Few approaches using raw video frames as input while other using spatiotemporal features for training the network. The multitask deep learning and transfer learning approaches (Karpathy et al. 2014; Simonyan and Zisserman 2014; Yan et al. 2014) were introduced which combines the two datasets for action classification to availability medium datasets like UCF101, or HMDB51. The multiple task learning uses two-softmax classification layer while in the transfer learning final fully connected layer is fine-tuned for a specific dataset.

In Feichtenhofer et al. (2016) proposed a spatiotemporal multi-stream based ConvNet architecture for video action recognition in HMDB51 and UCF101 dataset. They used multiplicative gating functions to utilise spatial and temporal information in the single forward pass. Wang et al. (2017) introduced an UntrimmedNet architecture for action recognition in untrimmed video. They implemented end-to-end training and avoided the temporal dependency of video clips on ActivityNet and THUMOS'14 datasets. Cherian et al. (2017) proposed a generalised rank pooling for action representation that extracts the features from intermediate CNN layers that are trained on subsequences. They optimised the model using the conjugate gradient of Grassmann manifold on the MPII Cooking dataset. In Wang et al. (2015) proposed view-invariant three-channel ConvNets architecture using weighted hierarchical depth maps for human action and interaction recognition. They projected spatiotemporal motion into the 2-D spatial structure and finally evaluate the performance on small datasets such as MSR Action 3D, UT Kinect, and MSR DailyActivity3D using fine-tuned on ImageNet architecture. In Lea et al. (2017) introduced a temporal convolutional network (TCNs) that utilised temporal convolutional to recognises fine-grained human–object interaction activi-

ties. They evaluated the performance on their architecture on 50 Salads and MERL Shopping Datasets. Liu et al. (2017) presented a view-invariant spatiotemporal deep network based using skeleton joints for human activity recognition. A CNN model used to extract the discriminative feature and validated on four datasets NTU RGB+D, MSRC-12, Northwestern UCLA, and UWA3D II.

Deep learning approaches have been famous in industrial and commercial applications for two decades. However, these solutions lack due small dataset and skills in deep algorithms. With the advent of the latest computer technologies, it is possible to train these models over millions of videos samples. Presently, human action recognition in videos with deep features become trends in vision community due to the availability of larger videos datasets such as YouTube1 M, YouTube8 M ActivityNet, NTU RGB+D, and PKU-MMD. Deep learning solutions let behind the handcrafted feature solutions regarding accuracy and classification of actions in videos.

In Table 11 some other famous publically available both RGB and RGB-D which are not described in this survey work. It can observe that from Table 11, with the advancement of low-cost depth sensors a massive increase in the RGB-D depth datasets as compared to conventional RGB datasets.

5.2 Advantages of RGB and RGB-D dataset

It can observe that that from the Table 4, five traditional human activity datasets are recorded with a small number of actions recognition from segmented videos under somewhat controlled conditions. Some benchmarks downloaded from online media such as YouTube, movies and social videos sharing sites represent a realistic action scene that is more practical for real-life applications. UCF 101 dataset is the largest dataset in the context of some classes, video clips than UCF 11, UCF 50, Olympic sports and HMDB51 datasets. The number of actions in larger datasets pretends recognition accuracy of particular activity class. MPII Cooking dataset focused on some practical human activities performed in a natural environment such as kitchen cooking activities. MOBISERV-AIIA dataset is targeting the ADLs of elderly people and malnutrition problem using multiple cameras in a smart home environment. They showed that their approach is better than sensor based ADLs recognitions while caring for elderly people in the independent environment. ActivityNet is large-scale RGB video dataset captured with complete annotated labels and bounding box.

The 3D datasets have advantages over visual 2D dataset as they are less sensitive to illuminations because they are captured with multiple sensors system such as visual, acoustical, and inertial sensors systems. It can be observed that from Table 8, that the fusion of information using different sensors increases the recognition accuracy on depth dataset at the cost of increased complexities, for example, UTD-MHAD depth dataset has various fusion information such as inertial sensors, accelerometers, and gyroscopes. i3DPost multi-view dataset recorded with multiple cameras set up and processed these views into a 3D human model for better representations. DAHLIA dataset is designed for assisted daily living activities in smarts homes. It consists of untrimmed long videos sequences recorded in a natural way such as ‘preparing lunch’ or ‘working in-house’ environment. The PARXIS Gesture benchmark is a unique one because it can use for both the Praxis medical test in elderly people as well as gesture recognition in videos. Human Manipulation Actions dataset focused on robotic activities and had RGB-D and acoustic data to recognise activities and used for object pose detection and tracking. Depth maps are viewpoint dependent in the context of human activity recognition, but UWA3D multi-view dataset is more independent of viewpoint variations.

Table 11 Other publically available important RGB and RGB-D action datasets

Datasets	Year	Modality	URL
CAVIER	2004	RGB	https://homepages.inf.ed.ac.uk/rbf/CAVIAR/gt.html
ViSOR	2005	RGB	http://classif.ai/dataset/visor/
Drinking/Smoking	2007	RGB	https://www.di.ens.fr/~laptev/download.html
ETISEO	2007	RGB	https://wwwsop.inria.fr/orion/ETISEO/download.html
CMU-MMAC	2008	RGB	http://kitchen.cs.cmu.edu
TV human interactions	2010	RGB	http://www.robots.ox.ac.uk/~alonso/tv_human_interactions.html
MuHavi	2010	RGB	http://velastin.dynu.com/MuHAVi-MAS/
VIRAT	2011	RGB	https://data.kitware.com/#collection/56f56db28d777f753209ba9f
ADL	2011	RGB	http://people.csail.mit.edu/hpirsiav/codes/ADLdataset/adl.html
ASLAN	2012	RGB	http://www.openu.ac.il/home/hassner/data/ASLAN/ASLAN.html
UT Kinect	2012	RGB-D	http://cvrc.ece.utexas.edu/KinectDatasets/HOJ3D.html
DHA	2012	RGB-D	http://mclab.citi.sinica.edu.tw/dataset/dha/dha.html
GTEA Gaze(+)	2012	RGB	http://ai.stanford.edu/~alireza/GTEA_Gaze_Website/
MSRC Kinect Gesture	2012	RGB-D	https://www.microsoft.com/enus/download/details.
MSRDailyActivity3D	2012	RGB-D	http://research.microsoft.com/en-us/um/people/zliu/ActionRecoRsrc/
SBU Kinect interaction	2012	RGB-D	http://www3.cs.stonybrook.edu/~kyun/research/kinect_interaction/index.html
TUM	2012	RGB-D	https://vision.in.tum.de/data/datasets/rgbd-dataset
ChaLearn gesture challenge	2012	RGB-D	http://gesture.chalearn.org/data
UCF Kinect	2013	RGB-D	http://www.cs.ucf.edu/~smasood/datasets/UCFKinect.zip
SKIG	2013	RGB-D	http://lshao.staff.shef.ac.uk/data/SheffieldKinectGesture.html
JHMDB	2013	RGB	http://jhmdb.is.tue.mpg.de/
Breakfast actions	2014	RGB	http://serre-lab.clps.brown.edu/resource/breakfast-actions-dataset
Huji EgoSeg	2014	RGB	http://www.vision.huji.ac.il/egoseg/videos/dataset.html
UR Fall detection	2014	RGB-D	http://fenix.univ.rzeszow.pl/~mkepski/ds/uf.html
Human 3.6 M	2014	RGB-D	http://vision.imar.ro/human3.6m/description.php
MANIAC	2014	RGB-D	http://www.dpi.physik.uni-goettingen.de/cns/index.php?page=maniac-dataset

Table 11 continued

Datasets	Year	Modality	URL
The ARENA	2015	RGB	http://www.cvg.reading.ac.uk/PETS2014/a.html
Human EVA-I	2015	RGB	http://humaneva.is.tue.mpg.de/
Actor and action dataset	2015	RGB	http://web.eecs.umich.edu/~jjcorso/r/a2d/index.html#downloads
G3D	2015	RGB-D	http://dipersec.king.ac.uk/G3D/G3D.html
TST Fall detection	2015	RGB-D	http://www.tlc.dii.univpm.it/blog/databases4kinect
TST TUG	2015	RGB-D	http://www.tlc.dii.univpm.it/blog/databases4kinect
K3 Da	2015	RGB-D	https://www.leightley.com/k3da/
IPATCH	2016	RGB	http://www.cvg.reading.ac.uk/PETS2016/a.html
CONVERSE	2016	RGB-D	http://csvision.swan.ac.uk/converse/

The LIRIS dataset is focused on complex human behaviour actions in an office environment and aims to classify activities as well as localise them. The CAD-60, CAD-120 datasets focused on daily human activities and face the cluttered background, viewpoint variations, occlusions, and intra-class variations. The NTU RGB+D dataset is having a large number of actions/actors among existing datasets and was captured with multiple modalities and different camera views. PKU-MMD is large scale benchmark focused on continuous multi-modalities 3D complex human activities with complete annotation information, and it is suitable for deep learning methods.

5.3 Disadvantages of RGB and RGB-D dataset

Currently, there are many video datasets, despite this, there are limitations to recognize and classify the human activities automatically. The main reasons of such limitations in at least one of the form are the number of samples for each action, the length of clips, capturing environmental conditions, background clutter and viewpoints changes, and some activities. The 2D datasets were recorded with a small number of actions to complex actions with a broad range of applications. The 2D datasets are faced with more challenges like view variations, intra-class variations, cluttered background, partial occlusions, and camera movements than depth datasets. Earlier, action recognition datasets consisted of less than ten or an equal number of different actions under well-maintained controlled conditions, e.g., Weizmann, KTH, and IXMAS datasets. Complete recognition accuracy achieves the state-of-art performance on such a dataset through different techniques. The MOBISERVE-AIIA dataset in which eating and drinking are monitoring with the multi-camera system is limited to smart homes only till now, so there is a need to such setup, which can be applied for the normal home environment. The i3DPost 3D human model constructed from human silhouettes occluded due to concavities in appearance in images. In DAHLIA dataset lower body parts of the subject occluded because videos were recorded in a kitchen environment. Due to objects occlusion in the kitchen, the Kinect sensor faces the irregularities in the body joints estimation while capturing the videos. PRAXIS Ges-

ture is a novel dataset in the field of ADLs for smart homes but gesture performed by the patients looks more trained and fixed, and lower body parts are impeded due to the table. Human activity recognition in web-based unconstrained videos datasets faces unambiguity and non-separable shapes such as UCF sports, UCF50, and UCF101 datasets. HMDB51 is more complicated than UCF sports action dataset due to additional meta-information about visible body parts/occlusion, camera motion, viewpoint. UCF sports datasets face the problem of low resolutions and detailed description of activities. These online datasets have trimmed videos, which makes some unrealistic approaches toward action recognition. The sports actions benchmarks are still challenging due to natural, realistic environmental conditions. The Olympic sports dataset is having more complex action classes than other repetitive activities sports datasets. Hollywood dataset collected from movies have less number of source movies and similarity of action in videos clips. Later on, a Hollywood2 dataset was gathered from a large number of movies than Hollywood. The THUMOS challenge datasets consist of negative background videos for each activity that make it harder to recognition tasks. The larger dataset YouTube-1M has more than five hundred action classes that are automatically annotated label videos. Besides this, it is only limited to sports categories videos and automatic labelling of videos produced unwanted noise in the dataset.

The RGB-D dataset is facing limitations of low resolutions, less training samples, the number of camera view, different actions, various subjects, and less precision. The depth frames fail to capture the colour of the object and texture information. It restricts depth sensors from recognising complex human activities such as human–object interaction, patients monitoring, tracking, surveillance, and so forth. Initial RGB-D datasets captured single actions videos frames under controlled indoor or lab environments. In comparisons to 3D datasets, 2D datasets are more publicly available. The RGB datasets are more realistic and useful for practical applications, but they are facing a problem with clutter background, illuminations variations, view angles, and changing background conditions. Most of the RGB-D dataset consists of a fewer number of actions as compared to the 2D dataset. The RGB-D dataset recorded with Kinect sensor device has limitations such as recording distance, and indoor environments. The 3D datasets are missing the mark to apply for practical applications. However, the overall classification accuracy of depth dataset is high in comparison to conventional 2D videos datasets. The MSR action 3D, CAD-60, CAD-120, Berkeley MHAD, UWA3D activity, LIRIS, UTD-MHAD, and NTU RGB+D datasets were recorded in indoor and controlled environmental conditions. MSR Action 3D is restricted to gaming actions depth frames only. Northwestern-UCLA dataset was recorded with more than one Kinect sensors at the same time to collect muti-view representations. Some 3D datasets focused on individual objects interactions such as 50 Salads, human manipulation, and SYSU-3D HOI addressing only specific applications only. Most of the latest RGB-D dataset have multiple modalities such as NTU RGB+D, M^2I, PKU-MMD datasets, therefore, it becomes a challenge to handle and synchronise all sensors data information simultaneously.

5.4 Future recommendation for action dataset

At present, a large number of techniques have been designed and tested on action recognition, in sports actions, surveillance video, object detection, abnormal human behaviour, human interactions and daily living activity datasets. However, it is still a challenge to compare these algorithms due to the lack of standard evaluation protocols and benchmarks. It is due to lack

of public data availability, and these algorithms lie on the particular applications domain. With the advancement of computer technology and low-cost devices, e.g. CPU, RAM, etc., it is possible to model and train deep learning approaches on larger samples datasets. So, there is a need for more actions with larger samples datasets which cover realistic scenarios and larger applications domains. It can be observed that the algorithm developed on single view is less prone to partial occlusion or a small variation in view training angles. A robust algorithm required to deal with these challenges like as view-variation, occlusion. These challenges can resolve if developed algorithms have to be trained for multiple views.

With the advent of Microsoft Kinect sensor, until now the RGB-D datasets are less public available in number, so there is a need for larger RGB-D datasets to the public domain. Most of the RGB-D benchmarks focusing only small and fixed unrealistic human actions/interactions, so it is required of such datasets that show some real action and human interactions classes. In future, it should be compulsory to introduce centralised dataset structure with proper annotation label videos and well defined standard evaluation protocols. The 3D datasets can be recorded with more number of actions in dynamic, and realistic conditions so that they can be useful for daily life, for example, sports, tracking, and surveillance applications. There is a need for robust evaluation techniques which can be verified for cross-dataset validations and implemented on realistic scenarios such as security and surveillance, patients monitoring applications.

6 Conclusion

A review of the various state-of-the-art datasets on human action has been presented. Human action datasets have been categorised into two major categories: RGB and RGB-D datasets. The challenges involved and specifications of these datasets have been discussed in details. The conventional RGB dataset is more challenging for human activity recognition due to the cluttered background, illumination variations, camera motion, viewpoints change, and occlusions. The earlier RGB or RGB-D datasets were recorded in controlled, static background environment with fewer activities as compared with the recent datasets. Latest HAR benchmarks recorded with a larger number of human action classes with more number of sample in realistic conditions which make them somewhat suitable to address the practical problem of the world. The various approached for human action recognition are developed in the past two decades on these datasets but no unique solution that can apply to both RGB and RGB-D datasets. The highest recognition accuracies on RGB and RGB-D datasets have been highlighted through various state-of-the-art techniques. It is a challenge with the advancements in the feature descriptors and generative methods in action recognition, a need for comprehensive datasets that reflect the variability of real-world recognition scenarios has emerged. It is required robust evaluation techniques for cross-dataset validation, which will be useful for realistic scenarios applications.

References

Abbasnejad I, Sridharan S, Denman S, Fookes C, Lucey S (2016) Complex event detection using joint max margin and semantic features. In: International conference on digital image computing: techniques and applications, Gold Coast

Agahian S, Negin F, Köse C (2018) Improving bag-of-poses with semi-temporal pose descriptors for skeleton-based action recognition. Vis Comput. https://doi.org/10.1007/s00371-018-1489-7

Aggarwal JK, Ryoo MS (2011) Human activity analysis: a review. ACM Comput Surv 43(3):1–43

Aggarwal H, Vishwakarma DK (2016) Covariate conscious approach for Gait recognition based upon Zernike moment invariants. IEEE Trans Cognit Dev Syst 10(2):397–407
Aggarwal J, Xia L (2013) Human activity recognition from 3D data-a review. Pattern Recognit Lett 48:70–80
Althloothi S, Mahoor MH, Zhang X, Voyles RM (2014) Human activity recognition using multi-features and multiple kernel learning. Pattern Recogn 47:1800–1812
Amin S, Andriluka M, Rohrbach M, Schiele B (2013) Multi-view pictorial structures for 3D human pose estimation. In: British machine vision conference
Awwad S, Piccardi M (2016) Local depth patterns for fine-grained activity recognition in-depth videos. In: International conference on image and vision computing New Zealand, Palmerston North
Baccouche M, Mamalet F, Wolf C, Garcia C, Baskurt A (2011) Sequential deep learning for human action recognition. In: Proceedings of the second international conference on human behavior understanding
Barekatain M, et al. (2017) Okutama-action: an aerial view video dataset for concurrent human action detection. In: IEEE conference on computer vision and pattern recognition workshops, Honolulu
Baró X, Gonzalez J, Fabian J, Bautista MA, Oliu M, Escalante HJ, Guyon I (2015) ChaLearn Looking at People 2015 challenges: action spotting and cultural event recognition. In: IEEE conference on computer vision and pattern recognition workshops, Boston, MA
Blank M, Gorelick L, Shechtman E, Irani M, Basri R (2005) Actions as space-time shapes. In: Tenth IEEE international conference on computer vision (ICCV'05), Beijing
Bloom V, Argyriou V, Makris D (2016) Hierarchical transfer learning for online recognition of compound actions. Comput Vis Image Underst 144:62–72
Blunsden B, Fisher RB (2009) The BEHAVE video dataset: ground truthed video for multi-person behavior classification. Ann BMVA 4:4
Bobick AF, Davis JW (2001) The recognition of human movement using temporal templates. IEEE Trans Pattern Anal Mach Intell 23(3):257–267
Borges PVK, Conci N, Cavallaro A (2013) Video-based human behavior understanding: a survey. IEEE Trans Circuits Syst Video Technol 23(11):1993–2008
Bux A, Angelov P, Habib Z (2016) Vision based human activity recognition: a review. Adv Comput Intell Syst 513:341–371
Chaquet JM, Carmona EJ, Caballero AF (2013) A survey of video datasets for human action and activity recognition. Comput Vis Image Underst 117:633–659
Chaudhry R, Ofli F, Kurillo G, Bajcsy R, Vidal R (2013) Bio-inspired dynamic 3D discriminative skeletal features for human action recognition. In: IEEE conference on computer vision and pattern recognition workshops, Portland
Chen L, Wei H, Ferryman J (2014) ReadingAct RGB-D action dataset and human action recognition from local features. Pattern Recogn Lett 50:159–169
Chen C, Jafari R, Kehtarnavaz N (2015) UTD-MHAD: a multimodal dataset for human action recognition utilizing a depth camera and a wearable inertial sensor. In: Proceedings of IEEE international conference on image processing, Canada
Cherian BF, Harandi M, Gould S (2017) Generalized rank pooling for activity recognition. In CVPR, Hawaii
Chéron G, Laptev I, Schmid C (2015) P-CNN: pose-based CNN features for action recognition. In: IEEE international conference on computer vision, Santiago
Cippitelli E, Gambi E, Spinsante S, Revuelta FF (2016) Evaluation of a skeleton-based method for human activity recognition on a large-scale RGB-D dataset. In: 2nd IET international conference on technologies for active and assisted living, London
Dalal N, Triggs B, Schmid C (2006) Human detection using oriented histograms of flow and appearance. In: Proceedings of European conference on computer vision
Das Dawn D, Shaikh SH (2016) A comprehensive survey of human action recognition with spatio-temporal interest point (STIP) detector. Vis Comput 32(3):289–306
Dollar P, Rabaud V, Cottrell G, Belongie S (2005) Behavior recognition via sparse spatio-temporal features. In: IEEE international workshop on visual surveillance and performance evaluation of tracking and surveillance
Donahue J, Hendricks L, Guadarrama S, Rohrbach MV, Saenko K, Darrell T (2015) Long-term recurrent convolutional networks for visual recognition and description. In: Proceedings of the IEEE conference on computer vision and pattern recognition
Du K, Shi Y, Lei B, Chen J, Sun M (2016) A method of human action recognition based on spatio-temporal interest points and PLSA. In: International conference on industrial informatics—computing technology, intelligent technology, industrial information integration, Wuhan
Duta IC, Ionescu B, Aizawa K, Sebe N (2017) Spatio-temporal vector of locally max pooled features for action recognition in videos. In: CVPR, Hawaii

Edwards M, Deng J, Xie X (2016) From pose to activity: surveying dataset sand introducing CONVERSE. Comput Vis Image Underst 144:73–105
Elmadany NED, He Y, Guan L (2016) Human gesture recognition via bag of angles for 3D virtual city planning in CAVE environment. In: IEEE 18th International workshop on multimedia signal processing, Montreal, QC
Feichtenhofer C, Pinz A, Zisserman A (2016) Convolutional two-stream network fusion for video action recognition. In: Proceedings of IEEE conference on computer vision and pattern recognition (CVPR), pp 1933–1941
Feichtenhofer C, Pinz A, Wildes RP (2017) Spatiotemporal multiplier networks for video action recognition. In: The IEEE conference on computer vision and pattern recognition (CVPR), Hawaii
Fernando B, Gould S (2016) Learning end-to-end video classification with rank-pooling. In: ICML
Fernando B, Gavves E, Oramas M, Ghodrati A, Tuytelaars T (2015) Modeling video evolution for action recognition. In: Proceedings of IEEE conference on computer vision and pattern recognition (CVPR)
Firman M (2016) RGBD datasets: past, present and future. In: Proceedings of the IEEE conference on computer vision and pattern recognition workshops
Fu L, Zhang J, Huang K (2017) ORGM: occlusion relational graphical model for human pose estimation. IEEE Trans Image Process 26(2):927–941
Gaglio S, Re GL, Morana M (2015) Human activity recognition process using 3-D posture data. IEEE Trans Hum Mach Syst 45(5):586–597
Gaidon A, Harchaoui Z, Schmid C (2011) Actom sequence models for efficient action detection. In: IEEE conference on computer vision and pattern recognition
Gao Z, Li S, Zhu Y, Wang C, Zhang H (2017) Collaborative sparse representation learning model for RGBD action recognition. J Vis Commun Image Represent 48:442–452
Gkalelis N, Kim H, Hilton A, Nikolaidis N, Pitas I (2009) The i3DPost multi-view and 3D human action/interaction. In: Conference for visual media production, London, UK
Goodfellow I, Abadie JP, Mirza M, Xu B, Farley D, Ozair S, Courville A, Bengio Y (2014) Generative adversarial nets. In: Proceedings of advances in neural information processing systems
Gopalan R (2013) Joint sparsity-based representation and analysis of unconstrained activities. In: IEEE conference on computer vision and pattern recognition, Portland
Gorban A, Idrees H, Jiang Y-G, Roshan Zamir A, Laptev I, Shah M, Sukthankar R (2015) {THUMOS} challenge: action recognition with a large number of classes. http://www.thumos.info
Gorelick L, Blank M, Shechtman E, Irani M, Basri R (2005) Actions as space-time shapes. In: The tenth IEEE international conference on computer vision (ICCV'05)
Goyal R, Kahou SE, Michalski V, Materzy´nska J, Westphal S, Kim H, Haenel V, Fruend I, Yianilos P, Freitag MM, Hoppe F, Thurau C, Bax I, Memisevic R (2018) The "something something" video database for learning and evaluating visual common sense. arXiv:1706.04261v2 [cs.CV]
Gross OK, Gurovich Y, Hassner T, Wolf L (2012) Motion interchange patterns for action recognition in unconstrained videos. In: ECCV, Firenze, Italy
Guha T, Ward RK (2012) Learning sparse representations for human action recognition. IEEE Trans Pattern Anal Mach Intell 34(8):1576–1588
Guo H, Wu X, Feng W (2017) Multi-stream deep networks for human action classification with sequential tensor decomposition. Sig Process 140:198–206
Hadfield S, Bowden R (2013) Hollywood 3D: recognizing actions in 3D natural scenes. In: IEEE conference on computer vision and pattern recognition, Portland
Hadfield S, Lebeda K, Bowden R (2017) Hollywood {3D}: what are the best {3D} features for action recognition? Int J Comput Vision 121(1):95–110
Haija S, Kothari N, Lee J, Natsev P, Toderici G, Varadarajan B, Vijayanarasimhan S (2016) YouTube-8M: a large-scale video classification benchmark. In: CoRR
Han F, Reily B, Hoff W, Zhang H (2017) Space–time representation of people based on 3D skeletal data: a review. Comput Vis Image Underst 158:85–105
Hao T, Wu D, Wang Q, Sun J-S (2017) Multi-view representation learning for multi-view action recognition. J Vis Commun Image Represent 48:453–460
Harris C, Stephens M (1988) A combined corner and edge detector. In: Fourth Alvey vision conference
Hassner T (2013) A critical review of action recognition benchmarks. In: IEEE conference on computer vision and pattern recognition workshops, Portland
Heilbron FC, Escorcia V, Ghanem B, Niebles JC (2015) ActivityNet: a large-scale video benchmark for human activity understanding. In: IEEE conference on computer vision and pattern recognition (CVPR), Boston, MA
Herath S, Harandi M, Porikli F (2017) Going deeper into action recognition: a survey. Image Vis Comput 60:4–21

Hongeng S, Nevatia R (2003) Large-scale event detection using semi-hidden Marko models. In: Proceedings of the international conference on computer vision (ICCV)
Hu JF, Zheng WS, Lai J, Zhang J (2015) Jointly learning heterogeneous features for RGB-D activity recognition. In: IEEE conference on computer vision and pattern recognition, Boston, MA
Hu JF, Zheng WS, Lai JH, Zhang J (2016a) Jointly learning heterogeneous features for RGB-D activity recognition. IEEE Trans Pattern Anal Mach Intell 99:1
Hu N, Bestick A, Englebienne G, Bajscy R, Kröse B (2016) Human intent forecasting using intrinsic kinematic constraints. In: IEEE/RSJ international conference on intelligent robots and systems, Daejeon
Idrees H, Zamir AR, Jiang Y-G, Gorban A, Laptev I, Sukthankar R, Shah M (2017) The THUMOS challenge on action recognition for videos "in the wild". Comput Vis Image Underst 155:1–23
Imran J, Kumar P (2016) Human action recognition using RGB-D sensor and deep convolutional neural networks. In: International conference on advances in computing, communications and informatics, Jaipur
Iosifidis A, Tefas A (2013) Dynamic action recognition based on dynemes and extreme learning machine. Pattern Recogn Lett 34:1890–1898
Iosifidis A, Tefas A, Pitas I (2013) Learning sparse representations for view-independent human action recognition based on fuzzy distances. Neurocomputing 121:344–353
Iosifidis A, Tefas A, Nikolaidis N, Pitas I (2014) Human action recognition in stereoscopic videos based on a bag of features and disparity pyramids. In: 22nd European signal processing conference, Lisbon
Iosifidis A, Tefas A, Pitas I (2014b) Regularized extreme learning machine for multi-view semi-supervised action recognition. Neurocomputing 145:250–262
Iosifidis A, Marami E, Tefas A, Pitas I, Lyroudia K (2015) The MOBISERV-AIIA Eating and Drinking multi-view database for vision-based assisted living. J Inf Hiding Multimed Signal Process 6(2):254–273
Jain M, Jegou H, Bouthemy P (2013) Better exploiting motion for better action recognition. In: CVPR
Jalal A, Kim Y (2014) Dense depth maps-based human pose tracking and recognition in dynamic scenes using ridge data. In: 11th IEEE international conference on advanced video and signal based surveillance
Jalal A, Kamal S, Kim D (2014) A depth video sensor-based life-logging human activity recognition system for elderly care in smart indoor environments. Sensors 14(7):11735–11759
Ji S, Xu W, Yang M, Yu K (2013) 3D convolutional neural networks for human action recognition. IEEE Trans Pattern Anal Mach Intell 35(1):221–231
Ji X, Feng CW, Tao D (2018) Skeleton embedded motion body partition for human action recognition using depth sequences. Sig Process 143:56–68
Jiang Y-G, Dai Q, Xue X, Liu W, Ngo C-W (2012) Trajectory-based modeling of human actions with motion reference points. In: Proceedings of the European conference on computer vision (ECCV)
Jiang YG, Wu Z, Wang J, Xue X, Chang SF (2017) Exploiting feature and class relationships in video categorization with regularized deep neural networks. IEEE Trans Pattern Anal Mach Intell 99:1
Junejo I, Junejo K, Aghbari Z (2014) Silhouette-based human action recognition using SAX-Shapes. Vis Comput 30(3):259–269
Kantorov V, Laptev I (2014) Efficient feature extraction, encoding, and classification for action recognition. In: Proceedings of the IEEE conference on computer vision and pattern recognition
Karpathy A, Toderici G, Shetty S, Leung T, Sukthankar R, Fei-Fei L (2014) Large-scale video classification with convolutional neural networks. In: IEEE conference on computer vision and pattern recognition, Columbus, OH
Kellokumpu V, Zhao G, Pietikinen M (2008) Human activity recognition using a dynamic texture based method. In: British machine vision conference
Kim YJ, Cho NG, Lee SW (2014) Group activity recognition with group interaction zone. In: 22nd International conference on pattern recognition, Stockholm
Kläser A, MarszaÅek M, Schmid C (2008) A spatio-temporal descriptor based on 3D-gradients. In BMVC08
Kong Y, Jia Y, Fu Y (2012) Learning human interaction by interactive phrases. In: European conference on computer vision
Kong Y, Liang W, Dong Z, Jia Y (2014) Recognising human interaction from videos by a discriminative model. IET Comput Vision 8(4):277–286
Kuehne H, Jhuang H, Garrote E, Poggio T, Serre T (2011) {HMDB}: a large video database for human motion recognition. In: Proceedings of the international conference on computer vision (ICCV)
Lan T, Wang Y, Mori G (2011) Discriminative figure-centric models for joint action localization and recognition. In: International conference on computer vision, Barcelona
Laptev I (2005) On space–time interest points. Int J Comput Vision 64(2–3):107–123
Laptev I, Lindeberg T (2004) Velocity adaptation of space-time interest points. In: Proceedings of the 17th international conference on pattern recognition

Laptev I, Lindeberg T (2004) Local descriptors for spatio-temporal recognition. In: ECCV workshop on spatial coherence for visual motion analysis
Laptev I, Marszalek M, Schmid C, Rozenfeld B (2008) Learning realistic human actions from movies. In: IEEE conference on computer vision and pattern recognition, Anchorage, AK
Lea C, Flynn MD, Vidal R, Reiter A, Hager GD (2017) Temporal convolutional networks for action segmentation and detection. In: The IEEE conference on computer vision and pattern recognition (CVPR), Hawaii
Li W, Zhang Z, Liu Z (2010) Action recognition based on a bag of 3D points. In: IEEE computer society conference on computer vision and pattern recognition, San Francisco
Li Y, Ye J, Wang T, Huang S (2015) Augmenting bag-of-words: a robust contextual representation of spatiotemporal interest points for action recognition. Vis Comput 31(10):1383–1394
Lin X, Casas J, Pard M (2016) 3D point cloud segmentation oriented to the analysis of interactions. In: The 24th European signal processing conference, Budapest, Hungary
Liu J, Luo J, Shah M (2009) Recognizing realistic actions from videos "in the Wild". In: IEEE international conference on computer vision and pattern recognition (CVPR)
Liu L, Shao L, Zhen X, Li X (2013) Learning discriminative key poses for action recognition. IEEE Trans Cybern 43(6):1860–1870
Liu Z, Zhou L, Leung H, Shum HPH (2016a) Kinect posture reconstruction based on a local mixture of gaussian process models. IEEE Trans Visual Comput Graph 22(11):2437–2450
Liu T, Wang X, Dai X, Luo J (2016) Deep recursive and hierarchical conditional random fields for human action recognition. In: IEEE winter conference on applications of computer vision, Lake Placid, NY
Liu C, Hu Y, Li Y, Song S, Liu J (2017) PKU-MMD: a large scale benchmark for continuous multi-modal human action understanding. arXiv preprint arXiv:1703.07475
Liu AA, Su YT, Nie WZ, Kankanhalli M (2017b) Hierarchical clustering multi-task learning for joint human action grouping and recognition. IEEE Trans Pattern Anal Mach Intell 39(1):102–114
Liu M, Liu H, Chen C (2017c) Enhanced skeleton visualization for view-invariant human action recognition. Pattern Recogn 68:346–361
Lopez JA, Calvo MS, Guillo AF, Rodriguez JG, Cazorla M, Pont MTS (2016) Group activity description and recognition based on trajectory analysis and neural networks. In: International joint conference on neural networks, Vancouver, BC
Lun R, Zhao W (2015) A survey of applications and human motion recognition with Microsoft Kinect. Int J Pattern Recognit Artif Intell 29(5):1555008
Ma S, Sigal L, Sclarof S (2016) Learning activity progression in LSTMs for activity detection and early detection. In: IEEE conference on computer vision and pattern recognition, Las Vegas, NV
Mademlis I, Tefas A, Pitas I (2018) A salient dictionary learning framework for activity video summarization via key-frame extraction. Inf Sci 432:319–331
Mahjoub AB, Atri M (2016) Human action recognition using RGB data. In: 11th International design & test symposium, Hammamet
Marszaek M, Laptev I, Schmid C (2009) Actions in context. In: IEEE conference on computer vision & pattern recognition
Mathieu M, Couprie C, LeCun Y (2015) Deep multi-scale video prediction beyond mean square error. In: CoRR
Matikainen P, Hebert M, Sukthankar R (2009) Trajectons: action recognition through the motion analysis of tracked features. In: IEEE 12th international conference on computer vision
Messing R, Pal C, Kautz H (2009) Activity recognition using the velocity histories of. In: Proceedings of the international conference on computer vision (ICCV)
Miech A, Laptev I, Sivic J (2017) Learnable pooling with context gating for video classification. In: CVPR workshop, Hawaii
Misra I, Zitnick C, Hebert M (2016) Unsupervised learning using sequential verification for Action Recognition. arXiv preprint arXiv:1603.08561
Mo L, Li F, Zhu Y, Huang A (2016) Human physical activity recognition based on computer vision with deep learning model. In: IEEE international instrumentation and measurement technology conference proceedings, Taipei
Mygdalis V, Iosifidis A, Tefas A, Pitas I (2016) Graph embedded one-class classifiers for media data classification. Pattern Recogn 60:585–595
Negin F, Rodriguez P, Koperski M, Kerboua A, Gonzàlez J, Bourgeois J, Chapoulie E, Robert P, Bremond F (2018) PRAXIS: towards automatic cognitive assessment using gesture recognition. In: Expert systems with applications, vol 106, pp 21–35

Ng J-H, Hausknecht M, Vijayanarasimhan S, Vinyals O, Monga R, Toderici G (2015) Beyond short snippets: deep networks for video classification. In: Proceedings of the IEEE conference on computer vision and pattern recognition

Ni B, Wang G, Moulin P (2011) RGBD-HuDaAct: a color-depth video database for human daily activity recognition. In: IEEE international conference on computer vision workshops

Ni B, Moulin P, Yang X, Yan S (2015) Motion part regularization: improving action recognition via trajectory group selection. In: IEEE conference on computer vision and pattern recognition, Boston

Niebles C, Chen W, Fei F (2010) Modeling temporal structure of decomposable motion segments for activity classification. In: 11th European conference on computer vision (ECCV)

Norouznezhad E, Harandi M, Bigdeli A, Baktash M, Postula A, Lovell B (2012) Directional space–time oriented gradients for 3D visual pattern analysis. In: Proceedings of the European conference on computer vision (ECCV)

Ofli F, Chaudhry R, Kurillo G, Vidal R, Bajcsy R (2013) Berkeley MHAD: a comprehensive multimodal human action database. In: IEEE workshop on applications of computer vision (WACV), Tampa, FL

Oreifej O, Liu Z (2013) HON4D: histogram of oriented 4D normals for activity recognition from depth sequences. In: CVPR, Portland, Oregon

Pei L, Ye M, Zhao X, Dou Y, Bao J (2016) Action recognition by learning temporal slowness invariant features. Vis Comput 32(11):1395–1404

Peng X, Zou C, Qiao Y, Peng Q (2014) Action recognition with stacked fisher vectors. In: ECCV

Pieropan A, Salvi G, Pauwels K, Kjellström H (2014) Audio-visual classification and detection of human manipulation actions. In: IEEE/RSJ international conference on intelligent robots and systems, Chicago, IL

Rabiner L (1989) A tutorial on hidden Markov models and selected applications in speech recognition. In: Proceedings of the IEEE 77 (2)

Rahmani H, Mahmood A, Huynh D, Mian A (2014) HOPC: histogram of oriented principal components of 3D point clouds for action recognition. In: European conference on computer vision (ECCV)

Reddy KK, Shah M (2012) Recognizing 50 human action categories of web videos. Mach Vis Appl 24(5):971–981

Rodriguez MD, Ahmed J, Shah M (2008) Action MACH: A spatio-temporal maximum average correlation height filter for action recognition. In: IEEE conference on computer vision and pattern recognition, Anchorage, AK

Rohrbach M, Amin S, Andriluka M, Schiele B (2012) A database for fine grained activity detection of cooking activities. In: Computer vision and pattern recognition

Ryoo MS, Aggarwal JK (2009) Spatio-temporal relationship match: video structure comparison for recognition of complex human activities. In: IEEE international conference on computer vision (ICCV), Kyoto, Japan

Ryoo MS, Chen CC, Aggarwal J, Chowdhury AR (2010) An overview of contest on semantic description of human activities. Recognizing patterns in signals, speech, images and videos, vol. 6388

Sadanand S, Corso J (2012) Action bank: a high-level representation of activity in video. In IEEE conference on computer vision and pattern recognition

Schuldt C, Laptev I, Caputo B (2004) Recognizing human actions: a local SVM approach. In: Proceedings of the 17th international conference on pattern recognition

Shahroudy A, Liu J, Ng TT, Wang G (2016) NTU RGB+D: a large scale dataset for 3D human activity analysis. In: IEEE conference on computer vision and pattern recognition, Las Vegas

Shan Y, Zhang Z, Yang P, Huang K (2015) Adaptive slice representation for human action classification. IEEE Trans Circuits Syst Video Technol 25(10):1624–1636

Shao L, Zhen X, Tao D, Li X (2014) Spatio-temporal Laplacian pyramid coding for action recognition. IEEE Trans Cybern 44(6):817–827

Shechtman E, Irani M (2005) Space-time behaviour based correlation. In: IEEE conference on computer vision and pattern analysis, Los Alamitos, CA

Simonyan K, Zisserman A (2014) Two-stream convolutional networks for action recognition in videos. In: Proceedings of advances in neural information processing systems

Singh B, Marks T, Jones M, Tuzel C (2016) A multi-stream bi-directional recurrent neural network for fine-grained action detection. In: IEEE conference on computer vision and pattern recognition (CVPR)

Somasundaram G, Cherian A, Morellas V, Papanikolopoulos N (2014) Action recognition using global spatio-temporal features derived from sparse representations. Comput Vis Image Underst 123:1–13

Soomro K, Zamir AR (2014) Action recognition in realistic sports videos. In: Computer vision in sports, pp 181–208

Soomro K, Zamir AR, Shah M (2012) UCF101: a dataset of 101 human action classes from videos in the wild. In: CoRR

Srivastava N, Mansimov E, Salakhutdinov R (2015) Unsupervised learning of video representations using LSTMs. In: CoRR

Stein S, McKenna SJ (2013) Combining embedded accelerometers with computer vision for recognizing food preparation activities. In: ACM international joint conference on pervasive and ubiquitous computing, Zurich, Switzerland

Sun C, Nevatia R (2013) ACTIVE: activity concept transitions in video event classification. In: Proceedings of the international conference on computer vision (ICCV)

Sung J, Ponce C, Selman B, Saxena A (2012) Unstructured human activity detection from RGBD images. In: IEEE international conference on robotics and automation, Saint Paul, MN

Tang K, Fei LF, Koller D (2012) Learning latent temporal structure for complex event detection. In: Proceedings of the IEEE conference on computer vision and pattern recognition (CVPR)

Tayyub J, Tavanai A, Gatsoulis Y, Cohn A, Hogg D (2015) Qualitative and quantitative spatiotemporal relations. In: ACCV

The TH, Le B-V, Lee S, Yoon Y (2016) Interactive activity recognition using pose-based spatio–temporal relation features and four-level Pachinko Allocation Model. Inform Comput Sci Intell Syst Appl 369:317–333

Tian Y, Cao L, Liu Z, Zhang Z (2012) Hierarchical filtered motion for action recognition in crowded videos. IEEE Trans Syst Man Cybern 42(3):313–323

Tran D, Sorokin A (2008) Human activity recognition with metric. In: European conference on computer vision, Marseille, France

Tran D, Bourdev L, Fergus R, Torresani L, Paluri M (2015) Learning spatiotemporal features with 3D convolutional networks. In: Proceedings of the international conference on computer vision

Vaquette G, Orcesi AL, Achard C (2017) The daily home life activity dataset: a high semantic activity dataset for online recognition. In IEEE international conference on automatic face & gesture recognition (FG 2017), Washington, DC

Varol G, Laptev I, Schmid C (2016) Long-term temporal convolutions for action recognition. arXiv:1604.04494

Vishwakarma S, Agrawal A (2013) A survey on activity recognition and behavior understanding in video surveillance. Vis Comput 29(10):983–1009

Vishwakarma DK, Kapoor R (2015) Hybrid classifier based human activity recognition using the silhouette and cells. Expert Syst Appl 42(20):6957–6965

Vishwakarma DK, Singh K (2017) Human activity recognition based on spatial distribution of gradients at sub-levels of average energy silhouette images. IEEE Trans Cognit Dev Syst 9(4):316–327

Vishwakarma DK, Kapoor R, Dhiman A (2016a) A proposed framework for the recognition of human activity by exploiting the characteristics of action dynamics. Robot Auton Syst 77:25–38

Vishwakarma DK, Kapoor R, Dhiman A (2016b) A unified framework for human activity recognition: an approach using spatial edge distribution and $\Re$-transform. Int J Electr Commun 70(3):341–353

Wang Y, Mori G (2011) Hidden part models for human action recognition: probabilistic versus max margin. IEEE Trans Pattern Anal Mach Intell 33(7):1310–1323

Wang H, Schmid C (2013) Action recognition with improved trajectories. In: Proceedings of the international conference on computer vision (ICCV)

Wang Y, Huang K, Tan T (2007) Human activity recognition based on R transform. In IEEE conference on computer vision and pattern recognition, Minneapolis, MN

Wang H, Ullah M, Kläser A, Laptev I, Schmid C (2009) Evaluation of local spa-tio-temporal features for action recognition. In: British machine vision conference

Wang J, Liu Z, Wu Y, Yuan J (2012) Mining actionlet ensemble for action recognition with depth cameras. In: IEEE conference on computer vision and pattern recognition

Wang H, Klaeser A, Schmid C, Liu C-L (2013) Dense trajectories and motion boundary descriptors for action recognition. In: IJCV

Wang J, Nie BX, Xia Y, Wu Y, Zhu S-C (2014) Cross-view action modeling, learning and recognition. In: Computer vision and pattern recognition, Columbus, Ohio

Wang P, Li W, Gao Z, Tang C, Zhang J, Ogunbona PO (2015) Convnets-based action recognition from depth maps through virtual cameras and pseudocoloring. In: ACM international conference on multimedia

Wang Z, Wang L, Du W, Qiao Y (2015) Exploring fisher vector and deep networks for action spotting. In: CVPR

Wang P, Li W, Gao Z, Zhang J, Tang C, Ogunbona PO (2016) Action recognition from depth maps using deep convolutional neural networks. IEEE Trans Hum Mach Syst 46(4):498–509

Wang L, Xiong Y, Lin D, Van Gool L (2017) Untrimmed nets for weakly supervised action recognition and detection. In: The IEEE conference on computer vision and pattern recognition (CVPR), Hawaii

Wang P, Li W, Ogunbona PO, Escalera S (2017b) RGB-D-based motion recognition with deep learning: a survey. Int J Comput Vis 99:1–34

Weinland D, Ronfard R, Boyer E (2006) Free-viewpoint action recognition using motion history volumes. Comput Vis Image Underst 104(2–3):249–257

Weinland D, Boyer E, Ronfard R (2007) Action recognition from arbitrary views using 3D exemplars. In IEEE 11th international conference on computer vision, Rio de Janeiro

Willems G, Tuytelaars T, Gool L (2008) An efficient dense and scale-invariant spatio-temporal interest point detector. In: Proceedings of the European conference on computer vision (ECCV)

Wolf C, Mille J, Lombardi E, Celiktutan O, Jiu M, Dogan E, Eren G, Baccouche M, Dellandrea E, Bichot C-E, Garcia C, Sankur B (2014) Evaluation of video activity localizations integrating quality and quantity measurements. Comput Vis Image Underst 127:14–30

Wu Z, Fu Y, Jiang YG, Sigal L (2016) Harnessing object and scene semantics for large-scale video understanding. In: IEEE conference on computer vision and pattern recognition (CVPR), Las Vegas, NV

Xu N, Liu A, Nie W, Wong Y, Li F, Su Y (2015) Multi-modal & multi-view & interactive benchmark dataset for human action recognition. In: Proceedings of the 23th international conference on multimedia, Brisbane, Queensland, Australia

Xu Z, Hu J, Deng W (2016) Recurrent convolutional neural network for video classification. In: IEEE international conference on multimedia and expo, Seattle, WA

Xu W, Miao Z, Zhang XP, Tian Y (2017) A hierarchical spatio-temporal model for human activity recognition. IEEE Trans Multimed 99:1

Yadav GK, Shukla P, Sethi A (2016) Action recognition using interest points capturing differential motion information. In: IEEE international conference on acoustics, speech and signal processing, Shanghai

Yan H (2016) Discriminative sparse projections for activity-based person recognition. Neurocomputing 208:183–192

Yan X, Chang H, Shan S, Chen X (2014) Modeling video dynamics with deep dynencoder. In: Proceedings of European conference on computer vision

Yeung S, Russakovsky O, Mori G, Fei-Fei L (2016) End-to-end learning of action detection from frame glimpses in videos. In: IEEE Conference on Computer Vision and Pattern Recognition, Las Vegas

Yilmaz A, Shah M (2005) Actions sketch: a novel action representation. In: IEEE computer society conference on computer vision and pattern recognition

Yu G, Yuan J (2015) Fast action proposals for human action detection and search. In: IEEE conference on computer vision and pattern recognition, Boston, MA

Yu Y, Choi J, Kim Y, Yoo K,Lee S-H, Kim G (2017) Supervising neural attention models for video captioning by human gaze data. In: The IEEE conference on computer vision and pattern recognition (CVPR), Hawaii

Yuan J, Ni B, Yang X, Kassim AA (2016) Temporal action localization with pyramid of score distribution features. In: IEEE conference on computer vision and pattern recognition, Las Vegas, NV

Zhang Z, Huang K, Tan T, Wang L (2007) Trajectory series analysis based event rule induction for visual surveillance. In: IEEE conference on computer vision and pattern recognition, Minneapolis, MN

Zhang Z, Huang K, Tan T (2008) Multi-thread parsing for recognizing complex events in videos. In: 10th European conference on computer vision: part III, Marseille, France

Zhang J, Li W, Ogunbona PO, Wang P, Tang C (2016) RGB-D based action recognition datasets: a survey. Pattern Recognit 60:86–105

Zhao G, Pietikainen M (2007) Dynamic texture recognition using local binary patterns with an application to facial expressions. IEEE Trans Pattern Anal Mach Intell 29(6):915–928

Zhou Y, Ni B, Hong R, Wang M, Tian Q (2015) Interaction part mining: a mid-level approach for fine-grained action recognition. In: IEEE conference on computer vision and pattern recognition, Boston, MA

Zhu Y, Zhao X, Fu Y, Liu Y (2011) Sparse coding on local spatial–temporal volumes for human action recognition. In: Proceedings of the Asian conference on computer vision

Zhu G, Zhang L, Shen P, Song J, Zhi L, Yi K (2015) Human action recognition using key poses and atomic motions. In: IEEE international conference on robotics and biomimetics, Zhuhai

Zhua F, Shao L, Xie J, Fang Y (2016) From handcrafted to learned representations for human action recognition: a survey. Image Vis Comput 55:42–52